

Pradeep Kumar Mallick
Preetisudha Meher
Alak Majumder
Santos Kumar Das *Editors*

Electronic Systems and Intelligent Computing

Proceedings of ESIC 2020

Lecture Notes in Electrical Engineering

Volume 686

Series Editors

Leopoldo Angrisani, Department of Electrical and Information Technologies Engineering, University of Napoli Federico II, Naples, Italy

Marco Arteaga, Departamento de Control y Robótica, Universidad Nacional Autónoma de México, Coyoacán, Mexico

Bijaya Ketan Panigrahi, Electrical Engineering, Indian Institute of Technology Delhi, New Delhi, Delhi, India
Samarjit Chakraborty, Fakultät für Elektrotechnik und Informationstechnik, TU München, Munich, Germany
Jiming Chen, Zhejiang University, Hangzhou, Zhejiang, China

Shanben Chen, Materials Science and Engineering, Shanghai Jiao Tong University, Shanghai, China
Tan Kay Chen, Department of Electrical and Computer Engineering, National University of Singapore, Singapore, Singapore

Rüdiger Dillmann, Humanoids and Intelligent Systems Laboratory, Karlsruhe Institute for Technology, Karlsruhe, Germany

Haibin Duan, Beijing University of Aeronautics and Astronautics, Beijing, China

Gianluigi Ferrari, Università di Parma, Parma, Italy

Manuel Ferre, Centre for Automation and Robotics CAR (UPM-CSIC), Universidad Politécnica de Madrid, Madrid, Spain

Sandra Hirche, Department of Electrical Engineering and Information Science, Technische Universität München, Munich, Germany

Faryar Jabbari, Department of Mechanical and Aerospace Engineering, University of California, Irvine, CA, USA

Limin Jia, State Key Laboratory of Rail Traffic Control and Safety, Beijing Jiaotong University, Beijing, China
Janusz Kacprzyk, Systems Research Institute, Polish Academy of Sciences, Warsaw, Poland

Alaa Khamis, German University in Egypt El Tagamoa El Khames, New Cairo City, Egypt

Torsten Kroeger, Stanford University, Stanford, CA, USA

Qilian Liang, Department of Electrical Engineering, University of Texas at Arlington, Arlington, TX, USA
Ferran Martín, Departament d'Enginyeria Electrònica, Universitat Autònoma de Barcelona, Bellaterra, Barcelona, Spain

Tan Cher Ming, College of Engineering, Nanyang Technological University, Singapore, Singapore
Wolfgang Minker, Institute of Information Technology, University of Ulm, Ulm, Germany

Pradeep Misra, Department of Electrical Engineering, Wright State University, Dayton, OH, USA
Sebastian Möller, Quality and Usability Laboratory, TU Berlin, Berlin, Germany

Subhas Mukhopadhyay, School of Engineering & Advanced Technology, Massey University, Palmerston North, Manawatu-Wanganui, New Zealand

Cun-Zheng Ning, Electrical Engineering, Arizona State University, Tempe, AZ, USA

Toyoaki Nishida, Graduate School of Informatics, Kyoto University, Kyoto, Japan

Federica Pascucci, Dipartimento di Ingegneria, Università degli Studi “Roma Tre”, Rome, Italy

Yong Qin, State Key Laboratory of Rail Traffic Control and Safety, Beijing Jiaotong University, Beijing, China
Gan Woon Seng, School of Electrical & Electronic Engineering, Nanyang Technological University, Singapore, Singapore

Joachim Speidel, Institute of Telecommunications, Universität Stuttgart, Stuttgart, Germany

Germano Veiga, Campus da FEUP, INESC Porto, Porto, Portugal

Haitao Wu, Academy of Opto-electronics, Chinese Academy of Sciences, Beijing, China

Junjie James Zhang, Charlotte, NC, USA

The book series *Lecture Notes in Electrical Engineering* (LNEE) publishes the latest developments in Electrical Engineering—quickly, informally and in high quality. While original research reported in proceedings and monographs has traditionally formed the core of LNEE, we also encourage authors to submit books devoted to supporting student education and professional training in the various fields and applications areas of electrical engineering. The series cover classical and emerging topics concerning:

- Communication Engineering, Information Theory and Networks
- Electronics Engineering and Microelectronics
- Signal, Image and Speech Processing
- Wireless and Mobile Communication
- Circuits and Systems
- Energy Systems, Power Electronics and Electrical Machines
- Electro-optical Engineering
- Instrumentation Engineering
- Avionics Engineering
- Control Systems
- Internet-of-Things and Cybersecurity
- Biomedical Devices, MEMS and NEMS

For general information about this book series, comments or suggestions, please contact leontina.dicecco@springer.com.

To submit a proposal or request further information, please contact the Publishing Editor in your country:

China

Jasmine Dou, Associate Editor (jasmine.dou@springer.com)

India, Japan, Rest of Asia

Swati Meherishi, Executive Editor (Swati.Meherishi@springer.com)

Southeast Asia, Australia, New Zealand

Ramesh Nath Premnath, Editor (ramesh.premnath@springernature.com)

USA, Canada:

Michael Luby, Senior Editor (michael.luby@springer.com)

All other Countries:

Leontina Di Cecco, Senior Editor (leontina.dicecco@springer.com)

**** Indexing: The books of this series are submitted to ISI Proceedings, EI-Compendex, SCOPUS, MetaPress, Web of Science and Springerlink ****

More information about this series at <http://www.springer.com/series/7818>

Pradeep Kumar Mallick · Preetisudha Meher ·
Alak Majumder · Santos Kumar Das
Editors

Electronic Systems and Intelligent Computing

Proceedings of ESIC 2020



Springer

Editors

Pradeep Kumar Mallick
School of Computer Engineering
Kalinga Institute of Industrial Technology
(KIIT) Deemed to be University
Bhubaneswar, Odisha, India

Alak Majumder
Department of Electronics and
Communication Engineering
National Institute of Technology
Arunachal Pradesh
Yopia, Arunachal Pradesh, India

Preetisudha Meher
Department of Electronics and
Communication Engineering
National Institute of Technology Arunachal
Pradesh
Yopia, Arunachal Pradesh, India

Santos Kumar Das
Department of Electronics and
Communication Engineering
National Institute of Technology Rourkela
Rourkela, Odisha, India

ISSN 1876-1100

ISSN 1876-1119 (electronic)

Lecture Notes in Electrical Engineering

ISBN 978-981-15-7030-8

ISBN 978-981-15-7031-5 (eBook)

<https://doi.org/10.1007/978-981-15-7031-5>

© The Editor(s) (if applicable) and The Author(s), under exclusive license to Springer Nature Singapore Pte Ltd. 2020

This work is subject to copyright. All rights are solely and exclusively licensed by the Publisher, whether the whole or part of the material is concerned, specifically the rights of translation, reprinting, reuse of illustrations, recitation, broadcasting, reproduction on microfilms or in any other physical way, and transmission or information storage and retrieval, electronic adaptation, computer software, or by similar or dissimilar methodology now known or hereafter developed.

The use of general descriptive names, registered names, trademarks, service marks, etc. in this publication does not imply, even in the absence of a specific statement, that such names are exempt from the relevant protective laws and regulations and therefore free for general use.

The publisher, the authors and the editors are safe to assume that the advice and information in this book are believed to be true and accurate at the date of publication. Neither the publisher nor the authors or the editors give a warranty, expressed or implied, with respect to the material contained herein or for any errors or omissions that may have been made. The publisher remains neutral with regard to jurisdictional claims in published maps and institutional affiliations.

This Springer imprint is published by the registered company Springer Nature Singapore Pte Ltd.
The registered company address is: 152 Beach Road, #21-01/04 Gateway East, Singapore 189721,
Singapore

Programme Committee

Patron

Prof. Pinakeswar Mahanta, Director, NIT, Arunachal Pradesh

Conference Chair

Dr. Preetisudha Meher, NIT, Arunachal Pradesh

Conference Co-chair

Dr. Alak Majumder, NIT, Arunachal Pradesh

Special Session Chair

Dr. Sanjeev Kumar Metya, NIT, Arunachal Pradesh

Women in Engineering Chair

Dr. Yang Saring, NIT, Arunachal Pradesh

Technical/Reviewer Committee Chair

Dr. Subhodeep Mukhopadhyay, NIT, Arunachal Pradesh

Finance/Registration Chair

Dr. Yaka Bulo, NIT, Arunachal Pradesh

Local Arrangement Chair

Dr. Abir Jyoti Mondal, NIT, Arunachal Pradesh

Industry Liaison Chair

Dr. Sahadeb Roy, NIT, Arunachal Pradesh

General Chairs

Prof. Bidyut K. Bhattacharyya (Fellow IEEE), NIT Agartala

Prof. K. K. Mahapatra, Dean (Acad), NIT Rourkela

Publication Chairs

Dr. Pradeep Kumar Mallick, Kalinga Institute of Industrial Technology (KIIT)
Deemed to be University
Dr. Santos Kumar Das, NIT Rourkela

Advisory Committee

Dr. Bhabani Sankar Swain, KU, South Korea
Dr. Benson Edwin Raj, Fujairah Women's College Fujairah, UAE
Dr. Mohd. Hussain, Islamic University, Madina, Saudi Arabia
Dr. Frede Blaabjerg, Aalborg University, Denmark
Dr. Yu-Min Wang, National Chi Nan University, Taiwan
Dr. Gabriele Grandi, University of Bologna, Italy
Dr. Steve S. H. Ling, University of Technology, Sydney, Australia
Dr. Hak-Keung Lam, King's College London, UK
Dr. Frank H. F. Leung, Hong Kong Polytechnic University, Hong Kong
Dr. Yiguang Liu, Sichuan University, China
Dr. Abdul Rahaman, Debre Tabor University, Ethiopia
Prof. Sanjeevikumar Padmanaban, Aalborg University
Dr. Bandla Srinivasa Rao, Debre Tabor University, Ethiopia
Prof. Pierluigi Siano, University of Salerno, Italy
Dr. Hussain Shareef, UKM, Malaysia
Dr. Anil Kavala, UKM, Malaysia
Dr. Hussain Shareef, Senior Engineer, Samsung Electronics, Seoul, South Korea
Prof. Michael Pecht, University of Maryland, USA
Prof. Josep M. Guerrero, Aalborg University, Denmark
Dr. Akshay Kumar Rathore, Concordia University, Montreal, Canada
Dr. Anup Kumar Panda, NIT Rourkela
Dr. Kishore Sarawadekar, IIT-BHU, Varanasi, India
Dr. Sachidananda Dehury, F.M. University, Odisha
Dr. Saroj Kumar Meher, ISI, Kolkata, India
Dr. Inderpreet Kaur, Chandigarh University
Dr. Debashish Jena, NITK, India
Dr. N. P. Padhy, IIT Roorkee
Dr. Sashikala Mishra, IIIT, Pune
Dr. Subhendu Pani, OEC, Odisha
Dr. Mihir Narayan Mohanty, ITER, SOA University
Dr. Sabyasachi Sen Gupta, Professor, IIT Kharagpur
Dr. P. Sateesh Kumar, Assistant Professor, IIT Roorkee
Dr. Swagatam Das, ISI, Kolkata
Dr. Sourav Mallick, NIT Sikkim
Dr. Ashok Kumar Pradhan, IIT Kharagpur
Dr. Bhim Singh, IIT Delhi
Dr. C. Sashidhar, CE, JNTUA
Dr. M. Sashi, NIT, Warangal

Prof. Rajshree Srivastava, DIT University, Dehradun, India

Dr. Kolla Bhanu Prakash, K.L. University, Andhra Pradesh

Dr. Bhabani Shankar Prasad Mishra, KIIT University, Odisha

Preface

It is our pleasure to introduce the proceedings of the First International Conference on Electronic Systems and Intelligent Computing (ESIC 2020) in relation to complex issues of electronic circuit and system with the analysis of computational techniques. The conference aims to create a forum for further discussion on integrated information in the significant field incorporating a series of issues.

The relevance of the conference theme, to a wide variety of disciplines, is reflected in the diverse range of papers submitted. The link between electronics and computing techniques strengthens the area of research to be presented and provides the precise information required for assessment. The international delegates and keynote speakers like Prof. Indranil Hatai, NUS, Singapore, Prof. Kamalakanta Mahapatra, NIT Rourkela, Prof. Goutam Sutradhar, Director, NIT, Manipur, Prof. Roy P. Paily, IIT Guwahati, Prof. Sarat Kumar Patra, Director, IIIT Vadodara, Prof. Sisir Kumar Nayak, IIT Guwahati, were highly impressed and have shown a high level of international interest in the subject.

The level of interest in the subject matter of the conference was maintained by submission of 225 papers at the conference through EasyChair. Every submitted paper went through a precise review process. Each paper received at least three reviews; where issues remained, additional reviews were commissioned. Finally, 140 papers were selected by 60 reviewers for presentation in four different tracks like microwave and devices, communication and networking, signal and image processing, and computations, mathematics, and control. Finally, 110 papers were registered for the conference.

Finally, we would like to record our appreciation to the organizing committee members for their work in securing a substantial input of papers to make the conference successful. We are also indebted to those who served as reviewers, faculties of our department, our students, and Prof. Pinakeswar Mahanta, Director

of NIT, Arunachal Pradesh, without their support the conference could not have been the success that it was. We also acknowledge the authors themselves, without their expert input there would have been no conference.

Bhubaneswar, India

Yupia, India

Yupia, India

Rourkela, India

Pradeep Kumar Mallick

Preetisudha Meher

Alak Majumder

Santos Kumar Das

About the Conference

Aim/Objective

The essential goal of the **International Conference on Electronic Systems and Intelligent Computing** (ESIC 2020) is to give a stage to both electronic hardware and software to communicate under one umbrella for further improvement of shrewd electronic frameworks. Effective and secure information detecting, stockpiling, and preparing play a significant part in the current data age. The cutting-edge savvy electronic frameworks take into account the requirements of effective detecting, stockpiling, and figuring. Simultaneously, effective calculations and programming utilized for quicker examination and recovery of required data are winding up progressively. Storing and handling of the gigantic measure of organized and unstructured information are getting progressively hectic. Simultaneously, post-CMOS technologies, Internet of things (IoT), and cyber-physical system (CPS) have been moving with synchronous advancement of hardware and programming and lie over ordinary customer gadgets. The exhibition and productivity of the present just as the future ages of figuring and data handling frameworks are generally reliant upon advances in both design and programming.

Contributions are sought in the following areas (but not limited to):

Track Details

Electronics, Devices, Circuits, and Systems

- Device modelling, post-CMOS devices
- Nano-technology, MEMS, and NEMS
- VLSI and microelectronic circuit design
- Hardware security
- Embedded systems and robotics
- System on chip (SoC)/network on chip design
- Field-programmable gate array (FPGA) design and applications

- Electronic instrumentations
- Electronic power converters and inverters
- Electric vehicle technologies, etc.

Communications Engineering and Vehicular Technology

- Wireline communication
- Computer networking
- Telecommunication systems
- Wireless ad hoc and sensor networks
- Network/information security
- Security protocol
- Cognitive radio
- Cooperative communications
- Radio resource management and optimization
- Vehicular communication systems
- Information theory and coding systems, etc.

Computing and IT

- Software engineering
- Cloud computing, fog computing, and big data
- Business/enterprise architectures
- Mobile computing
- Distributed systems
- Information systems
- Knowledge discovery and data mining
- Artificial intelligence
- Decision support systems
- Visualization and computer graphic
- Approximate computing
- Image processing, information retrieval
- Natural language processing
- Machine learning, etc.

Pervasive Computing and Internet of Thing

- Internet of things, everything, and nano-things
- Location-dependent/personalized application
- System architectures and platforms
- Embedded computing with applications
- Low-power, energy-aware pervasive computing
- Smart devices
- Spaces and objects
- Middleware services and agent technologies
- Positioning and tracking technologies
- Intelligent devices and environments

- User interfaces and interaction models
- Security and privacy issues for pervasive systems
- Ubiquitous computing, etc.

Control Systems

- Control theory and applications
- Robotics and autonomous systems
- Intelligent control
- Optimal control
- Robust control
- Adaptive control
- Linear and nonlinear control systems
- Complex adaptive systems
- Industrial automation
- Control systems technology, etc.

Energy and Power Systems

- Low-carbon power (CCS, nuclear, wind, solar, hydro, etc.)
- Low-carbon transport (fuel cells and hydrogen)
- Energy storage and network balancing
- Grid integration and infrastructure
- Distributed generation
- Energy efficiency and energy management
- Policy, targets, and resource efficiency
- Integrating finance, economies, and energy
- Computing, data, and ‘intelligent’ design
- Micro-grid operation
- System stability, dynamics, and control
- Power system protection and relaying
- Restructuring of power system, electricity, etc.

Engineering Education and Sustainable Development

- EESD and circular economy
- Global issues in EESD
- Overcoming barriers for EESD
- EESD and energy
- Stakeholders in EESD
- EESD and lifelong learning
- EESD and disciplinary approaches

Economics and Business Engineering

- Computational economics and finance
- FinTech
- Industrial and systems engineering
- e-commerce and e-business

- Business information systems
- Technopreneurship, technology, and innovation
- Supply change management technology, etc.

Contents

A Reliable and Secure Wireless Network for VoIP Applications	1
Vinod Kumar and O. P. Roy	
Interdisciplinary Approaches Incorporating Computational Intelligence in Modern Pharmacognosy to Address Biological Problems	11
Tathagata Adhikary and Piyali Basak	
Broadband Annular Ring Patch Antenna	21
Thingbaijam Rajkumari Chanu, Somokanta Hijam, and Maxon Okramcha	
Cooperative Spectrum Sensing with Improved Absolute Value Cumulation Detection Based on Additive Laplacian Noise in Cognitive Radio	27
Khushboo Sinha and Y. N. Trivedi	
Solar Power Plant Site Selection: A Systematic Literature Review on MCDM Techniques Used	37
Rajkumari Malemnganbi and Benjamin A. Shimray	
A FPGA-Based PUF Integrated Blockchain to Overcome the Challenges of Internet of Everything (IoE)	49
Lukram Dhanachandra Singh and Preetisudha Meher	
Biometrics-Based Pig Identification: From Invention to Commercialisation	63
Subhranil Mustafi, Pritam Ghosh, Sanket Dan, Kaushik Mukherjee, Kunal Roy, and Satyendra Nath Mandal	
Adoption of IoT in Vehicular Traffic Control: An Overview	77
Joyeeta Goswami and Ashim Saha	

Optimal Placement of FACTS Devices in the Power System Using ANN to Increase the System Loadability	89
Mohammad Khalid Saifullah, Md. Monirul Kabir, Nasim Mia, and Tanyir Ahmed	
Impact of Noise Levels on SVM-GMM Based Speaker Recognition System	99
Renu Singh, Utpal Bhattacharjee, Arvind Kumar Singh, and Madhusudhan Mishra	
Digital Payment System and the Millennial in a Smart City: An Antecedent to Technopreneurship.....	109
Anil Kumar Singh and Tagiya Mudang	
Efficient Fusion Based Multi-modal Biometric Authentication System Using Machine Learning	119
R. Sindhuja and S. Srinivasan	
An MOS-C Multifunction Filter Employing DXCCTA for High-Frequency Operation	133
Karam Bharat Singh, Manoj Joshi, and Ashish Ranjan	
Smart Car Parking Technique for Metropolitan City.....	143
Abu Shufian, Md. Asif Afroz, Md. Hasibuzzaman, Mehedi Al Miraz, Avijit Sarker, Md. Jahidul Islam Rashed, and Md. Aman Miah	
Implementation of Perturbation-Based MPPT Technique Using Model-Based Design	155
Sachin Angadi, Udaykumar R. Yaragatti, Yellasiri Suresh, and A. B. Raju	
QRS Complex Detection Algorithm for Wearable Devices	167
Lalita Gupta	
ORS: The Optimal Routing Solution for Smart City Users	177
K. Krishna Rani Samal, Korra Sathya Babu, and Santos Kumar Das	
An IoT-Based Pollution Monitoring System Using Data Analytics Approach	187
Harshit Srivastava, Shashidhar Mishra, Santos Kumar Das, and Santanu Sarkar	
Modeling the Hierarchical Fuzzy System for Suitable Crop Recommendation	199
R. Aarthi and D. Sivakumar	
Real-Time Emergency Vehicle Response System for Smart City Applications	211
Lima Priyadarsini, Prashant Deshmukh, and Santos Kumar Das	

Contents	xvii
Modified Aggressive Packet Combining Scheme with Repetition Code for Throughput Enhancement in High Error Rate Channel	221
Mancharla Ravi and Yaka Bulo	
Review on Silent Speech Recognition Using EMG Sensors and Voices After Laryngectomy	231
Pilla Devi Bhavani, V. Preethi, and Durgesh Nandhan	
CNN-Based Individual Ghungroo Breed Identification Using Face-Based Image	241
Kaushik Mukherjee, Sanket Dan, Kunal Roy, Subhajit Roy, Subhranil Mustafi, Pritam Ghosh, Satyendra Nath Mandal, Dilip Kumar Hajra, Santanu Banik, and Syamal Naskar	
Development of Image-Based Disease Scale of Phoma Blight of Potato Using <i>k</i>-Means Clustering	253
Kunal Roy, Sanket Dan, Kaushik Mukherjee, Subhranil Mustafi, Pritam Ghosh, Satyendra Nath Mandal, Subrata Dutta, and Ashis Chakraborty	
Power Quality Improvement of Cascaded Savonius Rotor Based Hydrokinetic Power System	265
Oying Doso and Sarsing Gao	
Design and Simulation of a Sub-6 GHz Low Loss Band Pass Filter Using Double Split Inductor for 5G Radio WLAN Applications	275
Venkata Raghunadh Machavaram and Bheema Rao Nistala	
Two Novel Configurations of Electronically Tunable Quadrature Sinewave Oscillator Using CDBA	285
Shekhar Suman Borah, Ankur Singh, and Mourina Ghosh	
Analog/RF and DC Performance Enhancement of a Pocket-Doped Junction-Less TFET for Low Power Application	295
Sneha Bharti, Suruchi Sharma, Abhishek Verma, Manisha Bharti, and Baljit Kaur	
A Study on Stability Analysis of QT Interval Dynamics of ECG Using ARMAX Model	307
A. Jyothisana and J. Sivaraman	
High Frequency Resonant Inverter with Shunt Active Power Filter for Harmonic Compensation	317
Rohan Sinha and Rahul Raman	
Modelling of Fiber Bragg Grating Sensor for Acoustic Pressure Wave Detection of Partial Discharge in Power Transformer	329
Sorokhaibam Nilakanta Meitei, Kunal Borah, and Saibal Chatterjee	

Design and Investigation of Tunnel Junction Engineered Dopingless-TFET with Improved DC and RF/Analog Parameters Analysis	337
Abhishek Verma, Suruchi Sharma, Sneha Bharti, Manisha Bharti, and Baljit Kaur	
The Role and Significance of Atrial ECG Components in Standard and Modified Lead Systems	347
Shaik Karimulla and J. Sivaraman	
Data Rate Enhancement Scheme and Mathematical Modelling for Data Communication Through Blood	357
Kauser Husainee and Tanmay Deshmukh	
A Novel Design of Fast and Low Power Pull-Up and Pull-Down Voltage Level Shifter	367
Vickey Kumar, Suruchi Sharma, and Baljit Kaur	
Modeling of Dual-Gate Carbon Nanotube Based Ion Sensitive Field Effect Transistor (DG-CNTISFET)	377
Hiranya Ranjan Thakur, Gaurav Keshwani, and Jiten Chandra Dutta	
A Novel Approach to Calculate TF-IDF for Assamese Language	387
Hsuvas Borkakoti, Chandana Dev, and Amrita Ganguly	
A Low-Power Third-Order Passive Continuous-Time Sigma-Delta Modulator Using FinFET	395
Sarangam Kunamalla and Bheema Rao Nistala	
Mitigation of Power Fluctuations in UPFC-Based Network	407
Rajen Pudur, Pallavi Kumari, and Mrinal Kanti Rajak	
An Efficient Approach for Barcode Encoding/Decoding Using Pattern Substitution	419
S. Ieswaria, R. Bhavani, and R. Priya	
Fabrication and Electrochemical Modeling of CNT-Based BioFET for Cholesterol Detection	429
Gaurav Keshwani, Kabyashree Hazarika, Hiranya Ranjan Thakur, and Jiten Chandra Dutta	
Design of LCL Filter for SPWM Inverter Based on Switching Frequency and THD Criterion	439
T. Saha, A. Mitra, and B. Halder	
Level Control of Hopper Tank Process Using Model-Based Controller	453
V. Murugananthan, M. Valluvan, and G. Sakthivel	

Contents	xix
Hybrid L + C Edge Detection Algorithm for Harnessing Large Image Datasets	465
Gurpartap Singh, Sunil Agrawal, and B. S. Sohi	
Resolution Selective 2–6-Bit Flash ADC in 45 nm Technology	475
Sarfraz Hussain, Rajesh Kumar, and Gaurav Trivedi	
Measurement of Heartbeats for Well-Being Assessment Using Photoplethysmographic Signals	485
Piyush Kumar, Arpan Sharma, Mayammi Zimik, Shivam Parashar, Renu Singh, Joyatri Bora, Aswini K. Patra, and Madhusudhan Mishra	
An Iterative Node-Pair Time Synchronization (INTS) for Wireless Sensor Networks	495
Sakuru K. L. V. Sai Prakash and N. Bheema Rao	
Image Captioning Methodologies Using Deep Learning: A Review	507
Virendra Kumar Meghwal, Namita Mittal, and Girdhari Singh	
Performance of Speaker Recognition System Using Kernel Functions Approach for Different Noise Levels	513
Renu Singh, Arvind Kumar Singh, and Utpal Bhattacharjee	
A Fuzzy Multicriteria Methodology for Selection Among Solar PV Adoption Barriers in India	521
Anbesh Jamwal, Akshay Patidar, Rajeev Agrawal, and Monica Sharma	
Suspension Modeling and Its Importance in Automotive Industries for Implementation of Modern Vehicular Technologies	533
Sujan Neroula and Santanu Sharma	
PIC Controller Based SVPWM Technique for Induction Motor Variable Speed Drive	541
Pabitra Kumar Guchhait, Suvadip Roy, and Abhik Banerjee	
A Neural Network Based Strategic Placement and Task Assignment for a Multi-agent System	555
Mukund Subhash Ghole and Anjan Kumar Ray	
Review and Analysis of Charge-Pump Phase-Locked Loop	565
Mriganka Gogoi and P. K. Dutta	
Image Fusion: Challenges, Performance Metrics and Future Directions	575
S. B. G. Tilak Babu, I. Chintesh, V. Satyanarayana, and Durgesh Nandan	
Factors Influencing Financing for Entrepreneurs	585
Raman Kumar, Rajasve Kaushik, Shivani, Rishi Kant Kumar, and Prashant Kumar	

Simulation and Analysis of Hybrid PEMFC and Solar PV Cell Model for Commercial Load Profile System	595
Archana Thoudam, Pabitra Kumar Guchhait, and Abhik Banerjee	
How Does Perceived Desirability and Perceived Feasibility Effects the Entrepreneurial Intention	607
Rajasve Kaushik, Raman Kumar, Manishankar Datta, Rishi Kant Kumar, and Prashant Kumar	
A New Topology for Photo Voltaic Energy Conversion System	617
Sudhir Maurya and Abhik Banerjee	
A User-Centric Task Allocation Approach in Mobile Crowdsensing	627
Moirangthem Goldie Meitei and Ningrinla Marchang	
Fault Classification Based Approximate Testing of Digital VLSI Circuit	641
Sisir Kumar Jena	
Image Processing Using Case-Based Reasoning: A Survey	653
Rahul Barman, Saroj Kr. Biswas, Sunita Sarkar, Biswajit Purkayastha, and Badal Soni	
Automatic Speech Recognition of Galo	663
Karter Nyodu and Samudra Vijaya	
Early Detection of Diabetic Retinopathy Using Machine Learning Techniques: A Survey on Recent Trends and Techniques	673
Dolly Das, Saroj Kr. Biswas, Sivaji Bandyopadhyay, and Sunita Sarkar	
GUI-Based Secure Architecture Design for Distributed Community Micro-grid	685
Praveen Tiwari, Maj Sunil Kumar Panwar, Bikram Paul, Pinakeswar Mahanta, and Gaurav Trivedi	
A Hybrid Protocol for Stop and Wait ARQ in Markov Two States Model	697
Sanjit Ningthoujam and Swarnendu K. Chakraborty	
Comparative Study on a U-Slot Miniaturized CPW-Fed Multi-band Antenna Applicable for 5G Communication	707
Kaushal Mukherjee, Amitesh Das, and Sahadev Roy	
An Experimental Investigation of FPGA-Based LMS Algorithm for Adaptive Noise Cancellation	719
Abinash Patnaik, Rajesh Kumar Patjoshi, and Rakhee Panigrahi	

ICI Mitigation with Fixed-Number (FN)- and Fixed-Region (FRgn)-Based BS Coordination and Cooperation in a Multi-cell Cellular Network	731
Janmoni Borah, Kshetrimayum Linthoinganbi Devi, and Joyatri Bora	
InGaAs-Based Square-Shaped Nanopillar Array for High Photodetector Performance.....	743
Smriti Baruah, Santanu Maity, and Joyatri Bora	
Identification of Approximable Program Components Using Edge Profiling	753
Priya Arundhati and Santosh Kumar Pani	
Bidirectional LSTM with Attention Mechanism for Automatic Bangla News Categorization in Terms of News Captions	763
Md Shopon	
Sentence Relation Classification Using Deep Learning Experiments ..	775
B. Haripriya and Kishorjit Nongmeikapam	
Spectral Analysis of Consonants in Arunachali Native Language—Adi.....	783
Sajal Sasmal and Yang Saring	
Double Gate Tunnel FET Versus Double Gate MOSFET: Electrical Properties Comparison	791
Menka Yadav	
Wireless Access Support for Distribution Management System (DMS) to Microgrid Communication in Power Network	805
N. Himabindu, Rajashekhar P. Mandi, Santoshkumar Hampannavar, and Swapna Manasani	
Implementation of a Charge Controller for Hybrid Electric Vehicle.....	813
Gautam and Brajagopal Datta	
Series-Stacked Non-parallel Multipath Differential Inductor for C Band Applications	823
Sunil Kumar Tumma and Bheema Rao Nistala	
Implementation of DCGAN to Generate Gamocha Design Patterns	831
Adarsh Pradhan, Arunav Buragohain, Uddipta Pathak, Sahil Ansari, and Manali Baruah	
Performance Evaluation of On-Grid Rooftop Solar PV System in GMCH, Guwahati, Assam	839
Israfil Hussain, Utpal Chandra Baro, Rupa Chhetri, Vanita Agrawal, and Abdul Latif	

Forced Alignment Method for Detection of Bodo Word Boundary	853
Raja Jwbthasa Daimari and Aniruddha Deka	
Fault-Tolerant Cascaded Asymmetrical Multilevel Inverter for the Solar-Based Electric Vehicle	863
Hillol Phukan, Tamiru Debela, and Jiwanjot Singh	
New H-Bridge for Symmetrical and Asymmetrical MLI with Reduced Number of Devices	875
Tamiru Debela, Hillol Phukan, and Jiwanjot Singh	
Different EDGE Detection Techniques: A Review	885
Chinmoy Ghosh, Suman Majumder, Sangram Ray, Shrayasi Datta, and Satyendra Nath Mandal	
Design and Analysis of an Improvised Fully Differential Amplifier	899
Swagata Devi, Koushik Guha, Naushad Manzoor Laskar, Sourav Nath, and Krishna Lal Baishnab	
Hyperspectral Band Selection Based on Variants of Rough Set Theory	909
Barnali Barman and Swarnajyoti Patra	
Performance Analysis of Interference Alignment-Based Precoding	919
Amlan Deep Borah, Md. Anwar Hussain, and Joyatri Bora	
Structural and Optoelectronic Properties of Spin-Coated $\text{CH}_3\text{NH}_3\text{PbCl}_3$ Thin Film Using Non-halide Source of Lead	929
Paramita Sarkar, S. K. Tripathy, and K. L. Baishnab	
Robust Gunshot Features and Its Classification Using Support Vector Machine for Wildlife Protection	939
Vivek Singh, Kailash Chandra Ray, and Somanath Tripathy	
Effect of pH Variations on Zinc Oxide (ZnO) Nanowire Dispersions	949
Vimal Kumar Singh Yadav and Roy Paily	
Intensity Modulated U-Shaped Bent Tapered Optical Fiber Concentration Sensor	957
Putha Kishore, D. Dinakar, Manchineellu Padmavathi, and L. Obulapathi	
Performance Enhancement for Scattering Effect in Perovskite Solar Cell with Distinct Cathode Materials	965
Sagar Bhattarai, Arvind Sharma, and T. D. Das	
Need of Techno-Preneurship and Innovations for Community-Level Cancer Screening in Arunachal Pradesh	973
M. S. Momocha and K. Chaitan	

Contents	xxiii
Phrase-Based Machine Translation of Digaru-English	983
Rushanti Kri and Koj Sambyo	
EMT Analysis of Heavy-Duty EVs in Charging Station	993
Swati Shukla and Gaurav Trivedi	
Analysis of the Transient Stability of a Multi-machine System with SVC	1003
Srishail K. Bilgundi, M. Shiva, H. Pradeepa, and M. V. Likith Kumar	
Projection-Based Throughput Computation of Three-Dimensional Geographical Routing Protocol for Multi-hop Wireless Sensor Networks	1017
Afruza Begum and Md. Anwar Hussain	
Digital Image Processing Based Automatic Fabric Defect Detection Techniques: A Survey	1029
Vaishnavi Raut and Indrasen Singh	
A Balanced Expert System to Manage Parkinson's Disease by Identifying Major Risk Factors: B-TESM-PD	1039
Arpita Nath Boruah, Saroj Kr Biswas, Sivaji Bandyopadhyay, and Sunita Sarkar	
Bioinformatics Advancements for Detecting Epidemic Disease Using Machine Learning Approaches	1051
Bikash Baruah and Manash Pratim Dutta	
A Strategic Community Control-Based Power Flow Between Grid-Integrated PV Houses	1061
Jatin M. Soni, Deep V. Patel, Rajendra V. Patel, and Hardik P. Modha	
Classification of Buildings and Vehicles in Google Map Satellite Images Using Random Forest Classifier	1073
Ritik Gautam, Saravanan Chandran, and Jose Hormese	
Addressing the False Positives in Pedestrian Detection	1083
N. J. Karthika and Saravanan Chandran	
Hybrid CR Network: An Approach Based on Interweave-and Underlay-Type CR Network	1093
Varun Kumar, Mangal Singh, Sarat Kumar Patra, and Poonam Singh	
Intensive Study on Compact Integrated Optic Couplers Using Grating Geometry	1105
Bidyut Deka, Aradhana Dutta, and Partha Pratim Sahu	
Effect of AlN Spacer Layer on the Proposed MIS-AIGaN/GaN HEMT	1115
Ravi Ranjan, Nitesh Kashyap, and Ashish Raman	

Enhancement of Isolation in MIMO Antenna System	1123
Neelima Koppala, Sree Lochan Kanthi Kumar Kuppachi, Rohith Sai Kumar Gajula, Bhanu Ravindranath Kasturi, and Rupa Sree Jangam	
Stochastic Frontier Model Approach of Technical Efficiency for Paddy Farming in Odisha	1135
Priyabrata Bhoi, Deepak Kumar Swain, Subhadra Mishra, Debahuti Mishra, Gour Hari Santra, and Samarjeet Borah	
Improving Security Concerns of Mobile Cloud Computing Environment with Quantum Cryptographic Techniques	1141
Sudhanshu Maurya, Kuntal Mukherjee, and R. Badlishah Ahmad	
Author Index	1151

About the Editors

Dr. Pradeep Kumar Mallick is currently working as Associate Professor in the School of Computer Engineering, Kalinga Institute of Industrial technology (KIIT) Deemed to be University, Odisha, India. He has completed Post-Doctoral Fellow (PDF) from Kongju National University South Korea, PhD from Siksha O' Anusandhan University, M. Tech. (CSE) from Biju Patnaik University of Technology (BPUT), and MCA from Fakir Mohan University Balasore, India. Besides academics, he is also involved various administrative activities, Member of Board of Studies, Member of Doctoral Research Evaluation Committee, Admission Committee etc. His area of research includes Algorithm Design and Analysis, and Data Mining, Image Processing, Soft Computing, and Machine Learning. He has published 10 books and more than 70 research papers in National and international journals and conference proceedings.

Dr. Preetisudha Meher is currently working as Assistant Professor in National Institute of Technology, Arunachal Pradesh, India. She has completed her PhD from National Institute of Technology, Rourkela, India in the year 2015. Her PhD research work is on “Design and analysis of improved domino logic with noise tolerance and high performance”. She has done M. Tech and B. Tech from BPUT Odisha. She has guided almost 10 BTECH and 8 MTECH projects in various domains. She has published 12 journals, 32 conference papers, 5 book chapters and 2 books during her industry and academic work. At present, she is working in the field of Low Power VLSI, Bio Informatics and IOT. She has been awarded as **Outstanding Woman in Engineering Award** conferred by Centre for Advance Research and Design at International Women Meet-2018 on 1st March 2018 held at Chennai, India. She has been awarded Best Paper in the year 2018 at International Conference on Information System Design and Intelligent Applications, Mauritius and also in the year 2019 at International conference on Intelligent System and Control Communication at Bangkok. She has organized a Workshop on “Recent Trends in VLSI Design” at NIT Arunachal Pradesh from 8th to 12th January 2018 and also International conference on Intelligent System and Control Communication at Bangkok on 27-28 June 2019 as convener.

Dr. Alak Majumder has completed his PhD degree from NIT, Arunachal Pradesh, India and is working there as an Assistant Professor in the Department of ECE. He earned his M-Tech in Microelectronics & VLSI and BE in Electronics & Telecommunication Engineering from NIT Agartala and TIT Agartala. He also served as Assistant Professor in the Department of ECE at ICFAI University, Agartala. He has 75+ technical articles, 6 filed Indian Patents and 1 US Patent to his credit. His current research interests include Analog-Digital VLSI, Clock Gating and Distribution and Wireline Communication Circuit. He is a Member of the IEEE, IAENG and IACSIT.

Prof. Santos Kumar Das is a R&D professional with more than 17 (1 years after BTECH, 7 years after MTECH (Foreign Industry), 5 years during PhD and 4 year after PhD) years of valuable experience on various Software developments and research activities both in industries and academics. At present, he is working at National Institute of Technology as an Assistant professor. He worked at SDSU, California, US as an adjunct faculty for one month on Software Defined Network. He is academically astute and technically brilliant with a Master Degree specializing in Electrical Communication Engineering from Indian Institute of Science (IISc) Bangalore, India and PhD Degree from National Institute of Technology, Rourkela, India. His PhD research work was on “Quality of service estimation for an Optical Virtual Private Network over WDM/DWDM network”. His current research work is on software defined network (SDN), IoT, sensor networking, optical networking, Smart City product development, and embedded system. He has guided almost 40 BTECH and 30 MTECH projects in various domains. He has published 12 journals, 25 conference papers, 8 patents (filed), and 4 book chapters during his industry and academic work. At present, he has submitted one PhD student and guiding 12 PhD ongoing students in optical networking, IoT and embedded domain. He is also managing three high value funded projects (440 lakh), where 30 to 40 students are working.

A Reliable and Secure Wireless Network for VoIP Applications



Vinod Kumar and O. P. Roy

Abstract In a wireless communication system, the Quality of Service (QoS) becomes an active area of research as the demand for real-time applications like voice or video communication increases day by day. In this paper, a new hybrid INTER-SR & INTRA-SR based reliable wireless network is designed for Voice over Internet Protocol (VoIP) applications. It is mainly consisting of one optimization algorithm named as Genetic Algorithm (GA) in conjunction with two classification approaches such as Artificial Neural Network (ANN) and Support Vector Machine (SVM). The proposed algorithm selects a reliable and more reliable route based on the nodes properties such as energy consumption and delay. In the end, three distinct QoS parameters such as routing overhead, delay and jitter are analyzed for two communication scenarios such as with attack and without attack in MANET simulator. The results demonstrate that the proposed algorithm performs with satisfying results compared to individual routing and optimization approaches.

Keywords Wireless network · Voice over internet protocol · Reliability · INTER-SR · INTRA-SR · GA · SVM · ANN

1 Introduction

The present day's society observes a revolutionary change in communication technologies to make life comfortable. VoIP is the technology to make communication possible over IP networks [1]. Using VoIP is very advantageous such as cost per call [2]. Further, VoIP technique suffers from many disadvantages, which makes people still remain on phone calls [3]. The major drawback faced by the VoIP calls is the packet loss and the delay that occurs during the congestion problem over IP networks. Another problem is the wastage of bandwidth [4]. A list of codecs along with their

V. Kumar (✉) · O. P. Roy
Department of EE, NERIST, Nirjuli, Arunachal Pradesh 791109, India
e-mail: vinodnerist@gmail.com

O. P. Roy
e-mail: oproy61@gmail.com

Table 1 Codec in general VoIP

Codec	Format size	Codec	Format size
G. 729	10	G. 729 A	10
LPC	14	G-723.1	30
G. 729 E	10	G-729 D	10

format size is listed in Table 1. The payload produced by VoIP is small as the VOIP is sensitive to delay; the larger is the size of the payload, more time is required by the VoIP to generate the payload, and hence increase the delay. VoIP systems still exist on data networks that means there may be a lack of security and types of attacks related to any data network [5, 6]. In the VoIP, the voice message is translated into IP packets. The data travels from different access points and chances of data loss increases within the route while transmitting the data from its source to destination [7]. From an existing survey, it has been observed that Denial of Service is one of the most common attacks that affect VoIP data. Therefore, it is necessary to design a reliable network.

2 Related Work

A number of protocols are coming into existence with improved security features, but still not meet the desired requirement. Gupta and Shmatikov [8] have presented a reliable network of VoIP protocol. The researchers started a replay attack that affects voice and break the security of the transport layer [8]. VoIP evaluation has also been performed by Audah et al. [9] using distinct codec schemes in NS-2 simulator. The author has examined the performance in terms of Quality of Service (QoS) [9]. Also, Ad hoc On-demand Distance Vector (AODV), Dynamic Source Routing (DSR), Temporally-Ordered Routing Algorithm (TORA) have been analyzed in OPNET simulator [10]. It has been concluded that the data VoIP packet transmission using the TORA protocol has been transmitted with better quality against the large data traffic [10]. Furthermore, for VoIP data transmission carried out using AODV and DSR routing mechanism has been conducted by Jasani [11]. The results indicate that data transmission using AODV routing is more suitable compared to DSR while VoIP packet is transmitted in the MANET network [11]. Sanchez-Iborra and Cano [12] have investigated the quality of MANET routing protocols in transmitting video data using OLSR and AODV [12].

3 Proposed Algorithm

The objective is to make VoIP data reliable and secure. A number of researchers have contributed in this direction but not attained desired security. To increase data security

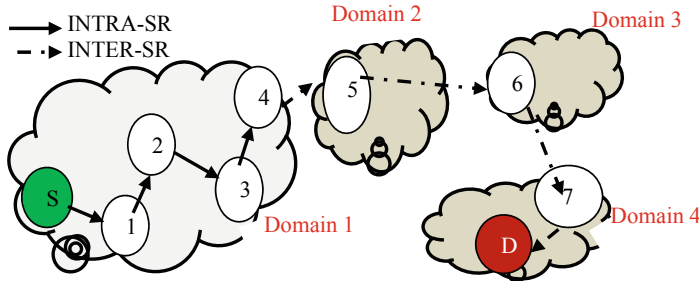


Fig. 1 Simulation area of $(1000 \times 1000 \text{ m}^2)$

of VoIP application, SVM and ANN are used for decreasing routing overhead and packet loss. The route has been selected based on the concept of INTER-SR (Inter-State Routing) and INTRA-SR (Intra State Routing). INTER-SR is a type of protocol in which the data is transmitted from one domain to another domain, whereas, in INTRA-SR, the data is transmitted within the domain.

3.1 Network Design

A network of $1000 \times 1000 \text{ m}^2$ is created with N number of nodes as shown in Fig. 1. Nine nodes are deployed denoted by (1–7), S and D. Nodes 1 to 4 and S comes under domain 1 and the route formation occurred due to INTRA-SR process. To reach data from source to destination, we also need INTER-SR technique in combination with INTRA-SR technique.

3.2 Security and Prevention

The problem of routing in VoIP-based communication model is solved by integrating INTRA-SR and INTER-SR approach. The problem of security and prevention is not covered by this approach, explained in the result and analysis.

To resolve this problem, we designed a hybrid mechanism using SVM and ANN techniques. SVM is a binary classifier for checking two conditions for the malicious node or genuine node. To validate the detection probability of SVM for the malicious or normal node, ANN and SVM are used as a classifier. In route formation, the data is transmitted to the nearby node as shown in Fig. 2, node 2 pass VoIP packet to node 3 by using the concept of distance. But, the routing mechanism of VoIP does not check whether the node is dropping the message or not. To degrade the VoIP packet drop of the proposed wireless network, an optimization scheme has been used with novel fitness function. The fitness function helps to select the node as in Table 2.

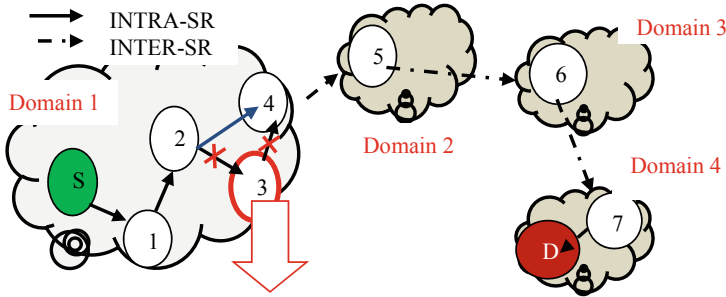


Fig. 2 Reliable network using GA with (SVM & ANN) approach

Table 2 Node's properties

Nodes	Energy consumption (mJ)	Delay (ms)
2	10	4
3	12	3
4	12	2

In domain 1, during route formation, VoIP message packet is forwarded by node 1 to node 3. But, node 3 is not an accurate node as it drops data packet. It is necessary to pass data to a genuine node, which has been performed here, using GA. The GA checks energy consumed by each nearby node as in our example, node 3 and node 4 consumes same energy, therefore, in such condition, one must go for checking other parameters that is a delay in this case. Node 4 forward data with less delay ($\cong 2$ s) and hence node 1 transmits data to node 4.

Malicious Detection of VoIP communication using GA with SVM and ANN

Required Input: $T \leftarrow$ Training Data as nodes properties. $C \leftarrow$ Target/Category in terms of communicating and non-communicating nodes. $N \leftarrow$ Number of Neurons, $MN \leftarrow$ Malicious Nodes,

Obtained Output: Start

- 1 **To optimized the T, Genetic Algorithm (GA) is used**
- 2 **Set up basic parameters of GA:** Population Size (P) – Based on the number of properties, CO – Crossover Operators, MO – Mutation Operators
OT – Optimized Training Data **Fitness Function:**

$$F(f) = \begin{cases} 1(True); & \text{if } F_s < F_t = \text{Threshold}_{Properties} \\ 0(False); & \text{Otherwise} \end{cases}$$

where F_s : Current Node Properties and F_t : Threshold properties for all nodes based on energy consumption, delay and position

```

3 Calculate Length of T for R
4 Set Optimized Training Data OT = [] For i in range of R
5    $F_s = T(i) = SelectedNodeProperties$ . // Current Data from N
6    $F_t = ThresholdProperties$ . // Average of All Data
7    $F(f) = FitFun(F_s, F_t)$ . Nvar = Number of variables
8   BestProp = OT = GA (F(f), T, Nvar, Set up of GA)
9 End - For SVM training data initialization OT - Nodes optimized
10 For I = 1 → All Nodes If Node Property (I) == Real
11 Define Cat category of training data Cat (1) = Node Properties (I)
12   Else Cat (2) = Node Properties (I) End - If
13 End - For Train_Struct=SVMTRAIN (T, Cat, Kernel function)
14 OT= Train_Struct.SupportVector //finding ANN training data
15 Initializing ANN basic parameters – Number of Epoch (E) // ANN Iterations – Number of Neurons (N)
16 F i = 1 → OT If T belongs to the properties of communicating nodes
17   Group (1) = Training data properties according to renodes
18   Else if T belongs to properties of non-communicating nodes
19     Group (2) = Training data properties for non-real nodes
20   Else Group (3) = Training data Extra properties End - If
21 End - For Initialize ANN for data
22 VoIP-Net = Newff (T, Group, N)
23 VoIP = Train (VoIP, Training data, Group) Testing:
24 Current Node = Nodes Properties in Cloud-Net
25 Authentication = simulate (Cloud-Net, Current Node)
26 If Authentication = True Genuine node not consider as a malicious
27 Else MN = Malicious Node
28 End Return: MN a list of Malicious Nodes
29 End

```

Above algorithm is designed using hybridization of SVM, ANN and GA. Algorithm first uses SVM using radial basis function (RBF) as a kernel and find the most helpful properties for ANN which are called support vectors. ANN is used to train and classify nodes authorization which helps in the improvement of network performance.

4 Results and Analysis

In this research, the performance of the communication system for VoIP message transmission is considered with two cases, one communication without attack and another communication with attack. The effect of occurring malicious node inside the network when making the voice call and data packet transmitted between the

source and destination node through different domain nodes have been discussed. The performance has been analyzed by constructing network with multiple nodes (5, 10, 15, 20, 25 and 30). The quality of transmitting VoIP message transmission has been observed on the basis of delay, packet loss and throughput. The network simulation environment consists of 30 numbers of nodes that were positioned randomly using random waypoint as a mobility model. The simulation parameters are mentioned in Table 3. The results such as routing overhead, average delay and average jitter have been computed in two scenarios that is communication with and without attack. To obtain accurate results, the network is simulated at least ten times and their average values are noted in the form of Tables 4, 5 and 6.

Figure 3 demonstrates the routing overhead for a reliable network that is used for VoIP application. A very close variation has been observed for three different approaches such as (1) with INTER-SR & INTRA-SR, (2) with GA and (3) for Proposed Algorithm. For route construction, INTER-SR with INTRA-SR has been used, which enables the user to communicate with the remote user that is located in different domains. The route optimization is performed with GA as an optimization technique. GA helps to find the properties of each node based on energy consumption, delay and node's coordinate and the data transmission is done based on node's properties rather than the concept of the closest node within the route. Later on, the problem of identifying the best node has been resolved using SVM in hybridization with the ANN algorithm. The graph is shown in Fig. 3 indicates that the proposed

Table 3 Simulation parameters

Considered parameters	Variation of parameters
Area	1000 × 1000 m ²
Nodes	5, 10, 15, 20, 25 and 30
Number of malicious nodes	10
Simulation time (s)	400 s
Routing protocol	INTER-SR and INTRA SR
Mobility model	Random waypoint

Table 4 Routing overhead analysis

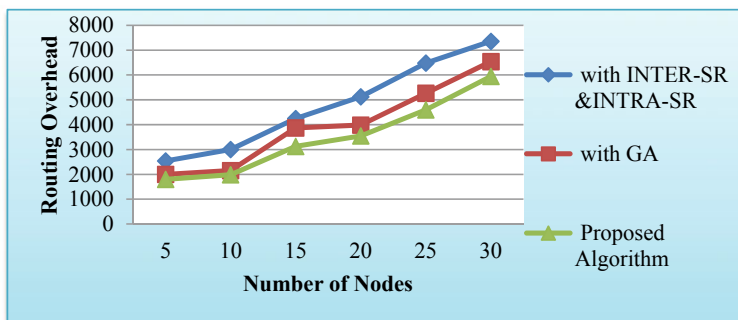
Number of nodes	Communication without attack			Communication with attack		
	INTER-SR & INTRA-SR	With GA	Proposed algorithm	INTER-SR & INTRA-SR	With GA	Proposed algorithm
5	2540	2000	1800	4521	3254	1726
10	3002	2154	1985	5264	3642	1875
15	4251	3869	3125	5728	4782	3745
20	5126	3985	3547	6357	4759	3675
25	6482	5264	4597	8581	5025	4871
30	7356	6542	5942	9264	6235	5297

Table 5 Delay analysis

Number of nodes	Communication without attack			Communication with attack		
	INTER-SR & INTRA-SR	GA	Proposed algorithm	INTER-SR & INTRA-SR	GA	Proposed algorithm
5	1	0.6	0.5	5	4	2
10	6	5	4	8	8	4
15	8.2	8	2	14	10	5
20	15	9	2	16	12	6
25	25	11	2.5	22	19	8
30	30	18	10	40	22	10

Table 6 Jitter analysis (ms)

Number of nodes	Communication without attack			Communication with attack		
	With INTER-SR & INTRA-SR	With GA	Proposed algorithm	With INTER-SR & INTRA-SR	With GA	Proposed algorithm
5	1.9	1	0.3	3.5	3	2.5
10	1.8	1.1	0.35	7	5.9	3
15	6.5	3.2	1.8	16	14	4.6
20	11.5	4	2.5	20	18	8.7
25	8	4.2	3	21	20	12
30	15	6.5	4.5	28	22	24

**Fig. 3** Routing overhead without Attack

algorithm transmits data with small routing overhead compared to individual routing and routing with optimization approach.

Figure 4 represents the routing overhead observed with the variation of the number of nodes in the presence of an attack. The graph indicates that with the increase in

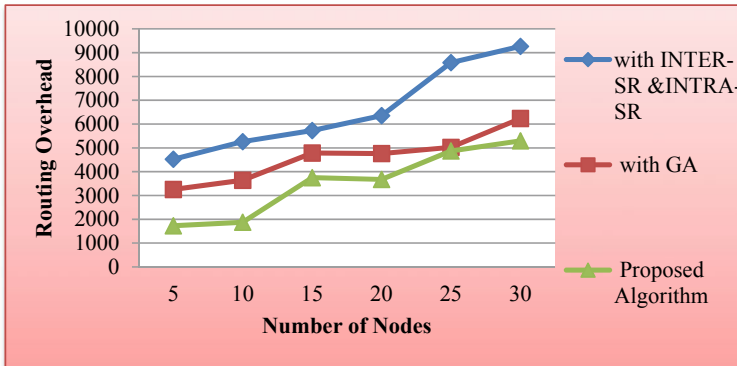


Fig. 4 Routing overhead with Attack

the communicating nodes within the network, the routing overhead increased and the maximum routing overhead measured for 30 numbers of nodes with INTER-SR and INTRA-SR, with GA and for the proposed algorithm are 9264, 6235, and 5297, respectively.

To show the effectiveness of the proposed algorithm, we evaluated average delay and jitter by generating VoIP messages in a large amount. The attained results related to average delay obtained without and with attack are shown in Figs. 5 and 6. The difference of delay values measured with INTER-SR and INTRA-SR, with GA and for combination of all that is proposed algorithm has been presented in Fig. 5. From the above graph, it has been observed that the average delay values recorded for with GA are almost twice and for the proposed algorithm almost thrice compared to the simple routing techniques performed by INTER-SR and INTRA-SR combination.

The jitter observed without attack and with the attack for VoIP application with three different algorithms is shown in Figs. 7 and 8, respectively. It is clear from Figs. 7 and 8 that when the classification algorithm in addition to the optimization approach is used, the occurrence of jitter has been reduced in a great extent.

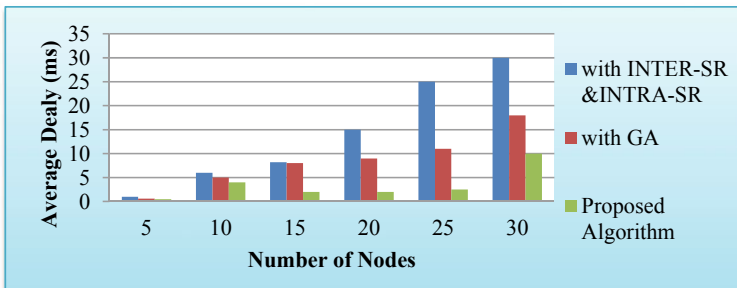
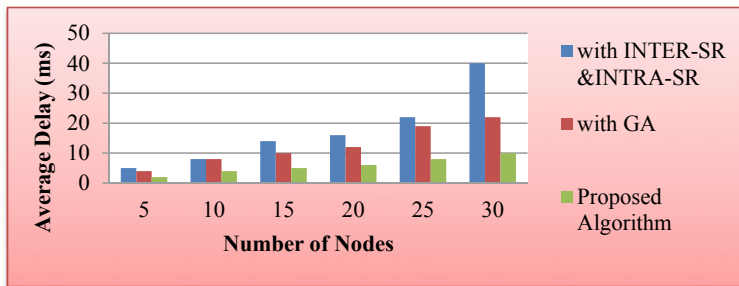
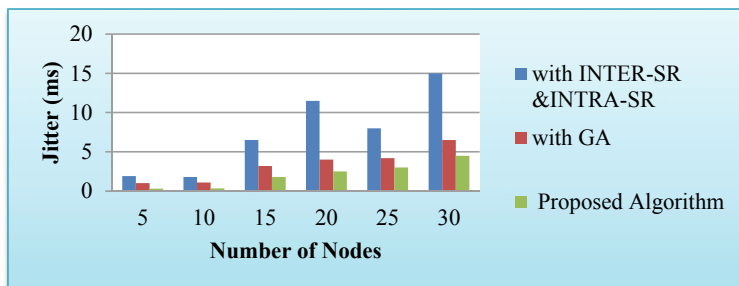
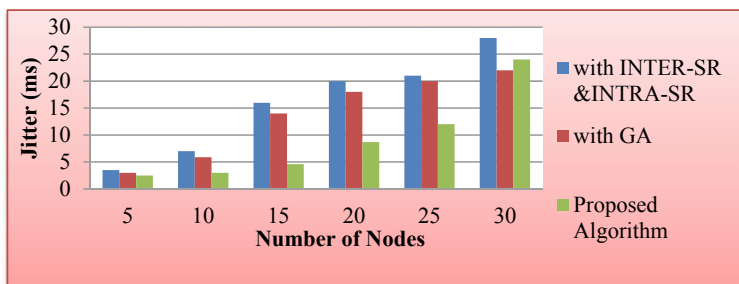


Fig. 5 Average delay without attack for VoIP application

**Fig. 6** Average delay with attack for VoIP application**Fig. 7** Average jitter without attack for VoIP application**Fig. 8** Average jitter with attack for VoIP application

5 Conclusion

In the paper, we have presented a reliable wireless network for VoIP-based applications. For routing, the concept of INTER-SR and INTRA-SR has been used to resolve the problem of handover as the data has to be transmitted from one domain to another domain. Two different scenarios of data communications such as in the presence

of with and without attack have been presented for three approaches as discussed in the results and analysis section. The performance of the designed network has been examined based on routing overhead, average delay and average jitter for VoIP application. The results demonstrated that better results compared to existing routing protocol has been obtained that guarantee the desired delay and jitter required for data transmission in VoIP applications in a wireless network.

References

1. Mohd Ali A, Dhimish M, Mather P (2019) WLAN protocol and network architecture selection for real-time applications (2019)
2. Chakraborty T, Misra IS, Prasad R (2019) VoIP over wireless LANs—Prospects and challenges. In: VoIP technology: applications and challenges, Springer, Cham, pp 71–93
3. Alsaadi MS, Alotaibi ND (2019) Routing protocols design and performance evaluation in wireless mesh networks. *Int J Technol Diffus (IJTD)* 10(1):60–74
4. Chakraborty T, Misra IS, Prasad R (2019) Technique for Improving VoIP performance over wireless LANs. In: VoIP technology: applications and challenges, Springer, Cham, pp 95–121
5. Abualhaj MM, Al-Tahrawi MM, Al-Khatib SN (2019) A new method to improve Voice over IP (VoIP) bandwidth utilization over Internet Telephony Transport Protocol (ITTP). In: Proceedings of the 2019 8th international conference on software and information engineering. ACM, pp 192–195
6. Estepa R, Estepa A, Madinabeitia G, Davis M (2018) Improving the energy efficiency of VoIP applications in IEEE 802.11 networks through control of the packetization rate. In: XIII Jornadas de Ingeniería telemática (JITEL 2017). Libro de actas, pp 23–29
7. Hsieh WB, Leu JS (2018) Implementing a reliable VoIP communication over SIP-based networks. *Wirel Netw* 24(8):2915–2926
8. Gupta P, Shmatikov V (2006) Key confirmation and adaptive corruptions in the protocol security logic. In: Proceedings of the Joint Workshop on Foundations of Computer Security and Automated Reasoning for Security Protocol Analysis (FCS-ARSPA'06), pp 113–142
9. Audah L, Kamal AAM, Abdullah J, Hamzah SA, Razak MAA (2015) Performance evaluation of voice over IP using multiple audio codec schemes. Asian Research Publishing Network (ARPN). *J Eng Appl Sci* 10:8912–8919
10. Ravikanti S, Preeti G (2015) Evaluating the performance of reactive unicast routing protocols with OPNET simulator in MANETS under VOIP. *Int J Innov Res Sci Eng Technol* 4(7) (2015)
11. Jasani H (2012) Evaluations of AODV and DSR for QoS requirements. In: Proceedings of the 1st annual conference on research in information technology ACM, pp 1–6 (2012)
12. Sanchez-Iborra R, Cano MD (2014) An approach to a cross layer-based QoE improvement for MANET routing protocols. *Netw Protocols Algor* 6(3):18–34

Interdisciplinary Approaches Incorporating Computational Intelligence in Modern Pharmacognosy to Address Biological Problems



Tathagata Adhikary and Piyali Basak

Abstract Computer simulations to address research problems have touched almost all the sectors of science. Ethnopharmacological data demands linkage with different biomedical databases for both prospective and retrospective studies. Computational intelligence bridges the gap between diverse resources already available (from the molecular level to macroscopic characteristics of drugs) marking its significance in computer-aided drug design and gives an insight into the mechanism of action of bioactive compounds. Computational methods are utilized to study the process of extraction, isolation, structure prediction, metabolomics, biosynthesis, dereplication, phytochemical library construction, and assessment of their bioactivity. Further, *in silico* models aim to minimize the cost and time associated with conventional screening techniques. Electronic structure determination, docking, geometry optimization are few methods to name that are popular in biological sciences. Softwares like Gaussian 94, MOPAC, GAMES, Spartan, and Sybyl showed their dominant role in deciphering the chemistry underlying a process. The complexity of collecting vast biological data and extracting the information of interest for subsequent knowledge provision and deduction of conclusions is mollified to a great extent using bioinformatics. This review discusses the hurdles, current progress, and potential of computational intelligence in drug discoveries/interactions.

Keywords Bioinformatics · Molecular simulation · Phytochemicals · Bioactivity · Statistics

1 Introduction

Pharmacognosy aims to develop databases on natural product-based drugs that primarily hold information about sources, geographical distributions, identification,

T. Adhikary · P. Basak (✉)

School of Bioscience and Engineering, Jadavpur University, Kolkata, West Bengal, India
e-mail: piyalibasak@gmail.com

T. Adhikary

e-mail: tatha.adhi@gmail.com

extraction/isolation, bioactivity, and toxicity profiling of drugs. Traditional recipes of medicine by apothecaries are still practiced ethnically but their scopes can be extended globally. The conventional techniques of drug discovery can be made less labor-intensive with minimal investment in terms of capital and time by the use of high-throughput technologies. Approximately one-third of the present literature on drugs involves plants as a source [1]. The immense data generated since centuries in the field of pharmacognosy remain scattered and thus limit the essence of strategic analysis of interlinked phenomena. Combining ancient manuscripts of ethnobotany with modern researches and subsequent implementation of data mining techniques forms a basic platform for logical representation of data.

Standing in the era of increasing pharmaceutical demands, computational intelligence bridges the gap between diverse resources already available (from the molecular level to macroscopic characteristics of drugs) marking its significance in computer-aided drug design. Multifold perspectives leading to an exponential growth of data demand for procedures to efficiently manage, integrate, visualize and analyze data. Combining the knowledge of genomics, proteomics, and metabolomics using bioinformatics advances in predicting pathways and accurate scientific reasoning of any process [2]. Further, *in silico* models aim to minimize the cost and time associated with conventional screening techniques.

Computer-assisted modeling of a physical entity or process has its own challenges also. The vastness of databases, accuracy of the information on pharmacokinetics, significance of assumptions, and their limitations influence the precision of prediction, i.e., success of such models. Keeping in mind the pros and cons, this review attempts to discuss the hurdles, current progress, and potential of computational intelligence in drug discoveries/interactions.

2 The Diversity of Databases

Initial efforts in the digitization of existing literature like the Biodiversity Heritage Library and the China-US Million Book Digital Library Project highlighted the challenges faced in gathering resources of interest from them. Automated character recognition and string-matching algorithms among many algorithms can be exploited to overcome such hurdles without semantic knowledge. The Encyclopedia of Life (EOL) and the Barcode of Life (BOL) provides a framework for taxonomic advancements that eliminate the linguistic challenge in existing literature [3]. An attempt to extract information from a semi-structured database of traditional Chinese medicines used ontology by an executable knowledge extraction language [4]. In addition, integration of heterogeneous data was achieved using Semantic Web technologies and semantic-based interoperable e-Science for identifying plant species in Chinese medicine having antidepressant activities and development of Traditional Chinese Medicine (TCM) system, respectively [5, 6].

Among simple file directories, object-oriented databases, and other types of databases, the relational database has gained popularity due to its efficient way of

storing and retrieving huge data via indexes, normalization, referential integrity, triggers, and transactions. MySQL and PostgreSQL are noteworthy relational database software that is free and quite popular in bioinformatics where data is assessed using a structured query language (SQL) [7]. Considering one or multiple parameters (like genomic data, the composition of bioactive compounds, ethnobotanical knowledge, medicinal uses, etc.), several databases are developed for integrating and indexing information. The International Ethnobotany Database (ebDB) is a non-commercial, multilingual, and primary repository for ethnobotanical data that supports translation and data entry by researchers. A large amount of experimental data in the field of natural products (biochemical and biological activity from *in vitro*, *in situ*, *in vivo*, and *in-human* experiments) is stored and analyzed by a relational database NAPRALERT [8]. The database developed by The United States Department of Agriculture (USDA) and maintained by Dr. Park provides information about secondary metabolites of selected medicinal plants used in inflammation, heart disease, obesity, hypertension, kidney disease, and diabetes whereas Dr. Duke's Phytochemical and Ethnobotanical Database at the USDA provides insights into a taxonomic classification of medicinal plants, their active metabolites, and pharmacological behavior. Protein Data Bank (PDB) being an important database in structural biology (for example, structural genomics) stores 3D structural data of proteins and nucleic acids. SCOP and CATH classify protein structures, while PDBsum provides a graphical overview of PDB entries. UniPort is a database of protein sequences derived mainly from genome sequencing projects, while KEEG specifies interactions and biosynthetic pathways of secondary metabolite. Herb Ingredient's Target (HIT) connects PDB, UniPort, Therapeutic Target Database (TTD), Pfam, KEEG, and other databases to analyze biological targets of herbal medicines listed in TCM.

Interestingly, the database CMKb is designed for aboriginal medicinal plants of Australia relating their taxonomy, phytochemistry, biogeography, biological activities, and images. Raintree is also a geographic region-based database specific to the plants of the Amazon rainforest [9]. Genome and transcriptome related data of medicinal plants from sequencing projects and plant Expressed Sequence Tags (ESTs) is analyzed by linking it with functional properties of plants and maintained by Plant Genomes Central (PGC) and EGENES database. Annotation of EST data with minimal redundancy is done in databases like KEGG genes, SwissProt, etc. to aid in the exploration of molecular markers [10]. A recent database, Medicinal Plants Genomics Resource (MPGR), collects transcriptomic and metabolomic data from diverse taxonomic plant species to key out putative genes and pathways involved in metabolite production. As a case in point, effector genes in the biosynthesis of ginsenoside in *Panax Ginseng* have been identified by analyzing EST data [11]. Further, the transcriptome data can be used to design a co-expressed gene network leading to gene discovery [12].

Instead of conventionally inspecting physical characteristics for bioscreening, the authenticity of a plant species is now done by DNA barcoding using DNA based markers due to its definitive results. For animals, the chosen sequence (i.e., DNA barcode) is from the mitochondrial gene cytochrome c oxidase subunit 1 (CO1) whereas matK-based barcode for angiosperms (representing a majority of land plants)

and ribulose-bisphosphate carboxylase gene (*rbcL*) were chosen as the plant barcode. Barcode of Life Database (BOLD) exhibits a platform for barcode-based classification. The Medicinal Materials DNA Barcode Database (MMDDB) combines data available on plants with their DNA barcodes making scopes for computational tools to search and sequence comparisons [9]. A database “MedHerb” is developed to manage information on genes, proteins, primers (used in Polymerase Chain Reaction (PCR)) and statistics related to some selected plant species with a scope of its expansion with time (a more feature-based database incorporating expressed sequence tags, active constituents, etc.) [13].

These diverse databases call for integration among multiple databases to link traditional information with experimental data of current researches in the field of medicinal plants. Currently, “omic” technologies consider genomics, transcriptomics, proteomics, and metabolomics related to a biological sample to understand complex systems underlying the whole process in a non-targeted and non-biased manner.

3 Approaches of Computational Intelligence (CI)

Generally, herbal remedies take into account a combination of medicinal plants which makes the systemization of these remedies difficult due to limited knowledge about the synergistic effect of active ingredients. Moreover, other influencing factors like availability, effective dose, price, etc. should be considered while documenting efficacious treatments. Chemical fingerprinting and characterization of chemical constituents can play a vital role in quality control to achieve an optimum combination of active metabolites for a specific biological activity. Lately, computational methods are utilized to study the process of extraction, isolation, structure prediction, metabolomics, biosynthesis, dereplication, phytochemical library construction, and assessment of their bioactivity (Fig. 1). Multivariate data analysis is addressed by reducing the dimensions of data and portraying the relationship between our observations and calculated parameters (i.e., molecular descriptors) [14].

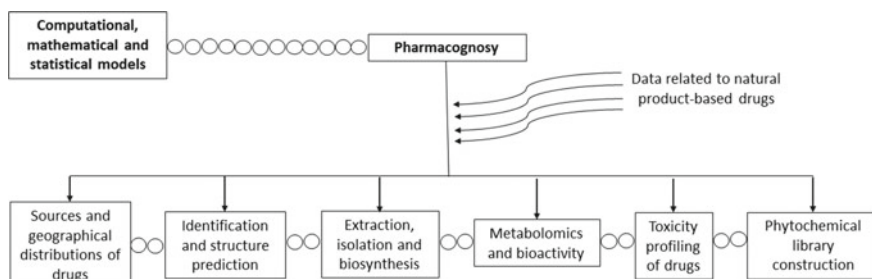


Fig. 1 The chain of interconnection between different sectors of pharmacognosy using bioinformatics

3.1 CI in Extraction, Isolation, and Dereplication

The foremost goal in pharmacognosy is to extract the phytochemicals from plant matrixes, later investigating their bioactivity and mechanism of action. The traditional way of trialing for optimization is tedious and often leads to erroneous results. Computational and mathematical models are applied to correctly value the parameters determining the quality of extraction. This ensures efficient optimization of process parameters to get maximum yield of desired bioactive compounds. Response Surface Methodology (RSM) is a popular model used to design experiments for obtaining an optimum response curve governed by multiple independent variables. Central Composite Design (CCD) or Box-Wilson design, Box-Behnken Design (BBD), Doehlert design, three-level full factorial, fractional factorial, and D-optimal are the commonly used RSM designs to identify and evaluate effects of factors involved in a process [15]. In a research work of extracting polysaccharides (ABP), CCD followed by multiple regression analysis was performed. A thorough analysis of the obtained 3D response surface plot and contour plot predicted the optimized extraction parameters (i.e., the independent variables namely extraction temperature, the ratio of water to raw material, number of extractions, and extraction time) [16]. Another study implemented ultrasonic extraction using red grape skins and combined BBD with high-performance liquid chromatography (HPLC) for maximizing the yield of flavonoids [17].

Recent trends are exploiting machine learning and probabilistic neural networks to classify and predict the occurrence of secondary metabolites leading to commercial drug designing [18]. Virtual screening of databases can also be used to mine therapeutic agents but its potential is restricted due to certain factors like large phytochemical data sets, variations in conformation of receptor molecules due rotatable bonds and complexities in calculating binding affinities [19]. Virtual High Throughput Screening (vHTS) can single out a probable drug from a large library of compounds based on the binding affinity of target receptors to accelerate drug discovery [20].

3.2 CI in Structure Prediction and Bioactivity Assessment

Chemometrics relates multiple parameters of a chemical system and includes various tools for basic statistics, factorial design, multivariate regression, signal processing, hierarchical cluster analysis, calibration curve fitting (using Principal Component Analysis (PCA), Partial least square regression (PLS), soft independent modeling of class analogy (SIMCA), etc.), factor analysis, pattern recognition and neural networks [16]. PCA offers dimensionality reduction of a data set to three subsets of variables namely principal components, scores, and loadings revealing variations among samples. Apart from the dominant usage of PCA in metabolic fingerprinting, computational models successfully discriminated cannabis varieties by performing PCA on the quantitative chemical data generated from gas chromatography flame

ionization of each variety [21]. These approaches proved to be cost-effective in discovering medicinal plants and their associated phytochemical patterns. This has led to relate phytochemistry and medicinal properties of herbs with phylogeny [22]. In a work involving phylogenetic analyses of 32 taxa of Amaryllidaceae tribe Galantheae, 6 taxa of other Eurasian genera of *Amaryllidaceae* and *Phaedranassa dubia* as an outgroup, plants to treat Alzheimer's disease were identified and reported a correlation between AChE inhibitory activity and alkaloid profiles of the plants [23].

Density functional theory (DFT) is a computational quantum mechanical modeling method greatly used for "ab-initio" calculations of molecular properties (like vibrational frequency, atomization energy), ionization potential, orbital energy and reaction paths [14]. The dominant role of bond dissociation energy of OH followed by hydrogen atom transfer (HAT) mechanism in antioxidant activity of a molecule was highlighted in a study to establish the relationship between structural electronic properties and antioxidant potentials of chosen isoflavonoids and isoflavonoid glycosides using DFT [24]. The use of DFT is also seen in identifying hepatoprotective phytochemicals of *Cucumis trigonus Roxb.* and *Cucumis sativus Linn.* by linking physicochemical properties with chemical reactivity and biological activity [15, 25].

Toxicogenomics relates genomics with toxicology to investigate the molecular mechanisms underlying toxicity and designs molecular expression patterns to predict it. Statistical learning methods like Probabilistic Neural Network (PNN), k-Nearest Neighbor (kNN), Support Vector Machine (SVM) and Decision Tree (DT) are employed to evaluate the genotoxicity of chemical compounds [26]. Docking predicts the orientation of a molecule (a candidate ligand) bounded to a receptor molecule forming a stable complex. Quantitative structure-activity relationship (QSAR) and docking studies were investigated on 75 compounds having a plant origin for computer-aided drug design against the dengue virus. QSAR studies reported 11 inhibitory molecules against NS5 protein and 8 inhibitory molecules against NS3 protein whereas docking studies revealed 13 inhibitory molecules against NS5 and three inhibitory molecules against NS3, out of which best-fit molecules were predicted [27]. Molecular docking using software ArgusLab was done to predict the anticancer activity of polytriterpenes namely triterpenes boswellic acid and ursolic acid [14]. In a study, three selected acetylcholinesterase-targeted flavonoids were addressed to Lipinski filter, ADME/Tox screening, molecular docking, and QSAR to predict the anti-Alzheimer's activity of the chosen pyranoflavonoids and the result was compared with in vitro analysis involving Ellman's method of bioactivity staining [28]. Apart from network-based analyses, the use of machine learning and fuzzy logic in Quantitative Composition–Activity Relationship (QCAR) is an initiative in this direction and seems to be more convenient than QSAR as, unlike QSAR it doesn't depend on the structural information of participating molecules.

In a study relating chemical composition and decreasing cholesterol effect of Qi-Xue-Bing-Zhi-Fang, experimental data validated that techniques like multiple linear regression, artificial neural networks (ANNs), and support vector regression showed a difference in the predictive accuracy of the models [29]. Experimental data on agrochemicals were analyzed by ANN using Kohonen based Self Organizing Map

(SOM) to study the accuracy of the model in predicting the agrochemical activity of various plant growth regulators [30]. A research conducted on the occurrences and oxidation patterns of 4700 flavonoids considered them as chemical markers for Asteraceae and taken as the input of SOM to establish phylogenetic relationships among the subfamilies and tribes of Asteraceae (i.e., for plant classification) [21]. A similar study combined Random Forest (RF) with SOM to classify 8411 phytochemicals from 240 herbs of TCM among 10 classes namely aliphatics, alkaloids, simple phenolics, lignans, quinones, polyphenols (flavonoids and tannins), and mono-, sesqui-, di-, and triterpenes (including sterols) [22].

The proteins separated are identified by using mass spectrometry (MS) nowadays for its high-throughput nature in large-scale protein identification than other protein identification practices like Edman degradation microsequencing. However, mass spectrometric data are complicated and identification of a protein from it mandates computational analyses of data. Computer-Aided Structure Elucidation (CASE) is an emerging technique that involves thorough data analysis of (Nuclear Magnetic Resonance) NMR, Mass spectroscopy (MS), and Infrared Radiation (IR) to extract all the possible structural information available from spectral data. Molecular docking simulations (MDSs) prognosticate time-dependent behavior of a system at the molecular level studying the structure, dynamics, and thermodynamics of biological molecules and their complexes from X-ray crystallography and NMR data [14].

The avenues of bioinformatics in solving research problems and examples discussed here reflect the necessity of computer-assisted simulations prior to the design of experiments. Its scope in the field of pharmacognosy is still explored encouraging the implementation of interdisciplinary approaches for a clear representation of scattered, unstructured data into a comprehensible form.

4 Summary

The immense data generated since centuries in the field of pharmacognosy remain scattered and thus limit the essence of strategic analysis of interlinked phenomena. Combining ancient manuscripts of ethnobotany with modern researches and subsequent implementation of data mining techniques forms a basic platform for logical representation of data. Multifold perspectives leading to an exponential growth of data demand for procedures to efficiently manage, integrate, visualize, and analyze data. Computational intelligence bridges the gap between diverse resources already available (from the molecular level to macroscopic characteristics of drugs) marking its significance in computer-aided drug design. Interdisciplinary strategies proved to be promising in solving scientific questions and are still at its infancy allowing scope for thorough researches in the recent future.

References

1. Strohl WR (2000) The role of natural products in a modern drug discovery program. *Drug Discov Today* 5(2):39–41
2. Saito K, Matsuda F (2010) Metabolomics for functional genomics, systems biology, and biotechnology. *Annu Rev Plant Biol* 61:463–489
3. Sarkar, IN (2009) Biodiversity informatics: the emergence of a field. S1
4. Cao C, Wang H, Sui Y (2004) Knowledge modeling and acquisition of traditional Chinese herbal drugs and formulae from text. *Artif Intell Med* 32(1):3–13
5. Samwald M et al (2010) Integrating findings of traditional medicine with modern pharmaceutical research: the potential role of linked open data. *Chin Med* 5(1):43
6. Chen H et al (2007) Towards semantic e-science for traditional Chinese medicine. *BMC Bioinf* 8(3):S6
7. Rhee SY, Dickerson J, Xu D (2006) Bioinformatics and its applications in plant biology. *Annu Rev Plant Biol* 57:335–360
8. Loub WD et al (1985) NAPRALERT: computer handling of natural product research data. *J Chem Inf Comput Sci* 25(2):99–103
9. Sharma V, Neil Sarkar IN (2012) Bioinformatics opportunities for identification and study of medicinal plants. *Brief Bioinf* 14(2):238–250
10. Zeng S et al (2010) Development of a EST dataset and characterization of EST-SSRs in a traditional Chinese medicinal plant, *Epimedium sagittatum* (Sieb. Et Zucc.) Maxim. *BMC Genom* 11(1):94
11. Chen S et al (2011) 454 EST analysis detects genes putatively involved in ginsenoside biosynthesis in *Panax ginseng*. *Plant Cell Rep* 30(9):1593
12. Mochida K et al (2011) Global landscape of a co-expressed gene network in barley and its application to gene discovery in Triticeae crops. *Plant Cell Physiol* 52(5):785–803
13. Rajoka MI et al (2014) Medherb: an interactive bioinformatics database and analysis resource for medicinally important herbs. *Curr Bioinform* 9:23–27
14. Mukherjee PK (ed) (2015) Evidence-based validation of herbal medicine. Elsevier
15. Sarker SD, Nahar L (2018) An introduction to computational phytochemistry. Computational Phytochemistry. Elsevier, pp 1–41
16. Liu J et al (2009) Optimization of polysaccharides (ABP) extraction from the fruiting bodies of *Agaricus blazei* Murill using response surface methodology (RSM). *Carbohydr Polym* 78(4):704–709
17. Tomaz I et al (2016) Multi-response optimisation of ultrasound-assisted extraction for recovery of flavonoids from red grape skins using response surface methodology. *Phytochem Anal* 27(1):13–22
18. Schwabe T et al (2005) Neural networks for secondary metabolites prediction in *Artemisia* genus (Asteraceae). *Internet Electron J Mol Des* 4:9–16
19. Shoichet BK (2004) Virtual screening of chemical libraries. *Nature* 432(7019):862
20. Subramaniam S, Mehrotra M, Gupta D (2008) Virtual high throughput screening (vHTS)—A perspective. *Bioinformation* 3(1):14
21. Fischbeck JT et al (2010) Metabolic fingerprinting of *Cannabis sativa* L., cannabinoids and terpenoids for chemotaxonomic and drug standardization purposes. *Phytochemistry* 71(17–18):2058–2073
22. Paton AJ et al (2004) Phylogeny and evolution of basils and allies (Ocimeae, Labiateae) based on three plastid DNA regions. *Mol Phylogene Evol* 31(1):277–299
23. Larsen MM et al (2010) Using a phylogenetic approach to selection of target plants in drug discovery of acetylcholinesterase inhibiting alkaloids in Amaryllidaceae tribe Galantheae. *Biochem Syst Ecol* 38(5):1026–1034
24. Do Minh T, Nguyen Van T (2019) Isoflavones and isoflavone glycosides: structural-electronic properties and antioxidant relations—A case of DFT study. *J Chem*

25. Gopalakrishnan SB, Kalaiarasi T, Subramanian R (2014) Comparative DFT study of phytochemical constituents of the fruits of *Cucumis trigonus* Roxb. and *Cucumis sativus* Linn. *J Comput Methods Phys*
26. Li H et al (2005) Prediction of genotoxicity of chemical compounds by statistical learning methods. *Chem Res Toxicol* 18(6):1071–1080
27. Mahendran R (2016) In silico QSAR and molecular docking studies of selected medicinal plant compounds against ns5 & ns3 protein of dengue virus: a comparative approach. *Int J Pharma Bio Sci, Sci*
28. Das S et al (2017) Prediction of Anti-Alzheimer's activity of flavonoids targeting acetylcholinesterase in silico. *Phytochem Anal* 28(4):324–331
29. Wang Y, Wang X, Cheng Y (2006) A computational approach to botanical drug design by modeling quantitative composition–activity relationship. *Chem Biol Drug Des* 68(3):166–172
30. Bushkov NA et al (2016) Computational insight into the chemical space of plant growth regulators. *Phytochemistry* 122:254–264

Broadband Annular Ring Patch Antenna



Thingbaijam Rajkumari Chanu, Somokanta Hijam, and Maxon Okramcha

Abstract This paper investigates an annular ring microstrip patch antenna with improved bandwidth from 2.61 to 38.15% at the range of 5.95–8.43 GHz by using pin-sorted using the same feeding point in each design. The obtained frequency range lies within the C-band.

Keywords Annular ring patch antenna · Bandwidth · Gain · Antenna efficiency · Impedance

1 Introduction

Microstrip Patch Antenna (MPA) is a coaxial probe-fed antenna that offers excellent segregation between radiating elements and the feed network, thus yielding a worthy front to back ratio [1]. The major advantage of this MPA is its lightweight, thin outlining, simplicity to fabricate, accordant to mounting surfaces, low cost and capable of being assimilated in active devices [1–3]. Due to these beneficial aspects the MPAs have versatile applications such as in space technology, satellite broadcasting, tracking systems, missiles, GPS monitoring systems, remote sensing and also in aircrafts [2, 3]. A small size circular MPA compared to a rectangular one conveys similar radiation pattern characteristics, thus indicating design compactness [2]. But, this circular MPA has a major drawback due to its narrow bandwidth in the range of 1–5%, which can be overcome by cutting the slots (the mechanism used to load the antenna) in various shapes. Al-Zoubi et al. [4] observed a 12.8% increase in bandwidth for circular MPAs when coupled with annular ring structures while bandwidth enhancement of 34% detected by Chang and Lien [5] using a stacked structured annular ring patch antenna. Another alternative, for improvement of bandwidth, is pin-shorting and is probably the modest technique to expand bandwidth without implementing any structural change in the patch antenna.

T. R. Chanu (✉) · S. Hijam · M. Okramcha
Manipur Technical University, Imphal, India
e-mail: rkchanu19@gmail.com

In this study, the properties of circular MPA and Annular Ring structure MPA are presented and compared. The designs have been simulated using the electromagnetic simulator, Zealand IE3D software.

2 Antenna Design

The conventional circular MPA is considered the reference antenna to compare the results that obtained from the proposed annular ring structure MPA. The geometry of the conventional circular MPA is shown in Fig. 1. The patch has the dimension of radius = 20 mm and is printed on FR4 of dielectric constant, $\epsilon_r = 4.4$ and the thickness of the substrate, $h = 1.6$ mm. A coaxial probe is used to connect the microstrip patch at coordinates and it is made fixed for both the conventional and the proposed MPA. The coordinate of the feeding point is (8, 0).

The geometry of the proposed to extend the bandwidth probe-fed patch antenna with embedding slots and pi-shorted is shown in Fig. 2. Impedance bandwidth of 38.15% can be obtained from the modified geometry. Its main advantage of this structure is that it produces wider bandwidth than the conventional circular patch with a single and simple topology. The feeding point and the shorted-pin coordinates are (-9.6, -8.5) and (9.6, 8.2), respectively.

Fig. 1 Conventional CPA

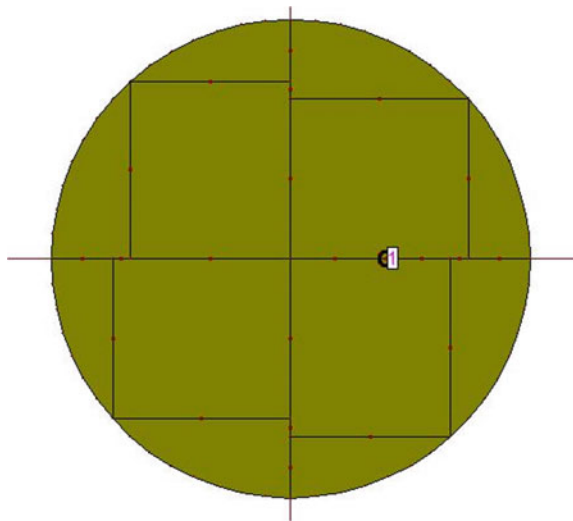
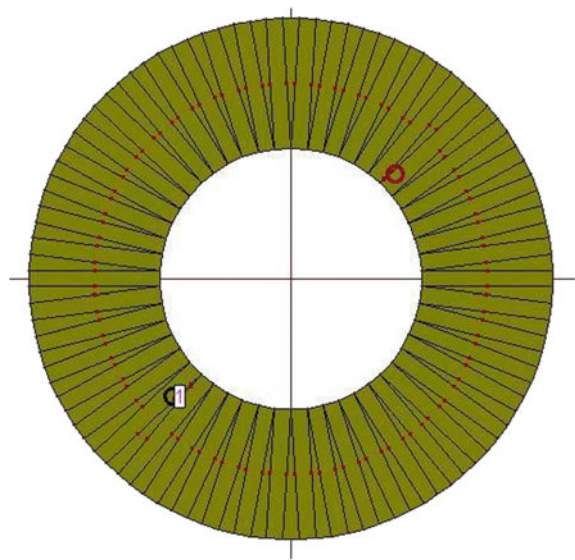


Fig. 2 Pin-shorted annular ring MPA



3 Simulated Results

3.1 Return Loss (S_{11}) and Impedance Bandwidth

The temp the Return Loss (S_{11}) shown in Fig. 3 of the conventional CPA is -21.46 dB

Fig. 3 Return loss (S_{11}) for conventional CPA

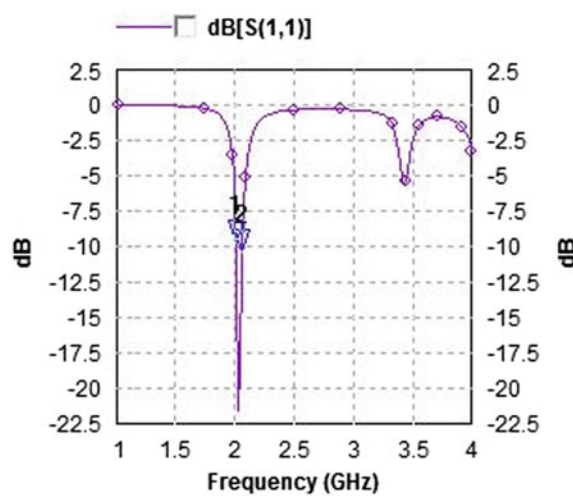
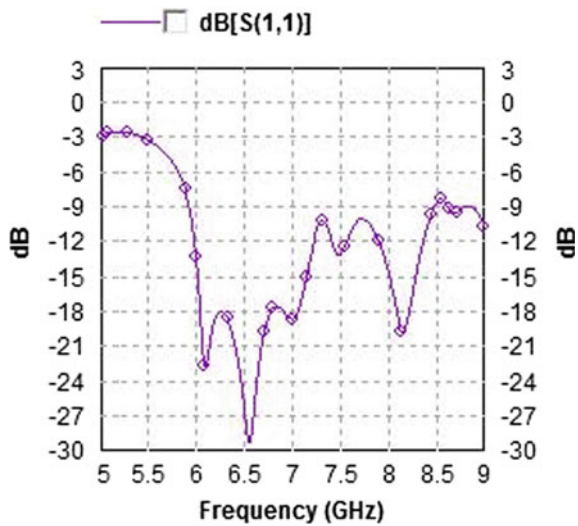


Fig. 4 Return loss (S_{11}) for pin-shorted annular ring MPA



at Resonating frequency at 2.03 GHz and the bandwidth obtained is 2.61%. For Pin-Shorted Annular Ring MPA the Return Loss (S_{11}) is -29.24 dB at 6.5 GHz and the bandwidth obtained is 38.15% which is shown in Fig. 4.

The BW of a patch antenna is calculated from the equation

$$\text{BW} = (f_h - f_l) * 100/f_r$$

where

f_h Higher Frequency at -10 dB Return Loss

f_l Lower Frequency at -10 dB Return Loss

f_r Resonating Frequency of the antenna at the lowest Return Loss.

3.2 Radiation Pattern

The microstrip antenna radiates normal to its patch surface. So, the elevation pattern for $\varphi = 0$ and $\varphi = 90$ degrees are important for the measurement. The simulated E-plane and H-plane pattern, 2D pattern view the conventional CPA and the proposed pin-shorted annular ring MPA are illustrated in Figs. 5 and 6, respectively.

3.3 Other Parameters

Positioning The Comparative study of a conventional CPA and Annular Ring MPA with and without pin-short after the simulation is given in Table 1.

Fig. 5 Radiation pattern for conventional CPA

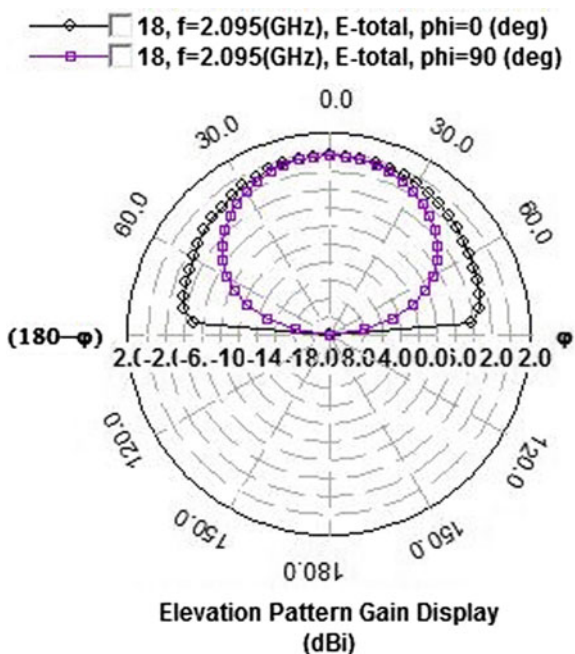


Fig. 6 Radiation pattern for pin-shorted annular ring MPA

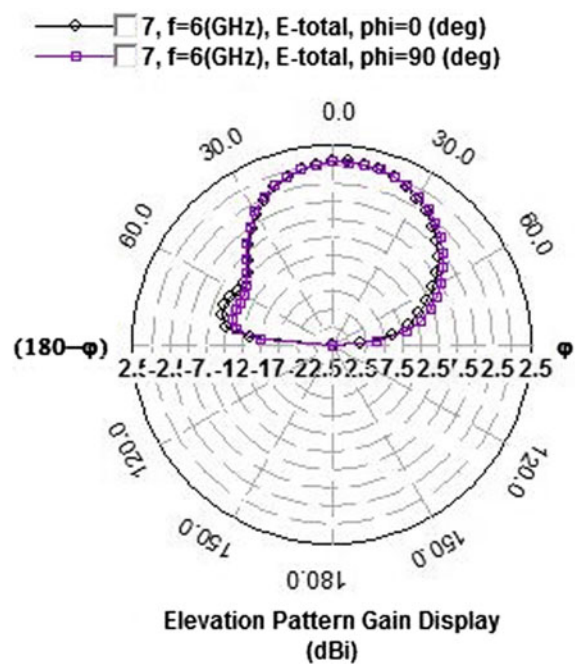


Table 1 Comparative results

S. No.	Parameter	Conventional CPA	Annular ring without pin-short	Annular ring with pin-short
1.	Gain (dBi)	-1.57	6.12	3.1
2.	Antenna efficiency (%)	18.44	39.74	38.15
3.	Impedance (Ω)	$55.3 + 8.5i$	$49.66 - 0.59i$	$47.35 + 2.05i$

4 Conclusion

The Pin-Shorted Annular Patch MPA is observed to have acquired the highest bandwidth and also the bandwidth has increased by 14.6 times than the conventional CPA. Considerable enhancement in gain from -1.57 to 3.1 dBi is detected, while the impedance of both nearly matched. Due to the insertion of a circular slot and pin-shorting technique, most of the parameters improved including a drastic enrichment observed in the Return Loss (S_{11}). These factors led to a change in current density on the circular patch and the path was also increased, hence the resonating frequency of the antenna changes from 2.03 to 6.5 GHz.

Thus, on modifying the conventional CPA the proposed circular annular ring patch antenna provided superior bandwidth of 38.15%. Also, the antenna was detected to remain stable over the entire bandwidth and finally, the most beneficial part is this antenna can be used for C-band applications.

References

1. Surmeli K, Turetkin B. U-slot stacked patched antenna using high and low dielectric constant material combinations in S-Band. Antenna Test and Research Center (ATAM)
2. Garg R, Bhartia P, Bahl I, Ittipiboon A. Microstrip Antenna Design Handbook. Artech House Publication, Boston London
3. Balanis CA. Antenna theory analysis and design, 3rd edn. Wiley
4. Al-Zoubi A, Yang F, Kishik A (2009) A broadband center-fed circular patch ring antenna with a monopole like radiation pattern. IEEE Trans Antennas Propog 57(3)
5. Chang D-C, Lien H-C (2004) The study of wideband single fed cp ring antennas. In: 4th Internal conference on microwave and millimeter wave technology proceedings

Cooperative Spectrum Sensing with Improved Absolute Value Cumulation Detection Based on Additive Laplacian Noise in Cognitive Radio



Khushboo Sinha and Y. N. Trivedi

Abstract In this paper, the performance of cooperative spectrum sensing (CSS) with absolute value cumulation detection (AVCD) based improved energy detector (IED) in additive Laplacian noise environment is proposed. Each cognitive radio (CR) uses improved AVCD (i-AVCD) as a test statistic. Decision from each CR is then forwarded to the fusion center (FC) where the final decision on the presence or absence of primary user (PU) is made. Performance of CSS in the form of receiver operating characteristic (ROC) and the total error probability (P_e) is discussed. Besides this, the optimum value of p , optimum number of CRs (n) out of K CRs, and optimum number of K to achieve a specified target total error probability (sum of false alarm probability and missed detection probability) is also obtained. Results are presented here using Monte Carlo simulations and it is concluded that by carefully choosing the optimum value of p , performance can be improved in case of CSS with OR rule while the same is not necessarily applicable in case of CSS with AND and majority rule (n/K) rule.

Keywords Spectrum sensing · Cooperative spectrum sensing · Cognitive radio · Receiver operating characteristic · Laplacian noise

1 Introduction

Cognitive radio is one of the most promising techniques for the efficient utilization of the available radio frequency spectrum. According to the FCC report [1], a large portion of radio frequency (RF) spectrum remains under-utilized. Motivated by it, the concept of cognitive radio (CR) was first proposed in [2] as a possible solution to the under-utilization of the limited RF spectrum. CR exploits the under-utilized frequency bands by identifying spectrum holes. Spectrum sensing is one of the most

K. Sinha · Y. N. Trivedi

Department of ECE, Nirma University, Ahmedabad, Gujarat, India
e-mail: yogesh.trivedi@nirmauni.ac.in

K. Sinha
e-mail: khusi.success@gmail.com

important functions of CR system where unlicensed user or secondary user (SU) at the CR terminal continuously monitors the spectrum to detect the presence or absence of licensed user or primary user [2]. Most spectrum sensing algorithms such as energy detection (ED) and improved energy detection (IED) [3], the eigenvalue based spectrum sensing [4], the goodness-of-fit based spectrum sensing [5] assumes Gaussian noise (AWGN) into consideration. In real scenarios, the noise may be non-Gaussian. Possible impairments which result in non-Gaussian background noise include artificial impulsive noise, co-channel interference from other PUs, emission from microwave ovens etc. [6]. Further, the previously mentioned detection schemes degrade heavily in non-Gaussian noise.

It has been shown in [6, 7] that Gaussian mixture model, Middleton class A noise model, and Laplace distribution (Laplacian noise) are used for approximately characterizing the statistics of multiple access interference (MAI) in TH-UWB communication system. It has been shown that Laplacian noise accurately model MAI than other noise models [7]. Motivated by it, Laplacian noise has been addressed by advanced test-statistics such as suprathreshold stochastic resonance (SSR) [8], polarity coincidence array (PCA) [9], non-linear function Kernel function [10], soft limiting PCA (SL-PCA) [11], AVCD [12], i-AVCD [13] among others. AVCD is based on fixed fractional lower order statistics (FLOS) while i-AVCD is based on a flexible FLOS strategy with exponent p ranging from 0 to 2 [13].

In this paper, i-AVCD based on the CSS scheme is proposed as a test statistic to improve the detection performance in additive Laplacian noise. Performance of CSS is shown for AND, OR, and majority (n/K) rule. Optimum value of p for all three CSS schemes (AND, OR, majority rule) is derived using simulations. Optimum number of CRs out of a specified number of CRs is also expressed analytically. Performance of CSS schemes for AVCD, i-AVCD, SL-PCA, SSR is compared and it is shown here that by choosing optimum p for CSS based i-AVCD test-statistics, performance can be improved greatly in case of CSS-OR rule but the same is not necessarily true in case of AND (CSS-AND) rule and majority (CSS- n/K) rule.

2 System Model

Let $y = [y_1, y_2, \dots, y_N]$ be a vector of N observations of a PU received at the cognitive terminal where $N \geq 1$. It is assumed that all the received observations are real, independent, and identically distributed (i.i.d.). Each received observations y_i can be represented as

$$\begin{aligned} H_0 : y_i &= w_i \\ H_1 : y_i &= \sqrt{\gamma} h x_i + w_i, \end{aligned} \quad (1)$$

where h is the channel coefficient and it is assumed to be constant ($h = 1$), $i = 1, 2, \dots, N$, γ denotes the average signal-to-noise ratio (SNR), w_i is Laplacian noise which

follows Laplace distribution with mean 0 and variance $2b^2$ i.e., $w_i \sim L(0, b)$, b is the scale parameter of Laplace distribution, x_i is BPSK PU signal, i.e., $x_i \in \{-1, 1\}$ p is the exponent (power) of received samples at the cognitive terminal (SU).

2.1 Decision Statistics

i-AVCD based decision rule can be expressed as

$$Z = \sum_{i=1}^N |y_i|^p. \quad (2)$$

Decision statistics of i-AVCD can be expressed as

$$\begin{aligned} H_0 : Z < \lambda, & \text{ PU absent,} \\ H_1 : Z \geq \lambda, & \text{ PU present,} \end{aligned}$$

where γ is the detection threshold of AVCD. It is should be noted that $p = 1$ denotes AVCD. Here, CSS scheme is applied where multiple CRs are present in a cognitive radio system. Each CR makes independent binary decisions in the form of 0 or 1. Then each CR forwards their independent binary decisions (hard decisions) to the fusion center (FC). FC then combines the received decisions to determine the presence or absence of PU as shown below:

$$S = \sum_{i=1}^K s_i, \quad (3)$$

where K is the total number of CRs present, S is the sum of independent binary decisions from each CR. s_i is the hard decision made by each CR based on i-AVCD test-statistics. The hypotheses H_0 (null hypothesis) and H_1 (alternative hypothesis) at the FC using the CSS scheme can be expressed as

$$\begin{aligned} H_0 : S < n, & \text{ PU absent,} \\ H_1 : S \geq n, & \text{ PU present} \end{aligned}$$

where $n < K$ denotes majority rule, $n = 1$ denotes OR rule and $n = K$ denotes AND rule.

3 Detection Probability and False Alarm Probability

Probability density function (pdf) of received samples y_i at each CR under hypotheses H_0 and H_1 can be expressed as

$$f_{|y_i|H_0}(x) = \frac{1}{2b} e^{-\frac{|x|}{b}} \quad (4)$$

$$f_{|y_i|H_1}(x) = \frac{1}{4b} \left[e^{-\frac{|x-\sqrt{\gamma}|}{b}} + e^{-\frac{|x+\sqrt{\gamma}|}{b}} \right]. \quad (5)$$

Using (4) $f_{|y_i|H_0}(x)$ can be expressed as [13]

$$\begin{aligned} f_{|y_i|H_0}(x) &= \frac{1}{b} e^{-|b^{-1}x|}, \\ &= 0, x < 0. \end{aligned} \quad (6)$$

Mean $E[|y_i|^p | H_0]$ and variance $D[|y_i|^p | H_0]$ can be expressed as [13]

$$E[|y_i|^p | H_0] = b^p \Gamma(p+1) \quad (7)$$

$$D[|y_i|^p | H_0] = b^{2p} \Gamma(2p+1) - b^{2p} \Gamma^2(p+1). \quad (8)$$

False alarm probability (P_F) at each CR can be expressed as

$$P_F = Q \left(\frac{\lambda - N \times E[|y_i|^p | H_0]}{\sqrt{N \times D[|y_i|^p | H_0]}} \right). \quad (9)$$

Similarly, detection probability (P_D) at each CR can be expressed as

$$P_D = Q \left(\frac{\lambda - N \times E[|y_i|^p | H_1]}{\sqrt{N \times D[|y_i|^p | H_1]}} \right). \quad (10)$$

Similarly, expressions of $E[|y_i|^p | H_1]$ and $D[|y_i|^p | H_1]$ can be derived [13] similarly as done in case of P_F .

Finally, at FC, detection probability (Q_D) and false alarm probability (Q_F) can be expressed as [14]

$$Q_F = \sum_{l=n}^K \binom{K}{l} P_F^l (1 - P_F)^{K-l} \quad (11)$$

$$Q_D = \sum_{l=n}^K \binom{K}{l} P_D^l (1 - P_D)^{K-l} \quad (12)$$

Total error probability (P_e) at the FC can be expressed as

$$P_e = Q_m + Q_F, \quad (13)$$

where $Q_m = 1 - Q_D$ is the missed detection probability at the FC.

3.1 Optimum Values of p , N , and K

Optimum values of $p(p^*)$ at each CR can be obtained by partially differentiating P_D w.r.t. p and equating it to zero.

$$p^* = \arg \max_p (P_D) \quad (14)$$

Similarly, optimum values of n can be obtained as

$$n^* = \arg \min_n (P_e) = \min \left(K, \left\lceil \frac{K}{1 + \alpha} \right\rceil \right) \quad (15)$$

where $\alpha = \frac{\ln(\frac{P_F}{1 - P_m})}{\ln(\frac{P_m}{1 - P_F})}$ and $\lceil . \rceil$ denotes ceiling function.

Thus, for specified values of K , and P_m , n^* can be easily found out.

4 Simulation Results

Figure 1 shows P_D versus SNR (in dB) comparison of i-AVCD with ED and AVCD using CSS- n/K (majority) rule at SNR of -4 dB, $N = 30$ and $P_F = 0.1$. It can be seen clearly that at low values of SNR, i-AVCD with n/K rule underperform the test-statistics without n/K rule. However, as SNR increases, n/K rule improves the performance of i-AVCD. Figure 2 shows P_D versus SNR comparison of i-AVCD using CSS-AND rule. It is clear from figure that AND rule of CSS doesn't perform better than that without AND rule in case of the test-statistics ED, AVCD and i-AVCD. Figure 3 shows P_D versus SNR comparison of i-AVCD using CSS-OR rule. It is clear from figure that OR rule of CSS improves the performance of ED, AVCD and i-AVCD significantly. Figure 4 shows optimum p of i-AVCD with CSS-OR rule for different P_F . It can be clearly seen from the figure that optimum $p(p^*)$ increases with decrease in P_F . Values p^* at different values of P_F and at $\gamma = -4$ dB are given

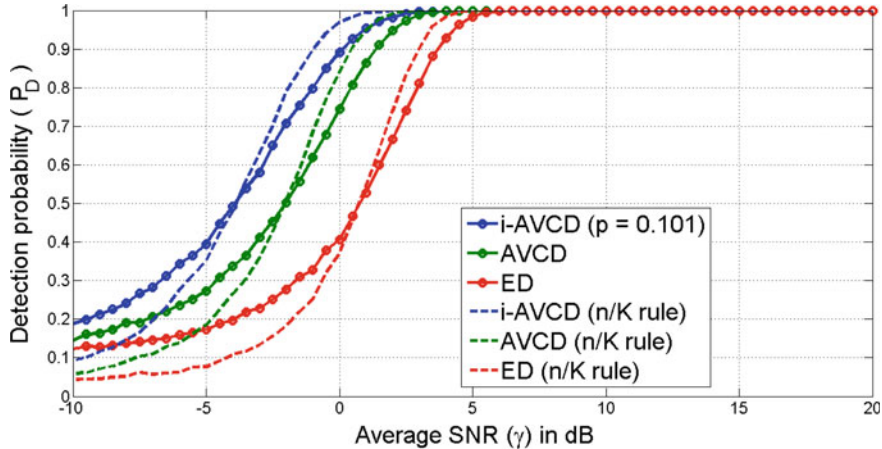


Fig. 1 Performance comparison of i-AVCD, AVCD and ED with CSS (n/K rule) for $n = 2$, $K = 3$ at $\gamma = -4$ dB, $N = 30$

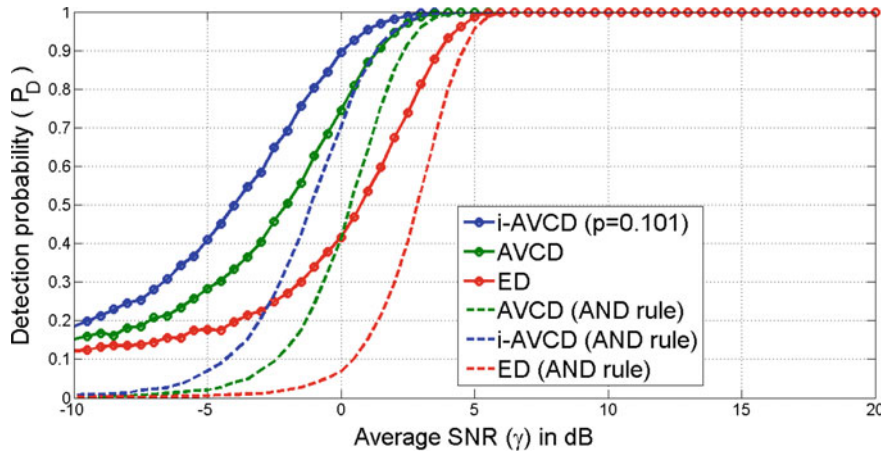


Fig. 2 Performance comparison of i-AVCD, AVCD and ED with CSS (AND rule) for $n = 3$, $K = 3$ at $\gamma = -4$ dB, $N = 30$

in Table 1. Figure 5 shows the optimum values of K comparison to achieve a certain target error probability for different P_F . From the simulation result, it is found that to achieve total error probability of 0.001739, optimum values of CR are 30 out of total 60 taken CRs. Similarly, to achieve an error target of 0.02311, only 15 CRs will be sufficient out of 60 CRs. Figure 6 shows performance comparison of i-AVCD with SL-PCA, SSR, ED, AVCD using CSS-OR rule at $P_F = 0.1$ and $N = 30$. i-AVCD at $p^* = 0.101$ shows better performance than all the mentioned test-statistics at optimum p . However, as p increases ($p = 1.5$), performance of i-AVCD decreases.

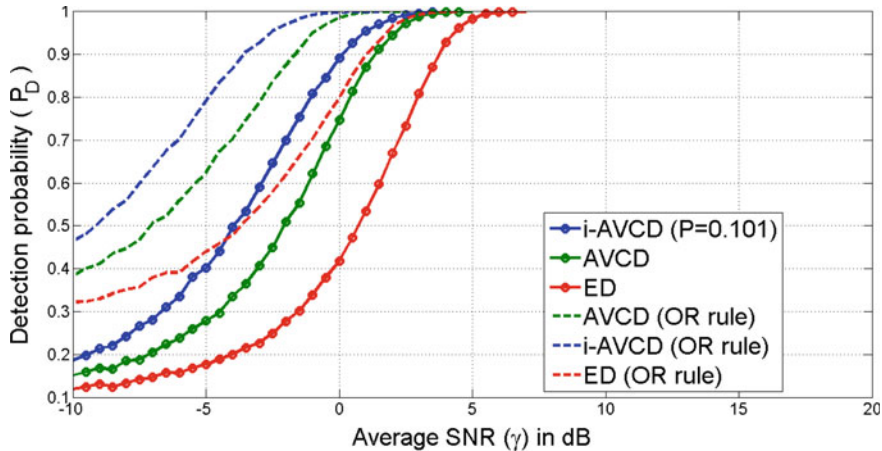


Fig. 3 Performance comparison of i-AVCD, AVCD and ED with CSS (OR rule) for $n = 1$, $K = 3$ at $\gamma = -4$ dB, $N = 30$

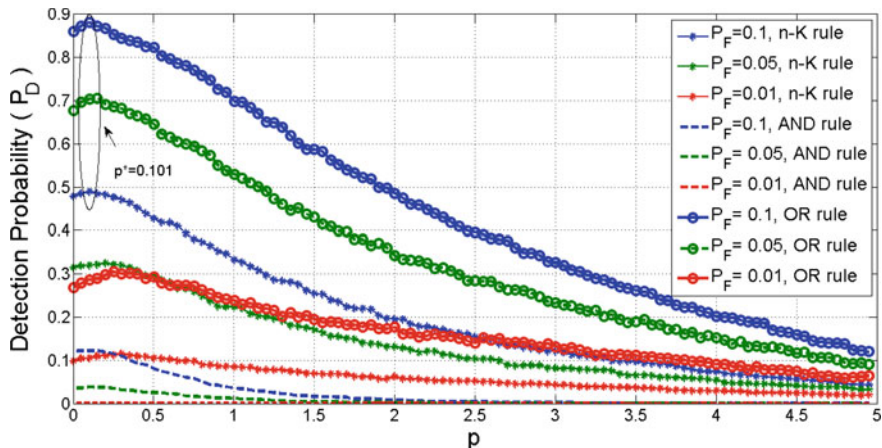


Fig. 4 P_D versus p at $\gamma = -4$ dB and $N = 30$ at different values of P_F showing optimum p

Table 1 Optimum values of p of i-AVCD with CSS at $N = 30$ and $\gamma = -4$ dB

P_F	Optimum $p(p^*)$			
	i-AVCD	i-AVCD with CSS-OR rule	i-AVCD with CSS-AND rule	i-AVCD with CSS-n/K rule
0.1	0.101	0.101	0.101	0.101
0.05	0.151	0.151	0.101	0.201
0.01	0.251	0.251	0.101	0.301

*denotes optimum value

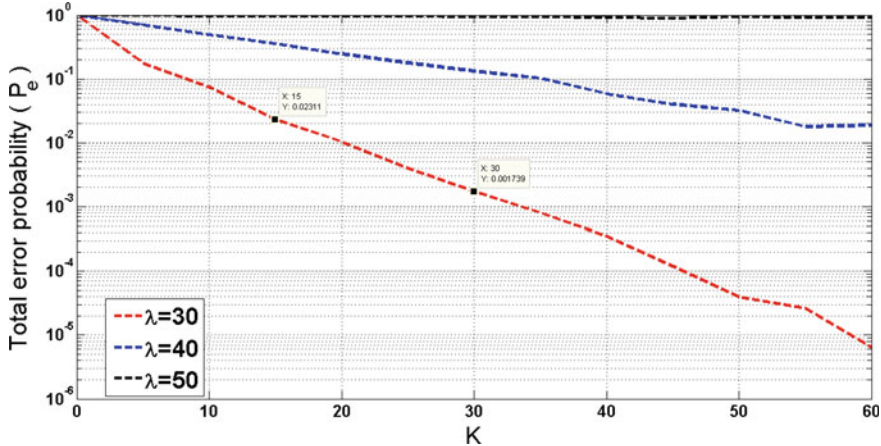


Fig. 5 P_e versus K at $\gamma = -4$ dB and $N = 30$ with i-AVCD at $p = 1$ for different detection threshold (λ)

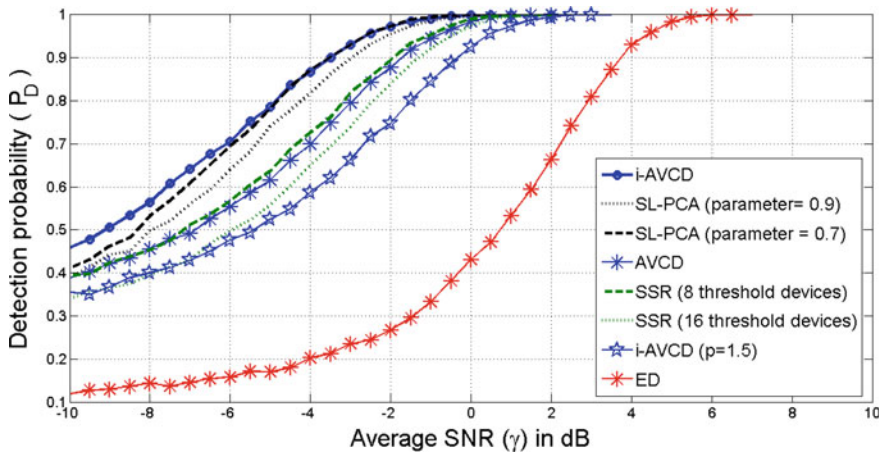


Fig. 6 Performance comparison of i-AVCD with other test-statistics using CSS scheme based on OR rule at $N = 30$ and $P_F = 0.1$.

Figure 7 shows receiver operating characteristic (ROC) plot of i-AVCD, AVCD, and ED at $N = 50$ and $\gamma = -4$ dB at different values of p . ROC improves as p decreases. Further, both simulations and analytical results closely match for the three compared test-statistics in the figure.

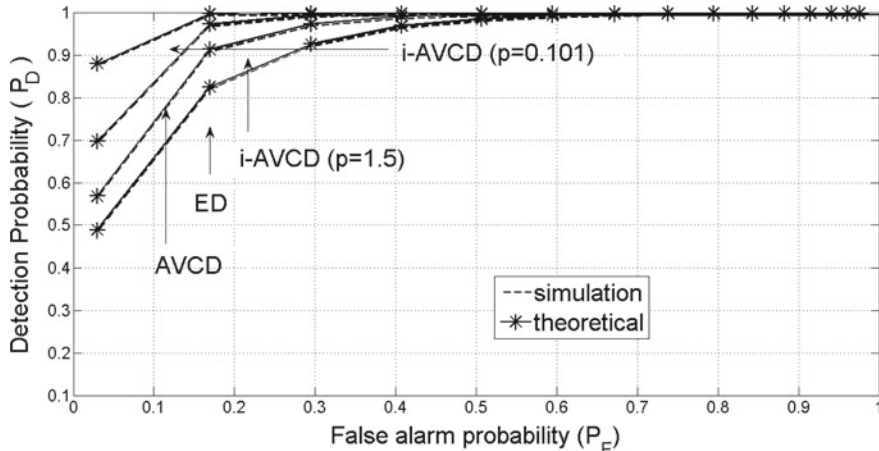


Fig. 7 ROC comparison of i-AVCD with other test-statistics using CSS scheme based on OR rule at $\gamma = -4$ dB, $N = 50$

5 Conclusion

Cooperative spectrum sensing with i-AVCD is discussed using different CSS rules: AND, OR, and majority (n/K) rule. It is concluded that optimum p increases with a decrease in P_F . Further, it is also concluded that OR rule shows better performance over a wide SNR range as compared to AND rule and majority rule. n/K rule also works well but shows improved performance over only a limited SNR range. i-AVCD is compared with ED, AVCD, SSR, SL-PCA and it is concluded that by carefully selecting optimum p , detection performance increases over a wide SNR range, as compared with other test-statistics in case of CSS-OR rule.

References

1. Federal Communications Communication (2004) Notice of proposed rule making. Unlicensed operation in the TV broadcast band. ET Docket No. 04-186 (FCC 04 113)
2. Mitola J, Maguire GQ (1999) Cognitive radio: making software radio more personal. IEEE Pers. Commun. 6(4):13–18
3. Chen Y (2010) Improved energy detector for random signals in Gaussian noise. IEEE Trans Wirel Commun 9(2):558–563
4. Liu C, Wang J, Liu X, Liang Y (2019) Maximum eigen value-based goodness-of-fit detection for spectrum sensing in cognitive radio. IEEE Trans Veh Technol 68(8):7747–7760
5. Trivedi YN, Patel DK (2015) Goodness-of-fit-based non-parametric sensing under Middleton noise for cognitive radio. Electron Lett 51(5):419–421
6. Shao M, Nikias CL (1993) Signal processing with fractional lower order moments: stable processes and their applications. Proc IEEE 81(7):986–1010
7. Hu B, Beaulieu NC (2008) On characterizing multiple access interference in TH-UWB systems with impulsive noise models. In: IEEE radio and wireless symposium, pp 879–882

8. Li Q, Li Z (2014) A novel sequential spectrum sensing method in cognitive radio using suprathreshold stochastic resonance. *IEEE Trans Veh Technol* 63(4):1717–1725
9. Wimalajeewa T, Varshney PK (2011) Polarity-coincidence-array based spectrum sensing for multiple antenna cognitive radios in the presence of non-Gaussian noise. *IEEE Trans Wirel Commun* 10(7):2362–2371
10. Magoosian A, Member S, Abouei J, Member S, Konstantinos N (2015) An Accurate kernelized energy detection in gaussian and non-Gaussian/impulsive noises. *IEEE Trans Signal Process* 63(21):5621–5636
11. Karimzadeh M, Rabiei AM, Olfat A (2017) Soft-limited polarity coincidence array spectrum sensing in the presence of non-Gaussian noise. *IEEE Trans Veh Technol* 66(2):1418–1427
12. Ye Y, Li G, Zhou F, Zhang H (2018) Performance of spectrum sensing based on absolute value cumulation in Laplacian noise. In: IEEE vehicular technology conference, pp 1–5
13. Ye Y, Li Y, Zhou F (2019) Improved energy detection with Laplacian noise in cognitive radio. *IEEE Syst J* 13(1):18–29
14. Zhang W, Mallik RK, Lataief KB (2009) Optimization of cooperative spectrum sensing with energy detection in cognitive radio networks. *IEEE Trans Wirel Commun* 8(12):5761–5766

Solar Power Plant Site Selection: A Systematic Literature Review on MCDM Techniques Used



Rajkumari Malemnganbi and Benjamin A. Shimray

Abstract Site Selection is a crucial step in installing Solar Power Plant (SPP) as it is determined by a set of quantitative and qualitative factors, which are vague in nature. In this review, various suggestions for site location of Photovoltaic Power System (PVPS) are studied. The solar power plants are mainly installed in remote regions where solar radiation is high. But these regions are far from the generation site and will face problems in transmission and distribution. Thus, various criteria/factors have to be considered in the site selection. Factors like solar radiation, location, climate, orography, environment, public acceptance have to be taken into account for optimal site selection. Every form of electricity generation has its strengths and weakness. The main objective in the site selection process is finding the optimum site satisfying the desired conditions given by the selection criteria. This review suggests how to define and classify particular criteria considered for Solar Photo Voltaic (PV) farm siting. The best criteria among all the other evaluations are obtained from the multi-criteria evaluation which gives scope for various applications. The aim of this paper is to define how the ideal locations for solar PV are selected using various Multi-Criteria Decision Making (MCDM) techniques. A large scale PV-project should generate at least 5 MW power. In site suitability, India ranks third next to China and Spain.

Keywords Solar Power Plant (SPP) · Photovoltaic Power System (PVPS) · Multi-criteria Decision-Making (MCDM) · Geographical Information System (GIS) · Site selection · Analytical Hierarchy Process (AHP)

R. Malemnganbi · B. A. Shimray (✉)

Department of Electrical Engineering, National Institute of Technology Manipur,
Imphal, India

e-mail: benjaminshimray@ieee.org

R. Malemnganbi

e-mail: rajkumarimalemnganbi@gmail.com

1 Introduction

In developing countries like India, the increasing need for electricity has become a major issue. At present many countries regarded fossil as the main source of energy. Because of its massive use, fossil fuels like natural gas, coal, and petroleum are getting depleted. Also, the burning of fossil fuels causes “**Green House Effect**” or “**Global warming**”. Thus, this issue and the rising demand for electricity leads to global effort. To meet the continuous requirement of electricity, we need to focus on other alternative renewable sources of RES. In many developed countries, we see that the use of renewable energy power supplies has decreased the global warming issue. Solar energy is one of the alternatives to a Non-Renewable source of energy that generates electric power from solar energy. Solar energy is found abundantly and is pollution-free. Recently solar energy plays have been playing an important role in the generation of electricity. In spite of all the advantages, as solar energy is uncertain the output characteristics of PV are non-linear and thus become complicated when the entire PV cell does not get uniform radiation and leading to more than one peaks.

India is a developing country and the need for energy has been increasing day by day. Since our country is developing, the demand will rise by approximately 10% on an installed base of 200 GW. We need to find other sources of electricity generation and renewable sources of energy which can fill this gap. Renewable sources of energy such as wind, solar, hydro, biomass, etc. play an important role to overcome the shortfall of energy. We need not set up solar PV in large utility-scale. Installing solar PV on the rooftop is amenable. By considering the solar resource data in the country, we can install solar PV on our commercial and residential rooftops for electricity production on a distributed basis. The energy generated from solar PV serves as the power source for homes and offices. It can also be used for electrification in off-grid sectors for rural India. As soon as this kind of project is set up, one can start distributing to other countries. There are entrepreneurs working on such models. India is considered one of the best suitable sites as renewable sources like sunlight; wind, hydro, and biomass are found in abundance. People have also become aware of the advantages of renewable energy. India is one of the countries that has the world’s largest scheme for renewable energy. The challenge for installing solar PVPP is the probable site selection for the annual production of electricity with financial viability.

The solar energy that requires massive areas of utilization, serves as one of the best sources of energy with low-density power supply among all renewable sources. Moreover, PV technology has the potential to deploy vast areas of land where the scope of global radiation is very high per year. Though solar power development has emerged as one of the leading renewable options for meeting demands in developing countries like India and China, one of the hindrances is its variation and unevenness of solar radiation which differs from site to site. Hence installing a PV project requires an in-depth analysis of the sites where the plant is to be located. Thus, a question arises, how one can select the optimal site for utility-size Solar PV? An extensive analysis is a foremost step towards an economical and well-performed solar project.

Therefore keeping a keen knowledge of the probable sites is a tactical breakthrough for the prediction of the annual power plant output and economic feasibility.

Geographical Information system (GIS) is software used to visualize, analyze, create, manage edit, and store the geographic data. Integrating GIS with various decision support systems will benefit to determine the ideal location for the solar power plant. Subsequently refining the performance of the solar PV project plays a vibrant role in maximizing the output power generated which will help in reducing the cost. Solar irradiation is considered one of the most important criteria while temperature plays a vital role in the PV performance. Locating the plant nearby ample consumer is one key factor that should be taken into account. From a location point of view, India ranks third next to China and Spain.

Shimray et al. [1] proposed an MLP neural network trained by the Genetic Algorithm for site selection of large Hydro Power Plant. In this paper, the author selected 19 criteria for analysis as a case study for site locating in Manipur, Arunachal Pradesh, Sikkim, and Himachal Pradesh. A paper on MLP-GA integrated with fuzzy is also presented for the four sites mentioned above. Criteria such as hostility, water quality, air quality, environmental conditions are considered [2].

2 Techniques Used in Solar Power Plant Site Selection

Though it is well-known that considering various factors in the decision criteria can enhance site selection, using the MCDM technique can ease site selection for an optimal power Plant. The various methods used may vary in the decision maker's goal and the data required and their respective characteristics. Table 1 gives detailed studies about different techniques used in site selection of solar PV plants. Various techniques used by different researchers are also described in the following section.

Hong Fang proposed TOPSIS based on variable precision rough set theory and prospect theory for selecting a suitable solar power Plant site. In this paper, a case study is also portrayed for four sites. Here four experts provide the crisp importance of the criteria chosen such as solar radiation, location, orography, policy support, environmental influence, etc. The weights of the criteria and the ranking order of the four sites are obtained by applying TOPSIS [33].

AHP is a decision an estimation method used for pairwise comparisons of specified criteria. Saaty [34] developed this method to measure vague factors relating to uncertainties. The comparative scale judgment helps in prioritizing an element over the other by taking the criteria into account. Thus, to make this choice, and to create prioritizing the following steps are carried out. The first step is to define the objectives and problems. Second, the decision hierarchy is created from the top, till the lowest level. The next step is constructing a pairwise comparison matrix. Now for every component, the priorities are used for every comparison done. Lastly, the weighted values for each comparison level are added and the overall priority is taken. The process of adding and weighing is done until the last level. Various application of AHP is studied. There are various ways to apply AHP. Kohara and Sugiyama

Table 1 Methods for site Selection

S. No.	Methods applied	Types of RES	Plant location	Grid	References
1	AHP	PV	South, Morocco	On	[3]
2	AHP-fuzzy TOPSIS	PV	India	On	[4]
3	Binary PSO	PV	Jaen, Spain	On	[5]
4	Grey cumulative	PV	Northwest, China	On	[6]
5	WLC	PV	Southwest, USA	On	[7]
6	Simulation scenarios	PV	India	On	[8]
7	AHP	PV	Ismailia, Egypt	On	[9]
8	GIS-join	PV-wind-biomass	United States	On	[10]
9	GIS-overlay	PV-hydro-bioenergy	Cumbria, United States	On	[11]
10	AHP	Solar-wind	China	On	[12]
11	GIS-NEAR	Solar-wind-hydro diesel	Nigeria	On	[13]
12	GIS-solar irradiation	Solar farms	Brazil	None	[14]
13	GIS-multiply	PV-wind-biomass	Appalachian Mountains, United States	On	[15]
14	WLC	PV	EU-28	On	[16]
15	GIS—Solar irradiation	Solar-wind-biomass-hydro	Salta, Argentina	None	[17]
16	GIS-intersect	PV	Rajasthan, India	On	[18]
17	AHP	Solar farms	Konya, Turkey	On	[19]
18	GIS—Solar irradiation	PV	Andalusia, Spain	On	[20]
19	Axiomatic design	PV	Turkey	On	[21]
20	GIS—Solar irradiation	Solar-wind-biomass	Kujawsko, Poland	On	[22]
21	FAHP	PV	Iran	On	[23]
22	WLC	PV, CSP-wind	Afghanistan	On	[24]
23	AHP	PV	Ismailia, Egypt	On	[25]
24	GIS-overlay	PV	Tibet, China	On	[26]

(continued)

Table 1 (continued)

S. No.	Methods applied	Types of RES	Plant location	Grid	References
25	FUZZY ANP and VIKOR	PV	Taiwan	Off	[27]
26	AHP	Solar-wind-geothermal	Indonesia	None	[28]
27	WLC	PV	Southwest, USA	On	[29]
28	NASA—Solar irradiation	PV	India	None	[30]
29	GIS-join	Solar farms	United Arab Emirates	On	[31]
30	AHP-fuzzy-WLC	Solar farms	Isfahan, Iran	On	[32]

(35) propose an AHP tool to establish countermeasure practices in the incident of a tragedy. Moreover, AHP can be improved by using optimization methods to specify an objective. For example, Sumabat et al. [36] presented the usage of AHP integrated with multiple response surface analysis to design a tool with reference to customer product property and preferences.

GIS-AHP application is one of the commonly used methods for incorporating GIS with other decision methods. AHP is considered a flexible and robust method that can solve complex decision problems [37].

Hassan Z. et al. used GIS-AHP application for weighing and computing the land suitability index (LSI) and estimate the probable site in Saudi Arabia. GIS integrated with MCDM techniques is one of the most used techniques that deal with rich topography information data and is one of the best methods to introduce the best sites for PVPP. Tahri et al. applied GIS integrated with AHP in evaluating solar farm sites. Jun et al. evaluated seven locations of solar-wind integrated power stations using elimination and choice transmission reality (ELECTRE-II) and concluded that the result had more improved exactness to the related research findings. Chang established a goal programming model for selecting suitable sites for various types of RE facilities. Ingudam et al. proposed an optimization process which provides electrification to rural areas of a particular state [38, 39]. Maleki et al. develop a framework that integrates GIS and artificial bee swarm optimization in determining the most probable sites for PVPP. Though the above-mentioned methods help ease the investors in selecting the most probable optimal locations in implementing the power plant projects, they are not able to deal with the uncertainties and vague environment as they use crisp values in signifying the unclear judgment of DM.

To manipulate the subjectivity of judgment and the vagueness, Fuzzy theory has been in use recently. Fuzzy theory permits the DM to integrate imperfect and unidentifiable information in the decision model. Lee et al. provided multi-criteria decision-making approach that incorporates interpretive structural modeling, Fuzzy Analytical Network Process and VIKOR for selecting the PVPP locations. Zoghi et al. optimized PV site selection using fuzzy Logic, MCDM process, and weighted linear

combination. Sanchez-Lazano proposed a fuzzy TOPSIS method in evaluating the site for PVPP to measure DM imprecision to enhance the subjective evaluations in selecting the Power plant site. In this context theory of Fuzzy set is appropriate as well as effective. However, in fuzzy, membership function and data distribution are predetermined, due to which it fails to determine the spontaneous changes of various decision-makers' suggestions. Rough Set Theory is also a method that uses rough intervals to define the uncertainties. Rough set theory is more objective and flexible than the Fuzzy set theory as prior information is not required. Because of its various advantages, rough set theory is used in various applications for solving vagueness like sustainable supplier selection, product service recommendation, etc.

3 Site Selection Criteria

While developing a utility-scale solar power plant, various factors or criteria have to be taken care of in selecting the site location. Probable Site Selection of Photovoltaic Power Plant (PVPP) is a complex MCDM process, as the required site has to be climatically and geographically acceptable. It must also have the highest generation potentials. Thus, decision-makers must have enough information to assess sites under different criteria, such as sunshine duration, sunshine radiation, soil, and transportation. The decision criteria reviewed here are deprived based on the existing literature and accessibility to the geo-referenced database. The factors considered are mostly related to climate and location. Solar irradiation is considered one of the most important decision criteria. Public acceptance is also one of the important factors that have to be considered. Various criteria used are shown in Table 2.

A large amount of solar energy will help in the generation of more electricity from the existing sources. Figure 1 shows the most used criteria that have been used in the selected power plant. Installing PVPP near the substation and power lines will enhance the accessibility to the grid. New transmission line need not be established, thereby reducing the overall cost and the power loss in the distribution and transmission line.

Air temperature is an important factor that determines the performance of the PV system. The air surrounding the PV system will cool the PV arrays and inverters' connectivity thereby improving the efficiency of the PV system. In order to avoid not in my backyard (NIMBY) opposition and its negative impact on the environment of urban areas, the most effective location for installing a Solar Power Plant is far away from cities for the development of Renewable energy. Some site selection criteria are reviewed under Table 2

From Fig. 1, it is known that solar radiation is one of the most important or used criteria by various DM followed by distance to power lines, main roads, and temperature.

Table 2 Criteria for site selection

Solar radiation	It is the energy emitted by the sun. The more energy it is emitted, higher is the potential for generation of power from the PVPP
Sunshine hour	It measures the duration of sunshine in a particular site in a given time period. Longer the duration higher will be the power generation
Temperature	The Plant Site has to be of suitable temperature for the panel. Higher the temperature, lower the efficiency
Wind speed	Wind can cause damage to the panel from dust or matters. On the contrary, the distribution of heat from the panel makes the panel's performance higher
Rainfall	Sites with high rainfall can deteriorate the efficiency of the solar panels
Distance to faults	The site near the fault line has a higher risk of earthquake thus resulting in damage of the plant
Distance to roads	Proximity to roadways can reduce the operational cost
Distance to urban and rural areas	Sites near rural and urban areas cause environmental problems and have a negative impact on the future development of the residential areas
Slope	Higher slope results in high investment and operational cost
Elevation	Higher areas have more potential than lowlands for solar energy. On the Contrary transportation and construction of the plant is difficult with the increase in altitude
Land availability	A PVPP requires a wide range of areas
Solar panel types	Monocrystalline cell is the most used cell because it gives the highest efficiency
Public acceptance	A site where the attitude of the public is positive is considered
Policy	Relevant law has to be considered to construct a solar power plant in that particular area

4 Unsuitable Sites and Restriction Factors

This stage is for eliminating the non-feasible sites that have barriers to the development and installation of the PVPP. Table 3 reviews the unsuitable or restricted factors for the solar power plant installation.

Figure 2 represents the most common restriction applied in the study of the most suitable site of PVPP. From the figure and the table above, it can be predicted that protected land, airport military zones, urban land, cultural heritage, higher slope areas, are the most omitted areas. Areas with high slope are excluded for their low financial viability. Railway network is also excluded because of traffic issues, more buildings in addition to a high-density population (Table 4).

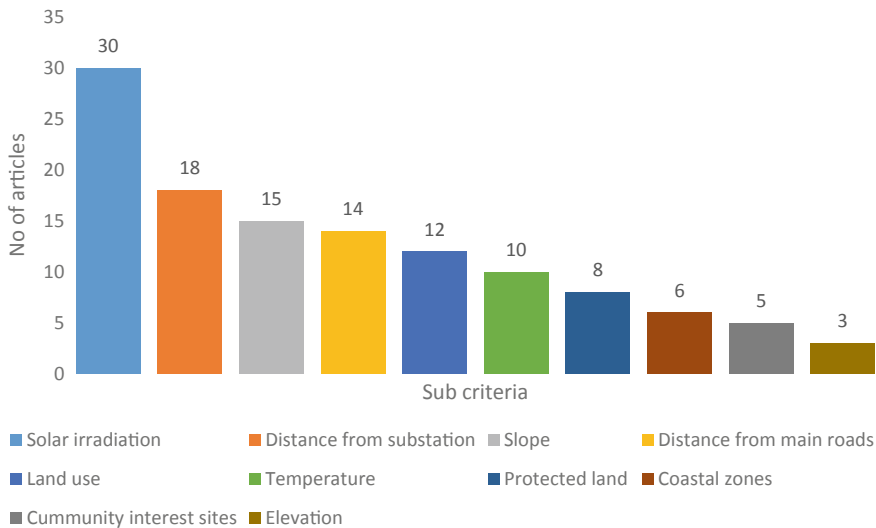
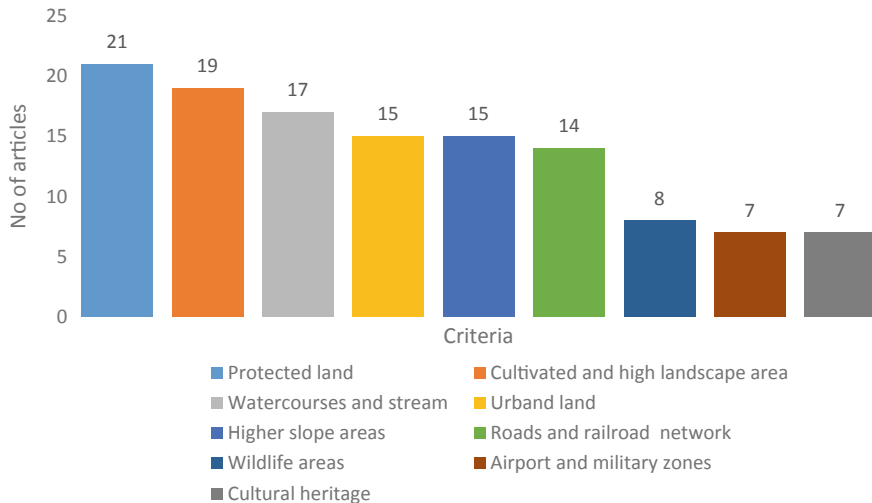


Fig. 1 Various selection factors for PVPP

Table 3 Restriction factors

S. No.	Limitations	References
1	The land aspect	[5, 6]
2	Dams	[28, 31]
3	Elevation	[23, 32]
4	Roads and railroad network	[20, 22, 32]
5	Airport and military zones	[32]
6	Watercourses and streams	[20, 22, 23]
7	Soft soil	[14, 15]
8	Natural disaster areas	[30, 37]
9	Cultural heritage	[3, 9]
10	Visual impact	[24, 35]
11	Mountains	[26, 29]
12	Water infrastructure	[17, 21]
13	Coastal zones	[22, 23]
14	Sand areas and sand dunes	[3, 33]
15	Community interest sites	[8, 30]
16	Protected land	[13, 17]
17	Biological significant areas	[23, 28]
18	Urban lands	[29, 31]
19	Paleontological sites	[17, 21]
20	Cultivated and high landscape	[17, 18, 29, 32]

**Fig. 2** Restriction factors**Table 4** Criteria for the selection of solar power plants

Factors	Sub-factors	References
Location	Distance from urban areas Distance from main roads Distance from substations Population density Distance from rivers	[4, 7, 10, 14, 16, 20, 30]
Climatic condition	Solar radiation Temperature Humidity Clearness index Annual dusty days	[4, 8, 9, 11, 19, 21]
Environmental factors	Land use Agrological capacity Emission level	[7, 8, 10, 12, 17, 19, 32]
Geographical feature	Slope Orientation Elevation Plot area	[5, 8, 11, 12, 19, 23, 29]
Economic condition	Energy saving Land cost Transmission losses Cost of energy Construction cost Energy generation Initial investment Demand for electricity	[3, 4, 7, 9, 11, 26, 29]

5 Conclusions

This paper reviews an in-depth assessment of various studies for a utility-scale PV power plant. It can be concluded that GIS-based MCDM tool continues to enhance the output for a proficient Decision Support system. It eases the Decision Makers and the developers to decide the probable and efficient sites to have a substantial technical performance with the least cost and less impact on the environment. Solar irradiation is considered to be the most important decision criteria. Land slope and Nearness to power lines are also considered as one of the most important factors while urban and protected land followed by watercourses and streams are considered the most restricted factors. In the last few years, the grid PV system has also overtaken the off-grid installation globally. The on-grid PV system utilization has gained favor where massive areas are available and solar radiation amount is high. Furthermore, in the context, about 85% of the surveys are concerned with on-grid PV. China is considered to be the world's largest solar energy producer with an installed capacity of 174 GW while Spain stands second with an installed capacity of 7011 MW. In the location point of view, India ranks third next to China and Spain.

6 Future Work

This review does not include textbook and papers that are not published and is limited to only English journals. It can be improved by taking real projects into account.

References

1. Shimray BA, Manglem K, Mehta RK (2017) Ranking of sites for installation of hydro power plant using MLP neural network trained with GA: a MADM approach. *Comput Intell Neuro Sci* 3:1–8
2. Shimray BA, Manglem K, Mehta RK (2017) A new MLP-GA-Fuzzy decision support system for hydro power plant selection. *Res Art Comput Eng Comput Sci* 43(12): 6823–6835
3. Tahri M, Hakdaoui M, Maanan M (2015) The evaluation of solar farm locations applying geographic information system and multi-criteria decision-making methods: case study in southern Morocco. *Renew Sustain Energy Rev* 51:1354–1363–1362
4. Sindhu S, Nehra V, Luthra S (2017) Investigation of feasibility study of solar farms deployment using hybrid AHP-TOPSIS analysis: case study of India. *Renew Sustain Energy Rev* 73:496–511
5. Gómez M, López A, Jurado F (2010) Optimal placement and sizing from standpoint of the investor of photovoltaics grid-connected systems using binary particle Swarm optimization, *Appl Energy* 87:1911–1918
6. Liu J, Xu F, Lin S (2017) Site selection of photovoltaic power plants in a value chain based on grey cumulative prospect theory for sustainability: a case study in Northwest China. *J Clean Prod* 148:386–397
7. Brewer J, Ames DP, Solan D, Lee R, Carlisle J (2015) Using GIS analytics and social preference data to evaluate utility-scale solar power site suitability. *Renew Energy* 81:825–836

8. Jain A, Mehta R, Mittal SK (2011) Modeling impact of solar radiation on site selection for solar PV power plants in India. *Int J Green Energy* 8:486–498
9. Effat HA et al (2013) Selection of potential sites for solar energy farms in Ismailia Governorate, Egypt using SRTM and multi-criteria analysis. *Int J Adv Remote Sens GIS* 2:205–220 (Cloud Public)
10. Niblick B, Landis AE (2016) Assessing renewable energy potential on United States marginal and contaminated sites. *Renew Sustain Energy Rev* 60:489–497
11. Gormally AM, Whyatt JD, Timmis RJ, Pooley CG (2012) A regional-scale assessment of local renewable energy resources in Cumbria, UK. *Energy Policy* 50:283–293
12. Yunna W, Geng S (2014) Multi-criteria decision making on selection of solar-wind hybrid power station location: a case of China. *Energy Convers Manag* 81:527–533
13. Menthis D, Welsch M, Fuso Nerini F, Broad O, Howells M, Bazilian M, Rogner H (2015) A GIS-based approach for electrification planning—A case study on Nigeria. *Energy Sustain Dev* 29:142–150
14. Martins FR, Pereira EB, Abreu SL (2007) Satellite-derived solar resource maps for Brazil under SWERA project. *Sol Energy* 81:517–528
15. Arnette AN, Zobel CW (2011) Spatial analysis of renewable energy potential in the greater southern Appalachian mountains. *Renew Energy* 36:2785–2798
16. Perpiña Castillo C, Batista e Silva F, Lavalle C (2016) An assessment of the regional potential for solar power generation in EU-28. *Energy Policy* 88:86–99 (2016)
17. Belmonte S, Núñez V, Viramonte JG, Franco J (2009) Potential renewable energy resources of the Lerma Valley, Salta, Argentina for its strategic territorial planning. *Renew Sustain Energy Rev* 13:1475–1484
18. Khan G, Rathi S (2014) Optimal site selection for solar PV power plant in an Indian state using geographical information system (GIS). *Int J Emerg Eng Res Technol* 2:260–266
19. Uyan M (2013) GIS-based solar farms site selection using analytic hierarchy process (AHP) in Karapınar region, Konya/Turkey. *Renew Sustain Energy Rev* 28:11–17
20. Carrión JA, Estrella AE, Aznar Dols F, Ridao AR (2008) The electricity production capacity of photovoltaic power plants and the selection of solar energy sites in Andalusia (Spain), *Renew Energy* 33:545–552
21. Boran FE, Menlik T, Boran K (2010) Multi-criteria axiomatic design approach to evaluate sites for grid-connected photovoltaic power plants: a case study in Turkey. *Energy Source B Econ Plan Policy* 5:290–300
22. Sliz-Szkliniarz B (2013) Assessment of the renewable energy-mix and land use trade-off at a regional level: a case study for the Kujawsko Pomorskie Voivodship. *Land Use Policy* 35:257–270
23. Noorollahi E, Fadai D, Akbarpour Shirazi M, Ghodsipour S (2010) Land suitability analysis for solar farms exploitation using GIS and fuzzy analytic hierarchy process (FAHP)—A case study of Iran. *Energies* 9:643
24. Anwarzai MA, Nagasaka K (2017) Utility-scale implementable potential of wind and solar energies for Afghanistan using GIS multi-criteria decision analysis. *Renew Sustain Energy Rev* 71:150–160
25. Effat HA (2013) Selection of potential sites for solar energy farms in Ismailia Governorate, Egypt using SRTM and multi-criteria analysis. *Int J Adv Remote Sens GIS* 2: 205–220 (Cloud Public)
26. Wang S, Zhang L, Fu D, Lu X, Wu T, Tong Q (2016) Selecting photovoltaic generation sites in Tibet using remote sensing and geographic analysis. *Sol Energy* 13385–13393
27. Lee A, Kang H-Y, Liou Y-J (2017) A hybrid multiple-criteria decision-making approach for photovoltaic solar plant location selection. *Sustainability* 9:184
28. Rumbayan M, Nagasaka K (2012) Prioritization decision for renewable energy development using analytic hierarchy process and geographic information system. In: 2012 International conference on advanced mechatronic systems (ICAMechS). IEEE, Tokyo, Japan, pp 36–41
29. Perpiña Castillo C, Batista e Silva F, Lavalle C (2016) An assessment of the regional potential for solar power generation in EU-28. *Energy Policy* 88:86–99

30. Chakraborty S, Sadhu PK, Pal N (2014) New location selection criterions for solar PV. *Int J Renew Energy Res* 4
31. Gherboudj I, Ghedira H (2016) Assessment of solar energy potential over the United Arab Emirates using remote sensing and weather forecast data. *Renew Sustain Energy Rev* 55:1210–1224
32. Zoghi M, Houshang Ehsani A, Sadat M, Javad Amiri M, Karimi S (2015) Optimization solar site selection by fuzzy logic model and weighted linear combination method in an arid and semi-arid region: a case study Isfahan-Iran. *Renew Sustain Energy Rev*
33. Fang H, Li J, Song W (2018) Sustainable site selection for photovoltaic power plant: an integrated approach based on prospect theory. *Energy Convers Manage* 174:755–768
34. Saaty TL (2008) Decision making with the analytical hierarchy process. *Int J Serv Sci* 1:83–97
35. Kohara K, Sugiyama T (2016) Simulating Tsunami evacuation with multi-agents and determining a countermeasure with AHP. *Int J Anal Hier Process* 8
36. Sumabat AKR, Manalac AJ, Nguyen NT, Kalaw ME, Tan RR, Promentilla MAB (2015) Optimizing geopolymmer-based material for industrial application with analytical heirarchy process and multi-response surface analysis. *Chem Energy Trans* 45
37. Hassan Z, Garni A, Arabia A (2017) Solar PV power plant site selection using GIS-AHP based approach with application in Saudi Arabia
38. Meitei IC, Singh TB, Denish K, Meitei HH, Singh NA (2019) Optimum design of photovoltaic system for a medical institute using HOMER. In: International conference on intelligent computing and smart communication, pp 1337–1346
39. Meitei IC, Irungbam AK, Shimray BA (2019) Performance evaluation of hybrid renewable energy system for supplying electricity to an institute and a hospital using HOMER. In: International conference on intelligent computing and smart communication, pp 1317–1326

A FPGA-Based PUF Integrated Blockchain to Overcome the Challenges of Internet of Everything (IoE)



Lukram Dhanachandra Singh and Preetisudha Meher

Abstract Today almost everything is upgrading into a smarter one, connecting them to the internet, which makes their data accessible to the network. Securing these data is the most important thing in the present day situation. Many researches have been proposing various solutions, PUF is one of them which is considered as hardware security primitives and on another side, blockchain technology is an advancing technology which is vigorously taken up by many applications such as financial applications for secure transactions, smart applications to secure the data by decentralizing them using some cryptography algorithm. But it is a bitter truth that the security issues do not end with them. It is high time for us to search for an alternate solution and to design a new better system that can bring these security issues to an end. So we proposed an FPGA based PUF to be implemented with Blockchain technology which can provide a better secure and reliable platform, which will be a decentralized platform consuming ultra-low-power and having efficient computational resources.

Keywords Blockchain technology · FPGA · Programmable unclonable function · Internet of things · Internet of everything

1 Introduction

The introduction of the Internet in commercial applications helps in the development of electronic commerce which encourages the financial trades among various entities [1]. A central entity takes all the responsibility to provide security both in communication and financial transaction among the different entities. And if any fraud or failure occurs, the central entity will be questioned and will remain responsible. In such centralized systems, at a single point of failure, it has a chance to cause

L. D. Singh (✉)

Electrical Engineering Department, National Institute of Technology, Manipur, India
e-mail: dhana.lukram0@gmail.com

P. Meher

Department of Electronics and Communication Engineering, National Institute of Technology, Tadepalligudem, Arunachal Pradesh, India

a terrible system failure. Thus, a central entity has challenges of being trusted and issues of security and privacy. The central entity also has slow processing during the transaction process [2].

To solve the issues of the central entity discussed above, it needs to be decentralized and for the same, blockchain technology was introduced which practices a decentralized ledger, in which all the members in the network uphold a synchronized copy of the whole or partial ledger. A cryptocurrency called Bitcoin was introduced in 2008 which was a blockchain-based cryptocurrency [3]. Since then numerous researches have been taken on to practice blockchain technologies in various applications of finance services, Internet of Things (IoT), Smart Healthcare, Smart Governmental schemes, etc. Every transaction achieved among multiple entities are deposited in the distributed ledger and after all positive transaction, the ledger is synchronized among all the nodes in the network. Now not only the industry is using cryptocurrency, but also the healthcare, military, and many more are implementing this blockchain technology, as it excludes the need of a central entity, and also the problems discussed above.

The Internet-of-Things (IoT) is known to be the pillar for various smart application areas, comprising smart healthcare, smart cities and smart transport. The IoT is a network formed with the interconnection of devices, which communicate and exchange data among each other through the internet for smart resolution. But lately, a new concept of interconnecting such various IoTs as one component of its architecture and environment has been presented [4], called the Internet of Everything (IoE).

The IoE consists of four components People, Data, Things and Processes. The Things in the IoE represent the devices that are associated with each other and the Internet exchanging data and decision making. People in the IoE come to be nodes inside the network. Countless devices belonging to the People are endlessly linked to the Internet and partake in performing communications among devices and other People. The remaining component is the Data which takes the role of information. The collected data is used for making intellectual choices in various phases of our daily life. Once the data is collected, transferring the correct data to the correct place at the accurate time is the Process in this IoE case. With every component of IoE, data collection, processing and security can aspect numerous potential threats. As an answer to all such problems, a FPGA based PUF integrated with Blockchain is considered and proposed.

2 Problem Definition

There is a common smash at the moment about the Internet of things (IoT) and its impact on almost everything we face in our day to day life from travelling to shopping and health. The IoT is a huge network that connects people and the things, all of which collect and share data about the way they are used. The collected data amount on the Internet of Everything rises every day.

The performance of devices used for these types of applications are low, which consumes less power, unable to deliver sufficient computational power for the architecture. To come up with all these concerns, researches are going on around the world which works on the development of solutions in which the computational requirements are unloaded to the edge of the network [5]. In such situations, the integration of edge datacenters assisted to remove the restrictions of resource-limited and low-performance devices [6].

2.1 Why Blockchain?

Privacy and security are two additional features of IoT architecture that require the highest consideration through the design level. Numbers of crypto graphical algorithms were suggested which can be used to reinforce the IoT security. But, IoT needs a central entity where all the data are stored and various devices or people communicated through; which is crucial if a cryptographic algorithm is used to secure the IoT architecture. Blockchain technology can be used to eliminate the necessity of a central entity from IoT architectures as the blockchain uses a decentralized public ledger for arranging the data and completing the transactions. As a copy of the ledger is shared with every node connected to the network, it helps to maintain consistency and security [1].

Blockchain technology is one among the emerging technologies worldwide which has the prospective to present it as a solution to several issues in multiple situations and everyday uses, such as the IoT.

In the blockchain, blocks are formed combining several transactions and nodes residing in the network produce blocks. All the blocks and their transactions should be authenticated by the identified node of the network as a portion of the consensus algorithm. Next to block confirmation, they are cryptographically linked with other blocks in the chain.

2.2 Why PUF Need to be Integrated into Blockchain?

Along with the advantages of blockchain, it also has some challenges which are essential to be solved prior to integration with any environment. More or less challenges require high computational resources, scalability, consumes more power, privacy and security. As an example, if we consider an IoT atmosphere, almost all these challenges are at the point of congestion for the integration of blockchain which comes up so fast and together at a time, which makes it hard to handle them quickly.

A Physically Unclonable Functions (PUF) is random functions which cause intrinsic properties of hardware to give unique response for a set of inputs (or challenges). A PUF is in charge of creating a unique key as an identity for the IoT device. A PUF can produce a sequence of unique keys that can only be generated from the

same PUF module. The set of keys produced by a PUF module can neither be duplicated nor produced from any other module. The PUF keys are not to be stored in the IoT devices memory. When it requires the keys, the PUF module will generate it and is forwarded to the module used for hash, which increases the security of the IoT device based on the architecture of PUF, an additional key can be created by varying the input. The output of the PUF key can be altered during the progress and several security threats can be dodged.

3 Type of Blockchain and Its Challenges

Blockchain technology is of several types. It is elaborated in Fig. 1 [2]. Blockchain technology uses the idea of a distributed ledger in which the replica of the whole ledger or a portion of it were shared with every node in the network. Central entity is substituted by a consensus algorithm in case of a blockchain network [2]. Every member in the network approves on the consensus algorithm which is like rules essential to authenticate the transactions. For a block of transactions to be authorized and added to the blockchain, the miner in the network runs the consensus algorithm and confirms the transactions.

3.1 Blockchain Technology Challenges

The blockchain practices cryptographic hashes to uphold consistency and security. When a block is added to the blockchain, it cannot be changed or removed. If anyone tries to modify the data in the blocks linked with the blockchain, the entire ledger will be destroyed signifying an inconsistency. There are several challenges for blockchain [7]. Several challenges of blockchain technology that demands energy or computation power or prevent its application have been found, such as, shortage of scalability, consumption of high energy, high latency, lack of privacy and fake block generation.

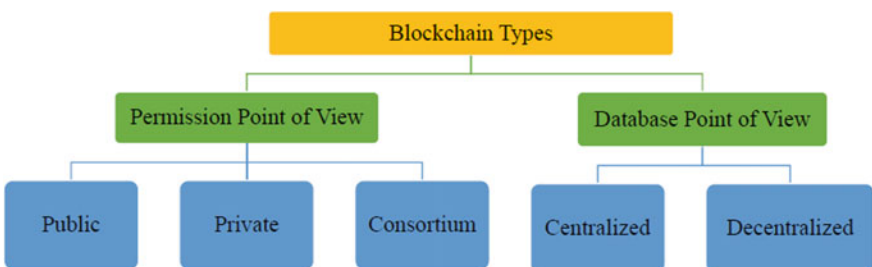


Fig. 1 Different types of blockchain [2]

Different transactions in the blockchain collectively form the blocks and when the block is formed at the nodes in the network, the process of mining begins which check and confirm the transactions in blocks and the blocks it selves. The process of mining needs higher computational power and dedicated hardware, consuming an enormous power. The scalability is also poor due to the needs of dedicated hardware. The latency also surges due to the rise in amount of data and nodes in the network. The time taken to authorize the transactions also surges with increases in the number of transactions which increases the issues too. There are also some issues where fake blocks can be made to attack the blockchain.

4 Review on Existing Consensus Algorithm

Consensus algorithms comprises various processes to create, check and confirm blocks. There are lots of key consensus algorithms, as shown in Fig. 2. We categorize them into three groups: (1) Validation based, (2) Voting based and (3) Authentication based.

Bitcoin practices Proof-of-Work (PoW) in which for consistent and secure transaction, it maintain miners inside the blockchain network and archive the same distributed ledger. In PoW algorithm, the participating nodes contest compared with each other to encrypt the new block into the prevailing chain [3]. New blocks are mandatory to be under a target value. It consumes a lot of resources; though provide security by determining the malicious nodes from inserting blocks into the blockchain. It verifies the new blocks depending on total computing power.

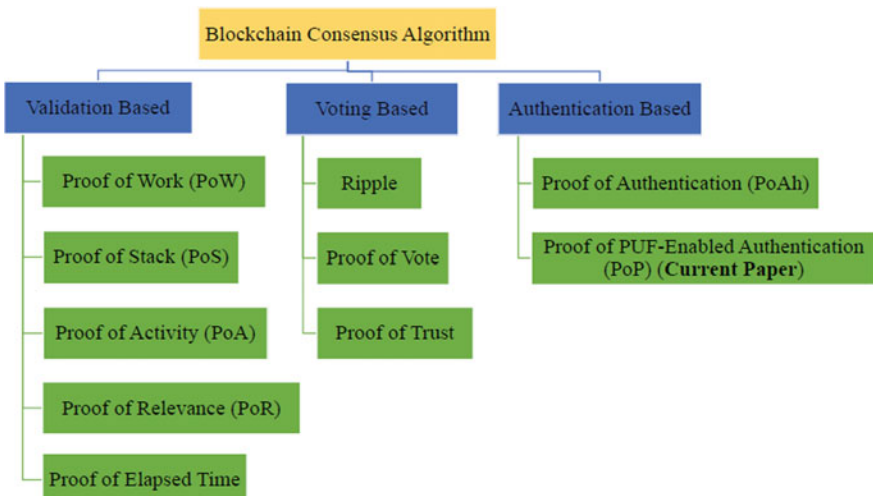


Fig. 2 Various consensus algorithms used in the blockchain

Etherium and Peercoin use Proof-of-Stake (PoS) which utilizes coinage (time for which the user held a particular currency) concept to determine the target value [8]. As in PoW, new blocks are mandatory to be under a target value but here it is determined individually. Higher the coinage is, it is easy for miner to find the solution. For every new solution provided by miner, a coinstake block that comprises a coin is referred back to the miner itself, which gives chance to miners [9].

The concept of PoW focused on rewarding the miners for validating the block, but it also increases the chances for them to win for on-line peers, but off-line peers cannot claim their reward as they are unable to sign their signature onto the blocks to claim the reward. Proof of Activity (PoA) was established to reduce the effect of these matters, whereby refining the security of the network [9].

Voting-based consensus algorithms consist of Ripple [10], Proof-of-Vote [11] and Proof-of-Trust [12].

Proof of Authentication (PoAh) implements an old-fashioned PoW consensus method for simple block confirmation [13]. The trusted nodes in the network act as miners which validate the blocks, trailed by authenticated nodes which drive the network peers to add block into the chain. This algorithm comprises two steps:

1. Validate the transactions in a block and respective sources, and
2. After positive validation, the corresponding trusted node's trust value is increased by one unit (Table 1).

Based on blocks from miners, the distributed ledger is shared to the network peers. Individual transactions in a block are confirmed by the trusted nodes in the networks. If it happens to be false identifications, after a certain number a trusted node will turn into normal node. The trust value of a respective trusted node is reduced by a unit for each false transaction.

However, for resource-limited IoT applications, any such consensus algorithm is not yet developed or tested. PoW and PoS are strong consensus algorithms and will not run in simple, battery-powered IoT devices.

Table 1 Comparison of different existing consensus algorithm

Consensus algorithm	Year	Types of blockchain used	Mining based on	Prone to attack
PoW [3]	2008	Permission less	Computation power	Bribe attack, Sibil attack
PoS [8]	2012	Permission less	Validation	DoS, Sibil
Ripple [10]	2014	Permissioned	Voting	DoS, Sibil
Proof of vote [11]	2017	Consortium	Voting	–
Proof of trust [12]	2018	Permission based	Probability and voting	DDoS
PoAh [13]	2019	Permission based	Authentication	–
PoP [14]	2019	Permission based	Authentication	–

Another consensus algorithm that is integrated with PUF termed as Proof of PUF enabled Authentication was proposed recently, which was permission-based blockchain and its mining was based on Authentication [14].

5 Physical Unclonable Functions (PUF) as Hardware Security Primitive

PUF was specially introduced for hardware security [15] as a random function which led to manufacturing variations in chip levels from the devices on the Integrated Circuit (IC). It introduces variations during the IC fabrication process which are random, inescapable, and uncontrollable and automatic. Due to these Nano-electronic manufacturing dissimilarities, none of the devices on a wafer are the same. The input challenge and its resultant response obtained from PUF circuit are termed as Challenge Response Pair (CRP). For evaluation of PUFs, three main figures of merit are measured as Uniqueness, Reliability, and Randomness, due to which PUF is considered as a hardware security primitives.

PUF can be categorized as Silicon PUFs and Non-Silicon PUFs based on fabrication and it is also classified as Strong, Controlled and Weak PUFs based on security-based. Many researches have been going on for efficient PUF designs according to their targets. Some of them are for Intellectual Property protection, anti-counterfeiting, test and debug security, device authentication, and key generation. And some are for implementing machine learning algorithm in it to provide more security and some researchers also seek to merge it in FPGA for low power consumption, to improve processing speed and also for size reduction [1]. Many review papers are also published on different architectures of PUF, like MUX based PUF, SRAM PUF, Butterfly PUF, Arbiter PUF, Ring Oscillator PUF and hybrid PUF which is a combination of two or more PUFs.

6 Contribution of the Paper

6.1 *PUF Integrated Blockchain–PUFchain*

The main target is to integrate the consensus algorithm for blockchain in IoE network which has a short form factor and less power for better security and data management. Figure 3 displays the structure of nodes in PUFchain. The network consist is client nodes that gather environmental data from devices and upload them to the network and trusted nodes that are accountable for mining and validation of devices collecting the data.

A high level of security can be attained with the integration of blockchain to the network. A hybrid oscillator arbiter PUF was used to implement a PUFchain [14]. A

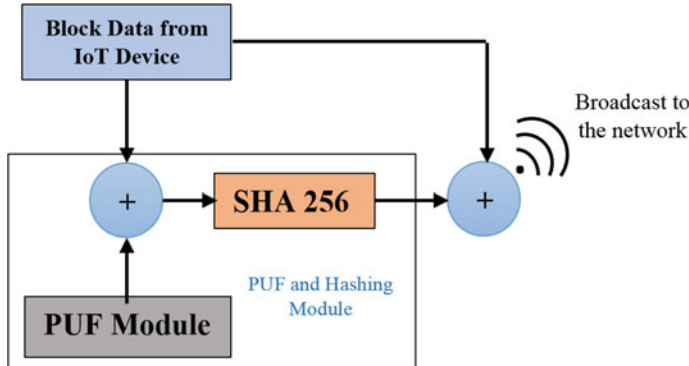


Fig. 3 Structure of nodes in PUFchain

Hashing module and PUF module is employed above the IoT device that improves the computation of cryptographic hashes. Addition of PUF module for unique key generation and cryptographic hash computation lessens the computational needs of the IoT devices. By selecting FPGA based PUF designs, FPGA based hashing module and optimization, we can significantly reduce the power consumption; improve security, scalability and latency of the blockchain. Figure 4 presents the architecture of the PUF-integrated blockchain.

The PUF and module used for hash consist of a cryptographic processor build up on FPGA and the FPGA based PUF module. The cryptographic processor collects the data from the IoT device and the PUF module supply the unique identification key. A sequence of transactions was commenced, authenticated and inserted to the blockchain which authorizes the consensus algorithm. Figure 5 shows the block structure of PUF integrated blockchain.

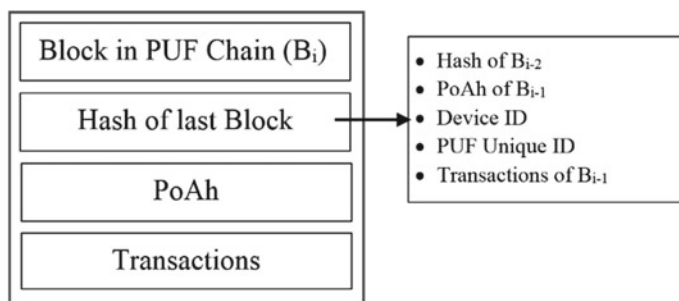


Fig. 4 Block structure of PUF integrated blockchain

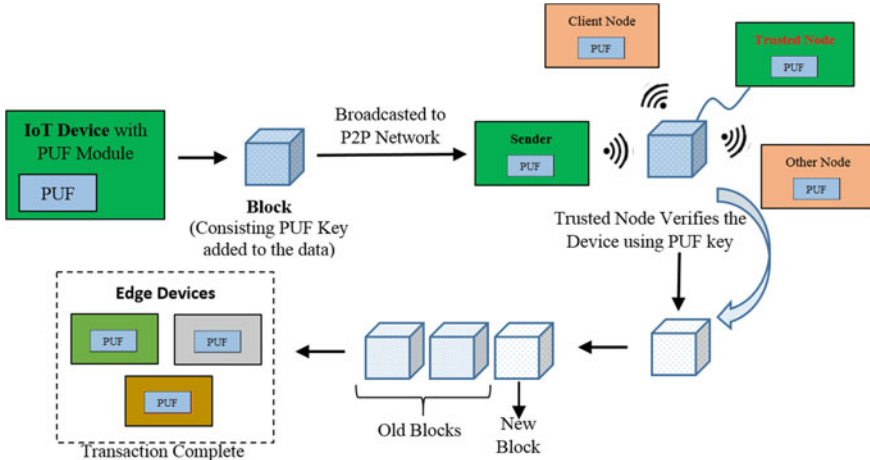


Fig. 5 Architecture of PUF-chain

6.2 Consensus Algorithm for PUF Integrated Blockchain

There are three phases in designing a consensus algorithm. First one is the device enrollment phase (E phase) in which it checks the IoT Device at the node if it can be selected or enrolled for PUF chain consensus algorithm. This can be achieved with PUF module. All the IoT devices in the PUF chain network should comprises PUF module to produce a unique identification key which is used later for authentication. So, in this E phase, a set of challenge inputs will be selected for PUF module and these challenges should satisfy a set of requirements to be considered as inputs to PUF [14]. And thus the corresponding CRPs are stored in a secured database which can be accessed later by trusted nodes. As soon as the IoT device is positively registered into the network, it is qualified for the initiation of transactions which will be authenticated by trusted nodes.

Second phase is the initiation of transaction (T phase) which will be generated after collection of data from the sensor device. The transaction data will consist of the collected sensor data and the device's MAC address. The MAC address works as identification for the remaining nodes in the network including trusted nodes. Just after the transaction is processed, hardware accelerator will receive it. It consists of the PUF which is proficient to compute the cryptographic hash. A challenge input (C_i) is chosen for the PUF which is one among the challenges saved in the secure database which can be accessed by the trusted nodes. The challenge is passed to the PUF module and it will collect the response. Then the data linked with the generated response are computed for hashing by the hardware accelerator. And it is directed reverse to the IoT device which further broadcast it to the network.

And the last phase is Authentication phase (A phase), which authenticates the block which is not broadcast to the network before adding to the blockchain. Just

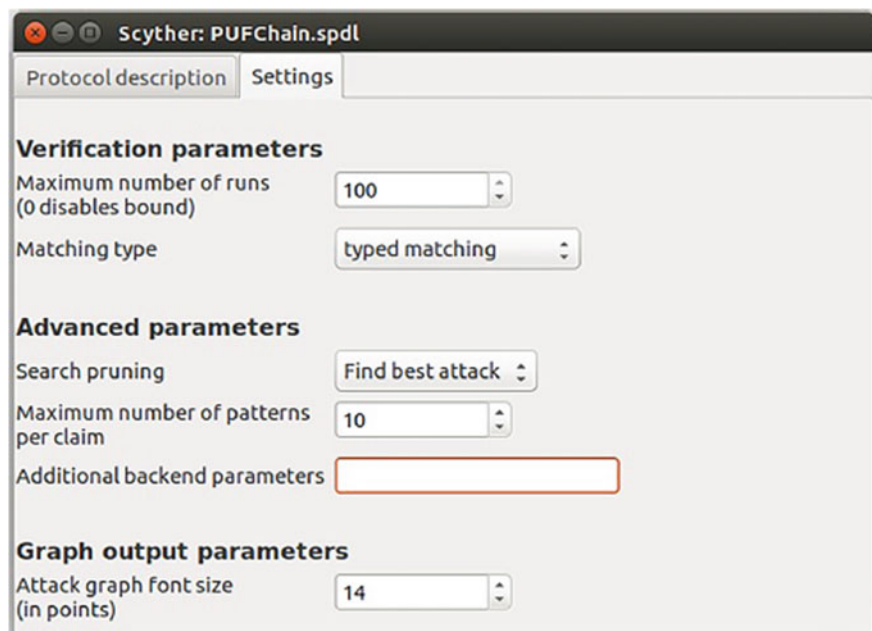
after trusted nodes received the block, the data (D_n which consists of the data collected by the node along with its MAC address) and the hash (H_n) are recovered which help of identification of the device. The trusted node obtained the PUF keys from the secure database with the help of the MAC address and it is sent along with the data to the hardware accelerator to perform the hashing part. The function used for hashing by the devices throughout the network should be the same. The resultant hash is checked for matching with the H_n received from the node. If both the hashes found to be a match, the device is authenticated and the block is added to the blockchain and it is broadcasted to the network. If they are found not to be matched with each other, the process carries on with all the PUF keys that are saved in the E phase. And if it cannot authenticate the device, the block will be released and not broadcast.

6.3 Evaluation and Analysis of Result

We can evaluate/analyses the result for the proposed PUF-chain using both software and hardware platform. We can develop a hardware accelerator containing PUF module and hashing module on an FPGA and we can use Raspberry Pi module as nodes as done in [14]. The consensus algorithm can be written in the Scyther simulator which is an automatic verification tool of security protocols. In this, we need to write the code in Security Protocol Description Language (.spdl), simulation can be done in Scyther v1.1.3 with a system running with Ubuntu 18.04.3 or higher version OS. The result can be checked as shown in Fig. 6 [14]. We can also perform analysis the transaction time and power consumption for the PUFChain. Table 2 gives the comparison of two existing consensus algorithms, i.e. PoAh [13] and PUFchain [14].

7 Conclusion and Future Directions

In this paper, we elaborate the steps in various phases of consensus algorithm which are required to authenticate the nodes in an FPGA-based PUF integrated blockchain network, providing better security, scalability, and reliability to and enhancing computational power of IoTs/IoE. We also promoted the ways to analyses the proposed PUF integrated Blockchain module. Some results of the existing consensus algorithm are also shown. We can implement SHA-256 on FPGA using blockchain concept as mentioned in [1] for hashing module we can provide far better security. And if we can implement the proposed consensus algorithm with machine learning then its security will be very strong that it takes years to have a breakdown of the barrier in the system.



(a) Experiment setup for PuFChain security verification

Claim				Status	Comments
PUFChain	D	PUFChain,D2	Secret ni	Ok	No attacks within bounds.
		PUFChain,D3	Secret nr	Ok	No attacks within bounds.
		PUFChain,D4	Commit S,ni,nr	Ok	No attacks within bounds.
Done.					

(b) Security verification results

Fig. 6 PUFchain security verification using Scyther

Table 2 Comparison of PoAh based blockchain and PUFchain

Parameter	PoAh based blockchain	PUFchain
Blockchain type	Permission based	Permission based
Mining	Authentication based	Authentication based
Security primitive	Hashing	Hashing and added PUF key
Over head	Device ID	Device ID
Hardware needed	IoT device capable of performing hashing	IoT device
<i>Time taken to add received the block (ms)</i>		
BlockPi	843	120.3
Clear Pi (Raspberry Pi 3)	85	46.5
Clear Pi (Raspberry Pi 1)	162.4	120.3
Time taken for a complete transaction	950	198
<i>Power consumption range</i>		
BlockPi	3.1 W 3.6 W	4.3 W 6.6 W
Clear Pi (Raspberry Pi 3)	2.1 W 2.5 W	3.3 W 5.6 W
Clear Pi (Raspberry Pi 1)	1.5 W 1.8 W	2.7 W 5 W

References

1. Singh LD, Meher P (2019) Advancement of blockchain security solution with FPGA. *Int J Adv Sci Technol* 28(3):276–283 (Elsevier)
2. Puthal D, Malik N, Mohanty SP, Kougiannos E, Das G (2018) Everything you wanted to know about the blockchain: its promise, components, processes, and problems. *IEEE Consum Electron Mag* 7(4):6–14
3. Nakamoto S (2009) Bitcoin: a peer-to-peer electronic cash system. *Cryptography Mailing List* 03
4. Miraz MH, Ali M, Excell PS, Picking R (2015) A review on Internet of Things (IoT), Internet of Everything (IoE) and Internet of Nano Things (IoNT). In: Proceedings of internet technologies and applications (ITA), Sept 2015, pp 219–224
5. Stanciu A (2017) Blockchain based distributed control system for edge computing. In: Proceedings of 21st international conference on control systems and computer science (CSCS), May 2017, pp 667–671
6. Wright K, Martinez M, Chadha U, Krishnamachari B (2018) SmartEdge: a smart contract for edge computing. In: Proceedings of IEEE international conference on Internet of Things (iThings) and IEEE green computing and communications (GreenCom) and IEEE cyber,

- physical and social computing (CPSCom) and IEEE smart data (SmartData), July 2018, pp 1685–1690
- 7. Zheng Z, Xie S, Dai H, Chen X, Wang H (2017) An overview of blockchain technology: architecture, consensus, and future trends. In: Proceedings of IEEE international congress on big data (BigData Congress), June 2017, pp 557–564
 - 8. King S, Nadal S (2012) PPCoin: peer-to-peer crypto-currency with proof-of-stake. [https://dec
red.org/research/king2012.pdf](https://decred.org/research/king2012.pdf). Last accessed on 17 May 2019
 - 9. Tschorisch F, Scheuermann B (2016) Bitcoin and beyond: a technical survey on decentralized digital currencies. *IEEE Commun Surv Tutor* 18(3):2084–2123
 - 10. Schwartz D, Youngs N, Britto A (2014) The ripple protocol consensus algorithm. In: Ripple Labs Inc white paper, vol 5
 - 11. Li K, Li H, Hou H, Li K, Chen Y (2017) Proof of vote: a high-performance consensus protocol based on vote mechanism & consortium blockchain. In: Proceedings of the IEEE 19th international conference on high performance computing and communications; IEEE 15th international conference on smart city; IEEE 3rd international conference on data science and systems (HPCC/SmartCity/DSS), pp 466–473
 - 12. Zou J, Ye B, Qu L, Wang Y, Orgun MA, Li L (2018) A proof-of-trust consensus protocol for enhancing accountability in crowdsourcing services. *IEEE Trans Serv Comput* 1–14
 - 13. Puthal D, Mohanty SP, Nanda P, Koulianios E, Das G (2019) Proof-of-authentication for scalable blockchain in resource-constrained distributed systems. In: Proceedings of IEEE international conference on consumer electronics (ICCE), Jan 2019, pp 1–5
 - 14. Mohanty SP, Yanambaka VP, Koulianios E, Puthal D (2019) PUFchain: Hardware-assisted blockchain for sustainable simultaneous device and data security in the Internet of Everything (IoE), Sept 2019. <https://arxiv.org/1909.06496.pdf>
 - 15. Pappu R, Recht B, Taylor J, Gershenfeld N (2002) Physical one-way functions. *Sci J* 297(5589):2026–2030

Biometrics-Based Pig Identification: From Invention to Commercialisation



**Subhranil Mustafi, Pritam Ghosh, Sanket Dan, Kaushik Mukherjee,
Kunal Roy, and Satyendra Nath Mandal**

Abstract The study aims to focus on the entrepreneurship possibilities in the live-stock sector (particularly *Pig*) in India. The existing individual pig identification system is tamperable, stressful, hurtful in nature resulting in low reliability among the insurance companies in providing the insurance claim as demanded by the farmers post animal's death. Thus, a new method of identification has been developed, which is tamperproof, reliable, unique, and non-invasive. Due to a large number of Pigs in India (approx. 9.06 million), there is an entrepreneurship possibility to commercialize the identification technology in the market. The market has been studied and was concluded that charging Rs. 100 per biometric tag, revenue of about INR 90.6 Crores can be generated pan India. Finally, after analyzing the Lifetime Value and Cost of Customer Acquisition, the break-even point was found near year two and was predicted a huge profit on and after the second year.

Keywords Entrepreneurship · Animal-Aadhaar · Innovation · Start-up · LTV · COCA

S. Mustafi (✉) · P. Ghosh · S. Dan · K. Mukherjee · K. Roy · S. N. Mandal
Department of Information Technology, Kalyani Government Engineering College, Kalyani,
Nadia, West Bengal 741235, India
e-mail: subhranilmustafi2011@gmail.com

P. Ghosh
e-mail: ghoshpritam25@gmail.com

S. Dan
e-mail: sanketdan@gmail.com

K. Mukherjee
e-mail: kaushik8.m@gmail.com

K. Roy
e-mail: kunalroy4mkolkata@gmail.com

S. N. Mandal
e-mail: satyen_kgec@rediffmail.com

1 Introduction

The Total Early-Stage Entrepreneurship has been 10.6 with a rank of 31 amongst the top 65 countries, according to the Global Entrepreneurship Monitor report in India 2017–2018. Invention when mixes with commercialization, leads to innovation. Entrepreneurs can also be proclaimed as innovators. They always tend to look for something better and more profitable ways [1]. The process of social, political, and environmental change expressed in the past 15 years of developing policy landscape has focussed on the difficulties in persisting with the traditional ‘productivist’ model and created an imperative for entrepreneurial opportunity-seeking behaviour [2]. “For de Lauwere et al. [3] it’s possible to categorize between groups of farmers:

- Economic entrepreneurs: people who can create significant economic change;
- Socially responsible entrepreneurs: for those who can recognize that success of the farm may be able to balance socio-environmental role;
- Traditional farmers: those farmers who grow by believing in ‘guaranteed’ successful activities;
- New growers: those farmers who tend to follow diversification but the similarity in areas of activity;
- Doubting entrepreneurs: those farmers who become disinclined to opt for and accept change.” [4]

The authors focus on the invention of the unique trait of the pig, from where a biometric tag can be generated for each animal which would help in identifying the individual uniquely without hurting it. After the invention of the unique trait of the species, the authors moved on to commercialize it and help the livestock (*particularly pig*) sector widely. Different traits were tested to be inferred to a unique result. However, the auricular venation pattern was proved the most feasible amongst them [5].

In this paper, the Primary Market Research has been conducted and market segments were identified. The pig breeding farms, the processors and the animal husbandries were the systematic market segments discovered, respectively. Among the first market segment, ‘DLG Farms [P] Ltd.’ was chosen to be the persona. The authors have chosen Kalyani, Nadia, West Bengal, India to be the demographics for the experiment of the invented product where pigs soon after weaning of about 2–3 months were taken throughout its lifetime till death, to validate the product. Both, the top-down and bottom-up approach of Total Addressable Market were calculated where the top-down approach proved to be more effective. However, if the economic buyer and the champion buyer agree upon the product and its technology, then the product can easily be handed over to the end-user, who has both the ability to pay and willingness to buy the product. The generation of the unique biometric tag is itself a core competency in this domain as now work of non-stressful, non-manipulative biometric tag for animals has not yet been generated till date, except the physical tagging system by the government.

Eventually, we found the uprising Life Time Value (LTV) and down steeping Cost of Customer Acquisition (COCA) coinciding at a breakeven point near the second year. According to Gerard McElwee [4], farmers should start entrepreneurship with strategic planning. And there should be a proper identification system for the customers to rely upon and buy the product which is non-tamperable at any point in time, and the authors are here to move into it of publishing a product based on such reliable, biometric identification system. This type of effort has not been made earlier in the pig sector. This is the reason for making this paper.

The paper is divided as follows: In Sect. 2, Systematic overview of the identification process is shown followed by technology description in Sect. 3. Information about the motivation for selecting pig is discussed. The fieldwork and motivation are pursued are discussed in Sect. 4 followed by Total Addressable Market in Sect. 5. The Value Proposition, which is described as the difference between the present state without the product and the future state after acquiring the product is shown in Sect. 6, followed by the decision-making journey in Sect. 7 and Core Competency in Sect. 8. The technical methodology is discussed in Sect. 9 and plot of LTV versus COCA in Sect. 10. The technology has been developed and validated under project “ImageIDGP”, funded by ITRA, Govt. of India.

2 Systematic Overview for Individual Identification

The overview of the unique pig individual identification is depicted in Fig. 1 where

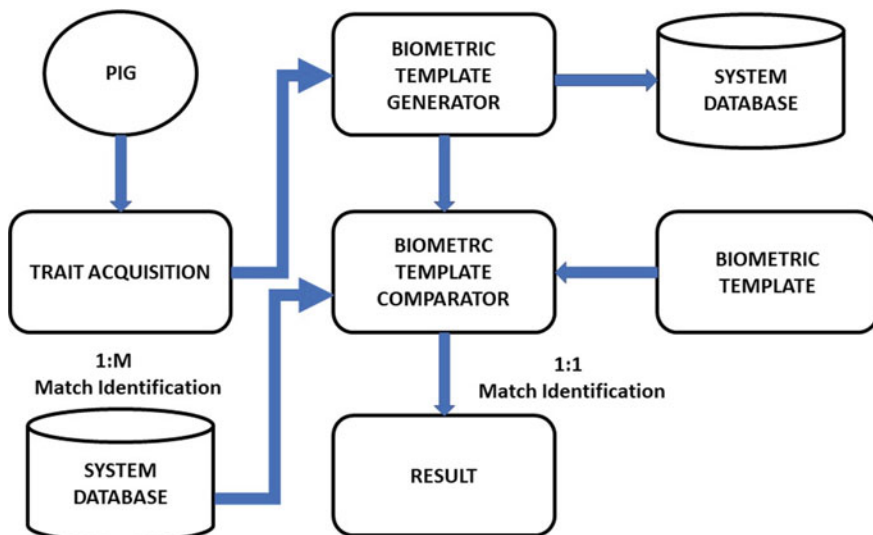


Fig. 1 Systematic overview for identification

after the trait acquired, a biometric template is generated which is stored in the database. The template generator is matched with the template of the new picture and is checked for equality.

3 Technology

Several traits had been examined but the auricular venation pattern of the pigs was found to be most feasible amongst them for individual identification. A threshold has thus been set to distinguish between the same or different pigs, based on the developed algorithms.

3.1 Trait Selection

There are two main auricular veins in pig ears and a number of branches and sub-branches arise from them. The number of branches, positions, and distances among them is unique for each pig. The identification system has been developed based on auricular venation pattern and it was found that branching up to secondary level remains fixed for the entire lifetime of the pig (Fig. 2).

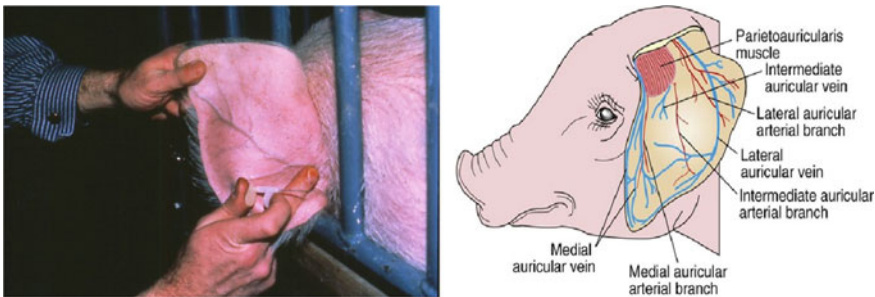


Fig. 2 Selecting ear vein pattern as the unique trait

3.2 Method of Identification

The ear vein image is taken as input and then processed through the phases of segmentation and normalization to get the principal branching as depicted in the picture and hence calculating the Euclidean distance to identify the threshold limit for the same and different pigs. Also, most interestingly, the ear vein pattern is completely different between the left and right ear of the same pig (Fig. 3).

4 Motivation and Field Work

This idea based on the technology push solves the problem where the traditional methods of identifying individual pigs are tamperable and such kind of manipulation creates a huge economic loss for the farmers as parent breeds can be manipulated during breeding. Again, after the death of any animal, the farmers are either underpaid or are refused to pay by the insurance company due to such unreliable identification

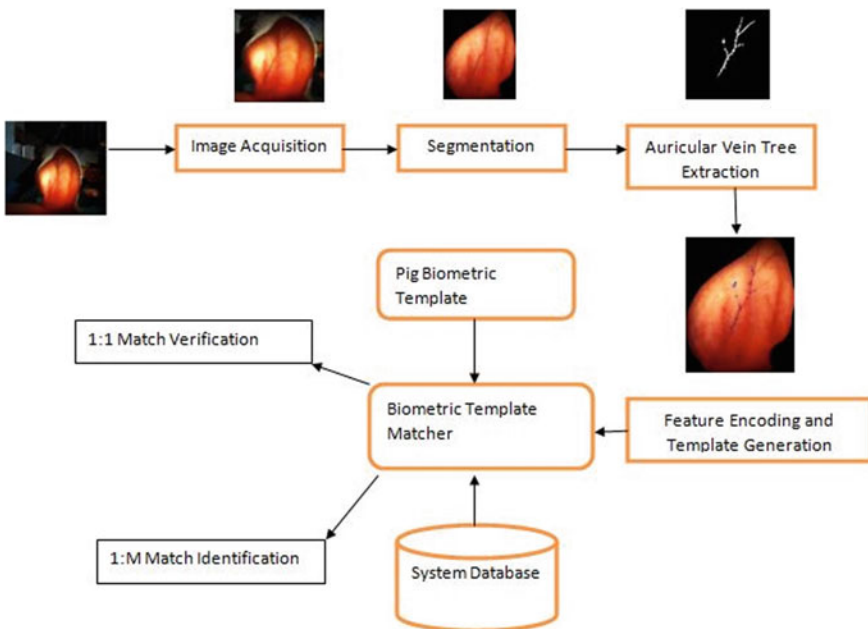


Fig. 3 Method of identification

systems, hence resulting in self-immolation for the farmers. The ability to solve the problems by helping the people and enhance the economy of the country through the livestock sector motivates the authors to pursue this opportunity, which may also be viable simultaneously.

Primary Market Research has been conducted and was found out that the breeding farms, organized farmers and animal husbandries can be identified as market segments wanting a solution against the traditional method of stressful physical tagging. Again, further research selected the breeding farms of West Bengal as the beachhead market for immediate validation and commercialization of the product. The demographics were chosen in Kalyani, Nadia, West Bengal and the Psychographics was the requirement for the replacement of the old traditional methods and hence an increase in the profit and economy of the farm widely. The proxy product was the pig restraining tool to minimize the utilization of the manpower in restraining the animal during taking the ear vein images (Fig. 4).

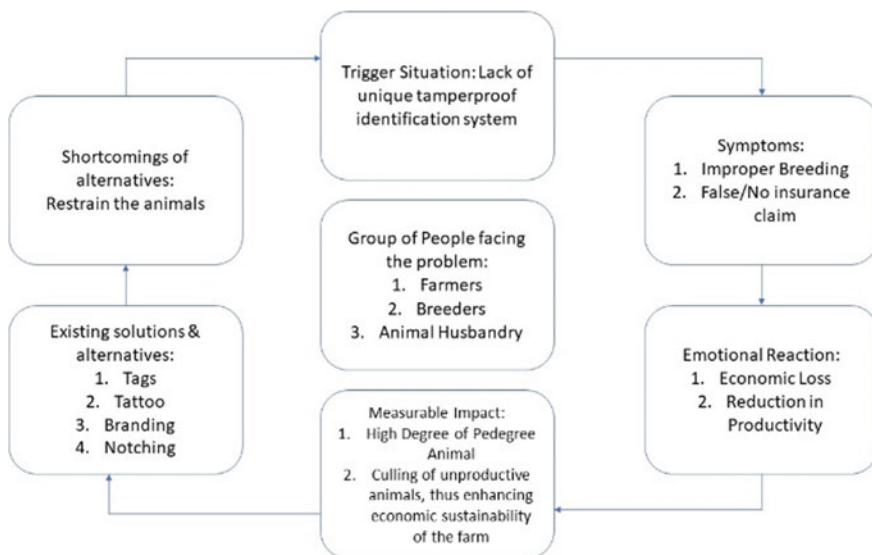


Fig. 4 Motivation and problem statement

5 Total Addressable Market

The concept here generally revolves around the estimation of the size of the universe (here considered as the total market), the product, and the technology would be able to capture without the presence of any of its competitors. The revenue that can be generated from such a 100% market share of the product helps in limiting the usage of the product and its usefulness in the market. Of this, 30% market which can be serviced at the present time denotes the service addressable market. Of the service addressable market, target market (mostly 10% market share) is taken into consideration for the most likely buyers at the very first instant. That target market provides feedback to other customers regarding the product and the rest of the revenue depends on that. This target market acts as advocates in the customer decision making journey to the decision-making process for the rest of the market in purchasing the product in nearby or distant future (Fig. 5).

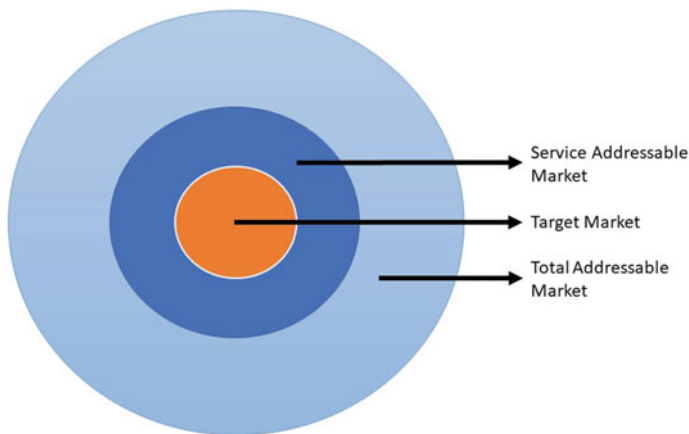
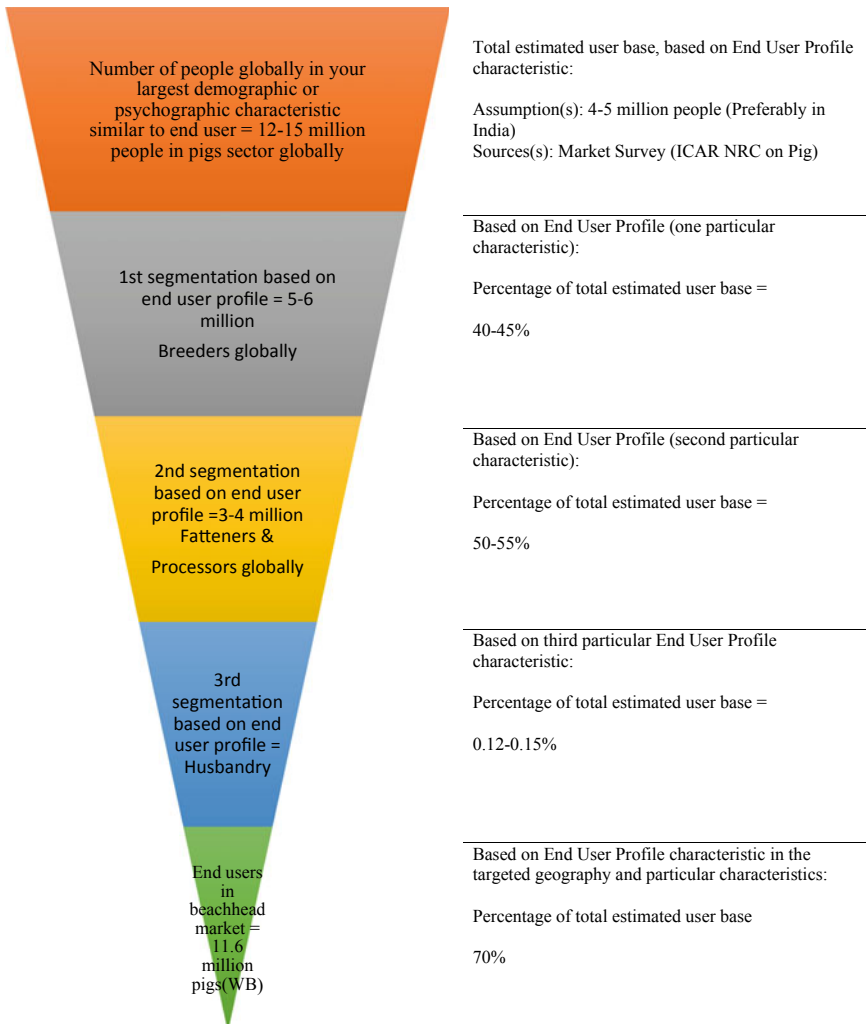


Fig. 5 Distinction between the markets

5.1 The Total Addressable Market in the Pig Sector as Per Latest Census



This TAM forms a major portion in anticipation the value proposition. It is the 100% market share of the product and 30% market share of the product forms service addressable market [6].

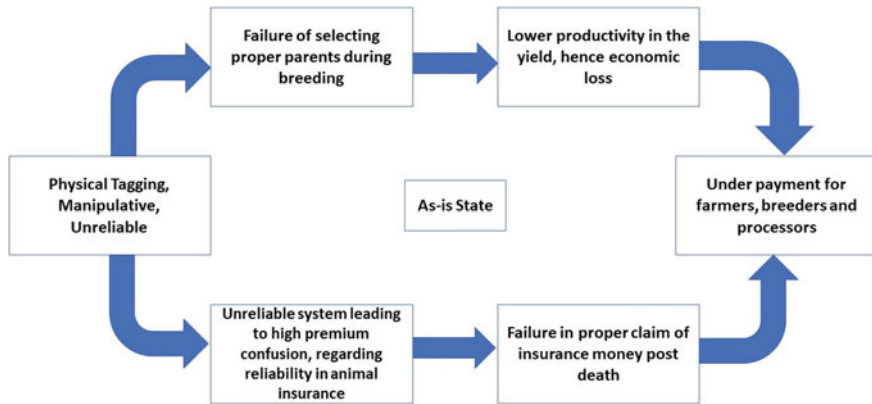


Fig. 6 ‘As-is’ state

6 Value Proposition

According to Frow and Payne [7], a value proposition is an offering to the customers through a series of benefits that the customer is going to receive after the usage experience. It is the change from the “as-is” state to the “possible” state on acquiring the product [8]. Now, here the customer wants (1) Unique identification of parent breeds of pigs to enhance the productivity and hence the economy of the breeding farm. (2) Creation of database against Unique ID for morphological and vaccination measures and (3) Proper claim of money for insurance post-death. Also, the customer fears the sign of the belief for the new tag, whether the product would be able to identify the animal uniquely, as per the statement. The drivers are the willingness and ability to pay for the unique individual identification tags which would help, making them economically stronger (Figs. 6 and 7).

7 Decision-Making Journey

The decision-making journey traverses from the Champion Buyer, the Gate Keeper, the Decider, the Economic Buyer, the Supplier, the End User, and finally the Influencer. The Gate Keeper helps in determining the type of information from various sources that are necessary for the product purchase. Then comes the decider, who helps in choosing the required supplier necessary for the purchase. The initiators are the ones who help in picking the problem and finding a solution to the problem. The champion buyer is the one who is willing to buy the product but is not sure about his/her ability to buy. The economic buyer has the ability to buy the product but depends on the willingness to buy the product from the champion buyer. When

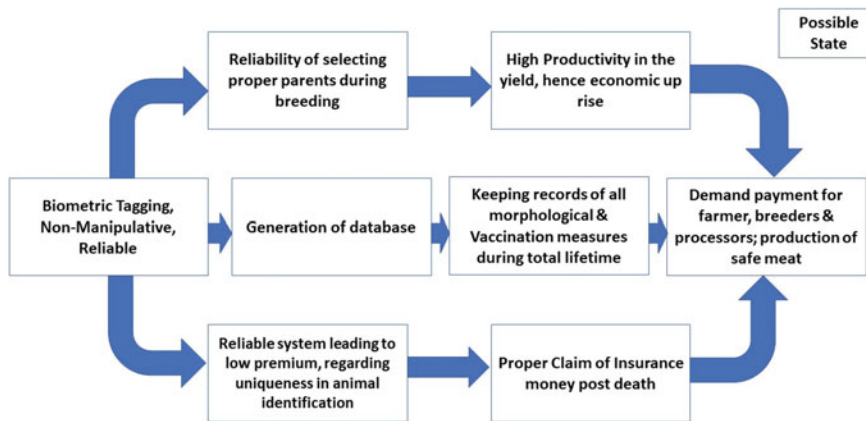


Fig. 7 ‘Possible’ state

willingness and ability combine, he/she becomes the end-user. Later on, getting the proper value, he/she advocates or influences others, wanting a product in the same domain, thereby completing the decision-making process (Fig. 8).

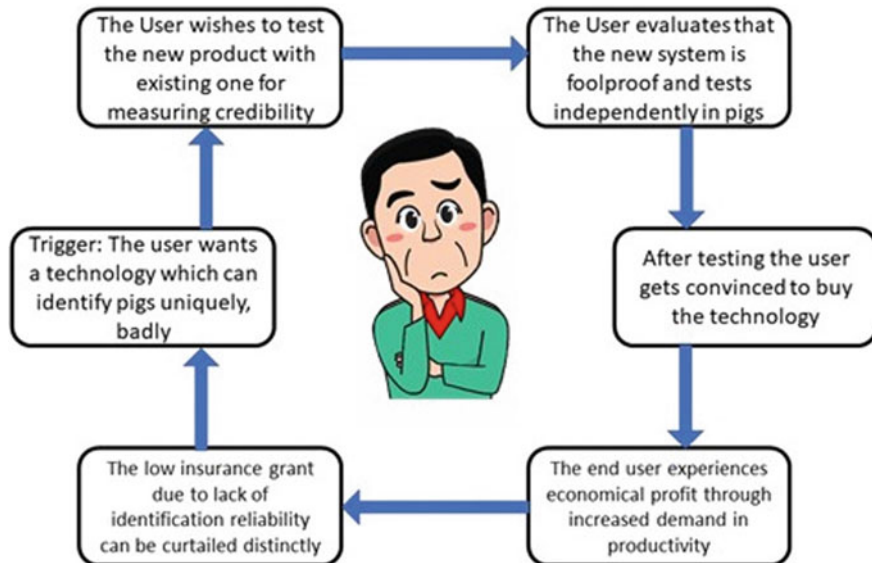


Fig. 8 The consumer decision-making journey

8 Analyzing Core Competency

The Core-Competency is itself the technology developed revolving around the unique character traits of Pigs & the technology used in developing the algorithm to produce the exact correct result for any number of samples. The algorithms in staking with the character traits are completely different from humans, and hence those human-based algorithms cannot be put to use absolutely.

Man et al. [9] [4] categorized entrepreneurial competences in six key areas of related competences. The key clusters are

- Opportunity recognition skills
- Relationship building
- Conceptual thinking and problem-solving skills
- Organizing
- Strategic competences.

Potential Competencies The potential competencies in this sector would be:

1. Creating a low-cost package plan for customers having more than 3000 animals
2. Providing a special service of handling and maintaining a database of the pedigree of large farms
3. Training the customers for any kind of first-aid technical issues with the first-hand experience.

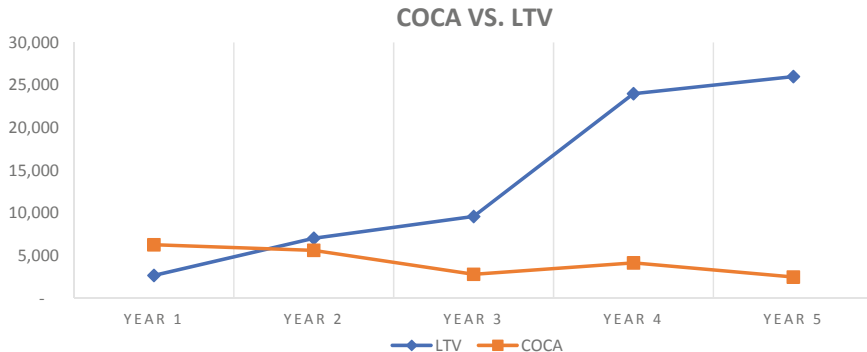
Since, there is no such revolutionary work done in this sector of the livestock, hence the product serves as a self-competent product and has covered nearly all the loopholes of the area, thereby validated in the aforesaid demographics of the market. Once commercialized, this would create an effective measure of verification during the distribution of animals by the government for breeding and taking return the same given individual after the breeding cycle. Also, since the technology revolves around taking images of the ear vein, the method is feasible than any other ‘fingerprints’ of the pig.

9 Plot of LTV [10] Versus COCA [11]

The lifetime value represents the total amount of money a customer is expected to spend on the entrepreneurship possibility. It is based on the products or technology they get and the value proposition satisfied to them after purchasing the product. The Cost of Customer Acquisition is the amount of money spent on acquiring customers through any way of advertisement or sales. As per our research, the LTV and COCA intersect near the second year (break-even point) (Table 1; Fig. 9).

Table 1 General overview and scaling of LTV and COCA

	Year 1	Year 2	Year 3	Year 4	Year 5
LTV	2680	7040	9600	24,000	26,000
COCA	6280	5620	2810	4149	2490

**Fig. 9** Plot of LTV versus COCA

10 Conclusion and Future Work

The best part of management is to motivate other people more than anything else. One can truly pursue such entrepreneurship opportunity in such a wide pig sector in India of 9.06 million pigs using such biometric-based individual identification technology, charging only Rs. 100 per biometric tag, which may consist of a unique code consisting of a database of morphological and vaccination information from birth till death, to guide to safe pork eventually. The point of intersection between LTV and COCA as discussed in Sect. 9 clearly shows that from year two, a margin of profit could be visualized which would grow in the later years. And most interestingly, no foolproof system has yet been developed which would be able to store information of the pig throughout the lifetime. This would be a flabbergasting opportunity to gain profit in such a sector which is of daily need to commons. Later the system may be extended globally to support the global pig population thereby generating a large revenue at the end of the day.

Acknowledgements The authors would like to thank ITRA (Digital India Corporation, formerly Medialab Asia), MeitY, Government of India, for funding, Padup Ventures Pvt. Ltd., and Dr. Amitabha Bandyopadhyay, Senior Consultant, ITRA Ag&Food for helping to carry out this research work.

References

1. Khan D (2012) Entrepreneurship in farming
2. Morris W, Henley A, Dowell Da (2017) Farm diversification, entrepreneurship and technology adoption: analysis of upland farmers in Wales. *J Rural Stud* 53:132–143
3. Lauwere C, & Enting I, Vermeulen, P, Verhaar K (2002) Modern agricultural entrepreneurship. International farm management association, 13th Congress, Wageningen, The Netherlands, July 7–12
4. McElwee G (2006) The enterprising farmer: a review of entrepreneurship in agriculture. *J R Agric Soc England*
5. Dan S, Mukherjee K (2020) Individual pig recognition based on ear images. In: Accepted at COMSYS 2020
6. Mauboussin MJ, Callahan D (2015) Total addressable market methods to estimate a company's potential sales. *Credit Suisse*
7. Frow P, Payne A (2011) A stakeholder perspective of the value proposition concept. *Eur J Mark* 45(1/2):223–240
8. Anderson J, Narus J, Van Rossum W (2006) Customer value propositions in business markets. *Harvard Bus Rev* 84(3):91–99
9. Man T, Lau T, Chan KF (2002) The competitiveness of small and medium enterprises: A conceptualization with focus on entrepreneurial competencies. *J Bus Ventur.* 17. 123-142.
10. Hoekstra JC, Huiizingh EKRE (1999) The lifetime value concept in customer-based marketing. *J Mark-Focused Manage* 3:257–274. <https://doi.org/10.1023/A:1009842805871>
11. Ang L, Buttle F (2010) Managing for successful customer acquisition: an exploration. *J Mark Manage* 22:295–317

Adoption of IoT in Vehicular Traffic Control: An Overview



Joyeeta Goswami and Ashim Saha

Abstract The number of consumer vehicles is ever-increasing, and traffic management is becoming a big challenge all over the world. In hilly or forest-covered areas, the natural calamities are also an addition to this traffic problem. This gives rise to economic difficulties as well as the environmental cataclysm of society. IoT (Internet of Things) presently became a promising technology to solve various serious problems by establishing the link between the environmental parameters with cloud intelligence. As the name, IoT or Internet of Things suggest it connects Hardware Devices like a small sensor to cloud server through the Internet or Network. It's like the cryptic wand of the technical world. In this paper, we have presented a comprehensive survey on IoT and different existing traffic management systems based on IoT and the complexities related to them. We have also tried to approach a power-efficient IoT based smart traffic management system which also incorporates the detection of different unforeseen natural events like landslides, flood, etc. for all kinds of roads in rural and urban areas, and will reduce the chances of road accidents.

Keywords IoT · Traffic control system · VANET · DSRC · LoRaWAN

1 Introduction

IoT, the modern span of technology combines all the available devices to communicate under one network using the internet. There are several reports and statistics published that indicate that IoT is one of the hottest technologies of the twenty-first century. The Term IoT is termed by Kevin Ashton, who is the co-founder of Auto-ID Centre at MIT. in 1999. As per Business Insider's Report [1], in the next five years, a whopping \$6 trillion will be invested in IoT based products and will give an ROI of \$13 Trillion by 2025. By 2020, M2M communication which is one of the fundamental

J. Goswami (✉) · A. Saha (✉)
National Institute of Technology, Agartala, India
e-mail: joyeetatit@gmail.com

A. Saha
e-mail: ashim.cse@nita.ac.in

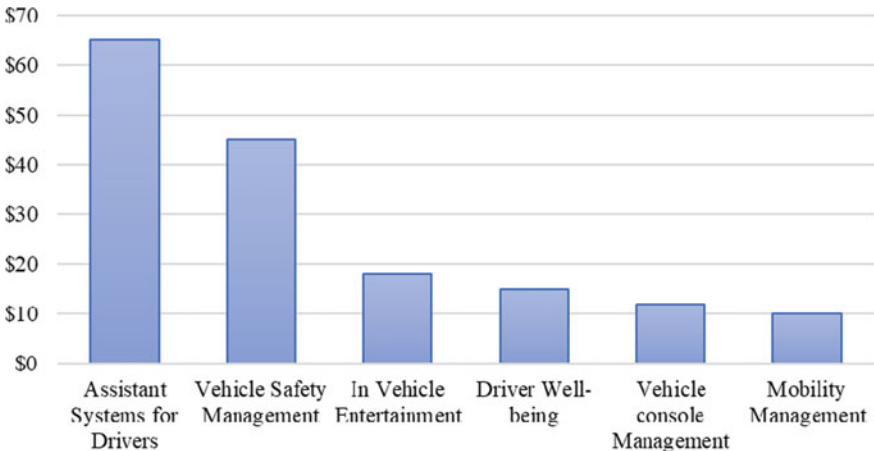


Fig. 1 IoV revenues in \$Billion

for IoT communication will grow to 12.2 Billion from currently 4.9Billion globally [2]. According to another report [3] published by Forbes IoT Market will reach up to 267billion USD in 2020. And domains like discrete manufacturing, Logistics, and transportation will drive more than 50% of total IoT expenses by the companies. Another report by McKinsey, suggests the total IoT market size in 2015 was up to \$900 M, growing to \$3.7 B in 2020 attaining a 32.6% CAGR.

Along with this, IoT has a significant role to play on Vehicular Ad Hoc Network or VANET. The use of Wireless Sensor Network (WSN) in VANET is widely popular nowadays. It is estimated that in 2017 the Market Value of the Internet of Vehicle (IoV) was \$66,075 million and it will increase to \$208,107 million by 2024 with a CAGR of 18% [4]. According to a report by IDC [5] more than 70% Light-duty Vehicles will be shipped with IoT and Internet-enabled with them. There are many applications of IoT including Agriculture, Automotive, Supply chain, Industrial Manufacturing, etc. In this paper, we will discuss the basic tech architecture of IoT along with a detailed survey on the traffic control system across the globe. At last, we will also discuss some areas researchers can work in this field. IoT based services are also generating new business stream and are expected to generate around \$152 B in 2020 (Fig. 1).

2 Communication Protocols

As an enormous and continuously advancing network, IoT has its range of protocols also transcend. From those protocols, some are not well known but some are very usual and used extensively in every field. These protocols establish communication between devices to exchange information with each other in a secured manner. There

Table 1 IoT Communication mediums comparison

Technology	Data rate	Range	Power use	Application
GPRS/HSDPA [39, 40]	Up to 10 Mbps	Long range	High	Cellular/Remote sensing
LTE [39, 40]	Up to 20 Mbps	Long range	High	Cellular/Remote sensing
Wi-Fi [40, 41]	Up to 54 Mbps	300 ft	High	Home automation/Remote device control
BLE (Bluetooth Low Energy) [39]	Up to 3 Mbps	300 ft	Low	Home automation/Wearables smartphone control/automotive
Xbee [39, 42]	Up to 250 Kbps	Up to 2 Kms LoS	Low	Home Automation/Mesh Network/Manufacturing/Traffic control systems
LoRA [6, 40]	Up to 50 Kbps	Up to 4 Kms LoS	Moderate	Remote sensing/Smart city/Industrial
Sigfox [39–41]	Up to 1 Kbps	Long Range	Moderate	Remote sensing/Smart city

are multiple communication channels available for both Near Field and Far Field Application. For devices that are in near proximity of each other, Bluetooth, Zigbee, and NFC are dominantly used for communication. And for far-field communication, technologies like Wi-Fi, Cellular. Recently Narrowband-IoT-based communication channels are also becoming very popular due to their low bandwidth requirements. Some of the technologies are LoRAWAN, Sigfox, Zwave, etc. Researches show that [6] for Smart Cities, using LoRA the scalability of the network can be significantly improved to get around 95% of the packet success rate for serving more than 15,000 nodes. The most popular communication technologies are tabulated here (Table 1).

3 Vehicular Ad Hoc Network (VANET) and Internet of Vehicle (IoV)

Vehicle-to-Vehicle or V2V communication is the rapidly growing technology that is possible by IoT as a foundation. In this type of communication, vehicles will communicate with each other by sharing their real-time information in the around 360-degree range [7]. By virtue of this V2V communication a new traffic Management technology has been established named ITS, i.e., Intelligent Transport System. The role of IoT technology here is to gather the information from various devices and analyze them to get the most preferable data and broadcast them to the unit or device where it needed. There are many technologies that are evolved or used in V2V Communication. One of such is VANET, which stands for Vehicular Ad hoc Network. VANET is the ad hoc network that supports Inter-Vehicular and Vehicle to Roadside Device Communication. It accumulates the real-time data from passing

by vehicles, analyze them, and produce some information message or alert message to the point where needed. VANET uses DTMAC protocol which is a distributed MAC protocol based on the TDMA scheme to establish communication between the moving vehicles by using the same frequency range without any interference [8]. It collects the real-time information of moving vehicles by using some combinations like Zigbee and GPS or DSRC and GPS, etc. In recent days and also for the future, the Dedicated Short Range Communication or DSRC protocol has taken a significant part in V2V communication. It is the wireless messaging technology of moving vehicles and operates on 5.9 MHz frequency. DSRC helps the drivers of moving vehicles to get the information about the surroundings (whether there is any vehicle or pedestrian is present or not) to control the vehicle according to the requirement, also gives the message about the coming vehicles to the pedestrians [9]. DSRC not only communicates between the vehicles but also sends the vehicle's data to nearby pedestrian and to VANET. VANET and DSRC commonly work together to control different causes of accidents such as Blindspot, Sudden lane change, Hard braking, Intersection movement, etc. For example, if any accident happens then DSRC will transmit the data to nearby devices and VANET collects this information and broadcast the message to the upcoming traffics so that they can control the vehicles and can avoid the congestion. VANET typically uses IEEE 802.11p, IEEE1609.1, 2, 3 and 4 communication standards [10].

IoV focuses on Intelligent integration of Vehicular communication with Environmental, drivers, and other parameters [8]. IoV integrates technologies like Telematics, Swarm Robotics, Machine Learning, Deep Learning, Artificial Intelligence, etc. to provide a credible, manageable and highly operational network which consist, multiple stakeholders, users, vehicle and decision-makers globally. A typical IoV implementation has two separate communication modes: Peer to Peer Model and Server-Client Model [11]. The communication between the Vehicles, i.e. V2V or Vehicle to Roadside Device or Control Unit communication works on Peer to Peer Model and Roadside Devices sends data to Cloud or Data Centre on Server-Client Model. Typically the Vehicle to Control Unit Communication is performed over IEEE 802.11 or IEEE 802.16 protocol [8]. The layer stack of IoV is as follows [11].

User Interaction Layer: This layer collects the data from Vehicles and it's environment.

Coordination Layer: Receives data from different sources and process them for analyzing.

Processing and Analysis Layer: Based on cloud, this layer performs all analyses and storage of the gathered data.

Application Layer: This layer offers intelligent services to end-users such as congestion management, alert, streaming, etc.

Business Layer: This layer is used for making business decisions and models from the IoV infrastructure (Fig. 2).

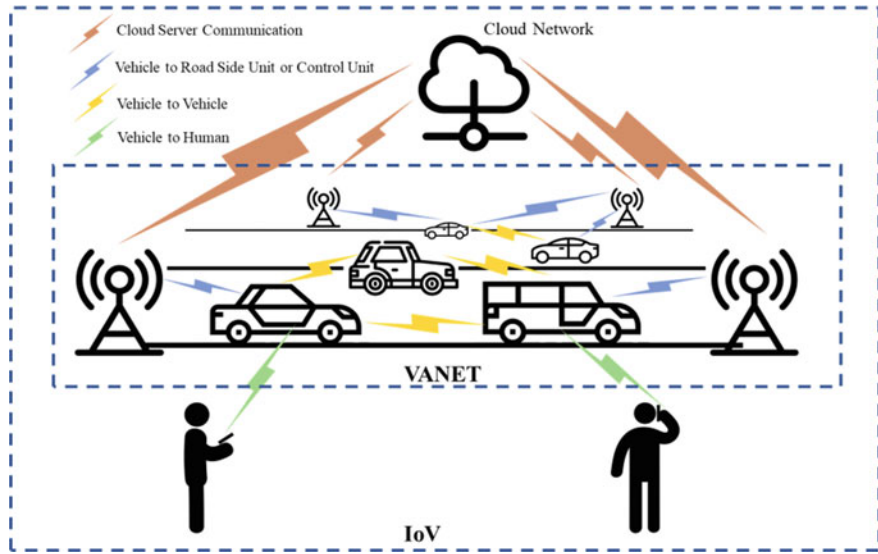


Fig. 2 VANET and IoV

4 Existing IoT Applications in Traffic Control

As day by day, the traffic problem is increasing, people from different corners of the world also developing advanced solutions with the help of the latest technologies. Some are trying to make it with wireless sensor networks [12, 13], some with RFID [14], some with the neural network [15], and so on. But the well-liked in recent times is the IoT based solutions. The Roadmap of IoT Based system is like this (Fig. 3).

Due to its mystic features, researchers are using this technology frequently. At the very beginning, people started with the M2M communication process, consisting of three parts: M2M devices, the server part, and a web-based user interface [16]. In this approach, the M2M server does the work to link the M2M devices with the authentication server or AAA (authentication, authorization, accounting), where authentication server will provide the number of vehicles in a particular area. The user interface (INVENTOR) gives all the information about the operation of the working unit to the authorized operator such as faulty units, errors, etc. [16]. After the basic



Fig. 3 IoV roadmap

structure, some improvisations had started. Cameras, snow sensors, fog monitors are placed in the place of normal sensors in the perception layers, in the network or server part cloud computing, data accuracy and validation has included, and the Service-Oriented Architecture (SOA) part was improvised with intelligent traffic control systems [17]. With the development people start to think of the separate parts of the traffic system using IoT. Some researchers thought about the crowd indexing system by using IoT structure to reduce the congestion on the roads [18]. Some started to think about the speed limit of vehicles to reduce accidents due to rash driving [19]. In [20] the system consisting of two parts the electronic system and the Software system. The electronic system detects and gathers the traffic data by utilizing the inductive loop detection method and transfers them to the base stations through Wi-Fi. And the second part consists of Green Light Phase Time (GLPT) Calculation Algorithm in cloud server which analyses the green light phase time and acknowledges back to the base station [20]. With the advancement of technology, people are analyzing the causes of traffic-related problems more deeply and try to solve them with more accuracy. Some are analyzing the accidents happen by sudden traffic slowdown due to other accidents, peak traffic time, work-in-progress, etc. [21]. Here it found that the sudden slowdown of traffic is mainly affected by inadequate visibility of drivers as a result of fog, tunnels, or any other reasons. In this case, Google maps are quite helpful but not for all kinds of roads. Here, the main focus is on the cloud server. By using the 4G network the real-time data from the sensors mounted in vehicles are transferred to an OpenGTS server which will load the information in a SQL database and gives a real-time OpenStreetMap traffic scenario [21]. In addition, those data are also put in a MongoDB distributed database by GeoJSON parsing, which will perform the marking of other vehicles on the same road in close proximity and to notify them about the sudden slowdown of traffic [21]. Some designs are working on the priority of traffic lanes using Wi-fi protocols [22], some are modifying the sensors to IR sensors [23]. As a whole of those modifications, the ultimate is the ITMS or Intelligent Traffic Management System to build a smart city. In this ITS or ITMS system the sensors (Ultrasonic, IR, Inductive loop detector) on the roads or in the moving vehicles will get the real-time information about the traffic density and broadcast them through IoT protocols (like wi-fi [22, 23], LoRaWAN [24, 25] and other above-mentioned protocols) to the nearest local units, other vehicles or pedestrian in the working range and also to the nearest communities, it means all the units in one system will get all the required information about other [26–29]. After collecting that information the cloud server analyzes them and works according to the given algorithm [29–32]. With the advancement, these smart systems have some challenges also like security, interoperability, connectivity, energy consumption, etc. [33]. But those problems are also been analyzed and solved by the researchers.

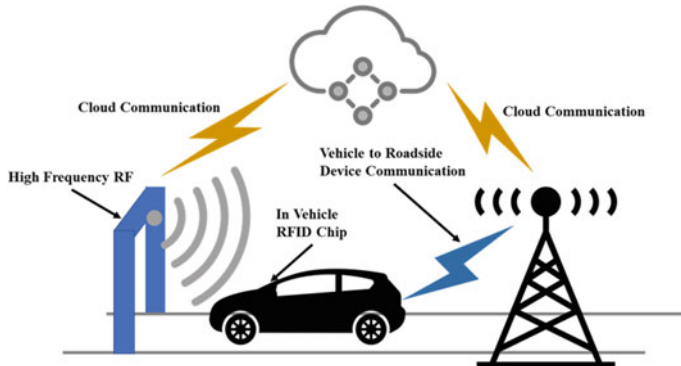


Fig. 4 Localization using RFID and vehicle to roadside communication

5 Way Forward

There are numerous researches performed in this field as discussed in the previous section. Many were also implemented nationally or internationally. Though in India due to several reasons, not many actual implementations are done.

5.1 Location Issues

In [34] many issues of Internet of Vehicle such as localization, security and Radio Propagation, etc. The GPS module has a location accuracy of 50 m in IoV systems. Also, the problem of signal loss is pretty dominant in dense areas. Using High-Frequency RFID along with GPS data can be helpful to mitigate localization issues. Some researchers are already conducting to use BLE beacon as an indoor navigation tool [35]. The security and privacy concerns are also important issues, that need to be taken care of. Researches may be conducted to implement a single global identifier and use the encryption algorithm for the same (Fig. 4).

5.2 Network Issues

As discussed in the last section, most of the system relies on the internet for communication between the sensor and cloud server. Based on the data sent from the sensors, the cloud server analyses the data and generates a proper flag based on the logic set by the administrator. This system heavily relies on internet connectivity but due to geographical extremities, it is very possible that in remote hilly areas the internet may not be available. So due to poor network connectivity, the cloud may not get

the sensor information and may not be able to generate an alarm. There are multiple ways to solve it. One approach could be using satellite communication instead of mobile networks as used by Ramesh [13]. But using VSAT increases the total cost of deployment. Also, the energy required for powering the VSAT satellites is also significant. To reduce the bandwidth requirement of the cellular network technologies like Narrowband IoT (NB-IoT) may be used. NB-IoT is an LP-WAN technology which uses an unused 200 kHz band and has a lower bit rate compared to LTE-M1. NB-IoT is supported by existing mobile networks and can support as long as 10 years of battery life [36].

5.3 Data Analytics

Data Analysis is the big challenge for the Internet of Vehicles as the Volume of Data generated is huge and mostly there is no trusted central authority. The automotive business and traffic controller authorities need to understand the type and nature of the data they required and integrate the solution to provide a rich contextual user interface in the IoV network. The trigger for any alarm should be contextual data-driven. That means the Analytical Model should be able to trigger the alarm based on the present data intent. Based on the data generated, the researchers may device predictive models which will help the drivers and other decision-makers to take informed decision about any situation.

6 Societal Impacts of IoV

With the Advancement of IoV along with Artificial Intelligence and Machine Learning, companies are coming up with autonomous vehicles, that will surely benefit the society by helping persons with special ability to commute easily and make driving a safer experience for all [37]. Around 90% of cases of car accidents are due to human error only [38]. IoV along with Autonomous technologies can help to save millions of people every year. The environment can also be less polluted by them as the usage of fossil fuel will reduce substantially.

7 Summary/Conclusion

In this paper, we have briefly discussed the various communication mediums used in IoT Implementation with their comparative study. We have discussed the overview of Vehicular Ad Hoc Network or VANET along with IoV. Then we reviewed some of the implementation and researches performed on the application of IoT in the traffic

Management system. Lastly, we have proposed multiple research options available for this domain, where researchers can work on the practical implementation of Traffic Management.

Acknowledgements This research work has been carried out in National Institute of Technology, Agartala, India sponsored by Department of Science & Technology(DST), Govt. of India under Interdisciplinary Cyber Physical System (ICPS) Program (Ref No: DST/ICPS/Cluster/IoT/2018/General Dated: 26.02.2019).

References

1. Here's how the Internet of Things will explode by 2020. <https://www.businessinsider.com/iot-ecosystem-internet-of-things-forecasts-and-business-opportunities-2016-4-28?IR=T>. Accessed 28 Apr 2016
2. Cisco visual networking index predicts near-tripling of IP traffic by 2020. <https://newsroom.cisco.com/press-release-content?type=press-release&articleId=1771211>. Accessed on 07 June 07
3. Columbus L. Internet Of Things market to reach \\$267B by 2020. <https://www.forbes.com/sites/louiscolumbus/2017/01/29/internet-of-things-market-to-reach-267b-by-2020/#403928ad609b>. Accessed on 29 Jan 292017
4. Internet of vehicles (IoV) market analysis and forecast 2019–2024 by: Ford Motor, Texas Instruments, Audi, Intel, SAP, NXP Semiconductors, Apple. <https://www.marketwatch.com/press-release/internet-of-vehicles-iov-market-analysis-and-forecast-2019-2024-by-ford-motor-texas-instruments-audi-intel-sap-nxp-semiconductors-apple-2019-10-16>
5. Worldwide connected vehicle shipments forecast to reach 76 million units by 2023, according to IDC. <https://www.idc.com/getdoc.jsp?containerId=prUS45092819>
6. Magrin D, Centenaro M, Vangelista L (2017) Performance evaluation of LoRa networks in a smart city scenario. In: 2017 IEEE international conference on communications (ICC). IEEE, pp 1–7
7. Preview the future of transportation-connected vehicles!. https://www.its.dot.gov/factsheets/pdf/Animation_preview.pdf
8. Fangchun Y, Shangguang W, Jinglin L, Zhihan L, Qibo S (2014) An Overview of Internet of Vehicles. In: China Communications. <http://sguangwang.com/PDF/An%20Overview%20of%20Internet%20of%20Vehicles.pdf>
9. Ashtaiwi A. Vehicle ad hoc networks. https://youtu.be/i2nGSUx9r_s
10. Borcoci E. From vehicular ad-hoc networks to Internet of Vehicles. https://www.aria.org/conferences2017/filesICN17/EugenBrcoci_NexComm2017_Tutorial.pdf
11. Gasmi R, Aliouat M (2019) Vehicular ad hoc networks versus Internet of Vehicles—A comparative view. In: 2019 International Conference on Networking and Advanced Systems (ICNAS)
12. Elmirini A, Amrani AG (2018) Wireless sensors network for traffic surveillance and management in smart cities. In: IEEE 5th international congress on information science and technology (CiSt)
13. Ramesh MV. Real-Time wireless sensor network for landslide detection. In: 2009 Third international conference on sensor technologies and applications. <https://doi.org/10.1109/sensorcomm.2009.67>
14. Guo L, Fang W, Wang G, Zheng L (2010) Intelligent traffic management system base on WSN and RFID. In: International conference on computer and communication technologies in agriculture engineering

15. Gilmore J, Abe N (2010) A neural networks system for traffic congestion forecasting., In: International conference on neural networks (IJCNN-93-Nagoya, Japan), 1993
16. Foschini L, Taleb T Corradi A, Bottazzi D. M2M-based metropolitan platform for IMS-enabled road traffic management in IoT. *IEEE Commun Mag* 49(11):50–57
17. Yu X, Sun F, Cheng X (2012) Intelligent urban traffic management system based on cloud computing and Internet of Things. In: International conference on computer science and service system. <https://doi.org/10.1109/CSSS.2012.539>
18. Zhang SJ, Chen SY (2014) Design and implementation of real-time broadcast system of urban public transport crowding index based on the Internet of Things. *Adv Mater Res* 1049–1050:1753–1758
19. Goswami J, Ghosh S, Katiyar S, Majumder A (2015) Development of a prototype to detect speed limit violation for better traffic management. In: Eighth international conference on contemporary computing (IC3). <https://doi.org/10.1109/ic3.2015.7346723>
20. Chong HF, Ng DWK (2016) Development of IoT device for traffic management system. In: IEEE Student Conference on Research and Development (SCORED)
21. Celesti A, Galletta A, Carnevale L, Fazio M, Ekuakille AL, Villari M (2017) An IoT cloud system for traffic monitoring and vehicular accidents prevention based on mobile sensor data processing. In: IEEE 1558-1748
22. Nagmode VS, Prof. Dr. Rajbhoj SM (2017) An IoT platform for vehicle traffic monitoring system and controlling system based on priority. In: 3rd International conference on computing and communication, control and automation (ICCUBEA)
23. Rani PJ, Kumar LK, Naresh M, Vignesh KS (2017) Dynamic traffic management system using infrared (IR) and Internet of Things (IoT). In: Third International conference on science technology engineering and management (ICONSTEM)
24. Kadir EA, Efendi A, Rosa SL Application of LoRa WAN sensor and IoT for environmental monitoring in Riau Province Indonesia, In: 5th International conference on electrical engineering, computer science and informatics (EECSI). <https://doi.org/10.1109/eecsi.2018.8752830>, 2018
25. Khattak HA, Farman H, Jan B, Din IU (2019) Toward integrating vehicular clouds with IoT for smart city services. *IEEE Netw* 33(2):65–71. <https://doi.org/10.1109/mnet.2019.1800236>
26. Sadhukhan P, Gazi F, An IoT based intelligent traffic congestion control system for road crossings. In: International conference on communication, computing and Internet of Things (IC3IoT). <https://doi.org/10.1109/ic3iot.2018.8668131>, 2018
27. Masum AKM, Chy KAM, Rahman I, Uddin MN, Azam KI (2018) An Internet of Things (IoT) based smart traffic management system: a context of Bangladesh. In: International conference on innovations in science, engineering and technology (ICISET)
28. Nafia HJ, Jacob SM, Nair N, Paul JJ (2018) Density based smart traffic system with real time data analysis using IoT. In: International conference on current trends towards converging technologies (ICCTCT)
29. Luo XG, Zhang HB, Zhang ZL, Yu Y, Li K (2019) A new framework of intelligent public transportation system based on the Internet of Things, vol 7. <https://doi.org/10.1109/access.2019.2913288>. Accessed on 17 April 2019
30. Mehmood Y, Ahmad F, Yaqoob I, Adnane A, Imran M, Guizani S (2017) Internet-of-Things-based smart cities: recent advances and challenges. *IEEE Commun Mag* 55(9):16–24. <https://doi.org/10.1109/mcom.2017.1600514>
31. Putra AS, Warnars HLHS. Intelligent traffic monitoring system (ITMS) for smart city based on IoT monitoring. In: The 1st 2018 INAPR international conference, 7 Sept 2018, Jakarta, Indonesia
32. Anitha, Babu KNRM (2018) IOT for ITS: an IOT based dynamic traffic signal control. In: International conference on inventive research in computing applications (ICIRCA)
33. Du R, Santi P, Xiao M, Vasilakos AV, Fischione C (2018) The sensible city: a survey on the deployment and management for smart city monitoring. *IEEE Commun Surv Tutor* 1–1. <https://doi.org/10.1109/comst.2018.2881008>

34. Kaiwartya O, Abdullah AH, Cao Y, Altameem A, Prasad M, Lin CT, Liu X (2016) Internet of vehicles: Motivation, layered architecture, network model, challenges, and future aspects. *IEEE Access* 4:5356–5373
35. Singh A, Shreshthi Y, Waghchoure N, Wakchaure A (2018) Indoor navigation system using bluetooth low energy beacons. In: 2018 Fourth international conference on computing communication control and automation (ICCUBEA). IEEE, pp 1–5
36. <https://www.gsma.com/iot/narrow-band-internet-of-things-nb-iot/>
37. Connected autonomous vehicles—How does their social impact generate innovation? <https://www.lexology.com/library/detail.aspx?g=df22bfc0-90e1-46f5-9da3-8ba891e6e607>
38. The social implications of driverless cars. <https://www.bbvaopenmind.com/en/technology/artificial-intelligence/the-social-implications-of-driverless-cars/>
39. 11 Internet of Things (IoT) protocols you need to know about. <https://www.rs-online.com/designspark/eleven-internet-of-things-iot-protocols-you-need-to-know-about>. Accessed on 20 Apr 2015
40. Hasan M. Top 15 standard IoT protocols that you must know about. <https://www.ubuntupit.com/top-15-standard-iot-protocols-that-you-must-know-about/>
41. Sakovich N (2018) Internet of Things (IoT) protocols and connectivity options: an overview. <https://www.sam-solutions.com/blog/internet-of-things-iot-protocols-and-connectivity-options-an-overview/>. Accessed on 22 Aug 2018
42. Rouse M. Zigbee. <https://internetofthingsagenda.techtarget.com/definition/ZigBee>. Accessed on June 2017

Optimal Placement of FACTS Devices in the Power System Using ANN to Increase the System Loadability



Mohammad Khalid Saifullah, Md. Monirul Kabir, Nasim Mia, and Tanvir Ahmed

Abstract Continuous monitoring of online voltage stability as well as increasing loadability of the existing electrical power system transmission lines are the most important issues for energy management systems in modern days. In this regard, the task of monitoring online voltage stability for various loading conditions is very much complex and time-consuming. This paper demonstrates an efficient voltage stability monitoring system using the computation of line voltage stability indices involving an artificial neural network (ANN) for reducing the complexity of an online voltage monitoring system that can provide warning information to the operator before voltage collapses. Comparative studies of system voltage stability and loadability at load point after placing the FACTS devices in the weakest lines of the power system are presented in this paper. In order to evaluate our proposed system how does it work; a series of experiments were conducted involving IEEE 14 bus power system network. The simulation result confirms that the proposed system can ensure power system operation security as well as reduce electrical power system installation cost by increasing system loadability.

Keywords Line voltage stability indices · Loadability · Voltage stability · FACTS devices · ANN

M. K. Saifullah · N. Mia · T. Ahmed

Department of EEE, Mymensingh Engineering College, Mymensingh, Bangladesh
e-mail: saifullahmec254@gmail.com

N. Mia

e-mail: iamnasim820@gmail.com

T. Ahmed

e-mail: tanvirahmed.eee15@gmail.com

Md. M. Kabir (✉)

Department of EEE, Dhaka University of Engineering & Technology, Gazipur, Bangladesh
e-mail: munir@duet.ac.bd

1 Introduction

Nowadays, appraisement and controlling of voltage stability of power systems have attained considerable attention although they are not new issues. The entire research works in this field can be divided into several parts among which estimating the distance towards voltage collapse is very important for the operators. For example, the demand for electrical energy is increasing day after day but there is a shortage in installed capacities. As a result, modern power systems are sometimes being operated very closed to the stability margins [1]. Therefore, maintaining voltage stability and managing demand has become major concerns for energy management systems (EMSs) of modern time [2].

As an important tool of online voltage stability appraisement, an artificial neural network (ANN) has earned worldwide attention to the scholars and researchers in recent years. The voltage stability assessment problems are non-linear in nature, therefore, the ANNs are considered as a better option over operable analytical methods of voltage stability monitoring [3, 4].

However, in this paper, an efficient voltage stability monitoring system has been presented called as VSMS that is formulated by four ways: (1) the computation of line voltage stability indices (LVSI) of a power system network, (2) generating a dataset of the particular network based on LVSI method with varying the loads, (3) performing the ANN training process on the intelligent dataset as well as achieving testing ANN for certain voltage collapsed load, (4) finding the ranking of different buses of the particular network on basis of the testing ANN, (5) finally, placing the FACTS devices in the weakest lines of the power system. The proposed VSMS reduces the complexity of an online voltage monitoring system that can provide warning information to the operator before voltage collapses. Comparative studies of improvement of system voltage stability and loadability at load point after placing the FACTS devices in the weakest lines of power system are presented in this paper.

The remainder of this paper is organized as follows. The proposed VSMS is briefly discussed in Sect. 2. Experimental studies are mentioned in Sect. 3. Experimental results are reported in Sect. 4. Short conclusions with few remarks are given in Sect. 5.

2 Proposed Voltage Stability Monitoring System (VSMS)

In this paper, an efficient voltage stability monitoring system (VSMS) has been demonstrated that is mainly formulated by computing the LVSI methods. Generally, LVSI methods are two types, such as the Jacobian matrix based LVSI method and system variables based LVSI method. The latter one was selected for the proposed VSMS because of its less complexity and less computational time. Two methods of LVSI (1) Line stability index (L_{mn}) shortly known as L -index method and (2) Fast voltage stability index shortly known as $FVSI$ have been used in this work. However, the major steps of VSMS are further explained as follows:

- Step-1 Select the suitable two methods of LSVI from various methods and selection of the optimum FACT device.
- Step-2 Calculate the LSVI value of all lines of IEEE-14 bus power system using verified data to generate the training data set for ANN.
- Step-4 Complete the data prediction process by trained ANN and ranking of the lines according to stability index to find out the weakest lines.
- Step-5 Place the selected FACT device in the weakest line in power system.
- Step-6 Compare the improvement of load point voltage stability and loadability of the power system with and without FACT devices.

It is now clear that the idea behind VSMS is straightforward, i.e., generating the training data and performing the ANN training and ranking the buses of power system network. The following section gives more details about the different components of our proposed system.

2.1 Selection of Stability Index and FACTS Device

As mentioned earlier, *L*-index method was chosen for training data generation of ANN, whereas, *FVSI* method was used for the verification of generated data because of their simplicity and popularity. A power system consists of two machine 100 and 5000 MVA, 50 Hz, 640 km transmission line, three buses with power system stabilizers (PSS) had been simulated in MATLAB/SIMULINK with various FACTS devices (UPFC, TCSC, SVC, STATCOM and SSSC) to find out the effective one. From simulation results and other research results, it has been noticed that UPFC is the quickest and most effective FACTS devices. Therefore, for the proposed system UPFC was selected to install in electrical power system to improve voltage stability.

2.2 Formulation of LSVI

Various types of LSVI methods have been proposed by the authors mentioned in [5–7]. In Fig. 1 a single line diagram of a simple single bus electrical power system has been shown that has been used in formulation of LSVIs.

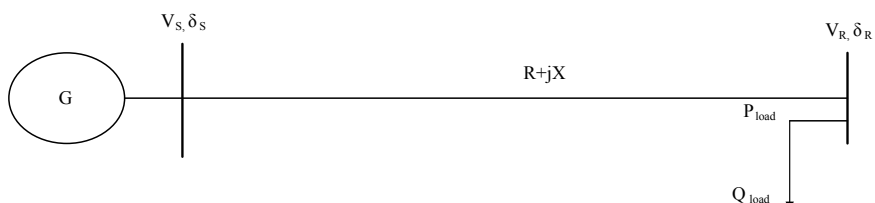


Fig. 1 Simple single line diagram of a single bus electrical power system

Here, line impedance, resistance, reactance and line impedance angle are denoted by Z , R , X and θ , respectively. V_R is voltages in the receiving end, V_S is denoted for voltage in the sending end, δ_R is phase angle at the receiving end and δ_S is phase angle at the sending end. Again, receiving end reactive power is denoted by Q_R and P_R is receiving end active power. The L -index method is presented in the Eq. 2.1 mentioned in [8, 9] that was proposed on the basis of reactive power flow in an electrical power systems transmission line. For the stability condition of line voltages, the values of the L -index or L_{mn} for the lines need to be equal or less than one. Here, the sending bus voltage phase angle is δ_m , the receiving bus voltage phase angle is δ_n , therefore $\delta = \delta_m - \delta_n$ and $\theta = \tan^{-1}(X/R)$. Fast voltage stability index ($FVSI$) method was provided by Musirin et al. [10]. The equation for $FVSI$ method is presented in Eq. 2.2. Here the parameters are the same as discussed before. For stability, the value of $FVSI$ should be equal or less than one.

$$L_{mn} = \frac{4XQ_R}{[V_s \sin(\theta - \delta)]^2} \quad (2.1)$$

$$FVSI = \frac{4Z^2Q_R}{V_s^2 X} \quad (2.2)$$

3 Experimental Studies

This section presents VSMS's performance on IEEE-14 bus power system network. In this section, the ANN structure, its training dataset structure, training performance, ranking of weakest line according to predicted output of ANN, and installation of FACTS devices process are briefly discussed. The result and its discussion are given in the next Sect. 4.

3.1 Experimental Setup

In this study, a feed-forward ANN was used including one input layer, one hidden layer and one output layer as shown in Fig. 2. In this ANN, the input variables are the variation of reactive loading conditions on the load buses and output or, target variables are the LSVI values of the interconnection lines or, power transmission lines between the buses of IEEE 14 bus power system. Here, the size of input layer, hidden layer and output layer were considered as 14, 10 and 20, respectively. In data generation, 10% of uniform increment the load variation was considered from 0% to 500% of input parameters. Furthermore, LSVI values of 20 interconnected lines in IEEE 14 bus power system were calculated for load variation of 0–500% as the

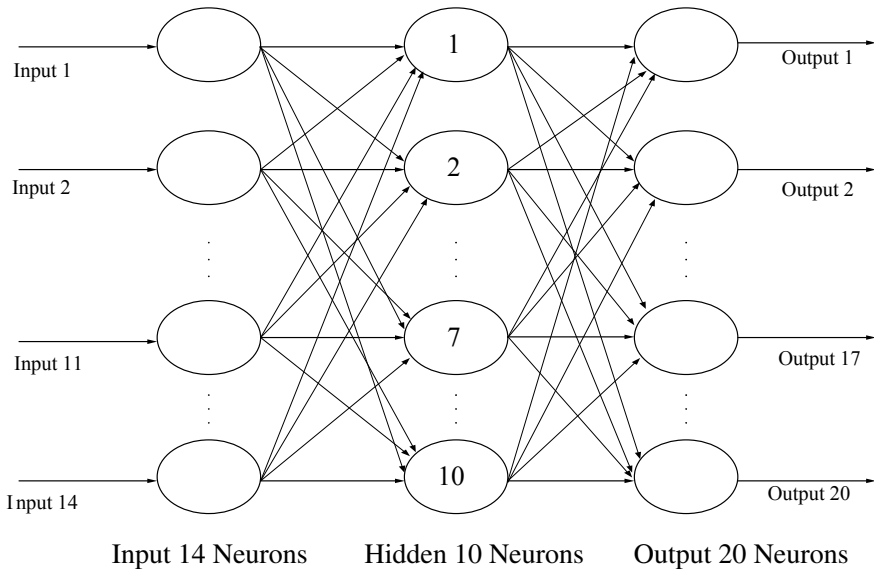


Fig. 2 ANN structure for IEEE 14 bus power system

output parameters. The *L*-index method and *FVSI* method were used for generating as well as verifying the training data, respectively.

3.2 ANN Training Performance

In this context, the total 51 patterns of training data for ANN were divided into three parts (1) training patterns, (2) validation patterns and (3) testing patterns. The ANN used the training data sets to train itself and used the validation data sets to update the weight (relations between the layers and neurons) and finally used test data sets to test itself. The permissible minimum error for the ANN was installed 10^{-9} . It is seen in Fig. 3 that the minimum error during validation was found at epoch 577. Therefore, the validation performance of the ANN network is satisfactory.

To verify the performances of the trained ANN two prototype data set of two different loading condition was given to the ANN. The graphical comparison of actual and predicted values of *L*-indexes (L_{mn}) for prototype Sample 1 and 2 input shown in Fig. 4. In the figure, it was seen that the actual and predicted data sets were all most same value except one small difference in line 19 for Sample 1.

For measuring accuracy criteria of prediction performances of the trained ANN for the two different loading conditions given to ANN in prototype Sample 1 and 2, the Mean Absolute Percentage Error (*MAPE*) of predicted output data were calculated according to the method given in Eq. 3.1. The less value of *MAPE* indicates the more accuracy of prediction performance of the trained ANN.

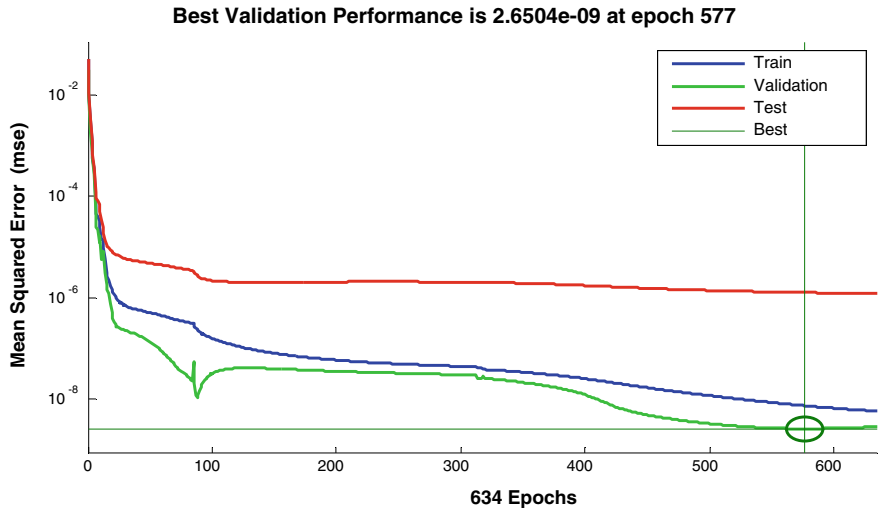


Fig. 3 Validation performance of the ANN network for IEEE 14 bus power system

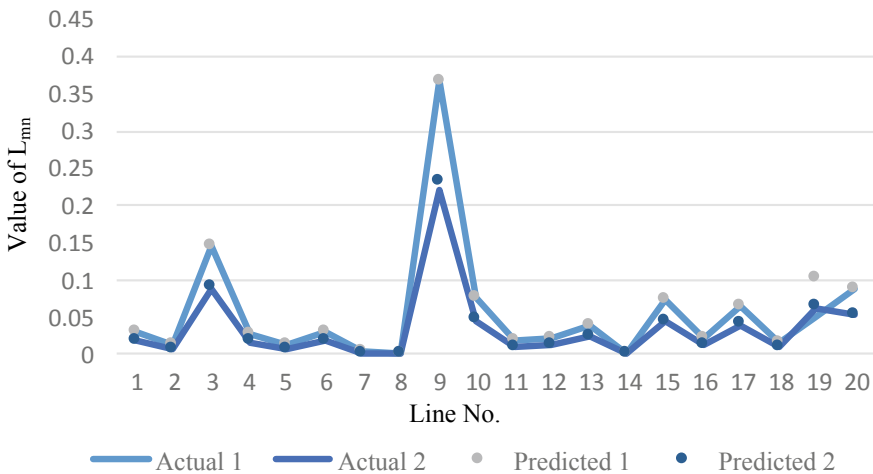


Fig. 4 Actual and predicted L_{mn} value for prototype input Sample 1 and Sample 2

$$\text{MAPE} = \frac{1}{N} \sum_{n=1}^N \left| \frac{A_n - P_n}{A_n} \right| \times 100 \quad (3.1)$$

Here, A_n represents the actual value of line voltage stability index and P_n represents the predicted value of line voltage stability index and N represents the total sample numbers available in the output samples. In Table 1 MAPE calculation results have

Table 1 MAPE calculation result of predicted outputs for prototype input Sample 1 and Sample 2

MRPE in (%)	
Sample 1	Sample 2
-0.27	-0.099640

Table 2 Ranking of the weakest lines of IEEE 14 electrical power system

Rank	Line No.	From bus	To bus
1	9	4	9
2	3	2	3
3	19	12	13
4	20	13	14
5	10	5	6

been mentioned. From Table 1 is seen that the error was very low, therefore the performance of trained ANN was satisfactory.

3.3 Ranking of Weakest Lines

Analyzing the simulation result of LVSI (value of L_{mn}) prediction by ANN of the IEEE 14 electrical power system, the 5 weakest transmissions lines have been identified those have the most probability of voltage collapse at rated baseload condition of buses in power system. The ranking of weakest lines has been shown in Table 2. As discussed before for voltage stability of transmission lines the value of L_{mn} should not gather than one. Therefore, the smaller value of L_{mn} signifies the better voltage stability of the lines in power system. Similarly, the line having bigger value of L_{mn} is weaker than the line having smaller value of L_{mn} . According to the values of L_{mn} , the weakest lines of the power system had been ranked that is mentioned in Table 2. From the predicted result it had been observed that the highest output value of L_{mn} was in line no. 9 which is the interconnection between bus no. 4 and bus no. 9, whereas, the second-highest value is in line no. 3 (interconnection between bus no. 2 and bus no. 3) and successively the other 3 weakest lines are 19, 20, and 10. These lines having the most probability of voltage collapse. Therefore, the selected FACTS devices UPFC should be installed in these lines. If the loading condition of the buses of power systems is changed, then the rank of the weakest line can be changed also.

3.4 Installation of FACTS Devices

Now, the FACTS device UPFC having capacitive reactance and inductive reactance $X_c = 0.05$ p.u. and $X_l = 0.05$ p.u., respectively was installed in the weakest power

Table 3 Voltage stability improvement data of the weakest lines after installing the FACTS devices

Line No.	Stability without FACTS	Stability with FACTS	Stability Improvement in %
9	0.36927	0.213183	42.27
3	0.14634	0.1120	23.47
19	0.10306	0.069994	32.08
20	0.08644	0.056124	35.05
10	0.075608	0.048052	37.07

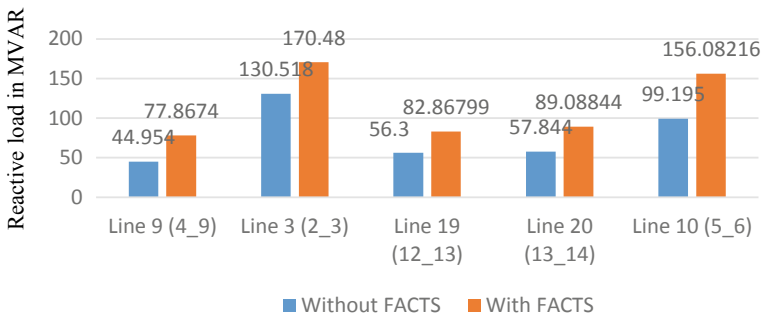


Fig. 5 Lodability improvement of the weakest lines after installing the FACTS devices

transmissions lines one after one those has been ranked in Table 2 earlier [11]. After installing the FACTS devices on the lines, the line voltage stability and lodability were improved as shown in Table 3 and Fig. 5.

4 Results and Discussions

The line voltage stability and reactive loadability of the electrical power transmissions lines have been significantly enhanced after installing FACTS devices. Voltage stability improvement of the weakest lines of IEEE 14 bus power system at baseload conditions showed in Table 3. The average improvement of the lines voltage stability is more than 33% for IEEE 14 bus power system. If the X_c and X_l value is changed then the amount of voltage stability improvement will change. In Fig. 5 the comparison between loadability of the weakest lines before FACTS devices installation and after FACTS devices installation in the weakest lines has been sowed for base loading conditions of IEEE 14 power system.

The average loadability improvement that had been calculated for each line was more than 37 MVAR (48%). The maximum line voltage stability improvement for FACTS devices installation was found more than 42% in line no. 9 that is interconnection line of bus no. 4 and bus no. 9. But the maximum line loadability improvement

for the FACTS devices installation was found more than 50 MVAR in line no. 10 that is interconnection between bus no. 5 and bus no. 6. The minimum line voltage stability improvement for FACTS devices installation was found more than 23% in the line no. 3 that is interconnection line of bus no. 2 and bus no. 3. But the minimum line loadability improvement for the FACTS devices installation was found more than 25 MVAR in line no. 19 that is interconnection between bus no. 12 and bus no. 13. The UPFC FACTS devices having $X_c = 0.05$ p.u. and $X_l = 0.05$ p.u. were installed in the lines as mentioned before. If the value of X_c and X_l is changed then the amount of loadability improvement will change. The improvement of lines loadability after FACTS devices installation in the weakest lines in IEEE 14 bus power system was calculated using LVSI method. Again, the amount of stability improvement and line loadability increment also depends on various parameters of the power system such as line impedance, line resistance, line reactance, and many more.

5 Conclusion

In this paper, an efficient voltage stability monitoring system, VSMS has been demonstrated. Incorporation of the system variables based LVSI method and ANN training, the proposed VSMS can easily find out the weakest electrical power transmissions lines that have the maximum probability of voltage collapse in the power system. After that, placing the suitable FACTS devices to the weakest lines improves the overall voltage stability and loadability of the power system. In the experimental studies, the proposed VSMS used standard IEEE 14 electrical power system, in where the experimental results for various loading conditions confirmed that a significant amount of improvement of system voltage stability and loadability was obtained after installing the UPFC FACTS devices in the weakest power transmissions lines (see Table 3 and Fig. 5). Furthermore, the proposed VSMS can minimize the complexity of LVSI calculation using ANN. Thus, an operator of a certain power system network can monitor and take necessary steps within the very shortest time. In Fig. 5, it was found that the loadability of the existing lines was increased by installing FACTS devices. Thus, new electrical loads can be added without installing a new power system network. Finally, it can be said that the proposed system may ensure secured and reliable service to the consumer as well as having economic significance by reducing the electrical energy cost.

References

1. Goh HH, Chua QS, Lee SW, Kok BC, Goh KC, Teo KTK (2015) Comparative study of line voltage stability indices for voltage collapse forecasting in power transmission system. *Eng Technol Int J Civil Environ Eng* 9:2–7
2. Ashraf SM, Gupta A, Choudhary DK, Chakrabarti S (2017) Voltage stability monitoring of power systems using reduced network and artificial neural network. *Electr Power Energy Syst* 87:43–51
3. Sobajic DJ (1993) Neural network computing for the electric power industry. Lawrence Erlbaum Associates, Publishers, Mahwah, NJ, USA
4. Jayasankara V, Kamaraj N, Vanaja N (2010) Estimation of voltage stability index for power system employing artificial neural network technique and TCSC placement. *Neurocomputing* 73:3005–3011
5. Ratra S, Tiwari R, Niazi KR (2018) Voltage stability assessment in power systems using line voltage stability index. *Comput Electr Eng* 1–13
6. Mohamed O, Jasmon AG, Yusoff S (1989) A static voltage collapse indicator using line stability factors. *J Ind Technol* 7:73–85
7. Goh HH, Chua QS, Lee SW, Kok BC, Goh KC, Teo KTK (2015) Evaluation for voltage stability indices in power system using artificial neural network. In: International conference on sustainable design, engineering and construction, procedia engineering, vol 118, pp 1127–1136
8. Moghavvemi O, Omar M, Omar F (1998) Technique for contingency monitoring and voltage collapse prediction. In: IEEE proceedings—generation on transmission and distribution, vol 145, pp 634–640
9. Moghavvemi M, Omar FM (1998) Technique for contingency monitoring and voltage collapse prediction. IEEE proceedings—Generation, transmission & distribution, pp 634–640
10. Musirin O, Rahman I, Rahman TA (2002) Novel fast voltage stability index (FVSI) for voltage stability analysis in power transmission system. In: IEEE student conference on research and development (2002)
11. Gerbex S, Cherkaoui R, Germond AJ (2001) Optimal location of multi-type FACTS devices in a power system by means of genetic algorithms. *IEEE Trans Power Syst* 16:3

Impact of Noise Levels on SVM-GMM Based Speaker Recognition System



Renu Singh, Utpal Bhattacharjee, Arvind Kumar Singh,
and Madhusudhan Mishra

Abstract Speaker recognition is one of the most popular voice biometric techniques used for security reasons in many areas like the banking system, online-shopping, database access, etc. The Speaker recognition system (SRS) works very well in noise-free environments as compared to noisy environments. In this study, the impact of noise levels has been studied by the application of support vector machine-Gaussian mixture model (SVM-GMM) based speaker recognition system. It has been observed that the recognition accuracy improves beyond SNR equals 10 dB with the use of the proposed hybrid system.

Keywords Speaker recognition system · Support vector machine-Gaussian mixture model · Mel-frequency cepstral coefficients · Signal-to-noise ratio

1 Introduction

Speaker recognition is the procedure of recognizing the voice of a speaker by utilizing explicit information encompassed in voice samples [1, 2]. The methodology can be used to verify the claimed identity of people for accessing the systems and enabling

R. Singh (✉) · A. K. Singh

Department of Electrical Engineering, North Eastern Regional Institute of Science and Technology, Nirjuli, Arunachal Pradesh 791109, India

e-mail: renumona08@gmail.com

A. K. Singh

e-mail: singharvindk67@gmail.com

U. Bhattacharjee

Department of Computer Science, Rajiv Gandhi University, Papum Pare, Arunachal Pradesh 791112, India

e-mail: utpalbhattacharjee@rediffmail.com

M. Mishra

Department of Electronics and Communication Engineering, North Eastern Regional Institute of Science and Technology, Nirjuli, Arunachal Pradesh 791109, India

e-mail: ecmадhusudhan@gmail.com

access control over various services by recognizing the voice. The various applications of the speaker recognition system are voice dialing, phone banking, phone shopping, database access, information and reservation facilities, voice mail, data security control, and remote access of PCs. The other significant use of this technology of speaker recognition is its utilization for criminological purposes [3].

Speaker recognition can be characterized into a number of classes, for example, open and closed set, speaker identification and speaker verification, text-dependent, and text-independent [4]. The recognition of a speaker using a machine comprises the extraction of features, modeling of speaker, and its testing [5]. The estimation of the specific features of the speaker from the speech signal is done using feature extraction. Thereafter, the speaker model is trained with the use of these features. Finally, in the stage of testing, recognition of the speaker is performed by matching with the pattern. The objective of the present work is to investigate the effectiveness of the speaker recognition system accuracy in different noise levels.

2 Speech Parameterization

The inspiration behind the speech parameterization for speaker recognition is to find the phonetic-discriminative attributes of voice signals while neglecting the untrustworthy parts. The best parametric illustration of acoustic waves can be obtained to create a superior performance of a recognition system. The proficiency of this stage influences the activity of the consequent phases. The importance of cepstral features particularly the mel-cepstral for speaker recognition has been studied by many researches [6, 7]. In spite of several limitations, in practical applications using the cepstral features due to high sensitivity in the channel and background noises [8]. Mel-frequency cepstral coefficients are the widely used feature both in speech and speaker recognition systems. Figure 1 represents the block diagram of Mel-frequency cepstral coefficients feature extraction process [9, 10].

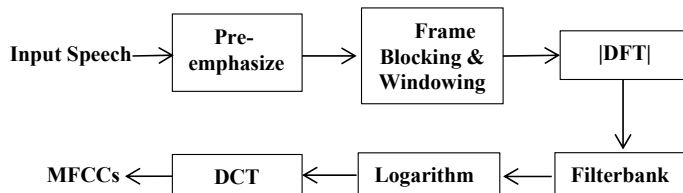


Fig. 1 MFCC feature extraction process

3 Database and Experimental Setup

In this work, the NIST 2003 SRE dataset of clean speech has been used. The voice samples are mixed with various kinds of noises ranging from 0 to 20 dB with an interval of 5 dB signal-to-noise ratio. The AURORA databases are used in preparing the sound noises. The different types of additive noises such as airport, car, exhibition, restaurant, street, and train are added to the clean database of NIST 2003. The following parameters viz. hamming window of length 20 ms, the frame rate of 1600 Hz with 0.97 pre-emphasis factors are considered for analyzing the speech signals. Apart from this for the computation of MFCC features 22 channel filter bank and cepstral features of 14-dimension with cepstral coefficients ranging from c_1 to c_{13} are used in this analysis. In order to achieve the final feature dimension of 39, the derivatives of the first- and second-order are added with the base features.

4 Hybrid Speaker Modeling

In this work support vector machine cum Gaussian mixture model has been used. The structure of SVM and GMM-UBM framework was performed in three phases, i.e., training the data using Support Vector Machine (SVM) classifier, building a Universal Background Model (UBM) as well as the speaker models. A gender-dependent 1024 component GMM-UBM has been offline trained for the used dataset considering expectation-maximization algorithm with 100 iterations.

5 Results and Discussion

The performance of a speaker recognition system is degraded in the presence of noisy conditions due to the acoustic mismatch between trained and testing conditions. The influence of noise levels at different noisy environments on SVM-GMM hybrid speaker recognition system is calculated using equal error rate (EER), detection cost function (DCF), and recognition accuracy. The estimation of the EER value of an SRS system depends on the computation of log-likelihood ratio (LLR) scores. Generally, a large number of testing samples are required for the evaluation of false reject rate (FRR) and false alarm rate (FAR), so that the EER can be determined. The DCF is determined as a weighted sum of the two error probabilities and the recognition accuracy as [11]:

$$\text{DCF} = C_{\text{miss}} P_{\text{miss}} P_{\text{target}} + C_{\text{false alarm}} P_{\text{false alarm}} (1 - P_{\text{target}})$$

$$\text{Recognition accuracy}(\%) = 100 - \text{EER}$$

The percentage EER values of SVM-GMM and GMM based speaker recognition systems in clean conditions are shown in Table 1. Table 2 represents the individual and average EER value of SVM-GMM based speaker recognition system at 0, 5, 10, 15, and 20 dB signal-to-noise ratios in various noisy environments viz. airport, car, exhibition, restaurant, street, street, and train noises, respectively. From the results, it has been observed that the impact of noise levels is varying for noisy environments. From the table, it is seen that at 0 dB noise level, the percentage equal error rate (% EER) is observed to be lowest for the street which equals 19.88, whereas the highest % EER has been obtained for exhibition noise and equals 26.80. It can also be seen that the percentage of EER is maximum at 5 dB for all the noises considered, and it decreases with an increase in SNR in the range of 10–20 dB. The values of DCF calculated falls in the range of 0.18–0.45.

The recognition accuracy percentage of SVM-GMM based speaker recognition systems at different noise levels and at different noisy environments are calculated and presented in Table 3. The recognition accuracy increases with an increase in SNR in the range of 5–20 dB considered in the study. The comparison of recognition accuracy of SVM-GMM based speaker systems of noisy environments with clean environments is shown in Table 4. The recognition accuracy percentage is seen to be closer for airport and restaurant when compared to a clean environment at 20 dB SNR.

Detection tradeoff function (DET) plots are attained considering the probabilities between “miss” and “false alarm” on a normal-deviate scale for all trials. Figures 2, 3, 4, 5, 6, and 7 show the DET plots between clean vs. noise at various noise levels. Figure 2 reveals that the pattern of DET plot is similar for all noise levels. Figure 3

Table 1 EER value of GMM and SVM-GMM based speaker recognition system in clean condition

Baseline system	Condition	EER (%)	DCF	Recognition accuracy (%)
GMM [12]	Clean	7.02	0.05	92.98
SVM-GMM	Clean	4.12	0.04	95.87

Table 2 EER (%) value of SVM-GMM based speaker recognition system at different noise levels and different noisy environments

Noise types	0 dB		5 dB		10 dB		15 dB		20 dB	
	EER	DCF								
Airport	20.62	0.24	22.68	0.27	17.52	0.18	14.43	0.15	9.27	0.09
Car	19.59	0.23	23.71	0.29	23.71	0.29	18.55	0.19	11.34	0.11
Exhibition	26.80	0.31	22.68	0.27	21.64	0.23	17.52	0.45	10.30	0.40
Restaurant	19.59	0.23	25.77	0.33	22.68	0.23	17.52	0.18	9.27	0.40
Street	19.58	0.22	23.71	0.29	19.58	0.29	19.58	0.29	11.34	0.40
Train	25.77	0.33	25.77	0.33	25.77	0.33	20.61	0.24	12.37	0.12
Average	21.99	0.26	24.05	0.30	21.82	0.27	18.04	0.25	10.65	0.25

Table 3 Recognition accuracy (%) of SVM-GMM based speaker recognition system at different noise levels and environments

Noise types	0 dB	5 dB	10 dB	15 dB	20 dB
Airport	79.38	77.32	82.48	85.57	90.73
Car	80.41	76.29	76.29	81.45	88.66
Exhibition	73.20	77.32	77.23	82.48	89.70
Restaurant	80.41	74.23	74.23	82.48	90.73
Street	80.42	76.29	76.29	80.48	88.66
Train	74.23	74.23	74.23	79.39	87.63
Average	78.00	75.94	76.79	81.97	89.35

Table 4 Recognition accuracy (%) difference of SVM-GMM based speaker recognition system between clean versus noisy environments at different noise levels

Noise types	0 dB	5 dB	10 dB	15 dB	20 dB
Airport	16.49	18.55	13.39	10.30	5.14
Car	15.46	19.58	19.58	14.42	7.21
Exhibition	22.67	18.55	18.55	13.39	6.17
Restaurant	15.46	21.64	21.64	13.39	5.14
Street	15.45	19.58	19.58	15.39	7.21
Train	21.64	21.64	21.64	16.48	8.24
Average	17.86	19.92	19.06	13.89	6.52

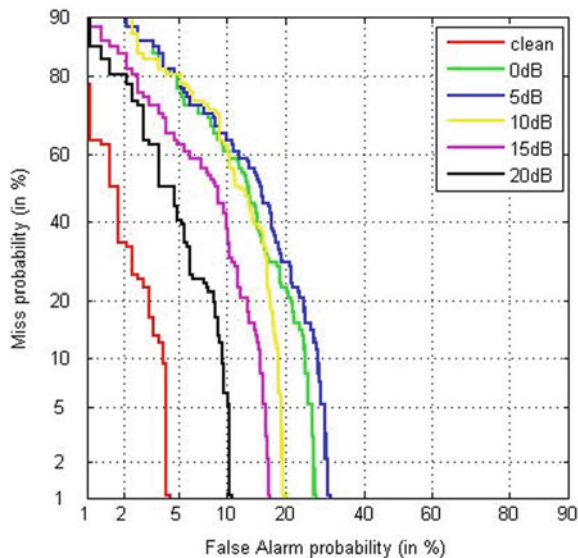
Fig. 2 DET plot clean versus airport noise

Fig. 3 DET plot of clean versus car noise

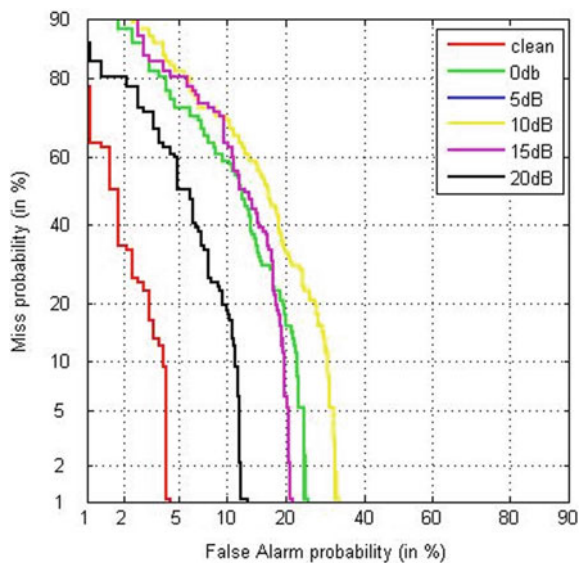
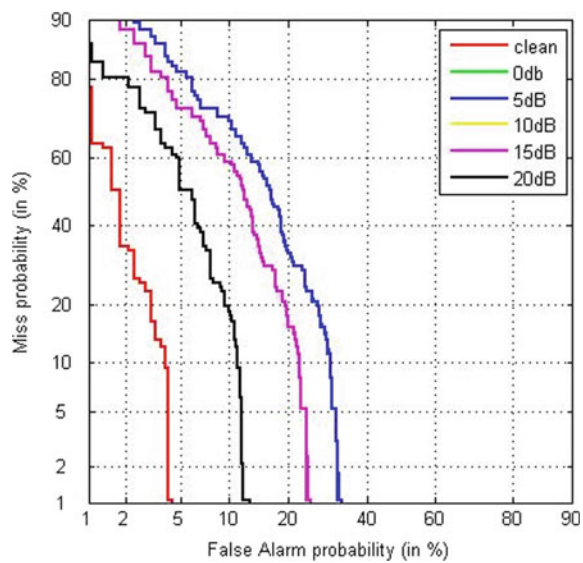


Fig. 4 DET plot clean versus street noise



represents the DET plot of clean versus car noise. In the above figure no separate visible curve line for 5 and 10 dB is noticed.

Fig. 5 DET plot of clean versus train noise

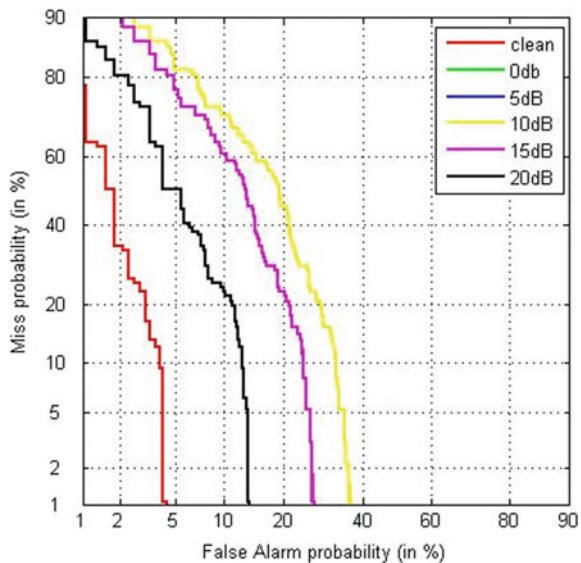
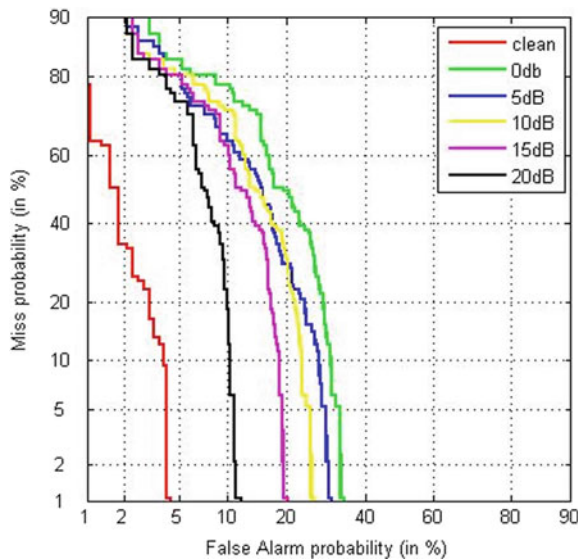


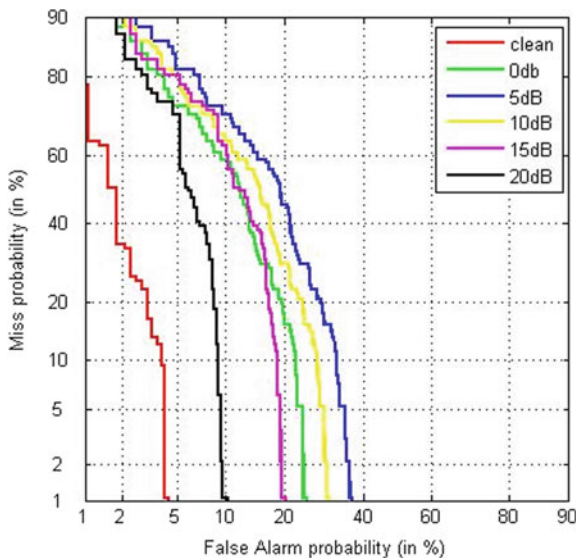
Fig. 6 DET plot clean versus exhibition noise



6 Conclusion

In the present work, an experiment has been performed using NIST 2003 and AURORA database for the impact of noise levels for SVM-GMM based speaker recognition system for various noisy environments. The recognition accuracy of SVM-GMM baseline system is seen to be increased to that of GMM based system

Fig. 7 DET plot of clean versus restaurant noise



for clean environment. From the results, it is also seen that recognition accuracy increases with an increase in SNR in the range of 5 dB to 20 dB for various noisy environments.

References

1. Furui S (1991) Speaker-dependent-feature extraction, recognition and processing techniques. *Speech Commun* 10(6):505–520
2. Vuppala1 AK, Rao KS (2013) Speaker identification under background noise using features extracted from steady vowel regions. *Int J Adapt Control Signal Process* 27:781–792
3. Kunzel H (1994) Current approaches to forensic speaker recognition. In: ESCA workshop on automatic speaker recognition, identification and verification, pp 135–141
4. Sturim DE, Campbell WM, Reynolds DA (2007) Classification methods for speaker recognition. In: LNAI vol 4343, pp 278–297
5. Shridhar M, Mohan Krishnan N (1982) Text-independent speaker recognition: a review and some new results. *Speech Commun* 1:257–267
6. Ghate PM, Sundar A, Kamble A (2013) Automatic speaker recognition system. In: Proceedings of ICAdC, AISC 174, pp 1037–1044
7. Furui S (1981) Cepstral analysis technique for automatic speaker verification. *IEEE Trans Acoust Speech Signal Process* 29(2):254–272
8. Wu Z, Cao Z (2005) Improved MFCC-based feature for robust speaker identification. *Tsinghua Sci Technol* 10(2):158–161
9. Gokay D, Zekeriya T, Lütfü S, Ulus C (2016) A review on feature extraction for speaker recognition under degraded conditions. *IETE Tech Rev* 1–12
10. Wang JC, Wang JF, Weng YS (2002) Chip design of MFCC extraction for speech recognition. *Integr VLSI J* 32:111–131

11. Rao KS, Sarkar S (2014) Robust speaker recognition in noisy environments. In: Springer briefs in speech technology http://doi.org/10.1007/978-3-319-071-5_3
12. Singh R, Bhattacharjee U, Singh AK (2019) Performance evaluation of normalization techniques in adverse conditions. Procedia Comput Sci 171:1581–1590

Digital Payment System and the Millennial in a Smart City: An Antecedent to Technopreneurship



Anil Kumar Singh and Tagiya Mudang

Abstract Developing select cities into “smart cities” is an ambitious mission of the current Indian government led by the Prime Minister, Shri Narendra Modi. It aims at improving the lifestyle, the standard of living, the quality of life of Indians, and elevating the possibilities of technopreneurship in the country. This research attempts to highlight the potential dimensions leading to the success and possible impediments ahead of this program, thereby estimating the level of success of the Digital India campaign. This research at the assessment of the attitude of young citizens towards digital payment systems. The study digs in to identify the factors leading to the popularity and limitations of the digital payment system amongst the millennials. The study is conducted in the proposed smart city of Itanagar, Arunachal Pradesh, India. Primary data is collected through a self-administered questionnaire built on a five-point Likert scale, and the secondary information is collected from various government bulletins and published reports. A theoretical model of factors determining the attitude towards digital payments is tested through confirmatory factor analysis (CFA). The goodness of fit indices achieved is within the cut-off limits. It is found that security concerns play the most significant role in determining the attitude of the millennials in the Itanagar region. The findings of this research update the existing literature on the acceptance and implementation of the digital medium of financial transactions in northeast India. The study outlines relevant factors that can determine the chances of success of the Digital India campaign in Itanagar.

Keywords IBM AMOS · Confirmatory factor analysis (CFA) · Digital payment system · Millennials · Smart city · Technopreneurship

A. K. Singh

Assistant Professor, School of Business, Assam Kaziranga University, Jorhat, Assam, India
e-mail: singhanilkumar@zoho.com

T. Mudang

Research Scholar, Department of Humanities and Social Sciences, North Eastern Regional Institute of Science and Technology, Nirjuli, India
e-mail: tagiyam@gmail.com

1 Introduction

The digitalization of data and seamless sharing of information has transformed the way we conduct our business today. This fact is noteworthy in the Indian context because unlike the developed countries in the west, information technology (IT) revolution is a relatively new phenomenon here. It surfaced only in the early 1990s during the liberalization, privatization, and globalization (LPG) era, and eventually became a nationwide buzz after the launch of the “Digital India” campaign by the Prime Minister Narendra Modi led Indian government in the year 2015. While some of the technological changes that have happened in India have so far succeeded, others have not [1]. One such significant technological switch is the digital payment system that gained fresh impetus in India after the controversial decision of the government on November 8, 2016, to demonetize high denomination Rs. 500 and Rs. 1000 bills accounted for nearly 86% of the total cash in the economy [2]. The nation witnessed a remarkable shift towards embracing alternate digital payment options of mobile wallets such as Paytm, MobiKwik, m-Pesa, Airtel Money, and much more post-demonetization [3]. By the year 2016, India had already become the world’s second-largest smartphone consumer market [4], but 68% of the Indian population continued to prefer cash to digital payments [1]. The transition from the traditional cash-based business model to a less-cash model is still a major challenge. An impediment to this initiative, however, would be the acceptability of digital mediums of payments, and other such related issues. The attitude of people towards digital systems is of considerable significance here. An individual’s perception of digital payment systems can affect the program to a great extent. As mobile phones are particularly popular amongst the generation Y, it no longer should be seen merely as a music player, a navigation device, or a camera device. It is now time to disrupt online payment systems through the immense possibilities of mobile devices [5]. But the matter that bothers IT enthusiasts worldwide is the fact that though mobile technology got warm and prompt reception worldwide, electronic payment services have witnessed a slower adoption rate [6]. A list of benefits of the electronic/digital payment system is listed in Table 1.

Table 1 Benefits of digital payment system

S. No.	Benefits	Supporting literature
1	Security	[7]
2	Reliability	[8]
3	Scalability	[9]
4	Anonymity	[10]
5	Acceptability	[11]
6	Privacy	[12]
7	Efficiency	[13]
8	Convenience	[12]

This study aims to assess the perspective of the millennials towards digital payment systems and predict the likelihood of success technopreneurship through the Digital India campaign.

2 Identification of Constructs

To realize the main objectives behind making cities smart, it is essential that people's attitude towards digital lifestyle remains positive. To assess the view of millennials towards digital payment systems, their technology readiness (TR) and adoption readiness (AR) need to be assessed [1]. While TR is people's tendency to welcome and use new technology [14], AR is the willingness of people to take up a digital platform for convenience and utility [15]. Apart from other measurements, security and trust are the two original dimensions that determine TR [9, 16].

Performance expectancy (benefits), ease of use (convenience), social influence, and facilitating conditions measure the AR [1]. Collectively AR and TR determine the attitude of users towards the digital payment system. Based on this theory, a conceptual research model to assess the attitude of millennials towards the digital payment system is proposed (Fig. 1).

3 Research Methodology

This study is empirical, using data from both primary as well as secondary sources. For secondary information, various authentic reports, high-end research papers were referred. The primary data was collected using a self-administered questionnaire. The questionnaire consisted of 15 close-ended items designed to measure the constructs

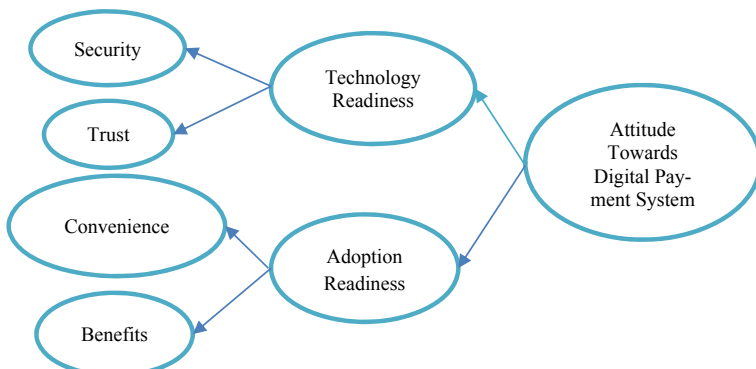


Fig. 1 Default relationship model

Table 2 Summary of factors measuring TR and AR

S. No.	Parameters	Constructs	Literature support
1	Technology readiness	Security	[9, 16–20]
		Trust	
2	Adoption readiness	Convenience	[1, 15, 21, 22]
		Benefits	

adapted from literature viz. security, trust, convenience, and benefits (refer to Table 2). The questions were developed on a five-point Likert Scale ranging from 1 = strongly disagree to 5 = strongly agree. The questionnaire was then checked for its face validity and content validity by sending it to the subject matter experts. Data analysis was carried out on the IBM SPSS v21 software platform.

3.1 Data Screening

Monotones are the responses collected that have no variance and hence should be dropped before further analysis [23]. After transferring the dataset to an excel sheet, the check for variances was done. All the response sets were found to have some deviation, and therefore, no monotones were identified.

Missing values are incomplete responses. The possibility of missing values was eliminated while preparing the questionnaire itself. All the items were marked as compulsory, thereby preventing incomplete form submission.

Common method bias (CMB) may lead to questionable inferences drawn out of the statistical analysis, and thereby posing a threat of wrong conclusions [24]. Harman's single-factor test, the statistical measure to test CMB, was also conducted on the IBM SPSS software platform. It was found that the percentage of variance accounted for the first component is 43.046%, which is less than 50%. This means that the instrument used for this study is statistically free from any significant common method bias.

3.2 Scale Reliability and Sampling Adequacy

Internal consistency, also known as scale reliability, is a valuable measurement property of questionnaires that intends to measure a single underlying construct by using multiple items [25], and the Cronbach's alpha (α) is the most common measure of scale reliability [26]. Literature suggests a minimum alpha (α) cut-off value at 0.5 [27, 28], and a more strict recommended value is 0.7 [29]. The observed Cronbach's alpha (α) value for the instrument used in this study obtained from SPSS is 0.906,

signifying excellent scale reliability. The KMO test for sampling adequacy value is found to be 0.899.

3.3 Construct Validity

Construct validity is tested by a convergent validity test and discriminant validity test. The convergent validity test is meant to determine the extent to which measures of the same construct are correlated. One can look at the standardized factor loading values in a CFA model and loadings of 0.7, and higher is considered excellent. Alternatively, one can calculate the average variance extracted (AVE) to assess convergent validity. The authors found out AVEs of the constructs using the following formula:

$$\text{AVE} = \frac{\sum_{i=1}^m L_i}{n}$$

where n is the number of items.

The discriminant validity test was not done in this study because it is done only in the case of first-order models, and the research model identified from the literature in this study is a third-order model. An AVE value of 0.5 and above is considered acceptable. A summary of validity and reliability test results is given in Table 3.

4 Analysis and Findings

From the literature, it was established that technopreneurship to succeed in India, people need to embrace technology-based business models, and technology readiness and adoption readiness are the key criteria to assess the situation. A conceptual model (Fig. 1) was developed and tested for acceptability through confirmatory factor analysis (CFA). The model was recreated on the IBM AMOS v21 software platform (Fig. 2). The four measurement dimensions viz. security, trust, convenience and benefits were loaded with four independent variables respectively (except on “benefits”, where only three measuring variables were loaded). The variables and their respective factor loadings are given in Table 4. The CFA tests were run on

Table 3 Validity and reliability test results

Measures	Items	Factor loadings	KMO	AVE	Cronbach's α
Security	4	0.72–0.93	0.899	0.69	0.906
Trust	4	0.69–0.79		0.58	
Convenience	4	0.54–0.69		0.40	
Benefits	3	0.61–0.74		0.47	

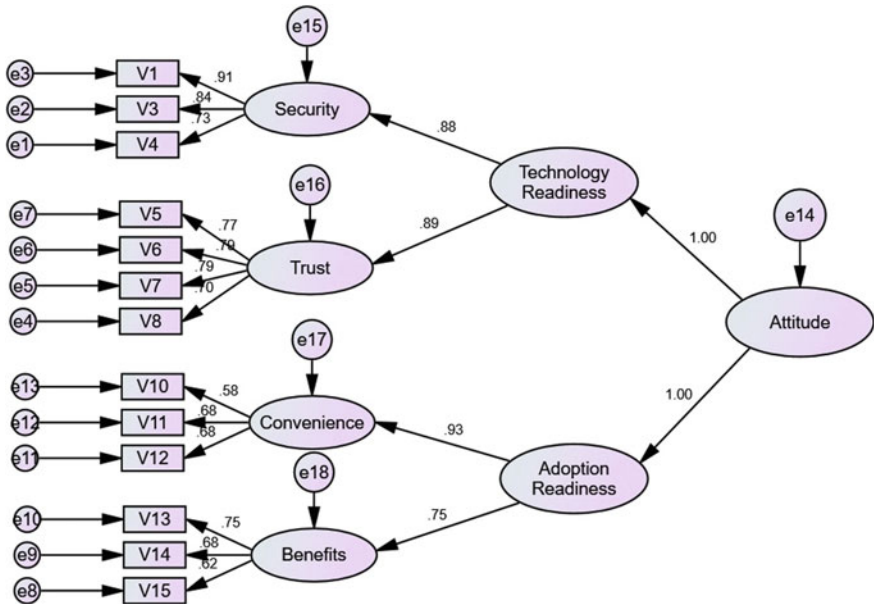


Fig. 2 IBM AMOS model

AMOS and the results are compiled in Table 5. After repeated improvements made to the model, the authors could obtain acceptable values of the crucial model fit indices.

4.1 Model Fit Indices

The proposed model has yielded encouraging fit indices. The absolute fit indices of the normative χ^2 (CMIN/DF) = 2.140, RMR = 0.023, GFI = 0.915, RMSEA = 0.076, and the SRMR = 0.046, all satisfying the threshold levels comfortably. At the same time, the incremental fit index CFI = 0.943 also satisfies the benchmark.

Conventionally, it is required to report one fit measure belonging to the absolute fit measures and one from the incremental fit measures, along with the normative χ^2 value. The results obtained from this study humbly satisfy that criterion. It may now be determined with confidence that the proposed model to assess the attitude of millennials towards the digital payment system is empirically validated, and the relationship between the different endogenous and exogenous variables involved is genuinely established.

Table 4 Constructs with their respective items' path loadings in the AMOS model

Constructs	Items	Standardized path loadings
Security	1. Safety of my data while using a digital payment system is vital for me (Code: V1)	0.91
	2. The risk of data theft while performing digital payments is low for me (Code: V2)	0.65
	3. I stop using digital options of payment whenever I learn about security breaches elsewhere (Code: V3)	0.84
	4. I make digital payments only if guaranteed by web assurance seals (e.g., Verisign, Tech Process, etc.) (Code: V4)	0.73
Trust	1. I trust the ability of digital payment systems to protect my privacy (Code: V5)	0.77
	2. I have full faith in reputed payment gateways like PayPal, BillDesk, Verisign, etc. (Code: V6)	0.79
	3. I prefer to use an internet security (antivirus) solution for data protection because I cannot trust the digital payment system's ability (Code: V7)	0.79
	4. I feel the risk associated with the digital payment system is low (Code: V8)	0.70
Convenience	1. Digital payment is much convenient and user-friendly as compared to the paper-based conventional payment system (Code: V9)	0.51
	2. The availability of a mobile-based digital payment system has enhanced the level of convenience (Code: V10)	0.58
	3. I find using a digital payment system complicated (Code: V11)	0.68
	4. It took me little time to learn using the digital payment system (Code: V12)	0.68
Benefits	1. I save my time and money by using a digital payment interface (Code: V13)	0.75
	2. The digital payment system has reduced my reliance on cash-based transactions (Code: V14)	0.68
	3. The digital payment system is quicker than the traditional payment system (Code: V15)	0.62

5 Practical Implications and Conclusion

This study started with an idea to assess the preparedness of an ordinary city to be transformed into a smart city and sustain technopreneurship. A city can be recognized as a truly smart city if the application of IT is found in almost all the spheres of life, including business and entrepreneurship. Attitude determines the chances of adoption and application of any novel idea and technology. In this study, the authors

Table 5 CFA model fit indices

Fit measure	Threshold values	Observed values	Background literature
CMIN/DF	≤ 5	2.140	[30, 31]
RMR	<0.05	0.023	[32]
GFI	>0.90	0.915	[32, 33]
AGFI	>0.90	0.873	[32, 33]
NFI	>0.90	0.900	[33]
RFI	>0.90	0.872	[33]
TLI	>0.95	0.928	[32]
CFI	>0.90	0.943	[33, 34]
RMSEA	<0.08	0.076	[32, 33, 35]
SRMR	<0.05	0.046	[36, 37]

focused exclusively on respondent attitudes towards digital payment systems. The authors chose to use AR and TR parameters only because of strong arguments in favor of them. By applying the inputs from the literature, a conceptual model was designed and later tested for confirmation using CFA on IBM AMOS. The results were highly encouraging, signifying that a proper model fit was achieved. Sound model fit indices indicated that the relational assumptions made in the theoretical model were correct. AR and TR indeed have a significant impact on the attitude of millennials towards the digital payment systems. TR values were slightly better than the AR values, meaning that the generation—Y in the city is technologically better prepared to embrace digital payment systems, but they need to be a little more convinced about its benefits in realtime. The government faces challenges while introducing technology into everyday business affairs. But it needs to spend more resources in improving the conviction in people about the endless benefits and utility of IT. Although the people give high importance to online security, the overall attitude of the millennials is in favor of the government's move to upgrade their city into a smart city. The Digital India campaign has excellent chances of success in this part of the nation if it can ensure enough and timely infrastructure. Technopreneurship is a solution to many issues in the Itanagar region, but its chances of success are shady now because of a lack of clarity in the minds of young people here about how IT can be best used for business and entrepreneurship. But at the same time, they are welcoming of technology applications in business, as evident from the AR and TR scores.

References

1. Sinha M, Majra H, Hutchins J, Saxena R (2019) Mobile payments in India: the privacy factor. *Int J Bank Mark* 37:192–209
2. Wade S (2017) How India is surviving post-demonetization. <https://www.forbes.com/sites/wadeshepard/2017/07/29/how-india-is-surviving-post-demonetization/#3f6841ee1164>. Accessed 30 May 2019
3. Nielsen Report (2016) Demonetisation: the Nielsen view (part II). <https://www.nielsen.com/in/en/insights/reports/2016/demonetisation-the-nielsen-view-part-two.html>. Accessed 01 June 2019
4. Iyengar R (2017) India poised for smartphone revolution. <https://money.cnn.com/2017/09/26/technology/india-mobile-congress-market-numbers/index.html>. Accessed 30 May 2019
5. Kazan E, Damsgaard J (2014) An investigation of digital payment platform designs: a comparative study of four european solutions. In: European conference on information systems
6. Guo J, Bouwman H (2016) An analytical framework for an m-payment ecosystem: a merchants' perspective. *Telecommun Policy* 40:147–167. <https://doi.org/10.1016/j.telpol.2015.09.008>
7. Chou Y, Lee C, Chung J (2004) Understanding m-commerce payment systems through the analytic hierarchy process. *J Bus Res* 57:1423–1430
8. Neuman BC, Medvinsky G (1995) NetCheque, NetCash, and the characteristics of Internet payment services. *J Electron Publ* 1
9. Tsiakis T, Sthephanides G (2005) The concept of security and trust in electronic payments. *Comput Secur* 24:10–15
10. Stroborn K, Heitmann A, Leibold K, Frank G (2004) Internet payments in Germany: a classificatory framework and empirical evidence. *J Bus Res* 57:1431–1437
11. Linck K, Pousttchi K, Wiedemann DG (2006) Security issues in mobile payment from the customer viewpoint. In: 14th European conference on information systems (ECIS 2006). Munich Personal RePEc Archive, Göteborg, pp 1–11
12. Kousaridas A, Parassis G, Apostolopoulos T (2008) An open financial services architecture based on the use of intelligent mobile devices. *Electron Commer Res Appl* 7:232–246
13. Cottelleer MJ, Cottelleer CA, Prochnow A (2007) Cutting checks: challenges and choices in B2B e-payments. *Commun ACM* 50:56–61
14. Colby CL, Parasuraman A (2001) Techno-ready marketing: how and why customers adopt technology. Simon and Schuster
15. Thakur R, Srivastava M (2014) Adoption readiness, personal innovativeness, perceived risk and usage intention across customer groups for mobile payment services in India. *Internet Res* 24:369–392
16. Kim C, Tao W, Shin N, Kim K-S (2010) An empirical study of customers' perceptions of security and trust in e-payment systems. *Electron Commer Res Appl* 9:84–95
17. Lim B, Lee H, Kurnia S (2006) Why did an electronic payment system fail? A case study from the system provider's perspective. In: Collaborative electronic commerce technology and research conference, Adelaide
18. Peha JM, Khamitov IM (2004) PayCash: a secure efficient Internet payment system. *Electron Commer Res Appl* 3:381–388
19. Yousafzai SY, Pallister JG, Foxall GR (2003) A proposed model of e-trust for electronic banking. *Technovation* 23:847–860
20. Zhou T (2011) An empirical examination of initial trust in mobile banking. *Internet Res* 21:527–540
21. Eastin MS (2002) Diffusion of e-commerce: an analysis of the adoption of four e-commerce activities. *Telemat Inform* 19:251–267
22. Chakravorti S (2003) Theory of credit card networks: a survey of the literature. *Rev Netw Econ* 2:50–68
23. Yeh K-JJ (2009) Reconceptualizing technology use and information system success: developing and testing a theoretically integrated model

24. Podsakoff PM, MacKenzie SB, Podsakoff NP (2012) Sources of method biases in social science research and recommendations on how to control it. *Annu Rev Psychol* 63:539–569. <https://doi.org/10.1146/annurev-psych-120710-100452>
25. Terwee C, Bot S, de Boer M, Van der Windt DA, Knol D, Dekker J, Bouter L, de Vet H (2007) Quality criteria were proposed for measurement properties of health status questionnaires. *J Clin Epidemiol* 60:34–42. <https://doi.org/10.1016/j.jclinepi.2006.03.012>
26. Field AP (2005) Discovering statistics using SPSS. Sage, London
27. Zaichkowsky JL (1985) Measuring the involvement construct. *J Consum Res* 12:341–352
28. George D, Mallery P (2010) SPSS for windows step by step: a simple guide and reference. Allyn & Bacon
29. Nunnally JC (1978) Psychometric theory. McGraw-Hill, New York
30. Wheaton B, Muthen B, Alwin DF, Summers GF (1977) Assessing reliability and stability in panel models. *Sociol Methodol* 8:84–136
31. Tabachnick BG, Fidell LS (2007) Multivariate analysis of variance and covariance. In: Using multivariate statistics, vol 3, pp 402–407
32. Hooper D, Coughlan J, Mullen MR (2008) Structural equation modelling: guidelines for determining model fit. *Electron J Bus Res Methods* 6:53–60. <https://doi.org/10.1037/1082-989X.12.1.58>
33. Hair JF, Black WC, Babin BJ, Anderson RE, Tatham R (2010) Multivariate data analysis. Pearson Prentice Hall, Upper Saddle River
34. Gefen D, Straub DW, Boudreau MC (2000) Structural equation modeling and regression: guidelines for research practice. *Commun Assoc Inf Syst* 6:1–30
35. MacCallum RC, Browne MW, Sugawara HM (1996) Power analysis and determination of sample size for covariance structure modeling. *Psychol Methods* 1:130
36. Byrne BM (2013) Structural equation modeling with LISREL, PRELIS, and SIMPLIS: basic concepts, applications, and programming. Psychology Press
37. Diamantopoulos A, Siguaw JA (2000) Introducing LISREL: a guide for the uninitiated. Sage

Efficient Fusion Based Multi-modal Biometric Authentication System Using Machine Learning



R. Sindhuja and S. Srinivasan

Abstract In the recent past, a multi-modal biometric authentication system plays a vital role in individual biometric authentication for private and public sections to assure security. The conventional multimodal biometric system performance is poor in various illumination conditions of biometric images during feature extraction. Fusion-based Multimodal biometric improves the accuracy and efficiency of security level, nonuniversality, variation of inter and intraclass, etc. In this paper, fusion-based multi-modal based biometric modality verification is proposed through incorporating modalities iris, fingerprint, and face based on Machine Learning (ML) algorithm. The proposed system is based on the individual scores estimated through every biometric modal and then normalized to receive score of fusion. Various statistical features can be estimated through every biometric modality modal based machine learning approach that can be applied for classification using ML. The biometric images are undergone for preprocessing to remove noise occurrence and to improve the quality of images even for various illumination conditions to achieve uniform illumination and contrast. The proposed system is used to achieve an extensively multimodal system with considering the improved wide range of quality of images. The segmentation algorithm is applied to segment the required region for statistical feature estimation. The fusion is applied using extracted features of biometric using pixel-based fusion. The proposed fusion technique capture takes the information of high frequency such as edges and slant textures of images for fusion. The estimated statistical features could be feed to ML to identify the given image is obtainable in a secured database or not. The various experimentation results are proof that the proposed methodology is improved efficiency and accuracy.

Keywords Multimodal biometric authentication · Machine learning · Region of interest (ROI) · Image enhancement · Image fusion

R. Sindhuja · S. Srinivasan (✉)
E&I, Annamalai University, Chidambaram, India
e-mail: Vasanaucdm@gmail.com

R. Sindhuja
e-mail: Sindhumeekna89@gmail.com

1 Introduction

Multi-modal biometric system (MBS) organized in necessary applications could be unimodal like they utilize a mono source of data for recognition such as fingerprint, voice, face, etc. Few of the disadvantages exposed by the unimodal biometric system may be overcome by improving several supplies of data for implementing uniqueness. The fingerprint and face authentication could make a better integration for a multimodal biometric system and utilized in the work for improving authentication by capture equipment, digital image processing unit, and personal computer. The software unit incorporates database and modules of implementation [1]. The MBS integrates data through various biometric modalities to enhance the efficiency of every entity multi-modal modality biometric environment and create network healthy to attacks of spoof. A secured MBS uses an integration of Convolutional Neural Network (CNN) and the supervised learning method of Q-Gaussian Support Vector Machine (QG-MSVM) is applied for the various status of fusion. Two recognition methods with two various fusion level algorithms are used for secured MBS with feature fusion level and decision level of the proposed system. The CNN algorithm is used for feature extraction of biometric images. These two layers of CNN are used for improving accuracy in that every layer is applied as descriptors of features. The inner fusion method is used to generate multimodal biometric templates [2]. The MBS may procedure in various multi-modal biometric signs through individual identification procedure detecting people. MBS gives a higher state of recognition than a traditional biometric system that applied only a single data of biometric information like fingerprint or face or some other information. The fingerprint and iris are used to score matching techniques [3]. In the Information Technology (IT), the high security is needed for every individual to ensure biometric model based scheme of authentication. The multi-factor recognition using multimodal biometric methodology is used to overcome the disadvantages related to single biometric system. The feature extraction from speech data is Mel Frequency Cepstrum Coefficient (MFCC) statistical feature extracted from the speech signal. In the iris image, the normalization is applied and the Daubechies wavelet scheme is applied to estimate the features for comparing between various individual biometric to reduce computational difficulties [4]. Fingerprint recognition is used for the forensic department to detect crime scenes. The entire crime scene fingerprint recognition method based on deep learning with CNN is useful for efficient recognition. The various directional images are captured at the crime site for further processing. The minutia extraction is used as features for machine learning approach for the precision image too difficult physical and compound chemical execution methods and stored as database. The proper enhancement method should be applied to improve the quality of fingerprint image for accurate recognition using ML [5]. The Gaussian and Poisson noises should be eliminated form the face database. The principle component analysis (PCA) algorithm is applied to calculate eigenfaces and eigenvectors to estimate features of face [6]. The computer vision and communication of an automatic control system is used to provide accurate and efficient recognition of face using face detection and face

authentication procedures. The face detection is done to identity face through an image that may have few attributes through the given image. Face detection is not only used for the biometric system and also used for expression recognition and tracking of face and pose. Face detection is a difficult task due to face is not rigid and it changes in various parameters such as shape, size, and color illumination [7]. The automatic identification based on speech is also one of the important biometric recognition systems in different languages. The Digital Signal Processing (DSP) unit is used to restore and enhance the speech signal to eliminate harmonics from a noisy speech signal. Features are applied to calculate various features from the filtered speech signal. The database is created for features to process recognition on a trained database. The testing signal is given to the DSP unit and proceeds all algorithms finally calculate features and those features are given to a testing unit of machine learning to give proper authentication if the features are already collected and stored in the database of recognition system [8].

2 Related Works

Classification and quality improvement methodology thus multimodal modality biometric verification network. Quality of image plays a vital role in the multimodal modality biometric verification network. An authentication technique used exclusively on only frequently capable is impossible convene structure concert needs feature in low-quality image. The SVM classification for fingerprint and face is used for outperforming considerably by applying image quality enhancement. Choras [9] has proposed a biometric authentication method for iris retinal images based on features and template matching. The multimodal biometric system is combining both iris and retinal images using Gabor transformation. The Gabor transform is used to spatial domain image into the frequency domain for calculating low and high-frequency coefficients for fusion. Toh et al. [10] have investigated various problems pertaining to the adaptive multimodal authentication system. The problems incorporate new user login, sensor decompose, and minute model information size. The less sample size issue is solved by applying a feature scaling space learning method. Viswanathan et al. [11] have presented a multimodal biometric verification system using the invariant moment fusion method authentication process. Without decreasing, preservation limitation novel methodology is implemented for biometric authentication system. The proposed system uses fingerprint and faces biometrics standard instant data could be estimated. The invariants are applied to fusion for creating mono identification data by applying the variance of coefficients. The mono data is recognized by estimating the variance, calculated based on the threshold data that is considered. Sarier et al. have described the initial security preservation multi-modal biometric recognition system protocol resistant to attacks of hill climbing. The biometric system is encrypted and stored for additional execution of the spatial domain of cryptography. The proposed system is working based on various cryptography parameters functioning on crypto biometric templates created either from a

single attribute such as fingerprint multimodal biometrics. Ma et al. have proposed that malicious attack highly damages the security and preservation of information of biometric systems making the authentication of biometric information is making highly demanding important. The watermarking based multi-stage recognition work is address to solve security problems. While information selection, modality is watermarked with fingerprint modality of information credibility token and recognition resource. The first stage authentication process is executed, at the second stage, the face pattern is further secured by applying the encryption method. The discrete wavelet transformation is applied to transfer time-domain information by frequency domain data to extract the low and high-frequency coefficients for further watermarking. The autocorrelation methodology is applied for watermarking and cross-correlation method is applied for recover of fingerprint image. Jagadiswary et al. have investigated patterns recognition method for multimodal biometric systems. The scanning equipment are used to capture images, to store unique characteristics of individuals. The methodology behind this can be utilized among various range of applications such as verification, health industry, passport verification, etc. such various field of application may be beneficial. Lokesh et al. have proposed speech recognition in different environments such as robotics, healthcare, unmanned vehicle, etc. The different speech recognition systems are implemented to solve different problems in application of real world. The novel speech signal recognition is implemented by the author by utilizing enhancement and feature extraction methodologies. The statistical feature estimation are applied as features extraction from the speech signal. The features considered as databases of various speech signals. The database is created for template matching for testing signals. The speech signal biometric authentication system provides a more range of efficiency and accuracy.

3 Modalities of Biometric Model

Various biometric modalities have been used that are widely utilized in multimodal modality biometric verification scheme. Speech, face, signature, fingerprint, ear, etc. are examples of biometric modalities. The biometric modalities are preprocessed properly to improve the quality and then it is segmented to extract useful information from biometric modality to extract the features and fused. The physical modalities stay static with instance while the behavioral modalities modify besides with instance. The multimodal modality biometric verification scheme utilizes various modalities for authentication and verification. The simplest methods are the singles that create utilize of a single biometric modality. The biometric authentication systems creating utilize of more than two biometric modalities are multi-modal methods. Every biometric system has its characteristics, advantages, and disadvantages.

4 Proposed Methodology

Multi-Modal Biometric Authentication and Verification System (MBAVS) can be proposed by integrating various multi-modal modalities biometric like fingerprint, iris, and face and fusion methodology. Various algorithms are applied to estimate statistical data about various modalities and template creation for authentication and verification using Machine Learning (ML). The fusion process of face, fingerprint, and iris in this paper are done using the status of several features is shown in Fig. 1, flow diagram of fusion methodology. The proposed system significantly consists of five different parts;

1. Feature-based Fingerprint enhancement and recognition
2. Retinal Iris recognition
3. PCA based Face recognition
4. Multi-modal fusion
5. Machine Learning verification.

5 Fusion Using Score Level (SL)

The score level (SL) fusion is used for fusing various biometric features for classification and recognition using machine learning. Various matching scores that could be estimated by various classifiers through various biometric standards could be applied fusion for matching at this status. Fusion at the level of matching could be involved in two different ways. First stage is classification issues and as data incorporation issue. In the classification method, feature extraction is estimated by applying a score matching method that is giving output using separate matches. In the next state, feature vectors are classified as acceptance level and rejection level, that is, genuine user and imposter classifications. In the data incorporation method, separate matching scores are applied for fusion to create decision making.

6 Fingerprint Recognition

Fingerprint recognition primarily consists of image restoration, image enhancement, image segmentation, feature extraction, and recognition using machine learning. We are performing fingerprint recognition using various techniques such as fingerprint minutiae extraction, orientation field, fingerprint thinning, etc.

7 Fingerprint Orientation Image

The orientation image of the fingerprint shows the exact ridge orientation in the fingerprint image in all areas. Here are a variety of approaches used to determine the fingerprint image orientation. The ridge orientation varies very slowly across the given fingerprint apart from in the area of singularities such as core and delta. Finally, there will be a full resolution of the orientation image. A single orientation that relates to the highly credible or main orientation of the block is processed instead of any non-overlapping block of size W/W of the image. Relatively, the horizontal and vertical direction gradients $AGx(x, y)$ and $BGy(x, y)$ are calculated based on simple gradient detection methods such as the Sobel edge detection technique.

The fingerprint minutiae block direction θ is given by $\theta = a\{1/2\} * \text{abs}\{\tan -1Gyy/Gxx\}$

$$Gxy = u \in Wv \in W2AGx(au, bv) \times BGy(au, bv) \quad (1)$$

$$Gxx = u \in Wv \in WAG2x(au, bv) \times BG2y(au, bv) \quad (2)$$

8 Iris Normalization

The next step is to rectify the segmented image measurements to allow assessments after successfully segmenting the iris region from a captured image. There are various reasons for variations between the eye's images. Some of them are due to dilation of the pupil, movement of the eyes, tilt of the head and rotation of the eye within the eyeball, and distance variations of the face. The most affected difference is due to variations in light intensity and illumination causes dilation of the pupil leading to stretching of the iris. To remove these inconsistencies, the segmented image is transformed. The standardization approach would produce iris regions with the same constant proportions so that two images of the same iris will have the same characteristics under different conditions. The next stage is called "segmentation," which is the separation of the portion of the iris from the eye image. It is a technique for isolating and excluding objects, as well as for identifying the iris' inner and outer boundaries. Standardization is the third stage. The product of the process of normalization is iris regions with the same constant dimensions so that at the same spatial location two iris images of the same individual will have characteristics under different conditions. The fourth stage is to remove the iris and pupil features from the segmented image by transforming the hair wavelet and the vector function (transforming wavelet output) by using Principle Component Analysis (PCA). Wavelets could be used to decompose information about the iris region into different components that appear at different resolution levels. In this work, hair wavelet transformation was used to extract the iris field characteristics. Decomposing wavelet images are each step results

in multi-resolution from accurate image to approximate images. The multilevel 2-D wavelet's decomposition output has four sub-images: LH, HL, HH represent detailed images for horizontal, vertical, and diagonal orientation, and LL corresponds to an approximation image as shown.

9 Iris Segmentation Using Modified Hough Transform

1. The image that helps process the valid region (ROI) is implied in the size map. It reduces the total number of pixels to handle, reducing processing time and memory use.
2. Symmetric division of image data allows searching the correct region effectively, thus reducing the complexity level and reducing the time CHT has to locate triplets.

The algorithm means that for each grid size P , the ROI only takes region from the starting point SP to the endpoint EP. Therefore, the reduction of the number of pixels to be processed to $M/PN/P$ reduces the time complexity of modified algorithms by order $O((M/P * N/P))$.

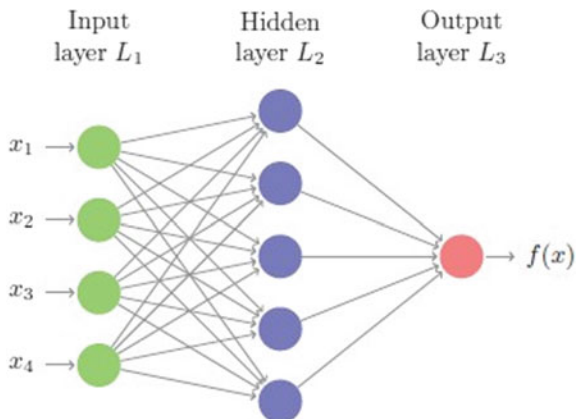
The proposed methodology pseudo-code can be written as Start

1. Write the $N M$ dimensions image matrix $f(x, y)$.
2. If P is the size of the row, then $Sp = (\text{floor}(P2)P)$ and $Ep = (\text{floor}(P2) + 1)P$.
3. Repeat steps 4 to 5 for $I = Sp$ M to $Ep[M]$.
4. For $j = Sp$, exit N to Ep , exit stage 5.
5. Find triplet (ho, ko, ro) and submit CHT.

10 Face Recognition Using Improved Principle Component Analysis (IPCA)

The techniques of Principle Component Analysis (PCA) and Linear Discriminant Analysis (LDA) are among the most popular techniques of extraction feature facial recognition. This paper involves two face recognition systems, one based on PCA followed by a feed-forward neural network (FFNN) called PCA-NN, and the other based on LDA followed by an LDA-NN FFNN. All systems consist of two phases, the PCA or LDA pre-processing phase, and the neural network classification phase. The systems proposed display improvement in recognition rates over standard Euclidean Distance-based LDA and PCA face recognition systems. Let a face image be a two-dimensional $N = N$ array. An image can also be viewed as a vector of the N^2 dimension. A series of images map a set of points in this huge space. In this enormous image space, face pictures, similar within an overall form, will not be distributed randomly and can, therefore, be represented by a low-dimensional subspace. The key idea of the PCA is to find the vectors that best account for the distribution of

Fig. 1 Feed forward neural network architecture



face images in the whole image space. These vectors define the face image subspace we call “face space.” By applying the Fisher’s linear discriminating criterion, the Fisher approach overcomes the drawbacks of the system’s own-face. This criterion seeks to maximize the ratio of the determinant of the in-class scatter matrix of the projected samples to the determinant of the projected samples. Fisher discriminants blend images of the same class and separate images from different classes. Images are projected from N^2 -dimensional space (where N^2 is the pixel number in the image) to $C - 1$ (where C is the number of classes in the image). Consider, for instance, two sets of points in two-dimensional space projected on a single line. As with proper space projection, the training images are projected into a subspace. The test images are projected and represented using a measure of similarity in the same subspace that varies with the subspace estimate. The neurons in FFNN are arranged as layers. The neurons receive input from the preceding layer in a layer and feed their output into the next layer. In this type of network, neuron connections in the same or previous layers are not allowed. Figure 1 shows the proposed face classification system’s architecture.

11 Results and Discussion

Figure 2 demonstrates the identification of fingerprints using the minutiae extraction feature. Figure 2b indicates this point’s result.

The fingerprint image is transformed into a skeleton of one pixel after thinning. Thinned image is the one that allows minutiae to be identified. The image is basically divided into 3×3 windows like Fig. 2c.

Figure 3 demonstrates the identification of iris by transforming modified Hough. Iris is the sclera-pupil area. The inner and outer edges can be loosely seen as rings. The method of position is to identify the centers and radii of the internal and external circles. In the suggested algorithm, we first get the center point and radius of the

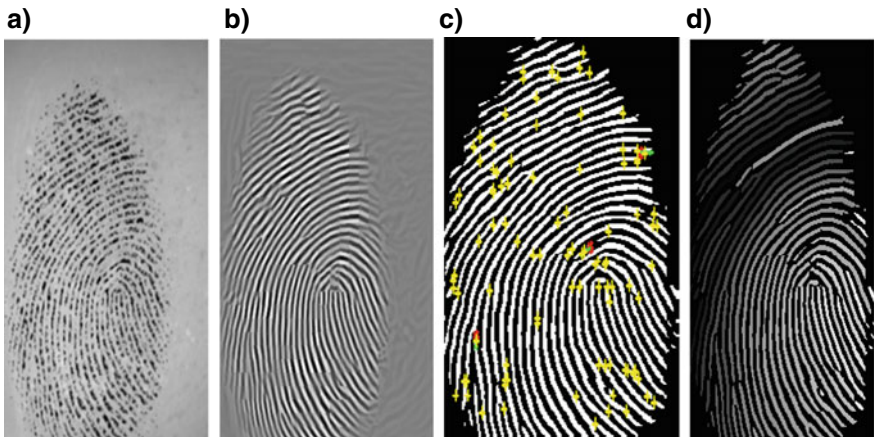


Fig. 2 **a** Input fingerprint image, **b** enhanced image, **c** minutiae feature extraction, **d** ridge mapping

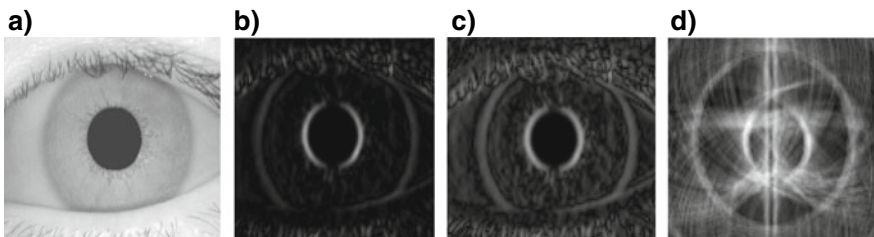


Fig. 3 **a** Input iris image, **b** Canny edge detection, **c** enhanced image, **d** modified Hough transform to detect iris circle

pupil. Then we get the center and radius of the iris using the pupil's center and radius information, the search scale. Iris images have some features in the distribution of gray values in different regions. In general, the gray value of the pupil is lower than the iris value, and the gray iris value is lower than the sclera value so that the pupil has the lowest gray value in the gray histogram. Based on the above element, we can differentiate between pupil and iris and sclera by taking binarization. The gray histogram of the iris image has clear multi-peak features. The highest valley behind the lowest peak gray value of the histogram is the threshold of segmentation of pupil-to-other sections. We use an iterative approach to find the first local minimum value on the left of the histogram's first peak value is the threshold. Choosing the initial seeds is a crucial step in the activity of the field. Generally speaking, when we get an image through the sensor, the yaw angle is not high and the pupil area is close to the center of the image. Therefore, it is needless to scan all the pixels in the image, and we can only search for far fewer points. This means that time is small in complexity. If all 0 (i.e., black) are the pixel values within the $5 * 5$ representation of the point, the point is considered to be within the pupil area. First, we look in the center of the

image, if the point meets the above requirements, it's called in the region of the pupil and the search is over otherwise, we're looking for the white pixels. Table 1 displays the feature extraction for fingerprint, iris, and face. The SL fusion method is used to fuse all features based on decision-making theory (Fig. 4).

Tables 2, 3, and 4 are displayed for False Acceptance Ratio (FAR) and False Rejection Ratio (FRR) for fingerprint, iris, and face. The thresholding value increases, FRR is increased and FAR is decreased and vice versa. Suppose, FRR and FAR are the same then it is known as Equal Error Rate (ERR). The ERR is decreasing the system accuracy and efficiency is improved as shown in Table 5.

Table 1 Fusion using score level (SL)

Features	Fingerprint	Iris	Face	Score level
Autocorrelation	63.9782	61.3839	64.9283	62.3899
Amplitude	2.3399	6.38933	2.2389	4.3899
Energy	1.2389	1.4888	1.2389	1.2793
Entropy	0.3783	0.3899	0.3878	0.3989
Homogeneity	7.4899	7.3899	7.4784	7.3989
Sum of squares	10.7989	10.2383	10.2398	10.2389
Sum of average	5.3787	5.9899	5.3989	5.3899
Sum variance	4.2899	4.2389	5.3289	4.5899
Normalization factor	0.2323	0.3544	0.3788	0.2389
Inverse normalization factor	1.2389	1.2899	1.2389	1.9899

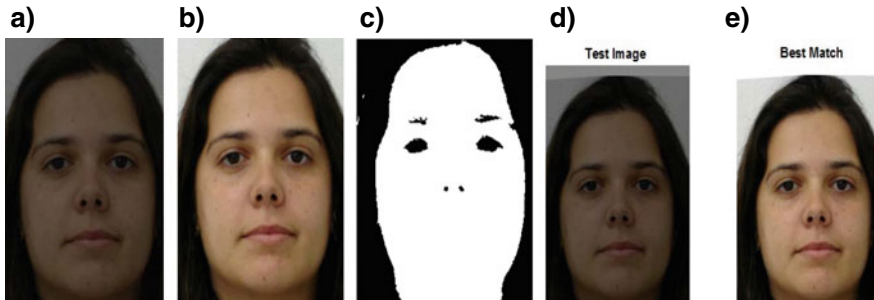


Fig. 4 **a** Input face image, **b** preprocessing image, **c** face detection, **d** authentication using best matching

Table 2 Parameter estimation for fingerprint biometric authentication system

FAR	FRR	Threshold
0.010000	98	0
0.011633	94	4
0.013265	90	8
0.016531	82	16
0.019796	74	24
0.024694	62	36
0.027959	54	44
0.031224	46	52
0.034490	38	60
0.037755	30	68
0.041837	20	78
0.043469	16	82
0.045918	10	88
0.048367	4	94
0.050000	0	98

Table 3 Parameter estimation for iris biometric authentication system

FAR	FRR	Threshold
0.010000	98	0
0.011633	94	4
0.013265	90	8
0.014898	86	12
0.015714	84	14
0.017347	80	18
0.018163	78	20
0.019796	74	24
0.021429	70	28
0.023061	66	32
0.024694	62	36
0.026327	58	40
0.027959	54	44
0.029592	50	48
0.031224	46	52

Table 4 Parameter estimation for face biometric authentication system

FAR	FRR	Threshold
0.010816	96	2
0.012449	92	6
0.013265	90	8
0.014898	86	12
0.017347	80	18
0.018163	78	20
0.020612	72	26
0.022245	68	30
0.023061	66	32
0.024694	62	36
0.027143	56	42
0.028776	52	46
0.029592	50	48
0.031224	46	52
0.032041	44	54

Table 5 Classifiers comparison

Types of classifier	Accuracy	Sensitivity	Specificity	ERR
KNN	86.3893	83.3993	82.2398	10.3893
BPNN	91.2398	91.2398	90.3939	5.3999
ML (proposed)	98.3989	98.2389	97.2398	0.3989

12 Conclusion

A Multi-Modal Biometric Authentication and Verification System (MBAVS) can be proposed using three biometric modalities including fingerprint, iris, and face based on fusion of matching score state is proposed in this paper. The proposed system provides an accurate and efficient authentication and verification than the unimodal biometric system. Face recognition system is achieved by applying PCA algorithm with FFNN based classification method (PCA-FFNN). The fingerprint image is applied to preprocessing to enhance the excellence of the image and feature extraction could be done for further recognition. The iris recognition is achieved by applying anisotropic diffusion filter preprocessing, segmentation of iris using Hough transform. The face image recognition is achieved using PCA-LDA hybrid algorithm for accurate recognition. The Score Level (SL) decision making fusion technique is applied to fuse all features of various modalities. The machine learning algorithm is used to give accurate and efficient authentication and verification.

References

1. Rahal SM, Aboalsamah HA, Muteb KN (2016) Multimodal biometric authentication system—MBAS. In: 2016 2nd international conference on information & communication technologies. IEEE. <https://doi.org/10.1109/iccta.2006.1684515>
2. Hammad M, Liu Y, Wang K (2018) Multimodal biometric authentication systems using convolution neural network based on different level fusion of ECG and fingerprint. Electronic ISSN: 2169-3536. IEEE. <https://doi.org/10.1109/access.2018.2886573>
3. Parkavi R, Chandees Babu KR, Ajeeth Kumar J (2017) Multimodal biometrics for user authentication. In: 2017 11th international conference on intelligent systems and control (ISCO). IEEE. <https://doi.org/10.1109/isco.2017.7856044>
4. Tayal A, Balasubramaniam R, Kumar A, Bahattacharjee A, Saggi M (2009) A multimodal biometric authentication system using decision theory, iris and speech recognition. In: 2009 2nd international workshop on nonlinear dynamics and synchronization. IEEE. <https://doi.org/10.1109/finds.2009.5227988>
5. Pavithra R, Suresh KV (2019) Fingerprint image identification for crime detection. In: 2019 international conference on communication and signal processing (ICCP). IEEE. <https://doi.org/10.1109/iccp.2019.8698014>
6. Aiman U, Vishwakarma VP (2017) Face recognition using modified deep learning neural network. In: 8th ICCCNT 2017, 3–5 July 2017. IIT Delhi, Delhi
7. Meena D, Sharan R (2016) An approach to face detection and recognition. In: 2016 international conference on recent advances and innovations in engineering (ICRAIE). <https://doi.org/10.1109/icraie.2016.7939462>
8. Dixit A, Vidwans A, Sharma P (2016) Improved MFCC and LPC algorithm for bundelkhandi isolated digit speech recognition. In: 2016 international conference on electrical, electronics, and optimization techniques (ICEEOT). ISBN 978-1-4673-9939-5/16/\$31.00 ©2016. IEEE. <https://doi.org/10.1109/iceeot.2016.7755413>
9. Choras RS (2010) Multimodal biometric personal authentication integrating iris and retina images, pp 121–131. Springer
10. Toh K-A, Tran Q-L, Yau W-Y (2004) Some issues pertaining to adaptive multimodal biometric authentication, pp 617–628. Springer
11. Viswanathan P, Venkata Krishna P, Hariharan S (2010) Multimodal biometric invariant moment fusion authentication system, pp 136–143. Springer
12. Mansour A, Sadik M, Sabir E, Jebbar M (2017) AMBAS: an autonomous multimodal biometric authentication system. In: 2017 13th international wireless communications and mobile computing conference (IWCMC). IEEE. <https://doi.org/10.1109/iwcmc.2017.7986607>
13. Xu Y, Chuang T-C, Lai S-H (2017) Deep neural networks for accurate iris recognition. In: 2017 4th IAPR Asian conference on pattern recognition (ACPR). 2327-0985/17 \$31.00 © 2017. IEEE. <https://doi.org/10.1109/acpr.2017.152>
14. Chanukya PSVN, Thivakaran TK (2019) Multimodal biometric cryptosystem for human authentication using fingerprint and ear. *Multimed Tools Appl.* <https://doi.org/10.1007/s11004-019-08123-w>
15. Elmir Y, Maadeed S, Amira A, Hassaine A (2012) A multi-modal face and signature biometric authentication system using a max-of-scores based fusion. Springer
16. Huang H, Li J, Ma Z, Feng H (2007) Incorporating image quality in multimodal biometric verification, pp 933–942. Springer

An MOS-C Multifunction Filter Employing DXCCTA for High-Frequency Operation



Karam Bharat Singh, Manoj Joshi, and Ashish Ranjan

Abstract This article introduces a biquad multifunction filter using an advanced current-mode building block termed as “Dual X Current Conveyor Transconductance Amplifier (DXCCTA)” which is a combination of dual X second generation Current Conveyor (DXCCII) followed by Operational Transconductance Amplifier (OTA). Single Input Multiple Output (SIMO) characteristics of the multifunction filter produce the filter responses and come with a single DXCCTA block with few grounded capacitors along with MOS-based resistors. All high-frequency responses of biquad multifunction filters are verified using CMOS model of DXCCTA as well as experimental verification using off the shelf ICs AD844 as “Current Feedback Operational Amplifier” and CA3080 as “Operational Transconductance Amplifier”.

Keywords DXCCTA · Multifunction filter · CFOA/ICAD844 · OTA/CA3080 · Frequency response

1 Introduction

An advance active block dominance in the current scenario is now considered as an important active device in microelectronics engineering which gives a suitable platform for the generation of signal processing circuits viz. active filters [1–13], oscillators [14–16], Schmitt trigger [17, 18], chaotic circuits [19, 20], active inductor design [21] and many more. Initially, voltage-mode op-amp has the major contribution for almost every electronic circuits but after the emergence of current-mode circuits [22] became a new trend for the design of active mode circuitry with low power dissipation, greater linearity, inbuilt tunability, wide bandwidth, higher frequency of

K. B. Singh (✉) · M. Joshi · A. Ranjan
National Institute of Technology Manipur, Imphal, India
e-mail: karambharatsingh@gmail.com

M. Joshi
e-mail: manojjoshi1506@gmail.com

A. Ranjan
e-mail: ashish.ism@rediffmail.com

operation and few others [23]. Some very popular advance active blocks are CCII [1, 4], CCCII [10], OTRA [24], FTFN [7, 13], CDTA [8], VDCC [9], DVCC [3, 12], CCTA [5], DDCCTA [25], DVCCTA [26], DXCCTA [27], FTFNTA [28] and few other. A wide array of second-order filters is available and can be treated as the fundamental filter circuitry in the analog domain. Moreover, literature is also enriched with different input–output combination filter as with SIMO [1–3], MISO [4–9] and MIMO [10–12]. In the case of multifunction filter, SIMO operation plays a significant role due to single input source which causes attractive design procedure without the selection of various input sources as in the case of MIMO and MISO. An intensive study of literature [1–28] have the following characteristics:

1. Excess number of active block elements [1, 2, 5, 6, 11]
2. More input signal to realize output filter [7–9]
3. Absence of electronic tenability [1, 24]
4. Low cut off frequency response [1, 4, 8, 24]
5. Component mismatch and circuit topology to get different responses [1, 5–9]
6. Necessary to use external passive components for measurement of different filter responses in current-mode topology [27].

This research paper brings a SIMO filter topology for the multifunction filter responses viz. Low pass (LP), Band Pass (BP) and High Pass (HP) filter by utilizing active MOS resistors and grounded capacitors with single active block DXCCTA. The proposed design is suitable for a very high-frequency operation up to 200 MHz. The examination of the frequency test of the multifunction filter is well executed through PSPICE simulation. An experimental test of the filter is also examined by using the ICAD844 and CA3080 to construct the DXCCTA for filter operation.

2 Circuit Description

A DXCCTA active block comprises a combination of DXCCII and an OTA. The schematic of DXCCTA and its internal MOS-based design is shown in Fig. 1, where the port characteristics can be mathematically defined as:

$$I_Y = 0, I_{X\pm} = I_{Z\pm}, V_{X\pm} = \pm V_Y, I_{O\pm} = \pm g_m V_{Z^-} \quad (1)$$

where g_m corresponds transconductance of DXCCTA and expressed as:

$$g_m = \sqrt{\mu_n C_{OX} \frac{W}{L} I_B} \quad (2)$$

The term μ_n , C_{OX} and W/L are the conventional parameters of a MOSFET and I_B be the input bias current.

A simple filter of the proposed SIMO filter is shown in Fig. 2. Where Z_1 , Z_2 and

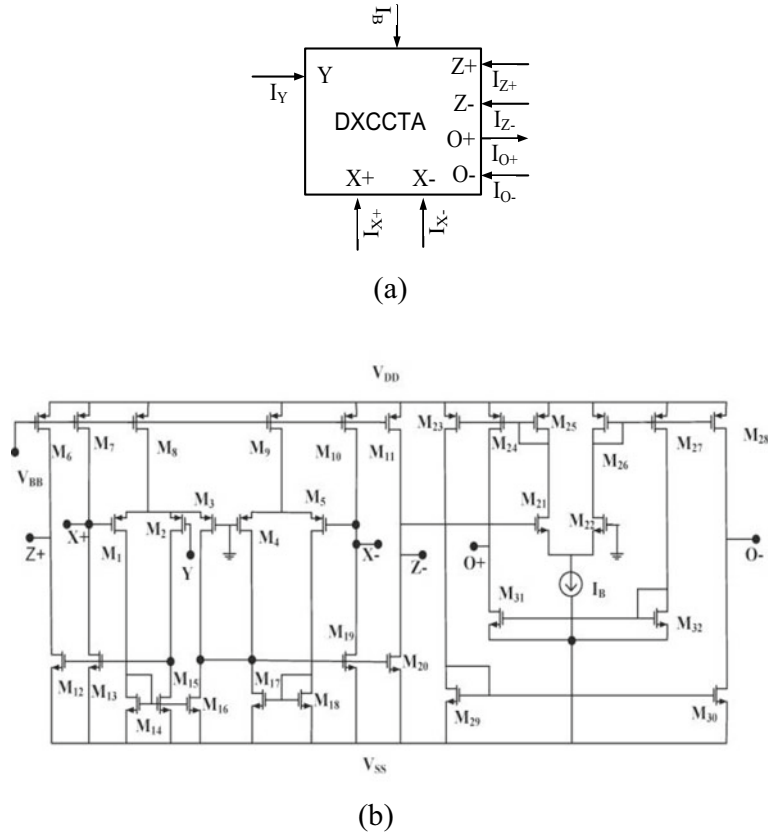


Fig. 1 DXCCTA **a** Schematic symbol, **b** internal CMOS circuit

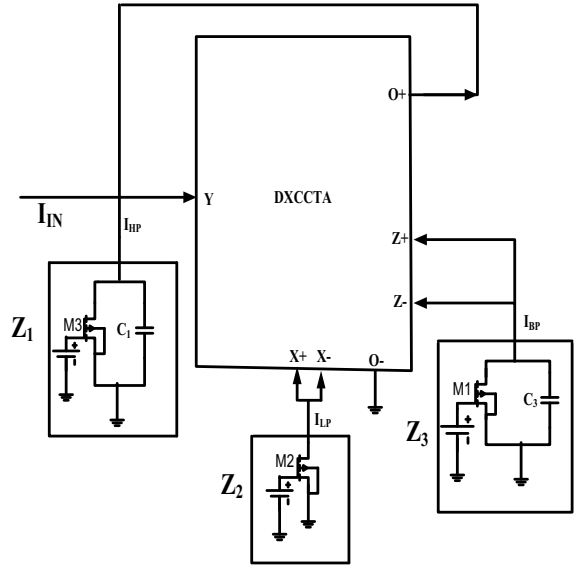
Z_3 represent the impedance term. Z_1 and Z_3 be the parallel combination of the active MOS resistor and capacitor and Z_2 be an active MOS resistor.

$$\left. \begin{aligned} Z_1 &= R_{\text{MOS1}} \left\| \frac{1}{sC_1} = \frac{R_{\text{MOS1}}}{1 + sC_1 R_{\text{MOS1}}} \right. \\ Z_2 &= R_{\text{MOS2}} \\ Z_3 &= R_{\text{MOS3}} \left\| \frac{1}{sC_3} = \frac{R_{\text{MOS3}}}{1 + sC_3 R_{\text{MOS3}}} \right. \end{aligned} \right\} \quad (3)$$

The MOS resistor exhibits a numerical resistance value in the saturation region as:

$$R_{\text{MOS}} = \frac{1}{2\mu_n C_{\text{Ox}} \left(\frac{W}{L} \right) (V_{\text{GS}} - V_{\text{Th}})} \quad (4)$$

Fig. 2 Proposed MOS-C current-mode multifunction filter



A simple routine analysis gives the transfer functions for LP, BP and HP as:

$$T_{LP}(s) = \frac{I_{LP}}{I_{IN}} = \frac{\frac{g_m}{R_{MOS1}R_{MOS2}R_{MOS3}C_1C_3}}{s^2 + \frac{g_m}{R_{MOS2}C_3}s + \frac{g_m}{R_{MOS1}R_{MOS2}R_{MOS3}C_1C_3}} \quad (5)$$

$$T_{BP}(s) = \frac{I_{BP}}{I_{IN}} = \frac{\frac{g_m}{R_{MOS2}C_3}s}{s^2 + \frac{g_m}{R_{MOS2}C_3}s + \frac{g_m}{R_{MOS1}R_{MOS2}R_{MOS3}C_1C_3}} \quad (6)$$

$$T_{HP}(s) = \frac{I_{HP}}{I_{IN}} = \frac{s^2}{s^2 + \frac{g_m}{R_{MOS2}C_3}s + \frac{g_m}{R_{MOS1}R_{MOS2}R_{MOS3}C_1C_3}} \quad (7)$$

The above equations of the filter function give the pole frequency (ω_0) and quality factor (Q_0) as:

$$\omega_0 = \sqrt{\frac{g_m}{R_{MOS1}R_{MOS2}R_{MOS3}C_1C_3}} \quad (8)$$

$$Q_0 = \sqrt{\frac{R_{MOS2}C_3}{g_m R_{MOS1}R_{MOS3}C_1}} \quad (9)$$

Here, the performance of (ω_0) and (Q_0) can be electronically tunable with a bias current that tune g_m and bias voltage for MOS resistors.

3 Non-Ideal Study

To study the non-ideal analysis, we have examined the transfer function using non-ideal characteristic of DXCCTA. In non-ideal characteristic condition, DXCCTA port relation is express as [27]

$$I_Y = 0, I_{X\pm} = \alpha I_{Z\pm}, V_X = \pm \beta V_Y, I_{O\pm} = \pm \gamma g_m V_{Z-}; \quad (10)$$

where (α , β and γ) be the current transfer gain, non-ideal voltage-transfer gains and transconductance inaccuracies present in the DXCCTA, respectively. By using non-ideal parameters (α , β and γ), the current-mode LP, BP and HP transfer function of the multifunction filters are observed as:

$$T_{LP}(s)|_{\alpha,\beta,\gamma} = \frac{I_{LP}}{I_{IN}} \Big|_{\alpha,\beta,\gamma} = \frac{\frac{\alpha\beta\gamma g_m}{R_{MOS1}R_{MOS2}R_{MOS3}C_1C_3}}{s^2 + \frac{\gamma g_m}{R_{MOS2}C_3}s + \frac{\alpha\beta\gamma g_m}{R_{MOS1}R_{MOS2}R_{MOS3}C_1C_3}} \quad (11)$$

$$T_{BP}(s)|_{\alpha,\beta,\gamma} = \frac{I_{BP}}{I_{IN}} \Big|_{\alpha,\beta,\gamma} = \frac{\frac{\alpha\gamma g_m}{R_{MOS2}C_3}s}{s^2 + \frac{\gamma g_m}{R_{MOS2}C_3}s + \frac{\alpha\beta\gamma g_m}{R_{MOS1}R_{MOS2}R_{MOS3}C_1C_3}} \quad (12)$$

$$T_{HP}(s)|_{\alpha,\beta,\gamma} = \frac{I_{HP}}{I_{IN}} \Big|_{\alpha,\beta,\gamma} = \frac{\alpha s^2}{s^2 + \frac{\gamma g_m}{R_{MOS2}C_3}s + \frac{\alpha\beta\gamma g_m}{R_{MOS1}R_{MOS2}R_{MOS3}C_1C_3}} \quad (13)$$

In this case, (ω_0) and (Q_0) becomes

$$\omega_0|_{\alpha,\beta,\gamma} = \sqrt{\frac{\alpha\beta\gamma g_m}{R_{MOS1}R_{MOS2}R_{MOS3}C_1C_3}} \quad (14)$$

$$Q_0|_{\alpha,\beta,\gamma} = \sqrt{\frac{\alpha\beta\gamma R_{MOS2}C_3}{\gamma g_m R_{MOS1}R_{MOS3}C_1}} \quad (15)$$

The influence of non-ideal parameter is reflected in (ω_0) and (Q_0). Moreover, the active and passive sensitivity of (ω_0) and (Q_0) are observed as:

$$\left. \begin{aligned} S_{\alpha,\beta,\gamma,g_m}^{\omega_0} &= \frac{1}{2}, S_{R_{MOS1},R_{MOS2},R_{MOS3},C_1,C_3}^{\omega_0} = -\frac{1}{2} \\ S_{\alpha,\beta,R_{MOS2},C_3}^{Q_0} &= \frac{1}{2}, S_{g_m,R_{MOS1},R_{MOS3},C_1}^{Q_0} = -\frac{1}{2}, S_{\gamma}^{Q_0} = 0 \end{aligned} \right\} \quad (16)$$

The sensitivity analysis (16) shows a low value that corresponds to good performances for filter design.

4 Simulation Results

To confirm the theoretical analysis, both simulation and experimental tests are performed for a multifunction filter. The first section of validation is done through PSPICE simulation in which DXCCTA is integrated with 0.18 μm CMOS TSMC parameters with supply voltage ± 1.25 V and bias voltage 0.43 V.

Multifunction filter frequency response for LP, BP and HP is observed for a very high frequency in the range of 100 MHz. The active resistor have 1 K Ω reactance value and traditional capacitance with 1 pF exhibits ω_0 of 177 MHz with a response in Fig. 3. The filter frequency response of BP filter is below 0 dB which can be improved by varying the bias current I_B values which gives freedom for independent gain control behaviour. The gain variation with different I_B values is well observed in Fig. 4 for the BP filter. Also, an experimental test for DXCCTA blocks is realized with CFOA (ICAD844) and OTA (CA3080) as shown in Fig. 5.

A time-domain verification for filter is performed for ω_0 100 MHz by selecting the components values for the LP filter as $R_{\text{MOS}1} = R_{\text{MOS}2} = R_{\text{MOS}3} = 2$ K Ω and $C_1 = C_2 = 1$ pF. As we have designed for 100 MHz cut off frequency, the filter output can pass the input signal which is less than 100 MHz frequency in LP filter. Figure 6 shows the experimental result of a LP transient response for 50 MHz input supply. For LP filter the input and output waveform will be in phase as shown in Fig. 6.

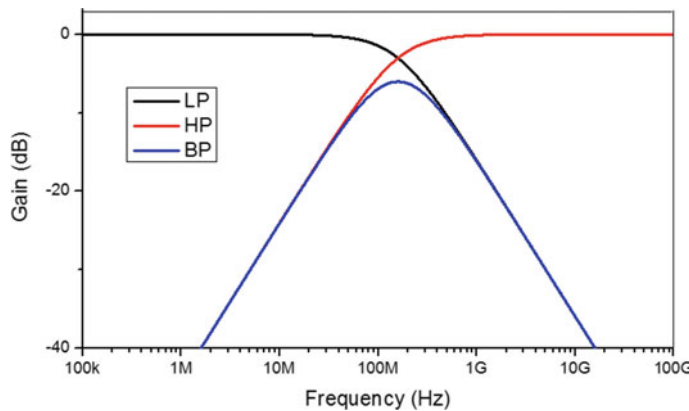


Fig. 3 Proposed CM-MF frequency response

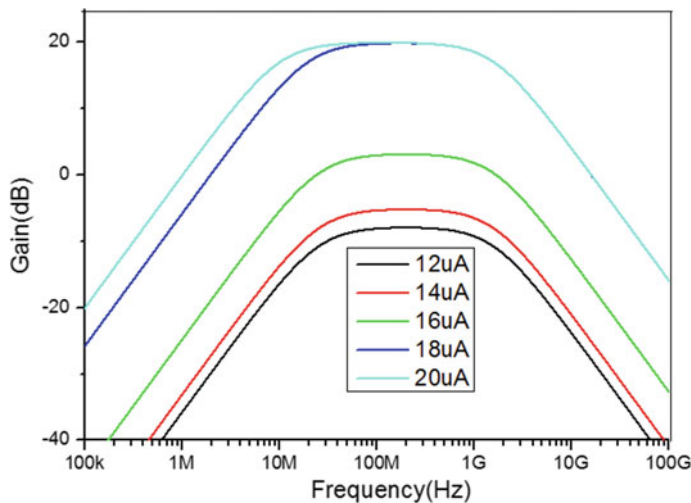


Fig. 4 Gain variation in BP with different bias current I_O

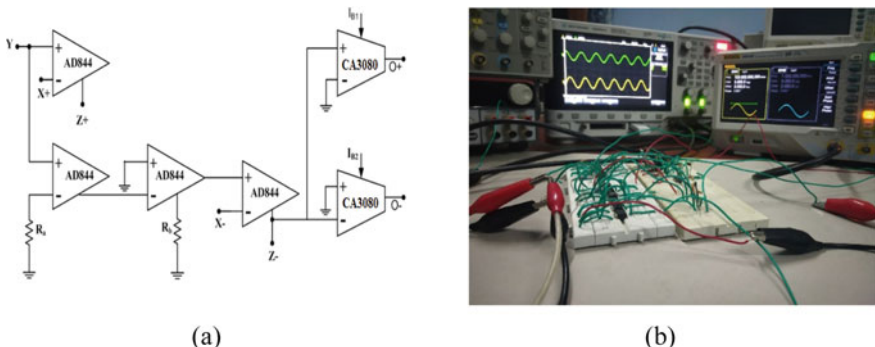
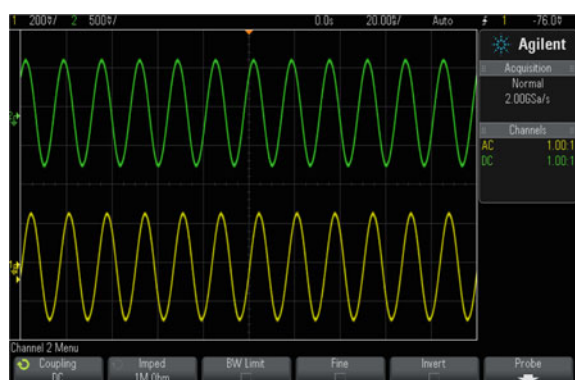


Fig. 5 DXCCTA using ICAD844 and CA3080 for experimental test. **a** Circuit diagram, **b** physical experiment set up

Fig. 6 Experimental LP transient response for 50 MHz input



5 Conclusion

This article brings a high-frequency second-order filter using MOS resistors and capacitors. The behaviour of the proposed design is simulated with the PSPICE simulation by utilizing TSMC 0.18 μm technology and experimentally performed using off the shelf ICs. The influence of non-ideal behaviour is also observed. The results follow a close agreement with the theoretical prediction. Some useful characteristics of the proposed filter are as follows:

1. Use of single DXCCTA.
2. With less passive components.
3. High-frequency response in 100 MHz.
4. Provides electronic tunability by using bias current.
5. No need to disturb the input signal for different output responses.
6. Suitable for LP, BP and HP filters.

Acknowledgements This work is supported by the Third Phase of Technical Education Quality Improvement Program (TEQIP-III) under the Collaborative Research Scheme (CRS ID: 1-5728068886), National Project Implementation Unit (NPIU), a unit of Ministry of Human Resource Development (MHRD), Government of India for implementation of World Bank assisted projects in technical education.

References

1. Cicekoglu O (1999) Multifunction filters using three current conveyors. *Microelectron J* 30:15–18
2. Chen HP (2014) Voltage-mode multifunction biquadratic filter with one input and six outputs using two ICCIIs. *Sci World J* (2014)
3. Abaci A, Yuce E (2016) Second-order voltage-mode universal filters using two DVCCs, two grounded capacitors and four resistors. *J Circ Syst Comput* 25(12)
4. Ozcan S, Kuntman H, Cicekoglu O (2000) A novel multi-input single-output filter with reduced number of passive elements using single current conveyor. In: Proceedings of the 43rd IEEE midwest symposium on circuits and systems, vol 3, pp 1030–1032
5. Tomar RS, Singh SV, Chauhan DS (2013) Current processing current tunable universal biquad filter employing two CCTAs and two grounded capacitors. *Circ Syst* 4:443–450
6. Ranjan A, Paul SK (2011) Voltage mode universal biquad using CCCII. *Active Passive Electron Compon*
7. Ranjan A, Perumalla S, Kumar R, John V, Yumnam S (2019) Second order universal filter using four terminal floating nullor (FTFN). *J Circ Syst Comput* 28
8. Shah NA, Quadri M, Iqbal SZ (2007) CDTA based universal transadmittance filter. *Analog Integr Circ Signal Process* 52:65–69
9. Uttaphut P (2018) Single VDCC-based electronically tunable voltage-mode second order universal filter. *Przeglad Elektrotechniczny* 1(4):24–27
10. Tangsrirat W (2007) Current-tunable current-mode multifunction filter based on dual-output current-controlled conveyors. *AEU-Int J Electron Commun* 61:528–533
11. Abaci A, Yuce E (2017) A new DVCC+ based second-order current-mode universal filter consisting of only grounded capacitors. *J Circ Sys Comput* 26

12. Horng JW, Jhao ZY (2013) Voltage-mode universal biquadratic filter using single DVCC. Hindawi Publishing Corporation, ISRN Electronics, London
13. Abuelmaatti AT (2000) Universal current-mode filter using single four-terminal floating nullor. *Microelectron J* 31(2):123–127
14. Joshi M, Bhatt V, Ranjan A, Benjwal P (2017) Realization of Colpitts oscillator using second generation current controlled current conveyor. In: The second international conference on research in intelligent and computing in engineering, pp 49–52
15. Kumari A, Ranjan A (2018) Realization of extra-X current controlled current conveyor based resistorless quadrature sinusoidal oscillator. *Int J Appl Eng Res* 13:80–84
16. Ghosh M, Bhattacharya S, Ranjan A, Paul SK (2011) CMOS sinusoidal oscillator using current conveyor. In: Proceedings of international colloquiums on computer electronics, electrical, mechanical and civil, Kerala, India
17. Ranjan A, Pamu H, Tarunkumar H (2018) A novel Schmitt trigger and its application using a single FTFN. *Analog Integr Circ Signal Process* 1–13
18. Pamu H, Ranjan A, Tarunkumar H (2018) Realization of schmitt trigger using IC AD844 based differential voltage current conveyor transconductance amplifier. In: Proceedings of international conference on innovations in electrical, electronics, power, smart grids and advanced computing technologies, 9–10 Mar 2018
19. Joshi M, Ranjan A (2019) An autonomous chaotic and hyperchaotic oscillator using OTRA. *Analog Integr Circ Sig Process* 101:401–413
20. Joshi M, Ranjan A (2018) Realization of multi scroll 2D chaotic oscillator using DVCC. In: Lecture notes in electrical engineering, vol 553, pp 1093–1101
21. Kumar N, Vista J, Ranjan A (2019) A tuneable active inductor employing DXCCTA: grounded and floating operation. *Microelectron J* 90:1–11
22. Sedra A, Smith KC (1970) A second-generation current conveyor and its applications. *IEEE Trans Circ Theory* 17:132–134
23. Toumazou C, Lidgey FJ, Haigh DG (1993) Analogue IC design: the current-mode approach. In: IEEE circuit and system series, vol 2. Peter Peregrinus Ltd., London, UK, pp 1–666
24. Bhatt V, Benjwal P, Joshi M (2017) OTRA based second order universal filter and its optimization like Butterworth, Chebyshev and Bessel. In: Second International conference on research in intelligent and computing in engineering, vol 10, pp 143–150
25. Pandey N, Paul SK (2011) Differential difference current conveyor transconductance amplifier: a new analog building block for signal processing. *J Electr Comput Eng*
26. Pandey N, Paul SK (2011) VM and CM universal filters based on single DVCCTA. Active Passive Electron Compon
27. Chaturvedi B, Kumar A (2016) DXCCTA: a new active element. In: 1st IEEE international conference on power electronics, intelligent control and energy systems
28. Tarunkumar H, Singh YS, Ranjan A (2019) An active inductor employing a new four terminal floating nullor transconductance amplifier (FTFNTA). *Int J Electron*



Karam Bharat Singh was born in 1994. He received his Bachelor of Technology in 2017 from the Department of Electronics and Communication Engineering, North Eastern Regional Institute of Science and Technology (NERIST), Nirjuli, India. His research interests include Current-Mode Analog circuit and filter design, Mixed-signal IC design, low power VLSI design, etc. At present, He is pursuing Master of Technology in VLSI and Embedded System from the Department of Electronics and Communication Engineering, National Institute of Technology Manipur, Imphal, India.



Manoj Joshi was born in 1989. He received his B.Tech. degree in 2011 from the Department of Electronics and Instrumentation Engineering, DIT University, Dehradun, India, and M.Tech. degree in 2014 from BTKIT, Dwarahat (Uttarakhand Technical University, Dehradun). His research interests include current-mode analog circuits and study of Chaos Theory, Chaotic and Hyperchaotic oscillator, Fractional-Order Devices, Mixed-signal IC design, filter designs. At present, He is pursuing a Ph.D. in VLSI in Electronics and Communication Engineering Department, National Institute of Technology Manipur, Imphal, India.



Ashish Ranjan was born in 1986. He received his Doctor of Philosophy (Ph.D.) degree in 2013 from the Department of Electronics Engineering, Indian Institute of Technology (Indian School of Mines), Dhanbad, India. His research interests include current-mode analog circuits, the study of fractional-order circuit, chaotic oscillators, filter designs, etc. At present, he is Assistant Professor in Electronics and Communication Engineering Department, National Institute of Technology Manipur, Imphal, India.

Smart Car Parking Technique for Metropolitan City



**Abu Shufian, Md. Asif Afroj, Md. Hasibuzzaman, Mehedi Al Miraz,
Avijit Sarker, Md. Jahidul Islam Rashed, and Md. Aman Miah**

Abstract The objective of this proposed model is to build a smart car parking system that will make the parking process easier and more effective for the users of the parking area. Due to the expansion of using car traffic problems mostly occur all over the world and to reduce the problem smart parking system can play a sustainable and innovative role. In the traditional parking system, the parking area's maximum works are dependent on manpower in the past. But now, it will reduce on a high scale and make the whole process automated by the bless of the smart system. A fire alarm process in the parking area makes this system more reliable and safer. Also, the smart car parking system provides a proper security system and proper parking area detection which are useful and makes the parking process more comfortable for the users.

Keywords Smart parking · Arduino · RFID sensor (tag, reader) · IR sensor · Flame sensor · Bill calculation and payment

1 Introduction

Science and technology mean innovation and it spreads its innovative manner also in the transportation sector. It changes all the transportation infrastructure and now in today's world a huge number of vehicles produce all over the world. Increasing of the rapid number of vehicles also produce transportation problem, which is normally known as traffic problem all over the world. So, to get a release from that problem

A. Shufian (✉) · Md. Hasibuzzaman · M. Al Miraz · A. Sarker · Md. J. I. Rashed · Md. A. Miah
Department of Electrical and Electronic Engineering, American International
University-Bangladesh, Dhaka 1229, Bangladesh
e-mail: shufian2aiub@gmail.com

Md. Hasibuzzaman
e-mail: hasibshuvo1995@gmail.com

Md. A. Afroj
Department of Computer Science and Engineering, United International University, Dhaka 1212,
Bangladesh
e-mail: shayon.asif@gmail.com

smart parking system is the most effective and coolest way to decrease the rate of traffic jams as most of the traffic problems normally occurred because of the parking car here and there. In this paper, all the features are combined which are gathered from the previous thoughts. The display will show the proper direction in which way the car has to move and it also shows the parking slot which is free and which is occupied [1]. In the parking area, an automatic counter system is provided that can measure the time and give a calculation of various charges for different kinds of cars for their parking time. In the smart parking process in and out gate can easily control. When the car comes to the gate sensor or RFID can use and when the authorized cars are detected the gate is automatically open and the same process is to open the out gate. Sometimes, it shows that the driver or the user parks the car and goes outside; then, there is no need to park on the load. A sensor can easily do the work. When there is a person, it detects the person and on the load like light, and when there is no one, it automatically offs the load. A fire alarm process can introduce in the parking area. If any fire accident occurs there, the sensor can easily detect this and the alarm will ring. This process makes the parking area more secure. Security is an important issue for car parking. Normally in the parking area, an authorized person can park. So, to make the parking process more secure sensor or RFID for an authorized person can introduce. So, not only the parking cars are safe and get proper security but also, unauthorized cars are easily detected and cannot park. In the parking area, various types of cars are parked and to depend on this the parking area can be divided into a different zone. If a different zone can introduce, it will easy to know which types of cars with their numbers are parked in a different parking zone.

2 Literature Review with In-Depth Investigation

The smart car parking system is a process in which the whole parking system is developed with merging of various features that make the parking process more innovative and comfortable and secure for the users [2]. The smart car parking system which is mainly implemented in Japan, USA, and Europe is developed with various research centers and technical institutions. This developing process was not started in a single day. It was a long-time process which was developed day by day. In 1951 automatic parking system was opened in Washington D.C. They have implemented some systems and they are still in use bowser, pigeon-hole systems, and roto park systems. In 1961 auto stacker was introduced in London. Advanced systems were implemented in South America and Asia in the 1970s. Japan has crossed all the records to implement more than 100,000 parking spaces which is a year from the 1990s which are fully automated [3]. In Hoboken, New Jersey robotic parking garage was implemented in 2002. In the recent 2015, few students of Jazan University have developed a computerized vehicle parking management and monitoring model which utilizes programmed number plate acknowledgment cameras to monitor the parking facilities of the University [4]. In 2018, a prototype car parking monitoring system using a camera network was developed with the help of visual detection and

communication of parking information [5]. In the same year, some researcher has developed a new localization approach that improved rear-view camera usage during automatic parking. They proposed a vehicle localization process using an interacting multiple model Kalman filter [6].

The smart parking system is considered the most beneficial, updated and innovative process that makes the parking too much easier. It reduces the time and effort to find out the parking slot. Also, it is helpful to reduce traffic jams. As in a smart parking system, users can easily find out the parking place so it also places an important role to decrease the emission of pollution. It also brings a revenue earning process for the owner of the parking area. This system is fully automated that is why it reduces the management cost and real-time data of users are stored in the system that makes the smart car parking process more secure and beneficial for the users [7].

There are various methods of smart parking systems such as parking information and guidance system, transit-based information system, smart payment system, an automated parking system. Parking guidance and information system is a system in which drivers can get proper information and direction sign or message sign to know about the parking place [8]. Necessary data or messages of real-time information on parking and departure times are provided in a transit-based information system [9]. The smart payment system is introduced to overcome the limitation of the accustomed payment process by reconstruction of the payment method via parking meter. It reduces the time limit of payment, maintenance, and staffing requirement. In the e-parking process, it shows the availability of parking space and the user can easily reserve place [10]. The main thought of this process is to ensure the vacant parking facility for the users via SMS and the user can pay the bill by the smart payment system. In the automatic parking system, the whole parking process is fully automated. Parking areas gate and other components are automatically worked through RFID sensors and make parking easier to give proper direction in display [11, 12].

2.1 Aim of Smart Car Parking

This proposed system is fully automated by a microprocessor. Also, it provides proper security protection with proper parking area detection which is useful and makes the parking process more comfortable for the users. The smart parking system is a suitable and efficient car parking system where cars are parked in a systematic and proper way. In this system, parking areas decrease and also make parking process easier and reduces parking time. A proper security system to detect authorized and unauthorized cars is the added advantage of the smart car parking system. There are some extra features like parking slot occupancy detection with a display, automatic billing process for parking of public cars, automatic load control and fire alarm system can add to make the parking system more effective. It can be introduced in public places such as educational institutions, offices, and shopping malls and so on with proper authorization. As a result, the parking process becomes more secure and it will also contribute a great part to reduce the traffic problem because in this

system the owner cannot park a car here and there. The smart car parking system is an adjustment of mechanical, electrical and control devices which can assure parking a large number of cars in a little space in a systematic and automatic way with proper direction.

3 Methodology and Designing of Smart Car Parking

The whole process was divided into various blocks and merged them to get the desired output. Two types of the process were used to fulfill that project. One process was the wireless connection and another was wired connection. In wireless process RFID tag and RFID reader were used and in wired connection was between Arduino, LCD, Flame sensor and other equipment. From the RFID tag information will send to the RFID reader and from RFID reader, Arduino will get the information. For the valid information, LCD will show information that had given to it from Arduino and the gate will be opened. At the same time, Arduino would get information from the IR Sensor about the vacancy of place and show the information in the LCD display. If any fire accident occurs in the parking place Arduino will get the information from the Flame sensor and the buzzer will ring. When the car will go out from the parking place again the RFID tag will have to punch and Arduino will get information from the RFID reader. Then parking time and money that have to pay to the users will show in the display. When the user will pay the money, Arduino gets the information and the gate will be opened (Figs. 1 and 2).

In smart parking system, the parking space is divided into a different slot and in every slot, IR sensor is used and the main purpose of IR sensor main is to identify if there any vacancy or not in parking space and an LCD display proper information can be seen that would give from the IR sensor. Suppose the parking area is divided into 6 slots and in every slot, the car was parked. So, LCD will show there is no

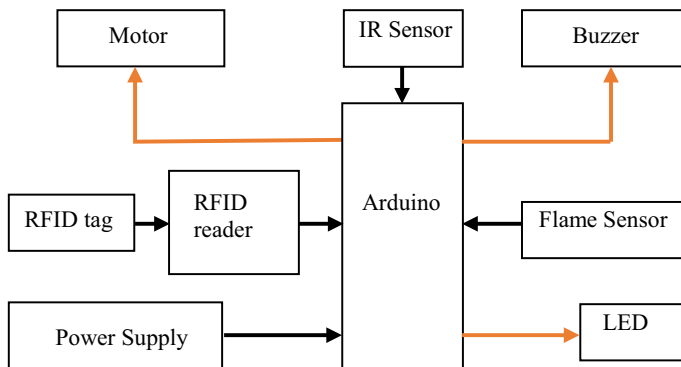
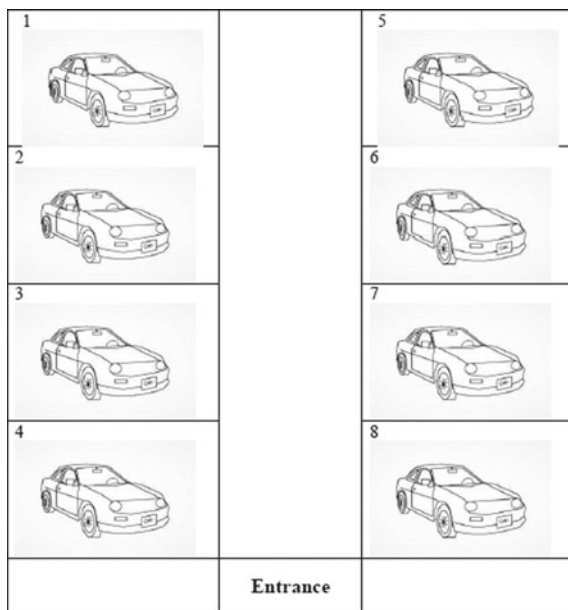


Fig. 1 Block diagram of the smart car parking system

Fig. 2 Different slot in the parking area



vacancy and parking is filled so extra no car can enter the parking area. Suppose there is a vacancy in 5 and 6 slots. So, LCD will show the vacancy of 5 and 6 slots and also give a proper direction of parking space thus a user can easily park their car (Fig. 3).

First, the LED display was connected to the Arduino and controlled it by Arduino. The input power was given to Arduino and RFID tag was used to control the gate. Here, a fire sensor in Arduino input and a buzzer was used in Arduino output from which a signal was found if there would any fire accident occur in the parking area. There was an IR sensor that was used to detect the occupancy of a parking slot and in LED display the user would easily see is there any free space or not in every slot. Bill calculation process was also set up in Arduino from which the user would see the amount of money in LED that would be paid to the owner of the parking area for parking the car. In block diagram whole process was given with proper connection and description thus how the system was going to be worked could easily understand for people Block diagram and the flowchart of the smart car parking system introduce the whole thought of this project in a shortage way. Step by step a process of this project and the working system is shown in the block diagram properly.

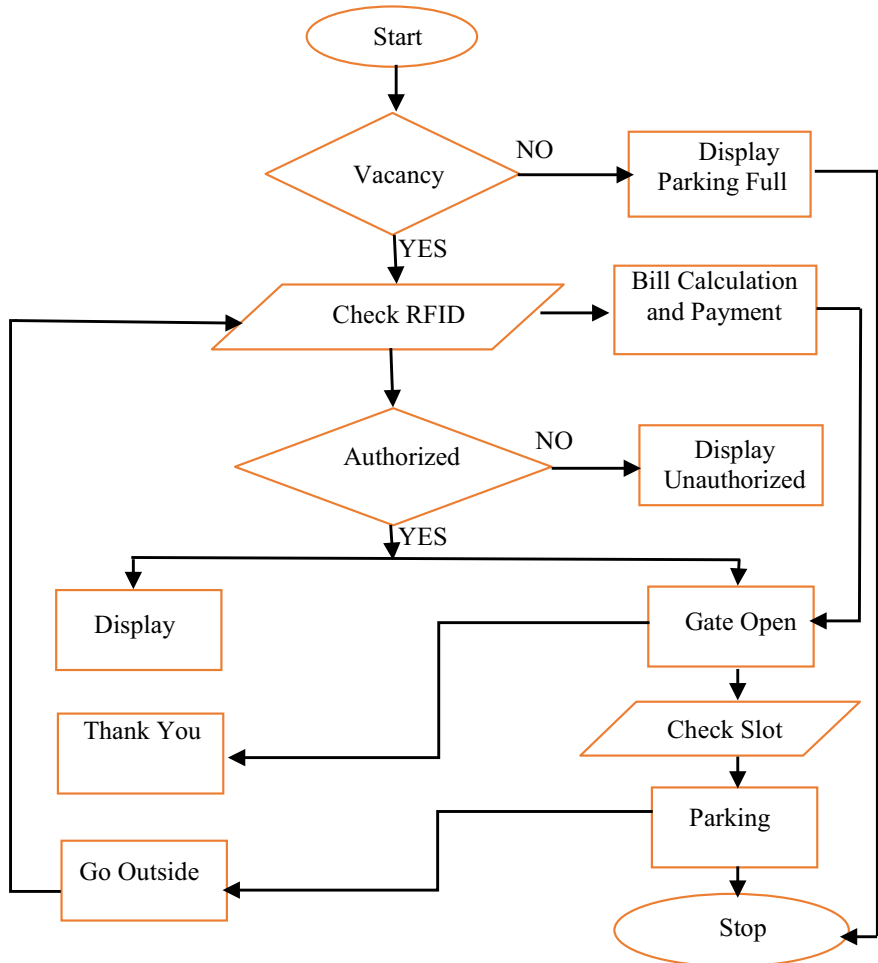


Fig. 3 Flowchart of the smart car parking system

4 Simulation and Structural Result of Smart Car Parking System

The simulation was the best way to find out the result in real-life circuits. For result analysis, Proteus 8 professional simulator was used. Figure 4 shows the schematic diagram of the proposed system where LCD display was attached to Arduino Uno. The RFID reader and Flame sensor were simulated by Proteus 8 and replaced in different combination pin number of Arduino through the wire. Red, yellow different color LED was used to show the variety of signaling different sectors.

Gate open section was shown in Fig. 4a. When a user would use the ID card the Arduino would justify the card pin number and give a result that the user was allowed

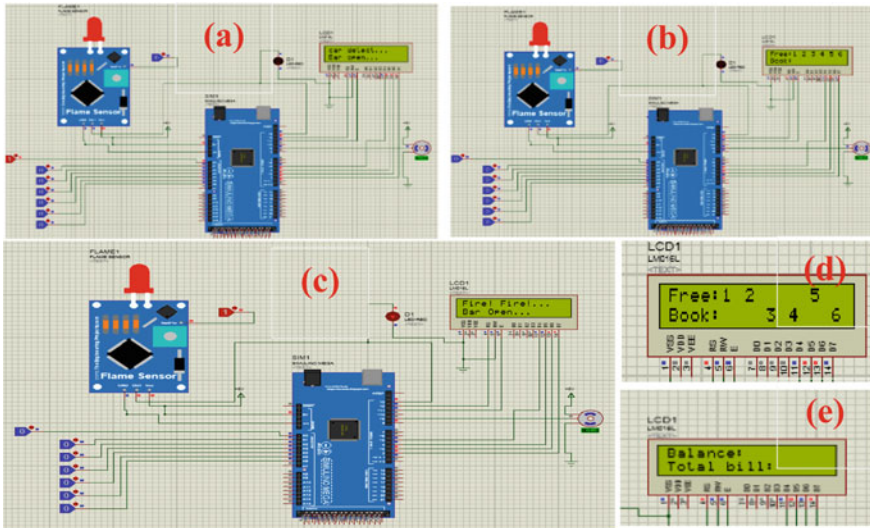


Fig. 4 **a** Car detect and bar open, **b** free slots in LCD display, **c** fire signal in LCD display, **d** car detect and bar open, **e** free slots in LCD display

or not. If the card was valid, the signal from Arduino would make the servo motor turn into the ninety-degree angle and the bar would open and the allowed users would go inside to the parking area and after some delay, the bar was automatically closed. The car parking free slots were shown in Fig. 4b. When valid user ID was punched then yellow LED was turned on and the gate was opened and user would go to the parking area.

In Fig. 4c, simulation was used for fire alarm purpose. The main purpose of the Flame sensor is to detect the fire accident in the parking area was connected to the Arduino and if any fire occurrence happened in parking area the occurrence was detected by Flame sensor and from the Arduino the result would go to buzzer and buzzer would make sound, Red LED would turn On and also in LCD display the fire signal was showed to make aware of the fire accident to its users.

In Fig. 4d, the free and booked slot for parking system was shown. In the display, there were six slots. In parking area, IR sensor was used to sense the vehicles and the result was justified in Arduino and an LCD display user would see the result that which slot was free and which slot was booked. In Fig. 4e, simulation was shown about the outgoing process of users from the parking area. When the user would want to go outside, the ID card was punched by the users and from the bill calculation process which was already installed in Arduino showed the amount of money in LCD display after calculating the parking time and money for per hour and user had to pay the money for parking the car and after receiving the money the bar was opened and user would go outside. After some delay, the bar was closed automatically.

In simulation part, the whole result was shown from which a total idea of the system which was merged with different parts such as gate control, free and book

slots detection, bill calculation and fire system can easily understand. In the hardware side, all the features were merged and a proper result of smart car parking system was shown.

The first stage of the hardware system was shown in Fig. 5a. Here, a card reader, servo motor, yellow LED and buzzer was connected to the Arduino according to the Arduino code pin number through the wire and it was the initial stage where no RFID was used to see the valid or invalid user ID and the gate was at its initial stage that means bar was closed. Figure 5b showed the validation process of the user ID card. When the valid ID was punched to the reader the information would go to the

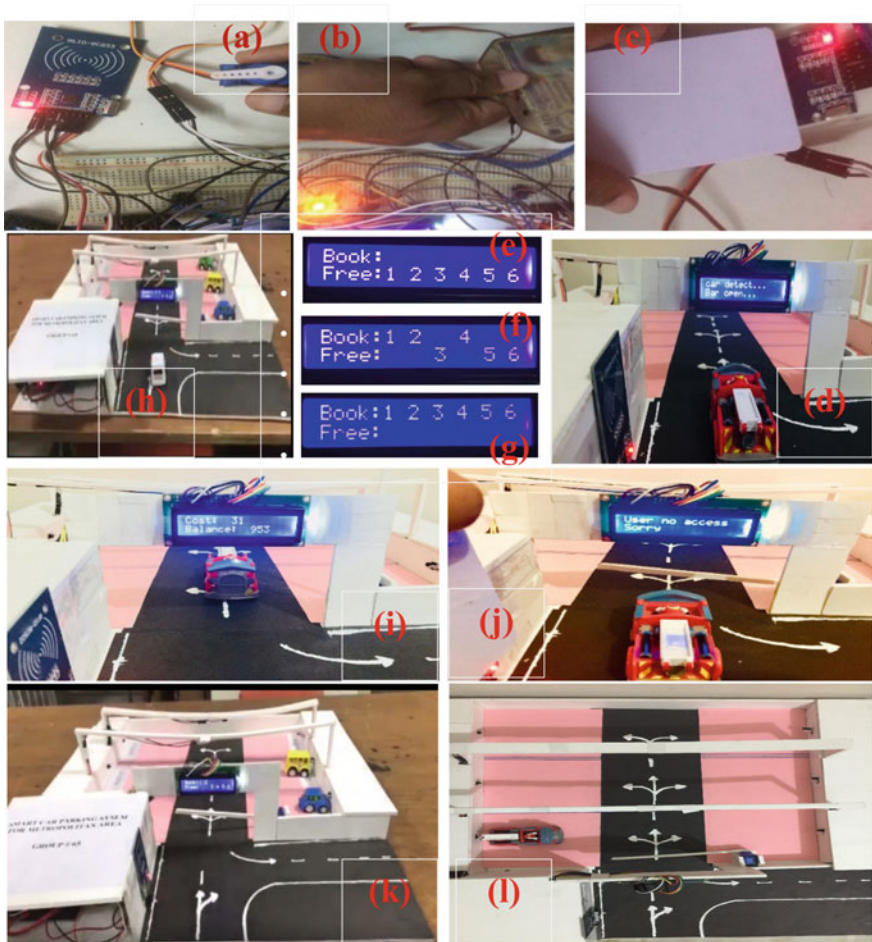


Fig. 5 **a** First stage of the smart car parking system, **b** valid RFID check, **c** invalid user ID check, **d** gate open, **e** free slots in LCD display, **f** free and booked slots in LCD display, **g** booked slots in LCD display, **h** car detection and bar open in LCD display, **i** estimated bill and remaining balance calculation, **j** invalid RFID check, **k**, **l** full hardware structure of the smart car parking system

Arduino and after checking the validity of the user ID the signal would go to the yellow LED and LED would turn ON. Figure 5c was about the invalid ID users. If any invalid id was punched in the RFID reader, the reader would detect the invalidity of the ID and the bar would not open and the red LED was also turned ON. After getting the valid ID signal from Arduino the gate would move into the ninety-degree angle and the car was allowed to go inside the parking area and in Fig. 5d the process was shown. When users have punched the ID, the validity was checked by the IR reader. After checking the validity user ID, the bar will be opened and it would be shown on display in Fig. 5d. When the valid ID was punched by the user, at the entrance user would see the LCD display where free or book slot as shown in Fig. 5e was usually shown in the free slot. That means every parking slot was empty and in any parking slot, the car would be parked. In Fig. 5f where some free and booked slots were shown. When the free slots were booked by the car, the IR sensor would detect it and the signal was sent to the Arduino and after justifying the signal in display, free and booked slot were shown. In Fig. 5g the booked slots are discussed. When all the slots were booked by the cars that were shown in the LCD display.

When the user would want to go outside from the parking area user had to punch the ID again and a particular amount of money was deducted from the user ID account and after deduction, the bar would open and the user would go outside. This part was shown in Fig. 5i. Figure 5j was about invalid ID users. If any invalid id was punched in the RFID reader, the reader would detect the invalidity of the ID and the bar would not open and the red LED was also turned ON.

4.1 Calculation

There is also a payment issue that users have to pay for using the parking space. The owner of the parking space may fix a value for hourly parking suppose it will be \$2 for one-hour parking. So, if the user parks the car for 2 h the user has to pay.

$$\text{Per hour parking cost} \times 2 \text{ h} = \$2 \times 2 = \$4.$$

So, when the user will want to go out from the parking area first user has to pay \$4 and the gate will automatically open thus a user can go outside.

An important part of a project has measured the cost. To start any project first rudiment was to select the equipment that would use in the project and calculate the cost of this equipment. That's why calculation was done and the total cost of the project and the price of all components were given in Tables 1 and 2.

Table 1 Cost estimation

Components	Quantity	Price (US dollar)
Arduino Mega 2560	01	10.6
LCD display 16 × 2	01	1.95
RFID reader	01	4.26
RFID tag	01	0.36
Flame sensor	01	9.20
Relay	03	2.56
Servo motor	01	2.20
Volume pot resistor	01	0.15
LED (pin type)	08	0.20
Buzzer	01	0.18
Miscellaneous		5.48
Total cost		37.15\$

Table 2 Compare with traditional models (list of car parking system and comparison table of car parking system)

Present all the method of car parking	Our proposed car parking method	Traditional car parking system	Smart car parking system
Transit-based information system, automated parking, E-parking, parking guidance and information system, smart payment system, parking lot, parking garages, carports, automated parking system, semi-automated parking system [3]	Smart car parking system	Dependent on manpower [4]	Whole process automated
		Cannot detect authorized and unauthorized cars [9]	Detect authorized and unauthorized cars
		Manually check free space for parking [10, 13]	Proper parking area detects automatically
		Cost and time calculation process are by hand [2]	Automatically calculate and give result instantly
		Non-smart and manual process [5]	Makes parking process easier and reduces time
		Some features like by hand gate controlling, manual load control [8, 13]	Extra feature like automatic billing process, automatic load control, and fire alarm system
		Security system is weak [6]	Provides a proper security system

5 Limitations and Future Enhancements

In this research work, the main focus was concerned about the development of the smart parking system. But there were some limitations also. There only one gate was used to gate in and out from the parking area. A problem was created for that when two users wanted to go and in at a time. In future improvements were carried out with this proposed model. Only six slots were shown in this model and all the components were accurately working with user demand. Sensors which were used to sense the car and in the display, free or booked slots were shown. For a large parking area, this model could be spread to fulfill the user demand in the future. Some of the techniques in which the circuit could be modified were such as, making the system with IoT and Wi-Fi based. Addition of more IR sensors for more car parking slots. Advanced parking slot booking system by SMS from mobile.

6 Conclusion

This designed framework is coordinated by Arduino, RFID tag, RFID reader, LCD display, servo motor, LED, buzzer, IR sensor, Flame sensor which make the parking system more effective and useful for the users. This design of the smart parking system will give proper direction, more security and provide an easy way of parking to its users and also it will play an important role to reduce the traffic problem of a country. On the other hand, this was an Arduino based project which would use in large areas like corporate offices, institutions, shopping mall or residential area to make the parking system easier. It would user-friendly and also the most effective. It would make the parking area more secure and could give a fire alarm to detect the fire with the flame sensor. For this purpose, the gate would automatically turn on and off with the proper validation of the user's ID card. So, it was not easy to make any violence in the parking area because it could be easily detected. So, a whole security system was created in the parking area through the project. The LCD display was used in the parking area to give the proper instruction about the parking slots that would make the parking process easier for the users because users would not have to search the parking slot in the large parking place. And the owner of the parking area would also earn money from the parking area easily. So, it was overall a friendly and effective prototype model for the car users to park the car easily and safely.

References

1. Lu R, Lin X et al (2009) SPARK—a new VANET-based smart parking scheme for large parking lots. In: IEEE conference on computer communications. <https://doi.org/10.1109/infcom.2009.5062057>
2. Yan G, Yang W et al (2011) Smart parking: a secure and intelligent parking system. IEEE Intell Transp Syst Mag 3(1):18–30
3. Pojani D, Stead D (2015) Sustainable urban transport in the developing world: beyond megacities. Sustainability 7(6):7784–7805
4. Aalsalem M et al (2015) An automated vehicle parking monitoring and management system using ANPR cameras. In: Conference on advanced communication technology. <https://doi.org/10.1109/icact.2015.7224887>
5. Hammoudi K et al (2018) Towards a model of car parking assistance system using camera networks: slot analysis and communication management. In: IEEE international conference on smart city. <https://doi.org/10.1109/hpcc.smartcity.dss.2018.00210>
6. Lee S et al (2018) Localization for automatic parking system using interacting multiple model Kalman filter with rear-view camera. In: International conference on control, automation and systems. Available: INSPEC accession number: 18345640
7. Roßnagel A (2019) Protection of fundamental rights in the smart car. In: Communication, security and data protection in the networked vehicle, p 84. <https://doi.org/10.1007/978-3-658-26945-6>
8. Geng Y et al (2013) New “smart parking” system based on resource allocation and reservations. IEEE Trans Intell Transp Syst 14(3):1129–1139
9. Rodier C, Shaheen S (2010) Transit-based smart parking: an evaluation of the San Francisco Bay area field test. Transp Res Part C Emerg Technol 18(2):225–233
10. Wang H, He W (2011) A reservation-based smart parking system. In: IEEE conference on computer communications workshops. <https://doi.org/10.1109/infcomw.2011.5928901>
11. Wei L et al (2012) Design & implementation of smart parking management system based on RFID & internet. In: International conference on control engineering & communication technology. <https://doi.org/10.1109/icect.2012.12>
12. Khan S et al (2019) A smart intruder alert system based on microprocessor and motion detection. In: International conference on robotics, electrical and signal processing techniques (ICREST). <https://doi.org/10.1109/icrest.2019.8644109>
13. Barno M et al (2019) An android subjugated compact self-driving semi-autonomous vehicle. In: IEEE region 10 symposium (TENSYMP). <https://doi.org/10.1109/tensymp46218.2019.8971224>

Implementation of Perturbation-Based MPPT Technique Using Model-Based Design



Sachin Angadi^{ID}, Udaykumar R. Yaragatti^{ID}, Yellasiri Suresh^{ID}, and A. B. Raju^{ID}

Abstract Maximum Power Point Tracking (MPPT) algorithms are imperative in solar Photovoltaic (PV) systems. This paper presents a simple approach for real-time implementation of perturbation-based MPPT algorithms employing model-based design (MBD) and Rapid Control Prototyping (RCP). To validate the proposed approach, classic Perturb and Observe (P&O) algorithm is tested. Altair's Embed software and low-cost Texas Instruments (TI) DSP controller is used for implementation. All the fundamental blocks required for the implementation of perturbation-based MPPT algorithms are discussed in detail. Hardware-in-Loop (HIL) simulation using Altair Embed for selection of appropriate sampling time and perturbation step size is demonstrated. The readers will also be presented with details of fundamental fixed point blocks of Altair Embed software for the implementation of other MPPT algorithms using low-cost controllers.

Keywords MPPT · Model-based design · Perturb and observe · Rapid control prototyping · Solar PV system

1 Introduction

The need for energy is continuously increasing owing to the lifestyle of the millennium and growing population. Exploring an alternative source of energy is the urgent demand of the hour for a sustainable future. The solar PV source is seen as one of the potential alternatives to meet the gap between energy demand and generation. India is bestowed with solar radiation capable of generating 5000 trillion kWh/year [1].

Several papers have discussed various MPPT algorithms with the aid of simulation results; however, developing code for a digital computer is still a challenge for many core engineers. MBD, a new approach for embedded development, is fast

S. Angadi (✉) · A. B. Raju
KLE Technological University, Hubballi, India
e-mail: sachin@kletech.ac.in

U. R. Yaragatti · Y. Suresh
National Institute of Technology Karnataka, Surathkal, Surathkal, India

emerging as alternative for code development. MBD is a model-centric approach to the development of controls for a dynamic system. It facilitates system-level design, RCP, automatic code generation and accelerated testing and verification [2]. Given preliminary simulation studies and design specifications, RCP and HIL testing can be performed on the system under test. If the simulation studies reveal substantial details about the system, then the model can be directly used for production code generation [3].

The rapid growth in MBD and rapid prototyping technology over the last few decades has motivated core designers to adapt MBD to develop code for their algorithms. Also, new MBD platforms like dSPACE, OPAL-RT are fast emerging to promote MBD and RCP to reduce the time for product development. MBD requires a hardware platform and dedicated software for performing necessary functions. The work of selected research articles using MBD for power electronics and MPPT is consolidated in Table 1. MATLAB-Simulink with embedded coder toolbox is the most commonly used host PC software with a wide variety of supporting hardware platforms like OPAL-RT, FPGA, DSP and microcontroller [4–10]. Few researchers have also explored LabVIEW for the implementation of MPPT algorithms using different compatible hardware platforms [11–13]. It is to be noted that backend software compatible with the chosen hardware platform is required to compile c-code generated by the embedded coder. In addition to automatic code generation, both MATLAB-Simulink and LabVIEW facilitate HIL simulation. However, only LabVIEW supports interactive HIL simulation. The development using LabVIEW is not viable for commercial application as the code generation is not available for low-cost microcontrollers.

Applications like MPPT requires real-time tuning of parameters like sampling time and perturbation step size for optimal performance. This paper presents a simple approach for RCP of perturbation-based MPPT algorithms. The proposed method uses a Altair Embed software, TI TMS320F28027 controller and Code Composer

Table 1 Summary of software and hardware platform used for embedded controller development employing MBD

References	Host PC software	Hardware platform	Backend software	Application
[4]	MATLAB-Simulink	FPGA	HDL	Inverter
[5]	MATLAB-Simulink	TMS320F28335	CC studio	Power electronics
[6]	MATLAB-Simulink	Spartan 3E (FPGA)	Xilinx	P&O (MPPT)
[7]	MATLAB-Simulink	STM32F4 board	ST-LINK	MPPT
[8]	MATLAB-Simulink	OPAL-RT OP4500	RT-Lab	Solar PV system
[9]	MATLAB-Simulink	STM32F429 board	ST-LINK	MPPT
[10]	MATLAB-Simulink	Arduino MEGA	–	Fuzzy MPPT
[11]	LabVIEW	MyRIO	–	Fuzzy MPPT
[12]	LabVIEW	cRIO-9075 kit	–	P&O (MPPT)
[13]	LabVIEW	NIcDAQ-9178	–	MPPT

Studio for the execution of MBD, automatic ‘C’-code generation and interactive HIL simulation for controller tuning and development. Blocks like PWM, ADC, unit delay, sample and hold, and digital filter required for the implementation of classic perturbation algorithms are discussed in detail. Further, the interactive HIL simulation feature of Altair Embed is explored to demonstrate live tuning of sample time and perturbation step size for optimal performance of MPPT algorithm.

2 Model-Based Design Framework

In this section, the system considered for the test using MBD is discussed. Also, the framework of the MBD using Altair Embed for ‘C’-code generation, interactive HIL simulation and data acquisition and monitoring is presented in detail.

2.1 System Description

The details of system implementation are shown in Fig. 1. The system consists of the solar PV source, DC-DC boost converter feeding resistive load, a TI TMS320F28027 controller and Altair Embed software. The communication link is established between the host computer and the controller using JTAG link at the rate of 100 Hz

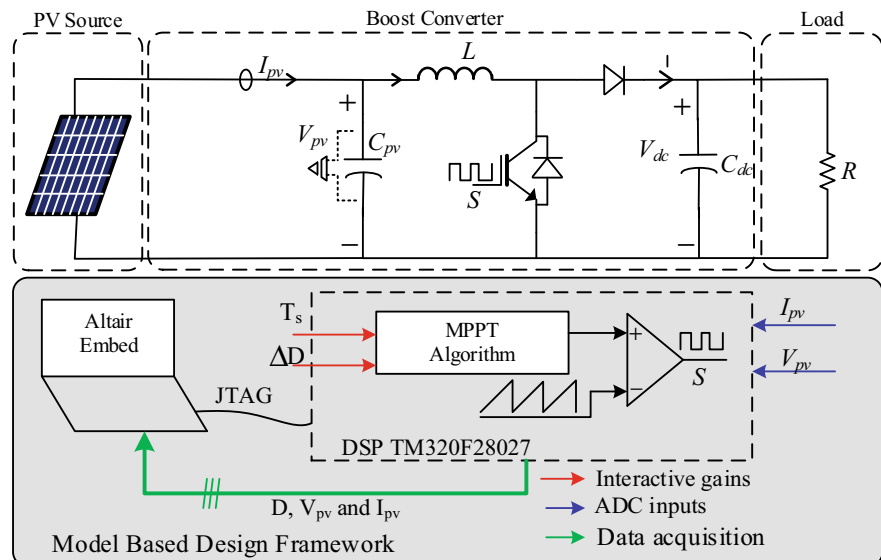


Fig. 1 Block diagram representation of the system under test

to facilitate RCP. System variables namely PV voltage (V_{pv}) and current (I_{pv}) are sensed and instantaneous power is calculated. The MPPT algorithm is processed to generate appropriate duty ratio (D) to ensure maximum power extraction from solar PV source.

2.2 MBD Using Altair Embed

The framework of MBD for controller design using Altair Embed is shown in Fig. 2. The MBD software and the backend software (Code Composer Studio) are installed on Host PC. A communication link is established between the target hardware (TMS320F28027) and Altair Embed using the JTAG communication protocol. The controller design and specifications are finalized before deployment using preliminary simulation studies. The MBD approach for controller design using Altair Embed involves following steps:

1. The designed controller is drawn as model using fixed point blocks in Altair Embed and is checked for logical, syntax error or any overflows.
2. The Altair Embed tool generates the c-code compatible with chosen target hardware.
3. The generated c-code is compiled using Code Composer Studio to generate .out file.
4. The .out file can either be used for interactive HIL simulation or can be burnt into flash of the target hardware for final deployment.

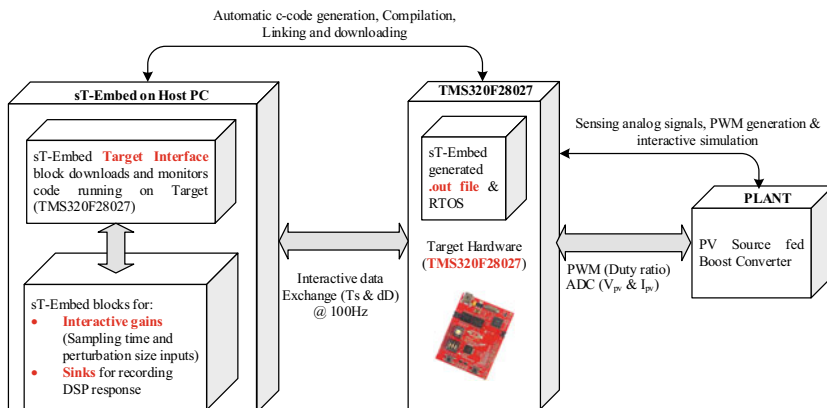


Fig. 2 Model based design framework for rapid prototyping with interacting HIL simulation

3 Rapid Control Prototyping

The classic P&O algorithm is presented in this section along with its Simulink and fixed point Altair Embed implementation. Also, the interactive HIL simulation using Altair Embed and TMS320F28027 is discussed in this section.

3.1 Perturbation-Based MPPT Techniques

Figure 3 shows the implantation details of P&O algorithm for Boost DC-DC converter. Direct duty ratio implementation is chosen for improved stability [14]. The Simulink implementation of the algorithm reveals the requirement of sample and hold, multiplier, unit delay, sign detector and saturation blocks for implementation of the algorithm. All the aforementioned blocks are available in fixed point block-set of Embed tool for implementation of the algorithm. The implementation of the model using fixed point blocks facilitates code generation for fixed point DSP/microcontrollers and reduced the memory utilization of the controller. The fixed

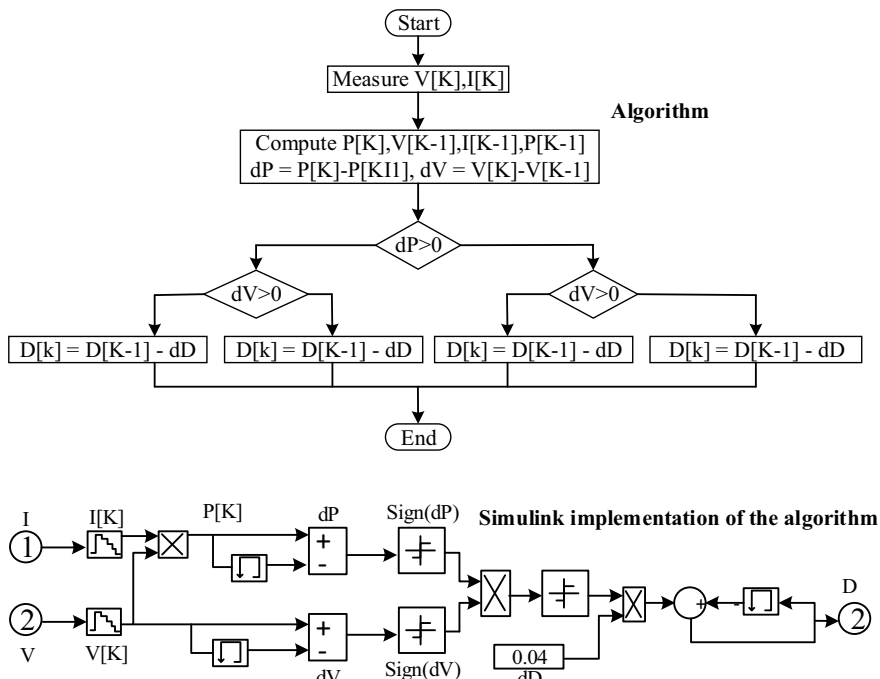


Fig. 3 Direct duty ratio based P&O algorithm and its Simulink implementation

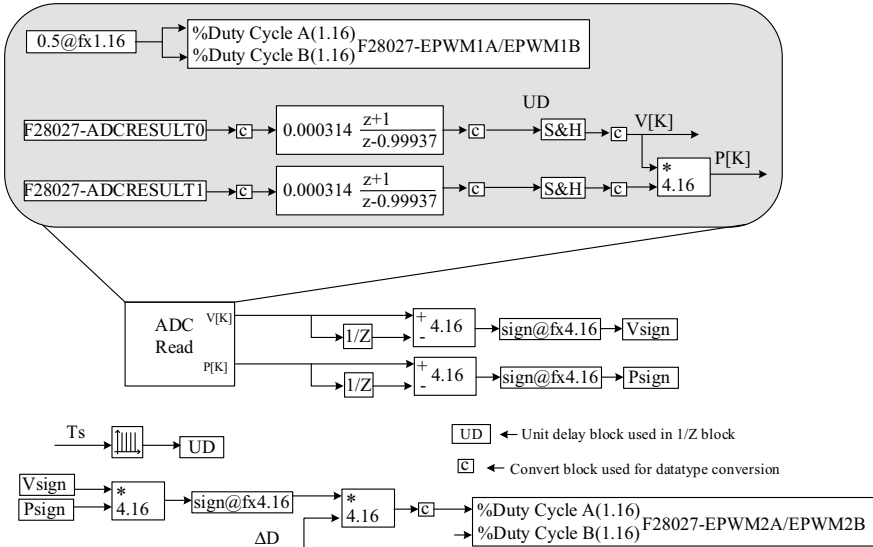


Fig. 4 Model based implementation of P&O algorithm using Altair Embed for TMS320F28027

point model developed using Altair Embed tool for TMS320F28027 is as shown in Fig. 4.

3.2 Hardware-in-Loop Simulation for RCP

Altair Embed is a user-friendly tool for developing embedded systems. It automatically generates a ANCI ‘C’-code compatible with the low-cost controller [15]. In addition to the code generation, interactive HIL simulation facilitates live parameter tuning and real-time data monitoring without data acquisition system. The software supports wide variety of low-cost controllers [16]. TI TMS320F28027 controller is chosen for study in this paper.

Figure 5 shows two files namely source file and the debug file. The source file consists of the detailed block-level implementation of the algorithm shown in Fig. 4. The source file is designed to facilitate interactive HIL simulation with real-time live

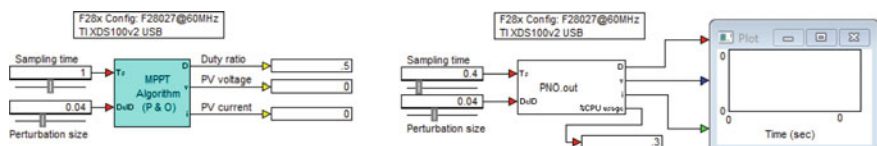


Fig. 5 Interactive HIL simulation setup in Altair Embed using TMS320F28027

data monitoring. The T_s and ΔD are chosen as two interactive inputs while D , V_{pv} and I_{pv} acquired in real-time for data monitoring. The ANCI ‘C’-code is generated using source file and compiled at the backend using Code Composer Studio software to generate an executable .out file. A separate debug file is created consisting of target interface block, interactive gains and display units for real-time data monitoring. The debug file allows execution of the .out in real-time and displays the selected data for monitoring in real-time at the rate of 100 Hz. The value of interactive gains can be changed using the slider and the impact of the gains on the system under test is monitored in the display units connected to the output of the debug file.

4 Results and Discussions

The details of the laboratory prototype developed for conceptual verification are discussed in this section. Also, the experimental results of the interactive HIL simulation studies are presented in detail to highlight the significance of the MBD approach and RCP in the implementation of the MPPT algorithms. Further, the pointers are given to the readers for the implementation of the other perturbation-based MPPT techniques.

4.1 Experimental Setup

The laboratory prototype developed for conceptual validation is shown in Fig. 6. The setup consists of a 1.5 kW Magna solar emulator, boost converter feeding a resistive

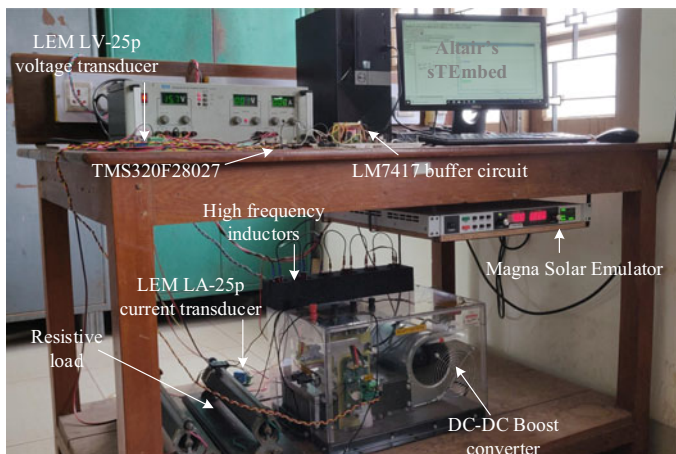


Fig. 6 Snapshot of laboratory prototype developed for conceptual validation

load, hall effect-based current and voltage sensors, TMS320F28027 controller and host PC with Altair Embed for HIL simulation. The PV current and voltage are sensed using LEM sensors and inbuilt ADC module of TMS320F28027 for processing of MPPT algorithm. The PV current, voltage and duty ratio are acquired using the Embed tool employing HIL simulation.

4.2 Results

Figure 7 shows the results obtained during the appropriate selection of T_s . Initially, the value of $T_s = 1$ s larger than system time constant is selected to obtain stable three-step output for the duty ratio around the maximum power point. Larger T_s increases the system response time, hence the value of T_s is reduced in steps of 0.1. It is observed that, stable output for the algorithm persists only up to value of T_s

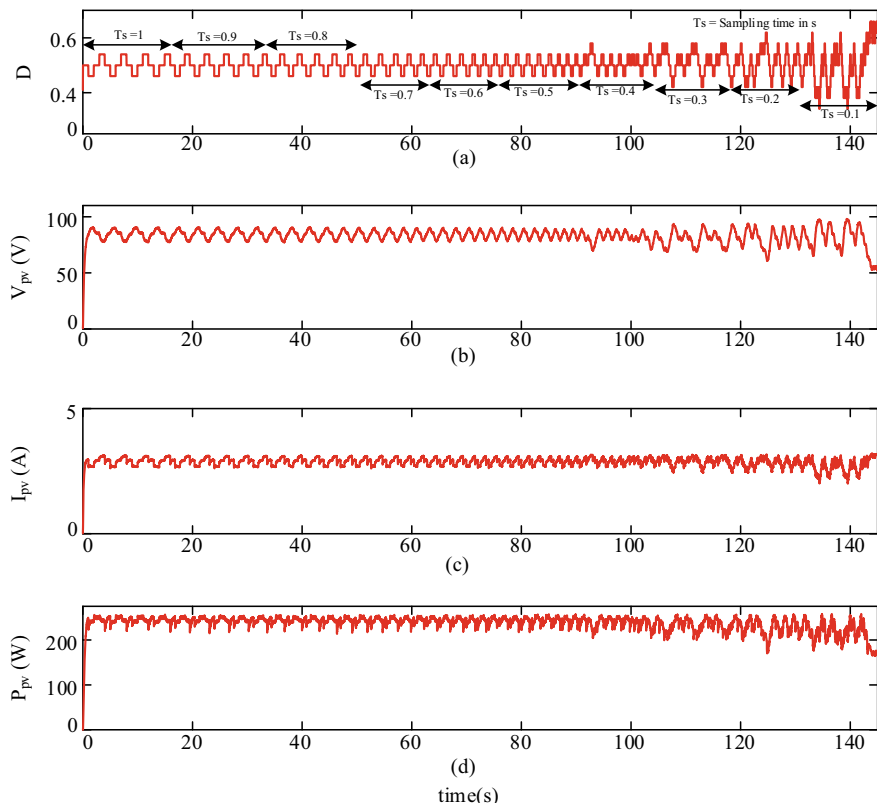


Fig. 7 Experimental results of **a** duty ratio (D), **b** PV voltage (V_{pv}), **c** PV current (I_{pv}) and **d** PV power (P_{pv}) for varying sampling time (1–0.1 s)

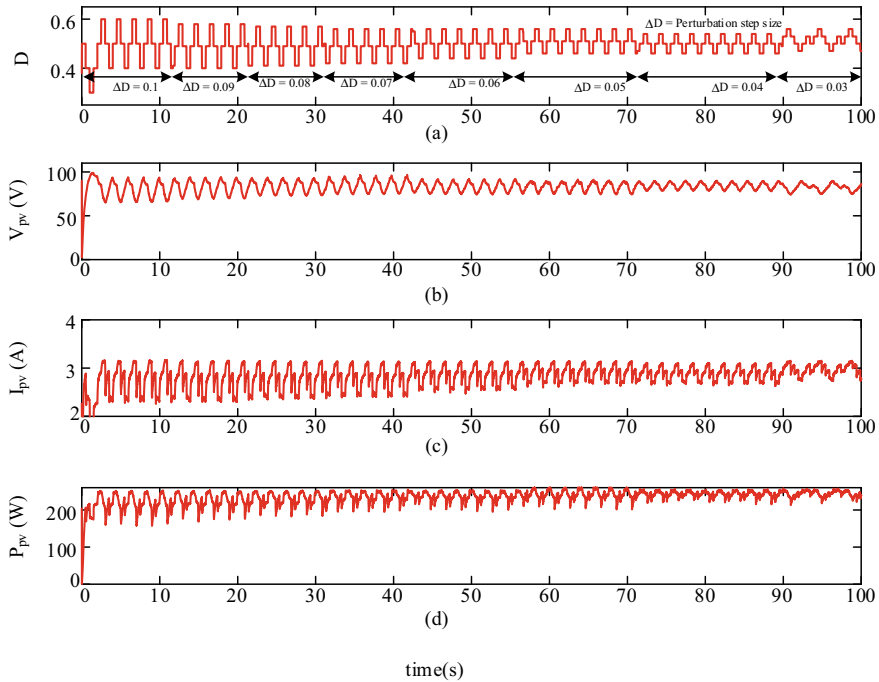


Fig. 8 Experimental results of **a** duty ratio (D), **b** PV voltage (V_{pv}), **c** PV current (I_{pv}) and **d** PV power (P_{pv}) for varying perturbation step (0.1–0.03)

$= 0.5$. The D , V_{pv} , I_{pv} start to exhibit larger perturbations leading to instability for value of $T_s < 0.5$ s.

The value of T_s is chosen to be 0.5 s for the system under test. Another parameter, which mainly decides the efficiency of the P&O algorithm, is the ΔD . Figure 8 captures the response of the system for different values of ΔD . Initially, the value of ΔD is chosen as 0.1. Further, the value of ΔD is reduced in steps of 0.01 and the response is captured in Fig. 8. For larger values of ΔD , the perturbations in V_{pv} and I_{pv} are larger leading to reduced power utilization. It is observed that the system exhibits a stable three-step waveform for the value of $\Delta D = 0.04$, beyond which the system tends to move towards instability, exhibiting random perturbations.

The values of two significant parameters of the P&O algorithm namely T_s and ΔD are chosen with the aid of interactive HIL simulation. For these optimal parameter values ($T_s = 0.5$ s and $\Delta D = 0.04$), the response of the system for the varying load is captured in Fig. 9. The system exhibits satisfactory performance for three different values of the load hence proving the validity of the controller and chosen parameter values.

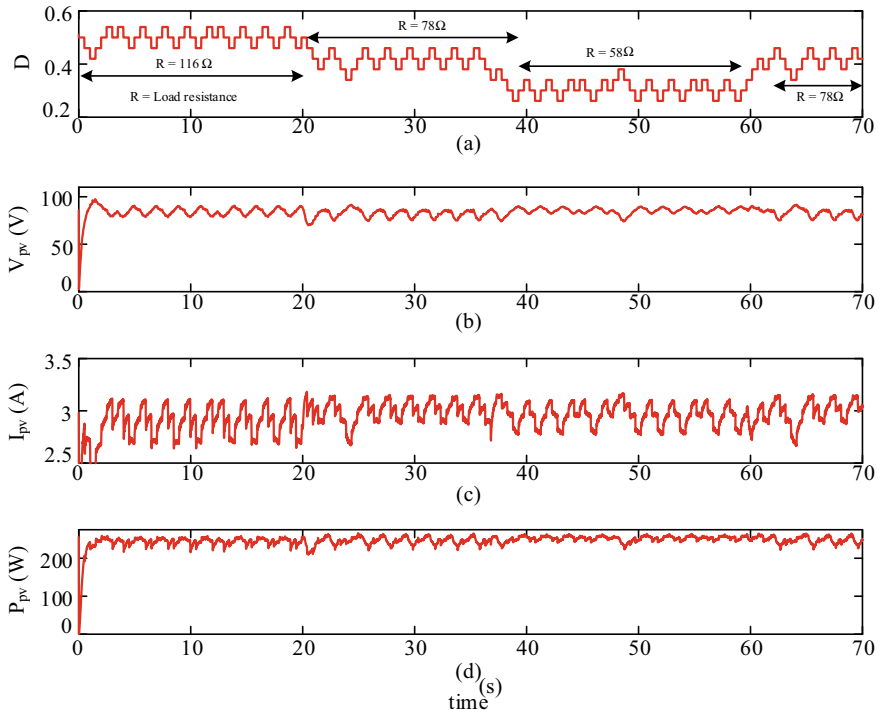


Fig. 9 Experimental results of **a** duty ratio (D), **b** PV voltage (V_{pv}), **c** PV current (I_{pv}) and **d** PV power (P_{pv}) for varying load resistor

4.3 Scope of the Study

In this paper, detailed implementation of the classic P&O algorithm for low-cost controller is presented in detail using Altair Embed. Block-level requirement and its fixed point implementation is conferred to the readers. The study can be further extended to other perturbation-based MPPT algorithms with minimal modifications [17–21]. Also, the impact of various parameters influencing the performance of the algorithm can be easily analysed using the concept of interactive HIL simulation.

5 Conclusions

This paper has presented a simple approach for real-time implementation of the P&O algorithm for low-cost controller TMS320F2027 using the concept of MBD and RCP. The usage of the Altair Embed tool for MBD, RCP and HIL simulation with interactive gains have been presented in detail. Results of the laboratory

prototype have been presented with the live tuning of sampling time and perturbation step size, demonstrating the significance of interactive gains for RCP. Sufficient details of fundamental fixed point blocks have been discussed for implementation of other perturbation-based MPPT algorithms with minimal modifications to the model discussed in this paper.

Acknowledgements Authors would like to thank KLE Technological University, Hubli—580031, Karnataka (INDIA) for funding this research project under Capacity Building Project (CBP-2019) scheme.

References

1. MNRE (2020) Solar energy systems. <https://mnre.gov.in/solarsystems>. Accessed 04 Jan 2020
2. Pulle DW, Darnell P, Veltman A (2015) Applied control of electrical drives. Springer
3. Roger A (2015) Managing model-based design. The MathWorks, Inc
4. Siwakoti YP, Town GE (2013) Design of FPGA-controlled power electronics and drives using MATLAB-Simulink. In: 2013 IEEE ECCE Asia Downunder. IEEE, pp 571–577
5. Dos Santos B, Araujo RE, Varajao D, Pinto C (2013) Rapid prototyping framework for realtime control of power electronic converters using Simulink. In: IECON 2013-39th annual conference of the IEEE industrial electronics society. IEEE, pp 2303–2308
6. Selvamuthukumaran R, Gupta R (2014) Rapid prototyping of power electronics converters for photovoltaic system application using Xilinx system generator. IET Power Electron 7(9):2269–2278
7. Motahhir S, El Ghzizal A, Sebti S, Derouich A (2017) MIL and SIL and PIL tests for MPPT algorithm. Cogent Eng 4(1):1378475
8. Jiang Z, Konstantinou G, Zhong Z, Acuna P (2017) Real-time digital simulation based laboratory test-bench development for research and education on solar PV systems. In: 2017 Australasian universities power engineering conference (AUPEC). IEEE, pp 1–6
9. Cheddadi Y, Errahimi F, Es-sbai N (2018) Design and verification of photovoltaic MPPT algorithm as an automotive-based embedded software. Sol Energy 171:414–425
10. Fannakh M, Elhafyani ML, Zouggar S (2018) Hardware implementation of the fuzzy logic MPPT in an Arduino card using a Simulink support package for PV application. IET Renew Power Gener 13(3):510–518
11. Bayrak G, Ghaderi D (2019) An improved step-up converter with a developed real-time fuzzy based MPPT controller for PV-based residential applications. Int Trans Electr Energy Syst
12. Roy S (2017) Hardware based real time implementation of perturb and observe algorithm in LabVIEW via cRIO-9075 interface. In: 2017 14th IEEE India council international conference (INDICON). IEEE, pp 1–6
13. Jeyapraba SB, Selvakumar AI (2017) Model-based MPPT for shaded and mismatched modules of photovoltaic farm. IEEE Trans Sustain Energy 8(4):1763–1771
14. Elgendi MA, Zahawi B, Atkinson DJ (2011) Assessment of perturb and observe MPPT algorithm implementation techniques for PV pumping applications. IEEE Trans Sustain Energy 3(1):21–33
15. Altair (2020) Altair Embed: visual environment for embedded systems. <https://solidthinking.com/product/embed/>. Accessed 03 Jan 2020
16. Altair (2020) Target hardware support for Altair EmbedTM: TI: F28x, MSP430, ARM Cortex M3 Arduino: Atmel ST Micro: STM32F3. <https://solidthinking.com/white-paper.aspx?id=8931>. Accessed 03 Jan 2020

17. Alik R, Jusoh A (2017) Modified perturb and observe (P&O) with checking algorithm under various solar irradiation. *Sol Energy* 148:128–139
18. Elgendi MA, Zahawi B, Atkinson DJ (2012) Assessment of the incremental conductance maximum power point tracking algorithm. *IEEE Trans Sustain Energy* 4(1):108–117
19. Killi M, Samanta S (2015) Modified perturb and observe MPPT algorithm for drift avoidance in photovoltaic systems. *IEEE Trans Ind Electron* 62(9):5549–5559
20. Killi M, Samanta S (2015) An adaptive voltage-sensor-based MPPT for photovoltaic systems with SEPIC converter including steady-state and drift analysis. *IEEE Trans Ind Electron* 62(12):7609–7619
21. Killi M, Samanta S (2018) Voltage-sensor-based MPPT for stand-alone PV systems through voltage reference control. *IEEE J Emerg Sel Top Power Electron* 7(2):1399–1407

QRS Complex Detection Algorithm for Wearable Devices



Lalita Gupta

Abstract Electrocardiography (ECG) is one of the best ways to obtain health information and monitor heart activity. QRS complex which is present in ECG is captured from the wearable devices consisting of sensors. Determination of QRS complex is crucial to understand the proper condition and functioning of the heart. Various QRS complex detection techniques are presented so far based on multiple transforms and designed filters. This paper presents an algorithm based on filtering and averaging methods which is able to deliver sensitivity and positive prediction of 99.84% and 99.52%, respectively. The error prediction (DER) is found to be 0.65%. This method is efficient in time when tested using MIT/BIH arrhythmia database.

Keywords Biometrics · ECG · QRS complex · Wearable sensors

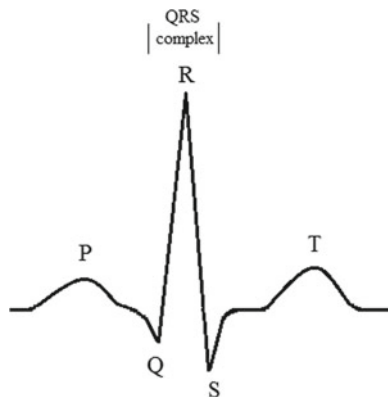
1 Introduction

The research in the field of electrocardiogram (ECG) signal applications for wearable devices has increased tremendously. Tiny electrical changes are observed on the surface of the skin which arises due to the electrical activity of the heart. These changes are recorded over a period of time by placing electrodes on the skin. These signals are collected with the help of wearable sensors, which are gaining popularity in biomedical science as bio-signal monitoring systems [1, 2]. Biometrics refers to the physiological and biological characteristics which are unique for each individual which can be used for their identification. ECG is the display of these recorded signals that helps in determining the present biological condition of heart. Analyzing the ECG signal is based on detecting the QRS complex (Fig. 1). The detection of QRS complex has been creating wide interest in the research field [3]. Computational efficiency and accuracy of the technique have been a major concern for the researchers over the past few years. As the ECG signal is collected from the patient, it gets contaminated by the presence of various noises which are basically other electrical signals arising due to

L. Gupta (✉)

Department of Electronics and Communications Engineering, Maulana Azad National Institute of Technology, Bhopal, Madhya Pradesh, India
e-mail: lalitagupta@manit.ac.in

Fig. 1 Components of ECG signal



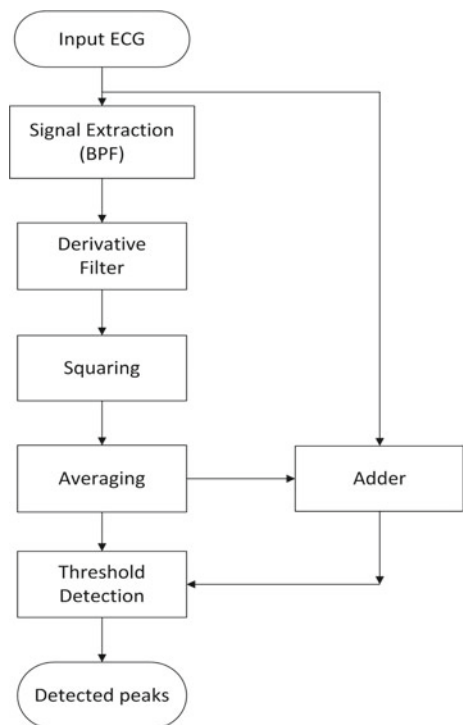
different activities or surroundings [4]. These noises can be classified predominantly as the electromyographic interference (EMG), baseline wander noise, and the power line interference.

The QRS complex significantly contains energy of frequency range of 3–40 Hz and even more for the Q, R, and S waves having sharp morphologies. The significant energy components present in the P wave and T wave start from 0.5 Hz and not more than 10 Hz. Power line interference is nothing but the harmonics of the 50 Hz power supply. However, baseline wandering and motion artifacts have low frequencies which range between 0.5 and 7 Hz. The ECG signal components get overlapped in this frequency range. Several algorithms have been presented which are based on Hilbert transform, wavelet transform [5], derivative filters [6], neural networks, digital filtering, and heuristic approaches which are based on nonlinear transformation [7–11]. Accuracy of these algorithms varies due to presence of all these noises. Besides accuracy and efficiency, computational complexity is a major concern for designing any algorithm. The most popular and primitive algorithm is given by Pan and Tompkins [12]. Similar method is proposed by Afonso et al. [13] and Hamilton et al. [14]. However, these algorithms were too complex to provide good battery efficiency in wearable devices. A novel dual slope QRS detection algorithm is proposed by Wang et al. which utilizes the fact that the largest slope in the ECG signal is found in the QRS complex (R peak) [15]. This method provides less complexity and high accuracy. However, the same can be achieved by the conventional method of successive filtering and processing the signal. This paper presents an algorithm which is able to reduce time complexity as well as give better battery performance with accurate results when applied for the MIT-BIH arrhythmia database.

2 Methodology

ECG is a quasi-periodic signal which is composed of heartbeats that has three main components: the P wave, the QRS complex, and the T wave. P wave is associated with the right and left atrial depolarization. The QRS complex has a series of three deflections that depicts the right and left ventricular depolarization, where conventionally the first negative deflection in the complex is Q wave. R wave is the following positive deflection, and a negative deflection after the R wave is called the S wave. The T wave denotes the repolarization (recovery) of ventricles, and its position depends on the heart rate of the person. This sequence of waves typically lasts for about 0.6–1 s. The morphology of the signal plays an important role, as the steepness, shape, and height of the signal are used as criteria to detect QRS complex according to the algorithm proposed by Wang et al. in [15]. The proposed algorithm is described briefly by the flowchart in Fig. 2 and is discussed as follows.

Fig. 2 Flowchart of the proposed algorithm



2.1 ECG Signal Extraction

An ECG signal energy lies between 5 and 12 Hz. Designing a band pass filter of given range increases complexity. So, the signal is passed through a band pass filter which consists of cascaded low pass and high pass filters. The lower cutoff frequency of the filter is kept 5 Hz, whereas higher cutoff frequency is 11 Hz with similar gains of both high pass and low pass filters. The transfer function of high pass and low pass filter is given by (1) and (2), respectively.

$$H_1(z) = z^{-16} - \frac{(1 - z^{-32})}{(1 - z^{-1})} \quad (1)$$

$$H_2(z) = \frac{(1 - z^{-6})^2}{(1 - z^{-1})^2} \quad (2)$$

2.2 Derivative Filter

The band pass filtered signal is then passed through the derivative filter to get the slope information of the QRS complex. The maximum slope in the ECG signal is found in the QRS complex only since the P and T waves do not possess such high peaks. The transfer function of the derivative filter used here is given by the following equation.

$$H_3(z) = \frac{1}{8}(-z^{-2} - 2z^{-1} + 2z + z^2) \quad (3)$$

It is a five point derivative which provides linear frequency response from DC to 30 Hz, which is favorable for the ECG signal.

2.3 Squaring Function

Squaring operation makes all the data points of the signal positive and gives a higher value for the R peaks since the slopes of P and T waves are small. The output of the derivative filter is nonlinearly amplified which emphasizes the higher frequencies. The squaring operation is performed by the following equation.

$$x_s(nT) = [x_d(nT)]^2 \quad (4)$$

2.4 Averaging and Threshold Detection

To detect peaks, a threshold value is required which is calculated on the basis of the signal received after averaging of the squared signal. The squared signal undergoes moving window integration to obtain the average value. An additional block adder adds this signal with the original signal. The threshold value is determined as the mean of the integrated signal after averaging and is applied on the output signal from the adder. The peaks exceeding the threshold value are considered as R peaks and are used in the calculation of accuracy, positive prediction sensitivity, and detection error.

3 Results and Discussion

The proposed algorithm is implemented in MATLAB using the MIT-BIH arrhythmia database. The database contains 48 half hour recordings of different patients for total 24 h of ECG data. These recordings have sampling rate of 360 Hz and have 11 bit resolution over 10 mV [16, 17].

The calculation of FP and FN helps to evaluate the false detection rate. FP is false detection of peaks, and FN is the count of those peaks whose detection has failed. TP stands for true positive which refers to the correct detection of peaks. All these parameters are used to calculate sensitivity (Se), positive prediction (+P), and detection error rate (DER) using the following equations (Fig. 3 and Tables 1 and 2).

$$\text{Se} (\%) = \frac{\text{TP}}{\text{TP} + \text{FN}} \quad (5)$$

$$+P(\%) = \frac{\text{TP}}{\text{TP} + \text{FP}} \quad (6)$$

$$\text{DER} = \frac{\text{FP} + \text{FN}}{\text{Total QRS}} \quad (7)$$

4 Conclusion

The algorithm presented in this paper gives faster results and better performance in terms of accuracy and sensitivity. The algorithm is able to extract the ECG signal from its accompanied noise signals. Hence, the processing of the ECG signal is done precisely, and truthful results are obtained. The application of ECG signal morphology can be extended for biometric application using feature extraction. The

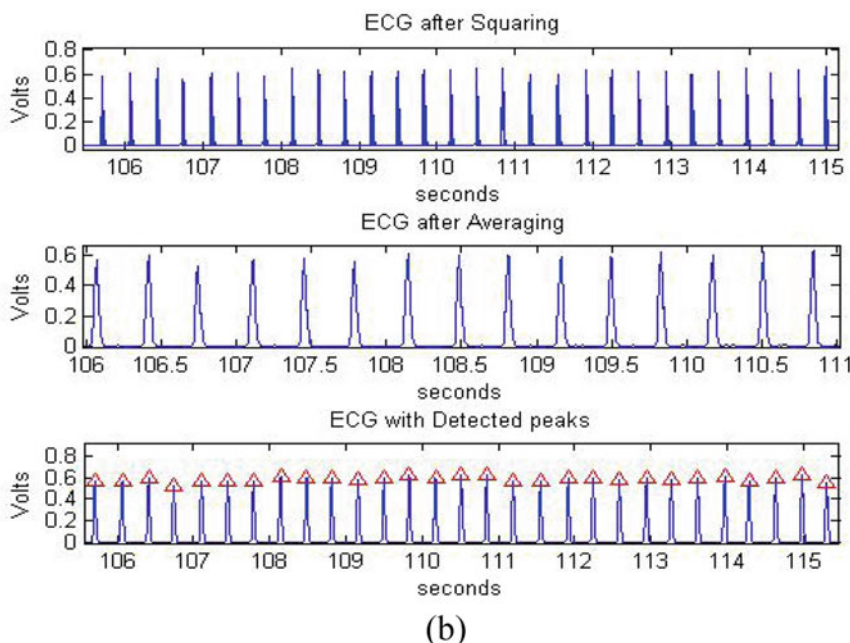
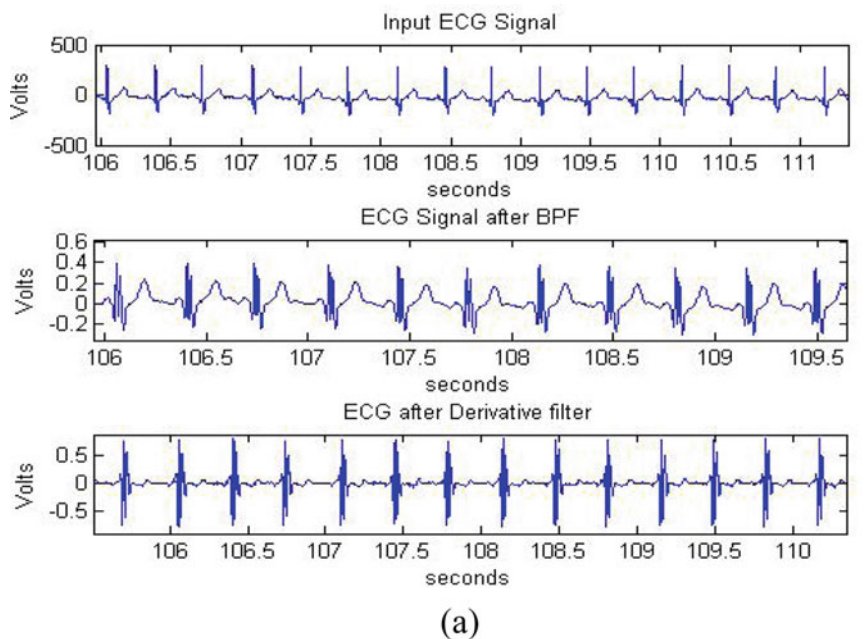


Fig. 3 Steps involved in QRS detection of tape 231 of MIT-BIH database

Table 1 Evaluation of implementation results of proposed algorithm

Tape No.	Total beats	FP	FN	Time (sec)	Se (%)	+P (%)	DER (%)
100	2273	3	3	2.03	99.87	99.87	0.26
101	1865	6	1	2.19	99.95	99.68	0.38
102	2187	0	3	2.43	99.86	100	0.14
103	2084	1	2	2.37	99.90	99.95	0.14
104	2229	59	2	2.67	99.91	97.42	2.74
105	2572	29	9	2.62	99.65	98.88	1.48
106	2027	7	2	2.19	99.90	99.66	0.44
107	2137	9	0	2.3	100	99.58	0.42
108	1774	123	33	2.12	98.14	93.40	8.79
109	2532	12	0	2.21	100	99.53	0.47
111	2124	3	0	2.51	100	99.86	0.14
112	2539	3	1	2.31	99.96	99.88	0.16
113	1795	1	2	2.26	99.89	99.94	0.17
114	1879	37	17	2.54	99.10	98.05	2.87
115	1953	1	1	2.17	99.95	99.95	0.10
116	2412	31	34	2.36	98.59	98.71	2.69
117	1535	5	1	2.37	99.93	99.68	0.39
118	2278	2	0	2.47	100	99.91	0.09
119	1987	3	2	2.15	99.90	99.85	0.25
121	1863	3	0	2.13	100	99.84	0.16
122	2476	1	0	2.15	100	99.96	0.04
123	1518	4	4	2.32	99.74	99.74	0.53
124	1619	3	0	2.41	100	99.82	0.19
200	2601	10	2	2.36	99.92	99.62	0.46
201	1963	6	2	2.51	99.90	99.69	0.41
202	2136	1	0	2.51	100	99.95	0.05
203	2980	86	2	2.63	99.93	97.19	2.95
205	2656	2	7	2.43	99.74	99.92	0.34
207	1862	0	0	2.65	100	100	0.00
208	2955	35	9	2.68	99.70	98.83	1.49
209	3004	7	3	2.37	99.90	99.77	0.33
210	2650	4	0	2.12	100	99.85	0.15
212	2748	2	0	2.33	100	99.93	0.07
213	3251	1	2	2.36	99.94	99.97	0.09
214	2265	1	0	2.47	100	99.96	0.04
215	3363	2	0	2.51	100	99.94	0.06

(continued)

Table 1 (continued)

Tape No.	Total beats	FP	FN	Time (sec)	Se (%)	+P (%)	DER (%)
217	2209	4	2	2.66	99.91	99.82	0.27
219	2154	2	3	2.64	99.86	99.91	0.23
220	2048	1	1	2.64	99.95	99.95	0.10
221	2427	2	0	2.35	100	99.92	0.08
222	2483	2	0	2.17	100	99.92	0.08
223	2605	2	4	2.13	99.85	99.92	0.23
228	2053	2	0	2.35	100	99.90	0.10
230	2256	2	0	2.14	100	99.91	0.09
231	1571	2	2	2.34	99.87	99.87	0.25
232	1780	2	0	2.33	100	99.89	0.11
233	3079	0	2	2.14	99.94	100	0.06
234	2273	0	3	2.11	99.89	100	0.11
Total	109,510	524	161	2.36	99.84	99.52	0.65

Table 2 Comparison of different methods for QRS detection

Methods	FP	FN	Se (%)	+P (%)	DER	References
BPF/search back	248	529	99.61	99.51	0.96	[12]
Filter banks	406	374	99.6	99.45	0.71	[13]
Dual slope	405	199	99.82	99.63	0.55	[15]
Multiscale morphology	213	204	99.81	99.80	0.39	[7]
Proposed method	524	161	99.84	99.52	0.65	–

implementation of a modified version of this algorithm along with hardware interface can enhance the automatic detection of cardiac diseases.

References

- Wahabi S, Pouryayevali S, Hari S, Hatzinakos D (November, 2014) On evaluating ECG biometric systems: Session-dependence and body posture. *IEEE Trans Inf Forensic Secur* 9(11)
- Rachim VP, Chung WY (December, 2016) Wearable noncontact armband for mobile ECG monitoring system. *IEEE Trans Biomed Circuits Syst* 10(6)
- Kohler BU, Hennig C, Orglmeister R (January–February, 2002) The principles of software QRS detection. *IEEE Eng Med Biol Mag* 21(1):42–57
- Tomasini M, Benatti S, Milosevic B, Farella E, Benini L (May, 2016) Power line interference removal for high-quality continuous biosignal monitoring with low-power wearable devices. *IEEE Sensors J* 16(10)
- Zhang F, Lian Y (2009) Wavelet and Hilbert transforms based QRS complexes detection algorithm for wearable ECG devices in wireless body sensor networks. *IEEE*

6. Arzeno NM, Poon CS, Deng ZD (2006) Quantitative analysis of QRS detection algorithms based on the first derivative of the ECG. In: IEEE Proceedings of 28th EMBS Annual International Conference in New York City, USA (August 30–September 3)
7. Zhang F, Lian Y (August, 2009) QRS detection based on multiscale mathematical morphology for wearable ECG devices in body area network. *IEEE Trans Biomed Circuits Syst* 3(4)
8. Kohama T, Nakamura S, Hoshiso H (1999) Preprocessing MAMD and RSEF for R–R interval detection of ECG. *IEEE TENCON*
9. Phukpattaranont P (2015) QRS detection algorithm based on the quadratic filter. *Elsevier Expert Syst Appl* 42:4867–4877
10. Rufas DC, Carrabina J (2015) Simple real-time QRS detector with the MaMeMi filter. *Elsevier Biomed Signal Process Control* 21:137–145
11. Zhang F, Wei Y, Lian Y (June, 2008) Efficient QRS detection in wearable ECG devices for body sensor network. In: IEEE Proceedings of 5th international workshop on wearable and implantable body sensor networks, in conjunction with the 5th International summer school and symposium on medical devices and biosensors HKSAR
12. Pan J, Tompkins WJ (March, 1985) A real-time QRS detection algorithm. *IEEE Trans Biomed Eng BME-32(3):230–236*
13. Afonso VX, Tompkins WJ, Nguyen TQ, Luo S (1999) ECG beat detection using filter banks. *IEEE Trans Biomed Eng* 46:192–202
14. Hamilton PS, Tompkins WJ (December, 1986) Quantitative investigation of QRS detection rules, using the MIT/BIH arrhythmia database. *IEEE Trans Biomed Eng BME-33(12)*
15. Wang Y, Deepu CJ, Lian Y (2011) A computationally efficient QRS detection algorithm for wearable ECG sensors. In: IEEE 33rd Annual International Conference EMBS Boston, Massachusetts USA (August 30–September 3)
16. Arefin MR, Tavakolian K, Rezai RF (2015) QRS complex detection in ECG signal for wearable devices. *IEEE*
17. Arefin MR, Rezai RF (2014) Computationally efficient QRS detection analysis based on dual-slope method. *IEEE*

ORS: The Optimal Routing Solution for Smart City Users



K. Krishna Rani Samal, Korra Sathyababu, and Santos Kumar Das

Abstract Road transport-related air pollution is one of the critical issues for most of the developing countries as the emission of air pollution during transportation causes severe physical and psychological health problems. Hence, the identification of pollution-free route is the most critical aspect in the case of air pollution management for smart city users. This research paper proposes an optimal routing solution algorithm (ORS) approach that predicts the pollutant value for the road network and includes a weight assignment function to measure the safety level of each route to build a developed transportation system for smart city users. The proposed method experimented with both geostatistical and non-geostatistical algorithm to predict the SPM pollutant level in each route. Each approach is evaluated to compute the weight function to determine the optimized routing solutions. The streamlined routing solution can be accessible by the developed Web applications to access the healthier path, which may not provide the shortest path every time but suggests a more robust route for smart city users.

Keywords Air pollution · Spatial analysis · Geostatistics · Transportation

1 Introduction

Road transportation is the oldest means of communication in India. In developing countries like India, it covers all the areas and facilitates to provide door to door services. Due to modernization, several ways have been developed to travel across

K. K. R. Samal (✉) · K. S. Babu

Department of Computer Science and Engineering, National Institute of Technology Rourkela,

Rourkela, Odisha 769008, India

e-mail: kkrani2009@gmail.com

K. S. Babu

e-mail: ksathyababu@nitrkl.ac.in

S. K. Das

Department of Electronics and Communication Engineering, National Institute of Technology Rourkela, Rourkela, Odisha 769008, India

e-mail: dassk@nitrkl.ac.in

roads. This modernization phenomenon has also brought several negative impacts on environments like the increasing level of air pollution due to overcrowded routes. These busy streets bring high risk to the general public, like adverse effects on the environment and human life. So, air pollution has become one of the most complicated environmental issues due to its negative impact on human health. The transportation system has become a severe issue in India, more specifically due to road congestion and the increasing level of pollution generated due to traffic congestion. Due to the high air pollution exposure, it is challenging to execute plans to develop a smart transportation system for smart city users as it causes severe health issues at nearby locations of toxic spots [1]. Therefore, there is a need to minimize traffic congestion that increases due to the high level of air pollution at highways. Hence, it is also essential to get notified of the air pollution level in routes, to prevent diseases and plan daily activities accordingly. Thus, transportation has become a basic challenging problem in everyday life of citizens in a smart city. This issue can be solved by spatial analysis of pollution levels at each location. As it is complicated to make the construction of roads for smart city users due to the limitation of resources and land use, it is better to enhance transportation quality by minimizing air pollution and its negative impacts.

Following the introduction, the rest is organized as follows. Section 2 represented state of the art, Sects. 3 and 4 include the proposed system model and results and discussion. Section 5 presents the conclusion and future work part of this research paper.

2 State of the Art for Routing Solutions

Zahmatkesh et al. [2] used air quality index as a standard to build urban travel route planning. The optimum route-finding based on the Dijkstra shortest path algorithm and AQI value. The author included a combination of both the parameters as a weight function to find the optimum path. Sharker et al. [3] also present a similar type of approach which differentiates the shortest route and the least air pollution exposure route in terms of distance, time, and air quality index. Determine the source of pollution level is also a crucial part of pollution management. Therefore, Briggs et al. [4] studied the causes of air pollution and proposed a regression-based approach for mapping traffic generated air pollution using spatial analysis techniques. Li et al. [5] also studied the source of increased levels of air pollution and its health impact during the different modes of transportation. The author suggested walking communication instead of motorcycles to minimize the pollution level. Vamshi et al. [6] attempted to reduce the pollution level by reducing its source of origin. He developed a framework based on Internet of things which distributes the traffic uniformly by providing diversion suggestion during peak traffic duration, and therefore, it reduces the traffic generated air pollution. Few types of research have been conducted to compute the real-time pollution value on each route. Ramos et al. [7] proposed a sensor network to identify the pollution level of each journey and provides all functionality that can

give the user all the facilities to trace the least polluted route among all possible ways.

Though all the existing work is made to alert citizens and focused on people's security, these applications are not user-friendly to access the analyzed information and also not able to compute global variations of air pollution to predict pollution level accurately. So, based on this study, the proposed work proposed a method to predict the pollutant value of each route more appropriately to find an optimal routing solution (ORS) for smart city users. The proposed system model is explained in the next section.

3 Proposed System Model

The proposed system model is a technology-based framework that consists of multiple components. Figure 1 represents the proposed framework consists of the geospatial data layer, data integration layer, geospatial analysis stage, and client application layer. Geospatial data layer includes data of air pollution monitoring stations, IoT-based devices. Data integration (DI) layer builds the data fusion model, which integrates study area coastline, natural, highway, administrative vector data, and IoT sensor device data. The geospatial analysis stage takes data fusion data as input and implements a geostatistical model to generate spatial interpolation maps. This stage provides map layer services that publish interpolation maps to the cloud server, where the navigation map will create a routing service based on the map service layer after the client application layer HTTP request. The client application

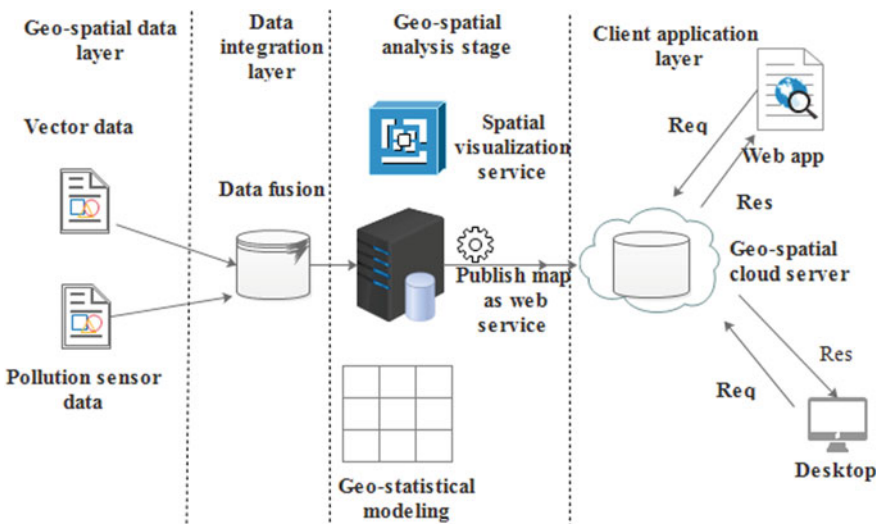


Fig. 1 Proposed system model

layer supports Web and desktop as a client to start request (Req)-response (Res) service with a cloud server to visualize the routing solution for a better decision.

Based on the system model, few things have been presented in the following subsection, such as study area, proposed spatial interpolation model, cross-validation, weight assignment, publish the map as a Web service.

3.1 Study Area

This study is carried out at Orissa (India). It extends between the latitudes (17.780 N and 22.730 N) and between longitudes (81.37 E and 87.53 E), which covers an area of 155,707 km². This state is in the northeastern part of India. A historical dataset of several pollution monitoring locations, collected from Odisha central pollution control board [8], is used to identify the spatial distribution of pollution levels across several geolocations of Odisha. Road networks also included in the base map during the spatial analysis of pollution over routes. During the study, it found that the SPM level is very high at Orissa as compared to other pollutants. Hence, SPM considered as a source of interest to identify the safety level at each route.

3.2 Spatial Interpolation Model

The Empirical Bayesian Kriging (EBK) model is used as a spatial interpolation model in the geospatial analysis stage. It is a geostatistical algorithm that automates the process of developing a kriging model. It follows the sub-setting and simulation procedure to adjust the parameter while developing a valid model automatically. It accounts for the error generated by the semivariogram model, which is possible by estimating and implementing many semivariogram models instead of one model. During the first iteration, it predicts a semivariogram model from the existing dataset and simulates a new value at each input location. Those simulated data are used to build a new semivariogram model and uses Bayes' rule to assign a weight to that model. The repetition of this process will compute standard prediction error at each unmeasured locations and generates a semivariogram spectrum. The distribution of such a semivariogram represented in Fig. 2, where blue crosses signify the empirical semivariances and solid red lines represent the median of the distribution.

EBK model utilizes three types of semivariogram model which are expressed as shown in Eqs. (1)–(3) [9]:

$$\text{Power } \gamma(h) = \text{Nugget} + b|h|^a \quad (1)$$

$$\text{Linear } \gamma(h) = \text{Nugget} + b(|h|) \quad (2)$$

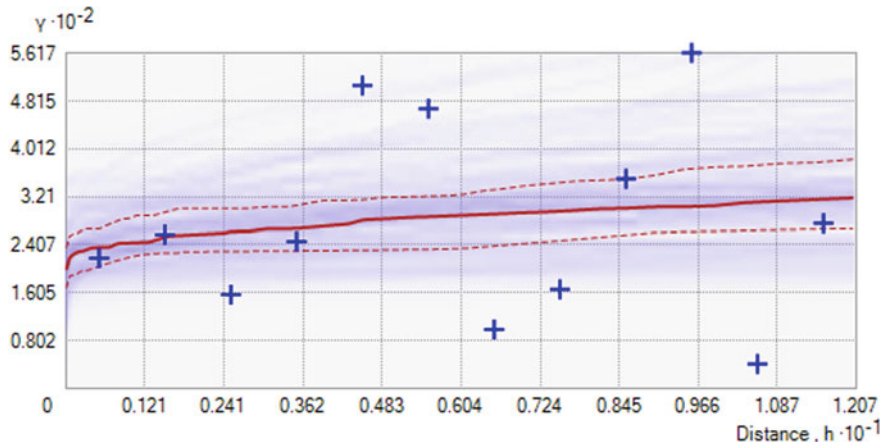


Fig. 2 Distribution of the semivariogram model shaded by density

$$\text{Thin plate spline } \gamma(h) = \text{Nugget} + b|h|^2 * \ln(|h|) \quad (3)$$

where h, b represent distance and slope, respectively. After the successful estimation of the semivariogram at each iteration, EBK generated an interpolation map with the help of some semivariogram model, as shown in Fig. 3, here color scale indicates the SPM value over the layer.

3.3 Cross-Validation

The leave-one-out cross validation (LOOC) technique is adopted to compare the performance of the proposed model with the inverse distance weighting (IDW) model in ArcGIS [10]. The achievement of those models is estimated based upon their standard prediction error, and therefore, root means square error (RMSE) and mean error (ME) evaluated to measure the performance. Table 1 shows the RMSE and MSE value for both the interpolation technique and found that EBK outperforms the IDW method for non-stationary data and provides better performance for generating the continuous surface.

3.4 Weight Assignment

Due to the non-uniform structure of air pollution monitoring stations, it is challenging to identify the spatial correlation among them and hence to determine the pollution level at each road segment for a given source and destination. This work followed

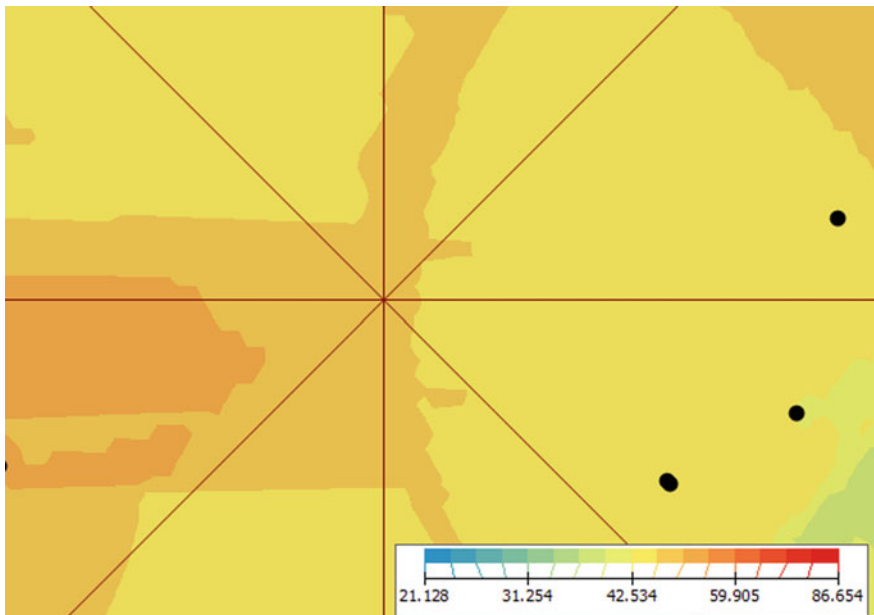


Fig. 3 SPM layer generated using EBK

Table 1 Comparison of error metrics

Interpolation/error metrics	Inverse distance weighting	EBK
Root mean square error (RMSE)	19.4994	16.3527
Mean error (ME)	0.8302	-2.1326

the weighting scheme and compared the weight of each route, to estimate the least polluted way among all possible paths. The weight computation method depends upon the interpolation value and travel distance to cover a segment. Therefore, EBK and IDW algorithms can be implemented for experimental purposes. Due to the high performance of EBK, it is considered to get SPM prediction value. During EBK implementations, the k -nearest neighbor technique is adopted to reflect the impact of interpolation points on the interpolated points. Here, four number of minimum neighbors and eight number of maximum neighbors are considered during EBK SPM spatial distribution. Algorithm 1 shows the spatial interpolation technique performed during the work. Once we get the continuous level of SPM value, it is possible to assign a weight to each route to quickly identify the optimal solution from source to destination, which is represented in Algorithm 2.

3.5 Optimal Routing Algorithm

Algorithm 1 Spatial-temporal interpolation algorithm

Input: Pollutant value at discrete points
Output: Continuous surface of pollutant

- 1: Temporal-spatial interpolation:
- 2: **if** time column values are not continuous **then**
- 3: **for** each measured point $\{a_1, b_1\}, \{a_2, b_2\}, \{a_3, b_3\}, \dots, \{a_n, b_n\}$ **do**
- 4: linear interpolation
- 5: **end for**
- 6: **end if**
- 7: **if** SPM value is sparse **then**
- 8: **for** each measured point $\{a_1, b_1\}, \{a_2, b_2\}, \{a_3, b_3\}, \dots, \{a_n, b_n\}$ **do**
- 9: Compute EBK interpolation
- 10: **end for**
- 11: **end if**
- 12: SPM prediction value \leftarrow unmeasured points $\{c_1, d_1\}, \{c_2, d_2\}, \dots, \{c_n, d_n\}$
- 13: **return** SPM polygon prediction map with class level c

Algorithm 2 Computing the least polluted route

Input: Source point, destination point, start time
Output: Optimal route, directions, distance, travel time

- 1: Perform spatial-temporal interpolation:
- 2: Continuous surface of SPM \leftarrow Call algorithm 1
- 3: **if** the user is a driver **then**
- 4: driving distance(d) \leftarrow transportation mode
- 9: **end if**
- 10: Estimate weight(w) of each route(i):
- 11: $\sum_{i=1}^n R_{\omega_i} = c * d$
- 12: $R_{\omega_i} \leftarrow$ Route
- 13: Find the optimal path, having $\min\left(\sum_{i=1}^n R_{\omega_i}\right)$
- 14: **return** The optimized route

3.6 Publish the Map as a Web Service

The interpolation output is projected to a WGS84 coordinate system to support the features on the Web. After generating the EBK interpolation polygon map, it can be published to ArcGIS Online as a Web service to design a Web application. The highly polluted area can be treated as barriers to provide the safest routing services to drivers

and pedestrians. Here, we have developed a Web map application, which computes the polluted area and considers it as barrier points for different transportation modes.

4 Results and Discussion

The navigation map is selected to find out the area of interest and intended navigation routes within that area. Direction service enables the user to display the direction while traveling toward the destination with an optimized travel time solution. High level interpolated polygon is treated as barriers points during different types of travel modes to obtain an optimal solution. Stops, barriers are the routing parameters that are intended to modify the waypoints for getting an optimized routing solution. Travel time is another most important feature, which is considered to get an optimized solution. The default transportation mode provides optimized travel time for small automobiles such as cars. This streamlined solution for a car driver represented in Figs. 4 and 5, with and without restrictions points.

The driver requires 1 h 45 min to travel from Khorda to Cuttack, Maa Mangala hotel, as shown in Fig. 4 without consideration of polluted area as a barrier and hence navigates to the highly polluted area, but in Fig. 5, the driver requires 2 h 15 min to

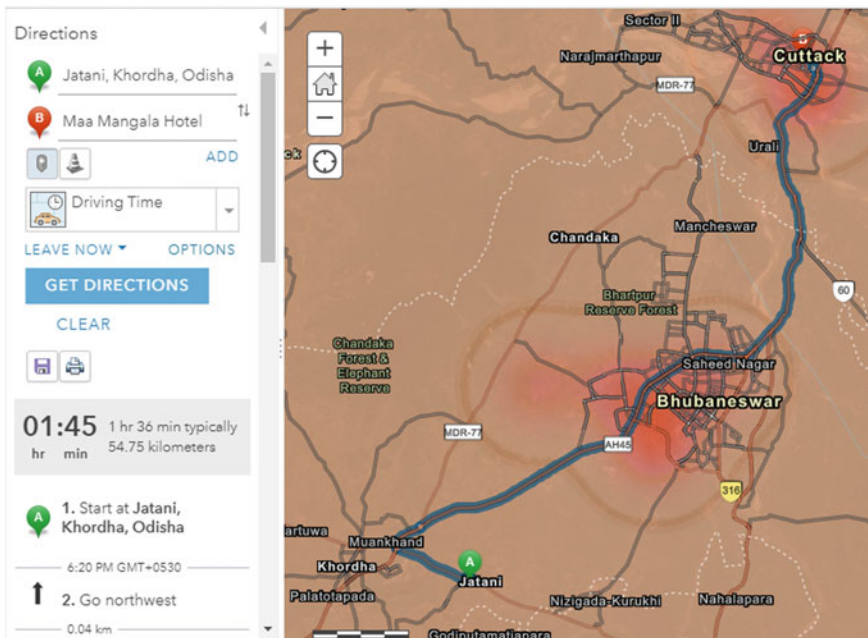


Fig. 4 Most SPM polluted route

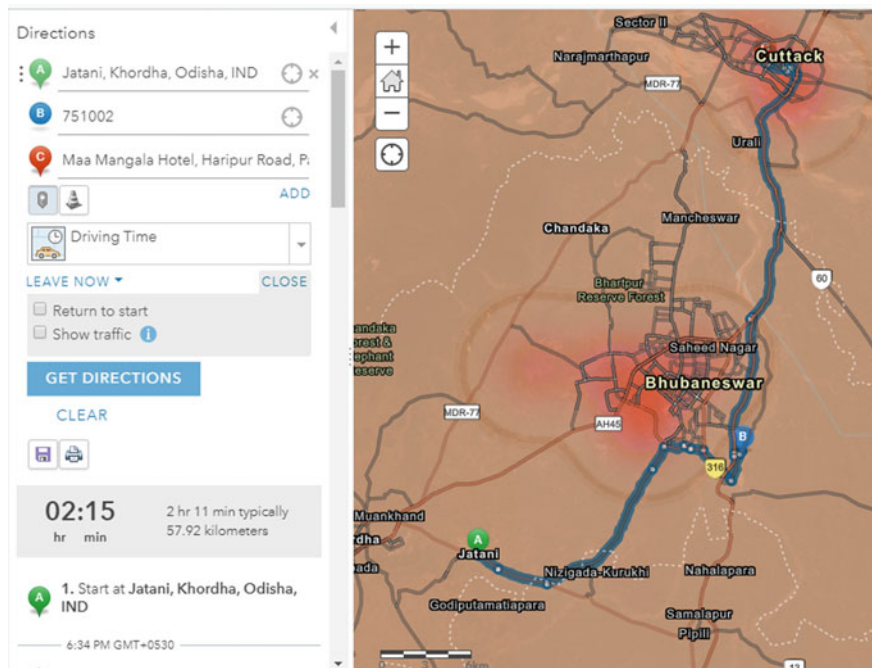


Fig. 5 Least SPM polluted route

cover that distance as he is considered the polluted area as barriers and followed the longest but healthiest path for a safe journey.

5 Conclusion and Future Work

The shortest distance may not be the best solution for smart city users every time. Some routes may cause severe health impacts while traveling. Hence, it is essential to identify the key features to determine the optimal path for smart city citizens. The presented proposed work based on geospatial science and cloud-based mapping service enables the user to generate network datasets and integrate spatial characteristics into the database to obtain such key routing parameters. This research was an attempt to find out the pollution exposure level at each route in Orissa. Therefore, it also used the EBK algorithm, which is the best suitable interpolation method for non-stationary data collected from unstructured sensors location than any other spatial interpolation technique to determine spatial correlation and spatial distribution of pollution level among those monitoring stations. Identification of the pollution level at each route is an efficient method for those patients who suffer from chronic diseases due to the high exposure of pollution. The final results of the work, which displays

as the least polluted route in the designed Web application, can be used by patients and any other smart city users to improve their health conditions. The proposed work has some limitations, which can be enhanced in our future work. The first and most critical issue is the number of active sensors available in Orissa, whose value can improve the performance of routing results. This work is limited to spatial analysis, which can be enhanced by spatio-temporal analysis with a multivariate pollution dataset.

Acknowledgements This research and product development work is financially supported by the IMPRINT (Grant No.-7794/2016), an initiative of Ministry of Human Resource Development, Government of India and Ministry of Housing and Urban Affairs, Government of India. The authors would like to thank once again.

References

1. Zhang J, Wang F-Y, Wang K, Lin W-H, Xu X, Chen C (2011) Data-driven intelligent transportation systems: a survey. *IEEE Trans Intell Transp Syst* 12(4):1624–1639
2. Zahmatkesh H, Saber M, Malekpour M (2015) A new method for urban travel route planning based on air pollution sensor data. *Curr World Environ* 10:699–704
3. Sharkeer MH, Karimi HA (2014) Computing least air pollution exposure routes. *Int J Geogr Inf Sci* 28(2):362
4. Briggs DJ, Collins S, Elliott P, Fischer P, Kingham S, Lebret E, Pryl K, Van Reeuwijk H, Smallbone K, Van Der Veen A (1997) Mapping urban air pollution using GIS: a regression-based approach. *Int J 225 Geogr Inf Sci* 11(7):699–718
5. Li HC, Chiueh PT, Liu SP, Huang YY (2017) Assessment of different route choice on commuters exposure to air pollution in Taipei, Taiwan. *Environ Sci Pollut Res* 24(3):3163–3171
6. Vamshi B, Prasad RV (2018) Dynamic route planning framework for minimal 230 air pollution exposure in urban road transportation systems. In: 2018 IEEE 4th world forum on the internet of things (WF-IoT), IEEE, pp 540–545
7. Ramos F, Trilles S, Muñoz A, Huerta J (2018) Promoting pollution-free routes in smart cities using air quality sensor networks. *Sensors* 18(8):2507
8. Central Pollution Control Board (6 January 2018) Air pollution. <http://cpcb.nic.in/air-pollution/>
9. Gunarathna M, Kumari M, Nirmanee K (2016) Evaluation of interpolation methods for mapping pH of groundwater. *Int J Latest Technol Eng Manag Appl Sci* 3:1–5
10. Esri, about ArcGIS (June, 2019). <http://www.esri.com/software/arcgis>

An IoT-Based Pollution Monitoring System Using Data Analytics Approach



**Harshit Srivastava, Shashidhar Mishra, Santos Kumar Das,
and Santanu Sarkar**

Abstract Air pollution occurs when harmful gases such as CO and NH₃ concentration levels increase above the threshold level specified by the World Health Organization (WHO). Among this, one of the very important parameters is particulate matter. These are tiny particulate that they reach directly to the lungs and cause breathing problems. The standard level of range for pollution is already given by the central governing body of India, i.e., Central Pollution Control Board (CPCB) in terms of the air quality index (AQI). In this paper, a system has been developed for detecting the air pollution index with the help of Raspberry Pi based on IoT technology which sends an emergency notification (EN) if there are any chances that the air pollution may raise above the given threshold in the future is developed which measures physical parameters like temperature, humidity, dew point, wind speed and pollutants parameters like suspended particulate matter (SPM) and carbon monoxide (CO) are monitored, and the effect of these parameters in pollution level is being predicted for pollution monitoring. The main objective of this is to apply the machine learning algorithm for the prediction and analysis of gas sensors concentration levels, the effect of physical environmental parameters so that we can analyze the future concentration levels (AQI) level of the gaseous pollutant, and based on this, an emergency notification (EN) is sent to the public as well as the concerning authorities. A system is developed for monitoring and alerting in real time. We are discussing the different methods used in machine learning algorithm, i.e., support vector machine (SVM) and random decision forests (RDF) to predict the multivariate time series for forecasting and to use these predicted values to send an emergency notification (EN).

H. Srivastava (✉) · S. Mishra · S. K. Das · S. Sarkar
National Institute of Technology Rourkela, Rourkela, Odisha 769008, India
e-mail: harshitsrivastava2345@gmail.com

S. Mishra
e-mail: 218ec5339@nitrkl.ac.in

S. K. Das
e-mail: dassk@nitrkl.ac.in

S. Sarkar
e-mail: sarkars@nitrkl.ac.in

Keywords Internet of things (IoT) · Raspberry Pi 3 · Support vector machine (SVM) · Random decision forests (RDF) · Central Pollution Control Board (CPCB) · Emergency notification (EN)

1 Introduction

Over the century, there has been a significant rise in the industries to fulfill the needs of the evergrowing population. As a result of large numbers of industries, it has caused a lot of major problems for the environment. As we know few of the impacts of air quality on the animals, human and environment, the governing body of the world, i.e., World Human Organization (WHO) has created guidelines to curb the health-related effects of air pollution on public by setting up the guidelines for the concentration of harmful air pollutants likes particulate matter, carbon monoxide, wind speed, temperature, humidity, etc. The first and the foremost effects that can be seen are the environmental pollution due to which there is a degradation of the atmosphere (breathable air) along with climate change with stratospheric ozone depletion and reduction in biodiversity, hydrological imbalance, freshwater, etc. Mobile sources and stationary releases chemical pollutants due to which suspended particulate matter (SPM), carbon monoxide (CO) and other toxic gases.

There are three important parts of integral design architecture in a system.

1.1 Perception Layer

This network layer primarily includes a stationary field sensor that works on a front-end acquisition device. As it can be realized by establishing a reliable as well as stable monitoring system, which includes site selection, sensor deployment over an area, and meteorological sensor deployment.

1.2 Network Layer

The importance of this is conveying the data related to the environment after assimilating all the sensor nodes which are deployed along an area for monitoring after this transmits the data received by the microcontroller to the data center in real time.

1.3 Application Layer

One of the primary focuses of this is to analyze and then process the pollutants. Then, calculate the air quality after which it should predict the trend which is to be followed. From the working prospective, the layer means pollution forecasts and air quality evaluation and then generating a notification to the concerning authorities.

2 Literature Survey

Hu et al. [1] presented an idea of how to trade off among the monitoring data quality and the cost of the notification message using the adaptive approach by taking the variance of the data received from the sensing nodes and adjusting the sensing rates. Yi et al. [2] where they have tackled the main problem with a pollution monitoring system is that, the presence of the limited amount of data available and non-scalability of the system available this been removed in our work by using advance sensing techniques like Wireless Sensor Networks (WSN). Hu et al. [3] presented an idea of the Haze Est-a model, which links with fixed-station data and data from the sensor to measure air quality, and the finding shows that decision tree and estimation accuracy of support vector regression (SVR) are equivalent. Rybarczyk et al. [4] presented an idea for the statistical correlation of particulate matter and wind after which it proposes a simple machine learning model to predict the level of particulate matter. Zhang et al. [5] presented an idea where they have used the advantage of a support vector machine of the classification and algorithm to overcome practical problems with which an algorithm proves the effectiveness of the algorithm. Saha et al. [6] presented an idea for a region implementing an IoT-stationed method to monitor the noise intensity and air quality index, a simple machine learning model to predict the level of particulate matter using Raspberry Pi Wi-Fi-enabled module. Zhang et al. [7] presented an idea of predicting the future outcome helps in reducing the harmful, so in this paper, they have used prediction techniques to avoid the effects of air pollution on the environment. Zhao et al. [8] presented a monitoring system for air pollution using sensors that can detect particulate matter, temperature and humidity, and when it crosses a safe range of the above parameters, then an alert signal is emitted. Yu et al. [9] presented an idea of the random forest in which due to its recursive partitioning to get many trees and then aggregate the total output to reduce the error. A Lyons et al. [10, 11] presented an idea that an alert notification will help in reducing the effects of air pollution. As they have used an alert notification to the people for high levels of air pollution so as to reduce the damage caused on the health and can be used to avoid such instances. Ayele et al. [12] presented a system that focuses on monitoring of air pollutants having an IoT-enabled system using recurrent neural network specifically Long Short-Term Memory (LSTM) which is a machine learning algorithm that shows a quick convergence and reduction in the training cycles that too with good accuracy.

3 Methodology

3.1 Architecture Model

The architecture model that we are using for our system will describe how the whole system is going to work. As shown in Fig. 1, the model will be used to take the environmental parameters reading, such as the particulate matter, temperature and few gas parameters. Now, these data will be taken up by our microcontroller and then will be sent to the cloud server through a modem. The model also has a display device that can be used to see real-time data. It also helps to detect the exact location of the device. The data sent in the server can be seen in the GUI interface that is a web-page that can be accessed from anywhere across the world.

Sensors Nodes: The different kind of parameters which are analyzed is taken by the different kind of the sensors, i.e., particulate matter sensing PM2.5 and PM10 (HPMA115S0), temperature sensor and humidity sensor (SHT10) and CO (carbon monoxide). The reason why these parameters have been considered is because we want to predict if there is an alarming situation in the near future so that necessary steps can be taken by the concern authorities.

Control and Processing Unit: It contains a microcontroller which is used to control the sensors to take values in real time. The microcontroller that we are using is Raspberry Pi 3 Model B. It features Broadcom BCM2837 SOC, which has an ARM Quad Cortex processor A53 with 1.2 GHz clock speed, and in addition to this, we are using an ARPI600 chip which converts analog to digital values.

Cloud Database and Cloud Server: The server will be used to store, host and manipulate the database along with a push notification that will be released when the future values increase a threshold which is being defined by the Central Pollution Control Board (CPCB) and to send an emergency notification to the concerned authorities. The server will store the pollution data received from the sensor node

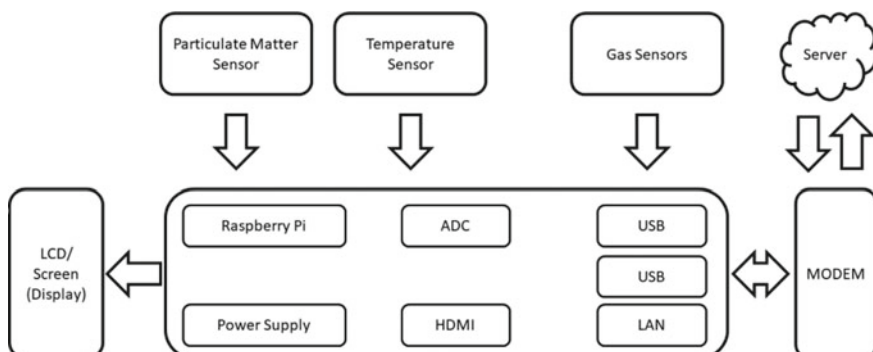


Fig. 1 System architecture model

through wireless links, and this data can be used by the front-end application which will then be used for the analytical purpose.

Android Emergency Notification: The data that is stored in the cloud database is stored from the sensor node through wireless links, and this data is used by the front-end application to analyze in which prediction algorithm is applied to trigger an Android emergency notification (AEN) with the help of an application program interface (API), which will be used to take proper precautions and to avoid the harmful effects of air pollutions.

3.2 Flowchart Model

The primary goal of the model is for monitoring the air quality index over an area and predicting the value to eliminate the problem of air pollution. As shown in Fig. 2, the data is taken from a different kind of the sensor and then given to the Raspberry Pi board and further, the AQI value is being calculated, and finally, the data is uploaded to the cloud where the prediction models will be used to forecast the future values, and if the values cross a certain threshold given by an IoT-based pollution Alert will be shown using Data Analytics Approach the CPCB (Central Pollution Control Board) in there website so that the concerned authorities can take the necessary steps.

3.3 Prediction Model

The prediction model can be explained by Fig. 3 whose working for each block is given below.

Data Preprocessing: First of all, remove all the irrelevant features and missing values from the database. Remove those values that are considered outside of the range to make sure that the credibility of the pollution dataset is not reduced.

Input Feature Engineering: After taking the sensor values from the ground station data splitting of the dataset into the hour, weekday/weekend and season by dividing it into different rows and columns so that as per the need, prediction model can be applied to get the desired output.

Target Preparation: In target preparation, we take an average of the data point received over an hour as the data we are getting is coming after 6 s, so there will not be a significant parameter change over such a short time, and then, the normalization is done on this data to avoid over-fitting.

Model Training: Here, we use Random Forest and SVM for classification and predicting the values with the help of Regression models based on the above methods

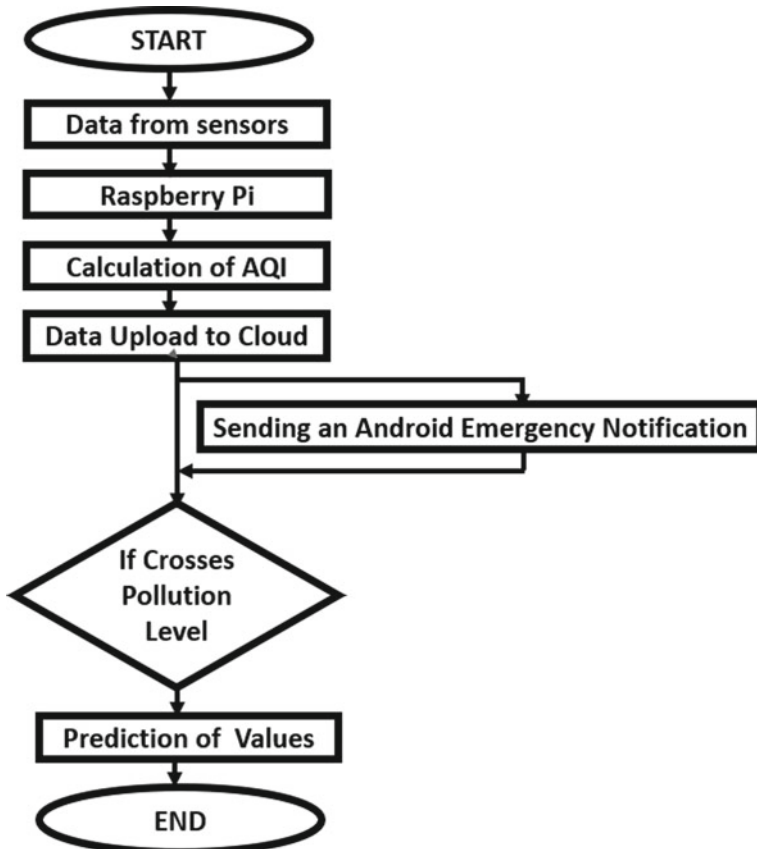


Fig. 2 Flowchart model diagram

now based on the output decision that will be taken to change the Hyper-parameters to improve the accuracy of the model.

3.4 Regression Models

Support Vector Regression (SVR): It is one of the much blooming supervised methods for the regression, support vector tries to give a mapping function which is nonlinear for plotting the given training data points, i.e., $D: (x_1, y_1), (x_2, y_2), \dots, (x_i, y_i)$ to a higher dimension. Over this higher dimension, a separating decision boundary hyperplane is defined which distinguishes all the dataset over the maximum margin function.

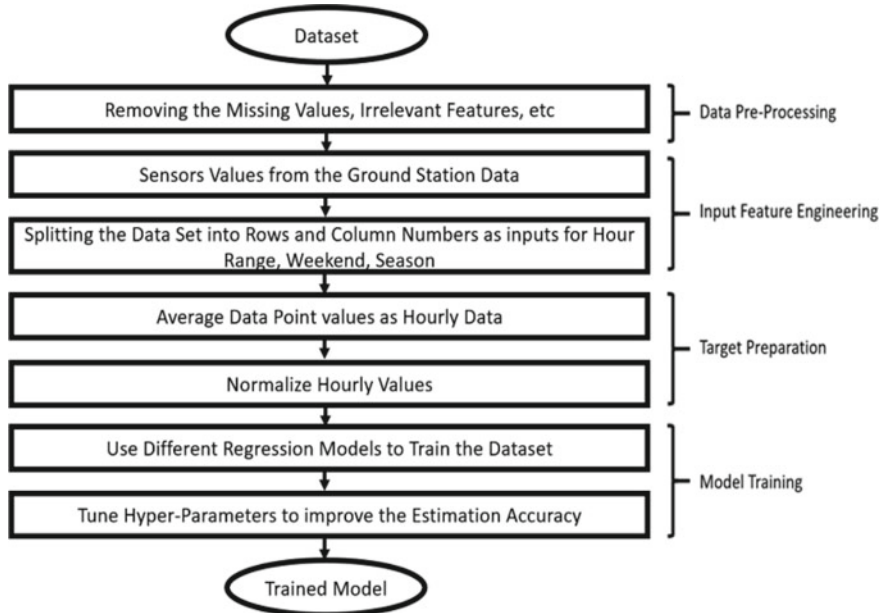


Fig. 3 Flowchart of prediction model

Random Forest Regression (RFR): It is an ensemble learning algorithm that is based on decision tree learning algorithm and bootstrap aggregating, which can be used for regression, classification and other tasks. The vital and important concept is to improve the prediction accuracy where subsamples play an important role. It is done by fitting a large number of decision trees on random subsets to the features available as a result of which it avoids over-fitting. As in this case, bootstrap aggregating is used (or named bagging) to continuously train decision or regression trees, with random feature subsets and sample subsets over which the algorithm is applied. Finally, after this, it predicts all the samples which have been taken into consideration by using the averaging technique and implying it to all the prediction from trees that have been trained.

4 Results

4.1 Firebase Server Database

As shown in Fig. 4, we have obtained some of the real-time parameters like temperature, humidity, dew point and particulate matter (PM2.5 and PM10) along with CO gas sensor values stored in the Firebase database after this prediction model is used.



Fig. 4 Real-time data packets in database

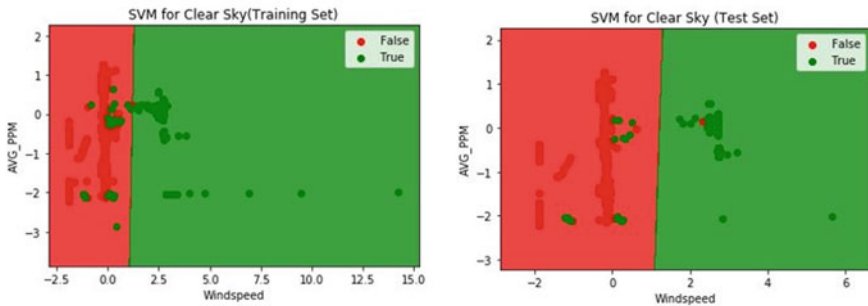


Fig. 5 Classification model of SVM

4.2 Support Vector Machine (SVM)

The primary function of this support is to identify a hyperplane in an N -dimensional hyperspace, which classifies the data points to distinguish the data points in between two classes, as it is visible in Fig. 5. Our main goal is to find a hyperplane that has the maximum margin as it is clear from the plot as the distance between data points of both the classes should increase significantly over the testing, so the accuracy is high. As shown in Fig. 6, the accuracy in our case is around 90%.

4.3 Random Forest Regression (RFR)

This technique uses a large number of decision trees in which these trees break a class of prediction, and then, the class over which maximum votes are considered

```
[[1551    12]
 [ 149    61]]
      precision    recall  f1-score   support

  False       0.91      0.99      0.95     1563
   True       0.84      0.29      0.43      210

accuracy                           0.91      1773
macro avg       0.87      0.64      0.69      1773
weighted avg    0.90      0.91      0.89      1773

accuracy = 90.91934574168077
```

Fig. 6 The accuracy of classification model of SVM

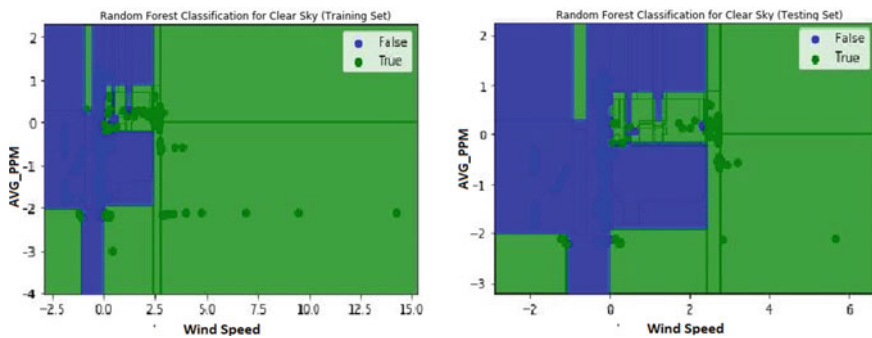


Fig. 7 Classification model of random forest regression

is considered as it is visible in our model for prediction in Fig. 7. The basic principle behind why the random forest model gives high accuracy is that when several uncorrelated trees will outperform any individual models. This can be explained as a wonderful effect of an individual tree that protects each other from their errors. There may be some trees that are wrong, and many others may be right, so overall, these trees can move in the right direction. As shown in Fig. 8, it is visible the accuracy that we are getting is around 99% which is indeed very good. Figure 9 shows the testing values and the predicted values of classification model of random forest.

4.4 *Android Emergency Notification (AEN)*

An AEN is send to the public based on the prediction algorithm that it is not safe for them move out for tomorrow based on the past data that has been received from the sensing node, this notification is sent based on the data that is received by the

```
[[1594    1]
 [ 3  175]]
      precision    recall   f1-score   support
  False        1.00     1.00     1.00      1595
   True        0.99     0.98     0.99      178

accuracy                           1.00      1773
macro avg        1.00     0.99     0.99      1773
weighted avg     1.00     1.00     1.00      1773

accuracy = 99.77439368302312
```

Fig. 8 Accuracy of classification model of random forest regression

Fig. 9 Testing values on the left side and predicted values on the right side of classification model of random forest

No.	y_test	No.	y_pred
0	38.4598	0	38.446
1	37.3202	1	37.2852
2	25.8971	2	25.9047
3	19.6317	3	19.6904
4	44.6964	4	44.6724
5	21.8763	5	21.8615
6	45.9081	6	45.9252
7	43.9372	7	43.959
8	41.7965	8	41.8002
9	30.7355	9	30.5352
10	43.2034	10	43.212
11	46.5866	11	46.575

Firebase, this data is being taken up with the help of the API key over which the data is being accessed, and then based on the threshold levels, a notification is sent as shown in Fig. 10.

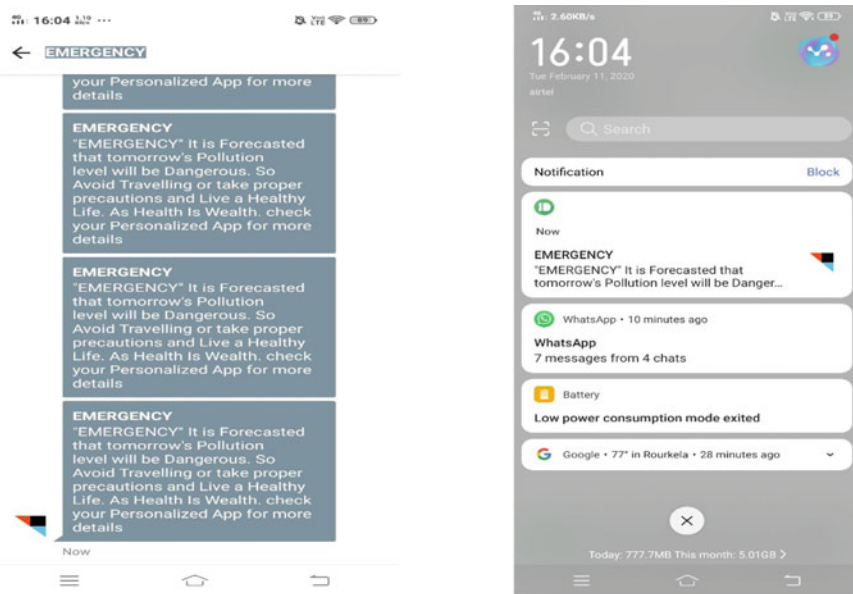


Fig. 10 Real-time images of emergency notification on left side and emergency pop-up on the right side

5 Conclusion

We have proposed a model which uses Raspberry Pi microcontroller along with the different kind of the sensors and then sending the data to the Firebase server over which prediction algorithm is used to predict the future values, and then based on the values, an emergency notification is sent. In an Internet of things (IoT)-based environment to measure air quality, this gives us a macro description of our proposed hardware and software module along with an explanation of the algorithm for calculation of values of different gas sensors, temperature sensors, humidity sensors, PPM data and predicts the value with the help of machine learning. Prediction model shows that RFR outperforms SVM which can be seen from Fig. 9 where the accuracy for this type of dataset is very high as it has to be the result because random forest model uses a lot of individual decision trees due to which it reduces the chances of predicting the wrong values overall due to considering an average result from a large number of decision trees of air pollution.

6 Scope for Future

Future work is to predict the AQI value for analyzing the air quality using machine learning with different techniques like LSTM, KNN and MLP and comparing the

accuracy of prediction. The real-time data is to be uploaded on a cloud server using a LAMP server model, and routing algorithm is to be implemented for finding the safest path based on environmental parameters from the similar nodes deployed across different location.

References

1. Hu SC, Wang YC, Huang CY, Tseng YC (November, 2011) Measuring air quality in city areas by vehicular wireless sensor networks. Elsevier J Syst Softw 84(1):2005–2012
2. Yi WY, Lo KM, Mak T, Leung KS, Leung Y, Meng ML (December, 2015) A survey of wireless sensor network based air pollution monitoring systems 15(12):31392–31427
3. Hu K, Rahman A, Bhrugubanda H, Sivaraman V (1 June, 2017) Haze Est: machine learning based metropolitan air pollution estimation from fixed and mobile sensors. IEEE Sensors J 17(11):3517–3525
4. Rybarczyk Y, Zalakeviciute R (2016) Machine learning approach to forecasting urban pollution. IEEE Ecuad Tech Chap Meet (ETCM), pp 1–6
5. Zhang Y, Liu C, Wang L, Yang A (November, 2012) Support vector machine classification algorithm and its application. In: Springer information computing and applications (ICICA 2012) communications in computer and information science, vol 308, pp 179–186
6. Saha AK, Sircar S, Chatterjee P, Dutta S, Mitra A, Chatterjee A, Chattopadhyay SP, Saha HN (2018) A raspberry Pi controlled cloud based air and sound pollution monitoring system with temperature and humidity sensing. In: 2018 IEEE 8th annual computing and communication workshop and conference (CCWC). Las Vegas, NV, pp 607–611
7. Zhang J, Ding W (January, 2017) Prediction of air pollutants concentration based on an extreme learning machine: the case of Hong Kong. Int J Environ Res Public Health 14(2):114
8. Zhao X, Zuo S, Ghannam R, Abbasi QH, Heidari H (2018) Design and implementation of portable sensory system for air pollution monitoring. In: IEEE Asia Pacific conference on postgraduate research in microelectronics and electronics (prime Asia), Chengdu, pp 47–50
9. Yu R, Yang Y, Yang L, Han G, Move OA (January, 2016) RAQ-a random forest approach for predicting air quality in urban sensing systems. Sensors (Basel). Int J Environ Res Public Health 16(1):PMCID: PMC4732119
10. Lyons RA, Rodgers SE, Thomas S, et al (May, 2016) Effects of an air pollution personal alert system on health service usage in a high-risk general population: a quasi-experimental study using linked data. J Epidemiol Community Health 70(12):1184–1190
11. Chen H, Li Q, Kaufman JS, Wang J, Copes R, Su Y, Benmarhnia T (January, 2018) Effect of air quality alerts on human health: a regression discontinuity analysis in Toronto, Canada. Elsevier Lancet Planet Health 2(1):19–26
12. Ayele TW, Mehta R (2018) Air pollution monitoring and prediction using IoT. In: 2018 second international conference on inventive communication and computational technologies (ICICCT), Coimbatore, pp 1741–1745
13. Yang Y, Zheng Z, Bian K, Song L, Han Z (2018) Real-time profiling of fine-grained air quality index distribution using UAV sensing. IEEE Internet Things J 5(1):186–198
14. Shaban KB (2016) Urban air pollution monitoring system with forecasting models. IEEE Sensors J 16(8)
15. Martinez-Espana R, Bueno-Crespo A, Timon I, Soto J, Munoz A, Cecilia JM (2018) Air-pollution prediction in smart cities through machine learning methods: a case of study in Murcia Spain. J Univers Comput Sci 24(3):261–276
16. Xiao Jun C, Xian Peng L, Peng X (2015) IoT-based air pollution monitoring and forecasting system. In: International Conference on Computer and Computational Sciences (ICCCS), Noida, pp 257–260

Modeling the Hierarchical Fuzzy System for Suitable Crop Recommendation



R. Aarthi and D. Sivakumar

Abstract To obtain successive sustainable agriculture, a farmer needs good practical and expert's knowledge regarding the modern farming technologies. As per the personal experience and traditional knowledge, the framers recommend a suitable crop for cultivation and this prediction may go wrong several times. Therefore, fuzzy expert system designed for crop recommendation systems for archiving the efficient crop recommendation. In the traditional single-layer fuzzy system, the rule is exponentially increased when the system variables are increased and a larger rule base will affect the system performance and transparency. Therefore, the multi-layer system is developed using the fuzzy hierarchical approach. The hierarchical fuzzy model is applied in a Mamdani fuzzy inference system for a suitable crop recommendation system. The crop recommendation system has 12 input variables, and it was decomposed into six fuzzy subsystems and arranged as per the priority. The final results show that a hierarchical crop recommendation system provides better performance than traditional fuzzy crop recommendation.

Keywords Fuzzy inference system · Crop recommendation · Hierarchical fuzzy system · Rule explosion · Soil properties

1 Introduction

Traditionally, the crop selection process is based on a farmer's own experience, but in most cases, the prediction went wrong due to lack of knowledge. Because the successful crop selection process is not only based on single criteria but also requires several agriculture factors. In general crop, recommendation involves several physical, chemical, and environmental factors. Crop selection is indirectly related to production and profit; this can be archived using the decision-making tool [1]. Developing the expert system is the best choice for crop recommendation because most of the farmers do not get farming advice and expert knowledge collected from a different

R. Aarthi (✉) · D. Sivakumar

Department of Electronics and Instrumentation Engineering, Annamalai University,
Chidambaram, Tamil Nadu 608002, India

e-mail: aarthi9025@gmail.com

field, scientist, and organization. The fuzzy-based expert system is widely used in the agriculture sector [2]. In the agriculture sector, most of the applications follow the nonlinear system, and the fuzzy system is the best choice for nonlinear applications. Therefore, fuzzy-based expert system is developed for the crop selection process. This type of expert system helps the farmers for the crop selection process. The major issue the fuzzy system faced is the rule explosion. If the number of input variables increased means, fuzzy rules also exponentially increased and affect the system performance. The fuzzy tree or hierarchical approach is a promising method to handle larger fuzzy variables spilled out into several subsystems; this will reduce the complexity and improve the system performances [3]. The fuzzy hierarchical system stared to evaluate the risk state in the driving assistant system [4]. In recent years, smart city development project is a major research field in India. However, maintenance and monitoring will cause several risks. To handle larger risk management in smart cities, a fuzzy hierarchical approach is used [5]. The author utilizes the hierarchical approach in the medical field that is designing a fuzzy system for diagnosing the arthritis diseases [6]. Roel Bosma et al. develop the hierarchical fuzzy layer in farming activity to improve the decision-making technique [7]. The author develops a novel hierarchical approach that is a cohesive hierarchical fuzzy system to monitor the water supply pipeline [8]. This study focused on the prediction of daily gas consumption in the Czech Republic based on climate conditions. The larger fuzzy system of the gas consumption model is decomposed into several subsystems and connected in hierarchical order [9]. Greenhouse climate control is a nonlinear approach and widely handled with the fuzzy system. The climate control system is partitioned into several small FIS based on the hierarchical approach [10]. The proposed work is to develop the crop recommendation system with 12 different agriculture parameters. This nonlinear approach is to deal with fuzzy systems. To accomplish precise and less complex systems designing, the hierarchical fuzzy model is employed for crop recommendation systems.

2 Material and Methodology

2.1 Hierarchical Fuzzy System

Rule generation is a fundamental part of a fuzzy system, but a larger number of input variables will cause the rule explosion. The rule explosion is a major limitation in the fuzzy system because it directly affects the system transparency and precision. In the standard fuzzy system, the rules are constructed in m^n manner, where n is an input variable and m is a membership function. Therefore, n increases will automatically overload the fuzzy rules and directly affect the system performance. The standard fuzzy system with a large rule base requires large memory and longer computation time. Fuzzy hierarchical or tree model is the only way to reduce the rule

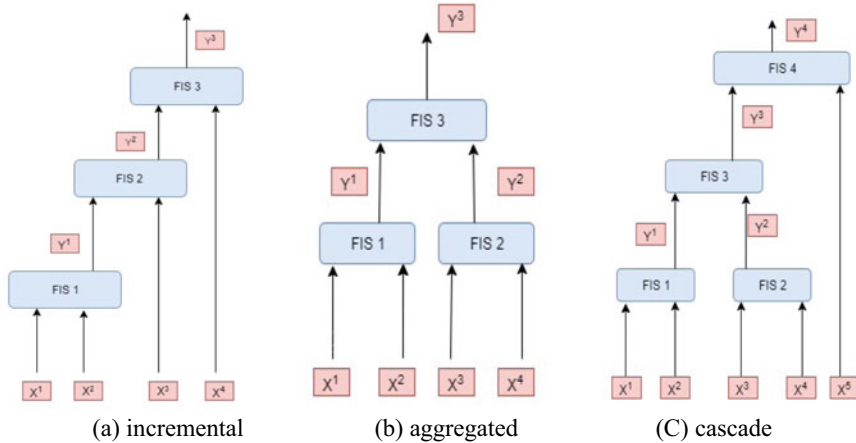


Fig. 1 Types of fuzzy hierarchical structure

explosion-related problem and improve the fuzzy system transparency and computation efficiency because a larger system splits into several small fuzzy systems [11]. Several approaches are present to decompose the larger fuzzy system into a small subsystem; they are incremental, aggregated, and cascade methods. The hierarchical structure design is based on this topology. The term hierarchical fuzzy system also named a fuzzy tree because the system is arranged in a tree-like structure. Figure 1 illustrates hierarchical fuzzy system structure.

In the incremental structure, the input variable is incorporated into multiple stages to define the output. The input fuzzy system is arranged in the order of contribution; the most important fuzzy input is arranged in the lower level and least at the top level. In an aggregated structure, the fuzzy system is formed in a group manner where a lower-level fuzzy structure is combined with a higher-level system [12]. In this structure, the subsystem is formed in the decision-making structure. The cascade structure also named as a combined structure because it groups together, both incremental and aggregated structure in the system. This fuzzy tree structure is suitable for both correlation and uncorrelated input.

2.2 *Methodology*

Rule explosion is a major issue in the standard fuzzy system because it creates the complexity of system designing. The crop recommendation requires the physical and chemical properties of soil. In the proposed paper, crop recommendation model developed using a fuzzy inference system. The block diagram of the standard fuzzy crop recommendation system is illustrated in Fig. 2.

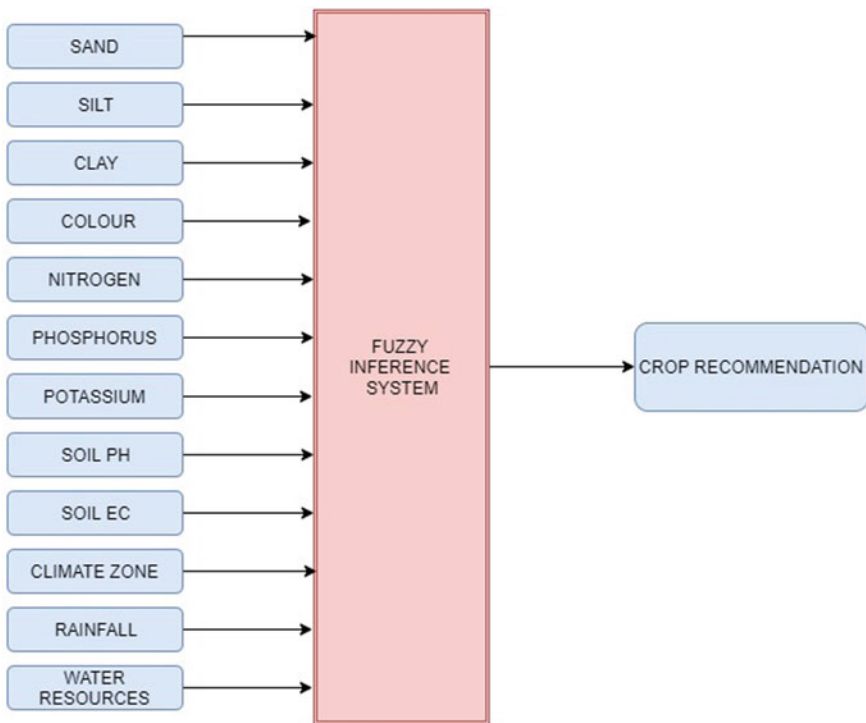


Fig. 2 Block diagram of standard fuzzy system

The system designed 12 input parameters to archive the effective result in crop recommendation. The input parameter is sand, silt, clay, nitrogen, phosphorus, potassium, soil color, soil pH, soil electrical conductivity, rainfall, climate zone, and water resources. This standard fuzzy model has two layers that are the initial layer or input layer and the final layer. As per the expert knowledge, each input variable has 3–4 membership functions. The total number of rules 499 for the crop recommendation system. To improve the crop recommendation system performance and reduce the complexity of rule formation, the fuzzy hierarchical system is proposed over the standard fuzzy system. The fuzzy hierarchical layout for crop recommendation system is illustrated in Fig. 3.

In the hierachical fuzzy model, the input variable is arranged in a lower-dimensional order instead of using higher order in the standard fuzzy system. This hierachical model of the output variable of the previous fuzzy system is given as the input variable to the next fuzzy system. And this work splits into three layers; they are input layer, intermediate layer, and final layer. The input layer consists of 12 variables, and intermediate layer is separated as five fuzzy inference systems; they are named as soil texture, soil type, soil nutrient, soil fertility, and environmental factor. The inputs of FIS 1 or texture class are sand silt and clay, and the outputs of the FIS 1 are given as input to FIS 2. For FIS 3 input variables are NPK and soil pH and soil EC is

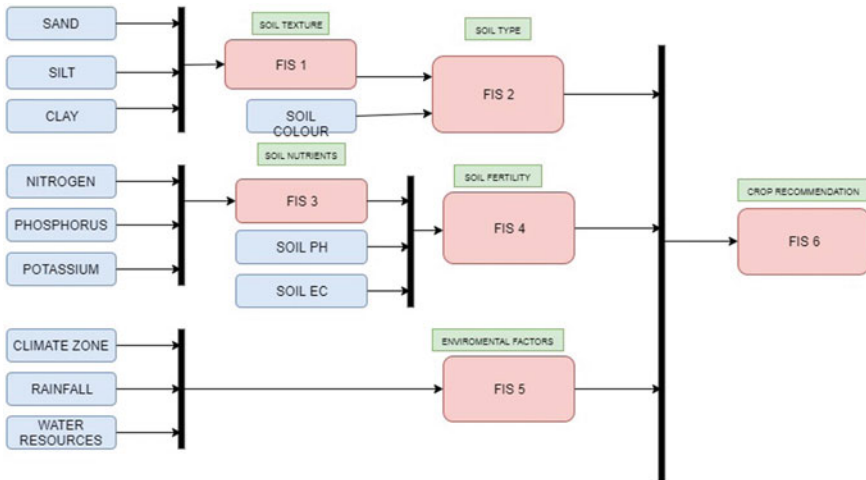


Fig. 3 Hierarchical fuzzy crop recommendation system

given as input parameter FIS 4. Climate zone, rainfall, and water resource are input parameters for FIS 5. Finally, the output parameters of FIS 2, FIS 4, and FIS 5 are given as input variables of FIS 6 that is a crop recommendation system. This fuzzy hierarchical crop recommendation system drastically reduces the number of fuzzy rules compared with the traditional fuzzy system.

3 Implementation and Discussion

The standard fuzzy model and hierarchical fuzzy crop recommendation system were developed in the fuzzy inference toolbox in MATLAB version 2018a. Table 1 represents the basic configuration of FIS designing for crop recommendation.

The input and output membership for FIS 1 are shown in Fig. 4, and its corresponding rule view is demonstrated in Fig. 5. In FIS 1, sand silt and clay are input variables, and each input variable has three membership functions. Texture classes are output variables and 12 membership functions. Totally, 12 fuzzy rules are developed.

Table 1 Basic FIS configuration

Configuration	Method
Membership function	Triangular
Input fuzzification	MIN and MAX
Implication	MIN
Aggregation	MAX
Defuzzification	Centroid

Final hierarchical crop recommendation FIS 6 rule viewer in Fig. 7. Output of fuzzy inference system FIS 2, FIS 4, and FIS 5 is applied as the input to FIS 6. The input and output variables soil type, soil fertility, environmental factor, and crop recommendation are illustrated in Fig. 6.

In this paper, five subsystems are designed for crop recommendation. They are soil texture, soil type, soil nutrient, soil fertility, environmental factor, and crop recommendation. The hierarchical fuzzy system rule table show in Table 2.

The rule table represents possible number rules in hierarchical system to numbers of rules which drastically reduced when compared with standard fuzzy model.

Traditional fuzzy model total number of rules: 439.

Hierarchical fuzzy model total number rules: 152.

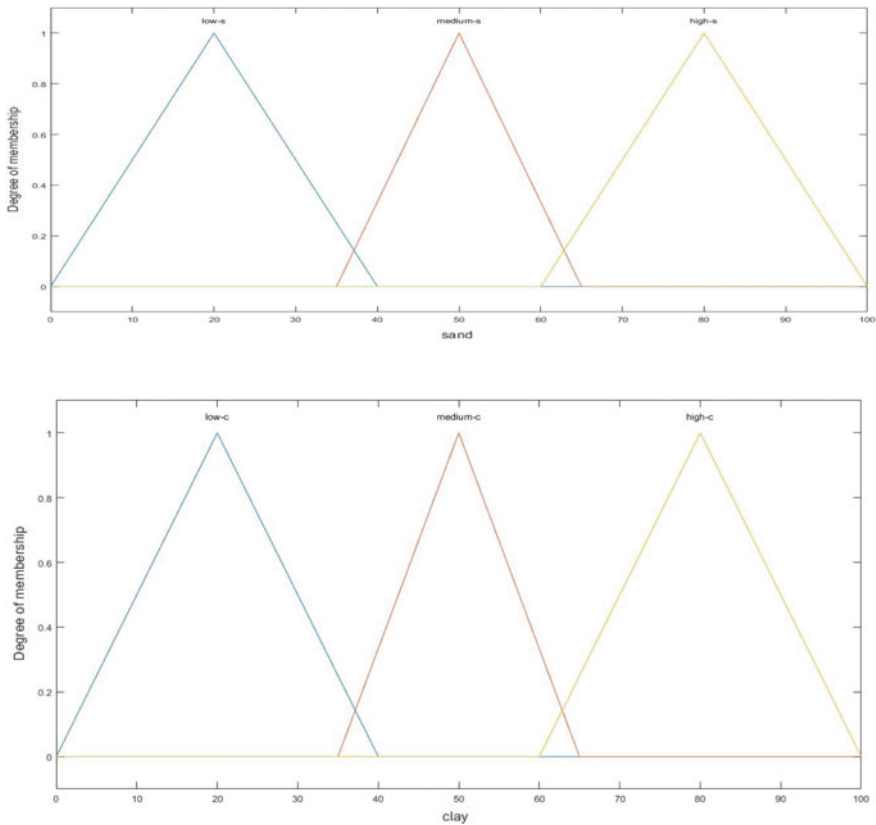
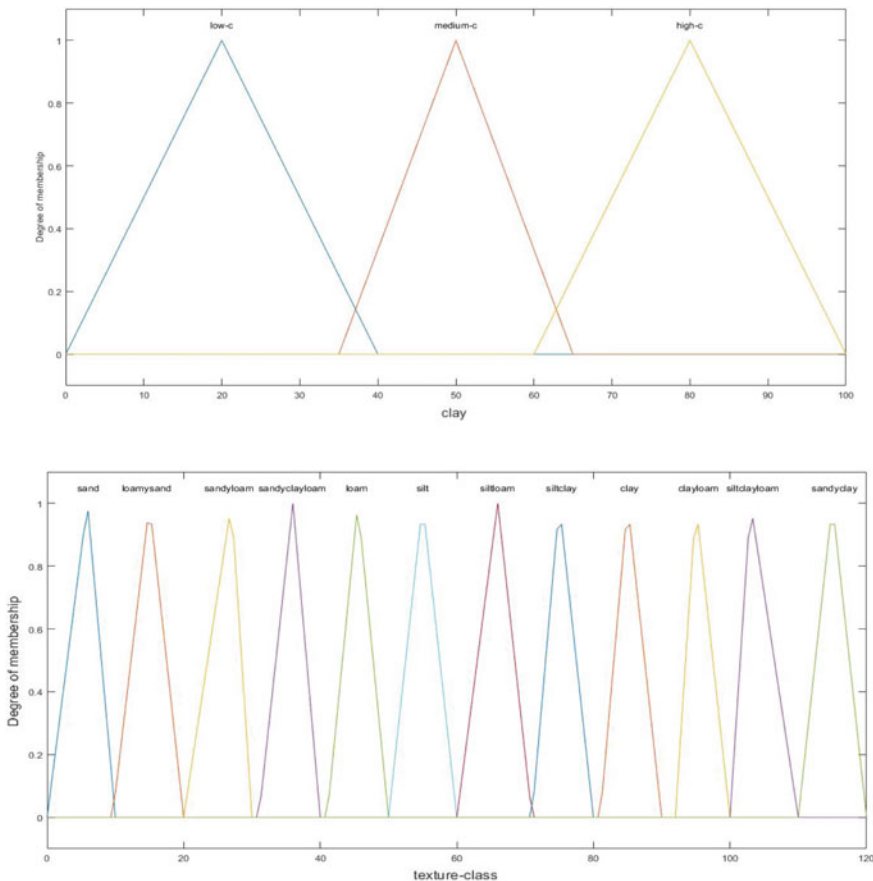
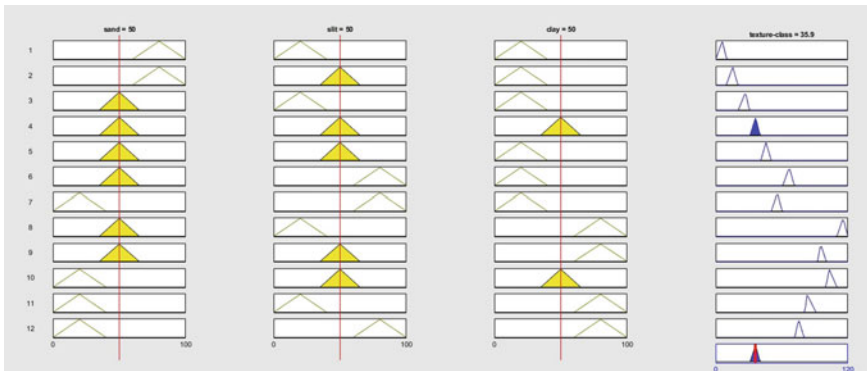


Fig. 4 Input and output membership function of FIS 1

**Fig. 4** (continued)**Fig. 5** Rule viewer of FIS 1

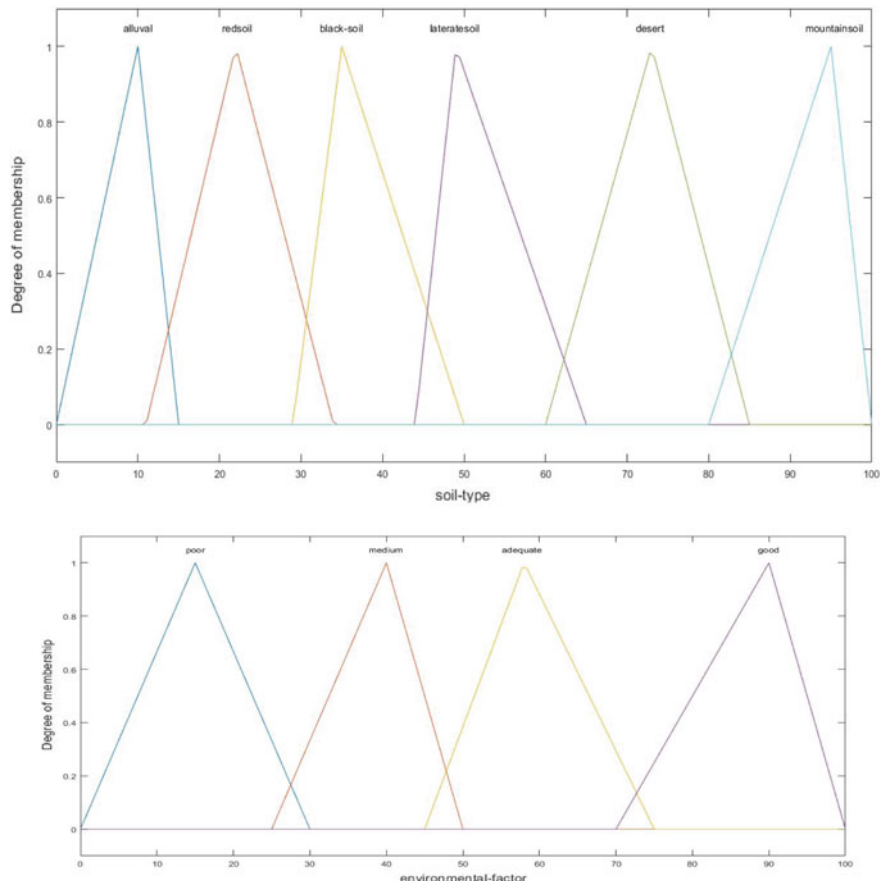


Fig. 6 Input and output membership function of crop recommendation

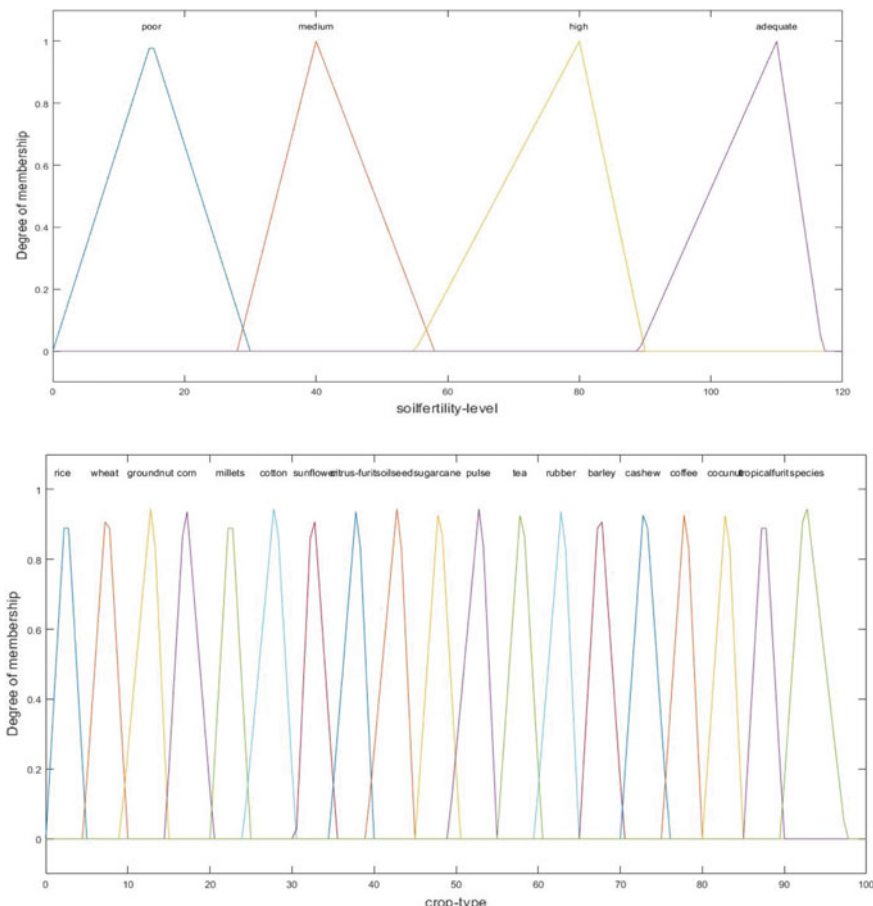
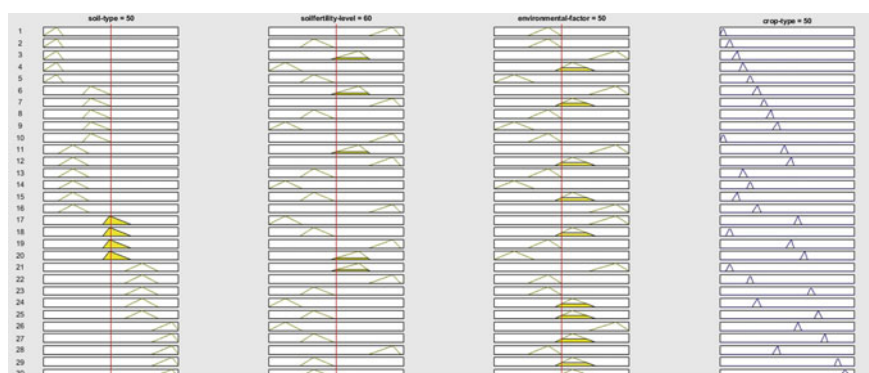
**Fig. 6** (continued)**Fig. 7** Rule viewer of crop recommendation system

Table 2 Rule formation in hierarchical fuzzy crop recommendation system

Model/fuzzy tree	No. of FIS unit	Input variable	Total no. of membership function	No of fuzzy rules
Soil texture	FIS 1	3	3	12
Soil type	FIS 2	2	3	15
Primary nutrient	FIS 3	3	2	38
Soil fertility	FIS 4	3	3	35
Environmental factors	FIS 5	3	3	12
Crop recommendation	FIS 6	3	20	40
Total number of rules				152

4 Conclusion

The hierarchical fuzzy-based suitable crop recommendation system was developed. This hierarchical model partitions the larger fuzzy system into several small subsystems. Therefore, the number involved fuzzy rules also reduced compared to the traditional fuzzy system for crop recommendation. The crop recommendation system complexity is reduced, and the system performance is improved in the hierarchical fuzzy system. The simulation results show that hierarchical fuzzy yields better performance than the tradition fuzzy system in crop recommendation application.

References

1. Deepa N, Ganesan K (2017) Decision-making tool for crop selection for agriculture development. *Neural Comput Appl*
2. Papageorgiou IE, Markinos A, Gemtos T (2009) Application of fuzzy cognitive maps for cotton yield management in precision farming. *Expert Syst Appl* 36:12399–12413
3. Chen Y, Abraham A (2010) Hierarchical fuzzy systems, tree-struc. Based Hybrid Com Intell 129–147
4. Dkhil MB, Wali A, Alimi AM (2018) A hierarchical fuzzy system for an advanced driving assistance system. *Comput Vision Pattern Recogn Artif Intell*
5. Ullah I, Fayaz M, Kim DH (January, 2019) Risk assessment based on hierarchical fuzzy inference and prediction using Kalman filter for underground facilities in smart cities. *Int J Innov Technol Explor Eng (IJITEE)* 8(3C)
6. Lim CK, Yew KM, Ng KH, Abdullah BJJ (2002) A proposed hierarchical fuzzy inference system for the diagnosis of arthritic diseases. *Australas Phy Eng Sci Med* 25(3)
7. Bosma R, Kaymak U, van den Berg J, Udo H, Verreth J (2011) Using fuzzy logic modelling to simulate farmers' decision-making on diversification and integration in the Mekong delta, Vietnam. *Soft Comput* 15:295–310
8. Fayaz M, Ahmad S, Hang L, Kim D (2019) Water supply pipeline risk index assessment based on cohesive hierarchical fuzzy inference system. *Processes* 7:182
9. Radek Sindel a.r, Hierarchical Fuzzy Systems, 16th Triennial World Congress, Prague, Czech Republic, Elsiver IFAC Publication, 2005 IFAC

10. Paulo Salgado J (2005) Boaventura Cunha, greenhouse climate hierarchical fuzzy modelling. *Control Eng Pract* 13:613–628
11. Lee M-L, Chung H-Y, Yu FM (2003) Modeling of hierarchical fuzzy systems. *Fuzzy Sets Syst* 138:343–361
12. Yager RR (February 1998) On the construction of hierarchical fuzzy systems models. *IEEE Trans Syst Man Cybern Part C: Appl Rev* 28(1)

Real-Time Emergency Vehicle Response System for Smart City Applications



Lima Priyadarsini, Prashant Deshmukh, and Santos Kumar Das

Abstract The city applications and services are targeting how to frame the upcoming Internet of things (IoT)-based applications and services for the perspective of the smart city. The acceptance, arrangement and execution of cutting-edge wireless services and applications have to be designed in the manner to allow facing the difficulties of smart cities. There is intelligence, analytical and conduct automation that permit the influencing better policy and smart deployment. Nowadays, various works are going on to detect health disease, accident, crime and fire for achieving the goal of smart cities. There are many individuals in the world to be alive if speedy notice would have given to emergency services. This detection system provides only alert to the respective authorities or their relatives but not able to implement real-time lifesaver services. The objective regarding this paper is to provide online cloud services to various emergency detection devices so that with the help of these devices, life can also be saved. The smartphone has become an important instrument in our life; with the help of a global position system (GPS) or cell phone location in mobile, human can be tracked. This work mainly deals with emergency vehicle networks for an ambulance, fire brigade and police vehicles like online cab services. In this work, a mobile application is proposed which is immediately triggered after detection of emergencies and provides real-time vehicle services for the nearby hospital, police control room and fire brigade.

Keywords Cloud services · Emergency vehicle response network · Mobile application · Google map

L. Priyadarsini (✉) · P. Deshmukh · S. K. Das

Department of Electronics and Communication Engineering, National Institute of Technology Rourkela, Rourkela, Odisha 769008, India

e-mail: lima.priyadarsini07@gmail.com

P. Deshmukh

e-mail: erprashantdeshmukh@gmail.com

S. K. Das

e-mail: dassk@nitrkl.ac.in

1 Introduction

Emergency vehicle armada dispatching and the board assume a significant job in occurrence reaction times and the nature of administration offered to end clients. The viability of the management procedure is important to limit the effect of occurrences on human lives and properties. Exact and opportune choices are along these lines required.

The key segment for crisis trade reaction scheme is the choice of stream ways for vehicles and materials, by the reason for well-being and brief time, moving, however, countless particular and vehicles influenced site could be expected under the circumstances is one of the instinctive models to quantify the plausibility of the arrangement [1]. Simultaneously, the city's unique street organization has just come to fruition; however, the development pace of vehicles is a lot quicker than that of new streets [2]. The connection between organic market reversals prompts the standardization and expanding the seriousness of urban clog.

The underdevelopment of data assortment innovation and the bother of data transmission and dissemination will all lead that coordinators of crisis reaction cannot take correct countermeasures; voyagers cannot acquire convenient, right and valuable data to choose the ideal way for departure; salvage powers cannot convey alleviation supplies to the scene in time [3–5].

To beat these issues, we propose a Real-Time Emergency Vehicle Response System, which gives ongoing administrations to penniless people, accommodating for diminishing the demise because of mishap cause, deferring of rescue vehicle administrations and police administrations.

2 Related Work

One commonly applied to use safe for vehicular ways are forms that recognize crisis channels. Such a request can reduce mishap risks through crisis effect hallucinations and help additional important time. They diagram a far-reaching structure of such a crisis channel warning structure that utilizes channel communication, yet additionally involves roadside foundation alike traffic lights. Within this structure, different vehicles do not only warned about moving toward crisis vehicles; they likewise get nitty-gritty course data. Given the data, the favorable and proper acknowledgment of various operators is understandable. A representation of this structure has been proposed in a rush-hour gridlock condition including crisis vehicles and traffic lights. To recognize prerequisites and assess the framework, this additionally led a point-by-point investigation of recordings from crisis reaction trips and a specialist review among individuals from a neighborhood crisis reaction association [6].

Urban crises are difficult to maintain a strategic distance from. Traffic crisis reaction after an episode assumes a significant job in decreasing misfortunes and is a key connection in urban crisis the executives. The framework, for the most part,

incorporates sub-frameworks, for example, staff clearing information assortment framework, vehicle activity information assortment framework, salvage material conveyance information assortment framework, faculty settlement place information assortment framework, traffic pike wise distinguishing proof framework and so on. It likewise devises the working projects for ordering the executives, faculty clearing and catastrophe transfer if there should arise an occurrence of crisis, and improves the urban crisis bolster the board framework. Accompanied by the Internet of everything and the details extract innovation, the trade crisis reaction framework is auspicious as well as precisely check streaming data for faculty and motor vehicles, rapidly with helpfully immigrate staff in addition to motor vehicle, adequately complete review salvage tasks, successfully upgrade salvage proficiency with enhancing the degree for the city administration [7–9].

Emergency circumstances require exact and opportune choices to lessen delay and the extra effect of episodes on human lives and common properties. Nonetheless, basic leadership in urban emergency circumstances is a difficult assignment because of the number of factors impacting the procedure and the unusual difference in some of them. This procedure trademark necessitates that leaders screen and change their choices for all time. In this manner, data accessibility and trade are basic to improve the basic leadership process. Despite refined enhancement commitments in unique emergency vehicle dispatching issue, not many of them have thought about their combination in intelligent transportation systems (ITS). In this unique circumstance, dynamic occasions and non-intermittent blockage could be better tended to. In this paper, we consider the dynamic crisis vehicles dispatching issues utilizing real-time data (DEVDP-RT). We propose a responsive methodology for vehicle dispatching dependent on a setting mindful and reconfigurable design. Our methodology is planned to help apportion emergency vehicles to urban crises and modify their courses as indicated by up and coming changes and unforeseeable occasions. Recreation results feature the advantages of the proposed dispatching model in improving the crisis reaction time and lessening delay [10].

Another framework identified with the traffic observing framework has been suggested by creators. During venture, the group planned cutting-edge trade checking framework as long as enhancing street trade stream accompanied by the point of gathering present and coming times essential requirements for street move. The framework expands this effectiveness of checking street trade conditions at giving permanent information on weather forecasting parameters of various areas. The article did not consider safety concerns by this cutting-edge trade observing framework [11, 12].

Intelligent transportation systems are the whole common significant use of every Internet of Everything empowered bright towns. It is dependent on a green wave framework that has been exhibited, which empowers the trade sign framework to use some signed field during a crisis channel which moves toward those trade signs. As a result of using these signed fields, a crisis channel gains every single green sign into the path. Creators exhibited this being a developing flow over a crisis channel. During the responsibility, this trade sign framework can identify any taken channel that goes through each developing sign. This significant burden from that

growing surge means that if this synchronization from this movement sign remains upset, this package produces an enormous road turned parking lot (over-immersion). To diminish the effect like non-having appropriate integration, RFID locate trade controller framework has been prescribed [13–15].

3 Proposed System

Google Mobile Services (GMS) is a collection of Google applications and application program interfaces that help support functionality across devices. The proposed system using the cloud, database and Google services for the emergency vehicle response platform. Smartphone and Internet are the common prominent things used by the people and become very important in this era. Figure 1 shows the system architecture of Real-Time Emergency Vehicle Response (RTEVR). In this left side, all the sensor devices for emergency detection are already available in the market. All the registered users having these devices with the Android phone have an emergency calling application installed, when the sensor sends a request to our cloud system, which is the middle of Fig. 1 shown, and detects emergency. The computing system of the cloud server classifies the emergency response and generates a broadcasting message for the corresponding vehicle response network, e.g., health-type request nearest available ambulance driver will be called, similarly for fire and police. The GMS provides the path to the driver to the victim using a real-time Google map and the nearest hospital. Our proposed system stores all the records in the database, e.g., driver's detail, user's detail, journey time, hospital database, etc.

Transportation of emergency supply is dynamic. The system built up a numerical model to depict the issue and afterward built up a database of the emergency organization on the base of the model. The database is the most significant piece of the product that shows dynamic transportation. Therefore, the paper portrays the plan of the database insistently. The database is the base of the emergency response system.

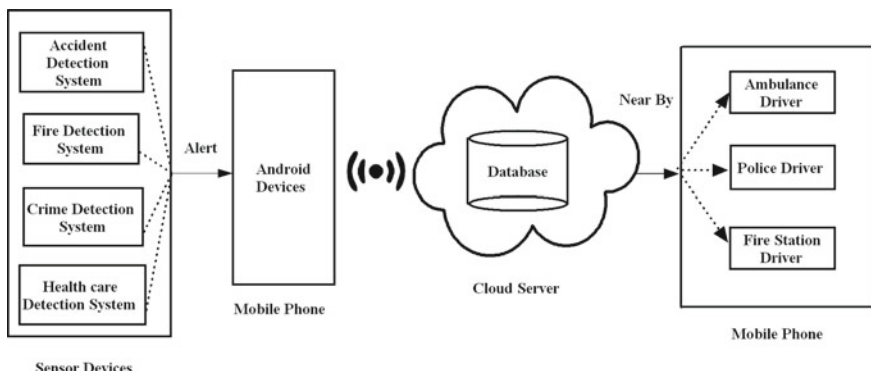


Fig. 1 System architecture of RTEVR

It very well may be utilized to store, recover and review the information shown in Fig. 2, so the emergency system can obtain information from it precisely. The information, which is associated with the paper, is examined through cluster hubs and associating sides, the database structure of the essential system. The proposed system uses MongoDB and Firebase database. MongoDB is the NoSQL database; therefore, the system can handle a huge amount of data, and it is easy to interface with Google services, an Android platform using the Atlas cloud or Parse server, and this system uses Parse server for communicating with Android to MongoDB. The system uses Firebase as a secondary data for providing an interface to sensor devices in the proper format because the microcontroller cannot directly communicate with MongoDB; therefore, firebase is a middleware between our system and emergency detection devices.

In Fig. 2, user and emergency vehicle driver's data is shown. The user database has data field user name, device ID and device type. The system uses the Mac address of sensor devices as device ID for classification of device type. The emergency vehicle database consists of all the vehicle driver details, e.g., application ID, mobile number, name and type in corresponding networks. Among the emergency organization, the most significant of all components are the logins and connecting sides. Figure 3 depicts the data processing unit of RTEVR, for data to be transmitted from one

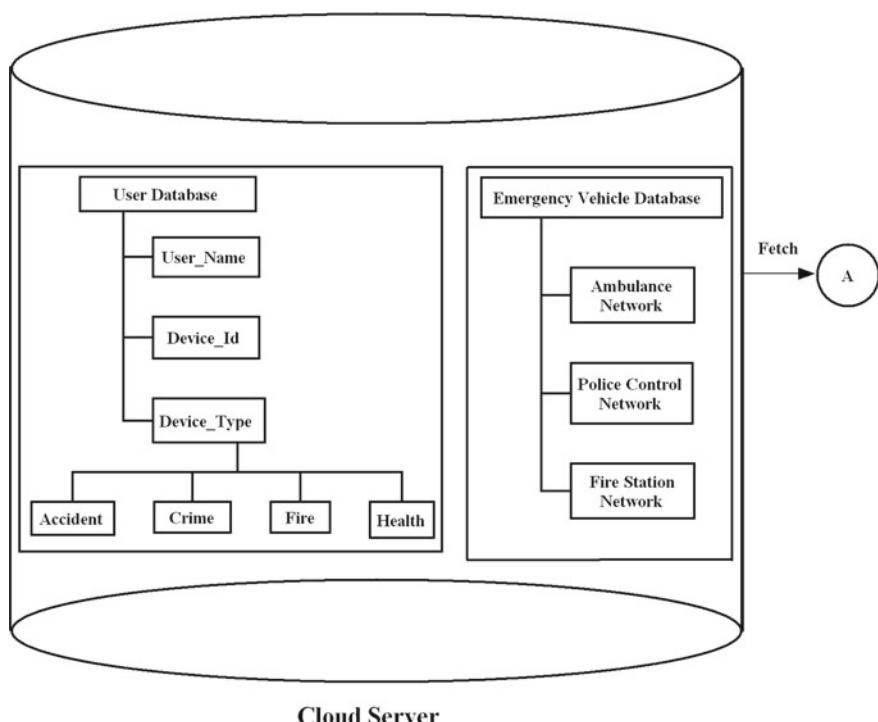


Fig. 2 Database design of RTEVR

Fig. 3 Data processing of RTEVR



platform to another need of protocols and computation unit; therefore in the proposed system, Amazon cloud is used as a computing platform and cloud services are using for communication between database and user interface, i.e., Android system or maybe Web interface.

4 Results and Discussion

Given the scientific model, the database of crisis organization is planned effectively. The product that is on the base of the scientific model above has been created. As indicated by the trademark and property of each component in the crisis arrangement, we made a comparing element relationship model and tried information with MongoDB server database and at last, built up the database of a crisis organization. The achievement of the database demonstrated the exactness and sensibility.

Figure 4 shows the entire registered user's database; it consists of a user-type field, which indicates user as driver or victim and also his gender.

Similarly, Fig. 5 shows emergency-type vehicles' database field which classifies the request type for ambulance, police and fire brigade and also respected linked driver details, e.g., e-mail, contact number.

Figure 6 indicates device ID database field link with a user profile for the respected emergency alert device for accident, crime, fire or healthcare. The Emergency Service Dashboard is displayed in Fig. 7, and all the requests are severed by response system using the query dashboard, i.e., all the sensor devices are linked and responded through the emergency dashboard.

User							Add Row	Refresh	Filter
	objectId	Gender	CurrentPosition	emailVerified	UserType	GpsEnable			
1	VNYhkFWJm2	Female	(22.2507179, 84.9017347)	True	Normal	True			
2	LqqXeQ2IeR	Male	(22.2505111, 84.9012445)	True	Driver	True			
3	P8ZI0889pd	Male	(22.250699, 84.9019369)	True	Driver	True			
4	zyJgjqamu	Female	(22.2602006, 84.902221)	True	Driver	True			
5	M1Xxfwz1OK	Male	(20.3348, 85.8229983)	True	Driver	True			
6	rFPaB0fDVY	Male	(20.3406967, 85.81914)	True	Driver	True			
7	g2p33yf1jl	Female	(22.2483408, 84.899996)	True	Driver	True			
8	GVS40fireB	Female	(22.2507228, 84.9018705)	True	Driver	True			
9	A1IWTTmpAm	Female	(20.3406969, 85.8209169)	True	Normal	True			

Fig. 4 User database field

CLASS SCEmergency 343 objects • Public Read and Write enabled					
	objectId	RequestState	DriverId	AcceptToStartDura...	StartToPatientLoca...
	String	String	String	AcceptToStartDura...	StartToPatientLoca...
0Id7LbbnAL	FINISH	zyjgjqxamu	8680	34	AMBULANCE
SI0QAXcYUL	REQUESTED	RDpwQjEUzJ	12892	5478	AMBULANCE
nReakzTvUi	FINISH	RDpwQjEUzJ	4012	339358	AMBULANCE
UUfUqlpygg	FINISH	pEdITOYurI	8225	2093	POLICE
qE7HLDxG0G	FINISH	pEdITOYurI	19684	736	AMBULANCE
sDtQYWLU6M	FINISH	lobPeZ7RZG	7432	5347	FIRE BRIGADE
hz43Twpbnx	FINISH	7WnkyYmUhX	8036	3411	AMBULANCE
goYQkma3aF	STARTEDFORHOSPITAL	RDpwQjEUzJ	1277	3076	AMBULANCE

Fig. 5 Emergency type vehicles database field

SCUserDevice 6 objects • Public Read and Write enabled						
	objectId	createdAt	updatedAt	ACL	DeviceId	OwnerId
	String	Date	Date	ACL	String	String
1gaZpkT72a2	20 Aug 2019 at 07:...	20 Aug 2019 at 07:...	Public Read + Write	12345	Wc40MpjU2g	Heart123
NEhhY1w1Kz	17 Apr 2019 at 07:...	17 Apr 2019 at 07:...	Public Read + Write	b8:27:eb:20:9e:9c	vTToSCNCX0	Accident Detection
qHOHbzB5T2	31 Jan 2019 at 07:...	31 Jan 2019 at 07:...	Public Read + Write	23#e45	S844UYf6UA	My Device
rTVa598FKc	28 Aug 2018 at 08:...	28 Aug 2018 at 08:...	Public Read + Write	Test555	vTToSCNCX0	Crime Test
AXdwNXK1Ek	23 Aug 2018 at 07:...	23 Aug 2018 at 07:...	Public Read + Write	60:01:94:5E:46:94	vTToSCNCX0	Fire Detection
aQTR7Gim60	2 Aug 2018 at 13:0...	2 Aug 2018 at 13:0...	Public Read + Write	2C:3A:E8:35:D1:B5	vTToSCNCX0	Fall Detection

Fig. 6 Device ID database field link with user

Send a test query
Try out some queries, and take a look at what they return.

What type of request?	GET
Which endpoint? Not sure what endpoint you need? Take a look at our REST API guide .	classes/_User
Use Master Key? This will bypass any ACL/CLPs.	No <input checked="" type="checkbox"/> Yes <input type="checkbox"/>
Run as... Send your query as a specific user. You can use their username or Object ID.	Username or ID
Query parameters Learn more about query parameters in our REST API guide .	where={"username":"johndoe"}

Fig. 7 Emergency service dashboard

5 Conclusion

During the evaluation, we developed the incident ID and mind-blowing salvage structure, which produces emergency alert and send it to the closest emergency communicator and will comparably send an SMS to emergency connection containing area addresses of the mishap. By consistent region following for both hurt person and communicator, the structure will develop the determination step of an event stunning misfortune by giving crisis assistant during the time. The framework will additionally assist in many crises, for example, when firing, crimes and different prosperity-associated crises. Urgency communicator directions are gifted branch location monstrous misfortune's region toward a Google chart coherently.

References

1. Guo D, Gao C, Ni W, Hu X (June, 2016) Max-flow rate priority algorithm for evacuation route planning. In: Proceedings of IEEE 1st international conference on data science in cyberspace, pp 275–283
2. Zhou Z, Lin S, Du W, Liang H (2019) Integration of regional demand management and signals control for urban traffic networks. *IEEE Access* 7:20235–20248
3. Zhou J, Beard C, Qian Y (July/August, 2018) Distributed device caching for information updating in emergency communications. In: Proceedings of 27th international conference on computer communication and network, pp 1–9
4. Oliveira A, Vazao T, Galao P, Varzea M (October, 2018) Performance evaluation of a hierarchical low rate emergency system. In: 2018 16th international conference on intelligent transportation systems telecommunications (ITST), pp 1–7
5. Yang B, Wang J, Ma W, Mao X (2018) Research on crowdsourcing emergency information extraction of based on events' frame. In: Proceedings of 10th International Conference on Computer Electronics and Engineering
6. Buchenscheit A, Schaub F, Kargl F, Weber M (2009) A VANET-based emergency vehicle warning system. In: IEEE Vehicular Networking Conference (VNC), Tokyo, pp 1–8
7. Sumi L, Ranga V (2016) Sensor enabled internet of things for smart cities. In: Parallel, distributed and grid computing (PDGC), 2016 fourth international conference on, IEEE, pp 295–300
8. Liu Z, Wang C (2019) Design of traffic emergency response system based on internet of things and data mining in emergencies. *IEEE Access* 7:113950–113962
9. Rani LPJ, Kumar MK, Naresh KS, Vignesh S (2017) Dynamic traffic management system using infrared (IR) and internet of things (IoT). In: 2017 third international conference on science technology engineering and management (ICONSTEM), pp 353–357
10. Yedder BH, Benyahia I (2017) Reactive emergency vehicles dispatching based real-time information dissemination. In: 2017 8th IEEE annual information technology, electronics and mobile communication conference (IEMCON), Vancouver, BC, pp 471–477
11. Costea I, Nemtanu F, Dumitrescu C, Banu C, Banu G (2014) Monitoring system with applications in road transport, in design and technology in electronic packaging (SIITME). IEEE 20th international symposium for IEEE, conference proceedings, pp 145–148
12. Aljawarneh S (2011) A web engineering security methodology for e-learning systems. *Netw Secur* 2011(3):12–15
13. Nemtanu F, Moise I, Banica C (8–12 May, 2013) Hybrid simulation in intelligent transportation systems. In: 36th international spring seminar on electronics technology (ISSE 2013), pp 106–107

14. Andreev S, Galinina O, Pyattaev A, Gerasimenko M, Tirronen T, Torsner J, Sachs J, Dohler M, Koucheryavy Y (2015) Understanding the IoT connectivity landscape: a contemporary M2M radio technology roadmap. *IEEE Commun Mag* 53(9):32–40
15. Mittal AK, Bhandari D (2013) A novel approach to implement green wave system and detection of stolen vehicles. In: IEEE Conference Proceedings in Advance Computing Conference (IACC), IEEE 3rd International, pp 1055–1059

Modified Aggressive Packet Combining Scheme with Repetition Code for Throughput Enhancement in High Error Rate Channel



Mancharla Ravi and Yaka Bulo

Abstract Aggressive packet combining (APC) scheme is a well-established scheme which reduces the number of retransmissions for receiving correct packet in error prone wireless link. It is a well-known fact that the retransmissions consume extra bandwidth and battery energy of the portable computer. Therefore, APC is an efficient technique which reduces number of retransmissions for a packet, thus reducing latency of the wireless system. In APC, three copies of a packet are transmitted, and receiver does bit-wise majority decision to get the combined copy. Least reliable bits identification is done in the combined packet if majority logic fails. Search the correct bit pattern for least reliable bits so obtained. APC provides higher reliability but at expense of throughput of the system. Therefore, major issue in APC is the lower throughput which at maximum is 33.33% ($\frac{1}{3} \times 100$). In this paper, modified APC with repetition code is proposed which addresses lower throughput issue of conventional APC. Simulation results show significant performance improvement in terms of throughput when packet combining scheme with repetition code is used in APC scheme.

Keywords Bit-by-bit majority logic · Bit error rate · Conventional aggressive packet combining scheme · Repetition code · Throughput

1 Introduction

The wireless networks suffer from high bit error rate 10^{-2} [1] to 10^{-3} [2]. In an automatic repeat request (ARQ) scheme, a packet is retransmitted if it gets corrupted due to transmission errors caused by the channel. Each retransmissions consume communication bandwidth and transmission energy. The bandwidth is a scarce resource

M. Ravi (✉) · Y. Bulo

Department of Electronics and Communication Engineering, National Institute of Technology Arunachal Pradesh, Arunachal Pradesh, India
e-mail: Mancharla.phd@nitap.ac.in

Y. Bulo
e-mail: yaka@nitap.ac.in

because many portable computers may be sharing a limited free space spectrum. The energy is also a scarce resource because the portable computer is usually powered by battery.

Therefore, it is desirable to reduce the number of retransmissions in order to utilize the bandwidth and battery energy efficiently. In many error control protocols, the receiver discards the erroneous packet and requests the transmitter for a retransmission. However, an erroneous packet may contain both erroneous bits and correct bits, and hence, it may still contain useful information. The receiver may be able to combine this information from multiple erroneous copies to recover the correct packet. In order to achieve the desirable quality in high bit error rate wireless channels, several modifications for applying basic ARQ are found in literature where erroneous packets are combined and by applying logic, the error location is identified. Once error location is identified, bit inversion is done to error so identified (Brute method). The technique is variably applied in packet combining scheme [3], multiple route packet combining scheme [4], and aggressive packet combining scheme [5]. In packet combining scheme [3, 6, 7], two copies of a packet are transmitted, and if at least one of the received copies are error free, it is accepted as a correct transmission. However, if both copies are received erroneous, bit-wise modulo-2 sum of the copies is computed to locate the errors in the combined copy. Thereafter, the packet is corrected by brute force bit-by-bit inversion of bit located as erroneous and checking for correctness using frame check sequence (FCS). However, PC scheme fails if there is at least one-bit position where both copies have an error (termed as double error in [3]), and the computational complexity increases when the number of errors in the combined copy exceeds a predefined value N_{\max} [3]. To deal with the latency issue in wireless network, Leung [5] proposed an efficient technique called aggressive packet combining scheme. In aggressive packet combining scheme, transmitter sends three copies of packet to the receiver. Receiver on receiving three copies of the packet will apply bit-by-bit majority voting on three received copies to obtain a combined packet. Receiver checks error on the combined packet, and if the packet is not corrected by majority logic, receiver will identify least reliable bits and search the correct bit pattern for the identified least reliable bits. If still correct copy is not obtained, it will request for retransmission of the packet. APC gives better error correction capability [8–14] with reduced latency, but suffers from low throughput. APC scheme requires at least three copies of a packet to successfully retrieve the correct copy of the packet, thus the best packet throughput of APC scheme is $T_{APC} = \frac{1}{3} \times 100\% = 33.33\%$ only.

In this article, we propose a modified technique of APC which increase the throughput of the conventional APC using the idea of packet combining and three-bit repetition code. We use the concept of packet combining scheme for incorrectly received copies to identify the error locations and then use three-bit repetition code when the retransmission call is received at the receiver side. We assume that the round-trip delay is negligible, the feedback channel is error free, and CRC provides perfect error detection capability.

2 Proposed Scheme

In proposed technique, instead of transmitting three copies of the original packet as in conventional APC, two copies are sent initially. If the received two copies are erroneous, then XORing of both the copies are done to locate the error positions as that of the conventional packet combining scheme. Bit-by-bit inversion of the error positions which is done in conventional PC is avoided because this step involves computational complexity which is equal to $C = 2^{2n\alpha} - 2$ [3] where n is packet size in bits and α is bit error rate. Thus, even for medium-sized packets and at moderate BER, random fluctuations of the channel may make the bit inversion procedure extremely complex. It also leads to battery energy consumption and delay of the system (as delay is not acceptable in real-time traffic). Conventional APC is an efficient technique with low latency, but it suffers from low throughput. Therefore, this proposal is an attempt to increase the throughput of conventional APC. It is observed that current wireless mesh network protocols retransmit whole of the packet when a retransmission call is received at the sender side [8]. These retransmissions end up sending bits that have already received correctly, wasting network capacity. Retransmitting entire packets work well over wired networks where bit-level corruption is rare and packet loss implies that all the bits of the packet were lost. However, in case of wireless network, all the bits in a packet do not share the same fate. Thus, it is wasteful to resend the entire packet. Therefore, in the proposed technique, instead of retransmitting entire packet when negative acknowledgement (NACK) is received, sender sends only that bits which are erroneous by using basic three-bit repetition code. After XORing, receiver sends NACK along with errored bit positions information to the sender and keeping the errored copies at its buffer. At the sender side, instead of retransmitting the whole packet, it sends only those bits which are detected to be error by repeating each bit three times. Receiver applies bit-by-bit majority logic in the third erroneous copy, and again error detection is done on the code obtained after majority logic. Incorrect positions are rectified by comparing the bits obtained after majority logic with those erroneous bit locations in any of the first two received copies. Flow diagram of the proposed scheme assuming return channel to be error free, the round-trip delay is negligible, and CRC used at the receiver provides perfect error detection with example is shown in Fig. 1. In Fig. 1, $P1_C1$ is the copy 1 of packet 1, and $P1_C2$ stands for copy 2 of packet 1. $P1_Repetition_code$ stands for retransmitted packet with three-bit repetition code.

In the proposed scheme, aggregate number of bits transmitted is lesser than the conventional APC, so the throughput improvement is very high as compared to the conventional APC. It gives satisfactory results when the packet is medium and large sized.

Majority logic applied in the transmitted packet is successful if no two bits out of three repetition code is error. Generally, codeword to have two bits flipped out of three bits, the medium would have to be extremely noisy of the order of 10^{-3} to 10^{-2} [1, 2]. And practically, channel does not happen to be extremely noisy all the

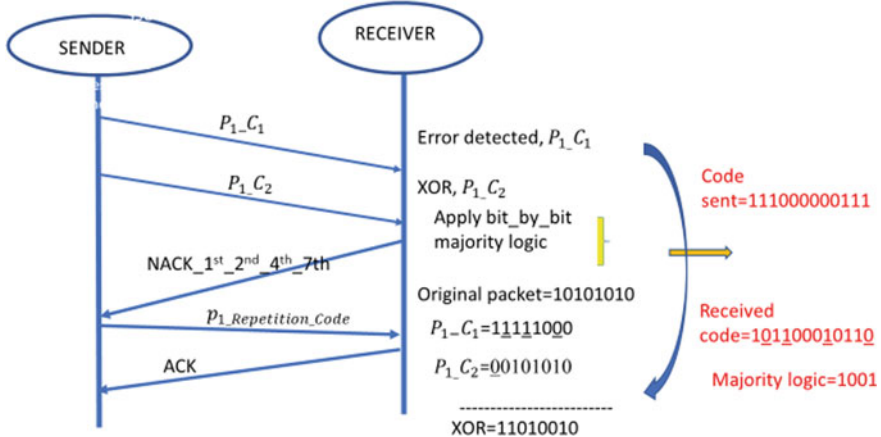


Fig. 1 Flow diagram of the proposed APC scheme with the bit repetition code

time. To understand the proposed scheme clearly, let us take an example showing proposed scheme.

An example showing proposed scheme for the packet $b_7b_6b_5b_4b_3b_2b_1b_0 = 11001100$

$$\text{Received copy, } b_7b_6b_5\bar{b}_4\bar{b}_3b_2b_1b_0 = 110\bar{1}1100$$

$$\text{Received copy, } b_7\bar{b}_6b_4b_5b_3b_2\bar{b}_6b_0 = 1\bar{0}0011\bar{1}0$$

$$\text{XOR} = 01010010$$

The incorrect positions are identified as second, fourth, and seventh bit locations from the left. Receiver now sends NACK along with this errored bit positions information to the sender. Sender sends three-bit repetition code of this errored positions as $111\ 000\ 000$. In receiver side, if the received code is $1\bar{0}1\ \bar{1}00\ 000$. Apply majority logic, we get code as 100 , and this code is sent for error detection. If found correct, receiver checks correct packet using this code in one of the erroneous copies stored in buffer of the receiver.

Error detection is done to check the packet.

3 Analysis and Simulation Results

In conventional APC scheme, three copies ($i = 3$) of a packet is transmitted at a time to get reliable packet at the receiver and the actual bit error rate, ξ (as then only double or triple bits in error cannot be detected leading to actual bit error rate) for APC is given by ζ [9]:

$$\zeta = \binom{3}{2}\alpha^2(1 - \alpha) + \binom{3}{3}\alpha^3 \quad (1)$$

Therefore, probability of erroneous transmission (P_{APC}) or packet error rate (PER) in conventional APC for packet size “ n ” is given by [9]:

$$P_{APC} = (1 - (1 - \xi)^n) \quad (2)$$

where “ α ” is bit error rate and ξ is the actual bit error rate. Throughput of the conventional APC is given by η_{APC} [15]:

$$\begin{aligned} \eta_{APC} &= \frac{(1 - P_{APC})}{(i + P_{APC})} \\ \eta_{APC} &= \frac{(1 - P_{APC})}{(3 + P_{APC})} \end{aligned} \quad (3)$$

where “ i ” is the number of copies transmitted.

In the proposed scheme, initially two copies are transmitted. At the receiver side, error detection is performed. If both the copies found erroneous, bit-wise modulo-2 sum is applied to find the error locations. Once error locations are identified, NACK is sent along with error location information. Therefore, probability of erroneous transmission P_{PC} for the first two copies assuming no double error occurs is given by [16]:

$$\begin{aligned} P_{PC} &= (1 - (1 - \alpha)^{ni}) \\ P_{PC} &= (1 - (1 - \alpha)^{2n}) \end{aligned} \quad (4)$$

Since two copies are transmitted in the first go therefore, $i = 2$.

For the third copy with three-bit repetition code, if any of the retransmitted bits cannot be recovered that is the case when two or all the three bits are erroneous. Therefore, bit(s) which cannot be recovered is written as β :

$$\beta = \alpha^3 + {}^3C_2\alpha^2(1 - \alpha) = \alpha^3 + 3\alpha^2 - 3\alpha^3 = 3\alpha^2 - 2\alpha^3 \quad (5)$$

Therefore, packet which is recoverable is given as ϕ :

$$\phi = 1 - \beta = 1 - (3\alpha^2 - 2\alpha^3) = 1 - 3\alpha^2 + 2\alpha^3 \quad (6)$$

Therefore, packet of k bits in error which are recoverable

$$= (1 - 3\alpha^2 + 2\alpha^3)^k \quad (7)$$

Probability of erroneous transmission for the proposed scheme P_{New} is given by:

$$P_{New} = P_{PC} \times [(1 - 3\alpha^2 + 2\alpha^3)^k] \quad (8)$$

Therefore, throughput of the proposed scheme is given by η_{New} :

$$\begin{aligned}\eta_{\text{New}} &= \frac{(1 - P_{\text{New}})}{(i + P_{\text{New}})} \\ \eta_{\text{New}} &= \frac{(1 - P_{\text{New}})}{[(2 + 3k) + P_{\text{New}}]}\end{aligned}\quad (9)$$

Performance evaluation is done in terms of packet error rate (PER) and packet throughput, as determined by the computer simulation using MATLAB R2012b tool. Bit error rate (α) in the range 10^{-5} to 10^{-3} (low error rate) and 10^{-3} to 10^{-2} (high error rate) is taken for different values of bits in error (k) for comparison. Simulation results show the effectiveness of the proposed scheme in terms of throughput improvement for large-sized packet ($n = 1000$). But PER is almost same as that of the conventional APC as observed from simulation results in Fig. 4.

Figures 2 and 3 show that the throughput of the proposed scheme increases with change of bit error rate from low-to-high bit error rate, and this increment is more for large-sized packet. Throughput of the conventional APC decreases with increase in bit error rate. Not much improvement can be observed in terms of packet error rate (P) in the proposed scheme as shown in Figs. 4 and 5. It becomes worst when the packet size and bit error rate increase as chances of more number of bits getting corrupted increase in wireless links.

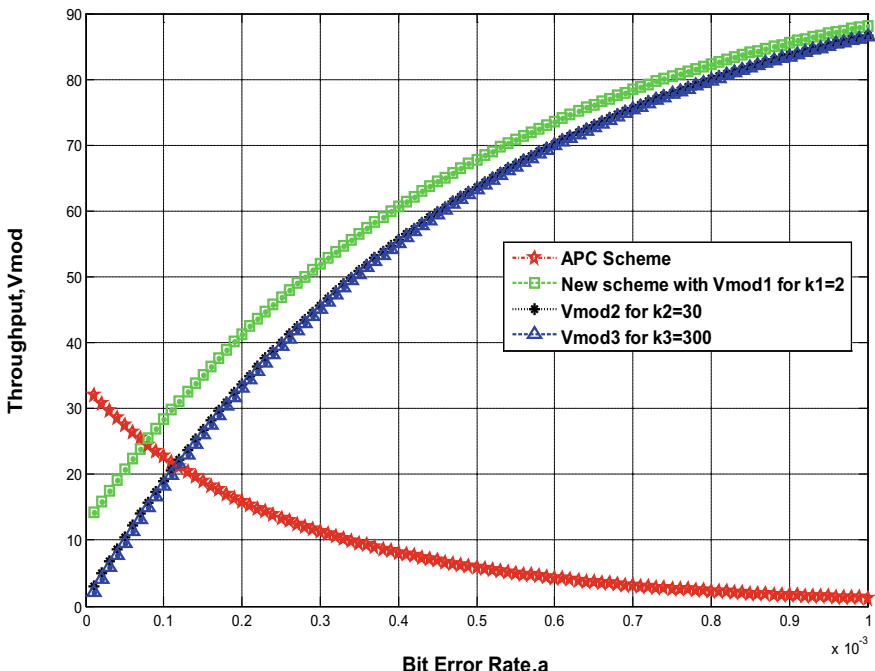


Fig. 2 Throughput plot of the proposed scheme for different values of k and APC scheme for $n = 1000$

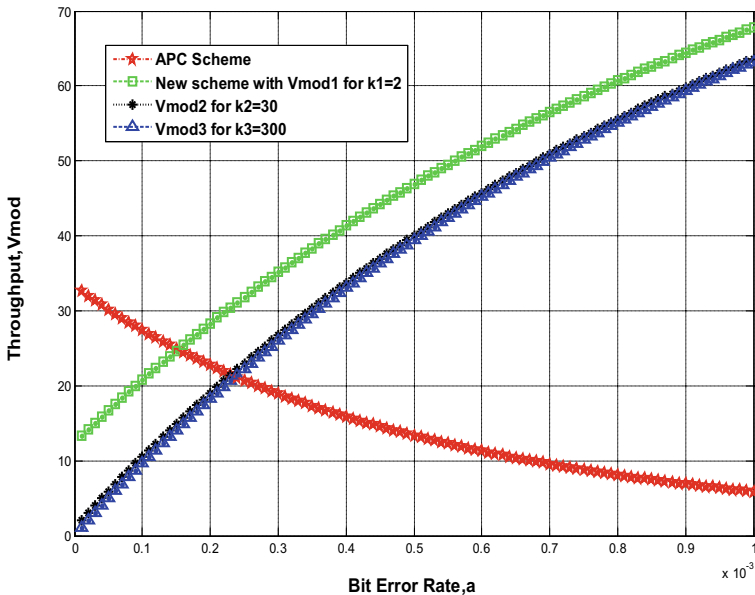


Fig. 3 Throughput plot of the proposed scheme for different values of k and APC scheme for $n = 500$

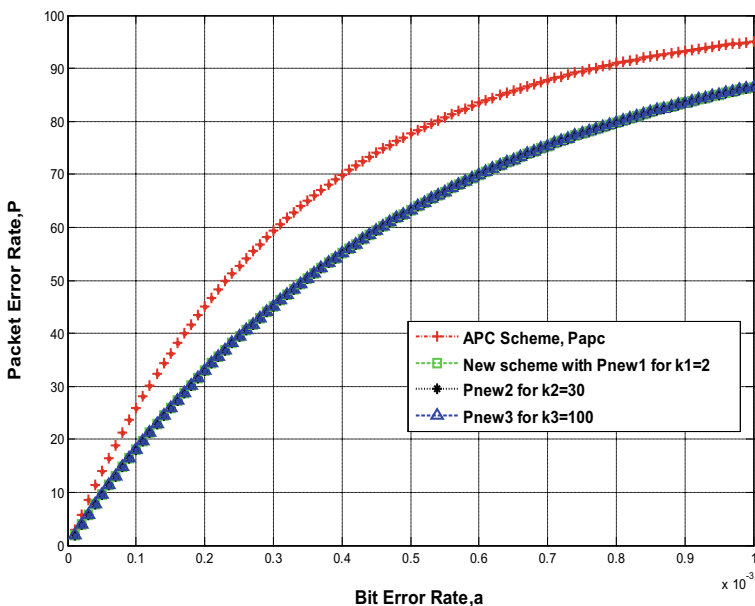


Fig. 4 Packet error rate plot for proposed scheme for different values of k and APC scheme for $n = 1000$

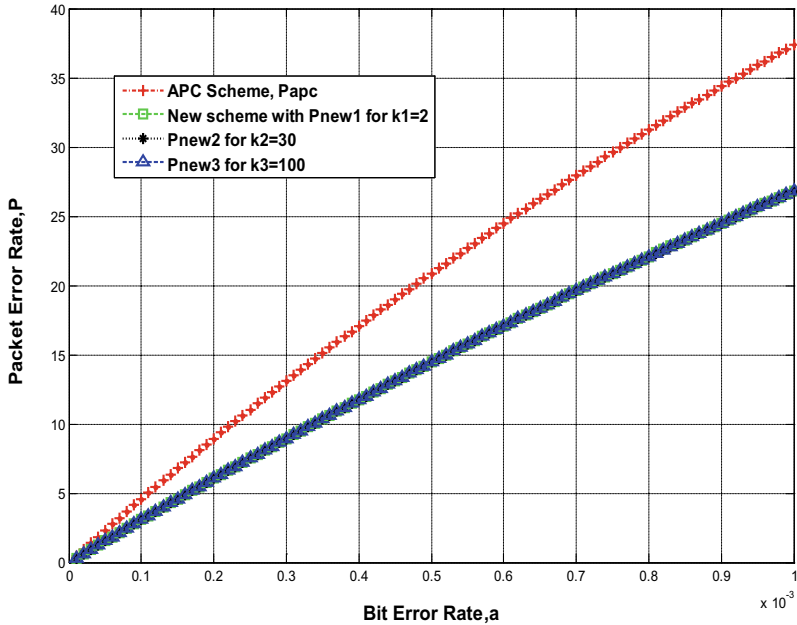


Fig. 5 Packet error rate plot for proposed scheme for different values of k and APC scheme for $n = 156$

4 Conclusion

The proposed scheme of bit repetition yields higher throughput as compared to APC scheme. Increment in throughput is prominent when the packet size and bit error rate increases as seen from Figs. 1 and 2. Not much improvement can be observed in terms of packet error rate (P) in the proposed scheme as shown in Figs. 3 and 4. It becomes worst when the packet size and bit error rate increase as chances of more number of bits getting corrupted increase in wireless links. The proposed scheme fails when double error occurs in the first two transmitted copies and two bits out of three transmitted repeated code get corrupted. Generally, codeword to have two bits flipped out of three bits, the medium would have to be extremely noisy of the order of 10^{-3} to 10^{-2} [1, 2]. And practically, channel does not happen to be extremely noisy all the time.

References

1. Liu H, Ma H, Zarki ME, Gupta S (1997) Error control schemes for networks: an overview. *Mob Netw Appl* 2:167–182
2. Yuen O (1996) Design trade-offs in cellular/PCS systems. *IEEE Comm Mag* 34(9):146–152

3. Chakraborty SS, et al (1995) An ARQ scheme with packet combining. *IEEE Comm Lett* 2(7):200–202
4. Hirayama Y, Okada H, Yamazato T, Katayama M (2005) Time-dependent analysis of the multiple-route packet combining scheme in wireless multihop network. *Int J Wirel Inf Netw* 42(1):35–44
5. Leung YW (2000) Aggressive packet combining for error control in wireless networks. *Trans Comm E83(2)*:380–385
6. Chakraborty SS, et al (1999) An exact analysis of an adaptive GBN scheme with sliding observation interval mechanism. *IEEE Comm Lett* 3(5):151–153
7. Chakraborty SS, et al (1999) An adaptive ARQ scheme with packet combining for time varying channels. *IEEE Comm Lett* 3(2):52–54
8. Jamieson K, Balakrishnan H (2007) PPR: partial packet recovery for wireless networks. *SIGCOMM'07*, Kyoto, Japan
9. Bhunia CT (2012) Several modifications of aggressive packet combining scheme for wireless network. In: Proceedings of the IEEE computer, information and telecommunication systems (CITS), pp 1–5
10. Saring Y, Bulo Y, Bhunia CT (2015) New modifications of aggressive packet combining scheme with improved performance. *Int J Appl Eng Res* 10(17):37610–37615
11. Khumukcham R, Goswami A, Saring Y (2015) Four new protocols for achieving better correction capability of APC scheme. In: Proceeding IEEE international conference of communication and signal processing, Melmaruvathur, Tamil Nadu, pp 741–745
12. Khumukcham R, Saring Y, Goswami A (2015) Combined APC-PC scheme for random and time varying channels. In: Proceeding IEEE international conference of communication and signal processing, Melmaruvathur, Tamil Nadu, pp 358–360
13. Bulo Y, Sharma P, Bhunia CT (2016) Improving error correction capability of aggressive packet combining scheme by using half-byte packet reverse technique and even–odd selection method. *Int J Comput Appl* 137(2):32–36
14. Saring Y, Singh SV (2019) Aggressive packet combining scheme with packet reversed and packet shifted copies for improved performance. *IETE J Res*
15. Bhunia CT (2005) IT, network and internet. New Age International Publishers India, New Delhi
16. Chakraborty SS, Liinaharja M, Ruttik K (2002) Selection diversity based ARQ schemes and their enhancements using packet combining in a slow rayleigh fading channel. *IEEE ICPWC* 192–195

Review on Silent Speech Recognition Using EMG Sensors and Voices After Laryngectomy



Pilla Devi Bhavani, V. Preethi, and Durgesh Nandhan

Abstract In this paper, there are four ways of speech rehabilitation techniques after laryngectomy. They are voice prosthesis, esophageal voice, electronic larynx, and silent articulation. After the surgical removal of the larynx, the person cannot speak. After laryngectomy, he/she cannot speak naturally. But using the four techniques mentioned above is helpful to a person without larynx.

Keywords Larynx · Laryngectomy · Dysarthria · Amatsu tracheoesophageal shunt · Electromyographic signals · Tracheophagical voice · Esophageal voice

1 Introduction

Speech is the most important tool for human beings to communicate with others. The main part of the human body which helps a person to communicate verbally is larynx. The larynx is also known as the voice box. In grown-up people, the larynx is found in the front neck at the degree of the C3–C6 vertebrae. It interfaces the second rate some portion of the pharynx (hypopharynx) with the trachea. The larynx broadens vertically from the tip of the epiglottis to the sub-par outskirt of the cricoid ligament. The voice box comprises of folds, which are known as vocal folds. The vocal folds are also called vocal strings. Main functions of vocal cords are:

1. To shield the airway from chocking on the material within the throat.
2. To control the flow of air into the lungs.
3. The creation of sounds utilized for speech.

P. D. Bhavani (✉) · V. Preethi

Department of Electronics and Communication Engineering, Aditya College of Engineering and Technology, Surampalem, Andhra Pradesh, India

e-mail: pilladevibhavani@gmail.com

V. Preethi

e-mail: preti.santhosh@gmail.com

D. Nandhan

Accendere Knowledge Management Services Pvt. Ltd, CL Educate Ltd, New Delhi, India

e-mail: durgeshnandano51@gmail.com

If anyone of the above functions is not going properly, it results in the problem of larynx. On earth, many people are suffering from throat disorders. Every year, thousands of people who are suffering from throat trauma (disease) require the surgical removal of larynx. The process of removing the larynx from the human body is called laryngectomy. In this process, the surgeons remove the damaged voice box. After laryngectomy, the patients require the alternative method of communication. For that purpose, they require software and augmentative. These include artificial voice sources after the loss of laryngeal function. But these kinds of artificial sources may provide an unnatural voice to the patient. These sources may also require the involvement of users' hands which is complex for the user [1].

There is an innovation that enables individuals with discourse to scatter is automatic speech recognition. In this innovation, the acoustic discourse is converted into the grouping of tokens utilizing design characterization strategies. In this procedure, there are numerical techniques for examining the connection between the vocal tract and its acoustic yield. The connection between the state of the vocal tract and the acoustic yield is spoken to with a scientific articulation that is $y = f(x)$, where y is the acoustic yield and x is the vocal tract shape. Here 'y' can be registered for any estimation of 'x.' Furthermore, for rearranging 'x,' there is a method. Reversal by PC arranging comprises of processing 'y' for some estimation of 'x' and arranging the subsequent (y, x) sets into an advantageous request as per y, x for a given y is then gotten by looking into y in the arranged information. Along these lines, the acoustic yield is arranged (interpreted) into the succession [2].

2 Literature Review

In 1992, Jan Noyes and Clive Frankish estimated that about 15 million people in the United States were suffering from throat disorder. The main application of automatic speech recognition (ASR) is helping people with disabilities. In this paper, it is discussed about the advantages of speech recognition. In the last decade, the recognition performance has been increased due to the increase in the processing power of the microcomputers. The processing power of microcomputers has been increased due to the development of more sophisticated techniques. Now, the speech recognizers are being considered in the industrial tasks and office and aerospace environments. Mainly in three areas, the disabled users are using the speech recognizers, and the areas are 1. communication, 2. environmental control, and 3. medical applications [3].

In 1997, Fangxin Chen and A. Kostov developed the methods for improving the performance of automatic speech recognition (ASR) of slurred speech (dysarthric speech) by exploring the residual vocal ability of people with severe dysarthria. The main application of this technology is to develop the communication and control devices for the dysarthric people. To detect the words in the high-level dysarthric speech, there is an algorithm. A discrete hidden Markov model (DHMM) was also adopted for speech pattern recognition [4].

In 1998, Mauro Becker presented a paper by explaining the importance of Amatsu tracheoesophageal shunt for the patients after laryngectomy. Previously, Radiotherapy and Hypopharynx lesions are employed for speech rehabilitation. By comparing the radiotherapy and hypopharynx lesions with the Amatsu tracheoesophageal shunt is much better. By using this Amatsu tracheoesophageal shunt 76% of vocalization was achieved. Since March 1991, this operation was done in 2 women and 33 men. And their ages are between 30 and 78 years. The main advantage of the Amatsu tracheoesophageal shunt is its inexpensive nature [5].

In 2005, P. D. Polur and G. E. Miller were presented about the Markov model which is helpful to increase the performance of the dysarthric speech recognition system. Dysarthric speech is also known as slurred speech. Dysarthria occurs due to neurological problems. The main aim is to allow the dysarthric patients to control assistive technology. Therefore, this dysarthric speech recognition system acts as a control tool. The fast Fourier transforms are used in dysarthric speech recognition [6].

In 2006, Szuchen Jou, Lena Maierhein, Tanja Schultz, Alex Waibel were presented about the classification of articulatory features based on electromyographic signals. The articulatory features are manner, place, voicing, rounding, front-back, static. The anticipatory behavior of electromyographic signals can be identified by using the recorded audible speech and electromyographic signals. Every articulator has its anticipatory behavior [7].

In 2009, James Heaton, Glen Colby was reported that five surface electromyography sensors were enough for automatic speech recognition. The main aim is to reduce the number of sensors because before 2009 authors reported that 11 surface electromyographic sensors are required for automatic speech recognition and they are fixed on the face and neck of the persons to recognize the speech. The sensors are located on the muscles which are responsible for speech production [8].

In 2010, Harsha Vardhan Sharma proposed the speaker-adaptive recognizers for the persons with spastic dysarthria. The spastic dysarthria is also known as upper motor neuron dysarthria. It occurs due to the strokes, trauma. In this, there are two modifications. They are (1) MAP (maximum a posterior) adaptation of speaker-independent systems, (2) transition-interpolated (linear interpolation between fully ergodic and left-right structures for both speakers adapted and speaker-dependent systems). Based on the above two modifications, there are four results after a few experiments [9].

In 2016, Tanmay Bhowmik reported that the two articulatory features have been identified by using training data. After the identification of features, phonemes are created by merging or combining the features. This experiment was conducted on two persons of Bengal and England, respectively [4].

3 Methodology

There is a well-known way to recognize silent speech by using surface electromyographic sensors. In this, there are two subways in which silent speech can be recognized. But the main component in both the ways is the surface electromyographic sensors. The first one is (a). silent speech recognition using 11 surface electromyographic sensors, and the second one is (b). silent speech recognition using six surface electromyographic sensors. The two ways are briefly described below.

3.1 Speech Recognition Using Eleven s-EMG Sensors

Firstly, eleven surface electromyographic sensors are used to recognize the silent speech. The positions of the s-EMG are fixed. In this case, four sensors are fixed on the face and the remaining seven sensors are fixed on the neck. The sensors which are placed on the face are EMG-8, EMG-9, EMG-10, EMG-11. The sensors which are placed on the neck are EMG-1, EMG-2, EMG-3, EMG-4, EMG-5, EMG-6, EMG-7. The positions of EMG sensors are as Fig. 1.

This experiment was conducted on nine different speakers. In that nine members, four were female and five were male. This experiment was conducted by using 65 words as given below in Table 1. When the experiment was conducted, there was a problem with the order of the words. That problem was, every speaker pronounced the same word for three times.

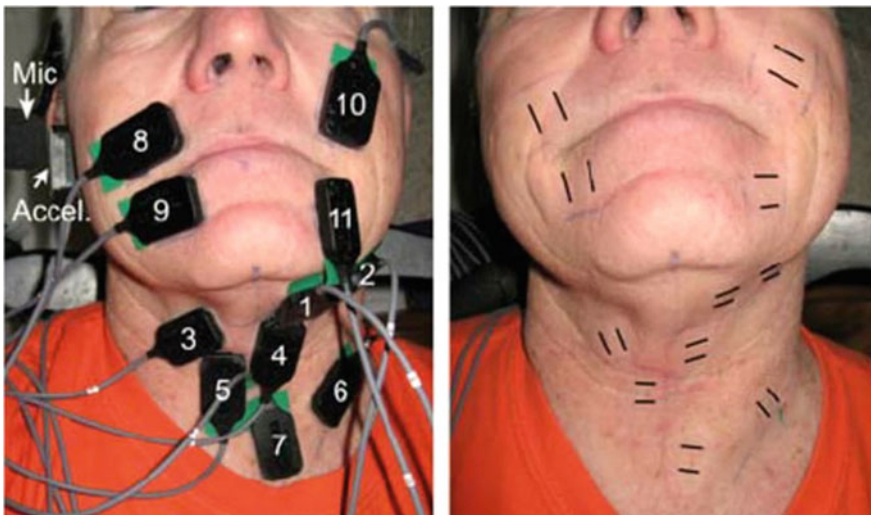


Fig. 1 Person with 11 s-electromyographic sensors

Table 1 65 words used for testing

No	Fire	That	Right	Forward	Negative	Maneuver
Go	Five	This	Seven	Latitude	Hibernate	Affirmative
One	Four	Zero	Target	Location	Position	Coordinates
Six	Help	Abort	Three	Measure	Proceed	Kilometers
Ten	Days	Block	Assist	Recover	Transmit	Rendezvous
Two	Nine	Eight	Brings	Reverse	Thousand	
Yes	Pull	Hours	Cancel	Seconds	Longitude	
Left	Push	Miles	Meters	Hundred	Standby	
Fast	Slow	Point	Collect	Monitor	Shutdown	
Feet	Stop	Reach	Advance	Continue	Accelerate	

Table 2 Recognition approximated accuracy of speakers

Speaker		Recognition approximated accuracy	
Number	Gender	Mouthed (%)	Vocalized (%)
1	Female	87	88
2	Female	83	93
3	Female	90	87
4	Male	78	91
5	Male	93	96
6	Male	91	98
7	Male	89	97
8	Female	89	85
9	Male	69	91
Mean value	-	85.44	91.77

Recognition: As this experiment was conducted on nine members, their speech modalities were calculated. The speech modalities are mouthed and vocalized. The recognition rate was also calculated (Table 2).

Graph: After getting the recognition rate. The graph was plotted by taking the subset size on the *x*-axis and the rate of recognition on the *y*-axis (Fig. 2).

3.2 Speech Recognition Using Six s-EMG Sensors

In this method, only six s-EMG sensors are used to recognize the silent speech. Electromyography is a medical technique used to record the electrical activities of the skeletal muscles. The positions of the six sensors are given below.

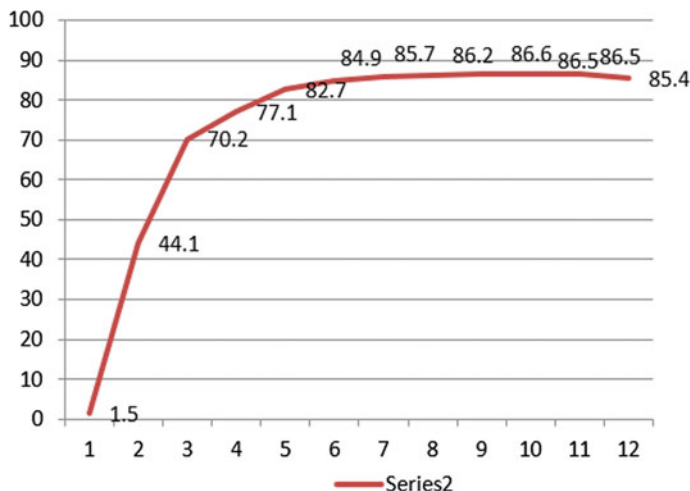


Fig. 2 Recognition rate

- EMG-1 => Under the chin
- EMG-2 => On the cheek (left side of the nose)
- EMG-3 => On the cheek (right side of the nose)
- EMG-4 => Below the EMG-3
- EMG-5 => Under the lower lip
- EMG-6 => On the neck.

This technique works very efficiently because of only six surface electromyographic sensors. This technique is affordable when compared with the technique of 11 sensors.

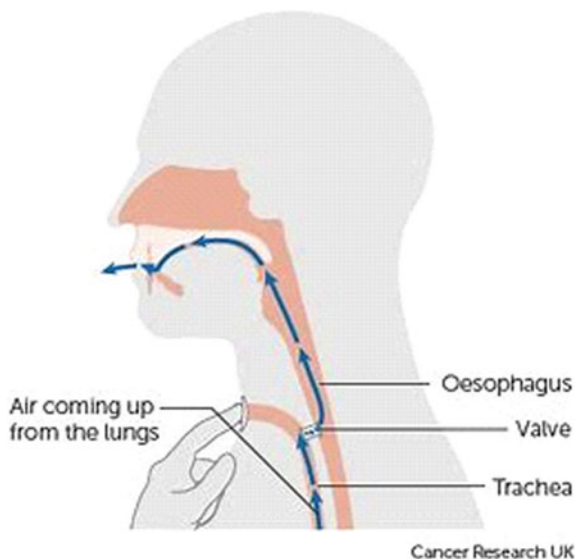
4 Speech Rehabilitation After Laryngectomy

There are four ways for the rehabilitation of speech after laryngectomy. The laryngectomy is the surgical removal of the larynx from the human body. The larynx is the most important tool for a person to communicate with others. The other name for larynx is the voice box. The larynx is located above the trachea and in front of the esophagus. With the removal of the larynx, a person cannot speak.

The four ways of speech rehabilitation are given below.

- Voice prosthesis
- Esophageal voice
- Electronic larynx
- Silent articulation.

Fig. 3 Air movement from lungs to mouth



4.1 Voice Prostheses

Voice prosthesis is also known as the speaking valve. This valve plays a major role in helping the person to speak after laryngectomy. The valve is made up of silicon. The valve is fixed inside the body of the patient at the position of the larynx. It is the fixed back of the stoma and connects the trachea with the esophageal fistula (Fig. 3).

When the person wants to speak, then he/she has to push the valve inside. Then, the airway will be formed between the windpipe and the esophagus. When the person pushes the valve, then the air from the lungs passes through the valve and reaches the esophagus which makes the person speak. But the voice of that person is not natural, and that voice is known as tracheoesophageal voice (Fig. 4).

4.2 Esophageal Voice

The person with an esophageal voice has to push the air from his/her mouth down to the esophagus. And he/she has to back up the air again. As the air passes, the pharyngoesophageal segment vibrates, which results in the production of speech. For this kind of speech, the person has to train very well. Because he/she has to swallow the air from the mouth and again he/she has to release it out all the time (when he/she want to speak). But this voice is not fluent and louder.

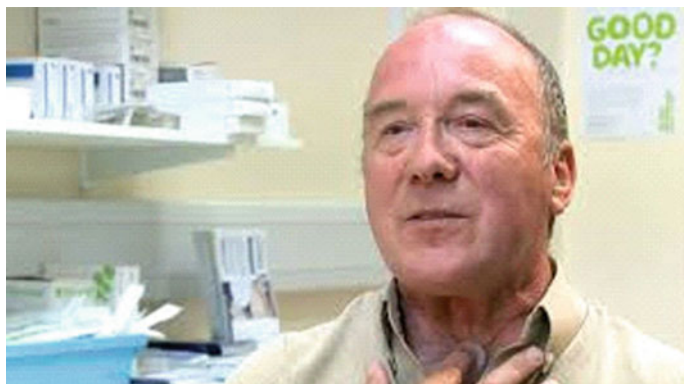


Fig. 4 Person with voice prosthesis

4.3 *Electronic Larynx*

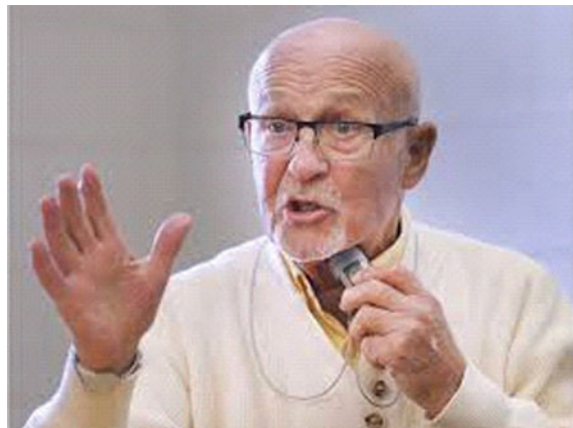
The electronic larynx is also known as servox. It is most commonly used in the UK. It is a mechanical vibrating device. It has no connection with the body. But the person has to carry it along with him (Fig. 5).

When the person wants to speak, then he/she has to place that device at the side of the neck. Then, the electronic signals pass through the tissues of the face and reach the mouth. Then, a kind of electronic sound (speech) will be produced (Fig. 6).



Fig. 5 Electronic larynx

Fig. 6 Person with electronic larynx



4.4 *Silent Articulation*

This is a kind of voice, in which a person may not speak using the speaking valve and he/she may not have the esophageal voice and he/she may not be able to have the electronic larynx. Then, that person will articulate silently. To understand what that person is telling, others should watch the person's lips very carefully.

5 Conclusion

This paper clearly shows the techniques of speech rehabilitation after laryngectomy. This paper also shows the types of voices after laryngectomy. It also consists of speech rehabilitation techniques using 11 surface electromyography sensors and six surface electromyographic sensors. Finally, as the speech is the most important thing for every human being, this paper clearly shows the way for the people with a laryngectomy.

References

1. Colby G, et al (2009) Sensor subset selection for surface electromyography based speech recognition. In: ICASSP, IEEE international conference on acoustics, speech and signal processing, pp 473–476
2. Atal BS, Chang JJ, Mathews MV, Tukey JW (1978) Inversion of articulatory-to-acoustic transformation in the vocal tract by a computer-sorting technique. J Acoust Soc Am 63(5):1535–1555. <https://doi.org/10.1121/1.381848>
3. Noyes JM, Frankish CR (1992) Speech recognition technology for individuals with disabilities. Augment Altern Commun 8(4):297–303. <https://doi.org/10.1080/07434619212331276333>

4. Bhowmik T, et al (2017) A comparative study on phonological feature detection from continuous speech with respect to variable corpus size. In: 2016 IEEE Students' Technol Symp Tech Sym, pp 311–316. <https://doi.org/10.1109/TechSym.2016.7872702>
5. Polur PD, Miller GE (2005) Predictive and cepstral coefficients in dysarthric speech 13(4):558–561
6. Vieira MBM et al (1999) Speech rehabilitation after laryngectomy with the Amatsu tracheo-esophageal shunt. *Auris Nasus Larynx* 26(1):69–77. [https://doi.org/10.1016/S0385-8146\(98\)00065-0](https://doi.org/10.1016/S0385-8146(98)00065-0)
7. Jou SC, Maier-Hein L, Schultz T, Waibel A (2006) Articulatory feature classification using surface electromyography. In: 2006 IEEE international conference on acoustics speech and signal processing proceedings, Toulouse, France, pp 605–608
8. Colby G, Heaton JT, Gilmore LD, Sroka J, Deng Y, Cabrera J, Roy S, De Luca CJ, Meltzner GS (2009) Sensor subset selection for surface electromyography based speech recognition. In: 2009 IEEE international conference on acoustics, speech and signal processing, Taipei, Taiwan
9. Meltzner GS et al (2017) Silent speech recognition as an alternative communication device for persons with laryngectomy. *IEEE/ACM Trans Audio Speech Lang Process* 25(12):2386–2398. <https://doi.org/10.1109/TASLP.2017.2740000>

CNN-Based Individual Ghungroo Breed Identification Using Face-Based Image



Kaushik Mukherjee, Sanket Dan, Kunal Roy, Subhojit Roy, Subhranil Mustafi, Pritam Ghosh, Satyendra Nath Mandal, Dilip Kumar Hajra, Santanu Banik, and Syamal Naskar

Abstract Convolutional Neural Network (CNN) is widely used as a strong framework for object classification. This framework is suitable for classification of group of objects which carry similar features like animal breeds, plant varieties, etc. In this paper, an attempt has been made to build a model of identifying individual Ghungroo pig (one of the most popular registered pig breeds in India) based on its face image using CNN. Individual Ghungroo pigs look very similar, and it is a very challenging task even for humans to identify them from a group of Ghungroo pigs. Ten Ghungroo pigs from ICAR-Indian Veterinary Research Institute (IVRI) Animal Farm Kalyani (Block B, Kanchrapara, West Bengal 741235) have been captured using a DSLR camera. The pigs have been captured in natural environment without any restriction. The Inception-v3 model with transfer learning has been used to build the individual pig identification model. The captured images have been separated with 90%:10% into training images and test images sets, respectively. It has been observed that the model has predicted individual pigs with 100% accuracy at 0.87 confidence level.

K. Mukherjee · S. Dan · K. Roy · S. Mustafi · P. Ghosh · S. N. Mandal (✉)
Department of Information Technology, Kalyani Government Engineering College, Kalyani,
Nadia, West Bengal 741235, India
e-mail: satyen_kgec@rediffmail.com

K. Mukherjee
e-mail: kaushik8.m@gmail.com

S. Roy
Gangarampur Government Polytechnic College, Gangarampur-Belbari Road, Kadighat,
Gangarampur, West Bengal 733124, India

D. K. Hajra
Department of Agronomy, Faculty of Agriculture, UBKV, Pundibari, Cooch Behar 736165, India

S. Banik
ICAR-National Research Centre On Pig, Rani, Guwahati, Assam 781131, India

S. Naskar
Indian Veterinary Research Institute (IVRI) Eastern Regional Station (ERS), 37, Belgachia Road,
Kolkata 700037, India

Keywords Deep learning · Convolutional neural network (CNN) · Object classification · Ghungroo pigs · Accuracy · Confidence level

1 Introduction

It is very obvious for any farm to track their animal (individual as well as breed) in an efficient manner; otherwise, it leads to some fraudulent activity. Traditional ways to identify the livestock animal such as ear tag (electronic/non-electronic), tattoo, etc., is not healthy enough with respect to sustainability and those are also distressing the animal. So there has always been a search for an optimized way to identify the livestock animal which will longlasting as well as not to distress the animal too much. Biometric models can play a vital role in this situation. There has been a tremendous effort on the research of finding a better biometric model to identify the livestock animal. Some of them are iris recognition, ear venation pattern, face recognition, etc. Some successfully identify the animal with good accuracy.

In this paper, face-based images of ten Ghungroo pigs have been captured by a DSLR camera without making any restriction. A total of 874 images have been capture in the natural environment. The ten distinct folders have been created with names Pig1, Pig2, ..., Pig9 and Pig10 to store captured pictures. The captured images have been stored into individual pig folders. The images kept in individual folders have been separated as training images: test images with 90%:10% ratio. That means if one individual pig folder contains 100 images; then, 90 images go to training images and the rest ten images kept for testing purposes which were not part of the training process. One model has been proposed based on the Inception-v3 model where ten separate outputs give ten values from 0.0 to 1.0. The feature extraction of Inception-v3 model kept intact, but the classification outputs have been changed into ten for ten pigs. The height value in one output has been indicated by the corresponding individual. The model has been trained in 200,000 iterations with learning rate 0.01. Once the training process was completed, the test process was run with the test images. This model has achieved the recognition accuracy of 100% with confidence level of 0.87. The CNN is generally used for set of objects classification, but the individual pig has been identified here. This type of effort has not been done earlier. This is the reason for making this paper.

The paper is divided as follows: In Sect. 2, previous work of the classification process is described followed by creation of image data set in Sect. 3. A brief description is discussed in the Sect. 4. Finally comes to architecture of proposed model which is shown in Sect. 5 followed by result and discussion and conclusion and future work in Sects. 6 and 7, respectively.

2 Previous Work

Recognition of human through face has been a popular research area for at least five decades [1]. Historically, geometric features extracted from face images have been used for face recognition [2, 3] and now the recent trend is to apply deep networks which has really improved the recognition performance in a high level. The fundamental idea of applying deep networks has come from the human nervous system (which is nothing but accumulation of infinite number of neurons). The face recognition system is widely used for “non-intrusive access control and monitoring/surveillance purposes and as such represents a potentially useful research area to apply to the problem of pig identification”. Although there has been a lot of related work done on livestock animals, few such as automatically identify the pig behaviours [4], biometric on livestock animal [5–10], breed identification on livestock animals [11] show very good result. Although there was little research on pig identification where pig face was used as a biometric tool, eigenface technique [12] was used and achieved 77% recognition accuracy on ten pigs, in this paper full manually cropped face was used. Another research was on the pig face [13] where augmented pig face was used as a data set for CNN and achieved 96.7%. In this paper, original data has been used without any augmentations and achieved 99.73% recognition accuracy.

3 Image Data set

Images were collected from ICAR-Indian Veterinary Research Institute (IVRI) Animal Farm Kalyani (Block B, Kanchrapara, West Bengal 741235) using DSLR camera (Nikon) with 18–55 mm lens (min focal length 18 mm and optical zoom 0.38X). The farm has been visited many times and collected face images of ten individual Ghungroo pigs. A total of 60–70 face images have collected per individual pig and collected 874 raw images in total. After that ten folders were created for ten individual pigs and renamed these folders as Pig1, Pig2, up to Pig10. The images are placed in respective folders, and all the ten folders are kept in a separate folder and renamed as “Pig Data” (Fig. 1).

4 Convolutional Neural Network and Inception V3 Model

Convolutional neural network (CNN, or ConvNet) is a special kind of multi-layer neural networks, designed to recognize visual patterns directly from pixel images with minimal preprocessing. It has two parts—one is feature extraction, and other is recognition. In this paper, Inception-v3 pretrained model developed by Google Inc. has been used to develop the proposed model. The architecture of CNN with



Fig. 1 Pig face image

convolution, max pooling and fully connected layer [14] is depicted in Fig. 2. In the convolution layer, kernel or filter K of specific dimension is applied over each position on the input image or feature map x . The function provides the following output (Eq. 1) [15]

$$x_n^k = \sum_{m \in M_n} x_m^{k-1} \times K_{mn}^k + b_n^k \quad (1)$$

where b_n represent bias, k is the layer number and M_n is the feature map from n channels. The size of the feature map can be estimated by using Eq. (2)

$$\text{size of feature map} = \frac{\text{input dimension} - \text{kernel dimension}}{\text{stride}} + 1 \quad (2)$$

The obtained feature maps from each layer are carried forward to subsequent convolution layer. This layer is responsible for feature extraction from an input image based on a mathematical calculation. The mathematical calculation is basically an element-wise multiplication with respect to filter and matrix. If the input image matrix is of dimension $[a \times b \times c]$ and filter matrix is of dimension $[f_1 \times f_2 \times f_3]$, then the dimension of output matrix will be

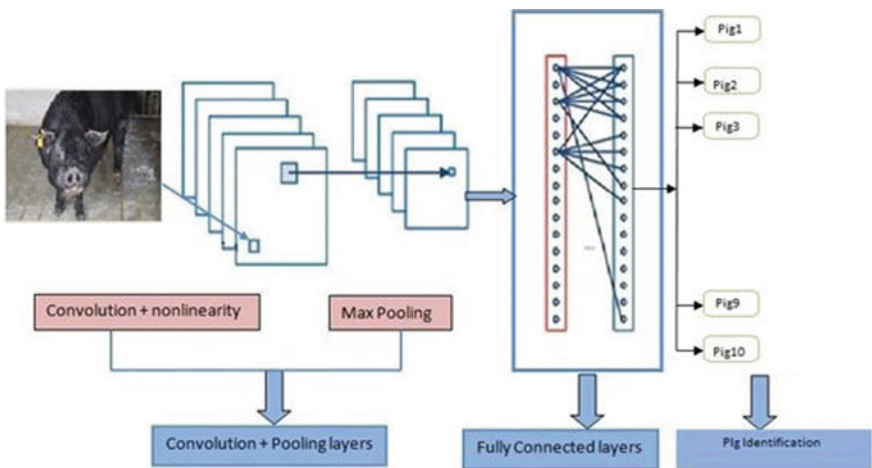


Fig. 2 Convolutional neural network for pig identification

$$(a - f1 + 1) * (b - f2 + 1) * 1 \quad (3)$$

Pooling layer (depicted in Fig. 3) is responsible for reduction in the dimension of the feature matrix obtained from the convolution layer in order to reduce computational cost as well as to prevent overfitting. Among different types of pooling, max pooling is popular and widely used for its ability to reduce the dimension without losing important information. After creating feature vector, it is then passed through a dense neural network for classification. This dense network is called fully connected layer (Fig. 4). Actually in fully connected layer, the classification is determined by the softmax which is nothing but an activation function. The softmax layer gives the output as 0 and 1. The following equation is responsible for the softmax function (Eq. 4).

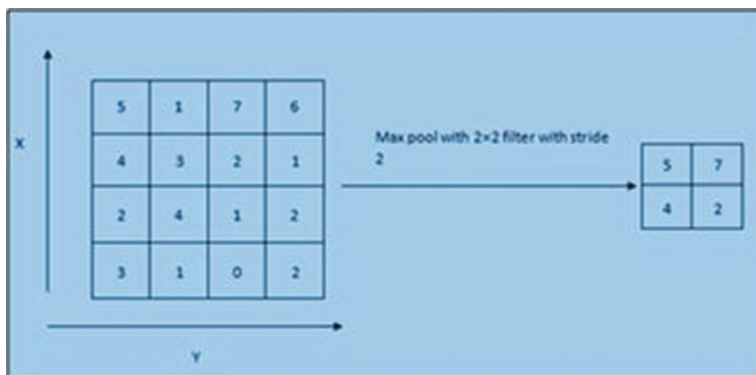
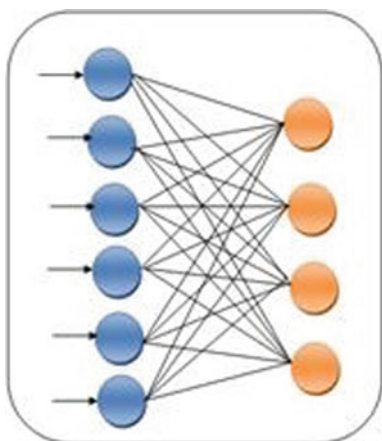


Fig. 3 Max pooling in CNN

Fig. 4 Fully connected (or dense) layer in CNN



$$\sigma(z)_j = \frac{e^{z_j}}{\sum_{k=1}^K e^{z_k}} \quad (4)$$

Above equation (Eq. 4) implies that the output activations are all positive, since the exponential function is positive. By contrast, if the output layer was a sigmoid layer, then certainly could not assume that the activations formed a probability distribution. This cannot explicitly be proved, but it might be plausible that the activations from a sigmoid layer will not be in general form of a probability distribution. And so a sigmoid output layer does not have such a simple interpretation of the output activations.

5 Proposed Model

In this paper, the prediction model has been proposed based on Inception-v3 pretrained model in transfer learning mode. The feature extraction layers of Inception-v3 have been kept intact, and the classification part has been changed for the individual pig identification. Finally, the pretrained Inception-v3 has been retrained with training pig image data set. The retrained model has been tested with pig image data set as shown in Fig. 5. The images of all individual pigs have been separated in certain distinct folders and renamed them to Pig1, Pig2, ..., Pig10 and put them in a folder called Pig Data. The subfolder names were written (as in the order in Pig Data) in the “retrained labels.txt” file. After training, a “tmp” folder was created automatically in the system disc drive where images were saved and labelled. From the “tmp” folder, the “output graph.pb” and “output labels.txt” files were copied and then pasted in the folder where “classify.py” file was located. This process enabled the programme to classify test images in the newly trained model.

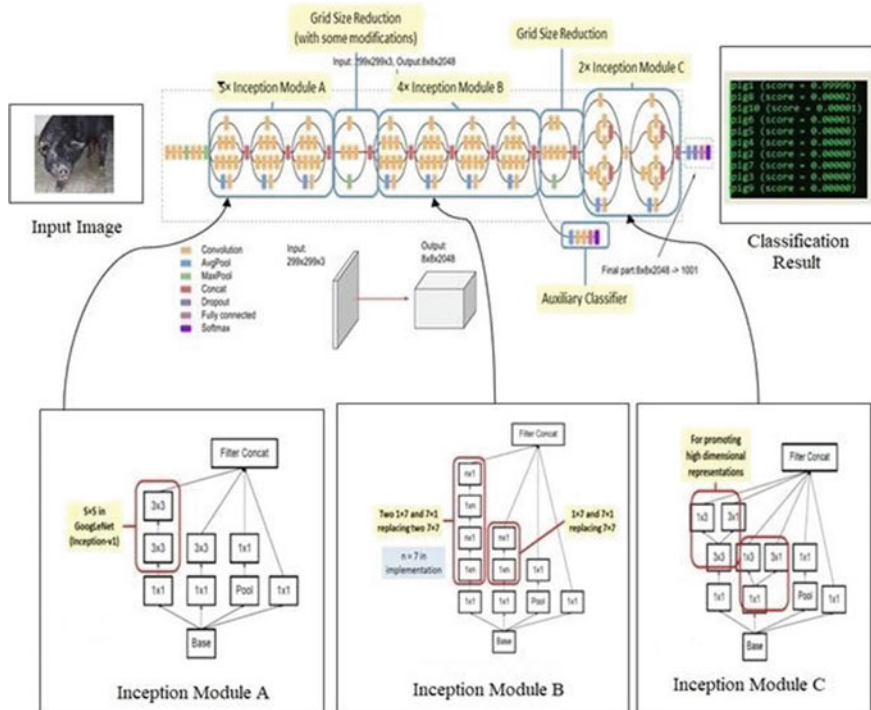


Fig. 5 Proposed architecture for individual pig identification based on Inception-v3

As there were ten subfolders, then there were ten output lines which gave the ten distinct values, and the highest value implies the respective pig.

6 Result and Discussion

The model has ten outputs for identification of ten individual pigs. There were ten distinct values for every result which has been produced from every test image. The maximum number of those results implies the respective pig. That means if the test result was 0.00004, 0.98863, 0.00013, 0.00009, 0.00026, 0.00431, 0.00059, 0.00402, 0.00089, 0.00104 (all are representing the confidence level) for Pig1, ..., Pig10, respectively, for a test image, then the result implies that the input test image was Pig2. Table 1 consists of the overall result. The model has been tested with various confidences levels from 0.87 to 0.99 for all test pig images as shown in Table 2, Fig. 6 depicts the graphical representation of accuracy vs. different confidence level with respect to pig, and Fig. 7 depicts the average accuracy vs confidence level. The accuracy of proposed model has been compared with some accuracies of different problem of object detection published in different research paper is shown in Table 3.

Table 1 Summary of training set and test set results (with confidence level 0.87)

Ghungroo_pig individual	Accuracy in training set (%)	Accuracy in test set (%)
Pig1	100	100
Pig2	100	100
Pig3	100	100
Pig4	100	100
Pig5	100	100
Pig6	100	100
Pig7	100	100
Pig8	100	100
Pig9	100	100
Pig10	100	100

The images of individual pig have been captured in natural environment without any restriction, and all captured images have been used in training and testing sets. There was no threshold of accepting images based on pixel resolution, lighting conditions and distance between camera and pig and also their movements. That is why the accuracies are decreasing with increasing of confidence level. The model has given lower accuracy in increasing the confidence level. The accuracy is given in published paper without mentioning confidence level.

7 Conclusion and Future Work

In this paper, the proposed model has given prediction accuracies from 100 to 76.67% with confidence levels from 0.87 to 0.99. The result has been given based on limited pig image data set (total 874 images). The pictures have been captured without restraining the pigs and without any control. The model has given better result compared to other results published in different research papers. The accuracies have been obtained from all captured images without image accepting threshold like pixel resolution, lighting conditions and distance between camera and pig and also their movements. The model will be applied for prediction on more pigs, and it will be tested on other pig breeds. The pig images will be collected from various ages of the same pig, from different organized farms for same or different pig breeds in future.

Table 2 Confidence level versus accuracy
Accuracy in various confidence levels (in %)

Sl. No	Pig	0.99	0.98	0.97	0.96	0.95	0.94	0.93	0.92	0.91	0.90	0.89	0.88	0.87
1.	Pig1	83.33	83.33	83.33	83.33	83.33	83.33	83.33	83.33	83.33	100	100	100	100
2.	Pig2	83.33	100	100	100	100	100	100	100	100	100	100	100	100
3.	Pig3	50	66.67	66.67	66.67	83.33	83.33	100	100	100	100	100	100	100
4.	Pig4	83.33	83.33	100	100	100	100	100	100	100	100	100	100	100
5.	Pig5	100	100	100	100	100	100	100	100	100	100	100	100	100
6.	Pig6	50	50	50	66.67	66.67	66.67	66.67	66.67	83.33	100	100	100	100
7.	Pig7	83.33	100	100	100	100	100	100	100	100	100	100	100	100
8.	Pig8	83.33	83.33	83.33	83.33	100	100	100	100	100	100	100	100	100
9.	Pig9	66.67	66.67	66.67	66.67	66.67	83.33	83.33	83.33	83.33	100	100	100	100
10.	Pig10	83.33	83.33	83.33	83.33	83.33	83.33	83.33	83.33	83.33	83.33	83.33	83.33	100
	Avg._accuracy	76.665	81.666	83.333	83.333	88.333	89.999	91.666	91.666	92.333	98.333	98.333	98.333	100

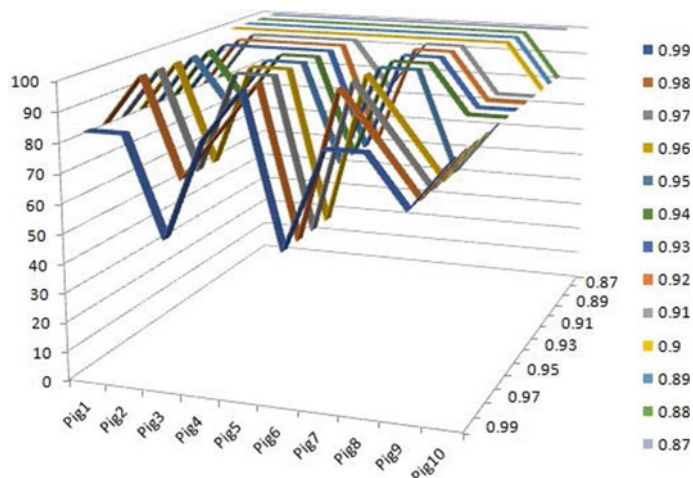


Fig. 6 Accuracy versus different confidence level with respect to pig

Fig. 7 Average accuracy versus confidence level

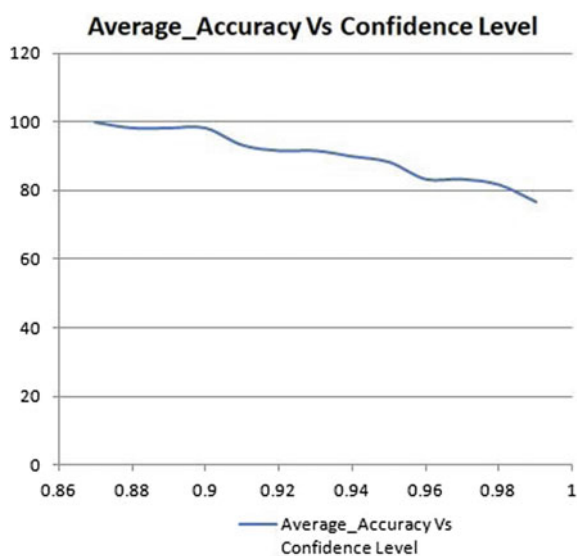


Table 3 Accuracy level different object prediction

Author	Crop	Deep learning model	Accuracy (%)
Liu et al. [15]	Apple	AlexNet precursors with inception module	97.62
Ma et al. [16]	Cucumber	DCNN, based on Lenet5	93.4
Aravind et al. [17]	Grape	AlexNet with SVM	99.23
Brahimi et al. [18]	Tomato	AlexNet	97.71
Lu et al. [19]	Rice	DCNN	95.48
Proposed algorithm	Individual pig identification	Proposed model (with confidence level 0.87)	100

Acknowledgements The authors would like to thank Dr. Amitabha Bandyopadhyay, Senior Consultant, ITRA Ag&Food for his valuable suggestions in this research work. The authors would also like to thank Dr. Sourabh Kumar Das, Principal, Kalyani Government Engineering College, Kalyani, Nadia, for his continuous support.

References

1. Bledsoe WW (1966) Man-machine facial recognition. Panoramic Research Inc., Palo Alto, CA
2. Turk M, Pentland A (1991) Eigenfaces for recognition. *J Cognit Neurosci* 3(1):71–86
3. Belhumeur PN, Hespanha JP, Kriegman DJ (1997) Eigenfaces versus fisher faces: recognition using class specific linear projection. *IEEE Trans Pattern Anal Mach Intell* 19(7):711–720
4. P. Ahrendt, T. Gregersen, H. Karstoft (May, 2011) Development of a real-time computer vision system for tracking loose-housed pigs. *Comput Electron Agric* 76(2):169–174
5. Gaber T, Tharwat A, Hassani AE, Snasel V (March, 2016) Biometric cattle identification approach based on Weber's Local Descriptor and AdaBoost classifier. *Comput Electron Agric* 122(Supplement C):55–66
6. Kumar S, Singh SK, Singh AK (October, 2017) Muzzle point pattern based techniques for individual cattle identification. *IET Image Process* 11:805–814
7. Tharwat A, Gaber T, Hassani AE (November, 2014) Cattle identification based on Muzzle images using Gabor features and SVM classifier, advanced machine learning technologies and applications, communications in computer and information science, Springer, Cham, pp 236–247
8. Allen A, Golden B, Taylor M, Patterson D, Henriksen D, Skuce R (July, 2008) Evaluation of retinal imaging technology for the biometric identification of bovine animals in Northern Ireland. *Livest Sci* 116(1):42–52
9. Gonzales Barron U, Corkery G, Barry B, Butler F, McDonnell K, Ward S (March, 2008) Assessment of retinal recognition technology as a biometric method for sheep identification. *Comput Electron Agric* 60(2):156–166
10. Kumar S, Singh SK (December, 2016) Monitoring of pet animal in smart cities using animal biometrics. *Future Gener Comput Syst*

11. Mandal SN, Ghosh P, Mukherjee K, Dan S, Mustafi S et al (2020) InceptGI: a ConvNet-Based classification model for identifying goat breeds in India. *J Inst Eng (India): Ser B*
12. Wada N, Shinya M, Shiraishi M (2013) Pig face recognition using Eigenspace method. *ITE Trans Media Technol Appl* 1(4):328–332
13. Hansen MF, Smith ML, Smith LN, Salter MG, Baxter EM, Farish M, Grieve B (2018) Towards on-farm pig face recognition using convolutional neural networks. *Comput Ind* 98:145–152
14. Szegedy C (2015) Going deeper with convolutions. Proceedings of the IEEE conference on computer vision and pattern recognition
15. Liu B, Zhang Y, He D, Li Y (2018) Identification of apple leaf diseases based on deep convolutional neural networks. *Symmetry* 10(1):11
16. Ma J, Keming D, Zheng F, Zhang L, Gong Z, Sun Z (2018) A recognition method for cucumber diseases using leaf symptom images based on deep convolutional neural network. *Comput Electron Agric* 154:18–24
17. Aravind KR et al (2018) Grape crop disease classification using transfer learning approach. International conference on ISMAC in Computational Vision and Bio-Engineering. Springer, Cham
18. Brahim M, Boukhalfa K, Moussaoui A (2017) Deep learning for tomato diseases: classification and symptoms visualization. *Appl Artif Intell* 31(4):299–315
19. Yang L, Yi S, Zeng N, Liu Y, Zhang Y (2017) Identification of rice diseases using deep convolutional neural networks. *Neurocomputing* 267:378–384

Development of Image-Based Disease Scale of Phoma Blight of Potato Using k -Means Clustering



Kunal Roy, Sanket Dan, Kaushik Mukherjee, Subhranil Mustafi, Pritam Ghosh, Satyendra Nath Mandal, Subrata Dutta, and Ashis Chakraborty

Abstract Disease identification of the plant at an early stage is a key to prevent the major diseases by minimal application of chemical pesticides. In West Bengal, phoma blight is now becoming an emerging dreaded disease of potato. Phoma blight is associated with development of numerous spots on leaflets, thereby reducing green photosynthetic area causing huge loss in potato tuber production. The disease rating scale for severity analysis has not been developed for this disease till now. In this paper, an image-based phoma blight disease rating scale has been developed using k -means clustering. The image of phoma blight affecting potato leaflets has been captured using a DSLR camera by placing white paper background of leaflets. The percentage of affected areas has been calculated and an image-based phoma disease scale has been developed. The number of affected leaflet images has been given to several plant pathologists and they have assigned disease rating scores based on eye estimations. The score has been assigned for each leaflet considering the maximum number of same scores assigned by plant pathologists. The disease rating has also been assigned based on the actual affected area within each leaflet image using k -means clustering. The comparison has been performed between eye estimated scoring and k -means-based scoring to verify the scale. Finally, it has been observed that the new developed disease rating scale has given 87% accuracy in disease estimation with plant pathologists.

Keywords Phoma blight · k -means clustering · Euclidean distance · Disease rating scale

K. Roy · S. Dan · K. Mukherjee · S. Mustafi · P. Ghosh · S. N. Mandal (✉)
Department of Information Technology, Kalyani Government Engineering College, Kalyani,
Nadia, West Bengal 741235, India
e-mail: satyen_kgec@rediffmail.com

K. Roy
e-mail: kunalroy4mkolkata@gmail.com

S. Dutta · A. Chakraborty
Department of Plant Pathology, Bidhan Chandra Krishi Viswavidyalaya, Mohanpur, West Bengal
741252, India

1 Introduction

Phoma blight is widely visible in many subcontinents which causes severe damages in the potato production. It is a fungal disease. The symptom of the disease is found on the leaflets. The early detection of the disease can be reduced the economic loss of the farmer. Traditionally, phoma blight is detected through the naked eye observation by the crop scout. The intensity of disease is measured by expert and plant pathologists. They are assigned numbers, 0, 1, 3, 5, 7 and 9 based on eye estimated affected area within leaflet, leaf and whole plant. k -means algorithm provides good clustering result based on the Euclidean distance between several data points [1]. Disease of the leaf spot can be identified using k -means clustering method as the color intensity of the spot is different from the leaf color [2]. Prajapati et al. had identified the rice plant disease using centroid feeding-based k -means clustering method and extract the various features like shape, color and texture. Based on different features, they have developed a support vector machine (SVM) for multiclass classification [3]. Manikrao et al. have identified disease of the cotton crop using image processing technique [4]. In their proposed method, HSV-based model has used and classification has done based on SVM method. Zhang et al. have used the k -nearest neighbor method classifier to recognize the plant disease. [5]. Khirade et al. in their paper have used the ANN method for classification of disease spot after considering H and B color feature from HSV and LAB image [6].

In this paper, images of the unaffected and affected potato leaves due to phoma blight have been captured with a DSLR camera placing white A4 paper below them. The captured pictures are sent to seven plant pathologists for assigning disease scores on each affected leaflet. One disease score has been assigned on affected leaflet after considering same maximum scoring assigned by maximum plant pathologists. The same affected leaflets have also been processed for calculating actual area affected by phoma using k -means clustering. At first, all captured images are resized to make them similar in size. The k -means clustering has been used to cluster green area and affected portion of leaflets. The affected area and whole area of each leaflet have been calculated and percentage of affected area has been measured. One new disease rating scale 0, 1, 3, 5, 7 and 9 has been proposed and image-based scoring has been assigned on same leaflets which have been sent to plant pathologists. One comparison has been made between eye estimated scoring and k -means-based scoring to verify the proposed scale. This type of effort has not been made in measurement of intensity of phoma blight earlier. This is the reason for making this paper. The paper is divided as follows: Introduction in Sect. 1. In Sect. 2, creation of Phoma Blight Image Dataset, disease rating scale and k -means clustering are described. A brief description proposed algorithm for image-based disease rating scale development is discussed in Sect. 3. Finally comes to result and discussion which is shown in Sect. 4 followed by conclusion and future work in Sect. 5.

2 Phoma Blight Dataset, Disease Rating Scale and *k*-Means Clustering

Phoma Blight Image Dataset

The unaffected and affected potato leaflets, leaves and plants have been captured by DSLR camera at c block farm, Bidhan Chandra KrishiVidyalaya, Kalyani, Nadia, West Bengal-741235. The 1000 potato leaflet has been captured during image acquisition and stored them at phoma blight potato leaflets database.

Disease Rating Scale

The intensities of diseases are measured using disease rating scales. The healthy leaves or plants are assigned scale “0” and dry leaves or plants or maximum portions which are affected by disease are assigned scale “9.” The scores between 0 and 9 are divided into either 1, 3, 5, 7 or 1, 2, 3, 4, 5, 6, 7, 8 scales. The scores are assigned by plant pathologists based on their eye estimation. The percentages of affected area along with their associated scores based on eye estimation are given in Fig. 1.

k-means Clustering

k-means is the simplest method to solve the clustering problem. Main idea of this clustering is to find out *k* centroid for each cluster. Centroid should be placed in the different location of the cluster space. Each pixel has a specified location. Assign each pixel to the group which is closest to the centroid. This grouping has been done based on the Euclidean distance metric. This algorithm aims at minimizing a squared error function. The equation is given in Fig. 2.

Fig. 1 Percentages of affected leaflets

		
0%(score:0)	1-10%(score:1)	10-20%(score:3)
		
20-30%(score:5)	30-50%(score:7)	>50(score:9)

$$J = \sum_{j=1}^k \sum_{i=1}^n \left\| x_i^{(j)} - c_j \right\|^2 \quad (1)$$

where $\left\| x_i^{(j)} - c_j \right\|^2$ is a chosen distance measure between a data point $x_i^{(j)}$ and the cluster centre c_j , is an indicator of the distance of the n data points from their respective cluster centres.

Fig. 2 Objective function of k -means clustering

3 Proposed Algorithm for Image-Based Disease Rating Scale Development

The algorithm named “IBPBRS” has been proposed to calculate actual phoma blight affected area of leaflet images of potato. The algorithm will take phoma blight affected leaflets and it will give percentage of affected area due to phoma blight. Finally, one disease scoring will be given based on percentage of affected area. The algorithm has been presented into flow chart in Fig. 3.

The detail descriptions of algorithm are as follows.

Image Acquisition

Images of both healthy and disease affected leaves have been captured using DSLR camera in different daylight conditions. The dry potato leaves and soil color are looked similar. To reduce this problem, the leaflets, leaves and plants have been captured by placing a white A4 paper below them. Images with low contrast, unwanted leaflets and noise were discarded. Image acquisition process is shown in Fig. 4.

Pre-processing

Both healthy and phoma affected leaf images acquisition process. The images with white background were resized into 1000×1280 pixel for making all pictures in same size. The unwanted area of the background; outside of A4 paper have been discarded for keeping the background as white (Fig. 5).

Affected Area Segmentation

In segmentation, the k -means clustering has been used for classification of the affected portion due phoma blight and unaffected part. At first RGB leaflet images have been converted into $L * a * b$ color space. $L * a * b$ color space consists of luminosity layer L^* which is lightness from black to white, chromaticity-layer “ a^* ” specify where the color falls along the red–green axis, and chromaticity-layer “ b^* ” specify where the color falls along the blue–yellow axis. All the color information has been stored in a and b layer which has been used for measuring the Euclidean distance metric for classification. In k -means clustering, each pixel has positioned a specified location in the cluster space. In this experiment, three clusters have been used. Out of these

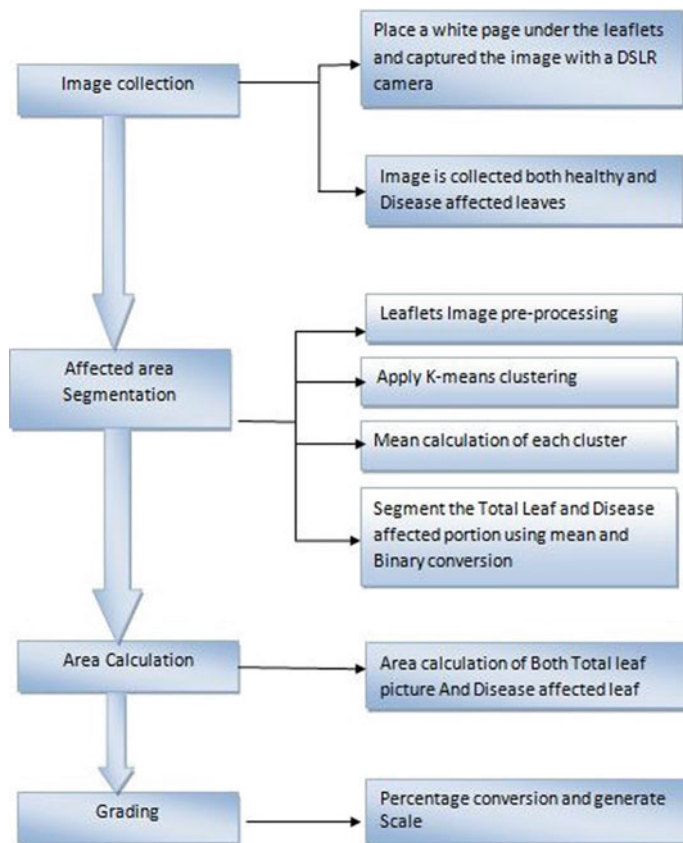


Fig. 3 “IBPBRS”—image-based phoma blight rating scale



Fig. 4 Image acquisition

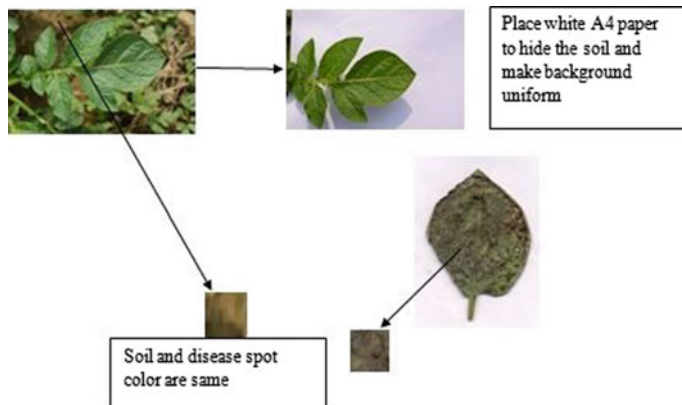


Fig. 5 Pre-processing

three clusters classification, two clusters have been used in this experiment whereas one cluster which only contains affected area, another has full outline of the leaf (shown in Fig. 6). The aim of this paper is to find out the total outline of leaf image and affected portion of leaflet. Mean of the each cluster was calculated. The total outline of the leaf images has the maximum mean value and affected portion of the image cluster has the minimum mean (Fig. 7). We can easily isolated total leaf and affected portion of the leaf.

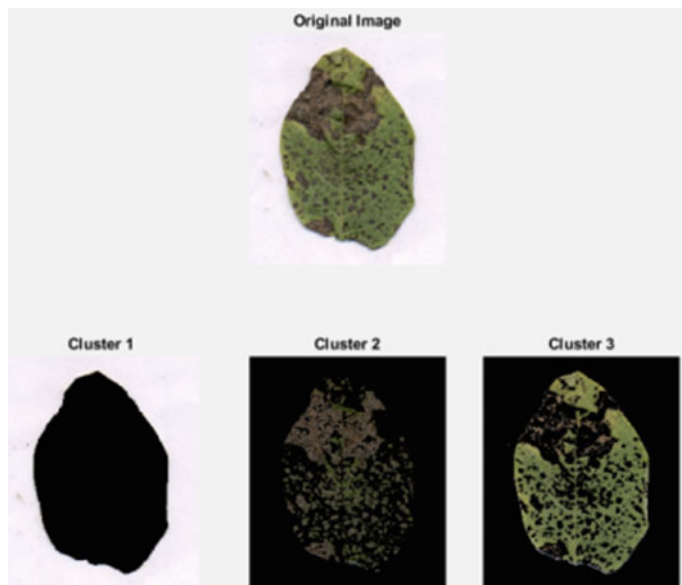


Fig. 6 Image segmentation using k -means clustering



Fig. 7 Disease affected leaf after segmentation

Calculation of image-based scoring of Phoma

Total outlined leaf image and affected portion images are considered for scoring. Total area each clustered image was measured, divided the affected leaf portion area by the total leaf area and calculate the percentage (shown in Fig. 8).

Proposed Disease Rating Scale

One disease rating scale for phoma blight is proposed at Table 1. The scale is divided into six grades 0, 1, 3, 5, 7 and 9 where score 0 indicates there is no disease and 9 indicates disease percentage greater than 55%. The proposed algorithm will be calculated the percentages of affected area due to phoma blight and announce the grade.

$$\text{Affected percentage value} = \frac{\text{affected portion area}}{\text{Total outlined leaf image area}} \times 100 \quad (2)$$

Fig. 8 Calculation of affected percentage

Table 1 Proposed disease rating scale

Score/Grade	Percentage	Disease intensity
0	0.0	No disease
1	0–10	Small disease area has been identified
3	10.1–25	Lesions area between 10.1 and 25% of total leaf
5	25.1–40	Lesions area between 25.1 and 40% of total leaf
7	40.1–55	Lesions area between 40.1 and 55% of total leaf
9	>55	Lesions area are greater than 55% of total leaf

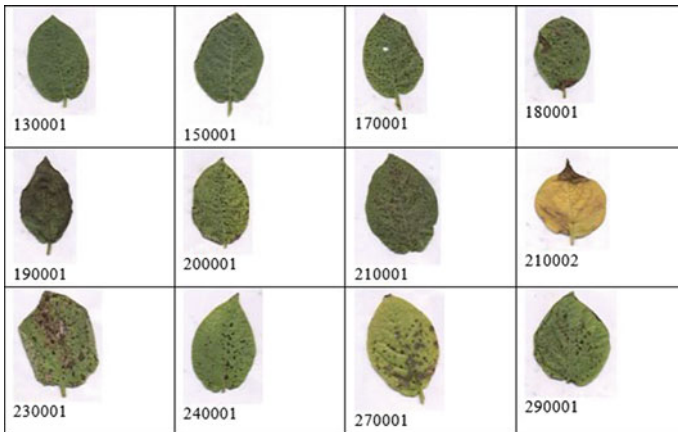


Fig. 9 Sample pictures from “phoma blight potato leaflets”

Phoma Blight affected Leaflets database

The leaflets have been captured keeping white A4 paper below them using DSLR camera. The captured phoma blight affected leaflets are about 1000 pictures and they are stored into “phoma blight potato leaflets” database. Some captured pictures with their picture identification number from database are shown in Fig. 9.

4 Result and Discussion

In this paper, the captured potato phoma affected leaflets have been processed based on proposed algorithm and scoring have been assigned on each leaflet using proposed disease rating scores. Same pictures are sent to seven plant pathologists to assign disease rating scores. The maximum number of scoring with the same values, the assigned scoring of plant pathologists and scoring based on algorithm is shown in Table 2. The matching comparison between plant pathologist scores and algorithm-based scores of twelve pictures is shown in Table 3. The 87 pictures have been tested and a percentage of matching scores of proposed algorithm with plant pathologist is given in Table 4. It is observed that the overall matching score is 87%.

5 Conclusion and Future Work

In this paper, proposed algorithm has been calculated percentage of affected area from phoma blight affected leaflets and disease scores have been assigned based on proposed disease rating scale. The algorithm has been given 87% accuracy with

Table 2 Disease rating of pathologists and proposed scale

Image ID	Plant pathologist 1	Plant pathologist 2	Plant pathologist 3	Plant pathologist 4	Plant pathologist 5	Plant pathologist 6	Plant pathologist 7	Maximum scoring with same value	Scoring based on proposed scale
130001	1	3	3	1	3	3	3	3	3
150001	3	3	3	3	3	3	3	3	3
170001	5	5	5	5	3	3	5	5	5
180001	5	7	7	7	5	7	7	7	7
190001	9	9	9	9	9	9	9	9	9
200001	7	7	5	7	7	7	7	7	5
210001	7	5	7	7	5	7	7	7	7
210002	9	9	9	9	9	9	9	9	9
230001	7	7	7	7	7	7	7	7	5
240001	3	3	3	5	3	3	3	3	3
270001	7	7	5	7	7	7	7	9	9
290001	5	5	5	5	7	5	5	5	5

Table 3 Plant pathologist score versus proposed disease score

Image ID	Plant pathologist score	Proposed disease score	Matching
130001	3	3	Yes
150001	3	3	Yes
170001	5	5	Yes
180001	7	7	Yes
190001	9	9	Yes
200001	7	5	No
210001	7	7	Yes
210002	9	9	Yes
230001	7	5	No
240001	3	3	Yes
270001	7	7	Yes
290001	5	5	Yes

Table 4 Matching percentage of different scoring between plant pathologist and scoring of image-based proposed scale

Total	0	1	3	5	7	9
87	100%	77%	86%	83%	76%	100%

assigned scores of plant pathologists. It is observed that proposed cluster-based algorithm has been given 100% accuracy on rating scale 0 and 9. The plant pathologists are confused for scoring 3 and 5. The matching percentages almost same of these two scoring. The database contained 1000 phoma blight affected potato leaflets pictures. All pictures will be assigned score values and the disease rating scale may be updated in future.

Acknowledgements The authors would like to thanks to Department of Higher Education, Science and Technology and Bio-Technology, West Bengal for funding this research work (Memo No. 33(Sanc)/ST/P/S&T/6G-41/2017 dated 12/06/2018). The authors would also like to thank Dr. Amitabha Bandyopadhyay, Senior Consultant, ITRA Ag&Food for his continuous valuable suggestions and Dr. Sourabh Kumar Das, principal, Kalyani Government Engineering College.

References

1. Sidqi HM, Kakbra JF (February, 2014) Image classification using K -mean algorithm. *Int J Emerg Trends Technol Comput Sci (IJETTCS)* 3(1)
2. Singh MK, Chetia S (February, 2018) Diseased leaf detection using K -mean clustering and texture features. *Int J Recent Sci Res* 24427–24429

3. Shah JP, Prajapati HT, Dabhi VK (2016) A survey on detection and classification of rice plant diseases. In: International conference on current trends in advanced computing (ICCTAC), pp 1–8, IEEE
4. Manikrao ND, Vyavahare AJ (2015) Disease detection of cotton crop using image processing technique: a survey. IJRASET 3(VI):ISSN: 2321–9653
5. Zhang SW, Shang YJ, Wang L (2015) Plant disease recognition based on plant leaf image. J Animal Plant Sci 42–45
6. Khirade SD, Patil AB (2015) Plant disease detection using image processing. In: IEEE, international conference on computing communication control and automation, Pune, pp 768–771

Power Quality Improvement of Cascaded Savonius Rotor Based Hydrokinetic Power System



Oying Doso and Sarsing Gao

Abstract Cascaded Savonius rotor based hydrokinetic power system is a novel method that used a vertical axis wind rotor used to generate power from running water. This article presents modelling and power quality study of Cascaded Savonius rotor based hydrokinetic power system aimed at supplying power without affecting the environment. The model is tested with load and with STATCOM with changing water velocity in MATLAB environment and its performance is found to be acceptable.

Keywords Hydrokinetic power system · Savonius rotor · Power quality

1 Introduction

India is one of the major producers of hydropower in the global scenario but there are many drawbacks related to traditional hydropower plants particularly large hydro plants. Therefore, the Hydro plant presented in this paper is a new technique where running river water is employed to push Savonius rotor that is usually developed for wind energy conversion systems (WECS). The Savonius rotor is directly connected to generators and working is the same as WECS except the driving force is running river water. Here in this hydro plant, there is no damming and thus does not cause a large area to be submerged. In addition to producing Hydro energy, this plant will fulfil the regular energy requirement of the rural area. Savonius hydrokinetic rotors can continuously yield power 24 h per day. Additional benefit is that water density is 835 times higher than air, hence if a swept area is equal energy generated by water is 835 times higher than wind [1]. Over 80% of the hydro capability of our nation (India) is circulated among the Himalayan state and the main rivers of the northeastern part of India continue flow throughout the whole year. So this scheme is expected to work well especially in North East India. The main advantage of this scheme is that it uses water as it comes so it is not harmful to nearby areas and is environment friendly.

O. Doso (✉) · S. Gao

Department of Electrical Engineering, North Eastern Regional Institute of Science and Technology, Nirjuli, Arunachal Pradesh 791109, India

e-mail: oyingdoso422@gmail.com

2 Savonius Rotor

Savonius rotor is an important tool for energy conversion in wind and hydropower systems. S. J. Savonius invented savonius rotor based on Flettner's rotor model. Savonius rotor is suitable in a condition where wind or water speed is low. Savonius rotors have the advantage of redirecting approaching debris instead of infusing it and thus, have reduced upkeep cost and do not require costly hydrofoil-shaped blades [2] and have higher starting torque [3]. Drag force is the vital thrust in Savonius rotor [4]. Savonius rotor produces higher torque even at low speeds and it is self-starting. The performance of Savonius rotor at the beginning is caused by the drag force after that rotation is caused by lift force. The aspect ratio is obtained by dividing the rotor height by its diameter. When used as a hydrokinetic rotor, aspect ratio should be between 1.5 and 2.0.

Output power of rotor is given by

$$P = 0.5C_P A_S \rho V^3 \quad (1)$$

Here P = power, C_P = power coefficient, A_S = swept area, ρ = air density, and V = velocity.

Rotor power output is greatly influenced by swept area A_S and is given by

$$A_S = H \times D \quad (2)$$

Here, H = height and D = diameter.

Rotational speed (n) is given by

$$n = \frac{60 * 2\pi}{\omega} \text{ (rpm)} \quad (3)$$

Tip speed ratio (λ) is

$$\lambda = \frac{\omega D}{2V} \quad (4)$$

Here, ω = angular velocity, D = diameter, and V = velocity.

The torque coefficient (C_T) is given by

$$C_T = \frac{T}{T_w} = \frac{T}{\frac{1}{2}\rho A_s V^2} \quad (5)$$

where T = rotor torque and T_w = torque available in wind.

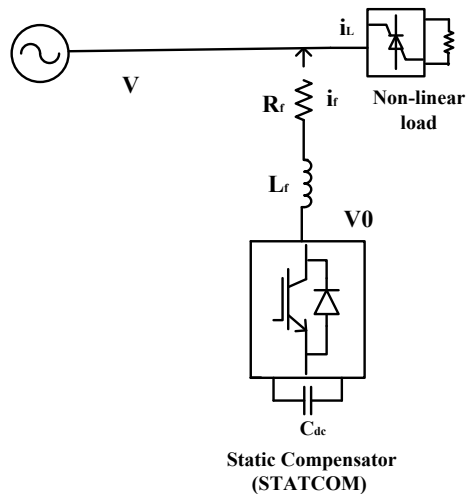
3 Static Synchronous Compensator(STATCOM)

STATCOM is a shunt device that basically works on the control of the voltage. It basically consists of a voltage source converter whose input is provided by a DC voltage source (Capacitor). V_0 is the generated voltage by the STATCOM and V is system voltage. By varying the output of V_0 reactive power can be controlled. If V_0 is greater than V current will flow from STATCOM to the system means the converter is generating the reactive power and vice versa. Under steady-state condition, no active power involve (if V is in phase with V_0). However, active power can also control by a slight phase shift between the V and V_0 . If V_0 lags V in that case STATCOM will absorb the active power and vice versa. In this way, STATCOM absorbs both active and reactive power. The modelled STATCOM is a three-legged IGBT based voltage source converter(VSC) with a DC link capacitor and filter. The STATCOM performance is fully dependent on its control scheme. The capacitance-voltage variation is because of power consumption by the voltage source converter(VSC) and filter. The change in DC capacitor voltage is examined, which indicates active power unbalance and direct axis component of current I_d . After that system peak voltage is compared with a reference value which indicates reactive power needed by the system and quadrature component of reference current, I_q [5]. The reference current I_d and I_q are changed to three-phase with Inverse Park's transformations (Fig. 1).

Inverse Park's transformation (dq0-abc) given by

$$I_{dq0} = T I_{abc} \begin{bmatrix} \cos(wt) & \cos(wt - \frac{2\pi}{3}) & \cos(wt - \frac{2\pi}{3}) \\ \sin(wt) & \sin(wt - \frac{2\pi}{3}) & \sin(wt - \frac{2\pi}{3}) \\ \frac{\sqrt{2}}{2} & \frac{\sqrt{2}}{2} & \frac{\sqrt{2}}{2} \end{bmatrix} \times \begin{bmatrix} I_a \\ I_b \\ I_c \end{bmatrix} \quad (6)$$

Fig. 1 STATCOM



Gating signals to the VSC is generated by comparing the reference source currents with that of measured currents in an HCC. The current controller output determines the switching pattern of the IGBTs of the VSC.

4 Proposed System and Simulation Result

The cascaded Savonius rotor based hydrokinetic power system is modelled and simulated in MATLAB software. The simulation is implemented using MATLAB 2016Rb (9.1.0.441655) in a discrete form with 5e-6 step size for 2.8 s. Figure 2 shows the schematic diagram of cascaded Savonius hydro plant where only 3 Savonius generator sets are presented. The modelled Cascaded Savonius plant consist of 6 unit and Each unit consist of 5 generators. Each unit can generate nearly 15 kW so from 6 unit nearly 90 kW can be generated. If the number of generation unit is increased it can generate more power up to large megawatt. The power quality issues have been analyzed with STATCOM and the result of the simulation is presented through the figure (Fig. 3).

Figure 4 shows the voltage with harmonic spectra and the current waveform of the system.

When a load of 60 kw +20 kVAR is loaded between 1.5 and 2.7 s voltage waveform is reduced up to 420 V as shown in Fig. 5

And with the use of STATCOM from 1 to 2.7 s. the voltage waveform is improved as given in Fig. 6.

The total harmonic distortion (THD) is used to quantify the presence of harmonics in the system. THD of the system voltage with load and STATCOM is within IEEE 519-1992 [6].

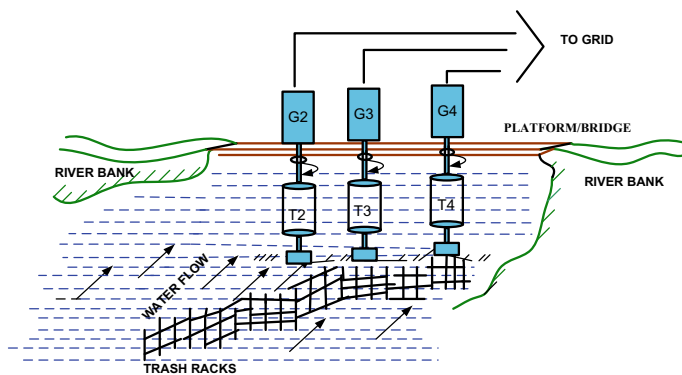


Fig. 2 Schematic diagram of Cascaded Savonius hydro plant

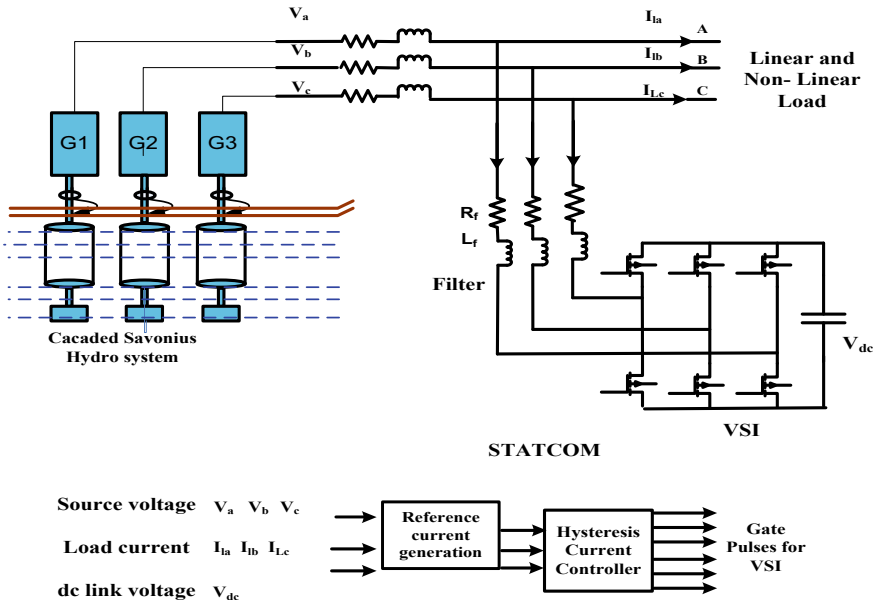


Fig. 3 Model of Cascaded Savonius hydro plant with load and STATCOM

5 Conclusion

The performance characteristics of the cascaded Savonius hydro system is found to be satisfactory and the result is presented in Table 1. Under no-load condition, the system voltage is very well maintained and when load is added there is some voltage drop but with the addition of STATCOM, the voltage waveform is improved. This Cascaded Savonius hydro system is feasible in powering rural locations as well urban locations.

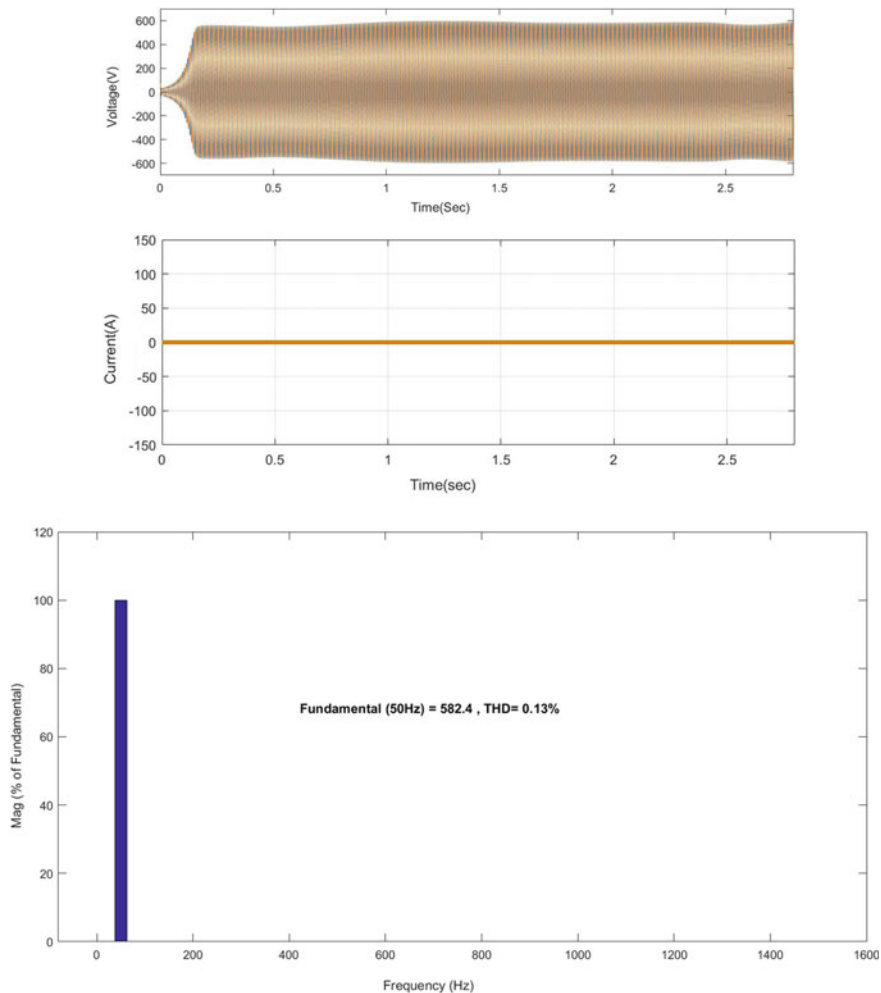


Fig. 4 Voltage waveform, current waveform and harmonic spectra of voltage of Cascaded Savonius hydro system

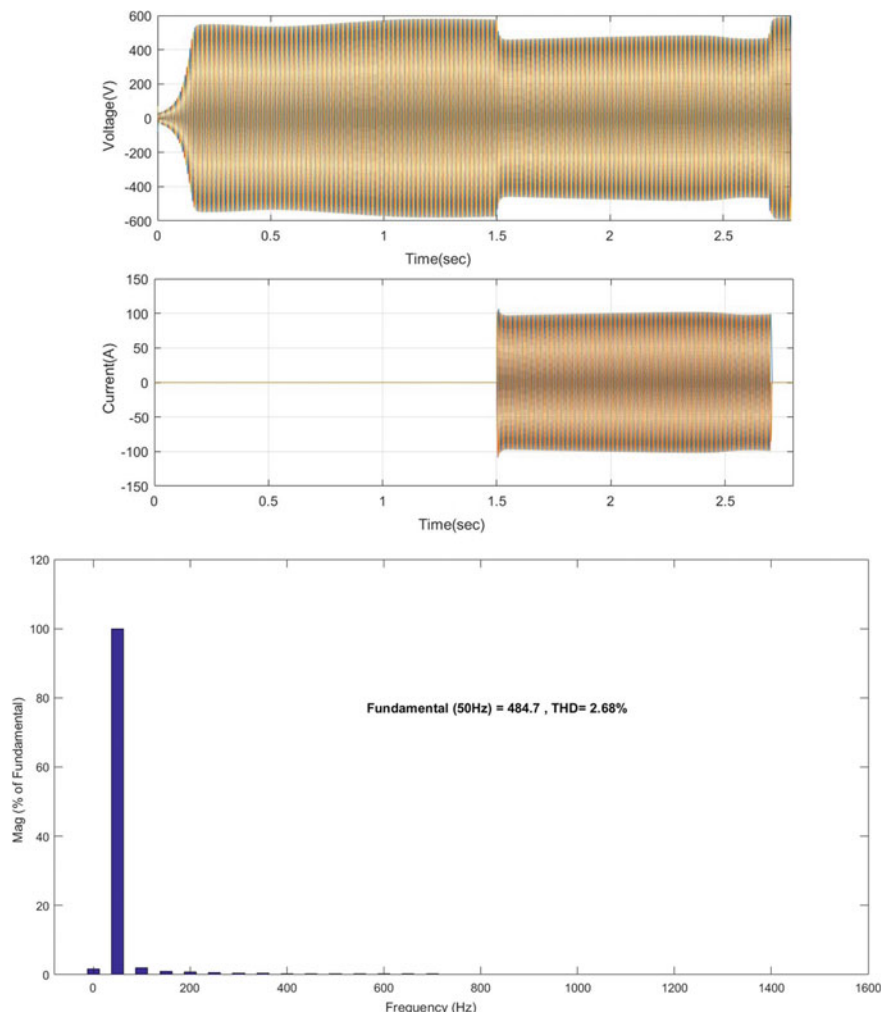


Fig. 5 Voltage, current waveform and harmonic spectra of voltage of Cascaded Savonius hydro system with load

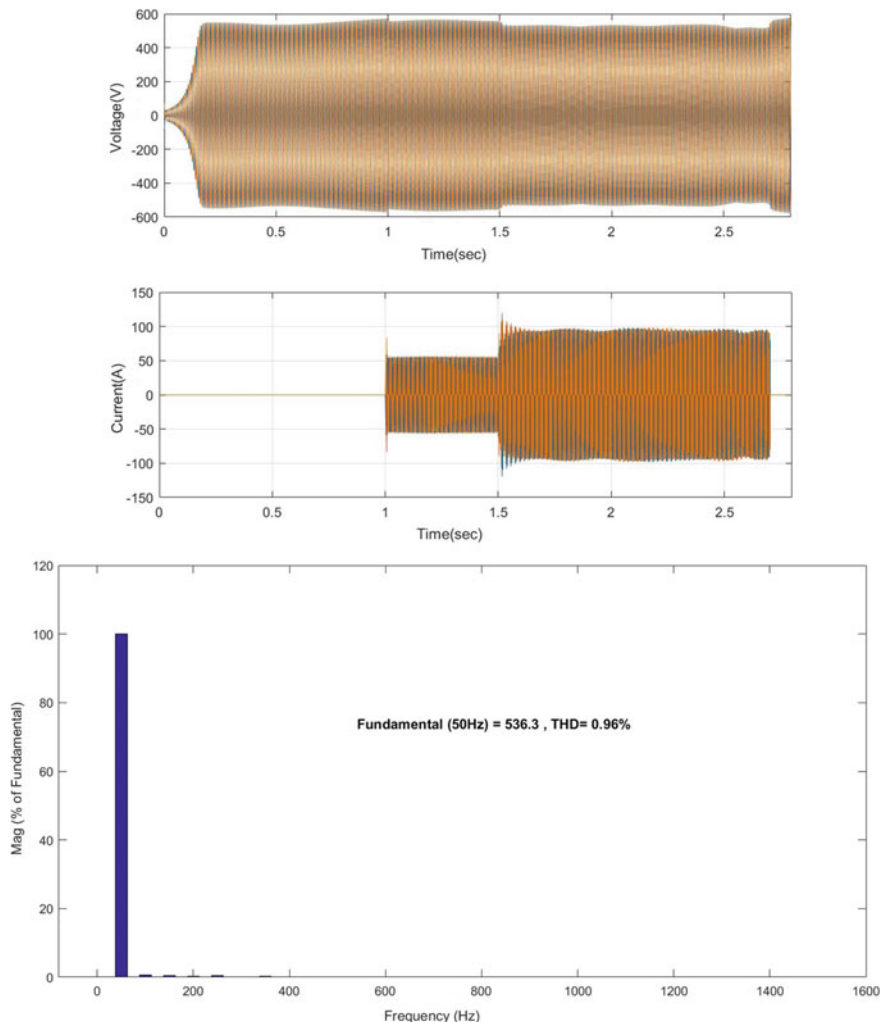


Fig. 6 Voltage, current waveform and harmonic spectra of voltage of Cascaded Savonius hydro system with load and STATCOM

Table 1 Performance result of the three models

S. No.	Frequency (Hz)	Voltage (V)	% THD of voltage
Without load and STATCOM	50	560	0.13
With load	50	420	2.68
With load and STATCOM	50	525	0.96

References

1. Doso O, Gao S (2019) Application of Savonius rotor for hydrokinetic power generation. ASME J Energy Resour Technol 142(1):014501 (2020). <https://doi.org/10.1115/1.4044555>
2. Zhou T, Rempfer D (2013) Numerical study of detailed flow field and performance of Savonius wind turbines. Renew Energy 51(3):373–381
3. Pudur R, Gao S (2016) Savonius rotor based grid connected hydrokinetic power generation scheme. Sustain Energy Grids Netw 5:148–155
4. Roy S, Saha UK (2013) Review of experimental investigations into the design, performance and optimization of the Savonius rotor. J Power Energy 227(4):528–542 (2013). (Proceedings of the institution of mechanical engineers, part A)
5. Mosobi RW, Chichi T, Gao S (2015) Power quality analysis of hybrid renewable energy system. Cogent Eng 2(1):1005000
6. IEEE Std. 519-1992 (1993) IEEE recommended practices and requirements for harmonic control in electric power systems. ©Institute of Electrical and Electronics Engineers, Inc

Design and Simulation of a Sub-6 GHz Low Loss Band Pass Filter Using Double Split Inductor for 5G Radio WLAN Applications



Venkata Raghunadh Machavaram and Bheema Rao Nistala

Abstract In this paper, a novel double split (2-split) inductor and a square spiral inductor are developed to design a low loss bandpass filter (BPF). The 2-split inductor has a quality factor of 23.858 at 5.1 GHz with a self-resonating frequency of 13.5 GHz. It shows a 32% improvement in quality factor and 17% improvement in inductance against the square spiral inductor. A planar square spiral capacitor is also designed, which has a capacitance of 0.206 pF and Q value of 27.42981 at 5.1 GHz. The double split inductor BPF had 1300 MHz bandwidth while square inductor BPF had 1900 MHz at 5.1 GHz. Both filters yielded a very good return loss of -25.644 dB and -17.943 dB, respectively. They also yielded an excellent insertion loss of -0.432 dB and -0.641 dB. The BPF designed using the 2-split inductor has 32% less insertion loss and 7.7 dB (30%) less return loss, when compared to the BPF with square spiral inductor. Both filters occupied lowest on-chip area of only 0.16 mm^2 . Simulation results prove that these BPFs possess excellent loss characteristics that suit the sub-6 GHz 5G radio WLAN applications.

Keywords Double split inductor · Quality factor · HFSS · Return loss · Insertion loss · On-chip area

1 Introduction

Implementation of low-cost and high-performance radio-frequency integrated circuits (RFICs) that suit the emerging 5G ultra-speed smart wireless devices and services is a big challenge for the RFIC designers [1]. Currently under development are miniaturized 5G radio BPF designs on silicon substrate CMOS ICs based on integrated passive device (IPD) technology. They enable small footprints, lowest

V. R. Machavaram (✉) · B. R. Nistala

Department of Electronics and Communication Engineering, National Institute of Technology

Warangal, Warangal, India

e-mail: raghu@nitw.ac.in

B. R. Nistala

e-mail: nbr@nitw.ac.in

power, flexible bandwidths, and easy integration. The spiral inductor and capacitor are most sought silicon passive components, which consume major areas of RFICs (60–70%). Low insertion loss, high-quality factor (Q) along with minimal on-chip area, is a challenging task for passive BPF designs [2]. Power handling, selectivity is traded with center frequency and on-chip area [3]. Good performing low-cost miniature passive devices are developed using IPD technology [4]. Compact passive LTCC BPFs are developed at high frequencies but suffer from heat and size [5]. IPD BPF and LNA circuits are now realized as co-located CMOS chips as a system in package (SIP). Such RFIC circuits have the least chip area with superior RF performance [6]. Therefore, passive 5G radio BPFs using Si IPD CMOS technology are being researched heavily to meet stringent 5G spectral demands.

A microstrip BPF demonstrated smaller insertion loss of 0.8 dB at 3.6 GHz but occupied large 99 mm^2 area [7]. Tapered inductors showed enhanced Q_{\max} from 22.8 to 26.7 with reverse excitation. But the Q_{\max} frequency increased to 8 GHz and resonant frequency to 14.6 GHz [8]. A 2.31 GHz BPF with inter-wined spiral inductor and capacitor had a good return loss of 26.1 dB but occupied 0.63 mm^2 area [9]. A quad BPF reported 22–33 dB return loss and 0.2–1.2 dB insertion loss in 1.8–4.2 GHz. It had a very large area of 545 mm^2 [10]. Another compact 3.3–3.8 GHz band 5G nRN78 BPF using Si IPD had produced smaller insertion loss of <1.8 dB but occupied a large area of 1.28 mm^2 [11]. An LC silicon IPD BPF resulted in 3–4 dB insertion loss but with 0.75 mm^2 area [12]. A GaAS substrate IPD BPF produced smaller 0.26 dB insertion loss and good return loss of 25.6 dB at 1.35 GHz but had a large chip area of 1.25 mm^2 [13].

We report here, the design and simulation of a spiral double split inductor and a spiral capacitor connected in cascade structure to form an LC resonator BPF. We found its S parameters in HFSS by concentrating the design for 5 GHz, as this sub 6 GHz radio band is being heavily explored for 5GnR N78 and N79 radio reception.

This paper comprises the Sects. 2, 3, and 4.

2 Design and Analysis of BPF

The inductance L , capacitance C , quality factor Q , and self-resonant frequency (SRF) depend on device geometrical parameters and technology process parameters: spiral diameter, type, and thickness of the substrate, conductor width, spacing, number of turns, ring shapes, metal ring thicknesses, etc. These are traded off [14]. Selection of thick substrate and thin oxide layers, decreasing permittivity of metal, not only reduces component losses but also enhances the capacitance and inductor Q value along with filter selectivity [15]. Analytical optimization techniques are performed by varying the geometrical parameters and technology process parameters to accomplish high performance [16].

A compact on-chip BPF is designed and simulated with a novel double split spiral inductor and spiral capacitor connected in a series configuration, in a single layer on the Si substrate. They are simulated in HFSS and the filter analysis is performed

with an equivalent lumped model. S parameters are employed as they are good at high-frequency analysis of RF circuits.

2.1 On-chip Double Split Spiral Inductor

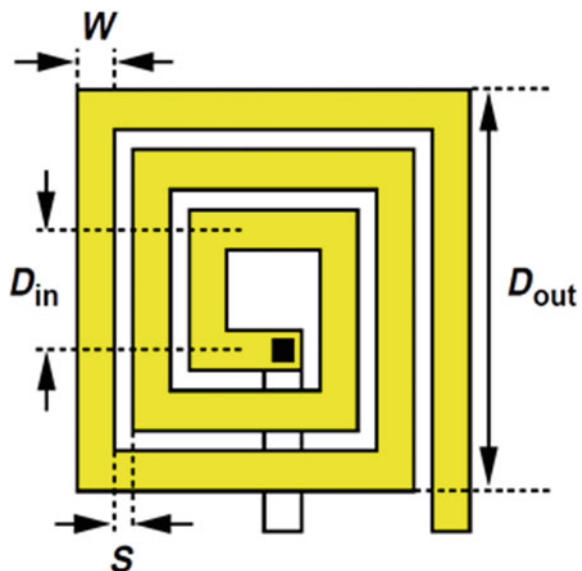
The inductor with more number of turns gives the best quality factor and inductance. In the double split inductors, the conductor width is reduced and the number of turns are increased within the same specified area. Reduction in the conductor width increases inductance value, so as to enhance the effective inductance. There is also an increase in number of turns due to which again the effective inductance is increased due to the mutual coupling between the tracks. Series stacked multi-turn spiral inductor structures shown in Fig. 1 possesses high inductance and Q around 10.

$$L_{\text{total}} = L_1 + L_2 + L_3 + M_{12} + M_{13} + M_{23} \quad (1)$$

$$Q = 2\pi \frac{\text{Peak Magnetic Energy} - \text{Peak Electric Energy}}{\text{Energy Loss}} \quad (2)$$

The proposed double split inductor has a novel double split structure (conductor path is split into two parallel tracks). The physical dimensions of the double split inductor are: width of each track – 4.5 μm , the spacing between the tracks – 1 μm and spacing between the turns – 2 μm . The width of the conductor strip is 10 μm .

Fig. 1 Typical on-chip passive spiral inductor structure- planar view



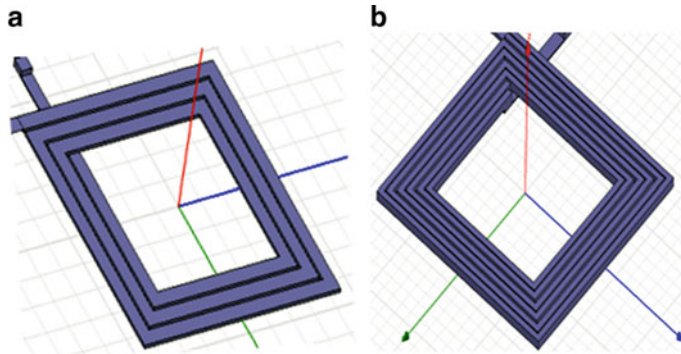


Fig. 2 On chip spiral inductors. **a** Square inductor. **b** Double split inductor (2-split)

We selected copper conductor on a thick Si substrate to reduce its parasitic resistance to enhance Q value. This double split inductor occupies an area of $180 \times 180 \mu\text{m}$ square on the chip footprint.

We also developed a square spiral inductor with similar geometrical parameters for performance comparison. The physical dimensions of the double split inductor are: width of each conductor track $-5 \mu\text{m}$ and spacing between the turns $-2 \mu\text{m}$. This square spiral inductor occupies an area of $180 \times 180 \mu\text{m}$ square on the chip footprint. The structures of both the inductors are shown in Fig. 2.

If mutual inductance increases then effective inductance also increases and can make it suitable for high-frequency applications. We have utilized the fact that mutual inductance depends on the space between the tracks. With the decrease in the space between the tracks the mutual inductance increases, thereby enhancing overall inductance. The same conductor width is chosen for all the 3 turns. Spacing between layers is selected so as to minimize the negative mutual inductance. The Q and L values for these inductors are found from the Y parameters (found from simulated S parameters) employing Eq. (2) [3].

$$Q = \frac{\text{Im}[Y_{11}]}{\text{Re}[Y_{11}]} \quad \text{and} \quad L = \frac{-1}{2\pi f \{\text{Im}[Y_{11}]\}} \quad (2)$$

Inductance and Quality factor variation against frequency for the simulated inductor structure are given in Figs. 3 and 4.

The value of inductance is 6.75 nH for the 2-Split double split inductor and 5.6 nH for the square inductor at 5.1 GHz . The self-resonant frequency is 13.5 GHz . The double split spiral inductor has an inductance of 1.21 times that of the square inductor. Both inductors have the same chip area of $180 \times 180 \mu\text{m}^2$.

The quality factor is 16.177 for a square spiral inductor and 23.858 for 2-split double split inductor. From simulation results, it is observed that the double split inductor has a quality factor of 1.48 times that of square spiral inductor. The double split inductor has an inductance of 1.21 times that of square spiral inductor.

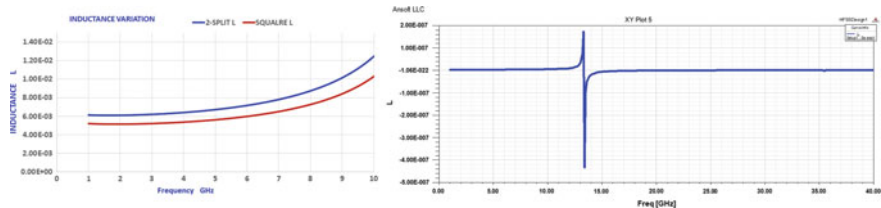


Fig. 3 Variation of inductance (nH) with frequency for on-chip square inductor and double split (2-split) inductor

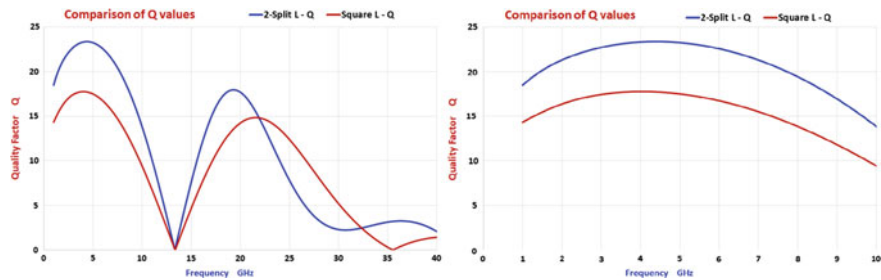


Fig. 4 Variation of a quality factor with frequency for on-chip square inductor and double split (2-split) inductor

2.2 On-Chip Spiral Capacitor

Proposed and simulated single layer square spiral capacitor is designed in HFSS. All turns are placed in the same layer, with the same conductor width. The capacitance value majorly depends upon material used, conductor dimensions in the annular geometry of spiral. The geometry of the spiral capacitor is given in Fig. 5.

The dimensions of planar on-chip capacitor are conductor width $-3\text{ }\mu\text{m}$, thickness $-2\text{ }\mu\text{m}$, the spacing between turns $-2\text{ }\mu\text{m}$. The occupied area of the on-chip capacitor

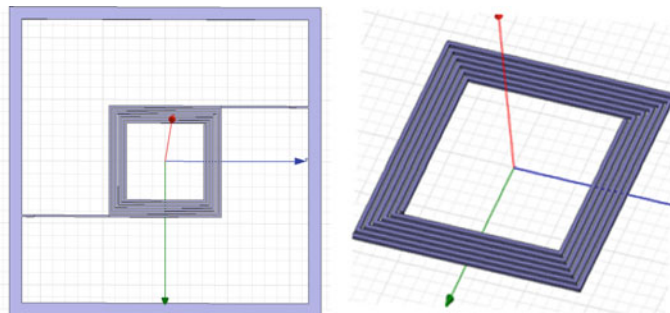


Fig. 5 On-chip square spiral capacitor

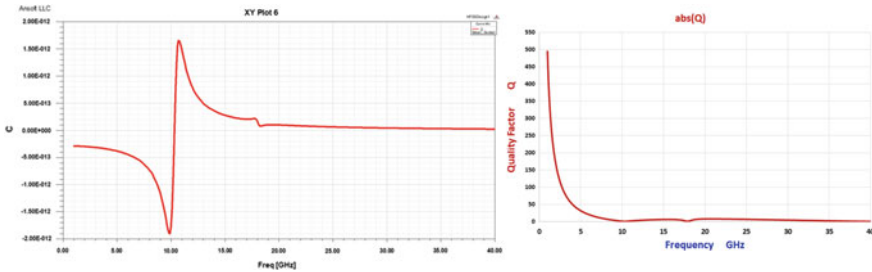


Fig. 6 Variation of the capacitance (pF) and the quality factor with frequency for on-chip spiral capacitor

is $180 \times 180 \mu\text{m}$ square. Capacitance and the quality factor Q for the capacitor are extracted from the S -parameters' as given in Eq. (3) [3].

$$C = \frac{-\text{Imaginary}[Y_{21}]}{\omega} \quad \text{and} \quad Q = \frac{\text{Imaginary}[Y_{11}]}{\text{Real}[Y_{11}]} \quad (3)$$

Change in the values of the capacitance and the quality factor w.r.t. the frequency for this proposed capacitor is shown in Fig. 6.

The simulated value of capacitance is 0.206 pF at 5.1 GHz. The capacitor HFSS simulation showed higher Q value of 27.42981 at 5.1 GHz and 10.3 GHz resonant frequency (SRF). Simulated response of this capacitor on 0.18 μm CMOS technology showed a significant enhancement of the quality Q and capacitances. Therefore, this capacitor is sure to satisfy the 5G radio lower band applications.

2.3 On-Chip Passive Band Pass Filter

We employed a series LC resonator model to simulate the BPF. This permits easier analysis and implementation to prove the filter performance. The simulation of BPF replaces the circuit elements L and C with the designed two split inductor and a spiral capacitor. The equivalent circuit for LC filter configuration. The filter simulation and optimization were carried out in HFSS tool. We found stable simulated values for the inductance and capacitance during the entire passband. Given below is the depiction of the simulated series LC bandpass filter using both the square and double split inductors with the same capacitor as shown in Fig. 7.

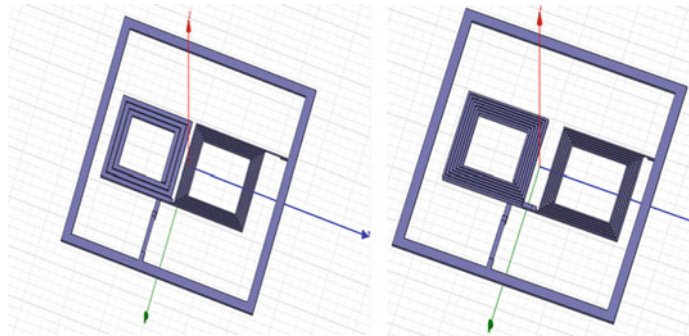


Fig. 7 Planar views of the series LC BPF employing both the on-chip square inductor and double split (2-split) inductor

2.4 Band Pass Filter Simulation

The first order series LC passive BPF is designed using a lumped LC model and simulated in HFSS for its S parameters. The obtained simulation results and theoretical values matched well for the proposed BPF. The insertion and return loss characteristics of the proposed BPF are shown in Fig. 8.

3 Results and Discussion

Both the double split and square spiral inductors and the spiral capacitor have their maximum quality factor value of 23.858, 16.177, and 495, respectively. It is observed that the proposed double split inductor showed an improvement of 32% in quality factor and 17% in inductance value. HFSS simulation of the 5.1 GHz BPF with 2.split inductor had shown 1400 MHz bandwidth from 4.5 to 5.9 GHz. The 5.1 GHz BPF using square inductor had shown 1900 MHz bandwidth from 4.1 to 6.0 GHz. The two filters yielded a very good return loss of -17.943 and -25.644 dB, respectively as per Fig. 8. They also yielded an excellent insertion loss of -0.432 dB and -0.641 dB, respectively at 5.1 GHz center frequency. Both the filters have lowest occupied on-chip area of only 0.16 mm^2 .

These simulation results of loss performance have clearly proven the two filters would definitely satisfy the performance requirements of a pre-6 GHz 5G bandpass filter. These simulation results demonstrate superior passband and stopband performance for the designed bandpass filter that yields good quality output signals suitable for a 5G radio (Table 1).

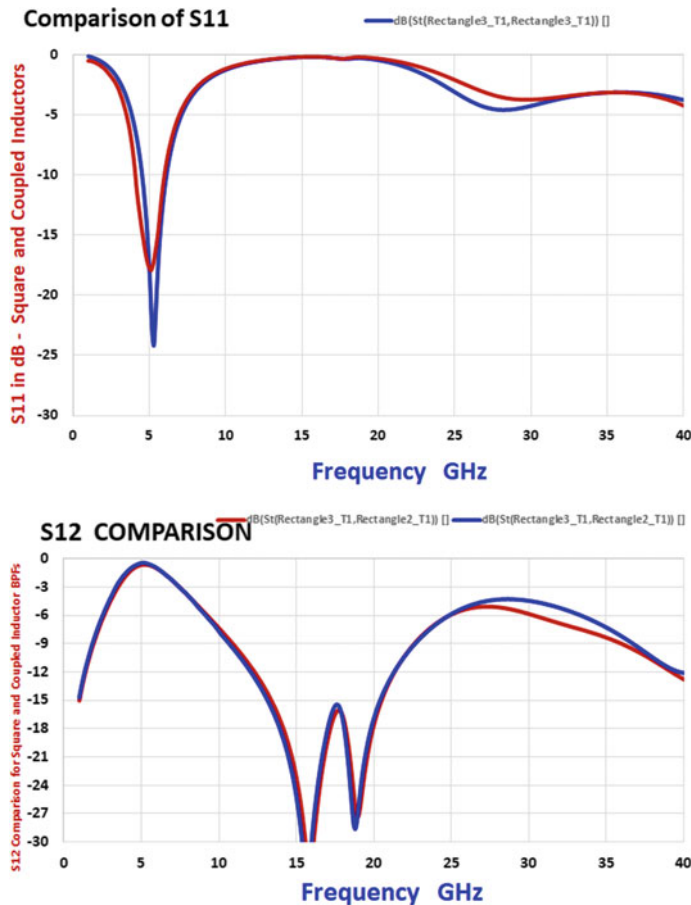


Fig. 8 Insertion and return loss variations of designed series LC passive BPF

Table 1 Summarized BPF parameters

5.1 GHz BPF	Design specifications	2-split L BPF simulation results	Square L BPF simulation results
Center frequency f_0 —GHz	4–5	5.1	5.1
Bandwidth Δf —MHz	1500	1400	1900
Fractional bandwidth—%	20–25	27	37
Quality factor Q	5–10	3.65	2.68
Return loss S_{11} dB	-20 to -30	-25.644	-17.943
Insertion loss S_{12} dB	<-1.0	-0.432	-0.641
On-chip area sq.mm	<1	0.16	0.16

3.1 Performance Comparison

The performance of our filter is compared with that of the corresponding filters in references reported, so as to prove its effectiveness to suit the requirements of 5G WLAN communications. The minimum and maximum fractional bandwidths reported in references [1–13] are 15 and 38%. Our filter had 27% fractional bandwidth. Minimum and maximum insertion loss reported in references [1–13] are –1.3 and –5.6 dB. Our simulated BPF yielded an insertion loss of –0.432 dB for double split inductor BPF. The minimum and maximum return loss reported in references [1–13] are –25 and –35 dB. Our BPF simulations produced a return loss of –25.644 dB for double split inductor BPF and –17.943 dB for square inductor BPF. The minimum and maximum on-chip filter occupied areas reported in references [1–13] are 0.852 and 4 mm². Our simulated BPF occupies only an area of 0.16 mm². These comparisons have proved that this proposed BPF employing double split inductor and a square spiral capacitor will surely meet the stringent spectral requirements of a sub-6 GHz 5G radio WLAN applications.

4 Summary and Conclusion

In this paper, a miniature IPD BPF is modeled and developed for the pre-6 GHz 5G radio access applications. A double split inductor has been proposed and compared with the square spiral inductor. The proposed inductor resulted in an improvement of 32% in quality factor and 17% in inductance value, compared to that of a square spiral inductor. So, the proposed inductor is useful for high-frequency applications. The filter is successfully simulated and its analysis is done in HFSS. The BPF designed using the 2_split inductor has 32% less insertion loss and 7.7 dB (30%) less return loss, when compared to the BPF with a square spiral inductor. Also, it had smaller bandwidth of 1400 MHz (26% less) against 1900 MHz bandwidth possessed by the BPF with a square spiral inductor. Due to several such key enhancements, this 5.1 GHz BPF will surely make the realization of RFICs for the pre-6 GHz 5G radio wireless access WLAN applications.

References

1. Lee CY, Chen TS, Deng JDS, Kao CH (2005) A simple systematic spiral inductor design with perfected Q improvement for CMOS RFIC application. *IEEE Trans Microw Theory Tech* 53(2):523–528
2. Lin CC, Huang CZ, Chen CY (2011) Compact and highly selective millimeter-wave meandered bandpass filter using 0.18-μm CMOS technology. In: Proceedings of Asia-Pacific microwave conference 2011, pp 49–52. ISBN: tel:978-0-85825-974-4">978-0-85825-974-4 © 2011 Engineers Australia

3. Nagesh Deevi BVNSM, Bheema Rao N (2016) Miniature on-chip band pass filter for RF applications. *Microsyst Technol* 23(3):633–638. <https://doi.org/10.1007/s00542-016-3052-7>
4. Xinhai B et al (2014) Fabrication and measurement of BPF using IPD technology. In: 2014 15th international conference on electronic packaging technology, pp 36–38. ISBN: 978-1-4799-4707-2/14/©2014 IEEE
5. Lin YC, Huang HH, Horng TS (2014) Synthesis of LTCC multi-band bandpass filter using reflection and transmission zeros. In: 2014 IEEE MTT-S international microwave symposium (IMS2014). ISBN: 978-1-4799-3869-8/14/ ©2014 IEEE
6. Wang S, Cho K-F (2016) CMOS, IPD switchable bandpass circuit for 28, 39 GHz fifth-generation applications. *IET Microwaves Antennas Propag* 10(14):1461–1466. <https://doi.org/10.1049/iet-map.2015.0806>
7. Al-Yasir YI et al (2019) Design, simulation and implementation of very compact dual-band microstrip bandpass filter for 4G and 5G applications. In: 2019 16th international conference on synthesis, modeling, analysis and simulation methods and applications to circuit design (SMACD), pp 41–44, ISBN: 978-1-7281-1201-5/19/ ©2019 IEEE
8. Vanukuru VN, Chakravorty A (2014) High-Q characteristics of variable width inductors with reverse excitation. *IEEE Trans Electron Devices* 61(9):3350–3354
9. Chuluunbaatar Z, Adhikari KK, Wang C, Kim NY (2014) Micro-fabricated bandpass filter using intertwined spiral inductor and interdigital capacitor. *Electron Lett* 50(18):1296–1297
10. Chen YW, Tai TC, Wu HW, Su YK, Wang YH (2017) Design of compact multilayered quad-band bandpass filter, pp 1815–1818. ISBN: 978-1-5090-6360-4/17 ©2017 IEEE
11. Shin KR, Eilert K (2018) Compact low cost 5G NR n78 band pass filter with silicon IPD technology. ISBN: 978-1-5386-1267-5/18 ©2018 IEEE
12. Mao C, Zhu Y, Li ZA (2018) Design of LC bandpass filters based on silicon based IPD technology. In: 19th international conference on electronic packaging technology, pp 238–240. ISBN: 978-1-5386-6386-8/18/ ©2018 IEEE
13. Quan CH, Wang ZJ, Lee JC, Kim ES, Kim NY (2019) A highly selective and compact bandpass filter with circular spiral inductor and an embedded capacitor structure using an integrated passive device technology on a GaAs substrate. *Electronics* 8:73. (MDPI, pp. 1–8). <https://doi.org/10.3390/electronics-8010073>
14. Wang C, Kim N-Y (2012) Analytical optimization of high performance and high-yield spiral inductor in integrated passive device technology. *Microelectron J* 43:176–181
15. Büyüktas K, Koller K, Müller KH, Geiselbrechtiger A (2010) A new process for on-chip inductors with high Q factor performance. *Int J Microwave Sci Technol*
16. Nagesh Deevi BVNSM, Bheema Rao N (2016) Analysis of miniature on-chip 3-D inductor for RF circuits. *ARPJ Eng Appl Sci* 11(5). ISSN: 1819-6608

Two Novel Configurations of Electronically Tunable Quadrature Sinewave Oscillator Using CDBA



Shekhar Suman Borah, Ankur Singh, and Mourina Ghosh

Abstract This paper presents two novel voltage mode quadrature sinewave oscillator configurations employing Current Differencing Buffered Amplifier (CDBA) as active elements and a few passive components. Tuning of frequency and condition of oscillation can be performed independently. The proposed CDBA-based quadrature sinewave oscillator circuit offers two voltage outputs with a 90° phase difference from high output impedance terminals and the performance of the proposed circuit is also valued by well-known Monte-Carlo simulations. The sensitivity analysis also carried out. The simulated and hardware verification is performed using PSPICE 0.5 μm CMOS process parameters and Current Feedback Operational Amplifier (CFOA) based IC AD844AN, respectively, to produce periodical sinewave oscillations.

Keywords Analog-integrated circuit design · Current differencing buffered amplifier (CDBA) · Quadrature sinewave oscillators

1 Introduction

The popularity attained by the Quadrature Sinewave Oscillators in various disciplines of electronic circuits such as signal processing and measurements, control systems, and to produces single sideband (SSB) as well as quadrature mixtures in the field of communication, etc. Based on the operational amplifier (Op-Amp) as an active element, many oscillator circuits have existed in the previously reported papers. But, the disadvantages of these circuits are not able to perform at higher frequencies

S. S. Borah (✉) · A. Singh · M. Ghosh
Department of Electronics and Communication Engineering, Indian Institute of Information
Technology Guwahati, Guwahati, India
e-mail: borahsumanshekhar90@gmail.com

A. Singh
e-mail: ankur1660@gmail.com

M. Ghosh
e-mail: mourina_06@rediffmail.com

because of limited gain-bandwidth product and slew rate [1–3]. This restricted gain-bandwidth product (GBWP) affects the oscillation frequency and its condition. To overcome these shortcomings, different oscillator circuits have been reported in the literature [4–7]. But, in those, the requirement of passive elements or active elements is more to generate oscillations. CDBA, a unique active ABB has attained much attention from the analog circuit designers [8]. It has the capability of working in both the current mode (CM) and voltage mode (VM) operations has a broad dynamic range and gives considerably wider bandwidth compared to other Analog Building Blocks (ABBs) [9, 10]. These advantageous characteristics of CDBA encouraged a far-reaching use of this ABB for the implementation of converters, oscillators, and filters as well as in the area of measurement and control system both adequately and efficiently.

In this work, two new configurations of CDBA-based sinewave oscillators are presented. The proposed oscillator circuits require two CDBAs and six passive components to produce the oscillations. Also, the simulations were performed using PSPICE 0.5 μm CMOS technology. The analysis of sensitivity determines that the proposed circuits have low-sensitivity. The performance of the proposed circuit is evaluated through Monte-Carlo simulations. The circuit is also verified experimentally using commercially available IC AD844AN.

2 Proposed Circuit Description

The electrical notation of CDBA [1] is shown in Fig. 1 and the relationship between current and voltage is represented by the following equation as:

$$V_p = V_n = 0, I_z = I_p - I_n, V_w = V_z \quad (1)$$

where I_p and I_n are the input currents, V_p and V_n are the input voltages at the terminals p and n , as well as z and w , are the current and the voltage output terminals, respectively. Terminal- w follows the voltage of terminal z . Current Differencing Buffered Amplifier (CDBA) is a current-controlled voltage source device and can be realized with CMOS technology. CDBA CMOS structure and 0.5 μm parameters are taken from ref. [11]. The analysis can be performed as a set of a non-inverting and an inverting current mode (CM) and a non-inverting voltage mode (VM) unity-gain cells. The two proposed quadrature sinewave oscillator circuits are shown in Fig. 2.

Fig. 1 Electrical notation of CDBA

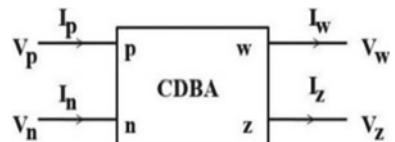
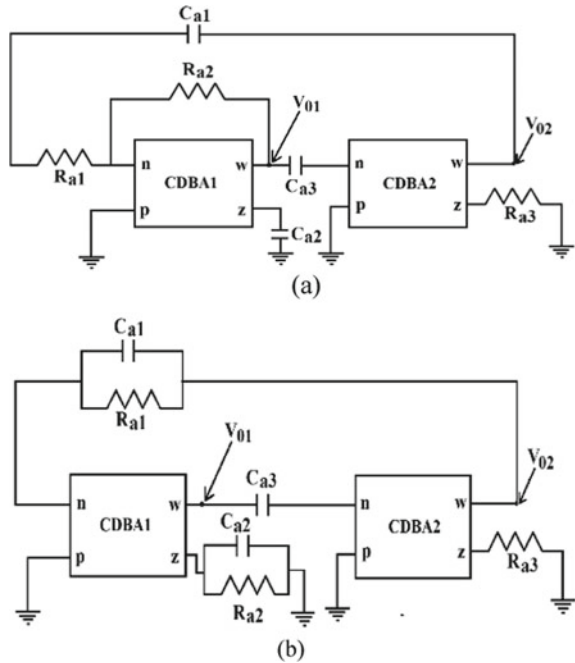


Fig. 2 Proposed sinewave oscillator circuits.**a** Configuration 1.**b** Configuration 2

The straightforward circuit analysis of the proposed configuration 1 as shown in Fig. 2a gives the characteristics equation as

$$s^2 C_{a1} C_{a2} C_{a3} R_{a1} R_{a2} + s(C_{a3} C_{a2} R_{a2} + C_{a1} C_{a2} R_{a1} - C_{a1} C_{a3} R_{a3}) + C_{a2} = 0 \quad (2)$$

Equation (2) implies the oscillation condition (OC) and oscillation frequency (OF) as

$$\text{OC : } C_{a3} C_{a2} R_{a2} + C_{a1} C_{a2} R_{a1} = C_{a3} C_{a1} R_{a3} \quad (3)$$

$$\text{OF : } f_o = \frac{1}{2\pi} \sqrt{\frac{1}{C_{a1} C_{a3} R_{a2} R_{a1}}} \quad (4)$$

Similarly, as shown in Fig. 2b, for the proposed configuration 2, the characteristics equation is,

$$s^2 C_{a1} C_{a3} R_{a1} R_{a2} R_{a3} + s(C_{a3} R_{a3} R_{a2} - C_{a2} R_{a1} R_{a2}) + R_{a1} = 0 \quad (5)$$

Therefore, from Eq. (5), oscillation condition (OC) and oscillation frequency (OF) is found to be

$$\text{OC} : C_{a3}R_{a2}R_{a3} = C_{a2}R_{a1}R_{a2} \quad (6)$$

$$\text{OF} : f_o = \frac{1}{2\pi} \sqrt{\frac{1}{C_{a1}C_{a3}R_{a2}R_{a3}}} \quad (7)$$

An essential performance measure of an integrated circuit is the study of sensitivity. Considering Eqs. (2) and (5), the sensitivities of OF (ω_0) to the variation of passive components such as resistances and capacitances are obtained as

$$S_{C_{a1}}^{\omega_0} = S_{C_{a3}}^{\omega_0} = S_{R_{a1}}^{\omega_0} = S_{R_{a2}}^{\omega_0} = S_{R_{a3}}^{\omega_0} = -\frac{1}{2} \quad (8)$$

From Eq. (8), it can be seen that the proposed configurations exhibit low-sensitivity performance and it is acknowledged as a good characteristic.

3 Non-ideality Analysis

For a complete review of the proposed circuit, it is pretty much necessary to analyze the non-idealities of CDBA [5]. Therefore, considering non-idealities, the voltage-current relationship given in (1) can be modified as

$$V_p = V_n = 0, I_z = Y_p I_p - Y_n I_n, V_w = \lambda V_z \quad (9)$$

where $Y_p = 1 - \beta_p$ and $\beta_p (|\beta_p| \ll 1)$ signifies the current-tracking error from p to z terminal, $Y_n = 1 - \beta_n$ and $\beta_n (|\beta_n| \ll 1)$ is the current-tracking error from terminal n to terminal z, $\lambda = 1 - \beta_v$ and $\beta_v (|\beta_v| \ll 1)$ is the voltage-tracking error from terminal z to terminal w. So, the revised transfer functions of the stated configuration 1 after examining the factors due to the non-idealities of CDBA presented in Eq. (2) can be described as

$$\begin{aligned} & s^2 C_{a1} C_{a2} C_{a3} R_{a1} R_{a2} + s(C_{a3} C_{a2} R_{a2} + C_{a1} C_{a2} R_{a1} \\ & - Y_{n1} Y_{n2} \lambda_1 \lambda_2 C_{a1} C_{a3} R_{a3}) + C_{a2} = 0 \end{aligned} \quad (10)$$

Therefore, modified

$$\text{OC} : C_{a3} C_{a2} R_{a2} + C_{a1} C_{a2} R_{a1} = Y_{n1} Y_{n2} \lambda_1 \lambda_2 C_{a1} C_{a3} R_{a3} \quad (11)$$

$$\text{OF} : f_o = \frac{1}{2\pi} \sqrt{\frac{1}{C_{a1} C_{a3} R_{a2} R_{a1}}} \quad (12)$$

Similarly, the modified transfer functions of the proposed configuration 2 given in Eq. (5) can be described as

$$\begin{aligned} & s^2 Y_{n1} Y_{n2} \lambda_1 \lambda_2 C_{a1} C_{a3} R_{a1} R_{a2} R_{a3} \\ & + s(Y_{n1} Y_{n2} \lambda_1 \lambda_2 C_{a3} R_{a3} R_{a2} - C_{a2} R_{a1} R_{a2}) + R_{a1} = 0 \end{aligned} \quad (13)$$

Therefore,

$$\text{OC : } Y_{n1} Y_{n2} \lambda_1 \lambda_2 C_{a3} R_{a3} R_{a2} = C_{a2} R_{a1} R_{a2} \quad (14)$$

$$\text{OF : } f_o = \frac{1}{2\pi} \sqrt{\frac{1}{Y_{n1} Y_{n2} \lambda_1 \lambda_2 C_{a1} C_{a3} R_{a2} R_{a3}}} \quad (15)$$

Also, while considering non-idealities the sensitivities of oscillator frequency ω_0 to the variation of passive components are

$$S_{C_{a1}}^{\omega_0} = S_{C_{a3}}^{\omega_0} = S_{R_{a1}}^{\omega_0} = S_{R_{a2}}^{\omega_0} = S_{R_{a3}}^{\omega_0} = -\frac{1}{2}, S_{Y_{n1}, Y_{n2}, Y_{\lambda1}, Y_{\lambda2}}^{\omega_0} = S_{\lambda_1, \lambda_2}^{\omega_0} = 0 \quad (16)$$

The above equation implies that the proposed sinewave oscillator configurations exhibit a low-sensitivity performance and the absolute measures ω_0 with respect to Y_{pi} , Y_{ni} and λ_i are within unity.

4 Simulated and Experimental Results

To validate the theoretical interpretation, the proposed circuits in Fig. 2a, b is simulated with PSPICE 0.5 μm CMOS parameters. The supply voltage $V_{DD} = V_{SS} = \pm 1.2$ V and the bias currents, $I_{B1} = 20 \mu\text{A}$, $I_{B2} = 20 \mu\text{A}$ and $I_{B3} = 25 \mu\text{A}$. In Fig. 3, the simulated transient response of the proposed oscillators during the initial state is shown. Simulated output waveforms (V_{01} and V_{02}) for configuration 1 and configuration 2 is displayed in Fig. 4. The simulated frequency of oscillation for both the circuits is 91.3 kHz and 16.4 kHz which closely agrees to the theoretical frequency of 91.88 kHz and 16.776 kHz respectively. The passive components values for both the circuits are $R_{a1} = R_{a2} = 1 \text{ k}\Omega$, $R_{a3} = 30 \text{ k}\Omega$, $C_{a1} = C_{a2} = 1 \text{ nF}$, and $C_{a3} = 3 \text{ nF}$.

The Fourier response of the output voltage, which verifies that the oscillations present at the desired frequency, are depicted in Fig. 5. The plot for voltage V_{01} versus V_{02} for both the configurations is shown in Fig. 6. The Monte-Carlo analysis, by considering 100 samples for 5% tolerance which provides the robustness in passive components is shown in Fig. 7.

The practical workability of this work is also verified using a macro model of commercially available IC of CFOA (AD844AN) [1] with supply voltage ± 5 V and the realization of the proposed oscillator configurations using AD844AN is shown

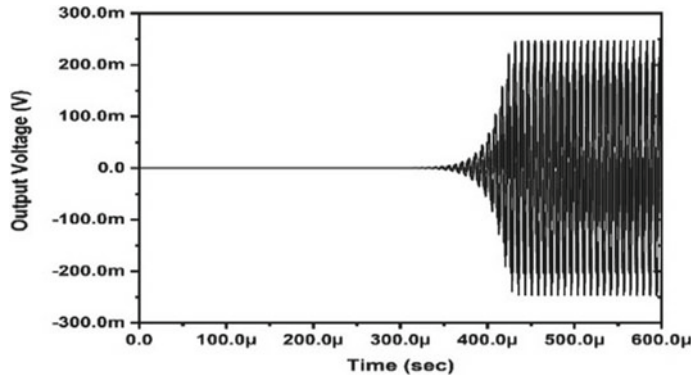


Fig. 3 The simulated transient response of the oscillators during initial state

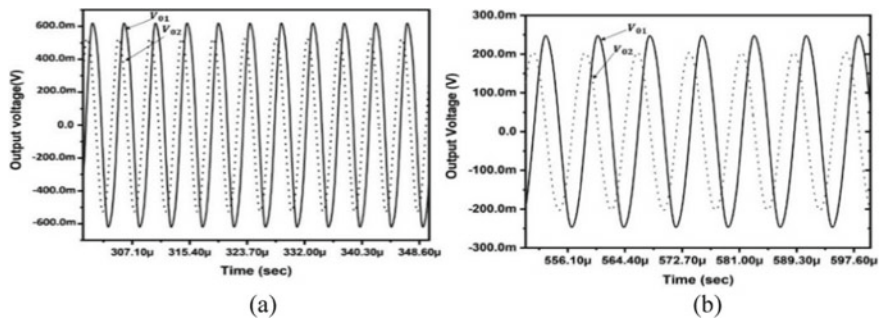


Fig. 4 Simulated quadrature output waveform of **a** configuration 1 **b** configuration 2

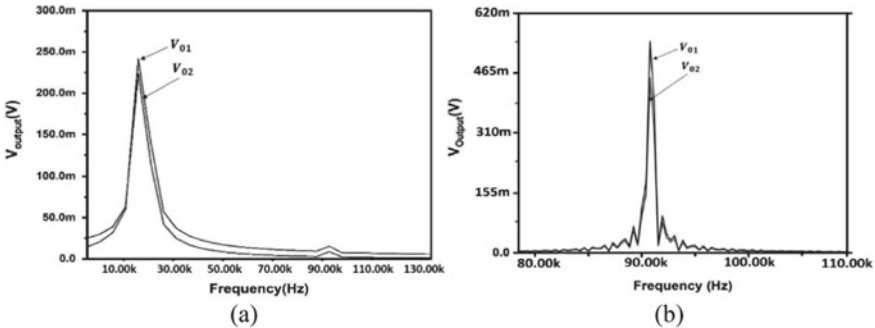


Fig. 5 Simulated frequency spectrum of **a** configuration 1 **b** configuration 2

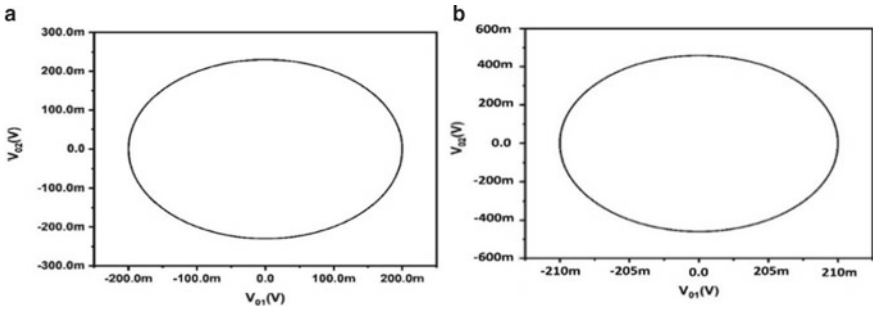


Fig. 6 Plot of V_{01} versus V_{02} for **a** configuration 1 **b** configuration 2

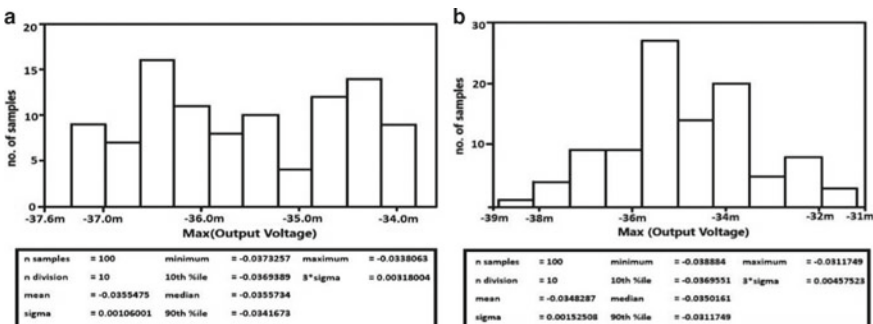


Fig. 7 Monte-Carlo analysis results for **a** configuration 1 **b** Configuration 2

in Fig. 8. The hardware arrangements for the proposed configuration 2 is shown in Fig. 9.

The passive elements values are, $R_{a1} = R_{a2} = 1 \text{ k}\Omega$, $R_{a3} = 30 \text{ k}\Omega$, $C_{a1} = C_{a2} = 1 \text{ nF}$ and $C_{a3} = 3 \text{ nF}$ and the oscillation frequency for both the circuit is 89.4 kHz and 15.2 kHz, respectively, which is close to the simulated results. The quadrature oscillations output waveform and the steady-state responses of the experimental circuits are shown in Fig. 10a, b, respectively.

In Table 1, a comparative analysis of the proposed work with the earlier reported work is shown. From this, it can be observed that, although the proposed work uses two ABBs which is similar to other reported works, but it uses less amount of transistors which can decrease power dissipation. Moreover, the use of passive components reported in ref [10] is more than the proposed topology. Therefore, these can be considered as useful characteristics of this proposed sinewave oscillator topology employing CDBA.

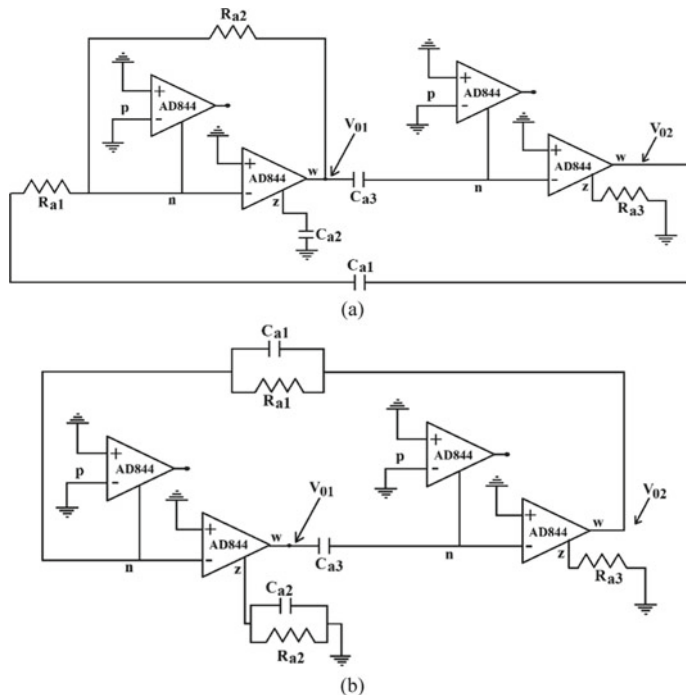
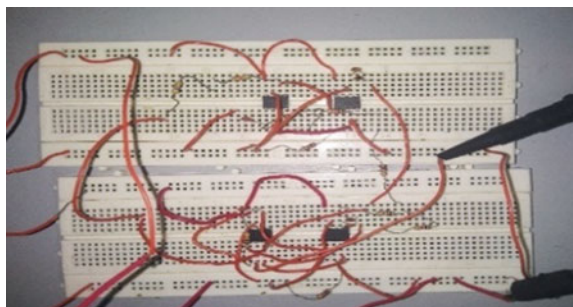


Fig. 8 Proposed oscillator circuits using AD844 **a** configuration 1 **b** configuration 2

Fig. 9 Hardware arrangements for the proposed configurations



5 Conclusion

This paper presents two CDBA-based quadrature sinewave oscillator configurations including low passive sensitivities. The proposed topology is simpler than the usual waveform generators which provide independent control of the frequency as well as the condition of oscillations. Here, CDBAs operate as active components and requires only three resistors and capacitors each as passive components. The

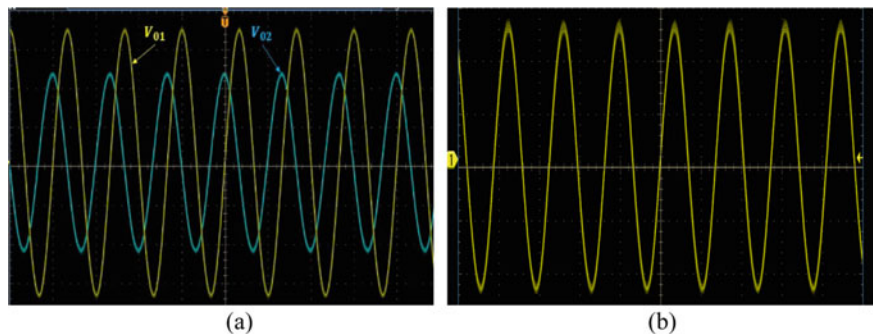


Fig. 10 Experimental results (using AD844): **a** quadrature output waveform **b** steady-state response

Table 1 Comparative study

References	No. of active elements (CDBA)	No. of passive components		Transistor	No. of transistors
		R	C		
[8]	2	3	2	CFOA(BJT)	76
[9]	2	4	2	CFA(BJT)	76
[10]	2	4	4	CFOA(BJT)	76
[12]	2	3	3	CFOA(BJT)	76
Proposed	2	3	3	CMOS	40

outcomes presented by the stated topologies are congruent with simulated and corresponding experimental results. Simulations were performed using PSPICE 0.5um CMOS technology and hardware experimentation was fulfilled using commercially available IC AD844AN. The grounded resistor is considered to be an additional feature from the integration point of view. Finally, the well-known Monte-Carlo analysis is performed to check the performance of the proposed work. Hence, the circuits can provide new possibilities to analog designers.

References

1. Acar C, Ozoguz S (1999) A new versatile building block: current differencing buffered amplifier suitable for analog signal-processing filters. *Microelectron J* 30:157–160
2. Pal D, Srinivasulu A, Pal BB, Demosthenous A, Das BN (2009) Current conveyor-based square/triangular waveform generators with improved linearity. *IEEE Trans Instrum Measur* 58:2174–2180
3. Senani R, Bhaskar DR, Singh AK (2014) Current conveyors: variants, applications and hardware implementations. Springer, New York
4. Sharma RK, Arora TS, Senani R (2016) The realization of canonic single-resistance-controlled oscillators using third generation current conveyors. *IET Circ Devices Syst* 11:10–20

5. Sotner R, Jerabek J, Prokop R, Kledrowetz V (2016) Simple CMOS voltage differencing current conveyor-based electronically tunable quadrature oscillator. *Electron Lett* 52:1016–1018
6. Keskin AÜ (2005) Voltage-mode notch filters using single CDBA. *Frequenz* 59(9–10):225–228
7. Gupta SS, Sharma RK, Bhaskar DR, Senani R (2010) Sinusoidal oscillators with explicit current output employing current-feedback Op-Amps. *Int J Circ Theor Appl* 38:131–147
8. Prasertsom D, Tangsrirat W (2010) CDBA-based sinusoidal quadrature oscillator with current controlled amplitude. In: 10th IEEE international symposium on communications and information technologies, pp 187–191. IEEE, Tokyo, Japan (2010)
9. Tangsrirat W, Pukkalanun T, Surakampontorn W (2008) CDBA-based universal Biquad filter and quadrature oscillator. *Act Passive Electron Compon* 2008:1–6
10. Keskin AU, Aydin C, Hancioğlu E, Acar C (2006) Quadrature oscillator using current differencing buffered amplifiers (CDBA). *Frequenz* 60(3–4):57–59
11. Keskin AÜ, Hancioğlu E (2005) Current mode multifunction filter using two CDBAs. *AEU Int J Electron Commun* 59(8):495–498
12. Tangsrirat W, Pisitchalermpong S (2007) CDBA-based quadrature sinusoidal oscillator. *Frequenz* 61(3–4):102–104

Analog/RF and DC Performance Enhancement of a Pocket-Doped Junction-Less TFET for Low Power Application



Sneha Bharti, Suruchi Sharma, Abhishek Verma, Manisha Bharti, and Baljit Kaur

Abstract The Junction-less tunnel field-effect transistor (JLTFET) is a captivating device due to its excellent electrical properties and less variability in comparison to MOSFET at the nanometer regime. In this regard, we investigate a silicon-based pocket doped JLTFET in which an InAs pocket is inserted across the source-channel junction to enhance tunneling probability. In this respect, we have considered analog/RF and DC Figure of merit analysis for the conventional and pocket doped JLTFET (PD- JLTFET) in terms of an electric field, transfer characteristics, transconductance, parasitic capacitances, cut-off frequency, gain-bandwidth product, and maximum oscillation frequency. Additionally, we have examined the effect of spacer length variation across the junction between source and channel. The ATLAS device simulator is used for the simulations of the conventional JLTFET and PD-JLTFET. The proposed PD-JLTFET has shown a higher I_{ON}/I_{OFF} ratio ($\sim 10^{13}$) and improved sub-threshold swing (~ 9.08 mV/decade). The notable characteristics demonstrated by PD-JLTFET make it an optimum device for low power and high switching application.

Keywords High-k dielectric material · InAs · Junction-less TFET · Sub-threshold swing

S. Bharti (✉) · S. Sharma · A. Verma · M. Bharti · B. Kaur

Department of Electronics and Communication Engineering, National Institute of Technology
Delhi, Delhi, India

e-mail: sneha2012bharti@gmail.com

S. Sharma

e-mail: SuruchiSharma@nitdelhi.ac.in

A. Verma

e-mail: abhishekverma355@gmail.com

M. Bharti

e-mail: manishabharti@nitdelhi.ac.in

B. Kaur

e-mail: baljitkaur@nitdelhi.ac.in

1 Introduction

Development in the field of semiconductors has led to an increase in the peremptory call for submicron devices for high switching speed and DC/analog applications [1, 2]. However, in deep submicron technology (due to reduction in device dimension) power dissipation and scalability have become the most critical factor due to an increase in transistor density on a chip, increasing leakage power and need of high speed of operation for the proper functioning of the device. For this reason, MOSFET is mostly used for the design of integrated circuits as it provides a simple fabrication process and is available at a cheaper cost to fulfill consumer demands. According to Moore's law, transistors density on a chip increases due to continued scaling of the device.

However, conventional MOSFET suffers from short channel effect, lowering of barrier potential caused by the drain voltage, low ON-OFF current ratio, and also it is not an energy-efficient device [3, 4]. Along with this, increment in leakage current occurs from one technology node to another, results in more static and dynamic power dissipation and also due to tunneling of charge carrier occurs over the barrier [5], conventional MOSFET provides minimum sub-threshold swing (>60 mV/decade), which doesn't provide high I_{ON}/I_{OFF} (ratio of ON-OFF current) required for application in low power devices. The reduction in power consumption is possible by scaling down the supply voltage but the reduction in supply voltage is also not possible after a particular technology node in the case of MOSFET because it reduces the competency of the device in carrying current [6]. So as to conquer these limitations, TFET is used over MOSFET.

The operation of TFET is based on the quantum mechanical tunneling(band to band) due to which it is immune from the short- channel effect and barrier lowering due to drain voltage [7, 8]. It also provides low OFF-state current and low sub-threshold swing [9–11]. The low sub-threshold swing of TFET enables it to reduce the supply voltage and threshold voltage to a value of less than 0.5 V [6, 12–14]. TFET, also known as "Green Transistors," can be operated at lower voltage source, so it is termed as a highly energy-efficient device [15].

While TFET has all these benefits, it suffers from low ON-state current that occurs due to insufficient quantum tunneling of charge carrier caused by large bandgap material present at the interface between source and channel [16]. Another disadvantage of TFET is its ambipolar behavior (current conduction for positive as well as negative voltage at the gate terminal) [17, 18]. Apart from all these, as the technology node reaches below 100 nm, fabrication complexity increases for such types of devices [19].

Thus, in order to overcome the limitations of fabrication complexity and low ON-state current with regards to TFET, a new transistor named JLTFET is used. It makes use of the concept of both JLFET and TFET [20]. It works on the principle of gate work function engineering, also termed as charge plasma concept [21]. As the name, JLTFET itself suggests that it does not have any metallurgical junction across drain-channel and source-channel interface, because of their equal doping concentration

throughout the region from drain-to-source. JLTFET does not have any junction, so it will be easier to fabricate [20] and has better performance than TFET.

Considering these advantages of JLTFET, we proposed a device pocket doped JLTFET (PD-JLTFET), which is composed of two gates, i.e., polarity-gate (*P*-gate) and control-gate (*C*-gate) in order to control the device operation. The *C*-gate is placed near the channel in this system, *P*-gate is placed near the source side, and its work functions are varied to inhibit ambipolar current. A pocket of InAs, which has a very low bandgap as compared to Si element, is inserted at the tunneling junction of the interface between source and channel to improve the current when the device is on. The proposed PD-JLTFET structure performance is analyzed and compared with conventional JLTFET [20]. The system suggested has better simulation results in terms of I_{ON}/I_{OFF} , I_{ON} , I_{OFF} , sub-threshold swing (SS), electric field, and transconductance.

PD-JLTFET design can be constructed using the steps specified by Daley et al. [22], as something of a single sheet piled up of several sheets of hetero components with a vertical structural layout.

The rest parts of this manuscript are structured as mentioned further: Sect. 2 elaborates device structure and simulation variables. Section 3 describes the results and discussion part, and at last, the conclusion is discussed in Sect. 4.

2 Device Structure and Simulation Variables

Figure 1a depicts the cross-sectional view of conventional JLTFET used in reference [20] and Fig. 1b shows the cross-sectional view of proposed PD-JLTFET with N⁺ doped structure. The device is shown in Fig. 1b is different from the structure shown in Fig. 1a by insertion of InAs as a pocket at the source-channel interface to shorten the bandgap at tunneling junction of the interface between source and channel, so that proper tunneling of charge carrier can occur at the junction. To obtain the enhanced device performance, InAs is used because it has low bandgap nearly equal to 0.36 eV (much less than Si having bandgap 1.1 eV) and also a high melting point. As InAs is a compound type semiconductor, so energy will be radiated in the form of light energy. The device parameters used in the simulation results are n-type heavily doped Si-channel, with a doping concentration of $1 \times 10^{19} \text{ cm}^{-3}$. In order to separate both the gates, i.e., *C*-gate and *P*-gate a spacer of 5 nm is used in the device structure. Few device simulation parameters and material constants are given in Table 1.

All the simulation results are carried out using 2D device simulator Silvaco Atlas 5.19.20.R [23]. Fermi-Dirac statistics are included in determining the required carrier concentration (intrinsic) in Shockley-Read-Hall (SRH) recombination expression [24]. In TFET current conduction, occur due to band to band tunneling. Therefore, the nonlocal BTBT (BBT.NONLOCAL) model is applied to determine the tunneling of charge carriers along the lateral direction for a particular device [25]. This nonlocal BTBT model is applied to simulate JLTFET [26]. Bandgap narrowing (BGN) model is taken into consideration due to excessive dopant mixing along the channel region

Fig. 1 Cross-sectional views of **a** conventional JLTFTET **b** proposed PD-JLTFTET

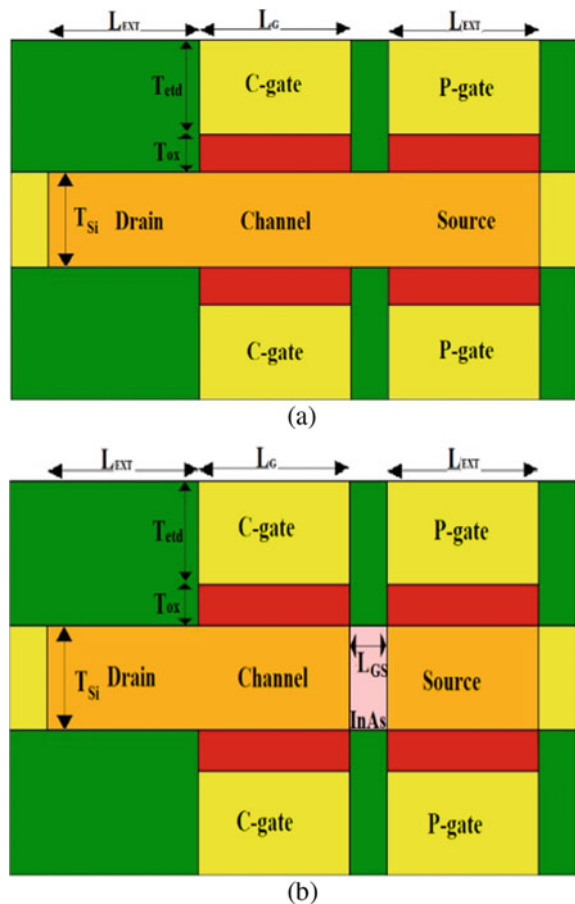


Table 1 Devices structure parameters

Parameters	Symbol	JLTFTET	PD-JLTFTET
Silicon film thickness	T _{Si}	5 nm	5 nm
Source/channel/drain doping concentration	N _D	1×10^{19} cm ⁻³	1×10^{19} cm ⁻³
Channel length	L _G	20 nm	20 nm
Drain/source length	L _{Ext}	20 nm	20 nm
Control-gate work function	W _{C-gate}	4.54 eV	4.3 eV
Polarity-gate work function	W _{P-gate}	5.93 eV	5.93 eV
Oxide thickness	T _{ox}	2 nm	2 nm
Electrode thickness	T _{etd}	5 nm	5 nm
Gate-source spacer	L _{GS}	5 nm	5–10 nm

in the device structure [23]. Because of the material having a large value of dielectric constant present at the gate electrode gate leakage model is exempted from the consideration. Shockley read hall (SRH) recombination model fits well due to high impurity atom present throughout the channel [23]. Quantum confinement model given by Hansch [23, 27] on BTBT is also taken into consideration, as the device dimension is less than 10 nm. Trap assisted tunneling model (SCHENK.TUN) given by Schenk is used to give the importance of trap assisted tunneling in the sub-threshold region [23, 28]. In this paper, the used nonlocal BTBT model uses Wentzel–Kramer–Brillouin method to calculate electron and hole tunneling probability [25]. The metalwork function for the proposed device is varied from 4.3 to 4.74 eV and 5.5 to 5.93 eV for *C*-gate and *P*-gate to create a layer just under the gates as *P*-type as well as intrinsic. Proposed device structure gives best outcome in view of sub-threshold swing and I_{ON}/I_{OFF} ratio at work function of 4.3 and 5.93 eV for corresponding control-gate and polarity-gate. As the sub-threshold swing is very less for the proposed device, hence it can be used for low power applications.

3 Results and Discussion

3.1 DC Analysis

This section describes the performance of proposed PD-JLTFT with the conventional JLTFT. The comparative analysis of carrier concentration in OFF-state for both the devices, i.e., PD-JLTFT and JLTFT is shown in Fig. 2a, from the concentration contour, This could be noted that the system looks like the layout N+-I-P+ [20]. In the proposed PD-JLTFT device structure InAs, having band-gap equal to 0.36 eV is used as a pocket at the source-channel interface that means bandgap will be very less as compared to Si when used at the interface of source-channel region hence electron concentration will be somehow more at source side in case InAs is used as pocket as have done in the case of the proposed structure. Figure 2b shows the comparison of OFF-state energy band diagram for conventional JLTFT with proposed PD-JLTFT. For both the device as There is a large tunneling barrier between source and channel, so tunneling is likely an electron from valance band of the source to conduction band of the channel will be negligible in this case. Therefore, the current will flow here is only due to diode leakage. As the bandgap of InAs is very less, hence some spike may occur at the junction between source and channel. The device operation is controlled by the application of a voltage on *C*-gate. As the device will be turned on, then the barrier existing between the channel and the source region will become narrow, so that proper tunneling of majority carrier can occur from source to channel. As Fig. 2c reflects the comparison of carrier concentration in ON-state for both the devices. From the figure shown below, we can note that on application of voltage on *C*-gate the concentration of electrons beneath the *C*-gate escalates and behaves like an n-type region. This results in a reduction of barrier

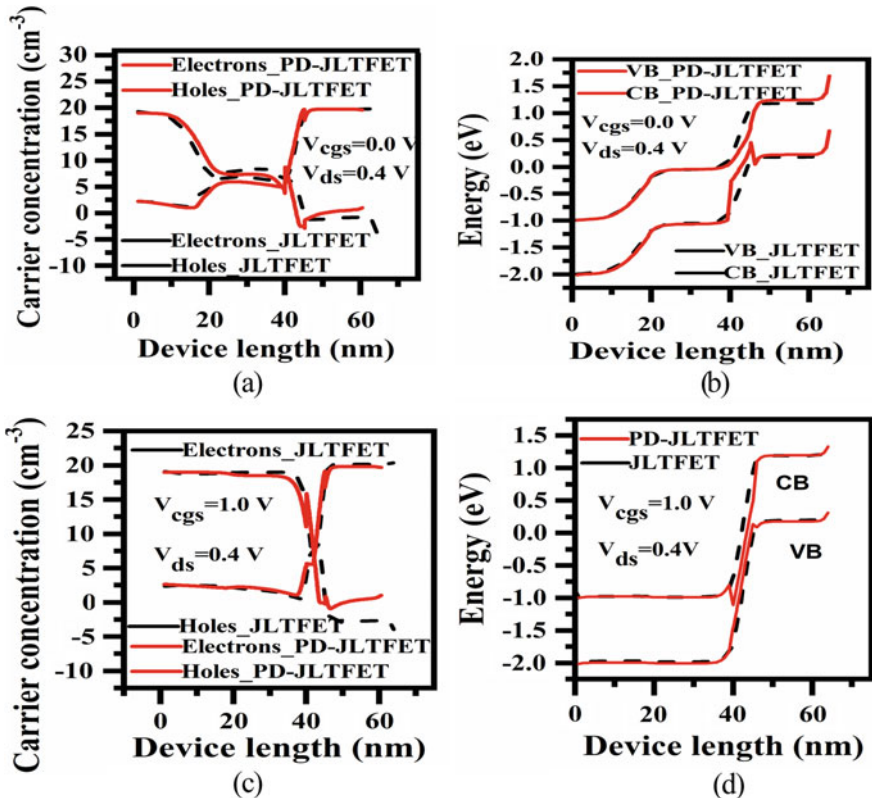
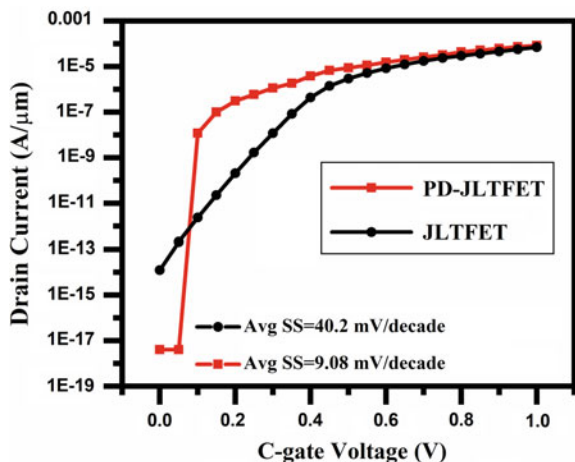


Fig. 2 Comparison between JLTFET and PD-JLTFET **a** Carrier concentration on OFF-state **b** Energy band diagram in OFF-state **c** Carrier concentration in ON-state **d** Energy band diagram in ON-state

between the source-channel junctions of the device due to the insertion of InAs also concentration of electron in the source region for PD-JLTFET will be more as compared to JLTFET. Figure 2d shows the comparative analysis of ON-state energy band diagram for both the devices. As we know that for TFET, as the barrier between source and channel tunneling region will decrease corresponding ON-current will increase, which can also be seen from the given figure. As the InAs has much lower bandgap as compared to Si, hence tunneling barrier in proposed PD- JLTFET will be less as compare to conventional JLTFET. So proper tunneling of the electron will occur in the case of PD- JLTFET compared to conventional JLTFET. For turning the device on the C -gate voltage is varied from 0 to 1 V, while P -gate voltage is kept at zero volts [20].

High-k dielectric material yields superior results in context to ON-current, SS, and OFF-current [5]. Interface trap effect is taken into consideration because of the direct exposure to material having high k-value with Si channel, as it leads to a kind of defect at the semiconductor-dielectric interface. Here in the structure, TiO_2

Fig. 3 Comparison of transfer characteristics between conventional JLTFET and Proposed PD-JLTFET



is considered as a dielectric material having a dielectric constant 80 [29]. Figure 3 depicts the transfer characteristics of existing JLTFET and intended PD-JLTFET. As the lower subthreshold swing of TFET reduces the supply and threshold voltage of a device to a value lower than 0.5 V [6, 12–14], hence as the device has very less sub-threshold swing equal to 9.08 mV/decade so the proposed device can be used at an input voltage less than 0.5 V, i.e., at 0.4 V. From the above characteristics it is clear that the proposed structure has higher ON-current and lower OFF-current as compared with conventional JLTFET.

Figure 4 shows the comparison graph of the electric field for JLTFET and PD-JLTFET at ON-state. From the graph, we can say that the proposed device has a better electric field in the source-channel tunneling junction due to the presence of narrow bandgap material as compared to conventional JLTFET. Whereas electric field in the other portion is the same.

Figure 5a displays the input to output characteristics of PD-JLTFET at various supply voltages (V_{ds}). Nanometer technology is perfect to use for low power applications as we can conclude from the graph that the intended structure gives better results for low supply voltage (0.4 V) than for high voltage (1.0 V). Figure 5b shows the transfer characteristics of PD-JLTFET at different isolation thickness. As the spacing between source-channel decreases, it leads to increase in tunneling probability of carriers, leads to escalates in ON-current and trails in subthreshold swing for lesser isolation thickness at the interface between source and channel, which can be seen from the graph that lesser isolation thickness of the provides more ON-current and as the isolation thickness at the interface increases, ON-current will decrease.

Transconductance (g_m) describes System operation capability. Therefore, the value of g_m must be high enough to achieve high linearity performance and high-frequency characteristics [1]. In this regard, Fig. 6 shows the comparison plot of g_m versus V_{gs} for both the devices. From the graph, it can be concluded that transconductance of PD-JLTFET is higher as compared to the JLTFET due to lesser work

Fig. 4 Comparison of Electric field under ON-state for JLTFET and PD-JLTFET

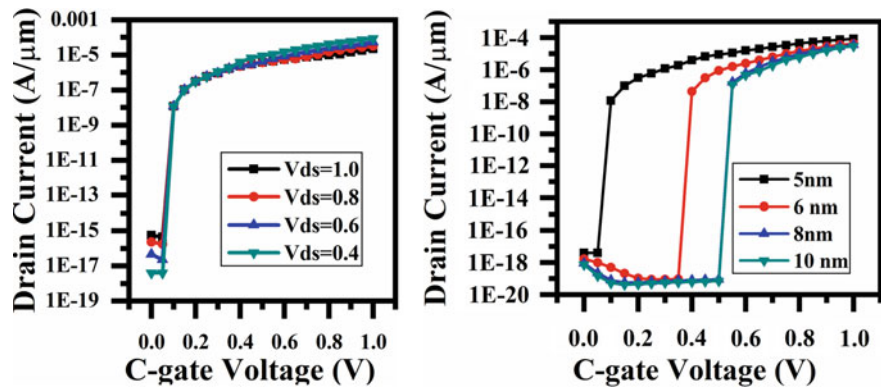
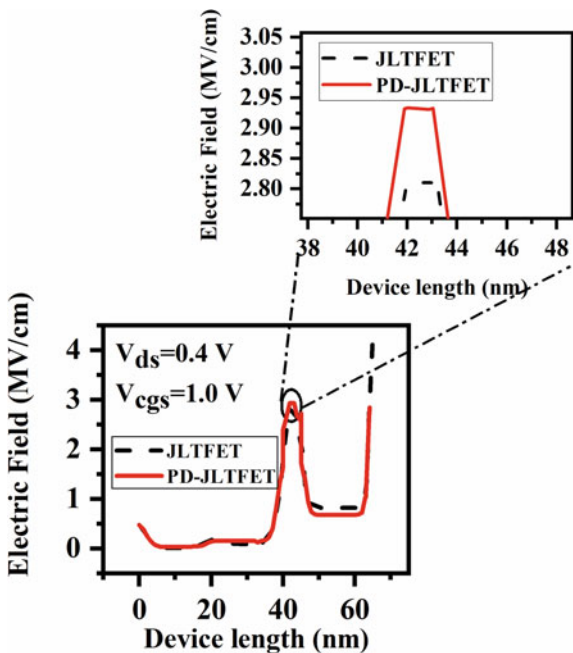
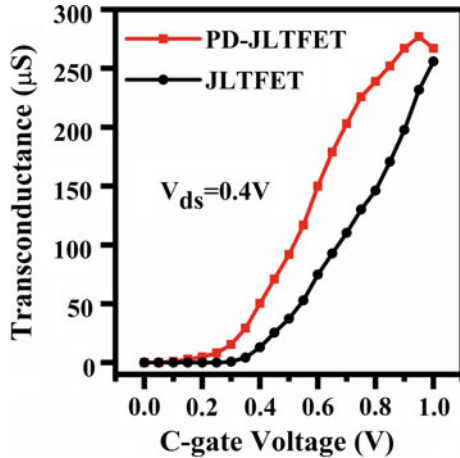


Fig. 5 Transfer characteristics for PD-JLTFET at **a** different supply voltage (V_{ds}) **b** different isolation thickness

function value of C -gate and material having less band gap present at the tunneling junction of the channel-source region, results in large current operating capability of the device, leading to high transconductance.

Fig. 6 Comparison of transconductance (g_m) between JLTFET and PD-JLTFET



3.2 Analog/RF Parameter Analysis

In the high-frequency region, parasitic capacitances play a significant role in device performance. Figure 7a shows the graph between C_{gd} versus V_{gs} for both the devices. From the graph, it can be observed that C_{gd} increase along V_{gs} due to significant barrier at drain channel interface created due to C -gate work function. The C_{gd} of PD-JLTFET is more as compared to JLTFET due to the presence of InAs at tunneling junction, which causes a relatively more parasitic effect on the devices. The parameter f_T and gain-bandwidth product (GBP) can be calculated using the formula as

$$f_T = g_m / 2\pi (C_{gd} + C_{gs}) \quad (1)$$

$$\text{and } \text{GBP} = g_m / 20\pi C_{gd} \quad (2)$$

Figure 7b, c shows the comparative analysis of cut-off frequency and Gain bandwidth product graph. Cut-off frequency for JLTFET is 16 GHz and for PD-JLTFET is 5.5 GHz. Corresponding gain-bandwidth product for JLTFET is 1.6 GHz and for PD-JLTFET is 0.55 GHz. F_{max} is the other constraints to determine the RF execution of the device. F_{max} (frequency) needed for power gain to be unity. It is defined as

$$F_{max} = \sqrt[3]{f_T / 8\pi C_{gd} R_{ds}} \quad (3)$$

Figure 7d depicts the graph of maximum frequency from which it can be concluded that F_{max} for JLTFET is 2.49 GHz and for PD-JLTFET F_{max} is 1.36 GHz due to parasitic effect in case of PD-JLTFET.

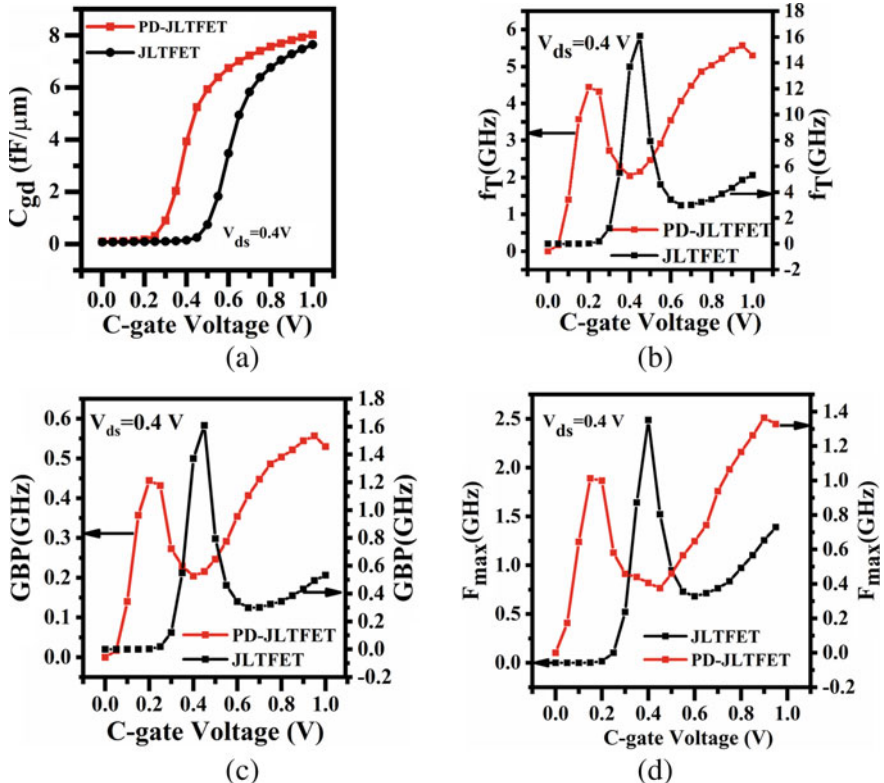


Fig. 7 Comparison between JLTFET and PD-JLTFET **a** gate-to-drain capacitance (C_{gd}) **b** cut-off frequency (f_T) **c** GBP **d** maximum oscillation frequency (F_{max}) versus V_{cg}

4 Conclusion

We have shown an effective technique to enhance the capability of the device in context to sub-threshold swing (SS), OFF-state current, ON-state current. The device performance of the intended PD-JLTFET is compared with the existing JLTFET. The device performance for the various spacing length between control-gate and polarity-gate is also analyzed. The SS of PD-JLTFET is 9.08 mV/decade, i.e., Very less as compare to conventional JLTFET, which has SS is equal to 40.2 mV/decade. The PD-JLTFET shows a significantly higher I_{ON}/I_{OFF} ratio, therefore improving its switching capability and makes it best suited for the use of low power applications.

Acknowledgements This work is supported by the SMDP-C2SD under the reference letter no. 9(1)2014-MDD (NIT Delhi, INDIA).

References

1. Kilchytska V et al (2003) Influence of device engineering on the analog and RF performances of SOI MOSFETs. *IEEE Trans Electron Devices* 50(3):577–588
2. Mohankumar N, Syamal B, Sarkar CK (2010) Influence of channel and gate engineering on the analog and RF performance of DG MOSFETs. *IEEE Trans Electron Devices* 57(4):820–826
3. Malili A, Chattopadhyay A (2012) The impact of fringing field on the device performance of a p-Channel tunnel field-effect transistor with a high-k gate dielectric. *IEEE Trans Electron Devices* 59(2):277–282
4. Bangsaruntip S, Cohen GM, Majumdar A, Sleight JW (2010) Universality of short-channel effects in undoped-body silicon nanowire MOSFETs. *IEEE Electron Device Lett* 31(9):903–905
5. Boucart K, Ionescu AM (2007) Double-gate tunnel FET with high- κ gate dielectric. *IEEE Trans Electron Devices* 54(7):1725–1733
6. Seabaugh AC, Zhang Q (2010) Low-voltage tunnel transistors for beyond CMOS logic. *Proc IEEE* 98(12):2095–2110
7. Bhuwalka KK, Schulze J, Eisele I (2005) Scaling the vertical tunnel FET with tunnel bandgap modulation and gate work function engineering. *IEEE Trans Electron Devices* 52(5):909–917
8. Nirschl T et al (2006) Scaling properties of the tunneling field effect transistor (TFET): Device and circuit. *Solid State Electron* 50(1):44–51
9. Choi WY, Park BG, Lee JD, Liu TJK (2007) Tunneling field- effect transistors (TFETs) with subthreshold swing (SS) less than 60 mV/dec. *IEEE Electron Device Lett* 28(8):743–745
10. Wang PF et al (2004) Complementary tunneling transistor for low power application. *Solid State Electron* 48(12):2281–2286
11. Zhang Q, Zhao W, Seabaugh A (2006) Low-subthreshold-swing tunnel transistors. *IEEE Electron Device Lett* 27(4):297–300
12. Kam H, King-Liu TJ, Alon E, Horowitz M (2008) Circuit-level requirements for MOSFET-replacement devices. In: 2008 IEEE international electron devices meeting 2008. IEDM, vol 11, no 6, p 1 (2008)
13. Mookerjea S, Datta S (2008) Comparative study of Si, Ge and InAs based steep subthreshold slope tunnel transistors for 0.25v supply voltage logic applications. In: 2008 device research conference. Dig. DRC, vol 567, no 2, pp 47–48 (2008)
14. Collet J, Tharaud O, Chapoton A, Vuillaume D (2000) Low- voltage, 30 nm channel length, organic transistors with a self- assembled monolayer as gate insulating films. *Appl Phys Lett* 76(14):1941–1943
15. Ionescu AM, Riel H (2011) Tunnel field-effect transistors as energy-efficient electronic switches. *Nature* 479(7373):329–337
16. Kao KH, Verhulst AS, Vandenberghe WG, Soree B, Groeseneken G, De Meyer K (2012) Direct and indirect band-to-band tunneling in germanium-based TFETs. *IEEE Trans Electron Devices* 59(2):292–301
17. Abdi DB, Kumar MJ (2016) Suppressing ambipolar conduction using dual material gate in tunnel-FETs having heavily doped drain. *Int J Electron Commun Eng* 10(5):594–598
18. Hrazia A, Vladimirescu A Amara, Anghel C (2012) An analysis on the ambipolar current in Si double-gate tunnel FETs. *Solid State Electron* 70:67–72
19. Tirkey S, Sharma D, Yadav DS, Yadav S (2017) Analysis of a novel metal implant junction less tunnel FET for better DC and analog/RF electrostatic parameters. *IEEE Trans Electron Devices* 64(9):3943–3950
20. Ghosh B, Akram MW (2013) Junctionless tunnel field effect transistor. *IEEE Electron Device Lett* 34(5):584–586
21. Saurabh S, Kumar MJ (2011) Novel attributes of a dual material gate nanoscale tunnel field-effect transistor. *IEEE Trans Electron Devices* 58(2):404–410
22. Daley DM, Tran HH, Woods WH, Zhang Z (2015) Tunnel field-effect transistors with a gate-swing broken-gap heterostructure. U.S. Patent 9,087,717 B2, 21 Jul 2015. (Online). Available: <https://www.google.ch/patents/US9087717>

23. Silvaco, Atlas user's manual, Silvaco, Inc., 408: 567–1000 (2016)
24. Raushan MA, Alam N, Siddiqui MJ (2019) Electrostatically doped drain junction less transistor for low-power applications. *J Comput Electron* 0123456789
25. Raushan MA, Alam N, Siddiqui MJ (2018) Dopingless tunnel field-effect transistor with over-sized back gate: proposal and investigation. *IEEE Trans Electron Devices* 65(10):4701–4708
26. Aghandeh H, Ziabari SA (2017) Gate engineered heterostructure junctionless TFET with Gaussian doping profile for ambipolar suppression and electrical performance improvement. *Superlattices Microst* 1(111):103–114
27. Mouritsen OG, Ipsen JH, Zuckermann MJ (1989) Lateral density fluctuations in the chain-melting phase transition of lipid monolayers. *J Colloid Interface Sci* 129(1):32–40
28. Schenk A (1992) A model for the field and temperature. *Solid State Electron* 35(11):1585–1596
29. Daineka D, Bulkin P, Girard G, Bour J (2004) High density plasma enhanced chemical vapor deposition. *Phys J* 9:3–9

A Study on Stability Analysis of QT Interval Dynamics of ECG Using ARMAX Model



A. Jyothsana and J. Sivaraman

Abstract The stability analysis of Electrocardiogram (ECG) intervals helps in determining its response to various disturbances in the cardiac cycle. ARMAX (Autoregressive with Moving Average and Exogenous Input) modeling of QT Interval (QTI) using RR Interval (RRI) as exogenous input shows the dependency of ventricular repolarization on heart rate. This study predicts the QTI using the ARMAX model, to evaluate the stability of QTI dynamics and then, to identify the factors responsible for causing instabilities. One minute-long ECG signals were recorded from Normal sinus Rhythm (NSR) subjects and the QTI of each signal are then modeled using the ARMAX approach. The stability of QTI dynamics was determined using the pole-zero plot. The proposed ARMAX model was capable of detecting unstable QTI in NSR subject and the unstable QTI was mainly due to Heart Rate Variability (HRV) within one-minute ECG.

Keywords ECG · Heart rate variability · QT interval · Stability analysis

1 Introduction

The action potential of cardiac muscle cells is obtained as an Electrocardiogram (ECG) recording. The QRS complex of the ECG signal is obtained as a result of depolarization of the ventricles and the *T* wave of ECG signal represents ventricular repolarization. Thus, the QT Interval (QTI) which consists of both QRS complex and *T* wave signifies the Action Potential Duration (APD) of the ventricle. The instability of cellular APD can be seen in the QTI of the ECG signal. The unstable QT Intervals (QTIs) increase the chances of arrhythmia in patients having different

A. Jyothsana · J. Sivaraman (✉)

Bio-Signals and Medical Instrumentation Laboratory, Department of Biotechnology and Medical Engineering, National Institute of Technology, Rourkela, Odisha 769008, India
e-mail: jsiva@nitrkl.ac.in

A. Jyothsana
e-mail: 218BM1001@nitrkl.ac.in

cardiovascular diseases like QT syndrome [1–3] and acute myocardial infarction [4–6]. In some studies, the instabilities of the QT interval (QTI) indicate Ventricular Tachycardia (VT) and Ventricular fibrillation (VF) in patients [7]. Any abnormalities in the ventricular repolarization of the ECG signal can be the root cause of different types of ventricular arrhythmia. APD restitution is the dependency of APD on its preceding Diastolic Interval (DI). The restitution slope detects the abnormality in APD. For a larger APD restitution slope (>1) even smaller variations in DI can cause an unstable APD [8]. The adaptability of the ventricular APD with the heart rate was studied by Halamek et al. [9] and the role of Premature Activation (PA) and QTI instability to the onset of VT was explored by Chen et al. [10]. The normal QT variability can change with the presence of PA in the ECG signal. The presence of such unstable QTIs can lead to arrhythmias such as sustained VT in cardiac patients.

Recently, Imam et al. [11] have conducted a study to analyze the stability of ECG interval and came up with the factors responsible for causing instability in QTI. From that study, they found that HRV is also responsible for causing unstable segments because HRV is more in healthy hearts and is more asymmetry as compared to an unhealthy heart. A methodology for determining the stability of PTA Interval (PTAI) was developed by Sivaraman et al. [12]. The authors studied the variation of atrial repolarization using ARX model and explored the role of PA and HRV in PTAI stability. Sivaraman et al. [13] had also studied the morphology of depolarization and repolarization wave of atria in healthy subjects using the signal-averaging method and they observed a decrease in the duration of repolarization wave with the increase in heart rate. They also concluded that the duration of the repolarization wave varies with the age of subjects. As ventricular arrhythmia continues for a longer time, the refractory period of ventricular tends to become shorter. This will have an impact on ventricular repolarization phase. The changes in ventricular repolarization can cause ventricular arrhythmia.

This study is performed to analyze stability in QTI dynamics in NSR subjects. The QTI dynamics are predicted using the ARMAX model. The equation derived using the ARMAX approach in the time domain is then converted to the Z-domain for assessing the stability. Further, the factors responsible for causing changes in the QTI variability is also investigated in this study.

2 Methods

2.1 Subjects

One minute-long ECG data of fifty NSR subjects were collected using the EDAN PC ECG system. The subject group had twenty-five males and twenty-five females of mean age 29.4 ± 5.3 years (range 20–40 years). The subjects were medically examined to exclude any form of cardiovascular disease. Smokers and patients with congestive heart failure, valvular disease, and other cardiopulmonary diseases that

may alter the ECG morphology were excluded from this study. ECG data with less noise is selected so that the QRS and *T* waves are visible and no further denoising process is required.

2.2 ECG Data Analysis

All the collected ECGs were imported to MATLAB(R 2018a) for further digital data analysis. The time duration from the beginning of the *Q* wave to the end of *T* wave was defined as the QTI. The QTI time series is extracted from the ECG signals and the RRI time series is extracted to detect the presence of PA and Huikuri et al. [14] proposed a method to find out the count of PA from the RRI time series.

PA was encountered when the RRI of a beat was smaller than the previous beat by at least 100 ms. The proposed methodology for detecting the instability in the QTI consists of two steps. First, the dependency of QTI on its previous QTIs and RRIs are represented using the ARMAX model. Second, the instability is determined by converting the derived ARMAX model equation into *Z*-domain.

2.3 ARMAX Modeling in QTI Dynamics

ARMAX approach is used to model the QTI in one-min ECG

$$\sum_{i=0}^A a_i \text{QTI}(K - i) = \sum_{i=1}^B b_i \text{RRI}(K - i) + \sum_{i=0}^C c_i e(K - i) \quad (1)$$

where *K* denotes the beats in 1 min ECG Segment. QTI and RRI are the discrete signals which represent APD and DI. QTI(*K*), QTI(*k* − *i*) and RRI(*k* − *i*) denotes the duration of the QTI and RRI for beat *k* and *k* − *i*, respectively. *e*(*K*) represents the discrete signal of error values which occurs between successive QTIs. *a_i*, *b_i* and *c_i* are the weight constants for QTI, RRI, and error terms, respectively, which contribute to QTI.

A, *B* and *C* represent the number of model parameters. The term $\sum_{i=0}^A a_i \text{QTI}(K - i)$ represents the autoregressive part, the term $\sum_{i=1}^B b_i \text{RRI}(K - i)$ represents the exogenous input and the last term $\sum_{i=0}^C c_i e(K - i)$ represents the moving average part of the ARMAX model. We have used *A* = *B* = *C* in this study where the value of *B* and *A* indicate the effect of heart rate and ventricular repolarization that are used in the model for the prediction of QTI duration as mentioned by Imam et al. [11]. We have used RRI instead of TQ Interval (TQI) because there is a chance for the TQI to get affected by the previous QTI hence; TQI is no longer an exogenous input. The system identification toolbox in MATLAB is used to determine the parameters of the ARMAX model.

$$\begin{aligned}
& a_0 \text{QTI}(k) + a_1 \text{QTI}(k-1) + \cdots + a_A \text{QTI}(k-A) \\
& = b_1 \text{RRI}(k-1) + \cdots + b_B \text{RRI}(k-B) + C_0 e(k) \\
& + C_1 e(k-1) + \cdots + C_c e(k-C)
\end{aligned} \tag{2}$$

Equation (2) shows the expanded form of Eq. (1)

For each iteration, the order of QTI, i.e., A was incremented by 1. Then the minimum value of A at which instability is obtained for the first time is denoted as A_{\min} . That is, the number of poles required to determine the instability for the first time is A_{\min} . Similarly, the value of A at which the predefined prediction value of QTI is obtained was denoted as A_{\max} . Hence, the number of poles required to predict the QTI accurately for the first time is A_{\max} . The Mean Square Error (MSE) between the calculated and measured QTI value should be less than 5 ms^2 for better accuracy.

2.4 Stability Analysis of QT Intervals

To evaluate the stability of QTI dynamics, the ARMAX model equation in the time domain is converted to Z-domain.

Equation (3) represents the Z-Transform of Eq. (2)

$$\begin{aligned}
& a_0 \text{QTI}(Z) + a_1 Z^{-1} \text{QTI}(Z) + \cdots + a_A Z^{-A} \text{QTI}(Z) \\
& = b_1 Z^{-1} \text{RRI}(z) + \cdots + b_B Z^{-B} \text{RRI}(Z) \\
& + C_0 e(z) + C_1 Z^{-1} e(Z) + \cdots + C_c Z^{-C} e(Z)
\end{aligned} \tag{3}$$

Equation (4) is obtained by rearranging Eq. (3)

$$\begin{aligned}
& \text{QTI}(Z)[a_0 + a_1 Z^{-1} + \cdots + a_A Z^{-A}] \\
& = \text{RRI}(Z)[b_1 z^{-1} + \cdots + b_B Z^{-B} + e(Z)[C_0 + C_1 Z^{-1} + \cdots + C_C Z^{-C}]] \tag{4}
\end{aligned}$$

The relationship between the output QTI and input RRI can be expressed using a transfer function based model as in Eq. (5)

$$G(z) = \frac{\text{QTI}(z)}{\text{RRI}(z)} = \frac{b_1 z^{-1} + b_2 z^{-2} + \cdots + b_B z^{-B}}{a_0 + a_1 z^{-1} + \cdots + a_A z^{-A}} \tag{5}$$

The solution of the numerator and denominator polynomials in Eq. (5) represents zeros and poles, respectively. If the values of poles and zeros are equal then they get canceled each other. This pole-zero plots can be used to determine the stability of ECG intervals and if any of the poles is having a magnitude greater than 1 or when it comes outside the unit circle then such a condition is considered to be unstable.

3 Results

ARMAX model was developed for each one-minute-long ECG of NSR subjects. The accuracy of predicted QTI is evaluated by measuring the MSE between the measured QTI and calculated QTI. The model order required to predict the measured QTI with better accuracy in one of the NSR subjects is $A_{\max} = 12$, whereas at $A_{\min} = 7$ the accuracy of prediction is less, as the MSE between the measured and predicted values of QTI is not less than 5 ms^2 . However, the model shows instability condition for the first time at $A_{\min} = 7$ in NSR subject. The measured and predicted value of QTI at $A_{\min} = 7$ and $A_{\max} = 12$ for NSR subject is obtained in Fig. 1a, b. In the pole-zero plot of NSR subject as the value of 'A' is increased from 7 to 12 it was observed that the number of poles is coming outside the unit circle is increased but the position of poles having a magnitude greater than unity obtained at $A_{\min} = 7$ remains the same as observed in Fig. 2a, b, respectively. The results are showing that the larger number of model orders are essential for better prediction of QTI but the instability can be found using the minimum number of model orders in the NSR subjects. The variation of the MSE with the number of beats for NSR subject is obtained in Fig. 3a.

4 Discussion

Chen et al. [10] used an autoregressive model with exogenous input as RRI to access the stability of the ventricular repolarization process and the model includes the ECG artifacts which can cause instability in QTI. The proposed ARMAX model is capable of separating the system dynamics from ECG artifacts. Imam et al. [11] found that PA is not the main cause for instabilities in QTI dynamics and is in agreement with the present finding of this study. He found that the HRV is more complex in healthy subjects as compared to VT subjects and hence, the PA beat is not the only factor for causing the unstable and stable conditions in QTI dynamics.

Using the ARMAX model, we have analyzed the effect of HRV on QTI in NSR subjects. Since the QTI affects the impending TQI, the focus of this study is on HRV based on analyzing RRIs as it covers both QTI and TQIs. Many studies have concluded that QTI dynamics can get affected by several factors such as respiration, age, temperature, gender, genetic profile, and autonomous nervous system [15, 16]. A study was conducted on the variations of PTaI dynamics with sinus rate, pacing, and drugs in heart block patients by Debbas et al. [17]. In a study conducted by Sivaraman et al. [13] on *P* and Ta wave morphology it was noted that with age there is a prolongation in the *P* and Ta wave duration and *P*-Ta interval get shortened with the increase in heart rate. Acharya et al. [18] have reported that HRV is more in a healthy heart and it is also more asymmetric as compared to the diseased heart. In this study, the impact of HRV has caused instability in the QTI dynamics of NSR subject whereas the chances of PA are minimum. In addition to HRV, the other intrinsic factors which are described in [15, 16] can also be held responsible for causing

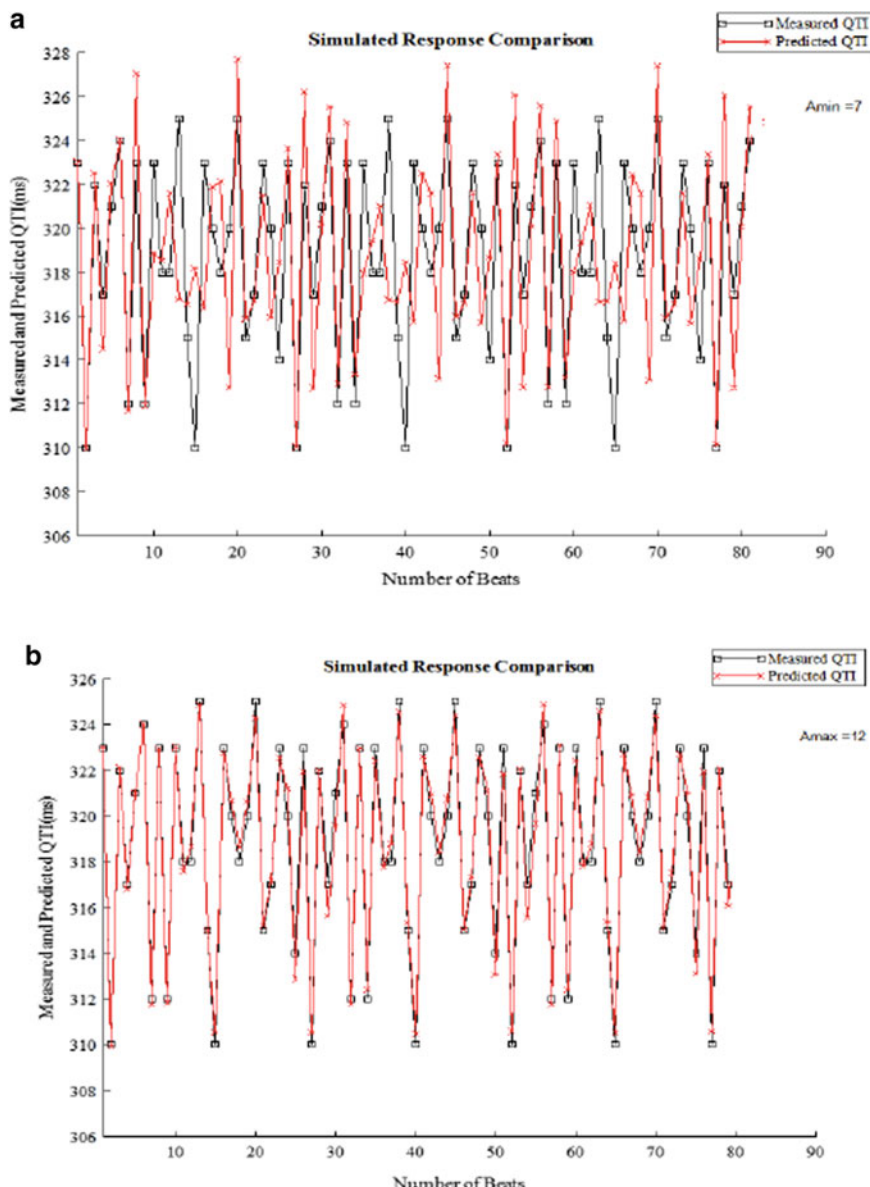


Fig. 1 **a** Measured and predicted value of QTI for NSR subject at $A_{\min} = 7$. **b** Measured and predicted value of QTI for NSR subject at $A_{\max} = 12$

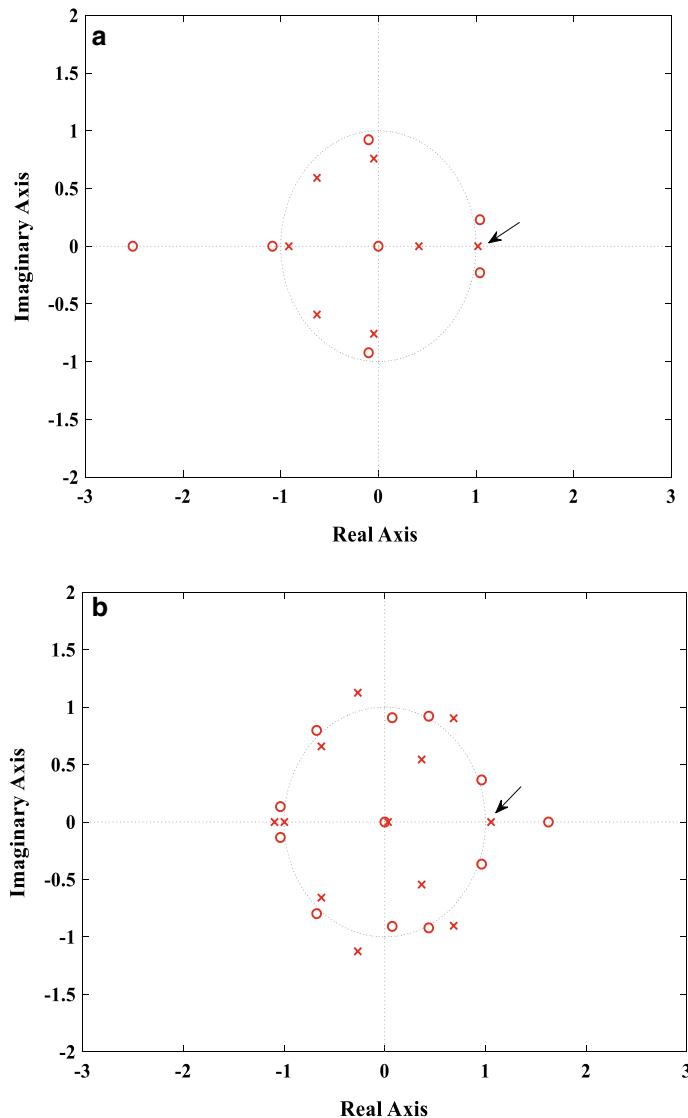


Fig. 2 **a** Pole-zero plot for NSR subject at $A_{\min} = 7$. **b** Pole-zero plot for NSR subject at $A_{\max} = 12$

instabilities in NSR subject which are in agreement with the study done by Imam et al.

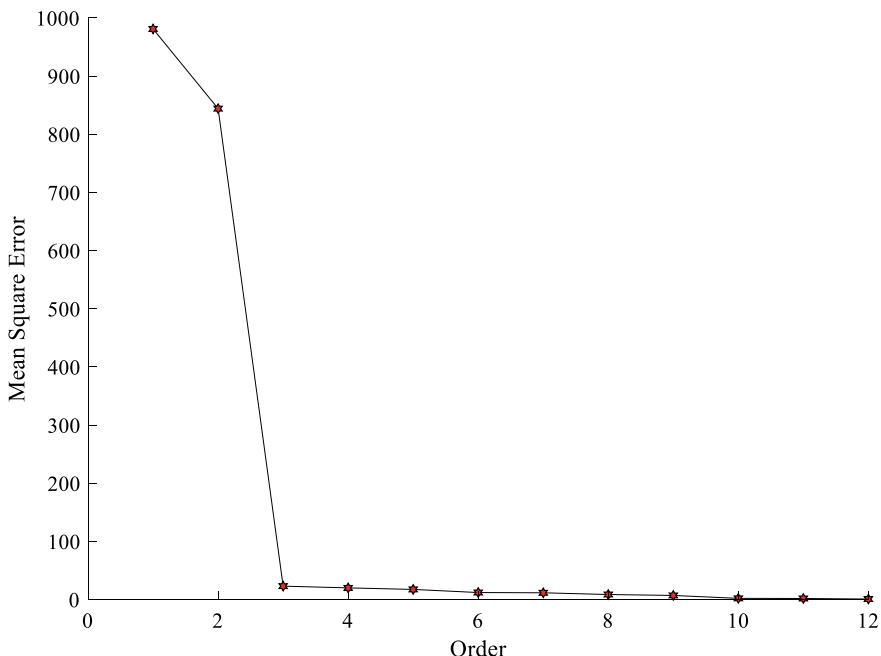


Fig. 3 a Variation of mean square error with the order

5 Conclusion

In this study, for the stability analysis of ventricular repolarization, the ARMAX model has been used in the determination of impending QTIs. The value of QTI predicted using derived ARMAX model was in agreement with the measured QTI in NSR subjects. In this study, we have found the instability condition in NSR subjects and the presence of instability in NSR subjects was mainly attributed to the presence of HRV. The result of this study indicates that the ECG signal predicted using the ARMAX model can be used to find out the development of instability in QTI due to HRV in healthy subjects. These instabilities are responsible for the development of arrhythmia risk. From this preliminary study, it was found that the ARMAX model was capable of predicting the QTI more accurately. Also, it determines the unstable intervals at minimum order which helps in saving the computational time.

Acknowledgements The authors acknowledge the support from MHRD, Government of India, for sponsoring the M.Tech. Programme of the first author. The present study was supported by financial grants from the Science Engineering Research Board (SERB), Department of Science and Technology, Government of India (EEQ/2019/000148).

References

1. Merri M, Moss AJ, Benhorin J, Locati EH, Alberti M, Badilini F (1992) Relation between ventricular repolarization duration and cardiac cycle length during 24-hour Holter recordings: findings in normal patients and patients with long QT syndrome. *Circulation* 85(5):1816–1821
2. Yamauchi S, Yamaki M, Watanabe T, Yuuki K, Kubota I, Tomoike H (2002) Restitution properties and occurrence of ventricular arrhythmia in LQT2 type of long QT syndrome. *J Cardiovasc Electrophysiol* 13(9):910–914
3. Chinushi M, Restivo M, Caref E, El-Sherif N (1998) Electrophysiological basis of arrhythmicity of QT/T alternans in the long-QT syndrome: tridimensional analysis of the kinetics of cardiac repolarization. *Circ Res* 83(6):614–628
4. Schwartz PJ, Wolf S (1978) QT interval prolongation as predictor of sudden death in patients with myocardial infarction. *Circulation* 57(6):1074–1077
5. Bonnemeier H, Wiegand UK, Bode F, Hartmann F, Kurowski V, Katus HA, Richardt G (2003) Impact of infarct-related artery flow on QT dynamicity in patients undergoing direct percutaneous coronary intervention for acute myocardial infarction. *Circulation* 108(24):2979–2986
6. Szydlo K, Trusz-Gluza M, Wita K, Filipecki A, Orszulak W, Urbanczyk D, Krauze J, Kolasa J, Tabor Z (2008) QT/RR relationship in patients after remote anterior myocardial infarction with left ventricular dysfunction and different types of ventricular arrhythmias. *Ann Noninvasive Electrocardiol* 13(1):61–66
7. Couderc JP (2009) Measurement and regulation of cardiac Ventricular repolarization: from the qt interval to repolarization morphology. *Philos Trans R Soc A Math Phys Eng Sci* 367(1892):1283–1299
8. Nolasco JB, Dahlen RW (1968) A graphic method for the study of alternation in cardiac action potentials. *J Appl Physiol* 25(2):191–196
9. Halamek J, Jurak P, Lipoldova J, Leinveber P (2010) QT/RR coupling and gender differences. *Comput Cardiol* 37(2010):365–368
10. Chen X, Trayanova NA (2012) A novel methodology for assessing the bounded-input bounded-output instability in qt interval dynamics: application to clinical ecg with ventricular tachycardia. *IEEE Trans Biomed Eng* 59(8):2111–2117
11. Imam MH, Karmakar CK, Khandoiker AH, Palaniswami M (2013) Effect of premature activation in analyzing QT dynamics instability using QT-RR model for ventricular fibrillation and healthy subjects. In: 2013 proceedings of annual international conference of the IEEE engineering in medicine and biology society (EMBC), pp 2559–2562
12. Sivarajan J, Uma G, Langley P, Umapathy M, Venkatesan S, Palanikumar G (2016) A study on stability analysis of atrial repolarization variability using ARX model in sinus rhythm and atrial tachycardia ECGs. *Comput Methods Programs Biomed* 137:341–351
13. Sivarajan J, Uma G, Venkatesan S, Umapathy M, Kumar NK (2014) A study on atrial ta wave morphology in healthy subjects: an approach using P wave signal-averaging method. *J Med Imaging Healthinfo* 4(5):675–680
14. Huikuri HV, Valkama JO, Airaksinen KE, Seppanen T, Kessler KM, Takkunen JT, Myerburg RJ (1993) Frequency domain measures of heart rate variability before the onset of nonsustained and sustained ventricular tachycardia in patients with coronary artery disease. *Circulation* 87(4):1220–1228
15. Almeida R, Gouveia S, Rocha AP, Pueyo E, Martinez JP, Laguna P (2006) QT variability and HRV interactions in ECG: quantification and reliability. *IEEE Trans Biomed Eng* 53(7):1317–1329
16. Porta A, Tobaldini E, Gnechi-Ruscone T, Montano N (2010) RT variability unrelated to heart period and respiration progressively increases during graded head-up tilt. *Am J Physiol Hear Circ Physiol* 298(5):1406–1415

17. Debbas NMG, Jackson SHD, De Jonghe D, Robert A, Camm AJ (1999) Human atrial repolarization: Effects of sinus rate, pacing and drugs on the surface electrocardiogram. *J Am Coll Cardiol* 33(2):358–365
18. Acharya UR, Joseph KP, Kannathal N, Lim CM, Suri JS (2006) Heart rate variability: a review. *Med Biol Eng Comput* 44(12):1031–1051

High Frequency Resonant Inverter with Shunt Active Power Filter for Harmonic Compensation



Rohan Sinha and Rahul Raman

Abstract This paper presents a high frequency resonant inverter which has been used as a power supply unit for an induction heating unit. Generally, power electronic devices being nonlinear loads introduce quite a high amount of harmonics, which in turn deteriorates the power factor. Therefore, this paper proposes a power filter stage has been devised for the mitigation of harmonics. As the main harmonic-related problem is with the input current, a shunt active power filter has been used. A voltage source inverter (VSI) has been used for the design of the filter, which has an additional control circuitry. The main aim here is to produce the compensating currents, which in turn governs the switching of the VSI. For this purpose, the instantaneous power theory (PQ theory) has been used for generation of compensating currents; these currents are then fed into a hysteresis controller (aversion of PWM) for generation of the gating signals. All the circuits are simulated using the PSIM platform and the results with and without the filter have been compared to obtain the desired results.

Keywords Resonant inverter · Shunt active power filter · VSI · Instantaneous power theory · Hysteresis control · THD · FFT · PSIM · Induction heating

1 Introduction

As the use of electronic and power electronic devices like is increasing at a steady rate, they pose some disorder in the utility supply because of their nonlinear nature. On such device is an inverter, a device which converts DC signals into AC signals. The inverter which will be discussed in this project is a high frequency resonant inverter, [1] which will be used as a power supply unit for induction heating. Induction heating is one of the most popular heating technologies used in the present

R. Sinha (✉)

Department of Electrical Engineering, Jorhat Engineering College, Jorhat, Assam, India
e-mail: sinharohan29@gmail.com

R. Raman

Department of Electrical Engineering, Indian Institute of Technology (ISM), Dhanbad, India
e-mail: rahulraman20@ee.ism.ac.in

era right from domestic heating to industrial heating. This is mainly because of the advantages associated with it like compact size, high power density, efficiency, easy controllability over power, etc. There are many configuration of the inverter which can be used for induction heating purpose like Class E resonant inverters [1], single ended resonant inverter [3], full bridge inverter [2–5], modified half bridge inverter [7], etc. For induction heating to be effective, the inverter concerned should switch at a very high frequency so as to be able to produce a high frequency AC output signal. This high frequency oscillating voltage signals induce eddy current in the workpiece causing the object to heat given by Joule's heating law. But being nonlinear loads and high frequency switching devices, they produce a high amount of harmonics. These harmonics have a natural tendency to flow back into the utility supply, thereby causing distortion of the input signal. Also, these harmonics are responsible for creating undesirable conditions in the grid, special when sensitive equipment is connected to the supply. Therefore, there is a need of circuits which can eliminate these harmonics making the utility supply sinusoidal. These circuits are referred to as filter circuits which are classified broadly as passive filters [5] and active power filters [6–9]. Passive filters do play a vital role in harmonic mitigation, but they come with some limitations such as large inductor or capacitor size, their tendency to undergo resonance with the source and the poor dynamic response of these filters. These are the reasons why passive filters fail to compensate for the harmonics under certain circumstances. Active power factors are therefore a preferable option which can overcome the limitations of passive filter and provide an effective harmonic compensation.

In this paper, the filter which will be coupled along with the high frequency resonant inverter is a shunt active power filter(SAPF). An SAPF [10] is a variant of power filters which is used for current harmonic mitigation connected between the nonlinear load and supply. This filter is generally preferred due to simplicity in design, easy control circuit and low cost. It basically consists of a voltage source inverter (VSI) for producing the compensating current and a control circuit which produces the reference current for generation of the gating pulse for the VSI. The instantaneous power theory has been employed for extraction of the current and a hysteresis current controller is used for generating the gating pulses. The shunt active power filter works by producing harmonics of equal magnitude but is 180° phase shifted. These signals generated by the filter are injected at the PCC and cancel out the harmonics making the utility supply near sinusoidal.

2 High Frequency Resonant Inverter

As it has been mentioned above, for the purpose of induction heating, the voltage signal to the load should be of high frequency. Therefore, a high frequency resonant inverter is employed for the purpose of generating this high frequency output [2, 5]. The inverter used here is a full bridge inverter (four IGBTs are used as switch) which is PWM controlled. The resonant condition created by the load, where the load forms

a parallel resonating circuit. Only when the resonant frequency of the load matches the switching frequency of the inverter, the inverter is said to be operating in the resonant state. This condition has to be fulfilled for the source to be able to transfer the maximum power to the load or the induction heater in this case.

2.1 Calculation of Switching Frequency and Load Parameters

For the resonant condition to deliver the maximum power to the load without power loss, the switching frequency of the inverter has to be precisely determined [2]. The switching frequency f_s should be near the resonance of the tank circuit. Here, the formula of parallel resonance is used for calculation. For it to satisfy the resonant condition, the susceptance part (imaginary) should be zero.

$$\omega = \sqrt{\frac{L_{\text{eq}} - C_{\text{eq}}R^2}{L_{\text{eq}}^2 C_{\text{eq}}}} \quad (1)$$

$$f_s = \frac{1}{2\pi} \sqrt{\frac{L_{\text{eq}} - C_{\text{eq}}R_{\text{eq}}^2}{L^2 C_{\text{eq}}}} \quad (2)$$

Always the capacitor and inductor value should be selected first because variable capacitors and inductors are expensive and easily available. On putting the values of the different parameters $R_{\text{eq}} = 1 \Omega$, $L_{\text{eq}} = 57.1 \mu\text{H}$, $C_{\text{eq}} = 0.2 \mu\text{F}$, the value of $f_s = 47 \text{ kHz}$. Therefore, Eq. (2) gives the resonant frequency which is essential for the inverter to resonate and to ensure ZVS.

3 Reference Current Generation

One of the most important part of the circuit is the control circuit based on which the gating pulses of the SAPF is determined. The proper control of the filter is required for effective compensation. To achieve the reference currents, the instantaneous power theory (PQ) has been used [6, 8, 10]. The instantaneous power theory was proposed by Akagi in the year 1983 and is a time domain analysis approach. This is a theory which is based on the conversion of abc coordinate to the $\alpha\beta\theta$ coordinate. And then define instantaneous power based on these coordinates. This control through current generation method can be used for both three-phase three-wire or four-wire systems. The main transformation consists of the Clark's transform given as,

$$\begin{bmatrix} V_o \\ V_\alpha \\ V_\beta \end{bmatrix} = \sqrt{\frac{2}{3}} \begin{bmatrix} \frac{1}{\sqrt{2}} & \frac{1}{\sqrt{2}} & \frac{1}{\sqrt{2}} \\ 1 & \frac{1}{2} & -\frac{1}{2} \\ 0 & \frac{\sqrt{3}}{2} & -\frac{\sqrt{3}}{2} \end{bmatrix} \begin{bmatrix} V_{sa} \\ V_{sb} \\ V_{sc} \end{bmatrix} \quad (3)$$

$$\begin{bmatrix} I_o \\ I_\alpha \\ I_\beta \end{bmatrix} = \sqrt{\frac{2}{3}} \begin{bmatrix} \frac{1}{\sqrt{2}} & \frac{1}{\sqrt{2}} & \frac{1}{\sqrt{2}} \\ 1 & \frac{1}{2} & -\frac{1}{2} \\ 0 & \frac{\sqrt{3}}{2} & -\frac{\sqrt{3}}{2} \end{bmatrix} \begin{bmatrix} I_{sa} \\ I_{sb} \\ I_{sc} \end{bmatrix} \quad (4)$$

After the above transformation is performed, the instantaneous powers have to be now calculated. As in a three-phase system, the current in $I_o = 0$ the power P_o is also equal to zero. So we have to now consider only the p and q part of the power. Therefore, the power can be given as follows,

$$\begin{bmatrix} p \\ q \end{bmatrix} = \begin{bmatrix} V_\alpha & V_\beta \\ -V_\beta & V_\alpha \end{bmatrix} \begin{bmatrix} I_\alpha \\ I_\beta \end{bmatrix} \quad (5)$$

As it is clear from the above equation, the instantaneous power consists of two main parts the oscillatory and the average components. The SAPF should be able to compensate for this oscillatory power. After the power calculation, an low pass filter (LPF) is required to eliminate the spurious components and extract the fundamental components from the power p . The next step is to determine the compensating currents given as,

$$\begin{bmatrix} I_{s\alpha} \\ I_{s\beta} \end{bmatrix} = \frac{1}{V_\alpha^2 + V_\beta^2} \begin{bmatrix} V_\alpha & V_\beta \\ V_\beta & -V_\alpha \end{bmatrix} \begin{bmatrix} p \\ q \end{bmatrix} \quad (6)$$

Having calculated the reference currents which are given by Eq. (6), these currents now need to be transferred back to the abc coordinate. For this purpose, the inverse Clark's transformation is used which gives back the compensating currents in abc coordinates.

$$\begin{bmatrix} I_{ca}^* \\ I_{cb}^* \\ I_{cc}^* \end{bmatrix} = \sqrt{\frac{2}{3}} \begin{bmatrix} 1 & 0 \\ \frac{-1}{2} & \frac{\sqrt{3}}{2} \\ \frac{-1}{2} & -\frac{\sqrt{3}}{2} \end{bmatrix} \begin{bmatrix} I_{s\alpha} \\ I_{s\beta} \end{bmatrix} \quad (7)$$

One of the issues associated in controlling the power filter is to maintain the DC link voltage. A separate controller has to be present in order to maintain a constant DC link. For this purpose, a proportional integral controller has been used which compares the voltage across the DC link capacitor and a reference voltage to produce a signal. This signal is than compared with the “ p ” part of the calculated power to obtain the required compensating power signal. So as to be able to mitigate the harmonics effectively, the reference voltage is always kept higher than that of the input utility supply. Therefore, the recommended reference voltage is always kept three to four times higher than the input.

4 Hysteresis Current Control

Hysteresis control is one of the most well known methods for controlling inverters and other switching devices [10]. It is actually an improvised version of PWM generation. In this proposed method, a Schmitt trigger has been used to form the PWM signal. A Schmitt trigger is a comparator with a positive feedback which forces the Op Amp into the saturation region. Using which a hysteresis band is formulated having two thresholds, the upper threshold and the lower threshold. Every time the error signals tries to cross these thresholds, the controller produces a change in the external signal. The error current deviate within the hysteresis band and forms the required pulsating signal (Fig. 1).

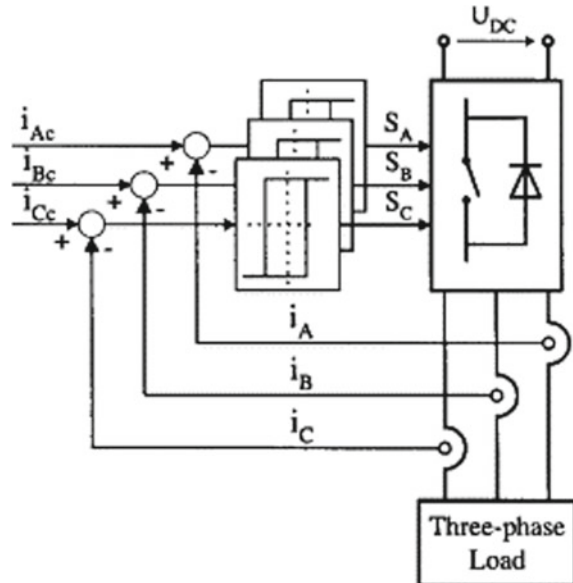
The hysteresis bands upper and lower thresholds can be determined by the formula given below. (A non-inverting type Schmitt trigger is used for this purpose)

$$V_{LT} = \frac{-(+V_{sat})R_1}{R_2} \quad (8)$$

$$V_{UT} = \frac{-(-V_{sat})R_1}{R_2} \quad (9)$$

$$V_H = \frac{R_1}{R_2}[+V_{sat} - (-V_{sat})] \quad (10)$$

Fig. 1 Hysteresis controller
[11]



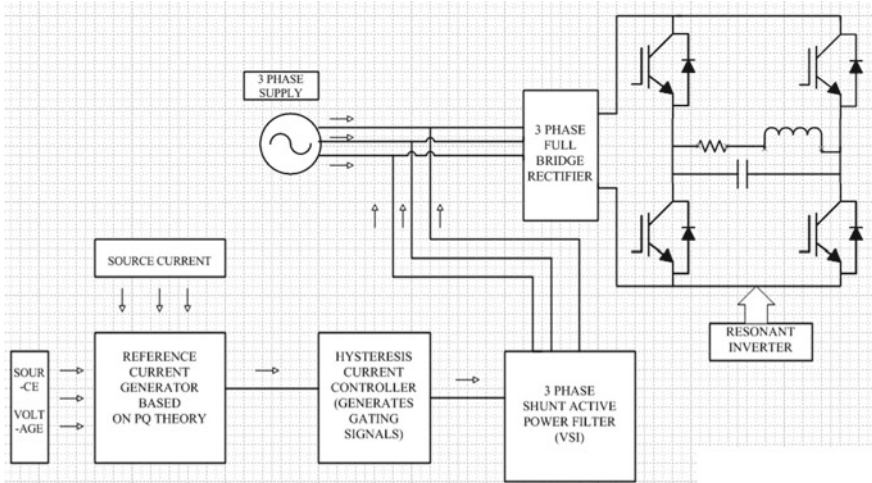


Fig. 2 General layout of the method used

5 Block Diagram of Method Used

The above general layout represents the method which has been used for the compensation of the harmonics produced by the high frequency resonant inverter. The control is divided into two parts, the reference current generation unit-based PQ theory and the hysteresis controller which is responsible for generating the switching pulses. These pulses are then fed into a three-phase VSI acting as the SAPF. The compensating currents are further injected at the point where the load is connected to the supply. The resonant inverter is fed from a three-phase power supply via a diode bridge rectifier which provides the pulsating DC supply for the inverter. For the reference current generation, the source voltages and currents are utilised (Fig. 2).

6 Simulation Diagrams and Experimental Results

All the simulation has been performed in PSIM platform. The simulation diagrams consist of high frequency resonant inverter without the filter and another one with the shunt active power filter. After that, the input currents are compared and their FFT analysis is done. The core motive of this work is to improve the signal quality of the input signal which is fed to the induction heater, which further says that the THD content of the signal has to be improved within some tolerable limit (Figs. 3, 4, 5, 6, 7 and 8).

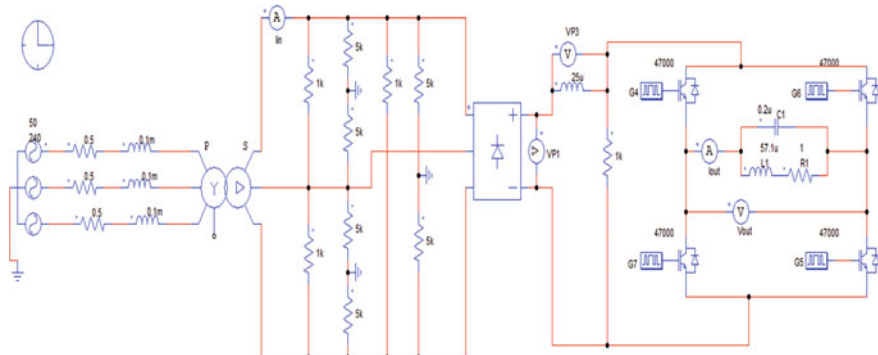


Fig. 3 High frequency resonant inverter without SAPF

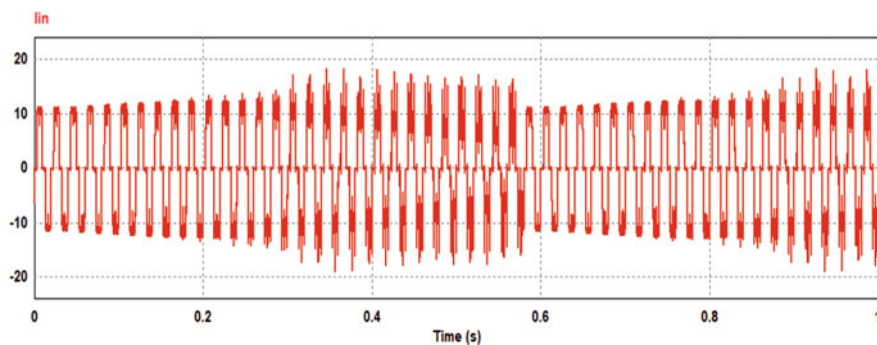


Fig. 4 Supply input current of inverter without SAPF

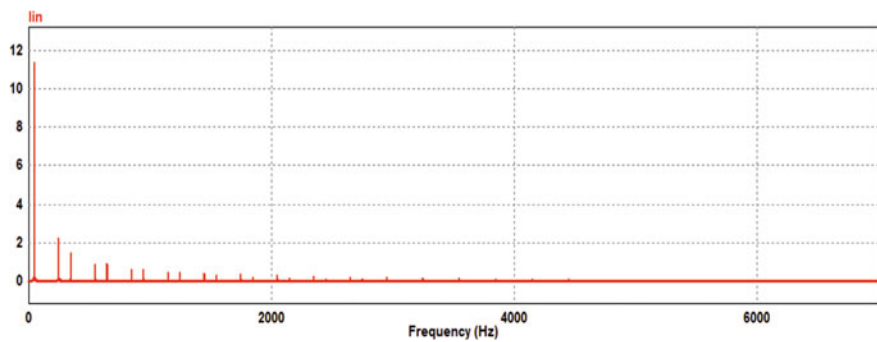


Fig. 5 FFT analysis of input current without filter

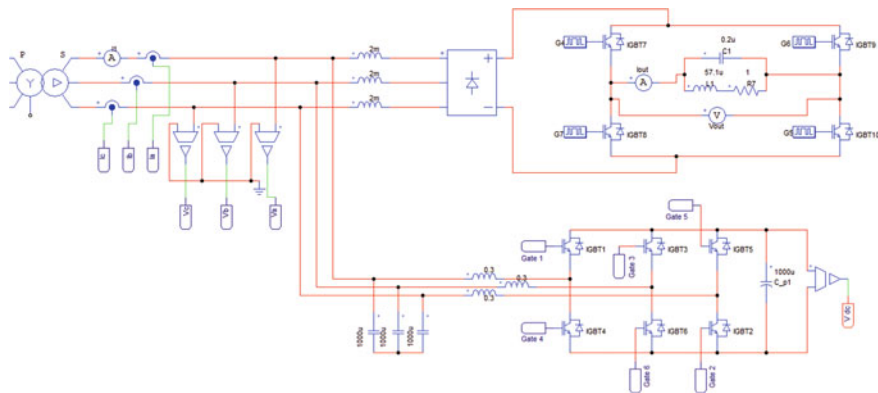


Fig. 6 Simulated circuit of the inverter with the SAPF

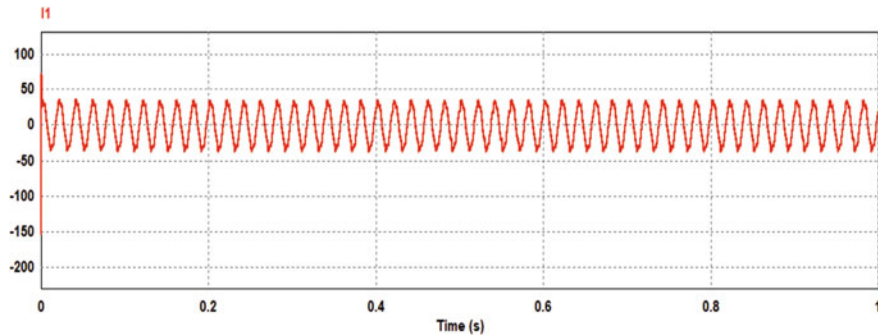


Fig. 7 Input current signal with SAPF

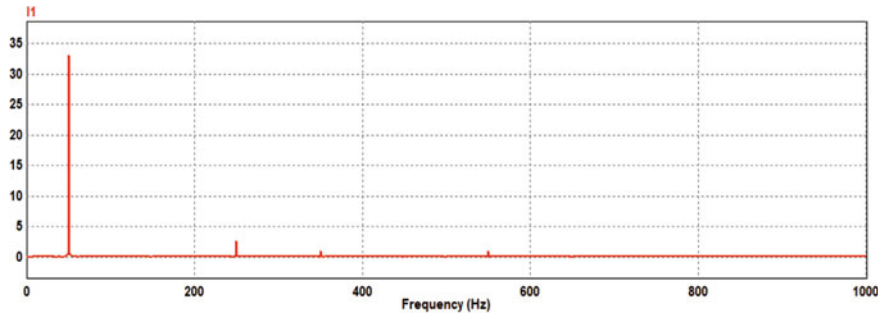


Fig. 8 FFT analysis of the input signal using SAPF

7 Calculation of Total Harmonic Distortion

As it is evident from the FFT analysis of the two signals, the one without the filter is quite non-sinusoidal and contains a high amount of harmonic. The one where the filter has been installed contains lower amount of harmonic and the utility power supply is almost near sinusoidal. The THD can be calculated as given below [5],

$$\text{THD} = \frac{\sqrt{\sum_{n=2,3}^{\infty} I_n^2 \text{ rms}}}{I_1 \text{ rms}} \quad (11)$$

7.1 THD Without Filter

$$\begin{aligned} \text{THD} &= \frac{\sqrt{5.208^2 + 2.8608^2 + 2.391^2 + 0.7332^2 + 0.6727^2}}{14.5} \\ &= 45.25\% \end{aligned}$$

7.2 THD with Filter

$$\begin{aligned} \text{THD} &= \frac{\sqrt{2^2}}{20.6} \\ &= 9.7\% \end{aligned}$$

8 Conclusion

This work therefore deals with the compensation of harmonics to improve the overall power factor and quality of the input current signal. Also, a controller has been designed based on the of instantaneous power theory to control the active filter. Then the experimental results of the simulation have been compared to determine the effectiveness of the filter. Without the filter the THD content has been found out to be at a 45.25% and with the SAPF the THD has been significantly brought down to 9.7%. So, it can be conclude that the filter has been able to reduce the harmonics, thereby improving the overall power factor.

References

1. Gorain C, Sadhu PK, Raman R (2018) Analysis of high-frequency class E resonant inverter and its application in an induction heater. In: 2nd international conference on power, energy and environment: towards smart technology, IEEE
2. Kumar A, Sadhu PK, Raman R, Singh J (2018) Design analysis of full-bridge parallel resonant inverter for induction heating application using pulse density modulation technique. In: International conference on power energy, environment and intelligent control, IEEE, 13–14 April 2018
3. Yeon JE, Cho KM, Kim HJ (2015) A 3.6 kW single-ended resonant inverter for induction heating applications. IEEE, 8–10 Sept 2015
4. Sugimura H, Sumiyoshi S, Mun SP, Kwon SK, Nakaoka M (2008) A novel one stage ZVS-PWM high frequency resonant inverter with boost single diode conducting mode passive ZCS-PFC scheme, IEEE, 10–13 Nov 2008
5. Raman R, Sadhu P, Kumar A, Kumar Sadhu P (2018) Design and analysis of EMI and RFI suppressor for induction heating equipment using vienna rectifier. In: 2nd international conference on power, energy and environment: towards smart technology, IEEE, 1–2 June 2018
6. Fujita H, Akagi H (1991) A practical approach to harmonic compensation in power systems-series connection of passive and active filters. IEEE Trans Indus Appl 27(6):1020–1025
7. Pal P, Sadhu PK, Pal N, Sanyal S (2015) An exclusive design of EMI-RFI suppressor for modified half bridge inverter fitted induction heating equipment. Int J Mechatron Electr Comput Technol (IJMEC) 5(15):2084–2100
8. Afonso JL, Pinto JG, Gonçalves H. Active power conditioners to mitigate power quality problems in industrial facilities. In: Power quality issues. IntechOpen
9. Budhrani AH, Bhayani KJ, Pathak AR (2018) Design parameters of shunt active filter for harmonics current mitigation. PDPU J Energy Manage 59–65
10. Shah A, Vaghela N (2014) Shunt active power filter for power quality improvement in distribution systems. Int J Eng Dev Res 1(2):23–27
11. Kazmierkowski MP (2002) Pulse width modulation techniques for three-phase voltage source. In: Krishnan R, Blaabjerg F (eds) Control in power electronics, 1st edn. Academic Press, 84 Theobolds Road, London WC1X 8RR, UK, pp 89–160



Rohan Sinha hails from Jorhat, Assam, India. He received his B.Tech degree in Electronics and Communication Engineering from DUIET, Dibrugarh University, Dibrugarh, Assam. He is currently pursuing his M.Tech degree in Electrical Engineering from Jorhat Engineering College, Assam, India.



Rahul Raman received the B.Tech degree in Electrical Engineering from National Institute of Technology, Agartala, India, and the M.Tech degree in Power System Engineering from Indian Institute of Technology (ISM), Dhanbad. He is currently a Doctoral Research Scholar with the Department of Electrical Engineering, Indian Institute of Technology (ISM), Dhanbad, and he is also working as an Assistant Professor in the Department of Electrical Engineering, Jorhat Engineering College, Assam, India. His area of research interest includes induction heating applications, power quality improvement, high frequency resonant inverter, filter designing, etc. He has several journal and conference publications at national and international levels along with a patent published in the same domain.

Modelling of Fiber Bragg Grating Sensor for Acoustic Pressure Wave Detection of Partial Discharge in Power Transformer



Sorokhaibam Nilakanta Meitei, Kunal Borah, and Saibal Chatterjee

Abstract Partial discharge (PD) detection in power transformer is a useful condition monitoring process. Various sensors like piezoelectric, optical fiber, capacitive and ultra-high frequency (UHF) sensors have been used for the monitoring of the power transformer. FBG sensor can be installed inside the transformer tank and is able to capture even low acoustic signal of PD due to its high sensitivity, small size and immunity to EMI. Hence in this work, an FBG sensor has been modelled for PD detection in transformer using COMSOL Multiphysics. Authors have studied the sensing performance of the model FBG sensor with different coating radii.

Keywords Power transformer · PD · Fiber Bragg grating (FBG) · Finite element method

1 Introduction

In the power grid, power transformers are costly and important equipment because of its working performance is direct influences the security and stability of the whole network [1]. Complete breakdowns of the transformer can happen without any signs, following in dangerous insulating oil spills, widespread damage to nearby apparatus and extreme interruption of service. Insulation breakdown is the main reason for

S. N. Meitei

Department of Electrical Engineering, North Eastern Regional Institute of Science and Technology, Nirjuli, Arunachal Pradesh 791109, India
e-mail: soroniameitei@gmail.com

K. Borah

Department of Physics, North Eastern Regional Institute of Science and Technology, Nirjuli, Arunachal Pradesh 791109, India
e-mail: kbnerist@gmail.com

S. Chatterjee (✉)

Department of Electrical and Electronics Engineering, National Institute of Technology Mizoram, Aizawl, Chaltlang, Mizoram 796012, India
e-mail: saibalda@ieee.org

the transformer failures, and frequently, PDs are included in such failure by deteriorating the dielectric characteristics of the insulating oil [2]. Therefore, continuously checking the health condition of the insulation system is necessary to protect from a complete breakdown and to avoid the huge cost. The most commonly adopted PD detection technique for power transformer is namely, electrical, chemical, acoustic, optical and opto-acoustic techniques [2, 3]. Among these PD detection methods of power transformer, the opto-acoustic method is adopted in this work.

The PD acoustic wave can be detected by using a PZT sensor. Recently, Meitei et al. [4] have modelled a piezoelectric sensor for PD detection and localization in distribution transformer using COMSOL Multiphysics software. An externally installed PZT sensor has the merits of a simple arrangement [5]. But it may deteriorate from surrounding noise like EMI and corona event, and it is also complicated in discovering the precise location of PD source due to its various routes of acoustic sound wave propagation in the transformer. To overcome these demerits of an externally installed piezoelectric sensor, an optical-based FBG sensor is applied for the application of PD detection [6]. FBG sensors have been designed for their application in different fields, like hydrogen gas detection in an oil-filled power transformer [7, 8], structural condition monitoring [9–11] and underwater acoustic detection [12]. Few researchers [13–15] have been experimentally investigated the PD detection in an oil-filled power transformer using Fiber Bragg Grating (FBG) sensor. Massimo Moccia et al. [16, 17] have been designed the FBG sensor using COMSOL Multiphysics software for the application of an underwater acoustic sensor. In this work, authors have designed an acoustic FBG sensor using FEM-based software COMSOL Multiphysics for PD acoustic wave detection in power transformer.

2 Theoretical Background and Simulation Model

FBG is a type of distributed Bragg reflector constructed in a short segment of optical fiber core [18]. When the broadband light is incident on the FBG, it reflects a particular wavelength and transmits all others. The reflected wavelength is known as the Bragg wavelength, and as follows [19].

$$\lambda_B = 2n_{\text{eff}}\alpha \quad (1)$$

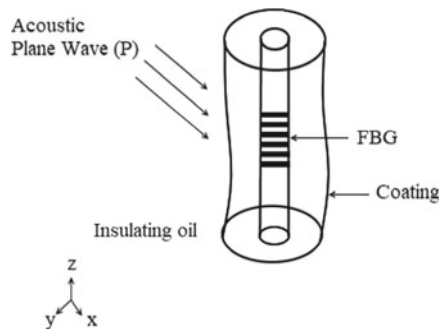
where α represents the grating period.

n_{eff} represents the effective refractive index.

The working principle of PD detection in a power transformer using an FBG sensor is presented in Fig. 1. Generally, it includes a complicated interaction of several physical phenomena.

When the PD acoustic wave distributing in an oil (i.e. transformer insulation oil) strikes on the composite structure of FBG sensor, its geometry gets mechanical deformation. The strain appears on the FBG due to mechanical deformation. In this work, transformer oil where PD acoustic pressure waves distribute is defined as an

Fig. 1 Working principle of PD detection using an FBG sensor



acoustic medium. The model FBG sensor consists of cylindrical shape optical fiber and coating is defined as the mechanical medium.

2.1 Power Transformer and FBG Sensor Model

The 3D model of 3-phase, 35 kV power transformer [20] is modelled using the CAD tools of COMSOL Multiphysics and is presented in Fig. 2. The sizes of the power transformer and its materials properties are given in Tables 1 and 2.

The 3D model of partial discharge acoustic FBG sensor is presented in Fig. 3. It is a composite structure which are consists of two-cylinder, inner cylinder which represents the optical fiber, and the another one is the outer cylinder which represents

Fig. 2 Power transformer model

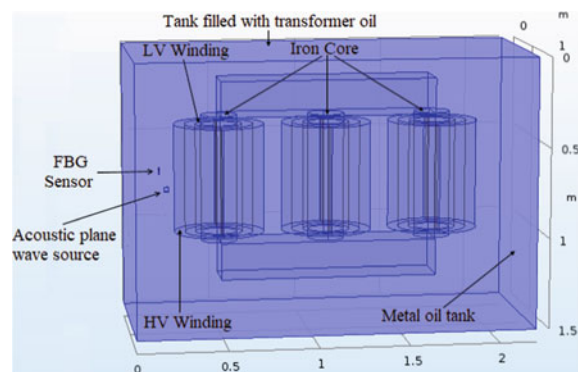
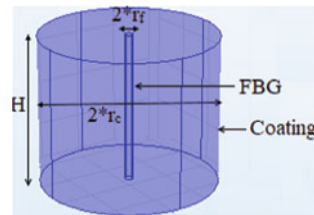


Table 1 Dimensions of 3D model of power transformer [20]

Component	Dimension (m)
Transformer tank ($L \times W \times H$)	$2.2 \times 1 \times 1.5$

Table 2 Properties of the material [20]

Components	Material	Density $\rho_0' (\text{kg/m}^3)$	Speed of sound (m/s)
Transformer tank and core	Structural steel	7850	5100
Winding	Copper	8700	4760
Oil	Insulating oil	890	1420

Fig. 3 3D model of FBG sensor

the coating of the fiber. The FBG model dimensions and its materials properties are given in Tables 3 and 4.

The modelled FBG sensor is installed inside the oil-filled power transformer at coordinate (0.2, 0.1, 0.7) to detect PD acoustic wave signal. Considering that the PD acoustic plane wave is incident on the FBG sensor in the form of an acoustic plane wave. At the boundary between the transformer oil and transducer emitting side, the constant acoustic pressure plane wave is defined (Dirichlet boundary condition) with the amplitude of 1 MPa [17]. The PD investigation is conducted within the frequency range of 80–200 kHz [3].

Table 3 Dimensions of 3D model of FBG sensor [17]

Components	Dimensions
Radius of optical fiber (r_f)	62.5 μm
Coating radius (r_c)	1.25 mm
Height of the optical fiber and coating (H)	5 mm

Table 4 Material properties of the model FBG sensor components [17]

Components	Young's modulus (E)	Poisson's ratio (v)	Density (ρ)
Optical fiber	72 GPa	0.17	2200 kg/m^3
Coating	78 MPa	0.3	1180 kg/m^3

2.2 Sensitivity Calculation of Model FBG Sensor

The sensitivity can be calculated by [17]:

$$S = \frac{\Delta\lambda}{\lambda_0 p_0} = \frac{1}{p_0} \left\{ \varepsilon_z - \frac{n_{\text{eff}}^2}{2} [p_{11}\varepsilon_x + p_{12}(\varepsilon_z + \varepsilon_y)] \right\} \quad (2)$$

where $\Delta\lambda$, λ_0 , p_0 and n_{eff} represent the Bragg wavelength shift, the central wavelength of the FBG, pressure amplitude, the effective refractive index (i.e. $n_{\text{eff}} = 1.465$), p_{11} and p_{12} represent elasto-optic parameters (i.e. $p_{11} = 0.121$, $p_{12} = 0.265$) and ε_i ($i = x, y, z$) are the coordinate at the FBG position where the strain components are calculated.

The sensitivity gain as follows [17].

$$\text{Sensitivity Gain} = 20 \log_{10} \left(\left| \frac{S}{S_{\text{bare}}} \right| \right) \quad (3)$$

where $S_{\text{bare}} = -2.76 \times 10^{-6} \text{ MPa}^{-1}$ [17].

3 Results and Discussion

To study the opto-acoustical response of the coated FBG sensor, the authors consider a specific sensor structure. For this first simulation case, the radius of the cylindrical shape coating is 1.25 mm, the radius of the optical Fiber Bragg grating is 62.5 μm , and the height is 5 mm [17]. The simulation is conducted in the frequency range of 80–200 kHz with an interval of 5 kHz [3].

When the acoustic plane wave produced by PD strikes on the FBG sensor, its geometry gets mechanical deformation due to its elastic properties, and the strain distributes on the surface of the model FBG sensor. The strain at the Bragg position defines the appear Bragg wavelength shift according to Eq. (2). Figure 4 shows the deformed structure of the model FBG sensor.

The sensitivity gain of the model FBG sensor is calculated using Eq. (3). The sensitivity gain curve of the model FBG sensor is presented in Fig. 5. The average sensitivity gain of the model FBG sensor was -230.43 dB, and the maximum sensitivity gain was -114.52 dB. From Fig. 5, obtained that the response of the model FBG sensor is decreasing from the lower frequencies to higher frequencies.

To analyze the sensing performance of the model FBG sensor, we have conducted the parametric study by changing the coating radius. In this study, dimensions and the material properties of the FBG sensor are kept as presented in Tables 3 and 4 except for the coating radius. The coating radius has been taken following a paper [17] to check the validity of our model based on COMSOL Multiphysics software. The

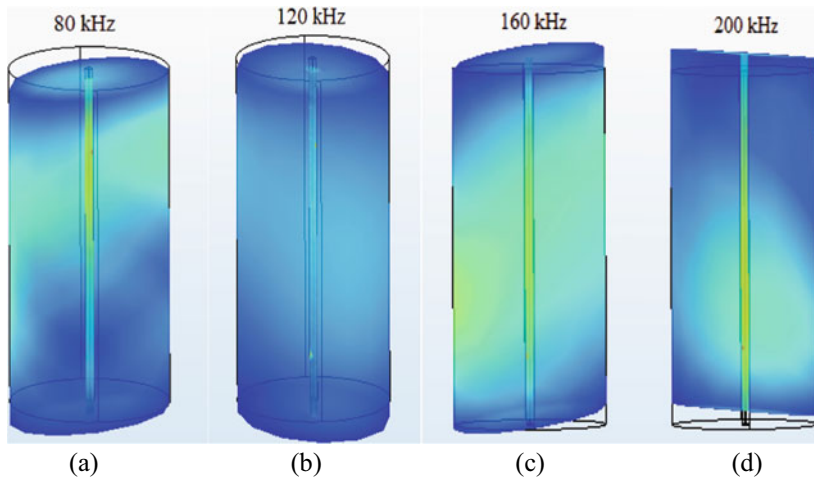
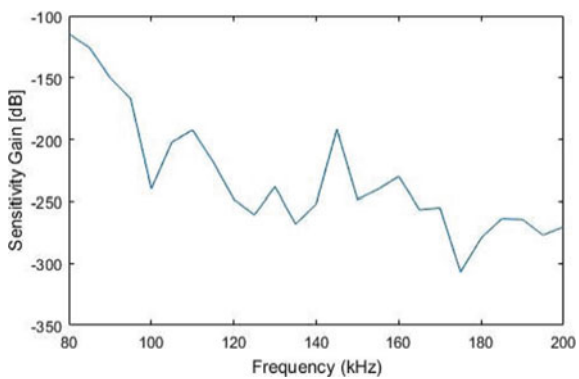


Fig. 4 Deformed structure and the z -strain distribution on the FBG sensor surface for various frequencies

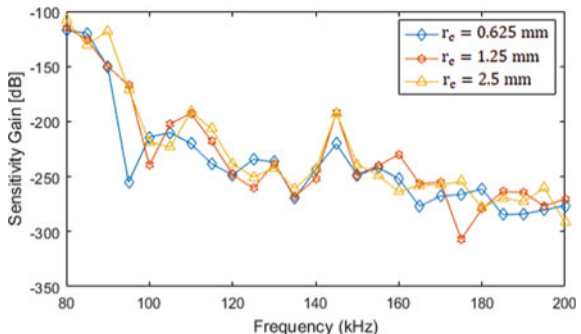
Fig. 5 Sensitivity gain curve



authors have investigated the sensing performance of the model FBG sensor by taking three different coating radii (i.e. $r_c = 0.625$ mm, $r_c = 1.25$ mm and $r_c = 2.5$ mm).

Figure 6 shows the sensitivity gain curve for different coating radii. It can be seen that the, when the coating radius is $r_c = 0.625$ mm, the average sensitivity gain of the model FBG sensor was -236.80 dB and the maximum sensitivity gain was -117.40 dB. When $r_c = 1.25$ mm, the average sensitivity gain was -230.43 dB and the maximum sensitivity gain was -114.52 dB. Similarly, when $r_c = 2.5$ mm, the average sensitivity gain was -227.53 dB and the maximum sensitivity gain was -107.72 dB. From the analysis, we found that increasing the radius of coating, enhancing the sensitivity of the model FBG sensor. Therefore, the model FBG sensor with coating radius $r_c = 2.5$ mm had a better sensing performance for partial discharge acoustic pressure wave detection. To the best authors' knowledge, there

Fig. 6 Sensitivity gain curve for different coating radii



exists no work on modelling of FBG as a PD sensor using COMSOL Multiphysics software. But, similar work on modelling of FBG sensor for underwater acoustic detection application using COMSOL Multiphysics software can be found in [16, 17] and the sensitivity performance of their underwater acoustic FBG sensor model is in good agreement with our model.

4 Conclusion

In this paper, modelled a coated FBG sensor for PD detection in power transformer using FEM-based software COMSOL Multiphysics. A parametric analysis was carried out by varying the coating radius of the FBG sensor to study its sensing performance. It obtained that increasing the radius of coating, enhancing the sensitivity of the model FBG sensor. Hence, the sensitivity response to the same acoustic wave signals in the frequency range of 80–200 kHz of the model FBG sensor with a radius of $r_c = 2.5 \text{ mm}$ has a better performance than the other two models. The proposed FBG sensor model shows the usefulness and effectiveness of the PD detection technique in a power transformer.

References

1. Xue N, Yang J, Shen D, Xu P, Yang K, Zhuo Z, Zhang L, Zhang J (2019) The location of partial discharge sources inside power transformers based on TDOA database with UHF sensors. IEEE Access 7(7):146732–146744
2. Deng J, Xiao H, Huo W, Luo M, May R, Wang A, Liu Y (2001) Optical fiber sensor-based detection of partial discharges in power transformers. Optics Laser Technol 33(5):305–311
3. Zhou HY, Ma GM, Zhang M, Zhang HC, Li CR (2019) A high sensitivity optical fiber interferometer sensor for acoustic emission detection of partial discharge in power transformer. IEEE Sens J
4. Meitei SN, Borah K, Chatterjee S (2020) Modelling of acoustic wave propagation due to partial discharge and its detection and localization in an oil-filled distribution transformer. Frequenz

- 74(1–2):73–81
- 5. Zheng Q, Ma G, Jiang J, Li C, Zhan H (2015) A comparative study on partial discharge ultrasonic detection using fiber Bragg grating sensor and piezoelectric transducer. In: 2015 IEEE conference on electrical insulation and dielectric phenomena (CEIDP), pp 282–285. IEEE (2015)
 - 6. Yu B, Kim DW, Deng J, Xiao H, Wang A (2003) Fiber Fabry-Perot sensors for detection of partial discharges in power transformers. *Appl Optics* 42(16):3241–3250
 - 7. Samsudin MR, Shee YG, Adikan FR, Razak BB, Dahari M (2016) Fiber Bragg gratings hydrogen sensor for monitoring the degradation of transformer oil. *IEEE Sens J* 16(9):2993–2999
 - 8. Jiang J, Ma GM, Li CR, Song HT, Luo YT, Wang HB (2015) Highly sensitive dissolved hydrogen sensor based on side-polished fiber Bragg grating. *IEEE Photon Technol Lett* 27(13):1453–1456
 - 9. Ma G, Li C, Quan J, Jiang J, Cheng Y (2011) A fiber Bragg grating tension and tilt sensor applied to icing monitoring on overhead transmission lines. *IEEE Trans Power Deliv* 26(4):2163–2170
 - 10. Goossens S, De Pauw B, Geernaert T, Salmanpour MS, Khodaei ZS, Karachalios E, Saenz-Castillo D, Thienpont H, Berghmans F (2019) Aerospace-grade surface mounted optical fibre strain sensor for structural health monitoring on composite structures evaluated against in-flight conditions. *Smart Mater Struct* 28(6):065008
 - 11. Tan CH, Shee YG, Yap BK, Adikan FM (2016) Fiber Bragg grating based sensing system: Early corrosion detection for structural health monitoring. *Sens Actuators A Phys* 1(246):123–128
 - 12. Bai X, Hu M, Gang T, Tian Q (2019) An ultrasonic sensor composed of a fiber Bragg grating with an air bubble for underwater object detection. *Optics Laser Technol* 112:467–472
 - 13. Ghorat M, Gharehpétian GB, Latifi H, Hejazi MA, Bagheri M (2019) High-resolution FBG-based fiber-optic sensor with temperature compensation for PD monitoring. *Sensors* 19(23):5285
 - 14. Ma G-M, Zhou H-Y, Shi C, Li Y-B, Zhang Q, Li C-R, Zheng Qing (2018) Distributed partial discharge detection in a power transformer based on phase-shifted FBG. *IEEE Sens J* 18(7):2788–2795
 - 15. Kanakambaran S, Sarathi R, Srinivasan B (2017) Identification and localization of partial discharge in transformer insulation adopting cross recurrence plot analysis of acoustic signals detected using fiber Bragg gratings. *IEEE Trans Dielectr Electr Insul* 24(3):1773–1780
 - 16. Moccia Massimo, Consales Marco, Iadicicco Agostino, Pisco Marco, Cutolo Antonello, Galdi Vincenzo, Cusano Andrea (2012) Resonant hydrophones based on coated fiber Bragg gratings. *J Lightwave Technol* 30(15):2472–2481
 - 17. Moccia M, Pisco M, Cutolo A, Galdi V, Bevilacqua P, Cusano A (2011) Opto-acoustic behavior of coated fiber Bragg gratings. *Opt Express* 19(20):18842–18860
 - 18. Ma G-M, Li C-R, Mu R-D, Jun J, Luo Y-T (2014) Fiber Bragg grating sensor for hydrogen detection in power transformers. *IEEE Trans Dielectr Electr Insul* 21(1):380–385
 - 19. Onn BI, Arasu PT, Al-Qazwini Y, Abas AF, Tamchek N, Noor AS (2012) Fiber Bragg grating sensor for detecting ageing transformer oil. In: 2012 IEEE 3rd international conference on photonics, pp 110–113. IEEE (2012)
 - 20. Gao C, Yu L, Xu Y, Wang W, Wang S, Wang P (2018) Partial discharge localization inside transformer windings via fiber-optic acoustic sensor array. *IEEE Trans Power Deliv* 34(4):1251–1260

Design and Investigation of Tunnel Junction Engineered Dopingless-TFET with Improved DC and RF/Analog Parameters Analysis



Abhishek Verma, Suruchi Sharma, Sneha Bharti, Manisha Bharti, and Baljit Kaur

Abstract Today's emerging trends of low power applications dopingless tunnel field-effect transistor (DLTFET) will replace MOSFET in the future. Hence, in this paper, we described a new tunnel junction engineered charge plasma-based DLTFET. A pocket of gallium arsenide (GaAs) is placed across the source and channel interface of the silicon film, thus increasing the likelihood of tunneling. Although GaAs bandgap is slightly more than silicon bandgap it has high electron mobility and low tunneling mass, resulting in increased current junction drivability. Besides, DC and analog/RF merit figures were evaluated in consideration of the carrier concentrations, energy bandgap diagram, parasitic capacitance, electric field, transconductance, transfer characteristics, cutoff frequency. Using the ATLAS device simulator, the simulation of conventional DLTFET and proposed device (TJE-DLTFET) was carried out. The proposed system showed a higher ON-current ($\sim 100 \mu\text{A}/\mu\text{m}$) and better subthreshold swing ($\sim 10.25 \text{ mV/decade}$). TJE-DLTFET showed a worthy choice for future high-frequency applications.

Keywords Non-local BTBT · GaAs · Dopingless-TFET · Subthreshold swing · Tunneling junction

1 Introduction

MOSFET continuous scaling down enables us to scale down supply voltage, enhancing current driving capacity with low power supply. Also, achieving a low OFF-state leakage current is useful. However, at the same moment due to its low ON-state current and its elevated subthreshold swing (SS) decreased to 60 mV per decade, the device is restricted to some extent. Along with this, it suffered from SCE, DIBL, and RDF because of doped regions MOSFET [1–5]. To reduce this limitation of MOSFET, further introduced conventional doped TFET with low OFF-state current that eliminates the problem of SCE, DIBL and it also reduces the subthreshold

A. Verma (✉) · S. Sharma · S. Bharti · M. Bharti · B. Kaur

Department of Electronics and Communication, National Institute of Technology Delhi, Delhi, India

e-mail: abhishekverma355@gmail.com

swing but increases the ON-state current by little amount because of poor BTBT [9–11]. For getting high ON-state current and to eliminate the RDF because of the doping mechanism, dopingless-TFET has been introduced. For the manufacture of dopingless-TFET, the annealing process and the ion implantation techniques do not need high temperature, this makes the dopingless-TFET realized with a low thermal budget [12–14]. The most delicate step in the fabrication of TFET is the formation of the abrupt junction for effective tunneling. Additionally, abrupt junction formation isn't an easy thing because of the massive diffusion of doping atoms existing in the drain and source section through the intrinsic doped TFET channel [6–8]. However, these problems related to doped TFET was solved by dopingless-TFET but for getting more tunneling efficiency and further increment in ON-state current, Tunnel Junction Engineered Dopingless TFET device is being proposed device (TJE-DLTFET).

For further comparative study purposes, the paper is broken down into four parts. Part 1.2 consist of device structure and simulation parameters, part 1.3 familiar of results and discussion which is sectioned into two subparts that is 1.3.1 DC analysis of transfer characteristics, carrier concentration, transconductance (g_m), energy band diagram, electric field, and 1.3.2 analog/RF study of the drain-gate capacitance (C_{gd}), gain bandwidth product (GBP), cutoff frequency (f_T), and maximum oscillation frequency (f_{max}) are addressed. Finally, the investigation throughout this paper will be concluded in the conclusion part 1.4.

2 Device Structure and Simulation Parameters

An intersectional overview of DLTFET and the suggested system (TJE-DLTFET) are included in Fig. 1a, b combined. Both devices are simulated using TCAD Silvaco tool [12, 17, 18, 22, 23]. The parameters considered for the device structures are shown in Table 1. Here, the charge plasma principle helpful to establish source p

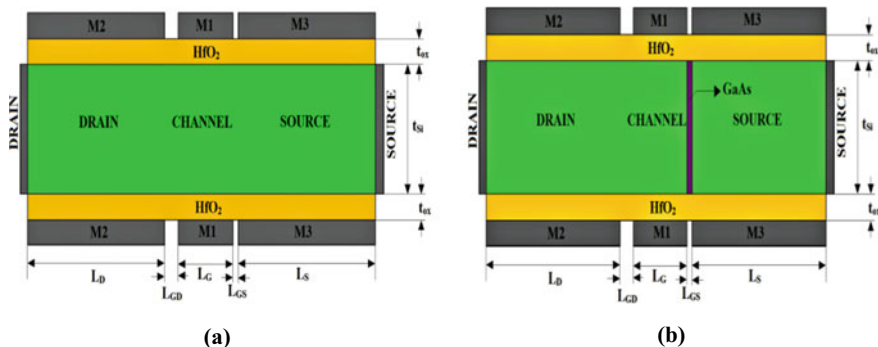


Fig. 1 Intersectional view of **a** DLTFET, **b** TJE-DLTFET

Table 1 Device structure and design parameters were seen in the simulation

Parameters	Values	Unit
Length of drain (L_D)	50	nm
Length of source (L_S)	50	nm
Length of channel (L_{CH})	20	nm
Drain and gate space (L_{GD})	5	nm
Source and gate space (L_{GS})	2	nm
The thickness of Silicon film (t_{Si})	10	nm
The thickness of physical oxide (t_{ox})/EOT	2	nm
Gate oxide material	HfO ₂ ($\epsilon = 21$)	unitless
The work function of drain (M2)	3.9	eV
The work function of source (M3)	5.93	eV
The work function of gate (M1)	4.3	eV
The thickness of inserted GaAs material	2	nm

+ region and drain $n+$ region. For source $p+$ region, platinum with work function as 5.93 eV is chosen to induce holes and for drain $n+$ region, hafnium with work function as 3.9 eV is chosen to induce electrons [15, 16]. In the proposed device (TJE-DLTFET), a vertical strip of gallium arsenide (GaAs) compound semiconductor material is incorporated across the source and channel of the thin silicon film tunneling junction. Although GaAs compound semiconductor material has a larger energy band gap than silicon, its inherent advantage of high electron mobility (8500 cm²/Vs) and smaller effective mass helps further enhancement of the band-band tunneling (BTBT) efficiency all over the source and channel tunneling junction [17]. The proposed device (TJE-DLTFET) can easily be fabricated in the same fashion as given to Daley et al. of IBM in a US patent, where a vertical structure is arranged as one layer stack composed of hetero-material surfaces [24]. The bandgap nature of GaAs components is direct, while the bandgap nature of silicon is indirect. The momentum corresponding to a minimum conduction band and also the maximum valence band is just the same indirect bandgap material. Thus, an electron can jump from conduction to valence band and vice versa by directly emitting or absorbing the photon.

However, the momentum corresponding to the conduction band minima and also the valence band maxima are different for an indirect bandgap material such as silicon. As a consequence, making a shift from one band to another needs a shift in momentum, and the electrons also need to absorb some additional energy from the crystal lattice vibrations to achieve the necessary momentum shift. This additional barrier in creating the transition significantly reduces the probability of the carriers for Band to Band tunneling (BTBT) [18]. The simulation models used for the simulation of the device in TCAD Silvaco include Fermi–Dirac,

Table 2 Material Parameters used in Simulation [10, 21]

Parameters	Silicon (Si)	Gallium arsenide (GaAs)
Bandgap, E_g	1.1 eV	1.42
Electron affinity, χ	4.07	4.07
Static dielectric constant, ϵ	11.7	13.2
Electron effective mass, m_e^*	0.522	0.072
Hole effective mass, m_h^*	0.44	0.55

Auger recombination, Shockley–Read–Hall (SRH) Recombination model, Lombardi (CVT) model, Concentration Dependent Recombination model, and Field Dependent mobility models are all included for additional precise and reliable simulation. Calculation of tunneling probability and the numerical solution is done by the Wentzel–Kramers–Brillouin (WKB) method [19–21] (Table 2).

3 Results and Discussions

3.1 DC Analysis

This part holds the analysis of the concentration of carrier and energy band diagram under OFF-state and also under ON-state. The impact of source and channel Tunnel Junction Engineering is used in TJE-DLTFET, it could be verified in Fig. 2a–d wherever it is seen that bandgap narrowed the same as DLTFET but a little sharp variation of the valence band of source and channel interface in TJE-DLTFET because the source and channel tunnel junction area comprises low effective mass material (GaAs). Under the OFF-state, between source and channel, the width of the tunneling barrier is high enough as shown in Fig. 2a, so charged carriers may not tunnel to channel conduction band from the source valence band in TJE-DLTFET and DLTFET which can be verified in Fig. 2b. Under ON-state condition, this can be seen as the positive bias applied through the gate electrode, the width of the barrier is reduced can be depicted in Fig. 2c which is sufficient to allow the majority of charge carriers to passageway easily to the channel conduction band from the valence band of the source region, it leads to an increase in the bulk of carriers charges across the channel, which Fig. 2d depict. The conduct of drain current (I_{DS}) concerning gate voltage (V_{GS}) for both DLTFET and TJE-DLTFET which can be verified from Fig. 3, which illustrates that the ON-state drain current (I_{DS}) of TJE-DLTFET showed better improvement compared to DLTFET. This increment in drain current (I_{DS}) is due to the availability of GaAs material across the source and channel tunnel junction. By keeping drain voltage $V_{DS} = 0.5$ V constant and gate voltage, V_{GS} varied where ON-state drain

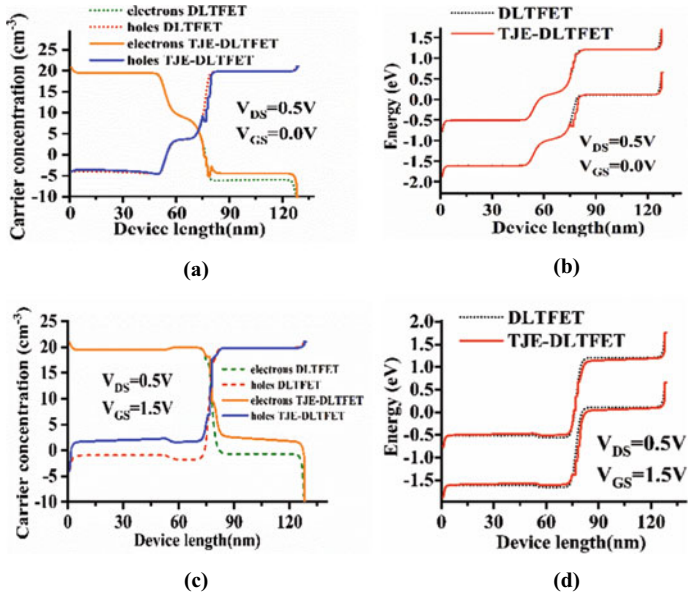
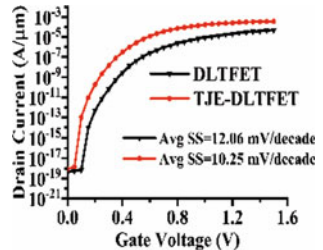


Fig. 2 **a** Carrier concentration in OFF-state, **b** energy band diagram in OFF-state, **c** carrier concentration in ON-state, **d** energy band diagram in ON-state for both DLTFTET and TJE-DLTFTET

Fig. 3 Transfer characteristics for both DLTFTET and TJE-DLTFTET



current (I_{DS}) for TJE-DLTFTET is recorded as $\sim 10^{-4}\text{ A}/\mu\text{m}$ and $\sim 0^{-5}\text{ A}/\mu\text{m}$ for that of DLTFTET at gate voltage $V_{GS} = 1.5\text{ V}$.

The spacer width (L_{GS}/L_{GD}) in both the gate/source electrode and gate/drain electrode, respectively must be chosen correctly as this is the primary factor across either junction for the tunneling of electrons. Reducing the gate/source spacer width (L_{GS}) increases tunneling of the majority of charge carriers at the source and channel interface, optimizing drain current (I_{DS}) under ON-state. [12]. In the ON-state, one can observe the electric field is maximum at the source/channel tunnel junction interface since the barrier range is reduced across it as well as the lesser effective mass of majority carriers. Consequently, there is an increment in tunneling efficiency; which in turn, allows the electric field across the source and channel interface to be reached at a peak, as shown in Fig. 4. Transconductance (g_m) is defined to be the rate at

Fig. 4 The electric field under ON-state for both and TJE-DLTFET and DLTFET

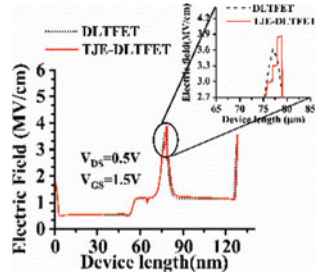
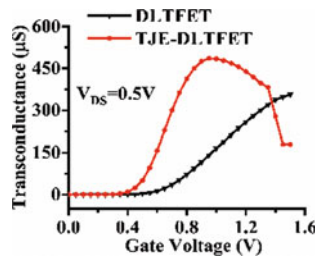


Fig. 5 Transconductance for both DLTFET and TJE-DLTFET



which gate voltage can be converted into drain current. TJE-DLTFET showed better sensitivity compared to DLTFET for the conversion of gate voltage to drain current because proposed TJE-DLTFET attains the maximum peak at lower gate voltage (V_{GS}) which starts decreasing at greater gate voltage (V_{GS}) due to degradation of mobility as depicted in Fig. 5.

3.2 Analog/RF Parameter Analysis

From the figure, it can be inferred that the proposed device has somehow the same parasitic capacitance as that of the DLTFET. The improvement in transconductance (g_m) has concluded the significant increment in the cutoff frequency (f_T) for the TJE-DLTFET compared to DLTFET because gate-to-drain capacitance (C_{gd}) as shown in Fig. 6. It shows a minimal increment in the C_{gd} value of TJE-DLTFET compared to DLTFET, therefore, the cutoff frequency of proposed TJE-DLTFET mainly dependent on the variation of transconductance (g_m) rather than the gate-to-drain capacitance (C_{gd}) as depicted in Fig. 7. The formula for the calculation of the cutoff frequency is as:

$$f_T = \frac{g_m}{2\pi(C_{gd} + C_{gs})} \quad (1)$$

However, Maximum oscillation frequency (f_{max}) is explained as the frequency where unit value for power gain. It can be formulated as:

Fig. 6 Gate to drain capacitance plot

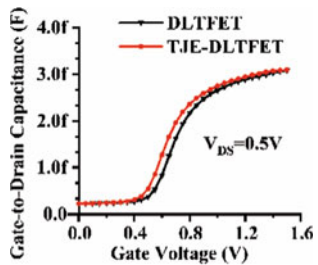


Fig. 7 Cutoff frequency plot

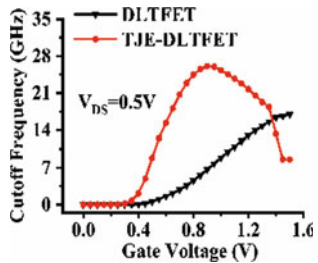
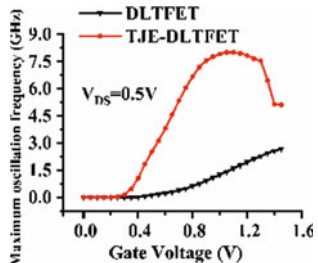


Fig. 8 Maximum oscillation frequency plot



$$f_{\max} = \sqrt{\frac{f_T}{8\pi C_{gd} R_{gd}}} \quad (2)$$

Gain Bandwidth Product (GBP) variation concerning gate voltage (V_{GS}) for both TJE-DLTFET and DLTFET is depicted in Fig. 9. It shows that the increment in gate

Fig. 9 Gain-bandwidth product (GBP) plot for both DLTFET and TJE-DLTFET

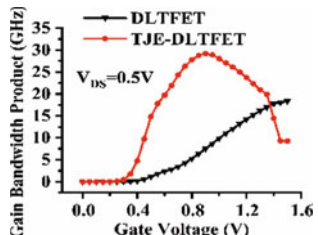


Table 3 Performance comparison for both the devices

Parameters	DLTFET	TJE-DLTFET
I_{ON} (A/ μ m)	$\sim 10^{-5}$	$\sim 10^{-4}$
I_{OFF} (A/ μ m)	$\sim 10^{-19}$	$\sim 10^{-19}$
I_{ON}/I_{OFF}	10^{14}	10^{15}
SS _{avg} (mV/decade)	12.06	10.25
V_T (V)	0.55	0.40

voltage (V_{GS}) result into initial increment in Gain Bandwidth Product (GBP) due to increase in the transconductance (g_m), but it starts decreasing for a higher value of gate voltage (V_{GS}) because of increment in gate-to-drain capacitance (C_{gd}). Therefore, TJE-DLTFET shows a higher GBP compared with DLTFET. The maximum value of GBP in TJE-DLTFET can approach to 29.17 GHz, which is higher as compared to 18.40 GHz in DLTFET. Thus, for high-frequency applications, TJE-DLTFET gives better performance.

$$\text{GBP} = \frac{g_m}{20\pi C_{gd}} \quad (3)$$

As depicted in Fig. 7, the maximum value of f_T for TJE-DLTFET is obtained at 26 GHz, which is higher than that for the DLTFET (of 17 GHz) obtained at the bias of $V_{ds} = 0.5$ V. Furthermore, Fig. 8 illustrates that the TJE-DLTFET exhibits a peak value of maximum oscillation frequency $f_{max} = 8.01$ GHz, and 2.68 GHz for the DLTFET for the bias of $V_{ds} = 0.5$ V (Table 3).

4 Conclusion

In this paper, DLTFET and TJE-DLTFET are explored by using the TCAD Silvaco simulation tool. In this regard, TJE-DLTFET (proposed device) has shown that the use of GaAs material through the source and channel tunnel junction, it facilitates the dropping of the energy band at the source and channel interface that also allows a strong tunneling efficiency of charge carriers due to high mobility and an effective mass of majority charge carriers. Thus, the enhanced drain current (I_{ds}), further showed the significant increment in the transconductance (g_m), which indicate the better current driving capability of the TJE-DLTFET compared to DLTFET. The result of TJE-DLTFET shows that the peak value of cutoff frequency (f_T) is 26 GHz, maximum oscillation frequency (f_{max}) is 8.01 GHz, and GBP is 29.17 GHz at lower gate voltage (V_{GS}), which offers the proposed TJE-DLTFET beneficial for high-frequency application. The threshold voltage (V_T) of TJE-DLTFET is 0.4 V which is lesser than compared to 0.55 V of DLTFET. Therefore, the proposed TJE-DLTFET opens the door for embedded ultra-low power device applications.

Acknowledgements The actual work is favored by the SMDP-C2SD under the specific reference letter No.9 (1)2014-MDD (NIT Delhi, Delhi, INDIA).

References

1. Choi WY, Park B-G, Lee JD, Liu T-JK (2007) Tunneling field-effect transistors (TFETs) with the subthreshold swing (SS) less than 60 mV/dec. *IEEE Electron Device Lett* 28(8):743–745
2. Wang PF, Hilsenbeck K, Nirschl T, Oswald M, Stepper C, Weis M, Schmitt-Landsiedel D, Hansch W (2004) Complementary tunneling transistor for low power application. *Solid-State Electron* 48(12):2281–2286
3. Bhuwalka KK, Schulze J, Eisele I (2005) Scaling the vertical tunnel FET with tunnel bandgap modulation and gate work function engineering. *IEEE Trans Electron Devices* 52(5):909–917
4. Verhulst AS, Vandenberge WG, Maex K, De Gendt S, Heyns MM, Groeseneken G (2008) Complementary silicon-based heterostructure tunnel-FETs with high tunnel rates. *IEEE Electron Device Lett* 29(12):1398–1401
5. Saurabh S, Kumar MJ (2009) Impact of strain on drain current and a threshold voltage of nanoscale double-gate tunnel field effect transistor. *Jpn J Appl Phys* 48(6):064503
6. Chiang M-H, Lin J-N, Kim K, Chuang C-T (2007) Random dopant fluctuation in limited-width FinFET technologies. *IEEE Trans Electron Devices* 54(8):2055–2060
7. Asenov A, Brown A, Davies J, Kaya S, Slavcheva G (2003) Simulation of intrinsic parameter fluctuation in decanometer and nanometer-scale MOSFETs. *IEEE Trans Electron Devices* 50(9):1837–1852
8. Shin C, Sun X, King Liu T-J (2009) Study of random dopant-fluctuation (RDF) effects for the tri-gate bulk MOSFET. *IEEE Trans Electron Devices* 56(7):1538–1542
9. Jhaveri R, Nagavarapu V, Woo JCS (2011) Effect of pocket doping and annealing schemes on the source-pocket tunnel field-effect transistor. *IEEE Trans Electron Devices* 58(1):80–86
10. Royer CL, Mayer F (2009) Exhaustive experimental study of tunnel field effect transistors (TFETs): from materials to architecture. In: 10th international conference on ultimate integration of silicon, pp 53–56 (2009)
11. Leonelli D, Vandoren A, Rooyackers R, Gendt SD, Heyns MM, Groeseneken G (2010) Optimization of tunnel FETs: impact of gate oxide thickness, implantation and annealing conditions. In: Proceedings of ESSDERC, Sep 2010, pp 170–173
12. Jagadesh Kumar M, Janardhanan S (2013) Doping-less tunnel field effect transistor: design and investigation. *IEEE Trans Electron Devices* 60(10):3285–3290
13. Damrongplasit N, Shin C, Kim SH, Vega RA, Liu TJK (2011) Study of random dopant fluctuation effects in germanium-source tunnel FETs. *IEEE Trans Electron Devices* 58(10):3541–3548
14. Damrongplasit N, Kim SH, Liu TJK (2013) Study of random dopant fluctuation induced variability in the raised-Ge-source TFET. *IEEE Electron Device Lett* 34(2):184–186
15. Krishnamohan T, Kim D, Nguyen CD, Jungemann C, Nishi Y, Saraswat KC (2006) High-mobility low band-to-band-tunneling strained-germanium double-gate heterostructure FETs: simulations. *IEEE Trans Electron Devices* 53(5):1000–1009
16. Yadav DS, Raad BR, Sharma D (2016) A novel gate and drain engineered charge plasma tunnel field-effect transistor for low subthreshold swing and ambipolar nature. *Superlattices Microstruct* 100:266–273
17. Shockley W, Read WT (1952) Statistics of the recombination of hole and electrons. *Phys Rev* 87:835–842
18. ATLAS device simulation software. Silvaco International, Santa Clara, CA (2012)
19. Saurabh S, Kumar MJ (2016) Fundamentals of tunnel field-effect transistors. CRC Press, London

20. Boucart K, Ionescu AM (2007) Double-Gate tunnel FET with high-k gate dielectric. *IEEE Trans Electron Devices* 54(7):1725–1733
21. Raad BR, Tirkey S, Sharma D, Kondekar P (2017) A new design approach of dopingless tunnel FET for enhancement of device characteristics. *IEEE Trans Electron Devices* 64(4):1830–1836
22. Raad BR, Sharma D, Kondekar P, Nigam K, Yadav DS (2016) Drain work function engineered doping-Less charge plasma TFET for ambipolar suppression and RF performance improvement: a proposal, design, and investigation. *IEEE Trans Electron Devices* 63(10):3950–3957
23. Li W et al (2015) Polarization-engineered III-nitride heterojunction tunnel field-effect transistors. *IEEE J Explore Solid-State Comput Devices Circ* 1(1):28–34
24. Daley D, Tran H, Woods W, Zhang Z (2015) Tunnel fieldeffect transistors with a gate-swing broken-gap heterostructure. 21 Jul 2015, US Patent 9,087,717. (Online). Available: <https://www.google.ch/patents/US9087717>

The Role and Significance of Atrial ECG Components in Standard and Modified Lead Systems



Shaik Karimulla and J. Sivaraman

Abstract Comparative study between Standard limb lead system (SLL) and Modified limb lead system (MLL) was carried out in this paper. Electrocardiograms (ECG) of Forty-five female subjects were recorded in sinus rhythm with SLL and MLL for 60 s with the help of EDAN SE-1010 PC ECG system. In MLL system, the amplitudes of *P* wave increased and the amplitude of ventricular components reduced. In PR interval atrial repolarization wave (Ta) wave was noticed and it is opposite to direction of *P* wave. There were no changes observed in durations of ECG wave. The MLL system with observable Ta wave improves the diagnosis of arrhythmias and atrial related diseases. The developed MLL system provides significant information related to atrial components. This study shows that MLL system is an alternate lead system to provide detailed information about atrial components of ECG.

Keywords Standard 12-lead system · Modified limb lead system · Atrial repolarization wave

1 Introduction

The positioning of Standard Limb Lead (SLL) was first introduced by Willem Einthoven [1], later positioning of precordial leads was introduced by Wilson et al. [2]. Limb leads are concerned with motion artifacts which affects the amplitudes of ECG. Placement of limb leads is not accessible in exercise and stress electrocardiogram and this problem was solved by Mason et al. [3] by placing the limb electrodes on torso. The placement of limb electrodes on torso affect the ECG amplitudes in frontal plane and false positive ECG changes also observed. No changes were

S. Karimulla · J. Sivaraman (✉)

Bio-Signals and Medical Instrumentation Laboratory, Department of Biotechnology and Medical Engineering, National Institute of Technology Rourkela, Rourkela, Odisha 769008, India
e-mail: jiva@nitrkl.ac.in

S. Karimulla
e-mail: 218BM1270@nitrkl.ac.in

observed in transverse plane and precordial leads [4] and many other lead systems were developed to record the atrial ECG components [5, 6].

Generally, Standard 12-lead system is used to record the electrical activity of heart and the placement of electrodes gives the view of all electrical axis of anatomical space of ventricles. It provides more information about ventricular components (i.e.) ventricular depolarization and ventricular repolarization and less information about atrial depolarization and repolarization. It is more important to study about atrial components and it is difficult to observe the activity of atrium in case of atrial arrhythmias. Study of entire cardiac cycle is essential for electro cardiologists to observe the electrical activity of entire heart and focusing more on ventricular components. The study related to ventricular disorders, arrhythmias and related diseases were studied widely but the disorders related to atria are not focused till recently.

The atrial depolarization wave (*P*) observed in standard 12-lead system is having less amplitude compared to ventricular depolarization wave (QRS complex) and is having major role in study of clinical information related to atrial arrhythmias. Furthermore, the standard 12-lead system is not able to provide information about atrial repolarization wave (Ta) because it is having very low amplitude and it coincides with the QRS complex as the activity of QRS complex starts before the ending of atrial repolarization [7]. The Ta wave was first observed in AV block patients and the observed Ta wave starts after end of *P* wave and it is opposite in direction to *P* wave. Ta wave is located in PR interval and is having duration nearly three times to *P* wave [8]. The Ta waves differ with different AV block patients. Standard 12-lead systems are not able to record Ta wave in normal sinus rhythm subjects (NSR) and only few studies describes the study of Ta wave in sinus rhythm subjects with different lead techniques. The study related to *P* and Ta wave improves clinical diagnosis related to atrial diseases. To observe the Ta wave in NSR subjects, Modified limb lead system (MLL) is developed by changing the positions of limb lead electrodes of SLL system. Recently Sivaraman et al., suggested MLL system describes the clinical standards of MLL system and studied about dynamics of atrial repolarization wave (Ta) in normal sinus rhythm (NSR) and atrial tachycardia subjects [9]. It is also noted atrial repolarization affected with that sinus rhythm and heart rate variability. The main goal of the present study is to explain the importance of MLL system in ECG diagnosis and on understanding the atrial ECG components. The lead placement in MLL system is placed in such a way where atrial repolarization wave is seen clearly which is absent in SLL system. MLL system improves in analyzing and diagnosis of atrial related diseases whereas SLL provides more information related to ventricular diseases.

Table 1 Subject details

Age details		
Total subjects	45 (24 ± 4.57)	(21.0, 25.0, 28.0)
All values are expressed in n (mean \pm SD), (minimum, median and maximum)		

2 Methods

2.1 Subjects

The experimental study included 45 healthy female subjects. The mean age of the subjects is 24 ± 4.57 years. There was a prior written consent taken from the volunteers before undergoing the study. None of the volunteers had any prior or ongoing medical issues (Table 1).

2.2 Data Collection

In MLL system the position of limb electrodes is changed and the position of chest electrodes remains same. The placement of electrodes as follows: Right arm (RA) electrode is placed on the third right intercostal space near the Left side of midclavicular line, left arm (LA) electrode is placed on fifth right intercostal space near the right side of midclavicular line, Right leg (RL) electrode is preferred for reference electrode is placed is same position like SLL system, left leg electrode is placed on fifth right intercostal space in midclavicular line [10].

The recording of the ECG signal was done with EDAN SE—1010 PC ECG instrument using surface Ag–AgCl electrodes. The subjects were in supine position and the duration of recording was 60 s for each subject with frequency response of 0.05–150 Hz. The recorded ECG signal was processed using EDAN software, and noise filtering was done using 25 Hz filter. The recording of ECG consists two-step process initially subjects were requested for to take 10 min rest after that ECG was recorded with standard limb lead system and by changing the position of limb lead electrodes ECG were recorded with modified limb lead system.

2.3 Statistical Analysis

The recorded data is mentioned as mean \pm standard deviation. For correlation analysis between ECG values Pearson correlation coefficient is considered. The data values are statistically significant with $P < 0.05$ for amplitudes and $P > 0.05$ for time

Table 2 Changes in amplitudes of ECG components in SLL and MLL ECG's

ECG wave	Standard limb lead ECG (μ V)		Modified limb lead ECG (μ V)		<i>P</i> value
	Mean	SD	Mean	SD	
<i>P</i> wave	141.47	22.24	84.84	25.41	<0.05
<i>R</i> wave	947	346.99	512.81	195.83	<0.05
<i>T</i> wave	266.55	99.10	134.39	58.30	<0.05

Table 3 No changes in temporal components of ECG with SLL and MLL ECG's

ECG intervals	Standard limb lead ECG (ms)		Modified limb lead ECG (ms)		<i>P</i> value
	Mean	SD	Mean	SD	
PR interval	141.47	22.24	142.15	21.33	>0.05
QRS interval	90.26	11.46	88.42	11.94	>0.05
QT interval	357.97	24.74	358.63	25.20	>0.05

durations of ECG components. All the statistical analysis was done using Origin Pro—8 of Origin Lab Corporations, 2016 version (Tables 2 and 3).

3 Results

The box and whisker plot shown in Fig. 1 describes the analysis of *P* and *R* wave in Standard Limb Lead system (SLL) and Modified Limb Lead system (MLL). Figure 1a) shows the *P* wave amplitude in SLL and MLL system. The minimum *P*

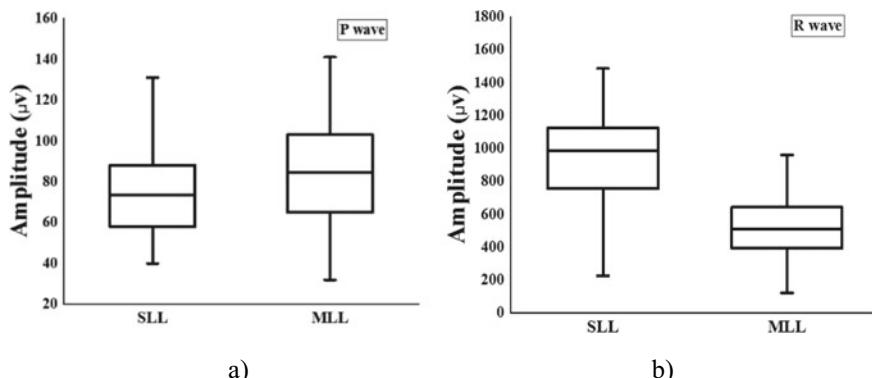
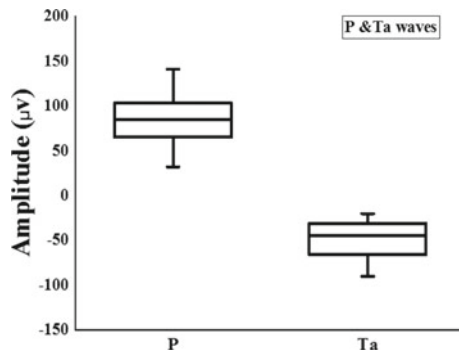


Fig. 1 Analysis of *P* and *R* wave in SLL and MLL. **a** Box plot of *P* wave amplitude in SLL and MLL system. **b** Box plot of *R* wave amplitude in SLL and MLL system

Fig. 2 Box plot of *P* and Ta wave amplitudes in MLL



wave amplitude value in SLL system is 40 μ V, mean value is 70 μ V and maximum value in SLL system is 130 μ V. The minimum, mean and maximum value in MLL system for *P* wave amplitude is 30 μ V, 77 μ V, and 140 μ V respectively. Figure 1b shows the *R* wave amplitude in SLL and MLL system. The minimum *R* wave amplitude in SLL and MLL system is 200 μ V and 190 μ V respectively. The mean *R* wave amplitude in SLL and MLL systems is 1000 μ V and 500 μ V respectively. The maximum *R* wave amplitude in SLL and MLL systems is 1500 μ V and 1000 μ V respectively.

Figure 2 shows the box and whisker plot of *P* and Ta wave amplitude in MLL system. The minimum, mean and maximum *P* wave amplitude in MLL system is 25 μ V, 75 μ V, and 149 μ V respectively. The maximum Ta wave amplitude in MLL system is -90μ V, mean Ta wave amplitude is -50μ V and minimum Ta wave amplitude is -3μ V.

Figure 3 shows the *T* wave amplitude in SLL and MLL system. The minimum *T* wave amplitude in SLL and MLL system is 100 μ V and 50 μ V respectively. The mean *T* wave amplitude in SLL and MLL systems is 250 μ V and 150 μ V respectively. The maximum *T* wave amplitude in SLL and MLL systems is 550 μ V and 350 μ V respectively.

Fig. 3 Box plot of *T* wave amplitude in SLL and MLL

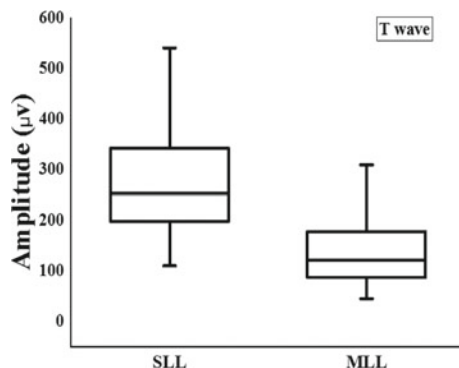


Fig. 4 Box plot of *P* wave duration in SLL and MLL system

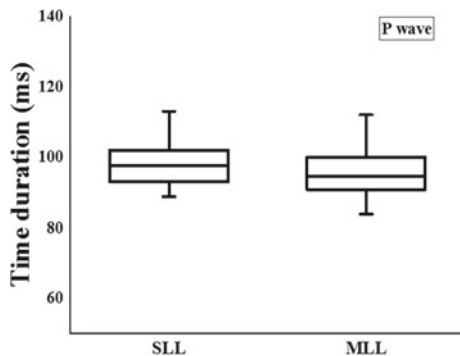


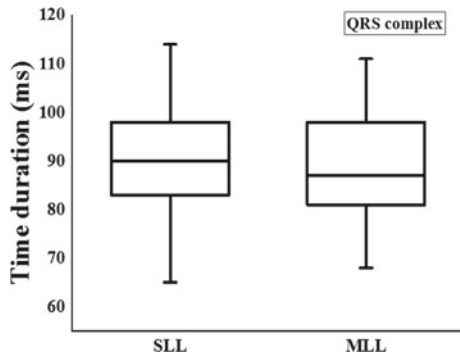
Figure 4 shows the *P* wave duration in SLL and MLL systems. The minimum, mean and maximum value in SLL system for *P* wave duration is 88 ms, 97 ms and 112 ms respectively. The minimum *P* wave duration in MLL system is 85 ms, the mean *P* wave duration in MLL system is 95 ms, and maximum *P* wave duration in MLL system is 110 ms.

Figure 5 expresses the box and whisker plot of QRS duration in SLL and MLL system. The minimum QRS duration in SLL and MLL system is 65 ms and 67 ms respectively. The mean QRS duration in SLL and MLL systems is 90 ms and 85 ms respectively. The maximum QRS duration in SLL and MLL systems is 115 ms and 108 ms respectively.

Figure 6a shows the box and whisker plot of PR interval duration in SLL and MLL system. The minimum PR interval duration in SLL system is 90 ms, mean PR interval duration is 140 ms, and maximum PR interval duration in SLL system is 180 ms. The minimum, mean, and maximum PR interval duration in MLL system are 100 ms, 135 ms, and 177 ms respectively.

Figure 6b illustrates the box and whisker plot of QT interval duration. The minimum QT interval duration in SLL and MLL systems is 290 ms and 320 ms respectively. The mean QT interval duration in SLL and MLL systems is 355 ms and

Fig. 5 Box plot of QRS interval duration in SLL and MLL system



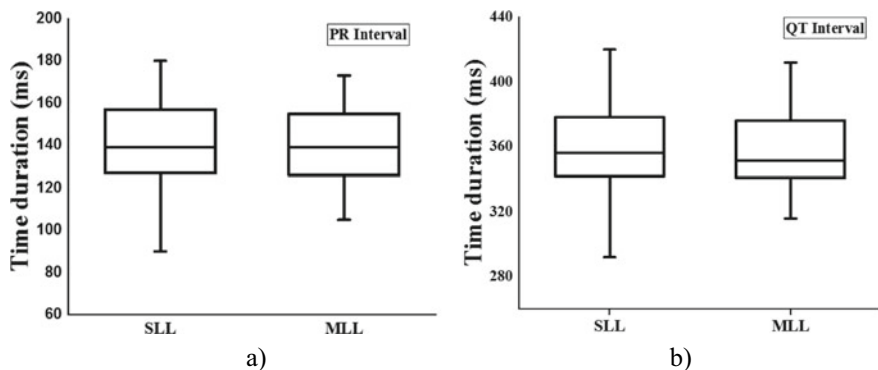


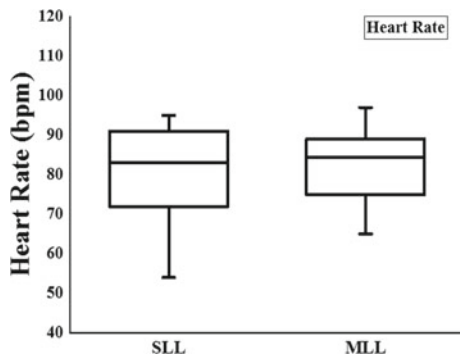
Fig. 6 Analysis of PR and QT interval duration in SLL and MLL. **a** Box plot of PR interval duration in SLL and MLL system. **b** Box plot of QT interval duration in SLL and MLL system

345 ms respectively. The maximum QT interval duration in SLL and MLL system is 420 ms and 410 ms respectively.

Figure 7 expresses the box and whisker plot of Heart rate in SLL and MLL system. The minimum heart rate in SLL and MLL system is 69 bpm and 65 bpm respectively. The mean heart rate in SLL and MLL systems is 85 bpm and 82 bpm respectively. The maximum heart rate in SLL and MLL systems is 100 bpm and 95 bpm respectively.

In general, heart rate plays major role in health of human body. It measures the number of contractions or beats per minute. The speed of heart rate varies with exercise, emotional responses etc. Resting heart rate denotes heart rate when body is relaxed. In SLL system heart rate is calculated by using RR interval, i.e., Heart Rate = $60/(RR \text{ interval})$, whereas heart rate in MLL system is calculated by using PP interval and is given as Heart Rate = $60/(PP \text{ interval})$. Heart Rate measurement in SLL and MLL system is same and there is no effect on heart rate with the type of lead system.

Fig. 7 Box plot of Heart rate (bpm) in SLL and MLL system



4 Discussion

Petrenas et al. described that modified Lewis lead system producing atrial amplitudes three times more than atrial amplitudes in Lewis lead system [10]. Kennedy et al. described *P* leads were derived from standard 12-lead systems by using transformations. *P* lead increases the *P* wave Root mean square (RMS) signal strength and AV RMS ratio in atrial activation. The increased signal strength and AV RMS results in accurate *P* wave detection and cancellation of QRST in standard electrocardiogram [11]. Sivaraman et al. presented a work in 2012 on two different lead systems (SLL and MLL) results in minimizing the atrial activity of ventricular QRS complex. The amplitudes of QRS complex in ECG reduced with MLL system [12]. Atrial repolarization wave was observed in PR segment having more duration than *P* wave and following the *P* wave in opposite direction [13]. Sivaraman et al. described that the amplitude of *P* wave increases in MLL system as compared with SLL system and there is axis shift in *P* wave also observed. The amplitude of QRS complex is reduced with MLL system. The *P* wave signal averaging method producing best explanation of *P* and Ta waves. The *R* peak algorithm gives the position of peak in *P* and *R* wave of all leads of MLL system. The MLL system changes the amplitudes of ECG waves and STa and also produces axis deviation in QRS complex and *T* wave [14].

5 Conclusion

The standard 12-lead system is not able to provide significant information about atrial components and the atrial repolarization wave (Ta) is not observed in ECG trace because it coincides with QRS complex in normal conditions. Ta wave was first observed in AV block patients. Recently developed MLL provides more information related to atrial depolarization wave and atrial repolarization (Ta) wave. Ta wave is clearly observed in MLL system which is opposite in direction to *P* wave and it improves the diagnosis related to atrial arrhythmias and related diseases. The Ta wave is useful in the study of dynamics of atrial activity change.

Acknowledgements The authors acknowledge the support from MHRD, Government of India, for sponsoring the M.Tech. program of the first author. The present study was supported by financial grants from Science Engineering Research Board (SERB), Department of Science and Technology, Government of India (EEQ/2019/000148).

References

1. Einthoven W (1912) The different forms of the human electrocardiogram and their signification. *Lancet* 179(4622):853–861
2. Wilson FN, Johnston FD, Macleod AG, Barker PS (1934) Electrocardiograms that represent the potential variations of a single electrode. *Am Heart J* 9(4):447–458
3. Mason RE, Likar I (1966) A new system of multiple-lead exercise electrocardiography. *Am Heart J* 71(2):196–205
4. Rautaharju PM, Prineas RJ, Crow RS, Seale D, Furberg C (1980) The effect of modified limb electrode positions on electrocardiographic wave amplitudes. *J Electrocardiol* 13(2):109–113
5. Takuma K, Hori S, Sasaki J, Shinozawa Y, Yoshikawa T, Handa S, Horikawa M, Aikawa N (1995) An alternative limb lead system for electrocardiographs in emergency patients. *Am J Emerg Med* 13(5):514–517
6. Szekely P (1944) Chest leads for the demonstration of auricular activity. *Br Heart J* 6:238–246
7. Sivaraman J, John R (2017) Effects of sinus rhythm on atrial ECG components using modified limb lead system. In: 4th international conference on signal processing, computing and control (ISPCC), pp 527–530 (2017)
8. Sprague HB, White PD (1925) Clinical observations on the T wave of the auricle appearing in the human electrocardiogram. *J Clin Invest* 1:389–402
9. Sivaraman J, Uma G, Venkatesan S, Umapathy M, Dhandapani VE (2015) Unmasking of atrial repolarization waves using a simple modified limb lead system. *Anatol J Cardiol* 15(1):2–6
10. Petrenas A, Marozas V, Jarusevicius G, Sornmo L (2015) A modified Lewis ECG lead system for ambulatory monitoring of atrial arrhythmias. *J Electrocardiol* 48(2):157–163
11. Kennedy A, Finlay DD, Guldenring D, Bond RR, McEneaney DJ, Peace A, McLaughlin J (2015) Improved recording of atrial activity by modified bipolar leads derived from the 12-lead electrocardiogram. *J Electrocardiol* 48(6):1017–1021
12. Sivaraman J, Uma G, Umapathy M (2012) A modified chest leads for minimization of ventricular activity in electrocardiograms. In: 2012 international conference on biomedical engineering (ICoBE) 2012, pp 79–82
13. Sivaraman J, Gandhi U, Sangareddi V, Mangalanathan U, Shanmugam RM (2015) Unmasking of atrial repolarization waves using a simple modified limb lead system. *Anatol J Cardiol* 15(8):605–610
14. Sivaraman J, Uma G, Venkatesan S, Umapathy M, Kumar NK (2014) A study on atrial ta wave morphology in healthy subjects: An approach using P wave signal-averaging method. *J Med Imaging Heal Inf* 4(5):675–680

Data Rate Enhancement Scheme and Mathematical Modelling for Data Communication Through Blood



Kauser Husainee and Tanmay Deshmukh

Abstract The data communication for medical purposes such as nano-surgical robots is being established by applying information theory on the kinetic, drift and diffusive molecular flow of blood. The modelling of blood flow can be used further for multiple scientific and medical research purposes. Modelling and simulation of blood flow is analysed in COMSOL Multiphysics tool using laminar flow model. Efficient scheme is developed for data rate enhancement in the field of molecular communication. Propagation delay is estimated using simulation results for communication establishment. Various differential equations are solved by modelling the blood pressure and velocity of blood.

Keywords Mathematical modelling · Molecular communication · COMSOL Multiphysics tool · Blood flow · Data rate enhancement

1 Introduction

In order to establish data communication for medical applications through nano-surgical robots placed inside the blood vessels of the human body using molecular fluid dynamics theory, a part of the cardiovascular system has to be studied, mathematically modelled, graphically plotted and simulated. A cardiovascular system implies the network of blood distribution in the human body. It consists of the heart, the blood and the blood vessels. The term blood pressure can be described as the pressure detected on the walls of the blood vessels when blood flows through them. It depends on the rate of blood flow, pressure gradient and vessels' size [1]. The types of blood vessels in the human body are the arteries, the arterioles and the veins. The arteries are relatively larger blood vessels which carry pure and oxygen-rich blood at high pressure to the body from the heart. Veins are the low-pressure blood collecting system which returns impure blood to the heart [2, 3]. The arterioles are the vessels which get divided into smaller vessels (to supply oxygen and nutrients to all small

K. Husainee · T. Deshmukh

Department of Electronics and Communication Engineering, Visvesvaraya National Institute of Technology, Nagpur, India

e-mail: kauserhusainee@gmail.com

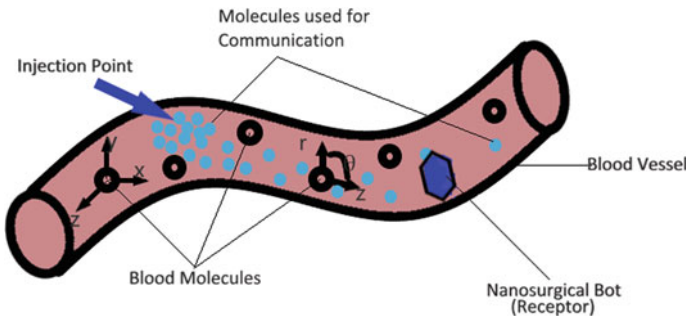


Fig. 1 Concept diagram

tissues). They are the constitutional units for the connection of arterial and venous systems with each other [1].

The approach is to inject a biodegradable solute into the blood stream from the transmitter side, and the volume rate of the solvent along with the time period for which it is transmitted is detected at the receiver side, through the sensors on the nano-surgical robots, which determine the analog value of the data sent as shown in Fig. 1. The data can be any symbol which can be exclusively designed for medical science purposes and not necessarily the characters that we use in keyboards or everyday life [4].

2 Data Rate Enhancement

The comparison of the conventional way of establishing molecular communication with the proposed model which uses quantization theory is done on the basis of baud rate and bit rate.

2.1 Conventional Model

In the convention model, general scheme followed as when the number of molecules above certain threshold is detected in certain time frame t can be taken as Logic-1 and the number of molecules below that threshold is taken as Logic-0. The time frame has to be decided as per the capabilities of hardware. The time frame directly gives us the data rate in the convention scheme. Total characters needed in the scheme are first defined, and then based on the corresponding character length, the baud rate is determined. Let the time frame which is the time required to receive 1 bit be $t = 10 \text{ ms}$.

$$\text{i.e., bit rate} = 100 \frac{\text{bits}}{\text{sec}}$$

If the maximum number of distinct input symbols available is 512, the number of bits per symbol is given by

$$\log_2 512 = 9 \frac{\text{bits}}{\text{symbol}}.$$

From this, time required to send 1 symbol, i.e. time required to send 9 bits, is

$$9 * t = 90 \text{ ms.}$$

$$\text{Baud rate} = \frac{1}{90} \left[\frac{\text{symbols}}{\text{msec}} \right] = 11.11 \frac{\text{symbols}}{\text{sec}}.$$

Therefore,

$$\text{Bit rate} = 100 \frac{\text{bits}}{\text{sec}}$$

If the total number of molecules detected at the receiver is above the threshold value, data is received as 1, otherwise 0. Let the 9 bits 100101011 represent one of the symbols as shown in Fig. 2.

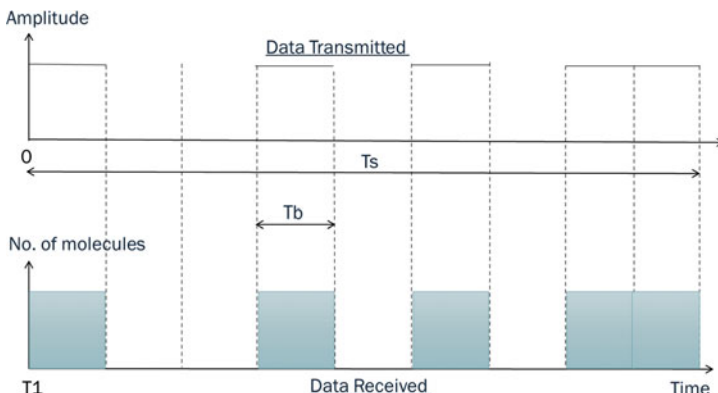


Fig. 2 Data transfer by conventional model for one symbol Tb—bit duration and Ts—symbol duration

2.2 Proposed Model

In our proposed model, as shown in Fig. 3, the earlier decided time frame is quantized in q_1 levels. Also, volume rate is quantized in q_2 . Here, again the quantization levels q_1 and q_2 depend on the hardware capability. Quantization levels in time frame q_1 depend on the sensor capabilities on the reception side. The fast response of the sensor is desired for the higher quantization levels. Similarly, the quantization levels in the volume rate depend on the injection capability of the device. High range volume rate injection may enable us for increase in quantization levels. So,

$$\text{the overall quantization levels} = q_1 * \left(\sum_{i=1}^{q_2} i \right) = 550 \text{ available symbols.}$$

Thus, here the maximum number of distinct input symbols available is 550. Here, we use 512 symbols out of these 550 symbols considering there may be high correlation between some symbols. Now in the same time frame, a complete symbol, i.e. characters, is transmitted instead of a bit.

Baud rate obtained for the above scheme is given by

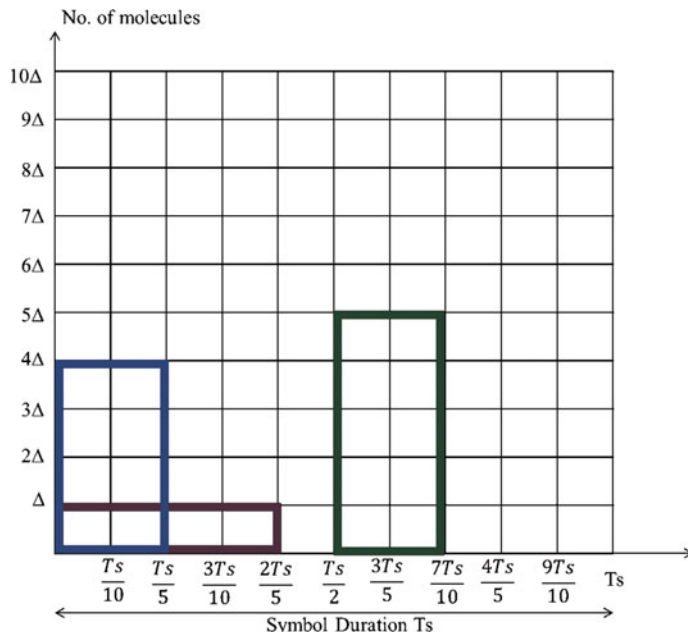


Fig. 3 Quantization levels in the proposed model and the possible cases of the symbols

$$\text{Baud rate} = \frac{1}{10} \left[\frac{\text{symbols}}{\text{msec}} \right] = 100 \frac{\text{symbols}}{\text{sec}}$$

The number of bits per symbol is given by

$$\log_2 512 = 9 \frac{\text{bits}}{\text{symbol}}$$

So, the bit rate obtained is 900 bits per sec.

Thus, there is an enhancement in the bit rate by 9 times.

According to the possible cases in Fig. 3, the molecule reception pattern in time frame can be correlated on the reception side with predefined symbol patterns to determine the symbol received.

3 Mathematical Modelling

3.1 Assumptions for the Fluid Characteristics

- Blood is contemplated as a ‘Newtonian fluid’ which has the relation that the viscous stress is directly proportional to the strain developed [5]. Such a system is governed by the conservation of momentum as well as mass relations which are represented by Navier–Stokes equation and continuity equation, respectively.
- The orientation of blood vessels in space and the effect of gravity have been neglected.
- Blood vessels are assumed to be non-deformable components cylindrical in shape. They do not change their shape as blood flows through them.
- Properties of blood before and after addition of oxygen from lungs are considered to be as it is.

In order to do the mathematical modelling, the characteristics of a particular section of the cardiovascular system has to be considered and studied [6]. In this model, we have studied the upper part of inlet and outlets of the aorta. For simulation purposes, these inlet and outlet blood vessels are placed inside the tissues which are particularly called as the ‘cardiac muscles’, which help to keep the vessels non-deformable. Hence, the blood fluid characteristics inside the vessels do not change [7, 8]. The modelling results give out the distribution of velocity of fluid inside the aortic section which is variable in space as well as time.

3.2 Navier–Stokes and Continuity Equation

Considering the assumptions as stated above, the blood is considered to be governed by the equations as given below

Continuity equation (conservation of mass):

$$\nabla \cdot \vec{V} = 0 \quad (1)$$

Navier–Stokes equation (conservation of momentum)

$$\rho \frac{D\vec{V}}{Dt} = -\nabla P + \mu \nabla^2 \vec{V} \quad (2)$$

where P , μ , ρ , V are the blood pressure, blood viscosity, blood density and velocity vector, respectively.

4 Simulation and Results

The function of heart beat which incorporates the functions of systole and diastole defined for the purpose of modelling is given in Table 1, which is graphically plotted in Fig. 4. The simulation is performed in COMSOL Multiphysics tool based on the heart beat function defined in Table 1 to get the result as shown in Fig. 5.

Table 1 Mathematical equation of heart beat function

Start	End	Function
0	0.5	$(1 - \alpha) * \sin(\pi t)$
0.5	1.5	$1 - \alpha * \cos(2\pi(t - 0.5))$

Fig. 4 Function of heart beat

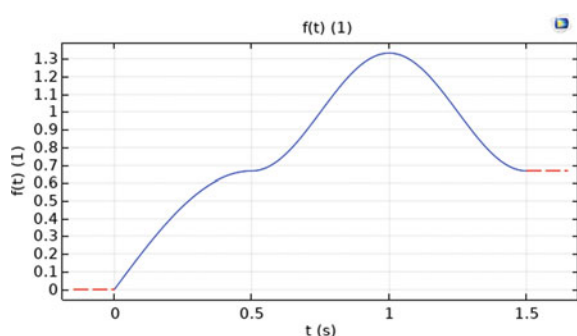
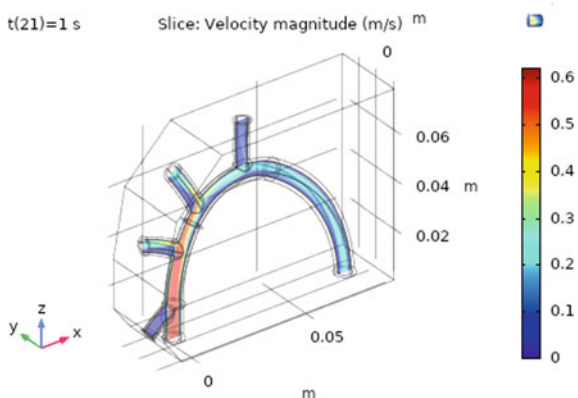


Fig. 5 Velocity distribution inside the aortic section



5 Modelling Based on Simulation

Using the simulation results obtained from Fig. 5, velocity distribution inside the aortic section, the mathematical modelling for axial and radial velocity is proposed as follows

For axial flow velocity component $w(z)$ in cylindrical coordinate system,

$$z = (a - w)^2 + (a - w)^4 + (a - w)^6 + (a - w)^8 + \dots \infty \quad (3)$$

where ‘ a ’ is the maximum axial velocity at the centre of the blood vessel.

$$\begin{aligned} z &= (a - w)^2 (1 + (a - w)^2 + (a - w)^4 + (a - w)^6 + (a - w)^8 + \dots \infty) \\ z &= (a - w)^2 (1 + z) \\ w(z) &= a - \sqrt{\frac{z}{z + 1}} \end{aligned} \quad (4)$$

For radial flow velocity component $f(r)$ in cylindrical coordinate system,

$$\frac{m - f}{q} = r^2 + r^4 + r^6 + r^8 + \dots \infty = \sum_{n=1}^{\infty} r^{2n} \quad (5)$$

where ‘ m ’ is the maximum radial velocity at the centre of the blood vessel and ‘ q ’ is a parameter which depends on the cross-sectional area of the blood vessel which varies throughout the different parts of the body.

$$f(r) = m - q \sum_{n=1}^{\infty} r^{2n} \quad (6)$$

For a particular small section of the cardiovascular system of length ‘ k ’, average velocity ‘ s ’ in the blood vessel can be calculated as,

$$s = \frac{\int_0^k w(z) dz}{\int_0^k dz} \quad (7)$$

$$\int(a)dz = az \quad (8)$$

Now, using Eq. (4),

$$\int_0^k w(z) dz = \int_0^k \left(a - \frac{\sqrt{z}}{\sqrt{z+1}} \right) dz \quad (9)$$

solving,

$$\begin{aligned} \int \left(\sqrt{\frac{z}{z+1}} \right) dz &= -\frac{\ln\left(\sqrt{\frac{z}{z+1}} + 1\right)}{2} \\ &\quad - \frac{1}{2\left(\sqrt{\frac{z}{z+1}} + 1\right)} - \frac{1}{2\left(\sqrt{\frac{z}{z+1}} - 1\right)} + \frac{\ln\left(\sqrt{\frac{z}{z+1}} - 1\right)}{2} \end{aligned} \quad (10)$$

Using Eqs. (8) and (10), we get

$$\begin{aligned} \int \left(a - \sqrt{\frac{z}{z+1}} \right) dz &= \frac{\ln(\sqrt{z+1} + \sqrt{z}) - \ln(|\sqrt{z+1} - \sqrt{z}|)}{2} \\ &\quad + \sqrt{z(z+1)} + az + c \end{aligned}$$

Thus, Eq. (9) becomes

$$\begin{aligned} \int_0^k w(z) dz &= \int_0^k \left(a - \frac{\sqrt{z}}{\sqrt{z+1}} \right) dz \\ &= \frac{\ln(\sqrt{k(k+1)} + k) - \ln(\sqrt{k(k+1)} - k)}{2} - \sqrt{k(k+1)} + ak \end{aligned} \quad (11)$$

Substituting Eqs. (8) and (11) in Eq. (7), the average velocity ‘ s ’ in the vessel is given by

$$s = \frac{\ln(\sqrt{k(k+1)} + k) - \ln(\sqrt{k(k+1)} - k)}{2k} - \sqrt{\frac{k+1}{k}} + a \quad (12)$$

So, the time delay between the transmission and reception ends required for synchronization in order to establish communication successfully is given by T , using Eq. (12)

$$T = \frac{k}{s} = \frac{k}{\frac{\ln(\sqrt{k(k+1)}+k) - \ln(\sqrt{k(k+1)}-k)}{2k} - \frac{\sqrt{k(k+1)}}{k} + \frac{ak}{k}}$$

$$T = \frac{k^2}{\frac{\ln(\sqrt{k(k+1)}+k) - \ln(\sqrt{k(k+1)}-k)}{2} - \sqrt{k(k+1)} + ak} \quad (13)$$

6 Conclusion

For the establishment of the communication, synchronization of data between transmitter and receptor is essential. In the mathematical model which represents the aorta in human cardiovascular system, the velocity distribution of axial and radial components is obtained using the simulations performed in COMSOL Multiphysics tool by solving Navier–Stokes equation and continuity equation using finite element method. From the velocity distribution expression, the estimation of propagation time from injection point to the reception sensor is derived. Using this propagation time, synchronization and thus communication can be established successfully. The proposed model for the communication gives the nine times enhancement in the data rate.

References

1. Ehrlich A, Schroeder CL (2004) Medical terminology for health professions, 5th edn, Thomson Delmar Learning, pp 131–132
2. Katila T, Magnin I, Clarysse P, Montagnat J, Nenonen J (2001) (eds) Functional imaging and modeling of the heart (FIMH'01). In: Lecture notes in computer science, vol 2230. Springer, Berlin
3. Magnin I, Montagnat J, Nenonen J, Katila T (2003) (eds) Functional imaging and modeling of the heart (FIMH'03). In: Lecture notes in computer science, vol 2674. Springer, Berlin
4. Taylor CA, Draney MT (2004) Experimental and computational methods in cardiovascular fluid mechanics. *Annu Rev Fluid Mech* 36:197–231
5. Sankar DS, Hemalatha K (2007) A non-Newtonian fluid flow model for blood flow through a catheterized artery—steady flow. *Appl Math Modell* 31(9):1847–1864
6. Jayaraman G, Tewari K (1995) Flow in catheterized curved artery. *Med Biol Eng Comput* 33(5):720–724
7. Sherwood L (2005) Fundamentals of physiology: a human perspective, 3rd edn. Thomson Brooks/Cole, pp 276
8. Yang BH, Asada HH, Zhang Y (1999) Cuff less continuous monitoring of blood pressure using hemodynamic model, the home automation and healthcare consortium” progress report no 2–3
9. Sultanov RA, Guster D (2009) Full dimensional compute simulations to study pulsatile blood flow in vessels, aortic arch and bifurcated veins: investigation of blood viscosity and turbulent effects. In: 31st annual international conference of the IEEE EMBS Minneapolis, Minnesota, USA, 2–6 Sep 2009

A Novel Design of Fast and Low Power Pull-Up and Pull-Down Voltage Level Shifter



Vickey Kumar, Suruchi Sharma, and Baljit Kaur

Abstract This article presents a low power consumption and fast voltage level shifter, which can increase the input voltage level lower or comparable to a threshold voltage to nominal voltage level and high voltage level to low voltage level. The proposed level shifter is based on a pull-up network which has regulated cross-coupled structure. This helps to enhance the switching speed and reduction of dynamic power. Furthermore, split input inverter and pMOS diode used to reduce the static power consumption. For proposed level shifter simulation results have performed in a 180 nm CMOS technology using cadence virtuoso tool. While converting supply voltage from low to the high voltage level of 0.4 V and 1.8 V, respectively at applied frequency 1 MHz, power consumption and propagation delays are 139.6 nW and 19.92 ns, respectively. And during conversion high to the low supply voltage are 1.8 V and 0.4 V, 120.2 nW and 15.31 ns, respectively.

Keywords Dual-supply · High speed · Low power · pMOS diodes · Up/down level shifter

1 Introduction

Power dissipation has become the most critical concern nowadays in integrated circuits (IC). Due to technology scaling, IC performance has increased but at a result of high power dissipation. One of the efficient ways of power reduction is the voltage scaling method [1–3]. By this dynamic power and static power consumption reduced. But the speed of the circuit also reduced. So where we need high-speed, we can't reduce supply voltage. Conventionally, limited power is reduced by supply voltage scaling well in the super threshold region, but in recent studies, it has been found that supply input voltage can be reduced near below than threshold voltage [4–13]. Different modules like digital, analog, passive circuits are fabricated on a single chip. And different modules have different requirements. For some modules, power

V. Kumar · S. Sharma (✉) · B. Kaur

Department of Electronics and Communication Engineering, National Institute of Technology
Delhi, Delhi, India

e-mail: sharma.suru91@gmail.com

consumption matters more as compared to the speed and vice versa. So two or more supply voltages were used for the efficient performance of SoC [2, 3]. Therefore, we need voltage level shifting between the two modules of SoC. For this purpose voltage level shifter is used which can revise low voltage comparable to the threshold voltage into high nominal voltage and vice a versa for the efficient performance of the SoC. There might be the use of many level shifters (LS) in SoC. Therefore, power demand, propagation delay and circuit area become the primary concern while designing the level shifter (LS). Hence, in short, power-efficient and fast level shifter is proposed which can increase low voltage level to high voltage level and vice versa, which is controlled by the applied voltage.

Further, this paper proceeds as follows: in Sect. 2, conventional LS circuits reviewed, Sect. 3 introduced the proposed LS and Sect. 4 shows the simulation results. In the end, in Sect. 5, conclusions are presented in brief.

2 Literature Review

Figure 1a represents the conventional-level shifter, which uses a pull-up network based on the current mirror structure. As it does not have regenerative interaction between a pull-down part and pull-up part in both sides of branches of the level shifter. Therefore, the operation speed of the circuit is very low. Moreover, because of the flow of static current in one of the circuit branches, it consumes high standby power according to the input state. Figure 1b shows level shifter having a pull-up network based on a cross-coupled structure. This pull-up part increases the difference between Q_1 and Q_2 . Due to this regeneration process, operation speed increases. When input rises to high MN_1 becomes on whereas MN_2 turned off. So Q_1 begins to discharge,

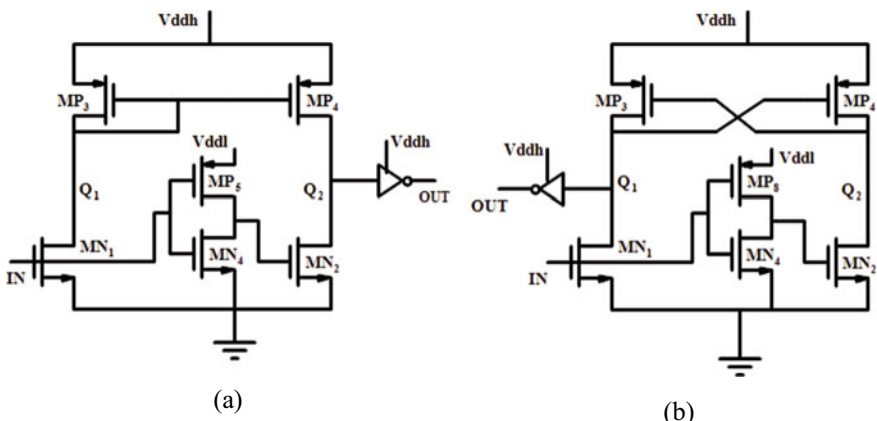


Fig. 1 Two different types of conventional LS architecture based on **a** current mirror **b** cross-coupled structure

which tries to switch on the MP_4 , so Q_2 starts to reach V_{ddh} , which turns off MP_3 . It results in a fast discharging of Q_1 . If the supply voltage range is of sub-threshold or less than that, then the contention problem comes into existence between pMOS and nMOS. To remove the contention problem size of MN_1 and MN_2 , we have to increase. Therefore, the overall efficiency of the circuit is reduced. One of the approaches to solve this problem is to reduce the drive strength of the pull-up circuit.

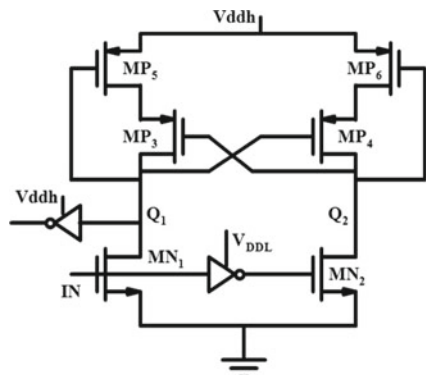
3 Proposed Circuit

Figure 2 represents a simplified proposed circuit schematic. This design uses a pull-up network having a cross-coupled regulated structure. The problem of making more size of NMOS in the pull-down network is resolved here by using MP_5 and MP_6 . By using these two PMOS transistors strength of the pull-up network is reduced. This charging and discharging of pull-up critical nodes becomes fast, which enhances the speed of switching and decreases dynamic power. Figure 3 explains the working of a simplified proposed level shifter in case of low to high voltage level conversion.

Initially, the voltage at a node Q_1 is V_H , which is slightly less than V_{ddh} and voltage at Q_2 is low. Therefore, MP_6 and MP_3 are on, and MP_4 and MP_5 are off. When there is the transition of input from low level to a high level then MN_1 becomes switched on and MN_2 switched off so Q_1 begins to discharge very fast because of the current flowing through MP_3 is very small, because of MP_5 and Q_1 discharge approximately from V_H to $V_{ddh} - V_H$ at this time MP_4 and MP_5 start to turn on.

So consequently, Q_2 begins to charge, and voltage at Q_2 increases. This flow causes MP_3 and MP_6 to start to turn off. This regenerative time process of pull-up network increase voltage at Q_2 very fast and caused MP_6 to turn OFF before Q_2 reaches V_{ddh} and Q_2 fixed at V_H . At the last step, MP_3 will be turned off because of Q_2 , and MN_1 would be able to discharge node Q_1 . The left and right branches do not contain any flow of static current due to switched OFF MP_5 and MP_6 . Moreover, interval nodes voltage remains at V_H always, which are lower than V_{ddh} , so dynamic

Fig. 2 Simplified proposed LS



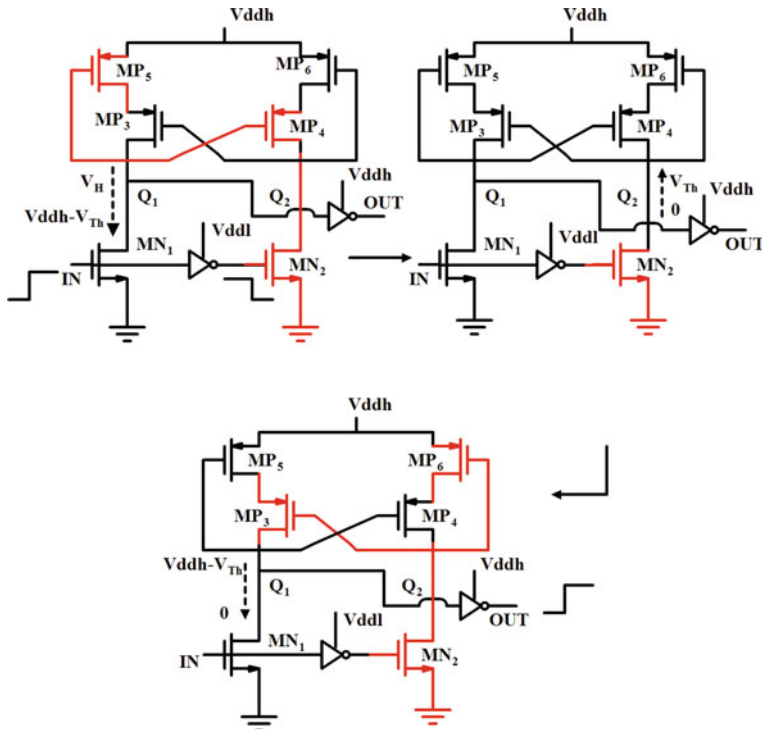


Fig. 3 Operation of a simplified schematic of proposed LS [14]

power also reduced. This flow will also be similar for high to low transition of input voltage exact reverse of it (Fig. 4).

4 Simulation Results

For the complete schematic circuit of voltage level shifter, which we have proposed, the transient waveforms are as depicted in Figs. 5 and 6, respectively. This is done by keeping $V_{ddl} = 0.4$ V and $V_{ddh} = 1.8$ V. In the proposed LS circuit, two PMOS diodes body connected to V_{ddh} are used. So that pMOS and nMOS of inverter do not switch on at the same time which results in small short circuit current and so power dissipation of LS circuit reduced. The transistors sizes are reported in Table 1. Figure 7 shows the effect of PVT variation on the overall power consumed and delay of the proposed LS structure for various values of V_{ddl} keeping supply frequency 1 MHz and V_{ddh} value 1.8 V. A fast pMOS and fast nMOS give the least delay contrarily slow pMOS and slow nMOS results the worst case. While Fig. 8 shows variation values concerning V_{ddh} at frequency 1 MHz and V_{ddl} value 0.4 V. Figures 9

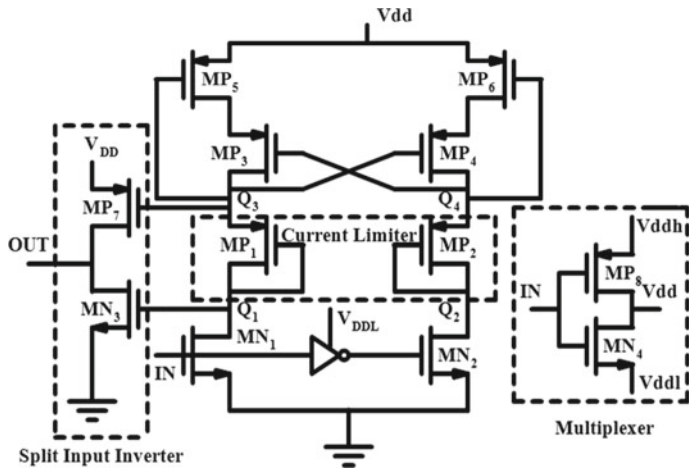


Fig. 4 Schematic of a complete proposed LS

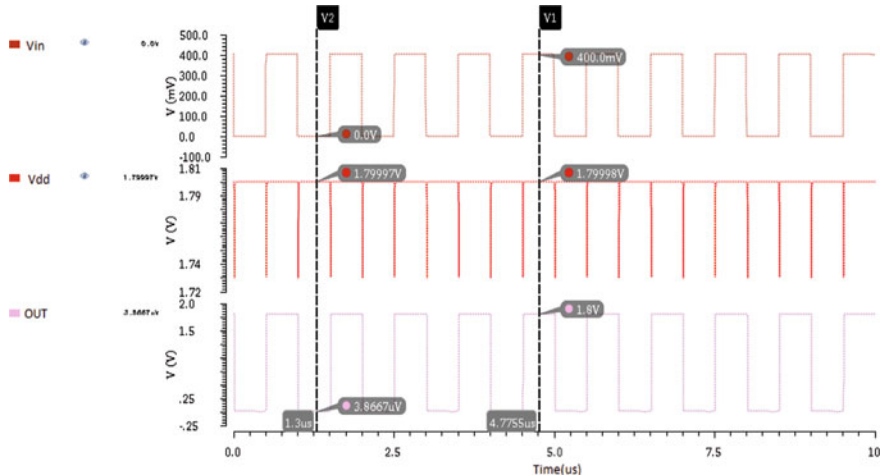


Fig. 5 Proposed level shifter simulated waveforms in case of low input voltage level

and 10 represents power and delay characteristics of LS at the typical corner for up and down voltage level conversion, respectively, for an applied frequency of 1 MHz.

Table 2 shows consumed power and delay, where P_s denotes the static power and P_t total power, in case of up voltage level, having input voltage value 0.4 V, $V_{ddl} = 0.4$ V, and $V_{ddh} = 1.8$ V at frequency 1 MHz at 27 °C typical corner. Moreover, Table 3 shows performance for converting voltage level down, having input voltage 1.8 V.

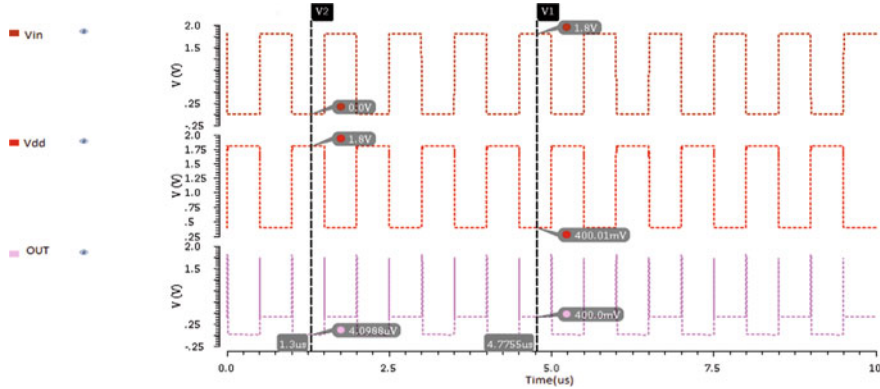


Fig. 6 Proposed level shifter simulated waveforms in case of high input voltage level

Table 1 Size of transistors

Transistors	W/L (in μm)	Transistor	W/L (in μm)
MN ₁ , MN ₂ , MN ₃ , MN ₄ , MP ₁ , MP ₂ , MP ₃ , MP ₄ , MP ₅ , MP ₆ , MP ₈	0.4/0.18	MP ₇	0.8/0.18

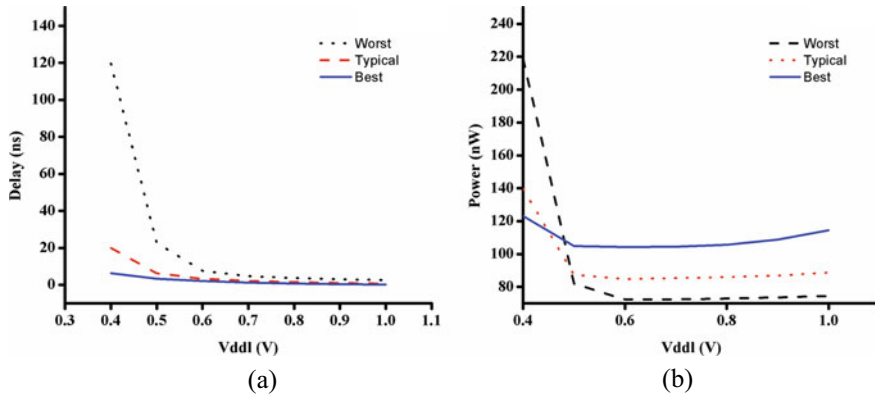


Fig. 7 Proposed LS PVT analysis **a** delay **b** power versus V_{ddl} for $V_{ddh} = 1.8$ V by keeping input supply voltage of 0.4 V at the frequency of 1 MHz for low to high-level shifting time

5 Conclusion

A novel up/down LS is proposed, which is fast and consumes low power. The proposed LS utilizes a pull-up network, which is based on the regulated cross-coupled circuit. Furthermore, it can convert supply input from a low threshold level to a high nominal voltages level, and it can also convert the supply voltage of high-level to

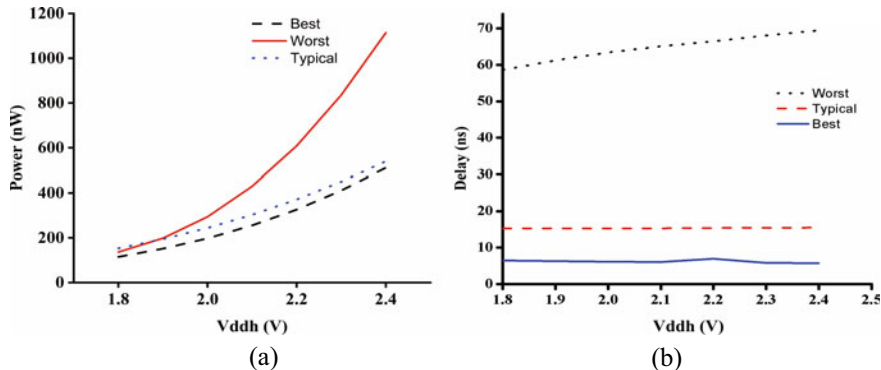


Fig. 8 Proposed LS PVT analysis **a** delay **b** power versus V_{ddh} for $V_{ddl} = 0.4$ V by keeping input supply voltage of 18 V at a frequency of 1 MHz for high to low-level shifting time

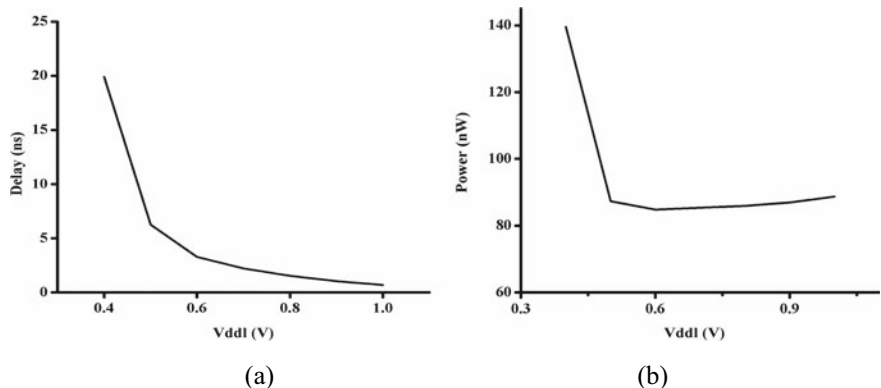


Fig. 9 Proposed LS characteristics **a** Delay **b** power versus V_{ddl} for $V_{ddh} = 1.8$ V and frequency of 1 MHz at the typical corner

low. Performed simulation results of the proposed up and down voltage level shifter using 180 nm CMOS technology indicates high performance and supports a wide range voltage level conversion. It can provide an up-conversion for the input signal as low as 80 mV and the input signal of high voltage level to about 0.4 V. Furthermore, corner analysis of the proposed circuit is performed to validate the superior performance over the conventional-level shifter.

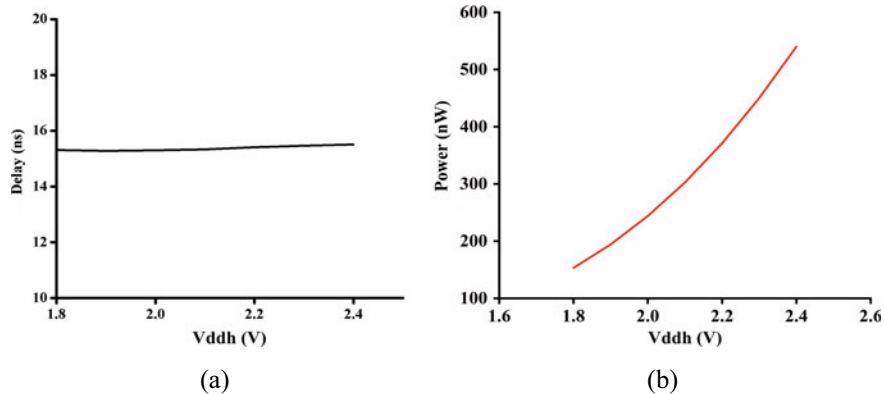


Fig. 10 Proposed LS characteristics **a** delay **b** power versus V_{ddh} for $V_{ddl} = 0.4$ V and frequency of 1 MHz at a typical corner

Table 2 Comparison with previous work ($V_{ddh} = 1.8$ V, $F = 1$ MHz)

References	Min V_{ddl}	Delay (ns)	P_s (nW)	P_t (nW)	PDP (nW ns)
Figure 5	0.28	19.92	0.36	139.6	2781
[13]	0.31	31.29	0.23	326.7	10,222
[15]	0.28	31.54	0.27	166.3	5245
[16]	0.29	29.85	0.06	139.3	4158
[17]	0.28	23.75	1	183.9	4368
[18]	0.3	29.59	0.78	631.4	18,683
[19]	0.3	28.83	0.23	218.3	6293
[20]	0.27	21.49	0.26	418.7	8998
[21]	0.29	25.23	1.76	137	3456
[22]	0.28	22.32	0.5	347	7745
[23]	0.38	41.12	0.13	228.1	9379
[24]	0.28	24.31	1.06	150	3646

Table 3 Performance parameters of the proposed LS

Delay (ns)	P_s (nW)	P_t (nW)	PDP (nW ns)
15.31	0.17	120.2	1840.26

References

1. Wang A, Chandrakasan AP (2005) A 180-mV subthreshold FFT processor using a minimum energy design methodology. IEEE J Solid-State Circuits 40(1):310–319
2. Usami K et al (1998) Automated low-power technique exploiting multiple supply voltages applied to a media processor. IEEE J Solid-State Circ 33(3):463–472

3. Zhang D, Bhide A, Alvandpour A (2012) A 53 nW 9.1-ENOB 1-kS/s SAR ADC in 0.13- μ m CMOS for medical implant devices. *IEEE J Solid-State Circ* 47(7):1585–1593
4. Wang A, Chandrakasan A (2005) A 180-mV subthreshold FFT processor using a minimum energy design methodology. *IEEE J Solid State Circ* 40(1):310–319
5. Raychowdhury A, Paul BC, Bhunia S, Roy K (2005) Computing with subthreshold leakage: device/circuit/architecture co-design for ultralow-power subthreshold operation. *IEEE Trans Very Large Scale Integr (VLSI) Syst* 13(11):1213–1224
6. Markovic D, Wang CC, Alarcon LP, Liu TT, Rabaey JM (2010) Ultralow-power design in the near-threshold region. *Proc IEEE* 98(2):237–252
7. Seok M, Jeon D, Chakrabarti C, Blaauw D, Sylvester D (2011) A 0.27 V 30 MHz 17.7 nJ/transform 1024-pt complex FFT core with super pipelining. In: Proceedings IEEE international solid-state circuits conference digest of technical papers (ISSCC), 20–24 Feb 2011, pp 342–344
8. Alioto M (2012) Ultra-low power VLSI circuit design demystified and explained: A tutorial. *IEEE Trans Circ Syst I Regul Pap* 59(1):3–29
9. Jeon D, Seok M, Zhang Z, Blaauw D, Sylvester D (2012) Design methodology for voltage-overscaled ultra-low-power systems. *IEEE Trans Circ Syst II Exp Briefs* 59(12):952–956
10. Klinefelter A, Zhang Y, Otis B, Calhoun BH (2012) A programmable 34 nW/channel sub-threshold signal band power extractor on a body sensor node SoC. *IEEE Trans Circ Syst II Exp Briefs* 59(12):941
11. Jeon D, Kim Y, Lee I, Zhang Z, Blaauw D, Sylvester D (2013) A 470 mV 2.7 mW feature extraction-accelerator for micro-autonomous vehicle navigation in 28 nm CMOS. In: 2013 IEEE international solid-state circuits conference digest of technical papers (ISSCC), 17–21 Feb 2013, pp 166–167
12. Craig K, Shakhsheer Y, Arrabi S, Khanna S, Lach J, Calhoun BH (2014) A 32 b 90 nm processor implementing panoptic DVS achieving energy efficient operation from sub-threshold to high performance. *IEEE J Solid-State Circ* 49(2):545–552
13. Hosseini SR, Saberi M, Lotfi R (2014) A low-power subthreshold to above-threshold voltage level shifter. *IEEE Trans Circ Syst II Express Briefs* 61(10):753–757
14. Kabirpour S, Jalali M (2019) A low-power and high-speed voltage level shifter based on a regulated cross-coupled pull-up network. *IEEE Trans Circ Syst II Express Briefs* 66(6):909–913
15. Lanuzza M et al (2017) An ultralow-voltage energy-efficient level shifter. *IEEE Trans Circ Syst II Express Briefs* 64(1):61–65
16. Maghsoudloo E, Rezaei M, Sawan M, Gosselin B (2017) A high-speed and ultra low-power subthreshold signal level shifter. *IEEE Trans Circ Syst I Regul Pap* 64(5):1164–1172
17. Hosseini SR, Saberi M, Lotfi R (2017) A high-speed and power-efficient voltage level shifter for dual-supply applications. *IEEE Trans Very Large Scale Integr (VLSI) Syst* 25(3):1154–1158
18. Luo SC, Huang CJ, Chu YH (2014) A wide-range level shifter using a modified Wilson current mirror hybrid buffer. *IEEE Trans Circ Syst I Regul Pap* 61(6):1656–1665
19. Lanuzza M, Corsonello P, Perri S (2015) Fast and wide range voltage conversion in multisupply voltage designs. *IEEE Trans Very Large Scale Integr (VLSI) Syst* 23(2):388–391
20. Huang CR, Chiou LY (2014) A limited-contention cross-coupled level shifter for energy-efficient subthreshold-to-superthreshold voltage conversion. In: International SoC design conference (ISOCC), 2014, pp 142–143
21. Lotfi R, Saberi M, Hosseini SR, Ahmadi-Mehr AR, Staszewski RB (2018) Energy-efficient wide-range voltage level shifters reaching 4.2 fJ/transition. *IEEE Solid-State Circ Lett* 1(2):34–37
22. Osaki Y, Hirose T, Kuroki N, Numa M (2012) A low-power level shifter with logic error correction for extremely low-voltage digital CMOS LSIs. *IEEE J Solid-State Circuits* 47(7):1776–1783
23. Lanuzza M, Corsonello P, Perri S (2012) Low-power level shifter for multi-supply voltage designs. *IEEE Trans Circ Syst II Express Briefs* 59(12):922–926
24. Wen L, Cheng X, Tian S, Wen H, Zeng X (2015) Subthreshold level shifter with self-controlled current limiter by detecting output error. *IEEE Trans Circ Syst II Express Briefs* 63(4):346–350

Modeling of Dual-Gate Carbon Nanotube Based Ion Sensitive Field Effect Transistor (DG-CNTISFET)



Hiranya Ranjan Thakur, Gaurav Keshwani, and Jiten Chandra Dutta

Abstract In this paper, modeling of a dual-gate carbon nanotube based ion sensitive field effect transistor (DG-CNTISFET) fabricated by electrochemical deposition (ECD) technique is discussed. The surface potential variation of the device was determined by using Bousse's model. The device showed high sensitivity because of large coupling ratio between top and bottom gate capacitances. High- κ and low- κ dielectric materials have been used as the top and bottom gate dielectrics, respectively, to achieve large coupling ratio. The high carrier mobility of CNT also contributed in achieving this high sensitivity of the device. The developed model was simulated in MATLAB environment. The simulated results were compared with the experimental results of the fabricated device and good fit was obtained.

Keywords CNT · High- κ · Modeling · DG-CNTISFET

1 Introduction

Among the various nanomaterials, field effect transistors based on carbon nanotube (CNT) have attracted lot of attention in the field of biosensors [1–3]. Some of the excellent properties of semiconducting CNT include ballistic transport, robustness, good thermal, mechanical, large surface area and high chemical stability [4–7]. The use of CNT in the channel can overcome the traditional ISFETs scaling limitations [8, 9]. The unique chemical bonding and surface stability of CNT impart high compatibility with high- κ dielectric material. Thus, the capacitance of CNTFET increases without using small film thickness. Consequently, the direct tunneling leakage current reduces [4, 5]. The drain current and on-off current ratio increases because of

H. R. Thakur (✉) · G. Keshwani · J. C. Dutta
Tezpur University, Tezpur, Assam 784028, India
e-mail: hrtnerist@gmail.com

G. Keshwani
e-mail: gauravkeshwani@gmail.com

J. C. Dutta
e-mail: jitend@tezu.ernet.in

increased capacitance. The combination of high- κ material with biocompatible and size compatible CNT leads to advanced miniature device [1, 4].

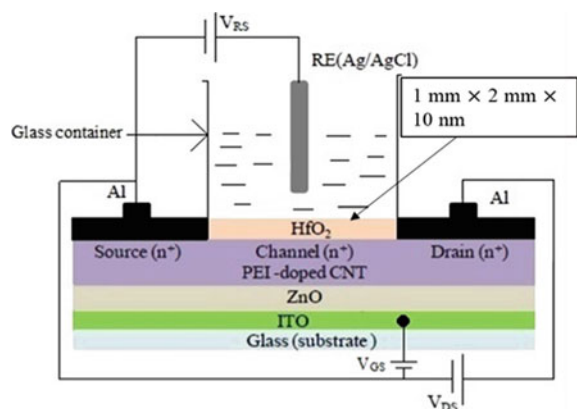
The single-gate CNTISFETs fabricated by using solution process showed near Nernstian sensitivity at room temperature [10]. Some application such as measurements of biological interactions or activities (e.g., DNA hybridization, protein function, cellular activity and DNA-protein interactions) requires highly sensitive device [11, 12]. Introduction of a second gate in single-gate CNTISFET can enhance this low sensitivity. The reference electrode and an electrolyte solution form the top gate. A metal layer is used as the bottom gate [13]. The sensitivity of the device improves due to the capacitive coupling. The capacitive coupling is enhanced with materials of high dielectric constant (κ) as top gate and bottom gate with low dielectric constant (κ).

Modeling of DG-CNTISFET helps in understanding the device physics and explains experimental data. The parameters to achieve high sensitivity and selectivity can be chosen properly [14]. The surface potential varies due to change in solution pH. Bousse's model was used to model this potential change. The drain current changes as a result. The current transport model of DG-CNTISFET was used to model the drain current change.

Thus, the modeling of DG-CNTISFET is discussed in this paper [15]. The schematic of the fabricated device is shown in Fig. 1.

Chemical solution process was used to fabricate the device. An ITO coated glass instead of (dimension $\sim 5 \text{ mm} \times 2 \text{ mm}$) was used as substrate. The substrate was cleaned by using a solution of water (H_2O), hydrogen peroxide (H_2O_2) and ammonium hydroxide (NH_4OH). A ZnO (dielectric constant ~ 1.5) layer (thickness $\sim 10 \text{ nm}$) was deposited on the substrate by electrochemical deposition(ECD) technique. This layer prevents current flow from channel (CNT) to ITO. ECD was carried out by using a three electrodes system. The three electrodes are reference electrode Ag/AgCl (silver/silver chloride), counter electrode Pt (platinum) wire, and working electrode ITO coated glass. 10 mg $\text{Zn}(\text{CH}_3\text{COO})_2$ (zinc acetate) was dissolved in distilled water of 10 ml to prepare ZnO solution. Ammonium hydroxide (NH_4OH) of 2 ml

Fig. 1 DG-CNTISFET with high- κ (HfO_2) top and low- κ (ZnO) bottom gate dielectric [15]



was then added to this solution. Gravimetric analysis technique was used to measure the thickness of the layer (~10 nm) [9]. PEI-doped COOH-functionalized MWCNT was deposited on this ZnO layer. PEI donates electrons to CNT as it is an amine rich polymer. The solution was prepared as: disperse CNT (5 mg) in PEI/methanol (5 ml). The *n* + S (source), D (drain), and channel regions were formed by this layer. The contact S and D regions were deposited on the top of the PEI-doped COOH-functionalized MWCNT layer with metal aluminum (Al) by PVD (filament evaporation) method. Quasi-ohmic contact was formed by Fermi-level depinning technique between CNT (work function ~4.8 eV) and Al (work function ~4.08 eV). HfO₂ (high- κ) layer of thickness ~10 nm as the sensing layer has been deposited after metallization process on the CNT channel. HfO₂ solution was prepared as: dissolve 10 mg HfCl₄ (solid) in de-ionized water (5 ml). This layer was heated (~180 °C) to form dry HfO₂ layer. The thickness was measured by gravimetric analysis method.

2 Modeling

Modeling in general can be described as the representation of real-world objects in terms of physical or mathematical equations. Modeling helps in understanding the operation of a device in details and reduces time as well as development cost. There are many models of ISFETs and BioFETs developed in SPICE. These are based on MOSFET models with modifications. However, the SPICE simulations do not include the electrochemistry of the device. The physical and chemical behavior of ISFET is modeled using physico-chemical condition by Grattarola et al. They have carried out the simulation in electronic circuit simulation program SPICE. Electrochemical models have been developed for silicon-based BioFETs only [16]. But, there is no electrochemical model for DG-CNTISFET.

2.1 Site-Binding Model

The concentration of H⁺ ions plays an important role in ISFETs. These ions determine the surface potential at the interface between the electrolyte and insulator depending on their binding with the surface sites of the gate insulator. The surface charge change can be well-explained by the site-binding model. Yates et al. [17] in 1973 introduced the site-binding model that described oxide and aqueous electrolyte interface properties. Fung et al. [18] in 1986 generalized this model to characterize the properties of ISFET with oxide insulators.

The relationship between the hydrogen ion (H⁺ ions) concentration at the oxide surface ([H⁺]_s) and the bulk ([H⁺]_b) is given by Eq. (1):

$$[\text{H}^+]_s = [\text{H}^+]_b \exp\left(\frac{-q\psi_0}{kT}\right) \quad (1)$$

where ψ_0 is the surface potential between the electrolyte and insulator interface, T denotes the absolute temperature, k denotes Boltzmann constant, and q denotes the elementary charge.

Hence, a surface potential, ψ_0 is developed as the H^+ ions present in electrolyte solution binds with the oxide surface sites. The potential developed at the interface changes with solution pH.

2.2 Model of Interfacial Potential

The potential developed at the electrolyte and insulator interface changes with the pH of the solution. Bousse et al. [19] developed a relationship based on the site-binding theory that describes the potential change with solution pH. The relation is given by Eq. (2) [21]:

$$\psi_0 = 2.3 \left(\frac{kT}{q} \right) \left[\frac{\beta}{\beta + 1} \right] (pH_{pzc} - pH) \quad (2)$$

where the value of pH for the oxide surface to be electrically neutral is pH_{pzc} ; β is a dimensionless parameter; k denoted Boltzmann constant; T denotes absolute temperature. The values of different parameters for determination of surface potential, ψ_0 of HfO_2 surface are listed in [20].

2.3 Current Transport Model of DG-CNTISFET

The drain current equation of DG-CNTISFET can be determined by modifying the equations of MOSFET drain current. The conventional MOSFET like behavior of DG-CNTISFET has been verified experimentally in [15]. The drain current through the channel region in DG-CNTISFET depends on the potential both at top and bottom gate.

Thus, the linear and saturation region drain current in DG-CNTISFET can be written as:

$$I_{DS,\text{lin,dual}} = \mu \frac{W}{L} V_{DS} \left[C_{\text{ox,top}} \{ (V_{GS,\text{top}} - V_{TH,\text{top}}) - 0.5V_{DS} \} \right. \\ \left. + C_{\text{ox,bottom}} \{ (V_{GS,\text{bottom}} - V_{TH,\text{bottom}}) - 0.5V_{DS} \} \right] \quad (3)$$

$$I_{DS,\text{sat,dual}} = \mu \frac{W}{2L} \left[C_{\text{ox,top}} (V_{GS,\text{top}} - V_{TH,\text{top}})^2 \right. \\ \left. + C_{\text{ox,bottom}} (V_{GS,\text{bottom}} - V_{TH,\text{bottom}})^2 \right] \quad (4)$$

In the above equation, $C_{\text{ox},\text{top}}$ is the top gate capacitance and $C_{\text{ox},\text{bottom}}$ is the bottom gate capacitance; $V_{\text{TH},\text{top}}$ is the top gate threshold voltage, and $V_{\text{TH},\text{bottom}}$ is the bottom gate threshold voltage.

In DG-CNTISFET, total threshold voltage is due to the sum of the threshold voltage of the top and bottom gates. The $V_{\text{TH},\text{top}}$ is given by ISFET's threshold voltage equation without the term $2\Phi_f$. The bottom gate V_{TH} is represented by MOSFET's threshold voltage equation except the term $2\Phi_f$.

$$V_{\text{TH},\text{top}} = E_{\text{ref}} - \psi_0 + \chi_{\text{sol}} - \frac{\Phi_{\text{CNT}}}{q} - \frac{Q_{\text{ox},\text{top}} + Q_{\text{ss},\text{top}} + Q_{\text{CNT}}}{C_{\text{ox},\text{top}}} \quad (5)$$

$$V_{\text{TH},\text{bottom}} = \frac{\Phi_M - \Phi_{\text{CNT}}}{q} - \frac{Q_{\text{ox},\text{bottom}} + Q_{\text{ss},\text{bottom}} + Q_{\text{CNT}}}{C_{\text{ox},\text{bottom}}} \quad (6)$$

where $Q_{\text{ox},\text{top}}$ is the top gate and $Q_{\text{ox},\text{bottom}}$ is the bottom gate insulator charge; $Q_{\text{ss},\text{top}}$ is the interface charge for insulator-CNT top gate and $Q_{\text{ss},\text{bottom}}$ is the interface charge for insulator-CNT bottom gate; Φ_M is the work function of bottom gate material; E_{ref} is the reference electrode potential; Φ_{CNT} is the CNT work function; q is the elementary charge; χ_{sol} is the solvent surface dipole potential; ψ_0 is the interfacial potential between the electrolyte and insulator interface. The value of ψ_0 depends on the analyte ions activity.

The total charge inside the carbon nanotube is given by Eq. (7)

$$Q_{\text{CNT}} = -qn_{\text{CNT}}L_{\text{CNT}} \quad (7)$$

where n_{CNT} is carbon nanotube carrier concentration; L_{CNT} is carbon nanotube length.

The oxide layer charge can be written as Eq. (8)

$$Q_{\text{ox}} = qn_{\text{ox}} \quad (8)$$

where, n_{ox} is the oxide layer carrier concentration.

2.4 pH Sensitivity of DG-CNTISFET

The device sensitivity due to the top gate can be determined using Eq. (2). However, the sensitivity of DG-CNTISFET depends on both the gates (top and bottom). The capacitive coupling ratio is high when the top gate capacitance is higher compared to bottom gate. As a result, the sensitivity of the device will be more. Large capacitive coupling ratio can be obtained with high- κ and low- κ as the top and bottom gate material, respectively. The thickness of the top gate dielectric should be less than the bottom gate dielectric material. The threshold voltage shift of DG-CNTISFET can be obtained by Eq. (9)

$$\Delta V_{\text{TH}} = -\frac{C_{\text{ox},\text{top}}}{C_{\text{ox},\text{bottom}}} \Delta \psi_0 \quad (9)$$

This equation shows that the threshold voltage change due to changes in the surface potential is increased by a factor of $C_{\text{ox},\text{top}}/C_{\text{ox},\text{bottom}}$. This enhanced sensitivity makes it advantageous to detect small changes.

Equation (9) can also be written as:

$$S_{\text{total}} = \frac{C_{\text{ox},\text{top}}}{C_{\text{ox},\text{bottom}}} S_{\text{top}} \quad (10)$$

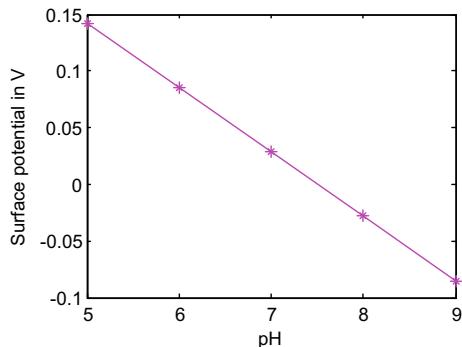
where S_{total} denotes sensitivity of the DG-CNTISFET and S_{top} is sensitivity of the device due to the top gate only.

3 Results and Discussions

The change of the device surface potential with pH change has been determined using Eq. (2). Figure 2 shows the variation of surface potential with pH change. The surface potential decreases with the increase of solution pH. Figure 3 shows the threshold voltage change of the top gate with pH. The threshold voltage increases with increase in pH value. This parameter acts as input for drain current variation of the device.

The sensitivity of the DG-CNTISFET was found to be 907 mV/pH compared to experimental value of 943 mV/pH using Eq. (10). The increased sensitivity compared to single-gate device is due to the dual-gate structure. Figure 4a shows the drain characteristics of the device in liquid medium. The experimental results have also been embedded in the plot. The plot shows the experimental and modeled results are in good agreement. Table 1 shows the values of different parameters that influenced the result most.

Fig. 2 Surface potential change with pH



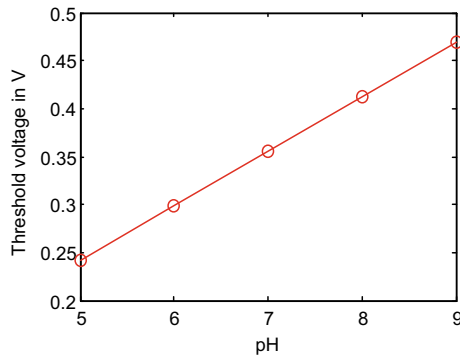


Fig. 3 Threshold voltage change of top gate with pH

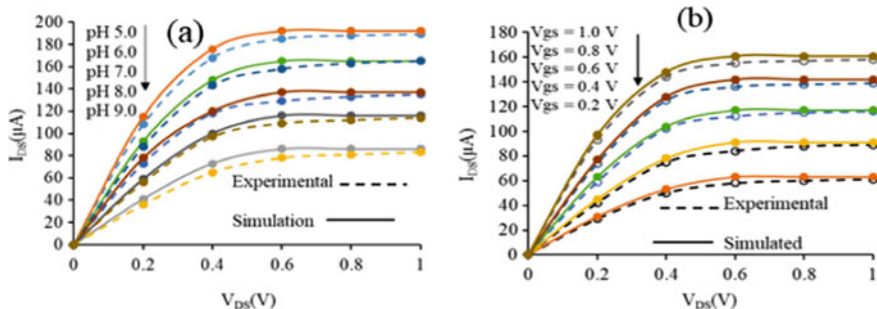


Fig. 4 **a** Drain characteristics of DG-CNTISFET in liquid **b** drain characteristics of DG-CNTISFET outside liquid

Table 1 Different influential parameters used in simulation

S. No.	Different parameter	Values
1	Reference electrode potential (E_{ref})	0.6 V
2	CNT work function (Φ_{CNT})	4.7 eV
3	Solvent surface dipole potential (χ_{sol})	0.2 V
4	Length of CNT (L_{CNT})	5 mm
5	Number of charge carriers in CNT (n_{CNT})	$9 \times 10^{15} \text{ cm}^{-3}$
6	Number of charge carriers in the oxide (n_{ox})	$9 \times 10^{12} \text{ cm}^{-2}$
7	HfO ₂ oxide thickness (t_{ox})	10 nm
8	Charges in the surface and interface states (Q_{SS})	$-3.5 \times 10^{-6} \text{ C/cm}^2$
9	ITO work function (Φ_M)	4.6 eV
10	Thickness of HfO ₂ ($t_{ox, top}$)	10 nm
11	Thickness of ZnO ($t_{ox, bottom}$)	10 nm
12	Dielectric constant for ZnO ($\kappa_{ox, bottom}$)	1.5
13	Dielectric constant for HfO ₂ ($\kappa_{ox, top}$)	25

The device drain characteristic outside liquid medium has also been investigated. For this, a metal Al gate has been deposited by physical vapor deposition (PVD) method on the top of the gate oxide layer. This is now similar to a MOSFET device. The threshold voltage was found to be 0.2 V. The drain characteristics were determined using Eqs. (3) and (4). The characteristics are similar to MOSFET. A comparison is shown in Fig. 4b between the modeled and experimental results. A good fit was obtained. Thus, it can be concluded that the device performance depends on the gate both in liquid and outside liquid.

4 Conclusion

A model was developed for DG-CNTISFET, which considers all the physical and electrochemical parameters of the fabricated device. The device showed good sensitivity with high- κ HfO₂ (dielectric constant ~25) as top gate (thickness ~10 nm) and low- κ ZnO dielectric material in the bottom gate. The enhanced sensitivity is due to the high coupling ratio. The drain current variation of the device is mostly due to the top gate of the device. The high mobility of CNT greatly contributes toward enhanced sensitivity so that the device can detect even small surface potential change. A small surface potential change causes a large change in drain current. A good fit was found between the experimental and the modeled results. Thus, this electrochemical model can be used for understanding DG-CNTISFET working.

Acknowledgements The authors thank the Department of Electronics and Information Technology, MCIT, Government of India for the support through Visvesvaraya PhD scheme and Tezpur University for providing the laboratory facilities.

References

1. Gruner G (2006) Carbon nanotube transistors for biosensing applications. *Anal Bioanal Chem* 384(2):322–335
2. Harvey JD, Jena PV, Baker HA, Zerze GH, Williams RM, Galassi TV, Roxbury D, Mittal J, Heller DA (2017) A carbon nanotube reporter of microRNA hybridization events in vivo. *Nat Biomed Eng* 1(4):0041
3. Allen BL, Kichambare PD, Star A (2007) Carbon nanotube field-effect-transistor-based biosensors. *Adv Mater* 19(11):1439–1451
4. Peng LM, Zhang Z, Wang S (2014) Carbon nanotube electronics: recent advances. *Mater Today* 17(9):433–442
5. Javey A, Kim H, Brink M, Wang Q, Ural A, Guo J, McIntyre P, McEuen P, Lundstrom M, Dai H (2002) High- κ dielectrics for advanced carbon-nanotube transistors and logic gates. *Nat Mater* 1(4):241
6. Javey A, Guo J, Farmer DB, Wang Q, Wang D, Gordon RG, Lundstrom M, Dai H (2004) Carbon nanotube field-effect transistors with integrated ohmic contacts and high- κ gate dielectrics. *Nano Lett* 4(3):447–450

7. Javey A, Tu R, Farmer DB, Guo J, Gordon RG, Dai H (2005) High performance n-type carbon nanotube field-effect transistors with chemically doped contacts. *Nano Lett* 5(2):345–348
8. Barik MA, Dutta JC (2014) Fabrication and characterization of junctionless carbon nanotube field effect transistor for cholesterol detection. *Appl Phys Lett* 105(5):1–6
9. Barik MA, Deka R, Dutta JC (2016) Carbon nanotube-based dual-gated junctionless field-effect transistor for acetylcholine detection. *IEEE Sens J* 16(2):280–286
10. Dutta JC, Thakur HR (2017) Sensitivity determination of CNT based ISFETs for different high- κ dielectric materials. *IEEE Sens Lett* 2(3):1–4
11. Spijkman M, Smits ECP, Cillessen JFM, Biscarini F, Blom PWM, De Leeuw DM (2011) Beyond the Nernst-limit with dual-gate ZnO ion-sensitive field-effect transistors. *Appl Phys Lett* 98(4):043502
12. Liu S, Guo X (2012) Carbon nanomaterials field-effect-transistor-based biosensors. *NPG Asia Mater* 4(8):e23
13. Jang H-J, Bae T-E, Cho W-J (2012) Improved sensing performance of polycrystalline-silicon based dual-gate ion-sensitive field-effect transistors using high- κ stacking engineered sensing membrane. *Appl Phys Lett* 100(25):253703
14. Dutta JC, Sharma PK (2018) Fabrication, characterization and electrochemical modeling of CNT based enzyme field effect acetylcholine biosensor. *IEEE Sens J* 18(8):3090–3097
15. Dutta JC, Thakur HR, Keshwani G (2019) High performance dual-gate carbon nanotube ion-sensitive field effect transistor with high- κ top gate and low- κ bottom gate dielectrics. *IEEE Sens J* 19(14):5692–5699
16. Sharma PK, Thakur HR, Dutta JC (2017) Modeling and simulation of carbon nanotube-based dual-gated enzyme field effect transistor for acetylcholine detection. *J Comput Electron* 16(3):584–592
17. Yates DE, Levine S, Healy TW (1974) Site-binding model of the electrical double layer at the oxide/water interface. *J Chem Soc Faraday Trans 1 Phys Chem Condens Phases* 70:1807–1818
18. Fung D, Cheung PW, Ko WH (1986) A generalized theory of an electrolyte-insulator-semiconductor field-effect transistor. *IEEE Trans Electron Devices* 33(1):8–18
19. Bousse L, De Rood NF, Bergveld P (1983) Operation of chemically sensitive field-effect sensors as a function of the insulator-electrolyte interface. *IEEE Trans Electron Devices* 30(10):1263–1270
20. Sharma PK, Thakur HR, Dutta JC (2016) Fabrication and characterization of a carbon nanotube based junctionless ion sensitive field effect transistor (CNT-JLISFET). In: International conference on computing, communication and automation (ICCCA), IEEE, Noida, pp 1450–1453
21. Dutta JC (2012) Ion sensitive field effect transistor for applications in bio-electronic sensors: a research review. In: 2nd national conference on computational intelligence and signal processing (CISP), IEEE, Guwahati, pp 185–191

A Novel Approach to Calculate TF-IDF for Assamese Language



Hsuvas Borkakoty, Chandana Dev, and Amrita Ganguly

Abstract TF-IDF is one of the earliest and most effective word vectorization techniques that provide the basis for many natural language processing (NLP) tasks. This paper provides a novel approach to create TF-IDF vectors for Assamese text. A considerable number of experiments are carried out throughout the process, and a significant result was found which is discussed here in detail.

Keywords TF-IDF · Assamese · Corpus · NLP

1 Introduction

Term frequency-inverse document frequency (TF-IDF) is one of the effective weighing factors in many natural language processing tasks, such as information retrieval and text mining. It calculates the probability of occurrence of the word in a document, which can be used to find the originality of the word. The strength of the value of TF-IDF vector of a word determines the relationship of the word in the document, and the stronger the value, higher the relation is. The approach described here tries to determine the TF-IDF value of documents in Assamese language, which is a morphologically rich Indo-Aryan language. The approach calculates TF-IDF based on the novel approach to find the frequency of the words in the document. The experimentation is carried out with different sets of data, with sentences, paragraphs and documents. The results produced to provide substantial information about the

H. Borkakoty (✉)

Jorhat Institute of Science and Technology, Sotai, Jorhat-10, India

e-mail: hsuvas@gmail.com

C. Dev · A. Ganguly

Department of Electrical Engineering and Industrial Engineering, Assam Engineering College, Jalukbari, Guwahati-13, India

e-mail: chandanaaec@gmail.com

A. Ganguly

e-mail: aganguly.ele@aec.ac.in

probability of occurrence of the word in the document(s). The following subsections cover different aspects of the approach. Section 2 covers a brief literature review of the topic. Section 3 sheds light on the methodology that is used to find the results. Section 4 provides information on the experimentation and results; finally, the conclusion is given in Sect. 5.

2 Literature Review

Spärck Jones [1] first revealed the relationship between exhaustivity of document description and the specificity of words in the document which first led to the idea of TF-IDF. The inherent relation was mathematically represented by Robertson [2], where he imprinted the IDF as log of total number of documents divided by the number of documents where the word occurs. Since then, TF-IDF has become a widely used word vectorization technique, used in many NLP tasks, such as classification, summarization, clustering and keyword extraction. Some of the uses are reviewed throughout this section.

Chan et al. [3] offered a classification system for Chinese news segments, where term frequencies are used to build the news words database, which in turn was used in classifier. Similarly, Abu-Errub [4] proposed a classification method to classify Arabic text documents where the categorization was done by using TF-IDF frequencies to find out the index terms, which were then used in the classifier. The classification task for Indian languages is also been done using TF-IDF. Notable work includes Dhar et al. [5] work on Bengali text classification where the features were determined using TF-IDF with dimensionality reduction using 40% of term frequencies of the word, which resulted in the highest of 97.78% accuracy in the classification of sports documents. Islam et al. [6] used a support vector machine [7] and a modified TF-IDF for feature selection which then used to classify a set of Bengali text documents with 92.57% of accuracy.

Apart from document classification, TF-IDF is also used in other language processing tasks for Indian languages. Notable works include Jayashree et al. [8] where they used TF-IDF along with GSS [9] coefficients to calculate the scores of the sentences in order to employ the extractive summarization technique. Sarkar [10] developed a summariser which ranked sentences according to their cumulative TF-IDF values which are then measured against a predefined threshold in order to find the thematic terms of a document. As for document clustering, Hannan et al. [11] used TF-IDF for vector space modelling of the words after the cleaning of corpuses. Hanumanthappa et al. [12] devised a keyword extraction mechanism using TF-IDF for three Dravidian languages, viz. Tamil, Telugu and Kannada, where TF-IDF was used to evaluate the importance of the word in the document and to model the vector space model for the vocabulary.

After reviewing all these literature, it has become evident that TF-IDF can serve as a very important pre-processing component in many language processing tasks.

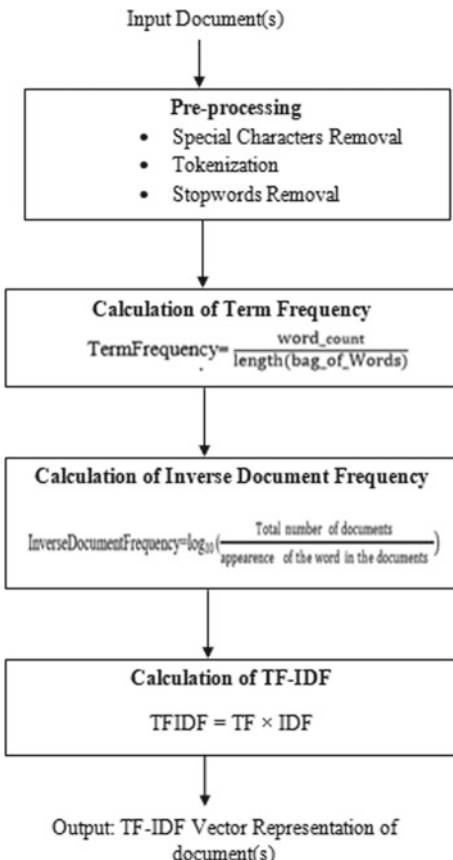
3 Methodology

Our proposed methodology is provided in accordance with the standard approach to find the TF-IDF of the document(s). The approach is divided into a set of steps as follows (Fig. 1).

3.1 Pre-processing

The pre-processing tasks that are carried out are tokenization and removal of stop words and special characters of words from the text. Since there is no predefined functions available to remove the stop words of Assamese language, hence a function is defined, which takes the text file as input removes special characters, etc., tokenizes the sentences using word tokenizer of NLTK [13]. After these two tasks, it uses a file

Fig. 1 Proposed methodology for calculation of TF-IDF



that contain the stopwords, obtained on request from the Indian Language Technology Proliferation and Deployment Centre (TDIL-DC) to find and remove the stop words. The output that is returned is in the form of a list of words with empty string for the stop words.

3.2 Computation of Term Frequency (TF)

A function is designed that takes a dictionary containing the pre-processed file (output of pre-processing function) and creates the term frequency of the words which is returned in the form of a dictionary. Term frequency is calculated as follows.

$$\text{Term Frequency} = \frac{\text{word count}}{\text{length(bag of Words)}}$$

3.3 Computation of Inverse Document Frequency (IDF)

The inverse document frequency (IDF) is calculated by converting the text files (documents) which are first to dictionaries and passed to the function as list of dictionaries. After that, the length of the list, that is, the total number of words in the dictionaries, is found. After that, IDF values of the words are calculated as per the formula mentioned below which is then stored in another dictionary against every word.

$$\text{Inverse Document Frequency} = \log_{10}\left(\frac{\text{Total number of documents}}{\text{appearance of the word in the documents}}\right)$$

3.4 Computation of TF-IDF

After calculating both TF and IDF for every word in the document, the calculation of TF-IDF is done using the following formula and the result is stored in another dictionary. The TF-IDF score is calculated by multiplying the TF and IDF score of the word.

$$\text{TFIDF} = \text{TF} \times \text{IDF}$$

4 Experiment and Results

The code, written in Python 3.7, contains the functions mentioned in the section above. The functions are defined to carry out the tasks from pre-processing till finding out the TF IDF, and inputs are given accordingly. The functions return the values after the calculation of respective components. The experiments are designed in accordance with the size of text, that is, starting with a set of sentences and continuing with set of paragraphs, a single document and ending with two different documents. All these data are accepted from the Assamese general text corpus obtained from the Indian Language Technology Proliferation and Deployment Centre (TDIL-DC). The sentences that are considered here are from an Assamese non-fiction named “Asomiya Upayashr Bhumika” which is also a part of the aforesaid corpora. The results of the experiments are given as a set of screenshots in Figs. 2, 3, 4 and 5. It has been observed that although the code works with efficiency for a set of inputs, with the increase of dataset, the time consumption goes higher. However, the results are quite satisfying and the program is scalable to accept n-number of documents to find the TF-IDF of the words contained in those documents.

The results seem promising and can be given as input to different NLP tasks. However, it is also noticed that with increase of documents, the TF-IDF values also increase for a certain set of words, whereas for some words, it shows the opposite result. This observation leads to the existence of certain frequent words and their use in different senses.

	অসম	কথা	কি	খায়	গছৰ	গোটা	ঠাই	দেশ	\
0	0.000000	0.0	0.000000	0.0	0.033448	0.0	0.000000	0.033448	0.033448
1	0.033448	0.0	0.033448	0.0	0.000000	0.0	0.033448	0.000000	0.000000

	দেশ	পাত	পাতে	বিষম	মানুহ				
0	0.000000	0.000000	0.033448	0.0	0.033448				
1	0.033448	0.033448	0.000000	0.0	0.000000				

Fig. 2 TF-IDF value for two sets of sentences

	অলপ্রদিনৰ	আগলৈকে	আৰ্হল	আনহাতে	আক	আৱাসৰ	ই	\
0	0.0	0.000000	0.000000	0.000000	0.0	0.000000	0.000000	
1	0.0	0.005376	0.005376	0.005376	0.005376	0.0	0.005376	0.005376

	উভয়ে	এই	...	সম্পাদন	সম্বন্ধ	সময়	সময়ত	সলনি	\
0	0.000000	0.0	...	0.000000	0.004855	0.004855	0.000000	0.000000	
1	0.005376	0.0	...	0.005376	0.000000	0.000000	0.005376	0.005376	

	হ্যান	স্থাপনৰ	হৈছে	হোৱাৰ	হয়				
0	0.000000	0.004855	0.000000	0.004855	0.0				
1	0.005376	0.000000	0.010751	0.000000	0.0				

[2 rows x 77 columns]

Fig. 3 TF-IDF value for words of two consecutive paragraphs. Taken from one file

	‘‘পদুম	‘অ’ব্দ	‘অকণদই’ত	‘অকণদই’ৰ	‘আইভানহো’ৰ	‘আলালেৰ	।	
0	0.00000	0.00005	0.00005	0.00005	0.0001	0.00005	0.00005	
1	0.30103	0.00000	0.00000	0.00000	0.0000	0.00000	0.00000	
	‘আসাম	‘আসামবন্ধু’	‘এলোকশী	...	কপেই	কপৰ	কপৰেখাৰপৰা	।
0	0.00005	0.00005	0.00005	...	0.00005	0.00005	0.00005	
1	0.00000	0.00000	0.00000	...	0.00000	0.00000	0.00000	
	বেখাক্ষন	বেখাপাত	বেবেকা	বেভাবেণু	ৰোগ	ৰোগগ্রস্ত,	ৰোগত	
0	0.00005	0.00005	0.00005	0.00005	0.00005	0.00005	0.00005	
1	0.00000	0.00000	0.00000	0.00000	0.00000	0.00000	0.00000	

[2 rows x 2832 columns]

Fig. 4 TF-IDF value for the words of one file

	‘‘The	‘‘এই	‘‘খৃত	‘‘গোৰক্ষ	‘‘তহতৰ	‘‘দৰিদ্ৰ	।	
0	0.00000	0.00000	0.00000	0.00000	0.00000	0.00000	0.00000	
1	0.000059	0.000029	0.000029	0.000029	0.000029	0.000029	0.000029	
	‘‘পদুম	‘‘বুচু	‘‘মৃচ্ছকটিকম	...	বেভাবেণু	ৰৈ	ৰোগ	।
0	0.00005	0.00000	0.00000	...	0.00005	0.00000	0.0	
1	0.00000	0.000029	0.000029	...	0.00000	0.000029	0.0	
	ৰোগগ্রস্ত,	ৰোগত	ৰোমাঞ্চকৰ	ৰোহসেনে	ৰোহসেনৰ	ভৃত	ৱাৰিয়ে	
0	0.00005	0.00005	0.00000	0.00000	0.00000	0.00000	0.00000	
1	0.00000	0.00000	0.000088	0.000029	0.000059	0.000029	0.000029	

[2 rows x 6577 columns]

Fig. 5 TF-IDF value for the words of two different files

5 Conclusion

This paper provides a novel approach to calculate TF-IDF feature vector for Assamese texts. The experimentation carried out on the code shows the word vectors for the words of the given corpus files. This can find applications in many NLP tasks such as document classification, named entity recognition and text summarization where the vectors can be fed as input parameters to the system. Thus, the future work should include the prospect of using the vectors to carry out the aforementioned NLP tasks.

References

1. Sparck JK (1972) A statistical interpretation of term specificity and its application in retrieval. J Documentation 28(1):11–21
2. Robertson S (2004) Understanding inverse document frequency: on theoretical arguments for IDF. J Documentation 60(5):503520

3. Chan TY, Chang YS (2017) Enhancing classification effectiveness of Chinese news based on term frequency. In: 2017 IEEE 7th international symposium on cloud and service computing (SC2). IEEE, pp 124–131
4. Abu-Errub A (2014) Arabic text classification algorithm using tf-idf and chi square measurements. *Int J Comput Appl* 93(6)
5. Dhar A, Dash NS, Roy K (2018) Application of tf-idf feature for categorizing documents of online bangla web text corpus. *Intelligent engineering informatics*. Springer, Singapore, pp 51–59
6. Islam MS, Jubayer FE, Ahmed SI (2017) A support vector machine mixed with TF-IDF algorithm to categorize Bengali document. In: 2017 international conference on electrical, computer and communication engineering (ECCE). IEEE, pp 191–196
7. Kecman V (2005) Support vector machine- an introduction. https://doi.org/10.1007/109846_97_1
8. Jayashree R, Srikanta KM, Sunny K (2011) Document summarization in Kannada using keyword extraction. *Proc AIAA* 11:121–127
9. Galavotti L, Sebastiani F, Simi M (2000) Experiments on the use of feature selection and negative evidence in automated text categorization. In: International conference on theory and practice of digital libraries. Springer, Berlin, Heidelberg, pp 59–68
10. Sarkar K (2012) Bengali text summarization by sentence extraction. arXiv preprint [arXiv:1201.2240](https://arxiv.org/abs/1201.2240)
11. Hannan A, Boro SR, Sarma JPSSK (2015) An approach to Bodo document clustering. *Int J Innovative Res Sci Eng Technol* (ISSN: 2319-8753) 4(12), <https://doi.org/10.15680/IJIRSET.2015.0412069>
12. Hanumanthappa M, Narayana Swamy M, Jyothi NM (2014) Automatic keyword extraction from Dravidian language. *Int J Innovative Sci Eng Technol* 1(8):87–92
13. Loper E, Bird S (2002) NLTK: the natural language toolkit. arXiv preprint [cs/0205028](https://arxiv.org/abs/cs/0205028)

A Low-Power Third-Order Passive Continuous-Time Sigma-Delta Modulator Using FinFET



Sarangam Kunamalla and Bheema Rao Nistala

Abstract FinFETs are known to be one of the promising devices for sub-50 nm regime. It involves better channel control, reduced short channel effects and low leakage current. A third-order continuous-time sigma-delta modulator presented in this paper is constructed by adding a capacitor to the stable second-order low-pass RC filter. It improves the quantization noise shaping and linearity of the modulator without increasing the power dissipation. A low-power, low-offset SR latch-based clocked comparator is used as quantizer. The designed modulator is implemented in FinFET 16 nm process, achieves the result of SNDR of 64 dB, ENOB of 10.5 bits, power dissipation of 48 μ W and operating with 1 V supply voltage. It is suitable for low-power ADC in biomedical applications with a signal bandwidth of 4 kHz.

Keywords FinFET · Continuous-time · Sigma-delta modulator · Low power · Analog to digital converter

1 Introduction

The development of embedded biomedical systems in recent years has increased the demand for low-power ADC [1]. The bio-potential signals are weak, and they require high resolution for accurate conversion. Sigma-delta modulators are commonly used for low-power ADC because of its simple circuitry, oversampling and noise shaping property [2]. There are two possible implementations of sigma-delta architectures. CT Modulators are more power efficient than discrete-time modulators because no need of anti-aliasing filter [3].

The basic architecture of a sigma-delta modulator is presented in Fig. 1. It comprises of loop filter, comparator and a DAC in the feedback path. The loop filter

S. Kunamalla (✉) · B. R. Nistala

Department of Electronics and Communication Engineering, National Institute of Technology

Warangal, Warangal, India

e-mail: sarangam_7@nitw.ac.in

B. R. Nistala

e-mail: nbr@nitw.ac.in

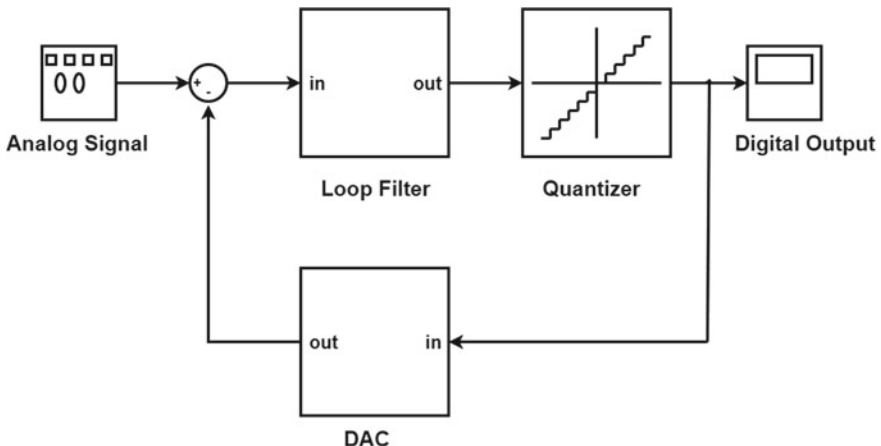


Fig. 1 Basic architecture of a sigma-delta modulator [4]

is mostly realized using active integrator. The comparator is a clocked comparator which is a 1-bit quantizer, and DAC is an inverter. Operational amplifier is the main building block in an integrator and consumes significant portion of the power in an overall sigma-delta modulator. The order of the filter depends on the number of active integrators. Each integrator requires one op-amp. As the order of the filter increases, the number of op-amps increases which limits the low power dissipation of the sigma-delta modulator.

The trend is towards smaller number of amplifiers than the order of the loop filter and without any amplifier [5–8]. A hybrid active–passive loop filter is implemented [9] with three active integrators and two passive integrators. This saves the power but resolution is restricted to 10 bits. In ref [10], a second-order passive sigma-delta ADC for low-power applications is implemented using cascade of two first-order RC circuits. This paper achieves simple circuit and low power but two poles in a single-loop cause stability problem. A 1 MHz continuous-time sigma-delta modulator using genetic algorithm approach is implemented by adding zero to the second-order filter to solve the problem of stability [11].

The passive filters are simple, no power consumption, linearity and operating at low supply voltage [12]. These filters are limited to second order only because it depends on the comparator gain. As the order of the filter increase, resulting a low voltage swing at its input. One solution to this is adding a capacitor to the second order to filter and pre-amplifier to the latched comparator. A third-order continuous-time sigma-delta modulator is implemented in this paper using passive only this achieves bandwidth using FinFET devices. FinFETs are promising devices in near future and have less short channel effects and low leakage currents than planar MOSFETs [13].

The paper is structured in the following manner. In Sect. 2, first- and second-order passive sigma-delta modulator architecture and its problems are described. The proposed third-order passive SDM architecture and its implementation details

are demonstrated in Sect. 3. In Sect. 4, the simulation results are discussed. Finally, the paper concludes in Sect. 5.

2 First- and Second-Order Passive Sigma-Delta Modulator Architecture

2.1 First-Order Passive Sigma-Delta Modulator

In this topology, the loop filter is realized with R_1, C_1 network as shown in Fig. 2. The input and feedback resistors are same value to get unity gain. Here, the integration function is performed by the capacitor C_1 . The main disadvantage of this topology is voltage across the capacitor is varying due to input and feedback resulting distortion present in the modulator output.

Equation (1) indicates the output voltage as related to input voltage, integration node voltage and quantization error voltage. The first-order STF, NTF, DTF is as shown below Eqs. (2), (3), (4), respectively.

$$V_{\text{out}} = \frac{V_{\text{in}}}{1 + SR_1C_1} + \frac{SR_1C_1}{1 + SR_1C_1} \cdot V_{\text{qe}} + \frac{-2}{1 + SR_1C_1} \cdot V_{\text{int}} \quad (1)$$

$$\text{STF} = \frac{1}{1 + SR_1C_1} \quad (2)$$

$$\text{NTF} = \frac{SR_1C_1}{1 + SR_1C_1} \quad (3)$$

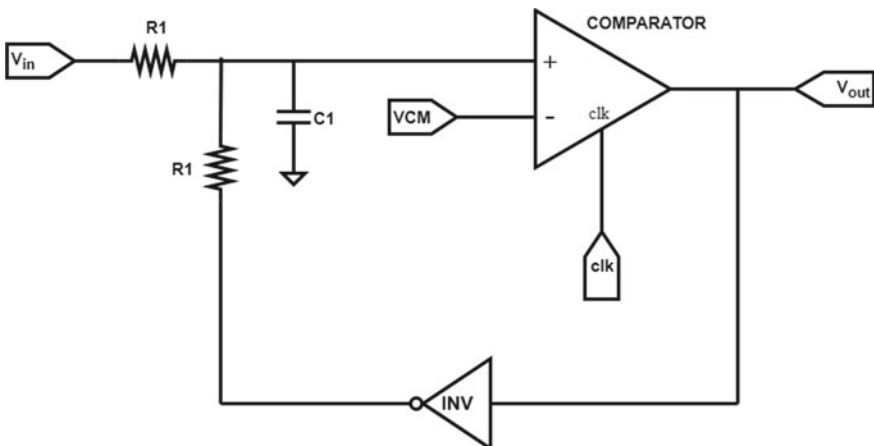


Fig. 2 First-order passive sigma-delta modulator architecture [10]

$$\text{DTF} = \frac{-2}{1 + SR_1C_1} \quad (4)$$

2.2 Second-Order Passive Sigma-Delta Modulator

This topology is obtained by cascading of two RC sections as shown in Fig. 3. It improves the linearity and reduces the distortion in the modulator output. The drawback of this topology is cascading of RC sections attenuates the input signal at the positive input of the comparator resulting the noise of the comparator increases. The second drawback is two poles in a negative feedback loop cause instability.

Equation (5) indicates the output voltage as related to input voltage, integration node voltage and quantization error voltage. The second-order STF, NTF, DTF is as shown below Eqs. (6), (7), (8), respectively.

$$V_{\text{out}} = \frac{(1 + SC_2R_2)}{1 + SR_2C_2 + SR_1C_1} \cdot V_{\text{in}} + \frac{S(SR_1C_1R_2C_2 + R_1C_1)}{1 + SR_1C_1 + S^2R_1C_1R_2C_2} \cdot V_{\text{qe}} + \frac{1}{1 + SR_1C_1 + (1 + SR_2C_2)} \cdot V_{\text{int}} \quad (5)$$

$$\text{STF} = \frac{(1 + SC_2R_2)}{1 + SR_2C_2 + SR_1C_1} \quad (6)$$

$$\text{NTF} = \frac{S(SR_1C_1R_2C_2 + R_1C_1)}{1 + SR_1C_1 + S^2R_1C_1R_2C_2} \quad (7)$$

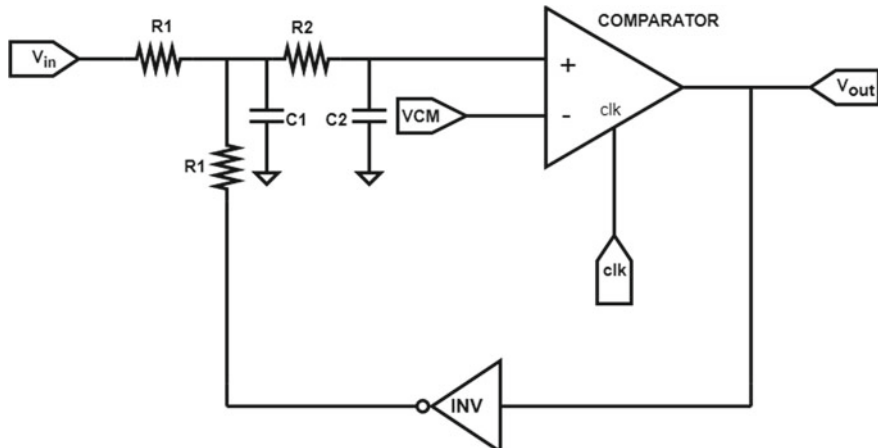


Fig. 3 Second-order passive sigma-delta modulator architecture [10]

$$\text{DTF} = \frac{1}{1 + SR_1C_1 + (1 + SR_2C_2)} \quad (8)$$

3 Proposed Third-Order $\Sigma\Delta$ Modulator

The proposed third-order $\Sigma\Delta$ modulator is demonstrated in Fig. 4. In this modified architecture, the conventional second-order $\Sigma\Delta$ modulator is stabilized by series R_3 and C_2 to create the left-hand zero. Now, in proposed topology, we add one more capacitor C_3 parallel to series R_3 and C_2 . By adding this capacitor, we are getting third-order $\Sigma\Delta$ modulator and less signal voltage at the positive node capacitor. In order to get the input signal at the output, a 2-stage RC filter is added to the modulator output. This topology saves a resistor when compared to cascading of three RC sections.

Equation (9) indicates the output voltage as related to input voltage, integration node voltage and quantization error voltage. The proposed third-order STF, NTF, DTF is as shown Eqs. (11), (12), (13), respectively.

$$V_{\text{out}} = \frac{(1 + SC_1R_2)}{D + (1 + SC_1R_2)} \cdot V_{\text{in}} + \frac{D}{D + (1 + SC_1R_2)} \cdot V_{\text{qe}} + \frac{(2R_1 + SC_3R_3R_1)(1 + SC_1R_2)}{D + (1 + SC_1R_2)} \cdot V_{\text{int}} \quad (9)$$

$$D = (2R_1 + R_3 + SC_3R_3R_1)(S(C_1 + C_2) + S^2C_1C_2R_2) + (1 + SC_1R_2) \quad (10)$$

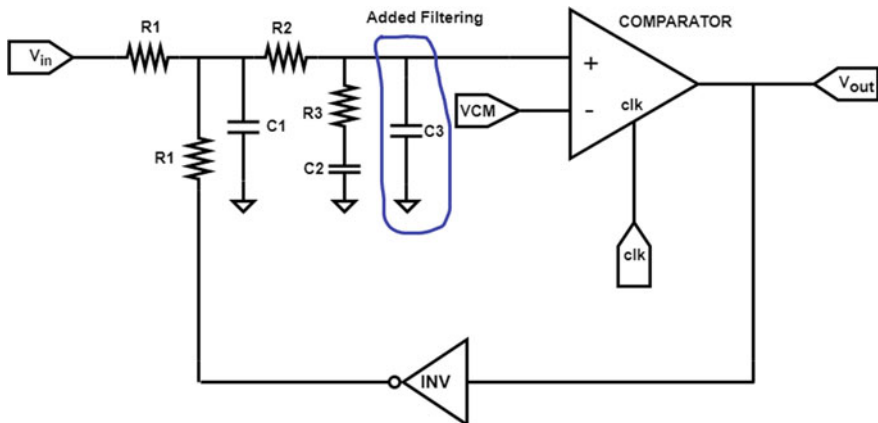


Fig. 4 Proposed third-order $\Sigma\Delta$ modulator

$$\text{STF} = \frac{(1 + SC_1 R_2)}{D + (1 + SC_1 R_2)} \quad (11)$$

$$\text{NTF} = \frac{D}{D + (1 + SC_1 R_2)} \quad (12)$$

$$\text{DTF} = \frac{(2R_1 + SC_3 R_3 R_1)(1 + SC_1 R_2)}{D + (1 + SC_1 R_2)} \quad (13)$$

3.1 Passive Filter Implementation

The dominant pole is coming through the resistance R_3 and the capacitor C_3 . We are choosing the values of R_3 and C_3 by criteria of $R_3 C_3 > 5T$ where T is input signal time period. The above condition is hold for proper integration. The values of R_1 , R_2 , C_1 , C_2 are selected based on resolution limit of the comparator and system stability.

The overall transfer function of the proposed SDM is displayed in Fig. 5. The bandwidth of the proposed modulator is 10 kHz. The first pole, second pole and third pole of this modulator are 3.8 kHz, 63 MHz and 350 MHz, respectively, and zero is compensated by second pole. The STF and NTF are low-pass and high-pass

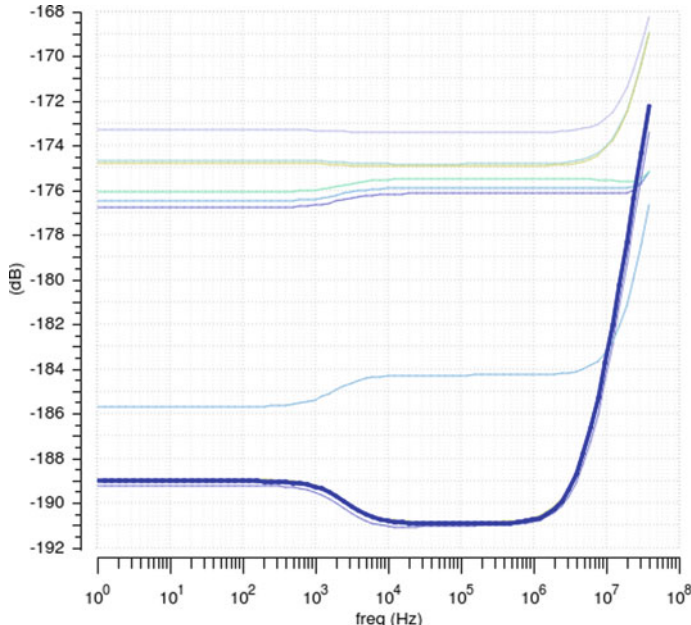


Fig. 5 Overall transfer functions of proposed modulator

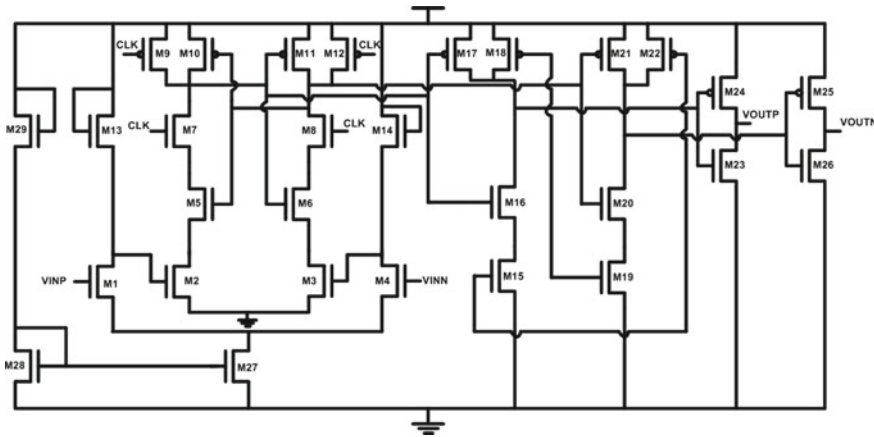


Fig. 6 Circuit diagram of comparator

characteristics, respectively, having a slope of 50 dB/decade with values of $R_1, R_2, R_3, C_1, C_2, C_3$ are set to $10 \text{ M}\Omega, 600 \Omega, 600 \Omega, 15\text{pF}, 2\text{pF}, 2\text{pF}$, respectively.

The sigma-delta modulator's critical portion is a comparator. The poor performance of comparator can degrade the resolution of the modulator. Figure 6 indicates the circuit diagram of the comparator. It comprises one pre-amplifier stage followed by a positive feedback latch and *S-R* flip-flop. The pre-amplifier stage is simple common source amplifier (M_1 and M_{13} , M_4 and M_{14}) having a gain of g_{m13}/g_{m1} and g_{m14}/g_{m4} to increase the resolution of the comparator. After the design of pre-amplifier stage, a cross-coupled latch (M_2 - M_3 and M_5 - M_{12}) together with an *S-R* latch built with NAND gates (M_{13} - M_{16} and M_{17} - M_{20}) to generate the accurate output signal. The *S-R* latch reduces the meta-stability occurrence in case of large regeneration time and output changes only raising edge of the clock. The inverters (M_{21} - M_{22} , M_{23} - M_{24}) increase the available output current. The current mirror (M_{25} - M_{27}) provides the bias current of $10 \mu\text{A}$.

The designed comparator has resolution limit of 5 mV , and simulation results are plotted in Fig. 7.

4 Simulation Results

The proposed architecture has been designed in a 16 nm FinFET process with a supply voltage of 1 V . Figure 8 shows the transient response of the proposed sigma-delta modulator for a sine wave input of $4 \text{ kHz}, 200 \text{ m } V_{pp}$. Resulting a pulse width modulated signal having more number of one's corresponding to 1 V and more number of zero's corresponding to 0 V . Intermediate values will get 1,0 transition.

The SDM modulator output spectrum with the sampling rate of 1 MHz is depicted in Fig. 9. From this plot, we are getting a gain of -34.54 dB at 4 kHz sine wave

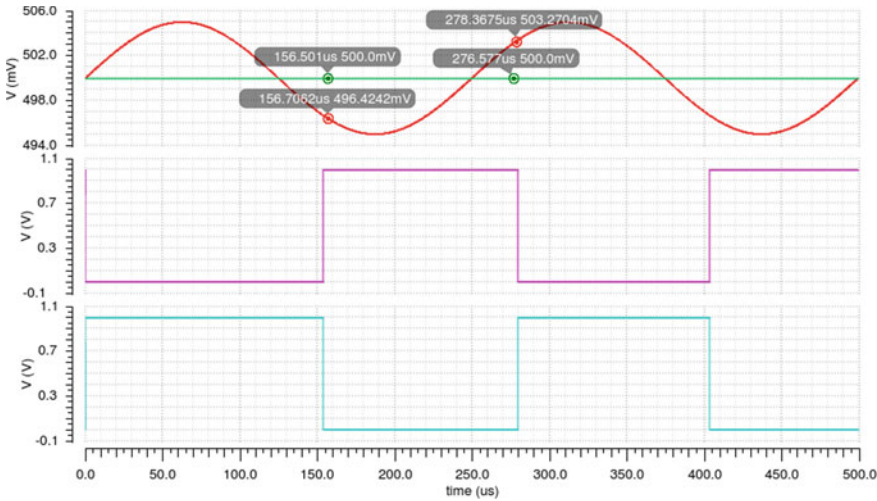


Fig. 7 Simulation results of the comparator

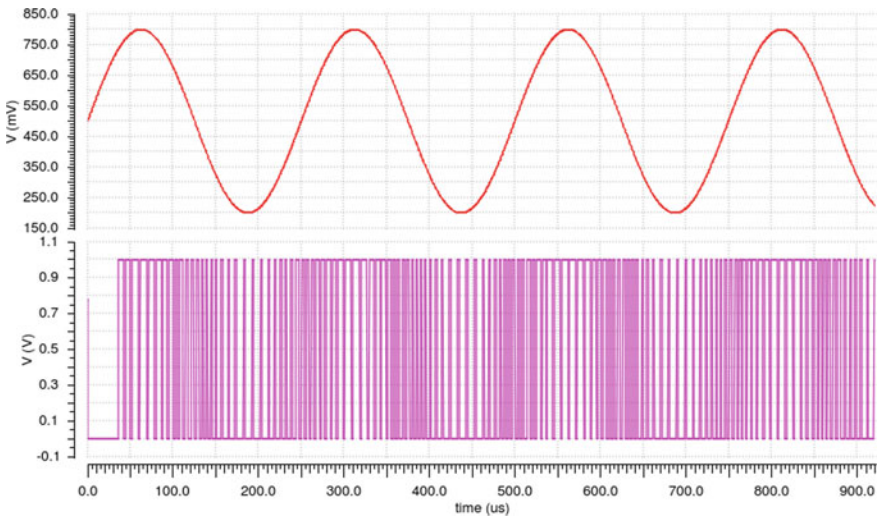


Fig. 8 Transient response of the proposed modulator

input signal and the average noise factor floor value is around -90 dB up to 10 kHz bandwidth.

Figure 10 depicts the FFT plot of PWM output waveform. Regarding dynamic performance of the modulator, a signal to noise and distortion ratio (SNDR) of 64 dB was achieved. This corresponds to the effective resolution of 10.5 bits and power dissipation $48 \mu\text{W}$.

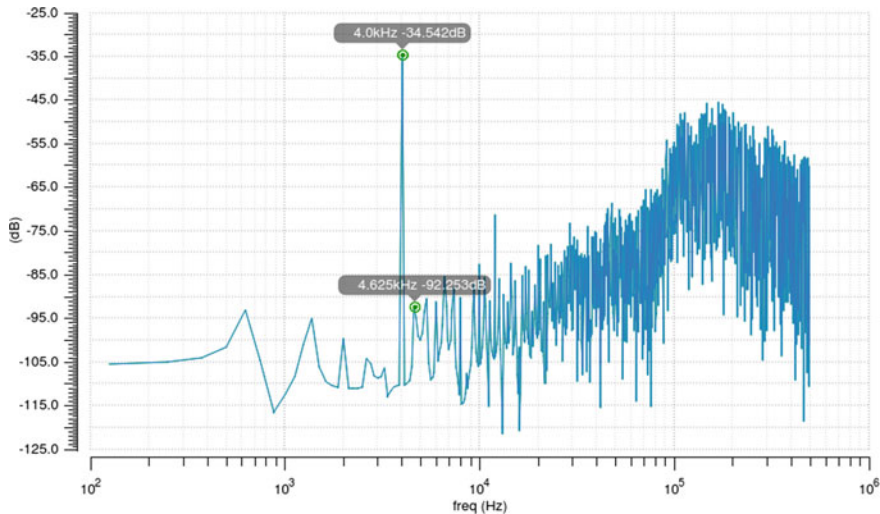


Fig. 9 SDM modulator output spectrum (4 kHz, 500mV_{pp})

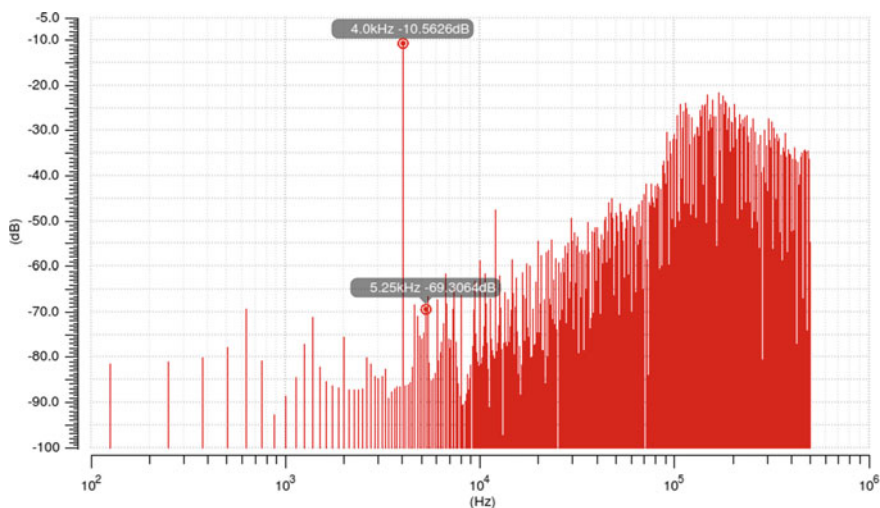


Fig. 10 FFT plot of the PWM output

The proposed SDM's performance is outlined and distinguished with the previous published passive sigma-delta modulator in Table 1. Based on the comparison Table 1, the proposed modulator achieves lower FOM and is designed in a lower technology.

Table 1 Performance comparison with previous published papers

S. No.	Parameter	This work	Ref [10]	Ref [14]	Ref [15]
1	Process	16 nm FinFET	500 nm	350 nm	500 nm
2	Signal BW	4 kHz	5 kHz	5 kHz	3 kHz
3	Sampling rate	1 MHz	10 MHz	1 MHz	1 MHz
4	Resolution (ENOB)	10.5 bits	8 bits	10 bits	–
5	SNDR	64 dB	50 db	–	57.6 dB
6	Power consumption	48 μ W	100 μ W	50 μ W	–
7	Supply voltage	1 V	5 V	3.3 V	2.5 V

5 Conclusion

A third-order sigma-delta modulator presented in this paper is designed by two cascaded passive RC circuits, a capacitor and comparator. The comparator is low-offset latched type implemented using FinFET devices. The stability of the modulator is achieved by overall transfer function plot. The designed modulator has an SNDR of 64 dB, effective resolution ENOB of 10.5 bits, power dissipation 48 μ W, and it is suitable for low area, low power dissipation and low-scale process ADC applications.

References

1. Benabes P, Kielbasa R (2002) Passive Sigma-Delta converters design. In: Proceedings of 19th IEEE instrumentation and measurement technology conference, IMTC 2002, Anchorage, AK, USA, 21–23, pp 469–474
2. Baker RJ (2009) CMOS mixed-signal circuit design, 2nd edn. Wiley, London, pp 59–60. ISBN: 978-0-470-29026-2
3. Schreier R, Temes GC (1997) Understanding delta-sigma data converters. IEEE press, Piscataway
4. de la Rosa JM (2011) Sigma-delta modulators: tutorial overview, design guide, and state-of-the-art survey. IEEE Trans Circ Syst I Reg Pap 58(1):1–21
5. Srinivasan V, Wang V, Satarzadeh P, Haroun B, Corsi M (2012) A 20 mW 61 Db SNDR (60 MHz BW) 1b 3rd-order continuous-time delta-sigma modulator clocked at 6 GHz in 45 nm CMOS. In: EEE international solid-state circuits conference (ISSCC), Digest of Technical Papers, pp 158–160
6. Zeller S, Muenker C, Weigel R, Ussmueller T (2014) A 0.039 mm inverter-based 1.82 mW 68.6 dB-SNDR 10 MHz-BW CT ADC in 65 nm CMOS using power- and area-efficient design techniques. IEEE J Solid-State Circ 49(7):1548–1560
7. Matsukawa K et al (2010) A fifth-order continuous-time delta-sigma modulator with single-opamp resonator. IEEE J Solid-State Circ 45(4):697–706
8. Weng CH, Wei TA, Alpman E, Fu CT, Tseng YT, Lin TH (2014) An 8.5 MHz 67.2 dB SNDR CTDSM with ELD compensation embedded twin-T SAB and circular TDC-based quantizer in 90 nm CMOS. In: Proceedings IEEE international symposium on VLSI circuits, pp 1–2
9. Song T, Cao Z, Yan S (2008) A 2.7-mW 2-MHz continuous-time modulator with a hybrid active–passive loop filter. IEEE J Solid-State Circ 43(2):330–341

10. Roy A, Baker RJ (2014) A passive 2nd-order sigma-delta modulator for low-power analog-to-digital conversion. In: 2014 IEEE 57th international midwest symposium on circuits and systems (MWSCAS), College Station, TX, pp 595–598
11. De Melo JL (2013) A low power 1-MHz continuous-time M using a passive loop filter designed with a genetic algorithm tool. In: Proceedings EEE international symposium on circuits and systems (ISCAS), pp 586–589
12. Sai T, Sugimoto Y (2009) Design of a 1-V operational passive sigma-delta modulator. In: 2009 European conference on circuit theory and design, Antalya, pp 751–754
13. Thakker RA, Srivastava M, Tailor KH, Baghini MS, Sharma DK, Rao VR, Patil MB (2011) A novel architecture for improving slew rate in FinFET-based op-amps and OTAs. *Microelectron J* 42(5):758–765
14. Guessab S, Benabes P, Kielbasa R (2004) Passive delta-sigma modulator for low-power applications. In: MWSCAS '04, pp 295–298
15. Gundel A, Carr WN (2007) A micro power sigma-delta A/D converter in 0.35 m CMOS for low frequency applications. LISAT 2007 pp 1–7

Mitigation of Power Fluctuations in UPFC-Based Network



Rajen Pudur, Pallavi Kumari, and Mrinal Kanti Rajak

Abstract Unified power flow controller which is the latest family in FACT family is used for real-time control and dynamic compensation of AC transmission system. UPFC controls all the parameters that affect power flow (voltage, phase angle and impedance) of transmission line by either selectively or simultaneously. But with conventional control schemes, the power fluctuation cannot be completely mitigated, and the time constant of damping is independent of real and reactive power feedback. In this paper, an attempt is made to validate the advance control scheme available for mitigation of the power fluctuation with MATLAB simulation. Complete model is prepared and analysed ignoring the dynamics of shunt device; the power fluctuation attenuation has been successfully achieved by simulation, and the results are presented.

Keywords Unified power flow controller · Power feedback control · Cross-coupling control

1 Introduction

The power transmission lines are in continuous improving to serve its best function of catering uninterrupted power to the consumers. These power systems are comprised of three major parts, generation, transmission and distribution which are governed by the demands of loads at different places, and their availability and controllability largely depend on the latest technology breakthrough. The Electric Power Research

R. Pudur (✉) · P. Kumari

National Institute of Technology Arunachal Pradesh, Yupia, Arunachal Pradesh, India
e-mail: rajenpudur@nitap.ac.in

P. Kumari

e-mail: pallaviumari426@gmail.com

M. K. Rajak

Department of Electrical Engineering, National Institute of Technology Arunachal Pradesh,
Yupia, Arunachal Pradesh, India
e-mail: mrinal2042@gmail.com

Institute (EPRI) has introduced a new concept which was called Flexible AC Transmission System (FACTS) [1] in the late 1980, which gives a concept or power to the existing power line supply more power to load up to its thermal capabilities. A FACTS device gives us freedom to choose how to control and increase the efficiencies of power line. Unified power flow controller (UPFC) is the youngest in the family of FACTS, and it can give both controls of real power and reactive powers independently in single go. Many researches have conducted to have smooth power flow without fluctuations, but it generally seems power fluctuation in these lines. Phase angle control and cross-coupling control are two known control methods which can give smooth flow of power, but power fluctuation has seen in power line [2]; hence, Hideaki Fujita [3] proposed an advance control scheme combining the two methods available to damp the power fluctuation in transient state.

In this paper, an attempt is made to validate the result obtained by Hideaki Fujita, with MATLAB simulation with the new value of additional feedback is presented with validates the experimental result obtained by Hideaki Fujita.

2 UPFC Generalized Configuration

UPFC is basically a dual converter system which is required for realistic implementation of the concept so that real power easily flows in two ends though reactive power can be changed in between the two converters. Using two voltage source converters, the UPFC can be easily realized, with common DC link in between as shown in Fig. 1; as shown in figure, the shunt converter is connected with grid by a shunt transformer and the series converter is connected with grid by series transformer. E_c is the voltage to be injected in the line for controlling the real power. The two

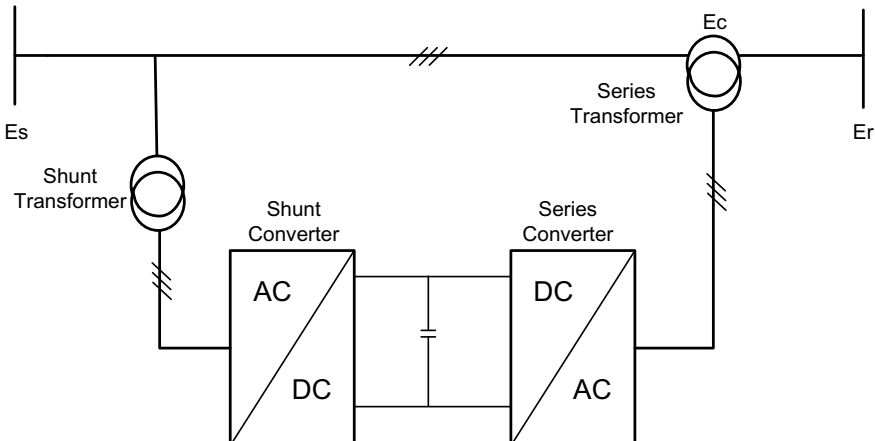


Fig. 1 Simplified diagram of UPFC

converters are connected with common DC line capacitor to keep the input voltage at series converter constant.

The UPFC plays a vital role in optimizing the operation of the transmission line system as it has multiple functions. The damping of the system will be boost by the UPFC, and it is also used to improve the transient margins. The shunt converter will control the bus voltage by absorbing or generating reaction power, and the series converter will control the power flow by injecting a controllable series voltage via a series transformer with the transmission line.

2.1 Operating Principle of UPFC

As we know that there are two numbers of the converter whichever are used in UPFC as shown in Fig. 1; the function of these converters is given in detail in the following

1. Shunt converter: Shunt converter will provide or consume the real power which is required by series converter at its common DC link which is to help the exchange of real power which comes from the series voltage injection. Shunt converter can also feedback the DC link voltage to AC line through shunt transformer, and shunt converter can also be used to produce or consume reactive power compensation; thus, an independent control can be achieved, and shunt converter is generally functioned as STATCOM.
2. Series converter: The main function of UPFC is to inject AC voltage (E_c) whose magnitude is controlled in the range $0 \leq E_c \leq E_{c(\text{Max})}$ and phase angle ρ in $(0 \leq \rho \leq 360)$ which is only possible using series converter. The voltage injection will be done by series converter connected with transmission line through series transformer at power frequency. The voltage injected will be taken as a synchronous AC voltage sources. There is an exchange of real and reactive power between series converter and AC line due to transmission line current. At the output of series transformer, there is an exchange of reactive power which is produced within the converter. At AC terminal, there is an exchange of real power which is converted into DC power which seems as positive or negative real power demand at DC terminal. This series converter basically functions as SSSC

There is an independent generation of reactive power at AC terminal by each converter and it is necessary to know that there is occurrence of closed—direct patch for the negotiation of real power through the action of injection of series voltage injection by shunt converter and series converter back to the line, and then, there is corresponding generation of consumption of reactive power exchange locally by series converter, and thus, it will not flow through the line. Therefore, shunt converter will act at unity power factor or will be controlled to acquire reactive power exchange with the line which is independent of the reactive power exchange by series converter.

2.2 Real and Reaction Power Control

Sending end voltage and phase angle:

$$E_s = E e^{-j\theta_1} \theta_1 = \frac{\delta}{2}$$

Receiving end voltage and phase angle:

$$E_r = E e^{-j\theta_2}, \theta_2 = \frac{\delta}{2}$$

The current phase is:

$$I = \frac{E_s - E_r}{Z},$$

where $Z = jX$ is the complex impedance of the line.

Receiving end complex AC power:

$$S = E_r I^* \quad (1)$$

$$P - j Q_r = E_r I^* \quad (2)$$

Receiving end transmitted power P and reactive power $-jQ_r$:

$$P - j Q_r = E_r \left(\frac{E_s - E_r}{jX} \right)^* \quad (3)$$

Substituting

$$E_s = E^{j\delta/2} = E \left(\cos \frac{\delta}{2} + j \sin \frac{\delta}{2} \right) \quad (4)$$

$$E_r = E^{-j\delta/2} = E \left(\cos \frac{\delta}{2} - j \sin \frac{\delta}{2} \right) \quad (5)$$

Since $E_s = E_r = E$

The final expression for real power transfer and reactive power transfer is:

$$P_o(\delta) = \frac{E^2}{X} \sin \delta$$

$$Q_{0r}(\delta) = -\frac{E^2}{X} (1 - \cos \delta)$$

3 Proposed Set-up of UPFC

A proposed circuit of UPFC is shown in Fig. 2; it is observed that a UPFC is connected between two sides of lines with voltage marked as E_s and E_r . Generally, the series converter is operated as controllable voltage source whereas shunt converter as the current source. By adjusting the bulk of real power in the line, the shunt converter is utilized to control the DC link voltage and also control the reactive power. IGBT is used to make series converter, and diodes are used to make shunt converter. A PWM inverter is used to generate six gate pulses, and its AC terminal will be connected via a matching transformer in series with the line, and a resistor and inductance are used to show the impedance (Z) of the line.

It is shown that we have one resistor (R) and inductor (L) which is used to show the impedance of transmission line. As the impedance of transmission line is much larger than the resistance of the line, it is acceptable to discard that line resistance at the overhead line.

Therefore, an expression for the line current phase will be given by,

$$I = \frac{E_s - E_r + E_c}{j\omega o L}$$

Single-phase current as shown in Fig. 3.

It is assumed here that sending end-side voltage, E_s equal to the receiving end side voltage, E_r for the account of ease as shown in the figure. From Fig. 4a, active power will be accomplished by adjusting the output voltage E_c which will be led

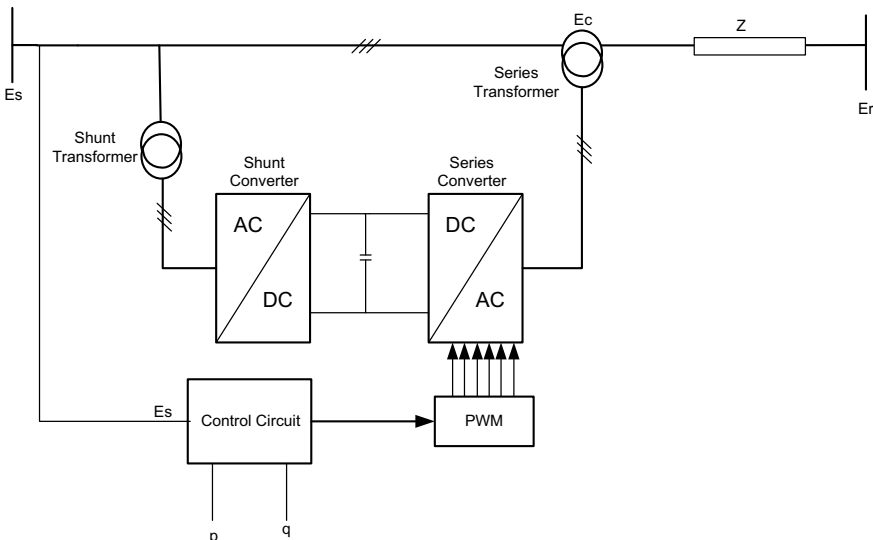


Fig. 2 Proposed to set up of UPFC

Fig. 3 Single-phase equivalent circuit

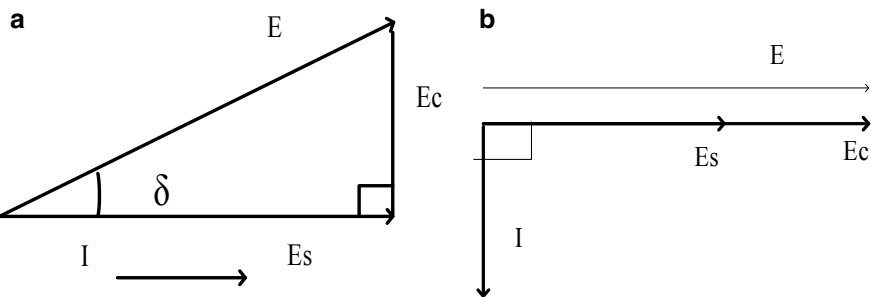
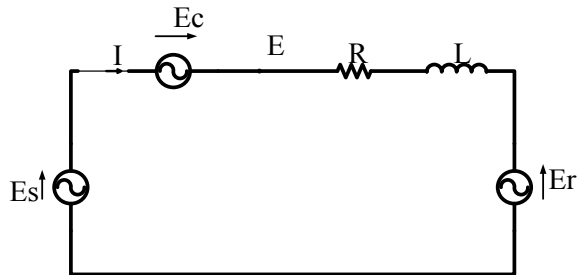


Fig. 4 Phasor diagram for **a** control of real power and **b** control of reactive power

by 90° as in relative to E_s in result I will be in phase with E_s . On the other hand, by adjusting E_c to be in phase with E_s , current I will lag by 90° ; then, it results in control of reactive power flow shown if Fig. 4b. The above discussion is not required because phasor vectors are used.

3.1 Phase Angle Control

In phase angle control, the control of real power will likely to be achieved by controlling the amplitude of 90° leading or lagging output voltage.

Consider a $d-q$ reference frame based on space vector in which q -axis voltage E_{cq} is utilized to control d -axis current i_d which is corresponding to real power.

Thus, for the series device, the voltage reference vector $E_c^* = E_{cd}^*, E_{cq}^*$ will be given as,

$$E_{cq}^* = K_p(i_d^* - i_d) \quad (K_p = [V/A] \text{ is an real power feedback gain})$$

(i_d^* = real current reference frame)

So, E_{cq} is used to control the phase angle between E_m and E_r which is given as

$$\delta = \tan^{-1} \left(\frac{E_{cq}}{E_s} \right)$$

3.2 Cross-Coupling Control

In this control which is comprised of both real power feedback loop and reactive power feedback loop, through the control of both the magnitude of E_m and phase angle δ , this control scheme can be described. Hence, the cross-coupling control empowers the UPFC to accomplish both control of real and reactive power, so on $d-q$ frame coordinates d -axis, voltage E_{cd} is used to control q -axis current i_q which is related to reactive power. Thus, for the series device, the voltage reference vector is given by

$$\begin{aligned} E_{cd}^* &= -K_q(i_q^* - i_q) \\ E_{cq}^* &= K_p(i_d^* - i_d) \end{aligned}$$

where K_q [V/A] reactive power feedback gain

4 Proposed Control Scheme

In this control scheme, for the series device, the voltage reference vector is given by

$$\begin{aligned} E_{cd}^* &= K_r(i_d^* - i_d) - K_q(i_q^* - i_q) \\ E_{cq}^* &= K_p(i_d^* - i_d) + K_r(i_q^* - i_q) \end{aligned}$$

In this scheme, both the schemes cross-coupling and phase control scheme are combined, with new power feedback gain K_r which will perform like a damping resistor across the current error.

Let us assume that the voltage of sending end will be the same as the voltage of receiving end, i.e. $E_s = E_r$.

$$\begin{bmatrix} E_{sa} \\ E_{sb} \\ E_{sc} \end{bmatrix} = \sqrt{\frac{2}{3}} E_s \begin{bmatrix} \cos \theta \\ \cos(\theta - \frac{2\pi}{3}) \\ \cos(\theta + \frac{2\pi}{3}) \end{bmatrix} \quad (6)$$

Here, $\theta = \omega \circ t$, $\omega \circ$ = supply angular frequency

$$E_{sa} = R_{ia} + L \frac{di_a}{dt} \quad (7)$$

$$E_{\text{sb}} = R_{\text{ib}} + L \frac{di_b}{dt} \quad (8)$$

$$E_{\text{sc}} = Ri_c + L \frac{di_c}{dt} \quad (9)$$

Now, applying d - q transformation in Eq. (6)

$$\begin{bmatrix} E_{\text{sa}} \\ E_{\text{sb}} \\ E_{\text{sc}} \end{bmatrix} = \sqrt{\frac{2}{3}} E_s \begin{bmatrix} \cos \theta \\ \cos(\theta - \frac{2\pi}{3}) \\ \cos(\theta + \frac{2\pi}{3}) \end{bmatrix}$$

Apply to apply d - q transformation

$$\begin{aligned} Ec_d &= Ri_d + L \frac{di_d}{dt} - \omega \circ Li_q \\ Ec_q &= Ri_q + L \frac{di_q}{dt} + \omega \circ Li_d \end{aligned}$$

Then, instantaneous real and reactive power is given by

$$\begin{aligned} p &= E_{\text{sd}} \cdot i_q + E_{\text{sq}} \cdot i_q = E_s \cdot i_d \\ q &= E_{\text{sd}} \cdot i_q - E_{\text{sq}} \cdot i_d = E_s \cdot i_q \end{aligned}$$

Taking the Laplace transform and assume initial condition $i_d(0) = i_q(0) = 0$, then

$$\begin{aligned} RI_d(s) - RI_d(0^+) + K_r I_d(s) - K_r I_d(0^+) \\ + sLI_d(s) - sLI_d(0^+) - \omega_0 L I_q(s) \\ - K_q I_q(s) = K_r I_d^*(s) - K_q I_q^*(s) \text{ As } Id(0^+) = 0 \end{aligned}$$

$$\begin{aligned} (R + Kr + sL)Id(s) - (\omega_0 L + K_q)I_q(s) &= K_r I_d^*(s) - K_q I_q^*(s) \\ (\omega_0 L + K_p)I_d(s) + (R + Kr + sL)I_q(s) &= K_p I_d^*(s) + K_r I_q^*(s) \end{aligned}$$

After solving the above equations.

$$\begin{aligned} &\{(R + Kr + sL)^2 + (\omega_0 L + K_p)(\omega_0 L + K_q)\}I_d(s) \\ &= \{K_r(R + Kr + sL) + K_p(\omega_0 L + K_q)\}I_d^*(s) \\ &\quad - \{K_q(R + Kr + sL) - K_r(\omega_0 L + K_q)\}I_q^*(s) \\ &\{s^2 L^2 + s(2RL + 2KrL) + (R^2 + Kr^2 + 2RK_r \\ &\quad + \omega_0^2 L^2 + \omega_0 L K_q + \omega_0 L K_p + K_p K_q)I_d(s)\} \\ &= \{sK_r L + (KrR + Kr^2 + \omega_0 L K_p + K_p K_q)\}I_d^*(s) \end{aligned}$$

$$-\{sK_qL + (K_qR + K_qK_r - \omega_0LK_r - K_rK_q)\}I_q^*(s)$$

Equation of the second-order system is $s^2 + 2\zeta\omega_n s + \omega_n^2$

$$\text{Here } 2\zeta\omega_n = \frac{2(K_r + R)}{L}$$

$$\text{Or, } \zeta \left[\frac{\sqrt{(\omega_0L + K_p)(\omega_0L + K_q) + (K_r + R)^2}}{L} \right] = \frac{(K_r + R)}{L}$$

$$\text{Or, } \zeta \text{ (Damping Factor)} = \frac{K_r + R}{\sqrt{(\omega_0L + K_p)(\omega_0L + K_q) + (K_r + R)^2}} \quad (10)$$

The equation for fluctuating frequency is given as,

$$\begin{aligned} \omega &= \omega_n \sqrt{1 - \zeta^2} \\ &= \omega_n \sqrt{1 - \frac{(K_r + R)^2}{L^2 \omega_n^2}} \\ &= \frac{1}{L} \sqrt{L^2 \frac{(\omega_0L + K_p)(\omega_0L + K_q) + (K_r + R)^2}{L^2} - (K_r + R)^2} \\ \omega &= \frac{\sqrt{(\omega_0L + K_p)(\omega_0L + K_q)}}{L} \end{aligned} \quad (11)$$

From Eq. (10), it can be observed that as larger the feedback gain K_r , then there will be ζ close to unity. And from (11), there is an increase in K_p and K_q ; there will be an increase in fluctuating frequency ω . The final control diagram is shown in Fig. 5.

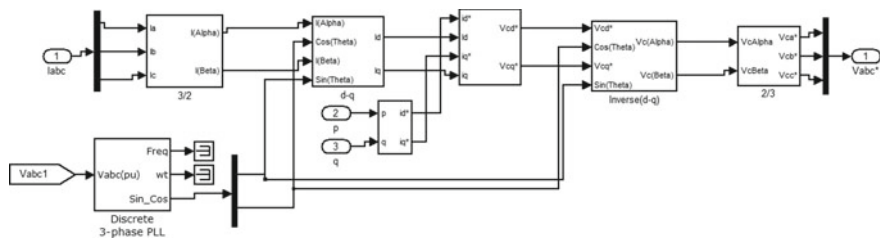


Fig. 5 Control scheme

5 Proposed Model of UPFC in MATLAB

A three-phase UPFC model is modelled in MATLAB software whose model is shown in Fig. 6. In this model, two generating units are taken which is of same rating, i.e. of 440 V. UPFC has two transformers—one is shunt transformer and series transformer where a series device is used to inject a voltage in series with the line. It consists of two converters, i.e. AC–DC–AC converter which is least expensive. This converter consists of the uncontrolled rectifier, and IGBT is used as voltage source inverter. The DC voltage at series converter should remain constant. A PWM inverter is used to give the gate pulse to the series inverter by which it will compare the carrier signal with a reference voltage. Also, a three-phase RLC load is used in order to show its effect in controlling real and reactive power.

5.1 Simulated Results

The model is run with the calculated value of additional power feedback gain one with ignoring the value of gain and other including it; the result clearly distinguished the active power and reactive power profile, and Figs. 7 and 8 show that the power profile is successfully attenuated.

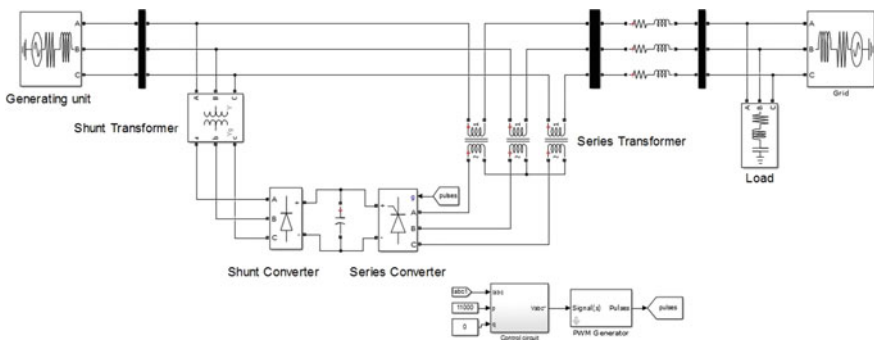


Fig. 6 Proposed UPFC model in MATLAB

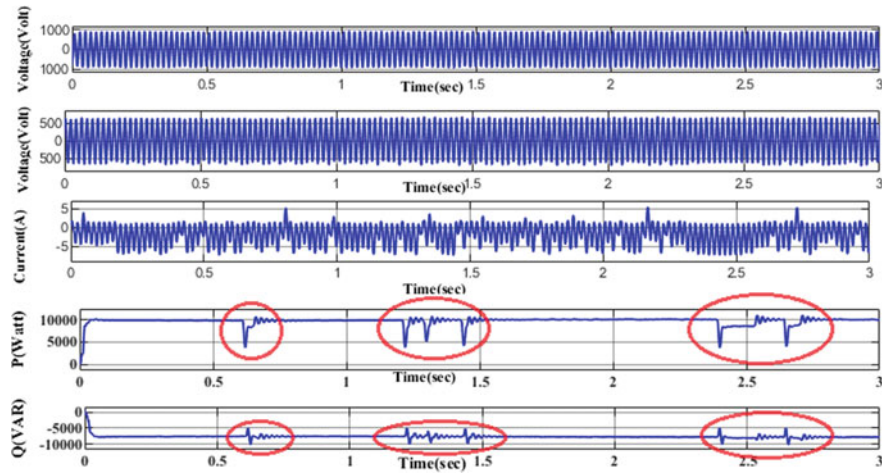


Fig. 7 Simulated waveform without the proposed control scheme with $K_p = K_q = 2.5$ [V/A] $K_r = 0$ [V/A]

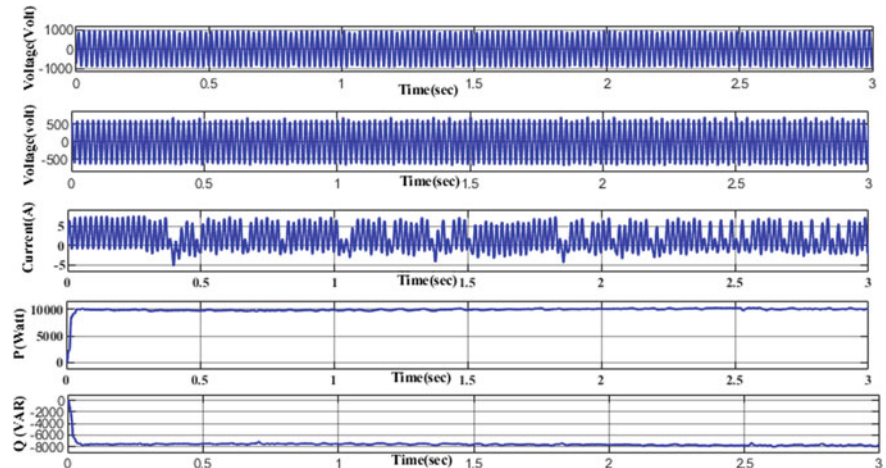


Fig. 8 Simulated waveform when the proposed control scheme is applied with $K_p = K_q = 2.5$ [V/A] $K_r = 4$ [V/A]

6 Parameters Used

Parameters	Ratings
Generating unit	440 V, 50 Hz
Rated power	10 KVA
Line reactance	$R = 0.04 \Omega, L = 1 \text{ mH}$
Shunt transformer ratio	1:1
Series transformer ratio	1:12
<i>Controller parameters</i>	
K_p	2.5 V/A
K_q	2.5 V/A
K_r	4 V/A
RLC load	$P = 5 \text{ kW}, Q_L = 800 \text{ VAR}, Q_c = 15,000 \text{ VAR}$

7 Conclusion

As here, a UPFC model is developed with a new control scheme where a new feedback gain is proposed, K_r . The proposed model is run without the implementation of the value of new power feedback gain K_r , and it has been observed that prominent distortion or fluctuation in the real and reactive power waveform. The value of K_r was calculated and implemented in the same model. After proper inclusion of K_r , it was observed that the unwanted fluctuation in real and reactive power has been reduced tremendously. Hence, the proposed control system gives smooth control of active and reactive power, and the same is tangibly advocated with all output graphs and validates the findings of Hideaki Fujita.

References

1. Gyugyi L (1992) Unified power-flow control concept for flexible AC transmission systems. In: IEE proceedings C (generation, transmission and distribution), vol 139, no 4. IET Digital Library, Jul 1 1992, pp 323–331
2. Yu Q, Round SD, Norum LE, Undeland TM. Dynamic control of a unified power flow controller. In: 27th annual IEEE power electronics specialists conference 1996, pp 508–514
3. Fujita H, Watanabe Y, Akagi H (1999) Control and analysis of a unified power flow controller. IEEE Trans Power Electron 14(6):1021–1027

An Efficient Approach for Barcode Encoding/Decoding Using Pattern Substitution



S. Ieswaria, R. Bhavani, and R. Priya

Abstract The storage of data with reduced space and faster retrieval has always been the main concern in every field. Barcodes ensure faster storage and retrieval of data in a secured form. This paper enlightens the importance of barcodes in every field of today's world and a proposed new barcode generation method with a picture embedded overcoming the traditional methods of storing information. Maintaining details of patient, student, etc., have always been into confusion due to manual maintenance. It would be a revolutionary change in maintaining patients' detail using barcodes in the form of a person's picture avoiding the manual error.

Keywords Barcodes · Picture-embedding · Modulation · Demodulation · Encoding · Decoding

1 Introduction

Manual records maintenance has always been a hectic task; apart from its difficulty in maintaining large amount of information and faster retrieval, it was also prone to unacceptable human error. Medical records include a variety of documentation of the patient's history, clinical findings, diagnostic test results, preoperative care, operation notes, postoperative care and daily notes of a patient's progress and medications. Student database with details is like admission, fees, marks, arrears, and courses.

Barcodes are of two types: (a) one-dimensional(1D) barcodes and (b) two-dimensional(2D) barcodes (quick response (QR) codes and as an extension of QR codes, an additional property of color). The one-dimensional barcodes though being the traditionally used one for a long period, QR codes took over every field since it

S. Ieswaria (✉) · R. Bhavani · R. Priya

Department of Computer Science and Engineering, Annamalai University, Chidambaram, India
e-mail: ieswaria@gmail.com

R. Bhavani
e-mail: bhavaniaucse@gmail.com

R. Priya
e-mail: prykndn@yahoo.com

is seen as an advancement of the former one with the capacity to store more data, requires less space, enabling it to be read from all angles and also with the advantage of including more languages than 1D barcodes such as numeric, alphanumeric, kana(Japanese character), and kanji(Chinese character).

The mapping between the barcodes and the message stores into it is called *symbology*. Barcodes though being classified broadly as 1D and 2D, various barcode symbologies exist like Code39, Code128, Codabar, Postnet, PDF417, Datamatrix, Maxicode, Aztec, and QR code.

Yang et al. [1] proposed an artcode with a dynamic color pallet by error diffusing algorithm and also performed shuffling to embed encoded modules and bits into color. Karthikeyan and Bender [2] introduced the embedding of molecular structures into QR codes by converting them into SMILES and compressing by Lempel–Ziv–Welch (LZW) and automatic chemical structure (ACS) for inventories in pharmaceutical laboratories. Gaikwad et al. [3] discussed embedding the image into barcodes and hiding information into them.

Divya et al. [4] proposed a technique to enhance security with the help of holography to recognize items. van der Westhuizen and Chai [5] introduced the ability to capture dynamic barcodes obtained from frames and produced the highest transmission rate of 622 bytes/s and 1% error for 720p. They have suggested ways in which the work could be extended like fault finding and amendment, live decoding, efficient data ordering, and more colors. Abdehnour et al. [6] combined barcode and radio frequency identification technology. Lee et al. [7] proposed a method to encode voice into binary digits, embedding them into barcode and vice versa achieved the lowest execution time of 18 ms for complex words.

This paper is organized by starting with an introduction to the problem and barcodes in Sect. 1 and followed by brief research works previously done on barcodes in Sect. 2 and proposed image embedded barcode model in Sect. 3. Section 4 provides the experimental results, and Sect. 5 concludes the work.

2 Literature Review

Various researchers have made continuous approaches to overcome the time and space complexity problem that is prevailing in the environment in storage and retrieval of data. The concept of barcodes has gone various domain-specific improvements to suit individual application requirements.

Chen et al. [8] proposed modulation method and demodulation method for Picode, which is a remarkable approach to embed a message into QR codes resembling the picture of the content that the barcode holds, achieving highest average successful detection probability (SDP) of 0.9964 and normalized data capacity (NDC) of 0.959. Chandran et al. [9] enhanced the Picode proposed before by amending the encoding/decoding algorithm with Bose, Chaudhuri, and Hocquenghem (BCH) algorithm, thereby strengthening the security.

Umaria and Jethava [10] discussed increasing the storage capacity of QR code by compressing and multiplexing, thereby producing it in 1 Kb and also providing a hint to extend it to audio and video files. Liu et al. [11] proposed an encoding method using pattern substitution for 2D barcodes. Chen et al. [8] proposed new modulation and demodulation techniques for Picode (picture-embedded barcode) and Vicode (video-embedded barcode).

Chu et al. [12] introduced a new encoding and decoding technique for barcodes that are visually relatable for humans and providing efficiency in terms of reliability and regularization with pattern assignment. Wasule and Metkar [13] proposed an encoding method for generating 2D barcodes in color with a better data capacity of grayscale QR codes to ‘ n ’ fold.

Xu et al. [14] proposed a barcode scanning method based on module scanning probability estimation model for binary, grayscale, and color images. Dinesh and Sharma [15] proposed a framework where three individual barcodes were displayed in R, G, and B channels, thus producing a color barcode with increased storage capacity.

Chen et al. [16] introduced a lightweighted encoding and decoding algorithm for generating color barcodes and also brought forth the importance of barcodes in M-commerce. Gabor Soros et al. [17] introduced a method that located 1D and 2D barcodes on smart phones. Garateguy et al. [18] optimized QR codes with halftoning techniques with multi-scale-structure similarity index measure (MS-SSIM) of 0.5590. Yu Zhang and Tong Lu proposed a model to detect color barcodes with an efficiency of 88.9%.

3 Proposed Method

This section gives the procedure followed in encoding and decoding the picture-embedded barcodes for binary images.

3.1 *Encoding Barcode*

The binary images that are used to encode are set for a uniform size of 126*126. The binary image is divided into equal size blocks. On the other hand, the message data undergoes channel encoding to avoid data loss/corruption. The encoded message along with the image blocks is passed for the modulation technique being proposed. Then finder pattern is applied to the modulated image in case of the binary image, otherwise passed through an intermediary binary to grayscale conversion. The final result giving the picture-embedded barcode. Figure 1 shows the block diagram of the encoding procedure done in this work to produce the picture-embedded barcode when provided with the picture and the message to be encoded.

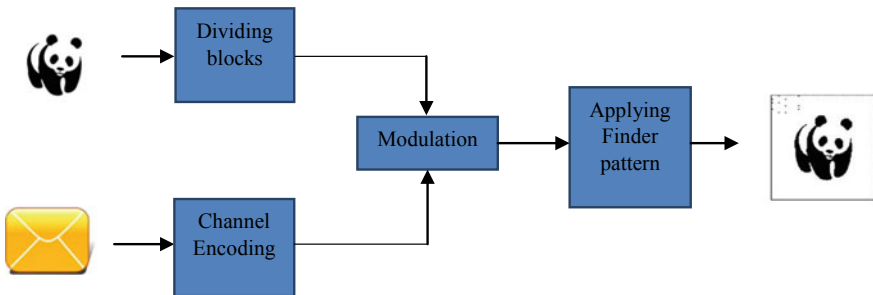


Fig. 1 Block diagram of barcode encoding process

3.1.1 Image Data

The original images are taken in the context from standard image processing picture, real-time personalities, and logo which are divided into blocks of 1×2 for modulation procedure. The message to be encoded undergoes channel coding for error correction. The encoding algorithm used here is Reed–Solomon encoding which is being traditionally used for channel coding [19]. The encoded data stream is then sent for modulation with the image.

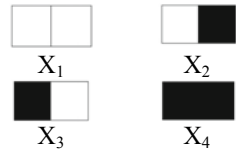
3.1.2 Proposed Modulation Procedure

Figure 2 depicts the procedural steps of the modulation process proposed in this paper. The proposed modulation process acts as the procedure for combining the image and message in a manner controlling visual distortion of the image and protecting the message stored in the barcode. The modulation process undergoes through three steps: pattern counter, pattern assignment, and pattern replacement. The human eye is sensitive to sharp changes; taking account of this, the images are processed in its binary form, and also, the block size is taken as per the intermediary pattern size. As per the block size, 4 patterns are analyzed to be repeated throughout the image, which is defined as X_1, X_2, X_3 , and X_4 . In the *pattern counter* step, the number of times the 4 patterns are being repeated is stored as $n(X_i)$ where, $i = 1, \dots, 4$. The result of the pattern counter gives the pattern enumeration of X_1 to X_4 . Based on this, the *pattern assignment* step assigns the highest repeating pattern as O and the second-highest repeating pattern as Z , in order to maintain the visual responsiveness and followed



Fig. 2 Proposed flow diagram of modulation process

Fig. 3 1*2 patterns defined in the binary image



by which the pattern replacement takes place according to the following:

$$\text{CB} \begin{cases} O, & M_k == 1 \\ Z, & M_k == 0 \end{cases}$$

where

CB represents current block,

M_k represents the k th element in the message data.

Figure 3 depicts the 1*2 block patterns X_1 , X_2 , X_3 , and X_4 that are being repeated throughout the image. The traditional pattern assignment is refined in order to maintain the visual similarity of the original image and the encoded barcode by not completely encoding all the blocks in the image. The encoding method is done by encoding every n th block according to the message bits. Thus, this modulation method acts as the new symbology that maps the encoded data to the message encoded into the barcode.

3.1.3 Barcode Generation

The modulated image is directly sent to the finder pattern generation consisting of the original image as binary. The finder pattern applied for the barcode is as followed in the data matrix, to leave the generated picture-embedded barcode undisturbed. The finder pattern is in the form of 'L'-shaped along the left and down and broken lines or dots along the right and up, acting as the alignment and timing pattern. Thus, the barcode has been generated and MS-SSIM was evaluated.

3.1.4 Barcode Encoding Algorithm

Step 1: Input message x

Step 2: Generate RS code for X

Step 3: Input image I

Step 4: Divide image blocks with block size $1*2$

Step 5: Define 4 patterns and obtain the value from pattern counter

Step 6: Assign, $O = \text{maximum repeated pattern}$

$Z = \text{second maximum repeated pattern}$

Step 7: For alternate blocks, replace current Block, $\text{CB} = \begin{cases} O, & M_k == 1 \\ Z, & M_k == 0 \end{cases}$

Where, M_k is the k th element in encoded message

Step 8: Generate finder pattern

Step 9: Calculate MS-SSIM

3.2 Decoding Barcode

The barcode generated undergoes the proposed demodulation procedure in accordance with the modulation proposed as shown in Fig. 4. The encoded image is extracted from the barcode that consists of potential regions; i.e., the finder pattern and the timing pattern that was applied to the encoded image during barcode generation. The image is then divided into a moving window of size $1*2$ with respect to the modulation procedure.

The demodulation contains the same steps as in the modulation with *pattern counter, pattern assignment, and pattern replacement*. Figure 5 shows the result of pattern counter that computes the number of times each pattern defined being repeated. But the pattern replacement step acts as a reversed process of barcode encoding pattern replacement. The demodulation takes place by pattern counting and assigning the highest and second-highest repeating patterns as O and Z . Here the pattern replacement in order to obtain the encoded message is carried by,

$$\text{Enc} \begin{cases} 1, & \text{CB} == O \\ 0, & \text{CB} == Z \end{cases}$$

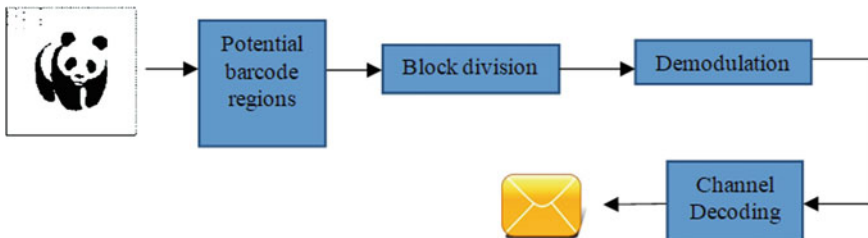
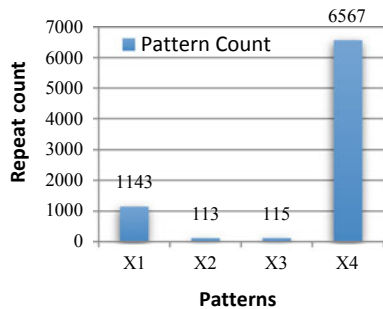


Fig. 4 Block diagram of barcode decoding process

Fig. 5 Result of pattern counter for panda image



where

Enc represents the encoded message.

The decoding also takes place by considering the n th block of the encoded message as it was taken during encoding. The encoded message is then decoded by the Reed–Solomon decoding algorithm giving the message that was encoded into the picture-embedded barcode.

3.2.1 Barcode Decoding Algorithm

Step 1: Input barcode image

Step 2: Remove finder pattern

Step 3: Input image I

Step 4: Divide image blocks of block size $1*2$

Step 5: Define 4 patterns and obtain the value from pattern counter

Step 6: Assign, O=maximum repeated pattern

Z= second maximum repeated pattern

Step 7: For alternate blocks, replace encoded message rsmsg(i,j)= $\begin{cases} 1, & CB == O \\ 0, & CB == Z \end{cases}$

Where, CB is the current block in the barcode image

Step 8: Decode rsmsg and obtain the message

4 Experimental Results

The model was implemented using MATLAB r2016a on Intel corei5 processor-based personal computer with 4 GB RAM. The images taken for encoding were binary with an uniform size of $126*126$ for pattern considered for modulation. The images are divided into a minimum rectangular block size of $1*2$ for which the patterns possible are shown in the figure. The proposed modulation procedure is carried out with the main aim to maintain the similarity to the original image as close as possible and at the same time securing the data encoded into the barcode, which is measured using MS-SSIM.

Figures 6a, 7, 8, and 9a show the original binary images sample taken and Figs. 6b, 7, 8, and 9b show the barcodes obtained for the original images, respectively, with MS-SSIM. Figure 10 compares the resulting MS-SSIM produced by the previous related research works, producing MS-SSIM of 0.46 for Halftone QR, 0.84 for QR image, and 0.49 for Picode with the proposed work which produces a result of 0.99. The proposed model was proved to produce higher MS-SSIM for binary images.

Fig. 6 **a** Original binary image **b** barcode with MS-SSIM = 0.9648



Fig. 7 **a** Original binary image **b** barcode with MS-SSIM = 0.9989

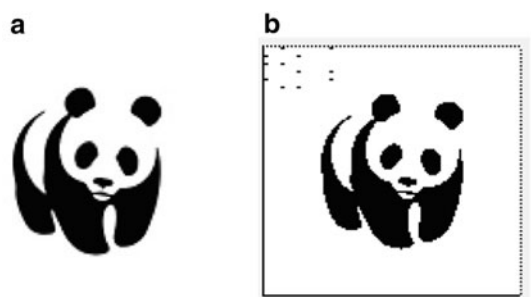


Fig. 8 **a** Original binary image **b** barcode with MS-SSIM = 0.9755

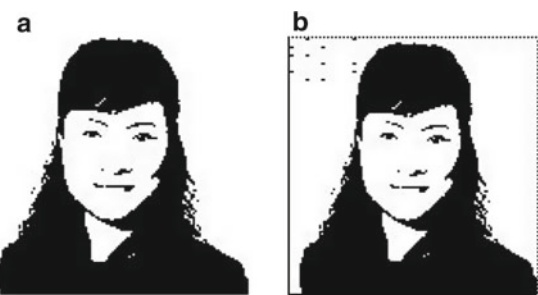


Fig. 9 **a** Original binary image **b** barcode with MS-SSIM = 0.9271

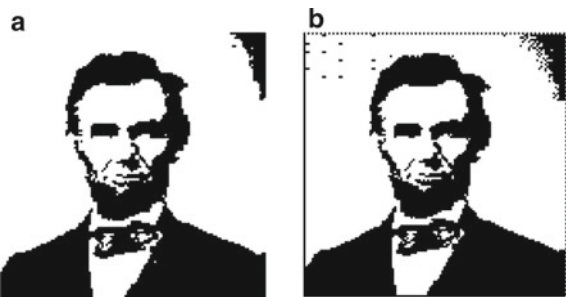
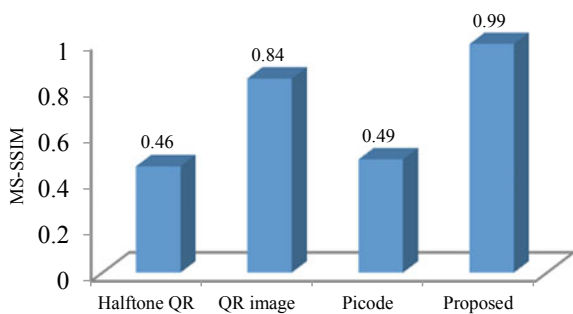


Fig. 10 Comparison results of MS-SSIM of proposed and previous works



5 Conclusion

The binary image was thus embedded with the encoded message through the proposed modulation procedure, and the resulting barcode was proved to produce high MS-SSIM in reference to the original image. The message was successfully decoded using the proposed demodulation procedure from the generated barcodes. Thus, facilitating data retrieval of databases is like medical, student, product, employee in the most efficient manner overcoming all traditional methods and manual errors.

References

1. Yang Z et al (2016) ARTcode : preserve art and code in any image. UBICOMP '16, pp 904–915
2. Karthikeyan M, Bender A (2005) Encoding and decoding graphical chemical structures as two-dimensional (PDF417) barcodes. J Chem Inf Model 45:572–580
3. Gaikwad AM (2015) Halftoning Technique. In: International conference on innovations in information, embedded and communication systems ICIIECS'15, vol 2
4. Divya PS, Sheeja MK (2013) Security with holographic barcodes using computer generated holograms. In: 2013 international conference on control communication and computing. Computers and security, pp 162–166
5. Van Der Westhuizen Y, Chai D (2018) 3D dynamic barcode. Electron Lett 54(17):1024–1026
6. Abdelnour A, Kaddour D, Tedjini S (2018) Transformation of barcode into RFID. IEEE Microw Wirel Compon Lett 28(5):398–400

7. Lee JR, Ruan S, Lin CH (2016) VoiceCode: a 2D barcode system for digital audio encoding. IEEE Glob Conf Consum Electron VoiceCode 5:2–3
8. Chen C, Huang W, Zhang L, Mow WH (2019) Robust and unobtrusive display-to-camera communications via blue channel embedding. IEEE Trans Image Process 28(1):156–169
9. Chandran V, Sekhar A (2017) A secure and reliable channel error correction technique for picode. In: 2017 IEEE international conference on electrical, instrumentation and communication engineering (ICEICE) 2017, pp 1–4
10. Umaria MM, Jethava GB (2015) Enhancing the data storage capacity in QR code using compression algorithm and achieving security and further data storage capacity improvement using multiplexing. In: 2015 international conference on computational intelligence and communication networks, CICN 2015, pp 1094–1096
11. Liu X, Luan R, Huang C (2011) A novel encoding method for visual two-dimensional barcode using pattern substitution. In: 2010 international conference on machine vision and human-machine interface, MVHI 2010, pp 662–665
12. Chu HK, Chang CS, Lee RR, Mitra NJ (2013) Halftone QR codes. ACM Trans Graph 32(6):1–8
13. Wasule S, Metkar S (2017) Improvement in two-dimensional barcode. Sādhanā 42(7):1025–1035
14. Xu M, Li Q, Niu J (2015) ART-UP: a novel method for generating scanning-robust aesthetic QR codes. J Latex Files 14(8):1–14
15. Dinesh K, Sharma G (2016) Per channel color barcodes for displays. IEEE, ICIP, pp 3992–3996
16. Chen B (2013) A lightweight color barcode algorithm and application in mobile E-commerce. Int Conf Comput Sci Educ 8:805–809
17. Soros G (2014) GPU-accelerated joint 1D and 2D barcode localization on smartphones. In: 2014 IEEE international conference on acoustics, speech and signal processing, pp 5095–5099
18. Garateguy GJ, Arce GR, Lau DL, Villarreal OP (2014) QR images: optimized image embedding in QR codes. IEEE Trans Image Process 1:1–11
19. Chen C, Huang W, Zhou B, Liu C, Mow WH (2016) PiCode: a new picture-embedding 2D barcode. IEEE Trans Image Process 25(8):3444–3458

Fabrication and Electrochemical Modeling of CNT-Based BioFET for Cholesterol Detection



Gaurav Keshwani, Kabyashree Hazarika, Hiranya Ranjan Thakur, and Jiten Chandra Dutta

Abstract In this work, a high sensitivity BioFET has been fabricated and modeled for cholesterol detection in serum samples. The device consists of indium tin oxide (ITO) coated glass as substrate, high κ -dielectric ($ZrO_2 \sim 25$) as gate insulator, PEI-doped MWCNT as transporting layer and K/PPy/CNT nanocomposite as sensing membrane. Alkali metal potassium (K) and conducting polypyrrole have been used to enhance the conductivity and dispersion property of the nanocomposite in order to get better response time and detection limit. The layers have been deposited by electrochemical deposition and spin coating technique. The morphology and characteristics of the deposited layers were characterized using Fourier transform infrared spectroscopy (FTIR), field emission scanning microscopy (FESM), scanning electron microscopy (SEM), X-ray diffraction (XRD), and cyclic voltammetry (CV). The modeling has been done using the enzymatic reactions between cholesterol substrate and cholesterol oxidase enzyme, site binding theory, pH dependency of surface potential, and current transport model.

Keywords Cholesterol · BioFET · Cholesterol oxidase · CNT · Modeling

1 Introduction

Cholesterol is an important lipid present in human cells majorly produced in the liver [1]. The level of cholesterol helps in the determination of diseases such as arteriosclerosis, myocardial infarction, hypertension, and coronary heart diseases

G. Keshwani (✉) · K. Hazarika · H. R. Thakur · J. C. Dutta
Tezpur University, Tezpur, Assam 784028, India
e-mail: gauravkeshwani@gmail.com

K. Hazarika
e-mail: kabyashreehazarika609@gmail.com

H. R. Thakur
e-mail: hrtnerist@gmail.com

J. C. Dutta
e-mail: jitend@tezu.ernet.in

[2]. At prescribed level, cholesterol is essential for proper metabolism of body but high concentration of cholesterol in blood serum can be life-threatening. Enzymatic methods offer better selectivity and specificity than analytical methods reported in the literature [3]. Cholesterol oxidase (ChOx) has emerged as an important tool for detection and measurement of cholesterol level in serums [4]. Few enzyme-based biosensors for cholesterol detection have been reported in past few decades but due to shortcomings such as short life span, high power consumption, narrow linear range, and sophisticated fabrication process could not be commercialized [5]. Thus, there is a need for a reliable, sensitive, and inexpensive biosensor for routine monitoring of cholesterol [6].

FET-based biosensors have gained a lot of attention due to its high amplification capability and possibility of ‘on chip fabrication.’ Traditional Si-based FET devices have drawbacks such as low sensitivity, scaling limitation, less carrier mobility, and incompatibility with high- κ dielectrics [7]. These drawbacks can be overcome to a large extent with the use of nanomaterials such as carbon nanotubes (CNT) [8–10]. With the use of nanomaterials, these devices can be used for the detection of enzymatic reactions, proteins, and other micro-molecules [11]. Moreover, CNT has high compatibility with high- κ dielectrics such as zirconia and hafnia which helps in further miniaturization of the device. High- κ dielectrics reduce tunneling current to a large extent even at nanometer thickness which makes it suitable as gate insulator and biosensor applications.

2 Experimental

2.1 Apparatus Used

For electrochemical deposition and layer characterization, AUTOLAB PGSTAT128N has been used. Spin coating has been done using SPIN NXG P28 spin coater. REMI RM centrifuge and SONAPROS PR-1000MP probe sonicator were used for sonication and centrifugation of prepared solutions. The samples were vacuum dried and heated using LABFREEZ vacuum oven.

2.2 Solution Preparation

Multi-walled carbon nanotubes (MWCNTs) with carboxyl group functionalization, zirconium (IV) tetrachloride ($ZrCl_4$), cholesterol oxidase (ChOx) enzyme, polyethylenimine (PEI) with average molecular weight Mn ~5000 g/mol, and polypyrrole (PPy) have been purchased from Sigma-Aldrich. All the other chemicals and reagents used were of analytical grade (Fig. 1).

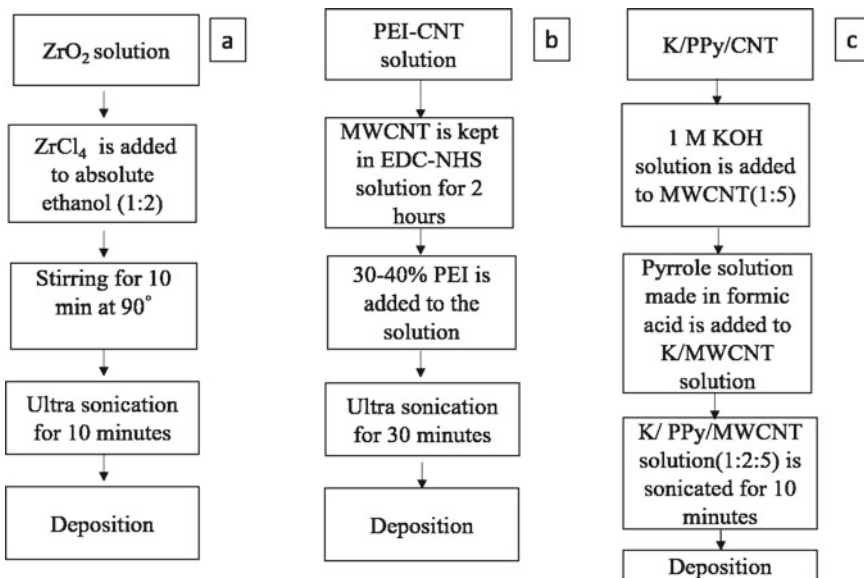


Fig. 1 Solutions for deposition of (a) top gate and bottom gate insulating layer (b) transporting layer (c) sensing layer

2.3 Fabrication

The high- κ dielectric cholesterol BioFET is fabricated on an ITO-coated glass substrate having sheet resistance \sim 50 ohm/cm². The layers have been deposited by solution process. High- κ zirconia layer and PEI-doped CNT channel have been deposited by electrochemical deposition technique using three electrode systems. The three electrode systems consist of Ag/AgCl reference electrode (RE), platinum wire counter-electrode (CE), and the deposition surface as the working electrode (WE). K/PPy/CNT sensing layer is deposited by spin coating technique. The various steps involved in fabrication of the BioFET are shown in Fig. 2. Gravimetric analysis is used to calculate the thickness of deposited layers. ChOx is covalently immobilized on carboxyl group of functionalized CNT by using EDC and NHS as crosslinking activators [5]. The deposited layer is washed using PBS solution to remove unbounded ChOx, dried for 12 h, and kept at temperature as low as 2–4 °C when not in use. The process of covalent immobilization of cholesterol oxidase on functionalized CNT is shown in Fig. 3. K/PPy/CNT layer facilitates the fast transfer of charge between reaction site and the oxide layer.

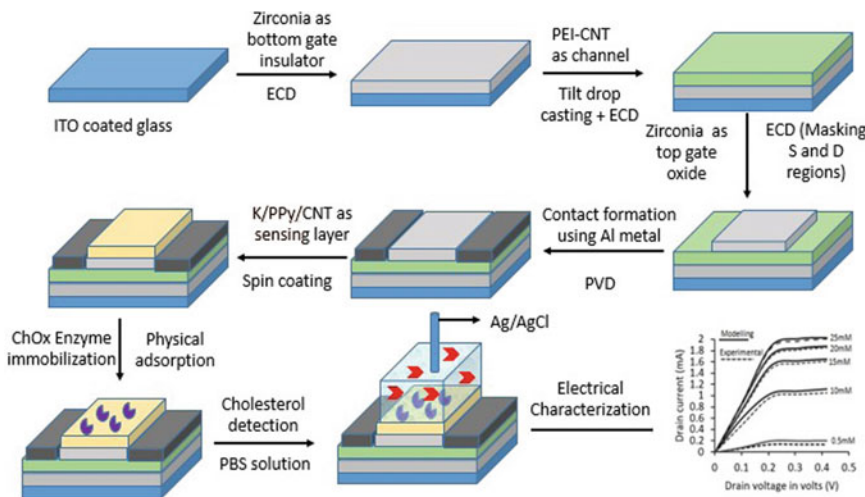


Fig. 2 Steps for fabrication and characterization of cholesterol BioFET

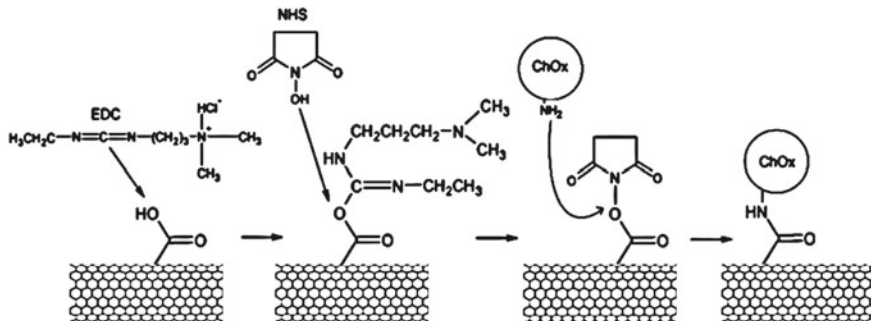


Fig. 3 Covalent immobilization of ChOx on MWCNT

2.4 Results and Discussions

The oxidation and reduction potential of the ceramic and nanocomposite were found out using cyclic voltammetry. Figure 4a, b shows the cyclic voltammetry plots for zirconia (ZrO_2) and PEI-doped CNT layer, respectively. The layers were deposited using chronoamperometric process. Zirconia was deposited keeping working electrode (WE) potential at -1 V (Fig. 4c) and PEI-doped CNT at WE potential at $+0.8\text{ V}$ (Fig. 4d). The deposition time was optimized by trial and error method.

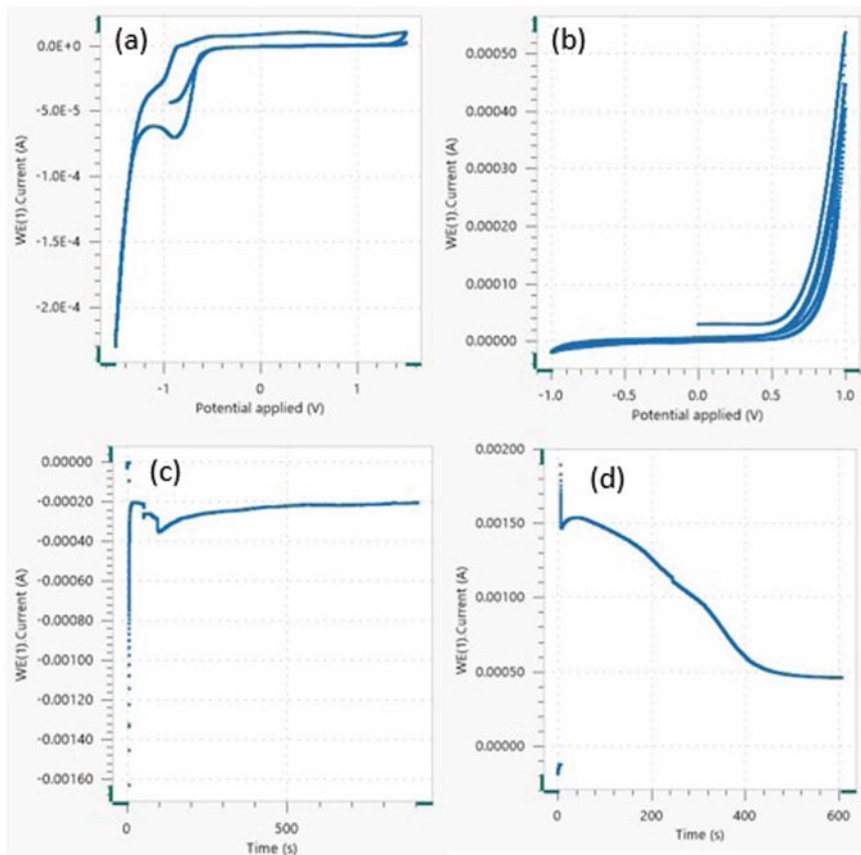


Fig. 4 Autolab waveforms showing (a) cyclic voltammetry of zirconia layer (b) cyclic voltammetry PEI-doped CNT layer (c) chronoamperometry process for deposition of zirconia layer (WE potential = -1 V), (d) chronoamperometry process for deposition of PEI-doped CNT layer (WE potential = 0.8 V)

2.5 Transport Layer Characterization

Fourier transform infrared spectroscopy (FTIR) and scanning electron microscopy (SEM) analysis have been used for chemical characterization of PEI-CNT transport layer. The peaks at 1750 and 3450 cm^{-1} may be attributed to CO and N–H stretching mode [12]. FESM results show uniform deposition but agglomeration can be seen at few sites. The FTIR and FESM results are shown in Fig. 5a, b.

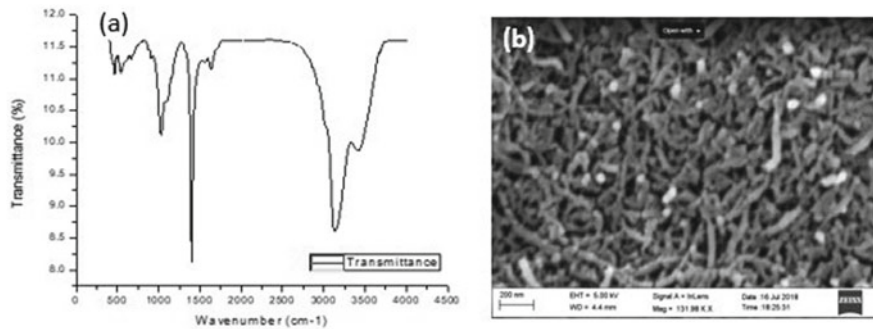


Fig. 5 (a) Fourier transform infrared spectroscopy and (b) field emission scanning microscopy of PEI-doped CNT layer

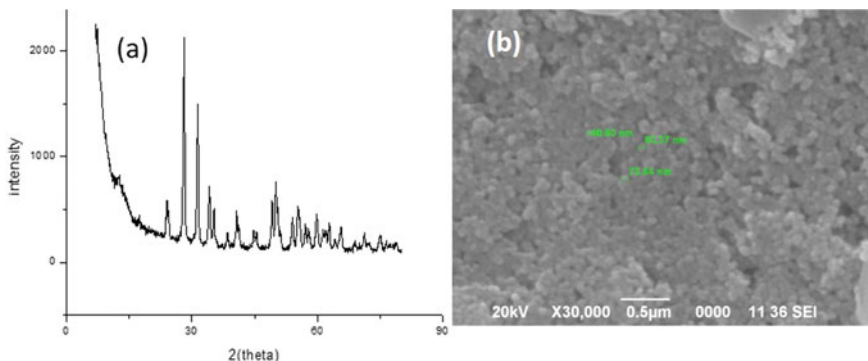


Fig. 6 Characterization of zirconia layer showing (a) XRD results (b) SEM image [13]

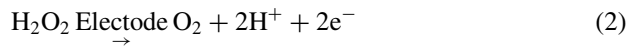
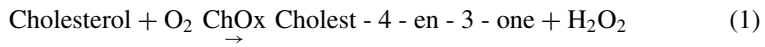
2.6 Oxide Layer Characterization

Scanning electron microscopy (SEM) results of deposited zirconia layer give information about the uniform deposition and fine particle size ranging ~40–90 nm. Peaks at $2\theta = 28^\circ$, 35° , and 50° show deposition of tetragonal phase and peaks at $2\theta = 32^\circ$ and 45° evidences monoclinic phase of zirconia [13]. The patterns are semi-amorphous containing a mixture of *t*-ZrO₂ and *m*-ZrO₂. The XRD and SEM images are shown in Fig. 6a, b.

3 BioFET Modeling

BioFET works on the basic principle of pH variations at the oxide surface of ISFET. The modeling has been done using the acid/base reactions, enzymatic reactions, and

the pH detection properties of ISFET [14]. The enzymatic reactions are shown in Eqs. (1) and (2). The reactions between substrate and enzyme release proton, which alters the surface potential and modulates drain current of the BioFET device.



Michaelis–Menten equation (Eq. 3) is used to model the enzymatic reaction which is responsible for cholesterol oxidation.

$$a = a_M \frac{[S]}{[S] + K_M} \quad (3)$$

Michaelis constant K_M is calculated using Lineweaver–burk plot and found out to be 2.1 mM. $[S]$ is the cholesterol concentration in PBS solution, and a_M is the maximal enzyme activity of ChOx enzyme. The pH value can be obtained by calculating the hydrogen ion concentration released in the solution using Eqs. (2) and (4).

$$\text{pH} = -\log[\text{H}^+] \quad (4)$$

Substrate and product concentration change with time. Decrease in substrate concentration increases the product concentration and the H^+ ion concentration resulting in decrease of pH in the solution. Variation of pH with substrate and product concentration is shown in Fig. 7 (Table 1).

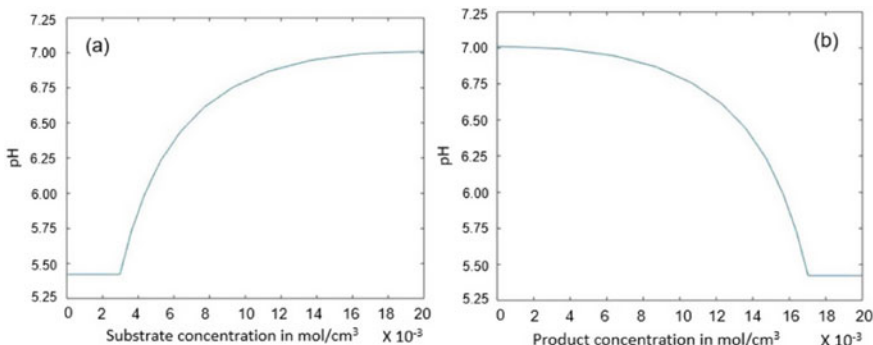


Fig. 7 Variation of pH with (a) substrate concentration, (b) product concentration

Table 1 Values taken for simulation of the device

S. No.	Parameter	Values for modeling
1.	Maximal enzyme activity a_M	16.68×10^{-9}
2.	Michaelis–Menten constant	2.1 mM
3.	Channel length	1 mm
4.	Reference voltage	0.2 V
5.	Acid dissociation constant	2.24×10^{-12}
6.	Substrate concentration	0–20 mM

4 Conclusion

In this work, CNT-based high sensitivity cholesterol BioFET has been fabricated and modeled. The electrochemical modeling of the device is in good agreement with the practical results obtained from electrical characterization of the device. Bonding structure between nanocomposites has been proposed in the paper. The deposited layers have been electrically and chemically characterized. The chemical characterization results of nanocomposite layer and oxide layer are in good agreement with the proposed structure. The thickness of the deposited layers is calculated using gravimetric technique and found to be in nanometer range. The use of carbon nanotubes in nanocomposites resulted in a better adhesion between the layers. FTIR, SEM, FESM, and CV results obtained for ZrO_2 oxide layer and PEI-MWCNT transporting layer validates uniform deposition and proposed structure.

Acknowledgements The authors would like to thank the Deity, MCIT, Government of India, for the support through Visvesvaraya PhD scheme and Tezpur University for providing laboratory facilities.

References

1. Narwal V, Deswal R, Batra B, Kalra V, Hooda R, Sharma M, Rana JS (2019) Cholesterol biosensors: a review. *Steroids* 143:6–17
2. Yıldırımoğlu F, Arslan F, Çete S, Yaşar A (2009) Preparation of a polypyrrole-polyvinylsulphonate composite film biosensor for determination of cholesterol based on entrapment of cholesterol oxidase. *Sensors* 9(8):64356445
3. Ansari AA, Kaushik A, Solanki PR, Malhotra BE (2009) Electrochemical cholesterol sensor based on tin oxide-chitosan nanobiocomposite film. *Electroanalysis Int J Devoted Fundam Pract Aspects Electroanalysis* 21(8):965–972
4. Vrielink A, Ghislia S (2009) Cholesterol oxidase: biochemistry and structural features. *FEBS J* 276(23):6826–6843
5. Keshwani G, Thakur HR, Dutta JC (2019) Fabrication and electrical characterization of carbon nanotube based enzyme field effect transistor for cholesterol detection. In: TENCON 2019–2019 IEEE region 10 conference (TENCON). IEEE, pp 1821–1824

6. Ibupoto ZH, Elhag S, Nur O, Willander M (2014) Fabrication of sensitive potentiometric cholesterol biosensor based on Co₃O₄ interconnected nanowires. *Electroanalysis* 26(9):1928–1934
7. Barik MA, Deka R, Dutta JC (2015) Carbon nanotube-based dual-gated junctionless field-effect transistor for acetylcholine detection. *IEEE Sens J* 16(2):280–286
8. Dutta JC, Thakur HR, Keshwani G (2019) High-performance dual-gate carbon nanotube ion-sensitive field effect transistor with high- κ top gate and low- κ bottom gate dielectrics. *IEEE Sens J* 19(14):5692–5699
9. Salaets N, Ervin M (2009) Solution deposition methods for carbon nanotube field-effect transistors (No. ARL-TR-4854). Army research lab Adelphi MD sensors and electron devices directorate
10. Dürkop T, Getty SA, Cobas E, Fuhrer MS (2004) Extraordinary mobility in semiconducting carbon nanotubes. *Nano Lett* 4(1):35–39
11. Dutta JC, Sharma PK (2018) Fabrication, characterization and electrochemical modeling of CNT based enzyme field effect acetylcholine biosensor. *IEEE Sens J* 18(8):3090–3097
12. Dutta JC, Thakur HR, Keshwani G (2019) High performance dual-gate carbon nanotube ion-sensitive field effect transistor with high- κ top gate and low- κ bottom gate dielectrics. *IEEE Sens J*
13. Keshwani G, Thakur HR, Dutta JC Characterization of thin zirconia films deposited by ECD on ITO coated glass for biosensing applications. In 6th international conference on signal processing and integrated networks, Amity University, Noida, Uttar Pradesh
14. Sharma PK, Dutta JC, Barik MA, Sarma MK (2017) Numerical modeling of potassium-doped polypyrrole/carbon nanotube graphene-based cholesterol enzyme field effect transistor. *Int J Numer Model Electron Netw Devices Fields* 30(6):e2223

Design of LCL Filter for SPWM Inverter Based on Switching Frequency and THD Criterion



T. Saha, A. Mitra, and B. Halder

Abstract Over the time, power generation from renewable energy sources and its grid integration is being increased rapidly. Subsequently, the quality of power has been degraded because of injected harmonic contents to the grid from large number of power electronic devices required for inverter applications. An optimized LCL filter can improve the quality of power for single-phase inverter connected with the utility. This perspective motivates the authors to design an LCL filter with optimum performance under the constraint of least switching frequency variation, total harmonic distortion (THD), size of the inductors, and power factor of the grid current. All the results have been obtained through MATLAB/Simulink environment in justification with the optimum satisfactory design.

Keywords SPWM inverter · LCL filter · Switching frequency · THD

1 Introduction

The upward global energy demand as well as saving the consumptions of fossil fuels is manipulating to drive renewable energy sources to meet the energy demand. Among them, the use of solar photovoltaic (PV) energy is most popular because of its several advantages. The energy is available in the form of DC source and requires converting through an inverter of suitable power rating as per demand by the consumers. Also due to non-sinusoidal AC output from the inverter, proper design of filter circuit is highly essential to make it sinusoidal to avoid unnecessary energy loss of the domestic appliances. On the other hand, when the PV inverter system is integrated with grid, the filter will provide a better power quality.

T. Saha · A. Mitra (✉) · B. Halder

Department of Electrical Engineering, Narula Institute of Technology, Kolkata, India

e-mail: arkendu.mitra@nit.ac.in

T. Saha

e-mail: tarinmoysaha07@gmail.com

B. Halder

e-mail: halder.biswajit@nit.ac.in

To lower the total harmonic distortion (THD) of the inverter current, LCL filter is most popular nowadays in comparison with L filter and LC filter [1]. Proper selection of the values of inductor and capacitor for an LCL filter is an important criterion for the betterment of inverter output current and grid current to maintain improved quality of power fed to the grid [2, 3]. The magnitude of current as well as active and reactive power of the inverter can be controlled through a closed-loop controller in comparison with a reference signal [4–6], where the THD of the current cannot be controlled without LCL filter. In the presence of the passive components of the filter, a small resistance is to be inserted in series with the filter capacitance for proper damping of the filter. Moreover, due to power losses caused by the passive elements of the filter, the introduction of active damping in the circuit is much preferable [7].

The THD can be controlled directly from the inverter through proper switching topology at higher switching frequency. The sinusoidal pulse width modulation (SPWM) and hysteresis band control technique can be a solution to lower the THD [8, 9].

In addition to this, the size of the filter will be lowered, but the switches of the inverter will experience high switching stress and high switching loss accordingly. Though this can be reduced by applying soft-switching technique, the circuit overall switching circuit will be more complicated. This proposed work makes a compromise between the switching frequency of the inverter and the size of the LCL filter with THD of the grid current.

2 Single-Phase SPWM Inverter

Among different switching topologies of inverters, sinusoidal pulse width modulation (SPWM) methodology is widely used because of its several advantages and low level of harmonic contents at its output. The output voltage from the inverter can be controlled by varying modulation index which is defined as the ratio between the peak of the modulating signal and carrier signal, and therefore,

$$m_a = \frac{\hat{v}_{\sin}}{\hat{v}_{\text{tri}}}, \quad (1)$$

where \hat{v}_{\sin} and \hat{v}_{tri} are the peak value of modulating sine wave and the peak value of carrier triangular wave, respectively. Since output voltage of the inverter is defined by the peak value of the modulating signal, the fundamental voltage from the inverter will accordingly be

$$V_{i_1} = \frac{m_a V_{\text{dc}}}{\sqrt{2}} \quad (2)$$

Figure 1 shows the development of the SPWM signal through the comparison of a sinusoidal signal with a triangular signal. Figure 2 is the enlarged view of a section

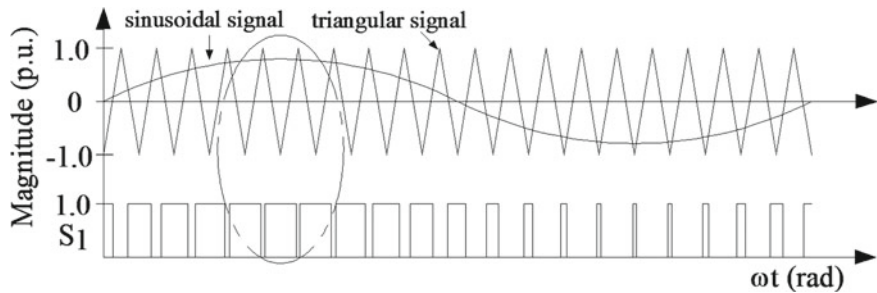
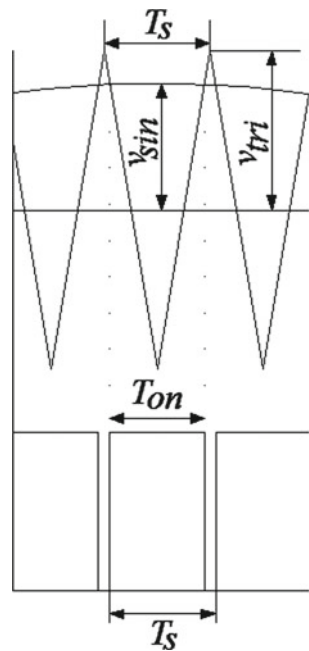


Fig. 1 Development of SPWM signal

Fig. 2 Enlarged view of sine-triangle comparison



of Fig. 2 to understand the relationship between the duty ratio and the modulation index.

3 LCL Filter Modeling

In general, the output of the inverter is not a sinusoidal and contains several harmonics. Figure 4 shows the circuit diagram of the LCL filter, which can be governed by the following equations

$$L_i \frac{di_i}{dt} = v_i - v_c - (R_i + R_f)i_i + R_f i_g \quad (3)$$

$$L_g \frac{di_g}{dt} = v_c - v_g + R_f i_i - (R_f + R_g)i_g \quad (4)$$

$$\frac{dv_c}{dt} = \frac{i_i - i_g}{C_f} \quad (5)$$

where v_i is the inverter-side AC voltage, v_g is the grid-side AC voltage, v_c is the voltage across capacitor, R_i is the internal resistance of the inverter-side inductor L_i , R_g is the internal resistance of the inverter-side inductor L_g , C_f is the filter capacitance, and R_f is the damping resistance.

The state matrix of the filter can be expressed as

$$\begin{bmatrix} \frac{di_i}{dt} \\ \frac{di_g}{dt} \\ \frac{dv_c}{dt} \end{bmatrix} = \begin{bmatrix} -\frac{R_i+R_f}{L_i} & \frac{R_f}{L_i} & -\frac{1}{L_i} \\ \frac{R_f}{L_g} & -\frac{R_f+R_g}{L_g} & \frac{1}{L_g} \\ \frac{1}{C_f} & -\frac{1}{C_f} & 0 \end{bmatrix} \begin{bmatrix} i_i \\ i_g \\ v_c \end{bmatrix} + \begin{bmatrix} \frac{1}{L_i} & 0 \\ 0 & -\frac{1}{L_g} \\ 0 & 0 \end{bmatrix} \begin{bmatrix} v_i \\ v_g \end{bmatrix} \quad (6)$$

which is expressed as $\dot{x} = Ax + Bu$. The transfer function of the filter circuit can be obtained by the following equation.

$$\frac{i_g}{v_i} = C[sI - A]^{-1}B \quad (7)$$

where

$$A = \begin{bmatrix} -\frac{R_i+R_f}{L_i} & \frac{R_f}{L_i} & -\frac{1}{L_i} \\ \frac{R_f}{L_g} & -\frac{R_f+R_g}{L_g} & \frac{1}{L_g} \\ \frac{1}{C_f} & -\frac{1}{C_f} & 0 \end{bmatrix}; B = \begin{bmatrix} \frac{1}{L_i} & 0 \\ 0 & -\frac{1}{L_g} \\ 0 & 0 \end{bmatrix} \text{ and } C = [0 \ 1 \ 0]$$

Neglecting the value of the internal resistance of the inductors, i.e., considering $R_i = R_g = 0$, the transfer function of the system can be written as

$$\frac{i_g}{v_i} = \frac{R_f C_f s + 1}{s[L_i L_g C_f s^2 + R_f C_f (L_i + L_g)s + (L_i + L_g)]} \quad (8)$$

The characteristic equation of Eq. (10) is written as

$$s^2 + R_f \left(\frac{1}{L_i} + \frac{1}{L_g} \right) s + \frac{1}{C_f} \left(\frac{1}{L_i} + \frac{1}{L_g} \right) = 0 \quad (9)$$

Comparing the equation with $s^2 + 2\xi\omega_n s + \omega_n^2 = 0$, the damping ratio can be estimated as

$$\xi = \frac{1}{2} R_f \sqrt{C_f \left(\frac{1}{L_i} + \frac{1}{L_g} \right)} \quad (10)$$

4 Design of Filter

To design LCL filter, several characteristics of the filter have to be considered, such as, current ripple, switching ripple attenuation, size of the filter, etc. The damping factor of an LCL filter is an essential criteria, and thus, a passive damping must be included by inserting a resistance in series with the capacitance as indicated in Eq. (10).

The parameters required to design the filter circuit are the DC link voltage V_{dc} , fundamental voltage output of the inverter V_{i_1} , rated active power P_n , switching frequency f_s , resonant frequency f_r , and grid frequency f_g .

The base impedance and the base capacitance are defined by the following equations.

$$Z_B = \frac{V_{i_1}^2}{P_n} \quad (11)$$

and

$$C_B = \frac{1}{\omega_g Z_B} \quad (12)$$

The filter capacitor is to be designed considering maximum variation of power factor at the grid side which is 5%, resulting the value of the filter capacitance will be $C_f = 0.05C_B$. If required the value of the filter capacitance may be considered higher than 5% of the base capacitance in order to compensate the inductive reactance of the filter.

The ripple current of the inverter-side inductor Δi_i can be estimated as

$$V_{dc} - V_o = L_i \frac{\Delta i_i}{DT_s} \quad (13)$$

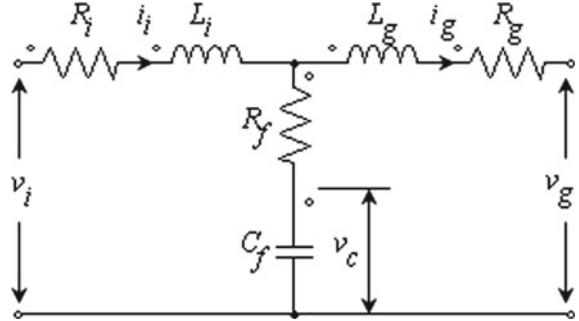
or,

$$\Delta i_i = \frac{D \times (V_{dc} - V_o)}{L_i \times f_s}$$

or,

$$\Delta i_i = \frac{D(1-D)V_{dc}}{L_i f_s} \quad (14)$$

Fig. 3 LCL filter circuit diagram



where V_o is the grid-side voltage referred to the DC side and is simply can be considered as DV_{dc} . Since the output voltage waveform of the inverter is the reflection of the duty cycle varied sinusoidally as shown in Figs. 2 and 3, the ripple current can be referred to the AC side can be written using Eq. (14) as

$$\Delta i_i = \frac{m_a(1 - m_a)V_{dc}}{L_i f_s} \quad (15)$$

It is evident from Eq. (15), that the maximum ripple current will occur at $D = 0.5$ and the value can be estimated as

$$\Delta i_{i\max} = \frac{V_{dc}}{4L_i f_s} \quad (16)$$

or,

$$L_i = \frac{V_{dc}}{4f_s \Delta i_{i\max}} \quad (16)$$

Most of the cases, the grid-side inductor is designed considering 20% of the inductor value connected at the inverter side. This will provide better attenuation particular at the frequency above 50th harmonic and can be calculated as

$$L_g = 0.2L_i \quad (17)$$

The natural frequency of oscillation can easily be estimated from Eq. (9) as follows

$$\omega_n = \sqrt{\frac{L_i + L_g}{L_i L_g C_f}} \quad (18)$$

From Eqs. (10) and (18), the damping resistance R_f can be calculated simply by considering the damping ratio $\xi = 0.5$, which gives

$$R_f = \frac{1}{\omega_r C_f} \quad (19)$$

Also, the active power and the reactive power flow through the inductor due to the fundamental component of the inverter current can be expressed as

$$P_i = \frac{V_{i_1} V_g}{x} \sin \delta \quad (20)$$

and,

$$Q_i = \frac{V_{i_1}}{x} (V_{i_1} - V_g \cos \delta) \quad (21)$$

where δ is the angle between the fundamental component of inverter output voltage and the grid voltage and x is the series inductive reactance of the filter equal to $L_i + L_g$.

5 System Specifications and Performance Analysis

The specifications of the proposed system are as follows:

DC bus voltage $V_{dc} = 100$ V

Fundamental voltage output from inverter $V_{i_1} = 50$ V

Active power output of the inverter $P_n = 200$ W

The modulation index from the output voltage from the inverter can be calculated as

$$m_a = \frac{\sqrt{2} V_{i_1}}{V_{dc}} = 0.707$$

The fundamental output current from the inverter

$$I_{i_1} = \frac{P_n}{V_{i_1}} = \frac{200}{50} = 4 \text{ A}$$

Allowing 5% ripple current of the peak value of the fundamental current of the inverter, $\Delta i_{i,\max} = 0.28$ A. Switching frequency of the inverter is studied to find a suitable design of inductors for LCL filter. Also, variation of THD and acceptable power factor has been taken into consideration for this work. The performance of the proposed LCL filter with respect to switching frequency, THD, and power factor has been given in Table 1.

Although switching frequency is appearing in Table 1 as integer multiple of 1 kHz, an incremental frequency of 125 Hz has been studied for the whole range. At lower switching frequency with a fixed percentage of ripple current, the size of inductors is

Table 1 Design criterion of LCL filter

Switching frequency (kHz)	Inverter-side inductance (mH)	Grid-side inductance (mH)	Filter bandwidth (kHz)	THD (%)	Power factor
3	29.46	5.89	0.81	0.09	0.93
4	22.1	4.42	0.93	0.08	0.97
5	17.68	3.54	1.05	0.13	0.98
6	14.73	2.95	1.15	0.19	0.99
7	12.63	2.53	1.24	0.38	0.99
8	11.05	2.21	1.32	0.18	0.99
9	9.82	1.96	1.4	0.21	0.99
10	8.84	1.77	1.48	0.21	0.99
11	8.04	1.61	1.55	0.36	1.00
12	7.37	1.47	1.62	0.43	1.00
13	6.8	1.36	1.69	0.33	1.00
14	6.31	1.26	1.75	0.36	1.00
15	5.89	1.18	1.81	0.43	1.00
16	5.53	1.1	1.87	0.37	1.00

so high that it may result in $\sin \delta > 1$, which is infeasible design. In this point of view, the minimum switching frequency has been considered to be 3 kHz, which causes a power factor of 0.93 and with significantly large inverter-side inductor of 29.46 mH. It is evident from Table 1, at the switching frequency of 4 kHz, the corresponding THD level is found significantly low along with the acceptable level of power factor of 0.97 and the required inverter-side inductor size of 22.1 mH. On the other hand, at higher switching frequencies greater than 4 kHz, significant improvement of THD level has not been found, although inductor sizing and the power factor remain in the acceptable level. However, due to an increase in the switching frequency, the switching losses of the inverter will increase accordingly and all the power electronic switches of the inverter will experience a high switching stress and may damage if proper snubber protection is not associated with the switches. Thus, the bolded part of Table 1 is showing the optimum design parameters for the LCL filter the switching frequency of 4 kHz.

To find out the value of the filter capacitor, base impedance and base capacitance are required to be calculated using Eqs. (11) and (12). From the above data, the value of base impedance will be $Z_B = 12.5$ ohm and the value of base capacitance will be $C_B = 255 \mu\text{F}$. Since the value of the filter capacitance will be considered as 5% of the base capacitance, $C_f = 12.7 \mu\text{F}$. Also from Eq. (19), the value of the damping resistance will be $R_f = 17.01$ ohm.

If the switching frequency of the inverter switches is considered as $f_s = 4$ kHz, from Eq. (16), the value of the inverter-side inductor will be $L_i = 22.1$ mH and from Eq. (17), the value of the inductor connected at the grid side will be $L_g = 4.42$ mH.

From Eq. (18), the resonant frequency of the system will be $f_n = 735$ Hz, which maintains the criteria $10f_g \leq f_n \leq \frac{1}{2}f_{sw}$ to avoid the resonant condition of the LCL filter, where f_g is the grid frequency.

From Eqs. (20) and (21), $\delta = 41.8^\circ$ and the reactive power flow from the inverter to the grid will be $Q_i = 76.36$ VAr.

For a ripple current of 5%, the variation of inverter-side and grid-side inductors with respect to the switching frequency is shown in Fig. 4. Also the variation of frequency bandwidth of the filter, THD and power factor are shown in Fig. 5 accordingly. Figures 6, 7, and 8 represent THD of the inverter current, frequency response of the LCL filter and THD of the grid current, respectively. Figure 9 shows the output voltage of the inverter and the inverter output current, filter capacitor current and the grid current are shown in Figs. 10, 11, and 12, respectively.

Fig. 4 Variation of inductance with respect to switching frequency

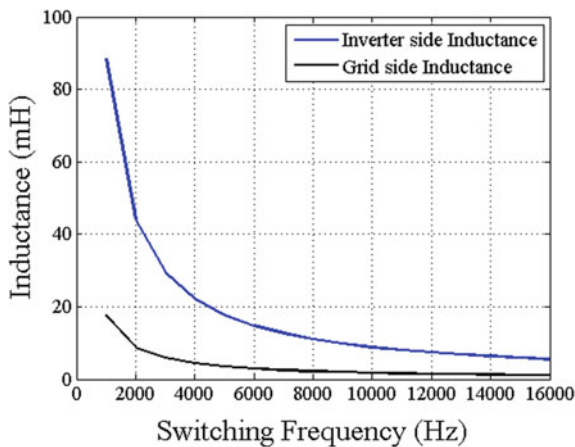
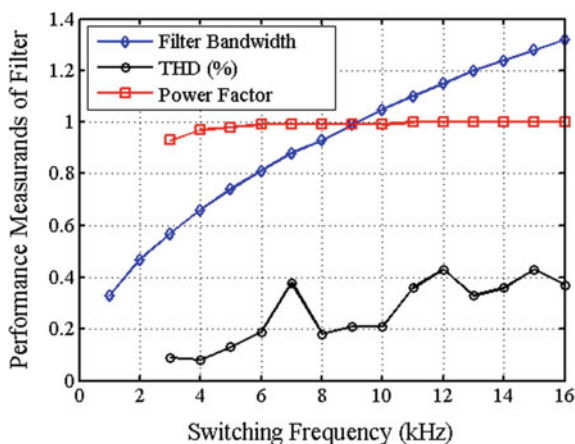


Fig. 5 Variation of frequency bandwidth, %THD and pf w.r.t. switching frequency



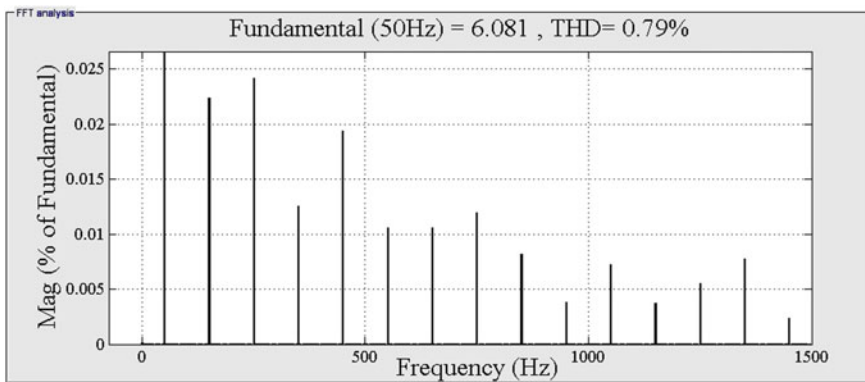


Fig. 6 THD of the inverter current

Fig. 7 Frequency response of LCL filter

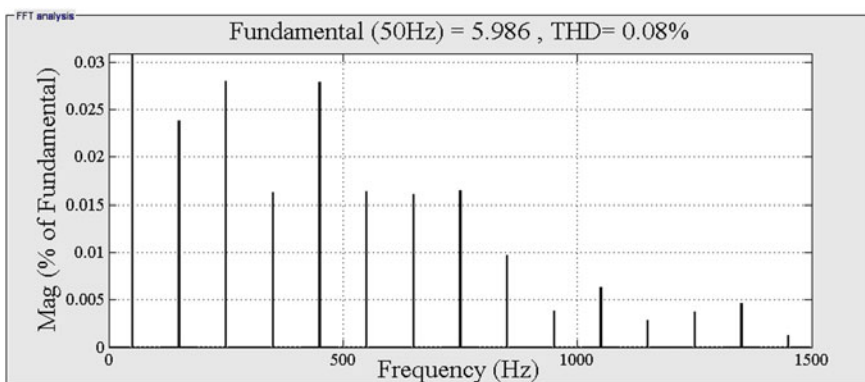
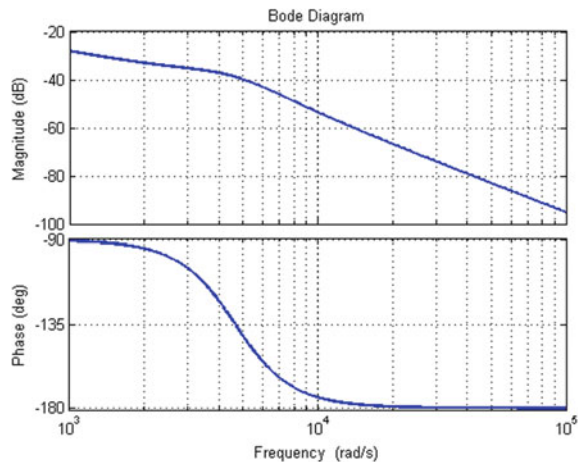


Fig. 8 THD of the grid current

Fig. 9 Inverter output voltage

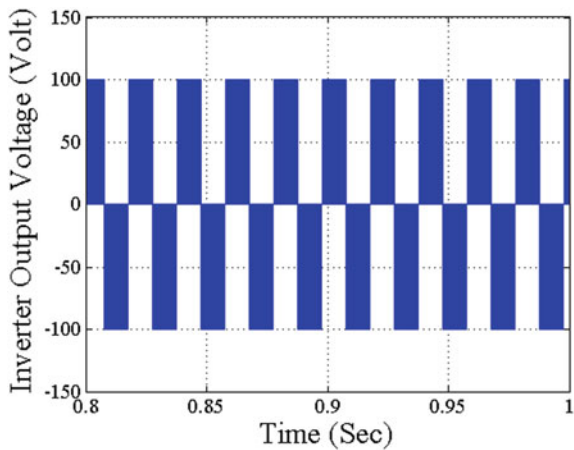
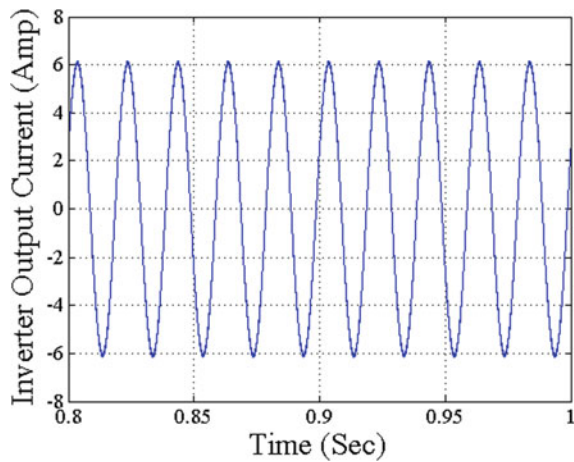
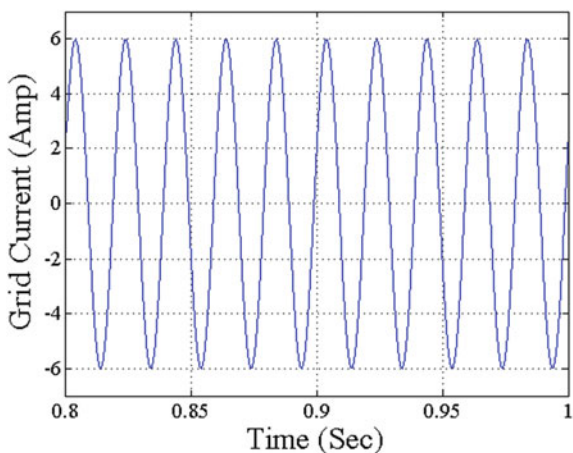
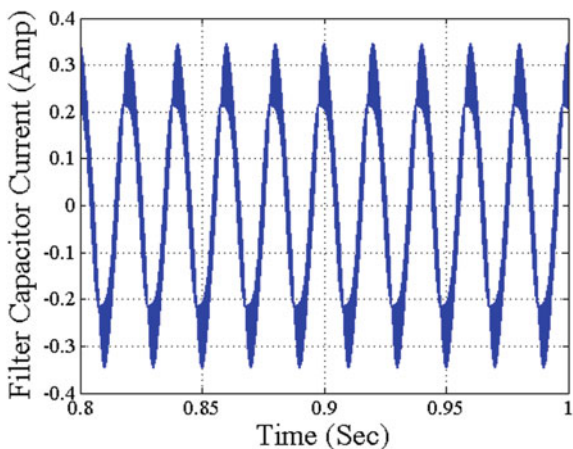


Fig. 10 Inverter output current



6 Conclusion

The proposed work shows that the choice of switching frequency at 4 kHz results in an inductor size of 22.1 mH at the inverter side and 4.42 mH at the grid side corresponding to a reduction of THD in the grid current of 89%. The designed filter also satisfies the choice of resonant frequency criteria. In this work, the minimization of the switching frequency of the inverter has been emphasized, which is unique in comparison with other research works in this area. In view of increase in single-phase quality power generation from renewable sources, the proposed work has high level of acceptability because of its cost-effectiveness and simplicity. In future, this performance will be experimentally validated through the implementation of single-phase grid-connected renewable power generation.

Fig. 11 Grid current**Fig. 12** Filter capacitor current

References

1. Hanju C, Vu TK (2010) Comparative analysis of low-pass output filter for single-phase grid-connected photovoltaic inverter. In: 25th annual IEEE applied power electronics conference and exposition (APEC), pp 1659–1665
2. Sedo J, Kascak S (2016) Control of single-phase grid connected inverter system. In: IEEE ELEKTRO, pp 207–212
3. Cossoli P, Cáceres M, Vera L, Firman A, Busso A (2018) Proportional-resonant controller and LCL filter design for single-phase grid-connected PV micro-inverters. In: IEEE PES transmission and distribution conference and exhibition
4. Liu X, Ma P, He G, Wang D (2018) Study on control strategy of LCL type single-phase grid-connected inverter. In: 3rd international conference on mechanical, control and computer engineering (ICMCCE), pp 37–42
5. Tang H, Zhao R, Tang S, Zeng Z (2012) Linear quadratic optimal control of a single-phase grid-connected inverter with an LCL filter. IEEE Int Symp Indus Electron, pp 372–376

6. Li X, Balog RS (2015) PLL-less robust active and reactive power controller for single phase grid-connected inverter with LCL filter. In: IEEE applied power electronics conference and exposition (APEC), pp 2154–2159
7. Cai P, Wu X, Yang Y, Yao W, Liu W, Blaabjerg F (2018) Design of digital filter-based highly robust active damping for LCL-filtered grid-tied inverters. In: IEEE 4th southern power electronics conference (SPEC)
8. Maghraby M, Ashour HA, Hossam-Eldin AA (2017) Analysis and implementation of discrete SPWM signals for grid-connected inverter with LCL filter. In: 9th international middle east power systems conference (MEPCON), pp 515–520
9. Sudhakar B, Satish Kumar GVS (2016) A unipolar fixed hysteresis band based sliding mode control of single phase grid connected LCL filtered voltage source inverter. In: IEEE international conference on power electronics, drives and energy systems (PEDES)

Level Control of Hopper Tank Process Using Model-Based Controller



V. Murugananthan, M. Valluvan, and G. Sakthivel

Abstract In industries, many processes are nonlinear, in-order to understand and analyze the process, linearization step is involved. The nonlinear process taken is Hopper tank process. This paper highly concentrates on level control of Hopper tank process. Conventional PID, internal model controller, modified internal model controller are developed and tested in MATLAB simulation environment. Time domain and error criterion analysis are done and better performances are highlighted.

Keywords Conventional PID · Internal model controller (IMC) · Modified internal model controller (MIMC) · Internal model control based PID(IMC-PID) · First-order plus dead time (FOPD)

1 Introduction

Nonlinear process tanks like conical tank process, Spherical tank Process, and continuously stirred tank process are highly in application of many process industries. The above-mentioned processes are nonlinear because they never follow linearization principle and superposition principle, in particular all the above-mentioned tank processes area is not fixed, i.e., radius of the tank has been varied at each and every level, thus area is also variable. Because of the above-mentioned reasons, those tanks are nonlinear in nature.

Hopper tank process is nonlinear in nature, this is because it never follows linearization and superposition principle, in its physical structure, it has cylindrical tank, which is mounted on a conical tank bottom. This kind of tank processes

V. Murugananthan (✉) · M. Valluvan · G. Sakthivel

Department of Electronics and Instrumentation Engineering, Faculty of Engineering and Technology, Annamalai University, Annamalainagar, Chidambaram 608002, India
e-mail: murugananthanva@gmail.com

M. Valluvan
e-mail: varunvalluvan@gmail.com

G. Sakthivel
e-mail: gsauei@gmail.com

are highly in use of petrochemical industries, pharmaceutical industries, and food processing industries. Those industries use this tank setup because it can store large amount of feed and at the same time, higher advantages of evacuation sludge material [1]. While coming to offline analysis, FOPD transfer function is taken into account.

Many research papers are available for spherical tank, conical tank and cylindrical tank process. But very limited articles are available for hopper tank process. Suresh et al. [1] studied this tank system and developed FOPD models for different levels and designed conventional PID using different tuning techniques, IMC-PID, then he compared time domain performance indices and suggested better tuning technique. Vinothkumar [2] applied Ziegler Nicholas and Cohen Coon tuning techniques for the linearized model, which are developed by Kesaven [1]. Wang [3] numerical model technique for hopper tank, then the results of pressure and flow dynamics are compared. Wang [4] developed discrete model for hopper tank by using discrete element method and finite element method and compared the results of pressure and flow pattern. Dinesh Kumar and Meenakshi Priya [5] took two spherical tank process and implemented gain schedule PID controller, Arasu et al. [6] took conical tank process and implemented model-based nonlinear controller.

1.1 Work Flow

The main objective of this paper is to implement basic model-based linear controllers IMC and MIMC, because in many papers, conventional controllers based on different tuning techniques are implemented for hopper tank process while compared with basic model-based linear controllers. The overall work of this paper is shown in Fig. 1

2 Hopper Tank Modelling

Any process can be model by means of three methods; they are

- i. Black box modelling
- ii. Gray box modelling
- iii. White box modelling.

White box modelling is applicable only if all process parameters are known. If partial process parameters are known means gray box modelling is applicable. Completely the process parameters are unknown means black box modelling can be applied. Here, black box modelling technique is applied.

The geometrical diagram of Hopper tank process is shown in Fig. 2 and the tank parameters [1] are

Overall height of the tank H is 100 cm.

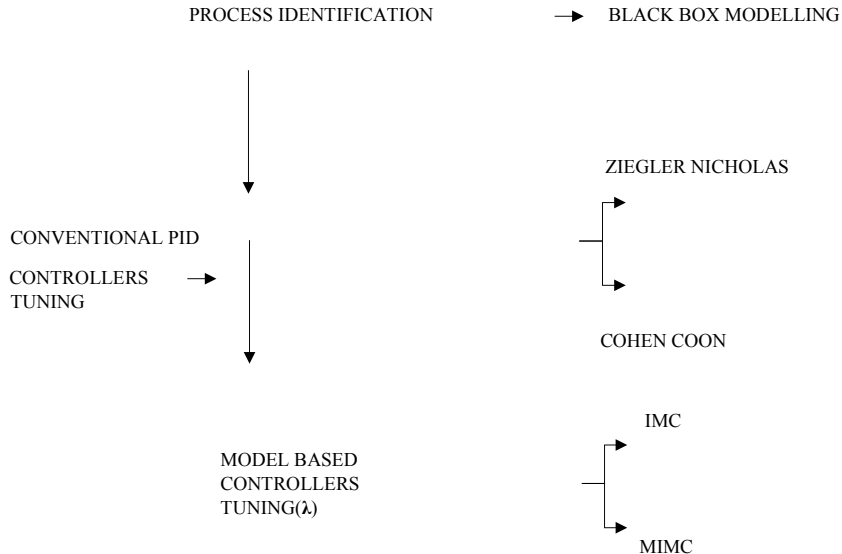


Fig. 1 Work flow diagram

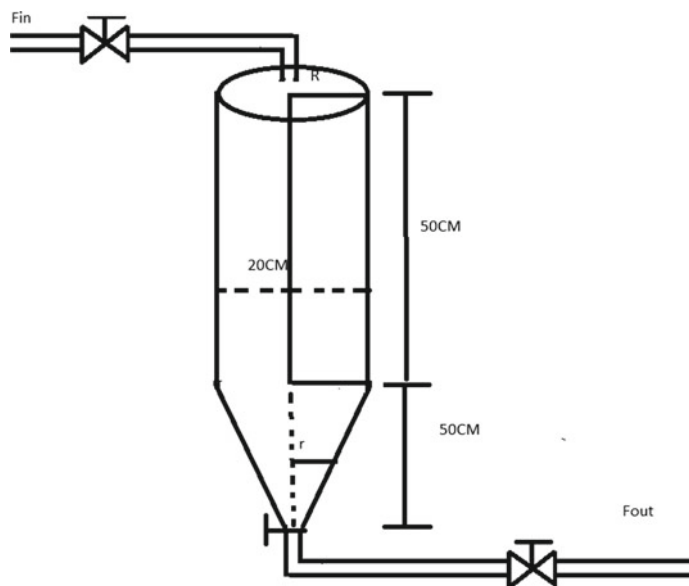


Fig. 2 Hopper tank process

Variable height h .

Top radius of cone and radius of cylinder R Diameter of cylinder is 20 cm.

Variable radius of cone is r .

F_{in} inflow rate.

F_{out} outflow rate.

Valve co-efficient is β .

Volume v .

Area A .

Based on the parameters taken [1], the mass balance equation of the process is

$$\frac{dv}{dt} = F_{\text{in}} - F_{\text{out}} \quad (1)$$

$$A \frac{dh}{dt} = F_{\text{in}} - \beta \sqrt{h} \quad (2)$$

The generalized FOPD transfer function model which relates input F_{in} and h variable height h is

$$G_p(s) = h(s)/F_{\text{in}}(s) = \frac{ke^{-\theta s}}{\tau s + 1} \quad (3)$$

By solving the mass balance Eqs. (1) and (2), then substitute the process parameters, the FOPD model for level step change 0–15 cm is [1],

$$G_p(s) = h(s)/F_{\text{in}}(s) = \frac{2.7e^{-0.15s}}{(0.75s + 1)} \quad (4)$$

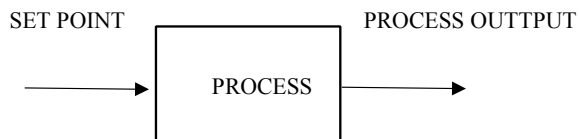
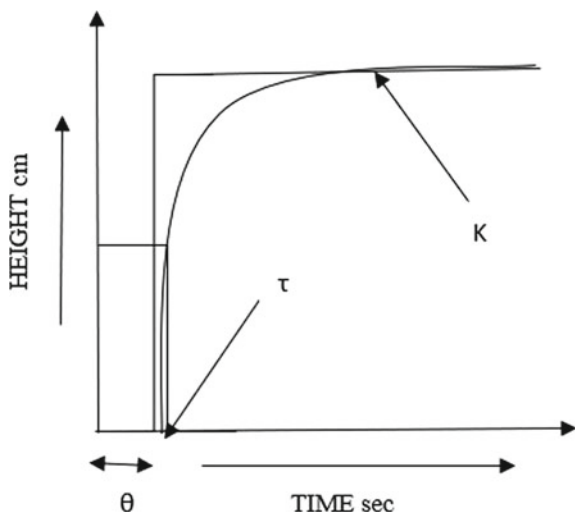
3 Controller Design

Three types of controllers are developed for obtained process model of setpoint change 0–15 cm; they are conventional PID, IMC, MIMC, and IMC-PID.

3.1 PID Controller

The PID controller parameters are obtained by reaction curve method, i.e., by getting open-loop response of the model, the tuning parameters are identified. In PID controller, process model does not have any influence on controller structure. The open-loop block diagram is shown in Fig. 3

The open-loop response FOPD is shown in Fig. 4,

Fig. 3 Open-loop structure**Fig. 4** Open-loop response

From the response, the tuning gain K , dead time is θ and time constant τ is obtained. Here, the time constant τ is 63% of rise time. The general tuning formulas for Ziegler Nicholas and Cohen Coon are given. In Table 1, based on the parameter obtained, the Ziegler Nicholas and Cohen Coon PID tuning parameters are given in Table 2.

Table 1 Ziegler Nicholas and Cohen Coon tuning formulas

Tuning techniques	P	$P + I$	$P + I + D$
Ziegler Nicholas	$\tau/K\theta$	-	-
	$0.9\tau/K\theta$	3.3θ	-
	$1.2\tau/K\theta$	2θ	0.5θ
Cohen Coon	$\tau/K\theta [1 + \theta/3]$	-	-
	$\frac{\tau}{K\theta} [0.9 + \theta/12\tau]$	$\theta[30 + 3\theta/\tau]/9 + 20\theta/\tau$	-
	$\tau/K\theta [4/3 + \theta/4\tau]$	$\theta[32 + 6\theta/\tau]/13 + 8\theta/\tau$	$4\theta/11 + 2\theta/\tau$

Table 2 Ziegler Nicholas and Cohen Coon tuning values

Tuning technique	PID
Ziegler Nicholas	$K_p = 0.01278, K_I = 0.000701, K_D = 0.0568$
Cohen Coon	$K_p = 0.016232, K_I = 0.00092, K_D = 0.0472$

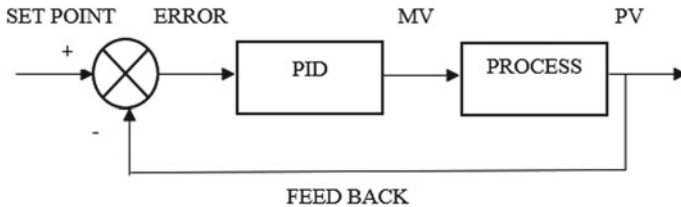


Fig. 5 Closed-loop structure

The parameters from Table 2 are applied to the PID controller in Simulink model. The closed-loop block diagram of the process is shown in Fig. 5,

In closed-loop, based on feedback process variable, the error is calculated, and the PID controller gives manipulated variable to the process to make process variable settle in the setpoint level given. The general PID controller structure is

$$G_c(s) = K_p e(t) + K_p / T_i \int e(t) + K_p * T_d de(t) dt \quad (5)$$

Here, K_p —proportional gain, T_i —integral time constant, T_d —differential time constant.

3.2 Internal Model Controller

Internal model control is a basic model-based control strategy, in which unlike PID controller, the controller is purely influenced by process model, i.e., the control is an inverse of the actual process model, so in IMC, the setpoint is tracked accurately, i.e., there is no steady-state error theoretically; the proof is as follows,

$$G_p(s) = \frac{y_{set}(s)}{u(s)} \quad (6)$$

Then,

$$G_p^{-1}(s) = \frac{u(s)}{y_{set}(s)} \quad (7)$$

So, we can write

$$\frac{y(s)}{y_{\text{set}}(s)} = \frac{u(s) G_p(s)}{y_{\text{set}}(s)} \quad (8)$$

Equation (8) can be written as

$$\frac{y(s)}{y_{\text{set}}(s)} = G_p^{-1(s)} * G_p(s) \quad (9)$$

$$\frac{y(s)}{y_{\text{set}}(s)} = 1 \quad (10)$$

From the above result, it is clear that, the output exactly tracks setpoint, i.e., theoretically no steady-state error but practically steady-state error cannot be eliminated but it can be minimized by using IMC. This is the major advantage of model-based controller over PID controller. While inverting our process model, there is a mismatch between numerator and denominator part of transfer function, i.e., numerator order is greater than denominator order, and to compensate this, a low pass filter is multiplied with the inverted process model. The controller model is as follows; from Eq. (4), the process model is

$$G_p(s) = h(s)/F_{\text{in}}(s) = \frac{2.7e^{-0.15s}}{(0.75s + 1)}$$

By inverting the above transfer function,

$$\hat{G}_p(s) = \frac{(0.75s + 1)e^{-0.15s}}{2.70} \quad (\text{system is unstable}) \quad (11)$$

To avoid transfer function mismatch, a low pass filter is included

$$\text{LPF} = \frac{1}{\lambda s + 1} \quad (12)$$

$$G_{\text{IMC}}(s) = \hat{G}_p(s) * \text{LPF} \quad (13)$$

It is clear that while we are inverting the process model, we get positive dead time which means it makes the system to give inverse response, so before inverting, pades approximation [7] is applied for dead time. The general transfer function of pades approximation for FOPD process is as follows

$$e^{0.15s} = \frac{-0.5\theta s + 1}{0.5\theta s + 1} \quad (14)$$

By solving Eq. (13), (14), we get IMC controller models as

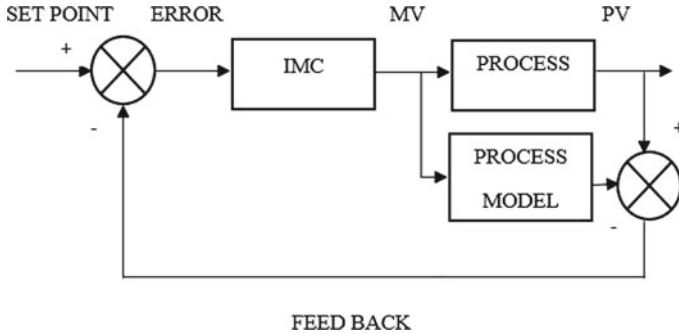


Fig. 6 Internal model control structure

$$G_{IMC}(s) = \frac{0.80625s + 1.075}{2.4975\lambda s + 2.4975} \quad (15)$$

λ is the filter co-efficient, generally its value lies between 0 and 2 [8], and for this work, the filter co-efficient we consider as 0.6, 1.2, and 1.5. The IMC structure is shown in Fig. 6.

3.3 Modified Internal Model Controller

The modified internal model controller block diagram is shown in Fig. 7. MIMC controller mathematical part is same as that of IMC and the only difference is in the structure, that is in IMC, actual process output and process model output is compared and given as feedback but in MIMC, the process model output is directly added with the controller output and given as input to the process.

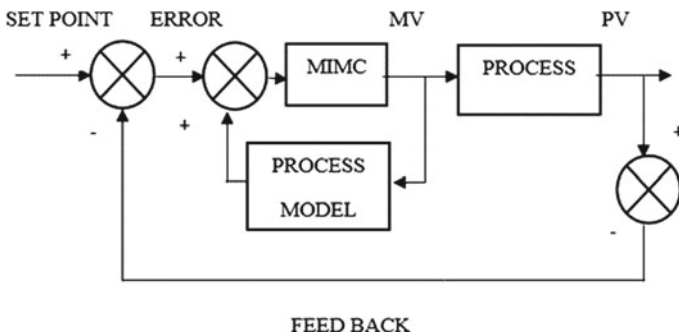


Fig. 7 Modified internal model control structure

4 Results and Discussion

The responses of all control strategies are given in Figs. 8, 9, 10 and 11. The time domain and error criterion of all control strategies are given in Table 3 and from the process response, it is clear that conventional PID using Ziegler Nicholas and Cohen Coon tuning technique, the time taken to settle the process in actual setpoint is very large and also the process attains initial settlement prior to actual setpoint for some time period and then starts rising and settles in actual setpoint. But in IMC and MIMC, smooth settling is achieved as well as settling time taken is highly reduced.

The responses of IMC and MIMC for different ζ are shown in Figs. 10 and 11, From the response, it is clear that higher ζ values increase the time taken by the

Fig. 8 Ziegler Nicholas tuning response

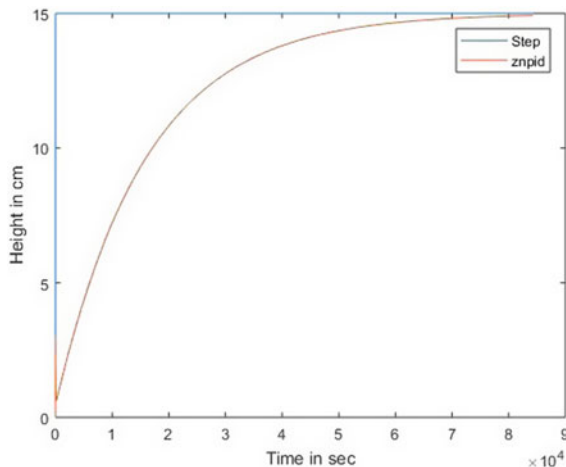


Fig. 9 Cohen Coon tuning response

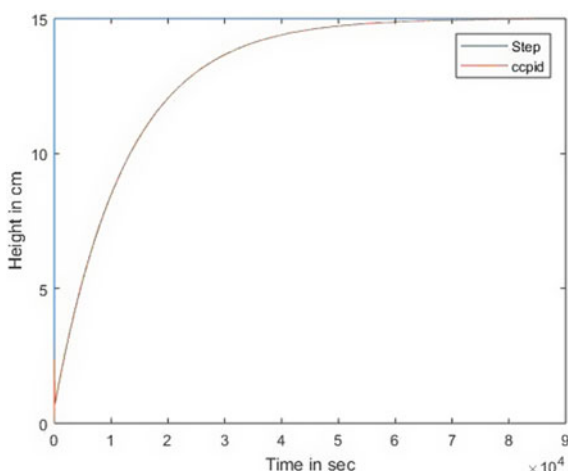


Fig. 10 IMC response for $\lambda = 0.6, \lambda = 1.2, \lambda = 1.5$

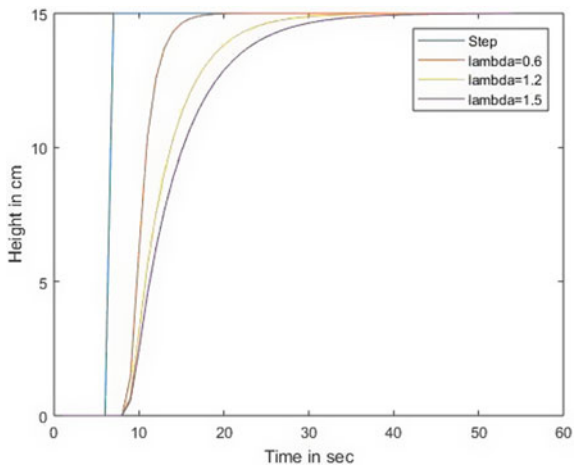
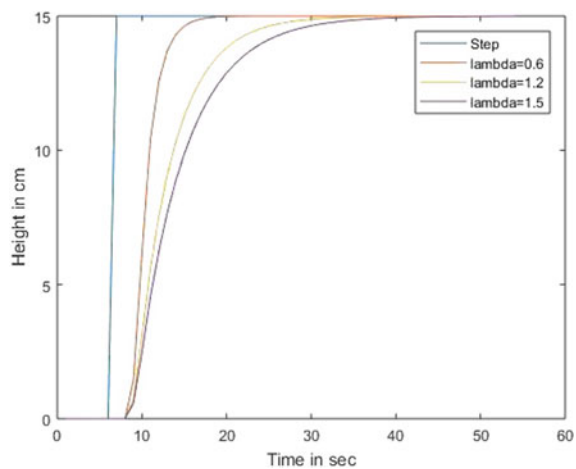


Fig. 11 MIMC response for $\lambda = 0.6, \lambda = 1.2, \lambda = 1.5$



process to settle at setpoint, and time domain criterion values also proven the same. From the response and time domain criterion, both IMC and MIMC are similar but when come to error criterion, MIMC gives better results. Overall MIMC outperforms IMC and conventional PID

5 Conclusion

The results of model-based controllers outperforms conventional PID controller; this is because the controller has the influence of process model. In this work, for model-based control structure, the FOPD model is taken as plant and process model

Table 3 Time domain and error criterion values

Controllers	Ziegler Nicholas PID	Cohen Coon PID	IMC				MIMC	
	$\lambda = 0.6$	$\lambda = 1.2$	$\lambda = 1.5$	$\lambda = 0.6$	$\lambda = 1.2$	$\lambda = 1.5$		
<i>Time domain specifications</i>								
Rise time in sec	3.5935e + 04	2.8393e + 04	3.8008	9.6265	12.4543	3.8008	9.6265	12.4543
Settling time in sec	5.8695e + 04	4.8168e + 04	15.3969	25.9288	30.9372	15.3969	25.9288	30.9372
Peak time in sec	84213	84208	53	54	54	53	54	54
<i>Error criterion</i>								
ISE	5.62e + 04	4.348e + 04	4906	4934	4949	78.1	133.9	162.7
IAE	7708	6031	376.8	378	378.5	7.95	15.49	19.6

approximated after pades approximation is taken as process mathematical model. In the future, the simulation parameters will be applied to real-time process. The scope of the work will be in model predictive controller mechanism and adaptive control mechanism.

References

1. Kesavan SM, Padmesh TV, Shyan CW (2014) Controller tuning for non-linear hopper process tank-A real time analysis design. J Eng Sci Technol (Special Issue):59–67 (2014). (EURECA 2013)
2. Vinothkumar C, Esakkiaappan C (2019) Level control of nonlinear hopper tank process in pharmaceutical industry using ziegler Nicholas and cohen coon tuning techniques. Int. J. Innovative Technol Explor Eng (IJITEE) 8(10). ISSN: 2278–3075
3. Wang Y, Lu Y, Ooi J (2013) Numerical modelling of dynamic pressure and flow in hopper discharge using the Arbitrary Lagrangian-Eulerian formulation. Eng Struct 56:1308–1320
4. Yin W, Ooib JY (2015) A study of granular flow in a conical hopper discharge using discrete and continuum approach. Sci Direct Proc Eng 102:765–772
5. Dinesh Kumar D, Meenakshi Priya B (2012) Design and implementation of non linear system using gain scheduled PI controller. Procedia Eng 38:3105–3112
6. Arasu SK, Panda A, Prakash J (2016) Experimental validation of a nonlinear model based control scheme on the variable area tank process. IFAC-PapersOnLine 49(1):30–34
7. Bequette BW (2003) Process control: modeling, design, and simulation. Prentice Hall, Englewood Cliffs
8. Jogwar SS (2018) NPTEL study Material, Department of Chemical Engineering, Indian Institute of Technology Bombay

Hybrid L + C Edge Detection Algorithm for Harnessing Large Image Datasets



Gurpartap Singh, Sunil Agrawal, and B. S. Sohi

Abstract The primary focus of this work is to improve the performance of pre-existing techniques used to crop fragments of images from a larger image or a form. The form mentioned here can consist of any number of rectangles having different dimensions and in varying arrangements. The requirement of such forms arises with the staggering growth in the application of artificial intelligence (AI). This growth has made the collection of large image datasets an essential task, as we need a colossal amount of data to train algorithms. These algorithms are in turn used in the trending AI applications. This has made collection of datasets a prominent task as any in the development of an AI. Therefore, in the field of handwriting recognition also we need a large dataset. To create such large datasets, we need general formats that can be applied anywhere around the globe and also do not require any special equipment. In this work, a hybrid approach with the above said attributes have been proposed to collect the Punjabi handwritten dataset. This proposed technique primarily uses pre-existing operators designed for edge detection and locates rectangles within the forms. Then, it matches the dimension and location of rectangles within the forms with pre-assigned values. On applying the proposed technique, the algorithm was able to extract segments with quite impressive accuracies and create large enough datasets for future work. The main reason for achieving such high accuracy is that the proposed technique exploits the robustness of both Canny and Laplace operators for edge detection.

Keywords Datasets · Handwriting · Dilation · Contours · Canny operator · Laplace operator · Edge detection

G. Singh (✉) · S. Agrawal
UIET, Panjab University, Chandigarh 160017, India
e-mail: gpsphd1990@gmail.com

S. Agrawal
e-mail: s.agrawal@hotmail.com

B. S. Sohi
Chandigarh University, Gharuan, Punjab 140413, India
e-mail: bssohi@gmail.com

1 Introduction

Image processing has been a prevailing field of research for decades because of its wide range of applications in almost every field. But recently, staggering growth in computer vision and artificial intelligence(AI) has led to tremendous growth in the field of image processing. These fields are entirely based on data and a significant amount of data is in the form of images. Hence, it is natural that image processing will be one of the most prominent research fields in the future [1]. Image processing includes several fundamental steps but this work is entirely focused on image retrieval/fragmentation. As we all know that most of the available data is not in a structured form neither, it is available in a format in which they can be used to train AI or computer vision algorithms. Most of the algorithms that are being used today are deep learning algorithms and they need very specific datasets so that they can learn the general and in-depth representation of datasets. Only then, these algorithms can be used in real-time applications. If the datasets used to train these algorithms is somewhat compromised, then it will create issues in achieving the ultimate goal of a generalized AI. This has made creating a dataset quite significant but yet a daunting task as any in the development of an AI.

Recently, some synthetic methods [2, 3] have also been developed to create image datasets that mimic the existing images. But the images obtained using synthetic methods cannot accurately represent the data encountered in the real-time scenarios. The main reason for above-mentioned issue is that synthetically generated datasets are nothing but anomalies created by introducing variance in the existing images. Even in recent experiments done by Jahanian et al. [4], it was observed that generative adversarial network's (GAN's) ability to introduce variance is limited which means GANs can introduce only a certain degree of variation in dataset. This clearly substantiate that the data generated using synthetic methods yet cannot represent the real-time data; it can only generate samples within the scope of existing data or extrapolate entirely outside the support of the training data.

Although the main feature of these synthetic techniques is that they learn the distribution from the existing data and then accordingly introduce variance in order to generate new data samples but even, then we cannot completely rely upon these techniques for future applications. Hence, this work is dedicated to find an approach using which data can be collected conveniently for automation in the future applications.

2 Literature Review

Since last few decades, a significant amount of work has been done in the field of image segmentation. In [5], authors have done inspection of several autonomous approaches which have been used for image segmentation and to what extent

they have achieved success. There are several application where image segmentation is required like preservation of historical handwritten text documents [6–8], vehicle number plate extraction from images [9], segmentation of handwritten words/alphabets for classification [10], etc. Based on applications, there are different algorithms that have been used for segmentation and these algorithms uses different techniques for segmentation [11]. In this work, the main aim is to crop rectangular segments from larger images. Hence, the techniques mentioned in [11], namely edge detection-based image segmentation techniques have great potential for yielding excellent results in the scenario considered in this work. The two most commonly used edge-based segmentation methods are Canny [12] and Laplace [13]. The main difference between these two techniques is that Canny is first derivative order-based edge detection whereas Laplace is a second order edge detection technique. Moreover in canny filter, Otsu's thresholding technique [14] is used in order to obtain better edges. The main reason for using Otsu's thresholding is that it generally searches for the threshold that minimizes the intra-class variance which is defined as a weighted sum of variances of the two classes. Hence, yielding a high accuracy in edge detection. Moreover, there are several variants of Laplace and Canny filters [15, 16] that have been used for several applications, which suggests that these techniques are quite versatile.

From literature survey, it is evident that these edge detection techniques are capable of extracting fragments of images from a larger image irrespective of the format of form being used for data collection. Hence, the work presented in this article is entirely based on edge detection techniques and also the proposed methodology is derived from these techniques only.

3 Methodology

Present work consists of a form printed on A4 page, but this method can be very easily extended for pages of any size. Here, we have considered three formats in which we have collected handwritten Alphabets/Vowels, digits, and words in Punjabi language. The formats used are as shown in Fig. 1a–c.

From the above figures, it is clear that we can place rectangles in different arrangements and in different sizes thus assuring wide range of applications. These forms are then printed on A4 size paper and are filled by school students. Later, the filled forms are scanned using a CanonMF246dn Digital Multifunction Laser Printer. A scanned image of the filled forms is shown in Fig. 2.

As we can observe from Fig. 2, there are several imperfections and noise that have been introduced while scanning hence, the algorithm must be able to identify them ideally. Otherwise, it will be difficult to extract the fragments accurately. The imperfections occurring at the time of scanning also include some rotation as well which makes quite difficult to pinpoint the exact location of rectangular boxes. Hence, the required methodology must be robust enough to locate the exact edges despite of

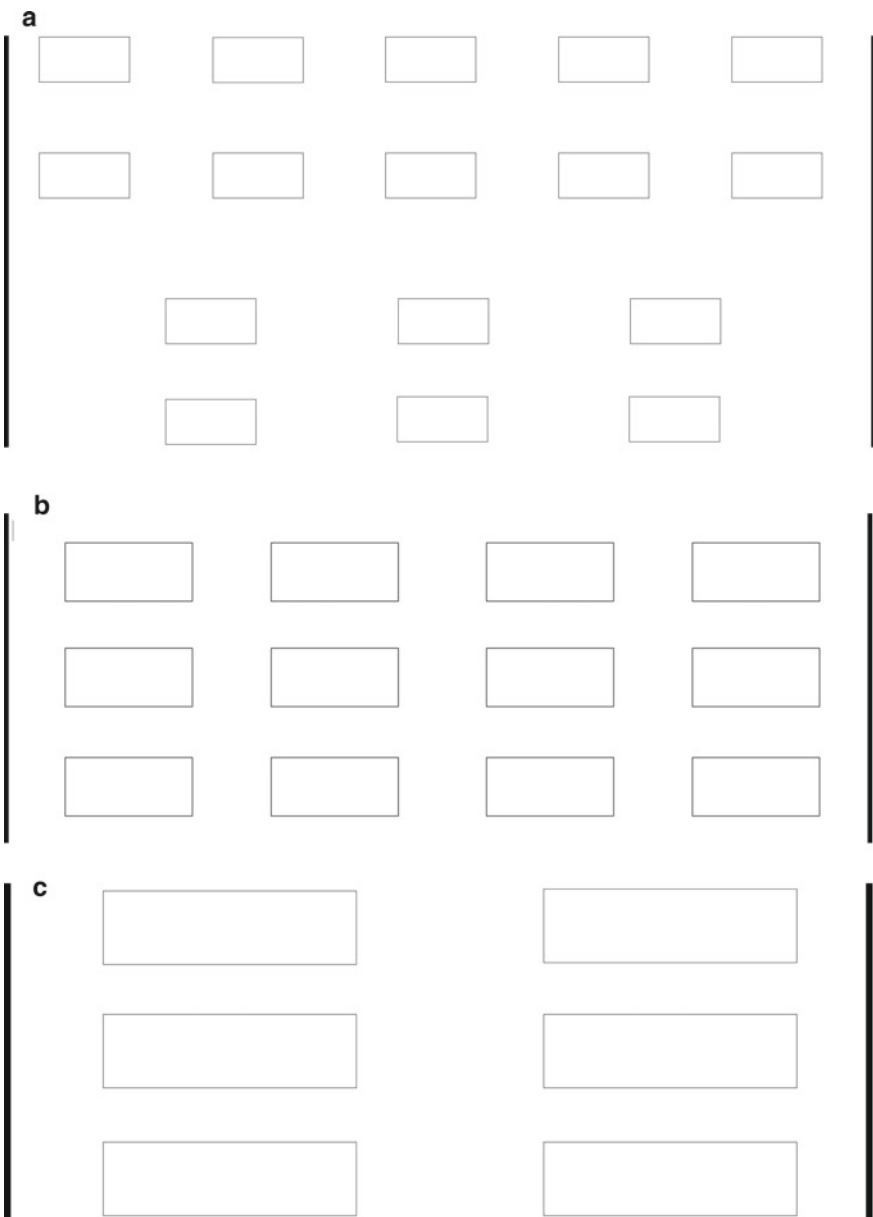


Fig. 1 **a** A segment of format for alphabet and vowel dataset collection. **b** A segment of format for collection digit dataset. **c** A segment of format for collection word dataset

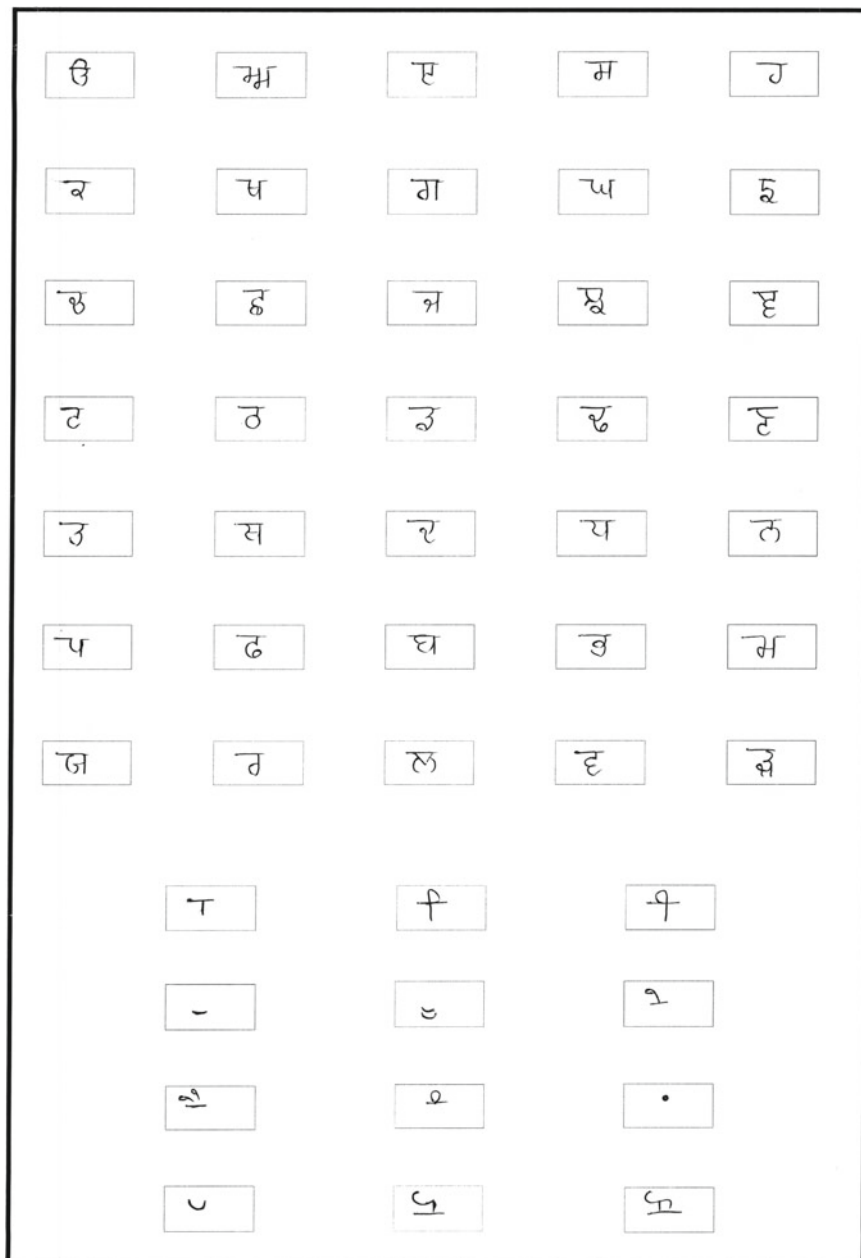


Fig. 2 A scanned image of format for alphabet and vowel dataset collection

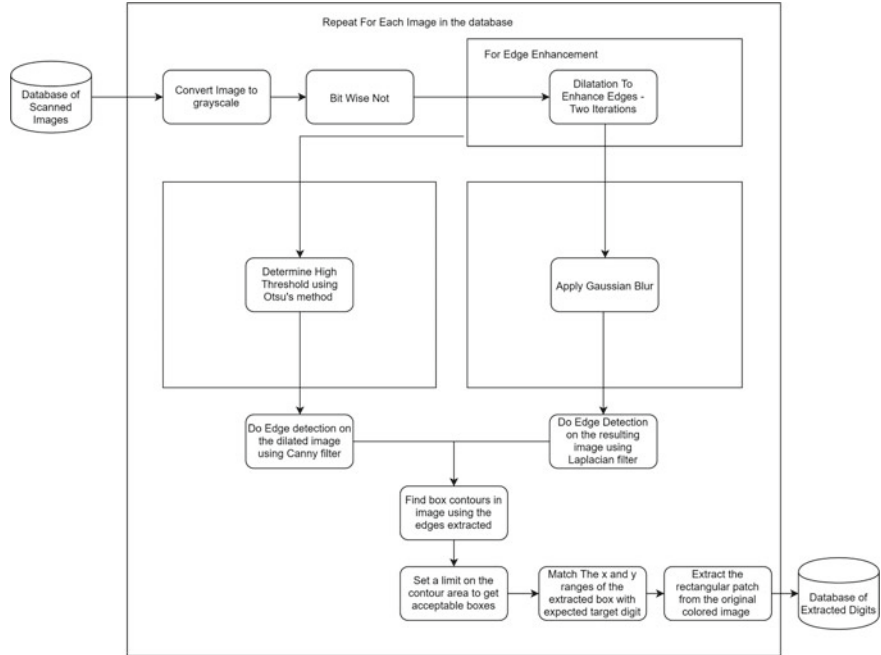


Fig. 3 Algorithm for extracting handwritten fragments from scanned images

all the deformations. Taking into consideration all these factors, the final algorithm used to extract images is shown in Fig. 3.

The algorithm shown in Fig. 3 comprises of features of both Laplacian and Canny filters for edge detector. The reason for using both the filter at the same time is that they both have excellent features but neither of them is individually capable of detecting all the edges from a noisy and deformed images. This has been demonstrated in the results mentioned in Table 2. That is the reason that we have combined both the edge detectors so that we can get better image extraction, which can be confirmed from the results mentioned in Table 3.

4 Results and Discussion

In this work, we have collected data from over 300 individuals. The details of forms filled by individuals and the number of fragments in the scanned images that have to be extracted are mentioned in Table 1.

After we have obtained the scanned images, the next step is to extract the fragments. We have initially used Canny and Laplace separately to extract the fragments. This also helps in analyzing how these algorithms individually and collectively perform. The details of extracted fragments are mentioned in Table 2.

Table 1 Details of image fragments within scanned images

S. No.	Type	Number of scanned IMAGES	Number of boxes in each format	Rectangle count
1.	Alphabets	323	47	15,181
2.	Digits	325	40	13,000
3.	Words	325	20	6500

Table 2 Details of extracted fragments using Laplace and Canny operators individually

S. No.	Type	Fragments extracted (Canny)	Accuracy (Canny)	Fragments extracted (Laplace)	Accuracy (Laplace)
1.	Alphabets	13,813	90.9	13,719	90.3
2.	Digits	11,641	89.5	11,609	89.3
3.	Words	5442	83.7	4113	63.2

As we can observe in both the cases, that the number of extracted fragments are quite less than the actual number. But there is another observation that the fragments extracted by both the filters are not exactly same. There are some images that are extracted only by either of the algorithms. Hence, all we need is to combine both the algorithms in a manner that we can extract relatively higher number of fragments. Therefore, in this work, both the filters have been used in unison in the algorithm suggested in this work; hence, we are able to integrate the mathematical foundations of both the filters in a single filter. After combining both the filters, we were able to extract more number of fragments than we were able to extract with individual filters. The details of extracted fragments from proposed algorithm are mentioned in Table 3.

Another important fact regarding this method is that the amount of scanned images will have no effect on the accuracy. So it will not matter if we are extracting fragments from 100 or 1000 scanned images. A comparison of accuracy for all the three algorithms is shown in Fig. 4 which indicates that the suggested algorithm has outperformed the existing algorithms.

From Fig. 4, it can be visualized that our proposed method is able to extract the fragments with higher accuracy as compared to Laplace and Canny individually.

Table 3 Details of extracted fragments using proposed algorithm

S. No.	Type	Extracted fragments using L + C	Accuracy (%)
1.	Alphabets	14,839	97.7
2.	Digits	12,635	97.1
3.	Words	5843	89.8

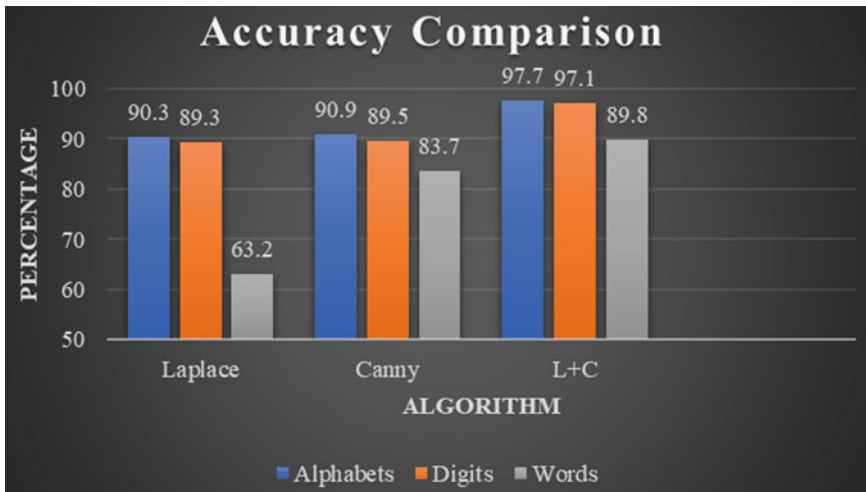


Fig. 4 Accuracy comparison of Laplace, Canny, and L + C algorithms for alphabets, digits, and words

This improvement can be attributed to the fact that the proposed method is able to combine the benefits of both the existing techniques.

5 Conclusion and Future Scope

From experimental results shown in this work, it can be observed that proposed algorithm did reasonably well. In order to make this technique easily accessible, hardware used in this work is quite ordinary. An improvement that can be made to this proposed methodology is by the use of noise cancellation techniques which would make edge detection facile. Also the quality of the scans can be improved by using hardware of superior grade.

The main advantage of this work is convenience in collecting large image datasets. Hence, the methodology proposed in this work will be of great help for researchers working on collection and segmentation of large data. For a futuristic technique, we can introduce adaptiveness as well, which will help in designing an edge detection algorithm capable of maintaining robustness even at the most sophisticated scenarios.

Acknowledgements This Publication is an outcome of the R&D work undertaken project under the Visvesvaraya Ph.D. scheme of Ministry of Electronics and Information Technology, Government of India, being implemented by Digital India Corporation.

References

1. Shih F (2011) Image processing and mathematical morphology. CRC Press, Boca Raton
2. Martin Arjovsky SC, Bottou L (2007) Wasserstein generative adversarial networks. In: International conference on machine learning, pp 214–223
3. Pu Y, Gan Z, Henao R, Yuan X, Li C, Stevens A, Carin L (2016) Variational autoencoder for deep learning of images, labels and captions. NIPS 2352–2360
4. Jahanian A, Chai L, Isola P (2019) On the “steerability” of generative adversarial networks. *ArXiv* abs/1907.07171
5. Zhang H, Fritts JE, Goldman SA (2008) Image segmentation evaluation: a survey of unsupervised methods. *Comput Vis Image Understanding* 110(2):260–280
6. Toledo JI, Carbonell M, Fornés A, Lladós J (2018) Information extraction from historical handwritten document images with a context-aware neural model. *Pattern Recogn* (2018)
7. Sánchez JA, Bosch V, Romero V, Depuydt K, De Does J (2014) Handwritten text recognition for historical documents in the transcriptorium project. In: ACM international conference proceeding series
8. Sastry PN, Krishnan R, Ram BV (2010) Classification and identification of Telugu handwritten characters extracted from palm leaves using decision tree approach. *J Applied Engn Sci* 5(3):22–32
9. Sharma C, Kaur A (2011) Indian vehicle license plate extraction and segmentation. *Int J Comput Sci Commun* 2(2):593–5999
10. Louloudis G, Gatos B, Pratikakis I, Halatsis C (2009) Text line and word segmentation of handwritten documents. *Pattern Recogn* 42(12):3169–3183
11. Zaitoun Nida M, Aqel Musbah J (2015) Survey on Image Segmentation Techniques. *Procedia Comput Sci* 65:797–806
12. Canny J (1986) A computational approach to edge detection. *IEEE Trans Pattern Anal Mach Intell* 6:679–698
13. Wang X (2007) Laplacian operator-based edge detectors. *IEEE Trans Pattern Anal Mach Intell* 29:886–890
14. Otsu N (1979) A threshold selection method from gray-level histogram. *EEE Trans Syst Man Cybern* 9(1):62–66
15. Rong W, Li Z, Zhang W, Sun L (2014) An improved CANNY edge detection algorithm. In: 2014 IEEE international conference on mechatronics and automation, pp 577–582
16. Fan P, Zhou RG, Hu WW, Jing N (2018) Quantum image edge extraction based on Laplacian operator and zero-cross method. *Quantum Inf Process* 18(1):27

Resolution Selective 2–6-Bit Flash ADC in 45 nm Technology



Sarfraz Hussain, Rajesh Kumar, and Gaurav Trivedi

Abstract This paper presents a 2–6-bit resolution selective flash ADC (RSA). A re-configurable or resolution selective flash ADC is designed for use with different applications. In this design, resolution for a particular application can be chosen without the need of replacing the ADC with another low or high resolution ADC. Speed, resolution, and power are inter-dependent; therefore, to maintain a good balance re-configurable ADCs are very much efficient. A resolution selective design gives user a choice for selecting the resolution according to the application and thus save the manufacturing cost. For full resolution of 6-bit the ADC consumes 1.57 mW and for the lowest resolution of 2-bit it consumes 268.9 μ W for 1 V supply voltage.

Keywords Mixed-signal circuits · Encoders · Flash ADC · Fat-tree encoder · Re-configurable ADCs

1 Introduction

Resolution is one of the most important factors in an ADC. Resolution is defined as 1 LSB which is the step size of an ADC. More the resolution, better the output. With performance comes trade-off. Speed decreases and power consumption increases with increase in resolution. For an n-bit Flash ADC, $2^n - 1$ number of comparators are required. For a 2-bit Flash ADC 3 comparators are required whereas for 6-bit flash ADC 63 comparators are required. High speed applications sometimes doesn't require high resolution therefore a low resolution ADC can give a good required

S. Hussain (✉) · R. Kumar

Department of Electronics and Communication Engineering, NERIST, Nirjuli, Arunachal Pradesh, India

e-mail: sarfrazenator@gmail.com

R. Kumar

e-mail: rk@nerist.ac.in

G. Trivedi

Department of Electrical and Electronics Engineering, Indian Institute of Technology Guwahati, Guwahati, Assam, India

e-mail: trivedi@iitg.ac.in

outcome. Similarly, in less speed and more accurate applications like CD read-write operation high resolution is required. Earlier two different ADCs are required for high speed and high accuracy applications but with resolution selective ADC a single ADC is sufficient. By selecting the resolution in accordance with our requirements we can get optimum results. 45 nm technology provides better speed performance and a torsion between different technologies.

In [1], a resolution selective flash ADC was proposed for a maximum resolution of 4-bit. It was designed for 90 nm technology. The proposed design has a higher resolution and is designed for 45 nm technology node. In [2], a portable application based 6-bit flash ADC is designed. Many ADCs have been and are being designed in bulk. TIQ-based comparators have an advantage of being fast [3, 4]. Therefore, a resolution selective TIQ based ADC can reduce the manufacturing cost as well as increase speed.

Section 2 describes the idea of resolution selective flash ADC. An algorithm is proposed for the selection of analog and digital part. Section 3 shows the simulated results and comparison table. All the simulations are carried out in Cadence Virtuoso IC 6.1.

2 Resolution Selective Flash ADC

In the proposed flash ADC, one can select the resolution from 2 to 6-bit as per the specific application. The main idea of the resolution selective ADC is to reduce the manufacturing cost by implementing the same ADC for multiple applications. A flash ADC has two main blocks: comparator block (analog part) and encoder block (digital part). The first step for designing such an ADC is to select the highest resolution. Once highest resolution ADC is designed then the proposed algorithm is applied to select the inner components for different resolutions. Algorithm 1 is used for analog part election and algorithm 2 is used for digital part selection.

2.1 TIQ Based Comparator

Threshold Inverter Quantizer is an Inverter based comparator proposed in [5] which is used in this paper. The algorithm used in [6] is used to select different transistor sizes for different thresholds. Such a comparator doesn't require resistor ladder circuitry and the threshold acts as a reference node voltage. The comparator selective circuit is shown in Fig. 1. The following equation is used to select the transistor sizes [4, 5]:

$$V_{th} = (\sqrt{k}(V_{DD} - |V_{tp}|) + V_{tn})/1 + \sqrt{k}$$

where $k = \mu_p W_p / \mu_n W_n$ (1)

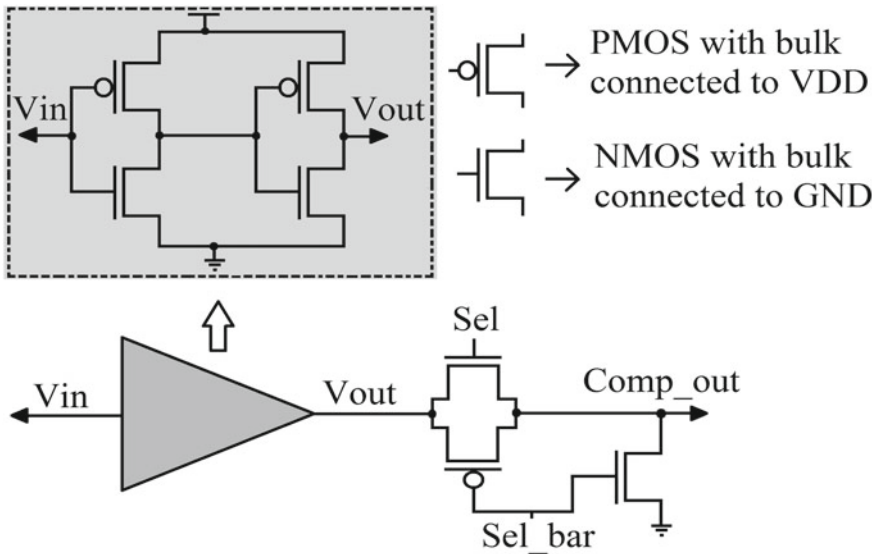


Fig. 1 Comparator circuit

Table 1 Step size for different resolutions for the same input range

Resolution	Step size (mV)
2	112
3	32
4	16
5	7.46
6	3.61

In [6], the transistor sizes are optimized by utilizing the property of INL and DNL. Optimization is required because of a vast range of transistor values for a specific threshold. For choosing a particular threshold or reference points for the comparator, the full scale range is selected by choosing the highest and the lowest input swing. $V_{DD} - |V_{tp}|$ is the highest input and V_{tn} is the lowest input. The input range for the proposed design varies from 368 to 592 mV. With this range step size is chosen by dividing it into $2^n - 2$ parts. Respective step size for different resolutions is tabulated in Table 1.

2.2 Encoder

Encoder is the digital part of an ADC [7–9]. Modified Fat-tree encoder is used along-with a bubble error corrector circuit for better results. The selection of output is done

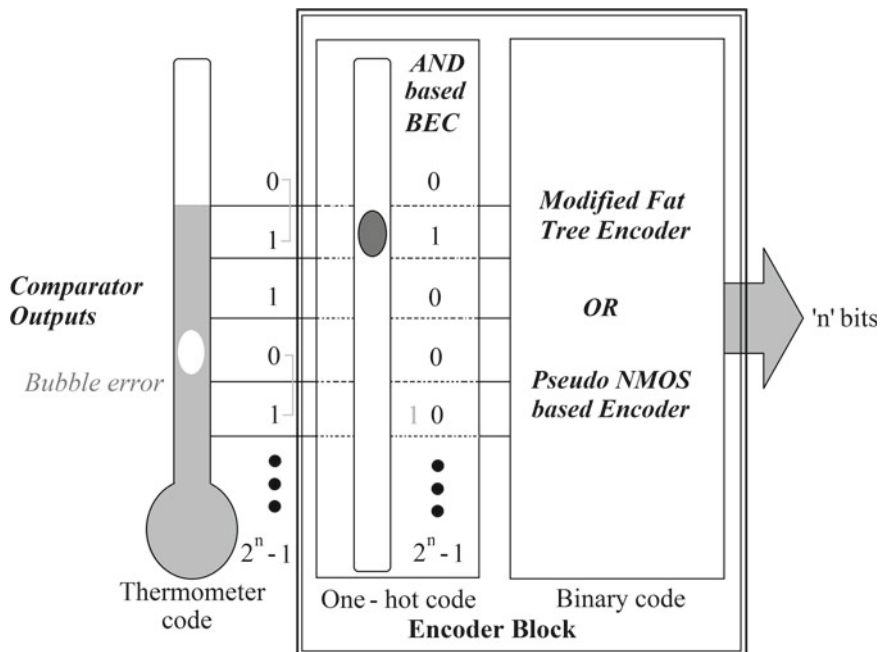


Fig. 2 Proposed encoder circuit

Table 2 Selection of binary outputs based on resolution

Resolution	MSB	LSB
2	B_5	B_4
3	B_5	B_3
4	B_5	B_2
5	B_5	B_1
6	B_5	B_0

through the proposed algorithm. Only the required components are chosen rest are turned OFF. For an encoder only the output block selection is made for easy and fast response. Selector block is added to the output of each of the successor blocks of the binary encoder. The proposed encoder is shown in Fig. 2. For different resolutions the MSBs and LSBs are tabulated in Table 2.

2.3 Proposed Algorithm for RSA

An algorithm is proposed for resolution selective flash ADC (RSA). It helps us select only the required components for a specific resolution thus saving power and

Table 3 Algorithm for analog part selection**Algorithm 1** Algorithm for selecting the comparators for varying resolution**Input:** Resolution in bits**Output:** Selected Comparator Array

Initialisation :

1: Initialise 6-bit array

'a[]'

Setting 6-bit array elements:

2: **for** $i = 0$ to 62 **do**3: $a[i] = i+1$ 4: **end for**

Selection of components from array 'a' based on the selected resolution :

5: Res = required resolution

6: $n = 2^{**res}$ 7: $b = []$ for k in range($n-1$)8: $b[0] = a[0]$

first element is always same

9: $x = 6-res$ 10: **for** $i = 1$ to length of b array **do**11: $j = (i+2)*(2^{**x})-2$ 12: $b[i] = a[j]$ 13: **end for**14: **return** b

****Note:** Total number of comparators in a block is 63 (i.e. $2^6 - 1$). Out of the 63 comparators, selection is being made.

manufacturing cost. Algorithm is tabulated in Tables 3 and 4. Separate algorithms are followed: Algorithm 1 is meant for comparator block selection while the algorithm 2 is meant for selecting digital part.

3 Simulated Results

The parameters considered for the simulations are: (i) 1 V supply for 45 nm technology, (ii) minimum channel length is taken as 45 nm and (iii) ramp input is given. In the proposed flash ADC, one can select the resolution from 2 to 6-bit as per the specific application. For 2, 3 and 4-bit resolution different graphs are obtained to show the selectivity results. The performance of the proposed resolution selective flash ADC is tabulated in Table 5. The normalized power-delay product (PDP) for 2-bit resolution is 1.8 and for 6-bit is 47.1. The outputs of ADC for different resolutions are shown in Figs. 3, 4 and 5. The results signify that it can be used for multiple applications. Compared to a TIQ flash ADC the proposed ADC shows more or less good results when 4-bit resolution is selected. Table 6 shows the comparison of both the 4-bit ADCs. Though, it has a drawback of consuming more power relative to ADC

Table 4 Algorithm for digital part selection**Algorithm 2** Algorithm for selecting the encoder outputs for varying resolution**Input:** Resolution in bits**Output:** Selected Binary Output Array

Initialisation :

1: Initialise 6-bit output array

'a[]'

Setting 6-bit array elements:

2: **for** $i = 0$ to 5 **do**3: $a[i] = i+1$ 4: **end for**

Selection of components from array 'a' based on the selected resolution :

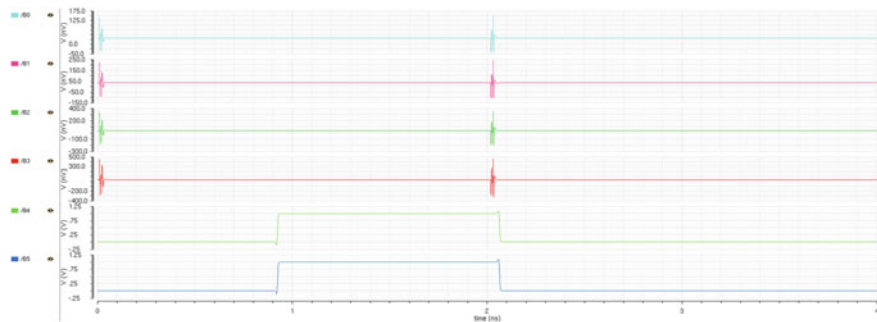
5: Res = required resolution

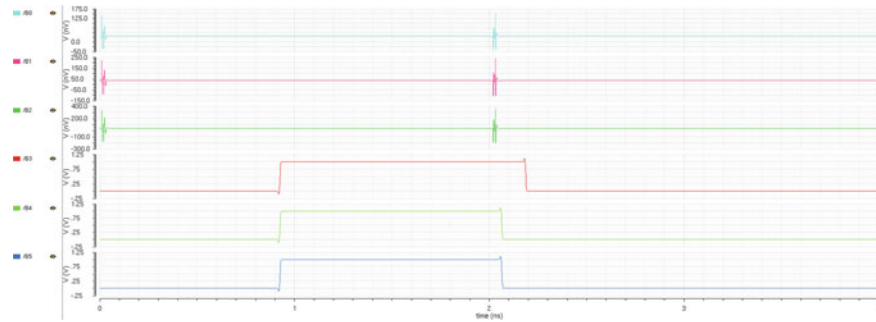
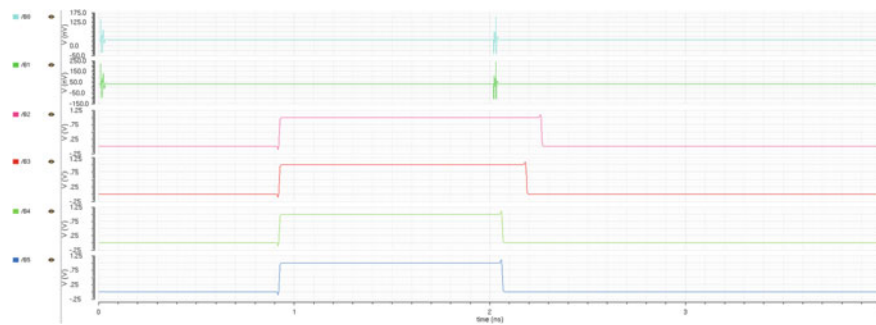
6: b= [] for k in range(0,res)]

7: x = 6 - res

8: **for** $i = 0$ to length of b array **do**9: $b[i] = a[i] + x$ 10: **end for**11: **return** b**Table 5** Performance chart for resolution selective flash ADC

Resolution	Delay (pico-sec)	Power dissipation (μ -W)	Normalized PDP	Normalized EDP
2	70	268.9	1.8	1.31
3	200	591.6	11.8	23.66
4	250	941.8	23.5	58.86
5	270	933.1	25.2	68.02
6	300	1570	47.1	141.30

**Fig. 3** 2-bit flash ADC output

**Fig. 4** 3-bit flash ADC output**Fig. 5** 4-bit flash ADC output**Table 6** Proposed 4-bit flash ADC performance comparison

ADC	Delay (pico-sec)	Power dissipation (μ -W)	Normalized PDP	Normalized EDP
4-bit flash ADC	252.8	740.4	1.87	47.31
Proposed 4-bit RSA	250	941.8	2.35	58.86

without the resolution selective blocks but it saves the manufacturing cost and can be utilized for multiple applications. Thus, a resolution selective ADC can be used with less cost of implementation for multiple applications. Table 7 exhibits the comparison of the proposed ADC with the recent flash ADC designs. We can observe that the chosen flash ADC design architecture is advantageous and the proposed design enhances the implementation capability of the ADC.

Table 7 4-bit flash ADC performance comparison

ADC	Proposed flash ADC (RSA)	Proposed flash ADC (RSA)	Wu et al. [10]	Varghese and Mahapatra [11]
Technology node	45 nm	45 nm	180 nm	90 nm
Resolution (in bits)	6	4	4	4
Max sampling rate (in GHz)	1.25	1.5	2	3
Supply voltage (in volts (V))	1	1	1.8	1.2
Power dissipation (mW)	1.57	0.94	42	2.42

4 Summary

The paper depicts the methodology for selection of different components for different resolutions. Two algorithms are proposed for the selection procedure. A 4-bit flash ADC without the selection block is compared with flash ADC with selection block having the same architectural components. The resultant of proposed ADC shows more power consumption due to the additional blocks. When compared to other recent 4-bit ADCs, the chosen architecture and the proposed design show improvement in the design. For the complete 6-bit resolution selective flash ADC (RSA), maximum sampling rate is 1.25 GHz with a power dissipation of 1.57 mW, and for a 4-bit RSA, it is 1.5 GHz with 0.94 mW. The objective of the design is to reduce the manufacturing cost and to use the same ADC for multiple applications. By selecting different resolutions it can be used for applications required.

Acknowledgements Authors would like to thank ECE department, NERIST, Arunachal Pradesh and EICT Academy, IIT Guwahati, Assam for their resource and assistance. We would also like to thank MeitY (under Govt. of India) for facilitating research grant under Visvesvaraya PhD Scheme.

References

1. Tiwari S, Kumar A (2018) Reconfigurable flash ADC using TIQ technique. In: 4th international conference on computing sciences (ICCS). Jalandhar, pp 204–208
2. Mishra SN, Arif W, Mehedi J, Baishya S (2013) A power efficient 6-bit TIQ ADC design for portable applications. In: IEEE third international conference on consumer electronics Berlin (ICCE-Berlin). Berlin, pp 235–239
3. Hussain S, Kumar M (2016) Design of an efficient 8-bit flash ADC for optical communication receivers. In: International conference on electrical, electronics, and optimization techniques (ICEEOT). Chennai, India, pp 449–453
4. Abumurad A, Ozdemir A, Choi K (2019) 10-bit flash ADCs and beyond: an automated framework for TIQ flash ADCs design. Circuits, Syst Signal Process 38(9):4314–4330
5. Lee D, Yoo J, Choi K (2002) Design method and automation of comparator generation for flash A/D converters. In: IEEE international symposium on quality electronic design, pp 138–142

6. Ozdemir Alrizah M, Choi K (2019) Optimization of comparator selection algorithm for TIQ flash ADC using dynamic programming approach. In: IEEE computer society annual symposium on VLSI (ISVLSI). Miami, FL, USA, pp 495–500
7. Lee D, Yoo J, Choi K, Ghaznavi J (2002) Fat tree encoder design for ultra high speed flash A/D converters. In: Proceedings of 2002 MWSCAS, vol 2. Oklahoma, USA, pp II-87-II-90
8. Sall E, Vesterbacka M (2008) Thermometer-to-binary decoders for flash analog-to-digital converters. In: 18th European conference on circuit theory and design. Seville, Spain, pp 240–243
9. Varghese GT, Mahapatra K (2016) A low power reconfigurable encoder for flash ADCs. Global colloquium in recent advancement and effectual researches in engineering, science and technology (RAEREST 2016), Elsevier Procedia Technology, vol 25, pp 574–581
10. Wu L, Huang F, Gao Y, Wang Y, Cheng J (2009) A 42 mW 2 GS/s 4-bit flash ADC in 0.18 μm CMOS. In: International conference on wireless communications and signal processing. Nanjing, China, pp 1–5
11. Varghese GT, Mahapatra K (2016) A low power reconfigurable encoder for flash ADCs. Procedia Technol 25:574–581

Measurement of Heartbeats for Well-Being Assessment Using Photoplethysmographic Signals



Piyush Kumar, Arpan Sharma, Mayanmi Zimik, Shivam Parashar, Renu Singh, Joyatri Bora, Aswini K. Patra, and Madhusudhan Mishra

Abstract Heart rate carries vital information for the diagnosis of cardiac abnormalities. By monitoring the heart rate, one can acquire crucial information regarding the health condition of a person. Expansion and contraction of the heart bring up variations in the volume of the blood flowing through the entire human body. On observing the blood flow via blood vessels, one can determine the rate by which heart pumps the blood. The proposed work built on an embedded platform is aimed to determine the heartbeat counts in order to detect cardiac abnormalities like arrhythmia in real-time scenario. The principle used in this study is based on photoplethysmography (PPG) which is a simple and non-invasive technique to achieve heartbeats information. It calculates the heartbeat by analyzing the change in the volume of blood flowing

P. Kumar · A. Sharma · M. Zimik · S. Parashar · J. Bora · M. Mishra (✉)

Department of Electronics and Communication Engineering, North Eastern Regional Institute of Science and Technology (NERIST), Nirjuli, Arunachal Pradesh 791109, India

e-mail: ecmadvusudhan@gmail.com

P. Kumar

e-mail: piyushkec28@gmail.com

A. Sharma

e-mail: arp.pok52@gmail.com

M. Zimik

e-mail: zimikmayanmi@gmail.com

S. Parashar

e-mail: shivam98.ece@gmail.com

J. Bora

e-mail: bhjoyatri@gmail.com

R. Singh

Department of Electrical Engineering, North Eastern Regional Institute of Science and Technology (NERIST), Nirjuli, Arunachal Pradesh 791109, India

e-mail: renumona08@gmail.com

A. K. Patra

Department of Computer Science and Engineering, North Eastern Regional Institute of Science and Technology (NERIST), Nirjuli, Arunachal Pradesh 791109, India

e-mail: aswinipatra@gmail.com

through the blood vessels. Arteries near the skin of the fingers are used for detection of the pulse. The density of blood in arteries changes with each beat of the heart. This variation is strengthened by the amplifiers and is fed to the microcontroller (Arduino Uno) for further analysis. An LCD display shows the heartbeat rate thereby paving a way to assist medical professionals for reliable and accurate treatment of cardiac abnormalities.

Keywords Heart rate · Arrhythmia · Arduino Uno · Photoplethysmography · Cardiovascular abnormalities

1 Introduction

Heart rate is defined as the rate by which the heart of an individual beats in a minute. It is also known as pulse. It depends on various factors like age, size, emotions, anxiety, body temperature, dehydration, etc. [1]. Generally, the heart rate is low for a healthy person. It is because of the efficient functioning of the heart muscles. A non-invasive technique like the ANFIS system is used to find out fetal heart rate [2]. Some surveys reported that a small increase in blood pressure leads to a rise in the risk of cardiovascular diseases (CVDs) [3]. The normal heartbeats for a human by age are given in Table 1 [4]. Arrhythmia is a very common cardiac disorder in peoples having heart-related issues. It is diagnosed when the heartbeat of a person varies from the normal heartbeat. About 80% of the heart attack incidents are due to arrhythmia, causing 12% of total deaths annually [5].

Arrhythmia may be of different types like bradycardia, tachycardia, premature contraction, atrial fibrillation, and ventricular fibrillation. When the heart rate of an adult goes below 60, then the person suffers from bradycardia. It does not show any symptoms until the heartbeat reaches below 50. The heart rate more than the normal range is referred as tachycardia. Even after so much technical advancement in medical science, cardiac arrest largely affects public health and is the leading cause of death globally [6–10]. A large number of studies have been performed to make arrhythmia detection processes uncomplicated [11–13]. Due to a large number of people who needs continuous monitoring, a self-operating diagnosis system is required. People of any age group may become the victim of arrhythmia. Common arrhythmia symptoms include premature rhythms, fatigue, weariness, giddiness, and

Table 1 Heart rates of healthy human for different age groups [4]

AG	40	45	50	55	60	65	70
AMHR	180	175	170	165	160	155	150
THR	90–153	88–149	85–145	83–140	80–136	78–132	75–128

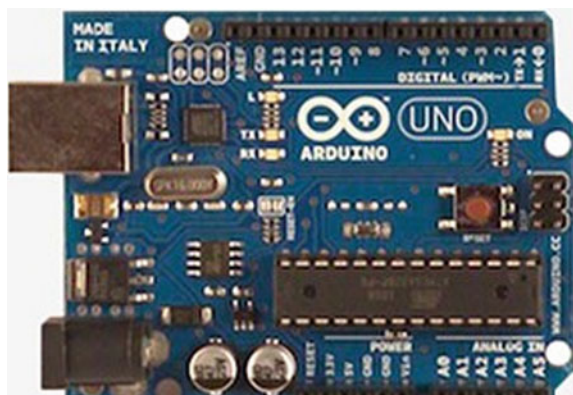
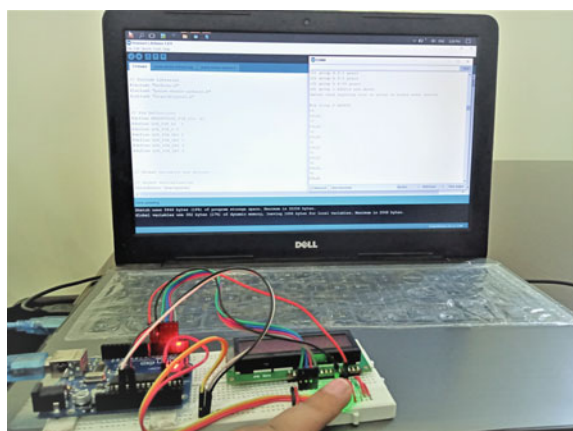
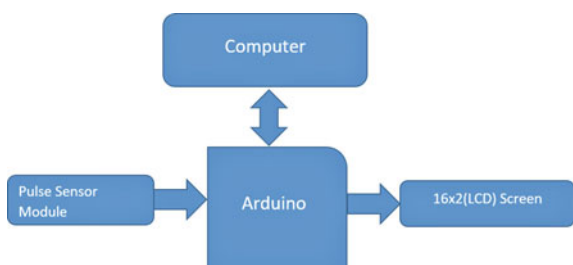
Here, *AG* age group, *AMHR* average maximum heart rate in beats per minute, and *THR* target heart range in beats per minute

fainting. Morphological arrhythmia and rhythmic arrhythmia are the two major categories of arrhythmia. Morphological arrhythmia refers to only one irregular heartbeat, while rhythmic arrhythmia refers consists of a series of irregular heartbeats.

2 Proposed Method

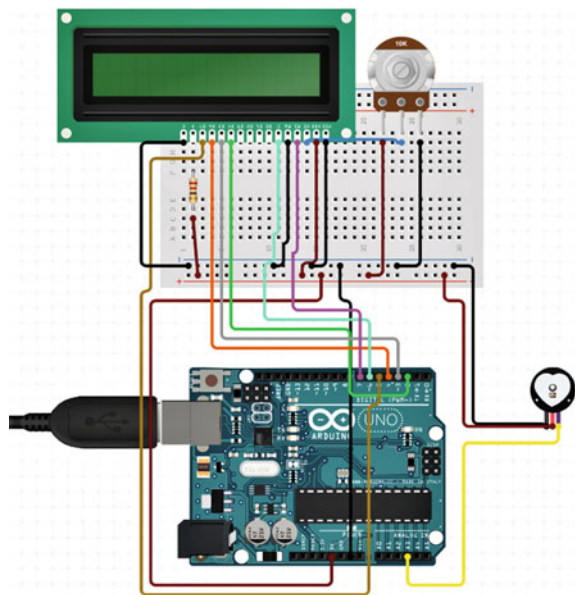
Heart diseases need a routine checkup and proper diagnosis by the physicians. By doing this, doctors can treat patients well. Some diseases like arrhythmia and prehypertension need continuous monitoring by the doctors. Prehypertension does not indicate any symptoms but damages the atrial wall and the nervous system [3]. For this type of diagnosis, a person has to stay in hospitals for a longer duration. This creates many problems such as a shortage of doctors and beds in hospitals for all the patients. Some other patients who need urgent treatment may not get admitted to hospitals. In this case, hospital authority usually discharges patients who are admitted only for medical examination. Due to technological advancement, health centers use wireless communications to control traffic [14]. Heartbeat is also an important parameter to know about the health condition of an individual in this context [15]. Electrocardiogram (ECG) recording-based heart monitoring system employed in hospitals usually leads to discomfort to the patients due to wiring arrangements. It is not applicable to wearable devices. PPG-based instruments are economical, easy to use and portable. PPG uses light rays for diagnosis purpose, and ECG uses electrodes to transmit and receive information. ECG-based bedside cardiac monitoring system mostly shows incorrect values, 86% approximately [16]. The PPG uses optical sensors, so it is used in wearable devices. Our proposed method is based on PPG which has mainly a pulse sensor module, Arduino board, and a display. A typical system comprising of these different units for heart rate measurement using PPG signals is illustrated in Fig. 3. The main objective of the proposed scheme is to measure the heart rates from PPG signals. Pulse sensor consists of light-emitting diode (LED) and light-dependent resistor (LDR), which generates potential difference when a tip of a finger is placed over the sensor for monitoring heartbeat. Arduino is an open-source microcontroller. It is used to design various electronic equipment. It has hardware as well as software. It consists of “Integrated Development Environment” (IDE), which is used to write and upload programs from computer to Arduino board. Arduino does not need separate hardware (programmer) to upload new code onto the board. Uno is the most used board among all in the Arduino family. It is mainly used by the novices because it is cheap and simple to learn (Fig. 2).

Arduino communicates with buttons, LEDs, motors, speakers, camera, GPS units, and even with TVs and smartphones. It has an Atmega 328 which is 28 pin IC consists of 14 digital I/O pins and 6 analog inputs and many more. Arduino Uno operates at a frequency of 16 MHz, and dimension of the board is 68.6×53.44 mm. It has a flash memory of 32 KB out of which 0.5 KB is used by the bootloader [17]. “Liquid crystal display” (LCD) screen is an electronic display unit. It can be found in many circuits wherever a display is required. A “ 16×2 ” LCD is very generic equipment and is

Fig. 1 Arduino Uno board**Fig. 2** Experimental setup for heart rate measurement**Fig. 3** Block diagram of a general system

commonly used in the countless number of devices. LCDs are more advantageous than seven-segment display and other multi-segment LEDs. It is because LCDs are cheap, easy to program, and have no limitations in showing alphabets and numerals and so on. In a “16 × 2” LCD screen, there are two lines. Each line can show 16 characters. To control the flow of current in the circuit, a resistor is used [18] (Fig. 4).

Fig. 4 Interfacing diagram
[17]



Heartbeat sensor converts the change in the amount of blood flowing in the human body into electrical pulses [19]. The sensor unit consists of an LED and LDR. A tip of a finger is placed over the sensor for monitoring heartbeat. LED transmits light, and some parts of it are absorbed by the blood cells inside the arteries within the finger, and rest of the light rays are reflected back to the receiving unit, i.e., LDR. The extent of light received by the LDR rest on the bulk of blood flowing over the arteries. So, when the heart pumps the blood into the body, then the amount of blood in blood vessels also changes. This change in the amount of blood leads to the change in intensity of light captured by blood cells and eventually, it leads to variation in the magnitude of light rays acknowledged by the LDR. The resistance of LDR changes according to the intensity of light received by it. This change in resistance of LDR can be converted into a varying voltage by using op-amps [20]. This change is very small such that it needs to be amplified before feeding into the microcontroller. An amplifier with large gain can amplify these small variations. The amplified signal is passed through a low-pass filter to filter out the unwanted signals. A computer is used to program the Arduino board and to select the age group of the person to be monitored. The low-pass filter consists of two stage op-amps having cutoff frequencies of 2.5 Hz each, which count up to $2.5 * 60 = 150$ BPM.

2.1 Formulae for Counting Heartbeat

$$\text{Pulse } A = \text{time } B - \text{time } A,$$

$$\begin{aligned} \text{Pulse } B &= \text{pulse } A/5, \\ \text{Rate} &= 60,000/\text{pulse } B \end{aligned}$$

where Pulse A = five-pulse time, Pulse B = single pulse time, Time A = first pulse counter value, and Time B = last pulse counter value.

Timer counter starts with the arrival of the first pulse. The first pulse counter value is recorded. After this, counter waits for five pulses. Then, the counter value for Time B is recorded. Time A is subtracted from Time B to get actual time taken by five pulses. Then, this five-pulse time is divided by 5 to get a single-pulse time. Finally, the pulse can be calculated by using the above rate expression, i.e., rate = 60,000/pulse. The pulse sensor module is supplied with 5 V and GND and the signal out pin is applied to A3 pin in Arduino module as an analog input pin. The digital output pins of Arduino pin 4, 5, 6, 7 is connected to dB4, dB5, dB6, dB7 of LCD as a data transfer pins and RS and E of LCD is also connected to the pins of 2 and 3 of digital I/O pins in Arduino module. VCC, GND, and contrast adjustment are also applied to the respective pins of LCD where potentiometer is adjusted to 10 K.

3 Results and Discussions

The heartbeat sensor counts the heartbeat of the patient in a minute and sends it to the filters. The final heartbeat is stored in the Arduino board by using five-pulse formula. Many countries are facing scarcity of doctors and hospitals due to the increase in population. Many patients do not get medical facilities, so this study is aimed to help reduce the crowd. It also decreases the cost of monitoring pulse, because it is a very easy and simple process of doing it. It is also very user-friendly to operate; it does not need any experts to do so. We have monitored the heartbeat of 32 persons of four different age groups. We have also calculated the heartbeat of the athletes, and we got the result as shown in Table 3. We have taken the heartbeat of three infants (0–1 years), eight children of age between 1 and 4 years, and four individuals of age between 4 to 9 years. We have also recorded pulse rate of 17 persons of age above 10 years old.

Finally, in our analysis of 32 different persons, all of them were found to be normal. Arrhythmia was not detected in any of them. These recorded values were cross-validated with the help of a fasttrack reflex smartwatch. The readings of the established market product (smartwatch) were close to that of our proposed method. This study was extended to measure the heat rate of four different persons at two different conditions as depicted in Table 3. The values were close to the readings obtained using smartwatch which validates the effectiveness of our proposed method.

Table 3 shows the heartbeat of three peoples in normal situations and after running for 20 min. The heartbeat of a person increases while running because the body cells demand more oxygen, so the heart starts to pump more blood in order to increase the supply of oxygen and other nutrients to all the cells present in the body. In our

```
Age bar select?  
(1) group A 0-1 years  
(2) group B 1-4 years  
(3) group C 4-9 years  
(4) group D above 10 years  
(5) group E Athletes  
(menu) send anything else or press on board reset button  
  
Now Group D TEEN AND ADULTS  
71  
PULSE  
68  
PULSE  
71  
PULSE  
71  
PULSE  
71  
PULSE  
78  
PULSE  
76  
PULSE  
76  
PULSE
```

Fig. 5 Output displayed on the computer screen of the experimental setup

experiment, all three persons were above 18 years old. The heartbeat of a normal adult person lies between 60 and 100 BPM. From Table 3, we can note that after running when the person is in an idle position or taking rest, the heartbeat starts decreasing and tends to attain normal heartbeat.

4 Conclusion

The significance of this device is that it can reduce the cost of monitoring heart diseases like bradycardia and tachycardia. It also reduces the physician's efforts and helps them to know about the heartbeat of the patients. The device is mobile and cost-efficient and only the knowledge of its working would be enough for a person to even use it at their home without any clinician's help. Thus, it could be also used by the general public who has almost no prior knowledge of medical equipment and terms associated with these diseases. As we are aware of the present-day scenario of

Table 2 Heartbeat recordings of 32 different persons of varying age group using proposed experimental setup

S. no.	Age group	Beats per minute	Status	Arrhythmia
1.	0–1	121	Normal	X
2.	-do-	111	Normal	X
3.	-do-	115	Normal	X
4.	1–4	108	Normal	X
5.	-do-	110	Normal	X
6.	-do-	92	Normal	X
7.	-do-	96	Normal	X
8.	-do-	97	Normal	X
9.	-do-	80	Normal	X
10.	-do-	93	Normal	X
11.	-do-	89	Normal	X
12.	4–9	62	Normal	X
13.	-do-	88	Normal	X
14.	-do-	86	Normal	X
15.	-do-	96	Normal	X
16.	Above 10	68	Normal	X
17.	-do-	71	Normal	X
18.	-do-	68	Normal	X
19.	-do-	61	Normal	X
20.	-do-	82	Normal	X
21.	-do-	92	Normal	X
22.	-do-	91	Normal	X
23.	-do-	98	Normal	X
24.	-do-	97	Normal	X
25.	-do-	69	Normal	X
26.	-do-	60	Normal	X
27.	-do-	62	Normal	X
28.	-do-	67	Normal	X
29.	-do-	61	Normal	X
30.	-do-	98	Normal	X
31.	-do-	99	Normal	X
32.	-do-	69	Normal	X

Table 3 Experimentally recorded four sets of heartbeat (measured per minute) for three different healthy persons at rest and unrest conditions

Heartbeats at rest condition			Heartbeats after running		
Person 1	Person 2	Person 3	Person 1	Person 2	Person 3
78	70	82	144	164	147
68	72	73	143	159	144
80	79	74	130	146	107
74	89	89	107	130	98

the less availability of doctors in many places, especially in the developing countries like India, this type of mobile biomedical devices can be a helpful for the people as well as for the clinicians at the local hospital where no physicians are present. This device is an example of a collaboration of medical science with engineering.

References

- Das S (2013) The development of a microcontroller based low cost heart rate counter for health care systems. *Int J En Trends Technol* 4(2)
- Marchon N, Naik G (2016) Detection of fetal heart rate using ANFIS displayed on a smartphone. In: 2016 IEEE region 10 conference (TENCON), Singapore
- Zhu Y, Chen Y, Qi L, Ma HT (2016) Spectral analysis of heart rate variability and its coherence with pulse transit time variability in prehypertension. In: 2016 IEEE region 10 conference (TENCON), Singapore
- <https://www.health.harvard.edu/heart-health/what-your-heart-rate-is-telling-you>
- Mehra R (2007) Global public health problem of sudden cardiac death. *J Electrocardiol* 40:S118–S122
- Owais V, Abou-Zied AH, Youssef A-BM, Kadah YM (2002) Robust feature extraction from ECG signals based on nonlinear dynamical modeling. In: Proceedings of the 23rd annual international conference of the IEEE, engineering in medicine and biology society
- Mishra M, Banerjee S, Thomas DC, Dutta S, Mukherjee A (2018) Detection of third heart sound using variational mode decomposition. *IEEE Trans Instrum Meas* 67(7):1713–1721
- Kumar P, Parashar S, Gautam AK, Bora J, Mishra M (2019) Techniques for lung sounds analysis to assist medical professionals: a study. *J Anal Comput* 12(1):1–8
- Mishra M, Pratiher S, Banerjee S, Mukherjee A (2018) Grading heart sounds through variational mode decomposition and higher order spectral features. In: 2018 IEEE international instrumentation and measurement technology conference (I2MTC), Houston, TX, pp 1–5
- Paul Nikita et al (2019) Advancements in signal processing techniques for detecting cardiac abnormalities: a study. *J Anal Comput* 12(1):1–9
- de Albuquerque VHC et al (2016) Robust automated cardiac arrhythmia detection in ECG beat signals. *Neural Comput Appl* 1–15
- Kora P, Krishna KSR (2016) ECG based heart arrhythmia detection using wavelet coherence and bat algorithm. *Sens Imaging* 17(1):1–16
- Daamouche A, Hamami L, Aljalil N, Melgani F (2012) A wavelet optimization approach for ECG signal classification. *Biomed Signal Process Control* 7(4):342–349
- Mamoon IA, Islam AKMM, Baharun S, Komaki S, Ahmed A (2016) A novel medical priority aware transmission mechanism for cognitive radio based hospital. In: 2016 IEEE region 10 conference (TENCON), Singapore

15. Jha RS, Singh VP, Mittal VK (2016) Discriminant feature vectors for characterizing ailment cough versus simulated cough. In: 2016 IEEE region 10 conference (TENCON), Singapore
16. Lawless ST (1994) Crying wolf: false alarms in a pediatric intensive care unit. Crit Care Med 22:981–985
17. Arduino Uno board specifications. <https://www.edgefx.in/arduino-uno-board-tutorial-and-its-applications/>
18. Burke MJ, Whelan MV (1987) The accuracy and reliability of commercial heart rate monitor. 21(1):29–32
19. Fezari M, Bousbia-Salah M, Bedda, M (2008) Microcontroller based heart rate monitor. Inte Arab J Inf Technol 5(4)
20. Adams TD, Yanowitz FG, Fisher AG, Ridges JD, Lovell K, Pryor TA, (1981 Noninvasive evaluation of exercise training in college-age men. Circulation 64:958–965

An Iterative Node-Pair Time Synchronization (INTS) for Wireless Sensor Networks



Sakuru K. L. V. Sai Prakash and N. Bheema Rao

Abstract An essential function of the spread sensor network is time synchronization. This paper presents a novel iterative node-pair time synchronization (INTS) algorithm that assists the sensor nodes in collaborating with the anchor node in synchronizing its clock. Even though the clocks on anchor and the sensor nodes are presumed to set to the universal time, they invariably have a different offset. However, in the present formulation, we make a simplifying assumption that all the anchor clocks and all the sensor clocks run at the same speed and taken as one. The varying clock offsets could lead to inconsistencies in data gathering in a distributed environment. A synchronization mechanism for a global ordering of the packets generated at different nodes is essential. Bounded but variable delays during the exchange of message packets between the sensor nodes prevent the determination of the exact clock offsets between the anchor transmitting node and the senor receiving nodes. Our algorithm tries to handle this problem by limiting the uncertainty bounds to minimum application-specific value by an iterative method. Finally, we present the simulation and the analytical results, which are identical and encouraging.

Keywords Time synchronization · Anchor node · Sensor node · Iterative · Uncertainty

1 Introduction

Effective collaboration and collection of data by the small form factor sensor nodes in the sensor field play an imperative role in sensor networks. Sensor nodes are composed of sensors and actuators, the computational module (microcontroller and

S. K. L. V. Sai Prakash (✉) · N. Bheema Rao

Department of Electronics & Communication Engineering,

National Institute of Technology, Warangal, Telangana State 506004, India

e-mail: sai@nitw.ac.in

N. Bheema Rao

e-mail: nbr@nitw.ac.in

memory), a communication module, and a power supply. To make the right interpretation of the data collected by the nodes, the time on the sensor nodes play a crucial role. In a distributed environment, any two sensor nodes will not have the same clock showing the same time, as different oscillators drive them. To fulfill the application demand, time synchronization of the distributed sensor nodes is of utmost priority. Time synchronization algorithms, contrarily, yield a beneficial solution to keep every networked node to the coincident time scale concerning a common clock. Typical cases to point up the need for time synchronization are:

1. Localization: The location of the randomly deployed distributed sensor nodes heavily depend on time synchronization. As the data generated by the node should have a tag from which location it belongs to, the node location plays a vital role. The localization algorithms use time of arrival information to calculate the position from different nodes; a firm agreement of time between the nodes highly required.
2. Network access: Scheduling and accessing the network in time division also demands a highly time-synchronized sensor network. Time-synchronized media sharing sensor nodes coordinate for collisions avoidance and conserve energy, as presented in Fig. 1.
3. The lifetime of sensor nodes: Duty cycling making the nodes to sleep and making them wake up for reception and transmission of packets will extend the life of the sensor node and also the network. For this operation, tight time synchronization is required.
4. Target localization: When a set of sensor nodes are trying to localize the target, time synchronization plays an essential role in calculating the position, direction, and velocity, as presented in Fig. 2.

Because of the importance of time synchronization, as illustrated by the above examples, we have developed a novel time synchronization algorithm that addresses the problem due to different offsets of the individual clocks.

The remaining of the paper written as follows: Sect. 2, a brief survey of the related work presented, and we introduce the system model, terminologies, and algorithm in Sect. 3. An iterative node-pair time synchronization procedure and statistical analysis are explained in Sect. 4. Discussion on the results is in Sect. 5, and finally concludes with the future direction of our work in Sect. 6.

Fig. 1 TDMA frame structure

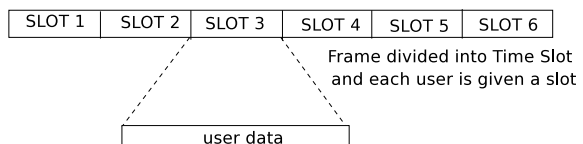
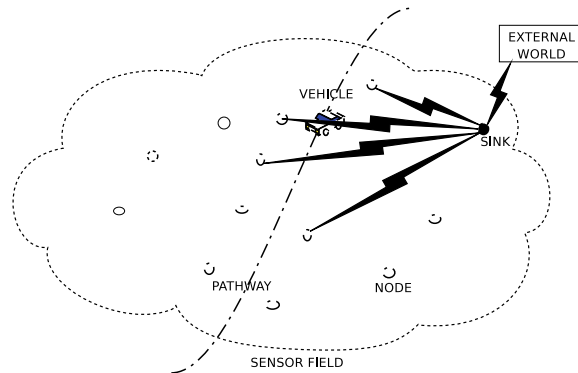


Fig. 2 Target localization

2 Related Work

For the last few years, several time synchronization algorithms have been proposed and evaluated for the performance of sensor networks. Most existing synchronization schemes considered a time-stamped message exchange process for obtaining the offset between two clocks in the distributed environment and used it as a correction factor. The exchange process can, therefore, classified as uni-directional, bidirectional, and receiver–receiver protocols [1, 2]. The network time protocol [3] and the global positioning system are not suitable for sensor nodes as they are power hungry and energy consuming. The predominant time synchronization algorithms, such as RBS [4], TPSN [5], DTSP [6], and FTSP [7], are all based on timestamp exchanges and tried to eliminate the uncertainty in exchange process such as: sent, access, propagate, and receive delays. The authors in RBS protocol [4] uses the broadcast nature of the wireless media to bring down the delays in the synchronization procedure. The reference node transmits a sync time-stamped message and the same received by every node in the communication range of the reference node. The nodes which received the packet note the arrival time and exchange this information among all the recipients and use it for finding the offset among themselves. In this method, the delays which are common at the transmitting side are eliminated, and only receiver side delay exists. The authors in the DTSP protocol [6] uses multiple transmitter timestamps and receiver timestamps at each receiver node and perform recursive least squares estimate to calculate associated time offsets and skews. The authors in the TPSN protocol [5] find the root node and generated a spanning tree. Under the assumption that all are symmetrical links in the spanning tree, a node-pair synchronization is run long the branch of tree between parent node and child node, and round trip measurements are performed. The communication overhead when compared to RBS, TPSN is more, and the node failure, makes the whole process of tree formation to repeat. The authors in the FTSP protocol [7] select the node having lowest ID as the reference node, and use its time as the reference for synchronization. The reference node periodically broadcasts the time-stamped messages. The receiver nodes

use these timestamps to calculate the offset and skew by linear regression. As the messages are periodically flooded, the node failure does not affect the performance of the algorithm.

Localization and synchronization in sensor networks are well studied and have many similarities, such as the message exchange process and use of mathematics to estimate position and time. Due to this correlation, a small survey of the literature on localization carried out.

In Refs. [8–10], iterative localization, range-free localization, and distributed localization algorithms are discussed. The authors in the iterative localization [5] uses a one-dimensional array of sensor nodes randomly placed and found the location of the nodes, using a communication range as a disk. Based on the disk information, an intersection method used to get the location information. Once the nodes are localized, they help the neighbor nodes to localize. The authors in the range-free localization [4] uses a two-dimensional array of sensor nodes randomly placed and found the location of the nodes, using a communication range as a circular disk. Based on the disk area intersection method, the location information is calculated. Once the nodes are localized, they help the neighbor nodes to localize. The authors in the distributed localization [11] uses a two-dimensional array of sensor nodes randomly placed found the location of the nodes. The unlocalized nodes only iteratively talk with localized nodes and use correlation technique to find their locations. A square intersection model is considered.

3 Terminology, System Model, and Algorithm

The distributed clocks which are present on the sensor nodes are to be synchronized utilizing message packet transmissions that undergo variable delays [4–7]. One transmission is sufficient if the application-dependant clock accuracy is more than the delay.

Considering node-pair for the time synchronization procedure, assuming the transmitter node referred to as anchor node represented by A and the clock on it by t_A , and receiver node referred to as sensor node by R and the clock on it by t_R are related as:

$$t_R(n) = m * t_A(n) + O + \delta(n) \quad (1)$$

where m defined as relative slope, O defined as relative offset, δ defined as the random transmission delay of the message packet amid the anchor node and the receiver node, and n is the n th packet transmissions. These delays hamper the synchronization process and consist of many components, inclusive of the sender processing delay caused by kernel processing, system calls, and context switches which are dependent on node load processing; media accessing delay depends on the MAC procedure and network load, media transmission delay by the radio frequency signal to transit from anchor to receiver node, receiver receiving delay at the receiver node, the time captured to receive the complete message and translate.

If the clocks on both the nodes are moving at the same frequency, i.e., m is 1, the relative offset is given by:

$$O = t_R(n) - t_A(n) - \delta(n) \quad (2)$$

If the clocks on both the nodes have no offset, i.e., O is 0, the relative skew is given by:

$$m = \frac{t_R(n) - \delta(n)}{t_A(n)} \quad (3)$$

We assume $\delta(n) \in [p_{\text{ar}}, P_{\text{ar}}]$ and $0 \leq p_{\text{ar}} \leq P_{\text{ar}} < \alpha$, i.e., $\delta(n)$ are bounded random variables and that p_{ar} and P_{ar} are known. Then, after receiving n time-stamped message packets, offset O should satisfy

$$O \in [t_R(n) - t_A(n) - p_{\text{ar}}(n), t_R(n) - t_A(n) - P_{\text{ar}}(n)] \quad \text{for } 1 \leq n \leq x \quad (4)$$

where x is the max value where the iterative process stops when the application specific uncertainty value is reached.

This means $O \in [\overline{O(n)}, \underline{O(n)}]$ where,

$$\overline{O(n)} = \max_{1 \leq n \leq x} \{t_R(n) - t_A(n)\} - P_{\text{ar}} = O - (P_{\text{ar}} - \max_{1 \leq n \leq x} \{\delta(n)\}) \quad (5)$$

$$\underline{O(n)} = \min_{1 \leq n \leq x} \{t_R(n) - t_A(n)\} - p_{\text{ar}} = O - (\min_{1 \leq n \leq x} \{\delta(n)\} - p_{\text{ar}}) \quad (6)$$

Let $\tilde{O}(n) := \overline{O(n)} - \underline{O(n)}$ denote the width of uncertainty in our estimate of O offset after n timestamps were received. The \underline{O} corresponds the left lower bound, and from here on, it will be represented as Le; \overline{O} corresponds the right upper bound of uncertainty interval and from hereon represented as Ri. Then, we have $\tilde{O}(n) = (P_{\text{ar}} - p_{\text{ar}}) - (\max_{1 \leq n \leq x} \delta(n) - \min_{1 \leq n \leq x} \delta(n))$. Note that, we have not made any assumptions on the random sequence $\delta(n)$ of delays experienced by the timestamp packets except that they are bounded.

4 Mathematics

4.1 Estimation Procedure

Let anchor node A be transmitting clock messages, and the same is collected by the sensor node R. The 1st timestamp message of the anchor node A is designated by $t_A(1)$, and the 1st packet collection time by the sensor node R is designated $t_R(1)$. The $\delta(1)$ is the random delay which is contributed by all the delays, experienced by the 1st packet at the destination sensor node R from the anchor node A and is

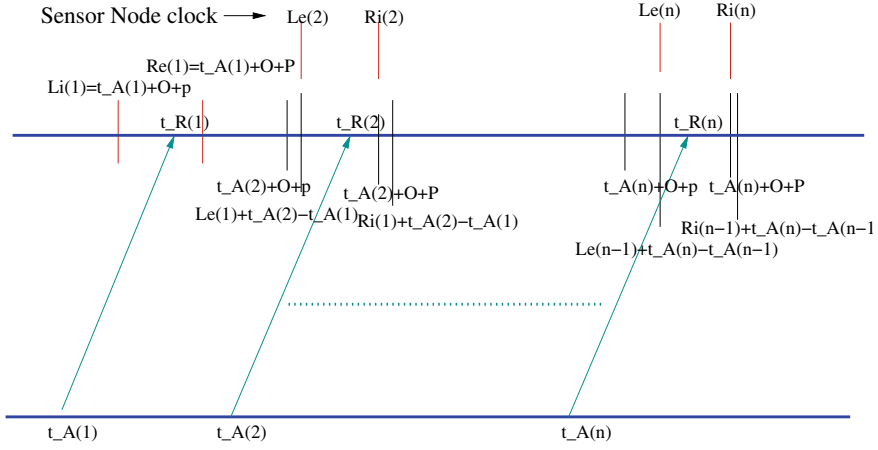


Fig. 3 Iterative time synchronization

confined by $[p_{ar}, P_{ar}]$. Given single anchor node A and single sensor node R pair under study, we discard the subscripts of the random delay bounds.

After first packet transmission, time $t_R(1)$,

$$t_R(1) \in [t_A(1) + O + p, t_A(1) + O + P] \quad (7)$$

$$Le(1) = \max\{t_A(1) + O + p, 0\} \quad (8)$$

$$Ri(1) = \min\{t_A(1) + O + P, \infty\} \quad (9)$$

under the assumption, the starting time of sensor R can be anywhere between $[0, \infty]$ (Fig. 3).

After second packet transmission, time $t_R(2)$,

$$t_R(2) \in [t_A(2) + O + p, t_A(2) + O + P] \quad (10)$$

and from advancing the first packet $t_R(2)$ lies in

$$t_R(2) \in [t_A(1) + O + p + t_A(2) - t_A(1), t_A(1) + O + P + t_A(2) - t_A(1)] \quad (11)$$

Now

$$Le(2) = \max\{t_A(2) + O + p, t_A(1) + O + p + t_A(2) - t_A(1)\} \quad (12)$$

$$Ri(2) = \min\{t_A(2) + O + P, t_A(1) + O + P + t_A(2) - t_A(1)\} \quad (13)$$

now substituting Eqs. 8 and 9

$$\text{Le}(2) = \max\{t_A(2) + O + p, \text{Le}(1) + t_A(2) - t_A(1)\} \quad (14)$$

$$\text{Ri}(2) = \min\{t_A(2) + O + P, \text{Ri}(1) + t_A(2) - t_A(1)\} \quad (15)$$

After n th packet transmission, time $t_R(n)$,

$$t_R(n) \in [\text{Le}(n), \text{Ri}(n)] \quad (16)$$

where

$$\text{Le}(n) = \max\{t_A(n) + O + p, \text{Le}(n-1) + t_A(n) - t_A(n-1)\} \quad (17)$$

$$\text{Ri}(n) = \min\{t_A(n) + O + P, \text{Ri}(n-1) + t_A(n) - t_A(n-1)\} \quad (18)$$

The important point here is to get the random variables and from Eqs. 17 and 18

$$\text{Le}(n) = t_A(n) + O + p + \delta(n) - \min\{\delta(n), \delta(n-1), \dots, \delta(1)\} \quad (19)$$

$$\text{Ri}(n) = t_A(n) + O + P + \delta(n) - \max\{\delta(n), \delta(n-1), \dots, \delta(1)\} \quad (20)$$

The uncertainty interval width $Z(n)$ can therefore be written as

$$Z(n) = \text{Ri}(n) - \text{Le}(n) \quad (21)$$

$$\begin{aligned} Z(n) &= P - p - \max\{\delta(n), \delta(n-1), \dots, \delta(1)\} \\ &\quad + \min\{\delta(n), \delta(n-1), \dots, \delta(1)\} \end{aligned}$$

If the a-priori bounds are accurately selected, it is intuitively clear that \max will go close to P and \min will go close to p , thereby $Z(n)$ converges to zero.

4.2 Statistical Analysis

Let

$$X(n) = \max\{\delta(n), \delta(n-1), \dots, \delta(1)\} \quad (22)$$

$$Y(n) = \min\{\delta(n), \delta(n-1), \dots, \delta(1)\} \quad (23)$$

Then

$$Z(n) = (P - p) - (X(n) - Y(n)) \quad (24)$$

Let $\delta(1), \delta(2), \dots, \delta(n)$ be independent random variables with identically distributed and has similar probability density function $f(z)$ and distribution function $F(z)$ having span $[p, P]$. Expectation of Z will be

$$E[Z] = (P - p) - E[X - Y] \quad (25)$$

Being continuous, the joint pdf of $F_{XY}(x, y)$ is

$$f_{XY}(x, y) = -\frac{\partial^2}{\partial x \partial y} \Pr[X \leq x, Y \geq y] \quad (26)$$

All the n random delays are i.i.ds, and variables possess similar PDF $f(z)$ with the support $[p, P]$.

$$\Pr[X \leq x, Y \geq y] = [F(x) - F(y)]^n \quad (27)$$

Differentiating

$$\frac{\partial^2}{\partial x \partial y} [F(x) - F(y)]^n = n(n-1)(F(x) - F(y))^{n-2} f(x)f(y) \quad (28)$$

The joint pdf

$$f_{XY}(x, y) = \begin{cases} n(n-1)(F(x) - F(y))^{n-2} f(x)f(y) & x \geq y \\ 0 & x \leq y \end{cases} \quad (29)$$

Expectation value of $[X - Y]$ is

$$\begin{aligned} E[X - Y] &= \int_{x \geq y} (x - y) f_{XY}(x, y) dx dy \\ &= n(n-1) \int_{x=p}^P \int_{y=p}^x (x - y)((F(x) - F(y))^{n-2} f(x)f(y)) dx dy \end{aligned}$$

Assuming uniform density in $[p, P]$, the distribution becomes

$$F(z) = \frac{z - p}{P - p} \quad z \in [p, P] \quad (30)$$

Expectation of $[Y - Z]$ is derived as

$$E[X - Y] = \frac{(n-1)(P-p)}{n+1} \quad (31)$$

Expectation of Z is shown by

$$E[Z] = \frac{2(P - p)}{n + 1} \quad (32)$$

The variance of Z is given by

$$\text{Var}[Z] = E[Z^2] - [E[Z]]^2 \quad (33)$$

$$= \frac{2(P - p)^2(n - 1)}{(n + 1)^2(+2)} \quad (34)$$

5 Results

The novel iterative node-pair time synchronization algorithm has analytically computed, and the same is simulated in MATLAB software. The uncertainty a-priori bounds considered as 0.3-time units as the lower bound and 0.9-time units as the upper bound. The anchor node transmits time-stamped message packets periodically with a regular interval of the 1-time unit. The process was monitored for the behavior of the uncertainty width as the message transmission packets are incremented. The i.i.d random delays assumed to take uniform density function with the above uncertainty support. Both the analytical and simulation studies carried out considering uniform distribution with the support of 0.3 and 0.9-time units and measurements made over 100 packets, as shown in Fig. 4.

The same is drawn in the log-log scale for the bounds on uncertainty interval with 0.3 and 0.9-time units and over 1000 transmission message packets. The graph is shown in Fig. 5:

6 Conclusion and Future Work

We present here an iterative node-pair time synchronization algorithm motivated by the localization methods in the WSN literature. Even though it is a node-pair time synchronization, it can also view it as a one to many single-hop synchronization approaches. It reduces the voluminous transmission, thereby reducing the energy at the forfeiture of the enhanced computation. From Fig 4, we can conclude that if the data of the uncertainty width of the interval, if carefully selected, they would much impact the convergence curve. The analytical and simulation results show that approximately 20 anchors transmitted time-stamped message packets are in a single-hop network for 10-time units to 1-time unit reduction in the uncertainty with the node clock times. This profound yield improvements compared to RBS method need 30 message packets for a pair of receivers, thereby reducing the uncertainty

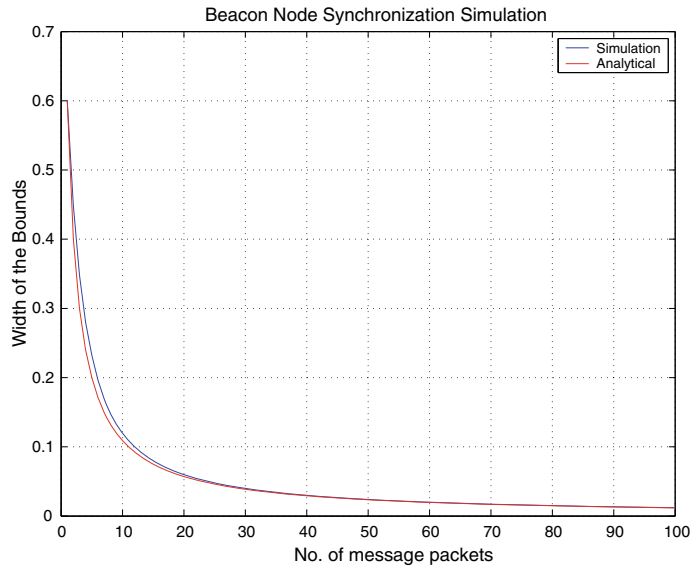


Fig. 4 Convergence characteristics

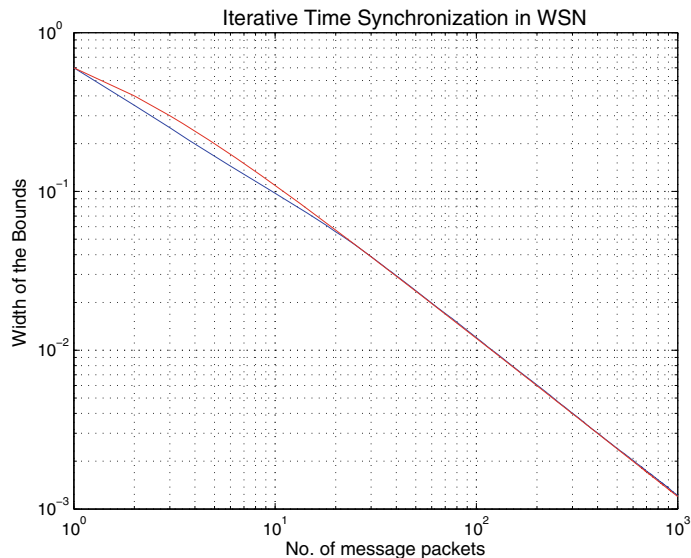


Fig. 5 Log–log convergence characteristics

width from 11-time units to 1.6-time units. Our INTS protocol uses unidirectional communication, while TSPN protocol employs bidirectional communication. Thus, our protocol halves of the transmission messaging time and thus increasing energy efficiency. The construction of a spanning tree process not necessary. In our method, the messages are broadcasted periodically by the anchor node in predetermined time periods, tree reformation either not required, in the event of failed node. The FTSP authors claimed a minimum requirement of six message packets for uncertainty reduction 10 to 1-time unit. Though these results seem to be better than ours, election procedure in the FTSP method incurs much communication and computational overhead. The clocks in FTSP only synchronized to the leader local time rather than global time. In our INTS protocol, GPS assumed to be present at the anchor node, and the time is universal. Every sensor node in the sensor network gradually synchronized to the global time present with the anchor node. The results are encouraging us to extend the work for whole network synchronization, and various strategies to cover the entire network are to be studied.

References

1. Simic S, Shankar Sastry S (2002) Distributed localization in wireless ad hoc networks. Technical report No. UCB/ERL M02/26. EECS Department, University of California, Berkeley
2. Feng Z, Leonidas G (2005) Infrastructure establishment, chapter 4, wireless sensor networks: an information processing approach. Elsevier
3. Sundararaman B, Buy U, Kshemkalyani AD (2005) Clock synchronization for wireless sensor networks: a survey. Elsevier J Adhoc Netw 3(3):281–323. <https://doi.org/10.1016/j.adhoc.2005.01.002>
4. Sivrikaya F, Yener B (2004) Time synchronization in sensor networks: a survey. IEEE Netw 18(4):45–50. <https://doi.org/10.1109/MNET.2004.1316761>
5. Mills DL (1994) Precision synchronization of computer network clocks. ACM SIGCOMM Comput. Commun. Rev. <https://doi.org/10.1145/185595.185651>
6. Jeremy E, Lweis G, Deborah E (2002) Fine grained network time synchronization using reference broadcasts. ACM SIGOPS Oper Syst Rev. <https://doi.org/10.1145/844128.844143>
7. Ganeriwal S, Kumar R, Srivastava MB (2003) Timing-sync protocol for sensor networks. In: SenSys'03: proceedings of the 1st international conference on embedded networked sensor systems, Nov 2003, pp 138–149. <https://doi.org/10.1145/958491.958508>
8. Solis R, Borkar VS, Kumar PR (2007) A new distributed time synchronization protocol for multihop wireless networks. In: 45th IEEE conference on decision and control. <https://doi.org/10.1109/CDC.2006.377675>
9. Miklos M, Branislav K, Gyula S, Akos L (2004) Protocol the flooding time synchronization, SenSys'04. Baltimore, Maryland, USA
10. Karnik A, Kumar A (2004) Iterative localization in wireless ad hoc sensor networks: one dimensional case. In: IEEE SPCOM, international conference on signal processing and communications, Dec 2004. <https://doi.org/10.1109/SPCOM.2004.1458387>
11. Stupp G, Sidi M (2004) The expected uncertainty of range free localization protocols in sensor networks. In: International symposium on algorithms and experiments for sensor systems, wireless networks and distributed robotics, ALGOSENSORS 2004. <https://doi.org/10.1016/j.tcs.2005.06.025>

Image Captioning Methodologies Using Deep Learning: A Review



Virendra Kumar Meghwal, Namita Mittal, and Girdhari Singh

Abstract Image captioning involves knowledge of both “Computer Vision” as well as “Natural Language Processing” to generate a caption for digital images. Various approaches have been used to generate captions for images. Among them, Deep Learning based approaches have shown impressive results in image captioning. This paper presents a concise review of recent image captioning methodologies based on Deep Learning to automatically generate captions and discusses the datasets and the evaluation metrics that are used to evaluate various methodologies in image captioning.

Keywords Image caption · Visual attention · Semantic attention · Deep Learning · CNN · LSTM

1 Introduction

Computer Vision deals with the study of digital images and videos in order to understand the content in them, so as to enable computers to understand images and videos like humans do. While, Natural Language Processing deals with the understanding of Natural Languages (languages used by humans), so as to enable the computer to interact with humans. Image captioning combines both these fields of study to enable the computer to generate captions for images. As both these tasks are difficult for computers, thus image captioning is a much more difficult and complex task for computers as it combines them both.

Image captioning using Deep Learning approaches automatically learns to extract various features from the data and then these features are used to generate captions for

V. K. Meghwal · N. Mittal (✉) · G. Singh
Malaviya National Institute of Technology, Jaipur, India
e-mail: nmittal.cse@mnit.ac.in

V. K. Meghwal
e-mail: 2018rcp9061@mnit.ac.in

G. Singh
e-mail: gsingh.cse@mnit.ac.in

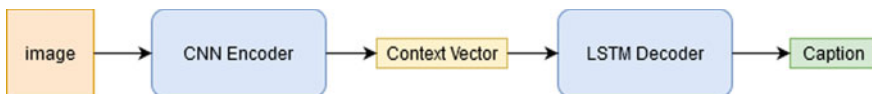


Fig. 1 A general image captioning framework

the given image. Most of these approaches use encoder–decoder framework (Fig. 1). In this framework, the input image is first fed into an encoder. The encoder, which is generally a CNN, finds various features and encodes it into a vector called context vector. This vector is passed as an input to the decoder, which decodes it and generates an appropriate caption for the given image. Attention-based encoder–decoder models instead of taking context vector as input, takes input from the last convolution layer of the CNN Encoder, so as to preserve spatial details of various features (Fig. 1).

2 Datasets

There are a few open-source datasets that are available to be used for image captioning. Three of them are listed below.

2.1 *Mscoco [1]*

This is the largest dataset available for image captioning. It contains around 330 K images and five captions per image. Most researchers who are working on image captioning prefer to work on this dataset as it is the largest dataset and has lesser noisy data.

2.2 *Flickr30k [2]*

This is the second most popular dataset in the image captioning domain. It contains around 31,783 images, with 158,915 crowd-sourced captions describing them.

2.3 *Flickr8k [3]*

It is a predecessor of the Flickr30k dataset. It contains eight thousand images with five captions each.

3 Evaluation Metrics

3.1 *Bleu* [4]

BLEU stands for Bi-lingual Evaluation Understudy. This evaluation metrics is popular in machine translation. As, the earlier no better metric was available for measuring image captioning, so BLUE was used for this purpose. It does not take grammatical correctness of sentences into account. It ranges from 0 to 1.

3.2 *Rouge* [5]

Recall-Oriented Understudy of Gisting Evaluation is a popular metric for summarization evaluation. It ranges from 0 to 1.

3.3 *Meteor* [6]

It stands for Metric for Evaluation of Translation with Explicit ORdering. It was developed for measuring machine translation. Compared to BLUE, it has a significantly better correlation with human judgments.

3.4 *CIDEr* [7]

Consensus-based Image Description Evaluation was developed for evaluating image captioning. It measures the similarity of a generated sentence against a set of ground-truth sentences written by humans.

3.5 *Spice* [8]

Semantic Propositional Image Caption Evaluation was developed for evaluating image captioning. It is based on semantic scene graphs and has shown that it correlates much better with human judgments.

4 Methods

Various methodologies have been proposed for generating captions from images. A few of the recent methodologies are discussed below.

Huang et al. [9] proposed a pipelined framework consisting of two cascaded agents in the decoder. In this model, the image is encoded using a Faster-RCNN, this encoded vector is then passed to the decoder for caption generation. The decoder consists of a semantic adaptive agent and a caption generating agent. In the semantic adaptive agent, this encoding is passed to an LSTM, the output of the LSTM is fed into the visual attention module to generate a vector which is passed to the semantic adaptive attention module along with the output of the LSTM to generate the output vector of the semantic adaptive agent. This output vector is then passed to the caption generating agent which consists of an LSTM followed by softmax, to generate the caption. Peri et al. [10] used a CNN for encoding image and an LSTM for encoding captions (during training) and then these features were projected into a Common Vector Space which aligns similar or correlated concepts in images and texts and dissimilar ones far apart. This CVS representation is then used by decoder LSTM to generate semantically similar captions. Huang et al. [11] proposed an attribute refinement network to model the correlation between attributes. For this, they utilized joint training on images and captions which helped them to boost the performance of their model. They used image features, object features and attribute distribution in their model. The model employs a combination of an attention LSTM, a visual attention module, a language LSTM along with attribute refinement and semantic attention to generate captions. He et al. [12] proposed Visual-Semantic Double Attention (VSDA) model with a new semantic attention model. This model uses two CNNs to extract visual attention features and semantic attention features which are then fed as an extra input to the LSTM for generating caption. These extra inputs help the LSTM to recognize the relevant semantic features and reduce the effect of irrelevant features. Shi et al. [13] proposed a cascade attention module that enables high priority inputs to affect the attention of other inputs to emphasize inequality among inputs. In this model, the encoder uses a Faster-RCNN to extract a feature vector representing features of each region of interest. Another feature vector representing features of the global context in the image is also extracted by encoder. The decoder consists of a cascaded attention module and two LSTMs—Language LSTM and Attention LSTM. In the decoder, the cascaded attention module attends to these regions of interest and global context based on the hidden state of the attention LSTM. The language LSTM builds a visual sentinel vector to represent semantic context information which helps to determine whether the language LSTM requires the visual features as input or not. Based on this language LSTM generates each output word of the caption.

Zhang et al. [14] combined spatial and adaptive attention into a transformer. This model uses a CNN to extract the image features into a context vector which is then fed into the adaptive transformer in place of LSTM in the decoder to generate captions. The transformer helps the model to determine when and where to use image features

and achieved better performance and boost in training speed. Li et al. [15] proposed a visual-semantic LSTM model. They used Region Proposal Network to extract low-level features and a CNN to extract high-level features. The low-level features are passed to LSTM-V to localize the objects in the image. The output of LSTM-V and the high-level features generated by CNN are passed to LSTM-S to generate the corresponding words in the caption.

5 Comparison of Evaluation Metrics

See Tables 1 and 2.

Table 1 Comparison among few recent methodologies in image captioning (dataset: MSCOCO)

Approach name	Methodology	Results
Show, translate and tell [10]	CNN + common vector space + RNN	B1 = 70.6, B2 = 53, B3 = 38.5, B4 = 27.9, M = 24.6
Visual-semantic double attention [12]	CNN (visual-semantic attention) + LSTM	B1 = 75.3, B2 = 59.1, B3 = 45.1, B4 = 34.4, M = 26.5, R = 55.2, C = 106.3
Attribute refinement [11]	CNN + visual Att + attribute refine + semantic Att + LSTM	B1 = 77, B2 = 61, B3 = 47.1, B4 = 36.3, M = 27.6, R = 56.6, C = 115.1, S = 20.9
Cascade attention [13]	R-CNN + cascade Att + (lang LSTM + Att LSTM)	B1 = 79.4, B2 = 63.7, B3 = 48.9, B4 = 36.9, M = 27.9, R = 57.7, C = 122.7
Two Cascaded Agents [9]	CNN + visual Att + LSTM + semantic Att + LSTM	B1 = 80.6, B4 = 38.2, M = 28.3, R = 58.4, C = 126.4, S = 21.7

Table 2 Comparison among few recent methodologies in image captioning (dataset: Flickr30k)

Approach name	Methodology	Results
Show, translate and tell [10]	CNN + common vector space + RNN	B1 = 61.1, B2 = 42.7, B3 = 29.3, B4 = 20.3, M = 19.3
Adaptive transformer [14]	CNN + transformer	B1 = 67, B2 = 49.6, B3 = 35.5, B4 = 25.2, M = 20.4, C = 53
Visual-semantic double attention [12]	CNN (visual-semantic attention) + LSTM	B1 = 68.1, B2 = 49.8, B3 = 35.7, B4 = 25.6, M = 20.8, R = 47.4, C = 53.2
Visual-semantic LSTM [15]	(Region proposal network + CNN) + LSTM	B1 = 75.5, B2 = 57.1, B3 = 42.9, B4 = 31.7, M = 22.9, C = 71.5

6 Conclusion

A lot of effort has been put by researchers in image captioning, thus, resulting in a vast improvement over the past few years. This paper reviewed some of these recent methodologies used in the image captioning domain. Despite the vast improvement, there is still scope for improvement in methodologies. Further research direction may be an improvement in visual and semantic attention, evaluation metric, etc.

References

1. MSCOCO Homepage. <http://cocodataset.org/>. Last accessed 02 Oct 2019
2. Plummer BA, et al (2015) Flickr30k entities: Collecting region-to-phrase correspondences for richer image-to-sentence models. In: Proceedings of the IEEE international conference on computer vision
3. Hodosh M, Young P, Hockenmaier J (2013) Framing image description as a ranking task: data, models and evaluation metrics. *J Artif Intell Res* 47:853–899
4. Papineni K, et al (2002) BLEU: a method for automatic evaluation of machine translation. In: Proceedings of the 40th annual meeting on association for computational linguistics. Association for Computational Linguistics
5. Lin CY (2004) Rouge: a package for automatic evaluation of summaries. Text summarization branches out
6. Banerjee S, Lavie A (2005) METEOR: an automatic metric for MT evaluation with improved correlation with human judgments. In: Proceedings of the ACL workshop on intrinsic and extrinsic evaluation measures for machine translation and/or summarization
7. Vedantam R, Lawrence Zitnick C, Parikh D (2015) Cider: consensus based image description evaluation. In: Proceedings of the IEEE conference on computer vision and pattern recognition
8. Anderson P, et al (2016) Spice: semantic propositional image caption evaluation. In: European conference on computer vision. Springer, Cham
9. Huang L, Wang W, Wang G (2019) Image captioning with two cascaded agents. ICASSP 2019 IEEE international conference on acoustics speech and signal processing (ICASSP). IEEE
10. Peri D, Sah S, Ptucha R (2019) Show, translate and tell. arXiv preprint [arXiv:1903.06275](https://arxiv.org/abs/1903.06275)
11. Huang Y, et al (2019) Image captioning with attribute refinement. In: 2019 IEEE international conference on image processing (ICIP). IEEE
12. He C, Hu H (2019) Image captioning with visual-semantic double attention. *ACM Trans Multimed Comput Commun Appl (TOMM)* 15(1):26
13. Shi J, Li Y, Wang S (2019) Cascade attention: multiple feature based learning for image captioning. In: 2019 IEEE international conference on image processing (ICIP). IEEE
14. Zhang W, et al (2019) Image caption generation with adaptive transformer. In: 2019 34rd youth academic annual conference of Chinese association of automation (YAC). IEEE
15. Li N, Chen Z (2018) Image captioning with visual-semantic LSTM. IJCAI

Performance of Speaker Recognition System Using Kernel Functions Approach for Different Noise Levels



Renu Singh, Arvind Kumar Singh, and Utpal Bhattacharjee

Abstract Speaker recognition is one of the most popular voices biometric technique used for security reason in many areas like banking system, online-shopping, database access etc. The recognition performance of speaker recognition system is very satisfactory in noise-free environments, whereas the improved performance in case of low level signal-to-noise ratio (SNR) is the need in the present days. Hence, in this study speaker recognition performance has been evaluated at different signal-to-noise ratios using SVM-based various kernel functions approach and principal component analysis (PCA). The proposed scheme has been applied on NIST 2003 and AURORA dataset and found that the recognition accuracy and running time improves at low level SNRs using kernel functions.

Keywords Speaker recognition system · SVM · Principle component analysis (PCA) · Signal-to-noise ratio

1 Introduction

Speaker recognition is a method of recognizing a speaker's voice by utilizing explicit information comprised in speech waves [1, 2]. This methodology can be used to substantiate the characteristics claimed by the person who wants to access the systems i.e. enabling the access control of different services with the help of voice. The various applications of speaker recognition system are voice dialing, phone banking, shopping over phone, database access services, reservation services, services on voice mail

R. Singh (✉) · A. K. Singh

Department of Electrical Engineering, North Eastern Regional Institute of Science and Technology, Nirjuli, Arunachal Pradesh 791109, India

e-mail: renumona08@gmail.com

A. K. Singh

e-mail: singharvindk67@gmail.com

U. Bhattacharjee

Department of Computer Science, Rajiv Gandhi University, Itanagar, Arunachal Pradesh 791112, India

e-mail: utpalbhattacharjee@rediffmail.com

and controlling security aspects for secret data and remote access of PCs. Another significant use of speaker recognition technology is its utilization for criminological purposes [3]. Generally, the speaker recognition by a machine comprises feature extraction, speaker modeling or training and testing [4]. The estimation of the speaker specific features from the speech signal is done using feature extraction. Thereafter, the speaker model is trained with the use of these features. Finally, in the stage of testing, recognition of speaker is performed by matching with the pattern.

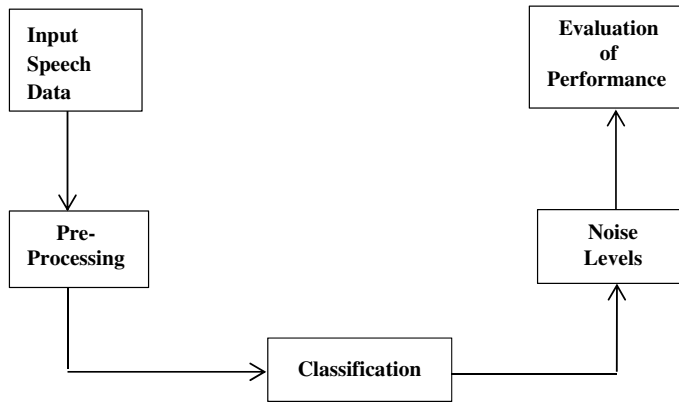
Support vector machine (SVM) is one of the highly used classification technique in analyzing the performance of speaker recognition [5–7]. The support vector machine provides a natural solution for binary class problems. It is one of the popular learning techniques for solving regression and classification problems. SVM has been applied in various areas viz. face, text, 3D object, speech, speaker recognition systems. SVM uses different kernel functions such as linear, nonlinear, polynomial, radial basis, sigmoid, Gaussian, cubic and quadratic etc. Astuti and Adiwijaya have carried out SVM with principal component analysis (PCA) for the classification of microarray data [8]. Bassma have used SVM for the improvement of vehicle localization in urban canyons [9]. Zhao et al. [10] have used nonlinear kernel nuisance attribute projection for speaker verification using NIST SRE data. Kernel PCA feature extraction along with support vector machine classification are effectively used for through-wall human being detection [11]. Das et al. have used linear polynomial and radial basis function kernels for the analysis of gene data set [12].

The focus of this work is to investigate the accuracy of the speaker recognition system in different noise levels using different kernel functions viz. linear, quadratic, cubic and Gaussian.

2 Speech Data Classification

The various steps in this analysis consist of pre-processing/feature extraction, classification and performance evaluation as shown in Fig. 1. In the feature extraction step, principal component analysis (PCA) has been used for dimension reduction which uses mapping function. The different processes which are used in this extraction are data centering, covariance matrix calculation, Eigen value and Eigen vector calculation. In classification, SVM helps in modeling the complex data set and separate different classes and maximize the margin. SVM uses a nonlinear mapping approach for converting the original data to a high dimension and helps in linear separation of data creating a hyperplane (decision boundary). The performance evaluation is executed in the final step.

In this work, two different types of experiments are performed. Initially the experiment is performed to analyze the effectiveness of number of components considered in PCA. The various experiments are carried out on NIST 2003 SRE clean data set to visualize the effect on the accuracy of various Kernel functions. The second experiment in the proposed method is performed to visualize the recognition accuracies as well as running time. The experiments are conducted on noisy data namely: 0, 5,

**Fig. 1** Performance evaluation steps

10, 15 and 20 dB signal-to-noise ratio. The total numbers of 12 scenarios of experiment were considered for each data set, as shown in Table 1. The general classifier characteristics for Kernel function operation has been given in Table 2.

Table 1 Experiment scenarios [8]

Scenario	Dimension reduction	SVM Kernels
1.	None	Linear
2.	None	Quadratic
3.	None	Cubic
4.	None	Fine Gaussian
5.	None	Medium Gaussian
6.	None	Coarse Gaussian
7.	PCA	Linear
8.	PCA	Quadratic
9.	PCA	Cubic
10.	PCA	Fine Gaussian
11.	PCA	Medium Gaussian
12.	PCA	Coarse Gaussian

Table 2 General classifier characteristics

Kernel function	Linear, quadratic, cubic, Gaussian
Kernel scale	Automatic
Box constraint level	1
Multiclass method	One-vs-One
Standardize data	True

3 Kernel Functions and Expressions

The various kernel functions used in the SVM classifier are linear, quadratic, cubic and Gaussian functions. The expressions of these kernel functions are expressed as follows [9];

Linear function:

$$k(x_i, x_j) = x_i^T x_j + c \quad (1)$$

Quadratic function:

$$k(x_i, x_j) = 1 - \frac{\|x_i - x_j\|^n}{\|x_i - x_j\|^n + c} \quad (2)$$

Cubic function:

$$k(x_i, x_j) = (x_i^T x_j + 1)^n \quad (3)$$

Gaussian function:

$$k(x_i, x_j) = \exp\left(-\frac{\|x_i - x_j\|^n}{2\sigma^2}\right) \quad (4)$$

where x_i and x_j are input space vectors, n is order of the kernel and c is a constant.

4 Results and Analysis

The effect of kernel function approach for the clean speech data and noisy data at different SNR has been studied in this paper. For the effective analysis, various scenarios with and without PCA are considered for clean speech data which can be seen in Table 3. It is clearly seen that accuracy percentage of scenario using PCA is found to be improved except linear case, whereas there are no changes in accuracy percentages for fine and coarse Gaussians. The comparison of accuracy for with and

Table 3 Accuracy (%) of SVM Kernel function in various scenarios

Case	Linear	Quadratic	Cubic	Fine Gaussian	Medium Gaussian	Coarse Gaussian
Without PCA	95	85	85	85	85	100
With PCA	90	90	90	85	100	100

without PCA are done at number of components after PCA equals 1 and variance kept after PCA equals 95%.

Here, total 9 numbers of experimental scenarios are considered for the calculation of the accuracies of 6 SVM Kernel functions. The various scenarios for different variance thresholds which are 36.5, 48.44, 66, 80.14, 90.34, 95.08, 97.52, 98.85 and 100% are considered as per Astuti and Adiwijaya [9]. To check the Kernel functions accuracy the first scenario chooses a minimum number of components and the corresponding value of the variance $\geq 36.5\%$, and so on. The results are calculated for 6 numbers of SVMs. The accuracies for various numbers of components and variance for different scenarios are presented in Table 4.

The experimental results for noisy speech data using various scenarios and SNRs are shown in Table 5. The accuracies with PCA are found to be increased for linear,

Table 4 Accuracy for PCA parameters for clean speech data

Components after PCA	1	2	4	8	16	25	34	39	39
Variance kept after PCA(%)	36.5	48.44	66	80.14	90.34	95.08	97.52	98.85	100
<i>Accuracy (%)</i>									
Linear	75	80	85	90	75	75	95	75	75
Quadratic	75	85	90	85	80	90	90	85	90
Cubic	70	85	90	90	80	95	85	85	90
Fine Gaussian	65	80	85	75	75	75	85	75	75
Medium Gaussian	75	80	95	90	75	75	75	75	75
Coarse Gaussian	75	75	75	75	75	75	75	75	75
Average	72.5	80.8	86.6	84.2	76.66	80.83	84.16	78.33	80

Table 5 Accuracy for proposed methods for noisy speech data

Scenario	Accuracy (%)				
	0 dB	5 dB	10 dB	15 dB	20 dB
1.	60	70	75	85	95
2.	65	70	85	90	90
3.	60	70	85	90	90
4.	60	65	60	85	85
5.	65	65	65	85	85
6.	60	65	60	85	95
7.	70	75	75	85	90
8.	75	75	80	85	85
9.	70	85	80	90	85
10.	60	65	60	85	85
11.	65	65	60	85	95
12.	60	65	60	85	95

Table 6 Training time for proposed methods

Scenario	0 dB	5 dB	10 dB	15 dB	20 dB
1.	0.5883	1.0826	1.0440	1.1933	1.1467
2.	0.5903	1.0258	1.0317	1.2308	1.0862
3.	0.6298	1.0316	1.0216	1.0771	1.0594
4.	0.7259	1.0421	1.1473	1.0756	1.0530
5.	0.5891	1.0299	1.0804	1.1434	1.0081
6.	0.6342	1.1789	1.0507	1.0156	1.1173
7.	0.5663	0.5293	0.5312	0.5538	0.6021
8.	0.5876	0.5774	0.6192	0.7662	0.6056
9.	0.5881	0.5767	0.5321	0.5983	0.5410
10.	0.5815	0.5412	0.6226	0.7907	0.6189
11.	0.5887	0.5477	0.5414	0.6390	0.5456
12.	0.6125	0.5477	0.5508	0.5913	0.5497

quadratic and cubic Kernels at 0 and 5 dB SNRs. However, it remains same for all the Gaussian Kernels. It is also seen that the accuracies do not improve for higher SNRs in the range of 10–20 dB. The running times for all the scenarios for different SNRs are depicted in Table 6. It is seen that PCA greatly reduces the running time for all the SNRs considered.

5 Conclusion

In the present work, experiments have been performed using NIST 2003 and AURORA database for the analysis of Kernel functions at various scenarios for different SNRs. The accuracy and running time of SVM using Kernel approach and PCA are found to be improved for low level SNRs. The quadratic Kernel function is found to be better at 0 dB, whereas Cubic Kernel function is found to be better at 5 dB SNR.

References

1. Furui S (1991) Speaker-dependent-feature extraction, recognition and processing techniques. *Speech Commun.* 10(6):505–520
2. Vuppala AK, Rao KS (2013) Speaker identification under background noise using features extracted from steady vowel regions. *Int J Adapt Control Signal Process* 27:781–792
3. Kunzel H (1994) Current approaches to forensic speaker recognition. In: ESCA workshop on automatic speaker recognition, identification and verification, pp 135–141
4. Shridhar M, MohanKrishnan N (1982) Text-independent speaker recognition: a review and some new results. *Speech Commun* 1:257–267

5. Wan V, Renals S (2005) Speaker verification using sequence discriminant support vector machines. *IEEE Transa Speech, Audio Process* 13(2):203–210
6. Sturim DE, Campbell WM, Reynolds DA (2007) Classification methods for speaker recognition. *LNAI* 4343:278–297
7. Chakroun R, Zouari LB, Frikha M, Hamida AB (2015) A novel approach based on support vector machines for automatic speaker identification. IEEE conference
8. Astuti W, Adiwijaya (2018) Support vector machine and principal component analysis for microarray data classification. *J Phys Conf Series* 971:012003
9. Bassma G, Hassan EG, Tayeb S (2018) Support vector machines for improving localization in Urban canyons. *MATEC Web Conf* 200:00004
10. Zhao X, Dong Y, Yang H, Zhao J, Lu L, Wang H (2008) Nonlinear kernel nuisance attribute projection for speaker verification. In: IEEE international conference on acoustics, speech, and signal processing, 4125–4128
11. Wang W, Zhang M, Wang D, Jiang Y (2017) Kernel PCA feature extraction and the SVM classification algorithm for multiple-status, through-wall, human being detection. *EURASIP J Wireless Commun Netw* 151:1–7
12. Das SR, Das K, Mishra D, Shaw K, Mishra S (2012) An empirical comparison study on kernel based support vector machine for classification of gene expression data set. *Procedia Eng* 38:1340–1345

A Fuzzy Multicriteria Methodology for Selection Among Solar PV Adoption Barriers in India



Anbesh Jamwal, Akshay Patidar, Rajeev Agrawal, and Monica Sharma

Abstract At present selection of energy policies of any country affect its environment and economic development. There is a need for the selection of the most appropriate energy policy which can promote the economic development of the country. In developing countries like India, there is a lack of energy resources and these sources are exhausting day by day due to an increase in population. To preserve the unconventional sources of energy Govt. of India is now promoting renewable sources of energy. In the last few years, studies were carried out which were focused on the best energy policy selection and these studies are based on the hybrid multicriteria decision-making techniques like Fuzzy-AHP. In the last few years, the fuzzy set theory has been proved out as a powerful tool to treat the uncertainty when information is vague or incomplete. In the present study fuzzy multicriteria decision making, the based methodology is suggested to assess the barriers which resist the adoption of Solar PV panels in the Himachal Pradesh region. The methodology is based on the AHP (analytical hierarchy process) under the fuzziness which allows the ranking of barriers from the industry experts and inputs from Govt. of Himachal Pradesh to be crisp, linguistic expressions and fuzzy number. In the application of this study, critical barriers are found which resist the implementation of Solar PV panels in Himachal Pradesh.

Keywords Solar PV · Barriers · Fuzzy-AHP · Triangular fuzzy numbers · India

1 Introduction

Energy is an important factor in the present time for the economic as well as social development of any nation [1]. At present, Electricity has become a promising energy

A. Jamwal · R. Agrawal · M. Sharma (✉)

Department of Mechanical Engineering, Malaviya National Institute of Technology, J.L.N. Marg, Jaipur, Rajasthan 302017, India
e-mail: msharma.dms@mnit.ac.in

A. Patidar · M. Sharma

Department of Management Studies, Malaviya National Institute of Technology, J.L.N. Marg, Jaipur, Rajasthan 302017, India

source to fulfil human needs. In the last few decades, the demand for electricity has grown due to the rapid advancement in technology [2]. Developing countries like India, where economic development is depending on industries [3]. All the major industries sectors such as the Information Technology sector and the Manufacturing sector consumes a large quantity of energy. India is the third largest producer of electricity [4]. But still, there are many areas in India that are far away from the regular supply of electricity [5]. The production level of Electricity in India is not enough to meet the rising demand from Industries and other consumers [6]. At present, India is focusing more on gas-based power, hydro energy and renewable sources of energy. However, Govt. of India is also looking for the adoption of clean coal technology to meet the rising demands of electricity. The generation of electricity from renewable sources of energy using PV systems is the major need of the present generation [7]. At a global level, Europe has the most developed PV market, where 3% of total electricity is generated by PV systems [8]. The electricity consumption level of any country indicates its economic prosperity. Himachal Pradesh is situated in the northern region of India. In Himachal Pradesh, the growing population and rapid growth in the industrial area, an increase in the standard of living in cities has increased the dependence on imported energy. Himachal Pradesh energy consumption has risen in the last 10 years because of the combined demand for urbanization and industrialization. Solar energy contributes to the power generation in the Himachal Pradesh, although this region of India receives the maximum sunlight exposure which has potential for the energy generation from Solar Photovoltaic systems. Govt. of Himachal Pradesh has launched several schemes to promote solar energy in state but sadly generation of energy from these sources remained narrow and unpractical when compared to conventional electricity generation because of a lot of Implementation barriers. Traditionally, solar energy in India has been only used for limited applications [9]. But as our fossil fuels are consuming rapidly due to an increase in the population of the world in the last few decades. Man is moving towards renewable sources of energy to secure the future of upcoming generations [10, 11]. Photovoltaic systems have become more popular and much competitive at the present time but the diffusion of PV systems is still less than in the comparison to conventional energy sources [12]. At present, the production of electricity is shifting from conventional sources of energy to renewable sources of energy to save the environment from the effect of fossil fuels. Another reason for shifting is to reserve fossil fuel sources for future generations [13]. Generation of electricity from renewable sources like solar energy a profuse means and use of PV systems is one means.

Diffusion research on a PV system is old since the 1980s. Few studies have carried out on the economic perspective and analysis of policies [14]. Many studies have been carried out in past not only based on the countries, for example, India [15], Pakistan [16], China [17], Sri Lanka [18] and Nepal [19], but also the type of applications like off grid systems and On-grid systems [20]. In past, the cost and technology of PV systems were not assumed to commercially competitive with conventional sources of energy but at present because of the maturity in technology and lesser production costs made the solar PV systems very popular [21]. However, after technology advancement and lesser costs still, the adoption of the solar PV

system is limited as compared to conventional sources of energy. There are always some barriers that affect the adoption of PV systems over conventional sources of energy [22]. The study of these adoption barriers has been a common interest in many studies which include renewable energy research. However, only a few studies report about the analysis of these barriers with the use of MCDM techniques and very fewer studies reported about the assessment of these barriers with the hybrid techniques like Fuzzy-AHP [23]. To fill this gap, the aim of the present study is to investigate the barriers in the adoption of Solar PV in Himachal Pradesh and the assessment of these barriers with Fuzzy-AHP. To address this, data is collected from industry experts, Govt. of Himachal Pradesh and academia related to this field. The rest of the paper has 5 Sections. There are 13 major barriers are found out in the study. These 13 barriers are divided into three criteria. The most influencing barrier is found out with the ranking of barriers done by Fuzzy-AHP.

2 Methodology

In the present paper, a fuzzy multicriteria decision making methodology is reconstructed to select the most influencing adoption barrier among all barriers. Fuzzy-AHP method is used in this study to prioritize the weights of adoption barriers. In the Analytical hierarchy process experts related to the research, the area has to give a definite input number which varies from 1 to 9 scale for the pairwise comparison which helps in finding the priority vector [24]. If the two factors in the study have equal importance then it has a scale of 1; if a factor is weakly important or strongly important than other than it has a scale of 3, 5, 7 and 9 on the basis of importance over another. The scale used in this study is discussed in Table 1. Even sometimes the scale of 2, 4, 6 and 8 also used when there is a slight difference between two classifications. Reciprocals of 1, 1/2, 1/3, 1/4, ..., 1/9 used for the reverse comparison in the study. Sometimes, factor comparison involves certainty and subjectivity which don't give accurate results of the study. For example, In a study may be expert know that one factor is important than another factor but he may not be able to give the definite scale for the comparison because he is not sure about the degree on factor A over the factor B. Experts provides a range of scale from 3 to 7 to compare the two factors but due to lack of adequate information sometimes it is difficult to do

Table 1 Saaty rating scale for study

Scale	Description
1	Equal importance
3	Less weakly importance
5	Strong weakly importance
7	Strongly importance
9	Very strongly importance

Table 2 Adoption barriers in solar PV systems in Himachal Pradesh

Barrier No.	Barrier name	Barrier notation
1.	Effect of temperature	Barrier <i>B1</i>
2.	Shadowing	Barrier <i>B2</i>
3.	Irradiance	Barrier <i>B3</i>
4.	High initial investment cost	Barrier <i>B4</i>
5.	Absorption and transmittance	Barrier <i>B5</i>
6.	Power efficiency	Barrier <i>B6</i>
7.	Cost of material used	Barrier <i>B7</i>
8.	Solar panel mounting	Barrier <i>B8</i>
9.	Cloud cover	Barrier <i>B9</i>
10.	Ineffective quality control	Barrier <i>B10</i>
11.	Competition with land used	Barrier <i>B11</i>
12.	Solar plant infrastructure	Barrier <i>B12</i>
13.	Humidity	Barrier <i>B13</i>

Table 3 List of criteria of barriers in the adoption of solar PV systems

Criteria No.	Criteria name
<i>C1</i>	Economic perspective
<i>C2</i>	Technical perspective
<i>C3</i>	Atmospheric perspective

comparison. In such cases, the AHP method failed due to the existence of Fuzziness or incomplete comparisons. [25] Fuzzy-AHP is an extension of the AHP method which was introduced earlier of 1983. With the development in MCDM over the years and application of these MCDMs in engineering, there is a lot of development in these techniques [26]. In the present study modified Fuzzy-AHP is used to find the most influencing barrier among all barriers which resist the adoption of Solar PV systems in Himachal Pradesh. Table 2 shows the barriers in the adoption of a Solar PV system. Table 3 shows the list of criteria.

2.1 Consistency Ratio Check for Pairwise Comparison

In the present study following steps are followed to measure the consistency ratio.

1. Calculation of relative weight and Eigen-vector and λ_{\max} for each of the matrix.
2. Computation of CI (consistency index) for each of the matrix by the following equation:

Table 4 CR calculation for criteria's

Criteria	3RD root	Priority vector
C1	1.0000	0.2583
C2	2.4662	0.6370
C3	0.4055	0.1047
Lambda max	3.0384	
CI	0.0192	
CR	0.0331	

$$CI = (\lambda_{\max} - n)/(n - 1) \quad (1)$$

3. The consistency ratio of each of the matrix is calculated by following mathematical equations.

$$CR = (CI/RI) \quad (2)$$

2.2 Questionnaire Design and Experts of Solar PV Industries Response Collection

The questionnaire survey for this study is carried out by preparing a questionnaire and responses are collected from 28 experts related to the Solar PV field. After the expert's selection for this study, detailed information about this study objective and reason for this study were sent to experts by mails. At last, 28 responses were collected related to this study from experts. The experience of experts were more than 10 years in this area. The nine-point scale was used to assign the relative weights for the pairwise comparison of both the criteria and barriers under criteria. Further, the consistency ratio calculation for criteria's and barriers under different criteria's is shown in Tables 4, 5, 6, and 7.

2.2.1 Conversion of Crisp Data into Triangular Fuzzy Numbers

From the data collected from experts and consistency ratio checked from the pairwise comparison, it is found that all the matrices are consistent. A TFN (triangular fuzzy number) is represented by (a, b, c) and the member function is defined as:

$$\mu_v(x) = \mu_v(x) = \begin{cases} \frac{x-a}{b-a}, & a \leq x \leq b \\ \frac{c-x}{c-b}, & b \leq x \leq c \\ 0, & \text{otherwise} \end{cases} \quad (3)$$

Table 5 Consistency ratio calculation for barriers under criteria C1

C1 Criteria	3RD root	Priority vector
B3	3.4087	0.5574
B5	0.0441	0.0441
B6	1.8481	0.3022
B8	0.5886	0.0962
Lambda max	4.202	
CI	0.0674	
CR	0.0748	

Table 6 Consistency ratio calculation for barriers under criteria C2

C1 criteria	3RD root	Priority vector
B3	4.2129	0.5574
B5	1.3161	0.2045
B6	0.6148	0.0955
B8	0.2934	0.0456
Lambda max	4.1901	
CI	0.0634	
CR	0.0704	

Table 7 Consistency ratio calculation for barriers under criteria C3

C3 criteria	3RD root	Priority vector
B4	1.6787	0.3020
B7	0.8027	0.1444
B10	1.5518	0.2792
B11	1.0845	0.1951
B12	0.4409	0.0793
Lambda max	6.7491	
CI	0.4373	
CR	0.3904	

The crisp data collected from the responses of experts were converted to fuzzy data by the use of TFN. The nine-point scale was used in the study for the pairwise comparison [27]. TFN is used for the pairwise comparison representation. The scale is given in Table 8.

The conversion of crisp data into the fuzzy numbers is done by a formula shown in the equation below:

$$A = \left(x - \frac{1}{2}, x, x + \frac{1}{2} \right) \quad (4)$$

Table 8 Conversion of crisp inputs to triangular fuzzy number

	Crisp number	Triangular fuzzy number		
		Alpha	Beta	Gamma
1	1.0000	1.0000	1.0000	1.0000
2	2.0000	1.5000	2.0000	2.5000
3	3.0000	2.5000	3.0000	3.5000
4	4.0000	3.5000	4.0000	4.5000
5	5.0000	4.5000	5.0000	5.5000
6	6.0000	5.5000	6.0000	6.5000
7	7.0000	6.5000	7.0000	7.5000
8	8.0000	7.5000	8.0000	8.5000
9	9.0000	9.0000	9.0000	9.0000
1/2	0.5000	0.4000	0.5000	0.6667
1/3	0.3333	0.2857	0.3333	0.4000
1/4	0.2500	0.2222	0.2500	0.2857
1/5	0.2000	0.1818	0.2000	0.2222
1/6	0.1667	0.1538	0.1667	0.1818
1/7	0.1429	0.1333	0.1429	0.1538
1/8	0.1250	0.1176	0.1250	0.1333
1/9	0.1111	0.1111	0.1111	0.1111

The alpha cut value of 0.5 is considered in the present case for the conversion of crisp data into fuzzy numbers. The alpha cut values of zero are considered for both upper bound and lower bound numbers.

Table 9 shows the fuzzy weight vector calculations for criteria; Table 10 shows the weight vector calculations for $C1$ criteria. Table 11 shows the fuzzy weight vector calculations for $C2$ criteria. Table 12 shows the fuzzy weight vector calculations for $C3$ criteria.

Table 13 shows the barriers affecting the adoption of Solar PV in Himachal Pradesh with their normalized global weights. Barrier $B1$ (effect of temperature) with an

Table 9 Fuzzy weight vector calculations for criteria's

	Alpha	Beta	Gamma
$C1$	0.8939	1.0000	1.1187
$C2$	2.2407	2.4662	2.6801
$C3$	0.3731	0.4055	0.4463
Sum	3.5077	3.8717	4.2450
Fuzzy weight vector	0.2106	0.2583	0.3189
	0.5278	0.6370	0.7640
	0.0879	0.1047	0.1272

Table 10 Fuzzy weight vector calculations for barriers under C_1

	Alpha	Beta	Gamma
B_3	3.1721	3.4087	3.6280
B_5	0.2551	0.2697	0.2876
B_6	1.7003	1.8481	2.0154
B_8	0.5362	0.5886	0.6448
Sum	5.6636	6.1151	6.5758
Fuzzy weight vector	0.4824 0.0388 0.2586 0.0815	0.5574 0.0441 0.3022 0.0962	0.6406 0.0508 0.3559 0.1138

Table 11 Fuzzy weight vector calculations for barriers under C_2

	Alpha	Beta	Gamma
B_1	4.0280	4.2129	4.3895
B_2	1.1959	1.3161	1.4382
B_9	0.5555	0.6148	0.6812
B_{13}	0.2756	0.2934	0.3152
Sum	6.0551	6.4371	6.8242
Fuzzy weight vector	0.5903 0.1752 0.0814 0.0404	0.6545 0.2045 0.0955 0.0456	0.7249 0.2375 0.1125 0.0521

Table 12 Fuzzy weight vector calculations for barriers under C_3

	Alpha	Beta	Gamma
B_4	1.4651	1.6788	1.8998
B_7	0.7028	0.8027	0.9221
B_{10}	1.3488	1.5518	1.7654
B_{11}	0.9607	1.0845	1.2332
B_{12}	0.4097	0.4409	0.4797
Sum	4.8870	5.5587	6.3002
Fuzzy weight vector	0.2325 0.1115 0.2141 0.1525 0.0650	0.3020 0.1444 0.2792 0.1951 0.0793	0.3887 0.1887 0.3613 0.2523 0.0982

Table 13 Normalized global weights of all barriers

Normalized global weights		
Barriers	Weight	×100
B1	0.4141	41.4062
B2	0.1297	12.9750
B3	0.1443	14.4274
B4	0.0322	3.2186
B5	0.0115	1.1476
B6	0.0787	7.8701
B7	0.0155	1.5500
B8	0.0250	2.5039
B9	0.0608	6.0842
B10	0.0298	2.9788
B11	0.0209	2.0913
B12	0.0085	0.8454
B13	0.0290	2.9016

approximate weight of 41% has the highest power among all the barriers. This is the most influencing barrier among all the barriers which resist the adoption of solar PV in Himachal Pradesh. On the other hand barrier, *B12* has approximately 0.84% weight which is the lowest among all the barriers. Barrier *B3* and *B2* are also influencing barriers with a weight of 14 and 12% approximately. Simulation of most influencing barrier with new parameters is discussed in below to overcome this barrier. It is expected that this simulation with new parameters can help to improve the performance of Solar PV which will help to overcome this barrier.

3 Results and Discussion

In this study Technical, economic and environment factors were categorized into 13 barriers. These barriers were then studied using the AHP-Fuzzy methodology to find the most critical barrier, which was affecting the implementation of solar panels in the Himachal Pradesh region. Temperature (*B1*) is the most critical barrier and Irradiance (*B3*) is the second most critical factor. With any change in the value of temperature the output power production of the solar panel gets affected such that its implementation in higher latitudes becomes uncertain due to a high variation in temperature and more cloud cover. Irradiance also affects the output power, as the value of currents varies linearly with any change in the amount of energy absorbed by the solar panel.

4 Summary/Conclusion

In the present study, 13 critical barriers were found from the data collected from Solar PV industry experts. These 13 barriers were categorized into 3 criteria. Further, hybrid Fuzzy-AHP methodology is adopted for the assessment of barriers that influence the adoption of Solar PV in Himachal Pradesh. Ranking of barriers was got by normalizing the global weights of barriers. It is found that Barrier B1 (Effect of temperature) is the major barrier among all barriers which influence the adoption of Solar PV in Himachal Pradesh. It is also found that B12 (Solar Plant Infrastructure) barrier is a very less influencing barrier among all barriers. The effect of temperature should be taken care of before the implementation of Solar PV in the city areas of Himachal Pradesh. This study was carried out in the city areas of Himachal Pradesh. Further, this study can be extended by the identification of barriers in both rural areas and urban areas of Himachal Pradesh using hybrid techniques.

References

1. Jamwal A, Aggarwal A, Gupta S, Sharma P (2019) A study on the barriers to lean manufacturing implementation for small-scale industries in Himachal region (India). *Int J Intell Enterp* 6(2–4):393–407
2. Sahu BK (2015) A study on global solar PV energy developments and policies with special focus on the top ten solar PV power producing countries. *Renew Sustain Energy Rev* 43:621–634
3. Jamwal A, Agrawal R, Gupta S, Dangayach GS, Sharma M, Sohag MAZ (2020) Modelling of sustainable manufacturing barriers in pharmaceutical industries of Himachal Pradesh: an ISM-Fuzzy approach. In: Proceedings of International Conference in Mechanical and Energy Technology, pp 157–167. Springer, Singapore
4. Zahedi A (2006) Solar photovoltaic (PV) energy; latest developments in the building integrated and hybrid PV systems. *Renew Energy* 31(5):711–718
5. Katiraei F, Aguero JR (2011) Solar PV integration challenges. *IEEE Power Energ Mag* 9(3):62–71
6. Tyagi VV, Rahim NA, Rahim NA, Jeyraj A, Selvaraj L (2013) Progress in solar PV technology: research and achievement. *Renew Sustain Energy Rev* 20:443–461
7. Nema P, Nema RK, Rangnekar S (2009) A current and future state of art development of hybrid energy system using wind and PV-solar: a review. *Renew Sustain Energy Rev* 13(8):2096–2103
8. Denholm P, Margolis RM (2007) Evaluating the limits of solar photovoltaics (PV) in electric power systems utilizing energy storage and other enabling technologies. *Energy Policy* 35(9):4424–4433
9. Wang G, Ciobotaru M, Agelidis VG (2014) Power smoothing of large solar PV plant using hybrid energy storage. *IEEE Trans Sustain Energy* 5(3):834–842
10. Nugent D, Sovacool BK (2014) Assessing the lifecycle greenhouse gas emissions from solar PV and wind energy: a critical meta-survey. *Energy Policy* 65:229–244
11. Tsoutsos T, Frantzeskaki N, Gekas V (2005) Environmental impacts from the solar energy technologies. *Energy policy* 33(3):289–296
12. Asif M, Muneer T (2007) Energy supply, its demand and security issues for developed and emerging economies. *Renew Sustain Energy Rev* 11(7):1388–1413
13. Rehman S, Bader MA, Al-Moallem SA (2007) Cost of solar energy generated using PV panels. *Renew Sustain Energy Rev* 11(8):1843–1857

14. Koppelaar RHEM (2017) Solar-PV energy payback and net energy: meta-assessment of study quality, reproducibility, and results harmonization. *Renew Sustain Energy Rev* 72:1241–1255
15. Sharma NK, Tiwari PK, Sood YR (2012) Solar energy in India: strategies, policies, perspectives and future potential. *Renew Sustain Energy Rev* 16(1):933–941
16. Bhutto AW, Bazmi AA, Zahedi G (2012) Greener energy: issues and challenges for Pakistan—solar energy prospective. *Renew Sustain Energy Rev* 16(5):2762–2780
17. Liu LQ, Wang ZX, Zhang HQ, Xue YC (2010) Solar energy development in China—a review. *Renew Sustain Energy Rev* 14(1):301–311
18. McEachern M, Hanson S (2008) Socio-geographic perception in the diffusion of innovation: solar energy technology in Sri Lanka. *Energy Policy* 36(7):2578–2590
19. Bhandari R, Stadler I (2011) Electrification using solar photovoltaic systems in Nepal. *Appl Energy* 88(2):458–465
20. Sohag MAZ, Kumari P, Agrawal R, Gupta S, Jamwal A (2020) Renewable energy in Bangladesh: current status and future potentials. In: Proceedings of International Conference in Mechanical and Energy Technology, pp 353–363. Springer, Singapore
21. Kabir E, Kumar P, Kumar S, Adelodun AA, Kim KH (2018) Solar energy: potential and future prospects. *Renew Sustain Energy Rev* 82:894–900
22. Weldekidan H, Strezov V, Town G (2018) Review of solar energy for biofuel extraction. *Renew Sustain Energy Rev* 88:184–192
23. Kahraman C, Kaya İ, Cebi S (2009) A comparative analysis for multiattribute selection among renewable energy alternatives using fuzzy axiomatic design and fuzzy analytic hierarchy process. *Energy* 34(10):1603–1616
24. Gautam N, Ojha MK, Swain P, Aggarwal A, Jamwal A (2019) Informal investigation of fourth-party and third-party logistics service providers in terms of Indian context: an AHP approach. In: Advances in industrial and production engineering, pp 405–413. Springer, Singapore
25. Tasri A, Susilawati A (2014) Selection among renewable energy alternatives based on a fuzzy analytic hierarchy process in Indonesia. *Sustain Energy Technol Assessments* 7:34–44
26. Sharm P, Jamwal A, Aggarwal A, Bhardwaj S, Sood R (2018) Major challenges in adoption of RFID for Indian SME's. *Int Res J Eng Technol* 5:2247–2255
27. Singh PL, Sindhwan R, Dua NK, Jamwal A, Aggarwal A, Iqbal A, Gautam N (2019) Evaluation of common barriers to the combined lean-green-agile manufacturing system by two-way assessment method. In: Advances in industrial and production engineering, pp 653–672. Springer, Singapore

Suspension Modeling and Its Importance in Automotive Industries for Implementation of Modern Vehicular Technologies



Sujan Neroula and Santanu Sharma

Abstract Losing traction by wheels while driving can deteriorate the vehicle efficiency and dynamic stability, and might lead to catastrophic outcomes in some cases. The traction provided by the tire is a function of the normal reaction force on a wheel and the Tire Road Frictional Coefficient (TRFC). Knowledge of the normal reaction force on the wheel can enable the vehicle to abide by the Acceleration Slip Regulation (ASR) while driving and can help in optimizing the performance in braking and traction control. A suspension being a linkage between the sprung and unsprung components of a vehicle and plays an important role in-vehicle system and dynamics. This paper presents a model of suspension taking into account different spring stiffness and damping coefficients. The behavior of the suspension has been analyzed for different obstacle heights, vehicle speed, and acceleration. The model has been further assessed on-road using a lightweight Electric Vehicle (EV).

Keywords Suspension modeling · Electric vehicle · Traction control

1 Introduction

A vehicle suspension system works as a linkage between the vehicle wheels and the chassis. The suspension system isolates the vehicle from the vibration and harshness arising due to the road surface and also nullifies the vertical acceleration arising due to road undulations [1]. A suspension must be rigid enough so it can withstand the static load effectively and on the other hand, it must be soft enough so as to ensure comfort and isolation from vibrations and harshness [2].

S. Neroula · S. Sharma (✉)

Department of Electronics and Communication Engineering, Tezpur University, Tezpur, Assam 784028, India

e-mail: santanu.sharma@gmail.com

S. Neroula

e-mail: sujanneroula1990@gmail.com

In [3, 4], a two-dimensional nonlinear model of MacPherson suspension is reported by analysis of the suspension kinematics and the dynamics have been derived using Euler-Lagrange's approach [5].

An electromagnetic suspension model has been reported in [6], wherein the optimization has been done by the introduction of constraints in current, voltage, and airgap.

The suspension of the vehicle can be mounted to the chassis through a load sensor that can sense the wheel load in real-time. The real-time data of the wheel load along with the vehicle TRFC can enhance the vehicle ASR by optimizing the deliverable torque and also can enhance the braking performance [7, 8].

The following sections present the vehicle suspension model using Newtonian mechanics and Lagrange's model, followed by the simulation and actual on-road analysis of the suspension system.

2 Suspension Modeling

2.1 Suspension Modeling by Newtonian Mechanics

Vehicle suspension modeling is crucial for the inclusion of technologies like traction control, rollover prevention, etc. Figure 1b illustrates the vehicle suspension model where b is the damping coefficient of the damper and K_S and K_W are the spring constants of suspension and wheel, respectively. The relation governing equations for the spring and the damper can be expressed as [9].

$$F = K dx, F = b\dot{x} \quad (1)$$

From the FBD illustrated in Fig. 1b, the equation for the suspension model can be derived as

$$F_1 = K_S(y - x), F_3 = K_W(x - r), F_2 = b(\dot{y} - \dot{x}) \quad (2)$$

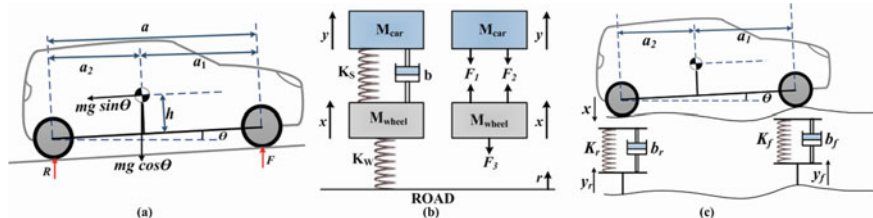


Fig. 1 Figure showing **a** a vehicle parked on an incline **b** free body diagram (FBD) of suspension model using Newtonian mechanics **c** dynamic off-road suspension model using Lagrange's model

Here, the damping force is proportional to the velocity of the piston. Further force F_3 , i.e., the force acting between the wheel and road can be expressed as

$$M_{\text{Wheel}}a_W = K_s(y - x) + b(\dot{y} - \dot{x}) - K_W(x - r) \quad (3)$$

$$M_{\text{Car}}a_c = -K_s(y - x) - b(\dot{y} - \dot{x}) \quad (4)$$

Here $(x - r)$ is the relative displacement of the wheel and the road surface. From the above equations, we can estimate the total force acting on the wheel and the vehicle. Equations 3 and 4 describe the suspension model using Newtonian mechanics wherein the mass of the tyre, suspension stiffness, and damping have been considered.

2.2 Suspension Modeling by Lagrange's Mechanics

Another very effective and lucid approach is an analysis using Lagrange's equation. When we neglect the mass of the tyre and its roll moment, a simple model can be formed by taking into consideration; the suspension damping and stiffness along with the vehicle pitch. The spring constant (front and rear) of the vehicle suspension systems has been measured as $K_s = 35,000 \text{ Nm}^{-1}$, and damping coefficient has been determined to be $b = 2000 \text{ N-sm}^{-1}$. Lagrange's model has been presented in Fig. 1c.

Here the index f and r refer to the front and rear of the vehicle, respectively. The vehicle moment of inertia I , for the designed vehicle has been measured to be 144.5 kg m^2 . The kinetic energy (KE) and the potential energy (PE) for the system can be formulated as

$$KE = \frac{1}{2}m\dot{x}^2 + \frac{1}{2}I\dot{\theta}^2 \quad (5)$$

$$PE = \frac{1}{2}K_f(y_f - x - a_1\theta)^2 + \frac{1}{2}K_r(y_r - x - a_2\theta)^2 \quad (6)$$

The energy (Q) dissipated in damper can be expressed by Rayleigh's function as

$$Q_{\text{damper}} = \frac{1}{2}b_f(\dot{y}_f - \dot{x} + a_1\dot{\theta})^2 + \frac{1}{2}b_r(\dot{y}_r - \dot{x} - a_2\dot{\theta})^2 \quad (7)$$

Further implementing the Eqs. 8 and 9, along with Eqs. 5, 6, and 7; the equation describing the motion for the suspension system can be obtained as (Eq. 10). (Here $P = KE - PE$) [10].

$$\frac{d}{dt}\left(\frac{\partial P}{\partial \dot{x}}\right) - \frac{\partial P}{\partial \dot{x}} = \frac{\partial Q_{\text{damper}}}{\partial \dot{x}} \quad (8)$$

$$\frac{d}{dt} \left(\frac{\partial P}{\partial \dot{\theta}} \right) - \frac{\partial P}{\partial \dot{\theta}} = \frac{\partial Q_{\text{damper}}}{\partial \dot{\theta}} \quad (9)$$

$$\begin{aligned} & \begin{bmatrix} m & 0 \\ 0 & I \end{bmatrix} \begin{bmatrix} \ddot{x}(t) \\ \ddot{\theta}(t) \end{bmatrix} + \begin{bmatrix} b_f + b_r & a_2 b_r - a_1 b_f \\ a_2 b_r - a_1 b_f & a_2^2 b_r + a_1^2 b_f \end{bmatrix} \begin{bmatrix} \dot{x}(t) \\ \dot{\theta}(t) \end{bmatrix} \\ & + \begin{bmatrix} K_f + K_r & K_r a_2 - K_f a_1 \\ K_r a_2 - K_f a_1 & a_1^2 K_f + a_2^2 K_r \end{bmatrix} \begin{bmatrix} x(t) \\ \theta(t) \end{bmatrix} \\ & = \begin{bmatrix} K_f & K_r \\ -K_f a_1 & K_r a_2 \end{bmatrix} \begin{bmatrix} y_f \\ y_r \end{bmatrix} + \begin{bmatrix} b_f & b_r \\ -b_f a_1 & b_r a_2 \end{bmatrix} \begin{bmatrix} \dot{y}_f \\ \dot{y}_r \end{bmatrix} \end{aligned} \quad (10)$$

The parameters that are considered for the simulation closely resemble the values obtained for the designed vehicle and data obtained from the manufacturers of various components that have been used in designing the vehicle. $K_f = K_r = 35,000 \text{ Nm}^{-1}$, $a_1 = 0.9 \text{ m}$, $a_2 = 0.8 \text{ m}$, vehicle gross mass, $m = 270 \text{ kg}$ (including the driver), $I = 145 \text{ kg m}^2$, and wheelbase of the vehicle is 1.7 m. The height of the CG for the vehicle designed has been measured to be 0.32 m.

MATLAB simulation is used to extract the solution for Lagrange's equation which describes the system's natural frequency and oscillations. Simulation of Eq. 10 with vehicle parameters yields the roots of the equation as; $-3.6552 \pm 16.4810i$, $-8.3448 \pm 7.3886i$.

From these roots, the first and second damped natural frequencies for the suspension system are obtained as

$$\begin{aligned} \omega_{d1} &= \omega_{n1} \sqrt{1 - \zeta_1^2} = 7.3386 \\ \omega_{d2} &= \omega_{n2} \sqrt{1 - \zeta_2^2} = 16.4810 \\ -\zeta_1 \omega_{n1} &= -8.3448 \text{ rad s}^{-1}, \quad -\zeta_2 \omega_{n2} = -3.6552 \end{aligned} \quad (11)$$

Negative sign that persists in the real part of the root signifies the decaying nature of the system oscillations. Using Eq. 11, the damping coefficient and damped natural frequency has been obtained to be

$$\begin{aligned} \zeta_1 &= 0.75, \quad \zeta_2 = 0.22 \\ \omega_{n1} &= 11.15 \text{ rad s}^{-1}, \quad \omega_{n2} = 16.88 \text{ rad s}^{-1} \end{aligned}$$

The system transfer function for the two natural frequencies and the damping coefficients has been obtained as

$$\begin{aligned} H_1(s) &= \frac{284.9}{s^2 + 7.43s + 284.9} \text{ and} \\ H_2(s) &= \frac{124.2}{s^2 + 16.7s + 124.2} \end{aligned} \quad (12)$$

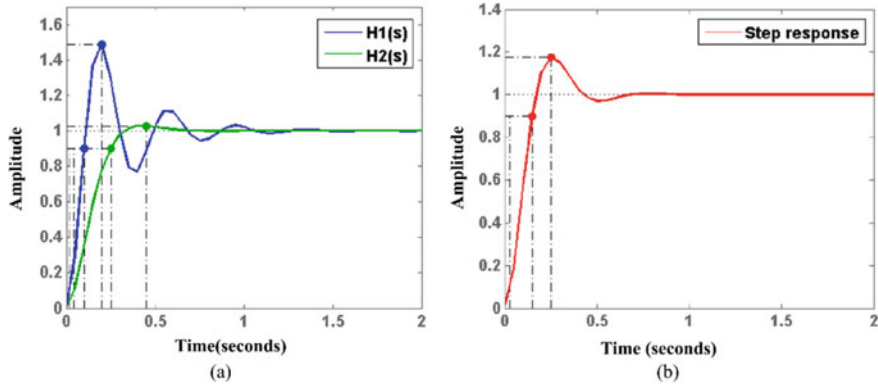


Fig. 2 **a** Step response for $H_1(s)$, and $H_2(s)$ **b** step response for the superposition of $H_1(s)$, and $H_2(s)$

The step response for these transfer functions $H_1(s)$ and $H_2(s)$ obtained has been illustrated in Fig. 2a. The actual step response (superposition) for the system has been illustrated in Fig. 2b.

3 Experimental Design

To illustrate these damping, we have considered an obstacle over which the vehicle will be passing at a uniform speed. This obstacle acts as a unit step input for the transfer function illustrated in Eq. 10. The variation in load at each wheel has been logged in real-time. The comparison of the two results (simulation and on-road) has been presented in the result section.

The vehicle drives over an obstacle of height 2.4 cm having width 500 cm at a constant speed of 5 m/s. The real-time force acting on the wheel and suspension has been plotted. This experiment is followed by a deceleration at a rate of 5 m/s² and the force on the front wheel has been recorded in real-time.

4 Results and Discussions

Figure 3a illustrates the experimental design which analyzes the responsiveness and damping of the suspension setup. Figure 3b shows the actual vehicle suspension setup equipped with a load sensor for the estimation of normal force in dynamic conditions. The following part presents in brief the mathematics involved to estimate the holding torque and the techniques employed.

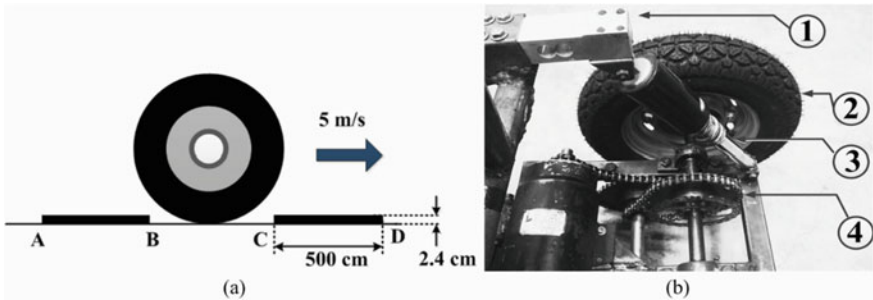


Fig. 3 **a** The designed obstacle for evaluation of suspension **b** the actual designed vehicle with 1-load cell, two-wheel, three-suspension, four-drivetrain

Accurate data acquisition from the load cell associated with each wheel is important and the results must comply with the simulation carried out in the previous section (Fig. 2a, b). The geometry of the suspension and swing arm introduces a deviation in the wheel load sensor output. Initially, the system was designed using a Kalman filter. As this filter is defined only for the linear systems, it was unable to filter out the error(s) introduced due to the suspension. The road grade estimated using this technique can be expressed as

$$\theta = f(F_i)_{i=\text{FL, FR, RL, RR}} \quad (13)$$

To eliminate the error introduced, an NLO has been adopted thus establishing a linear relation between the wheel load and sensor output. The actual sensor output, state estimation using Kalman filter and NLO has been illustrated in Fig. 4a, b. The use of NLO over the Kalman filter also reduces the computational speed and increases design flexibility [11]. Using the NLO, the nonlinearities, and the errors in estimated load have been reduced to a great extent. Figure 4c exhibits the results of the experiment design discussed in Fig. 3a. Rolling of the wheels over an obstacle of height 2.4 cm and width 50 cm; at speed of 5 ms^{-1} exhibits a considerable variation in the estimated wheel load. The evaluated damping coefficient and natural frequency from the real-time suspension response resemble the simulation results.

This test was followed by braking test wherein the vehicle was subjected to a high deceleration force of 5 ms^{-2} , creating a negative pitch. A subsequent increase in the front wheel load on the front wheels was registered is shown in Fig. 4d. Also, a comparison between the simulation result (expected) and the actual load has been presented.

With the knowledge of the wheel load, the gradient of a road surface can be determined, and technologies like Hill Start Assist (HSA), Traction control, and vehicle Eco-routing can be implemented effectively [12, 13].

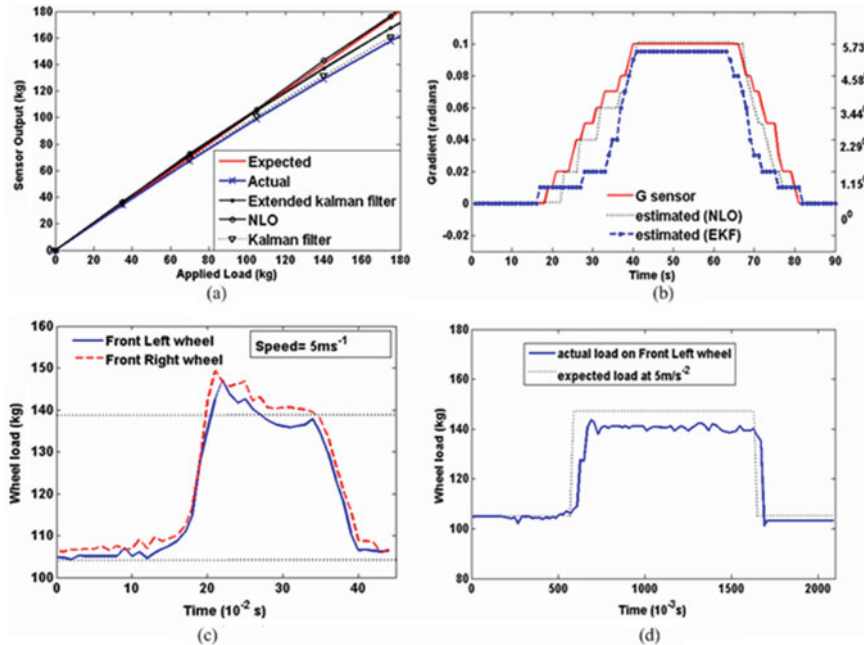


Fig. 4 **a** Load sensor linearization to mitigate undesired effect caused by vehicle suspension geometry **b** the estimated road grade using G sensor, the load cell output without linearization and with load cell output with adaptive calibration factor **c** variation in load on front left and front right wheel when passing over an obstacle of height 2.4 inches and 50 cm wide **d** variation in wheel load of front left during deceleration of 5 m/s^{-2}

5 Conclusions

This paper presents an approach to suspension modeling in lightweight vehicles and dynamic estimation of the real-time load on the wheel of a vehicle when vehicle passes over an obstacle. The novel contribution of the paper is as follows:

1. Lagrange's model provides a simple approach to suspension modeling and taking into consideration the spring stiffness, damping coefficient and vehicle parameters, the natural frequency and damping constant for a suspension can be derived.
2. From the on-road test results, it can be affirmed that the damping constant and natural frequency of the suspension is in close resemblance to the results obtained in simulation.

Future developments of this research will include the implementation of traction control and optimization of braking in lightweight electric vehicles based on the load on each wheel.

Acknowledgements We are immensely grateful to Dr. Chinmayee Hazarika, Assistant professor, Department of Electronics and Communication Engineering, GIMT, Guwahati, for her valuable inputs and suggestions in this work.

References

1. Vidya V, Dharmana MM (2017) International conference on circuit, power and computing technologies, ICCPCT
2. Turnip A, Setiawan IR, Amri MF, Tamba TA (2015) International conference on technology, informatics, management, engineering and environment, TIME-E
3. Ikonen E (2017) Active suspension control with state estimation using finite Markov chains. *Int J Adv Mechatronic Syst* 7(3):183–192
4. Ikonen E, Najim K, Garca-Cerezo A (2016) MacPherson suspension system modeling and control with MDP. In: IEEE symposium series on computational intelligence (SSCI)
5. Rankinen A, Ikonen E, Liedes T (2018) Validation of a nonlinear two-dimensional MacPherson suspension system model with multibody simulations. In: 2018 14th IEEE/ASME international conference on mechatronic and embedded systems and applications, MESA, pp 1–5. IEEE
6. Liang D, Zhang K, Jiang Q, Wang Y, Duan J, He H (2019) Mathematical model optimization of electromagnetic suspension system based on additional constraints. In: 14th IEEE conference on industrial electronics and applications, ICIEA, pp 2309–2314. IEEE
7. Neroula S, Sharma S (2019) Dynamic estimation of the tire-road frictional coefficient (TRFC) for acceleration slip regulation in a lightweight electric vehicle. In: TENCON 2019 IEEE region 10 conference, TENCON, pp 2582–2586. IEEE
8. Podder P, Das K, Neroula S, Barman P, Sharma S (2017) Development of an automated setup for dynamic evaluation of DC motor characteristics. In: 2017 IEEE Calcutta conference, CALCON, pp 190–195
9. Gillespie TD (1992) Fundamentals of vehicle dynamics. Society of Automotive Engineers, Warrendale, PA
10. Mohammadzadeh A, Haidar S (2006) Analysis and design of vehicle suspension system using MATLAB and SIMULINK. American Society for Engineering Education
11. Grip HF, Imsland L, Johansen TA, Kalkkuhl JC, Suissa A (2009) Vehicle sideslip estimation: design, implementation, and experimental validation. *IEEE Control Syst Mag* 36–52
12. Das K, Borah CK, Agarwal S, Barman P, Sharma S (2019) Road load model analysis for eco-routing navigation systems in electric vehicles. In: 2019 IEEE 89th vehicular technology conference, VTC2019, pp 1–5. IEEE, Spring
13. Sharma S, Pegu R, Barman P (2015) Electronic differential for electric vehicle with single wheel reference. In: 2015 1st conference on power, dielectric and energy management at NERIST, ICPDEN, pp 1–5

PIC Controller Based SVPWM Technique for Induction Motor Variable Speed Drive



Pabitra Kumar Guchhait, Suvidip Roy, and Abhik Banerjee

Abstract The Space Vector Pulse Width Modulation (SVPWM) technique is getting more popular than other classical PWM techniques because of its cleaner harmonic spectrum and higher level of output voltage. In this work, three phases of balanced AC has been generated with four different frequency levels using an 8-bit microcontroller to improve the performance of the system and also to minimize the cost of the inverter. Voltage/Hz (V/f) control for induction motor drive is also done by developing a suitable algorithm for generating the control pulses. Experimental results are provided to check the effectiveness of SVPWM technique.

Keywords Pulse width modulation · SVPWM · Inverter · Induction motor · Variable voltage and variable frequency control

1 Introduction

In the recent trend for the Variable Voltage as well as for the Variable Frequency controlled induction motor drives, pulse width modulated Voltage Source Inverter (VSI) techniques are universally used [1]. Among the various PWM techniques, sinusoidal PWM (SPWM) is widely accepted. In SPWM the maximum output voltage that can be reached up to 61.2% E_{dc} in linear modulation region. To get maximum output voltage, we have to keep the modulation index ($m = 1$) which will cause an increased amount of harmonics at the output resulting in inferior system performance [2]. In contrast to the SPWM technique, the space vector PWM (SVPWM) method

P. K. Guchhait (✉) · A. Banerjee

Department of Electrical Engineering, National Institute of Technology Arunachal Pradesh, Yopia, Arunachal Pradesh 791112, India

e-mail: pabitraguchhait@gmail.com

A. Banerjee

e-mail: abhik_banerjee@rediffmail.com

S. Roy

SMS India Private Limited, Gurugram, Haryana, India

e-mail: suvidip1991@gmail.com

provides superior harmonic quality as well as an extended linear range of operation. In SVPWM method, we can reach a maximum output voltage up to 91.2% E_{dc} in the linear modulation region [3]. There has been an upward trend in the use of SVPWM technique for the induction motor drive because the technique is less trouble to digital realization and also the better dc bus utilization. There are so many papers [4–6] where different approach has been taken to implement the SVPWM technique for induction motor drive using FPGA, DSP and microcontroller. Several literature [7, 8] also discusses the output results between different PWM strategies that have been carried out. In this present work, an SVPWM VSI fed V/f controlled induction motor drive has been designed and an 8-bit microcontroller has been taken into consideration to develop the inverter which may promise a very low cost-effective and efficient than the SPWM.

2 Theoretical Background of the Work

Here, a brief explanation of the theory of SVPWM has been given. Space Vector Modulation (SVM) deals with a special type of switching sequence based on the three upper switches of the VSI. Theoretically, a sinusoidal voltage is treated as the reference vector which rotates at a constant angular frequency and the average output voltage track the reference voltage with the minimum level of the harmonic disorder.

2.1 Space Vector Modulation

The concept of Space Vector (SV) is explained here by deducing its mathematical model with reference to three 120° phase-shifted sinusoidal signals. At first, three vectors are considered $R(t)$, $Y(t)$ and $B(t)$ which are 120° apart from each other in space such that at any instant, the summation of $R(t) + Y(t) + B(t) = 0$ as shown in the Fig. 1.

The resultant vector \mathbf{V} can be written as

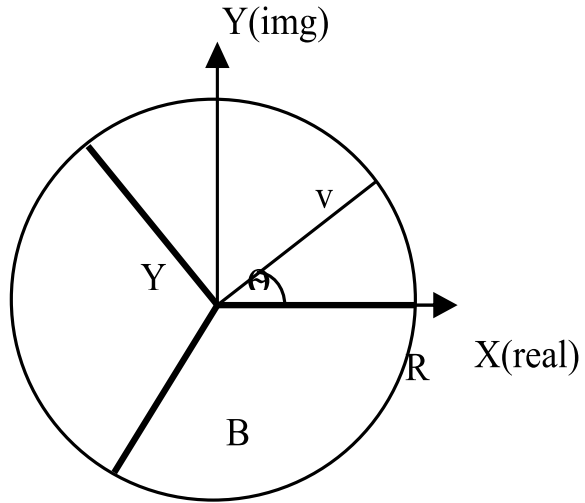
$$\mathbf{V} = \mathbf{V}_x + j\mathbf{V}_y \quad (1)$$

$$\text{Where, } V_x = R - (Y - B)\sin\frac{\pi}{6} \quad (2)$$

$$V_y = (Y - B)\cos\frac{\pi}{6} \quad (3)$$

This is equivalent to the following matrix form

Fig. 1 Orientation of R , Y , B and V



$$\begin{bmatrix} V_x \\ V_y \end{bmatrix} = \frac{2}{3} \begin{bmatrix} 1 & -\frac{1}{2} & -\frac{1}{2} \\ 0 & \sqrt{\frac{3}{2}} & -\sqrt{\frac{3}{2}} \end{bmatrix} \begin{bmatrix} R \\ Y \\ B \end{bmatrix} \quad (4)$$

where 2/3 in Eq. (4) represents the scaling factor.

The resultant vector V often known as the SV and also represents $\mathbf{V} = V e^{j\theta}$. Where,

$$\theta = \tan^{-1} \frac{V_y}{V_x} \quad (5)$$

$$V = \sqrt{V_x^2 + V_y^2} \quad (6)$$

The three-phase sinusoidal balanced voltages $R(t)$, $Y(t)$, $B(t)$ are as follows:

$$R(t) = V_m \sin(\omega t) \quad (7)$$

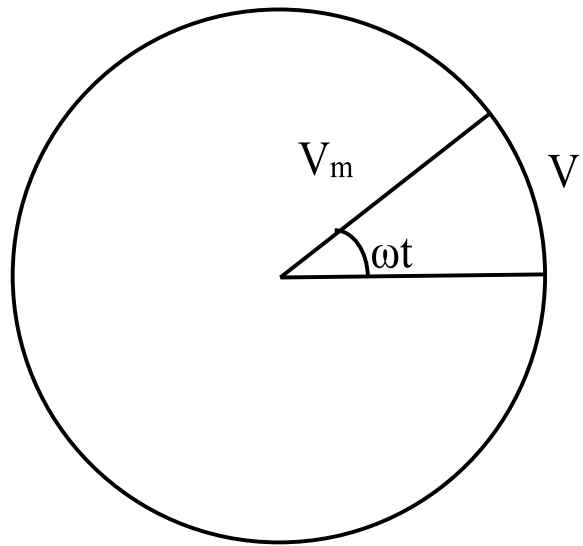
$$Y(t) = V_m \sin(\omega t - 120^\circ) \quad (8)$$

$$B(t) = V_m \sin(\omega t + 120^\circ) \quad (9)$$

The voltage SV obtained from these equations is given by,

$$\mathbf{V} = V_m e^{j\omega t} \quad (10)$$

Fig. 2 Trajectory of the space vector

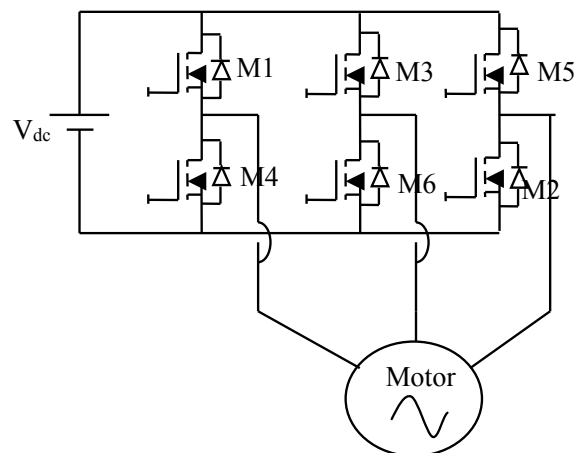


The SV rotates with constant speed and constant magnitude of ω rad/sec and V_m , respectively. Figure 2 represents the locus of SV. The radius of the circular path depends on the voltage amplitude.

2.2 Space Vector PWM in VSI

The schematic diagram of a typical VSI is shown in Fig. 3. S_1, S_3, S_5 and S_2, S_4, S_6 are the upper and lower leg switches, respectively. The pairs S_1-S_4, S_3-S_6 and

Fig. 3 Three phase VSI



$S5-S2$ are their complementary legs. So there will be eight possible switching states, two of them will be zero switching states ($V7, V8$), and the rest six states will be active switching states ($V1-V6$). The eight different switching states are tabulated in Table 1. Here the switches can be ON or OFF, meaning 1 or 0. From Table 1, we can see that magnitude of the inverter line voltage remains constant for different switching conditions only the vectors are shifted by a phase angle 60° with them. The SVs of the inverter line voltage are hexagonal in nature and depicted in Fig. 4 where the zero vectors ($V7, V8$) reside at the origin. The locus of the reference voltage space vector (V^*) (see Fig. 4) is circular in nature inside the hexagon. Let decides

Table 1 Switching states of the VSI

State	Status of the switches			Space voltage vector
	$S1$	$S3$	$S5$	
1	1	0	0	$\mathbf{V1} = \frac{2}{\sqrt{3}} V_{dc} \angle 30^\circ$
2	1	1	0	$\mathbf{V2} = \frac{2}{\sqrt{3}} V_{dc} \angle 90^\circ$
3	0	1	0	$\mathbf{V3} = \frac{2}{\sqrt{3}} V_{dc} \angle 150^\circ$
4	0	1	1	$\mathbf{V4} = \frac{2}{\sqrt{3}} V_{dc} \angle 210^\circ$
5	0	0	1	$\mathbf{V5} = \frac{2}{\sqrt{3}} V_{dc} \angle 270^\circ$
6	1	0	1	$\mathbf{V6} = \frac{2}{\sqrt{3}} V_{dc} \angle 330^\circ$
7	1	1	1	$\mathbf{V7} = 0$
8	0	0	0	$\mathbf{V8} = 0$

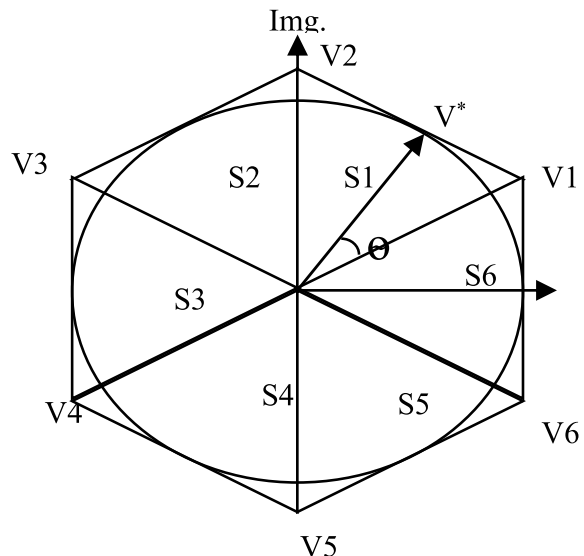
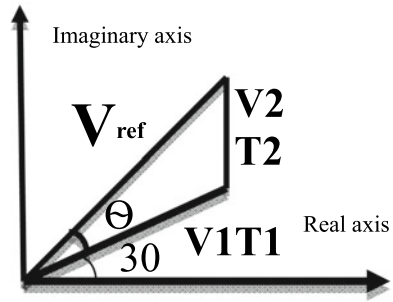
Fig. 4 Different sectors of operation

Fig. 5 Realization of RVV

that at any instant, the reference voltage vector (RVV) makes an angle θ w.r.t $V1$. This RVV can easily be constructed using the corresponding vectors $V1$, $V2$, and zero vectors $V7$, $V8$. For high switching frequency, the RVV can be considered to be fixed at its previous position for one switching period.

Therefore, now the RVV can be formed by taking the average between $V1$, $V2$ for the time period of $T1$ and $T2$, respectively whereas the time period considered for each zero vectors, i.e. $V7$, $V8$ as $T_0/2$ such that total sampling time will be $T_s = T_1 + T_2 + T_0$. From Fig. 5, the following equation can be formed.

$$V^* \cdot T_s = V_1 \cdot T_1 + V_2 \cdot T_2 + V_0 \cdot T_0 \quad (11)$$

In rectangular co-ordinate Eq. (11) can be expressed as

$$T_s M \begin{pmatrix} \cos\left(\frac{\pi}{6} + \theta\right) \\ \sin\left(\frac{\pi}{6} + \theta\right) \end{pmatrix} = T_1 \frac{2}{\sqrt{3}} \begin{pmatrix} \cos\left(\frac{\pi}{6}\right) \\ \sin\left(\frac{\pi}{6}\right) \end{pmatrix} + T_2 \frac{2}{\sqrt{3}} \begin{pmatrix} \cos\left(\frac{\pi}{2}\right) \\ \sin\left(\frac{\pi}{2}\right) \end{pmatrix} \quad (12)$$

From this equation, the following equations are derived

$$T_1 = T_s M \sin\left(\frac{\pi}{6} - \theta\right) \quad (13)$$

$$T_2 = T_s M \sin(\theta) \quad (14)$$

$$T_s = T_1 + T_2 + T_0 \quad (15)$$

$$T_0 = T_s - (T_1 + T_2) \quad (16)$$

Following these equations, the RVV (V^*) is constructed for $90^\circ > \theta > 30^\circ$ as shown in Fig. 5. The RVV is constructed for the other five sectors in the same way. To eliminate the even harmonics in the output line voltage spectra, the line voltage vectors are set for two sampling periods ($2T_s$) and the satisfied condition will be V_z

Fig. 6 Experimental Setup

$- V_n - V_{n+1} - V_z - V_z - V_{n+1} - V_n - V_z$ (where V_z will be anyone of the zero vectors ($V7, V8$) which are used alternatively and the each V_z is used for $T_0/2$ time).

3 Drives Implementations

3.1 Hardware Descriptions

The Hardware setup is figured in Fig. 6. Here, the dc supply is needed for the VSI which has been given from a 1Φ230 V; 50 Hz supply using a variac and a diode bridge rectifier. IGBT (H20R1203) is used as switching devices in three phases VSI Circuit. The gate pulse signals are generated from PIC18F4520 microcontroller device. Hybrid IC VLA542-01R is used for driving IGBT module. This amplifies the gate pulses as well as isolates the control circuit from power circuit. We have used 3-phase/4-pole/415 V/50 Hz/4.7 A/squirrel cage induction motor as load. A voltage divider circuit is used with the help of a potentiometer to provide 0–5 V dc to the ADC pin of the microcontroller as the reference voltage.

3.2 Firm Ware Development

To buildup the SVPWM technique for VSI, an algorithm has been developed. The programming is done on MPLAB C18 compiler, the details of the programming given in flowchart as in Fig. 7. The program has been developed under the four different frequency levels (20 Hz, 30 Hz, 40 Hz and 50 Hz, respectively). The frequency level is changed by changing the ADC input reference voltage (0–5 V). V/f ratio is kept constant for different frequency levels by varying modulation index (m_a). Here we consider sampling angle $\theta_s = 10^\circ$. So the output voltage SV is approximated at every

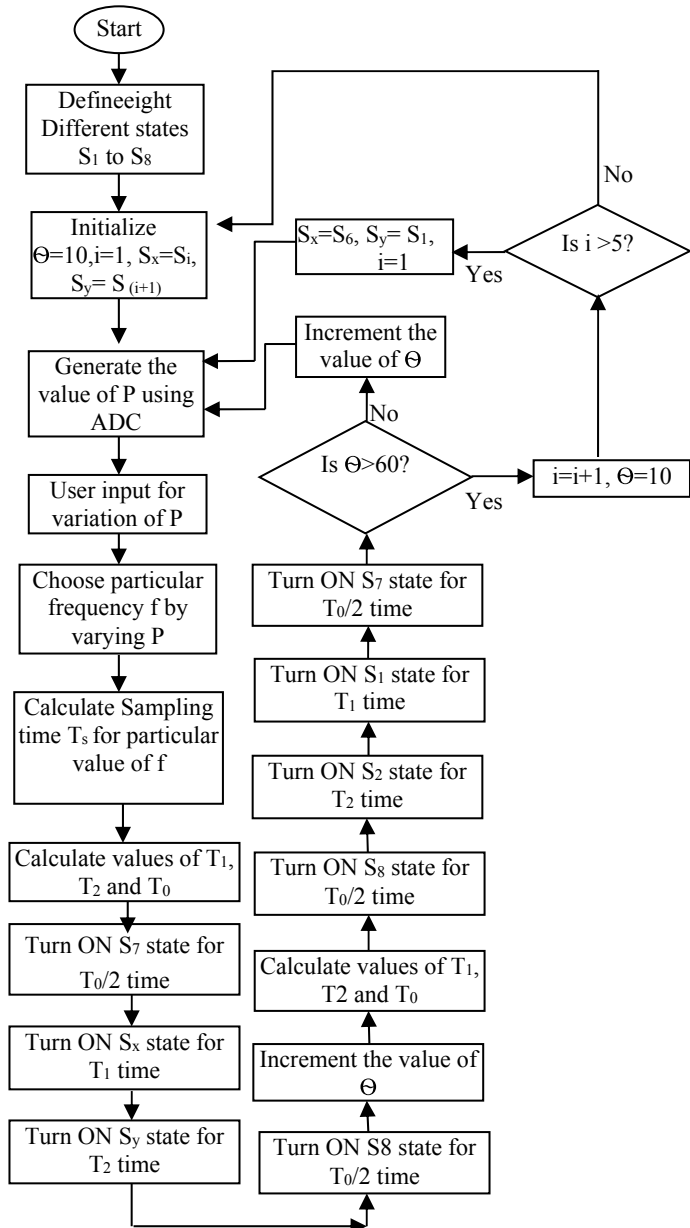


Fig. 7 Flowchart of the program

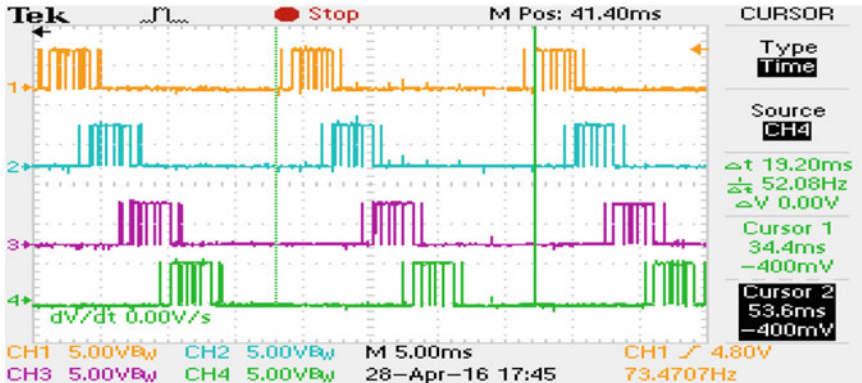


Fig. 8 State 1, 2, 3 and 4

10° of electrical rotation of reference voltage SV. Sampling time is calculated from eq. (17).

$$T_s = \frac{10^3}{f \times 6 \times \left(\frac{60}{\theta_s}\right)} \text{ms} \quad (17)$$

For every 10° of electrical rotation, the value of T_1 , T_2 and T_0 is obtained from the Eqs. (13)–(16). We have used these equations in our program in MPLAB C18 compiler to calculate the values of T_1 , T_2 and T_0 . To make the output voltage follow the reference voltage, state-7 (V_7) ($S1, S3, S5$) is activated for $T_0/2$ times, state-1 (V_1) ($S1, S6, S2$) activated for T_1 times, state-2 (V_2) ($S1, S3, S2$) is activated for T_2 times and state-8 (V_8) ($S4, S2, S6$) is activated for $T_0/2$ times. For next 10°, i.e. $\theta = 20^\circ$, the same procedure should be maintained to calculate T_1 , T_2 and T_0 and follow the reverse sequence V_8, V_2, V_1 and V_7 . To generate the output reference voltage for the first 60° rotation, i.e. for sector-1 the same procedure should be followed three times. For the remaining sectors, T_1 , T_2 and T_0 are calculated in the same way only the line voltage vectors used to construct the reference voltage SV are changed and the switching sequence is the same as discussed for sector-1. The switching states and gate pulses are shown in the following Figs. 8, 9 and 10. The whole setup is depicted in Fig. 11 schematically.

4 Experimental Results

The line voltage and current waveforms are shown in Figs. 12 and 13 for 50 Hz frequency. The output voltage is higher with SVPWM technique compared to Sinusoidal PWM (SPWM) technique for the same DC bus voltage. The line voltage nearly

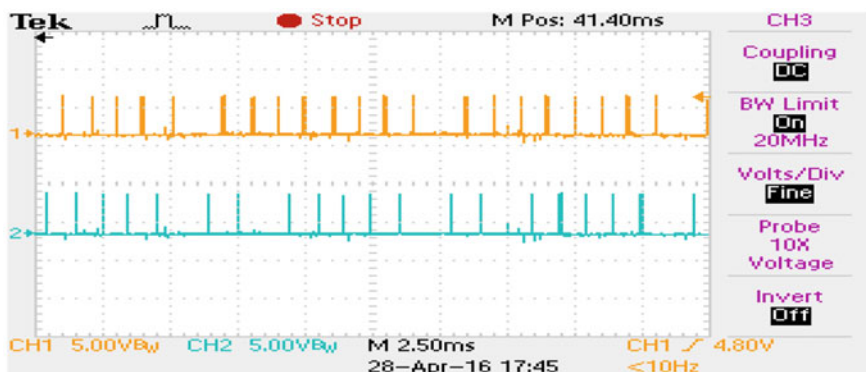


Fig. 9 State 7 and 8

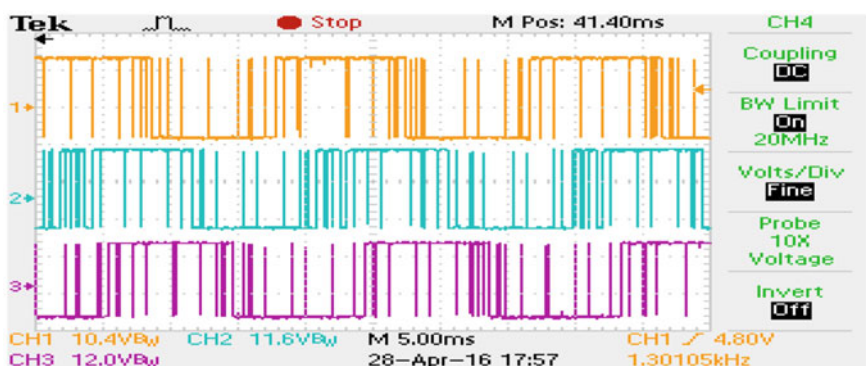


Fig. 10 Gate pulses

138 V for dc bus voltage 196 V whereas 105 V for the same dc bus voltage. The line current is 0.45 A for SVPWM technique as compared to 0.34 A for SPWM technique. It is clear from the figures that the harmonic content is low in output voltage and current using SVPWM technique. The V/f control is easily done here and the output line current remains almost constant for different frequency levels after putting constant load on the induction motor. The V/f control curve is given in Fig. 14. Therefore, it is evident from the results that SVPWM technique is very much convenient to implement for different frequency levels and for V/f control.

5 Conclusions

In conclusion, the development and implementation of space vector pulse width modulated VSI is successful. As we have encountered some problems for smooth

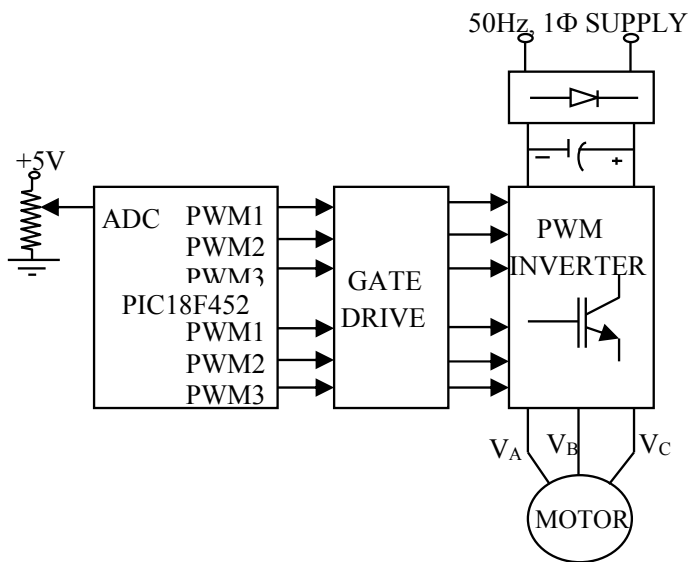


Fig. 11 Schematic diagram of whole set up



Fig. 12 Output line voltage

frequency variation from (0 to 50 Hz) with 8-bit microcontroller discrete frequency levels have been used instead of a smooth variation. Still the results are good with respect to other SVPWM industrial drives using DSP or FPGA. The V/f controlled has been done very easily and precisely. Drives with V/f techniques solve many applications in the area of compressor, pumps, fan, conveyor etc. and also save

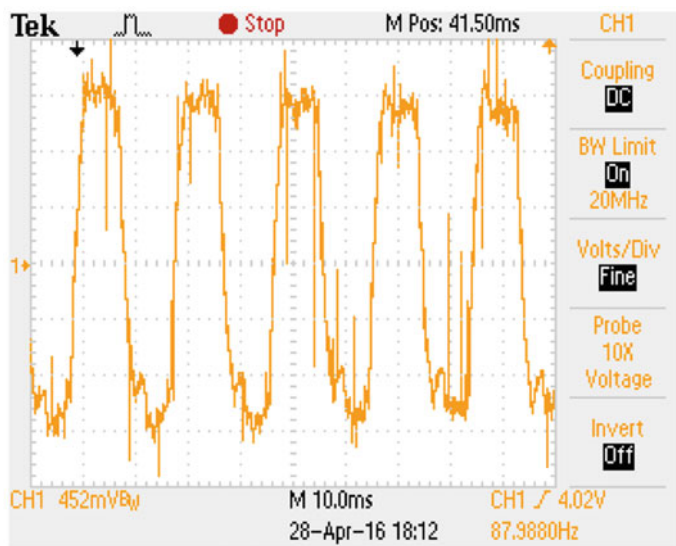


Fig. 13 Output line current

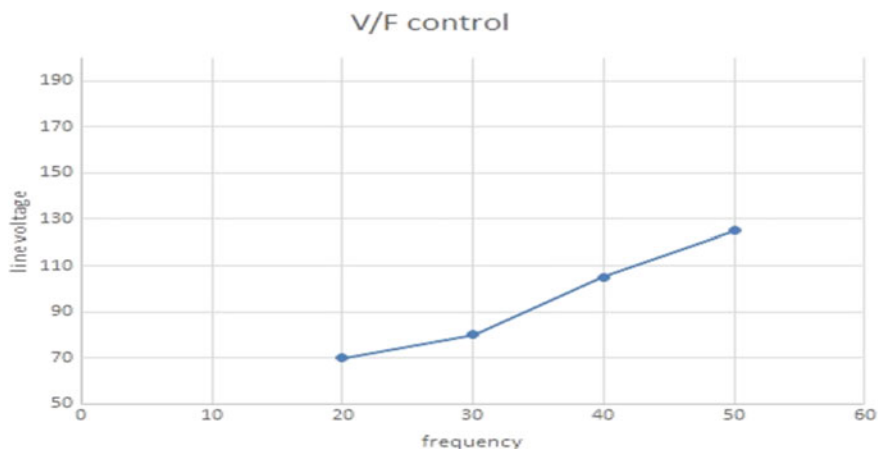


Fig. 14 v/f control of SVPWM

energy to reduce the cost. V/f drive with close loop techniques is used, where the load changing requires with constant speed.

References

1. Bose BK (2010) Power electronics and motor drives: advances and trends. Elsevier
2. Mohan N, Undeland TM, Robbins WP (2003) Power electronics: converters, applications, and design. Wiley
3. Buasre A, Subsingha W (2013) Double-sided linear induction motor control using space vector pulse width modulation technique. Energy Procedia 34:181–188
4. Dutta S, Chandra A, Chowdhury S (2016) Design and development of an 8 bit microcontroller based space vector PWM inverter fed Volt/Hz induction motor drive. CIEC, Kolkata
5. Loongk LK (May, 2008) Micro-controller based space vector modulation (SVM) signal generator. Faculty of Electrical Engineering University, Teknologi, Malaysia
6. Ali JA, Hannan MA, Mohamed A (2014) PSO algorithm for three phase induction motor drives with SVPWM switching and V/f control. In: 2014 IEEE international conference on power and energy (PECon), pp 250–254
7. Khan H, Miliani E-H, Drissi KEK (2012) Discontinuous random space vector modulation for electric drives: a digital approach. IEEE Trans Power Electron 27(12)
8. Tian K, Wang J, Wu B (2016) A virtual space vector modulation technique for the reduction of common-mode voltages in both magnitude and third-order component. IEEE Trans Power Electron 31(1)

A Neural Network Based Strategic Placement and Task Assignment for a Multi-agent System



Mukund Subhash Ghole and Anjan Kumar Ray

Abstract To provide surveillance, relief, and support, a multi-agent system (MAS) can be used. Therefore, task assignment and strategic placement become an essential part of the MAS. In this article, a method of attending the demands from the workspace is proposed in two modes of operations. One is operating MAS from its base camp through task assignment. Other is training the MAS using self-organizing map to place at its strategic position and address the demands of attending task. Distance and task execution overheads are included in the method for a more realistic situation. Extensive simulations are presented in 2D and 3D to validate the proposed work and comparative studies are presented to highlight the effectiveness of each mode of operation.

Keywords Task assignment · Self-organizing map (SOM) · Surveillance · Multi-agent system

1 Introduction

Natural disasters are painful and sudden events that come with little to no warning. The recent examples of such disasters are the floods that occurred in 13 Indian states in 2019 [1], the Nepal earthquake in 2015 [2], the Kedarnath flood in 2013 [3], and the Sikkim earthquake in 2011 [4]. Such disasters result in loss of human lives and resources. To provide relief and support, multi-agent system (MAS) can be used to do various tasks simultaneously. Task assignment (TA) becomes an essential part of MAS in pre and post-disaster events and for surveillance of several areas of interest.

MAS is a system composed of multiple interacting intelligent agents that can solve tasks that are difficult for an individual agent. A MAS has several applications

M. S. Ghole (✉) · A. K. Ray

Department of Electrical and Electronics Engineering, National Institute of Technology Sikkim, Ravangla, Sikkim 737139, India

e-mail: mukund.ghole@gmail.com

A. K. Ray

e-mail: akray.nits@gmail.com

such as support for pre/post-disaster events, warehouse management [5], robotic soccer cup [6], multi-robot patrolling, traffic and transportation management [7]. TA also has applications related to rescue robots [8]. In [9], a crowd intelligence based parcel delivery task assignment method was presented which includes ride-sharing-based delivery mechanism. Some applications of self-organizing map (SOM) include autonomous navigation in next-generation mars rovers [10], an attempt on developing human–robot interactions to classify and select autonomous behavior of the system [11]. In [12], a dynamic ambulance dispatching and redeployment system to assist real-time decision making is developed to solve real-life instances arising in Montreal. A multi-task allocation to participants while minimizing the total traveling distance was presented in [13].

In this work, a method of attending tasks is proposed by authors for two modes of operation. First, a multi-agent system is sent to the tasks directly from the base camp to attend the tasks by taking overhead for distance traveled and task execution. In the second mode, the agents are trained to place themselves strategically within the workspace and then they attend the tasks considering both overheads. In order to validate the proposed work, simulation studies are presented. A comparative study between the above two modes is also presented in 2D as well as in 3D simulation environments.

The paper is arranged as follows: in Sect. 2, the proposed method is presented. The validation of the proposed work in a simulated environment is presented in Sect. 3. In Sect. 4, the overall conclusion is made.

2 Methodology

A problem is considered based on the task to agent distance using a multi-agent multi-task assignment method. Consider an open workspace having a set of tasks, and a base camp is defined within the workspace, where the agents reside in the beginning. The agents can be placed at their strategic locations to better serve the tasks coming from the workspace by training these agents using SOM. The nomenclature used in the proposed method is tabulated in Table 1.

2.1 Overhead Costs

In order to make this method look more realistic, two overhead costs are added during auctioning as shown in Eqs. 2 and 3.

- Distance overhead cost

In order to attend a task, the agent has to travel a distance which could be directly or via completing other task(s), therefore an overhead dia is added, which is zero when the agent attends a task directly from its initial position.

Table 1 Nomenclature used

N	Total number of agents	$d_{j,k}$	Lattice distance between winner and j^{th} agent
M	Total number of demands/tasks	$h_{j,k(x)}$	Neighborhood function
t	time step	$\sigma(t)$	Width of the neighborhood function
t_{\max}	Maximum number of time steps	σ_0	Initial value of width function
x	Input position	$\eta(t)$	Learning rate
ω	Weights of an agent	η_0	Initial value of learning rate
m	Dimension of the search space	τ_1	Time constant of width function
$k(x)$	Index of the winner agent	τ_2	Time constant of learning rate
A	Set of all agents	T	Set of all tasks
T_r	Set of all remaining tasks	d_{jr}	Distance overhead for A_i from task T_{jr}
dia	Distance overhead for assigned tasks for i^{th} agent	d_{\min}	Closest task to agent distance
M_r	Number of remaining tasks	$\delta_{to(i)}$	Task completion overhead of i^{th} agent
γ	Task completion overhead value for $A_{(ir,\text{assigned})}$ to $T_{(jr,\text{assigned})}$		

- Task completion overhead cost

Every agent that attends a task, requires some amount of work to be done to complete that task, the more tasks an agent does, the task the completion overhead costs of that agent increases.

2.2 Multi-agent Task Assignment

- The following relations are considered for modeling the task assignment:

$$A_i \in A, \quad \forall i = 1, 2, \dots, N, \quad T_j \in T, \quad \forall j, \quad T_{jr} \in T_r, \quad \forall j_r \quad (1)$$

where, j is the ID of M number of tasks, j_r is the ID of M_r number of unassigned tasks. Initially $M_r = M$, $T_{jr} = T_j$, $dia = 0$ and $\delta_{to(i)} = 0$.

- Calculate the task to agent distance as

$$d_{ijr} = ||A_{ir}, T_{jr}|| + dia + \delta_{to(i)}, \quad \forall A_{ir}, \forall T_{jr} \quad (2)$$

- Find the closest task for each agent

$$d_{\min} = \underset{ir, jr}{\operatorname{argmin}}(d_{ijr}) \forall A_{ir}, \forall jr \quad (3)$$

then assign that task T_{jr} to the agent A_{ir} , which will henceforth be referred as $T_{(jr, \text{assigned})}$ and $A_{(ir, \text{assigned})}$, respectively. Exclude that task to form the $T_{jr} \in T_r$.

- Update the remaining tasks and the position of agents to the already assigned task as follows:

$$\begin{aligned} M_r &= M_r - 1 \\ A_{(ir, \text{assigned})} &\Leftarrow T_{(jr, \text{assigned})} \\ \text{dia} &= \|A_{(ir, \text{assigned})}, T_{(jr, \text{assigned})}\| + \text{dia} \\ \delta_{to(A_{(ir, \text{assigned})})} &= \delta_{to(A_{(ir, \text{assigned})})} + \gamma \end{aligned} \quad (4)$$

- Repeat the Eqs. 2 to 4, till all the tasks are assigned.

2.3 Strategic Placement

Several applications of TA like area surveillance or quick response to the demand for task execution, during emergency, require MAS to be placed strategically. This provides advantages such as swiftness in response and less distance to travel. Therefore, the SOM paradigm [14] is utilized here to train the MAS. Integration of overhead costs emphasizes the simulation's usefulness for real scenarios.

2.4 Lattice Structure of Agents and Their Weights

Every agent acts as a neuron in the SOM, and these agents are placed in a single-dimensional lattice. For each demand from the workspace, the agents move and place themselves in the vicinity of the demand. Every agent has a weight associated with it, which represents the co-ordinates in the workspace. Consider an m dimensional workspace, an agent i 's weight can be represented as:

$$\omega_i = [\omega_{i1}, \omega_{i2}, \dots, \omega_{im}] \quad \text{for } i = 1, 2, \dots, N \quad (5)$$

Each agent's initial weights are selected from the base camp.

2.5 Generation of Input Points

Simulated Environment: In a workspace of m -dimensions, an input is randomly generated in the workspace and it is defined as:

$$x(t) = [x_1, x_2, \dots, x_m] \quad (6)$$

where t is the sample. In this paper, for 2D and 3D workspaces, m is taken as 2 and 3, respectively.

2.6 Training of Agents Using SOM

Euclidean distance between each agent and input in a time step is calculated. The winner agent is decided based on the following equation [14]:

$$k(x) = \text{index} \left[\min_i \|x(t) - \omega_i(t)\| \right] \quad \text{for } i = 1, 2, \dots, N \quad (7)$$

The winner agent influences its neighboring agents to move towards the input point. A Gaussian function is used as a neighborhood function for each step which is given as

$$h_{j,k(x)}(t) = e^{-\frac{d_{j,k}^2}{2\sigma^2(t)}}, \quad \text{for } t = 0, 1, \dots, t_{\max} \quad (8)$$

As the training proceeds, the winner agent's influence on its neighboring agents should gradually decrease after each step, it is given by

$$\sigma(t) = \sigma_0 e^{-\left(\frac{t}{\tau_1}\right)} \quad (9)$$

Now, the weights of agents are updated in each step using the following equation

$$\Delta\omega_i(t) = \eta(t) h_{j,k(x)}(t) (x(t) - \omega_i(t)) \quad \forall i = 1, 2, \dots, N \quad (10)$$

In Eq. 10, $\eta(t)$ is the learning rate parameter and is given by

$$\eta(t) = \eta_0 e^{-\left(\frac{t}{\tau_2}\right)} \quad (11)$$

The weight of agent i is updated using the following equation:

$$\omega_i(t+1) = \omega_i(t) + \Delta\omega_i(t) \quad \text{for } i = 1, 2, \dots, N \quad (12)$$

3 Results

The proposed method is tested for 2D and 3D workspaces and the effects of the task assignment and strategic placement of a multi-agent system are presented and compared among themselves. In both cases, $\gamma = 20$. For the training with SOM, the parameters are $t_{\max} = 1000$, $\sigma_0 = 5$, $\eta_0 = 5$, $\tau_1 = 5$, $\tau_2 = 40$.

- In TA mode only, agents are attending the demands which originate from the whole workspace with the help of the proposed TA method. This demonstrated in Figs. 1 and 3 for cases I.a and II.a, respectively.
- In SP and TA mode, the agents are strategically placed in the workspace and then any demand that comes can be attended. A two-step process is followed. In order to place the agents strategically, they are first trained using the data taken from the whole workspace using SOM. After training, any demand that originates from the workspace can be attended. This is demonstrated in Figs. 2 and 4 for cases II.a and II.b, respectively.

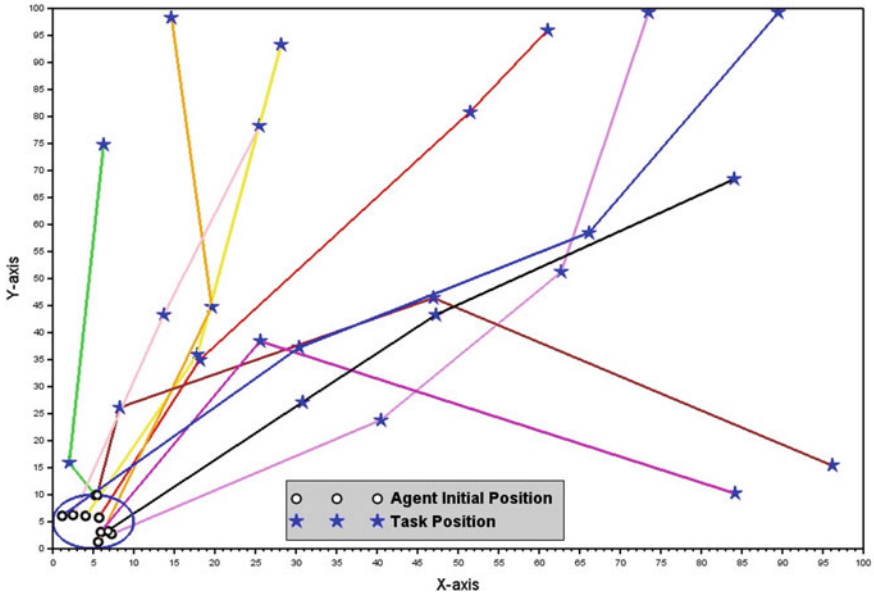


Fig. 1 (Case I.a) agents attending tasks coming from the whole workspace; base camp is at a corner place (TA mode only)

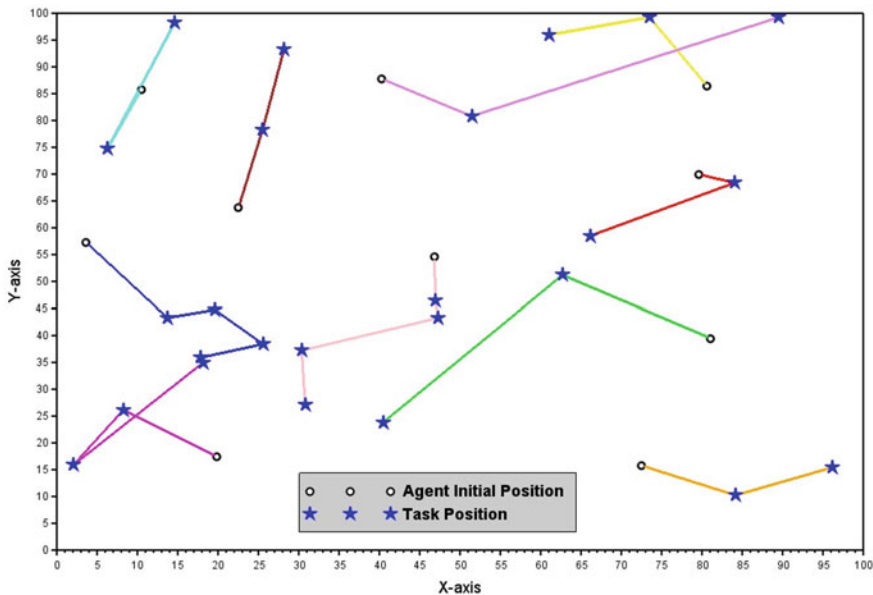


Fig. 2 (Case I.b) agents are placed at their strategic positions and then they attend the tasks coming from the whole workspace (SP and TA mode)

3.1 Case I

In Case I, the task assignment method is presented in 2D workspace for two scenarios. The TA mode only is shown in Fig. 1. The SP and TA mode is shown in Fig. 2. In this case, $N = 10$ and $M = 25$ are taken. The results of both scenarios are tabulated in Table 2.

3.2 Case II

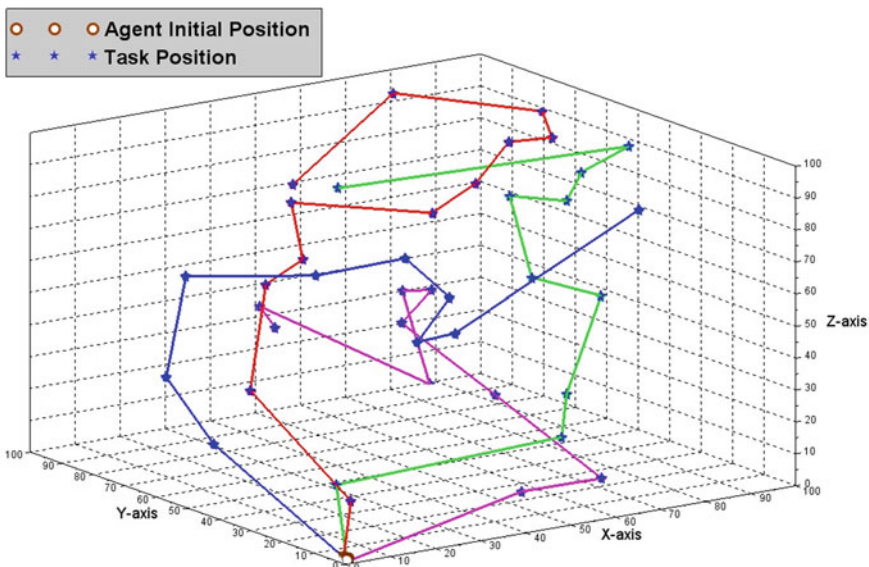
In Case II, the task assignment method is presented in 3D simulation in two scenarios as mentioned in Case I (Figs. 3 and 4). In this case, $N = 4$ and $M = 40$ is taken. The results of both scenarios are tabulated in Table 3.

4 Conclusion

In this work, SOM based strategic placement, a task assignment method of multi-agent system including two overhead costs are presented. From the results, it is

Table 2 2D workspace

Agent	Case I	
	TA only (units)	SP and TA (units)
A1	89.6466	57.0805
A2	85.0095	27.5807
A3	74.1462	25.0475
A4	100.0458	25.9360
A5	130.0413	55.5508
A6	108.9334	30.0736
A7	99.7778	51.3964
A8	120.0514	39.2868
A9	65.5974	40.2478
A10	117.4837	36.8788
Total distance	990.7332	389.0793

**Fig. 3** (Case II.a) agents attending tasks coming from the whole workspace; base camp is at a corner place (TA mode only)

observed that the agents which are already at their strategic locations respond quickly against demands. Incorporation of overhead costs exhibits its effect on realistic scenarios of surveillance. This phase of the work is focussed on a task assignment method for agents and comparison is provided. In the future, the inclusion of path planning of these agents along with collision avoidance will be considered.

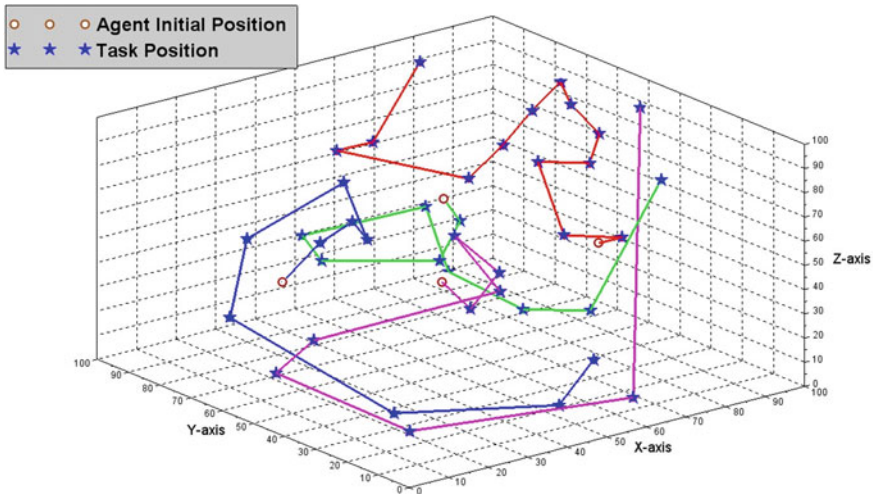


Fig. 4 (Case II.b) agents are placed at their strategic positions and then they attend the tasks coming from the whole workspace (SP and TA mode)

Table 3 3D workspace

Agent	Case II	
	TA	SP and TA
	(units)	(units)
A1	272.49377	324.6839
A2	314.2017	222.0405
A3	256.5464	244.0955
A4	278.5442	285.3438
Total distance	1121.7862	1076.1639

Acknowledgements This work is supported by the Visvesvaraya Ph.D. Scheme, Digital India Corporation (formerly known as the Media Lab Asia) for the project entitled “Intelligent Networked Robotic Systems”.

References

1. https://en.wikipedia.org/wiki/2019_Indian_floods. Accessed on 23 Dec 2019
2. Goda K, Kiyota T, Pokhrel RM, Chiaro G, Katagiri T, Sharma K, Wilkinson S (2015) The 2015 Gorkha Nepal earthquake: insights from earthquake damage survey. Front Built Environ, Front 1(8)
3. https://en.wikipedia.org/wiki/2013_North_India_floods. Accessed on 23 Dec 2019

4. Prajapati SK, Kumar A, Chopra S, Bansal BK (2013) Intensity map of Mw 6.9 2011 Sikkim–Nepal border earthquake and its relationships with PGA: distance and magnitude. *Nat Hazards* 69(3):1781–1801
5. <https://azbigmedia.com/business/economic-development/heres-a-look-at-the-economic-development-wins-of-2019>. Accessed on 23 Dec 2019
6. Asada M, Stone P, Veloso M, Lee D, Nardi D (2019) RoboCup: A treasure trove of rich diversity for research issues and interdisciplinary connections (TC spotlight). *IEEE Robot Autom Mag* 26(3):99–102
7. Burmeister B, Haddadi A, Matylis G (1997) Application of multi-agent systems in traffic and transportation. *IEE Proc Softw* 144(1):51–60
8. Amaya S, Mateus A (2019) Tasks allocation for rescue robotics: a replicator dynamics approach. In: Rutkowski L, Scherer R, Korytkowski M, Pedrycz W, Tadeusiewicz R, Zurada J (eds) Artificial intelligence and soft computing. ICAISC 2019. Lecture Notes in Computer Science, vol 11509. Springer
9. Wang F, Wang F, Ma X, Liu J (2019) Demystifying the crowd intelligence in last mile parcel delivery for smart cities. *IEEE Netw* 33(2):23–29
10. Dlouhy S, Arneson E (2019) Applications of autonomous navigation in next-generation mars rovers. In: International Telemetering Conference Proceedings
11. Jitviriya W, Hayashi E (2014) Application of self-organizing map for analysing robotic arm's action with consciousness-based architecture module. *J Robot Netw Artif Life* 1(2):135–139
12. Gendreau M, Laporte G, Semet F (2001) A dynamic model and parallel tabu search heuristic for real-time ambulance relocation. *Parallel Comput* 27(12):1641–1653
13. Liu Y, Guo B, Wang Y, Wu W, Yu Z, Zhang D (September, 2016) TaskMe: multi-task allocation in mobile crowd sensing. In: Proceedings of the 2016 ACM international joint conference on pervasive and ubiquitous computing, pp 12–16
14. Kohonen T (1990) The self-organizing map. *Proc IEEE* 78(9):1464–1480

Review and Analysis of Charge-Pump Phase-Locked Loop



Mriganka Gogoi and P. K. Dutta

Abstract A Charge Pump Phase-Locked Loop (CP-PLL) is one of the very important circuits used in the communication system. Its main purpose is to lock the phase and frequency of two signals one can be named as reference signal while other as a feedback signal. It comprises a phase-frequency detector (PFD), a charge pump (CP), a loop filter (LF), and a voltage control oscillator (VCO). In this paper, we are presenting a review and analysis of various configurations of CP-PLL made by different researchers. The analyses mainly emphasize on linear and nonlinear second and third-order CP-PLL.

Keywords Phase-locked loop (PLL) · Charge pump · S-domain · Loop filter · Phase noise · Jitter · VCO

1 Introduction

The significant use of phase-locked loop (PLL) is to match an input signal which is also considered as a reference signal with a feedback signal obtained from the voltage control oscillator in terms of their frequency and phase. Initially developed theories of PLL were analog-based [1], in which an analog mixer was used as a phase difference detector to multiply reference and feedback analog signal. A PLL can operate in three states, free-running state, capture state, and phase lock state. In free-running state, the frequency of the reference signal is zero, while in capture state the reference signal has a particular frequency and that affects the output frequency of VCO and in phase lock state the difference in reference signal frequency and that of output signal frequency is zero. Though analog PLL was faster, static error in that structure was a major concern. As a result further analysis made to digital

M. Gogoi (✉) · P. K. Dutta

Department of Electronics and Communication Engineering, North Eastern Regional Institute of Science and Technology, Nirjuli, Arunachal Pradesh, India
e-mail: mriganka.gogoi@dbuniversity.ac.in

P. K. Dutta
e-mail: pkdutta07@gmail.com

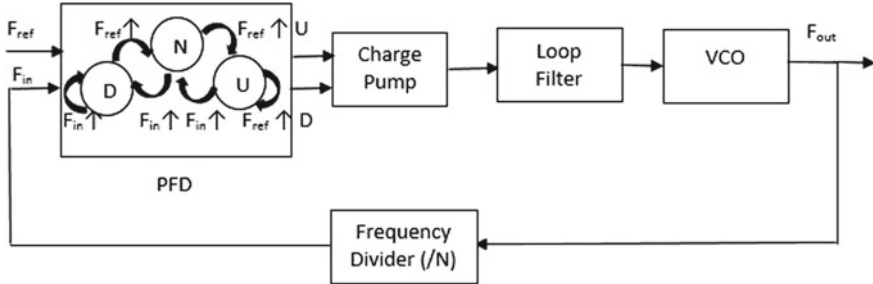


Fig. 1 A CP-PLL block diagram

PLL/CP-PLL. Hence one of the main reasons CP-PLL being widely used is that it provides zero static phase offset theoretically [2].

Figure 1 represents the fundamental blocks of CP-PLL. PFD compares the phase/frequency of reference (F_{ref}) and input signals (F_{in}). A charge pump is associated with PFD to convert its digital states to analog signal so that it can be used for controlling the VCO. Main function of LF is to remove and attenuate unwanted components like noise and high-frequency signal components obtained from the phase detector. The output signal of VCO is periodic with frequency ' F_{out} ', its is a linear function of the input control voltage. A frequency divider circuit is used to divide the clock frequency.

The paper is organized as, Sect. 2 describes a detailed understanding of PFD, Charge Pump, loop filter, and VCO along with their mathematical representation. Section 3 focuses on mathematical analysis of second-order CP-PLL, Sect. 4 describes the analysis of third-order modelling of CP-PLL, Sect. 5 gives the concluding remark.

2 Description of PFD, CP, LF, and VCO

The falling or rising edge of reference (F_{ref}) or VCO (F_{in}) signal triggers the PFD circuit. Its main task is to compare the phase or frequency of two signals and converts into three discrete states namely $-I_P$ (negative state), $+I_P$ (positive state), and 0 (zero state) that is shown in Figs. 2 and 3. A charge pump is associated with PFD to convert its digital states to analog signal so that it can be used for controlling the VCO. In 1980 Gardner presented two different charge pumps with passive filters [1] as shown in Fig. 4. Emphasis is given more on the charge pump with pump current $\pm I_P$, as the analysis is simplified and also configuration is practical in many real-life scenarios.

A loop filter may be an active or a passive filter, one of such passive filter is shown in Figs. 5 and 6, mathematical representation for the same is given in Eqs. (1) and (2).

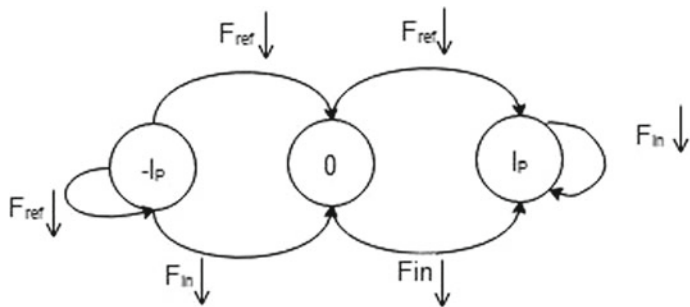
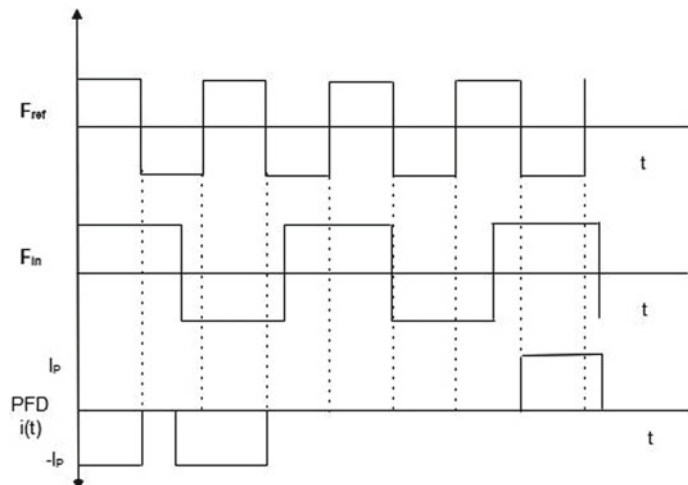
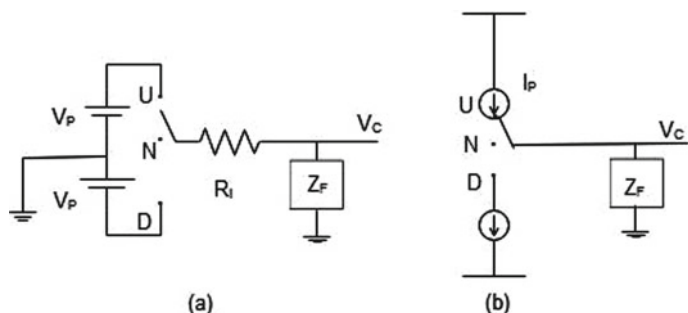
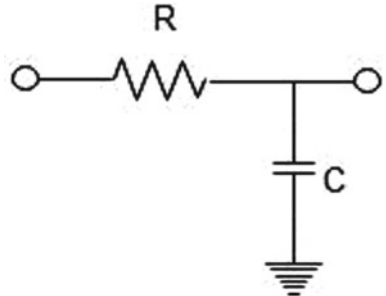
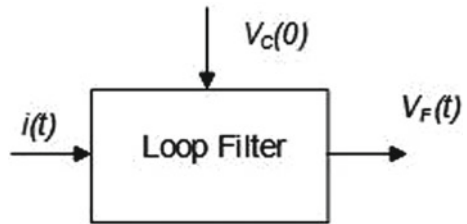
**Fig. 2** PFD state diagram**Fig. 3** PFD operation**Fig. 4** Charge pump with passive loop filters **a** pump voltage $\pm V_P$ **b** pump current $\pm I_P$ [1]

Fig. 5 Low pass RC filter**Fig. 6** Input and output signals of loop filter

$$H(s) = R + \frac{1}{Cs} \quad (1)$$

$H(s)$ is the response of the low pass RC filter in Laplace domain with R resistance and C capacitance [2].

$$V_F(t) = V_c(0) + Ri(t) + \frac{1}{C} \int_0^t i(\tau) d\tau \quad (2)$$

where $V_F(t)$ is the output of loop filter in volt and $V_c(t) = V_c(0) + \frac{1}{C} \int_0^t i(\tau) d\tau$ is capacitor voltage in time domain representation. $V_c(0)$ is the initial value of the capacitor.

Output signal of the loop filter $V_F(t)$ has control over the frequency of VCO. A VCO is presented in Fig. 7 [2].

$$\bar{\theta}_{\text{VCO}}(t) = W_{\text{VCO}}(t) \quad (3)$$

$$W_{\text{VCO}}(t) = W_{\text{VCO}}^{\text{fr}} + K_{\text{VCO}} V_F(t) \quad (4)$$

where $\bar{\theta}_{\text{VCO}}(t)$ is the differentiation of $\theta_{\text{VCO}}(t)$ which is phase of VCO output signal, $W_{\text{VCO}}^{\text{fr}}$ denotes VCO free-running angular frequency and K_{VCO} its gain. $\theta_{\text{VCO}}(0)$ is the initial value of phase of VCO.

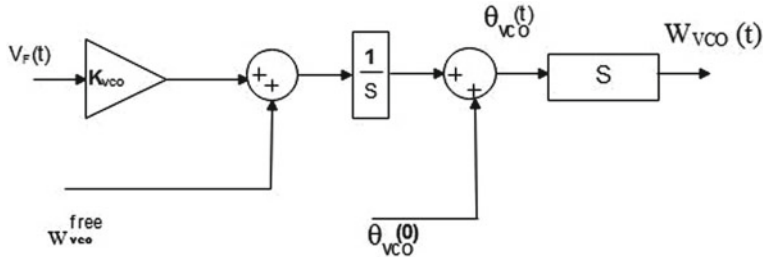


Fig. 7 Voltage control oscillator

Differential equations based mathematical model of CP-PLL are achieved based on the Eqs. (1), (2), (3), and (4) that are shown below [2].

$$\bar{V}_c(t) = \frac{1}{C} i(t) \quad (5)$$

$$\bar{\theta}_{\text{VCO}}(t) = W_{\text{VCO}}^{\text{fr}} + K_{\text{VCO}}(Ri(t) + V_c(t)) \quad (6)$$

3 Second-Order CP-PLL and Its Mathematical Analysis

In 1980 Gardner [1] presented a CP-PLL with a three-state phase detector, a charge pump with passive filters, and a VCO, without a frequency divider circuit. A continuous-time mathematical understanding of second-order CP-PLL filter was presented and found that the transfer function was the same as the conventional second-order PLL and it concluded that for any value of loop gain an analog, second-order CP-PLL is unconditionally stable. Zero static phase error is an essential requirement in PLL which can be achieved using an active filter with large gain. However, according to Gardner zero amplification is not a necessary condition for the charge pump to have zero phase error [3].

A new model with a proper approximation of discrete-time state variables was proposed in 1994 by Van Paemel [4] for CP-PLL of second order. Difference equations are used for representing discrete-time state variables without linearization or approximation. The model estimates the transient waveform of the VCO control voltage exactly and is valid for out of lock situation of PLL. However, the system gain becomes unstable for higher loop gain. The limit derived for stability is approximately 10% of the frequency associated with PLL input signal.

Armaroli et al. [5] presented behavioural modelling in the time domain for CP-PLL using the nonlinear elements. They have presented a simulated method by decomposing a network into a few number of one-way blocks. Proposed models for PFD and VCO were new, charge pump model was obtained based on changes between its

input signals. For a second-order PLL they made assumptions for closed-loop natural frequency, damping ratio, and calculated the cross over frequency. A simulated time required for the proposed algorithms is much faster than the conventional ones, CPU time required is 70 s. However, due to the discrete nature of the circuit, the system is noisier. Acco et al. [6, 7] proposed a discrete linear, and nonlinear model of CP-PLL. The analysis was made for CP-PLL with a frequency divider circuit. In discrete-time linear model VCO, the N-divider and filter equations appear to be linear and trivial while that of PFD characteristic is non-linear. The whole system is represented in linear form by making an approximation of the relation that exists between the phase error and the average current input. This model is suitable for locked state of CP-PLL. The above-described model is event-driven and nonlinear that allows to represent both unlock and overload state, it has high accuracy and requires less simulation time. It is also observed that there is a similarity between the discrete nonlinear model and event-driven model which estimates the state variables. They have illustrated the second-order model by non-linear piecewise set of independent difference equations based on small error signals.

Curran et al. [8] focussed on solving the stability issue of CP-PLL based on nonlinear and discrete-time model proposed by Paemal [4]. They emphasized on the first approximation of the nonlinear system and observed that Gardener's approach of linearization that leads to first approximation is invalid, while paemal's piecewise approach accurately determines the first approximation and is highly conservative. Their stability analysis gives a complete solution for the first approximation.

Leonov et al. [9] attempted to discuss and filled some of the spaces described by the theory of control system, dynamic systems, and engineering concepts of PLL. They have suggested an effective way to find a unique lock-in frequency that will eventually help to solve this problem existed in Gardener's PLL [1].

Homayoun et al. [10] presented a model of time-variant to calculate the small-signal loop transmission of second-order CP-PLL exactly. They have analyzed both small and large signal behaviour on the stability of the model. Observation was made on translational nature of the loop and found that it degrades the system's stability due to overlapping of replica transfer functions. It was shown stability of CP-PLL can be maintained with the loop bandwidth approaching half of the input frequency.

Niansong et al. [11] presented a design of a low jitter PLL for 802.11 a/b/g applications. Performance of VCO affects phase noise and spur of PLL. To reduce phase noise they replaced traditional tail current source by tail current source with source degradation. Spur of the PLL is also affected by the gain of VCO, so a 6-bits digital controlled capacitor array that will maintain lower gain is used. A comparison between phase noise with and without source degradation is found to be -70.37 dBc/Hz and -66.6 dBc/Hz at 10 kHz, -113.9 dBc/Hz and -112.4 dBc/Hz at 1 MHz. They also analyzed phase error occurred due to both static and dynamic current mismatch nature of charge pump and thus made necessary modifications in it to reduce the phase error. Further analysis also made to reduce phase error in Phase frequency detector. Overall phase error reduction in the PLL at 10 kHz and 1 MHz are -89 dBc/Hz and -118 dBc/Hz . RMS jitter in the same frequency band is found to be 757 fs.

Zhao et al. [12] proposed a new nonlinear second-order PLL that has nonlinear elements. It regulates the loop noise bandwidth adaptively through the non-linear module adaptively. Their results demonstrate the increase of tracking speed and as well as acquired bandwidth. Its bandwidth is 18.8 kHz which is much greater than the traditional PLL whose bandwidth is just 4 kHz. Thus it provides a balance between tracking, speed and accuracy.

4 Third Order CP-PLL and Its Mathematical Analysis

Gardner presented a mathematical model with linearized equations for third-order CP-PLL [1]. To mitigate the ripple in second-order CP-PLL, an additional filtering is required which is fulfilled by connecting a capacitor in parallel with RC impedance. The transfer function (TF) ‘ $F(s)$ ’ of the filter is given by Eq. (7) and the order of the overall transfer function of CP-PLL changes to three. A third-order CP-PLL is shown in Fig. 8, and its transfer function ‘ $P(S)$ ’ is given by Eq. (8) [4].

Lu et al. [13] performed jitter transfer analysis in z- domain for a high order giga-bit rate PLL. They have also used the impulse invariance method as used by Hanumolu et al. to obtain the z-domain equations for 3rd order PLL. Stability and frequency steps are analyzed using the discrete transfer function for 3rd order PLL [4].

$$P(S) = \frac{F_{\text{out}}(s)}{F_{\text{ref}}(s)} = \frac{K_{\text{PDF}} K_{\text{VCO}} \left(\frac{1+s\tau_2}{C+C_1} \right)}{s^3 + \left(\frac{1}{\tau_1} \right) s^2 + \left(\frac{K_{\text{PDF}} K_{\text{VCO}} \tau_2}{N(C+C_1)s + \left(\frac{K_{\text{PDF}} K_{\text{VCO}}}{N(C+C_1)\tau_1} \right)} \right)} \quad (7)$$

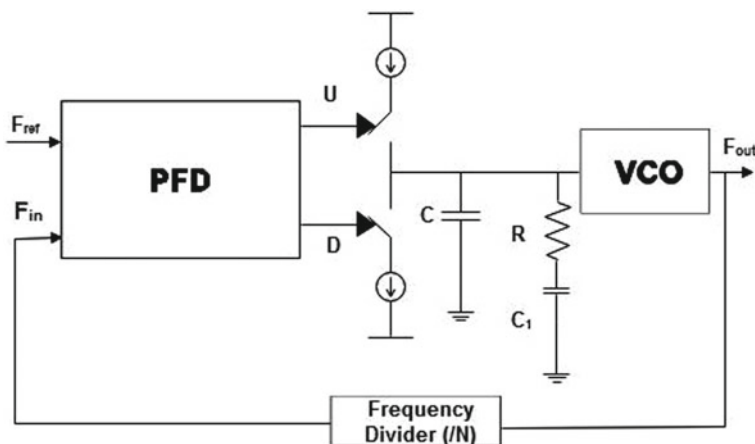


Fig. 8 A CP-PLL with loop filter of second-order [4]

where $\tau_1 = \frac{CC_1}{C+C_1}$ and $\tau_2 = RC$.

The TF of the closed-loop is as given by Eq. (8) [4].

$$F(s) = \frac{1 + sRC}{s(S^2RR_2CC_1C_2 + S(RC(C_1 + C_2) + C_2R_2(C + C_1)) + (C + C_1 + C_2))} \quad (8)$$

where K_{PFD} PFD's gain and K_{VCO} is VCO's gain respectively, N is the number of times VCO clock is divided by the frequency divider circuit.

Hanumolu et al. [14] presented a third-order CP-PLL with exact mathematical analysis and showed that z-domain representation of the state-space model in linear form is similar to the one obtained from the impulse invariant transformation [6]. Nonlinearity linearity effect and current mismatch were assumed to be negligible as a result the model cannot be used for simulation with modern-day PLL tools.

Xintian et al. [15] designed a new single-ended charge pump of low jitter with an opamp of 76 dB voltage gain for clock multiplication in Low voltage differential signalling (LVDS) transmitter [7]. The proposed PLL model comprised of the designed charge pump circuit, it is a full differential VCO, a PFD with dynamic logic, and a loop filter of second order with passive nature. The output parameters show optimal jitter-power consumption product, occupies small area, and large lockin range when compared with some of the existing PLL designs. Power consumption is 12 mW, jitter is 7.1 ps and 65 ps peak-peak at 350 MHz and lock-in range is 100–560 MHz.

Ji et al. [16] design a 1 GHz PLL based frequency synthesizer that is used in IEEE 1394b PHY (physical). For the generation of 1 GHz frequency 4-stage ring oscillator is employed. The final design is a third-order, type-2 charge pump PLL with a differential low ripple charge pump and ring oscillator based VCO. 1 GHz clock is divided into 200, 100, 50, and 25 MHz. Settling time is found to be 4 μs and rms value of period jitter is 2.1 ps. The main focus of the proposed methodology is on providing multi-frequency and multi-phase clock signals.

Armaroli et al. also extended its time-domain behavioural modelling of second-order CP-PLL to third-order [17]. New models for PFD and VCO that were proposed for second-order model were extended to third-order model. Shaktarin et al. [18] proposed an algorithm for PLL with a current detector and second-order loop filter describing the operation of the in-lock indicator. The proposed model of PLL comprised of FPD (Frequency Phase Detector), current-controlled source (CCS), filter (F), charge pump (CP) and controlled oscillator (CO). CCS and F together form the CP. Mathematical analysis is done by representing the model with differential equations, two types of third order CP-PLL are modelled by a different arrangement of resistors and capacitors in the loop filter. The model will help in analysing fine structure of signals in frequency and time ranges and solving stability issues of CP-PLL.

Comparative analysis shows that nonlinear second-order model coupled with nonlinear elements provides a balance between tracking, speed, and accuracy [12]. Third-order CP-PLL especially proposed in [18] solves stability issues of CP-PLL.

Many methodology are implemented by the research community to reduce measurement parameters like speed, dead zone, jitter, phase noise, current mismatch, power dissipation and area are also discussed here. Requirement of extensive analysis, mathematical clarity and optimized design are essential for further development of efficient CP-PLL design.

5 Conclusion

This paper describes the analysis of CP-PLL that has a PFD, a CP, a passive filter, and an Oscillators. Description of these fundamental blocks from mathematical perspective is presented. It gives an idea of various measuring parameters of PLL for its performance enhancement. In order to improve the efficiency, various examples of PLL are proposed by various researchers at different times, however, with the advancement of technology, improvement in the performance parameters is highly essential. Analysis of linear and nonlinear second and third-order CP-PLL presented by various researchers are discussed here. Further comparative analysis of different CP-PLL with the various parameters are elaborately presented.

References

1. Gardner FM (November, 1980) Charge-pump phase-lock loops. *IEEE Trans Commun COM-28(11):1849–1858*
2. Kuznetsov N, Yuldashev M, Yuldashev R, Blagov M, Kudryashova E, Kuznetsova O, Mokaev T (2019) Charge pump phase-locked loop with phase-frequency detector: closed form mathematical model. ArXiv:1901.01468, eess.SP
3. Garner FM (October, 1982) Phase accuracy of charge pump PLLs. *IEEE Trans Commun COM-30(10):2363*
4. Van Paemel M (1994) Analysis of a charge-pump PLL: a new model. *IEEE Trans Commun 42(7):2490–2498*
5. Armaroli D, Liberale V, Vacchi C (August, 1995) Behavioral analysis of charge pump PLLs. *Proc Midwest Symp Circuits Syst 893–896*
6. Acco P, Kennedy MP, Mira C, Morley B, Frigyik B (May, 1999) Behavioral modeling of charge pump phase locked loops. *Proc ISCAS'99 375–378*
7. Acco P (2003) Study of the loop a phase lock: hybrid aspects taken into account. PhD thesis, Toulouse, INSA
8. Curran PF, Bi Ch, Feely O (2013) Dynamics of charge-pump phase-locked loops. *Int J Circuit Theory Appl 41(11):1109–1135*
9. Leonov GA, Kuznetsov NV, Yuldashev MV, Yuldashev RV (2015) Hold-in, pull-in, and lock-in ranges of PLL circuits: rigorous mathematical definitions and limitations of classical theory. *IEEE Trans Circuits Syst-I: Regul Pap 62(10):2454–2464*
10. Homayoun A, Razavi B (2016) On the stability of charge-pump phase-locked loops. *IEEE Trans Circuits Syst I Regul Pap 63(6):741–750*
11. Niansong M, Yu S, Bo L, Yaohua P, Yumei H, Zhiliang H (2017) A low spur, low jitter 10 GHz phase-locked loop in 0.13 μm CMOS technology. *J Semicond 32(3):035004(1–5)*
12. Zhao L, Shi L, Zhu C (2018) New nonlinear second-order phase-locked loop with adaptive bandwidth regulation. *Electronics 7:346*

13. Lu J, Grung B, Anderson S, Rokhsaz S (May, 2001) Discrete z-domain analysis of high-order phase locked loops. Proc ISCAS'01 260–263
14. Hanumolu PK, Brownlee M, Mayaram K, Moon UK (September, 2004) Analysis of charge-pump phase-locked loops. IEEE Trans Circuits Syst I, Fundam Theory Appl 51(9):1665–1674
15. Shi X, Imfeld K, Tanner S, Ansorge M, Farine PA (2006) A low-jitter and low-power CMOS PLL for clock multiplication. In: Proceedings of 32nd European solid-state circuits conference, pp. 174–177
16. Ji JY, Liu HQ, Li Q (2012) A 1 GHz charge pump PLL frequency synthesizer for IEEE 1394b PHY. J Electron Sci Technol 10(4):319–326
17. Best RE (2007) Phase locked loops: design, simulation, and applications. McGraw-Hill Professional
18. Shakhtarin BI, Timofeev AA, Sizykh VV (2014) Mathematical model of the phase-locked loop with a current detector. J Commun Technol Electron 59(10):1061–1068

Image Fusion: Challenges, Performance Metrics and Future Directions



S. B. G. Tilak Babu, I. Chintesh, V. Satyanarayana, and Durgesh Nandan

Abstract Image fusion is a technique of fusing multiple images for better information and a more accurate image compared to source images. The applications of image fusion in the modern military, multi-focus image integration, pattern recognition, remote sensing, biomedical imaging, etc. In this paper discussed, advantages and drawbacks of newly arrived existing methods in the transform domain and spatial domain image fusion, universal acceptable flowchart for image fusion obtained from literature, different helpful datasets that are accessible to assess extensively image fusion algorithms, many performance metrics used to measure the performance of image fusion techniques and finally suggestions are made as per present research necessities of respectable performance with acceptable effort in image fusion.

Keywords Image fusion · Data fusion · Performance metrics · Image integration · Multiscale fusion · Medical image fusion · Multi-focus image fusion

1 Introduction

Image fusion helps to extract more information from a single composite image over two separate images [1–3]. The image fusion method having many applications like multi-modality (e.g. visible and infrared) image fusion, multi-focus image integration, multi-exposure image fusion, remote sensing, biomedical imaging, etc. Proper

S. B. G. Tilak Babu (✉) · I. Chintesh · V. Satyanarayana

Department of Electronics and Communication Engineering, Aditya Engineering College,
Surampalem, India

e-mail: thilaksayila@gmail.com

I. Chintesh

e-mail: chinteshjust@gmail.com

V. Satyanarayana

e-mail: vasece453@gmail.com

D. Nandan

Accendere Knowledge Management Services Pvt, Ltd, CL Educate Ltd, New Delhi, India

e-mail: durgeshnandan051@gmail.com

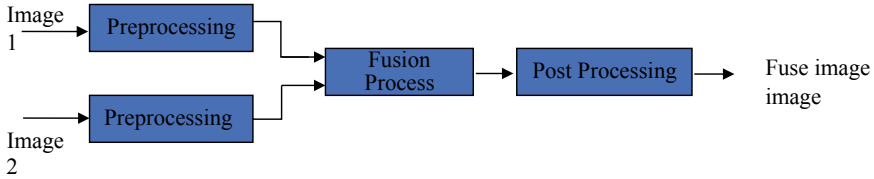


Fig. 1 General image fusion process

design of fusion rule for a specific application like multi-modality is a very important task in research.

Very few articles are identified in the literature on a fusion rule applied on multiple image fusion applications. Moreover, the efficient design of a fusion rule that applies to multiple fusion applications is much needed in the present scenario.

A simple fusion process is shown in Fig. 1, many image fusion methods use often preprocessing for image registration, very few articles have also existed in literature which does not require source image registration [4, 5]. Many of the available datasets consist of registered images so the recently arrived fusion methods not discussing registering of source images, but it is necessary to mention image registration as it impacts the final fused image if source images are not of the same size. There are many kinds of fusion rules proposed to fuse images such as Weight average, choose maximum, coefficient grouping, etc. Few fusion methods existed in the literature that uses more than one fusion rule in their algorithm based on applications [6, 7]. From literature, it is observed that the fusion of images can be efficiently obtained in the transform domain concerning the spatial domain. The simple three steps in the fusion process based on transform domain are (1) Applying transform domain on source images, (2) Fusing images in the transform domain, (3) Applying inverse transform on fused image to get spatial domain fused image. Usually, in post-processing inverse transform or final touches are given to get the final fused image.

Further, the paper is arranged as follows, in Sect. 2 various newly proposed image fusion schemes are discussed. Quality assessment parameters for image fusion are mentioned in Sect. 2. After the thorough study, the tabulated summary s presented with its significance and comparison of various fusion methods in Sect. 3. Finally, a review of the most significant conclusion and future directions are discussed. Articles in the literature conclusion are given in Sect. 4.

2 Image Fusion: Literature Survey

The image fusion methods can be broadly classified into two groups which are as follows:

1. Spatial domain fusion
2. Frequency domain fusion.

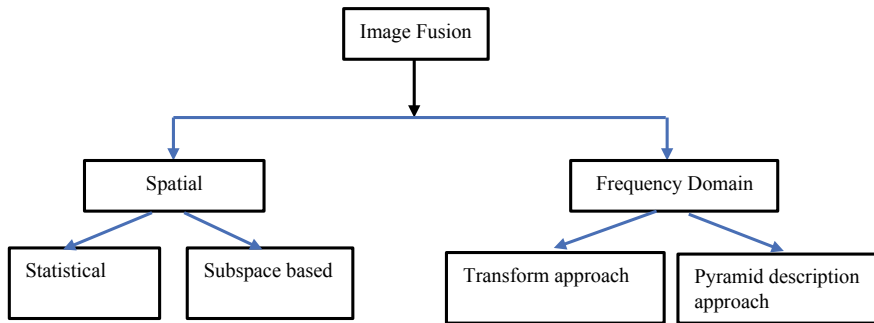


Fig. 2 Image fusion scheme categorization

Various existing approach categorization is as follows (Fig. 2).

As discussed earlier, image fusion having many applications such as multi-focus image integration, pattern recognition, remote sensing, biomedical imaging, etc. Many of the authors proposed to image fusion algorithms to a specific application but a universal algorithm much needed that apply to all types of applications in image fusion. Many algorithms have existed in literature with complexity varies from highly complex transform domain to a simple weighted average of pixels. Jin et al. [8], proposed a lightweight algorithm for fusing multi-focus images. This scheme works on a lesser number of images with the help of adaptive pulse-coupled neural networks local spatial frequency (PCNN-LSF) and Laplacian Pyramid Transform (LPT). Hou et al. [9] presented visible and infrared image fusion performed in the NSST domain. The shift-invariant technique NSST grabbed the properties from wavelet, source images are directly decomposed by NSST into high-frequency and low-frequency subbands. The fusion of low-frequency sub-band performed based on an improved edge saliency map, where high-frequency subbands fusion done by the MSF map. The multi-objective artificial bee colony (MOABC) algorithm with spinning cortical mode utilized to optimize fusion results. Finally, inverse NSST applied to obtain a time-domain fused image from the transform domain. The quantitative performance of the algorithm shows robustness over other existing methods.

Karsanina et al. [10] proposed soil image resolution enhancement by using various stochastic techniques, initially the soil images are rescaled by using bicubic interpolation then immediately segmented into micro-units. Immediately Direction correlation filters (DCF) are applied, the next superposition principle is used to fuse. As very few papers available in the literature on soil image resolution enhancement through image fusion, the authors mentioned key limitations to find solutions immediately. Lihua-jian et al. [11] proposed image fusion based on Joint Bilateral filter (JBF), Kirsch operator, Rolling Guidance Filter (RGF), Weight Average (WA) with global variance and multiplication of weight maps with detail layers. Initially, kirsch operator is used to extracting salience map from source images, by inputting salience maps to RGF, different subbands are obtained. In the iterative process, RGF can extract

edges. The salience maps are optimized by JBF and optimal correction. The performance of fusion is good in objective and subjective evaluation on different types of images, because of two separate fusion rules for base layers fusion and detail layers fusion. Tested on different images viz., multi-modal images, multispectral images, multi-focus images.

Huiqian et al. [12] proposed a fusion method based on two different decomposition techniques name NSST, Moving Frame-based Decomposition Framework (MFDF). Initially, the source images are applied to MFDF separately, and then it decomposed into texture/edge coefficients and approximation coefficients. The maximum Selection Rule (MSR) is used to integrate the texture features, where NSST is utilized in the integration of the approximation coefficients. The component synthesis process is used to obtain the final fused image from approximation fused coefficients and texture fused coefficients. From this proposed method, authors able to get good visual effects and objective values in the fused image compared to source images. In [13], Cartoon Texture Decomposition (CTD) technique results in a cartoon image and texture image from a source image. The combination of proportional calculating and spatial fusion is called spatial based fusion rule which was used to fuse cartoon coefficients. Structure information is preserved in cartoon components by this energy-based fusion rule. Sparse Representation (SR) based fusion rule is used to integrate texture components. The multi-modality image integration algorithm is tested on visible - infrared images, Medical images for medical diagnosis, multi-focus images. One pair or two pairs of MODIS and Landsat images can be fused by the Huihui et al. proposed algorithm [14]. Based on Deep Convolutional Neural Networks (DCNN) the proposed algorithm fuses the source images in two stages (1. Training stage, 2. Prediction stage). Initially, learn the NLM model in between low spatial resolution image and MODIS images. Usually, in the investigation of rapid variations in land surfaces, the main problems are poor atmospheric conditions, and frequent cloud cover is admitted in the proposed method. The authors mentioned that the proposed algorithm is unable to estimate the lost information in LSR MODIS images.

Robust Sparse Representation (RSR) and PCNN-based multi-focus image algorithm proposed by Yond yang et al. [15], RSR helps to decompose sources images into the reconstruction error matrix (residual matrix) and sparse coefficients matrix. PCNN results initial decision map where morphological opening and closing results final decision map. Weighted fusion rule is applied to get the final fused image. Baihong [16], proposed a fusion algorithm with acceptable registration errors and computational complexity for fusing Hyperspectral and multispectral images. The fusion process done by depends on the Low Rank constrained Gaussian Mixture Model (LR—GMM) (Table 1).

Table 1 Significant performance parameters for fused image

Name of metric	Formula	Value for best performance
RMSE	$\text{RMSE} = \sqrt{\frac{1}{MN} \sum_{i=1}^M \sum_{j=1}^N (I_r(i, j) - I_f(i, j))^2}$	Lower (close to zero)
SNR	$\text{SNR} = 10 \log_{10} \left(\frac{\sum_{i=1}^M \sum_{j=1}^N (I_r(i, j))^2}{\sum_{i=1}^M \sum_{j=1}^N (I_r(i, j) - I_f(i, j))^2} \right)$	Higher value
PSNR	$\text{PSNR} = 20 \log_{10} \left(\frac{L^2}{\sum_{i=1}^M \sum_{j=1}^N (I_r(i, j) - I_f(i, j))^2} \right)$	Higher value
CC	$\text{CC} = \frac{2C_{rf}}{c_r + c_f}$	Higher value (close T to $T + 1$)
MI	$\text{MI} = \sum_{i=1}^M \sum_{j=1}^N h I_r I_f(i, j) \log_2 \left(\frac{h I_r I_f(i, j)}{h I_r(i, j) h I_f(i, j)} \right)$	Higher value
SSIM	$\text{SSIM} = \frac{(2\mu I_r I_f + C_1)(2\sigma I_r I_f + C_2)}{(\mu^2 I_r + \mu^2 I_f + C_1)(\sigma^2 I_r + \sigma^2 I_f + C_2)}$	Higher value (close to $T + 1$)
QI	$\text{QI} = \frac{4\sigma_{xy}\bar{x}\bar{y}}{(\sigma_x^2 + \sigma_y^2)[(\bar{x})^2 + (\bar{y})^2]}$	Higher value (close to +1)
σ	$\sigma = \sqrt{\sum_{i=0}^1 (i - \bar{i})^2 h I_f(i)}$	Higher
HE	$\text{HE} = - \sum_{i=0}^L h I_f(i) \log_2 h I_f(i)$	Higher
FMI	$\text{FMI} = \text{MI}_{I_p I_f} + \text{MI}_{I_m I_f}$	Higher
FQI	$\text{FQI} = \sum_{w \in \epsilon} C(w) \begin{pmatrix} \lambda(w) \text{QI}(I_p I_f / w) + \\ (I - \lambda(w) \text{QI}(I_m I_f / w)) \end{pmatrix}$	Higher (close to 1)

3 Summary

In this section, it is the comparative analysis of all existing literature in the field of image fusion and its possible applications (Table. 2).

3.1 Quality Assessment Techniques

Qualitative analysis and quantitative analysis are the two popular ways to estimate the performance of fused images [18–21]. In the earlier analysis, the fused image is

Table 2 Significant measures for image fusion are shown

References	Preprocessing	Methods used	Fusion rule	Applications	Comments
Jin et al. [8] 2018	NA	LPI, PCNNLSF	Combination of MAX and AVERAGE fusion rules	Multi-Focus fusion on gray and colour images	Authors claims, with the help of a lesser number of images the algorithm achieves good performance with acceptable complexity
Hou et al. [9], 2018	NA	NSST, SCM with MOABC algorithm	Improved edge saliency map, MSF map	Visible and infrared image fusion	NSST, MOABC-SCM based algorithm performance is evaluated quantitatively and shows robustness over existing methods
Karsanina et al. [10], 2018	Bicubic interpolation (rescaling purpose)	Bicubic interpolation, segmentation, DCF, averaging	Superposition	Soil images	The key limitation is to find solutions immediately in the field of soil image enhancement through image fusion

(continued)

Table 2 (continued)

Refere nces	Preprocessing	Methods used	Fusion rule	Applications	Comments
Jian et al. [11], 2018	Kirsch operator (saliency map extraction purpose)	RGF (decomposition purpose), JBF	WA with global variance (base layers), multiplication of weight maps with detail layers	Multi-modal images, multispectral images, multi-focus images	In the iterative process, RGF can extract edges. The performance of fusion is good in objective and subjective evaluation on different types of images, because of two separate fusion rules for base layers fusion and detail layers fusion
Liu et al. [12], 2018	NA	MFDF (decomposition purpose), NSST, component synthesis	MSR—texture features, average fusion rule-approximate components	Medical diagnosis	With the help of two decomposition techniques, authors able to get good visual effects and objective values infused image compared to source images
Hongpe ng [13], 2017	NA	CTD	proportional calculating and spatial fusion, SR-based method	Visible and infrared image fusion, medical diagnosis, multi-modal images	Structure information is pre-served in cartoon components by energy-based fusion rule

(continued)

Table 2 (continued)

Refere nces	Preprocessing	Methods used	Fusion rule	Applications	Comments
Song et al. [14], 2018	Downsampling of landsat images	NLM-CNN, SR-CNN	SR-based method	Spatiotemporal fusion, landsat images, and MODIS images fusion	The main problems are poor atmospheric conditions and frequent cloud cover is admitted in the proposed method. The author directed that the proposed algorithm unable to estimate the lost information in LSR MODIS images
Yang et al. [15], 2018.	The authors considered two registered images	RSR, PCNN, morphological opening and closing	Weighted fusion rule	Multi-focus image fusion	The algorithm seems complex and consumes and authors mentioned average time around 73 s
Lin et al. [16], 2018	No need for image registration	GMM	LR-GMM based fusion rule	Hyperspectral image and multispectral image fusion	Image registration is not necessary. Acceptable computational complexity and image registration errors
Yongh et al. [17], 2018	NA	SPCA, MTF	SPCA based fusion rule	MS, PAN image fusion	With the help of spatial structures, this method efficient in the predication of lost spatial details

compared with the input images and testifies the quality of the fused image using various statistical parameters in terms of spatial information, geometric patterns, object size, colour spectral information, etc. The objective evaluation indication is a quantitative analysis that can overcome the influence of human's inaccurate vision judgment and make the indicators mathematically evaluate the effectiveness of image fusion. Significant measures for image fusion are shown in Table 1.

4 Conclusion

Several methods are reported in the literature to address issues in image fusion, many of them are on a specific application but a universal algorithm much needed that apply to all types of applications in image fusion. In this paper, advantages and drawbacks of image fusion literature, universal flowchart proposed to image fusion and performance metrics of image fusion are discussed. The universal flow charts are needed to test with various newly arrived feature extractor techniques, machine learning/optimization techniques need to add for efficient fusion.

References

1. Ghamisi P, Rasti B, Yokoya N, Wang Q, Hofle B, Bruzzone L, Bovolo F, Chi M, Anders K, Gloaguen R, Atkinson PM, Benediktsson JA (2019) Multisource and multitemporal data fusion in remote sensing: a comprehensive review of the state of the art, vol 7. Institute of Electrical and Electronics Engineers Inc., pp 6–39
2. Ma J, Ma Y, Li C (1 January, 2019) Infrared and visible image fusion methods and applications: a survey. *Inf Fusion* 45:153–178
3. Meher B, Agrawal S, Panda R, Abraham A (1 August, 2019) A survey on region based image fusion methods. *Inf Fusion* 48:119–132
4. Solanki V, Katiyar SK (2016) Pixel-level image fusion techniques in remote sensing: a review. *Spa Inf Res* 24(4):475–483
5. Wang Z, Wang S, Zhu Y, Ma Y (1 December 2016) Review of image fusion based on pulse-coupled neural network. *Arch Comput Methods Eng* 23(4):659–671
6. Yang B, Jing ZL, Zhao HT (2010) Review of pixel-level image fusion. *J Shanghai Jiaotong University (Sci)* 15(1):6–12
7. Zhou T, Ruan S, Canu S (2019) A review: deep learning for medical image segmentation using multimodality fusion. *Array* 3–4:100004
8. Jin X, Hou J, Nie R, Yao S, Zhou D, Jiang Q, He K (1 September 2018) A lightweight scheme for multi-focus image fusion. *Multimed Tools Appl* 77(18):23501–23527
9. Hou R, Nie R, Zhou D, Cao J, Liu D (1 October 2019) Infrared and visible images fusion using visual saliency and optimized spiking cortical model in non-subsampled shearlet transform domain. *Multimed Tools Appl* 78(20):28609–28632
10. Karsanina MV, Gerke KM, Skvortsova EB, Ivanov AL, Mallants D (15 March, 2018) Enhancing image resolution of soils by stochastic multiscale image fusion. *Geoderma* 314:138–145
11. Jian L, Yang X, Zhou Z, Zhou K, Liu K (1 June 2018) Multi-scale image fusion through rolling guidance filter. *Future Gener Comput Syst* 83:310–325

12. Liu X, Mei W, Du H (1 February 2018) Multi-modality medical image fusion based on image decomposition framework and nonsubsampled shearlet transform. *Biomed Signal Process Control* 40:343–350
13. Zhang Y, Chen L, Zhao Z, Jia J (1 February 2016) Multi-focus image fusion based on cartoon-texture image decomposition. *Optik* 127(3):1291–1296
14. Song H, Liu Q, Wang G, Hang R, Huang B (1 March 2018) Spatiotemporal satellite image fusion using deep convolutional neural networks. *IEEE J Select Topics Appl Earth Obs Remote Sensing* 11(3):821–829
15. Yang Y, Yang M, Huang S, Ding M, Sun J (2018) Robust sparse representation combined with adaptive PCNN for multifocus image fusion. *IEEE Access* 6:20138–20151
16. Lin B, Tao X, Duan Y, Lu J (16 March 2018) Hyperspectral and multispectral image fusion based on low rank constrained gaussian mixture model. *IEEE Access* 6:16901–16910
17. Kim Y, Kim M, Choi J, Kim Y (1 December 2017) Image fusion of spectrally nonoverlapping imagery using SPCA and MTF-based filters. *IEEE Geosci Remote Sensing Lett* 14(12):2295–2299
18. Tilak Babu SBG, Satyanarayana V, Srinivasarao C (2016) Shift invariant and Eigen feature based image fusion. *Int J Cybern Inf (IJCI)* 5(4)
19. Li H, Qiu H, Yu Z, Li B (1 September 2017) Multifocus image fusion via fixed window technique of multiscale images and non-local means filtering. *Signal Process* 138:71–85
20. Tilak Babu SB, Prasad KH, Gandeti J, Kadali DB, Satyanarayana V, Pavani K (2019) Image fusion using Eigen features and stationary wavelet transform. *Int J Innov Technol Explor Eng* 8(8)Special Issue 3:38–40
21. Zhang Q, Liu Y, Blum RS, Han J, Tao D (1 March 2018) Sparse representation based multi-sensor image fusion for multi-focus and multi-modality images: a review. *Inf Fusion* 40:57–75

Factors Influencing Financing for Entrepreneurs



Raman Kumar, Rajasve Kaushik, Shivani, Rishi Kant Kumar,
and Prashant Kumar

Abstract Financing is always a constraint for any entrepreneurs, especially for nascent entrepreneurs. They face various challenges and need to look towards various factors and in order to gain finance from investors in any country. However, very few studies have discussed what the factor which influences investors to provide finance to entrepreneurs in any country. In this paper, a model has been proposed which shows factors that influence financing for entrepreneurs. The model has been further verified from the dataset provided by Global Entrepreneurs Monitor (GEM). The result suggests that education and training, R&D and technology have a significant impact on financing for the entrepreneur in a country while culture, infrastructure, and service have a positive impact.

Keywords Financing · Government policies · Culture · Social support · GEM

1 Introduction

Traditionally, entrepreneurial activity was considered as a one-time process that creates new offerings, or even a completely new business—an demonstration that

R. Kumar (✉)
Lalit Narayan Mithila University, Darbhanga, Bihar, India
e-mail: ramansbi007@gmail.com

R. Kaushik
Pearl Consulting Services, Gurugram, India
e-mail: rajasve.kaushik@pearlconsulting.co.in

Shivani
Centre of Rural Development, Indian Institute of Technology, Delhi, India
e-mail: shivani1424@gmail.com

R. K. Kumar · P. Kumar
Department of Management Studies, Indian Institute of Technology, Delhi, India
e-mail: rishinit14@gmail.com

P. Kumar
e-mail: prashant@dms.iitd.ac.in

challenges or “creatively destroys” existing offerings and market relations. Yet, entrepreneurship today is bound to be seen as an instrument established in the culture of an enterprise than as an occurrence [1]. Therefore, in comparison to driving performance independently, entrepreneurship integrates with other organizational variables to achieve company results [2]. Rather than having a universal impact, entrepreneurship can be assumed as a job in the quest for superior performance in different types of organizations.

Entrepreneurship researchers are getting progressively interested in how region-explicit, cultural, economic, political, demographic, and social factors that are outside the ability to control individual specialists influence business activity [3]. Recently, such a phenomenon has been identified as external enablers; however, both current and prospective entrepreneurs are reliant on the ecosystem in which they work in such a way that ecological changes can affect their behavior [4]. Indeed, few growing research indicates that business formation is influenced by regional context or environmental conditions.

It should be noted that access to external or foreign funding is critical for business or enterprise. Studies on large-sized enterprises and small and medium-sized enterprises (SMEs) around the world are readily available for financing and capital structure. However, we know less about start-up companies’ external financing—especially those who are in the preliminary or pre-angle stage [4, 5]. Indeed, the literature often associates startups with angel investors or venture capital funding.

In the field of entrepreneurship, a well-documented argument is that entrepreneurial practices or strategies are drivers of financial achievement or economic development. Prior literature has invested a significant amount of effort into understanding how entrepreneurial development is influenced by designing government policies. In fact, institutions dictate entrepreneurial activities, like those that set the rules of the game [2]. While government strategies shape various degrees of the institutional system, those arrangements have a noteworthy capacity to impact business exercises. Innovation encouragement, trade regulations, financing, and taxation could be included by the government while designing the entrepreneurs’ related policies [6].

Government communities around the world are giving more consideration towards research and development subsidization by venture capital programs. In several knowledge-based high-tech markets, Venture Capitalists (VCs) put resources in the financing and growth of startups and early-staged enterprises [7]. All such factors generate a great deal of curiosity amongst researchers of entrepreneurship as to what an extent these factors can affect the business environment and how to generate a conducive environment for business development. So, in this paper, we have proposed a model that supports the context of financing for entrepreneurs.

From this point forward, the flow of this paper is as follows. In Sect. 2, we have reviewed the literature related to the area of study, followed by the hypothesis of the study has been presented. Section 3 presents the data collection procedure and method utilized to analyze the proposed model. In Sect. 4, we have presented the results of our study, followed by a discussion of the result that has been stated.

Lastly, in Sect. 5, we have concluded the paper and suggested a few implications of this research.

2 Literature Review

Financing is the biggest challenge for any entrepreneur especially the nascent one who does not have access to various other resources that a professional one has. We have presented different constructs through research available in the literature.

2.1 *Education and Training*

So, for these entrepreneurs, one way is the develop the expertise and skill through various sources. In this context, [8] has suggested that for creativity, innovation, and successful development of business, it is essential to go through education as well as professional training from time to time. Besides training and skills, motivates entrepreneurs to become more risk-averse and substantial move towards sustainable development [9]. Looking at the education and training in a country, we have formulated the hypothesis

H1: Education and Training significantly lead to gaining finance for entrepreneurs.

Entrepreneurs who seek outside funding and support need to move towards developing a successful innovation technically or empirically from research and development [5]. Because technical information sharing through a different medium, techno-commercial articles [10], articles and information selection different review techniques [11] help them in analyzing their various problems of business. This helps entrepreneurs in decision-making strategy and moving towards more financial risk advising path [12]. Besides, R&D helps them to move towards going various AI and machine learning [13] based technique which helps them in building a better mindset and predictive ability. Looking at the impact on R&D and technological development in a country, we have proposed our second hypothesis.

H2: R&D and Technological development in a country impact access to financing for entrepreneurs.

In this context, various entrepreneurs consider different ideologies towards accessing training and education through technology and research and development centers. So, we have formulated our third hypothesis as

H3: R&D and Technological development in a country significantly improves the propensity of gaining education and training for entrepreneurs.

2.2 *Cultural and Social Support*

Hult et al. [14] studied the impact of four variables, i.e. organizational learning, entrepreneurship, market orientation, and innovativeness on the cultural competitive edge in an organization. They developed ten different models of four variables that affect the performance of an organization and these models were examined on a full and segmented sample of 764 organizations. They used a correlation matrix on all four variables and Structural equation modeling (SEM) to test each of the ten models. Casson and Della Giusta[15] entrepreneurship play an important role in building cultural competitiveness in each type of organization but plays a different role in the performance of small/old organizations and large/old organizations. So, another hypothesis is as under:

H4: Cultural and social supports significantly impact the financing for entrepreneurs.

2.3 *Government Policies and Support*

Dai and Si [16] analyzed the influence of different policies related to startups and business, on the entrepreneurial orientation of Chinese private firms which is also majorly promoted by the government. Also, the author has implemented strategic choice theory to contemplate if and how entrepreneurial perceptions of positive national-level government strategies result in a greater level of entrepreneurial orientation. It was noted that a positive relationship exists between the entrepreneurs' perception of the adequacy of new policies and the commitment of their company in entrepreneurial activities. This supports the voluntarist view of the relationship between organizations and the environment. Therefore, they concluded the integration of institutional theory and strategic choice theory is helpful to understand the impacts of recently planned national policies or strategies on the entrepreneurial orientation of private firms.

Cumming [6] studied the comparison of Australian Innovation Investment Fund (IIF) Program visibility and progression with government venture capital programs in the US, UK and Canada. Also, they analyzed its performance along various dimensions such as the degree of risk undertaken by putting resources into the underlying stage and cutting edge ventures; the probability to assess and increase the value of investees through arranging syndication, and portfolio size per support chief and the leave achievement [17]. We have presented our next hypothesis as under:

H5: Government policies and support significantly push entrepreneurs towards gaining better financial assistance.

2.4 Infrastructure and Service Support

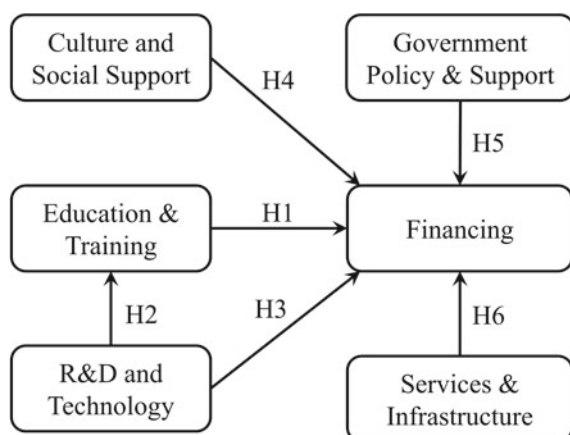
Bennett [18] studied the impact of infrastructure investments on entry rates and exit rates of establishments. Also, they ascertained the impact on job creation if new establishments enter and job destruction if establishments exit. They developed a theoretical model that depicts the External Enabler/Disabler (EED) Model with external factors such as technological change, policy change and institutional change. Research suggests that private infrastructure investment resulted in the creation of new businesses and increased job opportunities [19]. On the contrary, public infrastructure investment resulted in the destruction of business and permanent loss of jobs [20].

Nofsinger and Wang [3] analyzed how product type, production technology and experience of entrepreneurs affect the external investment made by the institutional investors and the informal investors along with the problems of information asymmetry and moral hazard faced by them. They used the survey data from the Global Entrepreneurship Monitor from 27 countries. They used Logit regression on the presence of institutional investors and informal investors along with the external financing ratio method. They concluded that problems of information asymmetry and moral hazard can be reduced by product type and entrepreneurial experience. Also, it was observed that the legal environment is also important for access to external financing. Institutional investors prefer to invest in businesses of experienced entrepreneurs. So, our last hypothesis is as follows:

H6: Infrastructure and various communication services significantly impact the financing for entrepreneurs.

So finally, collecting all the hypothesis, we have presented or model which is shown in Fig. 1.

Fig. 1 Proposed model for hypothesis formulation



3 Data Collection and Methodology

For this study, we have used secondary data which is made available by Global Entrepreneurship Monitor (GEM). These data are the assessment of different nationals' entrepreneur's activity which comprises data related to various themes from all around the globe. These data are publicly available after 3 years on their website which could be accessed through. The main indicator of this data in total early-stage entrepreneurs' activity (TEA). The GEM data is collected using two large surveys in which one is from the population from each individual and one is taken from experts. For our research, the data from the expert survey of the year 2015 which is the latest dataset available to us. In this dataset, we have extracted questions related to our hypothesis. A total of 34 questions from this dataset fall under our research category.

Once the database is created, we move towards validating our model using these data. We have selected Structural Equation Modeling (SEM) for analyzing our model. "Structural equation modeling (SEM) is an extremely flexible linear-in-parameters multivariate statistical modeling technique" [21]. This model is broadly used for multivariate statistical analysis techniques which basically uses regression and factor analysis in order to analyze the structural relationship between the constructs [22]. As we have a different set of questions and the set which is made available by the secondary method, so data contains many outliers and missing segments. SEM has features of manipulating those outliers and analyze the data with better accuracy [23].

Now, for analysis of the data through SEM, we have chosen the IBM AMOS tool [24] which a statistical software used to analyze SEM, path analysis, etc. through a different method like maximum likelihood, scale-free least-squares, etc. [25]. For our analysis, we have used the maximum likelihood to analyze our data.

4 Result and Discussions

The dataset consists of 34 elements from 2548 respondents. Once the model has been prepared and run on the IBM AMOS tool, it showed a chi-square value of 7142.458. The degree of freedom computed is presented in Table 1. Distinct sample moments from table shows show the portion of the output which is used to show the internal

Table 1 Computation of degrees of freedom

Number of distinct sample moments	629
Number of distinct parameters to be estimated	112
Degrees of freedom (629 – 112)	517
Chi-square	7142.458
Probability level	0.000

function of AMOS in order to analyze the desired output [24]. Another factor is the degree of freedom which gives “each of a number of independently variable factors affecting the range of states in which a system may exist, any of the directions in which independent motion can occur”. Lastly, the value of chi-square which shows the goodness of fit test of the model.

Tables 2 and 3 show the covariance and correlation between the constructs. Here the covariance and correlation between financing for entrepreneurs and education and training are 0.508 and 0.365 respectfully with standard error (S.E) of 0.038 which shows the positive covariance with minimum error. This shows that the country having better education and training for entrepreneurs shows a significant chance of gaining better financial availability from investors as, education and training provide skillset to build their business better. Now, for the second relationship, covariance and correlation between financing and R&D and technology are 0.760 and 0.437 respectfully. This shows the strong relationship between financing and R&D and technology in comparison to financing and education and training.

For our third hypothesis, education and training and research and technology have the highest relationship with covariance and correlation of 0.915 and 0.522. This shows a country having good research and development; technological support constitutes better educations and training for entrepreneurs. Covariance and correlation between financing and cultural and social support have a positive but weak relationship. Now, the government policies and support have some impact on financing as this has a covariance of 0.295 and a correlation of 0.267. Lastly, the infrastructure and service also have a weak relationship with the financing for entrepreneurs.

Table 2 Covariance relationship between the constructs

Factors	Estimate	S.E.	C.R.
Financing ⇔ education and training	0.508	0.038	13.439
Financing ⇔ R&D and technology	0.760	0.056	13.682
Education and training ⇔ R&D and technology	0.915	0.058	15.901
Financing ⇔ cultural and social support	0.270	0.045	5.957
Financing ⇔ government policies and support	0.295	0.033	8.840
Financing ⇔ services and infrastructure	0.254	0.043	5.866

Table 3 Correlation between the constructs

Factors	Estimate
Financing ⇔ Education and training	0.365
Financing ⇔ R&D and technology	0.437
Education and training ⇔ R&D and technology	0.522
Financing ⇔ cultural and social support	0.142
Financing ⇔ government policies and support	0.267
Financing ⇔ services and infrastructure	0.147

So, the country should more focused towards developing research and development facilities. The government should lean towards providing training and support to their better opportunity to entrepreneurs. The results from Tables 2 and 3 validate our proposed hypothesis and model. Out of six hypotheses, first three hypothesis shows significant relationship while the last three have an impact but little less than first three.

5 Conclusion

In this paper, we have presented the effect of different factors like education and training, R&D and technology, culture and social support, government policies and infrastructure, and service on financing. Our finding suggests that R&D and technological development in a country have a significant impact on financing in comparison to other factors. Other factors are also positively correlated with the financing, but R&D and Technological innovation have the highest one. At the same time, entrepreneurs should also focus on gaining better education and skills with more technological advancement.

References

1. Kang H (2012) Essays on entrepreneurial finance: the role of corporate venture capital and its performance implications. ProQuest Diss. Theses
2. Lerner J (2005) Venture capital and private equity: a course overview. SSRN Electron J
3. Nofsinger JR, Wang W (2011) Determinants of start-up firm external financing worldwide. J Bank Financ
4. Lago R, Saurina Salas J, Lopez JA (2007) Determinants of access to external finance: evidence from Spanish firms. SSRN Electron J
5. Scott JT, Scott TJ (2016) The entrepreneur's idea and outside finance: theory and evidence about entrepreneurial roles. Eur Econ Rev 86:118–130
6. Cumming D (2007) Government policy towards entrepreneurial finance: Innovation investment funds. J Bus Ventur 22(2):193–235
7. Bacq S, Lumpkin GT (2014) Can social entrepreneurship researchers learn from family business scholarship? A theory-based future research agenda. J Soc Entrep
8. Sarri KK, Bakourous IL, Petridou E (2010) Entrepreneur training for creativity and innovation. J Eur Ind Train 34(3):270–288
9. Byrne J, Delmar F, Fayolle A, Lamine W (2016) Training corporate entrepreneurs: an action learning approach. Small Bus Econ 47(2):479–506
10. Chatterjee S, Kumar P, Chatterjee S (2018) A techno-commercial review on grid connected photovoltaic system. Renew Sustain Energy Rev 81(2):2371–2397
11. Kumar P, Das U, Chatterjee S (2016) A brief study on control structure of grid connected PV inverter. In: 2016 international conference on energy efficient technologies for sustainability (ICEETS), 2016, pp 577–582
12. Färnstrand Damsgaard E, Hjertstrand P, Norbäck PJ, Persson L, Vasconcelos H (2017) Why entrepreneurs choose risky R&D projects—but still not risky enough. Econ J
13. Kumar P, Chatterjee S, Shah D, Saha UK, Chatterjee S (2017) On comparison of tuning method of FOPIID controller for controlling field controlled DC servo motor. Cogent Eng. 4(1)

14. Hult GTM, Snow CC, Kandemir D (2003) The role of entrepreneurship in building cultural competitiveness in different organizational types. *J. Manage*
15. Casson M, Della Giusta M (2007) Entrepreneurship and social capital. *Int Small Bus J Res Entrep* 25(3):220–244
16. Dai W, Si S (2018) Government policies and firms' entrepreneurial orientation: Strategic choice and institutional perspectives. *J Bus Res* 93:23–36
17. Tassabehji R, Hackney R, Popović A (2016) Emergent digital era governance: enacting the role of the 'institutional entrepreneur' in transformational change. *Gov Inf Q* 33(2):223–236
18. Bennett DL (2019) Infrastructure investments and entrepreneurial dynamism in the U.S. *J Bus Ventur* 34(5):105907
19. Bian J et al (2016) Mining twitter to assess the public perception of the 'internet of things. *PLoS One*
20. Dourish P, Bell G (2007) The infrastructure of experience and the experience of infrastructure: meaning and structure in everyday encounters with space. *Environ Plan B Plan Des* 34(3):414–430
21. Golob TF (2002) Structural equation modeling. In: *Transportation systems planning: methods and applications*
22. Asparouhov T, Muthén B (2009) Exploratory structural equation modeling. *Struct Equ Model A Multidiscip J* 16(3):397–438
23. Gefen D, Straub D, Boudreau M-C (2000) Structural equation modeling and regression: guidelines for research practice. *Commun Assoc Inf Syst* 4
24. IBM SPSS Amos (2012) IBM SPSS Amos. IBM Softw Bus Anal
25. Byrne BM (2013) *Structural equation modeling with AMOS*. Psychology Press

Simulation and Analysis of Hybrid PEMFC and Solar PV Cell Model for Commercial Load Profile System



Archana Thoudam, Pabitra Kumar Guchhait, and Abhik Banerjee

Abstract The performance and design optimization of a stand-alone PEM fuel cell (PEMFC) and PV power system to be used for commercial purposes is investigated in this paper. The main objective of the paper is to design a network of power systems that consists of renewable energy sources for its environmental impact. This paper shows the performance analysis of the hybrid PEMFC and solar PV cells under residential load demand variation, after which simulation is carried out.

Keywords PEMFC · PV cell · Hybrid-power system · Load profile

1 Introduction

The increasing population has necessitated the rise in commercial energy demand and the need for using the off-grid renewable power sources [1, 2]. Only one energy source proves insufficient to provide all-day power to the residents due to intermittent nature. The combination of fuel cell and solar PV is a possible option to meet the goal amongst other possible combinations [3–5].

Fuel cells are hydrogen-based devices. They convert the chemical energy of the fuel into electricity. In this case, we use hydrogen and oxygen as fuel. Fuel cells provide an edge over the conventional batteries in residential and portable applications. The main advantages of fuel cells are its static nature and noise pollution-free characteristics along with less atmospheric contamination of hazardous oxides. Fuel cells can be used for numerous off- and on-grid applications [6, 7].

A. Thoudam (✉) · P. K. Guchhait · A. Banerjee

Department of Electrical Engineering, National Institute of Technology Arunachal Pradesh,
Papum Pare, Arunachal Pradesh, India

e-mail: archana.thoudam@gmail.com

P. K. Guchhait

e-mail: pabitraguchhait@gmail.com

A. Banerjee

e-mail: abhik_banerjee@rediffmail.com

Out of all the varieties of fuel cells available in the market, proton exchange membrane FCs, also referred to, as polymer electrolyte membrane FCs, are most preferred due to their favourable characteristics for operation. A PEMFC is made up of a solid electrolyte which is sandwiched between two conducting electrodes coated with some catalyst. PEM fuel cell holds great promise for the use of small-scale energy generation sources and offers high energy density, low corrosion, reliability, rapid start-up, low operational temperature and no geographical limitations [8]. In this paper, Simulink model based PEM fuel cell model has been developed.

Photovoltaic (PV) cells are *p-n* junction devices which use energy from sunlight to produce power. This power is DC in nature. The main advantage of PV system is that it does not generate noise during operation and requires very little maintenance in comparison to other existing renewable energy sources. But we know that solar irradiation is intermittent in nature and hence, hybridization of the solar PV system with other renewable or non-renewable sources is necessary to provide continuous and reliable power [9].

In [10], a hybrid power system (HPS) merging Solar, Fuel cell and Ultracapacitors are created and modelled with controllers for power flow which can be applied for stand-alone, residential, micro-grid consumers. In [11], a HPS of PV (Solar) and Fuel cell is analyzed for applications in house-hold, i.e. micro-generation. The system comprises of PV modules, PEM type water electrolyzer, batteries and PEMFC. For a given location (Ankara) in Turkey, the working of the integrated hybrid system is predicted and thereby exhibited for varying climatic conditions. This paper indicates the strategy for power control of the PEMFC and solar PV cell-based-hybrid system for residential load conditions.

2 Hybrid Model of PEMFC and PV Model Under Study

The schematic model of hybrid PEM fuel cell and solar PV cell for better power quality service is presented in Fig. 1. We have a model of this hybrid power system in Simulink which is presented in Fig. 2.

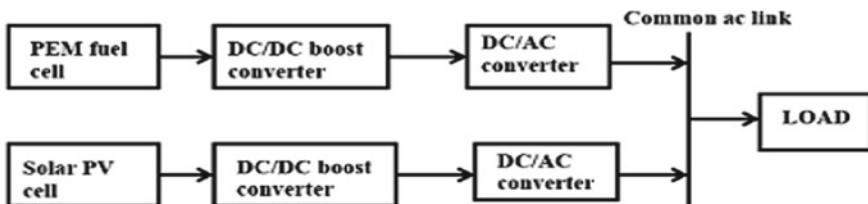


Fig. 1 Schematic diagram of hybrid PEM fuel cell and solar PV cell model

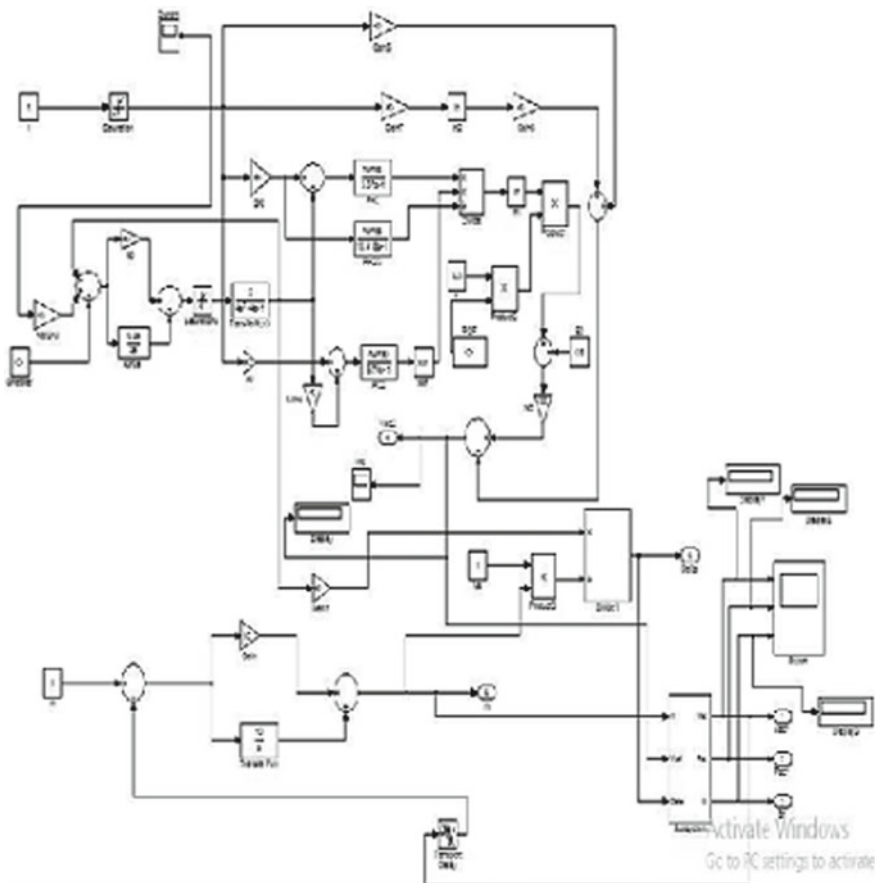


Fig. 2 Simulation diagram of PEM fuel cell

2.1 PEMFC Model

Various models of fuel-cells have been presented in the literature [12, 13]. But in these models, the partial pressures of the fuels, i.e. hydrogen (PH_2) and oxygen (PO_2) are taken as constant values, which are generally variable in nature in different conditions. So for better accuracy, it has to be modified for better results.

The PEMFC power scheme can be implemented as follows.

The flow of hydrogen (molar) going through the opening is proportional to the partial pressure of the hydrogen inside the channel which can be depicted as

$$\frac{q_{\text{H}_2}}{P_{\text{H}_2}} = \frac{K_{\text{an}}}{\sqrt{M_{\text{H}_2}}} = K_{\text{H}_2} \quad (1)$$

Considering various factors like input flow and output flow of hydrogen, and the rate at which the hydrogen is flowing during the reaction, a relationship can be established as follows:

$$\frac{d}{dt} P_{H_2} = \frac{RT}{V_{an}} (q_{H_2}^{in} - q_{H_2}^{out} - q_{H_2}^r). \quad (2)$$

The molar flow of hydrogen used during the reaction according to the electrochemical reaction can be obtained as

$$q_{H_2}^r = \frac{N_0 I_{FC}}{2F} = 2K_r I_{FC} \quad (3)$$

Substituting Eq. (3) in Eq. (2),

$$\frac{d}{dt} P_{H_2} = \frac{RT}{V_{an}} (q_{H_2}^{in} - q_{H_2}^{out} - 2K_r I_{FC}) \quad (4)$$

Now after applying Laplace Transformation on both sides of the Eq. (4), yields the following expression:

$$P_{H_2} = \frac{\frac{1}{K_{H_2}}}{1 + \tau_{H_2} s} (q_{H_2}^{in} - 2K_r I_{FC}) \quad (5)$$

In accordance with the given expressions, the partial pressures of the input variable, i.e. oxygen and water can be expressed as

$$\tau_{H_2} = \frac{V_{an}}{K_{H_2} RT} \quad (6)$$

$$P_{O_2} = \frac{1/K_{O_2}}{1 + \tau_{O_2} s} (q_{O_2}^{in} - 2K_r I_{FC}) \quad (7)$$

$$P_{H_2O} = \frac{1/K_{H_2O}}{1 + \tau_{H_2O} s} (2K_r I_{FC}) \quad (8)$$

The polarization curve of the PEMFC can be acquired by adding the three terms, i.e. Nernst instantaneous voltage (E), Activation overvoltage (V) and ohmic overvoltage (V_{ohmic}). The mathematical expression for obtaining the polarization curve of PEMFC is as follows:

$$V_{cell} = E + V_{act} + V_{ohmic} \quad (9)$$

where

$$V_{act} = -B \ln(C I_{FC}) \quad (10)$$

$$V_{\text{ohmic}} = -R^{\text{int}} I_{\text{FC}} \quad (11)$$

Nernst Voltage can be defined as in Eq. (12)

$$E = N_0 \left[E_0 + \frac{RT}{2F} \log \left\{ \frac{P_{\text{H}_2} \sqrt{P_{\text{O}_2}}}{P_{\text{H}_2\text{O}}} \right\} \right] \quad (12)$$

2.1.1 The Reformer Model with Its Controller

The fuel for the PEMFC power scheme should be pure hydrogen which will be fed to the system through an external assembly. The supply of pure hydrogen depends on the power requirement from the system and the reformer generates the same by undergoing a reforming process of methanol [14]. In [14], the author depicts a simple model. It is a transfer function of second-order and the model can be depicted mathematically as follows:

$$\frac{q_{\text{H}_2}}{q_{\text{meth.}}} = \frac{CV}{\tau_1 \tau_2 s^2 + (\tau_1 + \tau_2)s + 1} \quad (13)$$

The flow of hydrogen is controlled in accordance with the power requirement. A feedback stack current is required for the control. The correlation between the two can be calculated as:

$$q_{\text{H}_2}^{\text{req}} = \frac{N_0 I_{\text{FC}}}{2FU} \quad (14)$$

A PI controller is used for control of the rate of flow of methane [14]. The hydrogen which is utilized for this purpose is extracted from the reformer section. This can be depicted by the mathematical expression as

$$q_{\text{meth.}} = \left(k_1 + \frac{k_1}{\tau_3 s} \right) \left(\frac{N_0 I_{\text{FC}}}{2FU} - q_{\text{H}_2}^{\text{in}} \right) \quad (15)$$

2.1.2 Power Conditioning Unit (PCU) for PEMFC

The generated power by the PEM fuel cell power scheme is DC in nature, so it has to be converted to AC power for the use in residential applications as residential domestic loads are AC in nature. In some papers [15], a DC/DC boost converter is utilized to transform the DC power into AC power so that the system can gain better voltage regulation. But to simplify the complexity of the proposed system, only a

DC/AC converter is employed in this paper. We assume that the effect of time constant associated with the respective assembling units is negligible on the time response accuracy of the overall system [15]. The system's AC voltage and reactive power flow are regulated by the inverter modulation index. The system's active power flow can be controlled by the phase angle or power angle. The terminal voltage at load is assumed to have constant values. The inverter modulation index plays an important role in keeping the terminal voltage value constant and PI controllers are put into use for that.

The MI (Modulation Index) can be described mathematically as follows:

$$m = \frac{k_5 + k_6 s}{s} (V_{\text{ref}} - V_{\text{AC}}) \quad (16)$$

The PEM fuel cell power control mechanism can be explained briefly as follows:

$$P_{\text{AC}} = \frac{m V_{\text{cell}} V_s}{X} \sin(\delta) \quad (17)$$

$$Q = \frac{(m V_{\text{cell}})^2 - m V_{\text{cell}} V_s \cos(\delta)}{X} \quad (18)$$

Considering a lossless inverter system following assumptions can be drawn:

$$P_{\text{AC}} = P_{\text{DC}} = V_{\text{cell}} I_{\text{FC}} \quad (19)$$

From Eq. (14), (16) and (18), we get

$$\sin(\delta) = \frac{2 F U X}{m V_s N_0} q_{\text{H}_2}^{\text{req}} \quad (20)$$

The phase angle of o/p voltage and the rate of required hydrogen flow can be described by the following relationship, let's assume $\sin(\delta) \cong \delta$, which yields

$$\delta = \frac{2 F U X}{m V_s N_0} q_{\text{H}_2}^{\text{req}} \quad (21)$$

The feedback current of PEMFC system can be derived by establishing the relationship between the modulation index, load current, load phase angle and phase angle of the AC voltage.

$$I = m I_l \cos(\theta + \delta) \quad (22)$$

where

$$I_l = \frac{P_l}{V_s \cos(\theta)} \quad (23)$$

2.2 PV Cell Modelling

A solar PV cell is a device based on a *p-n* junction diode and it generates electricity when the energy of photons is higher than the energy level of the semiconductor bandgap. More than one PV cell is connected in a combination of series and parallel connections for the formation of a PV module. Various models have been discussed in the papers [16, 17]. Here, a single diode PV model structure has been used and is given in Fig. 3 and the Simulink model for the solar PV cell are given in Fig. 4.

The current in the output terminal of the PV cell can be written as given by (24)

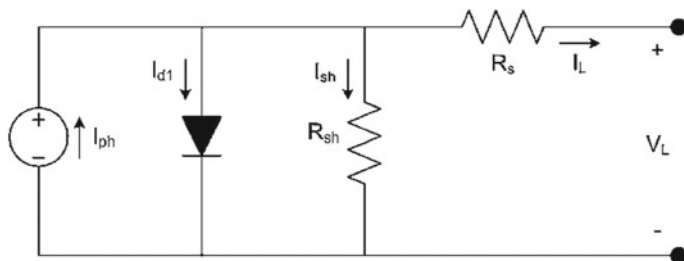


Fig. 3 Single diode solar PV cell

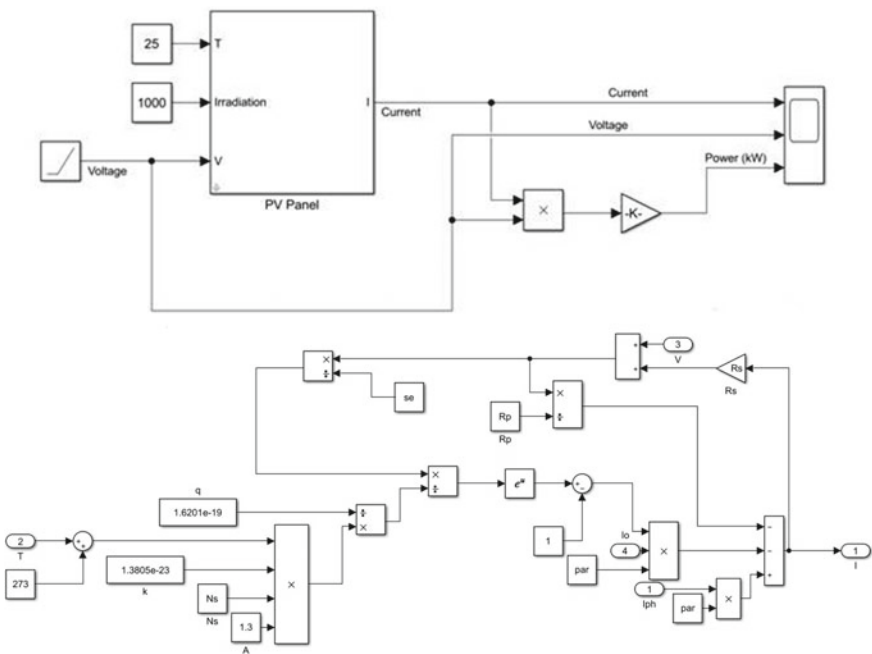


Fig. 4 Simulink model of solar PV cell

$$I_0 = I_{PV} - I_r \exp \left[\frac{q(V_0 + I_0 R_s)}{k T_c n} - 1 \right] \quad (24)$$

where the symbols represent: q signifies charge of the electron, its value is $1.6 * 10^{-19}$ °C, V_0 is the voltage at the output terminal, and I_0 is the current generated in the PV cell.

The photocurrent I_{PV} is dependent on (1) the solar irradiance and (2) temperature of the solar PV cell and may be written as

$$I_{PV} = [k * (T_c - T_r) + I_{sc}] * G \quad (25)$$

The reverse saturation current I_r of the PV cell can be defined as

$$I_r = I_{rs} * \left(\frac{T_c}{T_r} \right)^3 * e^{\left(\frac{q V_g * \left(\frac{1}{T_c} - \frac{1}{T_r} \right)}{n * k} \right)} \quad (26)$$

3 Results and Discussions

Here, the simulation for the PEMFC and PV hybrid system under different sources and load conditions in Simulink (MATLAB) environment are presented. The parameters associated with the PEMFC and the PV cell and their considered values are presented as shown in Table 1.

The considered load variation profiles are given in Fig. 5. The load profiles are considered as some of peak load demand variations at time 0.4–0.6 s and 1.2–1.4 s. The PEMFC output voltage according to the fuel cell feedback current is given in Fig. 6. From the figure, we can see that the maximum electrical power generated from the PEM fuel cell is 6 kW at the time of peak load demand. The flow of hydrogen and methane is also demonstrated in Figs. 7 and 8, and it is shown that the flow varies according to the load demand profiles.

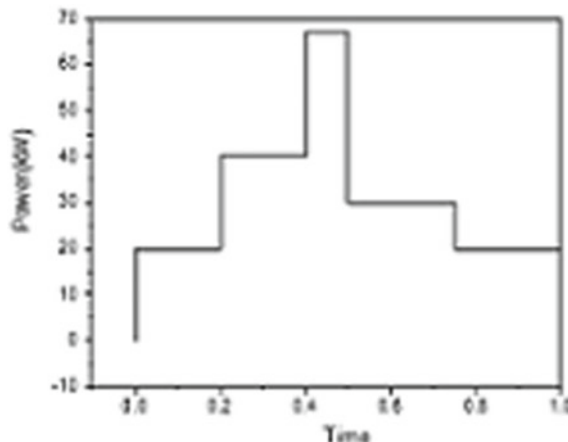
The characteristic I-V graph and P-V graph of the PV cell are also given in Figs. 9 and 10 for an irradiance 1000 W/m^2 (Fig. 11).

4 Conclusion

A hybrid model of PEMFC and PV cell has been developed in MATLAB Simulink. Further, it can be observed from the simulation result that the electrical power demand by the load is fulfilled with the aid of the proposed hybrid power system model. The distribution of solar PV power and PEMFC power can also be achieved individually with the help of MATLAB Simulink. Further, the convergence profile can also be

Table 1 The value of all the parameters of both the cells

Parameters of solar PV cell	Parameters value
Open circuit voltage of the solar PV module (V_{OC})	64.2
Short circuit current of the module (I_{SC})	5.96 A
Number of cells in series in a module	96
Number of modules in series and parallel (N_S and N_P)	5 and 66
Boltzman constant (k)	$1.38 * 10^{-23}$ J/K
Reference temperature (T_r)	25 °C
Series and shunt resistance of the module (R_S and R_P)	0.18 and 360 Ω
Parameters of PEMFC	Parameters value
Temperature of stack	343 K
Faraday's constant depicted by F	96,484,600 °C/kmol
No. of cells per stack, N_0 and No of stacks, N_{stack}	550 and 6
The constant $K_r = N_0/(4F)$	1.4251×10^{-6} kmol/(s A)
Universal gas constant (R)	8314.47 J/kmol/K
No load voltage (E_0)	0.8 V

Fig. 5 Load power profiles

achieved. So, it may be a permissive hybrid power system (HPS) to fulfil the electricity demand from the consumers in isolated mode or in grid- integrated mode. The control strategy of the output voltage can also be further improved with the help of different controllers.

Fig. 6 PEMFC output voltage

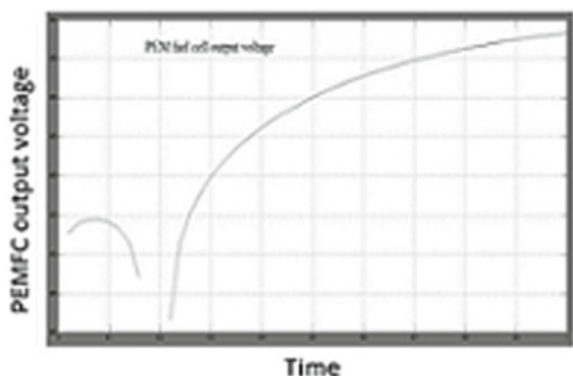


Fig. 7 Hydrogen gas flow profile

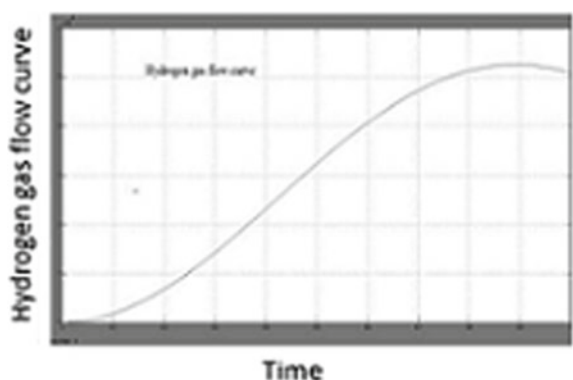


Fig. 8 Methane gas flow profile

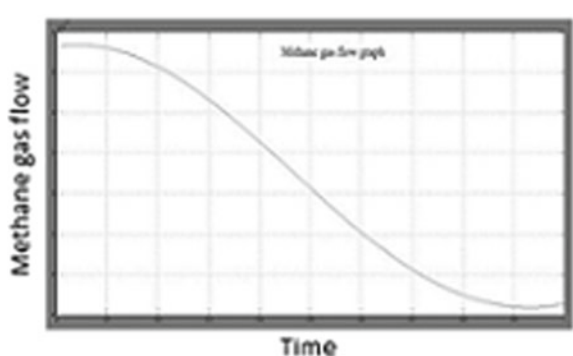


Fig. 9 Current characteristics of PV cell

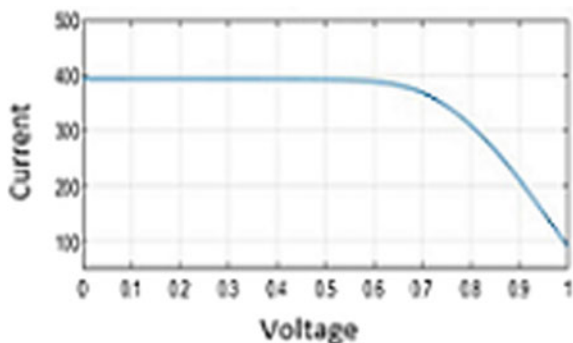


Fig. 10 Power characteristics of PV cell

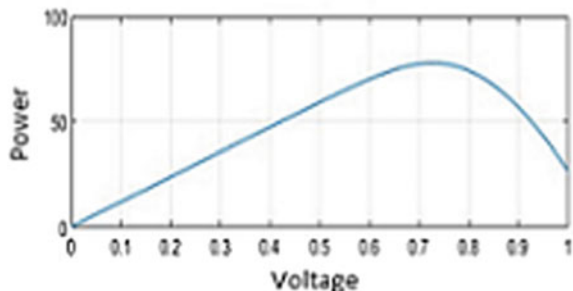
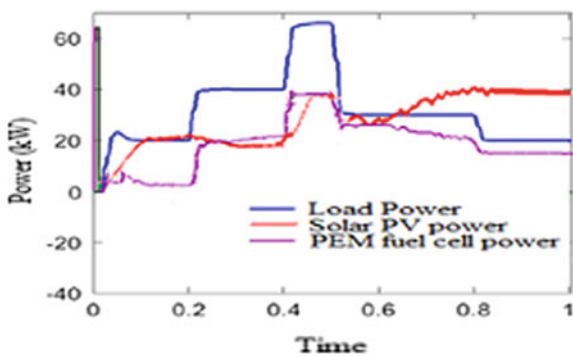


Fig. 11 Power distribution of the hybrid PEMFC and PV cell for the considered load power



References

1. Ghenai C, Janajreh I (2013) Comparison of resource intensities and operational parameters of renewable, fossil fuel, and nuclear power systems. *Int J Thermal Environ Eng* 5(2): 95–104
2. Sen R, Bhattacharyya SC (2014) Off-grid electricity generation with renewable energy technologies in India: an application of HOMER. *Renew Energy* 62:388–398
3. Lajnef T, Abid S, Ammous A (2013) Modeling, control, and simulation of a solar hydrogen/fuel cell hybrid energy system for grid-connected applications. *Adv Power Electron*

4. Uzunoglu M, Onar OC, Alam MS (2009) Modeling, control and simulation of a PV/FC/UC based hybrid power generation system for stand-alone applications. *Renew Energy* 34(3):509–520
5. Ahmed NA, Miyatake M, Al-Othman AK (2008) Power fluctuations suppression of stand-alone hybrid generation combining solar photovoltaic/wind turbine and fuel cell systems. *Energy Convers Manage* 49(10):2711–2719
6. Khan MJ, Iqbal MT (2005) Dynamic modeling and simulation of a small wind–fuel cell hybrid energy system. *Renew Energy* 30(3):421–439
7. Ganguly A, Misra D, Ghosh S (2010) Modeling and analysis of solar photovoltaic-electrolyzer-fuel cell hybrid power system integrated with a floriculture greenhouse. *Energy Build* 42(11):2036–2043
8. Corrêa JM, Farret FA, Canha LN, Simoes MG (2004) An electrochemical-based fuel-cell model suitable for electrical engineering automation approach. *IEEE Trans Ind Electron* 51(5):1103–1112
9. Jayalakshmi NS, Gaonkar DN, Nempu PB (2016) Power control of PV/fuel cell/supercapacitor hybrid system for stand-alone applications. *Int J Renew Energy Res (IJRER)* 6(2):672–679
10. Lagorse J, Paire D, Miraoui A (2009) Sizing optimization of a stand-alone street lighting system powered by a hybrid system using fuel cell, PV and battery. *Renew Energy* 34(3):683–691
11. Özgürin E, Devrim Y, Albostan A (2015) Modeling and simulation of a hybrid photovoltaic (PV) module- electrolyzer-PEM fuel cell system for micro-cogeneration applications. *Int J Hydrogen Energy* 40(44):15336–15342
12. Karami N, Moubayed N, Outbib R (2014) Energy management for a PEMFC–PV hybrid system. *Energy Convers Manage* 82:154–168
13. Khanh LN, Seo JJ, Kim YS, Won DJ (2010) Power-management strategies for a grid-connected PV-FC hybrid system. *IEEE Trans Power Deliv* 25(3):1874–1882
14. Hauer KH (2001) Analysis tool for fuel cell vehicle hardware and software (controls) with an application to fuel economy comparisons of alternative system designs
15. Hatzidioniu CJ, Lobo AA, Pourboghrat F, Daneshdoost M (2002) A simplified dynamic model of grid-connected fuel-cell generators. *IEEE Trans Power Delivery* 17(2):467–473
16. Natsheh EM, Albarbar A (2011) Photovoltaic model with MPP tracker for standalone/grid connected applications. In: IET conference on renewable power generation (RPG)
17. Nguyen XH, Nguyen MP (2015) Mathematical modeling of photovoltaic cell/module/arrays with tags in matlab/simulink. *Environ Syst Res* 4(1):24

How Does Perceived Desirability and Perceived Feasibility Effects the Entrepreneurial Intention



Rajasve Kaushik, Raman Kumar, Manishankar Datta, Rishi Kant Kumar, and Prashant Kumar

Abstract The motive of this work is to study the entrepreneurial intention among students using the Entrepreneurial Potential Model proposed by Krueger and Brazil. For this analysis, questionnaires were distributed among students of NIT Arunachal Pradesh. The questionnaire consists of six parts extracting information about perceived feasibility, perceived desirability, entrepreneurial intention, entrepreneurial capability, entrepreneurial ability and personal data. Five-point likert type scale is used to collect the data. Simple random sampling process is used for collection of the data. Confirmatory factor analysis is used to examine the reliability and validity of the Questionnaire. Multiple regression analysis used for data analysis. Findings show a positive impact of perceived desirability and perceived feasibility on the entrepreneurial intention of the students. The work suggests some action plans which can be executed for inspiring and strengthening the intent of graduate students.

Keywords Entrepreneurial intention · Skills · Perceived feasibility · Perceived desirability · Entrepreneurship

R. Kaushik (✉)

Pearl Consulting Services, Gurugram, India

e-mail: rajasve.kaushik@pearlconsulting.co.in

R. Kumar

Department of Economics, G.D. College, LNMU, Darbhanga, India

e-mail: ramansbi07@gmail.com

M. Datta · R. K. Kumar · P. Kumar

Department of Management Studies, Indian Institute of Technology, Delhi, India

e-mail: mdatta.nit@gmail.com

R. K. Kumar

e-mail: rishinit14@gmail.com

P. Kumar

e-mail: prashant@dms.iitd.ac.in

1 Introduction

Entrepreneurship refers to the activity of an individual for executing a new idea or endeavoring for a new opportunity. If any person wants to be an entrepreneur, they should closely observe the problem statements of society and have the problem identifying capability. This process of understanding what society wants helps to find the solution to address that issue, and if potential exists, it can be converted into a business opportunity. Entrepreneurship is a procedure of identifying and grabbing the opportunity, integrating resources and the team which will implement the plan [1]. Nurturing entrepreneurship is viewed as a key factor in promoting economic development and sustainable growth. For achieving sustainable economic growth, continuous harnessing of entrepreneurial activity is necessary else it will tend towards saturation. Entrepreneurs are wealth creators; they nurture the new business, which creates new employment, which results in solving the problems of unemployment [2].

Entrepreneurs play an important role in the growth of any country. In comparison to a developed country impact of entrepreneurship is more notified in a developing country as it constantly enhances the economic situation of a growing economy [3]. Entrepreneurship is continuously acquiring importance in India in the rouse of economic liberalization, and globalization. The government of India has embarked on 'The Make in India' initiative to boost up the entrepreneurial ecosystem in India [4].

The growing young generation in India has a huge potential for embracing the entrepreneurial ecosystem. The right place for inspiring, injecting the basic concept of entrepreneurship, and further assessing their intention towards entrepreneurship is the educational institutions [5]. Private, public and governmental organizations are implementing various measures to encourage more and more entrepreneurial activity in India. Educational institutions have started various programs on entrepreneurship. The current Government policies are focused towards institutional structure for ameliorating entrepreneurial skills, to hone entrepreneurial skills [6]. Vocational education and training have extended the area for more inclusion of youths in entrepreneurship. Many youths are looking towards different opportunities in control of renewable energy [7] are facing various difficulties which require various support in India [8].

The inclusion of entrepreneurship has taken such a deep route in our education system, that it has been included in the school curriculum now. The inclusion of entrepreneurship to the school level will help in the development of entrepreneurial intention, in the youth generation [9]. A push that is given at a younger age adds more power to any function. If there is a push from Government on Entrepreneurship, the process to initiate a new business is made simpler, this will bring in more opportunities and a new entrepreneur will find it more feasible to register a new business [10]. How much entrepreneurial intention will increase in the Product/Service industry will depend upon the policy of the ruling government in the country.

The literature on the entrepreneurial ecosystem in India is growing, and very few studies are being conducted to assess the entrepreneurial intention in the north-eastern part of India. Researchers widely endorsed that educational institutions must produce a grilling academic curriculum, which can act as a booster for emerging ventures, but still, a lot of improvement is required. After this, one of the most important constructs, which has evolved in the entrepreneurship, literature over the last few decades' research is entrepreneurial intention. Intention-based research models tried to give some good explanations of the amateur thought process of entrepreneurs and proven to be good compared to models based on individual variables. Looking as such intent it is necessary to find the impact of perceived desirability and perceived feasibility on entrepreneurs' intention.

From this point forward, the flow of this paper is as follows: Sect. 2 presents the literature review section of this paper in which various constructs of this paper are described Sect. 3

2 Literature Review

Hockerts [11] mentioned that major studies in the entrepreneurship area, before the intention model assessment are mainly trait approaches, psychological characteristics, ex-post conditions of entrepreneurs. Another lobby of researchers worked on demographic factors. They are largely criticized due to conceptual, methodological and lack of explanation. According to [12] the evolution of entrepreneurial intent in a person depends upon his/her perception of entrepreneurial feasibility and desirability which will later lead to entrepreneurial behaviour. Perceived desirability depends upon the individual's attitudes towards the result of any action. In the case of entrepreneurial action, the outcomes include revenue generation, autonomy, ownership, risk-taking ability, etc. Besides, entrepreneurs have desire to know various technocommercial [13] as well various new technology usage like Machine Learning [14] and artificial intelligence which provide them future skill and feasibility to utilize those technology [15].

Hill et al. [16] proposed Theory of Reasoned Action, which suggests that one's attitude is responsible for his/her behavioural intention towards that behaviour and along with that subjective norms (i.e., family influence, the influence of role models, etc.) are also responsible. It also suggested that individual's motivation and surrounding affects the constructs. Ajzen [17] proposed the theory of Planned Behaviour which is an extension of the Theory of Reasoned Action. He worked with three conceptually exclusive antecedents of one's intention which are the attitude for a behaviour, the degree of perceived level of behavioural control and subjective norms. According to the author, behaviour is related to the beliefs relevant to the behaviour. It is these accumulated beliefs that are reflected in a person's attitudes, intentions and behaviour. Performance of a behaviour is a connected function of intentions and perceived behavioural control [17]. Subjective norms can be simply explained as to how an individual perceives the external pressure of society to perform a specific behaviour.

Krueger and Brazeal [12] during his research on entrepreneurial intention proposed Entrepreneurial Potential Model. The researcher highlighted two important constructs in the study namely perceived feasibility and perceived desirability. During the study, they found that in the Theory of Planned Behaviour and the Entrepreneurial Event model few concepts are overlapping, and hence by integrating they proposed the EPM model. Findings show that credibility comes from the perception of desirability and with the understanding that this venture opportunity is feasible, which leads to a behaviour depending on the potential of the person, wants to start the entrepreneurial venture.

2.1 Entrepreneurial Intention

Entrepreneurship is an intention driven process. Intention of being self-employed or having a business of own makes a person inclined towards starting a new business. Entrepreneurial intent comes from one's willingness to solve a problem, to bring change, autonomy and from the present situation (Krueger and Brazeal [12]). Researchers tried to predict the intensity of the individual's entrepreneurial action and to construct an individual's intention to start a venture is being repeatedly used.

2.2 Perceived Desirability

Perceived desirability alludes to the intensity level to which a person is allured for performing behaviour to become an entrepreneur. Moreover, previous research states that cultural factors and social norms affect desirability. If one thinks that people from their surrounding environment endorse to accomplish the behaviour, this will augment one's attitude towards the behaviour. These social burdens are a hindrance to embark any entrepreneurial venture.

2.3 Perceived Feasibility

It can be defined as the degree at which one considers himself personally capable of carrying out a behaviour. The presence of guidance, mentors, and role models helps in establishing one's perception towards feasibility that there is potential, and the implementation can be done.

2.4 *Entrepreneurial Capability*

It refers to ones' ability to perform a task that comes after the creation of trust on a concept whose advantage and limitations have been understood properly. Literature shows that previous researchers use this concept to explain entrepreneurial credibility. It refers to one's skill of understanding the entrepreneurial process which helps in the implementation of a project.

Literature shows that previous researchers use this concept to explain the propensity to act as an entrepreneur. So, in this paper, we have proposed a model in order to find the objectives: (1) To study the entrepreneurial intention among students of NIT, Arunachal Pradesh. (2) To assess the effect of perceived desirability and perceive feasibility on entrepreneurial intention of students. (3) To study the effect of entrepreneurial ability on entrepreneurial intention of students.

3 Methodology

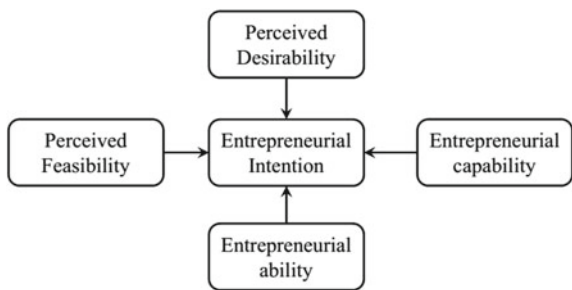
This section constitutes of two subsections. In first the proposed model has been discussed and in second data collection section has been described.

3.1 *Proposed Model*

Researchers like, [11, 17] stated that EPM meshes with two important pertinent antecedent models. The wide use of the Entrepreneurial Potential Model in previous studies supports EPM as the best robust model for the measurement of entrepreneurial intention. Entrepreneurial Potential Model [12] with little modification, is chosen as the base model for the study. The model conceptualizes that the occurrence of an entrepreneurial venture enquires potential and ability to start a business that is explained by three important constructs: perceived desirability, perceived feasibility and propensity to act. Here, the effect of the independent factors such as perceived feasibility, perceived desirability, entrepreneurial capability and entrepreneurial ability on the students' intention to start an entrepreneurial venture is tested.

Besides, Shapero [18] proposed Entrepreneurial Event Model, which is one of the earliest contributions in the field of intention-based behavioural study of entrepreneurs. The researchers irrespective of taking the entrepreneur as the unit of analysis took an entrepreneurial event for the study purpose. The model depicts the intention to embark on a new business as being dependent on three factors. (1) Perceived Desirability—the thoughts and perceptions of desirability—one's enthusiasm and attractiveness towards starting a new venture. (2) The propensity to Act—a

Fig. 1 Proposed research model



person's inherent qualities of mind and character strongly reflects in the decision-making process of the individual. (3) Perceived Feasibility—the state to which one feels to be personally competent to start a new venture. Based on these we have proposed our hypothesis as under and the model is presented in Fig. 1.

- H1 There is a significant impact of Perceived Desirability on Entrepreneurial Intention
- H2 There is a significant impact of Perceived Feasibility on Entrepreneurial Intention
- H3 There is a significant impact of Entrepreneurial ability on entrepreneurial intention
- H4 There is a significant impact of Entrepreneurial capability on entrepreneurial intention.

3.2 Data Collection

Entrepreneurial Potential Model is used in the study to assess the intensity of entrepreneurial intention among the undergraduate students of NIT Arunachal Pradesh. Desirability and feasibility, which are the significant determinants of entrepreneurial intention, are taken and to assess the impact on intention. Tested scales used in the Entrepreneurial Potential Model is used with little modification. The whole questionnaire is consistent of 06 (Six) portions, namely, perceived feasibility, perceived desirability, entrepreneurial capability, entrepreneurial ability, entrepreneurial intention, and personal data. Closed-ended questions with five-point likert scales were used. Simple random sampling was adopted. Responses were gathered from third year and final year students as they are on the verge of deciding on their professional career. The questionnaire was distributed among 120 students of NIT Arunachal Pradesh, out of which 100 successfully responded. In the beginning, a pilot study was conducted by distributing the questionnaire to 30 respondents to check the Cronbach's alpha.

4 Result

Regression analysis is used to find out the significant impact or influence of independent variables on the dependent variable [19]. So, equation of the proposed model is given in Eq. (1).

$$EI = \alpha + \beta_1 PD + \beta_2 PF + \beta_3 EC + \beta_4 EA + \epsilon \quad (1)$$

where EI—Entrepreneurial intention, PD—Perceived desirability, PF—Perceived feasibility, EC—entrepreneurial capability, EA—Entrepreneurial ability.

Table 2 represents the ANOVA analysis, which is computed to test whether the proposed model is statistically significant or not.

$$\begin{aligned} H_0 : \beta_1 &= \beta_2 = \beta_3 = \beta_4 = 0 (R \text{ square} = 0) \text{ and} \\ H_1 : \text{at least one } \beta &\neq 0 (R \text{ square} \neq 0) \end{aligned} \quad (2)$$

Analysis confirms the overall model fit of the study, revealing a significant *P*-value, which is 0.000. In the proposed model *R* Square value is 0.88 (from Table 1). Interpretation of which means 88% variation in EI is explained by all the four variables, i.e. PD, PF, EC, and EA. Now the statistical significance of each regression coefficient of the proposed model is checked (Table 5). Interpretation of the result of the analysis shows that all the independent variables except EC are statistically significant. The proposed model is shown below with the value of their respective coefficient (Table 3):

Table 1 Proposed Model 1 Summary

<i>R</i>	<i>R</i> square	Adjusted <i>R</i> square	Std. error of the estimate
0.940	0.883	0.878	0.370

Table 2 Anova table

Model	Sum of squares	<i>df</i>	Mean square	<i>F</i>	Sig.
Regression	98.822	4	24.706	180.79	0.000
Residual	13.118	96	0.137		
Total	111.941	100			

Table 3 Revised model summary

Mode 1	<i>R</i>	<i>R</i> Square	Adjusted <i>R</i> square	Std. error of the estimate
	0.939	0.881	0.877	0.371

Table 4 Anova table

Model	Sum of squares	df	Mean square	F	Sig.
Regression	98.611	3	32.870	239.20	0.000
Residual	13.329	97	0.137		
Total	111.941	100			

Table 5 Coefficients table for the regression analysis Dependent Variable: EI Predictors: (Constant), EA, PD, PF

Model	Unstandardized coefficients B (Stand. error)	Standardized coefficient beta	t	Sig.
(Constant)	-1.097 (0.277)		-4.047	0.000
PF	0.488.087	0.425	2.797	0.006
PD	0.309.081	0.259	4.526	0.000
EA	0.532.139	0.306	3.618	0.000

$$\text{EI} = -1.119 + 0.256 \text{PD} + 0.436 \text{PF} + 0.134 \text{EC} + 0.506 \text{EA} \\ (0.276) \quad (0.091) \quad (0.096) \quad (0.108) \quad (0.140) \text{ Standard error} \quad (3)$$

Values in brackets indicate individual standard error. A regression coefficient is statistically significant if the standard error is less than half of the regression coefficient. Regression analysis is again computed, and it is observed that the model is statistically significant shown in Table 4. Further removing EC from the model, R Square value is decreased by 0.002 (shown in Table 4), which is very negligible and insignificant. This shows that removing EC has the least effect on the predictive power of the model. The revised model is shown below (Table 3).

Since the coefficient of EC is found statistically insignificant, it has been removed from the model and the model has been revised to as follows:

$$\text{EI} = \alpha + \beta_1 \text{PD} + \beta_2 \text{PF} + \beta_3 \text{EA} + \epsilon. \quad (4)$$

$$\text{EI} = -1.097 + 0.488 \text{PD} + 0.309 \text{PF} + 0.532 \text{EA} \quad (5)$$

The interpretation of the value of the coefficient of PF is that keeping PD and EA constant if PF is changed for 1%, it brings a change in 48.8% in EI. Moreover, the beta value indicates that PF influences EI most followed by EA and PD. Therefore, PF is the most influencing factor among the independent factors taken in the study.

5 Discussion and Conclusion

This research used the EPM model of Krueger and Brazeal's with suitable modification, to study the entrepreneurial intention. Four constructs, such as perceived feasibility, perceived desirability, entrepreneurial capability, and entrepreneurial ability, have been taken as independent factors to study the entrepreneurial intent of the students. This study shows a significant impact of perceived feasibility, perceived desirability, and entrepreneurial ability on entrepreneurial intention.

The finding shows that perceived feasibility explains and influences most of the entrepreneurial intention of the students. Entrepreneurial education, support from the environment, understanding the potential of revenue generation of a new idea if implemented impacts the feasibility. To improve the perceived feasibility institute should give more exposure to the idea generation process, working process of start-ups, successful technology transfer process so that students can develop an in-depth understanding of the practicality of any project.

Desirability gets impacted by the student's own will to become self-independent, desire to build something of their own, which can generate revenue for them. The realization of less campus placement also gives a boost for desirability towards starting a new venture. It is also observed that due to less awareness, entrepreneurial intent is not growing. On the other hand, those who have grasped the depth understanding of the venture creation, skills to strategically implement, and have the propensity to act, though understand hindrances, shows strong entrepreneurial ability towards venture creation.

The entrepreneurship curriculum is creating an impact on the mindset of the students in NIT, but the intensity of that towards leading to the implementation behaviour is less. Absence of practical experience in incubators, less risk-taking skill, less awareness of Government policies, poor engagement with the entrepreneurial network is compelling them to step back from showing entrepreneurial behaviour.

Hence, it is recommended that the institute should follow up and grill the working process of the incubation center. Providing exposure to the entrepreneurial networks of the state and national level will boost the thought process of the students. Institute should also provide knowledge about existing Centre and state Government policies endorsing entrepreneurs and process to avail them. The curriculum designed should be aligned to develop entrepreneurial intention among the students. A similar course curriculum may be floated in other state control universities so that students will have a proper understanding of the entrepreneurial process.

References

1. Burns P (2018) New venture creation
2. Neck HM, Meyer GD, Cohen B, Corbett AC (2004) An entrepreneurial system view of new venture creation. *J Small Bus Manage* 42(2):190–208

3. Chaston I, Scott GJ (2012) Entrepreneurship and open innovation in an emerging economy. *Manage Decis* 50(7):1161–1177
4. Dasannacharya BA (2016) Make in India. *Curr Sci*
5. Trivedi R (2016) Does university play significant role in shaping entrepreneurial intention? A cross-country comparative analysis. *J Small Bus Enterp Dev* 23(3):790–811
6. Gupta VK, Guo C, Canever M, Yim HR, Sraw GK, Liu M (2014) Institutional environment for entrepreneurship in rapidly emerging major economies: the case of Brazil, China, India, and Korea. *Int Entrep Manage J* 10(2):367–384
7. Kumar P, Das U, Chatterjee S (2016) A brief study on control structure of grid connected PV inverter. In: 2016 International conference on energy efficient technologies for sustainability (ICEETS), pp 577–582
8. Surie G (2017) Creating the innovation ecosystem for renewable energy via social entrepreneurship: Insights from India. *Technol Forecast Soc Change* 121:184–195
9. Premand P, Brodmann S, Almeida R, Grun R, Barouni M (2016) Entrepreneurship education and entry into self-employment among university graduates. *World Dev* 77:311–327
10. Vilcov N, Dimitrescu M (2015) Management of entrepreneurship education: a challenge for a performant educational system in Romania. *Procedia Soc Behav Sci* 203:173–179
11. Hockerts K (2017) Determinants of social entrepreneurial intentions. *Entrep Theory Pract* 41(1):105–130
12. Krueger NF, Brazeal DV (1994) Entrepreneurial potential and potential entrepreneurs. *Entrep Theory Pract* 18(3):91–104
13. Chatterjee S, Kumar P, Chatterjee S (2018) A techno-commercial review on grid connected photovoltaic system. *Renew Sustain Energy Rev* 81:2371–2397
14. Kumar P, Chatterjee S, Shah D, Saha UK, Chatterjee S (2017) On comparison of tuning method of FOPID controller for controlling field controlled DC servo motor. *Cogent Eng* 4(1)
15. Duan Y, Edwards JS, Dwivedi YK (2019) Artificial intelligence for decision making in the era of Big Data—evolution, challenges and research agenda. *Int J Inf Manage* 48:63–71
16. Hill RJ, Fishbein M, Ajzen I (1977) Belief, attitude, intention and behavior: an introduction to theory and research. *Contemp Sociol* 6(2):244
17. Ajzen I (1991) The theory of planned behavior. *Organ Behav Hum Decis Process* 50(2):179–211
18. Shapero A (1975) The displaced, uncomfortable entrepreneur. *Psychol Today* 9(6):83–88
19. Hair JF, Ringle CM, Sarstedt M (2011) PLS-SEM: indeed a silver bullet. *J Mark Theory Pract* 19(2):139–152

A New Topology for Photo Voltaic Energy Conversion System



Sudhir Maurya and Abhik Banerjee

Abstract A new topology for solar photovoltaic (PV) energy conversion system is used in this paper. Various topologies are available nowadays which have several problems associated with using several blocks and in its performance analysis of the system from the stability point of view like DC-DC converter, low-frequency transformer, maximum power point tracking [MPPT] block, unfold circuit like push-pull circuit, etc. New types of topology for solar photovoltaic energy conversion systems have been shown which bypass the MPPT separate block units, unfold circuit, low-frequency transformer. By the use of current-controlled inverter integration of MPPT along with the DC-DC to AC conversion takes place inside a single block which reduces the number of blocks helping in getting a simple transformation block for the stability analysis. With the help of Phase Locked Loop (PLL) quadrature axis voltage can set to zero so that only direct axis voltage is used which corresponds to a single PI controller which again reduces one set point type tracking controller. Currents which are injected into the grid contains harmonics, THD generated form inverter is approximately 10% only, which can be further reduced by 5% by using simple suitable LC filter. MATLAB simulation depicts the whole work.

Keywords Current controlled inverter · Phase-locked loop · Integrated maximum power point tracking · Set-point controller

1 Introduction

MPPT controller (DC-DC circuit) can be of any type either isolated or non-isolated type. It ensures the load line attributes with respect to PV terminals so that maximum power can be drawn from the photovoltaic cell. An old topology that includes various

S. Maurya · A. Banerjee (✉)

Department of Electrical Engineering, National Institute of Technology, Yupia, Arunachal Pradesh, India

e-mail: abhik_banerjee@rediffmail.com

S. Maurya

e-mail: smdm6436@gmail.com

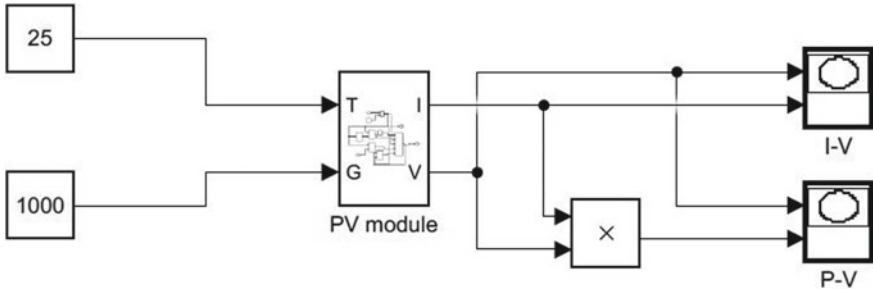


Fig. 1 PV module

blocks like separate MPPT block, DC-DC converter (Buck-Boost), Unfold circuit, push-pull circuit, low-frequency transformer is used. In the new topology, DC-DC converter and unfolding circuit are replaced by a single power stage block called current controlled inverter. Low-frequency transformer which is present at the right side is shifted to the high-frequency side, i.e. into the dc-dc converter. Low frequency transformer is bulky to use in this circuit. Isolation of transformer from the circuit is necessary from any type of discharging of currents which leads to shock, for this flyback converter topology is used which is an isolated version of buck-boost topology. DC-DC converter is eliminated by the use of current-controlled inverter. Inverter is doing current control with the help of inductor current which is actually being pumped into the grid is being controlled, then the MPPT algorithm can be used for the terminal currents of the photovoltaic panel. The stability analysis of the terminal voltage can be seen in [1–3], similarly the terminal voltage of the photovoltaic can be measured and the power that is obtained can be pass through the maximum power point tracking algorithm. The output of the reference current for the inverter will be appropriately modulated in such a way that the desired current flows through it and maximum power will be achieved from the photovoltaic panel [4]. In [5, 6], the simulink model of hybrid system can be observed and also in this way this topology works, where is only one power stage which is coming between the photovoltaic module and the grid (Figs. 1 and 2).

2 Three-Phase Grid Connection

The three-phase inverter, there are six gates (let we are using IGBT or MOSFET, for this six gate drive terminals are required, gate drive is getting the control signal from PWM block for RYB phases [7]. Now the input to the PWM will be control signals coming from the output of controllers. Now, to control the inductor current that is being pumped into the grid. Again, with the help of a comparator an I_g reference can be compared. Now, it compare current with the value of i_g reference and then pass it to the controller block it could be PI controller. Each phase of the

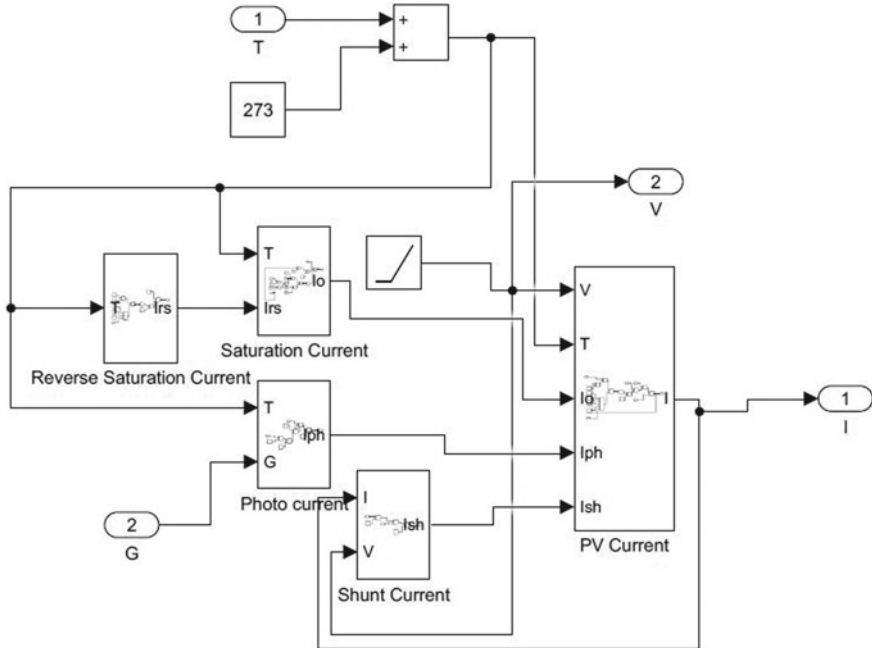


Fig. 2 PV module inside blocks

three phases are need to compare and control the output of controllers which will give it to the PWM block. So let us say each of the controllers is connected to PWM. Currents are sensed compared with a reference and based on the error the controller output will send the signal to the PWM which compares with the triangle carrier and then appropriately gives the PWM drive to each of the arms of the inverter with proper energy management [8]. These references i_{gR}^* , i_{gY}^* , i_{gB}^* are obtained from the MPPT algorithm. All the three currents are sensed by using a hall sensor or alternatively resistive shunt and differential amplifiers, instrumentation amplifiers can be used but hall sensor is better because it is contactless and has large bandwidth. V_T and I_T are measured by another hall sensor for MPPT block. Input to MPPT is V_T and I_T and output are i_{gR}^* , i_{gY}^* , i_{gB}^* (These are sinusoidal values).

3 Controller

However there are lots of drawbacks in this particular type of the circuit, first of all, the references i_{gR}^* , i_{gY}^* , i_{gB}^* are sinusoidal. They are not DC or setpoint value. The controller becomes a tracking controller it is no longer a setpoint controller reference current signal and feedbacks current signal all are AC sinusoidal in general.

Tracking controller needs to handle large signal deviation as the consequence the B.W of tracking controller will be lower compared to a similar setpoint controller, if i_{gR}^* and feedback signal have DC. So, design of tracking controller will be much more complex compare to a set point controller and DC to DC converter in power system [9]. It can also able to achieve intra cycle dynamics if one user setpoint controller but for the tracking controller only integral cycle dynamics can be achieved. Another problem is here three separate controllers one for each phase and the dynamics are coupled, so fining the three controllers simultaneously will become difficult as the dynamics are coupled. So those issues should be short out for the controller for three-phase photovoltaic grid-connected inverters [10] in the control methodology.

4 Current Controlled Inverter

Input to PWM is reference V_a , V_b , V_c (as desired) which will be compare with the carrier triangle which PWM has and then generate the necessary PWM signals (pulse). For the gate drive to switch ON and OFF accordingly and supply a voltage here such that i_a , i_b , i_c flows according to this control such that error just before PT is zero. Now to define ρ , angle between the d axis and α axis so that both coordinate systems rotates synchronously. α , β coordinate system has current space vector i_d get aligned along the current space vector that is i_q is equal to zero because i_d is aligned itself along grid current. We use V_a , V_b , V_c voltage waveforms to obtain ρ then i_d and i_q will be such that it will be with the respect to the voltage space vector as the d -axis and it has an advantage. Let we take angle ρ between V_α and α axis also V_g is not along V_d and V_q is not equal to zero. Then we get some error the PT activates and PI controller will work in such a way that error to PI tends to zero. Then V_q is equivalent to V_q^* which is equal to zero and d -axis will go and aligned along V_g voltage space vector and such a value of ρ (ρ will increase while aligning) will come up because of control action such that V_q is equal to zero here. In this way, ρ gives the value of difference between d_q axis and $\alpha\beta$ coordinate system such that d -axis aligned along the voltage space vector.

So, it becomes a robust mechanism because it is a close loop system and then there is PI component that has a history in it which will have a filtering effect on harmonics, surges, spikes, and uncertainties. So by incorporating this modification into our entire three phase grid-connected inverter block diagram, it will be a completely workable solution like other PV inverters used in [11, 12]. So we modify ρ -generation block.

5 SPWM (Unipolar PWM Technique)

According to IEEE—5/19/992—for household appliances total harmonic distortion (THD) is less than five percent. So we can just attach a simple AC filter like LC filter in order to reduce harmonics which is injected into the grid without using complex

AC filter also we can make THD less than five percent or by using base works as a filter. This can be achieved by using a sinusoidal PWM technique in which we should use less filter (Fig. 3).

6 Detailed Comparisons of Older Photo-Voltaic Conversion Topology with Respect to New One

Various topologies are available in the past in which separate DC-DC converter [9] which can be of any type of isolated or non-isolated type are present whose work is just to match load line to the PV terminals in such a way that maximum power [13, 14] can be drawn from the PV cell. Unfolding circuit which is basically a two-way switch type which switches ON alternatively can be replaced by a more popular bridge stage which is decoupled from the isolating stage. In the new topology, DC-DC converter and unfolding stage are replaced by a single power stage which is called the inverter. This leads to an increase in the efficiency of this model. Power transformer is of low frequency which is bulky, heavy, and expensive, so in this electronic model, the transformer is shifted to DC-DC converter so that it can work as high switching frequency which thereby reduces its weight, size, and works with increased efficiency. System becomes more compact. This leads to transformerless interface. In this high-frequency isolation flyback converter topology which is the isolated version of the buck-boost topology that can handle the entire first quadrant of the curve of the PV module is used. Further, improve on this topology by the use of current-controlled inverter, DC-DC converter is eliminated which is doing the job of maximum power point tracking. MPPT is done by the current-controlled inverter [15] itself, there is inductor current which is pumped into the grid is being controlled, then the maximum point algorithm is used for the terminal currents and the terminal voltage of the PV panel are measured and power that is obtained is pass through the maximum power point tracking algorithm..

7 Proposed Model of PV Energy Conversion System in MATLAB

See Fig. 4.

8 Simulated Result

See Fig. 5.

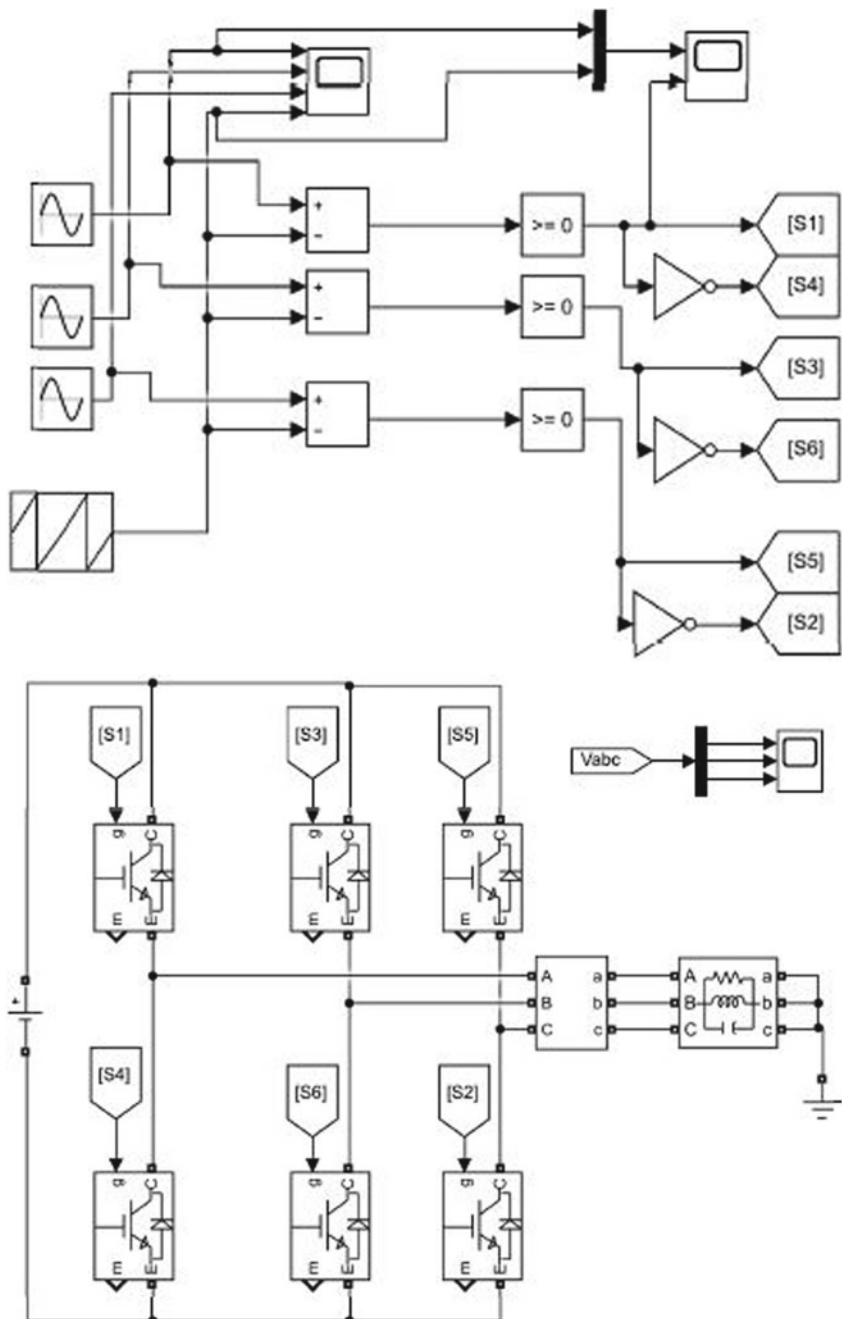


Fig. 3 Current-controlled inverter

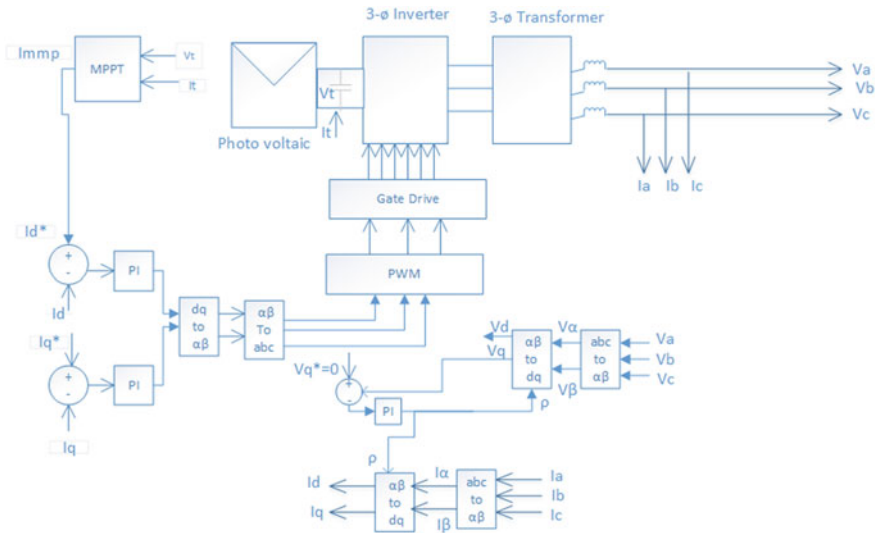


Fig. 4 MATLAB simulation model

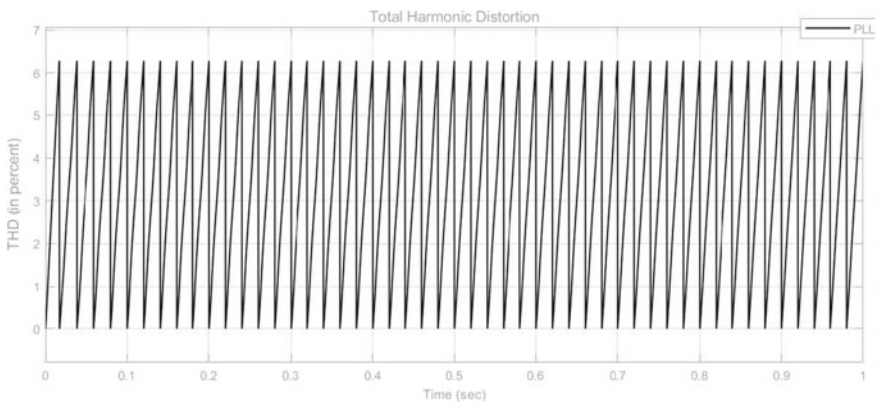


Fig. 5 PWM output

9 Parameters with Different Rated Values Used

See Table 1.

Table 1 Data sheet for PV module elements

Module type	BLD240-60P
Peak power	240 W _p
Maximum power voltage (V_{mp})	30.18 V
Maximum power current (I_{mp})	7.96 A
Open circuit voltage (V_{oc})	36.72 V
Open circuit current (I_{sc})	8.99 A
Cell η	16.50%
Module η	14.56%
Maximum system voltage	DC 1000 V
Temperature coefficient of $I_{sc} \alpha_1$	+0.045%/K
Temperature coefficient of $V_{oc} \alpha_v$	-0.34%/K
Temperature coefficient of $P_{max} \alpha_p$	-0.47%/K
Series fuse rating	15 A
Cells	6 × 10 pieces polycrystalline solar cells series (156 mm × 156 mm)
Junction box	With 3 bypass diodes

10 Conclusion

Setpoint controllers only two have been used (while we need three for AC tracking type controller). Working with DC values is easy because it is difficult to compare changing values of magnitude of AC which is changing with respect to time with the reference values for comparison. MPPT is integrated into the invertors by removing the DC-DC converter and power block is simple (just has one power stage) so that the analysis from the stability point of view becomes easy and the efficiency of the model is increased. Robust Phase Locked Loop (PLL) based on ρ determination is done as the current is injected into the grid via current terminals contain harmonics. So getting ρ we converted current terminals into voltage terminals with the help of proper transformation. In PLL open-loop becomes closed-loop by doing certain modifications, in this way it becomes robust a robust mechanism there is proportional-integral (PI) component there is history in it which will filtering the effect on harmonics, surges and spikes.

References

- IEEE TF Report (1982) Proposed terms and definitions for power system stability. IEEE Trans Power Appart Syst PAS-101:1894–1897
- Banerjee A, Mukherjee V, Ghoshal SP (2013) Modeling and seeker optimization based simulation for intelligent reactive power control of an isolated hybrid power system. Swarm Evol Comput 13:85–100

3. Kundur P et al (2004, Aug) Definition and classification of power system stability IEEE/CIGRE joint task force on stability terms and definitions. *IEEE Trans Power Syst* 19(3):1387–1401. <https://doi.org/10.1109/TPWRS.2004.825981>
4. Dinga Z, Houa H, Yua G, Hub E, Duana L, Zhao J (2019) Performance analysis of a wind solar hybrid power generation system. Elsevier
5. Onara OC, Uzunoglu M, Alama MS (2018) Modeling, control and simulation of an autonomous wind turbine/photovoltaic/fuel cell/ultra-capacitor hybrid power system. Elsevier
6. Tsai HL, Tu CS, Su YJ (2008) Development of generalized photovoltaic model using MATLAB/Simulink. In: Proceedings of the World Congress on Engineering and Computer Science (WCECS'08), San Francisco, USA, 22–24 Oct 2008
7. Figueres E, Garcera G, Sandia J et al (2009) Sensitivity study of the dynamics of three-phase photovoltaic inverters with an LCL grid filter. *IEEE Trans Ind Electron* 706–717
8. Dali M, Belhadj J, Roboam X (2010) Hybrid solar–wind system with battery storage operating in grid-connected and standalone mode: control and energy management—experimental investigation. *Energy* 35(6):2587–2595
9. Banaei M, Ardi H, Alizadeh R et al (2014) Non-isolated multi-input-single output DC/DC converter for photovoltaic power generation systems. *IET Power Electron* 7(11):2806–2816
10. Kroutikova N, Hernandez-Aramburo C, Green T (2007) State-space model of grid-connected inverters under current control mode. *IET Electr Power Appl* 1(3):329–338
11. Fazeli M, Ekanayake J, Holland P et al (2014) Exploiting PV inverters to support local voltage—A small-signal model. *IEEE Trans Energy Convers* 29(2):453–462
12. Fortunato M, Giustiniani A, Petrone G et al (2008) Maximum power point tracking in a one-cycle controlled single-stage photovoltaic inverter. *IEEE Trans Ind Electron* 55(7):2684–2693
13. Patel H, Agarwal V (2008) Maximum power point tracking scheme for PV systems operating under partially shaded conditions. *IEEE Trans Ind Electron* 55(4):1689–1698
14. Noguchi T, Togashi S, Nakamoto R (2002) Short-current pulse-based maximum-power-point tracking method for multiple photovoltaic-and converter module system. *IEEE Trans Ind Electron* 49(1):217–223
15. Feng J, Wang H, Xu J et al (2017) A three-phase grid-connected microinverter for AC photovoltaic module applications. *IEEE Trans Power Electron*

A User-Centric Task Allocation Approach in Mobile Crowdsensing



Moirangthem Goldie Meitei and Ningrinla Marchang

Abstract Mobile crowdsensing (MCS) refers to the process in which a collection of mobile devices share sensing data, which can then be aggregated to develop policies or applications that benefit a community. Traditionally, mobile crowdsensing has been deployed using a platform-centric task allocation approach. These platform-centric systems are primarily concerned with gaining profits for the platform by minimizing rewards given to users. Instead of this approach, this paper focuses on a more altruistic task allocation approach by proposing a user-centric task allocation approach. In this regard, we have developed two task allocation schemes: Nearest User Task Allocation (NUTA) and Nearest User Fair Task Allocation (NUFTA) in order to facilitate an optimized and equitable workload for the users.

Keywords Mobile crowdsensing · User-centric · Task allocation

1 Introduction

The growth of technology and the increasing availability of Internet access has led to large-scale production and consumption of data. Boom of consumer electronics, specifically mobile devices, provides a unique opportunity to gather data. These mobile devices come equipped with inbuilt sensors, e.g., camera, GPS, accelerometers, etc. Mobile crowdsensing (MCS) refers to a broad range of community sensing paradigms, which requires the active involvement of individuals to contribute sensor data (e.g., taking a picture, reporting a road closure) related to a large-scale phenomenon. Examples of such large-scale phenomena include traffic monitoring, air pollution level monitoring, noise pollution level monitoring, etc. [1].

Task allocation is the selection of tasks to be assigned to different participants. Task allocation can take on two approaches. The first approach can be referred to

M. G. Meitei (✉) · N. Marchang

Department of Computer Science and Engineering, NERIST, Nirjuli, Arunachal Pradesh, India
e-mail: ngmeitei@gmail.com

N. Marchang

e-mail: ningrinla@gmail.com

as a platform-centric approach. Prevalent architectures are mainly focused on the platform-centric task allocation approach. These systems are primarily concerned with profits gained by the platform, by minimizing rewards given to users. Examples of platform-centric systems include ride-sharing apps. The second approach can be defined as a user-centric approach. This user-centric system serves as the main focus of this study.

In user-centric approach, unlike the platform-centric ones, the main concern is not the financial benefit of the platform but rather, it follows an altruistic perspective and seeks to fulfill the interest of the users. It removes financial competition among users and instead places importance on collective work for the benefit of the environment or society. Examples include volunteer work, namely by non-governmental organizations (NGOs), or feedback regarding traffic or weather conditions.

For our proposed user-centric task allocation mechanism, the main goal is to reduce the workload on the users by minimizing the overall distance traveled to accomplish the allocated tasks. Additionally, we also seek to provide a fair mechanism for task allocation so that no users get flooded with tasks while other users are left underutilized.

This paper tackles the task allocation problem in MCS and proposes a user-centric task allocation strategy. The rest of the paper is organized as follows: Sect. 2 discusses the literature related to task allocation in MCS. Section 3 explains the user-centric task allocation mechanisms that are followed in this study. Section 4 briefly describes the experimental setup which yields the results in Sects. 5, and 6 provides the conclusion.

2 Related Work

The earliest work on mobile crowdsensing and the Internet of Things (IoT) was done by Ganti et al. in [1]. In their work, they identified a category of IoT applications that rely on data collection from a large number of mobile devices. They defined mobile crowdsensing and differentiated them from traditional IoT applications. They also identified unique characteristics of mobile crowdsensing, described the mobile crowdsensing process, and presented challenges of mobile crowdsensing and briefly discussed their solutions. Further, they presented the mobile crowdsensing architecture along with its features and problems and proposed the exploration of a unified mobile crowdsensing architecture to solve its problems.

Some works in MCS which deal with task allocation are [2–14]. He et al. proposed a methodology to address the problem of location-dependent task allocation and designed a local ratio based algorithm (LRBA) to solve the task allocation problem [2]. They designed the pricing mechanism based on the bargaining theory. Zhang et al. proposed a participant selection framework for mobile crowdsensing known as CrowdRecruiter [3]. They formulated the concept of piggyback crowdsensing in order to reduce energy consumption by leveraging smartphone app opportunities to perform sensing tasks and return sensed results. Liu et al. proposed TaskMe, a participant selection framework for multi-task mobile crowdsensing environments [4]. In

particular, two typical multi-task allocation situations with bi-objective optimization goals are studied: (1) For FPMT (few participants, more tasks), each participant is required to complete multiple tasks and the optimization goal is to maximize the total number of accomplished tasks while minimizing the total movement distance. (2) For MPFT (more participants, few tasks), each participant is selected to perform one task based on pre-registered working areas in view of privacy, and the optimization objective is to minimize total incentive payments while minimizing the total traveling distance. They adopted the Minimum Cost Maximum Flow (MCMF) model to solve the FPMT problem, and proposed the MT-MCMF and MTPMCMF algorithms to select the optimal participants. Also, they used the multi-objective optimization model to solve the MPFT problem, and proposed the W-ILP and C-ILP algorithms to select the best participants. Ding et al. defined the service node selection problem (SNSP) when selecting proper service nodes in mobile crowdsensing and formulated a multi-objective optimization model (MOOM), which converts SNSP to a multi-objective optimization problem (MOOP) [5]. Duan et al. worked on producing a joint pricing and task allocation system for mobile crowdsensing platforms [6]. They used Walrasian equilibrium to find the optimal solution for maximization problem of pricing and task allocation. They devised a distributed iterative algorithm based dual decomposition which was proven to converge to the optimal solution of social welfare maximization. Zhou et al. proposed an online primal-dual auction framework that connected a series of one-round auctions into an online auction [7]. They formulated an integer linear program (ILP) that characterized the winner determination problem (WDP) for social cost minimization in the online mobile crowdsensing auction. Amin et al. in 2016 looked to solve the task allocation problem in crowdsensing by maximizing the net reward of the platform under the time budget constraints of smart-phone users and different quality requirements of tasks [8]. They proposed a Harmony Search (HS) based meta-heuristic allocation algorithm to solve the task allocation problem. Cheung et al. proposed an Asynchronous and Distributed Task Selection (ADTS) algorithm to help the users plan their task selections on their own [9]. They focused on solving the distributed time-sensitive and location-dependent task selection problem, where users are heterogeneous in their initial locations, movement costs, movement speeds, and reputation levels. Xiong et al. proposed an energy-efficient piggyback crowdsensing task allocation framework called iCrowd to optimize task allocation [10]. The goal of iCrowd is to achieve maximum coverage and minimum incentive payment. Hassani et al. presented a Context-Aware Task Allocation (CATA) approach for task allocation by selecting the best participant set [11]. CATA also provides energy efficiency and privacy. Guo et al. proposed a worker selection framework called ActiveCrowd for multi-task allocation in MCS environments [12]. They studied the workers' intentional and unintentional movements for time-sensitive and delay-tolerant tasks, respectively, and proposed greedy genetic algorithms to solve them. Wang et al. introduced sparse mobile crowdsensing to make use of the spatial and temporal correlation among sensed data to reduce overall sensing cost while preserving the quality of data [13]. It selects a small area for sensing and infers the data of the remaining area using compressive sensing. Zhan et al. investigated the incentive mechanism for platform-centric MCS [14]. They also

analyzed the interaction between the platform and the users using Nash bargaining theory.

Some works that focused on the quality of sensed tasks are [15–18]. Kantarci et al. proposed using social network theory to evaluate the trustworthiness of crowd sensed data, as well as the mobile devices that provide sensing services [15]. They combined centralized reputation-based evaluation with collaborative reputation values based on votes and vote capacities. Wang et al. looked to solve the problem of scheduling different sensing tasks assigned to a smartphone with the objective of minimizing sensing energy consumption while ensuring Quality of SenSing (QoS) [16]. They formulated the Minimum Energy Single sensor task Scheduling (MESS) problem in which each sensing task only requests data from a single sensor and also presented a polynomial-time optimal algorithm for this problem. Further, they formulated the Minimum Energy Multi-sensor task Scheduling (MEMS) problem in which some sensing tasks request multiple sensors to report their measurements simultaneously and also presented an Integer Linear Programming (ILP) formulation and two effective heuristic algorithms to solve it. Liu et al. introduced Quality of Information (QoI) based satisfaction ratio to quantify the degree of how collected sensor data can satisfy QoI requirements [17]. They proposed a participant sampling behavior model to select participants in energy-efficient and QoI aware manner. Pouryazdan et al. introduced a new metric, collaborative reputation scores, to quantify crowdsensed data trustworthiness based on reputation scores [18].

Other works on MCS which do not directly deal with task allocation are as follows. Krontiris et al. performed a study on privacy and trust, incorporating both technical approaches and actual sharing behavior [19]. They highlighted three main challenges with respect to crowdsensing, namely privacy, sharing practices, and fairness which also serve as areas of research in the future. Wu et al. proposed a Dynamic Trust Relationships Aware Data Privacy Protection (DTRPP) mechanism for mobile crowdsensing [20]. They combined key distribution with trust management, by evaluating the trust value of a public key according to both the number of supporters and the trust degree of the public key. Wang et al. proposed ARTSense, a framework to solve the conflicting problem of trust versus privacy in mobile sensing [21]. Their solution consists of a privacy-preserving provenance model, a data trust assessment scheme, and an anonymous reputation management protocol where both positive and negative reputation updates can be enforced.

Whereas there are some existing task allocation schemes [2–18], all of them follow the platform-centric approach to the best of our knowledge. On the other hand, the proposed approach is user-centric. In several applications such as traffic monitoring, noise monitoring, weather monitoring, and so on, users are usually not paid for their participation in the sensing campaign [22]. Hence, task allocation must focus on improving the participation experience of the users which will further encourage better and long-term participation. This study attempts to exploit some motivating factors that will achieve this goal.

3 User-Centric Task Allocation

For the purpose of the study, the following three task allocation schemes have been developed:

- Nearest User Task Allocation (NUTA): Here, each task is assigned to the nearest user.
- Nearest User with Fair Task Allocation (NUFTA): Here, each user is allocated an approximately equal number of tasks while trying to assign a task to the nearest user as far as possible.
- Random User Task allocation (RUTA): Here, each task is assigned randomly to any user.

In each of the allocation schemes, a set of n users and m tasks are considered. A location is associated with each task, which is the location where the task has to be performed. Similarly, we also assume that a user has a location, from which she sets out for carrying out the tasks assigned to her. In Nearest User Task Allocation (NUTA), for each task, the nearest user is selected based on the Euclidean distance between their locations, and the task is assigned to the user. For each user, the minimum cost of performing all its assigned tasks can be found by solving the traveling salesperson problem (TSP).

Algorithm 1: Nearest User Task Allocation (NUTA)

```

1: dist ← 0
2: i ← 0
3: while i < m do
4:   task[i].distance ← 10000
5:   j ← 0
6:   while j < n do
7:     dist ← Euclidean(task[i], user[j])
8:     if task[i].distance > dist then
9:       task[i].distance ← dist
10:      task[i].user assigned ← j
11:    end if
12:    j ← j + 1
13:  end while
14:  i ← i + 1
15: end while

```

Algorithm 2: Nearest User with Task Allocation (NUFTA)

```

1: dist ← 0
2: i ← 0
3: while i < m do
4:   task[i].distance ← 10000
5:   j ← 0
6:   while j < n do
7:     if user[j].numTasks < numFairTasks then
8:       dist ← Euclidean(task[i], user[j])
9:       if task[i].distance > dist then
10:        task[i].distance ← dist
11:        task[i].user assigned ← j
12:      end if
13:    end if
14:    j ← j + 1
15:  end while
16:  i ← i + 1
17: end while

```

Algorithm 1 illustrates the working of NUTA. Each task i is initially assigned a large distance value, say 10,000. This distance is then compared (step 8) with the Euclidean distance between the task i and the user j , denoted by $\text{Euclidean}(\text{task}[i], \text{user}[j])$. If this Euclidean distance so calculated is smaller, the distance value belonging to the task is updated with the smaller value and the corresponding user is also saved. This comparison is done till all users are covered and finally, each task i is assigned to the user j with the shortest Euclidean distance among all the users.

A demerit of NUTA approach is that it may result in the skewness of task allocation, i.e., some users may get allocated a large number of tasks while other users may get assigned very few number of tasks. To mitigate this, NUTA is modified to incorporate a fairness task allocation policy. We call this modified scheme as Nearest User with Fair Task Allocation (NUFTA). Using this fairness task allocation policy, all users are assigned with approximately equal number of tasks. For this, once a user reaches a certain allocation of tasks (denoted by numFairTasks in step 7 of algorithm 2), it is not allowed to take on further tasks. For a task, if its nearest user has the maximum number of tasks already assigned, the next nearest user is then checked if it has exceeded its maximum number of tasks. If this user is eligible, then the task is allocated to it. Otherwise, the algorithm searches for the next nearest user and so on.

This approach is illustrated in algorithm 2. Again, each task i is initially assigned a large distance value, say 10,000. Now a user j is taken into consideration only if its number of tasks (denoted as $\text{user}[j].\text{numTasks}$) is less than the number of fair tasks that can be allocated to each user (denoted by numFairTasks). The number of fair tasks is given by the value m/n . Once it has been made sure that the number of tasks held by the user j does not exceed numFairTasks , we proceed to calculate the Euclidean distance between the task i and the user j , denoted by $\text{Euclidean}(\text{task}[i], \text{user}[j])$. The rest of the algorithm follows the same procedure as algorithm 1.

Lastly, Random User Task Allocation (RUTA) algorithm is also developed wherein each task is assigned randomly to any user. Whereas this algorithm is of no practical importance, it is used as a baseline algorithm for comparison with the other algorithms.

4 Experimental Setup

The implementation has been done in C. The simulation setup consists of the following arrangement:

- Area: 200×200 sq. units
- Setup A: Fixed number of tasks (m) and varying number of users (n)
- Setup B: Fixed number of users (n) and varying number of tasks (m)

For setup A, we first fix the number of tasks and vary the number of users. Then the tasks are allocated to different users using NUTA, NUFTA, and RUTA schemes. For each task allocation scheme, we measure five parameters which are explained below. We make a number of observations by varying the number of users from 5 till 25 (in intervals of 5) while keeping the number of tasks fixed to 100.

For setup B, we vary the number of tasks while keeping the number of users fixed. Then the task allocation is implemented according to NUTA, NUFTA, and RUTA schemes, and we measure the five parameters in each task allocation strategy. Observations are taken by varying the number of tasks in intervals of 20 while keeping the number of users fixed at 10.

The parameters that are measured for the simulation are as follows.

4.1 Overall TSP Cost

The overall TSP cost is the aggregated TSP cost of all the users combined. Once each task has been assigned to a user, we find the TSP cost for all users and add them to get the overall TSP cost of the setup. This is given by:

$$\text{Overall TSP cost} = \sum_{i=1}^n \text{TSP cost of user } i \quad (1)$$

4.2 Standard Deviation of TSP Cost

This metric computes the standard deviation of the TSP cost of all users.

4.3 Load Fairness Index (LFI)

We define the Load Fairness Index as the fairness of the load or tasks that are placed on a user. It measures the equitable distribution of tasks among the users. The higher the LFI value is, the more evenly the tasks are distributed and vice versa. This is represented as follows:

$$\text{LFI} = 1 - 1/n \left\{ \frac{(\sum_{i=1}^n t_{max} - t_i)}{t_{max}} \right\} \quad (2)$$

where t_i represents the number of tasks assigned to user i and t_{max} is the maximum number of tasks allocated to any user.

4.4 Standard Deviation of Load Fairness Index (SDLFI)

This parameter calculates the standard deviation of the LFI obtained above.

4.5 Average Traveling Distance (AvTD)

Average Traveling Distance is the average of the sum distance of all the users to their assigned tasks. The less the AvTD value is, the less a user has to travel to accomplish the allocated tasks. This is denoted as:

$$\text{AvTD} = \frac{1}{n} \left(\sum_{i=1}^n \text{Total distance of user } i \right) \quad (3)$$

5 Results and Discussion

This section gives the simulation results of the three different task allocation schemes NUTA, NUFTA, and RUTA w.r.t. setup A and setup B as discussed in the previous section. Each point in all the plots represents the average result of 30 simulation runs. Figures 1, 2, 3, 4, and 5 show the results for setup A, while Figs. 6, 7, 8, 9, and 10 show the results for setup B.

Figure 1 shows the overall TSP cost of the system across the three task allocation strategies. It can be seen that NUTA has the lowest cost as compared to the other two, and RUTA incurs a high cost as the number of users increases. The reason for this is because the traveling cost increases in RUTA as the tasks are located far

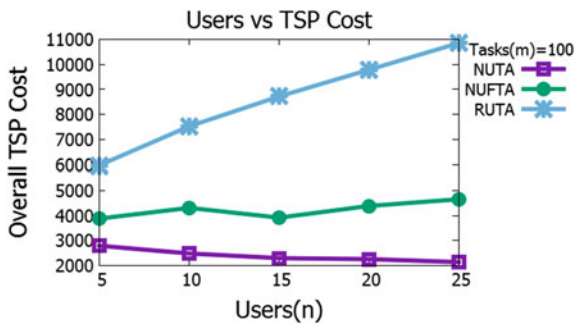
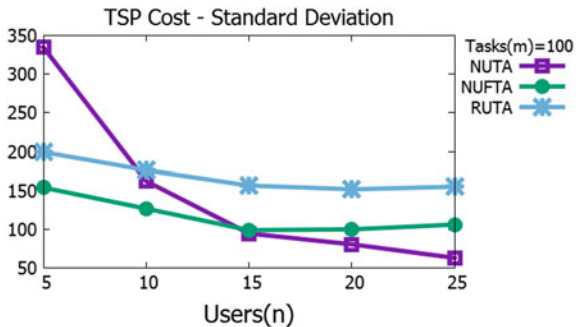
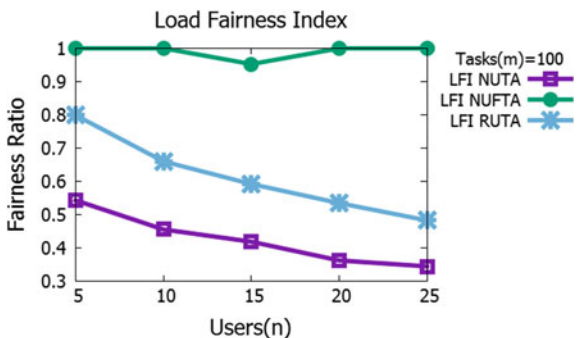
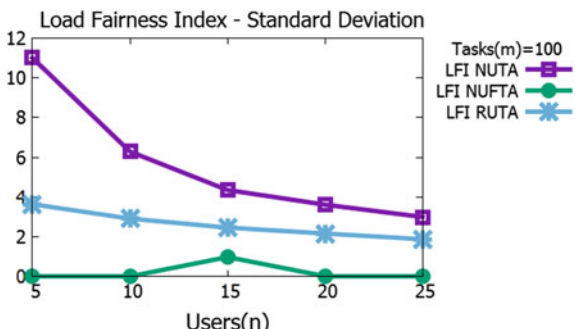
Fig. 1 Overall TSP cost**Fig. 2** Standard deviation of TSP cost**Fig. 3** Load fairness index**Fig. 4** Standard deviation of LFI

Fig. 5 Average traveling distance

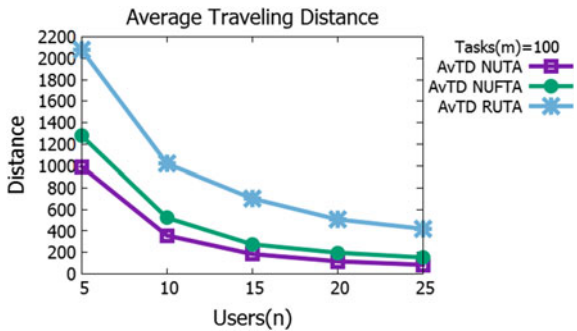


Fig. 6 Overall TSP cost

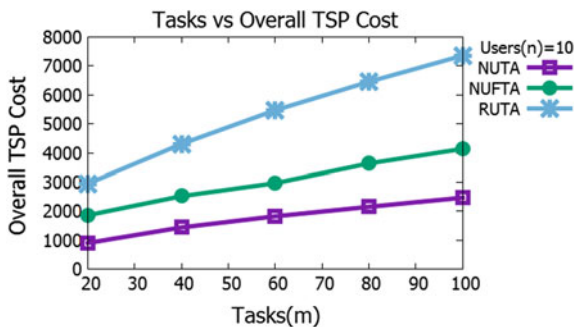


Fig. 7 Standard deviation of TSP cost

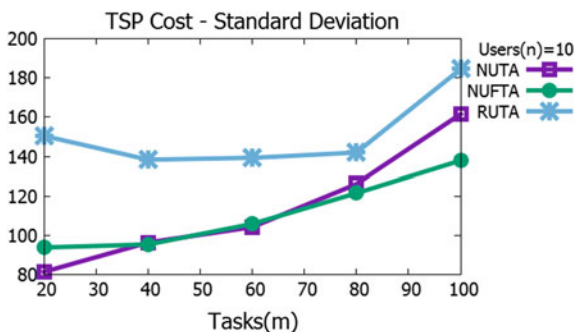


Fig. 8 Load fairness index

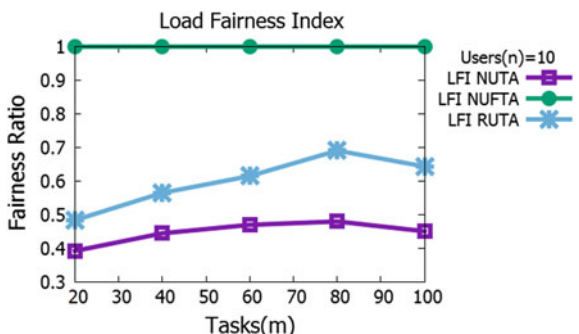


Fig. 9 Standard deviation of LFI

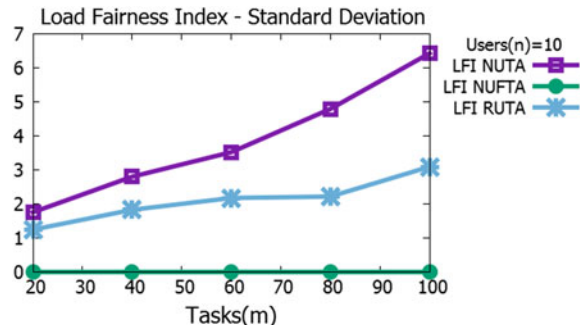
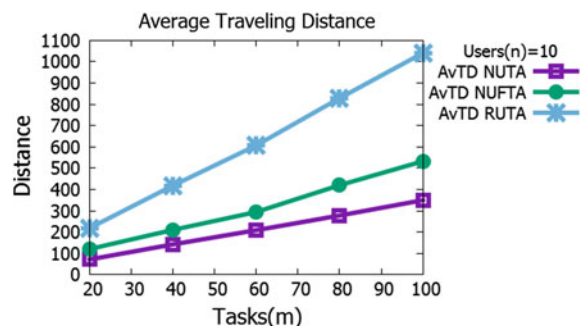


Fig. 10 Average traveling distance



apart from one another. Moreover, under NUFTA, due to the added constraint of allocating an approximately equal number of tasks to each user, a task may not be assigned to the nearest user. Thus, its overall TSP cost is higher than that of NUTA. Figure 2 shows the corresponding standard deviation for the TSP cost. The standard deviation illustrates the amount of variation in the TSP cost of the users. In NUTA, it tends to decrease as the number of users increases, whereas it is more uniform for NUFTA and RUTA across a varying number of users. This means that more uniform distribution of the number of tasks results in a more uniform TSP cost for the users.

The Load Fairness Index graph is shown in Fig. 3. It is seen that NUFTA has the highest fairness among the three schemes, with NUTA giving the lowest fairness. This is because fairness (equal distribution of tasks) is incorporated in the NUFTA algorithm itself, whereas it is not in both NUTA and RUTA. Figure 4 shows the corresponding standard deviation for the Load Fairness Index. As seen in Fig. 2, a more uniform distribution of tasks results in less variation in the LFI.

Finally, the Average Traveling Distance can be seen in Fig. 5. It is observed that NUTA has the least amount of Average Traveling Distance, with RUTA having the highest. Again, this is because of the proximity of the assigned tasks to the corresponding users. However, it can also be seen that NUFTA performs closely with NUTA in this regard.

The corresponding set of results for setup B are shown in Figs. 6, 7, 8, 9, and 10.

To summarize the results, it can be seen that NUTA gives the lowest overall TSP cost and AvTD, which implies that it outperforms other task allocation schemes regarding tasks that are allocated without fairness. However, NUFTA performs quite close to NUTA in terms of AvTD. Also, NUFTA scores highest in LFI, thereby indicating that it provides the highest amount of fairness in task workload among all the three schemes considered.

6 Conclusion

In this study, we have tackled the lack of alternatives to platform-centric task allocation strategies in MCS by proposing a user-centric approach to task allocation. Our proposal includes two task allocation schemes: NUTA and NUFTA. We found that NUTA performs better in situations when tasks are allocated without considering fairness. Additionally, we have seen that NUFTA may be more beneficial than NUTA in situations where the task workload is intended to be spread equally. In future research, we wish to examine the effects of introducing a time-sensitive task allocation approach, where each task has a set time by which it needs to be completed.

Acknowledgements This work is partially supported by DST-SERB, Government of India under grant EEQ/2017/000083.

References

1. Ganti RK, Ye F, Lei H (2011) Mobile crowdsensing: Current state and future challenges. *IEEE Commun Mag* 49(11):32–39
2. He S, Shin DH, Zhang J, Chen J (2014) Toward optimal allocation of location dependent tasks in crowdsensing. In: IEEE INFOCOM 2014–IEEE conference on computer communications. IEEE, pp 745–753
3. Zhang D, Wang L, Xiong H, Guo B (2014) 4W1H in mobile crowd sensing. *IEEE Commun Mag* 52(8):42–48
4. Liu Y, Guo B, Wang Y, Wu W, Yu Z, Zhang D (2016) TaskMe: multi-task allocation in mobile crowd sensing. In: Proceedings of the 2016 ACM international joint conference on pervasive and ubiquitous computing. ACM, pp 403–414
5. Ding S, He X, Wang J (2017) Multiobjective optimization model for service node selection based on a tradeoff between quality of service and resource consumption in mobile crowd sensing. *IEEE Internet Things J* 4(1):258–268
6. Duan X, Zhao C, He S, Cheng P, Zhang J (2016) Distributed algorithms to compute Walrasian equilibrium in mobile crowdsensing. *IEEE Trans Indust Electron* 64(5):4048–4057
7. Zhou R, Li Z, Wu C (2017) A truthful online mechanism for location-aware tasks in mobile crowd sensing. *IEEE Trans Mob Comput* 17(8):1737–1749
8. Amin RG, Li J, Zhu Y (2016) A new harmony search based allocation algorithm for location dependent tasks in crowdsensing. In: 2016 international conference on progress in informatics and computing (PIC). IEEE, pp 581–585

9. Cheung MH, Southwell R, Hou F, Huang J (2015) Distributed time-sensitive task selection in mobile crowdsensing. In: Proceedings of the 16th ACM international symposium on mobile ad hoc networking and computing. ACM, pp 157–166
10. Xiong H, Zhang D, Chen G, Wang L, Gauthier V, Barnes LE (2015) iCrowd: near-optimal task allocation for piggyback crowdsensing. *IEEE Trans Mob Comput* 15(8):2010–2022
11. Hassani A, Haghighi PD, Jayaraman PP (2015) Context-aware recruitment scheme for opportunistic mobile crowdsensing. In: 2015 IEEE 21st international conference on parallel and distributed systems (ICPADS). IEEE, pp 266–273
12. Guo B, Liu Y, Wu W, Yu Z, Han Q (2016) Activecrowd: a framework for optimized multitask allocation in mobile crowdsensing systems. *IEEE Trans Hum-Mach Syst* 47(3):392–403
13. Wang L, Zhang D, Wang Y, Chen C, Han X, M'hamed, A (2016) Sparse mobile crowdsensing: challenges and opportunities. *IEEE Commun Mag* 54(7):161–167
14. Zhan Y, Xia Y, Zhang J (2018) Incentive mechanism in platform-centric mobile crowdsensing: a one-to-many bargaining approach. *Comput Netw* 132:40–52
15. Kantarci B, Glasser PM, Foschini L (2015) Crowdsensing with social network-aided collaborative trust scores. In: 2015 IEEE global communications conference (GLOBECOM). IEEE, pp 1–6
16. Wang J, Tang J, Xue G, Yang D (2017) Towards energy-efficient task scheduling on smartphones in mobile crowd sensing systems. *Comput Netw* 115:100–109
17. Liu CH, Zhang B, Su X, Ma J, Wang W, Leung KK (2015) Energy-aware participant selection for smartphone-enabled mobile crowd sensing. *IEEE Syst J* 11(3):1435–1446
18. Pouryazdan M, Kantarci B, Soyata T, Foschini L, Song H (2017) Quantifying user reputation scores, data trustworthiness, and user incentives in mobile crowd-sensing. *IEEE Access* 5:1382–1397
19. Krontiris I, Langheinrich M, Shilton K (2014) Trust and privacy in mobile experience sharing: future challenges and avenues for research. *IEEE Commun Mag* 52(8):50–55
20. Wu D, Si S, Wu S, Wang R (2017) Dynamic trust relationships aware data privacy protection in mobile crowd-sensing. *IEEE Internet Things J* 5(4):2958–2970
21. Wang XO, Cheng W, Mohapatra P, Abdelzaher T (2013) Enabling reputation and trust in privacy-preserving mobile sensing. *IEEE Trans Mob Comput* 13(12):2777–2790
22. Mousa H, Mokhtar SB, Hasan O, Younes O, Hadhoud M, Brunie L (2015) Trust management and reputation systems in mobile participatory sensing applications: a survey. *Comput Netw* 90:49–73

Fault Classification Based Approximate Testing of Digital VLSI Circuit



Sisir Kumar Jena

Abstract Test data compression scheme plays a major role in testing digital VLSI circuits. Approximate Computing technique is a design technique that consumes less power, area, and provides better performance with a loss in the quality of the result. This paper combines the test compression scheme and the idea of approximation to test digital VLSI circuits. This testing technique is applied to the circuits that are used in error-tolerant applications like image/video processing. The basic idea is to construct a fault set that is more vulnerable to error and generate test patterns for them. After generating the test patterns, a conventional compression technique is applied to those patterns to reduce the pattern count drastically. The experimental result shows that the compression percentage is 70–80% compared to the traditional compression scheme. Finally, the circuit with the injected fault is used in the image processing application, and the result is generous.

Keywords Approximate computing · Approximate testing · VLSI testing · Fault classification · Output masking

1 Introduction

Reducing test application time (TAT) is the primary objective of a tester. Power consumption during testing of digital circuits is another issue that needs to be focused. Test data compression techniques play a major role in reducing test application time. According to [1], test data compression technique is classified into three groups: (i) Code-based scheme (ii) Linear decompression-based scheme and (iii) Broadcast-based scheme. Code-based scheme like Run- Length coding focuses on consecutive 0s or 1s and replaces it with x_0s or x_1s , where x represents the number of 0s or 1s, respectively. Golomb Coding [2], Frequency-Directed Run-Length coding [3], Alternate Run-Length coding [4] are some of the methods that follow Run-Length

S. K. Jena (✉)
DIT University, Dehradun, India
e-mail: sisiriitg@gmail.com

coding scheme. In the linear decompression-based schemes, there is a linear relationship between the uncompressed data and the compressed data which has to be generated by the help of LFSR (Linear Feedback Register) or XOR networks. Some of the decent works based on linear decompression-based scheme were presented in the literature [5, 6]. In broadcast-based scheme, the same values can be broadcasted to multiple scan chains [7, 8].

To tackle the problem of power issue, a subset of researchers is moving towards a different domain of research named as approximate computing. They are trying to propose different design paradigm, which takes the benefit of inherent tolerance property of some application like image processing, digital signal processing (DSP) and machine learning. Their objective is to design hardware that may not produce an accurate result but produce a result, which is acceptable for the specific application. By doing this, they achieve a considerable amount of power reduction as well as enhanced speed and area overhead [9]. Enhancing this idea, we define a new term approximate test which may be well as test time and test cost. The basic idea is we will not consider all fault to be tested rather we will test only those faults that affect the output most. In another word, we will leave some of the faults untested. By doing this, we may get some errors in the output, which we consider acceptable. The objective of our approach is to reduce test power consumption and test time drastically.

Let us consider a scenario where a semiconductor manufacturing company specifically design and fabricate a huge quantity of adder circuit that is used in DSP applications. We know that DSP applications such as image processing can tolerate some amount of errors. Assume that the fabricated adder circuit has a fault f . Due to the existence of fault f , the circuit does not produce accurate result rather it produces a result, which can be acceptable for image processing applications. If the traditional testing process is applied to test these circuits, then the entire manufactured circuits are considered as bad chip and discarded. By using an approximate testing approach, these bad chips can be made usable. Not only the chips are usable but also it takes very less time and power to test these circuits as compared to the traditional approach of testing.

The contribution of this paper includes the following:

- Introduce a new concept known as Approximate Testing which can be defined as the process of testing only those faults which are critical in nature and exclude the testing of faults which do not affect the normal working of the circuit.
- In the process of approximate testing, we provide an efficient methodology that can classify the faults into two groups: acceptable group and unacceptable group.
- Our process drastically reduces the most critical issues associated with testing that includes test power, test time, and test data volume. This is achieved by the test data compression technique applied to all the faults included in the unacceptable group.

The remaining section of the paper is organized as follows. Section 2 tries to give credit to some previous works that help in shaping our idea. Section 3 introduces the proposed approach in detail. Section 4 describes the details of fault classification

and automatic test pattern generation. Section 5 explains the test compression step and Sect. 6 shows the experimental result and finally Sect. 7 conclude the approach.

2 Motivation and Previous Works

Many research publications have focused on identifying those areas of a circuit which can be approximated. In [10], a gate-level pruning technique is used to design an approximated adder. Depending on the application's requirement the designer can choose how many gates to prune. The more gate you prune the more error you get in the output. In [11], presented an 8×8 multiplier using 4×4 multipliers and they called it a recursive multiplier. This multiplier was used in image processing application for sharpening images. All these approximation techniques are applied in designing a circuit. The same concept can be employed in testing a conventional circuit so that test time can be reduced. Consider an 8-bit Ripple carry Adder circuit shown in Fig. 1. According to approximate adder circuit design techniques, the errors present in LSB bits does not affect the result most. For an example, we want to add two numbers $a = 01110011$ and $b = 01100111$. In Fig. 1, Case-0 shows the actual output produced. Suppose the LSB bit produces an error due to some fault present in the 1st FA (Full Adder). Three different case arises. Case-1: For our example data $a = 01110011$ and $b = 01100111$, $F_0 = 1$ and carry = 1. Calculated error_significance = 1. Case-2: $F_0 = 1$ and carry = 0. Calculated error_significance = 1. Case-3: $F_0 = 0$ and carry = 0. Calculated error_significance = 2. The formal definition of error-significance is described in Sect. 3. From this example, we found that error in low order bit of an adder circuit does not affect the output. Hence, the low order circuit (FA1) does not require to be tested. Because this adder circuit will be used in error-tolerant applications like image processing, some amount of error in the circuit will be tolerated. So, all the fault associated with FA1 can be ignored and we don't require test patterns to test those faults. All these faults can be treated as acceptable faults. In the next section, we will propose our approach of testing digital circuits.

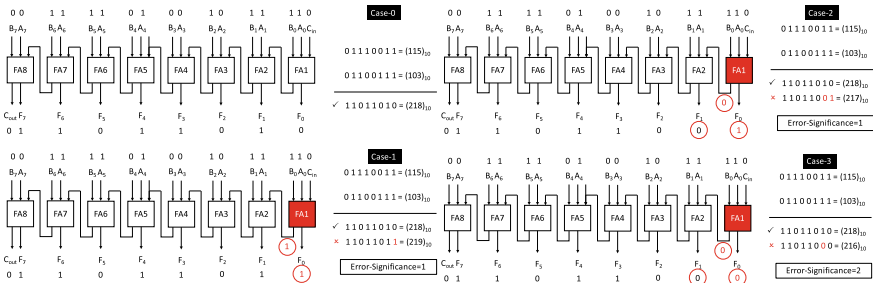


Fig. 1 Motivating example

3 Proposed Testing Methodology

To implement an approximate testing approach, we need to classify the faults. In [12] author introduced three measures (i) error-rate (ii) error-accumulation and (iii) error-significance. These measures are well known as RAS measures. Error-rate: The percentage of test vectors for which the output deviates from the corresponding error-free value, or a given circuit C , let we apply N test vectors and out of which, k test vector produces error, the error-rate for this circuit C :

$$\text{error-rate}(C) = \frac{k}{N \times 100}$$

Error-accumulation: It is defined as the change in error-rate over time. Error-significance: The absolute difference between the error-free output and erroneous output. For a given circuit C , let us apply a test pattern p , which produces output z . Assume that the error-free output for the pattern p needs to be z_p . Then the error-significance of fault f for which the pattern p is applied:

$$\text{error-significance} = |z_p - z|$$

Error-significance is generally represented with a numeric value. In this paper, we use error-significance as the measure for the classification of faults. In our approach, the faults are classified into two groups. (i) The first group (acceptable group) consider the faults whose error-significance should not exceed the threshold value provided by the application. Here threshold value is application-specific. For example, let the circuit C is an 8-bit adder and we fix the threshold as ± 3 . Assume that there is a fault f exist in the circuit and for any pair of the input vector, if the output produces an addition result within these threshold ranges then this fault f is included in an acceptable group. (ii) The second group (unacceptable group) considers the faults, which are critical in nature, i.e., due to the existence of these faults the circuit may behave abruptly. In our approach, we need to test these faults only. A fault classification method is presented in [13]. The objective of this paper [13] is to improve the yield. It is shown that the conventional ATPG which was used to generate test sets for the detection of unacceptable fault can also detect some acceptable faults. This is known as over-detection problem. So, the consequence is degradation in yield improvement. To deal with the over-detection problem some literature has been proposed [14–16]. Initially, we will generate the test set for unacceptable group, and then using a test data compression scheme, we will compress the test data so that it takes less amount of memory in our ATE. Hence, our approach provides a drastic reduction in test data volume.

The overall procedure of our proposed method is shown in Fig. 2. Initially an error-significance is specified by the designer depending upon the application where these circuits are used. Error-significance is calculated based on a threshold value specific to an application. For example, if our design is an adder that is to be used in

Fig. 2 Proposed testing methodology

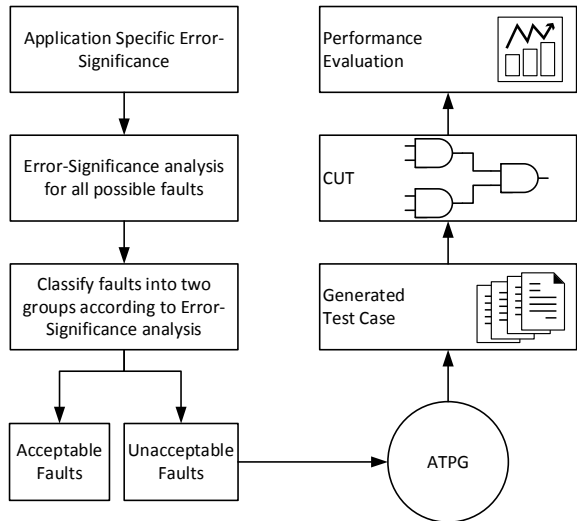


image processing application then threshold value may be ranged between 1 and 5. Generally, each color pixel of an image takes the value from 000 to 255, and any value between ± 5 does not change the perceptual view of a human eye. The next step of our process is to analyze error-significance for all possible faults. Depending on this analysis, fault classification is made. In the presence of a fault if the error-significance lies between the specified threshold value, then that fault is treated as a member of an acceptable set. The remaining faults are grouped into an unacceptable fault set. Our approach does not generate test patterns for acceptable faults. Unacceptable faults need to be tested properly. ATPG process is only applied to unacceptable faults. After generating the test set, it goes through a test data compression technique to further reduce the size of the test set. This step ensures a reduction in test application time. The resulting test set is then applied to CUT (circuit under test) and the performance is evaluated to see the performance gain in terms of test application time.

4 Fault Classification and ATPG

4.1 Fault Classification

We consider stuck-at-fault model for fault classification. Initially, we define a application-specific threshold value (T_h). For our case, it will be $(T_h) = 5$, because our circuit will be used for image processing applications. We take a 16-bit ripple carry adder for our purpose and intentionally induce single stuck-at-fault at each net. Our assumption here is either our circuit is fault free or it contains only a single stuck-at-fault. For each stuck-at-fault, the circuit is tested by some random inputs,

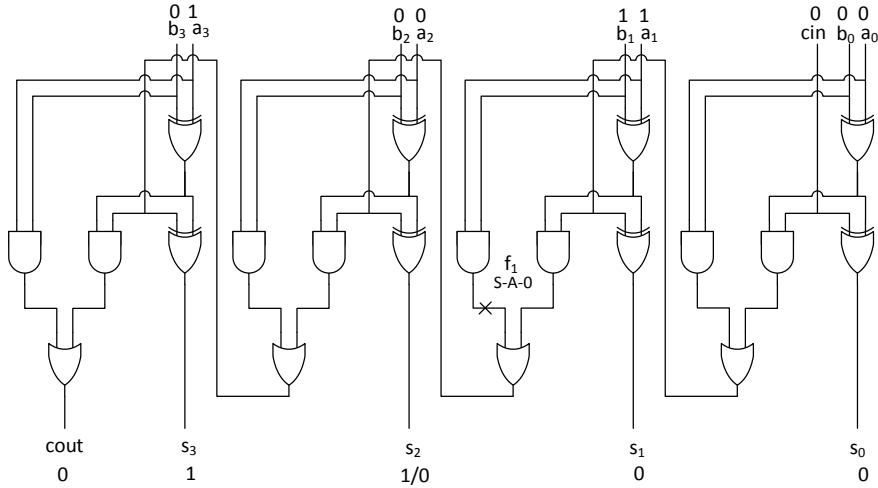


Fig. 3 4-bit Ripple carry adder

and error-significance is calculated. Consider a 4-bit ripple carry adder circuit (RCA) shown in Fig. 3 with fault set denoted by F . The inputs a_i and b_i are the binary numbers with carry-in (c_{in}).

The outputs s_i and carry-out (c_{out}) is the result of the adder which is defined as $R = c_{out} \times 2^i + s_i - 1 \times 2^{i-1} + s_{i-2} \times 2^{i-2} + \dots + s_0 \times 2^0$. Here i represents total number of bits in the adder. Similarly, the faulty circuit of the given circuit is given as RCA_f and the result of the fault circuit is denoted as R_f . The error-significance (E_s) is calculated as, $E_s = |R_f - R|$. For a given input $\{a_3, a_2, a_1, a_0\} = 1010$, $\{b_3, b_2, b_1, b_0\} = 0010$, $c_{in} = 0$, the output produced by the faulty circuit (shown in Fig. 3) is $\{c_{out}, s_3, s_2, s_1, s_0\} = 01000$ instead of 01100 . Hence $R = 12$ and $R_f = 8$. Thus, error-significance $E_s = |8 - 12| = 4$. As per the previously mentioned threshold value, this fault is an acceptable fault. This is just a simple test input to describe acceptability of a fault. As mentioned previously, we took a 16-bit RCA. In total, we tested 480 faults without considering fault collapsing for our circuit. 50 random number pairs are given as input in the presence of a single fault in the circuit and the error-significance is calculated.

4.2 ATPG

In this section, we will discuss the test pattern generation procedure. The objective is to target the predefined unacceptable faults and discard the acceptable fault. A deterministic test pattern generation scheme is used in our case because the random pattern may or may not detect all unacceptable faults. As we have already mentioned the pattern that detects an unacceptable fault may also detect an acceptable fault. This

is called the over-detection problem. In our case, the over-detection problem though not ignored but we did not guarantee that our approach is fully solved the over-detection problem. In [16], both deterministic and random test pattern generation is considered, and over-detection problem is fully solved to improve yield. In this paper our objective to reduce test pattern count as much as possible. We use the following notations for our discussion and the overall procedure is described in Fig. 4.

- UFS and AFS: The set of unacceptable and acceptable fault sets, respectively.

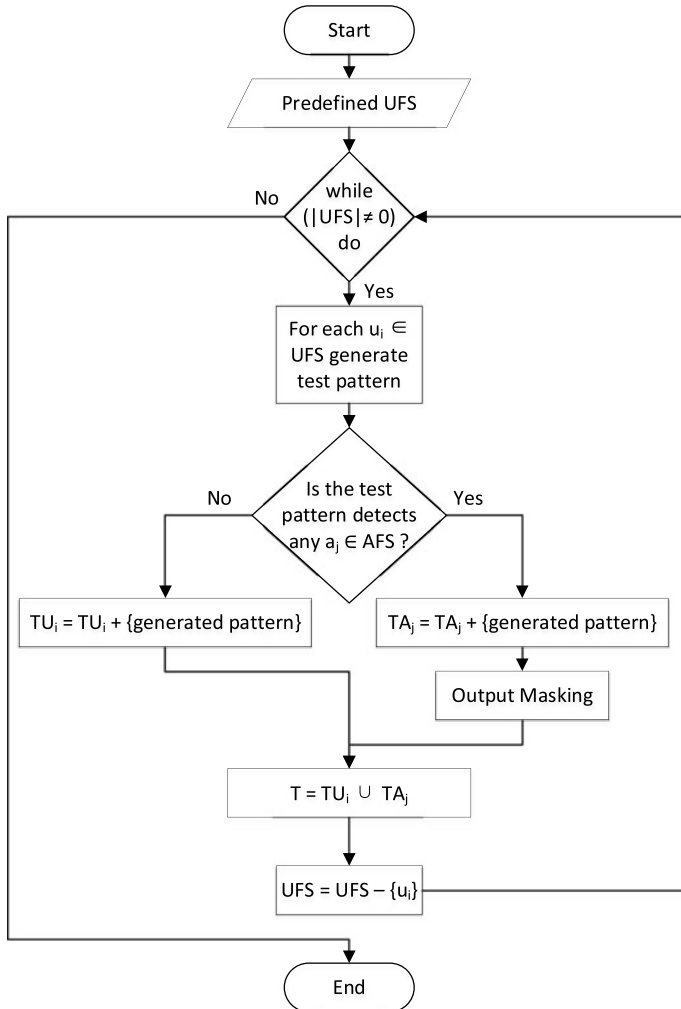


Fig. 4 Test set generation procedure

- u_i and a_j : Represents an element (s) of UFS and AFS, respectively. Where i and j vary from 1 to n and 1 to m , respectively.
- TU_i : Represents the set of a test pattern that only detects u_i but not a_i .
- TA_j : Represents the set of test patterns that detects at least one u_i and at least one a_i .
- T : Complete list of test patterns. $T = \text{TU}_i \bigcup \text{TA}_j$

Initially, we have an unacceptable fault list—UFS. Our loop will continue until we generate test patterns for all $u_i \in \text{UFS}$. Two possibility arises. (i) The pattern can detect only the unacceptable fault u_i without detecting any a_j . (ii) The pattern may detect at least one u_i and at least one a_j . In the first case, we directly add the test pattern to the test set TU_i . The second case is slightly handling the over-detection problem. For this case, we add the test pattern to the test set TA_j and apply an output masking technique presented in [13] to handle the over-detection. According to [13], when a test pattern generated to detect an unacceptable fault still detects an acceptable fault we use the output masking technique. Output masking means not observing a particular output line.

Output Masking Techniques—In general, a single fault can be detected by multiple test patterns and it is propagated through more than one output line. Hence, we can observe only one erroneous output for one particular test pattern and mask all other erroneous output lines which need not be observed and counted as redundant. This way we can avoid detecting an acceptable fault.

Example: An example that explains the output masking technique is presented in Table 1. Consider a CUT with two output lines O_1 and O_2 . In the first case, an unacceptable fault u_1 is targeted and as shown in the table, there are three patterns T_1 , T_2 and T_3 which can detect this targeted fault at the different observable points. By applying the test pattern T_1 we can observe u_1 and a_1 at output pin O_1 . Similarly, by applying the test pattern T_2 we can observe a_1 and a_2 at output pin O_1 , also we can observe u_1 and a_3 at output pin O_2 . Finally, by applying the test pattern T_3 we can observe u_1 at O_1 and a_2 at O_2 . All these three patterns are able to detect the fault u_1 but they also detect some acceptable fault. By analyzing all these patterns, we choose T_3 for detection of u_1 by masking O_2 , so that acceptable fault a_2 will not be observed. In the second case, u_2 is targeted and two test patterns T_4 and T_5 can detect u_2 along with some unacceptable fault. In this case, the masking is difficult,

Table 1 Output masking

Targeted faults	Test patterns	Observed OP		Remark
		O_1	O_2	
u_1	T_1	u_1, a_1	a_3, a_2	Choose T_3 and mask a_2
	T_2	a_1, a_2	u_1, a_3	
	T_3	u_1	a_2	
u_2	T_4	u_2, a_1	a_3	Difficult to mask. Unacceptable fault detected
	T_5	a_1	u_2, a_2	

hence we can mask any of the output pins which detect more number of acceptable faults.

After output masking step, finally, all the test patterns will be merged to form set T , which is nothing but the complete list of test patterns that detect all unacceptable faults but a very few acceptable faults.

5 Test Data Compression

This section basically describes the technique to compress the test set T obtained in Sect. 4. We have used the Huffman coding technique described in [17] to compress T . A Huffman code [18] is a statistical coding technique obtained by constructing a Huffman tree. For each leaf, a codeword is constructed by traversing from root to the corresponding leaf. A reader can refer [17] to know more about the construction of a Huffman tree.

6 Experimental Evaluation

Our experimental result is two-fold. With the first case, we show the benefits in terms of the compression ratio. For this purpose, we use iscas 85 benchmark circuits. First, we generate test vectors for the circuits using FastScan Tool by Mentor Graphics. Then we redesign those circuits using Verilog code and remove the gates that are not affecting/less affecting the final result. Again we generate the test vectors for the modified circuit and finally apply Huffman test compression code to the generated test vectors. The result is shown in Table 2. Data compression percentage (CP) will be calculated using the following equation:

$$CP = \frac{\text{Original Bits} - \text{Compressed Bits}}{\text{Original Bits}} \times 100$$

For the second case, we took a 16-bit ripple carry adder (RCA) and apply that circuit for image processing application, particularly for image smoothing.

Table 2 Experimental result ISCAS 85

Circuit	# Gate	# Test pattern	CP (Huffman)	CP (proposed)
C432	160	27	46.58	48.34
C499	202	52	69.47	71.84
C1355	546	84	71.49	76.21
C1908	880	106	51.83	65.23
C3540	1669	63	66.07	66.74



Fig. 5 Experimental result. **a** Original image with added noise. **b** Smoothen with accurate adder. **c** Fault injection-1st FA. **d** Fault injection-2nd FA. **e** Fault injection-5th FA. **f** Fault injection-8th FA

Smoothing is used to reduce the noise present in an image. We took a gate-level netlist of 16-bit RCA. We start by injecting fault from LSB bits and used that circuit to smooth an image. The entire image processing application will be implemented in Matlab R2018a. The result of the simulation is shown in Fig. 5. There are five gates (two XOR gate, two AND gate, and one OR gate) that drives the first LSB bit and having 16 fault sites where we can inject the fault. The second LSB (from right) drives by second FA (full adder). Here we consider the stuck-at fault model. As you can see when more and more fault injected in the circuit and propagating from left to right the image quality it gets distorted. Figure 5b, shows the image processed with the original accurate adder, and as we proceed from Fig. 5c–f, the image quality degraded. One thing we can notice in Fig. 5c that, when we inject fault in the LSB bit the image quality is very much similar to the original adder's image.

7 Conclusion

A new era of testing direction is presented in this paper which uses the concept of approximate computing. Though the proposed idea does not generate test patterns for the entire circuits but can able test a conventional circuit with very fewer test patterns which is objective a test engineer with a constraint that the circuit may produce some amount of when used in applications. Hence the proposed approach is only applicable to test those circuit which is to be used in error-tolerant applications.

References

1. Li X, Lee K-J, Touba NA, Chapter 6—test compression. In: Wang L-T, Wu C-W, Wen X (eds), VLSI test principles and architectures. Morgan Kaufmann, pp 341–396
2. Chandra A, Chakrabarty K (2001) System-on-a-chip test-data compression and decompres-sion architectures based on Golomb codes. IEEE Trans Comput Aided Des Integr Circ Syst 20(3):355–368
3. Chandra A, Chakrabarty K (2001) Frequency-directed run-length (FDR) codes with application to system-on-a-chip test data compression. In: Proceedings 19th IEEE VLSI test symposium. VTS 2001, Marina Del Rey, pp 42–47

4. Ye B, Zhao Q, Zhou D, Wang X, Luo M (2011) Test data compression using alternating variable run-length code. *Integr VLSI J* 44(2):103–110
5. Bayraktaroglu I, Orailoglu A (2003) Concurrent application of compaction and compression for test time and data volume reduction in scan designs. *IEEE Trans Comput* 52(11):1480–1489
6. Mrugalski G, Rajska J, Tyszer J (2004) Ring generators: new devices for embedded test applications. *IEEE Trans Comput-Aided Des* 23(9):1306–1320
7. Hamzaoglu I, Patel JH (1999) Reducing test application time for full scan embedded cores. In: Proceedings of international symposium on fault-tolerant computing, pp 260–267
8. Han Y, Hu Y, Li X, Li H, Chandra A, Wen X (2005) Wrapper scan chains design for rapid and low power testing of embedded cores. *IEICE Trans Inform Syst* E88D(9):2126–2134
9. Xu Q, Mytkowicz T, Kim NS (2016) Approximate computing: a survey. *IEEE Des Test* 33(1):8–22
10. Schlachter J, Camus V, Palem KV, Enz C (2017) Design and applications of approximate circuits by gate-level pruning. In: IEEE transactions on very large scale integration (VLSI) systems, 25(5), pp 1694–1702
11. Maheshwari N, Yang Z, Han J, Lombardi F (2015) A design approach for compressor based approximate multipliers. In: 2015 28th international conference on VLSI design, Bangalore, pp 209–214
12. Breuer MA, Gupta SK, Mak TM (2004) Defect and error tolerance in the presence of massive numbers of defects. In: IEEE design and test of computers, vol 21(3), pp 216–227
13. Hsieh T-Y, Lee K-J, Breuer MA (2007) Reduction of detected acceptable faults for yield improvement via error-tolerance. In: Proceedings of design automation test Europe, pp 1599–1604
14. Shahidi S, Gupta SK (2007) ERTG: a test generator for error-rate testing. In: Proceedings of international test conference, p 110
15. Shahidi S, Gupta SK (2008) Multi-vector tests: a path to perfect error rate testing. In: Proceedings of design automation test Europe, pp 1178–1183
16. Lee KJ, Hsieh TY, Breuer MA (2012) Efficient overdetection elimination of acceptable faults for yield improvement. *IEEE Trans Comput-Aided Des Integr Circ Syst* 31(5):754–764
17. Kavousianos X, Kalligeros E, Nikolos D (2007) Optimal selective Huffman coding for test-data compression. *IEEE Trans Comput* 56(8):1146–1152
18. Huffman DA (1952) A method for the construction of minimum redundancy codes. In: Proceedings of IRE, vol 40, pp 1098–1101

Image Processing Using Case-Based Reasoning: A Survey



Rahul Barman, Saroj Kr. Biswas, Sunita Sarkar, Biswajit Purkayastha, and Badal Soni

Abstract Case-based reasoning (CBR) is a technique which solves a problem using past experiences, where a case base stores these past experiences called cases. CBR is used to solve different kinds of problems where past information is available. With the advent of modern and efficient digital tools, huge amount of image data is being captured. Hence, huge amount of image data is stored in different application fields. Different organizations use CBR to find valuable and useful information from this image data. Therefore, in the recent times, there is a huge use of CBR in image data applications. This paper discusses the framework of CBR in image processing and reports different application models in different applications. From literature, it is observed that the performance of CBR in image processing is significant and acceptable.

Keywords CBR · Image processing · Artificial intelligence · Machine learning

1 Introduction

Digital image processing (DIP) is a method through which some useful information is retrieved from an image. DIP is used in different fields like space image

R. Barman (✉) · S. Kr. Biswas · B. Purkayastha · B. Soni

Department of Computer Science and Engineering, National Institute of Technology Silchar, Silchar, Assam 788010, India

e-mail: rahulbarman31.10.1994@gmail.com

S. Kr. Biswas

e-mail: bissarojkum@yahoo.com

B. Purkayastha

e-mail: biswajitpurkayastha1960@gmail.com

B. Soni

e-mail: soni.badal88@gmail.com

S. Sarkar

Department of Computer Science, Assam University, Silchar, Assam, India

e-mail: sunitasarkar@rediffmail.com

processing, computerized photography, medical/biological image processing [1], fingerprint recognition [2], face recognition [3], remote sensing [4], etc. Preprocessing, edge detection, segmentation, feature extraction, etc., are the main DIP techniques used to retrieve information from a digital image.

In the artificial intelligence field, case-based reasoning (CBR) is a technique which uses the past experiences and solves a new problem. CBR has been widely applied to different fields such as medical diagnostics, industrial manufacturing and question and answer systems. The working principle of CBR is very similar to the human brain, which compares the previous problems with the new problem to propose a solution to the new problem. CBR overcomes the problems of rule-based systems and inherits advantages from knowledge-based system. Besides CBR can learn by acquiring new cases through use, CBR does not need to create any rule to solve a problem and solution to a new problem can also be given through precedent. Therefore, since decades, there is trend of CBR in image processing to solve some image processing problems. This research article focuses on different applications of image processing using different CBR techniques. This paper also attempts to describe how CBR can be fitted in solving image processing problems.

2 Case-Based Reasoning

CBR maintains a case base where each case consists of problem details and the solution for the problem. Whenever a new problem arises, it takes the help of old problems and tries to solve it by its previous experiences. Hence, it is also called an experience-based problem. There are four stages of CBR: retrieve, reuse, revise and retain. In the retrieve stage, the most similar cases are retrieved from the case base by the system. In the reuse stage, the system uses the solution of the most similar case to solve the new case. In the revise stage, the applicability of the new proposed solution is tested by the administrator. And in the retain stage, the new proposed solution and problem are updated as a case for the future purpose. The working principle of CBR is schematically described in Fig. 1.

3 Framework of Image Processing Using Case-Based Reasoning

Nowadays, images are used in various fields due to the availability of images in abundance. Moreover, the human brain can recognize a familiar object only in 100 ms by looking at an image as image contains huge information about an event. So, image data are generally preferred to do certain jobs. Some features are extracted from an image by feature extraction technique and stored in the case base along with its known class. The combination of extracted features and the known class is called

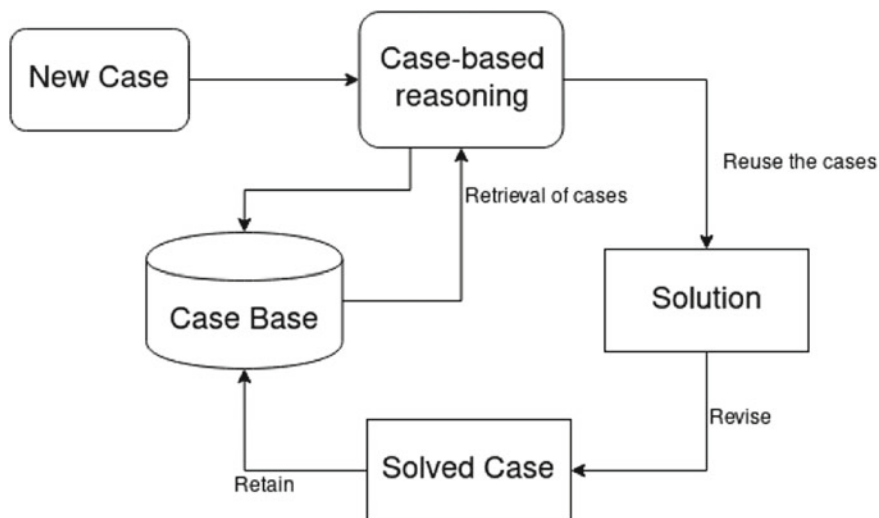


Fig. 1 Schematic representation of CBR method

a ‘case’ in the case-based reasoning technique. When the system receives a new image, it extracts the same features from the new image and compares them with the stored features. The system retrieves the most similar cases from the case base after comparing the features. The retrieved cases are reused to predict the class of the new image. If the new case is not present in the case base, then the features and the predicted class of the image are stored in the case base for future purpose. The framework of image processing using CBR is shown in Fig. 2.

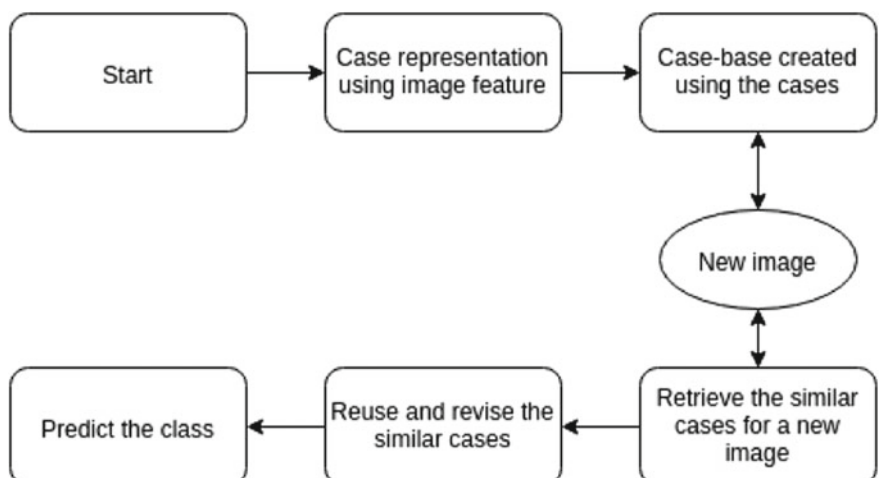


Fig. 2 Framework of image processing using CBR

4 Current Status of Image Processing Model Using CBR

Nowadays, image data are highly used in medical and industrial applications. CBR is one of the popular problem-solving techniques. CBR methodology allows different powerful ways to extract rich information from an image. Therefore, there is a trend of image processing using CBR in different application domains.

Surjandy et al. [5] have stated a solution for traffic congestion problem using CBR, where congestion data are taken from CCTV cameras. The pictures from the CCTV camera are converted into binary patterns using DECODE [17]. Each pattern from DECODE is identified as low, medium and high. The case base contains the binary patterns as the individual cases, where each case describes a street condition. The conditions are described as either empty (low), smooth (medium) or solid (high). Further pictures captured by the CCTV cameras are treated as a new case. The picture is converted into a binary pattern and compared with the present patterns in the case base. The system will give a traffic light solution, according to the comparison performed by DIFFNOW [18]. This proposed system shows that a solution to traffic congestion problem is obtainable from CCTV footage by use of CBR. The drawback being the image captured by the camera directly affects the performance of the system, and hence, can deteriorate from bad weather conditions and lowlight conditions.

Hongru et al. [6] have discussed a case representation method based on image information. Color of an image is not a very important feature but it is one of the perception characteristics. Although scaling, rotation and translation cannot affect the color characteristic of an image. Hence, this paper uses color as a feature of the image, and the case base is created by that feature. An image is represented either in RGB, i.e., red, green and blue color space or HSV, i.e., hue, saturation and value color space. HSV color model is very similar to the human vision where H (hue) represents different colors, S (saturation) represents the depth of color, and V (value) represents the degree of color shading. Therefore, the model converts the image to HSV color space from RGB color space, where the range of H is in $[0, 360]$, S is in $[0, 1]$, and V is in $[0, 1]$. Due to the range of H , S and V , the color dimensional histogram is also a large number. In CBR, if the retrieval procedure is done by the feature calculation, then the computation will be very large. Hence, using histogram, this calculation amount is much smaller. So qualify the HSV space to reduce the feature factor dimension before calculating the feature quantity. Hence, the color histogram of HSV space is used for describing the image characteristics, which is used as the attribute of case description, including the R , G , B , H , S and V of the pixel in RGB and HSV color space, respectively. For example, if we want to determine the fire pixel in a forest image, the R value should be greater than the G value and also there is a certain value for the H , S and V . If the conditions are matched, then we can say that the pixel is a fire pixel.

Chen et al. [7] have presented a paper on synthetic-aperture radar (SAR) image classification using CBR. There are mainly four steps used for SAR image classification, including image preprocessing, construction of case library, case-based classification and post-classification. In image preprocessing step, speckle removing and geometric correction are included. Frost adaptive filter [8] is used to remove the speckle which is harmful for image analysis, from the SAR image. During the case library construction, image attributes are used. Sensor platform, backscatters, entropy, polarization, SAR imaging time and variance of SAR systems are the attributes. The last three attributes are used for the case filtering that is when a new SAR image arrives for the classification, the sensor platform, polarization and imaging time of the new image are matched with the cases in the library, then the most similar cases are chosen for the classification. For case-based matching, similarity is measured by using some information which are variance, entropy and backscatters. Some isolated spots are present in the initial images which are already classified. An object-oriented post-classification method [9] is used to remove that. Thus, in this article, it is shown that the CBR method for SAR image classification is very promising where the overall accuracy of that experiment is 76.843%.

Khanum [10] has discussed about facial expression recognition system using CBR. Human emotion is a thing that machine is unable to identify correctly. Hence, if machine can understand the human facial expression, then it is possible to the machine for understanding human emotion. In this article, CBR is used to understand the human emotion by the facial expression, where eye, chin, cheeks, eyebrows, lips, teeth, nose and forehead are used to express mainly six emotions of human. The emotions which are detected in this paper are fear, joy, disgust, sadness, anger and surprise. Facial expression intensity is one of the main features to classify the emotion, and one of the major problems is to understand this feature. Humans produce different intensity to express variety of expressions. Hence, for the same expression of face, it should express different emotion if the intensity level is different. The eight facial elements are extracted from the facial image, where some range is there for different elements. The features from facial image are extracted by the image processing techniques. And that features are taken by the system as input and give output of expression state. A case consists of eight elements of the face with a value ranging from V_1 to V_n . There is also an efficiency index (e) and a frequency of past occurrence (f) present in a case which helps to retrieve cases from the case base. For the similarity measurement, three factors considered are frequency of occurrence, efficiency index and difference between the retrieved case and current case. The method is compared with the hidden Markov models (HMM), [11] and it is shown that the performance of CBR is better than the HMM method. The overall results for different facial expression are 92%.

Hijazi et al. [12] have presented an article where an approach based on histogram is used for classifying retinal images and CBR method is used for representing the histogram of retinal images to identify the age-related macular degeneration (AMD), where CBR has two stages. A histogram is created by the green and saturation values with blood vessels removed, which is present in the first case base and second case base consists of same histogram with optic disk (OD) removed. For a new retinal image, a dynamic time warping (DTW) technique is used for similarity matching in the first case base, for the remaining that cannot be classified in the first case base is repeated with second case base. In this paper, it is shown that a two-pass CBR approach is giving a better result than one pass CBR approach. However, two-pass CBR fails on a small dataset as the OD removal is not always correct, and it misclassifies the image. 82% sensitivity is the best average performance by the model.

Lee et al. [13] used the function of mask algorithm (Fmask) and case-based reasoning to improve the simple image simulation algorithm. Fmask is used to detect clouds, shadow of clouds and water areas. And CBR is used to select appropriate reference imagery to compare with the target imagery, selected by image simulation. There are four steps of improved simulation algorithm which are preprocessing, solar radiation modeling, selection of reference imagery and top-of-reflection simulation. Third step is done by using the CBR method which predicts the result of new case considering the result of past cases. The improved simulation algorithm creates a better result with 95.59% accuracy.

Abdoor et al. [14] have stated a solution for dish recommendation. It is seen that physical characteristics of a food can give a deep perception about the dish tastes. Hence, from the dish image, the aesthetic score is calculated by using image processing techniques. The aesthetic score is the weighted sum of three aesthetic attributes which are visual appeal score, colorfulness score and color spreadness score. After calculating the aesthetic score and taking some more attributes of the dish like flavor, texture, cooking style, price, etc., the system creates a case base using that features. The recommended system learns the food preferences of different users. The CBR system will give suggestions for food according to the preferences of individual users.

Waqr et al. [15] have discussed suggesting some wearable item for a person to look attractive and well-dressed using case-based reasoning technique. The system takes a photo of the user with a camera and extracts some facial features like skin tone, eye color, face shape, etc., with the help of image processing techniques. Beside this feature, the system also takes some more information about the user like height, weight, etc., that will help in reasoning. After collecting all the features from the user, the system finds the best matching case from the case base. All the cases stored in the case base are generated through some experts and also some old cases.

Raman et al. [16] have presented an article where mammogram images are used for detection tumor from it that provides support for the clinical decision to perform a biopsy of the breast. There are four stages of the process which are—first, mammograms are digitized and images are enhanced; second, suspicious areas are detected and localized; third, shape-based features are extracted in the mammogram which

is already digitized; and fourth, using case-based reasoning techniques features are analyzed. Here the region growing method is used to detect the mammographic mass. After the segmentation of mass, some useful features are taken for the decision making. Using the features which are extracted, obtain a matrix which has real values. This matrix is used in case-based reasoning to analyze the mammogram mass. The model generates results with 69.45% sensitivity and 69.2% specificity.

5 Summary

As a whole, it is shown that CBR is very useful in image processing techniques. Many of the work are done by the CBR, and in future many more work can be done by the CBR method. The summary of the all papers is given below in Table 1.

6 Conclusion

This paper discussed the image processing techniques using case-based reasoning method and showed fitness of CBR in image processing. It is observed from the literature that CBR performance in image processing is significant and acceptable. Different application domains of image processing using CBR are reported. In future, CBR can be used differently in many fields to improve the performance of systems. Digital image processing is also a very useful technique nowadays as the availability of images is in a huge amount. Hence, combination of CBR and image processing technique can make a promising system.

Table 1 Summary of survey papers in chronological order

SL No	Name of the paper and author	Year	Findings
1.	Khanum: [10] facial expression recognition system using case-based reasoning	2006	CBR is used to understand the human emotion by facial expression where eye, chin, cheeks, eyebrows, lips, teeth, nose and forehead are used to express mainly six emotions of human
2.	Chen et al. [7]: SAR image classification using case-based reasoning	2007	SAR image is classified using CBR where adaptive filter is used to remove speckle
3.	Raman et al. [16]: digital mammogram tumor preprocessing segmentation feature extraction and classification	2009	Region growing method is used to detect the mammographic mass, after that some useful features are taken for decision making and then CBR is used for classification
4.	Hijazi et al. [12]: retinal image classification using a histogram-based approach	2010	Two-phase CBR is used to identify age-related macular degeneration, where green and saturation histogram with blood vessels removed are used in first CB and same histogram with OD removed is used in second
5.	Hongru et al. [6]: research on case representation method based on image information	2013	Color histogram of HSV space is used for describing the image characteristics, which is used as the attribute of case description
6.	Waqar et al. [15]: wearable items suggestion system using case-based reasoning	2013	System takes a photo of the user through a camera and extracts some feature from the image, after that using CBR system suggests some wearable item for a person to look attractive
7.	Abdool et al. [14]: recommend my dish: a multi-sensory food recommender	2015	Aesthetic score of a dish image is calculated through some image processing techniques and the recommended system learns the food preferences of different users using CBR
8.	Lee et al. [13]: Improvement on image simulation from multitemporal Landsat images	2017	Using CBR and Fmask, improve the simple simulation algorithm. CBR is used in selection of reference imagery to predict the result
9.	Surjandy et al. [5]: CCTV traffic congestion analysis at Pejompongan using case-based reasoning	2018	Congestion data are taken from CCTV cameras, and the system gives a traffic light solution using CBR where the pictures are taken as a case

References

1. Kumar S, kumar B (2018) Diabetic retinopathy detection by extracting area and number of micro aneurysm from color fundus image. In: 2018 5th international conference on signal processing and integrated networks (SPIN)
2. Shetter A, Prajwalasimha SN, Swapna H (2018) Finger print image enhancement using thresholding and binarization techniques. In: 2018 second international conference on inventive communication and computational technologies (ICICCT)
3. Musa P, Al Rafi F, Lamsani M (2018) A review: contrast-limited adaptive histogram equalization (CLAHE) methods to help the application of face recognition. In: 2018 third international conference on informatics and computing (ICIC)
4. Peng L, Zhao Z, Cui L, Wang L (2004) Remote sensing study based on IRS remote sensing image processing system. In: GARSS 2004. 2004 IEEE international geoscience and remote sensing symposium
5. Surjandy, Anindra F, Soeparno H, Napitupulu TA (2018) CCTV traffic congestion analysis at Pejompongan using case based reasoning. In: 2018 international conference on information and communications technology (ICOIACT)
6. Hongru L, Xiaochen H, Yubin Z (2013) Research on case representation method based on image information. In: 2013 sixth international symposium on computational intelligence and design
7. Chen F, Wang C, Zhang H, Zhang B, Wu F (2007) SAR image classification using case based reasoning. In: 2007 IEEE international geoscience and remote sensing symposium
8. Frost VS (1982) A model for radar images and its application to adaptive digital filtering of multiplicative noise. *IEEE Trans Pattern Anal Mach Intell* 42(2):157–166
9. Benz U, Baatz M, Schreier G (2001) OSCAR-object oriented segmentation and classification of advanced radar allow automated information extraction. *Int Geosci Remote Sensing Symp (IGARSS)* 4:1913–1915
10. Khanum A (2006) Facial expression recognition system using case based reasoning. In: 2006 international conference on advances in space technologies
11. Zhou X, Huang X, Wang Y (2004) Real-time facial expression recognition in the interactive game based on embedded hidden Markov model. In: International conference on computer graphics, imaging and visualization (CGIV'04)
12. Hijazi MHA, Coenen F, Zheng Y (2010) Retinal image classification using a histogram based approach. In: The 2010 international joint conference on neural networks (IJCNN)
13. Lee SB, La HP, Kim Y, Dalgeun L, Kim J, Park Y (2017) Improvement on image simulation from multitemporal Landsat images. In: 2017 IEEE international geoscience and remote sensing symposium (IGARSS)
14. Abdool H, Pooransingh A, Li Y (2015) Recommend my dish: a multi-sensory food recommender. In: 2015 IEEE Pacific Rim conference on communications, computers and signal processing (PACRIM)
15. Waqar MM, Aslam M, Usman MG, Martinez-Enriquez AM (2013) Wearable items suggestion system using case based reasoning. In: 2013 10th international conference on electrical engineering, computing science and automatic control (CCE)
16. Raman V, Then P, Sumari P (2009) Digital mammogram tumor preprocessing segmentation feature extraction and classification. In: 2009 WRI world congress on computer science and information engineering
17. <https://www.decode.fr/binary-image>
18. <https://www.diffnow.com>

Automatic Speech Recognition of Galo



Karter Nyodu and Samudra Vijaya

Abstract The development of spoken language systems for the tribal languages of India is very beneficial to society. The details of the implementation of automatic speech recognition for Galo language, spoken in the northeast Indian state of Arunachal Pradesh, are presented here. A multi-speaker speech database of continuously spoken Galo sentences was specifically created for this purpose. The speech recognition system was implemented using Kaldi, a public domain software toolkit. The automatic speech recognition system recognizes Galo sentences spoken continuously by new speakers with an accuracy of about 80%.

Keywords ASR · Galo · Speech database · Kaldi · Speech-to-text

1 Introduction

Arunachal Pradesh is one of the states in the northeastern region of India. Being home to a large number of tribes and subtribes, a large number of languages are spoken in the state. Galo, a language of the Tani branch of the Tibeto-Burman language family, is spoken by the people belonging to the Galo tribe of Arunachal Pradesh. Galo is one of 12 tribal languages of Arunachal Pradesh, listed in the ‘The Scheduled Castes and Scheduled Tribes Lists’ published by the census of India [1]. Although 29,246 Indians stated Galo as their native language in 2011 [2], it is in the UNESCO list of ‘vulnerable’ languages [3]. Figure 1 shows the map of Arunachal Pradesh state wherein the primary area of Galo speakers is shaded [4].

Even though 7 of the 99 major, non-scheduled languages of India belong to the state of Arunachal Pradesh [2], study and technology development of the languages of the state are limited. A speech database of English, Hindi, and local language

K. Nyodu (✉) · S. Vijaya

Centre for Linguistic Science and Technology, Indian Institute of Technology Guwahati, Guwahati, India

e-mail: karter@iitg.ac.in

S. Vijaya

e-mail: samudravijaya@gmail.com

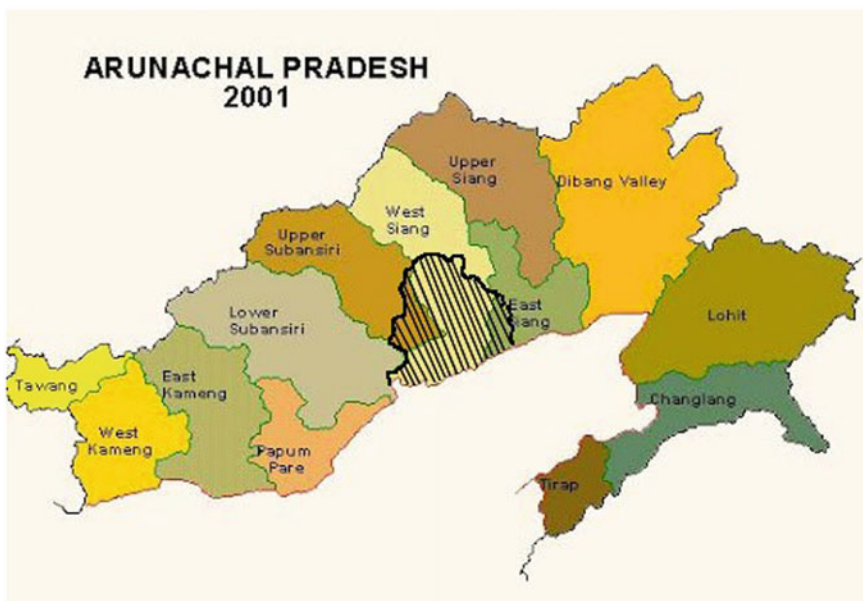


Fig. 1 Map of Arunachal Pradesh where the Galo speaking area is shaded. Sources [4, 5]

of Arunachal was created and used for speaker identification [6]. The same authors prepared a similar, but a larger database of speech from 200 speakers. This Arunchali language speech database was used for identifying the language of the input speech as one of the English, Hindi, Adi, Nyishi, Galo, and Apatani [7].

Very little research work on the Galo language has been reported in the literature. A book introducing the Galo language was written in 1963 [8]. A descriptive grammar of the Lare dialect of Galo was the theme of a recent Ph.D. thesis work [5]. The sole work on spoken Galo is an investigation of the acoustic features of Galo phonemes using formant frequencies and cepstral coefficients as features [9]. However, no spoken language system for Galo, whether it is speech-to-text or text-to-speech, has been implemented so far. The primary objective of this research work is to implement a speech-to-text system for Galo. A secondary objective was to create spoken language resources necessary for achieving the primary objective. Specifically, the following are the outcomes of the current research work:

1. A Galo speech database consisting of sentences read by many native Galo speakers.
2. Transcription of the speech data using the Galo script, which is a modified Roman Script.
3. A multi-speaker, continuous speech recognition system for Galo language.

The organization of the paper is as follows. The details of the spoken language resources developed for Galo language are given in Sect. 2. The implementation of ASR systems using various acoustic models and evaluation methodology is described

Table 1 Two examples of dialect-dependent transcription of words using modified Roman Script

Dialect		Gloss
Lare	Pugo	
‘aci	‘asi	brother
inrv	inye	to go

in Sect. 3. The results and discussion are also presented in Sect. 3. Section 4 draws some concluding remarks.

2 Spoken Language Resources

This section describes the steps for the development of linguistics resources for training and evaluating the Galo Automatic Speech Recognition (ASR) system. The subsections contain detailed descriptions of text and speech corpora.

2.1 Text Corpus

The text corpus contains a total of 200 short sentences, selected from the Galo-English dictionary [10]. The text corpus consists of 721 unique words. Galo script, which is a variety of modified Roman Script (MRS) [10], was used for writing the text.

M.W. Post, in his Ph.D. thesis, lists 6 dialects of Galo: lare, pugo, tai, gensi, karko, and zirdo [5]. Dialect-dependent variations in lexical terms were taken into account while writing the transcriptions of recorded speech. Table 1 shows two such examples of dialect-dependent variations.

2.2 Recording of Speech Data

Thirty-five Galo speakers were asked to read sets of 30–50 Galo sentences written in modified Roman Script. Speech data were collected at users’ locations using laptop, PC, and an earphone. The speech data were recorded at the sampling rate of 44.1 kHz, 16-bit, mono and were stored in wav format. The statistics of the number of speakers and the speech files is given in Table 2.

The set of 35 Galo speakers belonged to two broad categories of dialects: Lare and Pugo. The dialect-dependent statistics of the speech corpus is given in Table 3. The lexical transcriptions of the speech files were dialect-dependent.

Table 2 Statistics of the Galo speech corpora

Number of	Male	Female	Total
Speakers	20	15	35
Speech files	850	650	1500

Table 3 Distribution of speakers and files according to dialect

Number of	Dialect		Total
	Lare	Pugo	
Speakers	22	13	35
Speech files	930	570	1500

2.3 Pronunciation Dictionary

A pronunciation dictionary was created manually according to the format specified by Kaldi [11], the software toolkit used for the implementation of ASR systems. The entries in the dictionary specify the pronunciation of each word in the text corpus in terms of the phones or phone-like acoustic units of the language.

The Galo script [5] lists 7 vowels and 17 consonants. The script does not seem to distinguish between long and short vowels. In addition, diphthongs are also used in spoken Galo. Further, geminated consonants are present in the spoken Galo language. In order to have acoustic models of these acoustic–phonetic variations, we use a list of 19 (7 short + 7 long + diphthongs) vowel-like labels and 31 (17 single + 14 geminate) consonant-like labels. The labels follow the ILSL12 [12] convention, augmented with notations to mark tones of the language. Table 4 shows a few entries in the pronunciation dictionary.

Table 4 First two columns of the table show typical entries in the pronunciation dictionary

Word	Label sequence	Gloss
panam	p a n a m	To cut
paanam	p aa n a m	To hover
kai	k ai	Big
alo	a l o	Salt
allo	a ll o	Tomorrow

It illustrates the ILSL12 labels used to prescribe the pronunciation of Galo words involving long vowels, diphthongs, and geminated consonants

3 Implementation, Evaluation, and Results

The Kaldi software toolkit was used for the implementation of the ASR system. In this section, the details of the implementation, the evaluation methodology, the results, and the discussion are presented.

3.1 Feature Extraction

The default setting of the Kaldi toolkit was used for feature extraction. Thirteen mel-frequency cepstral coefficients (MFCC) were computed from every speech frame of 25 ms duration at a frame rate of 100/sec. Further, the first and second derivatives of 13 MFCCs were computed. As a result, a 39-dimensional feature vector was obtained.

3.2 Acoustic Modeling

For training the acoustics model, the default setting of the Kaldi toolkit was used. Six types of hidden Markov models (HMM) were trained. Each state of HMM is characterized by either a Gaussian mixture model (GMM) or a subspace GMM or a deep neural network (DNN). A brief description of each of these models is given below.

The simplest acoustic model (called **Mono**) models the context-independent phone-like units, also known as monophones. The second model (**Tri1**) is the first of a series of HMMs that model context-dependent phones (**triphone**). The third acoustic model (**Tri2**) uses linear discriminant analysis (LDA) and maximum likelihood linear transform (MLLT). The fourth acoustic model (**Tri3**) uses the speaker adaptive training and feature-space maximum likelihood linear regression (fMLLR). The fifth acoustic model (**SGMM-HMM**) employs subspace GMMs instead of GMMs. The last model is the **DNN-HMM**-based model which uses the posterior probability given by a DNN to compute the state-dependent likelihood of feature vector.

3.3 Language Model

Bigram language model was used to model the syntax. The parameters of this model are estimated using the transcription of the train data. IRSTLM software was used to train the language model [13].

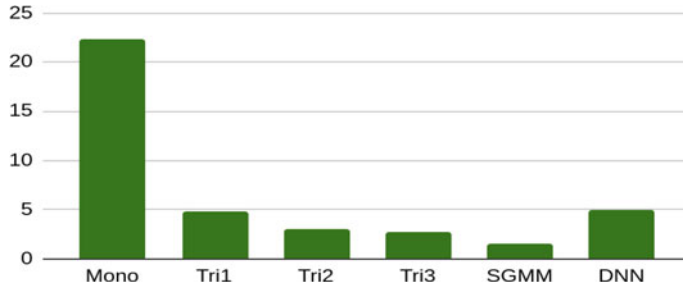


Fig. 2 WER (%) of the Galo ASR system for different types of acoustic models. Test data are the same as training data (entire speech corpus)

3.4 Results and Analysis

This section presents the performance of the Galo speech recognition system using various acoustic models. The word error rate (WER) is used as a measure of the performance of the ASR; lower the WER, the better the system is. The WER is computed as

$$\text{WER}(\%) = 100(D + S + I)/N$$

where D is the number of deletion errors, S is the number of substitution errors, I is the number of insertion errors, and N is the total number of words present in the reference transcription.

3.4.1 Performance on Training Data

The first evaluation was carried out using the same data for both training and testing. Here, the entire speech data were used for this purpose. The word error rates of the ASR system with different acoustic models are shown in Fig. 2.

The word error rate for the monophone model is 22%. The WER decreases drastically by using context-independent phone models (Tri*). The WER is the lowest (2%) for SGMM-HMM model. The WER of the DNN-HMM-based ASR system is slightly higher than that of the SGMM model. This is possibly due to the small size of the speech corpus, as DNN demands a large amount of speech data to adequately train a large number of parameters.

3.4.2 Performance on Test Data

In order to estimate the performance of the ASR system with respect to unseen speech data, a threefold cross-validation methodology was adopted. Accordingly, the entire

Table 5 Statistics of the three subsets of speech files used for threefold cross-validation of ASR

Number of	Fold 1		Fold 2		Fold 3	
	Train	Test	Train	Test	Train	Test
Utterances	990	510	1000	500	1010	490
Male speakers	13	6	12	6	12	7
Female speakers	10	6	11	5	11	5
Total	23	12	24	11	23	12

speech corpus was divided into three threefolds (subsets). These subsets were divided in such a way that each subset had an approximately equal number of speech files from both the female and male speakers. One subset was reserved/labeled as the test set. The system was trained with the remaining two subsets. The WER of the system with respect to the unseen test data is computed. This process is repeated for all three sets. Such a threefold evaluation is carried out for all the six acoustic models. The characteristics of the three subsets employed in our experiments are shown in Table 5.

The WERs of six types of acoustics models in threefold evaluation experiments are listed in Table 6. The WER of the ASR systems is around 20% for unseen data in all threefolds. This value of WER for unseen test data is an order of magnitude higher than that for the training data. Also, the difference between the WER of the context-independent (monophone) model and the best (tri3) model is negligible. Even though triphone models are more powerful, their potential is yet to be exploited due to lack of adequate amount of training data. The WER increases from 18% to 26% when SGMM-HMM acoustic model is used. A similar increasing trend in WER is observed when a DNN is used instead of a GMM.

The WERs of the ASR systems using six types of acoustic models are shown in the form of a bar chart in Fig. 3.

Table 6 WERs of various types of acoustic models in threefold experiments

Model	WER (%)			
	Fold 1	Fold 2	Fold 3	Average
Mono	19	21	17	19
tri1	18	23	17	19
tri2	21	25	19	22
tri3	17	20	15	18
SGMM	25	29	22	26
DNN-HMM	21	23	20	22

The WERs are around 20%

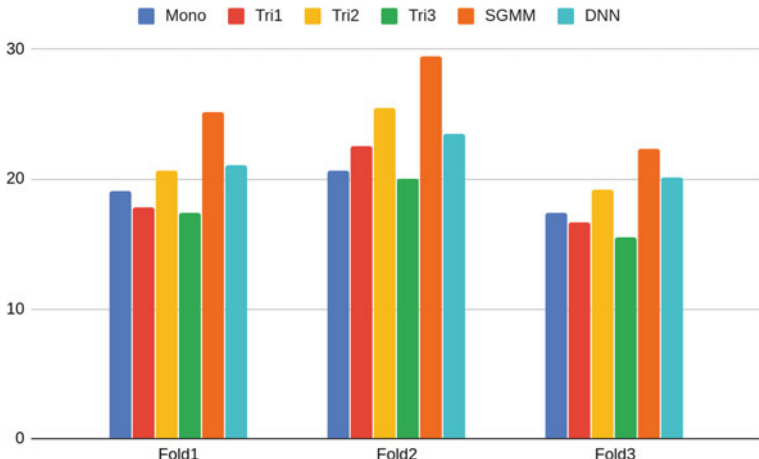


Fig. 3 WERs of various ASR systems in a threefold cross-validation experiment

4 Concluding Remarks

An automatic speech recognition system was implemented for Galo, a zero-resource language, spoken by Galo tribals in the state of Arunachal Pradesh. The system was trained using a preliminary multi-speaker speech database. The effectiveness of different types of acoustic models was investigated using a threefold cross-validation methodology. While the recognition accuracy of the ASR system is good for training data, the accuracy decreases significantly for all six types of acoustic models. This is due to the limited amount of speech data that could be collected in this initial effort. Future work includes expansion of the spoken language corpus and investigation of the utility of using prosodic features for machine recognition of this tonal language.

References

1. List of notified scheduled tribes, census of India. Online: http://censusindia.gov.in/Tables_Published/SCST/ST%20Lists.pdf
2. Office of the Registrar General and Census Commissioner India (2011) Statement-1 part-b languages not specified in the eighth schedule (non-scheduled languages). Online: <http://cen susindia.gov.in/2011Census/Language-2011/Statement-1.pdf>
3. Moseley C (ed.) (2010) Atlas of the world's languages in danger, 3rd edn. Paris, UNESCO Publishing. Online version: <http://www.unesco.org/languages-atlas/en/atlasmap/language-id-988.html>
4. Office of the Registrar General and Census Commissioner, India, State Maps. http://census india.gov.in/maps/State_Maps/StateMaps_links/arunachal01.html
5. Mark William Post (2007) A grammar of Galo. PhD Thesis, La Trobe University

6. Bhattacharjee U, Sarmah K (2012) A multilingual speech database for speaker recognition. In: 2012 IEEE international conference on signal processing, computing and control. <https://doi.org/10.1109/ispcc.2012.6224374>
7. Bhattacharjee U, Sarmah K (2013) Language identification system using MFCC and prosodic features. In: 2013 international conference on intelligent systems and signal processing (ISSP). <https://doi.org/10.1109/issp.2013.6526901>
8. Das Gupta SK (1963) An introduction to the Gallong language. Shillong, Northeast Frontier Agency
9. Sora M, Talukdar J, Talukdar PH (January, 2013) Formant frequency and Cepstral method estimation of Galo phonemes using acoustical cues. Int J Inf Electron Eng 3(1)
10. Rwbba I, Post MW, Rwbba I, Xodu M, Bagra K, Rwbba B, Rwbba T, Ado N, Keenaa D (2009) Galo-English dictionary with English-Galo index
11. Povey D, Ghoshal A, Boulian G, Burget L, Glembek O, Goel N, Hannemann M, Motlicek P, Qian Y, Schwarz P, Silovsky J, Stemmer G, Vesely K (December, 2011) The Kaldi speech recognition toolkit. In: IEEE 2011 workshop on automatic speech recognition and understanding. IEEE signal processing society. Online: <https://publications.idiap.ch/downloads/papers/2012/PoveyASRU20-112011.pdf>
12. Indian Language speech sound label set (ILSL12). Online: <https://www.iitm.ac.in/donlab/tts/downloads/cls/clsv2.1.6.pdf>
13. Federico M, Bertoldi N, Cettolo M (2008) IRSTLM: an open source toolkit for handling large scale language models. Proceedings of Interspeech, pp 1618–1621

Early Detection of Diabetic Retinopathy Using Machine Learning Techniques: A Survey on Recent Trends and Techniques



Dolly Das, Saroj Kr. Biswas, Sivaji Bandyopadhyay, and Sunita Sarkar

Abstract Diabetic Retinopathy (DR) is a medical condition which occurs due to diabetes mellitus. It causes severe blindness due to mutilation of the retina of human eye. According to statistics, 80% of the people, especially the working-age people have been suffering from this disease. Hence, currently, DR has become an important issue which needs to be solved at an early stage such that blindness can be prevented to a great extent among the working-age people. Various intelligent systems have been designed for early detection of DR as manual diagnosis is time consuming and error prone. Besides, the availability of ophthalmologist is not possible at any time and everywhere. Thus, the need of a highly optimized computer-assisted intelligent system is required that can be used for the early detection of DR. Various models have been proposed by researchers across the globe since decades. This paper aims to give an elaboration over the works that have been done earlier for the detection of DR and the recent technologies that have evolved for the same. This paper thus gives a state of the art on the features, causes, symptoms, various grades of DR and models that have been proposed and implemented for the early diagnosis of DR.

Keywords Diabetic Retinopathy · Diabetes · Image Processing · Machine Learning · Retinal Lesions

D. Das (✉) · S. Kr. Biswas · S. Bandyopadhyay
National Institute of Technology Silchar, Silchar, India
e-mail: das.dolly0019@gmail.com

S. Kr. Biswas
e-mail: bissarojkum@yahoo.com

S. Bandyopadhyay
e-mail: sivaji.cse.ju@gmail.com

S. Sarkar
Assam University, Silchar, India
e-mail: sunitasarkar@rediffmail.com

1 Introduction

Diabetic retinopathy is a chronic progressive disease which occurs due to diabetes mellitus. It causes damage to the retina of the human eye which leads to severe blindness. It is also known as diabetic eye disease. Statistically, 80% of the people who have been suffering from prolonged diabetes such as for 15–20 years suffer from DR [1]. DR is found to be highly prevalent among working-age people. Thus, such a medical condition requires early detection and diagnosis to prevent the disease from progressing into severe stages, thereby reducing the occurrence of blindness. DR can be detected on the basis of the existence of features and/or retinal lesions such as Microaneurysms (MA), Foveal Avascular Zone (FAZ), Exudates (EX) and Hemorrhages (HE) [2–6], in the rear view of the human eye, i.e., the fundus. Here, for the purpose of diagnosing the disease, a comprehensive eye examination is performed in which the human eye is dilated by injecting medically approved contrasting agents. The fundus images are then obtained using a digitized fundus camera [7]. The ophthalmologist examines these fundus images to identify features such as MA, HE, EX and FAZ and determines the severity of the disease. Besides these, certain other retinal lesions such as ruptured retinal blood vessels, Cotton Wool Spots (CWS), Intra Retinal Microvascular Abnormalities (IRMA) [2–6] can also be helpful for analyzing and identifying the severity of the disease. Of all the features mentioned above, manual analysis is feasible but time consuming. Thus, for faster analysis and detection, which can help experts as well as fill the absence of ophthalmologists in certain cases, the requirement of an intelligent system arises which can analyze and compute the severity of DR using fundus images. Hence, a system could be proposed that takes fundus images as input and classifies them into various categories of DR. Based on the presence and absence of the features mentioned above and also taking into consideration the severity level, the disease is identified and classified into five categories of DR such as No DR-0, DR-1, Mild Proliferative Diabetic Retinopathy (MPDR)-2, Proliferative Diabetic Retinopathy (PDR)-3 and Non-Proliferative Diabetic Retinopathy (NPDR)-4 [3, 4]. Some other methods [8, 9] have classified DR into two categories—DR and No DR. Thus, an intelligent system can be designed to identify DR using different features. Different kinds of works have been done since decades, proposing various intelligent and computer-assisted systems which can perform automated analysis of the disease. Various techniques have been proposed earlier for the detection and diagnosis of DR, such as fuzzy c-means clustering [5], Multilayer Perceptron (MLP) and Extreme Learning Machine (ELM) [10], neural network [10], Support Vector Machine (SVM) [8, 9, 12, 13], meta-SVM [11], Naive Bayes (NB) classifier [10, 12], probabilistic classifier, geometric classifier, K-Nearest Neighbor (KNN) classifier and tree-based classifier [12], Bayesian classifier [6, 14], Mahalanobis classifier [14], KNN classifier [12–14], Gaussian Bayes classifier [3, 4], genetic algorithm [16], AlexNet deep neural network (DNN) [17, 18], Convolutional Neural Network (CNN) [18] and various other Machine Learning techniques [10, 11, 13, 16, 19]. Figure 1 depicts different retinal lesions in human retina which appear due to DR [20]. Figure 2 shows the

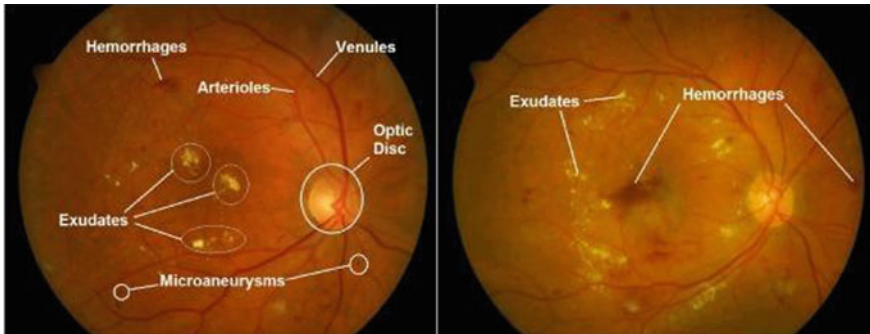


Fig. 1 DR retinal lesions

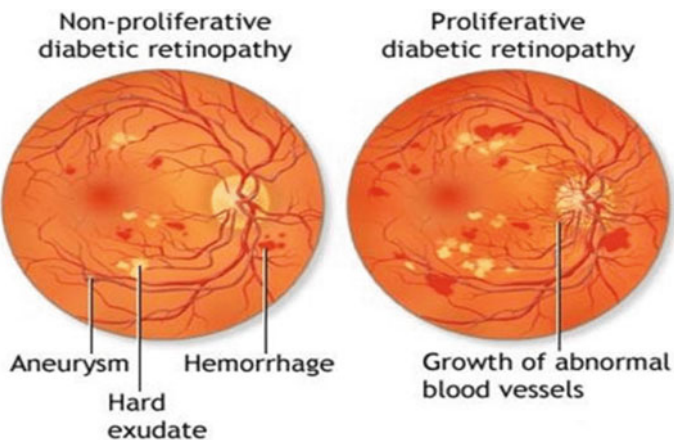


Fig. 2 Severe grades of DR

severe classes of DR as PDR and NPDR [21]. Figure 3a depicts DR classification, (b) depicts common method for DR detection and (c) [28] depicts DR detection using deep learning and CNN.

2 Features of DR

There are different features which can be used to identify DR at an early stage such that blindness can be prevented. A brief description on these features has been explained below:

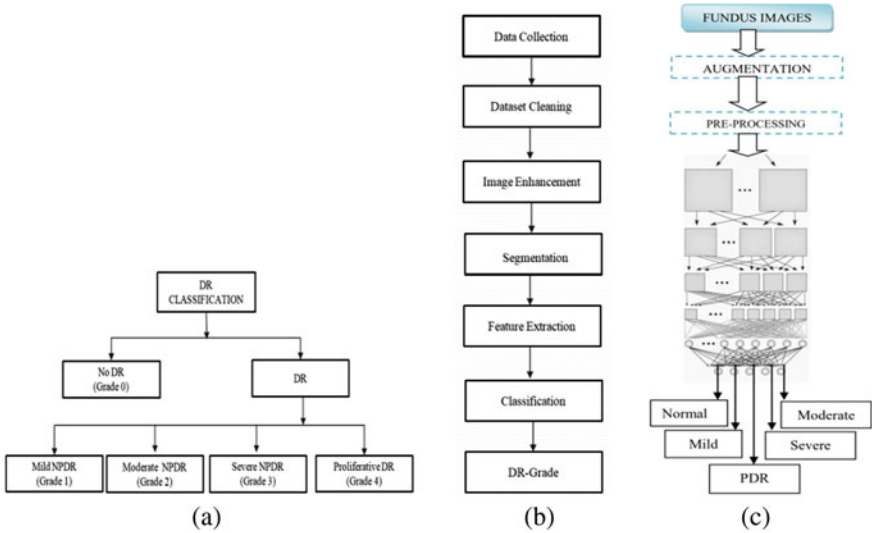
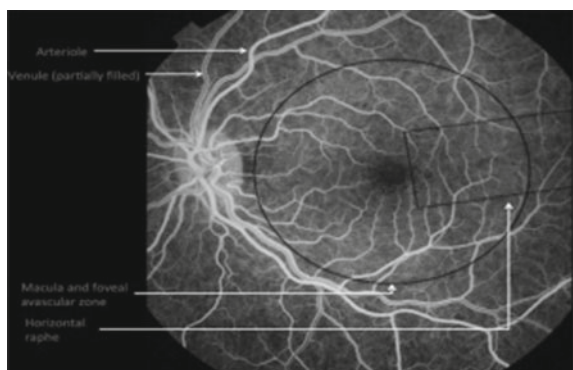


Fig. 3 **a** DR classification **b**. Common method for DR detection **c**. DR detection using deep learning and CNN

2.1 Foveal Avascular Zone (FAZ)

FAZ is a region situated within the fovea of the retina devoid of retinal blood vessels. It has a diameter of 0.5 mm and a Field of View (FOV) of 1.5° . The FAZ center also known as the macula center is the point of interest which is a significant landmark in Fluorescein Angiography (FA). Figure 4 shows the presence of FAZ in DR-affected retina [22].

Fig. 4 FAZ in DR retina



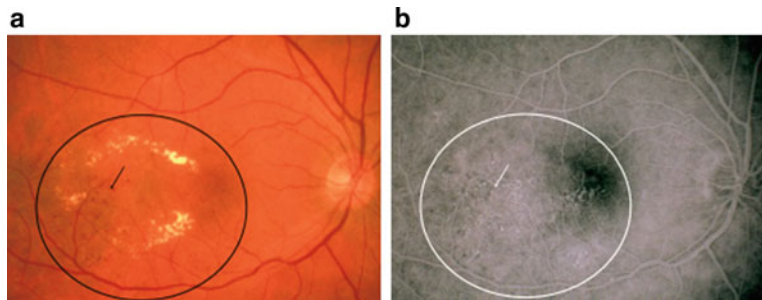


Fig. 5 **a** Presence of MA in DR. **b** Grayscale image of Fig. 5a

2.2 Microaneurysms (MA)

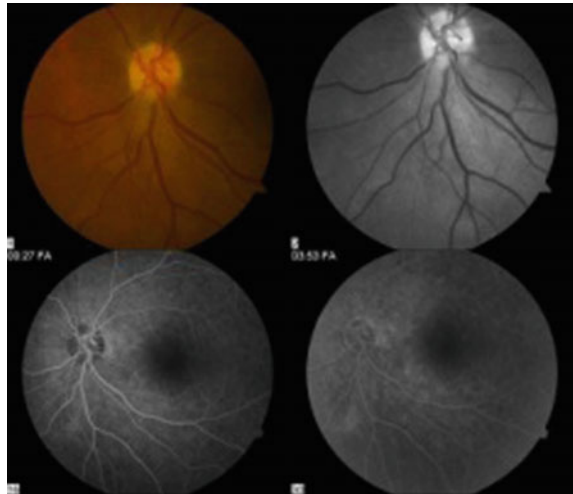
MA, also known as dot hemorrhage, is identified as the earliest symptom for the diagnosis of DR. They are the localized capillary dilations and saccular in structure. They generally appear in clusters as small red dots but may also appear in isolation. The region encircled black in Fig. 5a shows the presence of MA in DR retina. Figure 5b is the grayscale image in which the white dots spotted are MA [23].

2.3 Cotton Wool Spots (CWS)

CWS or soft EX are bloodless grayish speckles of contusion in the nerve fiber layer of the human retina. They are a consequence of ischemia causing disarray in the flow of axoplasm. Multiple CWS may count to nearly 6 or more than 6 in one eye and may specify pervasive ischemia in the retina. Figure 6 shows the presence of CWS in DR-affected retina [23].

Fig. 6 CWS in DR retina



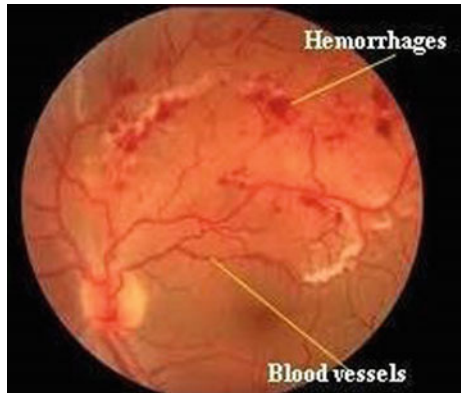
Fig. 7 IRMA in DR retina

2.4 *Intra Retinal Microvascular Abnormalities (IRMA)*

IRMA are the areas of capillary dilation and intraretinal new vessel formation, which arise within ischemic retina. Figure 7 shows the presence of IRMA in DR-affected retina [23].

2.5 *Hemorrhages (HE)*

HE is also known as intraretinal HE which may appear in shapes such blots, flames or dot-like structures depending upon its depth in the retina. HE appears as flame shaped when found in the nerve fiber layer of the capillary network, thereby following the divergence of the axons. However, it appears as dot shaped or blot shaped when found in the inner nuclear layer of the capillary network, aligned at right angles to the retinal surface. It is not exactly possible to differentiate between MA and HE; however, making use of Fluorescein Angiography (FA) shall help to discriminate MA by lighting up the MA when the human eye is dilated. The appearances of both these features do not affect vision. However, multiple blots HE may imply significant pre-proliferative retinopathy. Figure 8 shows the presence of HE in a DR-affected retina [22].

Fig. 8 HE in DR retina**Fig. 9** EX in DR retina

2.6 Exudates (EX)

EX or hard EX are prominent bloodless yellow intraretinal accumulations with variations in size such as from a tiny pinprick to wide-ranging speckle and may evolve into ring-like structures called circinate. They are a consequence of leakage composed of body fat or extracellular lipid (drusen) accumulation under the retina causing macular degeneration, arising from the abnormal retinal capillaries. Such a condition may lead to Diabetic Macular Edema (DME) [15] causing swelling and thickening of the macula in the retina. Figure 9 shows the presence of EX in DR-affected retina [23].

3 Different Methods for DR and Its Features Detection

Various works have been done with respect to premature recognition, detection and diagnosis of DR, thereby prohibiting the occurrence of blindness. Some of the important works have been stated below, which make use of various machine learning techniques.

Using Multilayer Perceptron (MLP), Extreme Learning Machine (ELM) and Naive Bayes (NB), Asha et al. [10] have performed the detection of DR using

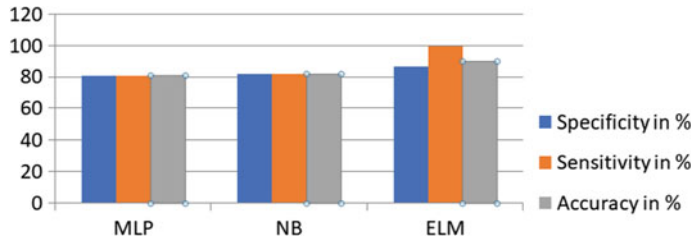


Fig. 10 Performance of MLP, NB and ELM in [10]

exudates. Experimental results show that the model built using ELM outperforms other two models, i.e., MLP and NB, and effectively detects the presence of EX in retinal images. Figure 10 depicts the performance of MLP, NB and ELM in [10].

Using meta-Support Vector Machine (meta-SVM), Li et al. [11] have simultaneously detected multiple types of lesions through fusion of classifiers and amalgamated the out-turn of every single SVM. It exploits the information using clustering to improve detection of lesions [11]. An accuracy of 99.44% has been achieved for detection of optic disk, and 93.49% has been achieved for detection of macula, for the detection of DR. Using Support Vector Machines (SVM), various systems have been proposed for detection of EX and non-EX in retinal lesions [8, 12], identification of HE trained on High-Resolution Fundus (HRF) and Standard Diabetic Retinopathy Database (DIARETDB1) datasets [9], detection of EX and MA using SVM and KNN classifier [13], detection of hard EX [24], for detection of DR and its severe stages. A sensitivity of 100%, a specificity of 94.6% and an accuracy of 96.66% have been attained in [8]. The sensitivity and specificity of HE detection are 94.76% and 99.85%, respectively, classification rate is 95% and Peak Signal-to-Noise Ratio (PSNR) of 51.45 dB in [9]. Different variants of SVM such as Gaussian SVM (GSVM), Cubic SVM (CSVN), Quadratic SVM (QSVM) and Linear SVM (LSVM) kernel functions have been trained, validated and tested on datasets such as e-ophtha, High-Resolution Image Set (HRIS), Methods to Evaluate Segmentation and Indexing Techniques in the field of Retinal Ophthalmology (MESSIDOR), DIARETDB1, Vascular Disease Image (VDIS), Digital Retinal Images for Vessel Extraction (DRIVE) and HRF, for detection of DR [12]. Figure 11 depicts the classification accuracy obtained for the variants of SVM to the corresponding dataset [8, 12]. Lachure et al. [13] have attained a specificity of 100% and a sensitivity of more than 90%.

Using probabilistic, geometric, KNN and tree-based classifier [12], retinal lesions have been identified and segregated as EX and non-EX region for detection of DR. Five probabilistic-based classifiers, namely NB, Bayesian Net(BN), NB updateable, Multinomial Naive Bayes (MNB) and Bayesian Logistic Regression (BLR) and three KNN Kernels (KNNK), namely Fine KNN Kernel (FKNNK), Weighted KNN Kernel (WKNNK) and Medium KNN Kernel (MKNNK) classifiers have been successfully deployed for classification of retinal lesions in the process of detection of DR. Figure 11 gives a representation of different variants of classifiers along with

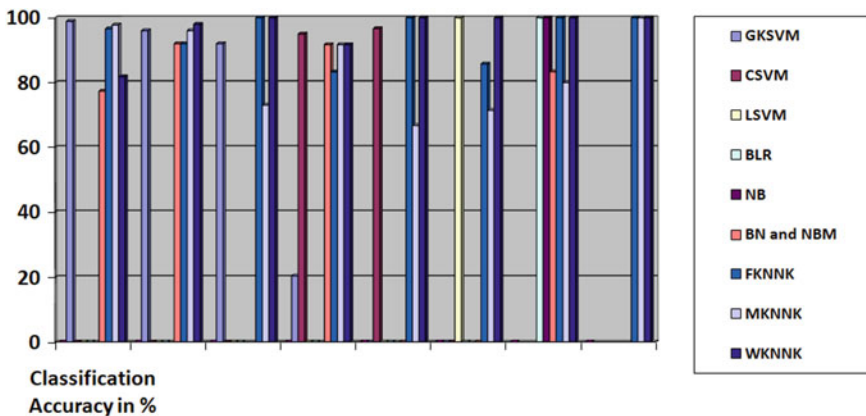


Fig. 11 Different variants of classifiers and their accuracy to the corresponding dataset

their classification accuracy to the corresponding dataset [12]. Ege et al. [6] have also proposed a DR screening system for identification of MA, HE, EX and CWS as dark and bright abnormalities. Various statistical classifiers such as the Bayesian classifier, the Mahalanobis classifier and the KNN classifier have been tested. The KNN classifier achieved a sensitivity of 93% for MA, 51% for HE, 100% for EX and 15% for CWS. Lachure et al. [13] have also proposed a methodology to detect EX and MA, for detection of DR using KNN classifier.

Using Bayesian classifier [6], Mahalanobis classifier [6], KNN classifier [6, 12, 13], DR detection has been performed by Ege et al. [6]. The Bayes classifier and Mahalanobis distance classifier have been used to estimate the covariance, mean and prior probability on the learning set. KNN classifier performs classification of dark and bright abnormalities on 134 retinal images. Mahalanobis classifier performed better classification of bright abnormalities than Bayes and KNN classifier. Figure 12 lists the performances of the three classifiers with respect to the sensitivity parameter [6]. Hsiao et al. [14] have proposed a detection scheme for optic disc in retinal images eliminating unacceptable contour segmentation, for detection of DR. The Supervised

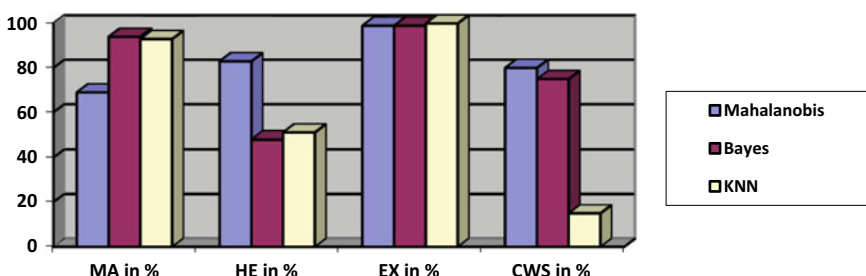


Fig. 12 Performances of the three classifiers with respect to the sensitivity parameter

Gradient Vector Flow (SGVF) is deployed for the edge detection of optic disc (OD). The Bayesian classifier identifies the correct and incorrect contour point and classifies them as edge points or non-edge points. Using Gaussian Bayes classifier [16, 17], the FAZ area is measured to detect DR. Frazil et al. [3, 4] performs pattern classification upon classes having Gaussian distribution. A sensitivity of 95%, a specificity of 97% and an accuracy of 98% have been obtained for various stages of DR using Log Posterior Probability Ratio (LPPR). The classifier shows a high specificity of 97% and a sensitivity of 84% for both mild and moderate NPDR. On an overall basis, the DR system can detect DR with a higher sensitivity of 90.81%, a specificity of 98.29% and an accuracy of 97.46%, for all the stages of DR.

Using AlexNet DNN, Mansour, R.F. et al. [19] have proposed that features can be extracted from Region of Interest (ROI) using Convolutional Neural Network (CNN) [11]. It models deep learning methods to detect ascribable DR in Kaggle dataset and MESSIDOR-2 database, exhibiting a better performance on the Kaggle dataset. Linear Discriminant Analysis (LDA) and Principal Component Analysis (PCA) have been used for feature selection and extraction of multidimensional features, thus outperforming Spatial-Invariant Feature Transform (SIFT)-based DR detection and other existing system with a highest classification accuracy of 97.93% [19]. It achieves a sensitivity of 99% and a specificity of 71% and area under the ROC curve of 0.97.

Various other ML [10, 13, 18, 20] techniques such as Adaptive Machine Learning (AML) [21], CNN [25] for identification of MA, EX and HE, deep learning Artificial Intelligence(AI) [26] and heat map generation for ConvNets [27] have been proposed for detection of DR. In [27], the area under the Receiver Operating Characteristic (ROC) curve, A_z of 0.954 and 0.949, for 2015 Kaggle Diabetic Retinopathy competition and e-ophtha, respectively, for detection of referable DR (rDR). CNN is trained using 128,175 images graded for DR and DME, using Eye Picture Archive Communication Systems (EyePACS-1) and MESSIDOR-2 dataset.

4 Conclusion

The paper gives an elaborate idea in brief about DR, its symptoms, features, shape, size and location of the features, various causes that lead to DR and how DR causes blindness. This paper also gives a brief introduction about the works that have been performed by various researchers and experts working on the domain of expert systems for DR since decades. The paper shows different prominent features responsible for DR detection. The models proposed by the researchers have introduced different grades for classification of DR. Besides, this paper focuses on the study and analysis of various machine learning techniques that have been deployed such as fuzzy c-means clustering, MLP and ELM, neural network, meta-SVM, SVM, NB classifier, probabilistic classifier, geometric classifier, KNN classifier and tree-based classifier, Bayesian classifier, Mahalanobis classifier, KNN classifier, Gaussian Bayes classifier, genetic algorithm, AlexNet DNN, CNN and various other ML techniques

to model systems for early DR detection and classification. Recent models such as SVM, AlexNet DNN and CNN have evolved with efficient results compared to rest of the models, thus making real-life application of such systems, easy and faster for detection. Thus, this paper is very helpful for new and young researchers who are working on the domain of DR.

References

1. Fong DS, Aiello L, Gardner TW, King GL, Blankenship G, Cavallerano JD, Ferris FL, Klein R (2004) Retinopathy in diabetes. *Diab Care* 27(Suppl 1):s84–s87
2. Kumar PS, Deepak RU, Sathar A, Sahasranamam V, Kumar RR (2016) Automated detection system for diabetic retinopathy using two field fundus photography. *Procedia Comput Sci* 93:486–494
3. Fadzil MHA, Ngah NF, George TM, Izhar LI, Nugroho H, Nugroho HA (2010) Analysis of foveal avascular zone in colour fundus images for grading of diabetic retinopathy severity. In: 2010 annual international conference of the IEEE engineering in medicine and biology, pp 5632–5635
4. Fadzil MA, Izhar LI, Nugroho H, Nugroho HA (2011) Analysis of retinal fundus images for grading of diabetic retinopathy severity. *Med Biol Eng Comput* 49(6):693–700
5. Sopharak A, Uyyanonvara B, Barman S (2009) Automatic exudate detection from non-dilated diabetic retinopathy retinal images using fuzzy c-means clustering. *Sensors* 9(3):2148–2161
6. Ege BM, Hejlesen OK, Larsen OV, Møller K, Jennings B, Kerr D, Cavan DA (2000) Screening for diabetic retinopathy using computer based image analysis and statistical classification. *Comput Methods Prog Biomed* 62(3):165–175
7. Goh JKH, Cheung CY, Sim SS, Tan PC, Tan GSW, Wong TY (2016) Retinal imaging techniques for diabetic retinopathy screening. *J Diab Sci Technol* 10(2):282–294
8. Senapati RK (2016) Bright lesion detection in color fundus images based on texture features. *Bull Electr Eng Inf* 5(1):92–100
9. Raja SS, Vasuki S (2015) Screening diabetic retinopathy in developing countries using retinal images. *Appl Med Inf* 36(1):13–22
10. Asha PR, Karpagavalli S (2015) Diabetic retinal exudates detection using machine learning techniques. In: 2015 international conference on advanced computing and communication systems, IEEE, pp 1–5
11. Li B, Li HK (2013) Automated analysis of diabetic retinopathy images: principles, recent developments, and emerging trends. *Curr Diab Rep* 13(4):453–459
12. Amin J, Sharif M, Yasmin M, Ali H, Fernandes SL (2017) A method for the detection and classification of diabetic retinopathy using structural predictors of bright lesions. *J Comput Sci* 19:153–164
13. Lachure J, Deorankar AV, Lachure S, Gupta S, Jadhav R (2015) Diabetic Retinopathy using morphological operations and machine learning. In: 2015 IEEE international advance computing conference (IACC), pp 617–622
14. Hsiao HK, Liu CC, Yu CY, Kuo SW, Yu SS (2012) A novel optic disc detection scheme on retinal images. *Expert Syst Appl* 39(12):10600–10606
15. Agurto C, Murray V, Yu H, Wigdahl J, Pattichis M, Nemeth S, Barriga ES, Soliz P (2014) A multiscale optimization approach to detect exudates in the macula. *IEEE J Biomed Health Inf* 18(4):1328–1336
16. Decencière E, Cazuguel G, Zhang X, Thibault G, Klein JC, Meyer F, Marcotegui B, Quellec G, Lamard M, Danno R, Elie D (2013) TeleOphta: Machine learning and image processing methods for teleophthalmology. *Irbm* 34(2):196–203

17. Mansour RF (2018) Deep-learning-based automatic computer-aided diagnosis system for diabetic retinopathy. *Biomed Eng Lett* 8(1):41–57
18. Rakhlil A (2018) Diabetic retinopathy detection through integration of deep learning classification framework. *bioRxiv* 225508
19. Porwal P, Pachade S, Kamble R, Kokare M, Deshmukh G, Sahasrabuddhe V, Meriaudeau F (2018) Indian diabetic retinopathy image dataset (IDRID): a database for diabetic retinopathy screening research. *Data* 3(3):25
20. Fraz MM, Jahangir W, Zahid S, Hamayun MM, Barman SA (2017) Multiscale segmentation of exudates in retinal images using contextual cues and ensemble classification. *Biomed Signal Process Control* 35:50–62
21. <https://www.glycosmedia.com/news/> 12–01–2020 to 13–01–2020
22. Kale P, Janwe N (2017) Detection of retinal hemorrhage in color fundus image. *Int J Adv Res Comput Commun Eng* 6(3)
23. Kaur J, Mittal D (2018) A generalized method for the segmentation of exudates from pathological retinal fundus images. *Biocybernetics Biomed Eng* 38(1):27–53
24. Tjandrasa H, Putra RE, Wijaya AY, Ariessanti I (2013) Classification of non-proliferative diabetic retinopathy based on hard exudates using soft margin SVM. In: 2013 IEEE International Conference on Control System, Computing and Engineering. IEEE, pp 376–380
25. Pratt H, Coenen F, Broadbent DM, Harding SP, Zheng Y (2016) Convolutional neural networks for diabetic retinopathy. *Procedia Comput Sci* 90:200–205
26. Takahashi H, Tambo H, Arai Y, Inoue Y, Kawashima H (2017) Applying artificial intelligence to disease staging: deep learning for improved staging of diabetic retinopathy. *PLoS ONE* 12(6):e0179790
27. Quellec G, Charrière K, Boudi Y, Cochener B, Lamard M (2017) Deep image mining for diabetic retinopathy screening. *Med Image Anal* 39:178–193
28. Chandrakumar T, Kathirvel R (2016) Classifying diabetic retinopathy using deep learning architecture. *Int J Eng Res Technol* 5(6):19–24

GUI-Based Secure Architecture Design for Distributed Community Micro-grid



**Praveen Tiwari, Maj Sunil Kumar Panwar, Bikram Paul,
Pinakeswar Mahanta, and Gaurav Trivedi**

Abstract Power generation from solar photovoltaic (PV) plants depends on multiple factors such as solar radiance and ambient temperature. Effective monitoring and control of the energy generated with the solar PV plants may augment the complete performance of the system. The local controllers regulate switching between solar PV, local battery, community battery, and grid according to the availability of power in each system. The sensor data and user information are stored in the cloud that can be accessed with the Internet of Things (IoT) device for further computation. A Web-based graphical user interface (GUI) has been developed for appropriate monitoring and control of energy flow and also to enable the power pooling. The app gets information from the cloud on which various sensor's data regarding energy pooling are stored by the local/community controllers, and it displays the information that is stored in the cloud. The primary task is to design and develop a Web-based application with sufficient data security. To secure the user data in the cloud, multi-factor authentication and symmetric key encryption are used for authorized access and data encryption. The basic model of the Web-based application is presented in this paper.

Keywords Distributed community micro-grid · IoT · GUI · Identity access management · Solar photovoltaic

P. Tiwari (✉)

Center for Energy, Indian Institute of Technology Guwahati, Guwahati, India

e-mail: praveen.tiwari@iitg.ac.in

M. S. K. Panwar · B. Paul · G. Trivedi

Department of Electronics and Electrical Engineering, Indian Institute of Technology Guwahati, Guwahati, India

P. Mahanta

Department of Mechanical Engineering, Indian Institute of Technology Guwahati, Guwahati, India

1 Introduction

The need for energy is rising rapidly in the developing countries [1]; consequently, effective energy conservation and management is desired in the modern power system operation [2]. This growing demand needs to be matched with additional energy resources. Renewable energy resources such as solar photovoltaic (SPV) are being promoted by the countries due to low production and maintenance costs, and also, it creates a lower impact on the environment by reducing the emissions of CO₂. SPV and fuel cells, which are the leading environment-friendly energies, produce a direct current (DC). Due to the development of highly efficient power converters, DC power distribution system is gaining interest over AC distribution [3]. Community smart DC micro-grid can increase and improve the performance of the network in multiple aspects, such as minimizing the power losses in transmission, reducing reliance on the grid, and economizing the upgrading of smart grid infrastructure. Since micro-grids do not send power over long distances, they require less metal indulge in heavy metal lines, which can make the best use of low to medium voltage systems [4, 5]. This system has to be user-friendly, remotely monitored, and controlled, and also, the appropriate energy trade model should be incorporated in it. Real-time monitoring of various parameters of energy generation with SPV plants is becoming important to augment the complete performance of the SPV systems. Smart home energy management system (SHEMS) augmented with IoT has been proposed for effective usage of SPV [6–8], which enables the user to monitor energy consumption. For the improved monitoring, graphical user interface (GUI) is to be designed, which includes graphically plotted real-time data like temperature, power, current, and voltage, and solar irradiance is reported [9–12]. The GUI applications must be secure to avoid any type of cyber-attack. Various methods to improve the security features of the GUI application are reported [13, 14]. However, there is scope for the development of a Web application for SHEMS with enhanced security. In this paper, the SHEMS is designed for the switching between SPV, battery, community storage, and distribution utility (DU) according to the availability of power in each system. The user information is stored in the ThingSpeak cloud (TC) [15] using IoT devices. When this system is connected to the community (society), the information about the energy consumption and the number of energy units consumed from the DU by each house in the community is sent to the same cloud but from a separate hardware system. The GUI reads information from cloud on which the data about the house power are stored and displays the respective values. It will also be able to calculate the total amount to be paid by the house owner until the current time. The Web-based application is secured with identity access management (IAM) system and two-factor authentication [14, 16]. The rest of the paper is organized as follows: Sect. 2 presents the architecture for GUI design and development. Section 3 describes the security architecture and its implementation. Section 4 presents the result/discussion on the implementation. Finally, the paper concludes with Sect. 5.

2 Architecture for GUI Design and Development

This section elaborates on the basic model, design, and hierarchy of a secure Web-based application. The framework is essentially flexible enough to fit in different application scenarios. Web server-based access is viable for a larger user base and remotely control ability or IoT/FPGA (e.g., Raspberry Pi/Zed board)-based approach where all the power management and transactions can be managed locally. In our current work, we demonstrate our framework and features on an only Web-based application. The GUI has real-time data like temperature, power, current, voltage, and radiance which are (Fig. 1).

Graphically presented using MS Visual Studio (ASP.net). These data are being collected by the sensors in real-time, and controllers push these data to particular cloud storage (e.g., TC) server on a regular interval (N.B. displayed data on Web GUI are a subset of data that are being collected by the storage server which is re-configurable from utility only). By retrieving data from the cloud, the Web application displays the most accurate percentage of power available in the SPV, community battery, and the real-time status of the power. The program flow for developing the Web application is as follows: (1) The first page of the application demands the user with the email id, password, and the time-based one-time password (TOTP). If the account does not exist, then it displays a popup menu saying that the account is invalid than the user needs to do the registration. (2) The application allows the user to create a new account by clicking the button. Do not have an account? Create new? This page demands the name, email id, password, and TOTP; once the user submits it, then these details get registered in the database. (3) If the account exists and user successfully logins, then the data regarding power and voltage of the house(user) are fetched from the ThingSpeak cloud and displayed. The information is then encrypted and stored in the database by a suitable symmetric key. This GUI application has the

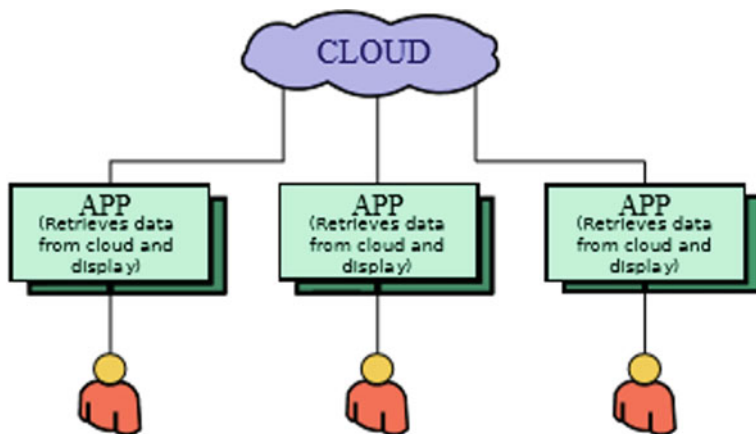


Fig. 1 Cloud-user data sharing framework

following security measures to counter any type of cyber-attack from any unwanted elements. The developed GUI is a Web-based application that is secured through HTTPS with the transport layer security (TLS) protocol for data transfer. My SQL is used for the database as backend, whereas MS Visual Studio is used as a front end to create the Web application. This model is working on identity access management (IAM), which checks both the authentication and the authorization of the user before providing access to the Web application and the data.

3 Security Architecture and Implementation

This section describes the security aspects of our proposed approach for DCM. The first level of security can be incorporated by implementing TOTP on the user login/registration portal. With two-factor authentication, the Web security enhances, as the threat of password interception, a man-in-the-middle attack or eavesdropping drops dramatically. The fundamental structure of two-factor authentication is described in Fig. 2 shown.

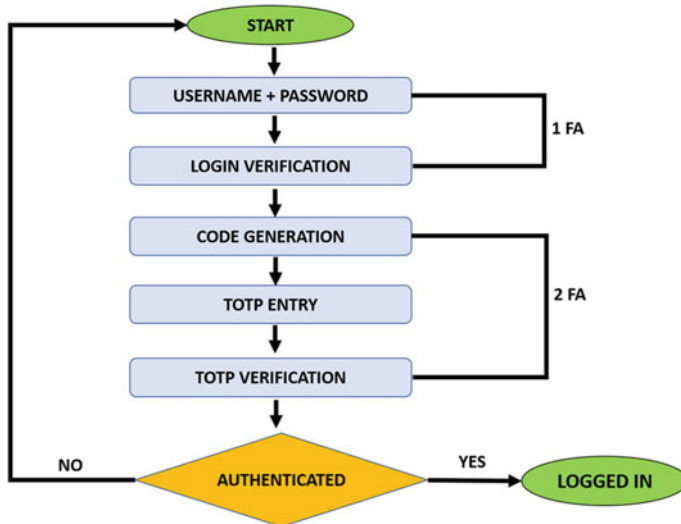


Fig. 2 Two-factor authentication

3.1 Data Sharing Security Using Robust Encryption Algorithm

For building a secure database, it is imperative to encrypt the raw data with some secure and robust encryption strategy. In this endeavor, we added the most commonly used secure symmetric encryption scheme Advanced Encryption Standards (AES)-128 bit [17]. For securing the local data server, symmetric encryption suffices whereas for remote data storage and data processing, private-public scheme can be adopted. The planned methodology is represented below, including the diverse components of the system that is working to process the user data. The projected system represents three major hierarchy units: distributed utility, community, and house. The user has to share data over the open cloud or grid with no security for accessing data. Therefore, in this paper, we have implemented protected data sharing methods on the micro-grid that can be executed for three entities which are as follows:

1. Distributed Utility (DU) Portal
2. Community Portal
3. House (User).

Portal: These entities perform different tasks and respond effectively to their assigned responsibilities. DU Portal: The distributed utility (DU) is the power distribution unit that regulates the operations among various communities. The DU portal acts as an administrator that can manage and grant access to data to various communities and the user. It is also responsible for simultaneously checking the reliable and systematic functioning of all the community and house portals.

Community Portal: The community is freelance to the user portal. All user activities are handled by the community, which means that the users are uploading or sharing their files on the cloud and have access rights given by the community. During this panel, the community can approve or decline the user requests. If the community granted permission to the user, then only the user accesses their account and uploads or shares the data. All files stored by the user can be viewed by the community.

House Portal: The house is the end-user who accesses the data on the cloud. A user is the only affected one whose sensitive data are stored on the cloud; hence, ensuring the safety of the user's data is a must as at the user side, and many actions need to be performed simultaneously like uploading, downloading, and updating of information.

All entities, including DU, community, and the house(user), need to verify the log in via user name/login Id, password, and TOTP, to get access to their respective account. As the authentication is successful, then it is redirected to the home page wherein the user can do various data operations. The security architecture for multi-level encryption process is demonstrated in Fig. 3.

Figure 3 illustrates the hierarchy of encryption applied for encrypting the data of the users. As and when the user uploads a file to the community, it gets encrypted using a symmetric key, which is shared among users by the approval of the community.

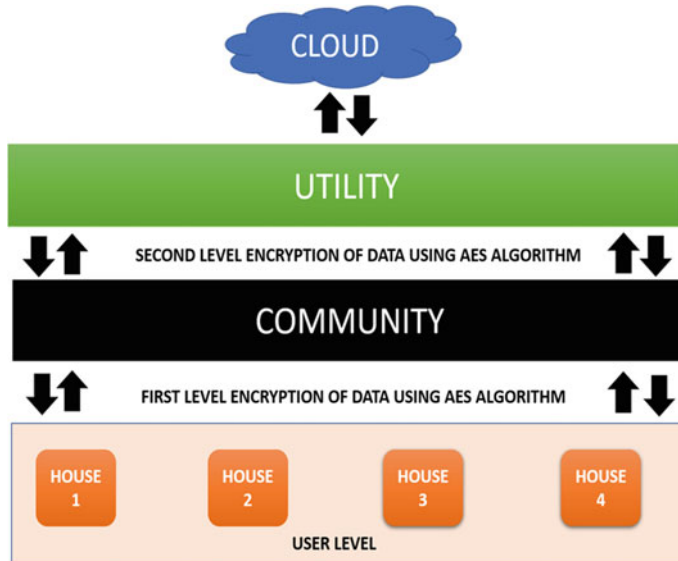


Fig. 3 Data encryption model

Similarly, when the community uploads any data to distribution utility or cloud, it gets encrypted again, using another symmetric key. In this way, the user data are encrypted twice before getting saved to the cloud. Access to the keys also has the same hierarchy. The house portal has only first level key; with this key, house can encrypt its data. Then, community portal has two pairs of keys, both house and community; with these pairs of keys, community can only encrypt data of the houses registered and the same structure for distributed utility who have a super-set of keys (three-layer keys) and have control over all the community registered under it. In the same way, for decryption, the community and the users have their symmetric keys.

3.2 *ThingSpeak Cloud Platform*

In this paper, we have incorporated the ThingSpeak platform as it is an IoT analytic platform that allows us to envisage, aggregate, and examine the live data streams in the cloud. TC provides instant visualizations of data posted by IoT devices to TC as it is often used for prototyping and proof of concept in IoT systems that require analytic. Since it is used in both cross-platform, it is quite reliable. Here, we used TC with Microsoft Visual Studio as a code editor. The system architecture consists of the home page that contains a channel that displays the graphs containing various values. The GUI is designed to take updated values from all sensors through the TC.

4 Implementation of GUI-Based Secure Architecture Design for DCM

In this paper, a Web-based GUI has been developed for DCM. A scaled-down model of DCM is designed to validate the working of the GUI platform. A sensor module is connected to the individual household to find the desired load demand of the respective house. The load demand of an individual house is then transferred to the TC. Another IoT sensor module is connected to a battery, which is considered as the community storage. An 8-channel relay is used for switching the power supply as per the control action of the SHEMS. A set of four houses has been considered for the present work. The setup of the rest houses is the same as the first one. The community controller is common for the four houses, which decides the power trading among the four houses. The detailed description of the experimental setup, including the working of the SHEMS, community controller, etc., is beyond the scope of this paper. For the illustration, two different graphs of user data retrieved from the ThingSpeak platform are presented.

The graphs explain the variation of the required power for a user with variation in time. By using the graph, we can find the values of the dynamic power demand of the house. Figure 4 gives the value of the state of charge of battery storage of community regulator.

The Web-based secure application is developed using Microsoft Visual Studio and C#. It is tested for its reliability while working with many users. The user data faces many security challenges before getting saved in the cloud. For securing user identity and user data, firstly, an HTTPS-based Web application is developed that uses transport layer security (TLS) for Web security. The screenshot of the Web application is presented in Figs. 5, 6, 7 and 8. Secondly, an OTP based authentication framework is used, which provides access to the user after checking its identity and authorization (IAM). Therefore, authorized and authenticated users can only log in to the environment using two-factor authentication.

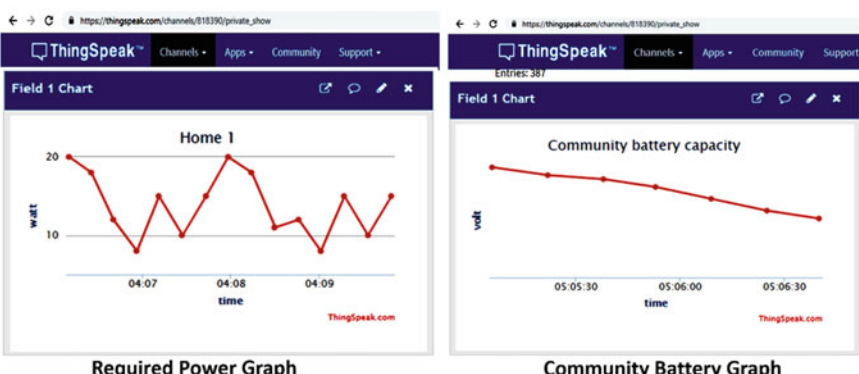
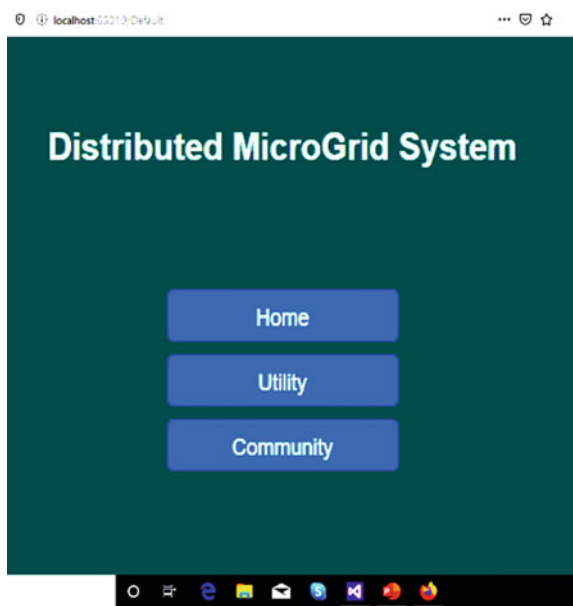
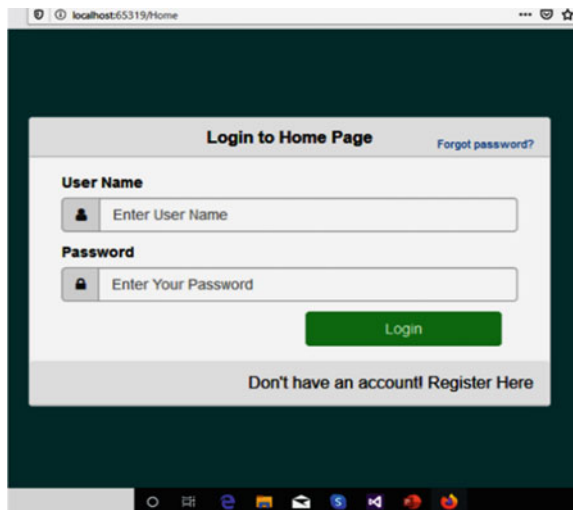


Fig. 4 Related IoT graphs using ThingSpeak

Fig. 5 Home page**Fig. 6** Login/registration page

For data flow and its security, an AES encryption [17] is used, which has consistency and scalability and is easy to implement. A Java-based application is developed to secure the user data by continuously monitoring the data at the server. When the migration of data took place or user uploads any data through an application over the cloud, the user data are then automatically encrypted Fig. 11 without user intervention using the AES-128-bit algorithm and sent to the respective cloud environment.

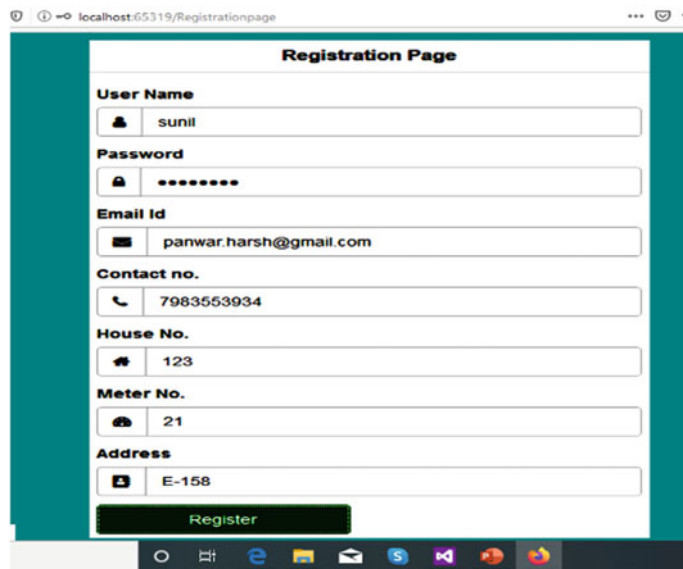
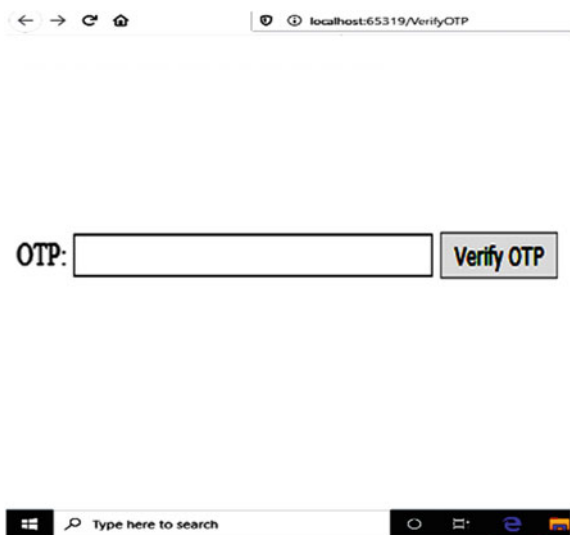


Fig. 7 First time user registration page

Fig. 8 OTP authentication page



If there are any requirements to read the data, it first is decrypted on the user's end. The plain text is not saved, written, or stored anywhere in the database or on to the cloud. The key is also not saved on the cloud since the key might get compromised. To store or save the keys, separate key management schemes are used. The results are shown in Figs. 9, 10 and 11.

Fig. 9 Encryption at cloud (server)

D:\demo\	
Name	Size
battery SoC.xlsx_e	7 KB
current.xlsx_e	7 KB
power generated.xlsx_e	7 KB
power load.xlsx_e	7 KB
user 1 details.xlsx_e	9 KB
user 2 details.xlsx_e	9 KB
user 3 details.xlsx_e	9 KB
user 4 details.xlsx_e	9 KB
voltage.xlsx_e	7 KB

Fig. 10 Encryption at house portal (user)

Network > 172.16.31.117 > demo		
	Name	Size
<input type="checkbox"/>	battery.xlsx_e	7 KB
<input type="checkbox"/>	current.xlsx_e	7 KB
<input type="checkbox"/>	power generated.xlsx_e	7 KB
<input type="checkbox"/>	power load.xlsx_e	7 KB
<input type="checkbox"/>	user 1 details.xlsx_e	9 KB
<input checked="" type="checkbox"/>	user 2 details.xlsx_e	9 KB
<input type="checkbox"/>	user 3 details.xlsx_e	9 KB
<input type="checkbox"/>	user 4 details.xlsx_e	9 KB
<input type="checkbox"/>	voltage.xlsx_e	7 KB

Name	Size
battery SoC.xlsx_e	7 KB
current.xlsx_e	7 KB
power generated.xlsx_e	7 KB
power load.xlsx_e	7 KB
user 1 details.xlsx_e	9 KB
user 2 details.xlsx_e	9 KB
user 3 details.xlsx_e	9 KB
user 4 details.xlsx_e	9 KB
voltage.xlsx_e	7 KB

Fig. 11 Auto checking of non-encrypted files (cloud)

5 Conclusion

In this paper, a Web-based GUI has been developed for distributed community micro-grid. Although the user data faces many security challenges before getting saved in the cloud/grid, for securing user identity and user data, firstly, an HTTPS-based Web application is developed that uses transport layer security (TLS) for Web security. Secondly, an OTP-based authentication framework is used, which provides access

to the user after checking its identity and authorization (IAM). Therefore, authorized and authenticated users can only log in to the environment using two-factor authentication. For data flow and its security, an AES encryption is used that has consistency and scalability and is easy to implement. AES encryption algorithm shows immunity against various kinds of cyber-attacks such as middle man attack, square attack, key, and critical retrieval attack. The user data are shared using multiple encryptions before it gets uploaded to the cloud. The system introduced in this paper provides decisions-based real-time data convention, thus eliminating manual data collection using TC. The Web-based GUI is developed for implementing more functionality in data management, visualization, and analysis to provide better interface and experience to the user.

References

1. Tiwari P, Manas M, Jan P, Nemec Z, Radovan D, Mahanta P, Trivedi G (2017) A review on microgrid based on hybrid renewable energy sources in south-Asian perspective. *Technol Econ Smart Grids Sustain Energy*
2. Anvari-Moghaddam A, Monsef H, Rahimi-Kian A (2016) Optimal smart home energy management considering energy saving and a comfortable lifestyle. In: 2016 IEEE power and energy society general meeting (PESGM), July 2016
3. Lotfi H, Khodaei A (2017) Ac versus dc microgrid planning. *IEEE Trans Smart Grid*
4. Wu L, Ortmeyer T, Li J (2016) The community microgrid distribution system of the future. *Electr J* 29(10)
5. Meena NK, Yang J, Zacharis E (2019) Optimisation framework for the design and operation of open-market urban and remote community microgrids. *Appl Energy* 252:113399
6. Basit A, Sidhu GAS, Mahmood A, Gao F (2017) Efficient, and autonomous energy management techniques for the future smart homes. *IEEE Trans Smart Grid* 8(2):917–926
7. Javaid N, Ullah I, Akbar M, Iqbal Z, Khan FA, Alraje N, Alabed MS (2017) An intelligent load management system with renewable energy integration for smart homes. *IEEE Access* 5:13587–13600
8. Safari A, Fotuhi-Firuzabad M, Lehtonen M (2016) Optimal residential load management in smart grids: a decentralized framework. *IEEE Trans Smart Grid* 7(4):1836–1845
9. Ramya AS, Periyasamy N, Vidhya A, Sundrapandian S, Raja P (2014) Design and development of a GUI for an optimal hybrid energy system. In: 2014 Eighteenth national power systems conference (NPSC) pp 1–6
10. Vallerio KS, Zhong L, Jha NK (2006) Energy-efficient graphical user interface design. *IEEE Trans Mobile Comput* 5(7):846–859
11. Viljoen M, Pienaar C (2013) Graphical user interface control for a solar/battery/hydrogen/fuel cell power plant. In: 2013 Africon, pp 1–5
12. Katole KR, Balwir SP, Badole M (2015) GUI based power management system with power line communication for industries. In: 2015 IEEE international advance computing conference (IACC), pp 1040–1043
13. Malviya S, Dave S (2018) Secure data sharing scheme using cryptographic algorithm for cloud storage. *Int J Appl Eng Res* 13(20):14799–14805
14. Patil A, Zambare K, Yadav P, Wasulkar P, Kimmatkar N (2015) Integration of encryption of file and one time password for secure file accession cloud. *Int J Ad Comput Sci Cloud Comput* 3(1):89–94
15. Mhatre L, Rai N (2017) Integration between wireless sensor and cloud. In: International conference on I-SMAC (IoT in social, mobile, analytics and cloud) (I-SMAC), pp 779–782

16. Aloul F, Zahidi S, El-Hajj W (2009) Two factor authentication using mobile phones. In: IEEE/ACS international conference on computer systems and applications, pp 641–644
17. Soliman SM, Magdy B, Abd El Ghany MA (2016) Efficient implementation of the AES algorithm for security applications. In: IEEE international system-on-chip conference (SOCC), pp 206–210

A Hybrid Protocol for Stop and Wait ARQ in Markov Two States Model



Sanjit Ningthoujam and Swarnendu K. Chakraborty

Abstract In this paper, a hybrid protocol is presented for improving the performance of Stop and Wait (S/W) ARQ with Aggressive Packet Combining (APC) schemes using Markov two states Model. APC protocols are not only implemented to get a correct copy but also to reduce retransmission of duplicate copies. To reduce the retransmission of duplicate copies in conventional ARQ protocols, Packet Combining (PC) and APC have been studied. Thus, the proposed protocol is considered under two states of Markov model i.e., good and bad states channel. The simulation results have shown that in the long period of bad state that the proposed protocol still obtains better in probability of packet error, mean energy consumption, and packet throughput over PC and APC schemes but lower throughput than S/W ARQ.

Keywords PC · APC · Throughput · ARQ · Energy

1 Introduction

Backward Error Correction (BEC) and Forward Error Correction (FEC) are used to transfer data reliably from transmitter (T_x) to receiver (R_x). It is well studied that BEC is good for short distance communication that is for wired network communication. Thus, many researchers have conclusively established that BEC should be attempted for wireless communication as it is cost effective. ARQ is the example of BEC in which erroneous copies are discarded by the receiver but by retransmission of duplicate copies, PC [1, 2] and APC [3] are studied in literature. PC provides 50% throughput which is greater than APC but lower error correction capability. However, in long distance communication, FEC strategy is used but it consumes huge amount

S. Ningthoujam (✉)

School of Computer Science and Engineering, VIT University, Amaravati, Andhra Pradesh, India
e-mail: sanjit.n@vitap.ac.in

S. K. Chakraborty

Department of Computer Science and Engineering, NIT Arunachal Pradesh, Papum Pare, India
e-mail: swarnendu.chakraborty@gmail.com

of energy for error correction code. Many modifications like Multiple Route Packet Combining [4], ARQs, and APC [5–17] have also studied for increasing throughput, tackling various error syndromes and enhancing fast error correction. But, these protocols do not address about energy efficiency. Therefore, to address stated above problem of APC, PC, and modified protocols, we propose this protocol to improve energy efficiency.

The paper is organized as follows. Reviews of conventional PC and APC are briefly described in Sect. 2. Proposed protocol is discussed in Sect. 3. The simulation results and conclusion are discussed in Sect. 4 and 5.

2 Related Works

2.1 *Packet Combining Scheme (PC)*

Let the first and second copies are erroneous and stored at R_x in order to perform XOR operation to identify the erroneous bit location. The identified locations will be applied bit inversion method by using brute force method. The example is shown here:

Assume that original copy: “00001111”

- 1st erroneous copy: “10001111”
 - 2nd erroneous copy: “00000111”
 - 10001111
 - 00000111
-

10001000 (erroneous bits are found at 1st and 5th bit positions from MSB)

- Bit inversion technique will be applied in 1st and 5th position from MSB (if 1 then 0 and vice versa)
- By this technique, original copy will be retrieved. The average number of brute force application will be $2^n - 1$ in general if n bits are found as erroneous. However, in PC technique, if two bits are identified in same position of two erroneous copies, then PC technique will fail. The example is shown here:

Assume original copy: “00001111”

- 1st erroneous copy: “00000111”
 - 2nd erroneous copy: “00000111”
 - 00000111
 - 00000111
-

00000000.

2.2 Aggressive Packet Combining Scheme (APC)

In APC scheme, we have divided into four sections.

- 1st section: assume original copy is “11110000”
- 1st copy—“11110000”
- 2nd copy—“11110000”
- 3rd copy—“11110000”.

In this case, all three copies are error free. Correction probability will be $(1 - P^3)$, where P is bit error probability. Therefore, correction is not required in this section.

- 2nd section: assume original copy is “11110000”
- 1st copy—“01110000”
- 2nd copy—“11110000”
- 3rd copy—“11110000”.

In this case, 1st copy is erroneous and 2nd and 3rd copies are error free. Correction probability will be $(1 - P^2) \times P$, where P is bit error probability. Therefore, correction is required and also possible.

- 3rd and 4th sections: assume original copy is “11110000”
- 1st copy—“01110000”
- 2nd copy—“01110000”
- 3rd copy—“11110000” in 3rd section and “01110000” in 4th section.

In these cases, correction probability will be given by $(1 - P) \times P^2$ and P^3 in 3rd and 4th section. Corrections are not possible in both sections.

3 Proposed Protocol

We assume that the proposed model will be Markov two states Model, good (G) and bad (B) states. The length of the good and bad period will be observed by transmitter. By independent geometrically distributed of random variables with parameter X and Y . It is also assumed that time required to transfer a packet of ‘ n ’ bit size will be having ‘ m ’ slots. Therefore, probability of good and bad period for ‘ n ’ packet size which contain ‘ m ’ slots will be given by Eqs. (1) and (2) (Fig. 1).

$$\text{Prob}(G) = (1 - X)X^m \quad (1)$$

$$\text{Prob}(B) = (1 - Y)Y^m \quad (2)$$

So, the mean length of G and B periods will be given by Eqs. (3) and (4)

$$\alpha = 1/(1 - X) \quad (3)$$

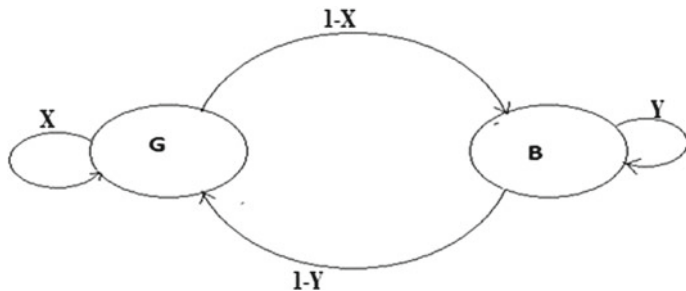


Fig. 1 Markov two states model

$$\beta = 1/(1 - Y) \quad (4)$$

/* Proposed protocol */

Input: P_i : the incoming packets, where $i = 1, 2, 3\dots j$

Output: correct or error packet

1. **If** ($P_{(i=\text{first packet})}$ = correct copy) **Then**
2. Current protocol (C.P) = stop and wait ARQ;
 - a. **If** (test) = correct copy **then**
 - b. C.P = stop and wait ARQ;
 - c. **Else**
 - d. C.P = APC protocol;
 - e. **End**
3. C.P = APC protocol;
 - a. **If** (test) = correct copy **then**
 - b. C.P = stop and wait ARQ
 - c. **Else**
 - d. C.P = APC protocol
 - e. **End**
4. **End**

3.1 Mathematical Analysis

Let ' μ ' be the bit error rate probability in wireless. Let single bit '1' is sent from T_x to R_x and it is received erroneously as '0'. Then, single bit error correction probability is given by Eq. (5).

$$P_{\text{ec}} = 1 - \mu \quad (5)$$

The error correction probability for the n packet size can be given by Eq. (6)

$$P_{\text{ec_}n} = (1 - \mu)^n \quad (6)$$

Therefore, the probability of packet error for n bit packet size is given by Eq. (7)

$$P_{\text{err_}n} = [1 - (1 - \mu)^n] \quad (7)$$

It is assumed that energy (E) consumption for one packet of transmission from T_x to R_x is unit. The energy consumption for transmission of packet is attained higher when retransmission of duplicate copies is occurred. Therefore, the mean energy (E) consumption for proposed protocol will be given by Eq. (8).

$$E = \frac{1}{[(1 - \mu)^{n \times i}]} \quad (8)$$

where i is the number of duplicate copies.

By Markov two states model, total mean length of good and bad states will always be unity.

$$\text{Therefore, } \alpha + \beta = 1 \quad (9)$$

In Stop and Wait ARQ, PC, and APC [18–21], the probability of packet error will be given by Eqs. (10)–(12)

$$\text{PE}_{\text{s/w}} = [1 - (1 - \mu)^n] \quad (10)$$

$$\text{PE}_{\text{pc}} = [1 - (1 - \mu)^n]^2 \quad (11)$$

$$\text{PE}_{\text{apc}} = [1 - (1 - \mu)^n]^3 \quad (12)$$

For the proposed protocol, the probability of packet error will be given by Eq. (13)

$$\text{PE}_{\text{Pro}} = \text{PE}_{\text{s/w}} \times \text{PE}_{\text{apc}} \quad (13)$$

Throughput (TH_{pro}) of the proposed protocol will be given by Eq. (14)

$$\text{TH}_{\text{pro}} = \text{TH}_{\text{s/w}} \times \alpha + \text{TH}_{\text{apc}} \times \beta \quad (14)$$

where $\text{TH}_{\text{s/w}} = (1 - \text{PE}_{\text{s/w}})/(i + \text{PE}_{\text{s/w}})$, $\text{TH}_{\text{apc}} = (1 - \text{PE}_{\text{apc}})/(i + \text{PE}_{\text{apc}})$

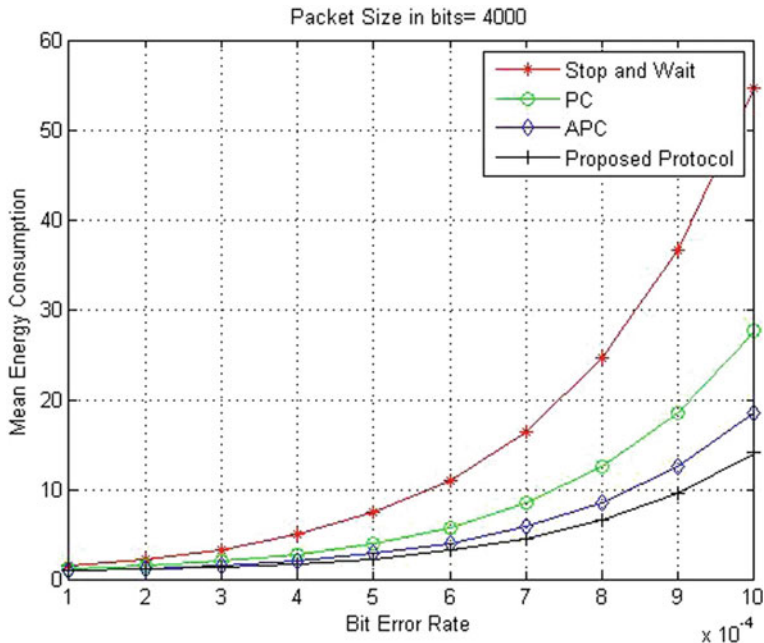


Fig. 2 Mean energy consumption ($\alpha = 0.3$, $\beta = 0.7$)

4 Results and Discussion

The proposed protocol is simulated using MATLAB. The probability of mean length in Bad (B) and Good (G) channel is taken as unity. Therefore, the mean length of ' G ', having short periods $\alpha = 0.3$ and mean length of ' B ', $\beta = 0.7$ having long periods have taken in simulation. The simulation results have shown in Figs. (2, 3 and 4). In the results, the proposed protocol has shown higher throughput than PC and APC but lower to S/W ARQ. Meanwhile, it also provides lower energy consumption by lowering the probability of packet error when bit error rate varies from 10^{-2} to 10^{-4} and packet size of 4000 bits.

5 Conclusion

In this paper, we have studied a new hybrid protocol (APC + S/W ARQ) for enhancing the performance of S/W ARQ using Markov two states model. The simulation results have shown that the proposed protocol obtains better performance in terms of mean energy consumption and probability of packet error. This protocol is attractive for wireless network as the bit error rate is very high. The transmitter will be switched from proposed protocol to S/W ARQ and vice versa as per the mean length

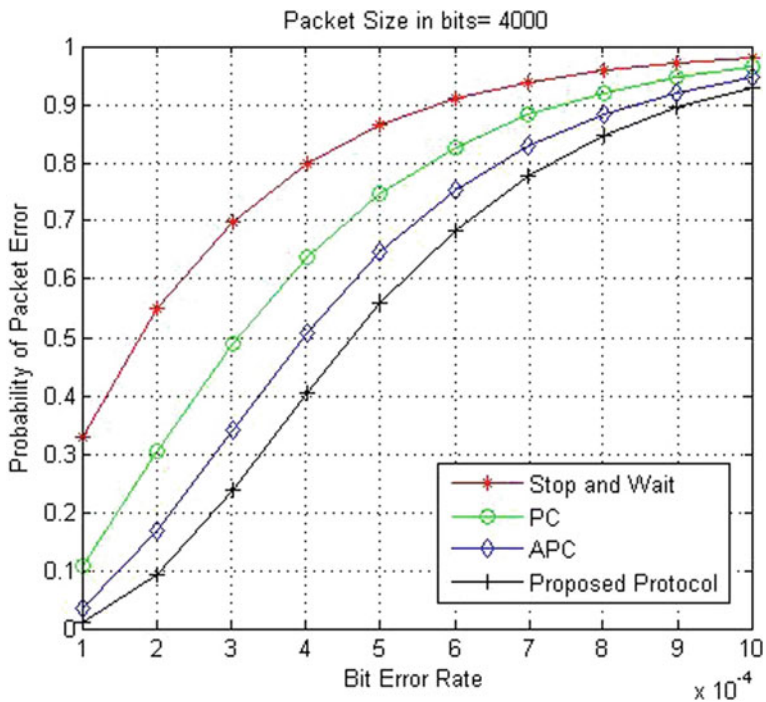


Fig. 3 Probability of packet error ($\alpha = 0.3$, $\beta = 0.7$)

of 'G' and 'B' periods. The proposed protocol is found a bit lower throughput than S/W ARQ but greater than PC and APC when long periods of 'B' and short period of 'G' states. Thus, little difference of throughput may not degrade the performance of proposed protocol due to lower energy consumption and lower probability of packet error.

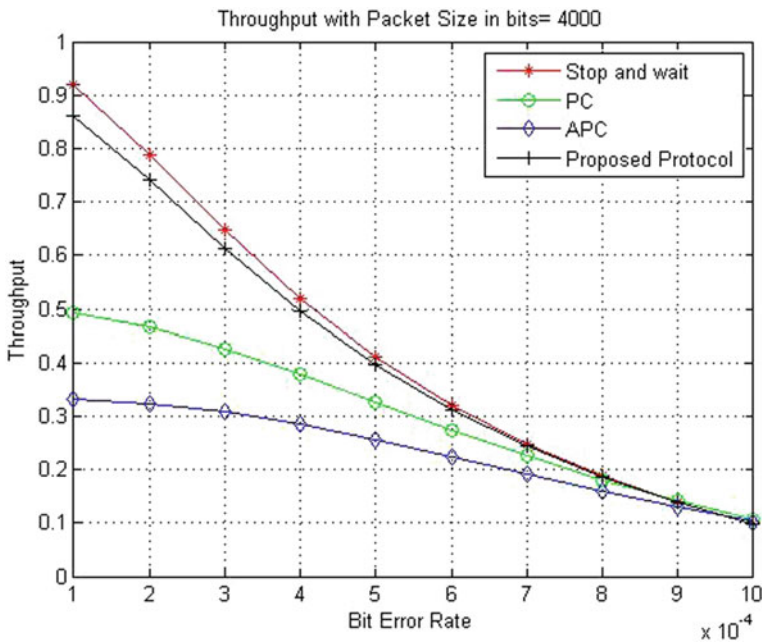


Fig. 4 Throughput ($\alpha = 0.3, \beta = 0.7$)

References

- Chakraborty SS et al (1995) An ARQ scheme with packet combining. *IEEE Comm Lett* 2(7):200–202
- Chakraborty SS (1999) An adaptive ARQ scheme with packet combining for time varying channels. *IEEE Commun Lett* 3(2):52–54
- Leung Y-W (2000) Aggressive packet combining for error control in wireless networks. *Trans Commun* E83(2):38–385
- Hirayama Y, Okada H, Yamazato T, Katayama M (2005) Time-dependent analysis of the multiple-route packet combining scheme in wireless multihop network *Int J Wirel Inf Netw* 42(1):35–44
- Bhunia CT (2001) ARQ-review and modifications. *J IETE Tech Rev* 18:381–401
- Sastry ARK (1974) Improving automatic repeat request (ARQ) performance on satellite channels under high error rate conditions. *IEEE Trans Commun COM-23*:436–439
- Chakraborty SK, Goswami RS, Bhunia A, Bhunia CT (2014) Investigation of two new protocols of aggressive packet combining in achieving better throughput. *J Inst Eng (India): Ser B* 15
- Chakraborty SK, Goswami RS, Bhunia A, Bhunia CT (2015) Studies of several new modifications of aggressive packet combining to achieve higher throughput, based on error correction capability of disjoint error vectors. *J Inst Eng (India): Ser B* 30
- Bhunia CT (2007) Packet reversed packet combining scheme. In: Proceedings of IEEE Computer Society, CIT'07. Aizu University, Japan, pp 447–451
- Ningthoujam S, Chakraborty SK, Bhunia CT (2014) New modified technique of aggressive packet combining scheme with multiple routes selection to get high error correction and throughput. *Int J Ad Electron Commun Syst* 3(5)
- Towsley Don (1979) The shutter go back-N ARQ protocol. *IEEE Trans Commun* 27(6):869–875

12. Wicker SB (1999) Adaptive rate error control through the use of diverse combining and majority logic decoding in hybrid ARQ protocol. *IEEE Trans Comm.* 39(3):380–385
13. Chakraborty SK, Goswami RS, Bhunia A, Bhunia CT (2014) New protocol of aggressive packet combining in gilbert two state model. *IEEE, CIEC, University of Calcutta*
14. Chakraborty SK, Goswami RS, Bhunia A, Bhunia CT (2013) Three new investigations of aggressive packet combining to get high throughput. *Int J Comput Appl USA* (0975–8887) 81(5):41–44
15. Chakraborty SK, Goswami RS, Bhunia A, Bhunia CT (2013) Two new modified schemes of aggressive packet combining schemes in achieving better throughput. In: IEEE, ITNG. IEEE Computer Society, Las Vegas, pp 729–730
16. Ningthoujam S, Chakraborty SK, Bhunia CT (2015) New protocol for aggressive packet combining in gilbert two state model using back up routes to achieve higher throughput. In: Proceedings of ICARCSET-2015, ACM, ICPS, March, 6th–7th, Eluru, Andhra Pradesh, India
17. Ningthoujam S, Chakraborty SK, Bhunia CT (2015) New investigation of aggressive packet combining scheme to reduce transmission delay and three states markov model using multiple routes to increase throughput. *Int J Future Gener Commun Netw* 8(5):157–166
18. Ningthoujam S, Chakraborty SK et al (2017) PC-APC schemes in multipath diversity system to get higher throughput. *Int J Electr Comput Eng* 7(1):337–343
19. Bhunia CT (2005) Information technology, networks and internet. New Age International Publishers, New Delhi
20. Ningthoujam S, Chakraborty SK (2019) Analysis of the adaptive three-modes for PC + MPC + APC techniques using retransmission cycle mechanism. *J High Speed Networks* 25(2):205–220 (IOS Press)
21. Ningthoujam S, Chakraborty SK (2019) A combined techniques of PC + MPC + APC to achieve higher error correction probability and throughput over APC and MPC techniques. *Wirel Pers Commun* 109(3):1–17

Comparative Study on a U-Slot Miniaturized CPW-Fed Multi-band Antenna Applicable for 5G Communication



Kaushal Mukherjee, Amitesh Das, and Sahadev Roy

Abstract In this paper, a compact ($17 \times 20 \times 1$) mm³ coplanar waveguide-fed multi-band antenna has been designed. This antenna consists of a U-Slot over the rectangular patch structure and frequency shifting strips. Various U-Slot structures have been studied in this work for the analysis of the antenna performances. A comparison table between the proposed antenna and similar antennas has been given in the result section. The proposed antenna resonates at 28 GHz, with a bandwidth of 2.62 GHz. Design and simulation of structures are carried out with the help of ANSYS HFSS software and other antenna parameters like field distributions, gain, directivity, impedance bandwidth, resonant frequencies, return loss, and VSWR are also reported in this study.

Keywords Coplanar waveguide (CPW) · Millimeter wave (mmW) · Reflection coefficient (S11) · U-Slot · 5G antenna

1 Introduction

5G is the latest arena of wireless communication standard ahead of today's 4G and 4.5G (LTE advanced) technology. This technology will facilitate users by improving the latency, speed, battery life, and power consumption of the mobile devices. As statistics show that the number of mobile devices in all over the world is expected to cross the 5 billion mark by 2019, so researchers have always looked one step forward beyond today's technology [1]. 5G technology (Fifth generation) will make a massive

K. Mukherjee

Department of Physics, The University of Burdwan, Burdwan, India
e-mail: mukherjeek95@gmail.com

A. Das (✉) · S. Roy

Department of Electronics and Communication Engineering, National Institute of Technology, Arunachal Pradesh, Yupia, India
e-mail: amitesh.engg.84@gmail.com

S. Roy

e-mail: sahadevroy@nitap.ac.in

difference with the existing 4G LTE (Long-Term Evolution) technology and will give birth to a Wireless World Wide Web (WWW) [2]. The major advantages of 5G over existing 4G LTE communication system are wider bandwidth, the finest quality of service, and a data transfer rate of more than 1 Gbps (Gigabits Per Second), etc. [3]. Shannon in his channel capacity theorem explains that data rate is equal to the bandwidth (BW) and the signal-to-noise ratio (SNR) value of the used modulation technique [4].

Some techniques have been suggested by researchers to increase the BW of an antenna for the 5G applications are: by increasing the substrate height [5], by using different size and shapes of ground planes (such as elliptical, circular, etc.) [6], by introducing partial ground planes [7], by the application of dielectric resonator antenna (DRA) [8], or by using the photonic band gap structures [9], etc. Recent researches have given some views on 5G antenna which are as follows: Ali et al. proposed a broadband printed slot antenna applicable for 5G communication [10], Zhang et al. proposed a DRA antenna based on MIMO technology for 5G applications [11], and Yassin et al. proposed a single fed antenna for both 4G and 5G communication [12].

In the present work, the slot technique has been used to develop an antenna for 5G applications. Further, a comparative study on the antenna performances for various sizes and shapes of U-Slot has also been studied here.

Section 2 describes the geometry of the antenna, Sect. 3 describes the simulation result and analysis, and Sect. 4 concludes this work.

2 Antenna Geometry and Parametric Analysis

The concept of bandwidth increment by the application of U-Slot [13] has been used here. Lee et al. proved that a wider bandwidth can be achieved by the application of a U-Slot and exciting the structure with co-axial feeding [14]. In his work, variation in bandwidth and matching in impedance frequency were obtained by tuning the probe position. In our proposed antenna, coplanar waveguide feeding has been used to excite the structure (as co-axial feeding is not suitable for mobile communication) [15] and instead of tuning the probe position, the sizes and shapes of U-slot have been varied to achieve the wider bandwidth. The basic structure of the reference antenna without strip and with strips are shown in Figs. 1 and 2, respectively.

The antenna without strip and U-Slot (Fig. 1) generates two resonant frequencies at 1.72 GHz and 5.37 GHz which are applicable for GSM and WLAN with impedance bandwidths of 0.25 GHz and 0.85 GHz, respectively. These narrow bandwidths do not satisfy the minimum BW requirements of 5G communication as 5G requires BW of almost 1000 times greater than the BW of today's 4G technology.

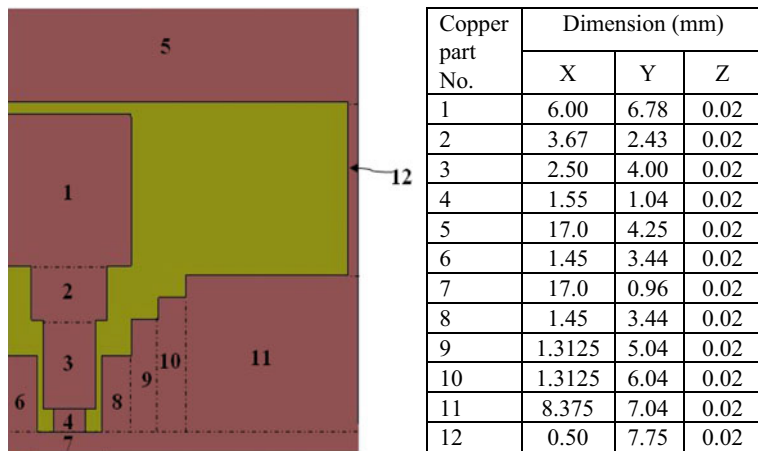


Fig. 1 Top view of antenna without strip

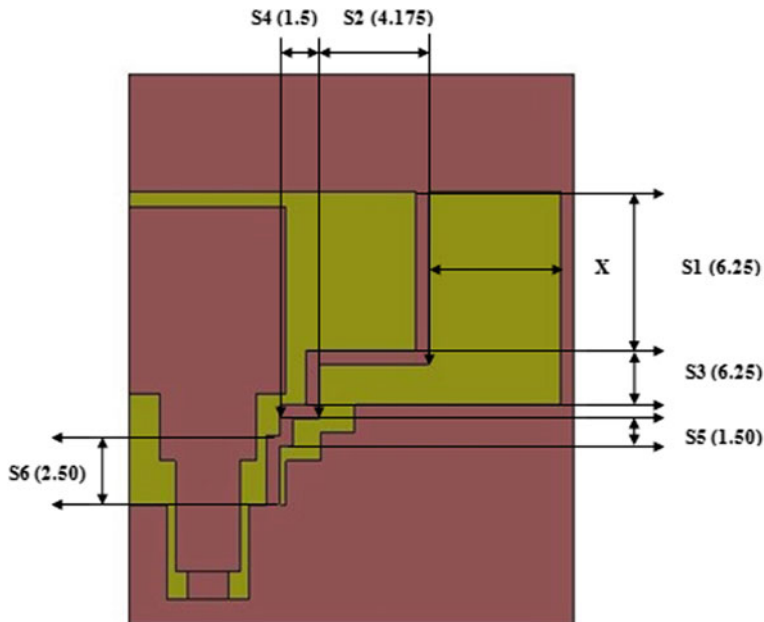


Fig. 2 Top view of antenna with additional strip (all dimensions are in mm)

2.1 Effect of Strip

The antenna without strip and U-Slot (Fig. 1) generates two resonant frequencies at 1.72 GHz and 5.37 GHz with impedance bandwidths of 0.25 GHz and 0.85 GHz, respectively.

The frequency shifting strip (FSS) is responsible for the generation of multiple bands and shifting of the frequency bands to the desired frequency range (Fig. 2). The strip lines can shift the resonant frequency either toward the upper frequency band or toward the lower frequency band, but it is not capable to increase the bandwidth of the antenna. So, the proposed antenna has been modified by the etching of a U-Slot over the patch.

2.2 Effect of U-Slot

This subsection describes the antenna performances due to the variations in size and shape of the U-Slot. As 5G communication always requires a wider bandwidth, so to increase the bandwidth of the proposed antenna, a U-Slot has been etched over the patch. These variations of U-Slot differ the antenna performances in terms of the amount of fringing field generation, the number of frequency band generation, etc. [16]. In the absence of U-Slot, the antenna will generate resonate frequencies within the desired bands, but does not satisfy the bandwidth requirements for 5G communication. By the application of U-Slot over the patch and by tuning the size and shape of the U-Slot, a wider bandwidth of 4.54 GHz is achieved in this work. In the absence of the U-Slot, maximum bandwidth of 2.62 GHz can be achieved.

2.3 Combined Effects of Strips and U-Slot

The combined effect of strips and U-Slot are explained here. These strips are responsible for the generation of multiple bands and shifting of the frequency bands to the desired frequency range. The strip line can shift the resonant frequency either toward the upper frequency band or toward the lower frequency band, but is not capable to increase the bandwidth of the antenna. So, the proposed antenna has been modified by etching of a U-Slot over the patch. In the presence of both the strips and U-Slot, the proposed antenna (Fig. 3) generates a wider bandwidth of 4.54 GHz. So, strips are used to shift the frequency range of the desired frequency band, and the combination of U-Slot and strip are used to achieve a maximum amount of bandwidth within the desired frequency band. The proposed antenna covers two 5G frequency bands, i.e., 28 GHz and 37 GHz (as announced by FCC) and also applicable for Wi-Fi.

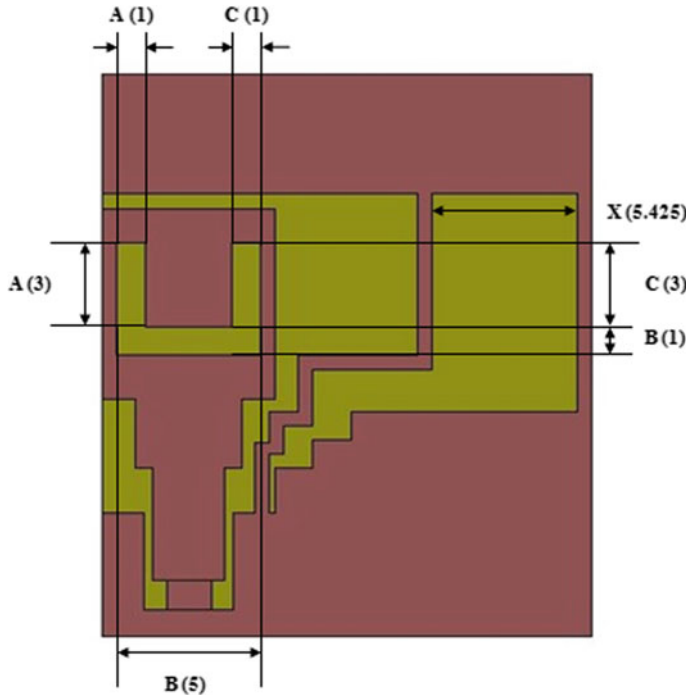


Fig. 3 Top view of proposed antenna

The antenna without strip and U-Slot (Fig. 4a) generates two resonant frequencies at 1.72 GHz and 5.37 GHz with impedance bandwidths of 0.25 GHz and 0.85 GHz, respectively.

The antenna with strips and without U-Slot (Fig. 4b) generates operating bands at 1.702 GHz and 5.802 GHz with reflection coefficients of -14.51 dB and -26.19 dB, respectively. Impedance bandwidth obtained from this antenna are of 0.57 GHz and 0.98 GHz. The antenna with U-Slot in reverse direction (Fig. 4c) generates resonant frequencies at 4.82 GHz, 12.58 GHz, 15.02 GHz, 18.34 GHz, 21.28 GHz, 27.12 GHz, 33.52 GHz, and 38.30 GHz with reflection coefficients of -16.93 dB, -16.46 dB, -16.25 dB, -19.54 dB, -22.37 dB, -15.61 dB, -16.87 dB, and -22.74 dB. Impedance bandwidths of the generated resonant frequencies are 0.32 GHz, 0.54 GHz, 0.82 GHz, 0.98 GHz, 1.08 GHz, 3.42 GHz, 3.06 GHz, and 2.36 GHz, respectively.

Antenna with narrow U-Slot (Fig. 4d) generates resonant frequencies at 5.18 GHz, 17.88 GHz, 20.58 GHz, 27.22 GHz, 33.74 GHz, and 38.40 GHz with reflection coefficients of -13.17 dB, -15.65 dB, -10.88 dB, -13.57 dB, -14.56 dB, and -11.22 dB respectively. Impedance bandwidths of the generated resonant frequencies are 0.10 GHz, 0.82 GHz, 1.66 GHz, 3.50 GHz, 3.72 GHz, and 0.9 GHz, respectively. The antenna is further investigated with Dual U-Slot (Fig. 4e), generates resonant

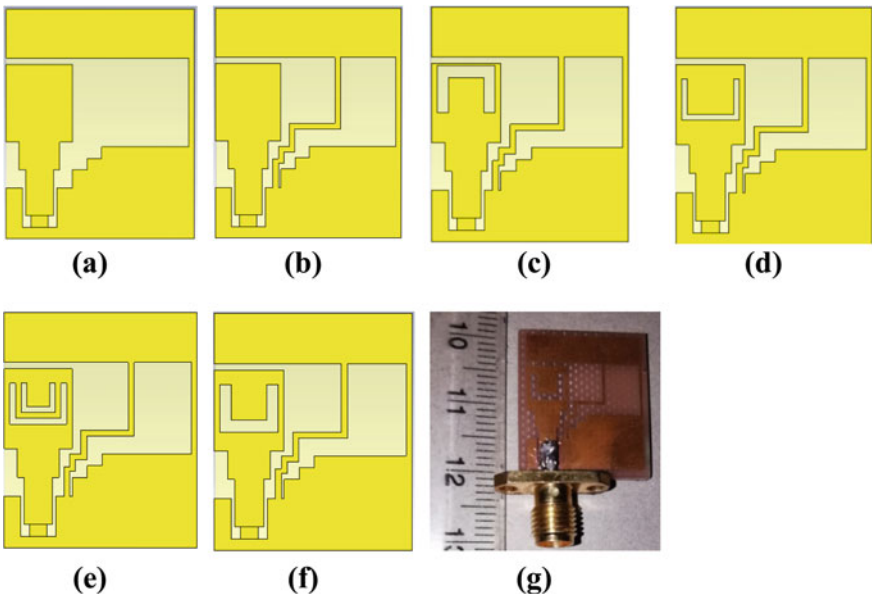


Fig. 4 Progress toward the proposed antenna **a** without strip and U-Slot, **b** with strip without U-Slot, **c** reverse U-Slot, **d** narrow U-Slot, **e** dual U-Slot, **f** proposed antenna, and **g** fabricated antenna

frequencies at 5.18 GHz, 16.46 GHz, 18.30 GHz, and 25.96 GHz with reflection coefficients of -13.10 , -18.78 dB, -36.92 dB, and -13.69 dB, respectively. Impedance bandwidths of the generated resonant frequencies are 0.12 GHz, 0.82 GHz, 1.66 GHz, and 3.49 GHz, respectively.

Proposed antenna (Fig. 4f) with single U-Slot generates resonant frequencies at 5.0 GHz, 17.62 GHz, 20.44 GHz, 28 GHz, and 37 GHz with reflection coefficients of -10.02 dB, -23.59 dB, -28.20 dB, -21.01 dB, and -29.08 dB, respectively. Impedance bandwidths are 0.02 GHz, 1.4 GHz, 1.28 GHz, 2.62 GHz, and 4.54 GHz, respectively.

3 Result Analysis and Discussion

By analyzing the design variations, it is observed that maximum bandwidth of 4.54 GHz with a reflection coefficient of -29.08 dB can be obtained from the proposed antenna with single U-Slot which is having length = 1 mm, width = 3 mm, and height = 1 mm as dimension as shown in Fig. 4f. If the length of patch increases, then the frequency will shift toward lower frequency band, and if the length of the patch decreases, then the frequency will shift toward the upper frequency band [17]. The mmW frequency band offers a wider bandwidth to the users which allow

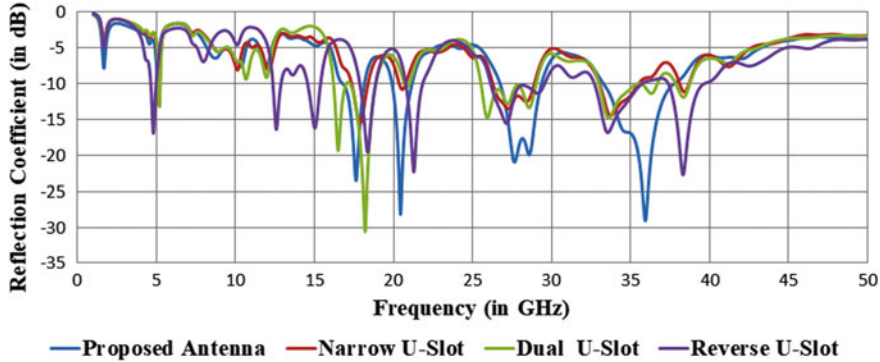


Fig. 5 Reflection coefficient plot by U-Slot variation

the users to connect their home appliances by using IoT and also provides faster transfer of data rate. The proposed antenna not only provides higher speed to the mobile users but also will be used in the fields such as medical, agricultural, and many others. This technology will facilitate people of urban and semi-urban areas by improving the traffic control system with real-time data processing.

The design theory involves the concept of three neighboring resonances, one of them is from TM_{01} mode of the patch, another one from the U-Slot, and the last one is from the strips. Using two neighboring resonance, an increment in the BW up to 30% is achievable. If a third resonance appears (that will appear if co-axial feeding is used instead of CPW feeding), then BW can be increased up to 40%.

In the presence of three resonances, BW is increased up to 42%. Achievable bandwidth with only one resonance is about 0.85 GHz, when two neighboring resonances appear, then the bandwidth is incremented up to 31% (2.62 GHz), and with three resonances, bandwidth is raised up to 42% (4.54 GHz) with a VSWR value within 1 to 2 (Fig. 5). Figure 6 represents the reflection coefficient plot which compares the simulated result with measured result.

The comparisons between proposed antenna and few relevant antennas have been summarized and presented in Tables 1 and 2.

As shown in Fig. 7, radiation patterns of the proposed antenna illustrate that far-field distribution and bandwidth are inversely related to each other. With the increment in bandwidth, the area covered by fields (both E and H) reduces linearly.

Surface current distribution of the proposed antenna at 28 GHz in Fig. 8a shows the charge accumulation and dissipation points. The far-field three-dimensional gain plot is presented in Fig. 8b with a maximum gain of -30 dB .

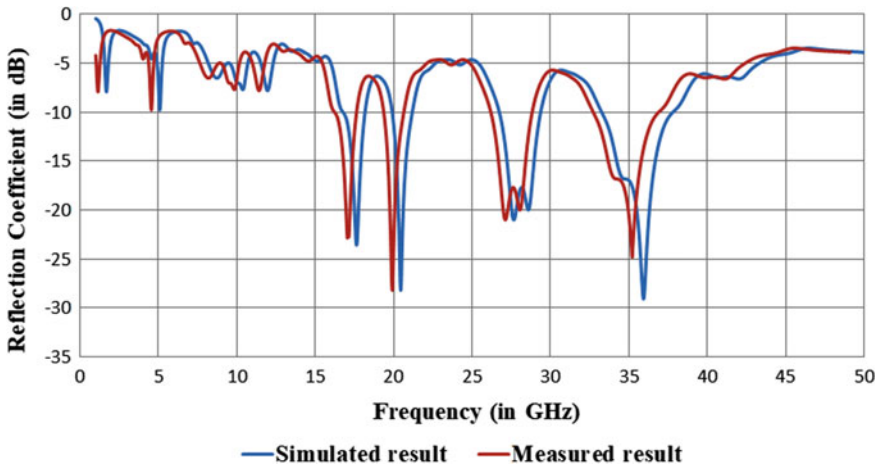


Fig. 6 Reflection coefficient plot of simulated and measured result

4 Conclusion

A miniaturized coplanar waveguide-ed multi-band antenna applicable for 5G communication is presented in this work. A comparative study of various sizes and shapes of U-Slot has also been reported here. The proposed antenna operates at 28 and 37 GHz of the 5G frequency band with a wider bandwidth (up to 4.54 GHz). An excellent far-field radiation pattern with a satisfactory amount of gain of 5 dBi is achieved. For better performances, the substrate material can be replaced by RT Duriod (dielectric constant of 2.2), but it will increase the cost of the antenna. The concept U-Slot has been used over the dual-band antenna to achieve a wider bandwidth up to near about 4.6 GHz. Again, mobile integration requires an antenna with compound semiconductor (such as GaAs) as a substrate material, which will also increase the cost of the antenna. To resolve these cost issues, the proposed antenna can be applicable in the cell towers also, where an antenna with FR4 as a substrate material, will overcome those problems. The proposed antenna is appropriate for both cellular and wireless applications.

Table 1 Analysis of performances between few relevant antennas

Antenna	Dimension (mm) ³	Frequency band at -10 dB (GHz)	Center freq. (GHz)	Bandwidth at -10 dB (GHz)	Applications
Ref. [7]	—	01.60–01.85	01.72	00.25	GSM
		04.95–05.80	05.37	00.85	Wi-Fi/WLAN
Antenna with FSS only	S1 = 0.50 × 6.25 × 0.02 S2 = 4.175 × 0.5 × 0.02 S3 = 0.50 × 6.25 × 0.02 S4 = 1.50 × 0.50 × 0.02 S5 = 0.50 × 1.50 × 0.02 S6 = 0.50 × 2.50 × 0.02	01.51–02.06 04.43–06.70	1.702 5.802	00.55 02.27	GSM1800/1900 Wi-Fi/WLAN 5.2, 5.5 & 5.8 GHz
Proposed antenna	FSS S1 = 0.50 × 6.25 × 0.02 S2 = 4.175 × 0.5 × 0.02 S3 = 0.50 × 6.25 × 0.02 S4 = 1.50 × 0.50 × 0.02 S5 = 0.50 × 1.50 × 0.02 S6 = 0.50 × 2.50 × 0.02 U-Slot A = 1.0 × 3.0 × 1.0 B = 5.0 × 1.0 × 1.0 C = 1.0 × 3.0 × 1.0	04.98–05.02	05.00	00.02	Wi-Fi
		16.76–18.16	17.62	01.40	5G
		19.90–21.18	20.44	01.28	
		26.74–29.36	28.00	02.62	
		34.26–38.80	37.00	04.54	

Table 2 Comparison between proposed antenna and few relevant antennas

Antenna	Substrate dimension (mm)	Frequency band at – 10 dB (GHz)	Center freq. (GHz)	BW at – 10 dB (GHz)	Application	VSWR	
[7]	17 × 20 × 1	1.51–2.06	1.702	0.55	GSM1800/1900	1.05	
		4.43–6.70	5.802	2.27	Wi-Fi/WLAN 5.2, 5.5 & 5.8 GHz	1.10	
[18]	6 × 6.2 × 0.5	37.03–38.97	38.00	1.94	5G	1.30	
		53–55	54.00	2.00	5G	1.64	
[19]	11 × 8 × 0.5	27.29–29.31	28.30	2.02	5G	1.53	
Proposed antenna	17 × 20 × 1	04.98–5.02	05.00	0.02	5G	Data rate	1.95
		16.76–18.16	17.62	1.40		06.24 Gbps	1.41
		19.90–21.18	20.44	1.28		05.70 Gbps	1.08
		26.74–29.36	27.66	2.62		11.68 Gbps	1.19
		33.26–37.80	35.92	4.54		20.24 Gbps	1.07

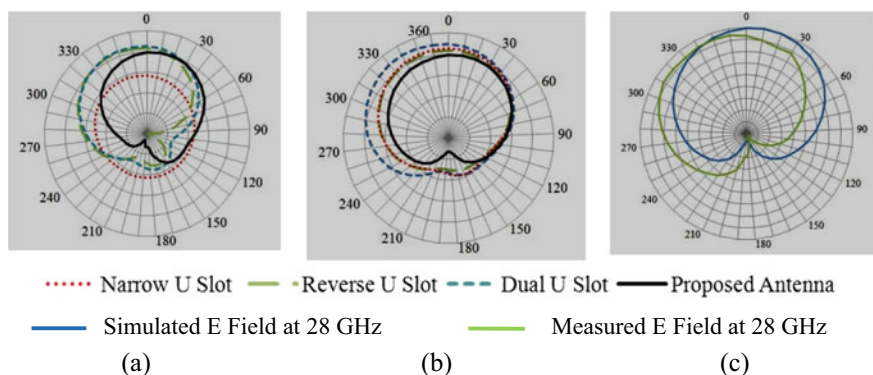


Fig. 7 Radiation pattern plots: **a** simulated H Field at 28 GHz, **b** simulated E Field at 28 GHz, and **c** measured E Field at 28 GHz

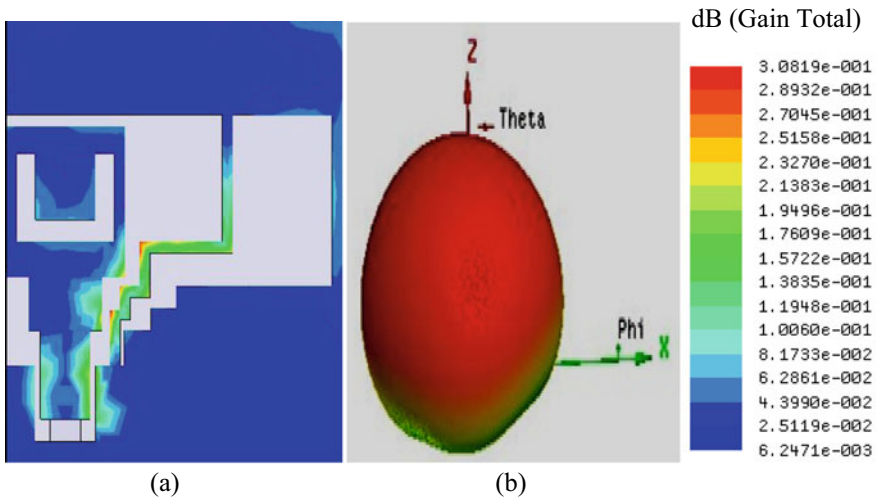


Fig. 8 Electric field distribution **a** and far-field gain plot **b** of the proposed antenna at 28 GHz

References

1. Zhang S, Cai X, Zhou W, Wang Y (2018) Green 5 g enabling technologies: an overview. *IET Commun* 13:135–143
2. Al-Turjman F (2019) 5G-enabled devices and smart-spaces in social-IoT: an overview. *Future Gen Comput Syst* 92:732–744
3. Feng M, Mao S (2019) Dealing with limited backhaul capacity in millimeter-wave systems: a deep reinforcement learning approach. *IEEE Commun Maga* 57:50–55
4. Paolo B, Stefano B, Giulio C, Andrea M, Rusek F, Alessandro U (2014) Modulation formats and waveforms for 5G networks: who will be the heir of OFDM?: an overview of alternative modulation schemes for improved spectral efficiency. *IEEE Signal Process Maga* 31:80–93
5. Colburn JS, Rahmat-Samii Y (1999) Patch antennas on externally perforated high dielectric constant substrates. *IEEE Trans on Antennas Propag* 47:1785–1794
6. Soranun J, George K (2004) A class of shaped deficit round-robin (SDRR) schedulers. *Telecommun Syst* 25:173–191
7. Koohestani M, Moghadasi MN, Virdee BS (2011) Miniature microstrip-fed ultra-wideband printed monopole antenna with a partial ground plane structure. *IET Microwaves Antennas Propag* 5:1683
8. Mashhadi SHH, Niaz MW, Jiao YC, Chen J (2019) Broadbeam coplanar-parasitic rectangular dielectric resonator antenna. *Progress Electromagnet Res* 81:55–66
9. Alam MS, Islam MT, Misran N (2012) A novel compact split ring slotted electromagnetic bandgap structure for microstrip patch antenna performance enhancement. *Progress Electromagnet Res* 130:389–409
10. Abd El-Hameed AS, Barakat A, Abdel-Rahman AB, Allam A, Pokharel RK, Yoshitomi K (2018) Broadband printed-dipole antenna for future 5G applications and wireless communication. In: IEEE radio and wireless symposium (RWS), pp 106–108
11. Zhang Y, Deng JY, Li MJ, Sun D, Guo LX (2019) A MIMO dielectric resonator antenna with improved isolation for 5G mm-wave applications. *IEEE Antennas Wirel Propag Lett* 18:747–751
12. Mohamed ME, Abdallah HA, El-Hennawy EA, H. S. (2018). Single-fed 4G/5G multiband 2.4/5.5/28 GHz antenna. *IET Microwaves Antennas Propag* 13(3):286–290

13. Khodaei GF, Nourinia J, Ghobadi C (2008) A practical miniaturized U-slot patch antenna with enhanced bandwidth. *Prog Electromagnet Res* 3:47–62
14. Chow YL, Chen ZN, Lee KF, Luk KM (1998) A design theory on broadband patch antennas with slot. *IEEE Antennas Propag Soc Int Sym* 2:1124–1127
15. Chu H, Li P, Zhu XH, Hong H, Guo Y (2019) Bandwidth improvement of center-fed series antenna array targeting for base stations in offshore 5G communications. *IEEE Access* 7:33537–33543
16. Radavaram S, Pour M (2018) Wideband radiation reconfigurable microstrip patch antenna loaded with two inverted U-slots. *IEEE Trans Antennas Propag* 67:1501–1508
17. Tighezza M, Rahim SKA, Islam MT (2018) Flexible wideband antenna for 5G applications. *Microwave Opt Tech Lett* 60:38–44
18. Imran D, Farooqi MM, Khattak MI, Ullah Z, Khan MI, Khattak MA, Dar H (2018) Millimeter wave microstrip patch antenna for 5G mobile communication. In: International conference on engineering and emerging technologies, pp 1–6
19. Outerelo DA, Alejos AV, Sanchez MG, Isasa MV (2015) Microstrip antenna for 5G broadband communications: Overview of design issues. In: IEEE international symposium on antennas and propagation and USNC/URSI national radio science meeting, pp 2443–2444

An Experimental Investigation of FPGA-Based LMS Algorithm for Adaptive Noise Cancellation



Abinash Patnaik, Rajesh Kumar Patjoshi, and Rakhee Panigrahi

Abstract Desirable along with undesirable information are carried through signals. Adaptive noise elimination is a substitute method for estimating signals spoiled through additive interferences and noise. This process necessitates two inputs such as primary input comprising polluted signal and reference input comprising desired signal. The primary input is filtered adaptively and deducted from the desired signal to attain error signal, and the adaptive algorithm performs in closed loop manner to reduce the error signal. The adaptive noise cancellation has been designed via two methodologies. One is model-centered methodology while another is FPGA-based methodology. In case of model-centered methodology, MATLAB/Simulink is employed, and the simulation results are observed through virtual oscilloscope. In FPGA-based methodology, Quartus II IDE tool of Altera is utilized for hardware implementation on Altera DE2 development board.

Keywords FPGA · Altera DE2 board · Matlab · Simulink · Adaptive filter · LMS algorithm · Verilog design

1 Introduction

Usages of digital signal processing enforce significant checks upon power disruption, area, speediness, and price [1]. Accordingly, model tool should be thoroughly selected. The most familiar tools for purpose of such applications are DSP, ASIC, and FPGA. The DSP utilized for mathematical tasks cannot handle excessive sampling

A. Patnaik (✉) · R. K. Patjoshi

Department of Electronics and Communication Engineering, National Institute of Science and Technology, Berhampur, India

e-mail: avinashpatnaik1998@gmail.com

R. K. Patjoshi

e-mail: rajeshpatjoshi1@gmail.com

R. Panigrahi

Department of Electrical Engineering, Parala Maharaja Engineering College, Berhampur, India

e-mail: rpanigrahi99@gmail.com

rate appliances owing to its serial architecture. However, ASIC meets shortage of flexibility and requires extended proposal cycle [2]. The FPGA can recompense the shortcomings of DSP as well as ASIC [3]. Henceforth, FPGA has developed the top platform for proposal of signal processing scheme owing toward their upper bandwidth and better liveness through their parallel design [4]. The primary aim of this paper is to explore usage of FPGA structure for adaptive noise cancellation through model-based and FPGA-based approaches. Two approaches are considered here, Model based and FPGA based. In model-built approach, MATLAB/Simulink is employed to observe the different outputs as continuous verification of adaptive noise cancellation system is achieved. In FPGA-based approach, there is a need of developing Verilog code for LMS algorithm [5], FIR filter, I2C controller [6], ADC, DAC, and mixed signal modules. These Verilog codes are compiled using Quartus II IDE tool of Altera and generate the configuration file, which are dumped into the FPGA to observe the operation [7]. The basic purpose of the paper is terminating the noise from a corrupted or tainted signal and getting preferred signal as output.

The paper has been structured as given below. Here, Sect. 2 defines proposal structure of the system. The system-level explanation is described in Sect. 3. Layout for model- and FPGA-built design is provided in Sect. 4. Hardware implementation process is described in this section. Conclusion and the forthcoming expansion of the paper are prescribed in Sect. 5 followed by References.

2 Algorithm Description

Adaptive filters are computational tools that effort to do the modeling of the correlation concerning dual signals occurring at actual time upon or using an iterative method. These filters, which are basically compatibility tools, are accomplished as an assembly of entailing program commands functioning on above of an arithmetical handling appliance. These devices can be a microprocessor or a chip functioning DSP. These devices can also be comprising of established logic operations, which has been realized upon a field-programmable gate array (FPGA) or has been executed on a VLSI integrated circuit [8]. Still, most important task of the above-mentioned filter has been measured independently then of the particular physical attainment that it receives [9, 10]. Because of this, the mathematical model of adaptive filter is decided as contrasting to their particular accomplishments in software or as well as hardware.

An adaptive filter can be distinct through only four features:

1. The *signals* can be managed through filter.
2. The *structure* describes the way the output signal, that is coming out from the computational tool, is calculated using its own input signal.
3. The affiliation among the input and output of the mentioned filter could be changed, by altering the structure which consists different *parameters*. The parameters are also very much accustomed from one particular time prompt to another, which is designated by adaptive algorithm.

Fig. 1 Block diagram of adaptive filter

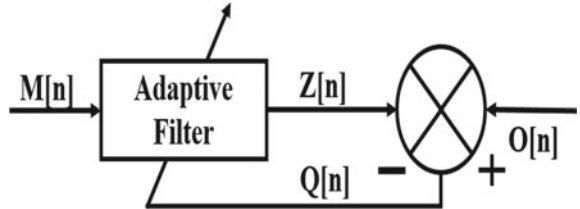


Figure 1 displays a block diagram, where an individual sample, i.e., a digital input signal $M[n]$, is given to adaptive filter. This device calculates the resultant output sample $Z[n]$ at time n . The arrangement is not significant for adaptive filter, excluding the point that it comprises modifiable factors whose amounts affect directly, how $Z[n]$ will be calculated. The output signal is related with another signal $O[n]$, which is known as desired signal, by deducting the two given sample signals at time n . This difference response is specified as follows.

$$Q(n) = O(n) - Z(n) \quad (1)$$

where $Q(n)$ is an error indication. Here, mentioned signal can be served through the way which modifies or adjusts the factors confined by filter which can be ranged in time, i.e., starts from n and goes until $(n + 1)$ through a precise method. Following method of reworking has signified through a slanted arrow which goes through filter block shown as above figure. When time catalog is increased, which is n , the output of the adaptive filter will become improved match as compared with preferred response signal is hoped via adaptation procedure, which may lead to decline of the value $Q[n]$ as time goes on. Here, in the prearranged framework, an adaptive process is responsible for the automatic adjustment of filter weights. Interrelated with other algorithms, LMS algorithm is comparatively easy and straightforward. It is not related with the computation of correlation function as well as inversion of matrix.

The steps regarding LMS algorithms are presented below.

1. Filter output

$$Z(n) = \sum_{l=0}^{k-1} M[n-l]w_l n \quad (2)$$

2. Estimation error

$$Q(n) = O(n) - Z(n) \quad (3)$$

3. Adaptation weight

$$W_l[n + 1] = W_l[n] + u_M[n - l]Q[n] \quad (4)$$

where $Z[n]$, $O[n]$, $Q[n]$, $W[n]$, $W_l[n + 1]$ and u represent output signal, desired signal, error signal, old value of weight, updated value of the weight, and step size of algorithm, respectively.

3 System-Level Description

Figure 2 displays a topmost level test arrangement, where peripherals have been interfaced with Altera DE2 equipment. The above-mentioned peripherals include a personal computer, an oscilloscope, and a waveform or signal generator. The pattern file of FPGA, which is contained by the personal computer, is downloaded via JTAG cable, and the input signal having noise is served from the signal generator [11, 12]. Also, the response of the filter is perceived through oscilloscope. This is a principal arrangement necessitated in FPGA for any sort of signal processing.

The LMS design architecture in FPGA [13, 14] is presented in Fig. 2. The I2C clock carrying a frequency of 10 kHz has been generated using 50 MHz clock. The external codec supplies a clock, bearing a frequency of 27 MHz which gotten into a FPGA clock PLL. This results in producing a AUDIO_XCK master clock having a frequency of 18.4 MHz. The realization of audio bit clock and as well as audio left ~ right clock is done using the master clock. Digitalization of the external noise is done with the help of audio codec, which goes into the FPGA as AUD_ADC_LRCK clock. Addition to this, using rate of audio bit clock, the AUD_ADC_DATA signals are also maintained. The AUD_ADC_DATA, which is a 16 bit serial data, is transformed as parallel via SIPO module. This data is then delivered to MUX 1, to pick external noise

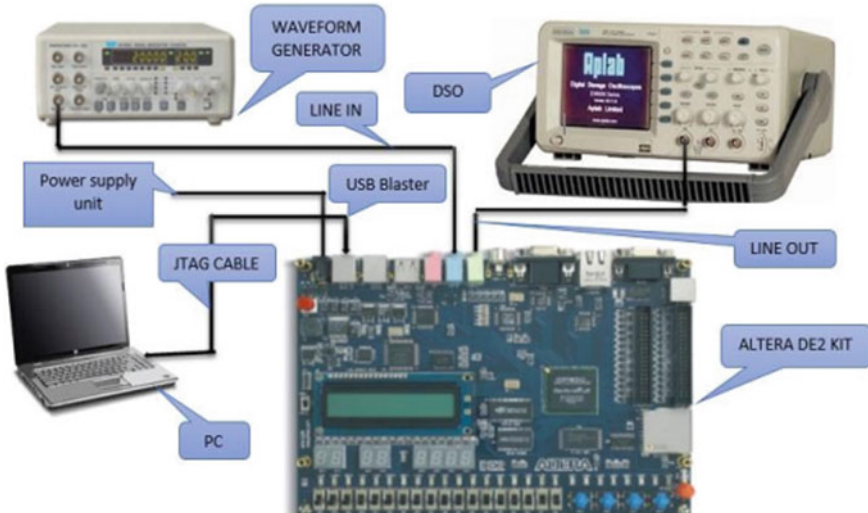


Fig. 2 Topmost level block diagram

mixed signal or internal noise mixed signal, which are the outputs of signal generator and sine LUT, respectively. $M[n]$, $O[n]$, $Z[n]$, and $Q[n]$ are the four parameters comprised by LMS adaptive filter block, which are applied upon MUX 2 to observe the outcomes using the switching process. MUX 3 is utilized for choosing only one signal, i.e., either adaptive output signal or external raw signal. After that, the output of MUX 3 is further delivered into MUX 4, where it will choose the internal pure sine wave signal or it will choose processed signal. PISO procedure is then performed for witnessing the outputs serially through oscilloscope (Fig. 3).

The present work considers the noise signal generated through Verilog program internally in FPGA, and hence, there is no external source connected to the FPGA setup. There are 18 DPDT switches totally accessible through DE2 board. Switch 13 is utilized to choose the internal sine wave or processed internal noisy sine wave. At the time, when switch 13 is made OFF, it will yield internal sine wave and yield processed noisy sine wave as input when it is made ON. Switch 17 is utilized to pick out internal sine signal or to pick out the adapted signal. Here, yielding of internal sine signal and adapted sine signal depends upon the OFF and ON condition of switch 17. It yields internal sine signal, when the switch is in OFF condition and vice versa.

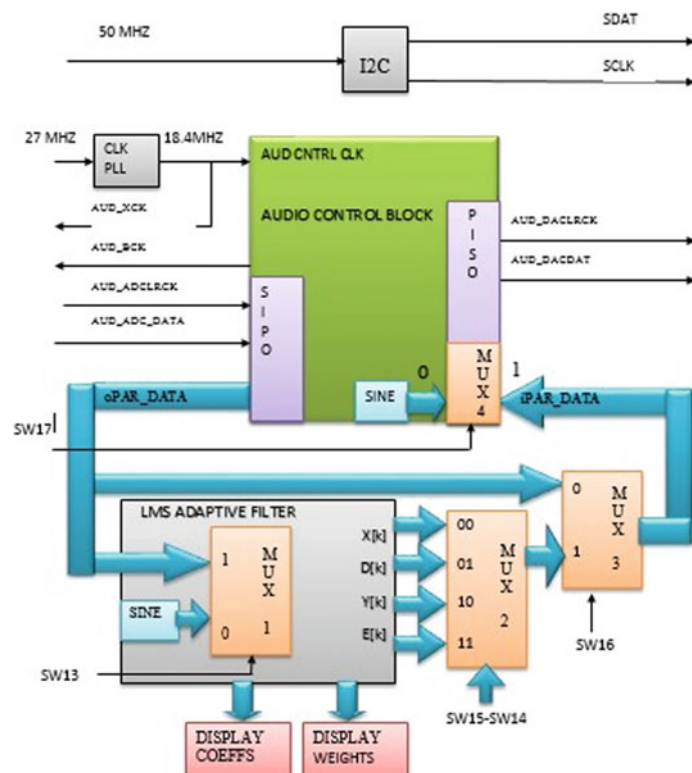


Fig. 3 Internal operation diagram

Switch 16 is used to choose the external signal or the adapted signal. When it is in OFF condition, receives the external signal and receives adapted signal when it is in ON condition as output. Since adapted output result is necessitated, switches 16 and 17 are remained to be ON. Switches 15 and 14 are used to realize all the outputs of mentioned filter. $M[n]$, which is the input signal, is displayed while switches 15 and 14 stay in OFF condition. When the prior switch is made OFF and the later switch is made ON, we get the $O[n]$ signal as output which is the desired signal, and we will get the $Z[n]$, which is the desired signal by using the vice versa condition. When both switches stay as ON, we can get the error signal $Q[n]$ in the oscilloscope. The peripherals are described as follows:

Oscilloscope: Digital oscilloscope has been used for showing the results. **Audio codec:** WM8731 is a stereo codec, which is also low power. It is also incorporated a headphone driver. This codec is generally considered for speech and MP3 players along with recorders. Stereo 24-bit multi-bit sigma delta ADCs and DACs are employed for over sampling of decimation filter, as well as digital interpolation. To maintain the digital audio input, the length of the word must stay between 16 and 32 bits, while the rate of sampling should be varying between 8 and 96 kHz. This codec device is existing in a 28 pin SSOP package.

Altera Cyclone II FPGA is planned for all layer copper, adjusted for minimum probable size of the die, and process containing 1.2 V SRAM. The Cyclone II FPGA deals with brilliant performance, greater densities, and profits of programmable logic under a price of an ASIC design.

MATLAB/Simulink: Simulink® is employed to execute model-built and multi-domain design and simulation. Simulink® provides system~ level scheme, embedded system confirmation along with spontaneous generation of code and continuous test. It also offers library consisting of customizable block, solvers, and an editor to model dynamic structures. When assimilate with the MATLAB, it permits us to use algorithms in different models and also allow us to export outcomes of different simulations into MATLAB to do further analysis.

4 Design and Simulation

Figure 4 shows the adaptive filter model used for noise cancellation. This model is done in system generator, using which we have got the VHDL code of the model that will be directly used in the FPGA. In the model-based design approach, Simulink model of adaptive noise elimination gives the simulation results of adaptive filter parameters. Figure 5 shows the input signal denoted as $M[n]$, which is the combination of both desired signal and noisy signal. Figure 6 shows the desired signal denoted as $O[n]$, which is removed from the $M[n]$ through adaptive filter. Figure 7 shows the output signal denoted as $Z[n]$, and Fig. 8 shows the error signal which we got by comparing the desired signal $O[n]$ and output signal $Z[n]$. Figure 9 shows the output of wave scope, and Fig. 10 shows the simulation results of Quartus (Figs. 11 and 12).

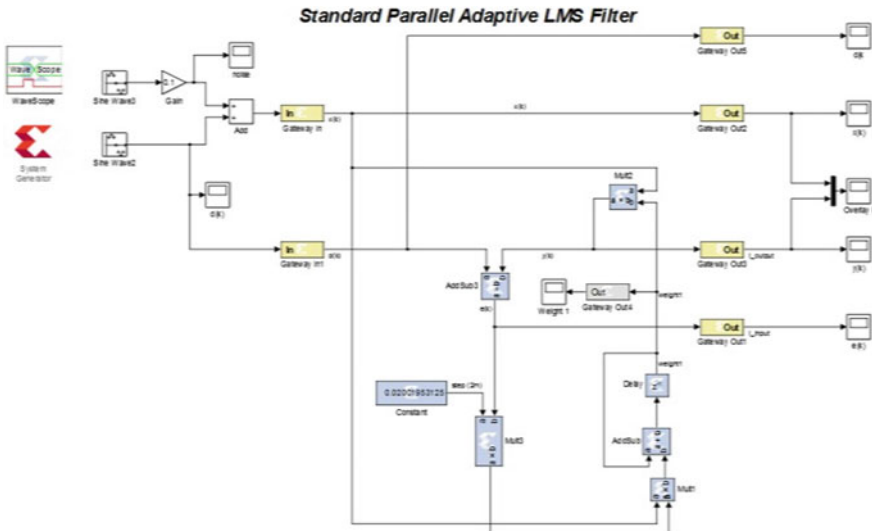


Fig. 4 Simulink model of the adaptive filter for noise cancellation

Fig. 5 Input signal waveform $M[n]$

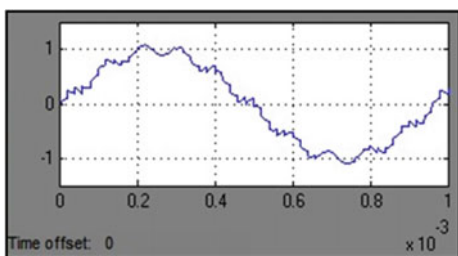
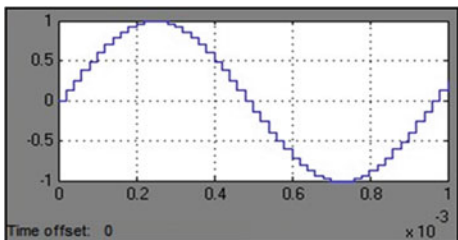


Fig. 6 Desired signal waveform $O[n]$



5 Hardware Implementation

In hardware setup (Fig. 13), the Altera DE2 kit is connected to the laptop by using JTAG cable through USB blaster port of DE2 board. A 3.5 mm audio jack is connected between line out and oscilloscope. The DE2 board is supplied via 9 V DC power

Fig. 7 Output signal waveform $Z[n]$

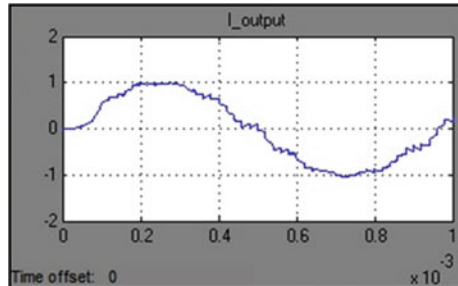


Fig. 8 Error signal waveform $Q[n]$

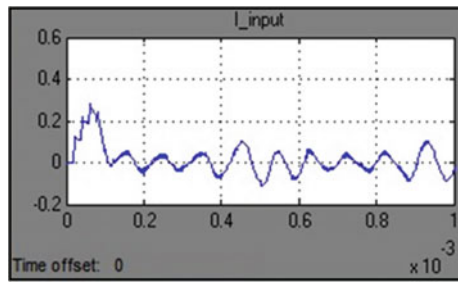
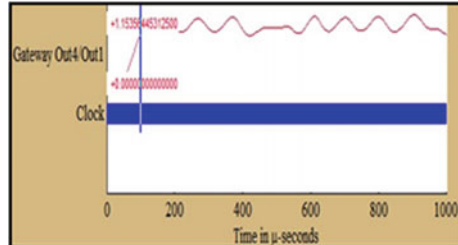


Fig. 9 Wave scope output



supply. After effective execution of the code, a soft file is created. This file desires to be dumped into the FPGA via USB blaster from laptop using programmer option given or provided by Quartus II. Figures 14, 15, 16, and 17 present the experimental results for input waveform, desired waveform, output waveform, and error waveform, respectively.

6 Summary/Conclusion

Execution of adaptive noise elimination by means of first-order LMS algorithm on FPGA is an effective process to cancel the noise and obtain the output exactly same as needed. LMS algorithm is very much easy, simple, and straightforward as compared

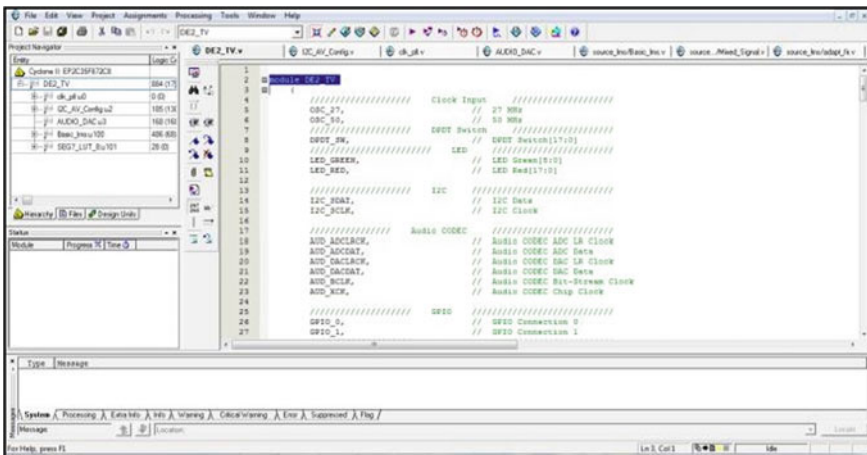


Fig. 10 Simulation results in Quartus environment

Fig. 11 Output signal waveform $Z[n]$

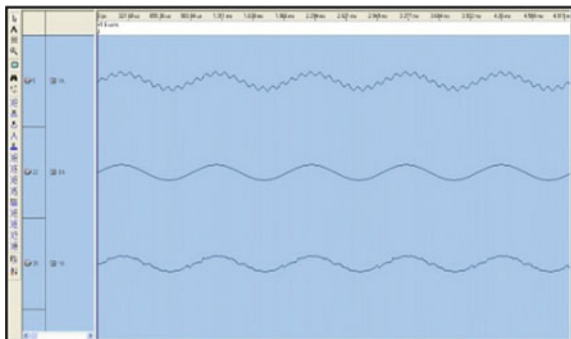


Fig. 12 Error signal $Q[n]$ waveform and corresponding weight update signal waveform

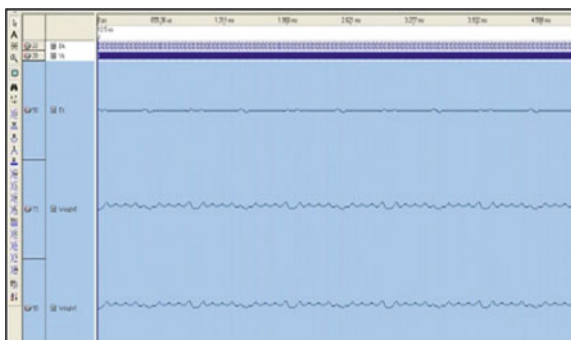
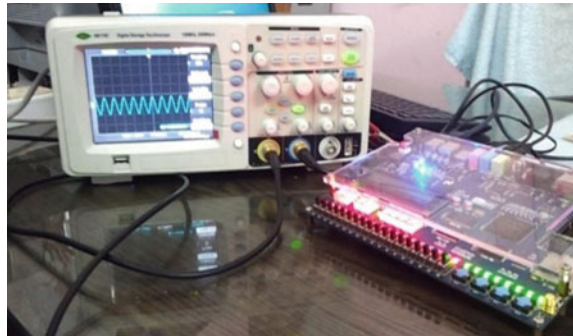
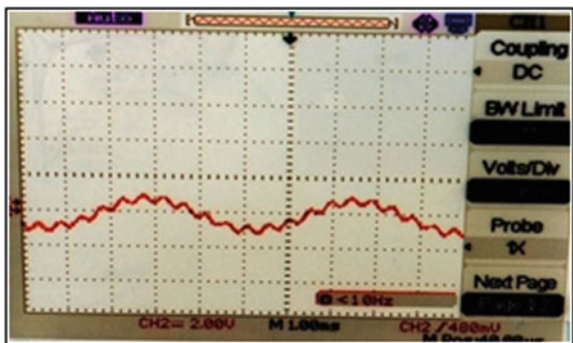
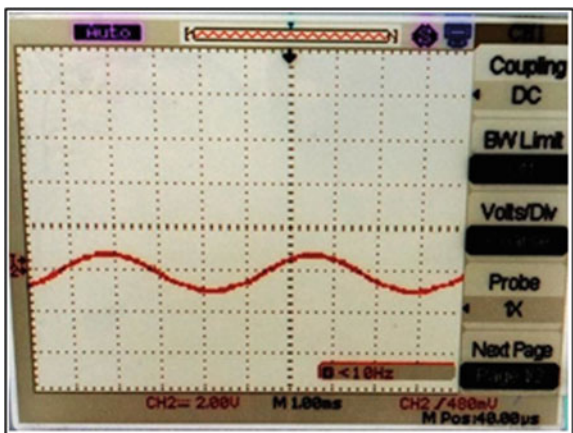


Fig. 13 Hardware setup**Fig. 14** Experimental result of input signal $M[n]$ **Fig. 15** Experimental result of desired signal $O[n]$ 

to other algorithms. This approach is more efficient toward energy saving and space facility for FPGA. This effort can be expanded toward multi-order LMS to generate output more perfect. Moreover, the external signal can be chosen as input for real-time processing.

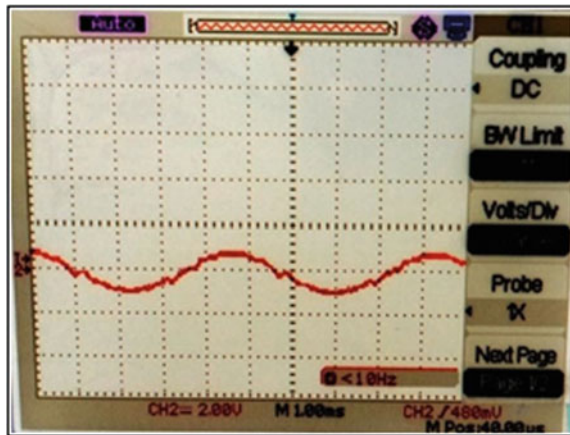


Fig. 16 Experimental result of output signal $Z[n]$

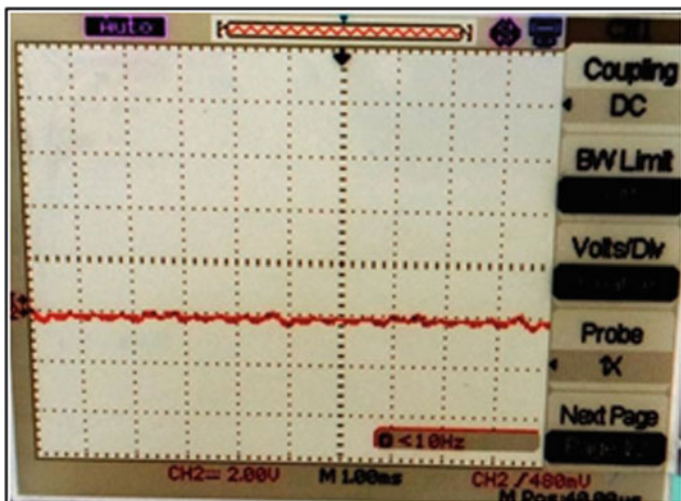


Fig. 17 Experimental result of error signal $Q[n]$

References

1. Mollaei Y (2009) Hardware implementation of adaptive filters. In: IEEE student conference on research and development (SCoReD). IEEE, pp 45–48
2. Patjoshi RK, Mohapatra KK (2010) FPGA implementation of fuzzy logic elevator group controller with traffic base system. 5th IEEE international conference on industrial and information systems (ICIIS), pp 366–371
3. Patjoshi RK (2010) Design and implementation of embedded based elevator control system. Ph.D. Diss. NIT Rourkela

4. Patjoshi RK, Panigrahi R (2019) Experimental investigation of microcontroller based elevator positioning control system using fuzzy-logic. *Int J Eng Adv Technol* 8(5):88–94
5. Kim CM, Park HM, Kim T, Choi YK, Lee SY (2003) FPGA implementation of ICA algorithm for blind signal separation and adaptive noise canceling. *IEEE Trans Neural Netw* 14(5):1038–1046
6. Patjoshi RK, Suvarsha CH, Ali SKI (2017) Design and analysis of novel high performance CMOS domino-logic for high speed applications. *ARPN J Eng Appl Sci* 12(17):5109–5114
7. Bahoura M, Ezzaidi H (2009) FPGA-implementation of a sequential adaptive noise canceller using Xilinx system generator. In: International conference on microelectronics-ICM, pp 213–216
8. Patjoshi RK, Vootla DH, Majety V (2017) A FDTD model for crosstalk analysis of dynamic CMOS and bootstrap gate-driven coupled RLGC interconnects. *Int J Pure Appl Math* 115(6):25–30
9. Lan T, Zhang J (2008) FPGA implementation of an adaptive noise canceller. In: 2008 international symposiums on information processing, pp 553–558
10. Elhossini A, Areibi S, Dony R (2006) An FPGA implementation of the LMS adaptive filter for audio processing. In: 2006 IEEE international conference on reconfigurable computing and FPGA's (ReConFig 2006), pp 1–8
11. Patjoshi RK, Mohapatra KK (2010) FPGA implementation of fuzzy logic controller for elevator group control system. In: International conference on future engineering trends
12. Ramos R, Lázaro AM, Río JD (2007) FPGA-based implementation of an adaptive canceller for 50/60-Hz interference in electrocardiography. *IEEE Trans Instrum Measur* 56(6):2633–2640
13. Patjoshi RK, Mohapatra KK (2015) Real time implementation of sliding mode based direct and indirect current control techniques for shunt active power filter. *WSEAS Trans Syst Control* 10(1):186–197
14. Diggikar AB, Ardhapurkar SS (2012) Design and implementation of adaptive filtering algorithm for noise cancellation in speech signal on FPGA. In: 2012 international conference on computing, electronics and electrical, pp 766–771

ICI Mitigation with Fixed-Number (FN)- and Fixed-Region (FRgn)-Based BS Coordination and Cooperation in a Multi-cell Cellular Network



Janmoni Borah, Kshetrimayum Linthoinganbi Devi, and Joyatri Bora

Abstract The paper investigates the effect of inter-cell interference on the user's downlink performances at cell-boundary areas specifically when the user is immobile at home cell or mobility occurs to adjacent and nearby cells. The regular and rearrangement of spectrums with well-known frequency reuse schemes in the 19-MCs network are presented. The paper also illustrates FN- and FRgn-based BS selection for coordination and cooperation among BSs. The simulated SINR and throughput being obtained with FN- and FRgn-based BS selection approach are appreciable.

Keywords ICI · Frequency reuse · BS coordination · BS cooperation

1 Introduction

Recently, network densification with overlaying of small-cells (SCs) seems to be a top priority for the network operator to meet the ever-growing demands of users. The limited spectrum, cell densifications, and augmentation in mobile users have led to some major network issues including inter-cell interference (ICI). ICI which typically arises due to utilization and allocation of the full or same spectrum in nearby and neighboring cells had been a basic cause of cell-edge user performance degradation mostly in heterogeneous cellular networks (HetCNs). The path loss, diffraction, reflection, and blockage of the signal have led to poor coverage of indoor and cell-edge regions in macrocell (MC). To overcome that, the operators are deploying SCs (e.g., picocells and femtocells) within MCs, particularly in cell-edge and indoor areas

J. Borah · K. L. Devi · J. Bora (✉)

North Eastern Regional Institute of Science and Technology, Nirjuli, India

e-mail: jb@nerist.ac.in; bjoyatri@yahoo.com

J. Borah

e-mail: borahh1989@gmail.com

K. L. Devi

e-mail: babythoi22@gmail.com

where MC is inadequate in providing services. SCs not only improves coverage of cell-edge and indoor regions (e.g., in shopping malls, in hospitals, residential homes, etc.) by reducing the serving distance from the base station (BS) to its user but also are easy to deploy, economical, and energy-efficient. SCs also seem to be efficient in providing services to isolated and outdoor places (e.g., mobile SCs with vehicles) [1–6]. On the one side, SCs found themselves in network performance improvements; on the other side, a relatively new approach specifically the Poisson point process (PPP) has been brought up for modeling and analyzing the HetCNs entities based on stochastic geometry (SG). The SG permits spatial and analytical modeling of network entities (e.g., BS and user) without worrying about pre-existing configuration and environments [7–10].

The diversifications from high transmit power MCs to low-powered femtocells BSs results in severe ICI effects in HetCNs. SCs with low coverage range although involve in ICI, but most dominant interferers are the high transmit powered MCs in HetCNs. Typically researchers, therefore, consider MCs based networks during ICI analysis and mitigation. The literature suggests various works related to ICI analysis and mitigation in MCs networks. Among well-known MC-based ICI mitigation techniques, the frequency reuse schemes, BS coordination, and BS cooperation are widely used. The static cell-edge user performance in a downlink network is analyzed with BS coordination strategy and allocation of frequency reuse (FR) schemes among cells [11]. The author proposes a fractional-coordinated fair scheduling scheme by using fractional frequency reuse (FFR) with sectorization for improving the cell-edge user's performance in the network [12]. In [13], the cell-edge user's performance in a downlink network is analyzed with an interference suppression strategy and FFR scheme of 1.5. In [14], the conventional centralized and distributed cellular network is planned and the ICI effect on a cell-edge user is discussed.

In [11], the performance of a static cell-edge user at the boundary of three MCs is analyzed with BS coordination along with FR methods. Motivated from work in [11], here, authors tried to investigate the ICI effect on the typical cell-boundary user during static or mobility in the 19-MCs network. In the previous work [16], authors present ICI analysis with the planning of spectrums with different FR schemes and 120° sectorization of MCs. The presented work is an extension of the authors' previous work [16] and illustrates ICI mitigation with FN- and FRgn-based BS selection in the 19-MCs network.

The paper subsequent sections are ordered as: Sect. 2 presents a schematic of 19-hexagonal cell planning with user distribution and FN- and FRgn-based BS selection algorithms. The schematic of spectrum planning in 19-MCs is presented in Sect. 3. The paper concluding remarks is given in Sect. 4.

2 System Model

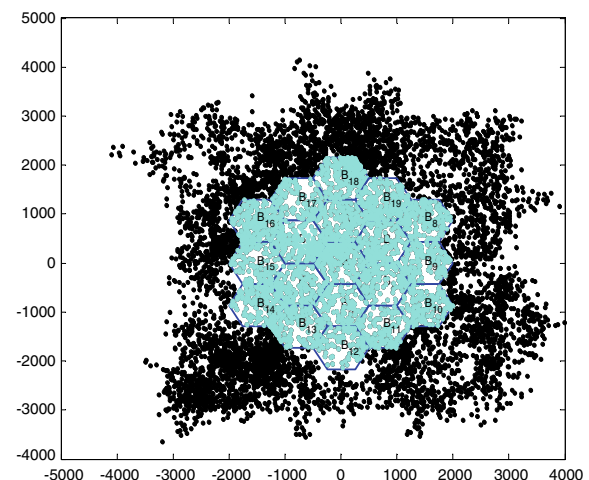
Figure 1 depicts the planning of regular hexagonal cells in an unplanned geographical area to analyze the performance of heterogeneously distributed users. The user heterogeneity so obtained is time-varying in nature which cannot be generated with a single-layer PPP, thus modeled with the Cox process [11]. The Cox process brings an additional layer to the Poisson point process (PPP) with a varying rate. The propagation is considered in the network with path loss, large-scale distances, and small-scale channel variations. The network is set up with regular 19-MCs as hexagonal grid sites of radius $R = 300$ m. The inter-site distance among MCs ($D = R\sqrt{3}$ m) is maintained in the network. The work mainly analyzes the severe ICI effects on a typical mobile user from adjacent MCs during mobility at the cell-edge and boundaries of two or more MCs. For ease of analysis, a typical mobile user of MC₁ is selected at the boundary, and random mobility is assumed to MC₄, and MC₃ (Fig. 2a).

During analysis, it is pre-assumed that either user is static/mobile within serving MC₁ or moving to adjacent MC₄ or MC₃. Assuming the round-robin algorithm, the network downlink metrics are analyzed with an allocation of full bandwidth (180 kHz) and 1-RB to each user. For the downlink scenario, say P_m is the transmitting power of all 19-MCs, network large-scale fading factor is C, and FR factor is δ . The downlink signal to interference plus noise ratio (SINR) received by the typical cell-edge user k served by BS j is given as:

$$\text{SINR}_k = \frac{P_m |h_{jk}|^2 C d_{kj}^{-\alpha}}{(I_k + N)\delta} \quad (1)$$

where d_{kj} is the k th user distance from j th BS; h_{jk} is rayleigh fading channel gain from j th BS to k th user; N is the noise power associated with the network. The first

Fig. 1 Schematic of regular hexagonal cells with user distribution



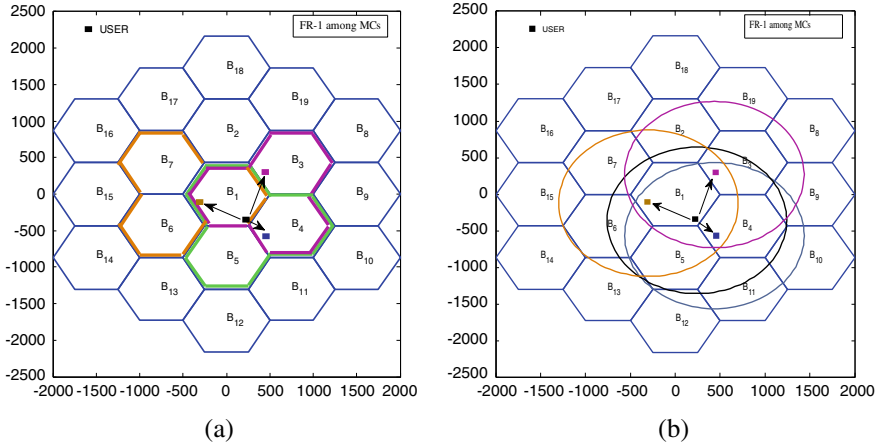


Fig. 2 Schematic of FR-1: **a** with FN-based BS selection, and **b** with FRgn-based BS selection

term in denominator I_k denotes the ICI effect on the k th user from adjacent MCs allocates with the same spectrum and is given by:

$$I_k = \sum_{\substack{j'=1 \\ j' \neq j}}^{N_m} P_m |h_{j'k}|^2 C d_{kj'}^{-\alpha} \quad (2)$$

Say, B is the bandwidth of each RB being allocated, then k th user downlink throughput being received from j th BS can be written as:

$$\gamma_k = \delta * B * \log_2(1 + \text{SINR}_k) \quad (3)$$

The effect of FN- and FRgn-based BS selection on user performance metrics could be understood from the Algorithms 1 and 2, respectively.

Algorithm 1: FN based BS coordination and cooperation

Initialization:

1. Number of MCs: $j = 1, 2, \dots, N_m$
2. The typical k^{th} user location at any point is: (U_x, U_y)
3. The signal received from serving j^{th} BS: $S_j \leftarrow 0$
4. The signal received from other nearest two BSs utilizing the same spectrum: $S_{j^*} \leftarrow 0$
5. The interferences from nearest two BSs utilizing the same spectrum: $I_{j^*} \leftarrow 0$
6. The interferences from other MCs in the network utilizing the same spectrum: $I_{j..} \leftarrow 0$

Main Algorithm:

7. The distance between user k and MC BSs is calculated as
for all $j \in N_m$ **do**

$$\text{find } d_{kj} = \sqrt{((U_x - B_{xj})^2 + (U_y - B_{yj})^2)}$$
end for
 8. Find two MCs nearest to the k^{th} user and are adjacent to serving MC with the same spectrum.
 9. **With BS coordination:** Two interfering MCs nearest to user k coordinates with serving j^{th} BS in data transmission and the overall received signal is given by

$$S_{k_FN(coord)} = (S_j) / (I_{j^*} + I_{j..} + N)$$
 10. **With BS cooperation:** Two interfering MCs nearest to user k simultaneously serves the user and overall received signal is

$$S_{k_FN(coop)} = (S_j + S_{j^*}) / (I_{j^*} + I_{j..} + N)$$
-

Algorithm 2: FRgn based BS coordination and cooperation**Initialization:**

1. Number of MCs: $j = 1, 2, \dots, N_m$
2. The region of cooperation: $R_{gn} \leftarrow 0$
3. The typical k^{th} user location at any point is: (U_x, U_y)
4. The signal received from serving j^{th} BS: $S_j \leftarrow 0$
5. The signal received from other BSs located within R_{gn} : $S_{j'} \leftarrow 0$
6. The interferences from BSs located within R_{gn} : $I_{j'} \leftarrow 0$
7. The interferences from BSs located outside R_{gn} : $I_{j''} \leftarrow 0$

Main Algorithm:

8. The distance between user k and MC BSs is calculated as
for all $j \in N_m$ **do**

$$\text{find } d_{kj} = \sqrt{((U_x - B_{xj})^2 + (U_y - B_{yj})^2)}$$

end for

9. **if** ($d_{kj} \leq R_{gn}$) **then**

$$S_{j'} \leftarrow I_{j'}$$

$$I_{j'} \leftarrow 0$$

- else if** ($d_{kj} > R_{gn}$) **then**

$$S_{j'} \leftarrow 0$$

$$I_{j'} \leftarrow I_{j''}$$

end if

10. **With BS coordination:** MCs within range of R_{gn} coordinates with serving j^{th} BS in data transmission and the overall received signal is

$$S_{k_FRgn(coord)} = (S_j) / (I_{j'} + I_{j''} + N)$$

11. **With BS cooperation:** MCs within range of R_{gn} simultaneously serves the user and the overall received signal is

$$S_{k_FRgn(coop)} = (S_j + S_{j'}) / (I_{j'} + I_{j''} + N)$$

3 Results and Discussion

The section presents an analysis of ICI effects with the available and modified arrangement of FR schemes [16]. The 19-MCs network with centralized macro-BS is set up and a typical user with a single transceiver antenna is assumed to be stationary or mobile to adjacent cells. The simulation parameters used during performance analysis in MATLAB are tabulated in Table 1 [15].

The schematic of full-spectrum (i.e., FR-1) allocation in 19-MCs with FN-based BSs selection is presented in Fig. 2a. The user during stationary at MC₁ receives severe interferences from adjacent MC BSs (B_4 and B_5). With FN-based coordination

Table 1 Parameters considered during simulation

Parameters	Values
Path-loss exponent (α)	2.7
Large-scale fading factor (C)	$10^{-3.53}$
Bandwidth of channel	1.4 MHz
Number of available subcarriers	12
Subcarrier's spacing	15 kHz
Bandwidth per resource blocks (B)	180 kHz
Total RB	6
RB allocation	1-RB/user
Power of noise (N)	-174 dBm/Hz
Number of MCs	19
Typical user mobility pattern	Random
Transmit power of MCs (P_m)	46 dBm

and cooperation, the interferences from B_4 and B_5 could be mitigated to an extent. Accordingly, when the user is mobile to adjacent cells, BSs are selected with the FN algorithm and coordination and cooperation among them take place. Figure 2b depicts an arrangement of FR-1 with FRgn-based BS selection. With FRgn, the interferences to a stationary user coming from BS B_3 to B_6 could be mitigated with coordination and cooperation among these BSs. The user during mobility within the cell or adjacent cells could be analyzed accordingly with FRgn.

The regular FR-3 (RegFR-3) and rearrangement of FR-3 (RearFR-3) with 120° sectorized 19-MCs are presented, respectively, in Fig. 3a, b. With FN-based Bs selection (Fig. 3a), it could be seen that the interferences to a stationary user coming from

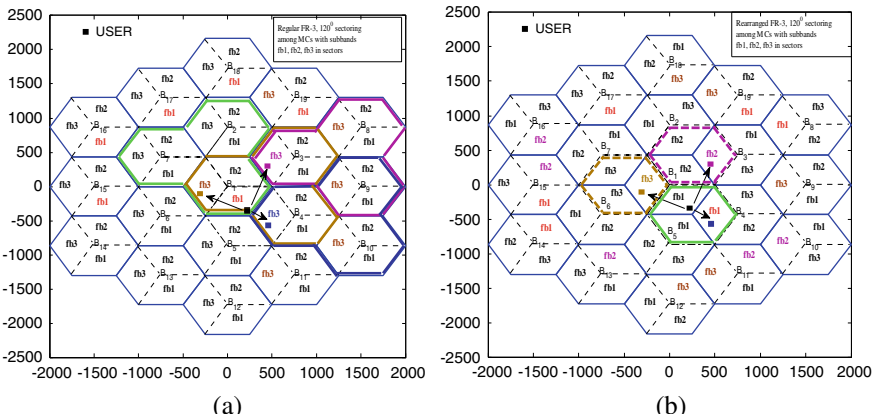
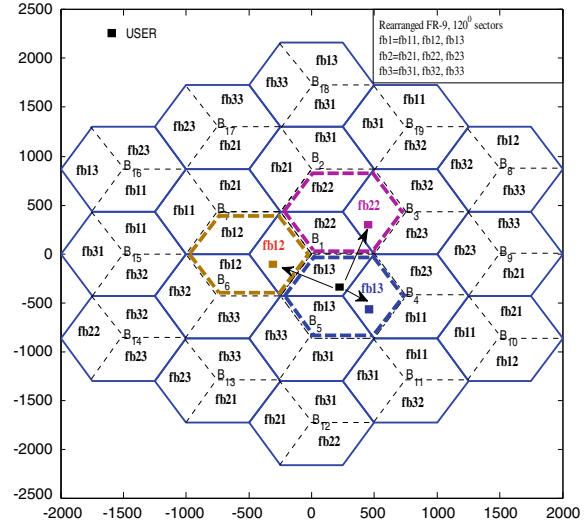
**Fig. 3** FN-based BS selection: **a** regular FR-3 (RegFR-3) planning, and **b** rearranged FR-3 (RearFR-3) planning

Fig. 4 Rearranged FR-9 planning with FN-based BS selection



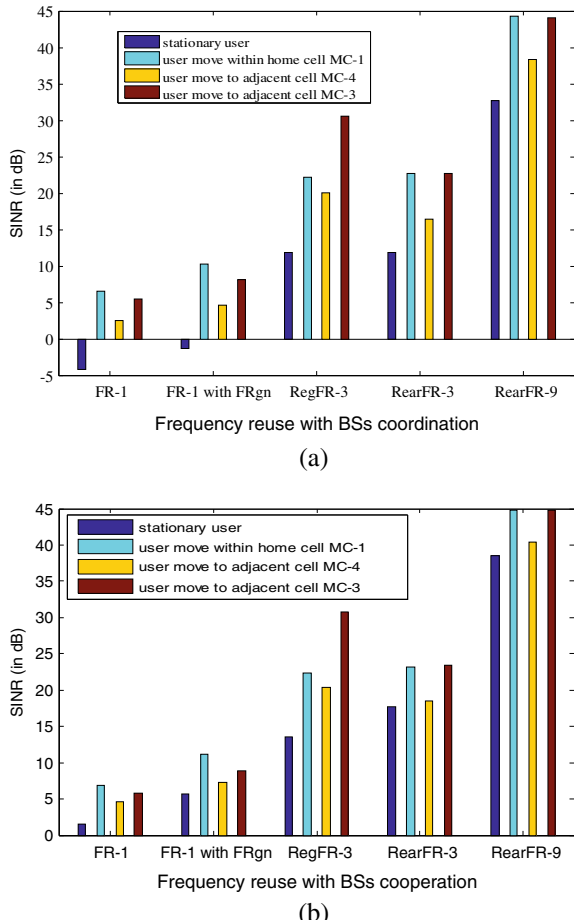
sectors of BS $B_{2,7}$ allocated with fb1 sub-band could be mitigating with coordination and cooperation among sectors of these BSs. The interferences to the user during mobility within the home cell (i.e., to the sector with fb3 sub-band) or adjacent sectors of MC_{3,4} could be analyzed and mitigate with FN accordingly. The FN-based BS selection for the typical user during stationary or mobility in RearFR-3 planning is presented in Fig. 3b. It is observed that the user which is stationary at the home cell in the sector with fb-1 sub-band face interferences from sectors with the same sub-band of MC_{4,5}. With FN-based BS coordination and cooperation, the interferences in RearFR-3 spectrums arrangements could be mitigated accordingly.

The modified rearranged FR-9 (RearFR-9 [16]) with 120° sectorized 19-MCs along with the planning of nine sub-bands is presented in Fig. 4. It is observed that the interferences to a stationary user coming from sectors of BS $B_{4,5}$ allocated with fb13 sub-band could be mitigated with FN-based BS coordination and cooperation among sectors of these BSs. As could be observed from Fig. 4, the interferences to the user during mobility within the home cell (i.e., to the sector with fb12 sub-band) or adjacent sectors of MC₃ with fb22 sub-band and MC₄ with fb13 sub-band could be analyzed and mitigate with FN-based BS selections accordingly.

The simulated SINR of a typical cell-boundary user is plotted in Fig. 5. Figure 5a depicts SINR of the stationary or mobile user obtained with FN- and FRgn-based BS coordination. The SINR obtained with FN and FRgn based BS cooperation is shown in Fig. 5b. The results depict that SINR being obtained with different FR schemes (in [16]) improves with FN- and FRgn-based BS coordination and cooperation.

Figure 6 shows the simulated downlink throughput of the typical cell-boundary user when it is static at home cell or moves to adjacent cells. The user throughput during stationary or mobility obtained with FN- and FRgn-based BS coordination is

Fig. 5 Simulated SINR of the typical user: **a** with FN- and FRgn-based BS coordination, and **b** with FN- and FRgn-based BS cooperation

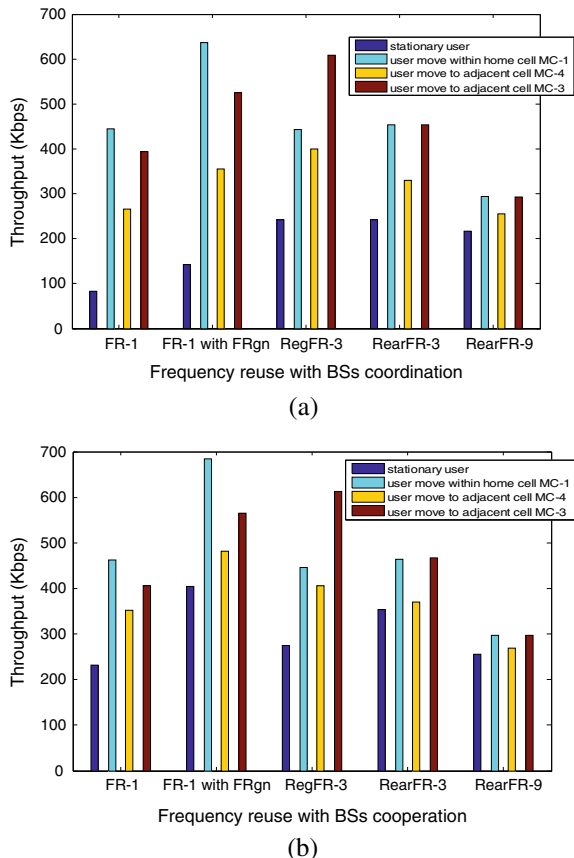


presented in Fig. 6a. The throughput obtained with FN- and FRgn-based BS cooperation is shown in Fig. 6b. The simulated results depict that the throughput of user improves with FN- and FRgn-based BS coordination and cooperation in the network in comparison to that obtained with different FR schemes (in [16]).

4 Conclusion

The ICI effect on stationary or mobile users near cell-boundary regions is investigated with the arrangement of different FR schemes (regular and rearranged of sub-bands) in the 19-MCs network. The paper discusses ICI mitigation with FN-

Fig. 6 Simulated downlink throughput of the typical user: **a** with FN- and FRgn-based BS coordination and **b** with FN- and FRgn-based BS cooperation



and FRgn-based BS coordination and cooperation in a multi-cell cellular network. The simulated SINR and throughput being obtained with FN- and FRgn-based BS selection approach are appreciable.

References

- Claussen H, López-Pérez D, Ho L, Razavi R, Kucera S (2017) Small cell networks: deployment, management, and optimization. Wiley-IEEE Press, London
- Anpalagan A, Bennis M, Vannithamby R (2015) Design and deployment of small cell networks. Cambridge University Press, Cambridge
- Quek TQ, de La Roche G, Güvenç İ, Kountouris M (2013) Small cell networks: deployment, PHY techniques, and resource management. Cambridge University Press, Cambridge
- Andrews JG (2013) Seven ways that HetNets are a cellular paradigm shift. IEEE Commun Mag 51(3):136–144
- Sui Y, Vihriala J, Papadogiannis A, Sternad M, Yang W, Svensson T (2013) Moving cells: a promising solution to boost performance for vehicular users. IEEE Commun Mag 51(6):62–68

6. Park Y, Heo J, Kim H, Wang H, Choi S, Yu T, Hong D (2014) Effective small cell deployment with interference and traffic consideration. In: 2014 IEEE 80th vehicular technology conference (VTC2014-Fall), Vancouver, Canada, pp 1–5
7. ElSawy H, Sultan-Salem A, Alouini M, Win MZ (2017) Modeling and analysis of cellular networks using stochastic geometry: a tutorial. *IEEE Commun Surv Tutorials* 19(1):167–203
8. Trigui I, Affes S, Liang B (2017) Unified stochastic geometry modeling and analysis of cellular networks in LOS/NLOS and shadowed fading. *IEEE Trans Commun* 65(12):5470–5486
9. Chen C, Elliott RC, Krzymień WA, Melzer J (2018) Modeling of cellular networks using stationary and non-stationary point processes. *IEEE Access* 6:47144–47162
10. Heath RW, Kountouris M, Bai T (2013) Modeling heterogeneous network interference using Poisson point processes. *IEEE Trans Sig Process* 61(16):4114–4126
11. Khan MHA, Chung Jin-Gyun, Lee MH (2016) Downlink performance of cell edge using cooperative BS for multicell cellular network. *EURASIP J Wirel Commun Netw* 2016(1):1–12
12. Abiri M, Mehrjoo M (2014) Improving the performance of cell edge users with fractional coordinated fair scheduling. *IET Commun* 8(13):2315–2321
13. Ghaffar R, Knopp R (2012) Interference suppression strategy for cell-edge users in the downlink. *IEEE Trans Wirel Commun* 11(1):154–165
14. You X, Wang D, Zhu P, Sheng B (2011) Cell edge performance of cellular mobile systems. *IEEE Trans Sel Areas Commun* 29(6):1139–1149
15. Chu NEX, Zhang J (2016) Small-cell deployment over existing heterogeneous networks. *Electron Lett* 52(3):241–243
16. Borah J, Hussain MA, Bora J (2020) ICI effects on user mobility with different FR schemes in a multi-cell cellular network. *IET Commun* 14(1):84–88

InGaAs-Based Square-Shaped Nanopillar Array for High Photodetector Performance



Smriti Baruah, Santanu Maity, and Joyatri Bora

Abstract Nanopillar arrays over the photodetector's surface ensure a greater injection of incident light by enhancing light trapping phenomenon due to multiple reflections from the nanopillars which contribute towards high-resolution optical communication. This paper reports the analytical investigation of the Indium Gallium Arsenide material based square-shaped nanopillar (NP) array over the detector's front surface for high-performance photodetection. The proposed structure exhibits an optimum 98% overall absorption of the incoming light. High EQE of about 55% and responsivity of 0.7 A/W has been obtained in 1.5 μm operating wavelength range with a minimum depletion width of 0.65 μm .

Keywords Photodetector · Nanopillar · Multiple reflections · Quantum efficiency · Responsivity

1 Introduction

Progressively, the majority of long-distance transmission nowadays operates in the (1300–1550) nm wavelength range as this corresponds to the minimum optical loss window for silica optical fibers [1]. In this respect, aggressive persuasion has been done to enable high bandwidth, high speed and low noise photodetector application in the efficient performance of the optoelectronic integrated circuit [2]. The proficient opto-electrical conversion quality of photodetector placed at the end of the optical path of an optical communication system greatly impacts the overall performance

S. Baruah (✉) · J. Bora

North Eastern Regional Institute of Science and Technology, Nirjuli, Arunachal Pradesh, India
e-mail: sbaruah1993@gmail.com

J. Bora

e-mail: jb@nerist.ac.in

S. Maity

Indian Institute of Engineering Science and Technology, Shibpur, West Bengal, India
e-mail: smaity@cegess.iests.ac.in

of the system [3]. However, the key issue that seriously limits the effective photodetector's functioning is the inadequate coupling of light on the surface due to the high refractive index mismatch at the air–semiconductor interface [4]. Conventional antireflection coatings (ARC) consisting of single and multilayer thin films coated on the semiconductor substrates operate only within a narrow range of wavelength and small variations of light incident angles [5]. Also due to the unavailability of the precise desired refractive index of the thin film materials, optimum reduction of light reflection losses is not achievable in a practical sense [6]. All these physical and structural constraints could be overcome by the nanostructure deposition to reduce reflectance losses [7]. The nanostructured material provides maximum flexible space for reconstruction [8]. Also, the light absorption mechanisms in these materials depend on the geometry of the structure which not only enhances the optical path length due to multiple scattering phenomena taking place within these array of structures but also produces an effective gradient refractive index [9]. Therefore, could serve as an omnidirectional broadband ARC for photodetector applications [10]. Intensive exploration for these nanostructures in minimizing optical losses includes: Silicon nanowire, nanohole, nanopyramids reducing light reflection losses and optical path enhancement owing to moderate filling ratios [11], Plasmonic silver nanostructured array ARCs attributing light Raman scattering [12], Low aspect ratio nano cylinders reducing reflection losses through forward Mie scattering [13], Broadband nanocone arrays mitigating reflection losses by providing effective refractive index medium [14] and excitation of localized surface plasmon resonances through InAsSb-coated Au nanopillar [15].

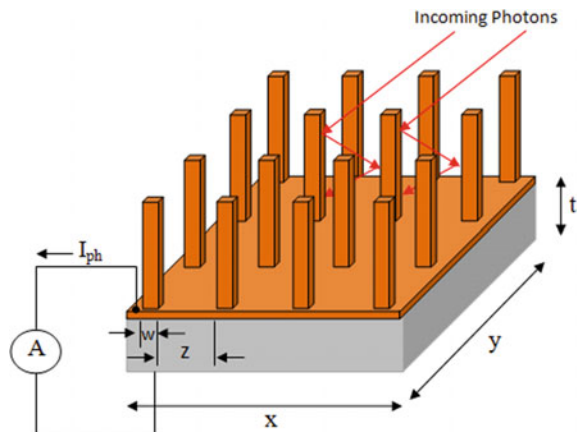
To date, the path followed by the incoming light during the multiple internal reflection phenomenons taking place within the interpillar spacing of the nanopillar arrays for enhancing photon reabsorption probability in the photodetector's surface has not been discussed in length.

This paper presents the analytical investigation of the multiple internal reflection phenomenons taking place within an InGaAs-based square-shaped nanopillar (NP) array deployed over the photodetector's surface of the same material for enhanced optical coupling. Optical modeling of the square-shaped nanopillar array as well as the mathematical analysis of the surface reflectance has been provided in Sect. 2. Section 3 investigates the various photodetector performance metrics with the nanopillar deployment through graphical representations.

2 Optical Modeling of the Nanopillar

Figure 1 provides the three-dimensional schematic representation of the InGaAs-based square nanopillar array with each of the pillar edge being ‘ s ’ height ‘ h ’ and interpillar spacing ‘ z ’ to be mounted over a photodetector's surface of $500\text{ nm} \times 500\text{ nm}$ area. The pillar arrangement over the surface has been done in a manner to achieve maximum absorption of the incoming light inside the device. As could be demonstrated from the figure, each of the four faces of the nanopillar would assist in

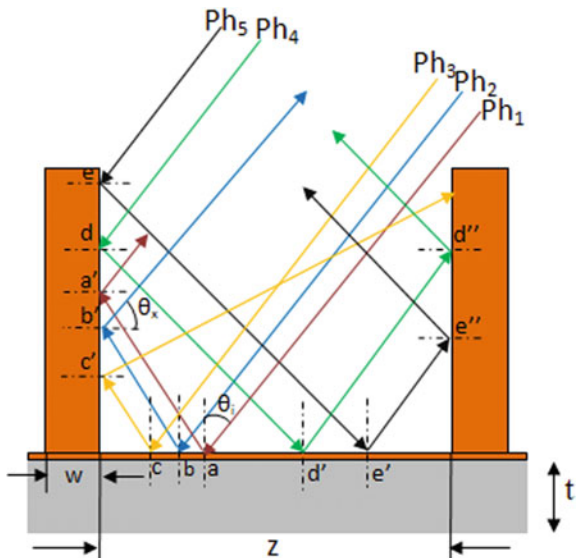
Fig. 1 Schematic of the proposed square-shaped nanopillar array



undergoing photon multiple internal reflections with their neighboring four square NPs.

The cross-sectional view of the NP showing the entire path followed by the incoming light during multiple internal reflections taking place within the interpillar gap ‘z’ has been provided in Fig. 2. For the simplified analysis of the reflectance pattern, five incoming photons are considered to capture inside the interpillar spacing. The reflected portion of the three of the incoming photons striking the planar detector’s surface with fixed incident angle ‘ θ_i ’ undergoes multiple reflections in the NP interfaces with striking angle ‘ $\theta_p = 90 - \theta_i$ ’. Similarly, two of the incoming

Fig. 2 Cross-sectional view of the NP array illustrating the light interaction mechanism within the NP array



photons striking the NP interface directly with incident angle ' θ_p ' get highly absorbed as it faced an effective gradient refractive index inside the NP structure. Thus, an overall enhancement of the light reabsorption probability due to the increased optical path length results in achieving optimum light coupling efficiency.

The total number of square nanopillars (N_p) that could be mounted over a fixed ' $x \times y$ ' area could be mathematically evaluated as,

$$N_p = \frac{\tan(90^\circ - \theta_i) \sqrt{\text{area}(x \times y)} + 2h}{s \tan(90^\circ - \theta_i) + 2h} \quad (1)$$

The overall light reflectance R' obtained with the deployed NP array structure considering the negligible transmission rate could be induced by combining the total reduced reflectance of the incoming photons striking initially the air-nanopillar interface (R_p) and the air- planar surface(R_s), respectively. Thus,

$$R' = R_p + R_s \quad (2)$$

$$R' = \sum_{i=1}^n R_{pi}[(1 - R_s) + (1 - (R_p - \Delta R_p))] + \sum_{i=n+1}^N R_{si}[1 - (1 - \Delta R_p)] \quad (3)$$

where ' $\Delta R'_p$ ' denotes the effective light reflectance obtained from the multiple internal reflections inside NP array, respectively, ' N ' denotes the total number of incoming photons and ' n ' denotes the total number of incoming photons striking the ' N_p ' number of nanopillars within a fixed detector's surface area which is given by,

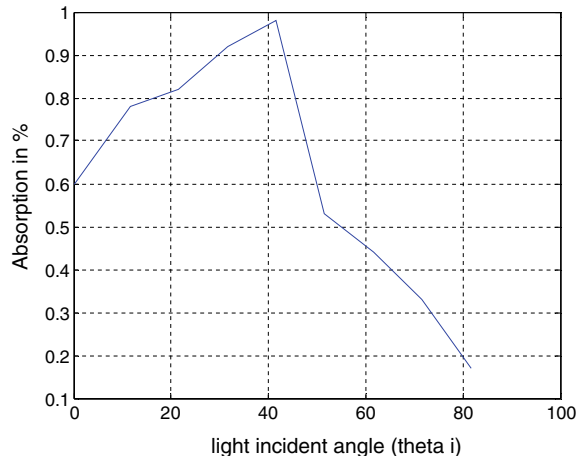
$$n = m[2\sqrt{N_p}(\sqrt{N_p} - 1)] \quad (4)$$

where m indicates the incoming photons trapped inside a single interpillar spacing.

3 Results and Discussion

The InGaAs-based square-shaped nanopillar is mounted over the planar surface of a photodiode of the same material with a filling factor of 0.22. The numerical, as well as the graphical representation in this paper, has mainly focused on the investigation of performance analysis of the detector's front surface in efficient light trapping. The numerical values of interpillar spacing ' z ' and NP height ' h ' have been calculated so as to allow most of the incoming photons to get trapped inside the array for maximum absorption without the shadowing effect. Figure 3 provides the amount of total light absorption (in %) within the NP array structures of fixed height and interpillar gap of 0.4 um and 0.5 um respectively with varying photon incident angle (θ_i) over '1 um \times 1 um' detector's surface area. The figure shows an increased absorption up to

Fig. 3 Variation of light absorption within a 0.4 μm high and with 0.5 μm interpillar gap NP array with increasing angle of light incidence (θ_i)



98% with increasing incident angle up to a certain value beyond which there is a gradual decrement in the overall light absorption due to the shadowing effect of the nanopillar which inhibits photon trapping. The incident angle at which maximum absorption took place depends on the distance between the nanopillar and striking point of the incoming photon at the plane of incidence.

Figure 4 shows the variation of interpillar ('z') spacing required for maximum light absorption inside the NP array structure for a different angle of incidence at a fixed pillar height. For larger light angles, there is a wider interring pillar gap required to trap as much as photon as compared to that of narrow incident angles so as to achieve optimum absorption. As could be demonstrated from the figure, the interpillar spacing required for the widest light incident angle is approximately five times larger than the value of pillar height.

Fig. 4 Maximum NP interpillar spacing required according to the light incident angle for pillar height varying from 0.1 to 0.4 μm for maximum absorption

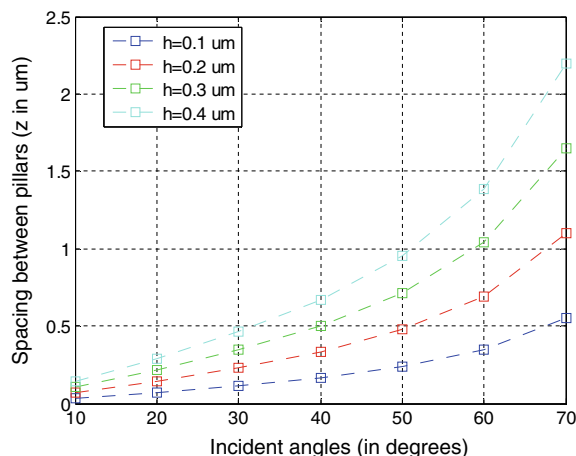


Fig. 5 Variation of maximum pillar height required according to the light incident angle with different interpillar spacing from 0.1 to 0.4 μm

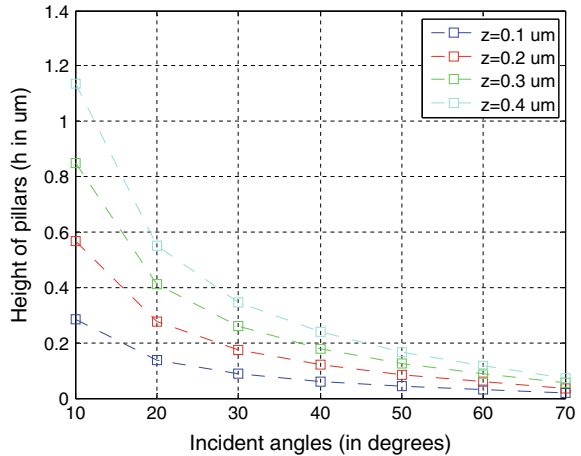
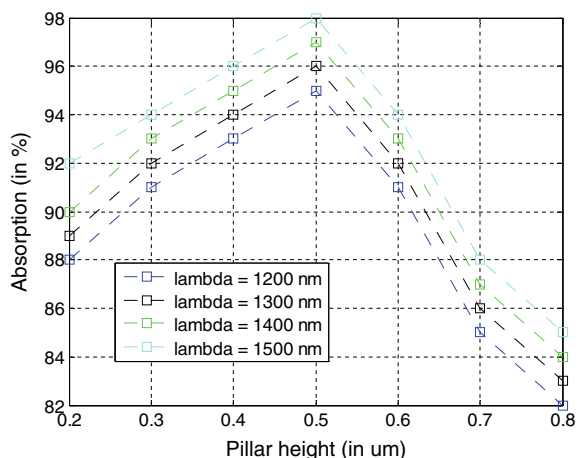


Figure 5 demonstrates the maximum number of nanopillars of fixed height and spacing that could be mounted over a detector's surface area of $1 \mu\text{m} \times 1 \mu\text{m}$ w.r.t to light incident angles. As could be evaluated from the figure, for wider incident angles, there is a continuous reduction of the total number of NPs that could be accommodated over a fixed surface area. Also, the number of longer NPs required for maximum light absorption is comparatively very less than that of shorter NPs.

The maximum absorption (in %) of light with an oblique incidence at '30°' considering zero transmission rate within an NP array with varying interpillar gap at different operating wavelength range (λ) is shown in Fig. 6. Within a certain spacing for fixed NP height, the overall photon absorption rate goes on increasing as more number of incoming photons could be trapped inside the structure. However, beyond a certain limit, increasing the pillar gap would not be helpful in contributing multiple

Fig. 6 Total photon absorption (in %) within the $0.4 \mu\text{m}$ high NP array with varying interpillar spacing for operating wavelength range from 1.2 to 1.5 μm



internal reflections and would affect the number of NPs that could be accommodated over the detector/s surface which will reduce the light absorption efficiency. InGaAs NPs operating at 1.5 μm wavelength exhibits the highest absorption of 98% by 0.4 μm long NP arrays at 0.5 μm fixed pillar spacing.

The variation of total photon absorption (in %) within the NP array with increasing NP height is well represented in Fig. 7. As could be demonstrated from the figure, longer NPs increases the probability of facing multiple internal reflections boosting the total light absorption rate but beyond the limit increasing, the pillar height would produce the shadowing effect which will inhibit the incoming photons to get trapped inside the structure which ultimately reduces the detector's performance. The 0.6 μm long NP array shows a maximum absorption of 98% with a fixed interpillar spacing of 0.7 μm at 1.5 μm operating wavelength.

Figures 8 and 9 provide the comparison of the performance efficiency of the photodetector with and without nanopillar array structure in terms of external quantum efficiency (EQE) and responsivity (A/W) metrics. Enhanced carrier absorption with the 0.4 μm long nanopillar array structure would provide a higher electron–hole pair generation. The higher quantum efficiency of a maximum 55% and responsivity of 0.7 A/W at 1.5 μm operating wavelength for a narrow 0.65 μm depletion width has been obtained in comparison to that of a planar detector's surface which shows only a maximum of quantum efficiency and responsivity of 0.22 and 0.14 A/W, respectively.

Fig. 7 Total photon absorption(in %) within the NP array with varying pillar height and fixed interpillar spacing of 0.7 μm for operating wavelength range from 1.2 to 1.5 μm

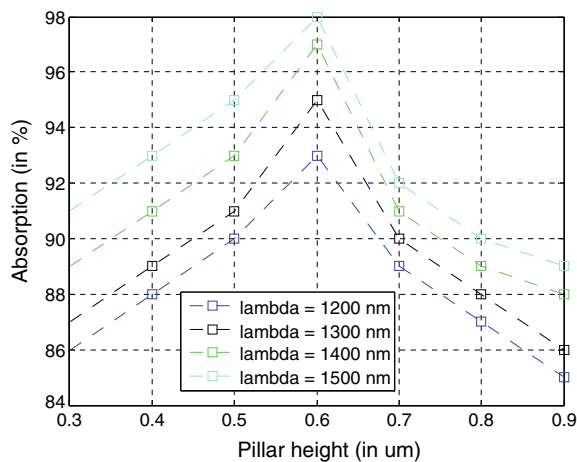


Fig. 8 Measured spectral responsivity of the PD with and without NP array surface for a detector's depletion width of 0.65 μm and 1 mw input optical power within a varying wavelength range of 1.2–1.8 μm

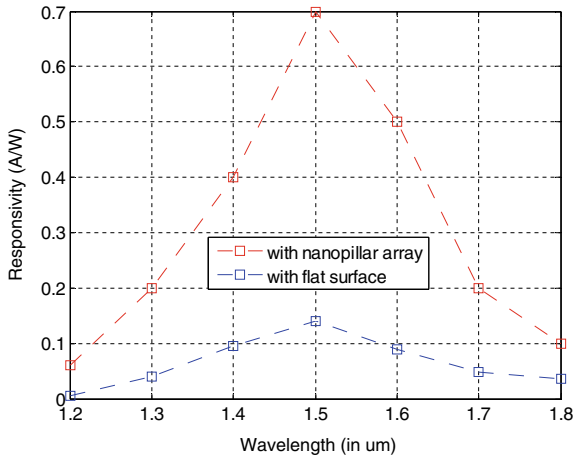
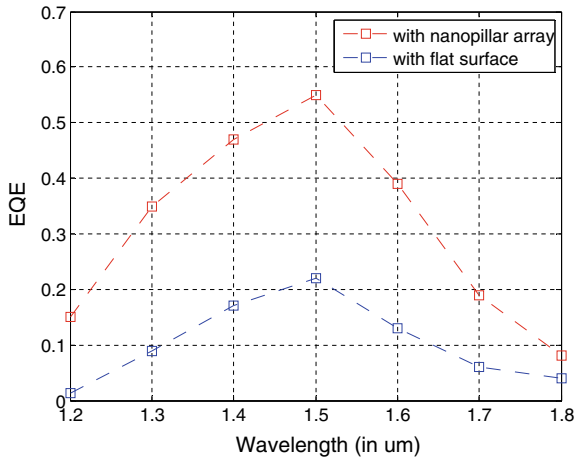


Fig. 9 EQE comparison curves of the PD with and without NP array surface with a detector's depletion width of 0.45 μm and 1 mw optical power



4 Conclusion

A high-performance InGaAs material-based square nanopillar array has been proposed to be deployed over the front surface of a photodetector of the same material composition. The overall absorption of the incoming light has been boosted to the greatest extent due to the multiple reflections of the light inside the NP array. Proper manipulation of inter-pillar spacing and height of the NP structure results in enhanced light trapping efficiency and thus minimizing the detector's reflection losses to a negligible level. The proposed structure shows a high light absorption of about 98%, The EQE of 55% and 0.7 A/W responsivity with a narrow depletion width of 0.4 μm , which is higher than that of a photodetector without NP array.

References

1. Dawson JW, Kiani LS, Pax PH, Allen GS, Drachenberg DR, Khitrov VV, Chen D, Schenkel N, Cook MJ, Crist RP, Messerly MJ (2017) E-band Nd 3 + amplifier based on wavelength selection in an all-solid micro-structured fiber. *Opt Express* 25(6):6524–6538
2. Zhao Z, Liu J, Liu Y, Zhu N (2017) High-speed photodetectors in optical communication system. *J Semiconduct* 38(12):121001–121005
3. Islam MM, Ahmed S, Islam A (2019) Performance analysis of 2.5 Gbps PIN and APD photodiodes to use in free space optical communication link. *Int J Thin Fil Sci Tec* 8(2):53–58
4. Kang Y, Liang D, Mehra S, Huo Y, Chen Y, Christoforo MG, Salleo A, Harris JS (2015) Efficiency enhancement of gallium arsenide photovoltaics using solution-processed zinc oxide nanoparticle light scattering layers. *J Nanomater* 2015:1–6
5. Jackson EM, Nolde JA, Kim M, Kim CS, Cleveland ER, Affouda CA, Canedy CL, Vurgaftman I, Meyer JR, Aifer EH, Lorentzen J (2018) Two-dimensional plasmonic grating for increased quantum efficiency in midwave infrared nBn detectors with thin absorbers. *Opt Express* 26(11):13850–13864
6. Schubert MF, Poxson DJ, Mont FW, Kim JK, Schubert EF (2010) Performance of antireflection coatings consisting of multiple discrete layers and comparison with continuously graded antireflection coatings. *Appl Phys Express* 3(8):082502–082503
7. Leung SF, Zhang Q, Xiu F, Yu D, Ho JC, Li D, Fan Z (2014) Light management with nanostructures for optoelectronic devices. *J Phys Chem Lett* 5(8):1479–1495
8. Ilyas N, Li D, Song Y, Zhong H, Jiang Y, Li W (2018) Low-dimensional materials and state-of-the-art architectures for infrared photodetection. *Sensors* 18(12):4163
9. Rani A, Reddy R, Sharma U, Mukherjee P, Mishra P, Kuila A, Sim LC, Saravanan P (2018) A review on the progress of nanostructure materials for energy harnessing and environmental remediation. *J Nanostruct Chem* 8(3):255–291
10. Kang JI, Kim H, Han CY, Yang H, Jeon SR, Park B, Cha HY (2018) Enhanced UV absorption of GaN photodiodes with a ZnO quantum dot coating layer. *Opt Express* 26(7):8296–8300
11. Buczyński R, Klimczak M, Stefaniuk T, Kasztelanic R, Siwicki B, Stępniewski G, Cimek J, Pysz D, Stępień R (2015) Optical fibers with gradient index nanostructured core. *Opt Express* 23(20):25588–25596
12. Yu R, Lin Q, Leung SF, Fan Z (2012) Nanomaterials and nanostructures for efficient light absorption and photovoltaics. *Nano Energy* 1(1):57–72
13. Bandarenka HV, Girel KV, Bondarenko VP, Khodasevich IA, Panarin AY, Terekhov SN (2016) Formation regularities of plasmonic silver nanostructures on porous silicon for effective surface-enhanced Raman scattering. *Nanoscale Res Lett* 11(1):262
14. Zhang D, Ren W, Zhu Z, Zhang H, Liu B, Shi W, Qin X, Cheng C (2015) Highly-ordered silicon inverted nanocone arrays with broadband light antireflectance. *Nanoscale Res Lett* 10(1):1–6
15. Lee WJ, Senanayake P, Farrell AC, Lin A, Hung CH, Huffaker DL (2016) High quantum efficiency nanopillar photodiodes overcoming the diffraction limit of light. *Nano Lett* 16(1):199–204

Identification of Approximable Program Components Using Edge Profiling



Priya Arundhati and Santosh Kumar Pani

Abstract Approximate computing is gaining popularity day-by-day due to its growing application area. One of the areas where it is required to give attention is program analysis techniques. Program analysis focuses mainly on program optimization and the correctness of the program. For program optimization, some transformation in the source code is carried out. In this paper, we have proposed a novel idea for transforming a normal program into an approximated program. The approximated version of the program can run in the non-approximated hardware and can decrease computation time, resource utilization, memory uses, and power consumption. Our method finds the cold segment of the original program by using Edge profiling and apply approximation as these parts have less effect on the final output value. The use of the distortion metric verifies the output quality of our transformation.

Keywords Program optimization · Approximate program transformation · Edge profiling · Distortion

1 Introduction

In today's era, everything is managed by machines. These machines are designed in such a way that they do not require human interaction, hence equipped with high computing power. The high computing machines require high power and energy consumption to produce the result. There are some applications where we may not require the exact result but a "good enough" result. For providing an exact result, the machine may require more energy, but for an acceptable result, it may require less energy. The computation of an exact result with energy-saving is known as "Approximate Computing." Nowadays, approximate computing is an integral part of the computing methodology. Approximate computing relaxes the correctness of

P. Arundhati (✉) · S. K. Pani

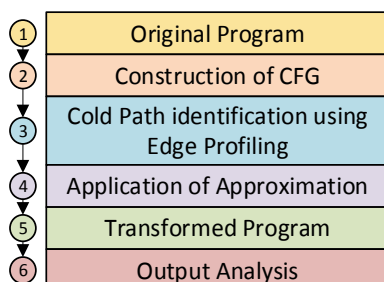
School of Computer Engineering, KIIT University, Bhubaneswar, India
e-mail: priyaarundhati87@gmail.com

S. K. Pani
e-mail: spanifcs@kiit.ac.in

the system by producing an acceptable result along with resource-saving. Approximate computing is applied in the area where the system is error-tolerant like multi-media processing, machine learning, signal processing, scientific computing, etc. Except these traditional application areas of approximate computing, researchers are thinking in a different way and trying to apply the concepts in the area where we can optimize resources like software engineering, program analysis, optimization, etc. However, most of the research in approximate computing is not related to software testing research. At the code level, the components (variable, code, loop, etc.) of a program need to be handled carefully and the section of code can be transformed into approximate code. Generally, program transformation changes the program to a different form without changing its semantics and used in reliability, maintenance, and extensibility of software. On the other hand, approximate program transformation (APT) changes the semantics of the original program within a specified error bound and this transformed program can take less computation time, less power to execute, and less memory. To make a non-approximate program into an approximate program, first, the components where the transformation should be applied must be found out. After identification of the program components, then only, the approximate techniques can be applied in the program without crossing the tolerable error limit. The transformed program is called as approximate program. Then the output of the original program and the approximate program is compared and the error is found out. If the error is within the specified bound, then the output is accepted.

In this paper, we will discuss the techniques by which we identify a suitable program component for approximation. For the identification of the components, we have taken the help of edge profiling algorithm [1] along with the edge selection criteria for control flow graph (CFG) [2]. When one component is identified for approximation, it can be replaced by some alternatives which produces approximated result with a tolerable error. Graphically, it is shown in Fig. 1. The detailed explanation of the process flow is discussed in Sect. 3. In Fig. 2, we are showing the error analysis process of our methodology. Here, x is the variable in the original program and it is replaced with x' in the transformed program. It must be noted that x should be the non-critical component (i.e., have less impact on the final output) of the program. It has some approximated error "err" associated with the input. The exact value of x can be replaced by x' by dropping some part of the large computation. In the final output, the error can be calculated as $\text{err} + x - x'$.

Fig. 1 Process flow to identify approximate program component and its transformation



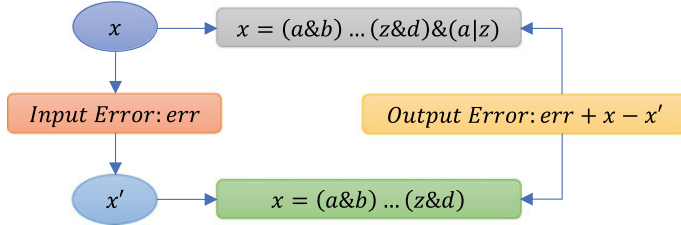


Fig. 2 Error analysis process

The remaining section is organized as follows. Section 2 focuses on the discussion of the related works. Section 3 describes the proposed method. Case study and experimental result are discussed in Sect. 4, and finally, Sect. 5 concludes the discussion.

2 Related Works

In [3], the authors introduce a new technique, named ApproxIMut, which combines the power of mutation testing with the feature of approximate computing. In [4], the approximate transformation is considered as the mutation operator and found that the same program behaves differently as that of the traditional mutation operator and the approximate transformation absorbs more mutants that are not done in traditional mutation operator. Another direction of approximate computing is approximate instruction processing(AIP) [5] which includes the techniques in compiler, algorithm, and code level. In [6], the authors propose a software framework which automatically finds the approximable program components by using statistical method. They find the range of the variables and by using binary instrumentation, the values of the variables are settled. They measured the new output against the actual output and which satisfied the QoS threshold they approximated that variable corresponding to the QoS threshold. In [7], the authors propose a static framework which finds the Degree of Accuracy (DoA) of program components and creates Component Influence Graph (CIG) to represent the relationship among various program components. In [8], the authors have used the concept of slicing to find the non-critical components of a program. After application of dependency slicing, they found the approximable program components and after that they have measured the output by using assertion metrics. Another new method is proposed in [9] where probabilistic reasoning is used to justify the approximate program transformation.

3 Proposed Methodology

For any program transformation, the first thing is the identification of the correct component on which the conversion is applied to achieve profitable trade-off without compromising much on the quality of the result. Our proposed methodology comprises of the following steps:

1. Components identification using edge profiling
2. Application of approximation transformation on the identified components.
3. Result verification.

3.1 Component Identification Using Edge Profiling

A control flow graph (CFG) describes the behavior of a program graphically. By the definition of a CFG, we know that a CFG is a directed graph (V, E) contains a set of vertices (V) and a set of edges (E). In CFG, the vertices or nodes represent the statements in a program, and edges represent the flow of control between the statements. An edge $x \rightarrow y$ in a CFG means that the program control can flow from node x to node y . Due to the simple structure of CFG, it is the most widely used representation of the program for the program analysis technique. Profiling is used to find the optimization candidate for a program. The profiler is used to monitor the dynamic behavior of a program, by instrumenting it and executing the program with some input and collects the execution traces. The output of a profiler is to give details of the computation like time consumed, space consumed, and many more. A profiler uses CFG for the analysis of the program. In this paper, we are using edge profiling [1] to identify the components for transformation. The edge profile of a CFG can accurately identify the cold paths in a program [10]. Before discussing the cold path, we must explain the definition of the path. A path in a CFG is a sequence of n vertices and $n - 1$ edges of the form $(v_1 e_1 v_2 e_2 v_3 \dots e_{n-1} v_n)$ where for each edge e_i , either $e_i = v_i \rightarrow v_{i+1}$ or $e_i = v_{i+1} \rightarrow v_i$ [event counting algorithm of ball-larus]. The cold paths of a CFG are the less frequently followed paths. Whereas the hot paths are the most frequently followed paths. We are choosing the cold paths for transformation because they do not have much impact on the final output of the program. A path is said to be cold if any edge in the path is cold. So, to identify the cold path first, we have to find the cold edges in the CFG. According to [2, 10], there are two criteria on which an edge is said to be cold. These are local criteria and global criteria.

- Local criteria: According to [10], an edge is cold if the ratio of its frequency to its source node frequency is below a threshold.
- Global criteria: An edge is cold if its frequency as a percentage of total program flow falls below a threshold.
- If either of these conditions satisfies, then an edge is said to be cold [2].

3.2 Application of Approximate Transformation on the Identified Components

After successful identification of the approximable component of a program, the next step is the actual application of approximation, which converts the original code into the approximated one. From the literature of approximate computing, we came to know about the direction of application of approximation in the program [11]. The directions are as follows: on the input of the program (Sampling), skipping some of the computation, and replacement of code. The choice of the selection of the method depends on the goal of the application. Under these three broad categories, there are various software-based approximation transformation techniques available such as as-loop perforation [12], task skipping or code perforation [13], memorization [14–16], precision degradation, etc. In this paper, we are using the concept of code perforation as approximation transformation. Code perforation is a method in which the particular section of code from a program is skipped. According to our proposed methodology, if the identified cold path contains a section of code, which has less impact on the final output of the program, then without executing the section of code we can discard or skip the execution. In [13], the authors have designed a compiler called SpeedPress to perform code perforation. Example 1 explains the concept of code perforation.

In the above example (Example 1), the final output is “r” and it depends on the value of “product” and “s”. The final value of “s” is produced by the function “fun()”. This function is again decrementing the value of “q”. For the application,

Example 1 Code perforation

<pre> 1. Read(p) 2. q=p 3. s=10 4. product=1 5. if (q mod 2=0) 6. { 7. fun () 8. { 9. s=q/s 10. q=q-1 11. write(s) 12. } 13. } 14. product=product*q 15. r=product + s 16. Write(r) </pre>	CODE PERFORATION 
-----------------------------------------------------------------------------------------------------------------------------------------------------------------------------------------------------------------------------------------	-------------------------------------------------------------------------------------------------------------

if the contribution of “s” produced by the function is very less then to increase the efficiency of the program, we can skip the condition checking segment (if statement). By doing this, we cannot get the accurate result of “r”. Some error will be associated with “r” and the associated error must be within the tolerable limit, but the time taken by this section of code to execute will be reduced. And this is the beauty of approximate computing.

3.3 Output Analysis

By the application of approximation, the program produces the inexact result. But the produced result must be within the user-defined threshold value so that the system can behave adequately and tolerate the inaccurate result. For the verification of the correctness of the system, several correctness metrics are used. From the literature [17], we came to know about various types of correctness verification metrics depending on the output type. In our proposed method, assuming that our output is of multimedia type, we are using PSNR [12, 18] as a quality metric. This model provides the probabilistic bound on the deviated output. The user can use this bound to find if the output is within the threshold or not.

4 Case Study and Experimental Evaluation

We implement our approach on the C code developed for image compression using selective-Huffman coding technique. The overall steps involved in this approach is shown in Fig. 3.

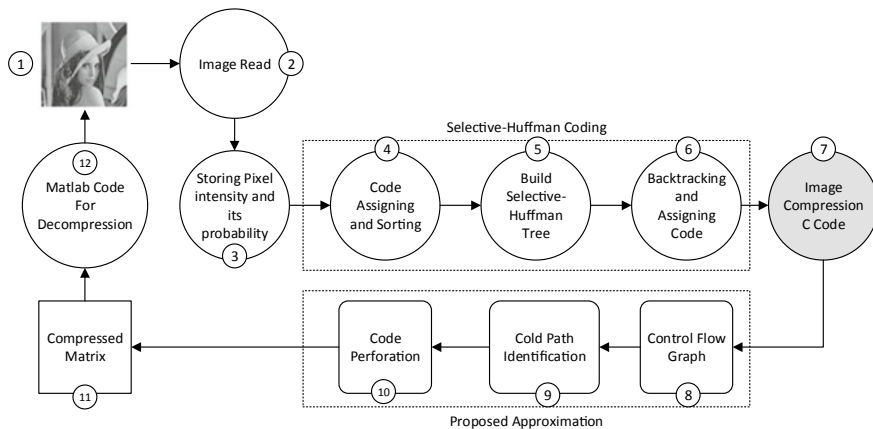


Fig. 3 Image compression process

For the image compression code block (highlighted in Image-3), we generate a control flow graph and identified the cold path using edge profiling algorithm proposed in [10]. After identifying the cold path, the corresponding C code is modified using code perforation technique and final compressed image matrix is generated. The compressed matrix is then decompressed using traditional MATLAB code for decompression and we get the original image. The entire process flow of encoding and decoding.

4.1 Control Flow Graph and Cold Path Identification

In this section, we will show you the cold edge and cold path in our control flow graph generated for image compression C code. The CFG for our code segment is shown in Fig. 4. The dashed edges indicate the cold edges generated from the algorithm described in [10].

Fig. 4 Control flow graph of our C code for image compression with dashed line showing the cold edges

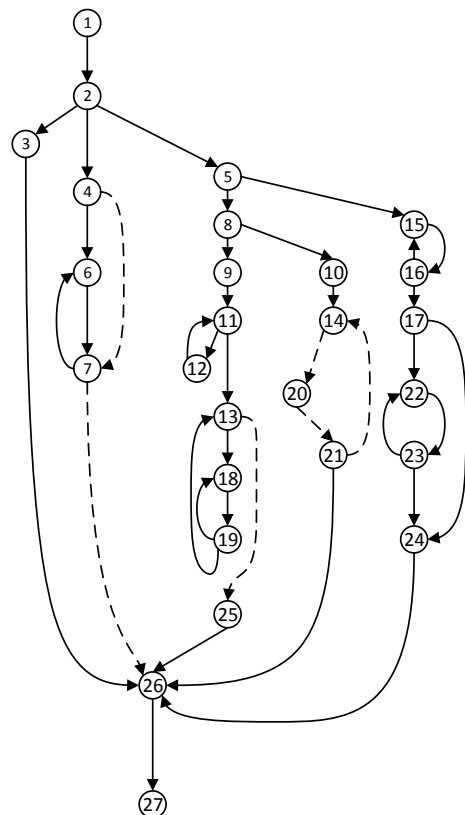




Fig. 5 Comparison of processed Lena image

After we find the cold edge, we have modified the code by reducing most of the loop to $n/2$ where n represents the number of iterations the loop executes. This concept is called loop perforation technique to reduce the execution time. By doing this, we will get a reduced version of the code and most of the loops in our code execute lesser time. The final code takes lesser processing time as compared to the original one. To compare the result of our process with the traditional process, we took the universally used Lena image and check for the visual clarity as compared with the traditional one. The overall result is shown in Fig. 5. These images will be generated after the decompression method corresponding to their compression.

Figure 5a shows the original image. Discrete cosine transform (DCT) is the widely used compression technique and it needs inverse DCT (IDCT) to obtain the original image. The result of Lena image for traditional DCT is shown in Fig. 5b. Figure 5c shows the result obtained which compressed using selective-Huffman coding. Finally, Fig. 5d shows the result obtained using our proposed technique.

5 Conclusion

We propose a program approximation technique that drastically reduces the original code. Reducing original code leads to higher processing power and take less time to produce a result. We got the result with slight reduction in the accuracy, but that is the theme of the approximate computing technique. We tested our approach on image compression through C code and found that the image clarity is quite acceptable. In the future, we are planning to apply this technique to other images and compare the result with traditional methods. The future plan also includes the calculation of peak signal-to-noise ratio (PSNR) of other images compressed using our approach, so that we can get compete analysis of the result we got.

References

1. Ball T, Larus JR (1994) Optimally profiling and tracing programs. *ACM Trans Prog Lang Syst (TOPLAS)* 16(4):1319–1360
2. Bond MD, McKinley KS (2005) Practical path profiling for dynamic optimizers. In: Proceedings of the international symposium on code generation and optimization. IEEE Computer Society
3. Gligoric M et al (2017) Mutation testing meets approximate computing. In: Proceedings of the 39th international conference on software engineering: new ideas and emerging results track. IEEE Press
4. Hariri F et al (2018) Approximate transformations as mutation operators. In: 2018 IEEE 11th international conference on software testing, verification and validation (ICST). IEEE
5. Barua HB, Mondal KC (2019) Approximate Computing: a survey of recent trends—bringing greenness to computing and communication. *J Inst Eng (India) Ser B* 1–8
6. Roy P et al (2014) Asac: automatic sensitivity analysis for approximate computing. *ACM Sigplan Notices.* vol 49, no 5. ACM
7. Roy P, Wang J, Wong WF (2015) PAC: program analysis for approximation-aware compilation. In: Proceedings of the 2015 international conference on compilers, architecture and synthesis for embedded systems. IEEE Press
8. Mitra S et al (2016) A verification guided approach for selective program transformations for approximate computing. In: 2016 IEEE 25th Asian test symposium (ATS). IEEE
9. Misailovic S, Roy DM, Rinard MC (2011) Probabilistically accurate program transformations. International static analysis symposium. Springer, Berlin, pp 316–333
10. Joshi R, Bond MD, Zilles C (2004) Targeted path profiling: Lower overhead path profiling for staged dynamic optimization systems. In: Proceedings of the international symposium on code generation and optimization: feedback-directed and runtime optimization. IEEE Computer Society
11. Venkatagiri R et al (2018) Impact of software approximations on the resiliency of a video summarization system. In: 2018 48th annual IEEE/IFIP international conference on dependable systems and networks (DSN). IEEE
12. Sidiropoulos-Douskos S et al (2011) Managing performance versus accuracy trade-offs with loop perforation. In: Proceedings of the 19th ACM SIGSOFT symposium and the 13th European conference on foundations of software engineering. ACM
13. Hoffmann H et al (2009) Using code perforation to improve performance, reduce energy consumption, and respond to failures
14. Brandalero M et al (2018) Accelerating error-tolerant applications with approximate function reuse. *Sci Comput Prog* 165:54–67
15. Sato Y et al (2015) An approximate computing stack based on computation reuse. In: 2015 3rd international symposium on computing and networking (CANDAR). IEEE
16. Tziantzioulis G, Hardavellas N, Campanoni S (2018) Temporal approximate function memoization. *IEEE Micro* 38(4):60–70
17. Akturk I, Khatamifar K, Karpuzcu UR (2015) On quantification of accuracy loss in approximate computing. In: Workshop on duplicating, deconstructing and debunking (WDDD). vol 15
18. Rinard M (2006) Probabilistic accuracy bounds for fault-tolerant computations that discard tasks. In: Proceedings of the 20th annual international conference on Supercomputing. ACM
19. Westbrook E, Chaudhuri S (2013) A semantics for approximate program transformations. arXiv preprint [arXiv:1304.5531](https://arxiv.org/abs/1304.5531)

Bidirectional LSTM with Attention Mechanism for Automatic Bangla News Categorization in Terms of News Captions



Md Shopon

Abstract The aim of any classification problem is to create a set of models that can classify the class of different texts and objects. Text classification is known as one such application. This problem can be used in various classification tasks, e.g., news category classification, identifying language, classification of text genre, recommendation systems, etc. In this paper, we propose a text classification method using bidirectional LSTM with attention mechanism to classify Bangla news articles. These news articles are collected from a renowned news portal Prothom Alo. The dataset consists of in total 383,304 news articles and there were total number of 12 different categories. Traditionally, news classification task is done in terms of news content. But in our work, we have performed classification based on the news captions which takes lesser amount of training time. We have achieved 91.37% accuracy using our approach. This is the state-of-the-art result that has achieved on this dataset.

Keywords Text classification · Bangla news categorization · News classification · Bidirectional LSTM · Attention mechanism

1 Introduction

Text categorization refers to the problem of categorizing some given text into some specific classes. The categories are mostly predefined and it depends on the text content in which category the text would fall into. With the recent advancement of textual data availability, processing these data automatically is now one of the most crucial tasks in the sector of machine learning and pattern recognition. The approach of using domain experts to classify and analyze the data to particular categories is both time and cost consuming, also it has some limitations.

M. Shopon (✉)
Department of Computer Science and Engineering,
University of Asia Pacific, Dhaka, Bangladesh
e-mail: shopon@uap-bd.edu

One of the most needed uses of text categorization is in electronic newspapers. In an electronic newspaper, a user is expected to read the articles from a computer screen that interests him/her the most. A reader may be interested to read news from different daily, weekly newspapers while being on move. It would most interest a user to receive articles or news from his/her favorite sources. Every user expects to have a custom personalized version of a newspaper with his/her favorable news in the front pages. This kind of task is being done on different international online news portals and blogging websites. So text categorization is a task that involves both business prospects and human labor reduction prospects.

There are not many Bangla news portals that use such an approach to interest their users in a more efficient way. In this work, we have introduced an approach to classify news categories from news captions. Many works have already conducted on text categorization based on the full news article. Text categorization from full news article is computationally expensive; this is why we have worked on classifying text category from news captions.

Several machine learning and statistical approach have been initiated for text classification. Among the most popular are regression model [1], support vector machine [2], decision tree, N-Grams [3–5], Naive Bayes classifier [6, 7], neural networks [8–10]. Most of this work is used on news class identification, authorship attribution, text genre classification [11], etc. But these tasks are mostly used in English languages. There are very little amount of task that has been done on Bangla news text classification. Bangla is known to be seventh most spoken language in this world. Due to lack of Bangla text dataset, not much amount of work has been done on Bangla text classification.

In this paper, we have introduced a bidirectional LSTM with attention mechanism-based news categorization in terms of news captions. The next parts of the paper are structured in the following manner: Sect. 2 discusses about the related works that have been done on Bangla text classification, Sect. 3 deals with the background terms for this work, Sect. 4 discusses about the corpus and working methodology that was used in this work, Sect. 4 states our approach for classifying the texts, in Sect. 5, we will discuss and compare our results with other works and finally, Sect. 6 will be the conclusion of this work.

2 Related Work

In this section, we will be discussing some of the work that has been done on Bangla text classification. Chy et al. [12] used a Naive Bayes classifier for classifying Bangla news text. Naive Bayes (Naive Bayes) classifier is often used in text classification experiments because of its effectiveness. The idea of Naive Bayes classifier is to adopt the joint probabilities of categories and words to predict the probabilities of different classes in a given document. In this work, they used their own developed RSS crawler to extract news articles from different online newspapers. After crawling the articles, they perform some preprocessing to make the text usable. Kabir et al. [13] Stochastic

Gradient Descent (SGD) classifier to classify texts. For feature extraction, they have used term frequency and inverse document frequency. Their used dataset consists of a total of 9127 articles and each of the articles was categorized in nine different categories. Mandal and Sen [14] used four different classification methods for his work. They are

- Naive Bayes classifier
- K-nearest neighbours (KNN) classifier
- Decision tree classifier
- Support vector machine (SVM).

They used 1000 articles as their corpus and their dataset was divided into five categories. They achieved the best result using SVM and decision tree. In text categorization, SVM classifier converts the original data into a higher dimension; from there, it can find a hyperplane for segregate the data by using important training details known as support vectors and then categorize the document. Mansur [15] used an N-Gram-based categorization method. They have used 1-year news articles from Prothom Alo news which were divided into 6 categories. An N-Gram is a subsequence of n number of items in the randomly given order.

3 Background

In this section, we will discuss the literature review of our used approach. We have used neural networks for text classification this is why this section will introduce you to the different methods and architectures we have used for classification. Neural network and deep learning are gradually taking over other traditional text classification algorithms. They have performed immensely well in the field of classification.

3.1 Fully Connected Neural Networks

Neural networks are inspired by mammalian cerebral cortex. Neural networks are generally formed in layers. These layers are built up of some interconnected ‘nodes’ which goes through an ‘activation function.’ Patterns are represented to the network via the first layer of neural network which is ‘input layer,’ it communicates to ‘hidden layers.’ There can be one or multiple hidden layers present in a neural network. The ‘hidden layer’ finally communicates with the ‘output layer’ which gives the output of the classification. Here, *Layer L₁* is the input layer, where $x_1, x_2, x_3, \dots, x_n$ is the input data. *Layer L₂* and *Layer L₃* is the hidden layer and *Layer L₄* is the output layer.

3.2 Recurrent Neural Networks

Recurrent neural networks (RNN) are a variation of fully connected neural network commonly used in different machine learning tasks such as speech recognition, image recognition and natural language processing (NLP). RNNs are designed to classify sequential characteristics and use specific patterns to predict the next possible scenario. RNN's input is not only the current input sample but also what they have anticipated previously. The terminology behind RNNs is to use sequential information. Usually, in a neural network, we consider that all the inputs and outputs depend on each other. But for many tasks, this assumption is wrong. If we want to predict the following word in a given sentence, it is necessary to know which word came before it. RNNs are termed recurrent because they perform the exact task for every component of a sequence, with the output being dependent on some of the previous calculations. RNNs have a 'memory' which keeps the information that was computed so far so that it can help to predict the next word.

3.3 Long Short-Term Memory (LSTM)

Hochreiter and Schmidhuber [16] proposed a modified version of a recurrent neural network for reducing the long-term dependency problem. LSTMs perpetuate the loss that is backpropagated through layers and time. By keeping a constant error, it allows recurrent neural networks to learn in many time steps continuously. LSTMs store information in a different way than a vanilla RNN. They store the information in a gated cell. It can perform three operations on the stored information,

- New information can be stored
- Information can be read
- Information can be erased or write.

This gated cell takes a decision which operation to perform. These analog gates can be either open or close. Being analog has some advantages over digital. As analog gates are differentiable, it is suitable for the backpropagation.

The RNN architecture can be defined using the deterministic flow from the previous to present hidden states. The deterministic flow is a function

$$\text{RNN: } H_T^{l-1}, H_{T-1}^l \rightarrow H_T^l$$

For vanilla RNNs, this function is given by

$$H_T^l = f(T_{n,n} H_T^{l-1} + T_{n,n} H_{T-1}^l), \quad \text{where } f \in \{\text{sigm, tanh}\}$$

On the other hand, the LSTM has intricate architecture that allows it to easily store information for a large number of timesteps. The 'long-term' memory is reserved in a vector of *memory cells* $c_t^l \in \mathbb{R}^n$.

LSTM in its core stores information from inputs that have already gone through it using the hidden state. This is called unidirectional LSTM. It only stores features or information of the past because the inputs it has seen are from the past. On the other hand, bidirectional LSTM(BiLSTM) follows a different architecture. In BiLSTM, the inputs run in both directions, one is from the past to future and the other one is from future to past and what alters in this approach from unidirectional is in the LSTM that runs in backward, we store information from the future and use the hidden states to combined information from both past and future.

3.4 Attention Mechanism

Attention is one of the most prominent ideas in the field of deep learning. Bahdanau et al. [17] first proposed the attention mechanism in their work for neural machine translation (NMT). This mechanism is proven to be very effective in different natural language processing tasks such as text completion, text generation and question–answer generation. Also, this mechanism works excellent for different computer vision tasks such as image captioning, image completion. Attention models imitate human behavior to process information by concentrating on some specific parts or segments of data that are most informative. To summarize attention networks, given a target hidden state h_t and source context vector c_t , we apply simple multiplication layer to concatenate the information from the two vectors in order to produce an attentional hidden state as follows:

$$\mathbf{h}_t = \tanh(W_c[c_t; h_t])$$

The attentional vector h_t is then passed to the softmax layer to generate the predicted distribution which is formulated as:

$$p(y_t|y_{<t}, x) = \text{softmax}(W_s h_t)$$

4 Corpus and Working Methodology

4.1 Corpus

The dataset we have used in this work is collected from Nabil [18]. This dataset consists of in total of 437,948 news articles from 32 different categories. Each dataset consists of ten different attributes. They are:

- Author
- Category Name in Bangladesh
- Category Name in Bangla

- Published Date
- Modification Date
- Tag
- Comment Count
- Title
- URL
- Main Content.

4.2 Dataset Preprocessing

Some of the categories in the dataset are not informative. So we preprocessed the data and removed 20 uninformative categories from the dataset. So in this work, we have worked with 12 different categories. Figure 1 shows the histogram representation of the dataset. Table 1 shows the category names and the number of samples in each category. Figure 2 shows some headline examples of different categories.

After that, we performed word-level tokenization. The maximum number word a headline has is 20. So we padded all the headlines to 20-word sequence and the labels were converted into one-hot encoded vector.

4.3 Model Architecture and Methodology

Standard long short-term memory networks are not able to identify the important parts for text classification. To resolve this issue, we introduced the attention mechanism which can capture the most important parts in a given sentence. Let $H \in R^D$ be a

Fig. 1 Histogram representation of the corpus

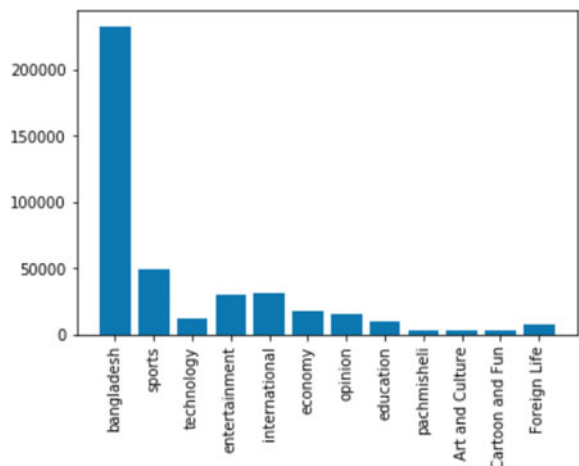


Table 1 Categories and number of samples

Category name	Number of samples
Bangladesh	232,504
Sports	49,012
International	30,856
Economy	17,245
Opinion	15,699
Technology	12,116
Education	9721
Foreign life	7402
Mixed news	3443
Art and cultural news	2702
Fun and cartoon	2604
Total samples	383,304

News Title	Category Name in English	Category Name in Bangla
ফরিদপুরে সড়ক দুর্ঘটনায় দুই নারী নিহত	Bangladesh	বাংলাদেশ
লর্ডসে দুর্দণ্ড শুরু অস্ট্রেলিয়ার	Sports	খেলা
রমজান মাস উপলক্ষে হিলি স্থলবদ্ধর দিয়ে পেঁয়াজ আমদানি	Economy	অর্থনৈতি
তিউনিসিয়ায় পার্ট্টাপার্ট সমাবেশ	International	আন্তর্জাতিক
প্রাথমিক শিক্ষা সমাপনীর প্রস্তুতি	Education	শিক্ষা
বেনকিউডের নতুন মনিটর বাজারে	Technology	বিজ্ঞান ও প্রযুক্তি
আমিরপুর জুনায়েদের বলিউড অভিযোগ!	Entertainment	বিনোদন

Fig. 2 News headlines of different categories

matrix of hidden vectors $[h_1, h_2, \dots, h_N]$ that the LSTM network produced. Here D is hidden layer size and N is the sentence length. The attention mechanism will result in an attention weight vector α and a hidden weighted representation r . The final sentence representation is given by:

$$h* = \tanh(W_p r + W_x h_N) \quad (1)$$

where $h* \in R^D$ and w_p and w_x are the projection of the parameters that were learned during the training phase. The attention mechanism helps the model to learn the most crucial part of a sentence when various aspects are considered.

The layer architectures are given below

1. Input Layer: The input layer receives a sentence.
2. Embedding Layer: The input vectors are then mapped into a lower-dimensional vector, where the maximum vocabulary size is considered 150,000.
3. Bidirectional LSTM Layer: We utilize bidirectional LSTM to get higher-dimensional features from the embedding layer. We have used two 100-dimensional BiLSTM layers.
4. Attention Layer: This attention layer is used for producing a weight vector and joins the word level features from every time step into a sentence-level feature vector by performing multiplication operation between the weight vector.
5. Flattening Layer: These sentence-level features are then converted into a one-dimensional vector.
6. FCNN Layer: After flattening, we fed the results into two 128-dimensional fully connected layers with 0.2 rate of dropout.
7. Output Layer: A probability distribution is produced in the output layer which is a softmax layer and it produces 12 different classes.

We have used categorical cross-entropy loss function and root mean squared propagation as the optimizer of our model.

5 Result Analysis

We have divided the dataset into two parts. One is for testing purpose and other one is training purpose. The dataset was divided into 70:30 ratio. Table 2 illustrates the division of the dataset.

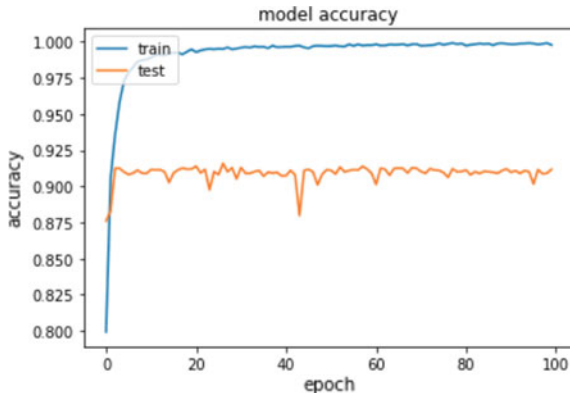
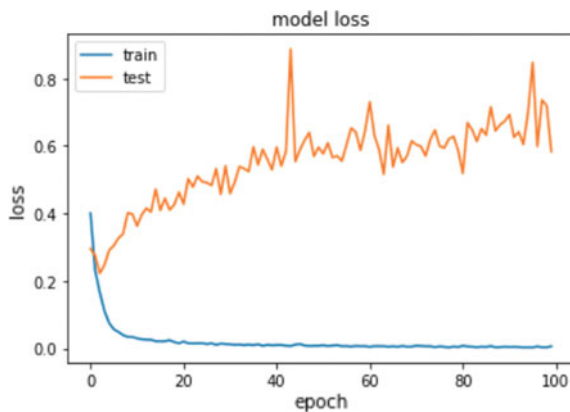
We have conducted three different experiments. The first experiment was done only by using LSTM networks, bidirectional LSTM networks and bidirectional

Table 2 Division of the dataset

Training sample	Testing sample
270,000	113,304

Table 3 Result and analysis

Method	Accuracy (%)
LSTM	86.06
Bidirectional LSTM	88.56
Bidirectional LSTM with attention mechanism	91.37

Fig. 3 Accuracy graph**Fig. 4** Loss graph

LSTM networks with an attention mechanism. We have trained all the experiments for 100 epochs. Table 3 shows the result of the different experiments we have conducted.

From the above table, we can see that bidirectional LSTM with attention mechanism performs better than other experiments. Figures 3 and 4 show the accuracy and loss graph for our experiment BiLSTM with an attention mechanism. This is the first work that has been done on this dataset. We consider our result as the state-of-the-art result for this dataset.

6 Conclusion

Text classification is a core research area in the deep learning field. Different approaches have been taken for English to achieve better automated classification performance. In this work, we evaluated the efficiency of bidirectional LSTM with attention mechanism-based text classification based on a news corpus of a renowned online news portal Prothom Alo. For Bangla, analyzing the accuracy of our approach has much better performance for text classification for Bangla. Most of the news classification tasks are done based on the news content. But in our work, we have done our work in terms of news captions. As the length of news captions is smaller than its content, the training time is lesser than training on news content.

Acknowledgements Thanks to Institute of Energy, Environment, Research and Development (IEERD), University of Asia Pacific for providing funding for this research.

References

- Genkin A, Lewis DD, Madigan D (2007) Large-scale bayesian logistic regression for text categorization. *Technometrics* 49(3):291–304
- Joachims T (1998) Text categorization with support vector machines: learning with many relevant features. In: European conference on machine learning. Springer, pp 137–142
- Fürnkranz J (1998) A study using n-gram features for text categorization. *Aust Res Inst Artif Intell* 3(1998):1–10
- Náther P (2005) N-gram based text categorization, institute of informatics. Comenius University
- Sebastiani F (2002) Machine learning in automated text categorization. *ACM Comput Surv (CSUR)* 34(1):1–47
- Mooney RJ, Roy L (2000) Content-based book recommending using learning for text categorization. In: Proceedings of the fifth ACM conference on Digital libraries. ACM, pp 195–204
- Forsberg M, Wilhelmsson K. Automatic text classification with Bayesian learning
- Lai S, Xu L, Liu K, Zhao J (2015) Recurrent convolutional neural networks for text classification. In: Twenty-ninth AAAI conference on artificial intelligence
- Zhang X, Zhao J, LeCun Y (2015) Character-level convolutional networks for text classification. In: Advances in neural information processing systems, pp 649–657
- Zhou C, Sun C, Liu Z Lau F (2015) A c-LSTM neural network for text classification. <http://arxiv.org/abs/1511.08630>
- Cavnar WB, Trenkle JM, et al (1994) N-gram-based text categorization. In: Proceedings of SDAIR-94, 3rd annual symposium on document analysis and information retrieval, vol 161175. Citeseer
- Chy AN, Seddiqi MH, Das S (2014) Bangla news classification using naive Bayes classifier. In: 16th International conference on computer and information technology. IEEE, pp 366–371
- Kabir E, Siddique S, Kotwal MRA, Huda MN (2015) Bangla text document categorization using stochastic gradient descent (SGD) classifier. In: 2015 International conference on computing and information processing (CCIP). IEEE, pp 1–4
- Mandal AK, Sen R (2014) Supervised learning methods for Bangla web document categorization. <http://arxiv.org/abs/1410.2045>
- Mansur M (2006) Analysis of n-gram based text categorization for Bangla in a newspaper corpus. Ph.D. thesis, BRAC University

16. Hochreiter S, Schmidhuber J (1997) Long short-term memory. *Neural Comput* 9(8):1735–1780
17. Bahdanau D, Cho K, Bengio Y (2014) Neural machine translation by jointly learning to align and translate. <http://arxiv.org/abs/1409.0473>
18. Nabil ZAN (2019) Bangla newspaper dataset

Sentence Relation Classification Using Deep Learning Experiments



B. Haripriya and Kishorjit Nongmeikapam

Abstract There are existing problems of finding relation between sentences for quite a few years. A system that can find the relation between a phrase and a document can be used for search engines, article finder and many more. This paper is focused on the problem statement of deciding whether given two sentences or two set of sentences are unrelated or related and if related whether it is mutually agreeing, disagreeing or neutral relation will be the classification outcome. Specifically, an attempt to find the title body consistency of a news article is done in this paper. For which, a deep transfer learning-based approach is proposed where the problem of detecting title body consistency is taken from the viewpoint of textual entailment (TE) where the title is considered as a hypothesis and news body is treated as a text. The framework used is bi-directional long short-term memory (LSTM) network which is a type of Recurrent Neural networks in deep learning with experiments with transfer learning technique.

Keywords Classification · Textual entailment · Bi-directional long short · Term memory · LSTM · Recurrent neural networks · Transfer learning

1 Introduction

The problem which is being taken into consideration deals with the study of the credibility and authenticity of information increased on the Web these days. For example, if a user inputs a phrase or claim in the Web app like “the US is the most powerful country in the world” or “Barak Obama is a gentleman” or “steps to follow to study abroad with scholarship.” These claims are taken and searched for many articles concerning that subject. If there are many reputed (and well known) sources

Supported by TEQIP-III.

B. Haripriya (✉) · K. Nongmeikapam

Indian Institute of Information Technology Senapati, Senapati, Manipur, India
e-mail: haripriya@iiitmanipur.ac.in

K. Nongmeikapam

e-mail: kishorjit@iiitmanipur.ac.in

which all “agree” with this claim, then the particular claim is most probably true. More concisely, the task can be defined as given a claim and a body of text (like news article), the system has to decide whether the body of the text generally “agree,” generally “disagree,” generally “neutral” or is completely “unrelated” to the claim. This problem is typically called a stance-detection problem. Given two pieces of texts, one being the premise (P) and another one is the hypothesis (H), the system has to decide whether:

- the H is the logical consequence of the P or not
- H is true in every circumstance (possible world) in which P is true.

The term entailment is used in the context of logical reasoning [1]. Entailment refers to when two statements are there and when one of them is true then the other is true and supports the former statement. For example, P: Johns assassin is in jail entails H: John is dead.

The main approach used is transfer learning which uses supervised features that have been used in several computer vision applications like face recognition, question answering, sentiment analysis and many more. These applications need to comparatively fewer data to be trained and tested. The features or the semantic information is stored in a neural network and will be used for a similar task but on a different corpus.

For this, standard recurrent models like long short-term memory (LSTM) models are used. Many basic concepts of natural language processing and deep learning were studied and this approach was picked. The different recurrent neural networks and making of those models were learnt in depth. The data set is having the title and body pairs with its labels (agree, disagree, discuss, unrelated). The back-end classification algorithm used is logistic regression with the word to vector embedding. Using the knowledge from an external embedding can enhance the precision of an LSTM because it can use the information that has been trained and distilled on a very large corpus of data. The pre-trained embedding used here is from fastText.

1.1 Recurrent Neural Networks

Figure 1 shows one unit of recurrent neural network (RNN). From bottom to top: input state (x), hidden state (h), output state (o). U , V and W are the weights of the network. Compressed diagram on the left and the unfold version of it on the right. Basically, RNNs are best fit for sequential data but they do have some drawbacks. Firstly, since they process inputs in temporal order, their outputs tend to be mostly based on previous context; secondly they have trouble learning time-dependencies more than a few time steps long [2]. As a solution, LSTM and bi-directional LSTM [3] were discovered which solves these drawbacks of RNNs.

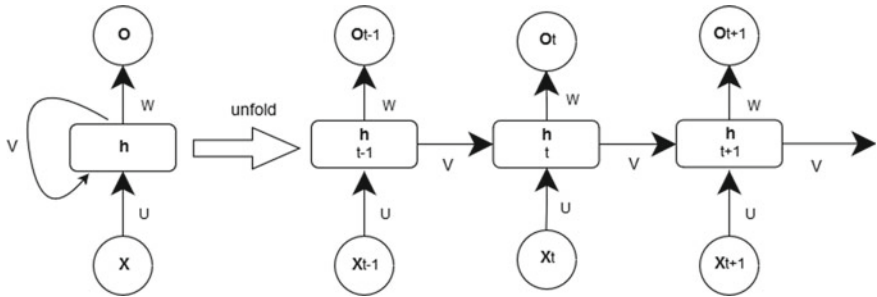


Fig. 1 Recurrent neural networks interior mechanism

1.2 LSTM

LSTM [4] is a variant of RNN architecture introduced to deal with long time-dependencies. It was motivated by an analysis of error flow in existing RNNs, which had a problem of long time lags and were inaccessible to existing architectures, because the back-propagated error either blows up or decays exponentially. LSTM contains hidden layers known as memory blocks that remember the input to the cells. Each of the memory cell consists of an input gate, output gate and forget gate. These can be imagined as write, read and reset operations for the cells.

1.3 Bi-Directional LSTM

Bi-LSTM connects two hidden layers of opposite directions to the same output. With this the output layer can get information from past (backwards) and future (forward) states simultaneously. This feature finely fits the problem statement of this paper.

In Fig. 2, O_1, O_2, O_3, O_4 are the output layers of each LSTM layer and X_1, X_2, X_3, X_4 are the input layers. Each LSTM layer is connected with the neighbor LSTM layer.

2 Related Works

The task of finding relation between any two entities has been done using various neural network architectures. The paper by Zeng et al. [5] a convolutional deep neural network(CNN) was used to extract lexical and sentence level features. Firstly, the word tokens are transformed to vectors by taking up word embedding. Then, lexical level features are extracted according to the given nouns. Meanwhile, sentence-level features are learned using a convolutional approach. These two-level features are concatenated to form the final extracted feature vector. Finally, the features are

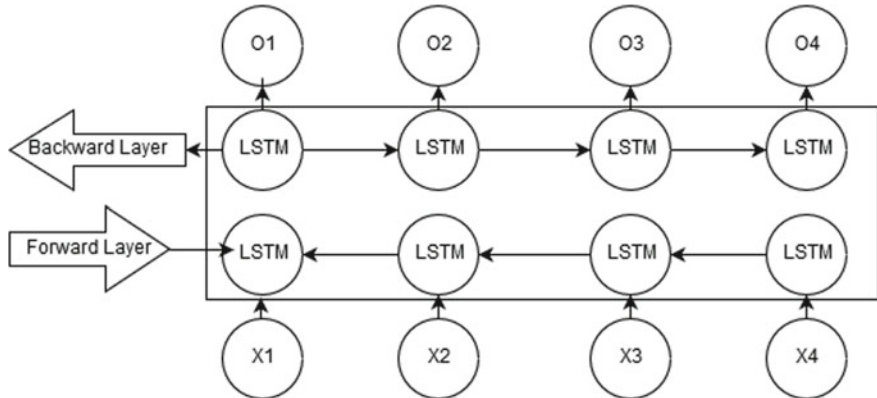


Fig. 2 Bi-directional LSTM interior mechanism

fed into a softmax classifier to predict the relationship between two marked nouns. Another paper by Augenstein et al. [6] focuses on stance detection as a task of classifying the attitude expressed in a text toward a target. Another paper [7] also utilizes 2D convolution to sample more meaningful information of the matrix. Experiments are conducted on six text classification tasks, including “sentiment analysis,” “question classification,” “subjectivity classification” and “newsgroup classification.”

3 Mechanisms

3.1 Initial Setup

The data sets taken for this project are Stanford Natural Language Inference (SNLI), Fake-News corpus, Facebook word to vector file (fastText-300dim). Stanford Natural Language Inference (SNLI) is a corpus created by Stanford NLP group which is available for free to download and use. It is a collection of 570 k human-written English sentence pairs manually labeled for balanced classification with the labels entailment, contradiction, and neutral, supporting the task of natural language inference (NLI), also known as recognizing textual entailment (RTE). News corpus is derived from the emergent data set created by Craig Silverman. The fastText vector file is freely available for download.

3.2 *Text-Pre-processing*

Generally, text pre-processing is done for transferring text from human language to machine-readable format for further processing. Removing punctuation, accent marks and other diacritics are only done because the special characters are least important in this paper and considering these might decline the flow of data analysis.

Firstly, the SNLI data set is split into hypothesis and text/body. Then the length of the longest sentence is found. Next, the classes will be encoded with sequence of 0 and 1 s. Later FastText vector representation is used to map each word to the corresponding vector representation in the data set and a new embedding matrix that contains only the embedding for words of the SNLI data set is present. These same initial steps are taken for News corpus also.

3.3 *Experiments*

The embedding matrix of the input data set is reshaped into three dimensions and given as input to the Bi-LSTM network. Bi-LSTM works on two passes, i.e., forward and backward. The outputs obtained from such networks for premise/document and title/hypothesis are concatenated. The concatenated vector is further given to feed-forward neural network (dense layer in this case) with ReLu [8] activation function. Later the output will be connected to the output layer, adding a fully connected hidden layer which is a usually an effective way of learning nonlinear combinations of these features.

Domain Adaption: This approach is a Naive approach where the training corpus and the testing corpus are different. The output obtained from the Bi-LSTM layer represents high level features of the data, while that output will be connected to the output layer, adding a fully connected hidden layer which is a usually an effective way of learning nonlinear combinations of these features. Since this was done for testing purpose, it is not that much efficient.

Transfer Learning: In this approach, two models with Bi-LSTM architecture are built and one of them is trained on SNLI corpus and the weights of the dense layers of this model were freezed and transferred to the second model. The second model is being trained and tested on Fake-News corpus. This way, the semantics learned from the SNLI corpus is used to detect stances (unrelated, discuss, agree, or disagree) between an unknown example pair. The basic idea of this approach is that the pre-trained embedding used has certain features that are common for all text based classification, like spam detection and many more. Those featured are freezed and used according to the needed classification task is transfer learning technique. This approach is well known in the problem condition where less data is available to train and test the system for new application. So for this, a standard data set is used to get the common features among the new examples.

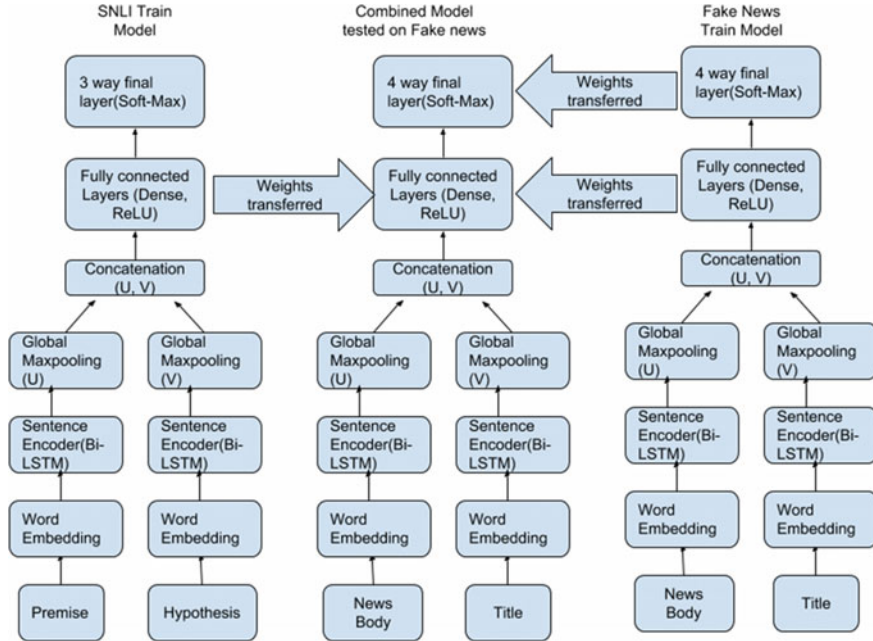


Fig. 3 Architecture of the hybrid model. Combined weights of two models are tested with the News corpus

Hybrid(Combined): At first, the models are built following the same process as described earlier. The first model is trained on SNLI corpus which is having four dense layers. The weights of the first two lower layers are saved and transferred to the third model. Then transfer of the two lower layers is done, as the SNLI corpus is very large, the vanishing gradient problem in the lower layers will be less compared to upper layers. The second model is trained on Fake-News corpus which is also having four dense layers. Here, transfer of the weights of upper two dense layers is done as shown in Fig. 3 to the dense of third model. Following this strategy, the benefits of both SNLI and Fake-News corpus are leveraged which are further utilized to train and test another model.

4 Results

Implementation includes the use of few necessary Python libraries for mathematical calculations and open source API for construction of deep learning models. The following are the verified results given by the proposed model:

1. Domain Adaption

Label/Label	Agree	Disagree	Discuss	Unrelated
Entailment	1	0	0	1
Contradiction	12	18	12	34
Neutral	1890	679	4452	18,314

Accuracy: 17.72%

2. Transfer Learning

Label/Label	Agree	Disagree	Discuss	Unrelated
Agree	23	0	1739	141
Disagree	17	2	572	170
Unrelated	3	0	18,176	170
Discuss	4	0	3355	1105

Accuracy: 76%

3. Hybrid (Combination)

Label/Label	Agree	Disagree	Discuss	Unrelated
Agree	502	98	1150	153
Disagree	207	108	307	75
Unrelated	135	25	17,520	669
Discuss	47	29	2241	2147

Accuracy: 79.789%

From the hybrid results, it has achieved the best accuracy among the results obtained from the three proposed models. In this model, the knowledge of semantically enriched corpus's (SNLI) is incorporated. Here, transfer of the weights from the upper two layers is done, because as the training corpus (Fake-News corpus) is comparatively less in size, the vanishing gradient problem in the upper layers will be less as compared to the lower layers. Then transfer of the weights of four-way final (with softmax activation) layer of the second model to the third model's final layer is done as the actual classification is performed in the third model. The justification of transferring this final layer's weights is empirical. Using these weights training and testing of the third model on News corpus is done.

No system is correct in all respect. All systems have their own advantages and disadvantages too. The proposed system is not the exception of that the state of

the art is 82.04% but the result got was 79.789% which could be due to less efficient pre-processing or any problem in the internal layers of model. The proposed system is fully deep learning-based approach which avoids any hand-crafted feature engineering and also we mitigate the data paucity problem of the target task by incorporating the concept of TE/NLI with this task which is conceptually similar to this task and making use of NLI benchmark data (SNLI) through transfer learning techniques.

5 Conclusion

In this paper, there was an attempt to investigate the role of textual entailment in news title body consistency through stance detection. As the problem of stance detection is quite similar with the problem of textual entailment. Framing this problem with the problem of textual entailment and utilizing the notion of it is done. For that purpose, various deep neural network-based transfer learning approaches were fostered. Typically, such kind of analysis leads to many researches upcoming in the field of artificial intelligence and machine learning. Future direction of this research includes enrichment of the best performing model by incorporating the relevance score between the title and body texts which is awaited to be resolved by future upcoming papers. Furthermore, testing of the best performing model in other kinds of corpus is also one of the future research scope of this paper.

References

1. Sammut C, Webb GI (2011) Encyclopedia of machine learning. Springer, Boston
2. Hochreiter S, Schmidhuber J (1997) Long short-term memory. *Neural Comput* 9(8):1735–1780
3. Hochreiter S, Bengio Y, Frasconi P, Schmidhuber J, Kremer SC, Kolen JF (2001) Gradient flow in recurrent nets: the difficulty of learning long-term dependencies. A field guide to dynamical recurrent neural networks. IEEE Press, New York
4. Graves A, Schmidhuber J (2005) Framewise phoneme classification with bidirectional LSTM and other neural network architectures. *Neural Netw* 18(5–6):602–610
5. Zeng D, Liu K, Lai S, Zhou G, Zhao J (2014) Relation classification via convolutional deep neural network. *zeng2014relation*
6. Augenstein I, Rocktäschel T, Vlachos A, Bontcheva K (2016) Stance detection with bidirectional conditional encoding. [arXiv:1606.05464](https://arxiv.org/abs/1606.05464)
7. Zhou P, Qi Z, Zheng S, Xu J, Bao H, Xu B (2016) Text classification improved by integrating bidirectional LSTM with two-dimensional max pooling. [arXiv:1611.06639v1](https://arxiv.org/abs/1611.06639v1) [cs.CL]
8. Cui J, Qiu S, Jiang M, Pei Z, Lu Y (2017) Text classification based on ReLU activation function of SAE algorithm. In: Cong F et (eds) AI advances in neural networks—ISNN 2017. Lecture notes in computer science, vol 10261. Springer, Cham

Spectral Analysis of Consonants in Arunachali Native Language—Adi



Sajal Sasmal[✉] and Yang Saring[✉]

Abstract In this article, an attempt has been made to analyze the spectral properties of consonants of Adi, which is one of the most common native languages of Arunachal Pradesh, India. The formant frequencies and spectral properties of consonants in Adi language like /t/, /k/, /p/, /d/, /g/, /b/, /n/, /ng/, /m/, /ny/, /r/, /s/, /h/, /j/, /y/, /l/ were studied. Also, the speech samples were analyzed in a wideband spectrogram. The first formants frequencies (F0) were observed to be varied from 538 Hz to 1228 Hz and the second formants frequencies (F1) range from 1190 to 2822 Hz for /k/, whereas for /d/, we found the ranges of F0 and F1 to be in the range from 303 to 1621 Hz and 1710 to 2732 Hz, respectively. It was observed that the formants frequencies of consonants (unvoiced part) are much higher than the formants frequencies of vowels (voiced part).

Keywords Adi · Formant · Phonemes · Spectrogram · ASR · Pitch

1 Introduction

Automatic speech recognition (ASR) system allows a machine to recognize the words spoken by an individual and converts it into text. ASR system is found in different types of applications like handsfree control and operation (as in airplanes and modern cars), telephone communication with information systems, automatic query answering system, automatic dictation, government information system, etc. Owing to advances in computing devices and architectures, the success of algorithm development and availability of large quantities of data ASR system has seen a rapidly rising figure of practical applications as well as commercial markets [1].

S. Sasmal (✉) · Y. Saring

Department of Electronics and Communication Engineering, National Institutes of Technology
Arunachal Pradesh, Yupia 791112, India
e-mail: sajal.sasmal@gmail.com

Y. Saring
e-mail: ys.nitap@gmail.com

Since the first ASR system was developed in 1952 for small vocabulary digits, ASR systems have been developed in several languages like English, Arabic, German, Mandarin, Spanish, and French, etc. India is linguistically very rich with eighteen constitutional languages written in ten diverse scripts [2]. In India, machine-oriented interfaces are restricted to the computer usage to a miniature fraction of the citizens, who are both computer skilled as well as familiar with on paper English. So there is a particular necessity for the ASR system to be developed in different languages spoken in India [2]. In a special reference to northeastern part of India, 350 languages have been identified in this region, and several types of research are going on in different northeastern languages such as Assamese [3], Mizo [4], Manipuri [5], Bodo [6], and Khasi [7].

Linguistically, Arunachal Pradesh is very rich and diverse; around 50 distinct languages are spoken in along with innumerable dialects and sub-dialects thereof. However, at a time of rapid globalization when languages are dying at the rate of one language every fortnight, many of the languages in Arunachal Pradesh are endangered; Adi is one of the endangered languages [8] with around only 100 thousand people speaking this language. Therefore, for the preservation of such endangered languages technical intervention such as digital archiving, implementing ASR in such language is of utmost importance. To implement ASR in any language, the analysis of its vowels and consonants are of utmost importance. Legoh et al. had created “Speech Corpus of Adi” and studied linguistic phoneme characteristics [9]. In 2018, Bordoloi et al. performed a spectral analysis of “vowels of Adi” in their work [10].

There are approximately 50 phonemes in Adi language with 16 consonants, 7 long vowels, 7 short vowels, 19 diphthongs (transition between two vowels), and 1 triphthong [9–11]. The Adi consonants [9, 11] are shown in Table 1.

In the Adi language, there is no dental and labio-dental fricative, retroflex, and aspirated types sound. For example, [s] and [h] are fricatives but one can swap in Adi speech without any variation in meaning.

Table 1 List of Adi consonants

	Alveolar	Glottal	Velar	Bilabial	Palatal
Stops (v) (uv)	/t/ /d/		/k/ /g/	/p/ /b/	
Nasals (v)	/n/		/ng/	/m/	/ny/
Roll (v)	/r/				
Fricatives (uv)	/s/	/h/			
Affricates (v)	/tʃ/				
Approximant (v)					/y/
Lateral approximant (v)	/l/				

v voiced part, uv unvoiced part

2 Formant Frequency of Speech

Formant frequencies were computed using the linear predictive coefficient technique [10]. Different vowels and consonants have a different set of formant frequencies. Similar sounds /e/ and /a/ are close by similar formant frequencies but distinct sounds have a different range of formant frequencies. So formant frequencies can be considered as the signature of vowels and consonants to recognize them. High-pass filtering of log power spectrum yields pitch harmonics, i.e., useful for pitch estimation and low pass filter is used to measure formants information of the speech. The pitch frequencies may be ignored and formant frequencies may be considered at the time of typical speech sound recognition. In this article, an attempt has been made to find the range of the formant frequencies of different consonants of Adi, which would be useful in the design of an ASR system of Adi language.

In this paper, an analysis was done for the first 3–4 formants for different consonants, and scatter plots are shown. The formant frequencies were measured using “WaveSurfer” and “Praat-6.1.09”.

3 Data Set

For spectral analysis of Adi language, we have recorded 684 Adi sentences from 7 native Adi speakers. Among the 7 speakers: 3 speakers are male and 4 are females. The speech samples were collected with a sampling rate of 8 kHz and were stored in .wav format.

4 Spectral Analysis

The Adi sentence “no kape aidun” uttered by an Adi female speaker (AD-F-01) is shown in Fig. 1. The total duration of the sentence is 5 s but the speaker response starts from 1.05695 s and ends at 2.08816 s. So the speaker’s involvement was 1.03121 s only. The word “no” exists from 1.05695 s to 1.2370 s and among this, the consonant /n/ lies between 1.0569 s and 1.1118 s.

Time is represented along the X-axis and amplitude along the Y-axis of the speech signal. We look into the spectral properties to compute formant frequencies, pitch, and energy intensity of different consonants. In Fig. 1, all four formants are shown by red dots for the Adi sentence “no kape aidun.” The first formant exists just above X-axis then second formant, third formant, and fourth formant are spread above all. From the spectrum in Fig. 1, it is observed that the formants follow a sequence for the speech part but there is no uniformity for noise part of the sound. Pitch is shown by the blue line in the spectrum, whereas the variation of intensity in the dB scale is represented by the yellow line. So we can observe that the speech part intensity has

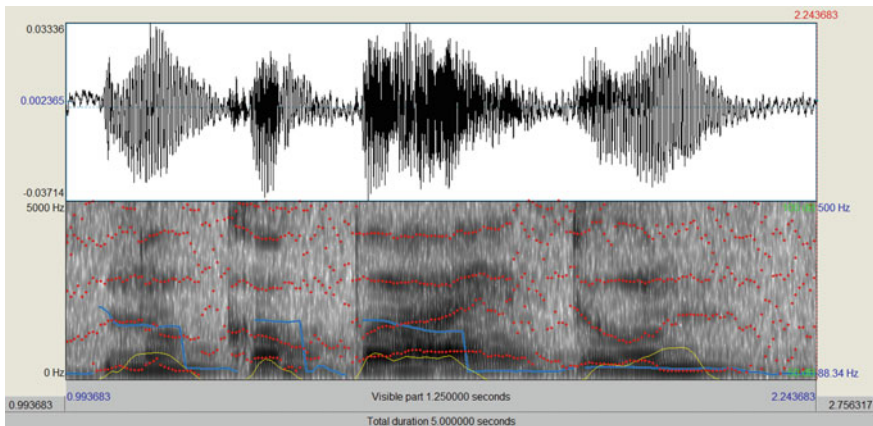


Fig. 1 Sound waveform and spectrogram with formant plot of Adi sentence “no kape aidun”

high value but it is very low for the noise section. Here, /n/ was uttered for 0.0549 s. In this duration, first formant frequency (F0), second formant frequency (F1), third formant frequency (F2), forth formant frequency (F3) have been calculated using 8 formants position in the spectrogram. F0 lies between 261 and 365 Hz, i.e., mean in this section is 306 Hz. Mean of F1, F2, F3 in the selected part are 1608 Hz (1576–1665 Hz), 2795 Hz (2717–2909 Hz), 4095 Hz (3855–4437 Hz), respectively. The minimum pitch in this section is 204 Hz and the maximum is 243 Hz but the mean pitch is 213 Hz. Mean energy intensity in the section is 53.88 dB (51.83–56.31 dB). In the word “kape” consonant /k/ is found in between 1.2652 s and 1.2996 s, so /k/ was uttered for 0.0344 s only. For /k/ the mean of formant frequencies F0, F1, F2 is 748 Hz (483–1328 Hz), 1425 Hz (1311–1968 Hz), 2739 Hz (2594–3031 Hz), and 4318 Hz (4155–4523 Hz), respectively. The minimum pitch in the section is 96 Hz and the maximum is 101 Hz giving mean to be 98 Hz. Mean energy intensity in the section is 46.02 dB (44.68–46.71 dB). The details of formant frequencies of /k/ are shown in Table 2.

Table 2 Details of formant frequencies of /k/ in the word “kape” by “AD-F-01”

Time (sec)	F0 (Hz)	F1 (Hz)	F2 (Hz)	F3 (Hz)
1.266827	1328	1968	3031	4523
1.273077	680	1304	2595	4488
1.279327	651	1311	2675	4271
1.285577	696	1358	2754	4245
1.291827	714	1388	2760	4233
1.298077	483	1341	2682	4155
	748(mean)	1425(mean)	2739(mean)	4318(mean)

The formants frequencies: F0, F1, F2, and F3 of consonant /k/computed for all seven speakers by considering more than twenty /k/phoneme uttered by each speaker is shown in Table 3.

The formant frequencies F0–F3 of consonant /b/were computed and the scatter plot of F0 versus F1 is shown in Fig. 2. We observed that the F0 lies in the range from 235 Hz to 492 Hz, F1 lies in the range from 1266 Hz to 1782 Hz, F2 in the range from 2428 Hz to 3750 Hz and F3 in the range from 3749 Hz to 4341 Hz. We notice that the range of F0 is 235–492 Hz and F1 is 1266–1782 Hz considering all four speakers. The frequency range of F2 and F3 are 2428–3750 Hz and 3749–4341 Hz respectively.

The scatter plot for F0 versus F1 for consonant /k/ is shown in Fig. 3 and it is observed that the formant frequencies F0 lies between 538 Hz and 1228 Hz and F1 lies in the range from 1190 Hz to 2822 Hz.

In Fig. 4, we have plotted F0 versus F1 for consonant /n/and it is observed that F0 lies in the ranges from 261 to 485 Hz and F1 lies in the range from 1256 to 1922 Hz, whereas for consonant /s/the variation of F0 and F1 are in the range 343–1738 Hz and 1802–3120 Hz, respectively, as shown in Fig. 5.

The range of formants frequencies F0, F1, F2, and F3 of different Adi consonants: /b/, /k/, /n/, /s/, /ng/, /t/, and /d/ were computed and listed in Table 4.

Table 3 Average of formant frequencies of consonant /k/

Speaker	Average F0 (Hz)	Average F1 (Hz)	Average F2 (Hz)	Average F3 (Hz)
AD-F-01	846.25	1806.94	2991.94	4247.50
AD-M-01	717.67	1608.33	2783.75	4154.00
AD-F-02	910.20	2052.53	3022.67	4412.92
AD-M-02	825.67	1782.27	2974.27	4154.00

Fig. 2 F0 versus F1 plot for consonant /b/of 4 speakers

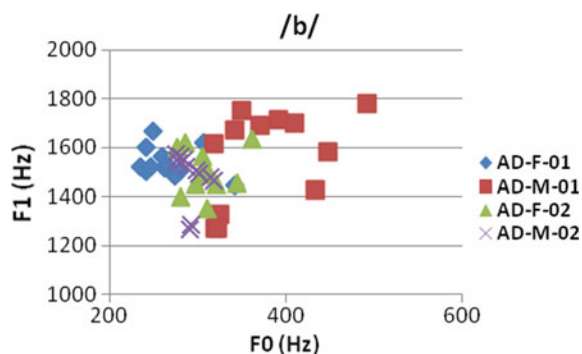


Fig. 3 F0 versus F1 plot for consonant /k/ of 4 speakers

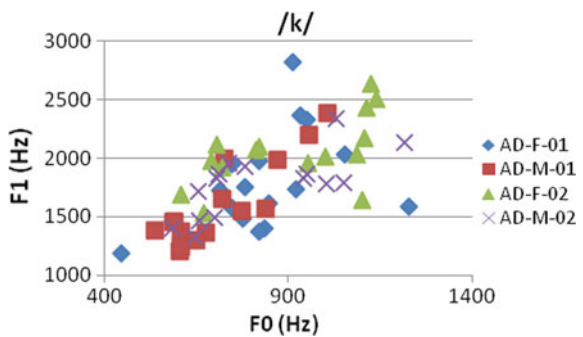


Fig. 4 F0 versus F1 plot for consonant /n/ of 4 speakers

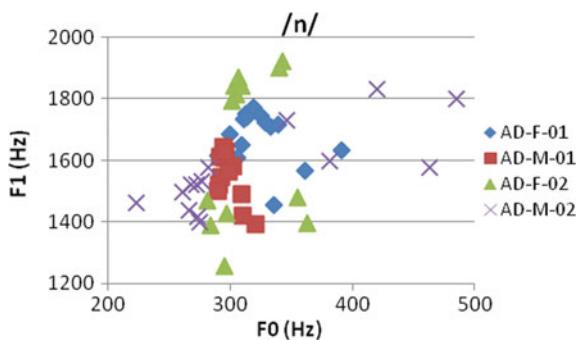
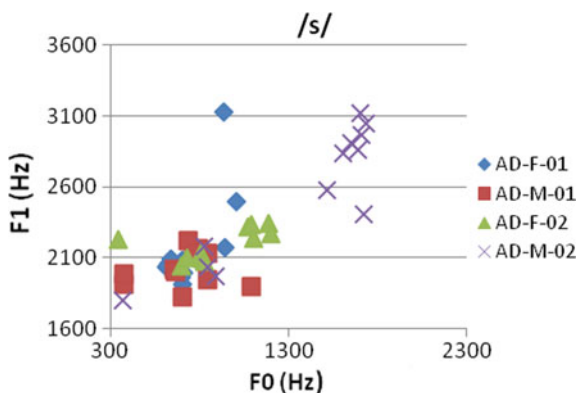


Fig. 5 F0 versus F1 plot for consonant /s/ of 4 speakers



5 Conclusion

In this article, we have studied the formant frequencies of consonants in Adi language. For this work, we recorded 684 Adi sentences from 7 Adi speakers and detected different consonants from those speech samples. The first four formants frequencies: F0–F3, pitch period and mean energy intensities were computed. By analyzing the

Table 4 Range of formants frequencies of different Adi consonants

Adi consonant	Range of F0 (Hz)	Range of F1 (Hz)	Range of F2 (Hz)	Range of F3 (Hz)
/b/	235–492	1266–1782	2428–3750	3749–4341
/k/	538–1228	1190–2822	2149–3698	3817–4826
/n/	261–485	1256–1922	2525–3277	3579–4549
/s/	343–1738	1802–3120	2739–4554	4163–5123
/ng/	280–542	1289–1664	2533–2932	3915–4357
/t/	658–1470	1524–2715	2501–3613	4077–5061
/d/	303–1621	1710–2732	2672–4099	4057–5667

spectrogram, we detected all formant frequencies of consonants like /b/, /k/, /n/, /s/, /ng/, /t/, and /d/. The range of F0 is from 235 Hz to 492 Hz and F1 is from 1266 Hz to 1782 Hz for /b/. The ranges of first two formant frequencies: F0 and F1 for consonants /k/, /n/, /s/, /ng/, and /t/ are 538 Hz to 1228 Hz and 1190 Hz to 2822 Hz; 261 Hz to 485 Hz and 1256 Hz to 1922 Hz; 343 Hz to 1738 Hz and 1802 Hz to 3120 Hz; 280 Hz to 542 Hz and 1289 Hz to 1664 Hz; 658 Hz to 1470 Hz and 1524 Hz to 2715 Hz; 303 Hz to 1621 Hz and 1710 Hz to 2732 Hz, respectively. We observed that the formants frequencies of consonants (unvoiced part) are much higher than the formants frequencies of vowels (voiced part).

References

1. Baker JM, Deng L, Glass J, Khudanpur S, Lee C, Morgan N, O'Shaughnessy D (2009) Developments and directions in speech recognition and understanding, Part 1 [DSP Education]. IEEE Signal Process Mag 26(3):75–80
2. Chandrasekar M, Ponnavaikko M (2008) Tamil speech recognition: a complete model. Electron J (Tech Acous)
3. Sarma MP, Sarma KK (2011) Assamese numeral speech recognition using multiple features and cooperative LVQ-architectures. Int J Electr Electron 5(1):27–37
4. Lalhminghlui W, Das R, Sarmah P, Vijaya S (2017) A Mizo speech database for automatic speech recognition. In: Conference of the oriental chapter of international committee for co-ordination and standardization of speech databases and assessment technique (O-COCOSDA), pp 302–306
5. Ningthoujam N, Prathim VR (2016) Designing of a feature extraction system for Manipuri language. Int J Sci Res Dev 4 (2)
6. Thakuria LK, Acharjee P, Das A, Talukda PH (2014) BODO speech recognition based on hidden Markov model Toolkit. Int J Sci Eng Res 5(1)
7. Arjunasor S, Deka GK, Ismail T, Singh LJ (2016) Khasi dialects identification based on Gaussian mixture model. Int J Eng Sci Comput 6(4):3882–3885
8. Post M (2011) A documentation of the upper belt variety of Minyong (Adi), Arunachal Pradesh, North East India. Endangered Languages Archive
9. Legoh K, Bhattacharjee U, Tuithung T (2013) Development of multi-variability speech corpus of Adi language for speech recognition researches. Int J Adv Res Comput Sci Softw Eng (IJARCSSE) 3(10):604–610

10. Bordoloi S, Saring Y (2018) Spectral analysis of vowels of Adi language of Arunachal Pradesh. In: 2nd international conference on electronics, materials engineering and nano-technology (IEMENTech), pp 1–4
11. Lalrempuii C (2005) Morphology of the Adi language of Arunachal Pradesh (Doctoral dissertation)

Double Gate Tunnel FET Versus Double Gate MOSFET: Electrical Properties Comparison



Menka Yadav

Abstract In this manuscript, an investigation, with the help of extensive device TCAD Sentaurus simulations, is presented for comparative analysis to understand the effects of variations in gate and drain potential on the device electrical properties of such silicon double gate tunnel field effect transistor (DG TFET) as well as DG MOSFET. The study is mainly focused at electrical properties like electrical channel potential, electric channel field, electron density, electron quasi-fermi potential in channel, drain current, and threshold voltage calculation. From the TCAD simulated study, it is found that electrical properties in the channel region of DG TFET are quite different from DG MOSFET. It is observed that the central channel potential of DG TFET is not pinned to a fixed potential even after threshold voltage (as in case of DG MOSFET occurs), but it initially increases and later on decreases with increasing gate voltage. It is also observed that the threshold voltage extracted with maximum transconductance method or linear extrapolation (LE) and electron quasi-fermi potential of DG TFET are much higher than the DG MOSFET's one. It is also observed that just on-set of inversion is not sufficient condition for DG TFET threshold voltage. These differences are explained in this paper with proper physics reasoning.

Keywords BTBT · DG tunnel FET · Electric potential · Electron density · Electric field · Threshold voltage · Electron quasi-fermi potential · Drain current

1 Introduction

Nowadays, we are living the era of More-Moore and More than Moore, this is because of the continuous down scaling of the benchmarked device—metal–oxide–semiconductor field effect transistor (MOSFET) which inevitably leads to fundamental physical limits that can no longer be overcome by technology innovation alone. Limits for conventional MOSFETs are: subthreshold leakage which limits the subthreshold

M. Yadav (✉)

Department of Electronics and Communication Engineering, Malaviya National Institute of Technology Jaipur, Jaipur, Rajasthan, India
e-mail: Menka.er@gmail.com

swing (SS_{MOSFET}) to 60 mV/dec at room temperature and higher OFF state device current, I_{off} , at lower device dimensions. Hence, new device concepts are needed.

The tunnel FET, based on the interband tunneling effect, has recently been subject to a variety of both theoretical and experimental studies [1–4]. It is being demonstrated that the device has several superior properties as compared to the benchmarked MOSFET device.

TFETs have the possibility to overcome the drawbacks of MOSFET; therefore, they are widely studied in recent years [5, 6]. TFETs may have SS_{TFET} lesser than MOSFET at room temperature because SS_{TFET} is independent of temperature, therefore, TFETs can be a good option to operate at higher temperatures, without any compromise on reliability. TFETs works on band to band tunnelling (BTBT) principle; therefore, it could be scaled down without any degradation in its electrical properties [7]. For example, I_{off} and threshold voltage (V_{Th}) in MOSFET depend on the gate length scaling but in case of TFET, these properties do not change with further gate length scaling [8]. Because of its superior properties, TFETs can be used in lower power applications such as SRAMs.

In this manuscript, electrical properties of DG TFET like electric potential, electric field, electron density, electron quasi-fermi potential, etc., in channel region are comparatively studied with DG MOSFET. Threshold voltage for both devices using maximum transconductance method or linear extrapolation method (LE) is also presented, as explained in [9].

The organization of the paper is as follows: Sect. 2 describes the device structure and simulation setup, Sect. 3 describes simulation results and discussions and Sect. 4 concludes the work.

2 Device Structure and Simulation Setup

The DG TFET device structure under study is presented in Fig. 1. Here, a transverse cut AA' is taken. Cut AA' is used to explore the results at point A, which is termed as surface or Si-oxide interface and at the mid of the channel, i.e., at mid of cut AA' , which is termed as the mid-channel point. The device parameters are listed in Table 1. For DG MOSFET also same device parameters are used, except phosphorus source doping is used.

Fig. 1 Double gate tunnel FET device structure

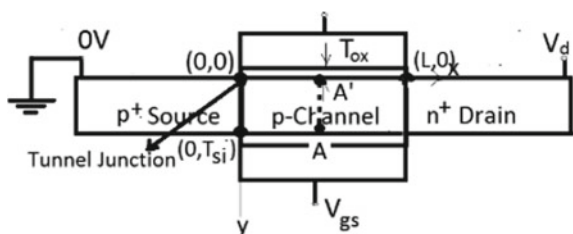


Table 1 Double gate tunnel FET device parameters

	Parameter	Value
1.	Gate length, L_g	50 nm
2.	Source doping, p -type	$10^{20}/\text{Cm}^2$
3.	Channel doping- p -type	$10^{17}/\text{Cm}^2$
4.	Drain doping. n -type	$5 \times 10^{18}/\text{Cm}^2$
5.	Gate oxide, HfO_2 , ϵ_{ox}	$22, \epsilon_0$
6.	Gate oxide thickness, T_{ox}	3 nm
7.	Silicon body thickness, T_{Si}	10 nm

Two-dimensional TCAD device simulations are done using TCAD device simulator Sentaurus [10]. To model BTBT, electric field dependent Kane's [11]- model is used for physics of the device. Since the source and drain regions are heavily doped and tunneling current is strongly dependent on band gap, band-gap narrowing model, *OldSlotboom*, is also included. High field saturation mobility model for electrons and holes is included. Shockley Reed Hall (SRH) model is used as carrier recombination model. Simulations are done for various gate voltage and drain voltages. The doping in the n -drain, p -source, and p -layer is kept constant at the optimum value and doping profiles used are abrupt. For n -type impurity, phosphorus, boron as a trivalent impurities are used and gate work function is set as 4.25 eV.

3 Simulation Results and Discussions

In this section, the simulated results for DG TFET at the surface, i.e., at point A and at the mid of the channel are presented and compared with DG MOSFET results. Electric properties at Silicon- HfO_2 interface of AA' cut, i.e., at point A are termed as surface electric properties and at mid of AA', i.e., center of the channel are termed as mid-channel properties.

3.1 Drain Current and Gate Threshold Voltage

Gate voltage, V_{gs} versus drain current, I_{ds} is shown in Fig. 2 for DG MOSFET and DG TFET. In Fig. 3, gate threshold voltage versus drain voltage is shown for both devices. We observed that DG TFET has higher threshold voltage than DG MOSFET. Here, the threshold voltage is extracted using maximum transconductance method, as given in [9], for MOSFETs. DG MOSFET has lower threshold voltage as compared to DG TFET because in DG MOSFET after on-set of inversion device becomes ON, while in case of TFET, on-set of inversion is not sufficient condition to make the device ON, as given in [12]. A saturation in the drain current is seen

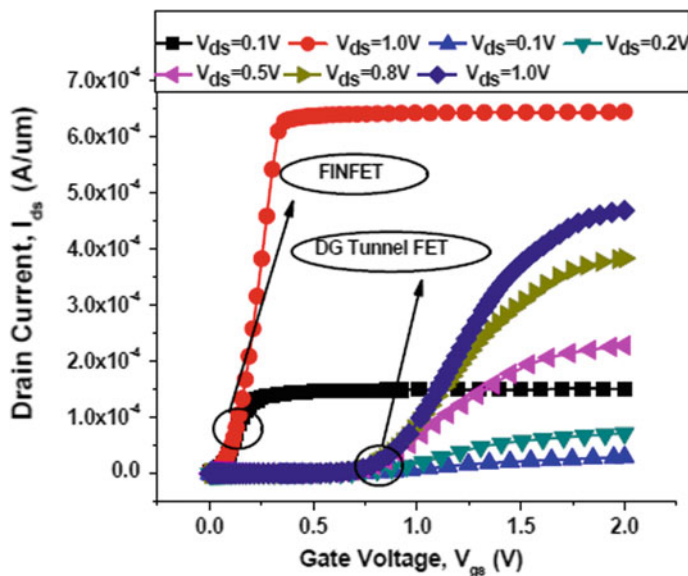


Fig. 2 Drain current versus applied gate voltage for DG TFET and DG MOSFET

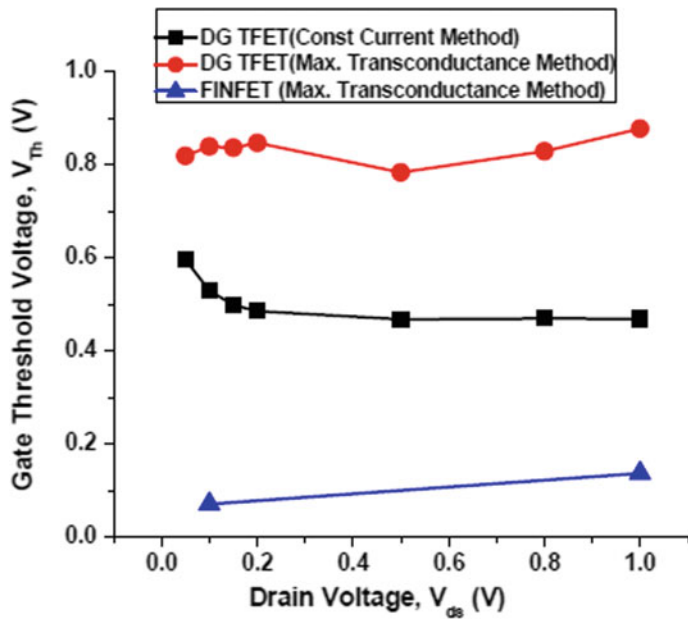


Fig. 3 Threshold voltage for DG TFET and DG MOSFET

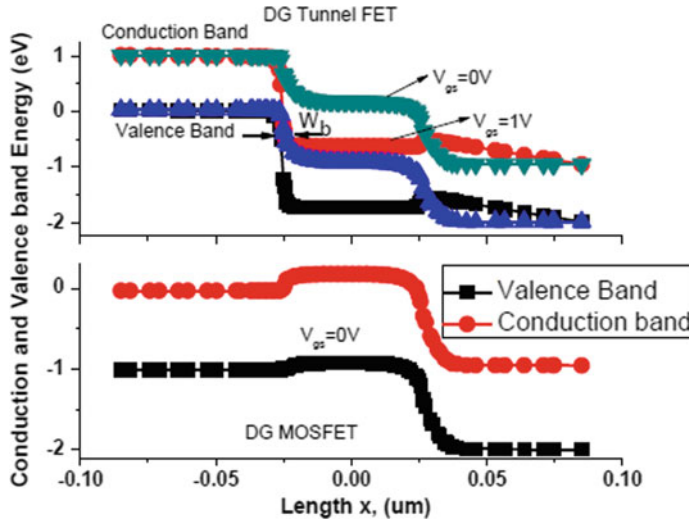


Fig. 4 Energy band diagrams for DG tunnel FET and DG MOSFET at $V_{ds} = 1.0$ V

after a particular applied gate voltage, in DG MOSFET. This is because velocity saturation is obtained by electrons, hence the (drift) current starts to saturate. While in DG, TFET current is increasing with increase in applied gate voltage, V_{gs} , this is because after threshold voltage (which is higher than DG MOSFET), the band to band tunneling (BTBT) generation rate, G_{btbt} , increases at a rapid pace and this rate is also controlled by applied drain voltage, therefore, as we increase drain voltage the tunnel barrier width, w_b decreases, as shown in Fig. 4; hence, average electric field across the tunnel junction gets increased and we get

-larger current for larger drain voltages [13–15]. The tunneling generation rate is given in Eq. (1).

$$G_{btbt} = A \frac{E_{avg}^2}{\sqrt{E_g}} \text{Exp}\left(B E_g^{3/2} / E_{avg}\right) \quad (1)$$

where

$$A = 3.5 \times 10^{21} \text{ eV}^{0.5}/\text{cm s V}^2$$

$$B = 22.6 \times 10^6 \text{ V/cm-eV}^{3/2}$$

$$E_g = \text{Silicon energy band gap}$$

$$E_{avg} = \text{Average electric field along tunnel path}$$

Here tunneling is occurring at source end denoted by circles in Fig. 1.

3.2 Electron Quasi-Fermi Potential

In Fig. 5, electron quasi-fermi potential (eQFP) versus drain voltage is shown for DG TFET. For DG MOSFET, eQFP although varies with applied drain voltage, V_{ds} its range is between 0 and 0.1 V even when V_{ds} is varied between 0 and 1.0 V. This is because the applied drain voltage sees a reversed biased $p-n$ junction at the drain/channel junction, therefore, whole drain voltage is applied across this junction and channel eQFP remains zero always.

In case of DG TFET, $p-n$ junction is formed at source/channel junction, therefore, the applied drain voltage can be seen at the junction and this sets channel eQFP equal to drain voltage, below threshold voltage as shown in Fig. 5. After gate threshold, there is enough tunneling current to make the device ON and hence the channel/drain region will act as a series connected resistance, since now channel is a resistive region so there will be a potential drop equal to the drain current times of the channel resistance. This will make the channel eQFP $\neq V_{ds}$; hence, there is a drop as seen at higher gate voltages, and this pattern is also followed at higher drain voltages with same physics.

But, in subthreshold regime, a hip hop change at higher drain voltages is seen. This is because for higher drain voltages, the whole channel p -type (since inversion is not set for lower gate voltages, as is clear from Fig. 6a) will work like a potential barrier, therefore, a fall in eQFP seen for higher drain voltages, which after onset of inversion follows the same physics as described in above paragraph.

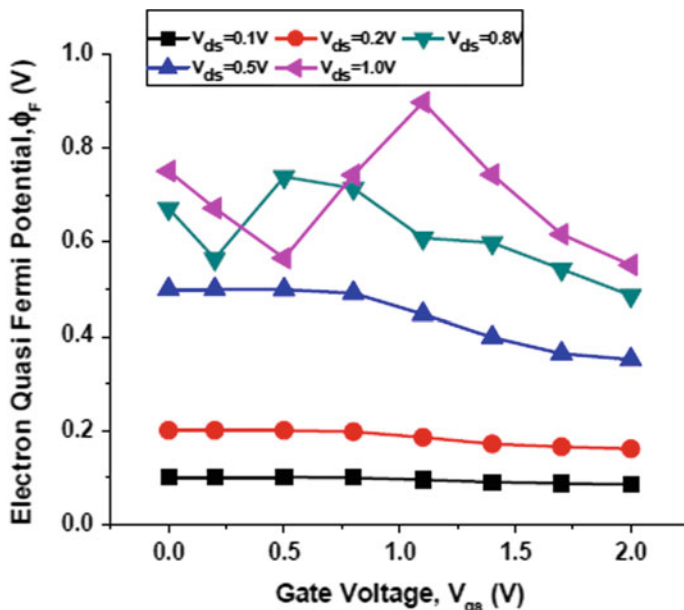


Fig. 5 Electron quasi-fermi potential at AA' cut for DG TFET

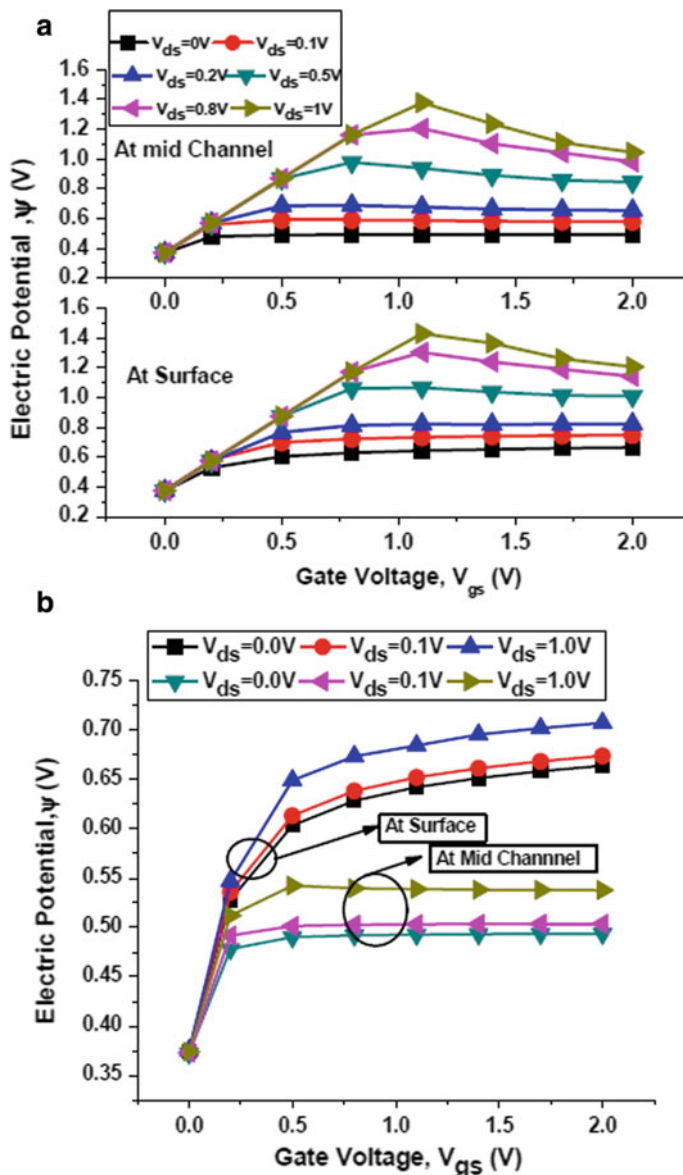


Fig. 6 Electric potential at surface and the mid-channel point for DG TFET and DG MOSFET. **a** Electric potential at surface and the mid-channel point for DG TFET. **b** Electric potential at surface and the mid-channel point for DG MOSFET

3.3 Electric Potential

Surface electric potentials and mid-channel potentials for 50 nm gate length DG TFET and DG MOSFET are shown in Fig. 6. For DG MOSFET, the surface potential always monotonically increases with increasing gate voltage, while mid-channel potential gets pinned to a fixed value for a fixed drain voltage, after threshold voltage as shown in Fig. 6b. It is also observed that the surface potential is always greater than mid-channel potential at any drain or gate voltage. This pattern of potential is also seen in literature [16, 17]. The shape of the pattern of potential will not change with the applied drain voltage, but for higher drain voltages, higher channel potentials are obtained. Since source/channel and drain/channel junctions in DG MOSFET are symmetric, therefore, there will be attraction of electrons from both source and drain regimes hence the symmetric pattern in the mid-channel and surface potential is found even if we change the drain voltage from 0.1 to 1 V.

In case of DG TFET as shown in Fig. 6a, surface potential and mid-channel potentials for lower V_{ds} (upto 200 mV) is seen constant, however, when we increase the drain voltage V_{ds} to 0.5 V and beyond this value, a monotonic decrease in -surface and mid-channel electric potentials is seen, this property of DG TFET is different from the potential pattern of DG MOSFET. At the same time, the surface potential is always greater than the mid-channel potential in DG TFET (i.e., the parabolic shape of the potential profile along AA' cut line). However, it is observed that the potential profiles for both DG TFET and DG MOSFET are parabolic in shape along AA' cut line, but still we are observing a different pattern in surface potentials and mid-channel potentials in both the devices. This is because a crossover point in potential is observed in case of DG TFET in oxide regime after gate voltage is further increased beyond threshold voltage as is clear from Fig. 6a.

It is also observed that surface potentials and mid-channel potentials for DG TFET are always much higher than surface and mid-channel potentials of DG MOSFET respectively. Potentials for DG TFET increase much more at higher applied drain voltages as compared to DG MOSFET, this happens because of sharper energy band bending in case of TFET, as shown in Fig. 3.2.

The possible reason for this decrease in both surface and mid-channel potential is the asymmetric device structure of TFET. Because of asymmetric device structure when the applied gate voltage is increased (below threshold voltage), since there is no tunneling from source to channel regime, therefore, the charge from drain/channel junction is attracted at surface (this is because of drain/channel tunneling at very low gate voltages or direct electrons are attracted from drain after inversion layer is formed), since there is no tunneling below threshold voltage, both surface and mid-channel potentials will increase monotonically as in case of DG MOSFET but after gate voltage goes beyond threshold voltage of the DG TFET device, the tunneling junction width at the source/channel junction gets lowered and more electrons will come to the channel, and these are related by Eq. (2) for both DG MOSFET and DG TFET. Since in DG MOSFET, there is zero eQFP hence surface potential increase, but in case of DG TFET eQFP is non zero and decreasing after threshold voltage (as

mention in Sect. 3.2), but electron density increases due to excess electrons generated from BTBT. This will decrease the channel potential as the gate voltage is increased.

In case of DG TFET, the nonzero eQFP will make its channel potential higher than the DG MOSFET's one.

3.4 Electric Field

In this subsection, total electric field ($E = (E_x^2 + E_y^2)^{0.5}$) versus applied gate voltage is presented for various drain voltages, V_{ds} for both devices. As shown in Fig. 7, surface electric field for DG MOSFET is almost independent of the applied drain voltage, while it decreases for DG TFET with applied drain voltage. While the mid-channel electric field increases with applied drain voltage in both the devices.

Because of symmetry in Double gate structures, the y -component of electric field will be zero at the mid channel and from x -component is more depending on the applied drain voltage. Hence, as the drain voltage increases, a corresponding increase in total electric field is solely due to E_x -component in both the devices. In DG TFETs, for lower gate voltages, the shape of the surface potentials as shown in [18] is not constant in the mid channel, due to sharp energy band bending in the device, as shown in Fig. 3.2, therefore higher mid-channel electric field is seen for lower gate voltages for DG TFETs. In case of surface electric field, a stronger E_y —component for lower drain voltages makes the total electric field higher. As the drain voltage is increased, it will make E_x stronger and E_y will become a bit weaker, since higher the drain voltage means, we need to apply higher gate voltage to make the surface potential constant, as shown in [12], therefore, the curves are shifted downwards for surface potential.

3.5 Electron Density

In this subsection, electron density for both devices is comparatively studied. Analytical expression for electron density in the channel is given by Eq. (2).

$$n(x, y) = \frac{n_{i,\text{eff}}^2}{N_a} e^{\left(\frac{\psi(x, y) - \varphi_{\text{FB}}(x)}{V_T}\right)} \quad (2)$$

where

$n(x, y)$ channel electron density/cm³

$n_{i,\text{eff}}$ effective intrinsic concentration of channel region per cm³

N_a channel doping per cm³

$\psi(x, y)$ channel potential at any point (x, y) , V

$\varphi_{\text{FB},n}(x)$ channel eQFP at x , V

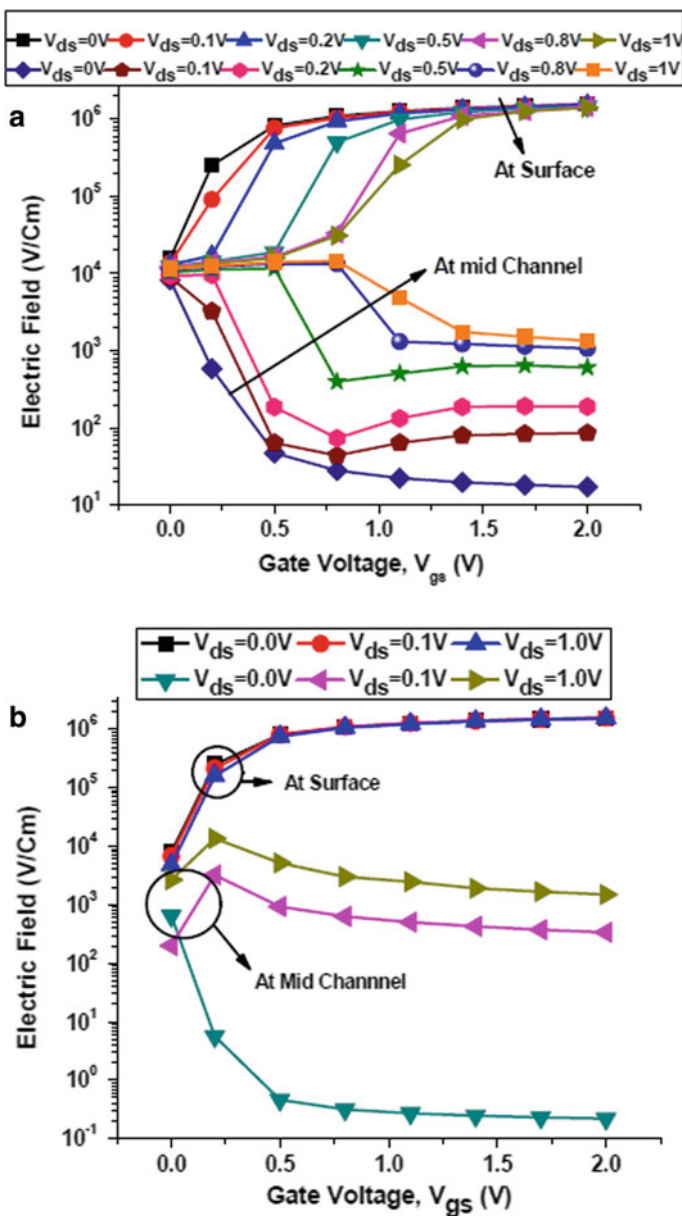


Fig. 7 Electric field at surface and the mid-channel point for DG TFET and DG MOSFET. **a** Electric field at surface and the mid-channel point for DG TFET. **b** Electric field at surface and the mid-channel point for DG MOSFET

V_T thermal voltage, V

It is clear from Fig. 8, DG MOSFET's electron densities are almost independent on applied drain voltage but DG TFET electron densities are strong function of drain voltages. This is because of higher quasi-fermi potentials seen in DG TFETs. As

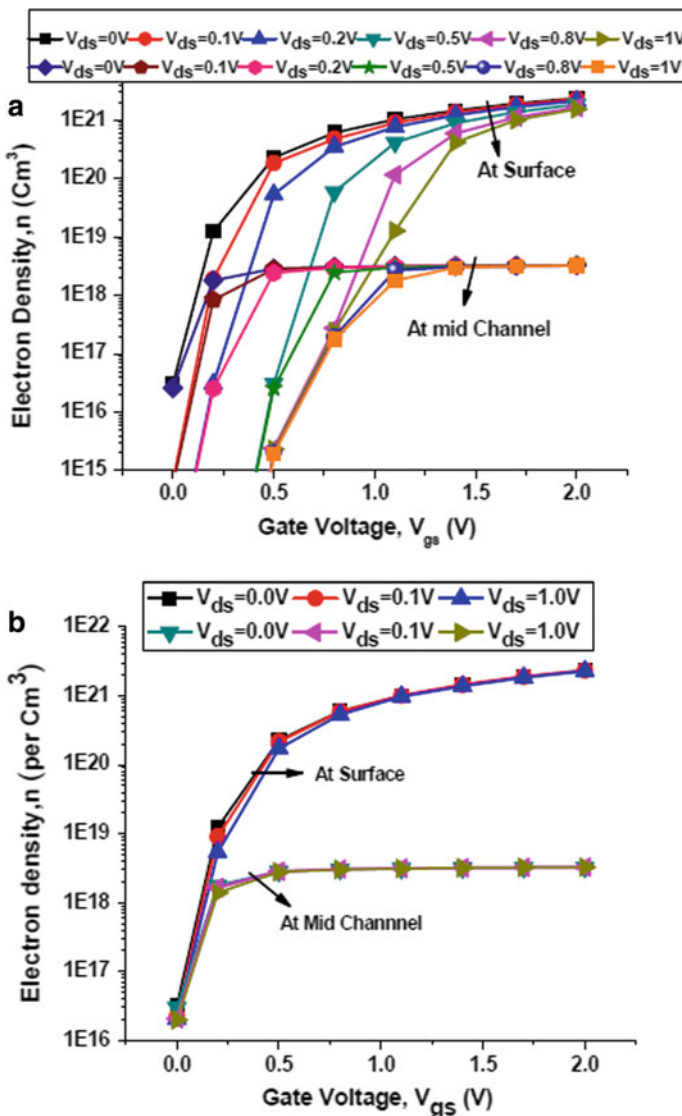


Fig. 8 Electron density at surface and the mid-channel point for DG TFET and DG MOSFET. **a** Electron density at surface and the mid-channel point for DG TFET. **b** Electron density at surface and the mid-channel point for DG MOSFET

shown in Sects. 3.2 and 3.3, an increase in drain voltage increases channel potentials and eQFP. But, we see, increase in channel potentials is lesser as compared to eQFP, hence from Eq. (2), electron density of DG TFET decreases with increasing drain voltages. As the applied gate voltage is increased, more electrons will be generated (due to BTBT) at the tunneling junction and will be attracted by vertical electric fields near the surface hence electron density will always increase with gate voltage, but mid-channel electron density will always be lesser than surface density.

4 Conclusion

Comparative study based on TCAD simulations for DG TFET and DG MOSFET devices with 50 nm gate length is carried out in this paper. It is found that although the channel (transverse) potential shape is parabolic in nature, its quality and quantity are different for both devices. In DG TFET, we found that the surface as well as mid-channel potential decreases after a particular gate voltage, which is different for different drain voltages. Unlike DG MOSFET, the mid-channel potential is not pinned to a fixed value after threshold voltage, but it decreases with increasing V_{gs} . Unlike DG MOSFET, a nonzero e —quasi-fermi potential is seen for DG TFET, which increases with applied drain voltage, but decreases at higher gate voltages. Gate threshold voltage for tunnel FETs is very high as compared to DG MOSFET and it is not depending on the on-set inversion charge theory. DG TFETs have very high I_{ON}/I_{OFF} ratios, and steeper subthreshold swing. Electron density and electric field properties are also different for both the devices.

References

1. Anghel C, Gupta A, Amara A, Vladimirescu A (2011) 30-nm tunnel FET with improved performance and reduced ambipolar current. *IEEE Trans Electron Devices* 58(6):1649–1654
2. Boucart K, Ionescu AM (2008) A new definition of threshold voltage in tunnel FETs. *Solid-State Electron* 52(9):1318–1323
3. Gupta SK, Kulkarni JP, Datta S, Roy K (2012) Heterojunction intra-band tunnel FETs for low-voltage SRAMs. *IEEE Trans Electron Devices* 59(12):3533–3542
4. Boucart K, Ionescu AM (2007) Double-gate tunnel FET with high-k gate dielectric. *IEEE Trans Electron Devices* 54(7):1725–1733
5. Born M, Bhuwalka KK, Schindler M, Abelein U, Schmidt M, Sulima T, Eisele I. Tunnel FET: a CMOS device for high temperature applications. In: 2006 25th international conference on microelectronics 14 May 2006, pp 124–127
6. Vandenberghe WG, Verhulst AS, Sorée B, Magnus W, Groeseneken G, Smets Q, Heyns M, Fischetti MV (2013) Figure of merit for and identification of sub-60 mV/decade devices. *Appl Phys Lett* 102(1):013510
7. Boucart K, Ionescu AM (2007) Length scaling of the double gate tunnel FET with a high-k gate dielectric. *Solid-State Electron* 51(11–12):1500–1507

8. Li YC, Zhang HM, Hu HY, Zhang YM, Wang B, Zhou CY, Lou YL (2013) Effect of high-k material on gate threshold voltage for double-gate tunnel FET. *Appl Mech Mater* 275–277:1984–1987 (2013)
9. Ortiz-Conde A, García-Sánchez FJ, Muci J, Barrios AT, Liou JJ, Ho CS (2013) Revisiting MOSFET threshold voltage extraction methods. *Microelectron Reliab* 53(1):90–104
10. Sentaurus TCAD Manual, Mar 2010
11. Kane EO (1960) Zener tunneling in semiconductors. *J Phys Chem Solids* 12(2):181–188
12. Anand B, Dasgupta S (2012) A TCAD approach to evaluate channel electron density of double gate symmetric n-tunnel FET, pp 577–581 (2012)
13. Yadav M, Bulusu A, Dasgupta S (2013) Two dimensional analytical modeling for asymmetric 3T and 4T double gate tunnel FET in sub-threshold region: Potential and electric field. *Microelectron J* 44(12):1251–1259
14. Bulusu A, Dasgupta S (2015) Insights into channel potentials and electron quasi-Fermi potentials for DG tunnel FETs. *J Semicond* 36(1):014005
15. Yadav M, Bulusu A, Dasgupta S (2015) Super-threshold semi analytical channel potential model for DG tunnel FET. *J Comput Electron* 14:566–573
16. Taur Y (2000) An analytical solution to a double-gate MOSFET with undoped body. *IEEE Electron Device Lett* 21(5):245–247
17. Taur Y (2001) Analytic solutions of charge and capacitance in symmetric and asymmetric double-gate MOSFETs. *IEEE Trans Electron Devices* 48(12):2861–2869
18. Bardon MG, Neves HP, Puers R, Van Hoof C (2010) Pseudo-two-dimensional model for double-gate tunnel FETs considering the junctions depletion regions. *IEEE Trans Electron Devices* 57(4):827–834

Wireless Access Support for Distribution Management System (DMS) to Microgrid Communication in Power Network



N. Himabindu, Rajashekhar P. Mandi, Santoshkumar Hampannavar,
and Swapna Manasani

Abstract With indispensable and rapid ingress of renewable energy sources in power systems, the communication between the distributed energy sources has become very crucial to have a reliable distribution management system (DMS). In this paper, wireless access support is proposed for Distribution Management System (DMS) and microgrid control center (MGCC) using WiMAX protocol. MATLAB/Simulink was used to model the WiMAX physical layer. The bit error rate (BER) v/s signal-to-noise ratio (SNR) curves were plotted and promising results were obtained.

Keywords Microgrid · Distribution management system (DMS) · Distribution generation (DG) · Distributed energy resource (DER)

1 Introduction

The policy of deregulation in electric power systems has allowed participation of private players in generation of power and this resulted in rapid penetration of distributed energy resources (DER) in the power grid at medium and low-voltage networks. The distribution system plays a vital role in smartgrid/microgrid which includes: (i) DER integration to the grid; (ii) load demand control; and (iii) efficient usage of network assets. Distribution system (DS) is too complex in nature and it is difficult to control, monitor, and handle it. The difficulties associated with DS are:

N. Himabindu (✉) · R. P. Mandi · S. Hampannavar
School of Electrical and Electronics Engineering, REVA University, Bengaluru, India
e-mail: himabindu@reva.edu.in

R. P. Mandi
e-mail: dir.eee@reva.edu.in

S. Hampannavar
e-mail: santoshkumar.sh@ieee.org

S. Manasani
National Institute of Technology Silchar, Silchar, India
e-mail: swapnamansani@gmail.com

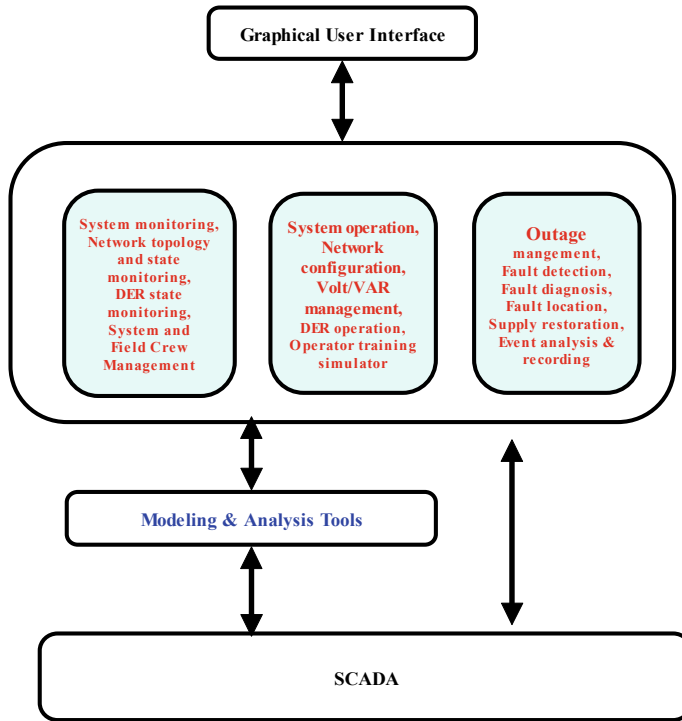


Fig. 1 Components of DMS

(i) often meshed but operate radically at times (because of the faults and expansion of the network) and (ii) difficulty in predicting time varying load demand. Distribution management system (DMS) is a set of applications adopted by the distribution network operators (DNO) to control and enhance the performance and manage its complexity. Figure 1 gives the key components of the DMS.

DER greatly impacts network performance and depends on DER-DS interface. It can be connected to the grid through an power electronic interface/microgrid (MG).

2 Microgrid

A MG is a network of small modular distributed generation (DG), storage, and loads. Microgrid central controller (MGCC) acts as an interface between DMS and microgrids. MG integration with DMS through MGCC [1] is shown in Fig. 2.

There are two operating modes: (i) grid-connected and (ii) islanded mode.

Grid-connected mode: In grid connected operating mode, the power is supplied to loads connected to MG and excess power is transferred back to the grid. The total MG system load is supported by MG and the grid.

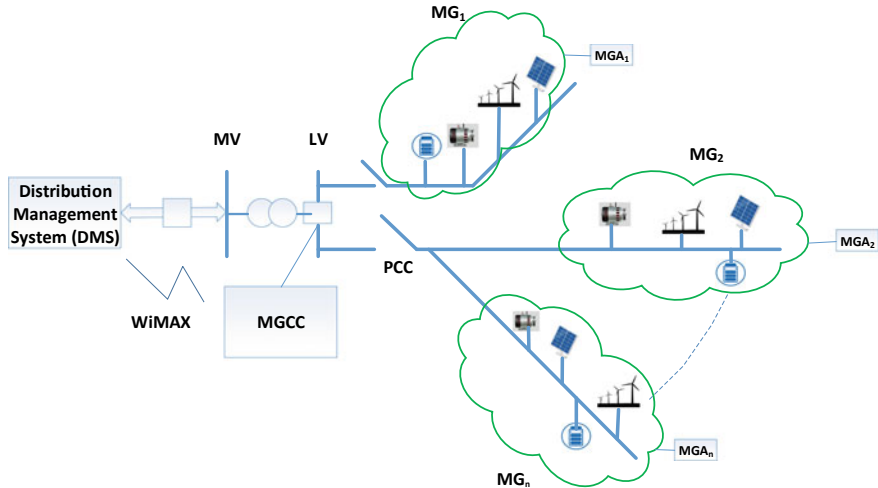


Fig. 2 MG integration to DMS via MGCC

$$V_{\text{PCC}} = V_{\text{grid}}$$

$$P_{\text{load}} = P_{\text{DG}} + P_{\text{grid}}$$

$$Q_{\text{load}} = Q_{\text{DG}} + Q_{\text{grid}}$$

where

- V_{PCC} is voltage at point of common coupling
- V_{grid} is grid voltage
- $P_{\text{DG}}, P_{\text{load}}, P_{\text{grid}}, Q_{\text{load}}, Q_{\text{DG}}, Q_{\text{grid}}$ are inverter, grid, load active/reactive powers in kW and KVar, respectively.

If DGs are generating excess power than the MG system load, then the excess power will be transferred to the grid.

$$P_{\text{DG}} = P_{\text{load}} + P_{\text{grid}}$$

$$Q_{\text{DG}} = Q_{\text{load}} + Q_{\text{grid}}$$

Standalone/Islanded mode:

In this mode, grid does not have any role to play and MG starts energizing the small network segment and supplies the power to the critical loads to be addressed. The voltage and frequency levels are maintained as per the IEEE 1547-2003 standard and PCC voltages are equal to the inverter front end voltage.

$$V_{\text{PCC}} = V_{\text{DG}}$$

$$P_{\text{load}} = P_{\text{DG}}$$

$$Q_{\text{load}} = Q_{\text{DG}}$$

If the MG system load is greater than the DGs generated power, then the system will enter the unstable region.

$$P_{\text{load}} > P_{\text{DG}}$$

$$Q_{\text{load}} > Q_{\text{DG}}$$

The recent literature elucidates DG integration issues, MG integration and control strategies, long-term evolution (LTE) protocol for MGCC to DMS communication, grid control center to the aggregator, and an aggregator of EV communication [2–5]. The MGCC to DMS communication is very crucial in deciding the MG integration to the grid. WiMAX protocol for MGCC's communication with DMS in the power network has been proposed in this paper. Also, the corresponding path loss models are simulated. The physical layer of the WiMAX downlink is modeled in MATLAB/SIMULINK. The curves pertaining to bit error rate (BER) and signal to noise (SNR) are also plotted.

3 WiMAX Protocol

WiMAX standard works in the frequency range of 2–6 GHz. The standard uses OFDM, 256-FFT, and handles 70 Mbps of data flow and coverage area of up to 50 km. The coverage area is 5–7 km at 7 Mbps. An OFDM system has three subcarriers: (i) pilot, (ii) data, and (iii) null.

The transmission of physical layer data vectors requires (randomization, interleaving, RS coding, and error correction) for modulation schemes (M-QAM) and for distinct coding rates (convolution coding and concatenated Reed–Solomon). OFDM symbols, demodulate waveform, deinterleave decode (RS and Viterbi), and bit scrambling process inversion [6–9] are used to retrieve the receiver data. WiMAX physical layer is shown in Fig. 3.

The fixed WiMAX protocol is chosen for the communication and the parameters used for simulation are shown in Table 1.

Signal-to-noise ratio (SNR) is represented as

$$\text{SNR} = P_{\text{signal (dB)}} / P_{\text{noise (dB)}}$$

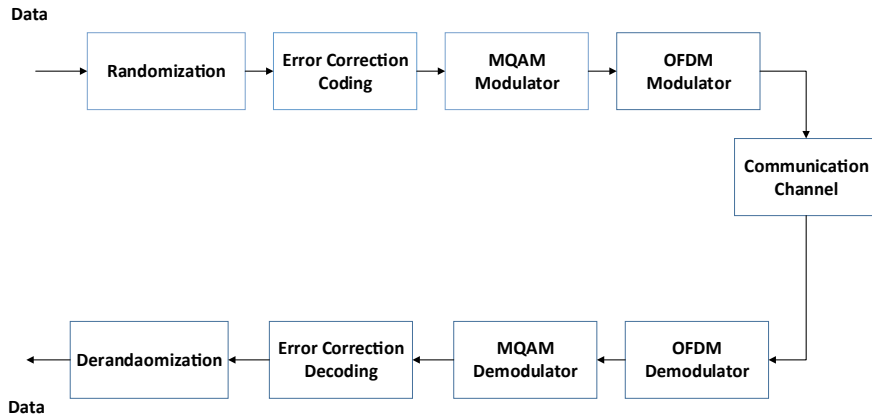


Fig. 3 WiMAX physical layer block diagram

Table 1 IEEE 802.16-2004 (fixed WiMAX)

Parameters	Value
Frequency band	2–11 GHz fixed
OFDM carriers	OFDM: 256 OFDMA: 2048
Modulation	16QAM, 64QAM, QPSK
Channel bandwidth	(1, 4, 8, 12) × 1.25 MHz (1, 2, 4, 8) × 1.75 MHz 8.75 MHz
Transmission rate	1–75 Mbps
Duplexing	TDD/FDD

In dB it is represented as

$$\text{SNR}_{\text{dB}} = P_{\text{signal (dB)}} - P_{\text{noise (dB)}}$$

4 Results and Discussion

MATLAB/SIMULINK is used to model and simulate the physical layer of WiMAX protocol. Figure 4 shows the plotted curves for BER v/s SNR. In order to achieve BER of 10^{-2} both BPSK $\frac{1}{2}$ needs 7.5 dB, QPSK $\frac{1}{2}$ needs 12 dB, QPSK $\frac{3}{4}$ needs about 15 dB, and 16QAM $\frac{1}{2}$ needs about 16.5 dB. The QPSK $\frac{1}{2}$ and 16 QAM $\frac{1}{2}$ are less susceptible to errors than other modulation schemes [10–13].

The transmitter and receiver antenna heights are 30 m and 10 m, respectively. Figure 5 shows the results of transmitter power which is 43 dBm. The SUI model

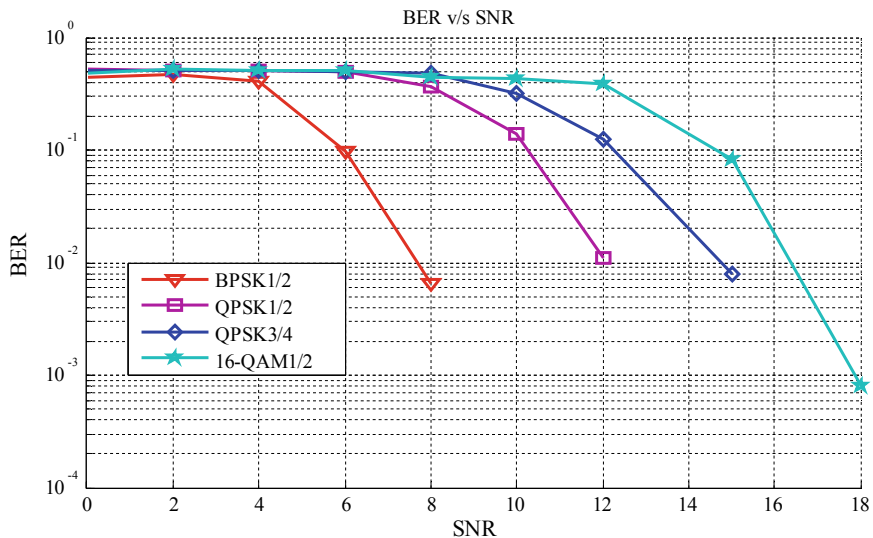


Fig. 4 BER v/s SNR for GCC to aggregator Link

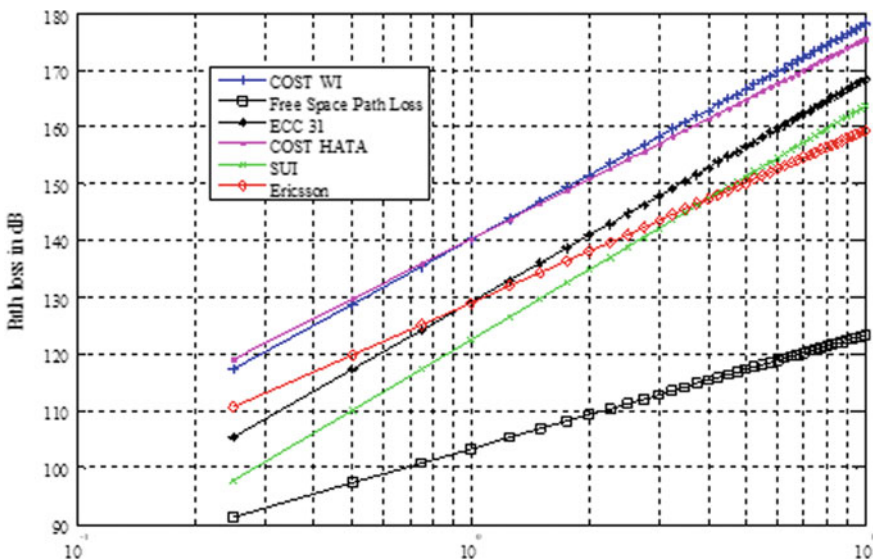


Fig. 5 BER v/s SNR for GCC to aggregator link

shows a lower path loss of 142 dB and 162 dB, respectively, for suburban and urban environments. The COST WI, COST HATA, and ECC-31 show, respectively, a path loss of 162 dB, 158 dB, and 164 dB, respectively. Ericsson model depicts comparatively higher path loss of 204 dB for suburban environment but interestingly in case of urban environment, it shows path loss of 160 dB which is less when compared to all other models. Compared to other models in urban environment, the COST HATA and COST WI, respectively, exhibit higher path loss of 176 and 178 dB for 10 m height receiver antenna.

5 Conclusion

The wireless access support for MGCC to DMS communication incorporating WiMAX protocol is discussed. For various bandwidth and path loss models BER v/s SNR graphs were plotted. This study helps the researchers associated in developing wireless infrastructure model for MG communication in distribution network.

References

1. Ekanayake J, et.al (2012) Smart grid technology and applications, 1st edn. Wiley Ltd
2. Kumar S, Udaykumar RY (2015) Modeling and comprehensive analysis of WiMAX protocol for grid control center to aggregator communication in V2G. *Int J Renew Energy Res (IJRER)* 5(1):133–138
3. Kumar S, Udaykumar RY (2013) IEEE 802.16-2004 (WiMAX) protocol for grid control center and aggregator communication in V2G for smart grid application. In: IEEE international conference on computational intelligence and computing research
4. Kumar S, Udaykumar RY (2013) IEEE 802.16 protocol for grid control center and aggregator communication in V2G for smart grid application. In: IEEE international conference on computational intelligence and computing research, Madurai, (IEEE-ICCIC), India
5. Ali-Yahiya T (2011) Understanding LTE and its performance. Springer Science and Business Media, Heidelberg, Germany
6. Kumar S, Udaykumar RY (2015) Performance analysis of LTE protocol for EV to EV communication in vehicle-to-grid (V2G). In: 2015 IEEE 28th Canadian conference on electrical and computer engineering (CCECE), Halifax, Canada, pp 1–6
7. Kumar S, Udaykumar RY (2013) Long term evolution protocol for grid control center and aggregator communication in V2G for smart grid application. In: IEEE international conference on computational intelligence and computing research, Madurai, India
8. Hamid M, Kostanic I (2013) Path loss models for LTE and LTE-a relay stations. *Univers J Commun Netw*
9. Zyren J (July, 2007) Overview of the 3GPP long trem evolution physical layer. Freescale Semicond
10. Hampannavar S, Chavhan S, Yaragatti U, Naik A (2017) Gridable electric vehicle (GEV) aggregation in distribution network to support grid requirements: a communication approach. *Int J Emerg Electr Power Syst*
11. Santoshkumar H, Udaykumar RY, Selvakumar S, Teshale A (2018) A framework for microgrid to distribution management system (DMS) communication in smart distribution network. In: IEEE international conference on computational intelligence and computing research

12. Kumar S, Chavhan S, Udaykumar RY (2019) A stochastic model based on markov chain to support vehicle-to-grid (V2G) operation in smart distribution network. *Int J Emerg Electr Power Syst*
13. Kumar S, Chavhan S, Swapna M, Udaykumar RY (2020) Electric vehicle traffic pattern analysis and prediction in aggregation regions/parking lot zones to support V2G operation in smart grid: a cyber physical system entity. *Int J Emerg Electr Power Syst*

Implementation of a Charge Controller for Hybrid Electric Vehicle



Gautam and Brajagopal Datta

Abstract A hybrid electric vehicle (HEV) is a vehicle which is the combination of more than one supply source. In this HEV, two batteries each of 24 Vs are used, one battery is connected to load which provide power to drive motor, and another battery is connected to charging system which takes power for charging. In the present work, the main controller of HEV is based on Arduino software which is used by the microcontroller. The system uses a battery swap circuit which increases the performance of the electric vehicle. Battery swap circuit measures the voltage level of both batteries, if the voltage level of load connected battery gets lower than the changing connected battery, then the connection of both the batteries get interchanged. The recharging system contains BLDC and solar panel which provides constant 24 Vs to the battery.

Keywords Hybrid electric vehicle · Brushless DC generator · Solar panel · Battery swap circuit · Microcontroller · Controller behavior · Battery management

1 Introduction

In present time, electric vehicles are the need for the transportation system. The demand of non-renewable energy (petrol, diesel, coal, etc.) is increasing day by day, so it is necessary to find out other energy resources. Renewable energy like solar is the most important and available in the large amount on earth which is very useful for hybrid electric vehicles. It provides an alternative source of energy which is used to feed extra energy to charge the battery or directly used to feed motor. Investigation of PV-Fed Hybrid Electric Vehicles with Various Power Electronic Circuits (2017) [1]. In this paper, the hybrid electric vehicle is based on conventional

Gautam · B. Datta (✉)

Department of Electrical Engineering, National Institute of Technology Arunachal Pradesh,
Yupia, Arunachal Pradesh, India
e-mail: brajagopal@nitap.ac.in

Gautam
e-mail: ggautam30@gmail.com

and non-conventional energy sources. It is using solar PV modules and petrol- or diesel-based engine, which is not fully renewable energy-based electric vehicle. The demand for non-conventional energy is increasing day by day, so it is necessary to find out another alternative source of energy which should be renewable based and it must be eco-friendly.

Energy Management in a Fuel Cell-based Hybrid Electric Vehicle using a Fuzzy Logic Approach (2017) [2]. An energy management strategy is provided for an HEV. This is based on a fuel cell as well as a Li-ion battery. These energy management's, based on the fuzzy logic approach, aim is to increase the performances of the hybrid electric vehicle. Here, the fuzzy logic-based controller has three inputs: the power error, load power, and battery.

A Rapid Charging System with Bidirectional Power Flow for Plug-in Hybrid Electric Vehicle (HEV) (2017) [3]. This paper shows the capability of the rapid battery charging technology with bidirectional power flow for HEV. It is used rectangular phase shift method with PWM (RPPWM) for zero voltage switching based on the dual-active bridge.

It controls the capability of power flow in both directions and reduces the complexity. Here, boost converter is used to regulate the constant DC output voltage which also improves the power factor. Here, boost converter plays another important role, and it provides the bidirectional power flow.

Real-time Power Hardware-in-the-Loop Emulation of a Parallel Hybrid Electric Vehicle (2017) [4]. This paper shows the control and coordination of several sources of the hybrid electric vehicle. This paper put light on a real-time emulator for parallel hybrid electric vehicle. Here, every system is modeled and controlled to balance the performance and control as per torque and speed.

Energy Management And Strategies For Hybrid Electric Vehicle Using Photovoltaic, Ultra-capacitor, And Battery (2017) [5]. In this paper, three sources are using PV, battery, an ultra-capacitor. During daytime, when solar panel provides maximum voltage, then at that point of the time, PV runs the motor as well as it also charges the battery and capacitor. When the power output of the PV get reduced, then battery and an ultra-capacitor provide power to the motor.

Here, regenerative braking technology is also applied which is very useful for hybrid electric vehicles. In this method, when the brakes are applied, then at that point in time, motor acts as a generator and starts feeding supply to the battery and an ultra-capacitor. As compared to others, this type of electric vehicle provides high performance, and battery backup will be improved. But, this is not a permanent solution. If the vehicle is running in the night, then the solar panel will be unable to provide power, and then, after sometime, battery will be low which is the major disadvantage of the electric vehicle.

From literature survey it is evident that more than one input sources can be used to drive an electric vehicle [7–11]. The sources are internal combustion engine (ICE) and electric motors. But, both the sources are separately connected to the motor. When battery gets discharged, ICE starts providing supply to the motor.

The pollution from the vehicles is one of the main cause of air pollution [12]. Day by day, the graph of pollution in traffic area is increasing very sharply. To prevent this,

the electric car must run in the city, so that the maximum pollution will be reduced. The amount of greenhouse gases as well as the global warming will be decreased.

2 Working of Proposed Recharging System

To increase the overall performance of the hybrid electric vehicle, it is necessary to increase the battery performance or its backup. According to this charging system, this hybrid vehicle uses two battery, so the charging of one battery and discharging of second battery which is connected to load occurs at the same time. This controller has recharging unit which is divided into two phases. In phase 1, two input sources like solar panel and brushless DC generator are connected. Both sources are again connected to relay via voltage sensor, and this voltage sensor is connected to the microcontroller, as shown in Fig. 1.

Phase 1

As shown in Fig. 2, another microcontroller is used in phase 2 with a voltage sensor, relay, and boost converter. The coming voltage is directly connected to relay

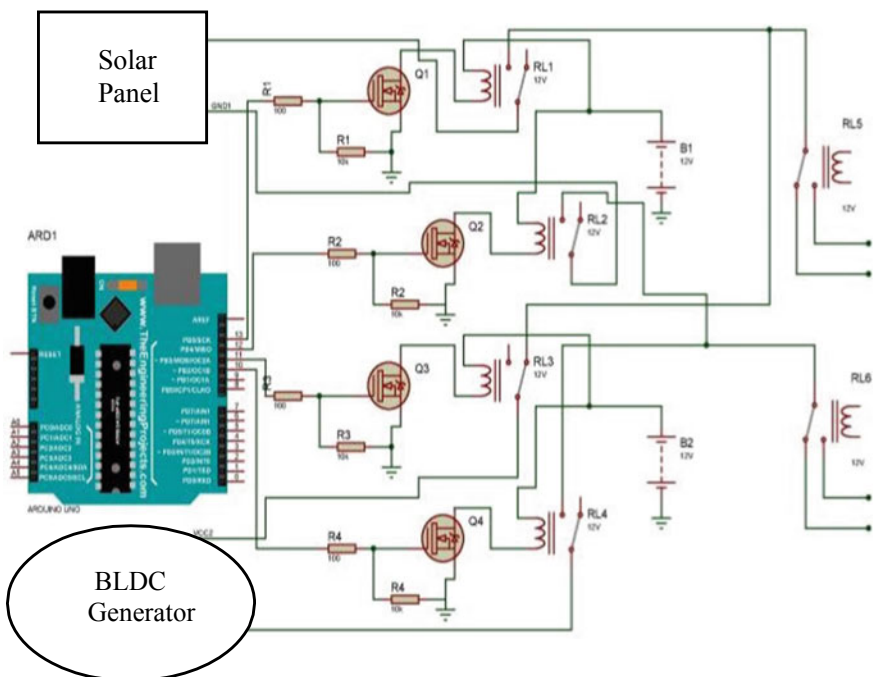


Fig. 1 Circuit diagram of phase 1

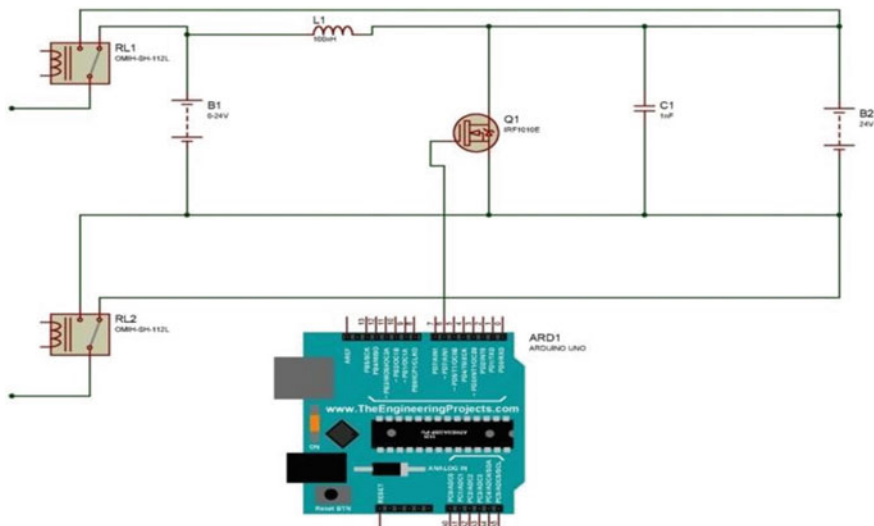


Fig. 2 Circuit diagram of phase 2

via voltage sensor. If the coming voltage is less than or equal to 23 V, then microcontroller feeds the voltage to boost converter via a relay. If the voltage is 24 V or more, then microcontroller bypasses the boost converter and directly feeds to the battery.

The ATMEL 8-bit microcontroller contains 32 kB flash memory with the capability of read-while-write, 1 kB of EEPROM, 2 kB of SRAM, 23 general purpose I/O lines. The device operates between 1.9 and 5.5 V. The programming is written inside the microcontroller in such a way that, which input sources provide the higher voltage, the microcontroller will proceed that voltage source to next level via a relay. If both the incoming sources provide the same amount of voltage, then at that point of time, microcontroller will proceed the voltage of BLDC generator because the preference is given to the BLDC generator in the programming. Here, BLDC generator and solar panel both deliver voltage which is shown in Fig. 3. The value of the voltage of both sources continuously varies according to time. Here, the microcontroller compares both voltages and selects the higher voltage with the help of relays.

The response of controller with different conditions.

Condition 1

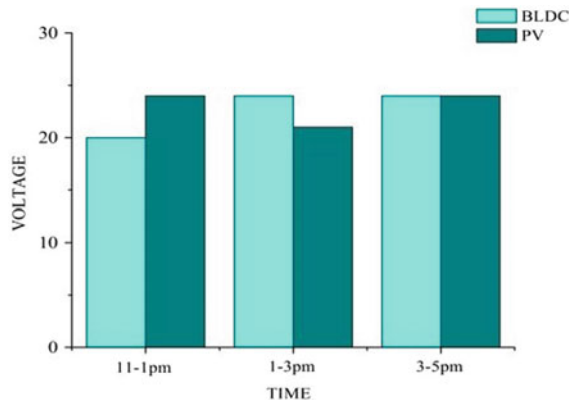
If the vehicle is in running condition (During Day).

Here, BLDC generator and solar panel both deliver voltage which is shown in Fig. 3. The value of the voltage of both sources continuously varies according to time. Here, the microcontroller compares both voltages and selects the higher voltage with the help of relays.

Condition 2

If the vehicle is in stationary condition (During Day Time).

Fig. 3 Different input values during running conditions (day)



As shown in Fig. 4, solar panel delivers supply, and output of BLDC generator is almost zero. The supplied value of BLDC generator is less than solar panel, so the microcontroller selects only higher supply value.

There are two pairs of the relay which are connected with solar panel and BLDC generator, and these relays are controlled by the microcontroller as per programming is installed in it. Here, V1 stands for the supply of BLDC generator, and V2 stands for solar panel's supply. Relay 1 and 2 are connected with BLDC generator, and relay 3 and 4 are connected to the solar panel. If the conditions ($V1 > V2$ and $V1 = V2$) are as given in Table 1, then relay 1 and 2 will on and relay 3 and 4 will be off and

Fig. 4 Different input values during a traffic jam or in parking conditions

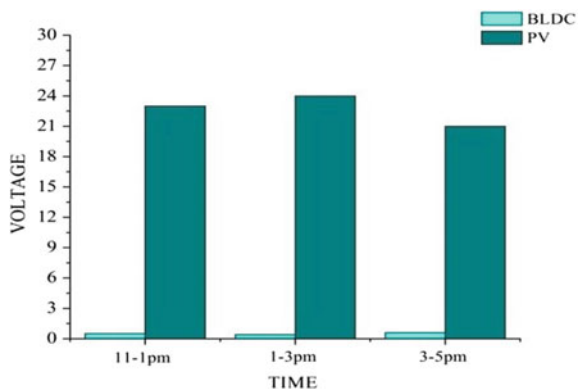
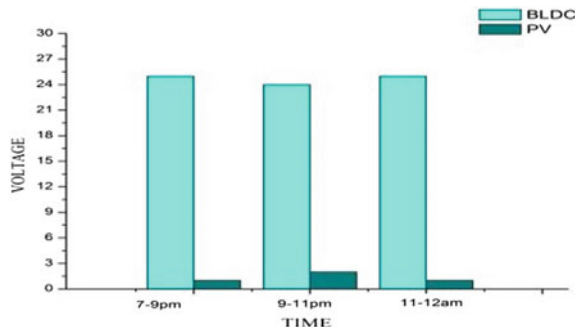


Table 1 Switching mode of the relay according to the supply voltage

Condition	Relay 1	Relay 2	Relay 3	Relay 4
$V1 > V2$	On	On	Off	Off
$V1 = V2$	On	On	Off	Off
$V1 < V2$	Off	Off	On	On

Fig. 5 Different input values during running conditions (night)



vice versa.

Condition 3

If the vehicle is in running condition (During Night Time).

In this condition, only BLDC generator provides supply, and the output of the solar panel is almost zero as shown in Fig. 5.

3 Battery's Connection Swapping System

This technology is useful for HEV which increase the battery backup, range, and the performance. Here, one battery, which is connected to the charging system, and another battery, which is connected to a load, both are also connected to the micro-controller via voltage sensor. The voltage sensor measures the voltage level of the batteries and sends the information to the microcontroller. Here, the microcontroller will decide that which battery is going to connect the load and which will connect to the recharging system via a relay. The circuit diagram of battery swap technology is given in Fig. 6.

The switching mode of the relay of battery swap circuit is controlled by the microcontroller as given in Table 2.

4 Results and Discussion

The output of recharging system with respect to variable input source for the battery is 24 V which is shown in Fig. 7. The image of a hardware implementation of battery swap system is shown in Fig. 8. The image of a hardware implementation of battery swap system is shown in Fig. 9. This system is controlled by Arduino.

- Recharging system and battery connection swap method increases the performance and efficiency of the HEV.
- The recharging system provides constant output to the battery as shown in Fig. 9.

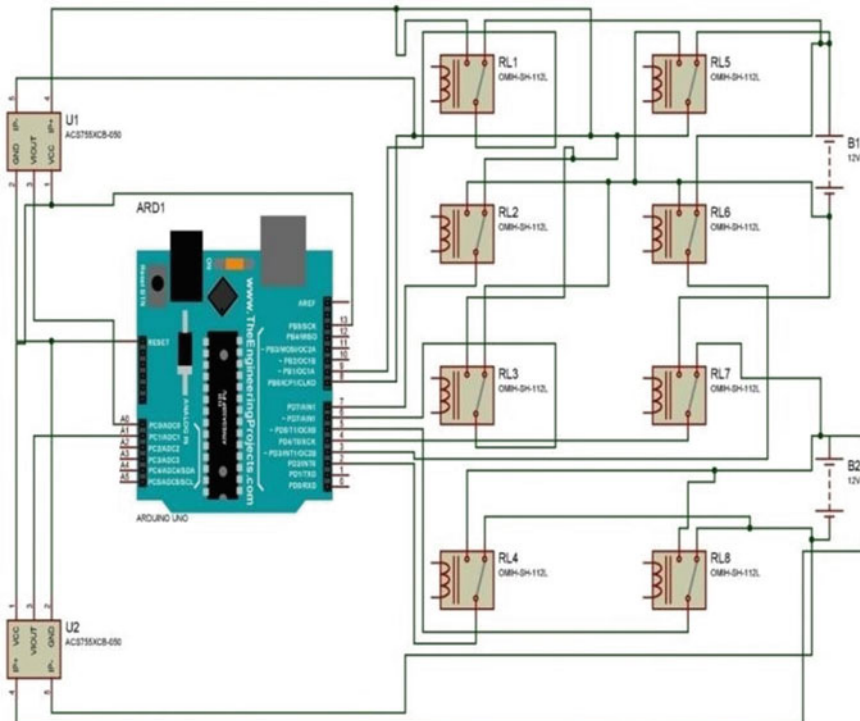


Fig. 6 Circuit diagram of batteries swap system

Table 2 Switching mode of the relay with respect to the voltage level of batteries

Condition	R1	R2	R3	R4	R5	R6	R7	R8
$V1 > V2$	Off	On	On	Off	Off	On	On	Off
$V1 = V2$	Off	On	On	Off	Off	On	On	Off
$V1 < V2$	On	Off	Off	On	On	Off	Off	On

- It increases the range of HEV.

5 Conclusion

The main source of pollution is the internal combustion-based vehicles which is the main cause of air pollution. The traffic area is more polluted. So, it is prevented by electric vehicle. So, the level of pollution will be low. Both greenhouse gases, as well as global warming, will decrease, and it also improves the quality of the environment. Due to addition of recharging system with battery, the overall range of the vehicle

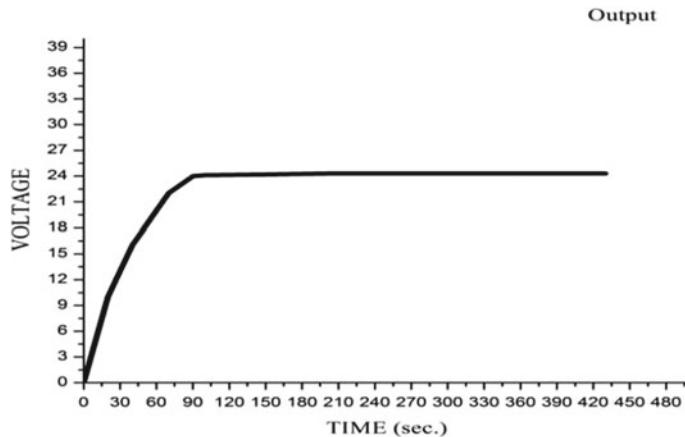


Fig. 7 Output of recharging system to feed battery

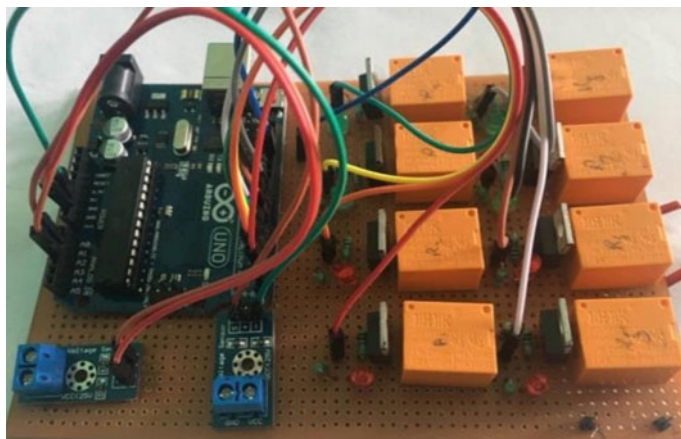


Fig. 8 Image of batteries connection swap system

will increase. The solar panel is used as a source in this system. As recharging system provides the sufficient amount of power to the battery in small period of time, it also improves the positive characteristics as well as driving range of the whole system. Hence, with this phenomenon, a large amount of energy saving is possible. The cost-effectiveness of this system is increased due to large number of components used, but the cost impact of recharging system will increase fuel economy and decrease harmful emissions. It also saves the overall cost because of long life cycle.

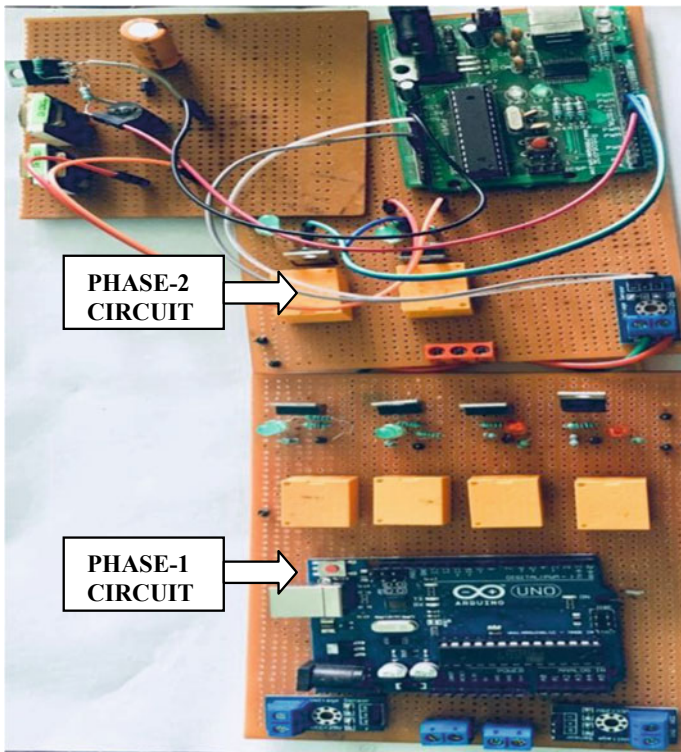


Fig. 9 Image of recharging system

References

1. Kaleeswari M, Madheswaran M, Vijayakumar K (2017) Investigation on PV fed hybrid electric vehicles with various power electronic circuits Kaleeswari. In: IEEE international conference on advances in electrical technology for green energy, pp 49–55
2. Saib S, Hamouda Z, Marouani K (2017) Energy management in a fuel cell hybrid electric vehicle using a fuzzy logic approach. In: The 5th international conference on electrical engineering
3. Naresh M, Bai VS, Pandey AK (2017) A rapid charging system with bi-directional power flow for plug-in hybrid electric vehicle. In: International conference on innovations in power and advanced computing technologies, pp 01–05
4. Kaarthik RS, Pillay P (2017) Real-time power hardware-in-the-loop emulation of a parallel hybrid electric vehicle drive train. IEEE transportation electrification conference
5. Liu M, Huang J, Cao M (2017) Handling stability improvement for a four-axle hybrid electric ground vehicle driven by in wheel motors. IEEE Access
6. Pancholi G, Yadav DK, Chaturvedi L (2017) Energy management strategies for hybrid electrical vehicle using PV, ultracapacitor, and battery. IEEE transportation electrification conference
7. Senthilnathan A, Manohar R, Mohanavel J, OmeshHeman Kumar A, Saravana Kumar R (2017) Smart hybrid electric vehicle. In: IEEE international conference on Innovations in green energy and healthcare technologies, pp 01–06

8. Shaikh MZ, Kodad SF, Jinaga BC (2008) Performance analysis of Piezoresistive MEMS for pressure measurement. *J Theor Appl Inf Technol* 227–231
9. Yan J, Li C, Xu G, Xu Y (2009) A novel on-line self-learning state-of-charge estimation of battery management system for hybrid electric vehicle. IEEE transportation electrification conference, pp 1161–1166
10. <http://www.circuitstoday.com/working-of-electric-cars>
11. <https://www.arduino.cc/>
12. <https://www.wikipedia.org/>

Series-Stacked Non-parallel Multipath Differential Inductor for C Band Applications



Sunil Kumar Tumma and Bheema Rao Nistala

Abstract Radio frequency-integrated circuits built on silicon require an inductor with high-quality factor and miniaturized on-chip area. This paper introduces series-stacked non-parallel multipath differential inductor to resolve this problem. The proposed inductor decreases the parasitic capacitance among the adjoining metal layers and also reduces the conductor's current crowding effects at high frequencies, leading to higher quality factor and self-resonance frequency. The proposed inductor manages to achieve a raise of 35% in quality factor and 25% gain in self-resonance frequency as compared to conventional series-stacked multipath inductor occupying the equivalent on-chip area for uniform inductance. High-frequency structural simulator (HFSS) is used to design and simulate the proposed inductor using 0.18 μm CMOS technology.

Keywords Quality factor · Self-resonance frequency · Series stack · Multipath

1 Introduction

On-chip inductors are used in wireless communication systems, micro-electromechanical systems (MEMS), and in few RFIC circuits such as mixers, voltage-controlled oscillators, and low-noise amplifiers. With an increased demand for personal mobile communications, RFIC requires high-performance on-chip inductors to reduce the total system size and assembly cost.

A CMOS radio frequency (RF) circuit design benefits from one or more on-chip inductors having a high-Quality factor (Q), a small occupied on-chip area, and a high self-resonance frequency (f_{SR}). At high frequency of operation, the skin and proximity effects and substrate losses degrade the performance of the on-chip

S. K. Tumma (✉) · B. R. Nistala

Department of Electronics and Communication Engineering, National Institute of Technology

Warangal, Warangal, India

e-mail: sunil.ajay1@gmail.com

B. R. Nistala

e-mail: nbr.rao@gmail.com

inductor [1]. Several methods were proposed to overcome these drawbacks which include implementation of the inductor in multilayers [2], usage of high thickness and high conductivity metal strip to form an inductor [3], usage of patterned ground shield underneath the inductor [4], and employing variable width in inductor turns [5]. Multipath inductor lowers the proximity effect and increases the Q without altering inductance (L) [6, 7]. Symmetric (differential) inductor structure which is excited differentially is less affected by substrate parasitics which improves both Q and f_{SR} for miniaturized on-chip area [8]. The symmetric trace differential-stacked spiral inductor (SDSSI) further enhances the Q and f_{SR} of the symmetrical inductor; however, it is unable to achieve higher inductance value [9]. Series-stacked spiral consists of two or more spirals overlaid one on top of the other increases the inductance value to a large extent for the miniaturized on-chip area for small degradation in Q value [10, 11]. Series-stacked multipath spiral inductors with crossover interconnection method improves the Q and f_{SR} without affecting the inductance for the miniaturized on-chip area as the current crowding effects are very less [12]. The performance of the series-stacked multipath inductors is further enhanced by using the proposed series-stacked non-parallel multipath differential inductor. In conventional series-stacked multipath inductors, the divided paths (segments) are parallel which forms the parasitic capacitance. However, in the proposed inductors, the segments are not parallel that decreases the parasitic capacitance and improves the Q and f_{SR} of the inductor to a significant extent. The proposed inductor is centered in C band which ranges from 4–8 GHz. C band is used for frequency allocation for satellite communications, cordless phones, and surveillance systems.

The construction of single-layer multipath symmetrical inductor is discussed in Sect. 2. The construction of the proposed series-stacked non-parallel multipath symmetrical inductor is depicted in Sect. 3. Section 4 describes simulation results, and conclusions are given in Sect. 5.

2 Multipath Differential Inductor

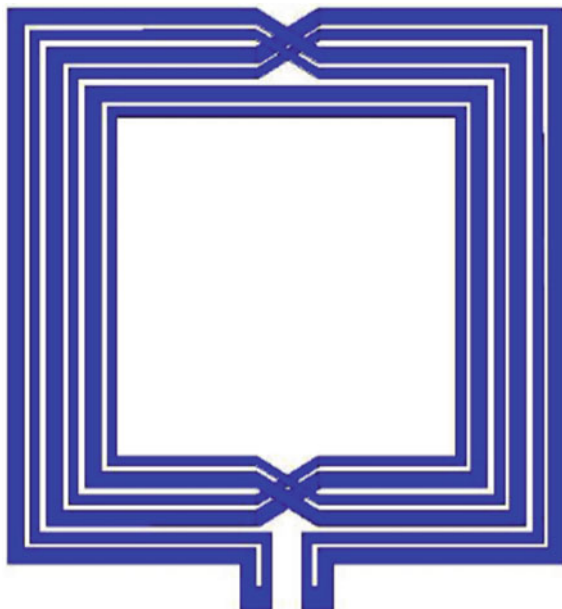
In a planar multipath differential inductor, the conductor width (metal strip) is partitioned into various current paths based on skin depth and minimum design rule as shown in Fig. 1. The path width is selected as less than the skin depth of the conductor.

At very high frequencies (>1 GHz), the skin depth for good conductors becomes tiny, and it is less than a micrometer. The skin depth (δ) is expressed as:

$$\delta = \sqrt{\frac{2\rho}{\omega\mu}} \sqrt{\sqrt{(1 + (\rho\omega\epsilon)^2) + \rho\omega\epsilon}} \quad (1)$$

where ρ is the resistivity, ω is the angular frequency, and ϵ and μ are the permittivity and permeability of the free space, respectively.

Fig. 1 Single-layer multipath differential inductor

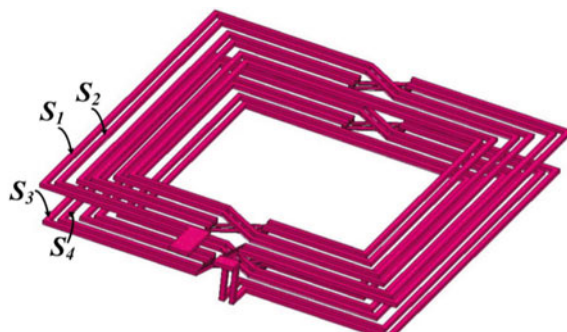


The multipath structure reduces the current crowding effects and contributes to the high Q [6]. The conductor is partitioned into multiple segments. The width of the segment is selected as below or equal to the skin depth.

3 Series-Stacked Non-parallel Multipath Differential Inductor

The proposed series-stacked non-parallel multipath differential inductor is shown in Fig. 2. The top and bottom layer each consists of one differential inductor, and these

Fig. 2 Proposed series-stacked non-parallel multipath differential inductor



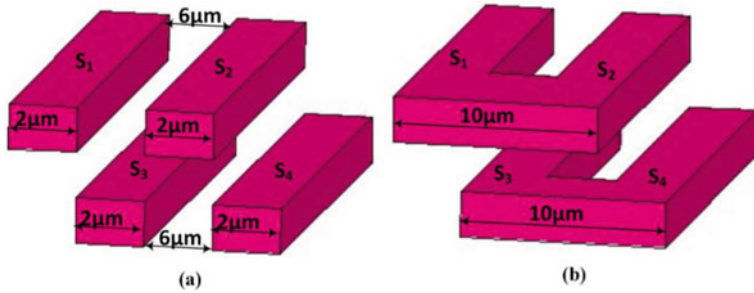


Fig. 3 **a** Partition of conductor width **b** non-parallel metal layers

are connected in series using vias. As shown in Fig. 3a, the conductor width is 10 μm, and it is partitioned into two segments, each segment has 2 μm width and spacing between the segments is 6 μm. The top layer consists of two segments denoted as S_1 and S_2 , and the bottom layer consists of two segments denoted as S_3 and S_4 as shown in Fig. 3a. The segments in the top and bottom layers are not parallel to each other as shown in Fig. 3b.

The non-parallel segments arrangement reduces the parasitic capacitance, and the multipath technique lowers the current crowding effect. Hence, the proposed inductor achieves high Q , high f_{SR} for almost same inductance value compared to existing series-stacked multipath inductor. The Q is often used to give an indication of its performance in an RF or another circuit is represented as:

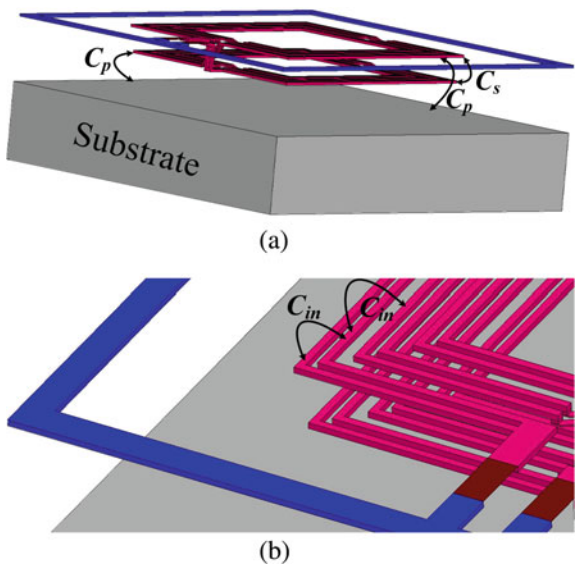
$$Q = \frac{\omega L_s}{R_s} \quad (2)$$

L_s is the inductance, and R_s is the D.C. series resistance of the inductor. The multipath structure also reduces the D.C. resistance (R_s) of the inductor which leads to a desirable increase in the inductor's Q . Self-resonance frequency (f_{SR}) is characterized as the point where the inductor ceases to offer inductive reactance, and it is represented in (3). The bandwidth of any designed application depends on f_{SR} .

$$f_{SR} = \frac{1}{2\pi\sqrt{L_s C_{eq}}} \quad (3)$$

From (3), C_{eq} is the sum of interlayer capacitance (C_s), metal to substrate capacitance (C_p), inter-winding capacitance (C_{in}) which are shown in Fig. 4a, b. The proposed inductor reduces the C_s and C_p , which leads to increase in f_{SR} . The performance of the proposed inductor is improved by modifying the number of segments, turn width, and the spacing between the turns throughout the spiral length.

Fig. 4 **a** Interlayer capacitance (C_s) and metal to substrate capacitance (C_p)
b inter-winding capacitance (C_{in})



4 Results and Discussion

The proposed inductor is constructed for an outer diameter of 180 μm and has 3 turns. The design and simulation of the proposed inductor is performed in HFSS using 0.18 μm CMOS technology. The differential impedance [13] of a differential inductor is obtained by using (4). The simulated L and Q values for the proposed symmetrical inductor are obtained by using (5) and (6).

$$Z_{\text{Diff}} = \left(\frac{Y_{11} + Y_{12} + Y_{21} + Y_{22}}{Y_{11}Y_{22} - Y_{12}Y_{21}} \right) \quad (4)$$

$$Q_{\text{Diff}} = \frac{\text{Im}(Z_{\text{Diff}})}{\text{Re}(Z_{\text{Diff}})} \quad (5)$$

$$L_{\text{Diff}} = \frac{\text{Im}(Z_{\text{Diff}})}{2 * \pi * \text{freq}} \quad (6)$$

The Q and inductance plots of the proposed inductor are shown in Figs. 5 and 6. From the results shown in Fig. 5, the proposed inductor with non-parallel segments achieves 25% improvement in f_{SR} for the same inductance value over conventional series-stacked multipath inductor. From Fig. 6, it is noted that the Q -factor of the proposed inductor is 33% greater than the conventional series-stacked multipath inductor. The maximum Q frequency ($f_{Q\max}$) of the proposed inductor is 4.8 GHz. The proposed inductor f_{SR} is 11.5 GHz which covers the entire C band.

Fig. 5 Comparison of Q -factor

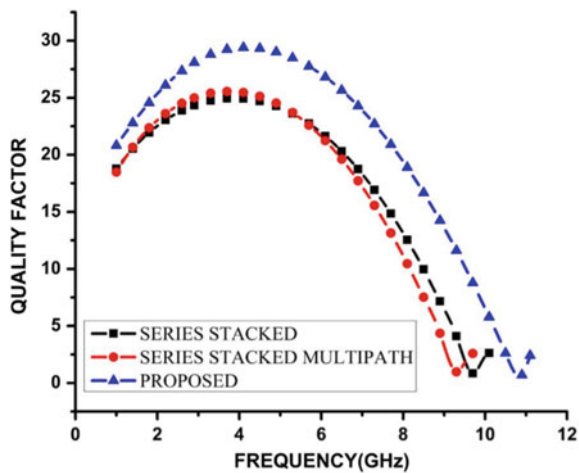
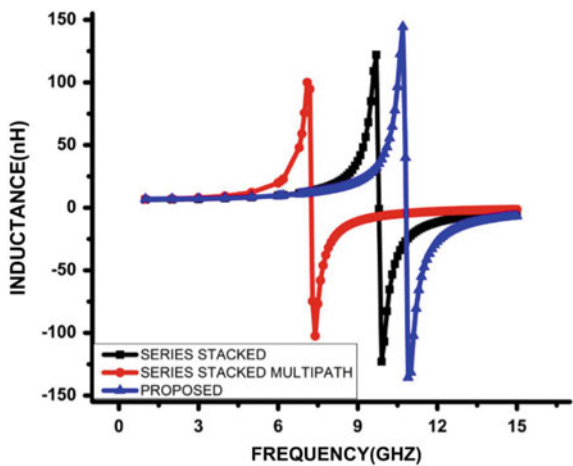


Fig. 6 Comparison of inductance



The simulation results for series-stacked multipath inductor, conventional series-stacked inductor, and the proposed inductor for an on-chip area of $180 \mu\text{m}$ are tabulated in Table 1.

5 Conclusion

In this paper, series-stacked non-parallel segmented multipath differential inductor has been proposed and simulated using $0.18 \mu\text{m}$ CMOS Technology. The proposed inductor gains 35% advancement in Q and 25% enhancement in f_{SR} over conventional series-stacked multipath inductor with an on-chip area of $180 \mu\text{m}$ for the inductance

Table 1 Comparison of performance with state-of-the-art inductors

Inductor	L (nH)	Q_{\max}	$f_{Q_{\max}}$	f_{SR}
Conventional series-tacked inductor [11]	7.09	22.52	3.6	9
Series-stacked multipath inductor [12]	7.8	25.07	4.1	9.2
Proposed inductor	7.9	29.87	4.7	11.5

The bold is used to represent the proposed inductor to differentiate it from the other works in the literature

of 7.9 nH. The peak Q frequency ($f_{Q_{\max}}$) is 4.7 GHz and f_{SR} is 11.5 GHz, which are within the C band. As the proposed inductor covers the entire C band, it is suitable for applications which include satellite communications, Wi-Fi, and radar systems.

References

1. Yue CP, Wong SS (2000) Physical modeling of spiral inductors on silicon. IEEE Trans Electron Dev 47:560–567
2. Tang C-C, Wu C-H, Liu S-I (2002) Miniature 3-D inductors in standard CMOS process. IEEE J Solid-State Circuits 37:471–480
3. Vanukuru VNR (2015) High Q inductors utilizing thick metals and dense-tapered spirals. IEEE Trans Electron Dev 62:3095–3099. <https://doi.org/10.1109/TED.2015.2458772>
4. Yue CP, Wong S (1998) On-chip spiral inductors with patterned ground shields for Si-based RF IC's'. IEEE J Solid-State Circuits 33:85–86
5. Pei S, Wanrong Z, Lu H, Dongyue J, Hongyun X (2011) Improving the quality factor of an RF spiral inductor with non-uniform metal width and non-uniform coil spacing. J Semicond 32:064011
6. Xu X, Li P, Cai M, Han B (2012) Design of novel high- Q -factor multipath stacked on chip spiral inductors. IEEE Trans Electron Dev 59:2011–2018
7. Vanukuru VNR, Chakravorty A (2014) Design of novel high- Q multipath parallel-stacked inductor. IEEE Trans Electron Dev 61:3905–3909
8. Danesh M, Long JR (2002) Differentially driven symmetric microstrip inductors. IEEE Trans Microwave Tech 50:332–341. <https://doi.org/10.1109/22.981285>
9. Kim J, Kim H (2010) CMOS symmetric trace differential stacked spiral inductor. Electron Lett 46:1005–1006
10. Akhendra Kumar P, Bheema Rao N (2017) Fractal series stacked inductor for radio frequency integrated circuit applications. Electron Lett 53:1387–1388
11. Zolfaghari A, Chan A, Razavi B (2001) Stacked inductors and transformers in CMOS technology. IEEE J Solid-State Circuits 36:620–628
12. Vanukuru VNR, Chakravorty A (2015) Series stacked multipath inductor with high self resonant frequency. IEEE Trans Electron Dev 62:1058–1062
13. Teo TH, Choi YB, Liao H et al (2004) Characterization of symmetrical spiral inductor in 0.35 μ m CMOS technology for RF application. Solid State Electron 48:1643–1650

Implementation of DCGAN to Generate Gamocha Design Patterns



Adarsh Pradhan, Arunav Buragohain, Uddipta Pathak, Sahil Ansari, and Manali Baruah

Abstract Generative adversarial network (GAN) [1] can learn to mimic any kind of distribution of data. The main motive of GAN is to generate images of a particular class on its own. One of the most popular and successful network of GAN is DCGAN [2], termed as deep convolutional generative adversarial network. It consists of deconvolutional and convolutional layer in the generator and discriminator network instead of dense layers. The generation and discrimination of DCGAN is more precise compared to the other GANs, as it features the minute details of the image. In this paper, we implement the DCGAN network to generate new Gamocha (traditional towel of Assamese tribe) design patterns. The design patterns made by DCGAN are as indistinguishable and unique as the human-made Gamocha. This GAN can follow the pattern structure of art to create new designs.

Keywords GAN · DCGAN · Gamocha

1 Introduction

The vivid art of creating and generating new images, patterns as well as designs plays a significantly important role in the day-to-day life of an artist. As the rate of development of artificial intelligence is blooming like an orchid these days, the

A. Pradhan (✉) · A. Buragohain · U. Pathak · S. Ansari · M. Baruah

Department of Computer Science and Engineering, Girijananda Chowdhury Institute of Management and Technology, Azara, Guwahati, India

e-mail: adarsh@gmit-guwahtini.ac.in

A. Buragohain

e-mail: arunavburagohain16@gmail.com

U. Pathak

e-mail: bkashyap.69@gmail.com

S. Ansari

e-mail: ansarisahilixvi@gmail.com

M. Baruah

e-mail: manalibaruah02@gmail.com

work pressure and the amount of work for humans is decreasing. But these changes failed to put shadow on the luminosity of lucid artistic nature of human creation. In the context of the algorithm of generative adversarial network proposed by Ian Goodfellow [1], the generation of artificial image took an enormous leap by providing realistic and specific output of the required class. With this very algorithm, images and arts can be created like a symphony by training the generative network with the training data provided.

The GAN consists of two different networks, i.e., generator and discriminator network. The generator network provides random images, and the discriminator distinguishes whether the image of that given class is fake or real. Here both the generator and the discriminator are trained simultaneously. The generator and discriminator consist of simple multi-layer perceptrons in Vanilla-GAN. The algorithm in Vanilla-GAN is simple, and it optimizes the mathematical equations using stochastic gradient descent.

For semi-unsupervised learning of GAN, Alec Radford and Luke Metz proposed the paper for DCGAN [2] where the classes consist of CNN called deep convolutional generative adversarial network. It is one of the most precise and successful implementation of GAN. It consists of ConvNets in place of multi-layer perceptrons. Here, the generator architecture consists of deconvolutional layer which upsamples the image and the discriminator architecture consisting of convolutional layer which downsamples the image.

In this paper, we implement the deep convolutional generative adversarial network to generate artificial texture of Gamocha design patterns. Gamocha is one of the most easily recognizable cultural symbol of Assam. ‘Ga’ means ‘body’ and ‘Mosa’ means ‘wipe.’ Gamocha is mainly a rectangular-shaped cloth with two colors, i.e., white in the body and red in the borders. Gamocha has historic significance in Assamese culture and is presented as a token of appreciation and respect. It is also used as a piece of water-absorbent cloth in daily household. By using the DCGAN, we recognize and design patterns from the Gamocha dataset and generate new design artificially. The generator here will try to produce new designs for Gamochas by generating random noises and deconvoluting, while the discriminator will distinguish it between real or fake by comparing and convoluting with the real dataset.

2 Related Works

Over the past few years, GANs have been implemented in various fields of art. Since GANs have the ability to learn from a data distribution and then create new data that is related to that data distribution, it can easily learn the underling patterns of an art or an image of clothing design. Various different models of GANs have been used to generate astonishing new art, for example, by training the network to learn from variety of other art, like CAN [3], where they use a modified version GAN to generate new artworks that are different from the training samples but are flawless to the human eye. GANs have also been implemented to generate new texture mosaics,

GANosaic [4]. There is also the work of Zalando Research on texture synthesis using SGAN [5] which is used for learning various repeated patterns in an image.

3 Generative Adversarial Network

Generative adversarial network is a class of unsupervised deep learning networks used to generate images proposed by Ian Goodfellow [1]. This neural network consists of two networks generator and discriminator. The generator generates images, while the discriminator distinguishes between fake or real of that particular image. Both the networks learn simultaneously.

In Fig. 1, blue box denotes the generator which provides random noises as the sample and this is sent to the red box, i.e., discriminator which discriminates the image to be real or fake and learns the features from the real-world dataset (blue cylindrical box) while the generator learns to generate more realistic images based on the output of the discriminator.

In deep convolutional generative adversarial network (DCGAN), the generator consists of deconvolutional layer [6] and the discriminator consists of convolutional layer [7] instead of dense layers. In DCGAN, the CNN architecture [7] is adopted and modified with three changes. The architecture of DCGAN is:

- In the pooling layers, both strided convolutions (discriminator) and fractional strided convolutions (generator) are used.
- Batchnorm is used by both the generator and discriminator.
- The removal of fully connected hidden layers are done for deeper architectures.
- Generator in all the layers uses ReLU activation function except the output as it takes Tanh.

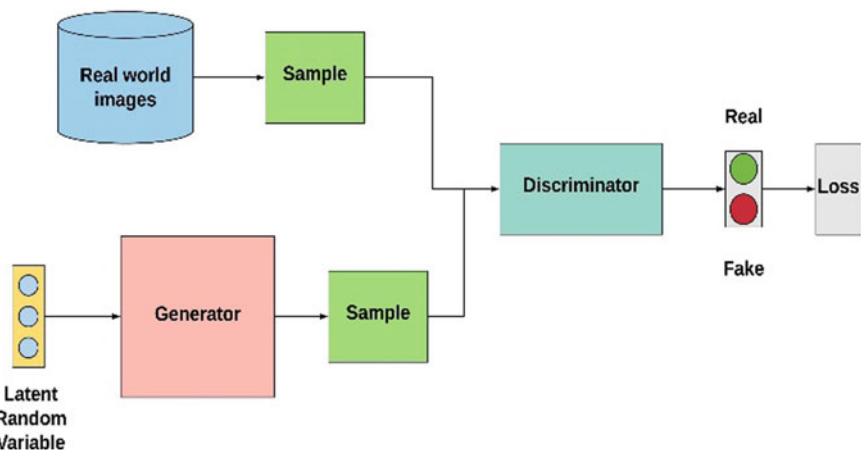


Fig. 1 Generative Adversarial Network architecture diagram

- In all the layers of discriminator, LeakyReLU activation is used.

Figure 2 represents the architecture of the generator in DCGAN. This diagram shows how an image is generated of a resolution of $64 \times 64 \times 3$. The generator consists of 10 layers.

Figure 3 represents the architecture of discriminator in DCGAN. Discriminator is a CNN containing 10 layers that takes $64 \times 64 \times 3$ and downsamples it using 2D convolution.

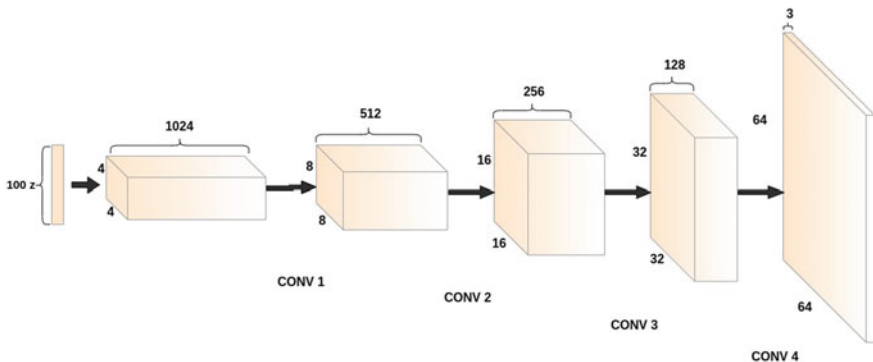


Fig. 2 Generator layer architecture diagram

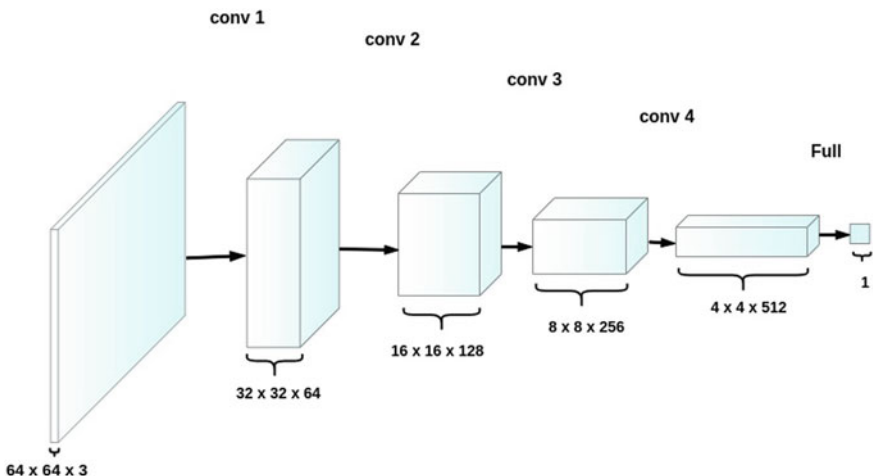


Fig. 3 Discriminator layer architecture diagram

4 Experiments

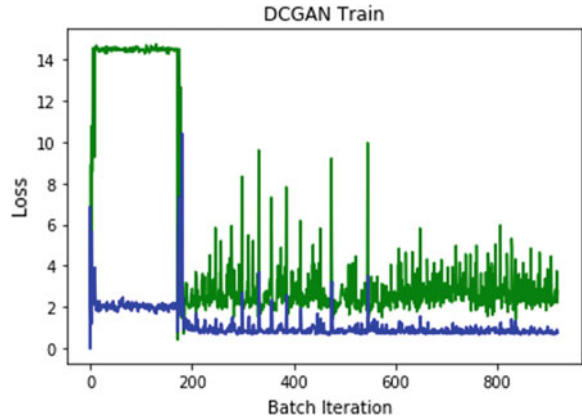
In this section, analysis and evaluation of the experiment is approached. The details of the dataset and implementation are presented.

4.1 Dataset

We have collected the design pattern dataset from Europeana collection [8] and combined it with some of the design patterns scraped from Google image and Pinterest to increase the variety of designs. A total of 318 images (Fig. 4) are collected with unique styles. These design patterns are then resized to a dimension of 64×64 to implement in the DCGAN.



Fig. 4 Sample of the real dataset

Fig. 5 Graph after 10 epoch

4.2 Design Pattern Generation

Training and testing of the model is performed on the environment configuration as follows: OS-Windows 10, CUDA10.0, cuDNN7.6.5, GPU (NVIDEA 1060) 6 GB memory, Python 3.7, 8 GB memory. Model parameter settings are: batch 64, image shape (64, 64, 3), epochs 190. Deep learning library used is: Keras [9].

In the generator network, the activation function used is ‘ReLU’ [10] with batch normalization momentum of 0.5. The last layer of the generator function uses ‘tanh’ activation function. In the discriminator network, the activation function used is ‘LeakyReLU’ [11] with batch normalization momentum of 0.5. After the flattening layer, the discriminator network uses ‘sigmoid’ activation function. Adam optimizer [9] is used in both the generator and discriminator network.

For training the model, the generator function and the discriminator function are run simultaneously loading the real dataset. During the process of training, the generated images are saved after an interval of (batch number % 50).

The graphs of Figs. 5 and 6 show the difference of results produced by the loss and batch iteration in DCGAN model after 50 epochs and 190 epoches.

Figure 7 is the result of the images produced by the DCGAN model after 190 epochs. It took almost six (6) hours to completely execute the program on our system with the configuration as mentioned earlier. Here, we see that the generated images, as shown in Fig. 6, have distortions and the design pattern cannot be distinctly observed, but they show uniqueness in them. Our dataset has only 318 unique images, and if we had larger number of images in the dataset, then the new design pattern generated will also be of better quality. These new design patterns can be used to craft new Gamocha with a different look and feel. With these uniquely designed patterns, every Gamocha can have a new appearance and will enhance the beauty of the traditional Gamocha.

Table 1 shows the results of generator loss and discriminator loss after several epochs.

Fig. 6 Graph after 190 epoch

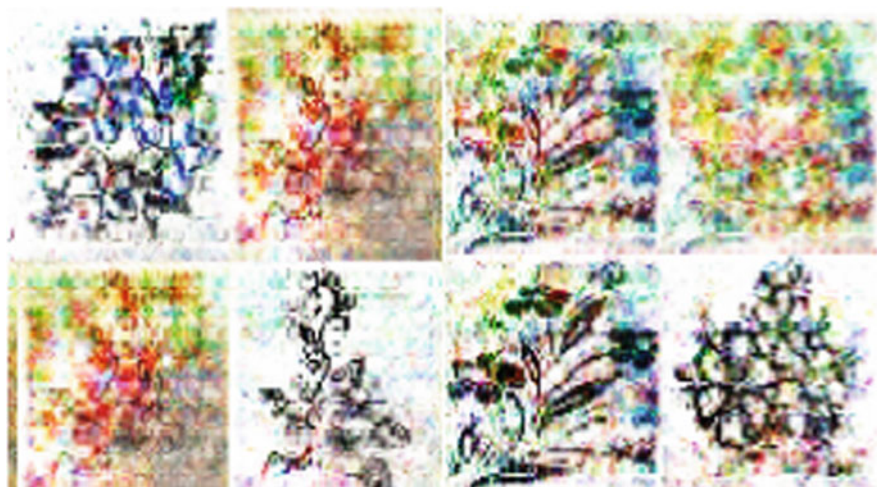
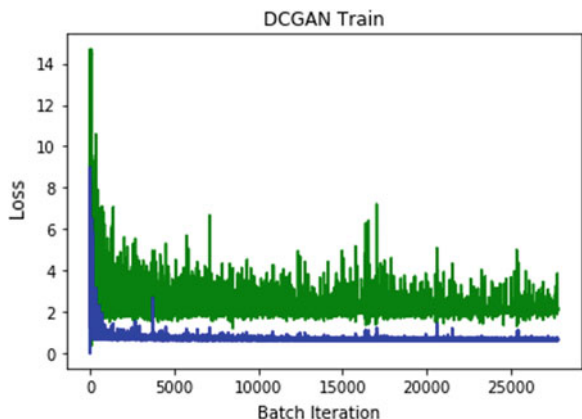


Fig. 7 Design patterns produced by DCGAN

Table 1 Shows the results of generator loss and discriminator loss after several epochs

Epoch	Generator loss	Discriminator loss
10	3.769013	0.9742602
100	2.111452	0.7276244
190	1.363392	0.6452213

The results produced by the DCGAN are distorted but have uniqueness in it. As our training dataset has only 318 unique images, so due to the lack of a larger training dataset, the DCGAN model could not generate new noise-free images. We expect that as the size of dataset will increase, the model will also obtain better results.

5 Conclusion

Generative adversarial networks are a stimulating and redefining recent innovation in deep learning. In this paper, we pragmatically focused on generating new and innovative design patterns for Gamocha implementing effective deep convolutional generative adversarial network. The generation of textures, different fibers and fabrics and designs for clothing using GANs can benefit and acknowledge the artificial intelligence to learn more and practically contemplate about the art patterns. The generation of new and variable designs produced by the DCGAN can be more unique if fed with proper design datasets.

Acknowledgements We would like to thank the developers of NVidia and TensorFlow for the immensely useful hardware and software which were used to implement our project.

References

1. Goodfellow I, Pouget-Abadie J, Mirza M, et al (2014) Generative adversarial nets. NIPS
2. Radford A, Metz L, Chintala S (2015) Unsupervised representation learning with deep convolutional generative adversarial networks (CNN). arXiv preprint [arXiv:1511.06434](https://arxiv.org/abs/1511.06434)
3. Elgammal A, Liu B, Elhoseiny M, Mazzone M (20–22 June, 2017) Eighth international conference on computational creativity (ICCC). Atlanta, GA
4. Jetchev N, Bergmann U, Seward C (2017) 31st conference on neural information processing systems (NIPS 2017). Long Beach, CA, USA
5. Bergmann U, Jetchev N, Vollgraf R (2017) Learning texture manifolds with the periodic spatial GAN. In: Proceedings of the 34th international conference on machine learning
6. Zeiler DM, Krishnan D, Taylor GW, Fergus R Deconvolutional networks. <https://arxiv.org/abs/1311.2901>
7. Zeiler MD, Fergus R Visualizing and understanding convolutional networks. <https://arxiv.org/pdf/1311.2901.pdf>
8. Europeana collection. <https://www.europeana.eu/portal/en>
9. Chollet F, et al (2015) Keras. <https://keras.io>
10. Ramachandra R, Zoph B, Le QV Searching for activation function. <https://arxiv.org/abs/1710.05941>
11. Nwankpa CE, Ijomah W, Gachagan A, Marshall S Activation functions: comparison of trends in practice and research for deep learning. <https://arxiv.org/pdf/1811.03378.pdf>

Performance Evaluation of On-Grid Rooftop Solar PV System in GMCH, Guwahati, Assam



Israfil Hussain, Utpal Chandra Baro, Rupa Chhetri, Vanita Agrawal, and Abdul Latif

Abstract In this paper, 500 KWp On-Grid Rooftop Solar PV plant installed and commissioned in 2018 at Guwahati Medical College Hospital (GMCH), Guwahati, Assam which is one of the largest in Assam is studied based on the information or the data in the report of Assam Energy Development Agency (AEDA) and its performance evaluation is carried out using PVsyst. Then we have compared the parameters with the one simulated by PVsyst for varying seasonal tilt i.e 20° in summer and 60° in Winter season and also for the fixed-tilt of 22°. Here the azimuth angle is taken 0° subject to the direction of the panel facing towards the south. The mean global horizontal radiation for the site is 4.72 KWh/m²/day with the average annual temperature is 24.6 °C. This study includes the design and performance analysis of the plant and then compares it with the obtained simulation values. The study uses different techniques and methods of a PV system for performance analysis and optimizes the operational behavior of PV systems.

Keywords PV system · On-grid · Performance ratio · Annual energy yield

1 Introduction

In a tropical country like India, the possibility of solar power generation is huge. In most parts of the region, it receives around 300 days of sun annually with 7–8 h of sunshine every day. The average incident radiation in India is between 4 and 7 kWh/m²/day [1]. The solar system received around 5000 Tera KWh of energy per year. The Ministry of Power (MoP), under Indian Government in November 2009 has launched a solar mission in the name of Jawaharlal Nehru with an aim for

I. Hussain (✉) · V. Agrawal
Royal Global University (RGU), Guwahati, Assam, India
e-mail: israfil.hussain@rgu.edu.in

U. C. Baro · R. Chhetri
EE Department, RGU, Guwahati, Assam, India

A. Latif
National Institute of Technology Silchar, Silchar, Assam, India

sustainable growth of solar power generation. The aim of the mission is to make the country strong in the fields of solar power by 2020 [2].

Government of India aims at installing 40 GW of Solar Rooftop grid-connected systems throughout the country by the year 2022. In fact, 250 MW Grid-tied Solar Rooftop projects have been provided in the state under the supervision of the Ministry of New and Renewable Energy (MNRE) and will be completed by the year 2022. Out of 250 MW, MNRE has sanctioned 14 MW grid-connected Solar Rooftop Program to Assam Energy Development Agency to implement the project in the state of Assam for the year 2017–2018 with 70% subsidy for Residential, Institutional (Non-Govt.) and Social Sectors Institutes. The “Smart City” initiatives by GOI have provided an unprecedented choice for the municipalities to use the modern technologies for better livelihood and better connectivity of the cities where we live. Before undertaking the program, the decision-maker predicts the solution to some of the key questions like “What we are planning to do?” and “What are the priorities for the city?”

The ‘Solar City’ development program initiated by the MNRE under India Government has aimed at developing the Guwahati city as the ‘Solar City’ in Assam by Assam Energy Development Agency (AEDA) through Guwahati Municipal Corporation in 2010. The 14 MWp Solar Rooftop Project has been sanctioned to Assam Energy Development Agency (AEDA).

Due to various land variations, the insertion of solar PV system on the geometrical area results in less efficiency. Hence, the rooftop area is emerging as a good option for energy generation. This rooftop grid-connected network will not only solve the failure of power but simultaneously it minimizes the environmental hazards generated by traditional fossil fuel based generation systems [3].

The plant performance work is described into two stages as follows:

1. Manual extraction of the parameters for electricity generation at a fixed-tilt.
2. Then, comparing the parameters with the one simulated by PVsyst in varying seasonal tilt and fixed-tilt. PVsyst is software that deals with the analysis of data, PV system sizing for grid-tied, independent, solar PV pumping as well as DC grid system.

2 Literature Review

Schaefer et al. [4] studied the performance, availability, and maintenance of 10 solar PV plants in U.S. Performance ratios, capacity factors are discussed here. The photovoltaic energy cost is mentioned which is followed by investment/maintenance costs, and capacity factor, and depends on the location, availability of plant, and the tracking system. Marion et al. [5] studied the performance indicators for grid-tied PV networks. The research focused on the importance of four performance indicators required for the total system performance assessment corresponding to the production of energy, solar reserve, and overall outcome of system losses which includes the absolute PV unit yield, base yield, performance factor, and PVUSA grading. Tudorache et al. [6] investigated the performance evaluation of sun-tracking PV panels of

single-axis type. The efficiency of sun-tracking PV system is then equated with the fixed PV system. The device identifies the fittest PV unit position with reference to the sun via a DC motor which is governed by a smart drive unit that will receive input signals from LDR light sensors. Cristaldi et al. [7] studied the economical evaluation of PV system losses that occurs because of dust and pollution. This article presents a technique for the maintenance of a PV plant that includes the cleaning expenses of the panels, then compares them to the economic losses in order to increase the efficiency. Kumar et al. [8] illustrated the performance evaluation of a 20 kWp grid integrated solar photovoltaic which is installed in an industry, located in Tiruchirappalli, India that describes some important features of the plant and the performance as well as economic analysis has also been done perfectly. Finally, the results are obtained for energy generation per month, different factors (performance and capacity), economic as well as maintenance features, etc. Bharathkumar et al. [9] studied the performance assessment of grid-tied 5 MW Solar PV unit in the regions of Karnataka where, the grid-tied solar PV unit set up by the Karnataka Power Corporation Limited, is described, and the evaluation of performance is done correspondingly. Sundaram et al. [10] studied the performance assessment of 5 MWp grid-tied PV units in the Southern part of India wherein the real-time analysis of the plant parameters is done and is verified by RET screen plus software environment. Bahaidara et al. [11] reported the analyses of the performance of PV unit for the climatic scenario of Dhahran in Saudi Arabia. EES software is leveraged to compute the parameters like cell temperature, maximum power position current/voltage/efficiency, and power. The values were then equated with the simulated results extracted by placing the PV modules to its environmental condition. Khalid et al. [12] studied the importance of performance ratio in grid-tied PV units efficiency. It determines the efficiency and output power. It has highlighted some economic and environmental benefits of using PR by framing a scenario example from the project named ‘SolMap project’ in India. Vasisht et al. [13] studied the performance of solar PV installation in seasonal variations. This attempt emphasizes the performance analyses of PV units leveraging the Capacity Utilization Factor (CUF) and Performance Ratio (PR). Sharma et al. [3] studied the performance of a grid-tied PV unit (capacity: 11.2 kWp) in Eastern India. This paper presents the parameter results for the month in between September 2014 to August 2015 of the installed plant. PV panels/inverter efficiency, PV array yield, final yield, and PR of the unit are also described perfectly. Nirwan et al. [14] addressed the performance analysis of grid-tied solar PV unit employing PVsyst software. The performance evaluation has been done with PVsyst for 1 MW grid-tied power plant set up at PEC University of Technology. He studied the performance evaluation at the given tilt angle for which the plant is installed and compared it with the optimum tilt according to the site with and without the Horizon considerations.

Hussain et al. [15–20] studied the performance analysis of Autonomous Hybrid System using renewable energy sources. Hereby the author uses the Artificial Intelligence techniques for optimization of the parameters of the different controllers. Finally, the comparative performance of Artificial Intelligence controllers for the hybrid model is presented.

3 Depiction of Solar PV Grid Scheme

The installed rooftop grid-tied PV plant employs solar panels, dc to ac conversion system (inverters), a power conditioning unit, and grid-tied equipment. The system has no energy storage. When the grid-connected PV system generates surplus amount then it supplies the excess power to the utility grid (Fig. 1; Tables 1 and 2).

According to data available on the NASA website, the monthly average isolation falling on a horizontal surface at the location is $4.72 \text{ kWh/m}^2/\text{day}$ and the average annual temperature is 24.6°C .

3.1 Plant Layout of the Established PV System

The total capacity of the proposed GMCH rooftop PV plant is of 500 kWp with a total of 3567 m^2 rooftop area. The plant is characterized into three different blocks of the hospital building. Each building is characterized by different solar generation capacity in accordance with the rooftop area available, as shown below



Fig. 1 Site location—GMCH, Guwahati

Table 1 Site information and Meteorological data

Site name	Rooftop of Guwahati Medical College Hospital
Coordinates	$26^\circ 10' 34 \text{ N}, 91^\circ 45' 46 \text{ E}$
Elevation	72 m above mean sea level
Altitude	43 m above ground level

Table 2 The table below showing the meteorological data of the located plant

	Jan	Feb	Mar	Apr	May	Jun	July	Aug	Sep	Oct	Nov	Dec
Hor. global	123.0	125.1	168.1	164.6	163.5	144.1	145.2	151.9	147.8	135.4	136.8	132.4
Hor. diffuse	42.4	53.2	73.0	85.9	93.8	86.6	80.5	82.5	69.7	70.3	34.5	23.3
Extraterrestrial	203.6	219.0	284.4	311.8	343.1	338.6	346.2	330.3	289.4	256.8	207.1	191.7
Cleanness index	0.604	0.571	0.591	0.528	0.477	0.426	0.419	0.460	0.511	0.527	0.660	0.691
Amb. temp.	16.8	19.4	23.1	24.8	27.2	28.0	28.9	29.0	27.8	26.2	22.0	18.6
Wind velocity	0.3	0.6	0.9	1.3	0.9	0.7	0.7	0.7	0.7	0.6	0.5	0.3

1. Main building (rooftop)—370 kW (operating)
2. Main building (5th floor)—80 kW (operating)
3. Tin roof—50 kW (operating).

So, the total plant generation capacity as 500 kW (Fig. 2).

A total of 1516 solar panels and 10 string inverters that include two inverters of 60 kW, seven inverters of 50 kW, and one inverter of 30 kW. The efficiency of the inverter is 95%. These inverters convert the DC power to AC power and the extractable output is supplied to the 11 kV grids utility.

The solar modules used are of “SOVA SOLAR” of the type SS330P polycrystalline with open-circuit voltage (V_{oc}) given as 45.27 V and short circuit current (I_{sc}) given as 9.29 A (Table 3).



Fig. 2 Picture of 500 kWp grid-tied rooftop PV unit

Table 3 PV module and Inverter specification (Report of AEDA)

PV module parameters	Specification	Inverter parameters	Specification
Type of modules	Polly crystalline	Model BG50KTR	INVT
P_{max}	330 W	Maximum DC Input power	53,000 W
I_{mp}	8.89 A	Maximum DC Input voltage	1100 V
V_{mp}	36.78 V	MPPT range	200–900/750
I_{sc}	9.29 A	No. of MPPT/strings/MPPT	2/5
V_{oc}	45.27 V	Starting voltage	200/150 V
Cell temperature	25 °C	Rated output power	50,000 W
Array area	50,000 sqft	Max. AC output current	72 A
No. of modules	1516	Frequency of grid	50 Hz
Efficiency	15%	Max. efficiency	98.60%
Weight	21.20 Kgs		

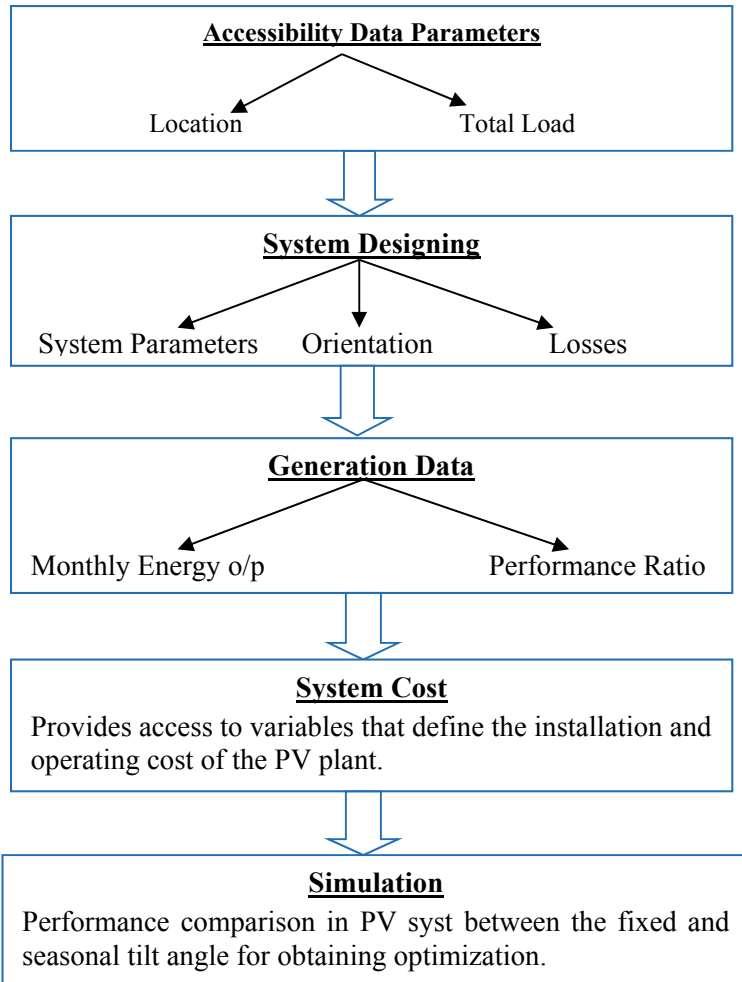


Fig. 3 Flowchart of the research work

3.2 Flowchart of the Work

See Fig. 3.

3.3 Plant Orientation

The tilt angle for the solar panels is inclined at 22° . The azimuth degree is 0° since the panels are facing towards the south. For optimization, the tilt angle is taken as 22° .

for summer and 60° for winter with azimuth of 0° that means the panels are facing towards the south (Figs. 4 and 5).

Monthly energy generation of the installed plant for tilt angle 22° is shown below for the last four months Since the RMS is activated in July 2019.

Figure 6 is collected from TrackSo [21], an IoT based energy management platform to track the performance of the remote plants provide a full control without actually being present there. The fig. shows that in the month of October has the record for the highest solar energy yield, by considering 4 months from August 2019 to November 2019.

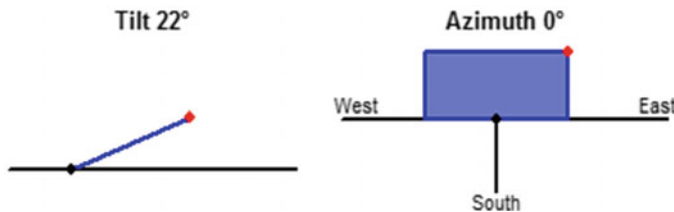


Fig. 4 Original tilt angle

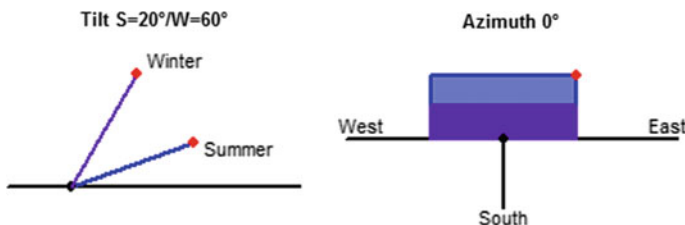


Fig. 5 Seasonal tilt angle

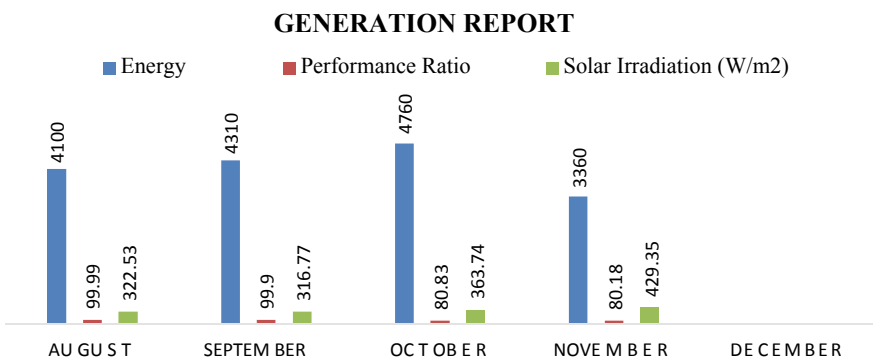


Fig. 6 Monthly energy generation and performance ratio

Table 4 Average energy yield for the specified months

Months	Monthly energy o/p	Avg. monthly extractable energy o/p (MWh)	Avg. annual extractable energy o/p (MWh)
August 2019	4.1	4.1	49.2
September 2019	4.3		
October 2019	4.7		
November 2019	3.3		
Total	16.4 (MWh)		

The average annual energy yield can be calculated by the product of the average monthly extractable energy output with the number of total months throughout the year. Thus, the annual energy yield is tabulated as in Table 4.

4 Performance Analysis

The solar PV plant performance depends on the various parameters that result in the true possibility of solar power generation variability. The calculation of the power, energy, and yield of the grid-tied PV power plants requires some important parameters. The required parameters given by [3] are shown below

1. PV array yield

The PV array yield is referred to as the PV array extractable output, divided by its rated power. The output represented (in a day, month or year) is given by [3]

$$Y_a = E_{DC,d} / P_{pv\text{ rated}}$$

2. PV final yield

The PV final yield is referred to as the output energy of the entire PV unit divided by the maximum (rated) power of the established PV array. Thus, the final yield is given by [3]

$$Y_{Fd} = E_{AC,d} / P_{pv\text{ rated}}$$

3. PV segment efficiency

The efficiency of PV segment (module) is given as

$$\eta_{pv} = (P_{DC} / G_t * A_m) * 100$$

4. DC-AC conversion (Inverter) Efficiency

The dc-ac conversion efficiency (η) is given as

$$\eta_{inv} = P_{AC} / P_{dc}$$

5. Efficiency of system

The overall system efficiency is given by

$$\eta_{\text{sys}} = \eta_{\text{pv}} * \eta_{\text{inv}}$$

6. Performance Ratio (PR)

PR is referred to the energy supplied to the network or grid divided by the energy produced by the unit in DC power, for the maximum peak hours/day [12]. The expressed is given as-

$$\text{PR} = Y_{\text{F}} / Y_{\text{R}}$$

7. CUF

It is a ratio of energy produced in a year by the PV unit to the aggregate of energy the PV unit will produce when operated under full rated power/day/year is known as the Capacity Utilization Factor (CUF). It is given as [13]

$$\text{CUF} = (E_{\text{ac.a}} / P_{\text{pv rated}} * 24 * 365) * 100$$

5 Simulated Results

The simulation is carried out for the comparison, using the PVsyst software by considering the total installed capacity, PV array area, field parameters, system sizing, etc.

Case 1 For fixed tilted plane field parameters include 22° angle with azimuth angle as 0° as the panels are south facing.

Case 2 For Seasonal Tilt the summer tilt is given as 20° and winter tilt as 60°. The azimuth is 0° as well.

As seen from Figs. 6 and 7, the optimized energy generated from the PV array with seasonal tilt is 4.54 kWh per kWp per day and the energy generated from fixed-tilt is 4.43 kWh per kWp per day. But the PR of fixed-tilt system shows quite a significant increase as compared to the performance ratio of the optimized tilt system (Fig. 8).

5.1 Loss Diagram Analysis

Figs. 9 and 10.

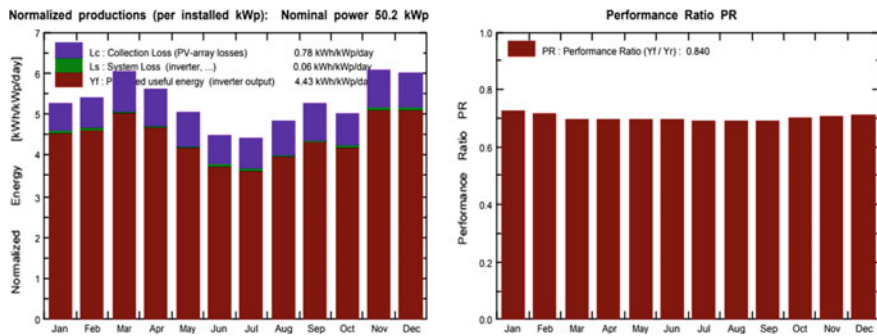


Fig. 7 Normalized production and performance ratio of original tilt

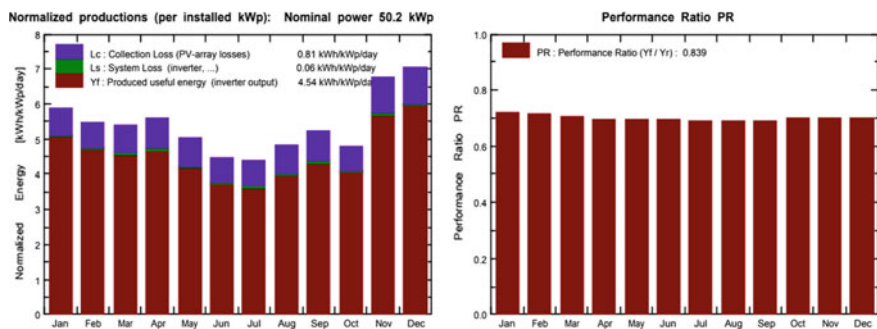


Fig. 8 Normalized production for seasonal tilt

6 Cost Analysis

As per the Electricity Regulatory commission for Assam the cost per watt of solar power is Rs. 53/Watt. The total cost of the plant is 2.65 crore with the MNRE capital subsidy of 70% of the project cost. The overall energy fed into the grid from the solar PV (SPV) plant is given as 81.1 MWh or 81,100 units per annum. The total time for the payback period is 7 years for the installed 22° tilt and south orientation with azimuth angle 0°.

7 Conclusion

The installed 500 kWp grid-tied PV unit at the rooftop of Guwahati Medical College Hospital, Assam was commissioned and monitored since August 2019 and its performance parameters are studied month wise. Then the PV system performance has been

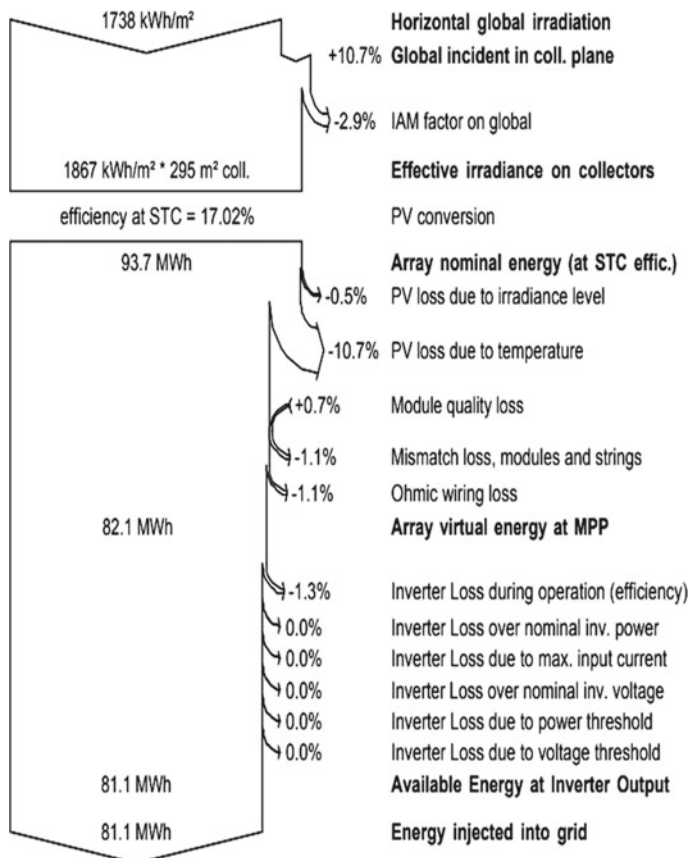


Fig. 9 Loss diagram for fixed-tilt angle

compared with the simulated values. Thus, the important features from this study are provided below-

1. The installed solar PV plant by using PVsyst shows that the 500 KWp power plant generates more energy for seasonal tilt angle equal to 22° for summer and 60° for winter.
2. The important factor to consider for designing the plant is that the energy produced is $1.92 \approx 2\%$ more in the case of a seasonal tilt than the original tilt angle.
3. The energy supplied to the grid is 2000 kWh more for seasonal tilt than that of the fixed tilted system.
4. Moreover, the mounted whole PV unit in GMCH has reduced about 25.22 ton of CO_2 from the atmosphere per year.

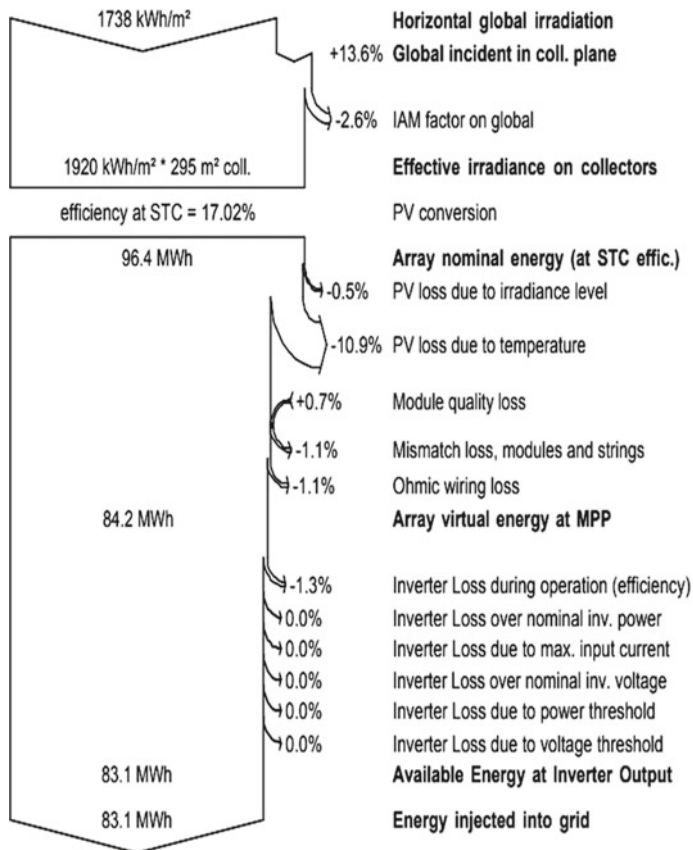


Fig. 10 Loss diagram for optimized tilt angle

Acknowledgements The authors are very much grateful to the authority of the Assam Energy Development Agency (AEDA) for giving such facilities for carrying out this research study.

References

1. Mahtta R, Joshi PK, Jindal AK (2014) Solar power potential mapping in India using remote sensing inputs and environmental parameters. *Renew Energy* 71:255–262
2. Akoijam AS, Krishna VV (2017) Exploring the Jawaharlal Nehru National Solar Mission (JNNSM): impact on innovation ecosystem in India. *Afr J Sci Technol Innov Dev* 9(5):573–585
3. Sharma R, Goel S (2017) Performance analysis of a 11.2 kWp roof top grid-connected PV system in Eastern India. *Energy Reports* 3:76–84
4. Schaefer JC (1990) Review of photovoltaic power plant performance and economics. *IEEE Trans Energy Convers* 5(2):232–238

5. Marion B et al (2005) Performance parameters for grid-connected PV systems. In: Conference record of the thirty-first IEEE photovoltaic specialists conference, 2005. IEEE
6. Tudorache T, Oancea CD, Kreindler L (2012) Performance evaluation of a solar tracking PV panel. Univer “Politehnica” Bucharest Sci Bull Ser C: Electr Eng 74(1):3–10
7. Cristaldi L et al (2012) Economical evaluation of PV system losses due to the dust and pollution. In: 2012 IEEE international instrumentation and measurement technology conference proceedings. IEEE
8. Kumar KA, Sundareswaran K, Venkateswaran PR (2014) Performance study on a grid connected 20 kWp solar photovoltaic installation in an industry in Tiruchirappalli (India). Energy Sustain Dev 23:294–304
9. Bharathkumar M, Byregowda HV (2014) Performance evaluation of 5 MW grid connected solar photovoltaic power plant established in Karnataka. Int J Innov Res Sci Eng Technol 3(6) (2014)
10. Sundaram S, Babu JSC (2015) Performance evaluation and validation of 5 MWp grid connected solar photovoltaic plant in South India. Energy Convers Manag 100:429–439
11. Bahaidarah H et al (2015) Performance evaluation of a PV module under climatic conditions of Dhahran, Saudi Arabia. Energy Explor Exploit 33(6):909–929
12. Khalid AMohd et al (2016) Performance ratio—Crucial parameter for grid connected PV plants. Renew Sustain Energy Rev 65:1139–1158
13. Vasisht MS, Srinivasan J, Ramasesha SK (2016) Performance of solar photovoltaic installations: effect of seasonal variations. Solar Energy 131:39–46
14. Nirwan D, Thakur T (2017) Performance evaluation of grid connected solar PV plant using PVsyst. Int Res J Eng Technol (IRJET) 4:3190–3194
15. Hussain I, Das DC, Sinha N (2017) Reactive power performance analysis of dish—Stirling solar thermal—Diesel hybrid energy system. IET Renew Power Gener 11(6):750–762
16. Hussain I, Ranjan S, Das DC, Sinha N (2017) Performance analysis of flower pollination algorithm optimized PID controller for wind-PV-SMES-BESS-diesel autonomous hybrid power system. Int J Renew Energy Res (IJRER) 7(2):643–651
17. Hussain I, Das DC, Latif A, Sinha N, Ranjan S (2020) FPA optimized controller for frequency control of dish stirling/diesel/fuel cell/energy storage based autonomous hybrid system. In: Dawn S, Balas V, Esposito A, Gope S (eds) Intelligent techniques and applications in science and technology. ICIMSAT 2019. Learning and analytics in intelligent systems, vol 12. Springer, Cham
18. Latif A, Pramanik A, Das DC et al (2018) Plug in hybrid vehicle-wind-diesel autonomous hybrid power system: frequency control using FA and CSA optimized controller. Int J Syst Assur Eng Manage 9:1147–1158. <https://doi.org/10.1007/s13198-018-0721-1>
19. Latif A, Das DC, Ranjan S, Hussain I (2018) Integrated demand side management and generation control for frequency control of a microgrid using PSO and FA based controller. Int J Renew Energy Res (IJRER) 8(1):188–199
20. Latif A, Das DC, Ranjan S, Barik AK (2019) Comparative performance evaluation of WCA-optimised non-integer controller employed with WPG-DSPG-PHEV based isolated two-area interconnected microgrid system. IET Renew Power Gener 13(5):725–736
21. Solar.trackso.in

Forced Alignment Method for Detection of Bodo Word Boundary



Raja Jwbthasa Daimari and Aniruddha Deka

Abstract Word Boundary Detection is one of the most important problems in the field of speech processing. There may be many methods for word boundary detection developed to date. But most of them are in languages like English, German, Hindi, etc. We know that language features are different for different languages, so a single method cannot be considered efficient for all languages. This paper proposes a new approach to Word Boundary Detection in Bodo Language (tonal language) in a noise-free environment. In a tonal language, a slight variation in pitch may change the meaning of the word completely. From the analysis of the results of male and female data, it is found that 80.56% of word boundaries are correctly detected for male data and 81.11% of word boundaries are correctly detected for female data. The proposed algorithm is developed using Forced Alignment Method using Hidden Markov Model (HTK) toolkit.

Keywords Word boundary detection · Tonal language · Forced alignment · Pitch · HTK toolkit

1 Introduction

word Boundary Detection can be defined as identifying the start and end of a spoken word in an utterance. The detection of a word boundary is one of the most challenging works in the area of speech processing. The accurate detection of word boundaries is challenging in the sense that the speaker does not pause consciously between the words. Also, the method developed for a particular language may not work for other languages as different languages possess different features. It is more challenging in the case of a tonal language. Tonal languages are unique in the sense that they have

R. J. Daimari (✉) · A. Deka

Department of Computer Science and Engineering, Royal School of Engineering and Technology, Guwahati, India

e-mail: trgenjiraja@gmail.com

A. Deka

e-mail: aniruddha.deka@rgi.edu.in

two tones for certain words. Bodo [1] is a tonal language and the tonal language features for Bodo will also be explored to a certain extent. In this paper, we propose a method to detect word boundary for Bodo Language using the Forced Alignment Method in common speech signal environments. Hidden Markov Model Toolkit (HTK) is used in the proposed system for the detection of word boundaries.

2 Previous Research

Jain et al. [2] developed an algorithm for Word Boundary Detection in the Hindi Language which was based on intensity and pitch. Their algorithm was designed to work in a noisy environment by considering three prosodic parameters which are “defined pitch contour”, “undefined pitch on silence zone” and “intensity contour”.

Mandal et al. [3] proposed a method of detecting word boundaries by using Suprasegmental features for the Bengali language, which is a stress bound language. While detecting word boundaries for the Bengali language, the authors’ Intonation, Stress and rhythm of the language. After their research, they found that 87.8% of word boundaries have been correctly detected. The drawback of this method is that it can be used only for stress bound language.

Kacur and Rozinaj [4] discussed a method for Word Boundary detection using cepstral matrices. They proposed that the method is efficient for detecting word boundaries in a noisy environment. In this method, speech signals are divided into consecutive segments, which are overlapped by a certain part of their length to keep the feature vectors behaviour smooth in the time and moreover not losing any speech information.

Ramana Rao and Srichand [5] proposed a method for word boundary detection using pitch variation, which determines the highness and lowness of a tone in a spoken utterance for Hindi, Bengali, Marathi, Telugu and German. They used the frequency of pitch for each word and found that more than 85% of word boundaries were correctly determined for the Indian languages and about 65% word boundaries were correctly determined for German language. The authors attributed the low detection rate in German to the fact that the misses occurred more often between words with only one vowel in that particular word and the next word.

3 Proposed System

3.1 Data Preparation

Data Preparation, which is also known as the preprocessing step is the first step in the detection of word boundaries as shown in “Fig. 1”. For generating a set of HMMs, the speech data files and the transcriptions associated with those files are required.

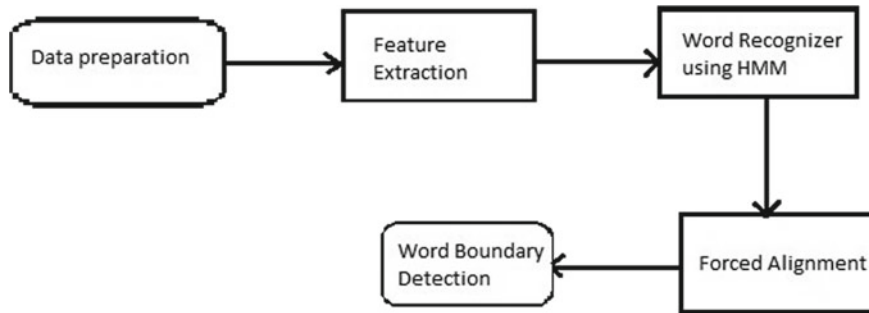


Fig. 1 Block diagram of the proposed model

Therefore, data preparation is essential and before the data can be used for training it should be converted into the appropriate parametric form along with its associated transcriptions in the correct format and use the required labels. Thus, before the data is recorded, a phone set for the words is defined, a dictionary is constructed to cover both training and testing which consists of the list of unique words present in the sentences and a task grammar is to be defined. Our database consists of 10 sentences which contain a total of 41 unique words in which certain words possess tonal features. Therefore, the dictionary consists of 41 words, and they are kept in the standard HTK format [6].

3.2 Data Recording Plan

The training and test data are recorded using the tool Wavesurfer. Wavesurfer is a waveform recording and trimming tool. For the purpose of recording, 10 sentences are taken in Bodo where certain words have tonal features. The data is recorded from 10 speakers where the number of male speakers is 5 and the number of female speakers is 5. Each sentence is recorded from each speaker 10 times. The resulting database consists of 1000 chipped files (500 male and 500 female utterances). In our research, four male speakers and four female speakers are used for training and one male and one female speaker is used for testing. This means 800 files (Male: 400, Female: 400) are used for training. And the remaining 200 will be used for testing. The word boundaries will be detected from the test data using the Forced Alignment Method.

3.3 Creating Transcription Files

To train a set of Hidden Markov Models (HMM) [6], every file of training data must have an associated phone level transcription. As a result, transcription files are necessary. To do this, a set of phone transcriptions are required. Each word should be written in a single line and each utterance should be terminated by a single period of its own. These transcriptions are kept in a file known as Master Label File (MLF) which is a single file containing a complete list of transcriptions. When HTK processes speech files, it expects to find a transcription with the same name but a different extension. For example, when the file /root/raja/speech_test_new/bodo_female_1.wav was being processed, HTK would look for a label file called /root/raja/speech_test_new/bodo_female_1.lab. When MLF files are used, HTK will look for a pattern in a file that matches the required label file name. In our research MLF files are created for both training and testing data for each chipped wav file.

3.4 Feature Extraction

In the detection of word boundaries in Bodo Language with our data, Mel Frequency Cepstral Coefficient (MFCC) is used for feature extraction. MFCC is chosen for feature extraction as compared to other methods because MFCC is derived on the concept of logarithmically spaced filter bank which resembles the concept of the human auditory system and hence produces better results as compared to Linear Predictive Coding (LPC). The MFCC parameters are given in the configuration file where the Fast Fourier Transform (FFT) should use a Hamming window and the signal should have first-order pre-emphasis applied using a coefficient of 0.97. The filter bank has 28 channels and 12 MFCC coefficients will be the output. This is specified in the configuration file. In HTK, the tool HCopy is used to automatically convert its input into MFCC vectors. In order for HCopy to work, some of the source file with its respective output file is to be used (Fig. 2).

3.5 Word Recognizer Using HMM

The word recognizer is built-in HTK with the help of HMM. The significance of a recognizer is to map between sequences of speech vectors and the wanted underlying speech utterance. A word recognizer is built using 41 unique words as the dataset consists of 10 sentences containing 41 unique words.

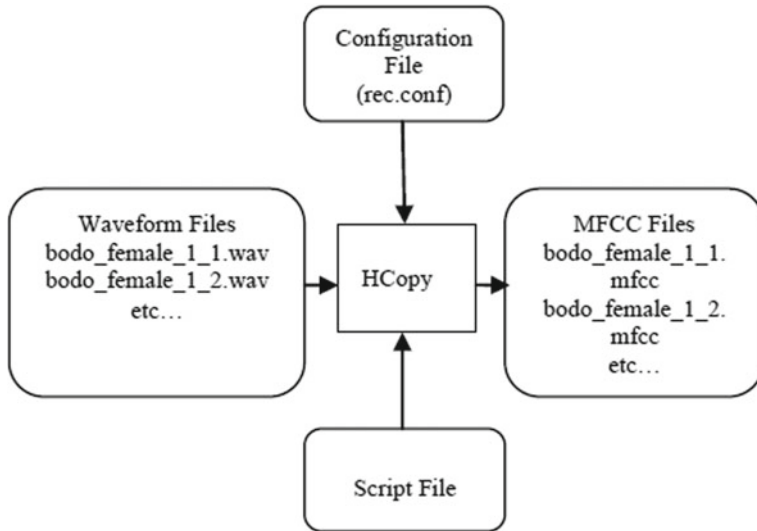


Fig. 2 Construction of MFCC feature vectors

3.6 *Forced Alignment*

In the determination of word boundaries, we have used the Forced Alignment Method. With the help of this method, the timestamp information of the sentence is found out. This method involves spotting the words which are recognized with the help of HMM and thereby marking the boundaries at the appropriate places. Forced Alignment Method is an effective method for labelling the word boundaries for a large speech database. In this method, the words are checked and compared with the language model which is developed and if the word matches the language model, the timestamp for that particular word is marked and if it does not match the language model which we have developed, it proceeds to check in the word. After forced alignment is performed on the test files, a file with the word boundaries is created by HTK.

4 Results and Discussion

In our research, two measures are defined for the detection of word boundaries. They are the hit rate and false alarm rate. In our hypothesis, a hit occurs when the hypothesis contains the correct word along with the correct timestamp information. The hit rate determines the percentage of word boundaries correctly detected. On the other hand, False Alarms in the word boundary hypothesis occur when the hypothesis does not contain the actual word boundaries to be detected. It occurs when the word boundary is detected but the detection is wrong. It specifies the percentage of error in the word

boundary hypothesis. Hit Rate and False Alarm rates are defined for a single test speech file as follows.

$$\text{Hit Rate} = \frac{\text{No. of Word Boundaries Correctly Hypothesized}}{\text{No. of Word Boundaries Present}}$$

$$\text{False Alarm Rate} = \frac{\text{No. of error in Word Boundary Hypothesis}}{\text{No. of Word Boundary Hypothesis}}$$

In “Fig. 3” for the utterance “Musua nokorni fichijagra junat”, the waveform for the sentence is shown along with the word boundaries after each word. In the sentence, the word “Musua” has its word boundary from 0.05 to 0.82 s, the word “nokhorni” has its word boundary from 0.82 to 1.27 s, the word “fichijagra” has its word boundary from 1.27 to 1.91 s and the word “junat” has its word boundary from 1.91 s to 2.3 s. As can be seen from “Fig. 3” for this sentence, the words along with the word boundary information are correctly detected thereby giving a hit rate 4/4, i.e. 100% and no false alarm is generated as no miss occurred in the detection of boundaries.

In “Fig. 4” for the utterance “Bharatni rajdhania gwdan delhi”, the waveform for the sentence is shown along with the word boundaries. In the sentence, the word “Bharatni” has its word boundary from 0.04 to 0.56 s, the word “rajdhania” has its word boundary from 0.56 to 1.12 s, the word boundary for the word “gwdan” is wrongly detected as “gandani” along with its boundary from 1.12 to 1.69 s and the word “delhi” has its word boundary from 1.69 to 2.12 s. As it can be seen from

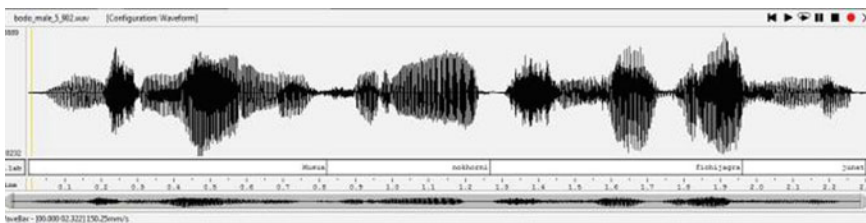


Fig. 3 Waveform of the utterance “Musua nokorni fichijagra junat” with timestamp

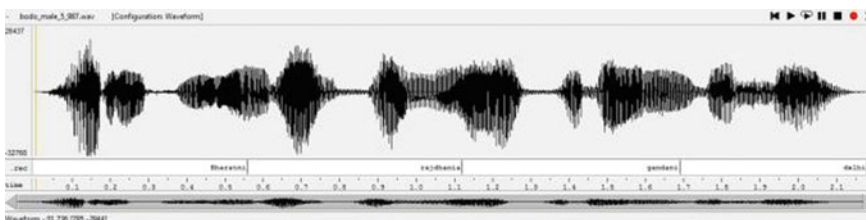


Fig. 4 Waveform of the utterance “Bharatni rajdhania gwdan delhi” with timestamp

“Fig. 4”, the word “gwdan” is wrongly detected as “gandani”. This results in a miss, thereby generating a false alarm. As we have highlighted that Bodo is a tonal language, the false alarm may be attributed to the tonal features of the language. Therefore, the hit rate, in this case, is 3/4, i.e. 75% and the false alarm is 1/3, i.e, 33.33%.

For the whole corpus which consists of 1000 chipped wav files, the overall results from the test data files are shown in “Table 2”. The hit rate is marginally higher in the case of male data as compared to female data. This can be because of the fact that the pitch of a female voice is higher as compared to male and pitch is also a measure to analyze word boundaries. Therefore, the variation of pitch is related to the difference in hit rate for male and female data. The result is represented graphically in “Fig. 5”. As it is already emphasized that Bodo is a tonal language, therefore a slight change in variation of pitch in certain words can change the meaning of the word completely. After analysis of the results, it is found that the false alarms are mainly due to the tonal variations. Basically, in our study false alarms have been raised for the words which are highlighted in “Table 1”.

Fig. 5 Graphical representation of hit rate and false alarm rate

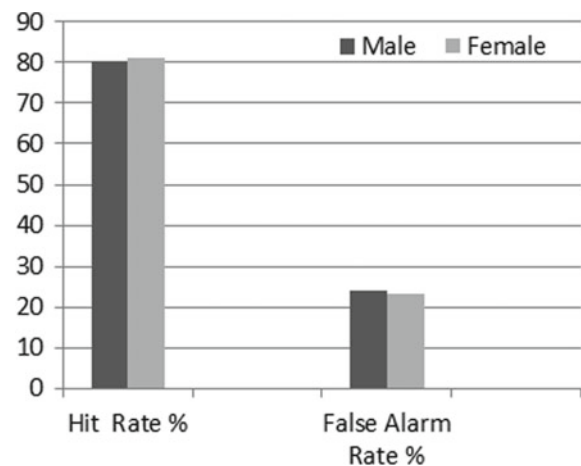
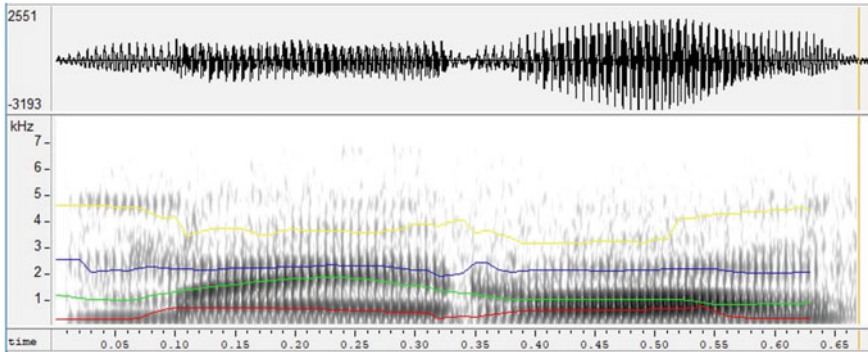


Table 1 Variation in actual and detected word boundary

Actual word	Detected word
asama	asomia
mache	munche
harini	gandani
mache	sache
gwdan	gadani
musua	mache
asama	rama
mache	gongshe

Table 2 Overall results

Sex	Hit rate (%)	False alarm rate (%)
Male	80.56	24.14
Female	81.11	23.28

**Fig. 6** Speech analysis of the word “mairong”

In “Fig. 6” shows the speech analysis of a single word “mairong”. The first part of the diagram shows the waveform of the word which ranges from -3193 to 2551 Hz. The second part is the spectrogram of the same word plotted in a log scaled spectrogram varying amplitude with time (ms). Here, we can divide the word in smaller frames say 0.05 ms and then we can eliminate the frames which do not reach the required frequency range.

5 Conclusion

In this paper, it is shown that word boundaries are detected in Bodo Language with the help of HTK. Moreover, a few tonal features of Bodo Language have been explored. The hit rate for male and female data is found out to be 80.56% and 81.11% respectively. Also, the false alarm rate is found out to be 24.14% and 23.28% respectively. Moreover, the reasons for variation in hit rate for male and female data have been mentioned. Also, false alarm rates have been discussed. The hit rate can be increased by improving the recording environment and as such a studio environment can be chosen. Also, due to the variation in speaker’s pronunciation and accents, the hit rate is affected.

6 Future Scope

The future scope of this work is that after the word boundaries have been successfully detected, the individual words with accurate boundaries can be extracted and it can be used for detecting regions out of vocabulary words and also for Keyword Spotting.

References

1. Sarmah P (2004) Some aspects of the tonal phonology in Bodo. Central Institute of English And Foreign Languages, Hyderabad
2. Jain A, Agrawal SS, Prakash N. Performance evaluation of word boundary detection for Hindi speech database. GGSIP University, Delhi, India
3. Mandal SKD, Gupta B, Datta AK (2006) Word boundary detection based on Suprasegmental features: a case study on Bangla speech. Int J Speech Technol
4. Kacur J, Rozinaj G. Word boundary detection in stationary noises using cepstral matrices. Department of Electrical Engineering and Information Technology, Slovak University of Technology
5. Ramana Rao GV, Srichand J (1996) Word boundary detection using pitch variations. Department of Computer Science and Engineering, IIT Madras
6. Young S, Kershaw D (2000) The HTK book. Microsoft Corporation, pp 27–49

Fault-Tolerant Cascaded Asymmetrical Multilevel Inverter for the Solar-Based Electric Vehicle



Hillol Phukan, Tamiru Debela, and Jiwanjot Singh

Abstract Fault-tolerant asymmetrical multilevel inverter (FTAMLI) has been performed. Multicarrier selective harmonic elimination pulse width modulation (MC-SHEPWM) has been adopted to generate the output voltage levels for an FTAMLI. The fault-tolerant algorithm has been adopted. Both during and after fault, the voltage remains constant by using this algorithm; to analyze the implementation of the propound algorithm with MC-SHEPWM scheme, faults have been assumed as open circuit and short circuit in semiconductor switches. Evaluation of output voltage, total harmonic distortion (THD), blocking voltage, and efficiency has been performed for both normal and fault condition. Further, improvement due to fault-tolerant algorithm in blocking voltage, THD, and efficiency has been demonstrated. In this paper, simulation is done in MATLAB/Simulink software.

Keywords Blocking voltage · Fault-tolerant asymmetrical multilevel inverter · Selective harmonic elimination pulse width modulation · Total harmonic distortion

1 Introduction

Due to the major growth of semiconductor power devices, the power electronic systems are now extensively used in medium and high voltage. Multilevel inverters (MLI) are power electronic equipment used to create high power quality for renewable power systems, photovoltaic systems, STATCOM, marine electric systems, and for industrial application [1, 2]. The first multilevel inverter has been invented as a neutral point clamped (NPC) to create three levels in the output voltage. Successively, the flying capacitor multilevel inverter (FCMLI) and cascaded H-bridge inverter (CHBI) become mature [3]. The NPC and FCMLI use extra diodes and capacitors in its structure unlike CHBI. CHBI has modular structure using semiconductor switches and it does not need any extra passive components. But, the disadvantage of CHBI is that it uses ample quantity of semiconductor switches and DC sources as the power

H. Phukan · T. Debela · J. Singh (✉)

Department of Electrical Engineering, National Institute of Technology, Silchar, Assam, India

e-mail: jiwanjot18@yahoo.co.in

quality increases in the output voltage [4]. Further, ample number of switches and DC sources decreases the reliability due to increase in the fault probability. To increase the power quality using n DC sources, a cascaded asymmetrical MLI using $2(n + 1)$ bidirectional switches has been implemented [5]. Further to increase the reliability, complexity, and cost, a sub-MLI-based topology has been reported [6].

First segment of asymmetric multilevel inverter (AMI) is to shoot up the levels in output voltage by reducing overall cost of AMI and to maintain the power quality at load end has been described [7–17]. In addition, another segment of an AMI is reliability and the AMI has to maintain the power quality in normal and fault condition. To increase the reliability of multilevel inverter, new topology has been proposed with fault-tolerant ability [18]. Reconfiguration of gating signal of semiconductor device for multilevel inverter in faulty condition has been reported [19]. The open-circuit fault is assumed, and fault tolerant strategy has been adopted for T-type 3-L inverter [20].

In this paper, fault-tolerant asymmetric topologies of MLIs have been proposed. In Sect. 2, basic structure of topology has been given and principle of incorporation and diminution of DC sources has been described. In Sect. 3, details of the proposed modulation scheme have been explained. Section 4 includes proposed fault-tolerant algorithm for fault-tolerant asymmetrical multilevel inverter (FTAMLI). Section 5 includes the simulation results of output voltage, THD, and blocking voltage in normal and fault condition using three DC source FTAMLI. The simulation results of two DC source FTAMLI have been discussed in detail. Section 6 summarize the results.

2 Basic Structure of FTAMLI

The proffer topology of FTAMLI is shown in Fig. 1. This topology is based on H-bridge. Several H-bridges have been concatenated in cascade to acquire the elevated number of levels and hence the total harmonic distortion in output voltage is reduced. If number of level increases, the THD becomes decreases. This topology has advantage that it produces ample number of levels using less DC sources or semiconductor devices. This topology uses unidirectional devices instead of bidirectional devices. The proposed topology of asymmetrical MLI is shown in Fig. 1. The magnitude of the output voltage levels in DC-DC converter are different, due to which the number of levels in the output voltage is high. If N numbers of DC sources are used:

$$\text{Numbers of unidirectional semiconductor devices} = 4N \quad (1)$$

The number of levels produced by the proposed topology elevates with the escalation in number of basic units.

$$\text{No. of levels in output voltage} = 3^N \quad (2)$$

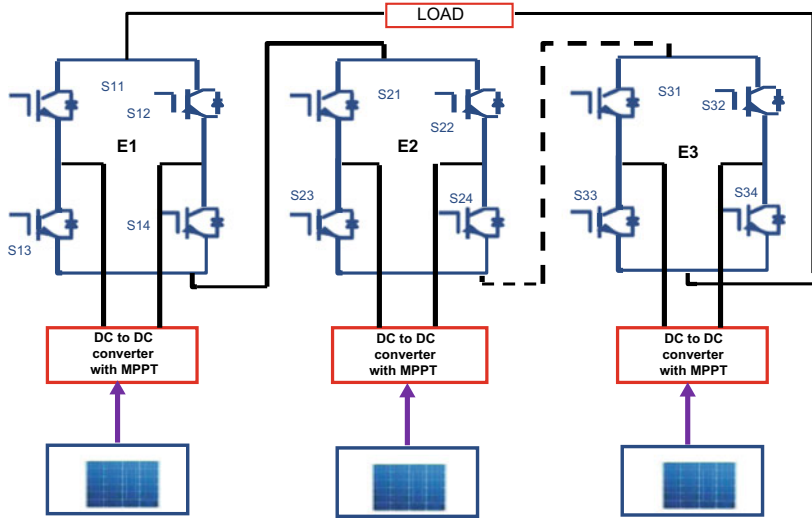


Fig. 1 Structure of FTAMLI for PV application

3 MC-SHEPWM for FTAMLI

Selective harmonic elimination (SHE) PWM technique is utilized to minimize selected harmonics levels by optimizing the conduction angles of the output voltage [21, 22]. Many PWM techniques are popular for MLI to minimize the THD [23]. These techniques are classified by two categories as a high frequency and fundamental frequency techniques. Under the category of high-frequency-based sinusoidal PWM (SPWM) is used for seven-level cascaded MLI. It has been reported that phase shifted SPWM gives better results than other SPWM techniques [24].

MC-SHEPWM scheme is employed to acquire output voltage levels of FTAMLI. The FTAMLI uses MC-SHEPWM to create twenty-seven levels of output voltage. The levels in positive half-cycle are obtained by comparing constant wave C_1, C_2, \dots, C_{13} with sinusoidal wave and levels in negative half-cycle have also been achieved by using the similar principle. The carrier wave has a constant level and reference wave is a sinusoidal wave. To obtain L number of levels in output voltage, $L - 1$ carrier waves are required.

G_1, G_2, \dots, G_{13} have been defined as pulse modes (PM). Corresponding to each pulse mode, the semiconductor switches will be in ON state to create desired level at output voltage of FTAMLI as shown in Table 1. Pulse modes G_1-G_{13} can be obtained by following Boolean operations:

$$G_1 = C'_1 \oplus C'_2 \quad (3)$$

$$G_2 = C'_2 \oplus C'_3 \quad (4)$$

Table 1 Switching table of three DC source FTAMLI

PM	DC source combination $E_1 > E_2 > E_3$	Switch states 1 = ON, 0 = OFF											
		S11	S12	S13	S14	S21	S22	S23	S24	S31	S32	S33	S34
G_1	$-E_2 - E_3 + E_1$	1	0	0	1	0	1	1	0	0	1	1	0
G_2	$+E_3$	1	0	1	0	0	0	0	1	1	0	0	1
G_3	$-E_2 + E_1$	1	0	0	1	0	0	1	0	0	1	0	1
G_4	$+E_2 - E_3$	1	0	1	0	1	1	0	1	0	1	1	0
G_5	$-E_2 + E_3 + E_1$	1	0	0	1	0	0	1	0	1	0	0	1
G_6	$+E_2$	1	0	1	0	1	1	0	1	0	1	0	1
G_7	$+E_1 - E_3$	1	0	0	1	0	1	0	1	0	1	1	0
G_8	$+E_3 + E_2$	1	0	1	0	1	0	0	1	1	0	0	1
G_9	$+E_1$	1	0	0	1	0	0	0	1	0	1	0	1
G_{10}	$+E_1 + E_3$	1	0	0	0	0	0	0	1	1	0	0	1
G_{11}	$+E_2 - E_3 + E_1$	1	0	0	1	1	1	0	1	0	1	1	0
G_{12}	$+E_2 + E_1$	1	0	0	0	1	1	0	1	0	1	0	1
G_{13}	$+E_2 + E_3 + E_1$	1	0	0	1	1	1	0	1	1	0	0	1
G_0	0	0	0	0	0	0	0	0	1	0	0	0	0
G_1	$+E_2 + E_3 - E_1$	0	1	1	0	1	1	0	1	1	0	0	1
G_2	$-E_3$	0	1	0	1	0	0	0	1	0	1	1	0
G_3	$-E_1 + E_2$	0	1	1	0	1	1	0	1	0	1	0	1
G_4	$-E_2 + E_3$	0	1	0	1	0	0	1	0	1	0	0	1
G_5	$-E_2 + E_2 - E_3$	0	1	1	0	0	0	0	1	0	1	1	0
G_6	$-E_2$	1	0	1	0	0	0	1	0	0	1	0	1
G_7	$-E_1 + E_3$	0	1	1	0	0	0	0	1	1	0	0	1
G_8	$-E_2 - E_3$	0	1	0	1	0	0	1	0	0	1	1	0
G_9	$-E_1$	0	1	1	0	0	0	0	1	0	1	0	1
G_{10}	$-E_1 - E_3$	0	1	1	0	0	0	1	0	0	1	0	1
G_{11}	$-E_2 - E_2 + E_3$	0	1	1	0	0	0	1	0	1	0	0	1
G_{12}	$-E_2 - E_2$	0	1	1	0	0	0	1	0	0	1	0	1
G_{13}	$-E_2 - E_2 - E_3$	0	1	1	0	0	0	1	0	0	1	1	0

$$G_3 = C'_3 \oplus C'_4 \quad (5)$$

$$G_{12} = C'_{11} \oplus C'_{12} \quad (6)$$

$$G_{12} = C'_{12} \oplus C'_{13} \quad (7)$$

Here, \oplus stands for EX-OR operation and C_1, C_2, \dots, C_{13} are carrier waves. $C'_1, C'_2, \dots, C'_{13}$ are the logical outputs. When sinusoidal wave is greater than that of carrier waves, logical output will be high. The MC-SHEPWM is combination of fundamental frequency and higher frequency for the proposed topologies.

$$V_{\text{out}}(wt) = \frac{4V_{\text{dc}}}{n\pi} \sum_{n=1,3,5,\dots}^{\infty} [\cos(n\alpha_1) + \cos(n\alpha_2) + \dots + \cos(n\alpha_{13})] \quad (8)$$

$$\text{THD} = \sqrt{\frac{\sum_{n=2}^{40} (V_n)^2}{v_1^2}} \quad (9)$$

In Eq. (8), $\alpha_1, \alpha_2, \dots, \alpha_{13}$ are the angles of output voltage V_{out} . By varying these angles, the magnitude of fundamental output voltage (v_1) and THD in output voltage V_{out} given in Eq. (9) can be varied. These angles have been changed by varying sinusoidal wave or carrier wave in MC-SHEPWM technique. From the above discussion, for this topology, modulation index (MI) is defined as:

$$\text{MI} = \frac{\text{Magnitude of reference wave}}{\text{Magnitude of carrier wave, } C_{13}} \quad (10)$$

Figure 2 shows that by changing the modulation index from 0 to 2, the magnitude of the fundamental output voltage v_1 and THD could be varied. It has been observed that with the elevation of modulation index, v_1 elevates. The THD of output voltage is more at low and high modulation index and THD is less than 5% between when the modulation index ranges from 0.48 to 1.2.

4 Proposed Fault-Tolerant Algorithm

Figure 3 shows fault-tolerant scheme for FTALI. The role of fault-tolerant algorithm is to maintain the voltage at load side in fault condition or in normal condition without changing the structure of FTALI. To show the effectiveness of fault-tolerant scheme, two types of faults have been considered, i.e., open-circuit fault and short-circuit fault. Open-circuit fault has been considered by opening of different semiconductor switches in the FTALI. The open-circuit fault has been assumed when one or

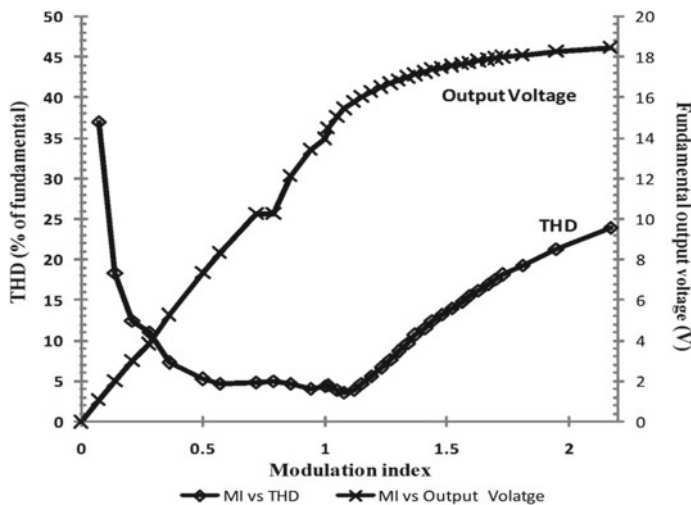


Fig. 2 Variation in THD and magnitude of fundamental output voltage accompanied by the variation of modulation index

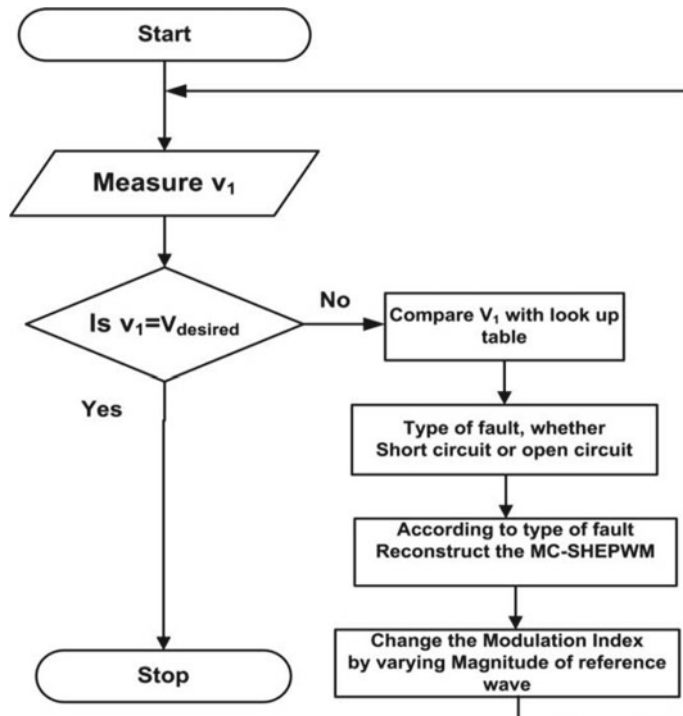


Fig. 3 Fault-tolerant algorithm for FTAMLI

two semiconductor switches are opened simultaneously. Short circuit is considered when one or two semiconductor switches have been shorted simultaneously.

In this algorithm, first the output voltage is computed, now if the fundamental output voltage is not equal to the $V_{desired}$ then v_1 goes to the look up table. The look up table or decision unit has preselected values of voltage obtained by simulation by taking open-circuit and short-circuit faults for FTAMLI. The v_1 is compared with the preselected values and decision is taken about type of fault that has been initiated. According to the type of fault, the MC-SHEPWM changes its switching strategy to decrease the total harmonic distortion in the output voltage V_{out} . After reducing THD, the modulation index is selected according to $V_{desired}$. This process will be stopped when V_{out} is approximately equal to $V_{desired}$.

5 Simulation Results

In this paper, fault analysis of FTAMLI has been done using three basic units of FTAMLI connected as shown in Fig. 4. To examine the capability of proposed algorithm for FTAMLI, the fault is assumed as open circuit in semiconductor switch S_{32} , S_{34} and short circuit in semiconductor switch S_{32} , S_{34} as shown in Fig. 4.

The circuit simulation has been done using MATLAB/Simulink software by connecting resistive load. The frequency of the output voltage is 50 Hz and RON_{switch} of each semiconductor switch is selected as 1 milliohm. Here, $V_{desired}$ is assumed as 15.3 V by choosing E_1 as 8.1 V, E_2 as 5.26 and E_3 as 1.78 V. Figure 5a shows the 27-level output voltage and its THD by using three DC source FTAMLI

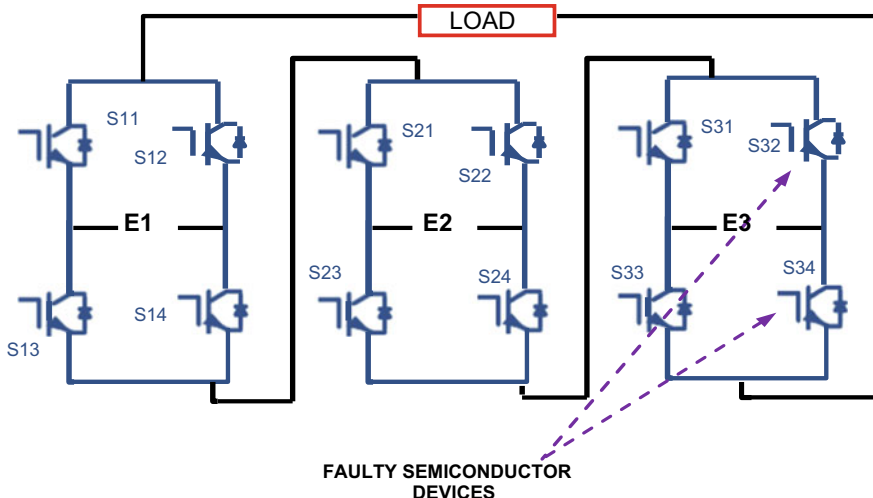


Fig. 4 Three DC source FTAMLI

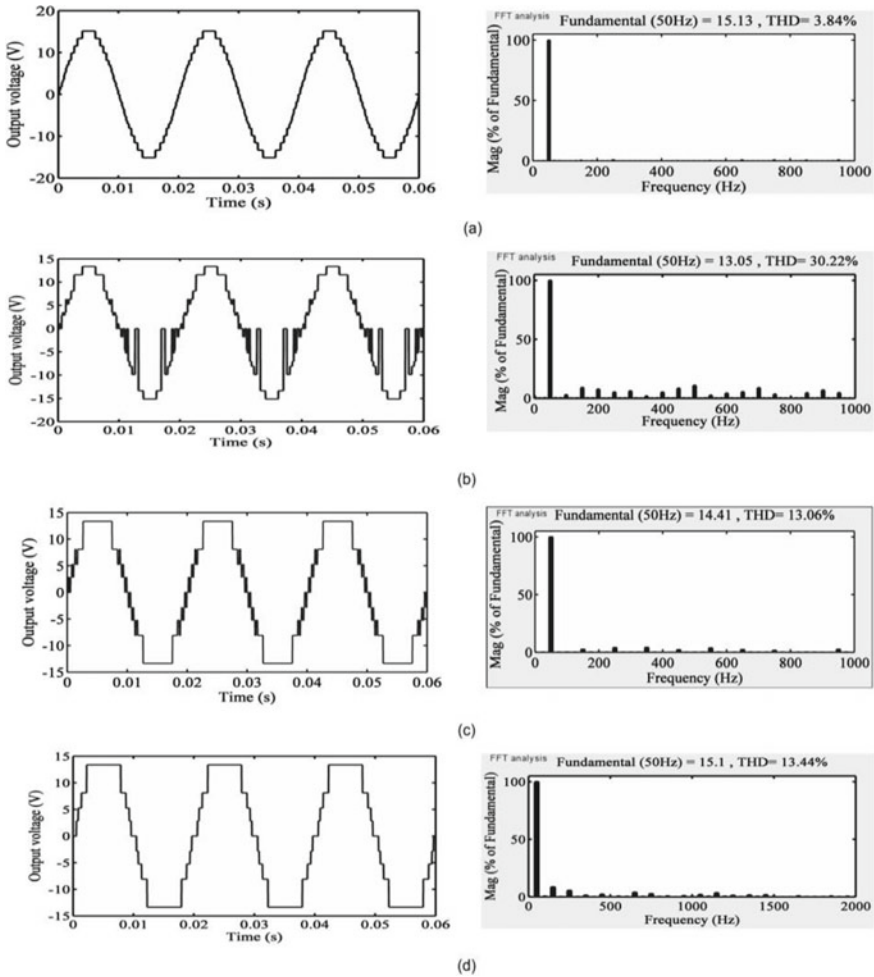


Fig. 5 Simulation results: **a** Twenty-seven-level output voltage and THD of voltage in standard condition, **b** output voltage and THD in switch fault condition (switch S_{34} , open), **c** output voltage and THD in fault condition (switch S_{34} , S_{32} , shorted), and **d** output voltage and THD using the proposed algorithm in fault condition (switch S_{32} , S_{34} open or shorted)

in normal condition. Figure 5b shows that without application of the proposed algorithm, the fundamental voltage decreases to 13.05, THD increases to 30.05% when semiconductor switch S_{34} is opened. Figure 5c shows that without application of the proposed algorithm, fundamental voltage decreases to 14.41 V and THD increases to 13.06% when S_{32} and S_{34} is shorted.

Figure 5d shows that when the proposed algorithm has been applied, the fundamental output voltage remains constant under fault condition and THD in output voltage also reduces than that of without algorithm.

It has been observed from Fig. 5, the lower-order harmonics are less by utilizing the propound algorithm. The detailed results of fundamental voltage, THD of output voltage, efficiency, and blocking voltage in fault condition have been compared in Table 2 using the proposed algorithm and without proposed algorithm. It has been observed from Table 2 that fundamental voltage remains constant is equal to 15.13 V, but in fault condition the voltage does not maintain its desired voltage.

THD and blocking voltage remain constant with proposed algorithm. The efficiency increases in fault condition by using the proposed algorithm which is equal to 99.9% whereas in short circuit of switch S32 and S34 condition, it reduces to 0.6 and 0.35%, respectively.

6 Conclusion

Fault-tolerant asymmetrical multilevel inverter topology using principle of addition and subtraction of DC sources has been presented in this paper. The output voltage and THD have been calculated for the three DC source FTAMLI by varying modulation index. It has shown that lower-order harmonics are eliminated under normal and fault condition. Fault-tolerant scheme has been adopted for FTAMLI. The FTAMLI has been analyzed by taking open-circuit condition and short-circuit condition in semiconductor switches. It has been analyzed that the propound algorithm gives less THD and it maintains desired voltage at load side without any change in structure of FTAMLI under normal and fault condition. It has been concluded that the blocking voltage of FTAMLI is less and efficiency is more when the proposed algorithm has been applied in fault conditions than that without proposed algorithm.

Table 2 Detailed simulation results by incorporating open-circuit fault and short-circuit fault in semiconductor switches of FTAMLI

Faculty semiconductor switch open circuit (OC) short circuit	Without algorithm					With algorithm			Efficiency η
	Fundamental output voltage (v_1)	THD of V_{out} (%)	Total max. blocking voltage	Efficiency η	Fundamental output voltage (v_1)	THD of V_{out} (%)	Total max. blocking voltage		
S_{32} (OC)	11.07	49.96	7.24	99.9	15.13	13.44	53.44	99.9	
S_{34} (OC)	13.04	30.32	7.24	99.9	15.13	13.44	53.44	99.9	
S_{32}, S_{34} (OC)	9.05	64.03	80.16	99.9	15.13	13.44	53.44	99.9	
S_{32} (SC)	15.12	8.19	57	0.6	15.13	13.44	53.44	99.9	
S_{34} (SC)	14.42	9.05	57	0.6	15.13	13.44	53.44	99.9	
S_{32}, S_{34} (SC)	14.41	13.06	53.44	0.35	15.13	13.44	53.44	99.9	
Normal condition	15.13	3.85	63.56	99.9	—	—	—	—	—

References

1. Kouro S, Malinowski M, Gopakumar K, Pou J, Franquelo LG, Wu B, Rodriguez J, Perez MA, Leon JI (2010) Recent advances and industrial applications of multilevel converter. *IEEE Trans Ind Electron* 57(8):2553–2580
2. Nabae A, Takashi I, Akagi H (1981) A new neutral point clamped multilevel inverter. *IEEE Trans Ind Appl* 17(5):518–523
3. Rodriguez J, Lai JS, Peng FZ (2002) Multilevel inverter: a survey of topologies, controls and application. *IEEE Trans Ind Electron* 49(4)
4. Ruderman A, Schlosberg S (2008) A hybrid asymmetric cascaded multilevel inverter comprising high resolution and symmetric low resolution parts. In: IEEE 25th convention of electrical and electronics engineers in Israel, Dec 2008, pp 21–25
5. Babaei E, Hosseini SH, Gharehpetian GB, Haque MT, Sabahi M (2007) Reduction of DC voltage sources and switches in asymmetrical multilevel converters using a novel topology. *Electr Power Syst Res* 77(8):1073–1085 (Elsevier)
6. Babaei E, Hosseini SH (2009) New cascaded multilevel inverter topology with minimum number of switches. *Energy Convers Manage* 50(11):2761–2767 (Elsevier)
7. Hinago Y, Koizumi H (2016) A single-phase multilevel inverter using switched series/parallel DC voltage sources. *IEEE Trans Ind Electr* 57(8)
8. Gupta KK, Jain S (2013) A multilevel voltage source inverter (VSI) to maximize the number of levels in output waveform. *Electr Power Energy Syst* 44:25–36 (Elsevier)
9. Gupta KK, Jain S (2014) A novel multilevel inverter based on switched DC sources. *IEEE Trans Ind Electron* 61(6)
10. Alishah RS, Nazarpour D, Hosseini SH, Sabahi M (2014) Novel topologies for symmetric, asymmetric and cascade switched-diode multilevel converter with minimum number of power electronic components. *IEEE Trans Ind Electron* 61(10)
11. Babaei E, Alilu S, Laali S (2014) A new general topology for cascaded multilevel inverters with reduced number of components based on developed H-bridge. *IEEE Trans Ind Electron* 61(8):3932–3939
12. Banaei MR, Salary E (2011) New multilevel inverter with reduction of switches and gate driver. *Energy Convers Manage* 52(2):1129–1136 (Elsevier)
13. Babaei E, Kangarlu MF, Mazgar FN (2012) Symmetric and asymmetric multilevel inverter topologies with reduced switching devices. *Electric Power Syst Res* 86:122–130 (Elsevier)
14. Babaei E, Dehqan A, Sabahi M (2013) A new topology for multilevel inverter considering its optimal structure. *Electr Power Syst Res* 103:145–156 (Elsevier)
15. Kangarlu MF, Babaei E, Sabahi M (2013) Cascaded cross-switched multilevel inverter in symmetric and asymmetric conditions. *J IET Power Electron* 6(6):1041–1050
16. Esfandiari E, Mariun NB (2013) Experimental results of 47-level switch-ladder multilevel inverter. *IEEE Trans Ind Electron* 60(11):4960–4966
17. Suresh Y, Panda AK (2013) Investigation on hybrid cascaded multilevel inverter with reduced DC sources. *Renew Sustain Energy Rev* 26:49–59 (Elsevier)
18. Chen A, Hu L, Chen L, Deng Y, Yao G, He H (2004) A multilevel converter topology with fault tolerant ability. IEEE applied power electronics conference and exposition, vol 3, Feb 2004, pp 1610–1616
19. Ma M, Hu L, Chen A, He X (2007) Reconfiguration of carrier based modulation strategy for fault tolerant multilevel inverters. *IEEE Trans Power Electron* 22:2050–2060
20. Choi V, Blaabjerg F, Lee KB (2015) Reliability improvement of a T-type three level inverter with fault tolerant control strategy. *IEEE Trans Power Electron* 30:2660–2673
21. Kumar J, Aggarwal P, Das B (2010) Implementation of cascade multilevel inverter-based STATCOM. *IETE J Res* 56(2):119–128
22. Shen K, Zhao D, Mei J, Tolbert LM, Wang J, Ban M, Ji Y, Cai X (2014) Elimination of harmonics in a modular multilevel converter using particle swarm optimization-based staircase modulation strategy. *IEEE Trans Ind Electron* 61(10):5311–5322

23. Colak I, Kabalci E, Bayindir R (2011) Review of multilevel voltage source inverter topologies and control schemes. *Energy Convers Manage* 52:1114–1128 (Elsevier)
24. Rushiraj GJ, Kapil PN (2016, March) Analysis of different modulation techniques for multi-level inverters. In: 2016 international conference on electrical, electronics, and optimization techniques (ICEEOT). IEEE, pp 3017–3024

New H-Bridge for Symmetrical and Asymmetrical MLI with Reduced Number of Devices



Tamiru Debela, Hillol Phukan, and Jiwanjot Singh

Abstract A novel symmetrical and asymmetrical single-phase five-level (5LSA) converter has been presented in this paper. Along with one dc source and one capacitor, a bidirectional switch is used in order to obtain the five levels in the output voltage. The proposed multilevel inverter has two circuits, namely single H-bridge circuit or main circuit and special combination of switching devices called auxiliary circuits. Main advantages of the proposed MLI are it constitutes single DC source, reduced number of switching devices, low switching system scores, reduces the complexity, low cost and enhances overall performance. The effectiveness and feasibility of the proposed topology are validated by simulations under different condition.

Keywords Isolated DC sources · Multilevel inverter · Multi-carrier pulse width modulation · Reduced switches · Symmetrical topology

1 Introduction

Inverter at multilevel (IM) plays a vital role to achieve superior power standard with appropriate control technique and tie of various semiconductor devices. These inverters use low-rated components, generate high-quality staircase voltage, and reduce the electromagnetic interference (EMI) to a large scope [1–3]. The major disadvantage of these types of inverters (MLI) is requirement of isolated DC source, increased cost, and hence decreased reliability. Therefore, a lot of effort has been made with different topologies to reduce the number component while improving performances [4–6]. Multilevel inverter is effectively employed in applications, such as active power filters [7], AC motor drive [8–10], and linked of renewable energy

T. Debela · H. Phukan (✉) · J. Singh

Department of Electrical Engineering, National Institute of Technology, Silchar, Assam, India
e-mail: phukanhillol@gmail.com

J. Singh
e-mail: jiwanjot18@yahoo.co.in

with the grid [11, 12]. Growth of multilevel has played a vital role in the field photovoltaic (PV) [13, 14], topologies [15–17], static compensator [18, 19], and control and modulation techniques [20–25]. Figure 1 indicates different topology by which the device count of multilevel inverter reduced.

Out of all multilevel (ML) topologies, the CMI stands out because of voltage rating devices, possibility of using low, its modular structure, and its developed high-magnitude voltages. The topology suggested is for both symmetrical and asymmetrical multilevel inverter (MLI) structures. The recommended topology minimizes the number of devices, cost, and complexity as estimated with conventional topologies.

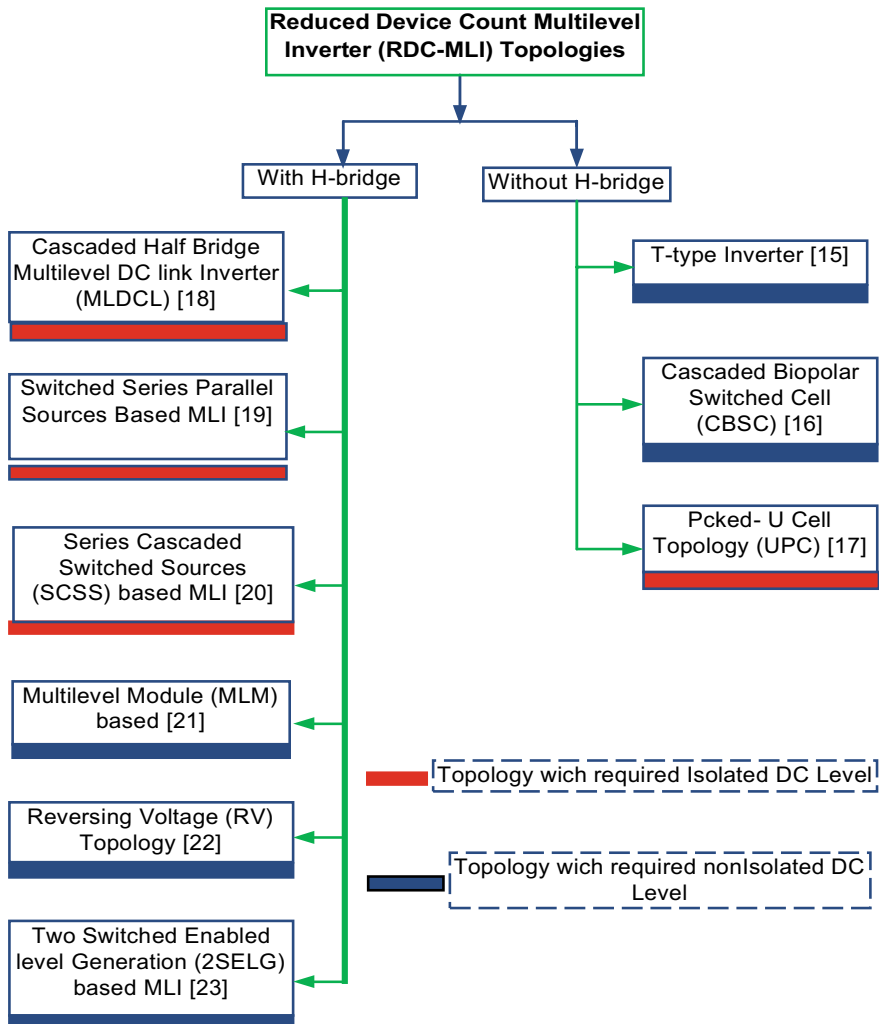


Fig. 1 Classification of reduced device count multilevel inverter topologies

The characteristics of propound topology and modulation schemes used to

1. Decrease total power count.
2. Increase reverse voltage at each switches limited to V_{in} .
3. Less power losses because number of components, the number of switch on state is reduced.
4. The voltages of the capacitor are independent of load power, and the voltages are self-balanced through the condensers.

2 Proposed MLI Topology

The suggested topology is mostly used for improvement of self-balancing, reduced components and uniform voltage blocking ability at all switches. Figure 2a indicates the configuration of conventional three-level cascaded H-Bridge which consists of 4 switches and one separate DC source. Figure 2b is the proposed topology five levels, which is also composed of four switches and one separated DC source, capacitor, and an auxiliary switch.

The auxiliary switches are attached in series with the capacitor; the capacitor is discharged at the beginning. It slowly starts to charge 0.5 V when the inverter switch becomes ‘ON.’ The capacitor maintains 0.5 V at each cell. Figure 2c shows the general framework designed to achieve higher output levels. Figure 3 shows the modes of operation of the proposed symmetric topology for 5L performance. The highlighted red indicates the current path in all from (i) to (x).

2.1 Proposed Symmetrical Topology

In the proposed symmetrical only one DC source is required for new five levels. Extended category of the propound cascaded configuration is shown in Fig. 2c. Table 1 indicates the comparison between different five-level topologies, and mode of operation is given in Table 1.

For ‘N’ number of cells, the general proposed symmetric topology is given by

$$(V_{S1} = V_{S2} = V_{S3} = \dots = V_{SN}) \\ V_{DC\ total} = \text{Capacitor}_{total} = N \quad (1)$$

$$V_{DC\ total} = \text{Capacitor}_{total} = N \quad (2)$$

$$\text{Diodes}_{total} = 4 \times N \quad (3)$$

$$\text{Output}_{level} = 4 \times N + 1 \quad (4)$$

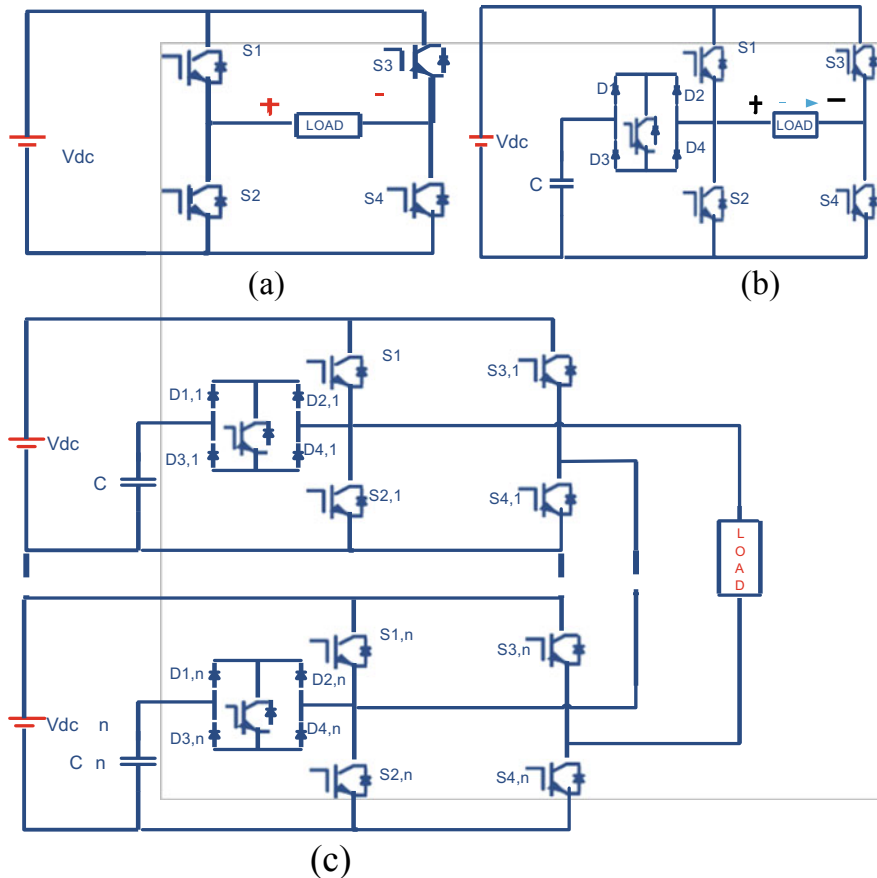


Fig. 2 **a** Three-level structure of conventional CHB. **b** Five-level structure of propound topology. **c** Extended proposed topology

2.2 Proposed Topology for A Symmetrical MLI

For asymmetrical topology, the DC sources are more and have different values. In this asymmetrical MLI, the values of DC source are assigned in three different algorithms as shown in Table 2. For conventional asymmetric MLI, value of DC source is increasing in binary combination (2:1) or tertiary combination (3:1). Table 2 shows that in addition to binary and tertiary the new and novel algorithm is proposed to achieve highest number of output (Table 3).

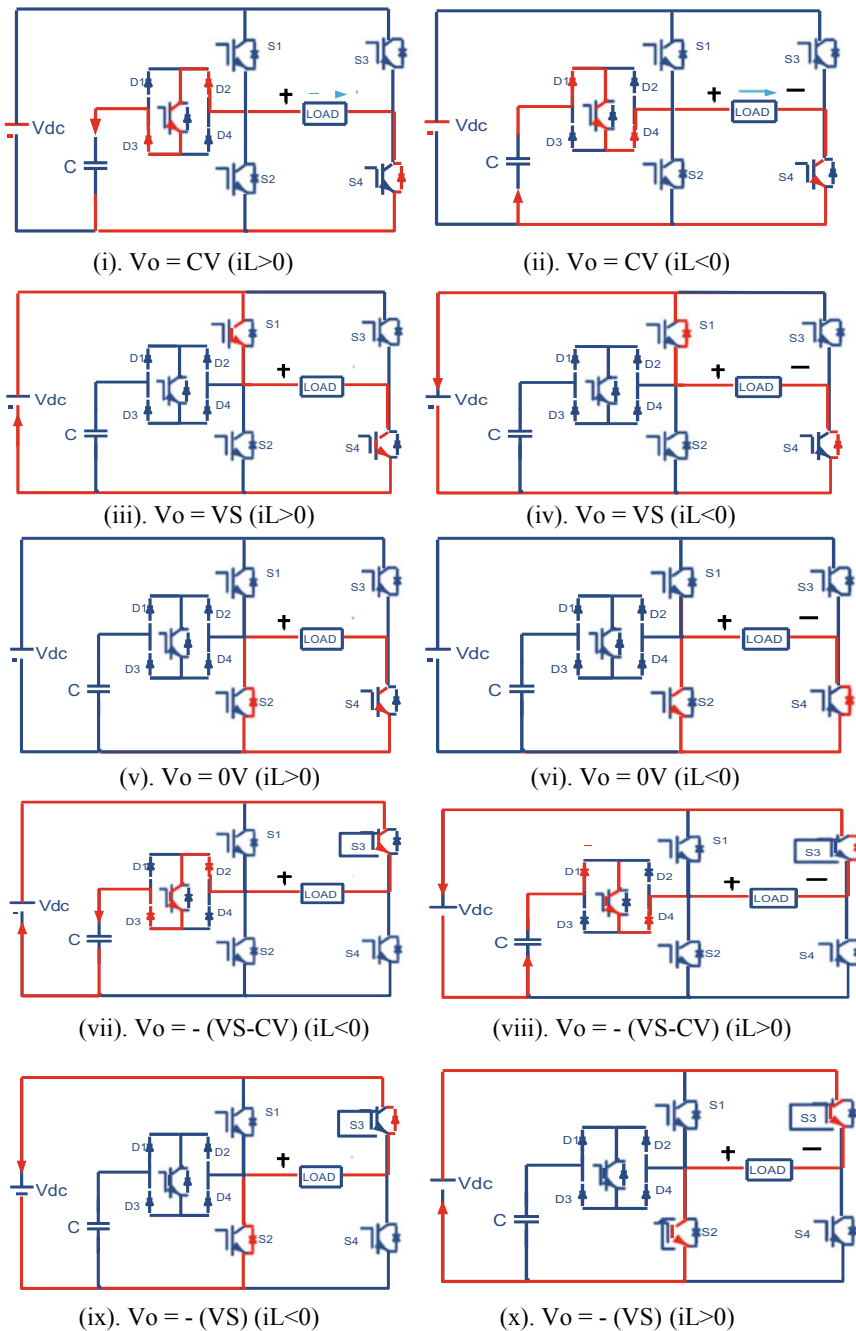


Fig. 3 Proposed symmetrical topology operation modes for five-level performance

Table 1 Comparison between different five-level inverter topology for symmetrical MLI

Components	NPC	CHB	FC	[26]	[27]	[28]	[4]	[5]	Proposed
PS	8	8	8	6	6	6	8	6	4
AS	0	0	0	0	0	0	0	0	1
DC sources	1	2	1	2	1	2	1	1	1
Capacitors	4	–	10	0	1	–	1	1	1
Diodes	20	8	8	6	7	6	8	6	4

NPC-Neutral Point Clamped, CHB-Cascaded H-bridge, FC-Flying Capacitor, PS-Power Switches, AS-Auxiliary Switch

Table 2 Mode of operation states for Fig. 3

Output voltage	Switches state ‘ON’	Capacitors State when “iL” < 0	Capacitors state when “iL” > 0
(C _v)	S4 and S5	Capacitor charges (Fig. 2 (ii))	Capacitor discharges (Fig. 2 (i))
V _s	S1 and S4	No effect (Fig. 2 (iv))	No effect (Fig. 2 (iii))
V ₀	S2 and S4	No effect (Fig. 2 (vi))	No effect (Fig. 2 (v))
(V _s – C _v)	S3 and S5	Capacitor charges (Fig. 2 (vii))	Capacitor discharges(Fig. 2 (viii))
(V _s)	S2 and S3	No effect (Fig. 2 (i))	No effect (Fig. 2 (x))

Table 3 The proposed topology with different level incorporates with ‘N’ number of cells

Algorithm	DC source values	Number of output level	Configuration
1st	$\frac{V_{S1}}{2^0} = \frac{V_{S2}}{2^1} = \dots = \frac{V_{SN}}{2^{N-1}}$	$2(N + 1) - 1$	Asymmetrical
2nd	$\frac{V_{S1}}{3^0} = \frac{V_{S2}}{3^1} = \dots = \frac{V_{SN}}{3^{N-1}}$	$2N$	Asymmetrical
3rd (Proposed)	$\frac{V_{S1}}{5^0} = \frac{V_{S2}}{5^1} = \dots = \frac{V_{SN}}{5^{N-1}}$	$5N$	Asymmetrical

2.3 Conduction Losses

The one important part during design of the system is calculation of losses. MLI operates in three different modes, namely blocking mode, switching mode, and conduction mode. In blocking mode, no current will flow across the devices. The transition of switch is called switch losses, i.e., transistors from ‘ON’ to ‘OFF,’ and conduction mode is the power losses during ON state. At instant ‘t,’ the device losses are given.

$$C_T(t) = [V_T + R_T \times i^\beta(t)] \times i(t) \quad (5)$$

$$C_D(t) = [V_D + R_D \times i^\beta(t)] \times i(t) \quad (6)$$

where

- C_T transistor conduction losses
- C_D Diode conduction losses
- V_T ON state of voltage transistor
- V_D ON state of voltage diode
- R_T Forward resistance of transistor
- R_D Forward resistance of diodes
- β Constant.

2.4 Power Losses

Power loss is directly proportional to blocking voltage and switching frequency

$$P_{\text{LOSS}, i} \propto V_B \& P_{\text{loss}, i} \propto f_S \quad (7)$$

For symmetrical 5-level topology loss is given by

$$P_{\text{LOSS}} = C \times V_B \times f_S \quad (8)$$

Let f_S is switching frequency and is fundamental frequency, and the above equation can be written as (Table 4)

$$\begin{aligned} P_{\text{LOSS, PROPOSED, 5 - LEVEL}} &= C \\ (V_{DC} \times f + 2 \times 2 \times V_{DC} \times f_S + 2 \times 2 \times V_{DC} \times f_o) \end{aligned} \quad (9)$$

But $(f_S \gg f_o)$ So Eq. (9) becomes

$$P_{\text{LOSS, PRO, 5 - LEVEL}} = C \times V_{DC} (5 \times f_S + 4 \times f_o) \quad (10)$$

Table 4 Parameters of the simulated model

Components	Value	Unit
Input voltage	20	V
Output voltage	20	V
Capacitors	3300	μF
Frequency	50	Hz

$$P_{\text{LOSS,PRO,5 - LEVEL}} = 5 \times C \times V_{\text{DC}} \times f_s \quad (11)$$

3 Simulation Results

Figure 4a–c displays the output parameters for 5L-MLI, respectively. Figure 5a, b indicates the output parameters under dynamic change of load. Note as the load inductive load is added in parallel to the resistive load, only the magnitude of current will change.

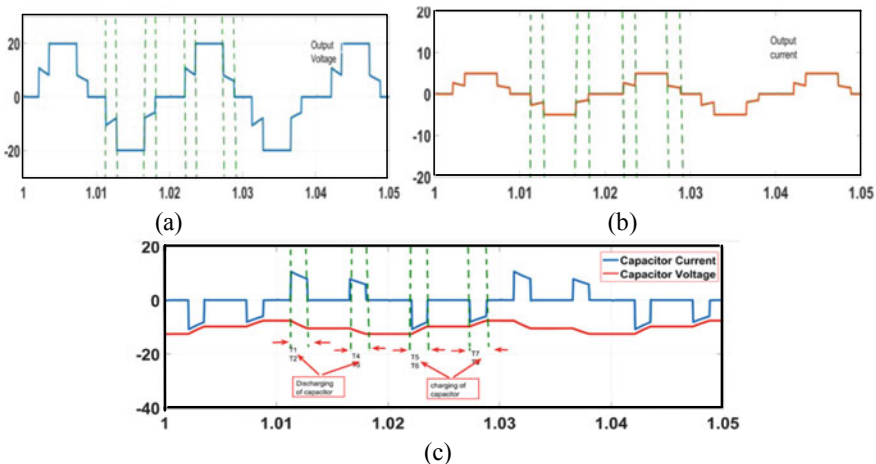


Fig. 4 Simulation results. **a** Output voltage under resistive condition, **b** output current under resistive load, **c** Result for five-level inverter charging and discharging capacitor

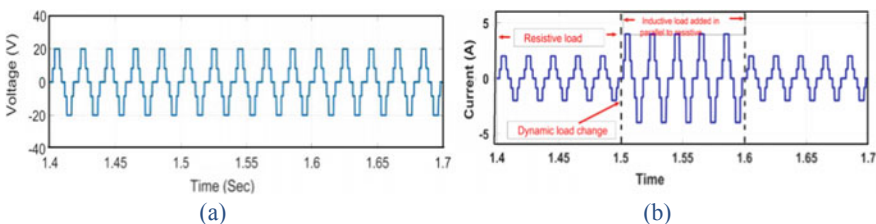


Fig. 5 Simulation results. **a** Output voltage under dynamic load. **b** Inverter output current for five level inverter under dynamic load in the proposed topology

4 Conclusion

Both symmetrical and asymmetrical MLIs are discussed. Supported topology was connected in a cascade manner for medium to high voltage. At the beginning, the symmetrical five-level inverter is presented. The operation of propound topology and generalized structure of symmetrical description has been described in detail. At last, the asymmetrical proposed topology has been presented. The propound topology utilizes lesser number of device count when compared with recent topologies, thus reducing the cost. Additional superiority of the propound topology is self-balancing, minimum number of switches, complexity is reduced. Finally, the developed proposed topology confirmed the feasibility and has been verified through simulation.

References

1. Akagi H (2011) Classification, terminology, and application of the modular multilevel cascade converter (MMCC). *IEEE Trans Power Electron* 26(11):3119–3130
2. Franquelo LG, Rodriguez J, Leon JI, Kouro S, Portillo R, Prats MAM (2008) The age of multilevel converters arrives. *IEEE Ind Electron Mag* 2(2):28–39
3. Nami A, Zare F, Ghosh A, Blaabjerg F (2011) A hybrid cascade converter topology with series-connected symmetrical and asymmetrical diode-clamped H-bridge cells. *IEEE Trans Power Electron* 26(1):51–65
4. Ebrahimi J, Babaei E, Gharehpetian GB (2012) A new multilevel converter topology with reduced number of power electronic components. *IEEE Trans Ind Electron* 59(2):655–667
5. Najafi E, Yatim A, Samosir AS (2008) A new topology—reversing voltage (RV)—for multi level inverters. In: Proceedings of IEEE 2nd international power energy conference, 1–3 Dec 2008, pp 604–608
6. Kangarlu MF, Babaei E (2013) A generalized cascaded multilevel inverter using series connection of sub multilevel inverters. *IEEE Trans Power Electron* 28(2):625–636
7. Alepuz S, Busquets-Monge S, Bordonau J, Gago J, Gonzalez D, Balcells J (2006) Interfacing renewable energy sources to the utility grid using a three-level inverter. *IEEE Trans Ind Electron* 53(5):1504–1511
8. Gupta KK, Ranjan A, Bhatnagar P, Kumar Sahu L, Jain S (2016) Multilevel inverter topologies with reduced device count: a review. *IEEE Trans Power Electron* 31(1):135–151
9. Hagiwara M, Nishimura K, Akagi H (2010) A Medium-voltage motor drive with a modular multilevel PWM inverter. *IEEE Trans Power Electron* 25(7):1786–1799
10. Cheng Y, Qian C Crow, ML, Pekarek S, Atcity S (2018) A comparison of diode-clamped and cascaded multilevel converters for 2168-6777 (c) 2018 IEEE
11. Barrena JA, Marroyo L, Vidal MAR, Apraiz JRT (2008) Individual voltage balancing strategy for PWM cascaded H-bridge converter-based STATCOM. *IEEE Transactions Ind Electron* 55(1):21, 29
12. Choi W, Kang F (2009) H-bridge based multilevel inverter using PWM switching function. In: Proceedings of 31st international telecommunications energy conference, 18–22 Oct 2009, pp 1–5
13. Ristow A, Begovic M, Pregelj A, Rohatgi A (2008) Development of a Methodology for improving photovoltaic inverter reliability. *IEEE Trans Ind Electron* 55(7):2581–2592
14. Rodriguez J, Lai J-S, Peng FZ (2002) Multilevel inverters: a survey of topologies, controls, and applications. *IEEE Trans Industrial Electron* 49(4): 24–738

15. Gupta KK, Jain S (2013) Multilevel inverter topology based on series connected switched sources. *IET Power Electron* 6(1):164–174
16. Manjrekar MD, Steimer PK, Lipo TA (2000) Hybrid multilevel power conversion system: a competitive solution for high-power applications. *IEEE Trans Ind Appl* 36(3):834–841
17. Lai J-S, Peng FZ (1996) Multilevel converters-a new breed of power converters. *IEEE Trans Ind Appl* 32(3):509–517
18. Liu C-H, Hsu Y-Y (2010) Design of a self-tuning PI controller for a STATCOM using particle swarm optimization. *IEEE Trans Ind Electron* 57(2):702, 715
19. Walker GR, Sernia PC (2004) Cascaded DC-DC converter connection of photovoltaic modules. *IEEE Trans Power Electron* 19(4):1130–1139
20. Gupta KK, Jain S (2014) Comprehensive review of a recently proposed multilevel inverter. *IET Power Electron* 7(3):467–479
21. Ruiz-Caballero DA, Ramos-Astudillo RM, Mussa SA, Heldwein ML (2010) Symmetrical hybrid multilevel DC–AC converters with reduced number of insulated DC supplies. *IEEE Trans Ind Electron* 57(7):2307, 2314
22. Hinago Y, Koizumi H (2010) A single-phase multilevel inverter using switched series/parallel DC voltage sources. *EEE Trans Ind Electron* 57(8):2643–2650
23. Najafi E, Yatim AHM (2012) Design and implementation of a new multilevel inverter topology. *IEEE Trans Ind Electron* 59(11):4148–4154
24. Rahim NA, Chaniago K, Selvaraj J (2011) Single-phase seven-level grid connected inverter for photovoltaic system. *IEEE Trans Ind Electron* 58(6):2435–2444
25. Hinago Y, Koizumi H (2010) A single-phase multilevel inverter using switched series/parallel DC voltage sources. *IEEE Trans Ind Electron* 57(8):2643–2650
26. Babaei E (2008) A cascade multilevel converter topology with reduced number of switches. *IEEE Trans Power Electron* 23(6):2657–2664
27. Ounejjar Y, Al-Haddad K, Gregoire LA (2011) Packed U cells multilevel converter topology: Theoretical study and experimental validation. *IEEE Trans Ind Electron* 58(4):1294–1306
28. Gui-Jia S (2005) Multilevel DC-link inverter. *IEEE Trans Ind Appl* 41(3):848–854

Different EDGE Detection Techniques: A Review



**Chinmoy Ghosh, Suman Majumder, Sangram Ray, Shravasi Datta,
and Satyendra Nath Mandal**

Abstract An image is represented by an important feature called EDGE which is very much useful for understanding the image properly. Edge can be considered as the discontinuity from one image pixel to another. So, edges are the boundaries between textures and accordingly edge detection is very much useful for segmentation, object detection and recognition purpose. Several methodologies exist using which the information about the edges can be extracted. This paper presents a brief study of different edge detection methodologies along with their performance issues and limitations. A detail discussion related to benefits and drawbacks of each algorithm are also discussed.

Keywords Edge detection · Fuzzy Inference System (FIS) · Genetic Approach (GA) · Line Segment Detector (LSD) · Xilinx System Generator (XSG) · Adaptive Network-based Fuzzy Inference System (ANFIS)

C. Ghosh

Department of Computer Science & Engineering, Jalpaiguri Government Engineering College, Jalpaiguri 735102, India

e-mail: chinmoy.ghosh@cse.jgec.ac.in

S. Majumder (✉) · S. Ray

Department of Computer Science and Engineering, National Institute of Technology Sikkim, Ravangla, Sikkim 737139, India

e-mail: suman.majumder3014@gmail.com

S. Ray

e-mail: sangram.ism@gmail.com

S. Datta

Department of Information Technology, Jalpaiguri Government Engineering College, Jalpaiguri 735102, India

e-mail: shravasi.datta@gmail.com

S. N. Mandal

Department of Information Technology, Kalyani Government Engineering College, Kalyani, Nadia, India

e-mail: satyen_kgec@rediffmail.com

1 Introduction

Edge detection procedure is utilized to identify an edge of an image [1–10]. For solving the issues related to lack of stability, differences and distinguishing operations of an image, edge detection technique is used mainly in applications of image processing for different organizations to symbolize the meaningful features and significant information of edges [1–5]. This procedure is mainly used to keep only the appropriate structural features of an image and diminish the size of an image after filtering the unnecessary information. At the time of detection and reconstruction of edges, the redundancies are removed that present within most of the images. To segregate the images into respective regions using the image segmentation procedure, the edge detection procedure is used as it represents the boundary of objects [1, 5–8, 11, 13].

2 Literature Review

In this section, different edge detection techniques are analyzed and the details are mentioned below.

One of the widely used edge detection algorithm is Canny Edge detection method invented by Canny [1]. Canny Edge detection has more engineering and mathematical concept using gradients. It is an optimal edge detection technique with important criteria such as good edge detection. It is kept in mind at the time of detection of edges that is as close as possible to the true values and maintaining the accuracy of the localization. On the other hand, there should not be multiple responses and the detector must return one point only for each edge. For doing any operation using canny edge detection, at first it is required to make the edge as smooth applying Gaussian filters. Thereafter computations are performed for the derivative of the filtered image in both X and Y coordinate using Sobel operator. Further, magnitude and direction is obtained using the equation $|G| = |G_x| + |G_y|$ and $\theta = \text{inv} \tan(G_y/G_x)$ followed by applying suppression procedure of non-maximum. The main concept is to suppress the pixels which are not local maximum. Finally “hysteresis threshold” are applied. There are two types of thresholds (high and low) and based on the two threshold values the gradient is calculated. If the gradient of the pixel is higher than the upper threshold then this is an edge pixel otherwise it is a non edge pixel. If the threshold of the pixel is between high and low and connected to an edge pixel, then it is also considered to be an edge pixel.

In 2012, Sriramakrishnan and Shanmugam [2] proposed an algorithm based on neuro-fuzzy system where Sobel and Laplacian methods are applied on input images. Further, fuzzy rules are applied on the respective output. Neural network is used on input layer. Accordingly, Dhir [3] proposed another algorithm based on Neuro-Fuzzy Inference system. Using the method of global thresholding, the binary images in term of either numerical zero (0) or one (1) are derived from the gray label. On the other

hand, an adaptive network-based fuzzy inference system (ANFIS) can be used with 3×3 masks to prepare the network to higher level.

Rani and Tanwar [4] proposed another algorithm based on neuro-fuzzy system. Using the back propagation method, an adaptive network-based fuzzy inference system (*ANFIS*) can be constructed based on *FIS* and its respective membership function values are adjusted accordingly. It can be derived from the 4 inputs and 1 output based *FIS* system. Using the gray levels which is denoted as L , an intensity of edge is normalized between the range [0 to $(L - 1)$] and the relevant pixels under the edge are partitioned to two different sets S_0 and S_1 .

Later, Petrova and Hostalkava [5] proposed an edge detection technique using wavelet transformation. This technique can be used in medical images for efficient edge detection. It is the most appropriate method for non stationary signal. The fundamental functionality may vary both in frequency and spatial range. In this case, low frequency (average intensity values) and high frequency component (for the edges) are obtained after designing the wavelet transformation. On the other hand, for an original image, a low pass filter in rows as well as columns is applied. As a result approximated image is achieved. The simplest method is to replace approximated image by zero and remove all low frequency components, and reconstruct the image. The remaining component is of high frequency (refers an edge). Another method is to pass the approximated images through a good edge detector (especially canny) where modified approximated pixels and the remaining pixels are used in reconstruction which leads to an edge.

In 2014, Bar et al. [6] proposed an application based on Mumford–Shah model for implementation of image segmentation and image restoration process. Segmentation is the process of labeling the images and paints it with gray values. While detecting an edge there maybe two types of penalties—(1) Penalty for edges and (2) Penalty for errors. The basic concept of this model is to write basic formula to compromise between representations of image to a simplified image which is not too far from the original image. The Mumford–Shah model is also used in image restoration. Due to simplicity and efficiency, Mumford and Shah model is also used in Chan Vase segmentation [6, 7]. In 2012, Getreuer [7] proposed the performance of Chan-Vese segmentation. Although many methods are reliant on the Chan-Vese segmentation but some of them do not work properly on edges. On the other hand, this scheme affords an efficient two-phase model for image detection. This segmentation technique is very much efficient than Snake methods [7, 9] and works even if the topology has transformed and derived from Mumford–Shah model. However, the technique introduced by Osher and Sethian [7], can crack this problem applying the level set function as the zero crossing rather than declaring the boundaries explicitly [7, 8].

In 2012, Chan and Vese [8] proposed an active contour model without edges. The process of labeling the location in the image where change rate is higher than adjacent locations is known as edge detection. With the gradient of the image we get the information about the location where major change in intensity in the image exists. So, the gradient gives the local information. The aim of active contour is to integrate the local measurements. Edge integration is the process of combining local preferably sparse and non contiguous edges into a meaningful edge curve for

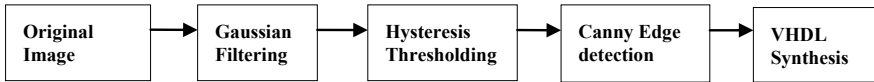


Fig. 1 VHDL based canny edge detection

segmentation. There is also a relationship between local edges and active contours that are going to compute it. Based on the curve evolution, this new model picks up the respective objects from an offered image and Mumford–Shah function is utilized to segment and position the levels of the corresponding object whose boundaries are not distinct by gradient. This, this model attempts as active contour models combining different lively models along with Mumford–Shah model.

Alvarez et al. [9] proposed the Snake algorithm that is based on real-time system. For modeling the snake evolution, a level set approach is used. To solve using level set methods for the partial differential equations (PDE), the Euler-Lagrange equation is exercised. Using the standard methods for estimation of contour distance function, various problems regarding the PDE is solved. Morphological operators associated with PDE components and an advanced morphological approach that is based on simple and fast numerical analysis has been proposed for the evolution of the PDE snakes approach. In this method, distance function of a contour cannot be estimated because the level set is just a binary constant function.

In 2014, Rashid et al. [10] recommend an algorithm which is VHDL based Canny edge detection method. The aim of this algorithm is to detect the edge automatically of a digital image and works based on the concept of canny edge detector algorithm followed by the Gaussian filtering on Xilinx System Generator (XSG). After that the VHDL synthesis is done for detecting the edge of the digital images efficiently. It mainly used for edge detection of brain tumors. The detail procedure is given in Fig. 1.

Further, Priyadarshini and Sahoo [11] proposed a new technique of edge detection based on the method of addition and division. The method is simple and based on the automatic computation of threshold during edge detection. It uses single dimensional array for storing the computations those are performed on the image pixels for calculation of the image threshold. The proposed method was applied on a number of images giving good and satisfying results compared to Sobel method [2, 11]. Later, Biswas and Sil [12] suggested an improved canny edge detection algorithm that stands on type-2 fuzzy sets. The algorithm is effective in handling the uncertainties arising in automatic threshold value selection for image segmentation using canny algorithm. Using type-2 fuzzy logic, it selects single threshold from image histogram and it efforts on gradient histogram produced by Sobel operator. The algorithm was found effective for many images especially hand radiography image. Moreover, Rashmi et al. [13] discussed an algorithm called Bilateral Filtering which calculates the weighted average intensity values of neighboring pixels of an image to replace with the intensity value of the pixel. The algorithm has better noise removing capability as well as better edge preserving capabilities than traditional canny operator.

In 2014, Shamlee [14] proposed an algorithm that removes the entire dependency between the blocks and it is referred to as a split canny detection of edges. For the distribution of gradient of the block and compute the block type based on predefined threshold values, the above said algorithm is used. To calculate the thresholds values of hysteresis related to block, histogram is used. This algorithm has reduced latency and can possibly be pipelined with other block based codes. The algorithm is scalable and has high edge detection performance even full HD videos. In 2014, Liu et al. [15] proposed a modified canny edge detection iterative algorithm. Using arithmetical iteration, it calculates optimal high and low dual threshold and then using mathematical morphology the images are made with sharp quality edges. It has good noise suppression and interference reduction capability. The algorithm is effective for edge detection for medical cell image to detect characteristics of roundness, size and number of cells but not good for Lena that needs extraction of image details.

Further, Gao et al. [16] proposed an algorithm based on alpha weighted quadratic filter. The positive alpha power is known for its ability to enhance image contrast and the negative alpha power is also used for suppressing the non edge portion. Thus, positive/negative power law can be utilized in the filter design for further enhancing the desired portions. In 2014, Dollár and Zitnick [17] proposed a new model using structured forests method that is used for the detection of edges rapidly. It tries to patch of edges as straight lines or T -junctions to form the local structure such are detected clearly and applied in discrete space to get real time.

Later, Maladakara and Vanamala [18] proposed an algorithm to design an improved Canny Edge detection algorithm. It is same as the actual canny algorithm but the only difference is it is applied at the block level. Blocks are classified into smooth, texture, hybrid and strong. This classification helps to minimize the computation using fuzzy logic for block classifications. The required steps of canny edge detections are all performed at first. Then fuzzy logic for block classification is applied. Later hysteresis threshold is applied and this is calculated on the basis of percentage of strong edges present in a block.

In 2017, Yu et al. [19] proposed a method called Deep Category—Aware Semantic Edge Detection (CASENet) which is based on deep semantic learning based edge detection method. In this method two or more semantic classes are connected by each edge pixel and follow an architecture where edge activation is performed based on different category at the top convolution layer. These layers share and fuse with the same set of bottom layer feature using convolution neural network (CNN). On the other hand, from the given K numbers of semantic edge categories, CASENet maintains a deep network. The network generally constructs K numbers of separate edge maps where each map indicates the edge probability of a certain category. CASENet also maintains similar network like deeply supervised network (DSN).

Later, Liu et al. [20] proposed a convolutional neural network (CNN) based edge detection technique which is called richer convolutional features (RCF). Based on the information obtained by different convolution layers in edge detection, a network is formed to produce outputs of intermediate layers using VGG16 network which has five numbers of convolutional layers. Further the layers are segregated into five numbers of stages and within the stages pooling layers are connected after each stage.

The RCF generally takes an image with any arbitrary size as an input and produce an edge as output with same size.

In 2018, Agrawal and Rosepreet [21] proposed a method to detect edges of dental radiographs using three different techniques—(1) Sobel type (2) Fuzzy Logic System Type 1 (T1FLS), and (3) Interval Type 2 Fuzzy logic System (T2FLS). To obtain image information or pixels as a form of dental radiographs or X-ray of different patients regarding the healthy and effective teeth, the aforesaid three techniques are used for edge detection. Sobel type mainly works on the gray scale values and computes gradients of every pixel for digital image. T1FLS is mainly used in less contrasted images related to biomedical application and easy detection of edges. However, T1FLS faces many difficulties where edges are not continuous, not very clear or blurred. But T2FLS is more efficient than T1FLS. Based on some predefined selected threshold values, a comparison is done among the three types and it is found that more pixels related to edges are obtained from T2FLS and analyzed easily than Sobel and T1FLS methods [1, 2, 11, 21].

In 2019, Halder et al. [22] used a novel approach for the detection of edges based on Richardson's extrapolation technique to quantify the strength of edges. This extrapolation is used to pick up convergence rate which is related to some sequence and a numerical analysis is done using this aforesaid method. In this method, the strength based on the neighboring pixel value is calculated in relation to the formula obtained from Richardson's extrapolation technique. On the other hand, to calculate the strength of gradient in different directions related to detection of edges, Richardson's extrapolation is utilized. For the identification of respective edges of a binary image this technique is also used.

A novel spatial FFT-based filtering approach as well as a boundary point detection algorithm is introduced in 2019 by Mineo et al. [23] for direct production of low noise supported surfaces from point cloud data which is not based on predefined threshold values. For this purpose, two methods are used—(1) Detection of boundary points and (2) Edge reconstruction. To detect boundary points, the BPD algorithm is used and the main benefit of this algorithm is that it does not dependent on any predefined threshold values. The algorithm identifies maximum numbers of boundary points from the region under every cloud application. The algorithm permits and merges the unlabeled surface points under the cloud into two numbers of groups—(1) internal points and (2) boundary points. This algorithm is mainly used to detect the boundary points and performs better than the existing methods. The boundary points are detected by BPD algorithm are further clustered and grouped together to order the points under the respective cluster. Later on, from every cluster, the closed boundary paths are collected. To resemble the real surface borderlines, the boundary curves are used to make it smooth. For this purpose and further reconstruct of the surface points under the borderline of the respective cloud, a novel boundary smoothing algorithm termed as RBS was introduced. Afterward, the closed boundaries are created using the clustering of the boundary points and the relative edges are created using the RBS algorithm after identifying each closed boundary.

Later, a novel methodology is applied to measure system Modulation Transfer Function (MTF) directly from natural or live scenes like camera or CCTV, using the

Table 1 ROI parameters

Parameters	ISO 12233	Proposed scheme
ROI size	$>64 \times 80\text{--}500$ Pixels	27×4 Pixels
Angle	$<45^\circ$	$2.5\text{--}42.5^\circ$
Constant	$<10:1$	No such constant limit
Number of edge points in ROI	Not applicable	15

Slanted Edge Method and ISO 12233 algorithm [24]. In this method edge detection techniques are used to select and extract suitable step edges from pictorial images. The system performance scheme-Spatial Frequency Response (SFR) is used in ISO 12233. Different edge selection techniques are proposed in ISO 12233 for digital imaging systems for SFR. However, in this case slanted edge SFR is used that works mainly on edge charts as an input. The chart is captured including at least one gray scale that is taken as a photograph with an angel. Another term used in slanted edge SFR is Region of Interest (ROI) that is a pre-processing activity which includes image linearization with respect to input luminance and edge selection. In this case, two edge detection methods are used—(1) Canny approach and (2) a matched filter. The maximum MTF in the database should be optimum performance of the imaging system derived from a perfect edge. The ROI parameters are described in Table 1.

The advantage of this type of system is that it can derive the system performance in real-time condition instead of any laboratory condition.

In 2020, Shi et al. [25] proposed a novel method related to edge detection for polarimetric synthetic aperture radar (PolSAR) images to pull out all the features related to edge. This method creates a limitation for the speckle noise within heterogeneous areas for weak and strong edges. For this purpose two methods are implemented—(1) To detect weak edges, polarimetric constant false alarm rate (IP_CFAR) is used and (2) To detect edges in heterogeneous areas but it is unable to maintain some of the weak edges, weighted gradient-based (WG) detector is used. But it sometimes produces false alarm rate due to speckle noises. There are three numbers of methods are used for PolSAR images—(1) feature-based edge detection methods, (2) multiple-channel fusion based methods and (3) statistics based edge detection methods. For this first method, some edge details are lost as it omits some weak edges. For the second method, it is unable to detect the edge details in heterogeneous terrain types such as the thin roads in the urban area. To overcome these limitations, a wavelet-based hybrid edge detection method is used [5, 25].

In 2020, Bausys et al. [26] proposed a multi-criteria based decision-making (MCDM) platform called suitability for satellite images. MCDM works mainly on the concept of visual features of edge detection algorithms. Using the neutrosophic weighted aggregated sum product assessment (WASPAS) method, the algorithms

ranked according to their suitability and there algorithms are selected based on primitive six numbers of criteria- contrast, roughness, density, number of different regions, size of the individual image regions and processing time.

3 Tabulated Review

In this section a tabulated review on several methodologies using which the information about the edges can be extracted is given. The tabulated review is summarized as Table 2 that includes different methodologies, algorithms used and performance analysis related to benefits and drawbacks. There is no perfect methodologies regarding edge detection are found so far but it depends on the requirements and adaptability.

4 Conclusion

Edge detection is the basic concept that needs to be focused in most of the image processing work. In this paper, an effort has been made to provide the brief overview about some of the robust, well known and successful edge detection techniques. It is observed that most of the recent algorithms are based on/modification of well known Canny edge detection algorithm. However, after blooming success of deep learning, the deep learning based edge detection techniques is gaining attention nowadays.

Table 2 Tabulated review

Schemes	Algorithm (s) used	Performance analysis
Canny [1]	Canny edge detection	It is one of the basic algorithms. It was the first edge detection algorithm which was based on second order derivation. It is motivated by human vision and has the ability to detect edges within wider ranges in all direction. However, this scheme is sensitive to noise and there is localization problem
Sriramakrishnan and Shanmugam [2]	Hybrid approach of neuro-fuzzy-1	For the input purpose, both the Laplacian and Sobel methods are imposed. On the other hand, for the output purpose, Fuzzy rules are incorporated. Neural network is applied on input layer
Dhir [3]	Hybrid approach of neuro-fuzzy-2	Using the method of global thresholding, the binary images in term of either numerical zero (0) or one (1) are derived from the gray label. Further, Adaptive network-based fuzzy inference system (ANFIS) can be used along with 3×3 masks to train the network to higher level
Rani and Tanwar [4]	Hybrid approach of neuro-fuzzy-3	Using the back propagation method, an adaptive network-based fuzzy inference system (ANFIS) can be constructed based on FIS. It can be derived from the 4 inputs and 1 output based FIS system. Moreover, using the gray levels denoted as L , an intensity of edge is normalized between the ranges [0 to $(L - 1)$]. The respective pixels under the edge are partitioned into two different sets S_0 and S_1
Petrova and Hostalkava [5]	Edge detection in medical images using the wavelet transform	Modification of approximation coefficient by zero gives false edges but approximation with canny edge detectors gives better result. This scheme is appropriate for non stationary signal

(continued)

Table 2 (continued)

Schemes	Algorithm (s) used	Performance analysis
Bar et al. [6]	Mumford and Shah Model is used for image segmentation and image restoration	Through this algorithm we can obtain an image near about the actual image which has less noise and less errors. This scheme is widely used in image restoration
Getreuer [7]	Chan-Vese segmentation	Using the set function of any level, the boundary of segmentation is generally depicted where the segmentation technique is very much efficient than Snake methods and works even if the topology has changed
Chan and Vese [8]	An active contour model without edges	This model is inspired by level sets and it has wide use in medical fields. The objects whose boundaries are not defined by gradient are mainly detected by this system. As the boundaries related to the location are detected very healthy, there is no need to formulate the image in a smooth form though some noise component is present within the image
Alvarez et al. [9]	A real-time morphological snake algorithm	Here the level set is binary piecewise constant and no need of defining the contour distances, i.e., no need of geodesic distance computation. So, this approach becomes easier to implement
Rashid et al. [10]	VHDL based Canny edge detection algorithm	This edge detection technique automatically detects edges of digital images. This is also very efficient and used in medical image detection
Priyadarshini and Sahoo [11]	Additions and divisions based edge detection method	This algorithm computes threshold by simple calculations which is easy compared to Sobel operator. This algorithm needs fewer computations

(continued)

Table 2 (continued)

Schemes	Algorithm (s) used	Performance analysis
Biswas and Sil [12]	Improved canny edge detection using type-2 fuzzy logic	The algorithm considers the uncertainties in the image and computes the threshold to the segment of the gradient image. The algorithm helps in selecting threshold besides the uncertainties in an image
Rashmi et al. [13]	Bilateral filter based adaptive Canny edge detector	The algorithm computes weighted average of intensity of a pixel using its nearby pixels and reduces noise in a digital image. The algorithm works well for high resolution images and has noise reduction capacity but it is not good for low resolution images
Shamlee [14]	A split canny edge detection	To reduce the loss of edges within the specific regions and compute the threshold values, a histogram is used. The algorithm has low memory requirements, low latency, high throughput and great edge detection performance
Liu et al. [15]	Canny edge detection based on iterative algorithm	The algorithm computes dual threshold—high and low by iterative computation. The detected edges are sharpen using this algorithm. It reduces the noise interference and gives the best threshold for image segmentation using mathematical morphology but cannot involve large calculations if needed
Gao C et al. [16]	Alpha weighted quadratic filter based edge detector	Positive alpha is used for enhancing image contrast whereas negative alpha is used for suppressing the non edge portion. This scheme safeguards contrast while concurrently get rids of noise Positive/Negative power law can be utilized in the filter design for further enhancing the desired portions

(continued)

Table 2 (continued)

Schemes	Algorithm (s) used	Performance analysis
Zitnick and Dollár [17]	Using the Structured Forests method, detection of edges is done	Applied in discrete space to get real-time performance. Local image patches are used to form the structure. It is a computationally efficient edge detector
Maladakara and Vanamala [18]	Improved canny edge detection algorithm	The canny is used at the block level and the total image is differentiated into several blocks and thus reduces the computational time and helps in more appropriate detection of edges
Yu et al. [19]	Deep semantic learning based edge detection method	Category wise edge detection is performed
Liu et al. [20]	Richer convolution features (RCF) based edge detection method	This RFC method produces high quality edges and also exploits multilevel and multi scale information of objects for prediction
Agrawal and Rosepreet [21]	Three different techniques are utilized—(1) Sobel type (2) Fuzzy Logic System Type 1 and (3) Interval Type 2 Fuzzy logic System (T2FLS)	To obtain image information or pixels as well as detection of edges regarding dental radiographs or X-ray of patients regarding the healthy and effective teeth, those three techniques are used
Halder et al. [22]	Richardson's extrapolation technique is used to measure the strength of edges	It is used for the identification of respective edges of a binary image
Carmelo et al. [23]	BPD algorithm, RBS algorithm and spatial FFT-based filtering	This algorithm does not depend on any predefined threshold values and reduces the chance of selecting any polynomial function for curve fitting
Van Zwanenberg et al. [24]	Modulation Transfer Function (MTF) and ISO 12233 algorithm	This scheme can derive the system performance in real-time condition instead of any laboratory condition
Shi et al. [25]	Polarimetric constant false alarm rate edge detector and weighted gradient-based (WG) detector	This scheme is very effective to suppress the noises and enhance the edge information
Bausys et al. [26]	Adaptive selection based edge detection algorithms	It is useful to get visual characteristics like—size of the individual regions, contrast, roughness, density, and the number of different regions.

References

1. Canny J (1986) A computational approach to edge detection. *IEEE Trans Pattern Anal Mach Intell* 679–698
2. Sriramakrishnan C, Shanmugam A (2012) A fuzzy neural approach for medical image retrieval. *J Comput Sci* 8(11):1809–1813. <https://doi.org/10.3844/jcssp.2012.1809.1813>
3. Dhir R (2012) Novel edge detection using adaptive neuro-fuzzy inference system. *Int J Comput Appl* 2(5)
4. Rani P, Tanwar P (2013) A novel hybrid approach for edge detection. *Int J Comput Sci Eng Surv* 4(2):27
5. Petrova J, Hostalkova E (2011) Edge detection in medical image using the Wavelet transform. Report of Research, Department of Computing and Control Engineering, Czech Public
6. Bar L et al (2014) Mumford and Shah Model and its applications to image segmentation and image restoration. In: *Handbook of mathematical methods in imaging*, pp 1–52
7. Getreuer P (2012) Chan-vese segmentation. *Image Process Line* 2:214–224
8. Chan TF, Vese LA Active contours without edges. *IEEE Trans Image Process* 10(2):266–277. <https://doi.org/10.1109/83.902291>
9. Alvarez L et al (2012) A real time morphological snakes algorithm. *Image Process Line* 2:1–7
10. Rashid SS et al (2014) VHDL based Canny edge detection algorithm. *Int J Curr Eng Technol* 4(2)
11. Priyadarshini S, Gadadhar S (2010) A new edge detection method based on additions and divisions. *Int J Comput Appl* 9(10):10–13
12. Biswas R, Sil J (2012) An improved canny edge detection algorithm based on type-2 fuzzy sets. *Procedia Technol* 4:820–824
13. Rashmi MK et al (2013) Performance analysis of adaptive canny edge detector using bilateral filter. *Int J Innov Res Comput Commun Eng* 1(4):931
14. Shamlee VJ (2014) A split Canny edge detection: algorithm and its FPGA implementation. *Int J Sci Res (IJSR)* 3:1198–1205
15. Liu X et al (2014) Canny edge detection based on iterative algorithm. *Int J Secur Appl* 8(5):41–50
16. Gao C et al (2011) New edge detection algorithms using alpha weighted quadratic filter. In: *IEEE international conference on systems, man, and cybernetics*. IEEE
17. Dollár P, Zitnick CL (2014) Fast edge detection using structured forests. *IEEE Trans Pattern Anal Mach Intell* 37(8):1558–1570
18. Maladakara DK, Vanamala HR (2015) Design of improved Canny edge detection algorithm
19. Yu Z, Feng C, Liu MY, Ramalingam S (2017) Casenet: deep category-aware semantic edge detection. In: *Proceedings of the IEEE conference on computer vision and pattern recognition*, pp 5964–5973
20. Liu X et al (2017) Richer convolutional features for edge detection. In: *Proceedings of the IEEE conference on computer vision and pattern recognition*, pp 3000–3009
21. Agrawal A, Rosepreet KB (2018) Edge detection techniques in dental radiographs (Sobel, T1FLS & IT2FLS). In: *International conference on communication, networks and computing*. Springer, Singapore
22. Halder A, Bhattacharya P, Kundu A (2019) Edge detection method using Richardson's extrapolation formula. In: *Soft computing in data analytics*. Springer, Singapore, pp 727–733
23. Carmelo M, Pierce SG, Summan R (2019) Novel algorithms for 3D surface point cloud boundary detection and edge reconstruction. *J Comput Des Eng* 6(1):81–91
24. Van Zwanenberg O, Triantaphillidou S, Jenkin R, Psarrou A (2019) Edge detection techniques for quantifying spatial imaging system performance and image quality. In: *Proceedings of the IEEE conference on computer vision and pattern recognition workshops*

25. Shi J, Jin H, Xiao Z (2020) A novel hybrid edge detection method for polarimetric SAR images. *IEEE Access* 8:8974–8991
26. Bausys R, Kazakeviciute-Januseviciene G, Cavallaro F, Usovaite A (2020) Algorithm selection for edge detection in satellite images by neutrosophic WASPAS method. *Sustainability* 1(2):548

Design and Analysis of an Improvised Fully Differential Amplifier



Swagata Devi, Koushik Guha, Naushad Manzoor Laskar, Sourav Nath, and Krishna Lal Baishnab

Abstract This work proposes the design of an amplifier intended for low power applications, operating at an ultra-low voltage and exhibiting a low input-referred noise. The suggested structure implements a flip voltage follower (FVF) implemented in its biasing circuit and thereby demonstrates improvised design parameters as compared to the conventional single-stage fully differential amplifier (FDA). The design is an attempt to enhance the transconductance, slew rate and gain-bandwidth product (GBW). All the devices are operating in a weak inversion region such that the entire design is appropriate for low power applications. The circuit simulations have been performed in 180 nm CMOS SCL Cadence environment and are working at 0.6 V supply voltage. The simulation results report an increased gain by 7.81 dB and an enhanced phase margin by 3.85°. The design consumes a power of 1.07 μW with a total input-referred noise of 6.56 $\mu\text{V}/\sqrt{\text{Hz}}$ @ 1 Hz. The gain-bandwidth product and slew rate are measured to be 485.28 kHz and 26.85 V/ms.

Keywords Flip voltage follower (FVF) · Weak inversion region · Gain-bandwidth (GBW) · Input-referred noise · Slew rate

1 Introduction

In the modern era; there is a demand for compact and portable gadgets. These criteria arise the need for implantable battery-operated devices, which should have low power consumption and low noise. Low power ensures longer battery lifetime, while the requirement for low noise is to minimize the disturbances caused by skin-electrode contact as well as external noises due to EEG recording electrodes attached to the human body. Furthermore, low area is also a major concern in device implantation, to avoid damage to tissues during surgery [1]. The EEG signals have very low amplitude, in order of few microvolts to millivolts, with a frequency range of a few

S. Devi (✉) · K. Guha · N. M. Laskar · S. Nath · K. L. Baishnab

Department of Electronics and Communication Engineering, National Institute of Technology Silchar, Silchar, Assam, India

e-mail: swagatadevi90@gmail.com

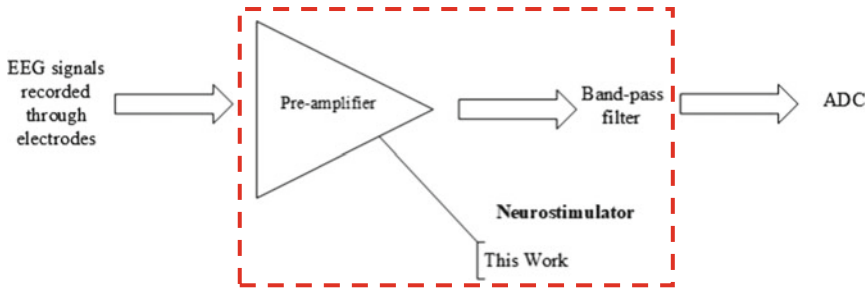


Fig. 1 Block illustration of a neurostimulator

hundred hertz. So, the primary idea of this work is to design a power noise efficient amplifier, which can be used as a preamplifier in neurostimulators of epilepsy seizure detection systems [2]. Epilepsy is a neurological disorder in which a person experiences periods of abnormal brain activity, and sometimes loss of awareness. The Center for Disease Control and Prevention (CDC) has described epilepsy as a “common neurological condition” characterized by recurrent seizures [3] and it has affected 50 million people worldwide as reported by World Health Organization in 2016. The pictorial illustration in Fig. 1 is the analog block representation of a neurostimulator. It comprises of a preamplifier and a band-pass filter. The preamplifier continuously records the EEG signals, by maintaining a low input-referred noise. The frequency range from the amplifier stage can be further narrowed down to the required bandwidth with the help of a band-pass filter if necessary.

Researchers worldwide have proposed various preamplifiers and, as reported by Qian et al. [4], a two-stage OTA low noise amplifier has been put forward which incorporates the multiple stages, thereby increasing of die area. Another work presented by Niranjala et al. [5] provides a low input-referred noise, but the power consumed is extremely high; which therefore acts as a constraint as it impacts the battery-life of the design. Similar work by Bano et al. [6] reports very high input-referred noise but a low power consumption. Wattanapanitch et al. [6] have mentioned in the article that the input-referred noise of the amplifier should be lower than the background noise of neural recording site, i.e., (5–10) μ V. The power of an amplifier is proportional to $\frac{1}{v_n^2}$, where v_n is the input-referred noise of the amplifier, which establishes that low noise is achievable at the expense of power. Therefore, power becomes a controlling criterion for a complete neural amplifier system. Thus, the power noise trade-off is also a major challenge for designers considering the demand of wearable and implantable devices [7].

The circumvention of multiple stages can resuscitate area but the output swing will be degraded. Therefore, this work suggests a flip voltage follower in the biasing circuit of a fully differential folded cascode amplifier (FDA), to enhance its transconductance, gain-bandwidth product and slew rate. The paper follows up with a brief description of FDA with CMFB circuit in Sect. 2, while Sect. 3 enumerates the

proposed structure. Section 4 is an articulation of the results and observations, followed by Sect. 5 which concludes this paper.

2 Fully Differential Folded Cascode Amplifier

Fully differential amplifiers have advantages in contrast to single-ended amplifiers. They are less susceptible to common-mode noise, provide larger output voltage swing and do not have even order nonlinearities. The FDA with a CMFB ensures proper functioning of the circuit and stabilizes common-mode output voltages at all operating range of frequencies. The output V_{OC} from the FDA block is fed into the CMFB block. V_{OC} is the average of V_{OC}^+ and V_{OC}^- . The difference of V_{OC} and desired V_{CM} is amplified by a factor of A_{CM} and then fed back to the op-amp, which is shown through pictorial depiction in Fig. 2 [8]. The CM block senses the common-mode voltage, which is expressed in Eqs. (1) and (2) as:

$$V_{OC} = \frac{V_{O1} + V_{O2}}{2} \quad (1)$$

$$V_{cms} = a_{cms}(V_{OC} + V_{CM}) + V_{CS\ bias} \quad (2)$$

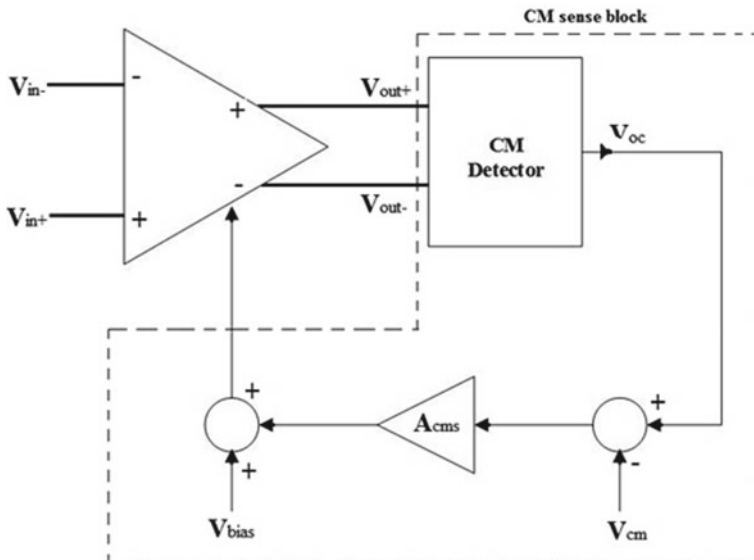


Fig. 2 Block representation of FDA with CMFB circuit

where, $V_{CS\text{ bias}}$ is the additional dc bias voltage. The V_{cms} output of CM sense block is required to drive the V_{cmc} input of op-amp. Thus, by varying V_{cms} and V_{OC} can be changed but V_{od} is not affected if the circuit is perfectly balanced. Hence, both V_{cmc} and V_{cms} have equal values for voltages.

3 Proposed Topology

In this work, flip voltage follower (FVF) is introduced in the structure, as illustrated in Fig. 3, while the schematic of its CMFB circuit is shown in Fig. 4. The circuit operates in the weak inversion region; hence the intrinsic gain becomes limited but the threshold voltage does not change. The low power supply voltage will restrict the voltage swing of the amplifier. A solution to overcome the issues is to use multistage op-amp, but it will consequence in a larger area which is not desirable. An alternative is to use a flip voltage follower which can enhance the driving capability of the structure, as shown in this work. The flip voltage follower circuit is a combination of two alike transistors, which is a modification of a conventional source follower. It provides a very low output impedance at the output node: $\frac{1}{g_{mA}r_{0A}g_{mB}}$ and hence is capable of sinking a large amount of current, and is unaffected by noise [9]. These

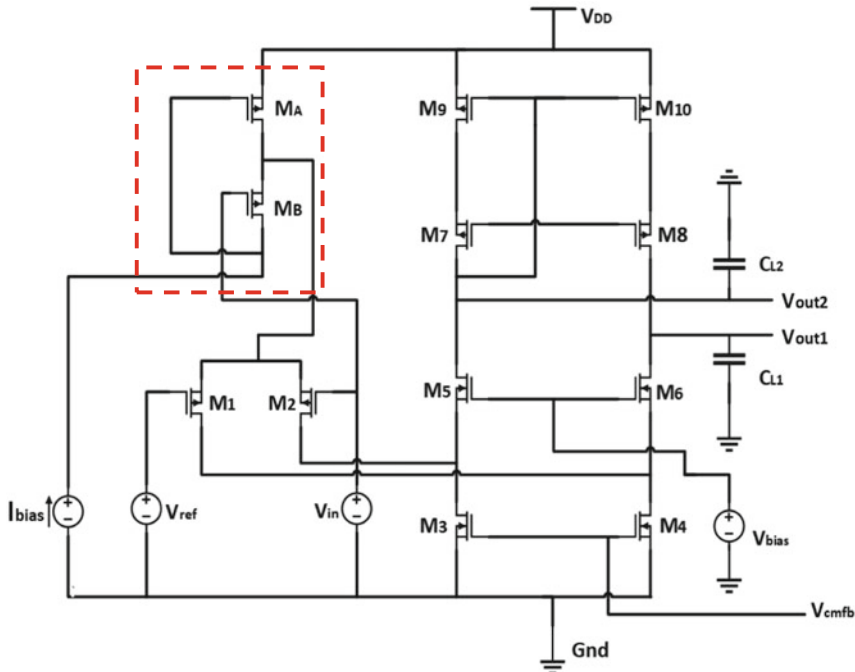


Fig. 3 Schematic of the proposed amplifier circuit

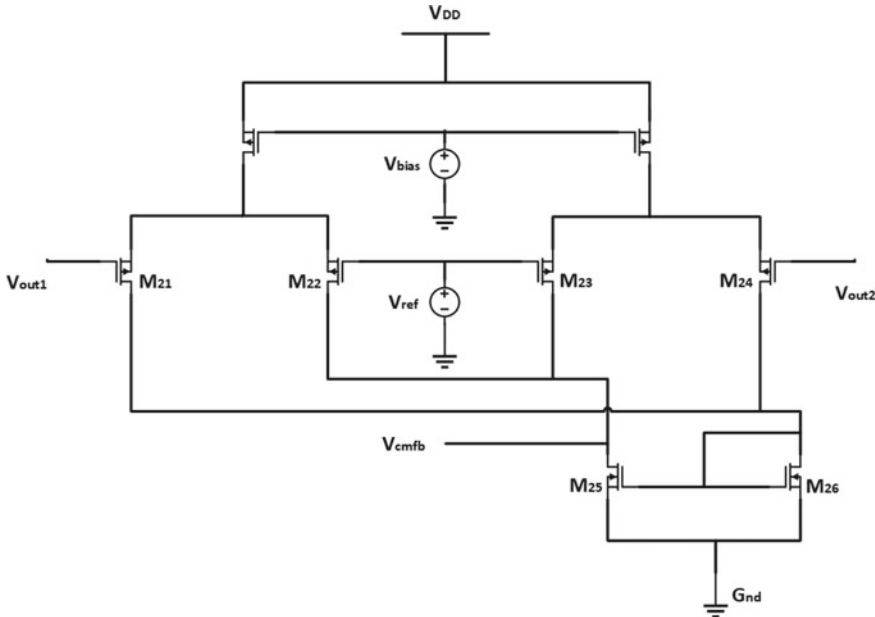


Fig. 4 Schematic of the CMFB

circuits are capable of functioning at a very low voltage and are therefore efficient for low power applications. The use of the FVF in the differential amplifier design results in increased transconductance and gain-bandwidth, as well as an enlarged voltage swing. The load capacitor will discharge by $\frac{(2k-1)}{C_L} I$ for positive output and charge by $\frac{I}{C_L}$ for negative output. Thus, the total slew rate is given by Eq. (3):

$$SR = \frac{6I_d}{C_L} \quad (3)$$

Again, as depicted in Fig. 3 the gate of MB is connected to the input transistor M2, therefore this current will change with respect to the input voltage, and therefore will remain self-biased.

$$I_d = I_D + i_d \quad (4)$$

The increased current which is proportional to the input voltage correspondingly result in a slight rise in consumed power. Now, when an ac input is being applied to source terminals of input transistors, it will result in doubling of the transconductance of its input stage, when compared to its conventional design. Thus, the ac current of its input stage is shown in Eq. (4).

$$I_d = 1 + \frac{g_{mOA} r_{oOA} - 1}{g_{mOA} r_{oOA} + 1} \quad (5)$$

Equation (5) states that the ac current is twice as compared to its conventional structure without FVF. Thus, its slew rate improves. The FVF circuit also introduces an additional pole but since the devices have very low impedance hence this pole is forced to high frequency, without affecting the frequency response [10].

The entire design is realized specifically for low power applications. Therefore, all the devices are operating in the weak inversion region, where V_{GS} is somewhat less than V_{th} . This signifies that $V_{GS} - V_{th}$ generates a smaller value than zero, but it allows a detectable drain current to flow through, which results in a degradation in frequency response and an increase in flicker noise. The degradation in frequency is due to very low currents, while flicker noise increases as it is the dominant noise at low frequencies [11]. Flicker noise reduction can be achieved by increasing the length of MOSFET devices, but at the expense of low current. This increase can be compensated either by increasing transistor width or gate-source voltage. Again, with an increase in transistor width, there is degradation in phase margin, which means more power will be consumed due to increased parasitic capacitances, also silicon area will be increased. On the other hand, an increase in gate-source voltage will increase input-referred flicker noise, but the impact of increase in transistor length is much more, hence noise can be effectively reduced without the increased cost of die area [12]. The expression of drain current for devices working in weak inversion region is shown in Eq. (6), where, V_{GS} is the gate-source voltage, V_{DS} is the drain-source voltage, V_{th} is the threshold voltage with a value of 26 mV at room temperature and I_S is the current with constant dimensions at $V_{GS} = V_{th}$, and the width and length of a transistor device is denoted by W and L .

$$I_D = I_S \left(\frac{W}{L} \right) e^{\left(\frac{V_{GS} - V_{th}}{nV_T} \right)} \left[1 - e^{-\frac{V_{DS}}{V_T}} \right] \quad (6)$$

Thus, the overall transconductance G_m of the amplifier can be calculated to be as g_{m1} , which is shown in Eq. (7) as:

$$G_m = g_{m1} = \frac{\delta I_D}{\delta V_{GS}} = \frac{I_D}{n V_{th}} \quad (7)$$

where g_{m1} is the transconductance for the input transistor: M1. The dominant pole ω_{p1} for the amplifier is given by the high output resistance and high capacitance that occurs at the output node, while the other pole ω_{p2} have a frequency much greater than dominant pole frequency shown by Eq. (8):

$$\omega_{p2} = - \frac{g_{m5}}{C_{gs5}} \quad (8)$$

Again, at low frequencies, flicker noise is the dominant noise over thermal noise. The additional silicon and silicon dioxide energy states contribute to an increase in flicker noise making it dominant. The overall input-referred noise is denoted by Eq. (8) where the first term is the total thermal noise and the second term is the entire flicker noise.

$$\overline{i_o^2} = \left[4K_B T \gamma g_m + \frac{K_F g_m^2}{C_{\text{OX}} W L f} \right] \Delta f \quad (9)$$

The overall flicker noise can be determined by expanding the second term in Eq. (9) and then replacing terms g_{m3} and g_{m9} with their respective expressions of transconductances as depicted in Eq. (7). Equation (10) is the illustration of total flicker noise in the amplifier:

$$\overline{V_{\text{if, proposed}}^2} = 2 \frac{K_{\text{FP}}}{C_{\text{OX}}^f} \left[\frac{1}{(WL)_{\text{a1}}} + \frac{K_{\text{Fn}} g_{m3}^2}{K_{\text{Fp}} g_{m1}^2} \left(\frac{I_{s3}}{n_3 V_T} \right)^2 \frac{W_3}{L_3^3} e^{2\left(\frac{V_{GS3}-V_{th}}{n_3 V_T}\right)} \right. \\ \left. + \frac{g_{m9}^2}{g_{m1}^2} \left(\frac{I_{s9}}{n_9 V_T} \right)^2 \frac{W_9}{L_9^3} e^{2\left(\frac{V_{GS9}-V_{th}}{n_9 V_T}\right)} \right] \Delta f \quad (10)$$

4 Simulation Results

Table 1 is a comparative summary of all the design parameters between a fully differential amplifier circuit with and without a flip voltage follower, and with a few recent works. The simulation has been performed in the Cadence 180 nm SCL technology @0.6 V supply voltage. The measured gain has improved by 7.81 dB is due to the doubling of transconductance and the phase margin by 3.85°, as compared to the conventional design. There is an increase in power consumption as a result

Table 1 Comparison of design parameters

Parameters	Conventional	Proposed	[12]	[5]
Supply voltage (V)	0.6	0.6	1	0.8
Overall gain (dB)	40.16	47.97	82	44.6
Phase margin (°)	85.67	89.52	84	—
GBW (kHz)	243.22	485.28	768	—
Power consumption (μW)	0.593	1.07	0.834	18.74
Input-referred noise (μV/√Hz)	13.45	6.56	80	1.24
Slew rate (V/ms)	15.49	26.85	—	—
Technology (nm)	180	180	150	180

of the increased current due to the implementation of the FVF. However as there exists a trade-off between noise and power, so the increased power reflects in the decrease in noise. As for the intended application the power does not exceed the requisite criterion, so is acceptable. The frequency response of both conventional and proposed design has been represented in Fig. 5.

The increase in transconductance also impacts the flicker noise by bringing it down by a significant value, as depicted in Eq. (10). Figure 6 shows the variation in input-referred flicker noise with frequency, and exhibits decreased value as compared to conventional design. The step response for V_{out} is illustrated in Fig. 7. The change in its biasing circuit puts an impact upon average slew rate and gain-bandwidth product

Fig. 5 Frequency responses of proposed and conventional structure

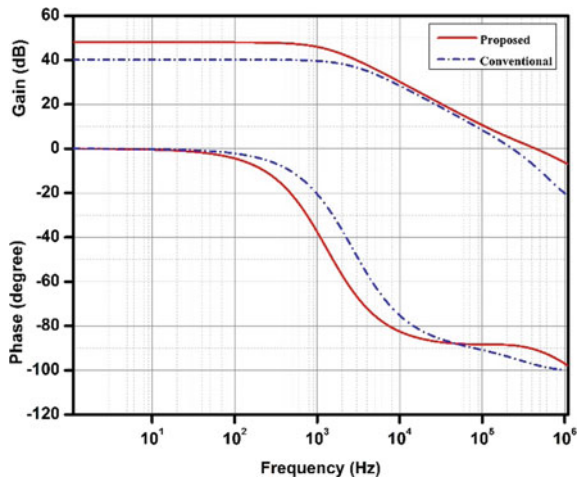


Fig. 6 Spectral density of the input-referred noise for amplifiers

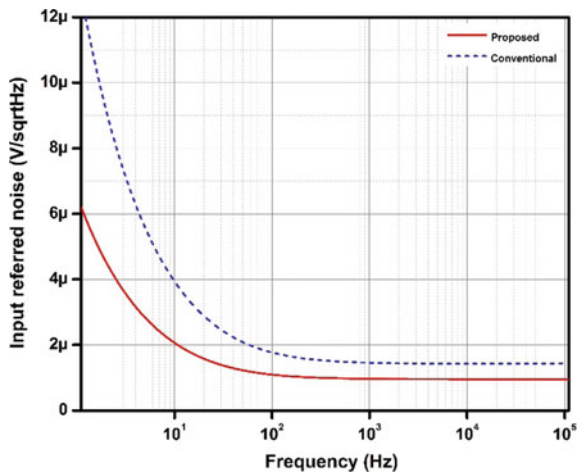


Fig. 7 Step response for V_{out}

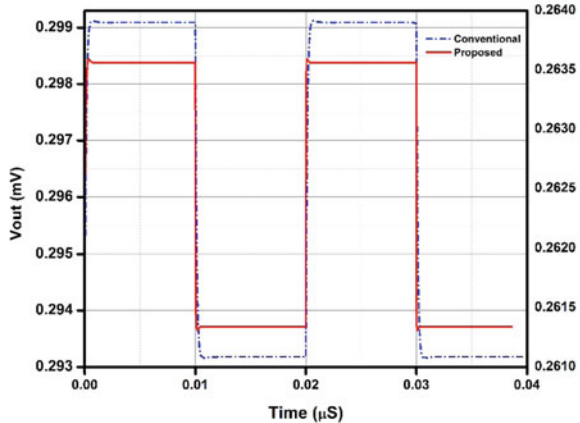


Table 2 Comparison of design parameters

Devices	Sizing (W/L)	Devices	Sizing (W/L)
MA MB	45/1	M9 M10	10/1
M1 M2	60/1	M21 M24	5/1
M3 M4	1/2	M22 M23	5/0.18
M5 M6	15/1	M25 M26	½
M7 M8	30/1	M27 M28	1.2/1

due to the increased transconductance, that can be observed. The device sizing values have been listed in Table 2 accordingly.

5 Conclusion

The proposed preamplifier is designed in weak inversion region to exhibit a low power of $1.07 \mu\text{W}$ with an input-referred voltage of $6.56 \mu\text{V}/\sqrt{\text{Hz}}$ @ 1 Hz, an open-loop gain of 47.97 dB and a phase margin of 89.52° . The overall improvement in gain, slew rate, and the gain-bandwidth product is by 7.81 dB, 242.06 kHz and 11.35 V/ms due to the FVF implementation. The use of FVF is to avoid the use of a multistage amplifier and enhance both increase voltage swing and gain. The designed prototype has been simulated in 180 nm SCL CMOS technology: higher technology can be incorporated based on availability. The design is an open-loop topology, while a closed-loop topology can be used for further analysis and comparison. Hence, the results suggest that the design is an improvisation over a conventional fully differential amplifier designed under same conditions.

References

1. Sarapeshkar R, Wattanapanitch W, Arfin SK, Rapoport BI, Mandal S, Baker MW, Andersen RA (2018) Low-power circuits for brain-machine interfaces. *IEEE Trans Biomed Circ Syst* 2(2):173–183
2. Qu H (1994) Self-adapting algorithms for seizure detection during EEG monitoring. Department of Electrical Engineering, McGill University, Canada
3. Amudhan S, Gururaj G, Satischandra P (2015) Epilepsy in India I: epidemiology and public health. *Ann Ind Acad Neurol* 18(5):263–277
4. Qian, C, Parramon, J, Sanchez-Sinencio E (2011) A micropower low-noise neural recording front-end circuits for epileptic seizure detection. *IEEE J Solid St Circ* 46(6):1392–1405
5. Niranjala M, Mohana D (2018) Epileptic seizure prediction using fully integrated neural signal acquisition amplifier. *Int J Res Dev Eng Sci Mng* 1(12):826–830
6. Bano S, Narejo GB (2017) Low power fully differential folded cascode OTA with CMFB circuit. *J Multi Eng Sci Technol* 4(7)
7. Wattanapanitch W, Fee M, Sarapeshkar R (2018) An energy-efficient micropower neural recording amplifier. *IEEE Trans Biomed Circ Syst* 1(2):136–147
8. Gray PR, Hurst PJ, Lewis SH, Meyer RG (2005) Analysis and design of analog integrated circuits, 4th edn. Wiley
9. Sarkar A, Panda SS (2017) Design of a power efficient, high slew rate and gain boosted improved recycling folded cascode amplifier with adaptive biasing technique. *Microsynt Technol* 23(9):4255–4262
10. Vij S, Gupta A, Mittal A (2014) A highly adaptive operational amplifier with recycling folded cascode topology. In: International conference on computer science and application engineering pp 135–145
11. Akbari M, Biabanifard S, Hashemipour O (2014) Design of ultra-low-power CMOS amplifiers based on flicker noise reduction. In: 2014 22nd Iranian conference on electrical engineering
12. Rajput SS, Singh A, Chandel AK, Chandel R (2016) Design of low-power high-gain operational amplifier bio-medical applications. In: IEEE computer society annual symposium on VLSI

Hyperspectral Band Selection Based on Variants of Rough Set Theory



Barnali Barman and Swarnajyoti Patra

Abstract To deal with the arduous task of hyperspectral image classification band selection is a prominent approach broadly used in the literature. Rough set (RS) theory is a paradigm suitable for handling uncertain, incomplete, and vague data. By incorporating various concepts, classical RS has been extended for band selection capable of handling those problems that classical RS cannot deal with. Four forward greedy hyperspectral band selection algorithms are empirically studied in this paper achieved using the rough set, variable precision rough set, tolerance rough set, and neighborhood rough set. The usefulness of these state-of-the-art techniques is gauged in terms of average overall classification accuracy, average kappa accuracy, and standard deviation acquired by using support vector machine classifier on two real hyperspectral data sets.

Keywords Hyperspectral image · Rough set theory · Variable precision rough set · Tolerance rough set · Neighborhood rough set · Support vector machines

1 Introduction

Presence of a large number of bands in the hyperspectral image (HSI) has driven the attention of the researchers to the area of dimensionality reduction. HSI with hundreds of bands provides the better discriminating capability of the land cover objects compared to the multispectral images. Due to the availability of limited label samples, ‘curse of dimensionality’ is a significant problem to be dealt with. It also suffers from high computational cost and storage issues. These problems are resolved by reducing the dimensionality of HSI. Out of two traditional dimensionality reduction techniques, feature or band selection is found to be more advantageous for its semantics preserving nature over feature extraction. Band selection that selects a

B. Barman (✉) · S. Patra

Department of Computer Science & Engineering, Tezpur University, Tezpur, Assam 784028, India
e-mail: barnali.gu@gmail.com

S. Patra

e-mail: swpatra@tezu.ernet.in

subset from original band set is divided into supervised [5] and unsupervised [12] categories. Supervised band selection techniques generally produce better accuracies compared to unsupervised band selection techniques as they employ the label information. Several supervised wrapper and filter methods for HSI band selection are presented in the literature [5, 11].

Rough set (RS) theory proposed by Pawlak [9] is a tool used to compute data dependencies to select a feature subset having the same predictive capability as that of the entire data set without any additional information [8]. Application of RS is found to be rare in the field of remote sensing [3, 8]. RS uses the crisp concept of equivalence classes. Before using continuous band values, it requires discretization due to its ability to deal with only discrete values. Besides, it cannot find the extent of similarity between the attributes. Therefore, based on relaxation on the subset operator, similarity, tolerance relation, or capable of handling continuous values, variants of the classical rough set (RS) have been proposed. Variable precision rough set (VPRS) provides modification on the subset operator of RS with additional allowed error information while selecting the feature subset [3, 14]. RS and VPRS need data to be discretized before performing feature selection which can cause loss of valuable information. This problem is mitigated with the help of tolerance rough set (TRS) [13]. Instead of indiscernibility relation of RS, TRS uses a similarity relation and a manually defined similarity threshold value to handle continuous data. Discretization problem can also be mitigated using another variant of RS, i.e., neighborhood rough set (NRS) with neighborhood granulation concept. It needs a neighborhood threshold and distance metric function as the extra information during feature selection [1, 2]. This empirical study focuses on such variants of the rough set for HSI band selection.

2 Basic Notions of Variants of Rough Set Theory

2.1 Rough Set (RS)

A data set can be expressed in a tabular form, where each row identifies an object and each column an attribute is known as information system denoted by (U, A, V, f) . The tuples represent the universe, attribute set, value domain, and information function, respectively. RS uses the concept of equivalence or indiscernibility relation [9]. A pair of objects belongs to the indiscernibility relation signifies that the knowledge of the used attribute set cannot make the two objects discernible.

Given (U, A, V, f) , $B \subseteq A$ and $X_w \subseteq U$. Let $\text{IND}(B)$ define the equivalence classes generated using indiscernibility relation denoted as $[x_i]_B$ ($x_i \in U$). On the basis of the knowledge in B , all the objects can be partitioned into two sets. The first set, i.e., B -lower approximation contains only the objects that surely belong to X_w also known as positive region (denoted by $(\text{POS}_B(X_w))$), and the other set, i.e., B -upper approximation contains all the objects that possibly belong to X_w [9]

$$\underline{B}X_w = \cup\{[x_i]_B | [x_i]_B \subseteq X_w\} \quad (1)$$

$$\overline{B}X_w = \cup\{[x_i]_B | [x_i]_B \cap X_w \neq \phi\} \quad (2)$$

The inclusion operator for computing both the approximations using RS sometimes becomes too restrictive as in real-life application decision making the objects of classes often overlap. Therefore, a variant of RS known as variable precision rough set is proposed.

2.2 Variable Precision Rough Set (VPRS)

Variable precision rough set proposed by Ziarko [15] provides relaxation on the subset operator. It allows partial classification rather than complete classification required by RS. Given $X, Y \subseteq U$, where $X, Y \neq \phi$. The relative classification error of X in Y is given by [15]

$$e(X, Y) = \begin{cases} 1 - \frac{|X \cap Y|}{|X|}, & |X| > 0 \\ 0, & |X| = 0 \end{cases} \quad (3)$$

Given an information system (U, A, V, f) , $B \subseteq A$ and $X_w \subseteq U$. Considering β to be the allowed level of error, the lower and upper approximation are defined as [15]

$$\underline{B}^\beta X_w = \cup\{[x_i]_B \in U | e([x_i]_B, X_w) \leq \beta\} \quad (4)$$

$$\overline{B}^\beta X_w = \cup\{[x_i]_B \in U | e([x_i]_B, X_w) < 1 - \beta\} \quad (5)$$

RS and VPRS cannot deal with continuous band values directly without applying a suitable discretization technique which can cause valuable information loss. This problem is mitigated by using the following two techniques.

2.3 Tolerance Rough Set (TRS)

Tolerance rough set (TRS), another variant of RS, can be applied successfully on real-valued data. Instead of using indiscernibility relation, TRS employs the concept of similarity relation. According to a specified threshold value, tolerance classes can be achieved. TRS requires a suitable similarity relation defined for the features. Given (U, A, V, f) , $a \in A$, $x_i, x_j \in U$. A standard similarity measure is given by [10]

$$\text{SIM}_a(x_i, x_j) = 1 - \frac{|a(x_i) - a(x_j)|}{|\max(a) - \min(a)|} \quad (6)$$

For $B \subseteq A$ feature set that contains more than one feature, the combined similarity measure is given by any of the following equation

$$(x_i, x_j) \in \text{SIM}_B^\tau \Leftrightarrow \prod_{a \in B} \text{SIM}_a(x_i, x_j) \geq \tau \quad (7)$$

$$(x_i, x_j) \in \text{SIM}_B^\tau \Leftrightarrow \frac{\sum_{a \in B} \text{SIM}_a(x_i, x_j)}{|B|} \geq \tau \quad (8)$$

where τ is known as a global similarity threshold representing the required similarity level for insertion within the tolerance classes. An object x_i uses a similarity relation for generating the tolerance classes is defined as $\text{SIM}_B^\tau(x_i) = \{x_j \in U | (x_i, x_j) \in \text{SIM}_B^\tau\}$.

Given (U, A, V, f) , $B \subseteq A$, $X_w \subseteq U$ and τ . The lower and upper approximation are defined as

$$\underline{B}^\tau X_w = \{x_i | \text{SIM}_B^\tau(x_i) \subseteq X_w\} \quad (9)$$

$$\overline{B}^\tau X_w = \{x_i | \text{SIM}_B^\tau(x_i) \cap X_w \neq \emptyset\} \quad (10)$$

2.4 Neighborhood Rough Set (NRS)

Neighborhood rough set (NRS), an another variant of RS, is also capable of handling real-valued attributes effectively. It mitigates the loss of valuable information that occurs during the discretization of continuous band values using RS. Given an arbitrary sample $x_i \in U$ and feature set $B \subseteq A$. Neighborhood granule generated by sample x_i for the B feature space is denoted by $\delta_B(x_i) = \{x_j | x_j \in U, \Delta^B(x_i, x_j) \leq \delta\}$ [7], where δ is a threshold value, and Δ is a distance metric function. The above equation shows that $\delta_B(x_i)$ the neighborhood information granule centered with x_i is influenced by δ and Δ , determining the shape and size of neighborhood granules, respectively. With the increment in δ value, the number of samples in the neighborhood of x_i will also increase. Given an information system (U, A, V, f) , $B \subseteq A$, $X_w \subseteq U$ and $\delta_B(x_i)$. The lower approximation and upper approximation are defined as [7]

$$\underline{B}^\delta X_w = \{x_i | \delta_B(x_i) \subseteq X_w, x_i \in U\} \quad (11)$$

$$\overline{B}^\delta X_w = \{x_i | \delta_B(x_i) \cap X_w \neq \emptyset, x_i \in U\} \quad (12)$$

Hyperspectral band selection using RS, VPRS, TRS, and NRS

Let the set of n patterns associated to the n pixels of the HSI with label be $U = \{x_1, x_2, \dots, x_n\}$ and the set of m bands be $C = \{b_1, b_2, \dots, b_m\}$ that indicate each pixel of the image. An HSI data set can be represented by $H = \{h_{ij} | i = 1, \dots, n; j = 1, \dots, m\}$ matrix, where h_{ij} is the value of pattern $x_i \in U$ for band $b_j \in C$. A hyperspectral data set can be expressed by a decision system $(U, C \cup D, V, f)$, where C, D, V and f indicate condition attribute, decision attribute, value domain, and information function, respectively.

Given a decision system $(U, C \cup D, V, f)$ and $B \subseteq C$. Let $X_{w_1}, X_{w_2}, \dots, X_{w_c}$ be the object subsets in U with decision classes w_1, w_2, \dots, w_c , respectively. The dependency degree of D w.r.t. B is defined as [9]

$$\gamma_B(D) = \frac{|\text{POS}_B(D)|}{|U|} \quad (13)$$

where $\text{POS}_B(D)$ denotes the positive region computed using Eqs. (1), (4), (9) and (11) for RS, VPRS, TRS, and NRS, respectively. $|\cdot|$ represents the number of objects present in a set. Informative attributes can be selected from the conditional attribute set using the above dependency measure. If the bands are chosen based on dependency criterion only, it may contain redundant information. Therefore, a significance criterion is defined to remove the irrelevant attributes as follows [7]

$$\sigma_B(D, a) = \gamma_{B \cup a}(D) - \gamma_B(D) \quad (14)$$

An attribute with the highest significance value is considered to be the most useful attribute. If the significance of an attribute is zero, then it is uninformative.

Algorithm (1) introduces a greedy forward search technique by exploiting the properties of RS, VPRS, TRS, and NRS for selecting an optimal hyperspectral band subset. Initially, an empty subset is considered, and in each iteration bands with the highest significance value are added. This process continues until a criterion to abort is encountered.

Algorithm 1: Hyperspectral band selection using RS, VPRS, TRS, and NRS

1. Initialize $P = \{\phi\}$, $C = \{b_1, b_2, \dots, b_m\}$ and $S = C$.
 2. Repeat
 3. For each and every band $b_i \in S$, calculate significance $\sigma_P(D, b_i)$ using (14).
 4. Select informative band $b_j = \arg \max_{b_i \in S} \{\sigma_P(D, b_i)\}$.
 5. Upgrade $P \leftarrow \{P \cup b_j\}$ and $S \leftarrow \{S - b_j\}$.
 6. Until a criterion to abort is encountered.
-

Table 1 Basic details of Botswana and KSC data sets

Data set	Sensor type	Spatial resolution (m)	Image size	Total spectral bands	Total classes
Botswana	Hyperion	30	1476×256	145	14
KSC	AVIRIS	18	512×614	176	13

3 Details of Data Sets

Two hyperspectral data sets used in our experiment to compute the effectiveness of the variants of rough set theory based band selection techniques described in Sect. 2 are Botswana [6] and KSC [6]. The details of these two data sets are listed in Table 1.

4 Experimental Results

4.1 Experimental Setup

Effectiveness of the three different variants of rough set theory is investigated on two aforementioned hyperspectral image data sets. To scale the spectral band values between 0 and 1 initially, normalization is performed. The variants of RS, i.e., VPRS, TRS, and NRS, are dependent on manual setting of additional parameters β , τ and δ , respectively. β value can be chosen from range $[0, 0.5]$, whereas τ and δ from $[0, 1]$. $\beta = 0, \tau = 0$ and $\delta = 0$ forces VPRS, TRS, and NRS to behave completely like RS, respectively. To train the SVM classifier, we have selected 50% labeled samples as the training set, and the rest are considered as the test set. The classifier is executed ten times for different training sets. Thus, it reduces the irregularities present in the result.

Three measures, i.e., average overall classification accuracy (\overline{OA}), its standard deviation (STD), and average kappa accuracy (\overline{KA}) are used for evaluating the performance of all the variants of RS for band selection. The percentage of the number of test samples correctly classified by the classifier is the overall classification accuracy (OA). Standard deviation is the variation of OA produced on ten runs. Using Kappa accuracy (KA) also, we can compute the accurate classification of samples in the test set.

In the experiment, we have used (7) to compute the combined similarity between bands and Euclidean distance to calculate the neighborhood granule of the patterns for TRS and NRS, respectively. In this paper, we have displayed results for bands 5–35 in the interval of 5 bands. After selecting the required number of bands from the band selection techniques, we tried to find out how much accurate they are. The standard one-against-all (OAA) architecture of support vector machine (SVM) classifier is used for this purpose. It assumes the radial basis function (RBF) as the kernel function. The variance parameter and the penalization factor of SVM classifier

for various data sets are approximated by applying a grid search via a ten-fold cross-validation technique. The LIBSVM library is used in implementation [4]. This paper has adopted the MATLAB environment for presenting all the results.

4.2 Results

The techniques are analyzed with the help of Botswana, and KSC data set is described in Sect. 3. Tables 2 and 3 show the results in terms of \overline{OA} , \overline{KA} and STD of classical rough set (RS), variable precision rough set (VPRS), tolerance rough set (TRS), and neighborhood rough set (NRS) for Botswana and KSC data sets, respectively. From the tables, it is visible that with the increment in band numbers, the classification accuracy also increases. Result of the VPRS technique is dependent on a manual parameter (β) that allows a certain level of error. This β value is manually considered to be 0.1 from the range [0, 0.5). We have observed that for $\beta = 0.1$, VPRS

Table 2 Average overall classification accuracy (\overline{OA}), average kappa accuracy (\overline{KA}), and standard deviation (STD) of RS, VPRS, TRS and NRS for Botswana data set (for manually considered parameters)

Number of bands	RS			VPRS ($\beta = 0.1$)			TRS ($\tau = 0.7$)			NRS ($\delta = 0.1$)		
	\overline{OA}	\overline{KA}	STD	\overline{OA}	\overline{KA}	STD	\overline{OA}	\overline{KA}	STD	\overline{OA}	\overline{KA}	STD
5	86.02	0.849	0.49	86.51	0.854	0.562	79.91	0.783	0.305	85.7	0.845	0.371
10	89.93	0.891	0.316	90.53	0.897	0.235	86.37	0.852	0.434	90.04	0.892	0.237
15	90.72	0.899	0.285	90.97	0.902	0.263	93.13	0.926	0.308	94.25	0.938	0.402
20	91.44	0.907	0.349	91.61	0.909	0.351	94.3	0.938	0.274	95.04	0.946	0.361
25	92.3	0.917	0.297	92.49	0.919	0.369	94.79	0.944	0.218	95.92	0.956	0.398
30	93.87	0.934	0.264	94.24	0.938	0.283	95.51	0.951	0.316	96.17	0.959	0.217
35	95.32	0.949	0.203	95.87	0.955	0.306	96.23	0.959	0.351	96.76	0.965	0.252

Table 3 Average overall classification accuracy (\overline{OA}), average kappa accuracy (\overline{KA}) and standard deviation (STD) of RS, VPRS, TRS, and NRS for KSC data set (for manually considered parameters)

Number of bands	RS			VPRS ($\beta = 0.1$)			TRS ($\tau = 0.7$)			NRS ($\delta = 0.1$)		
	\overline{OA}	\overline{KA}	STD	\overline{OA}	\overline{KA}	STD	\overline{OA}	\overline{KA}	STD	\overline{OA}	\overline{KA}	STD
5	79.67	0.773	0.37	84.28	0.824	0.286	73.15	0.699	0.569	69.11	0.653	0.714
10	85.59	0.839	0.497	89.21	0.88	0.224	87.62	0.862	0.294	76.32	0.735	0.438
15	87.93	0.865	0.326	90.27	0.891	0.234	92.38	0.915	0.204	84.55	0.827	0.282
20	89.97	0.888	0.212	91.74	0.908	0.192	93.67	0.929	0.226	86.52	0.85	0.33
25	91.25	0.902	0.332	92.61	0.918	0.217	94.24	0.936	0.236	90.54	0.895	0.465
30	92.11	0.912	0.368	93.09	0.923	0.226	94.75	0.942	0.243	93.31	0.925	0.383
35	93.01	0.922	0.246	93.48	0.927	0.207	95.06	0.945	0.314	93.76	0.93	0.321

produces better result compared to RS for both the data sets. VPRS produces better result compared to RS as it provides relaxation on the subset operator of RS. Here, the similarity threshold (τ) value is manually considered to be 0.7 from the range [0, 1]. In the case of TRS, $\tau = 0.7$ produces better result compared to RS and VPRS while having more than ten bands for both the data sets. It is due to the fact of using continuous band values directly without applying any discretization method. It exploits the concept of similarity between objects. For NRS, results are shown by considering δ value manually to be 0.1. When the number of selected bands are more than ten, it produces better result compared to all the other three techniques for Botswana data set. Thus, the concept of neighborhood granule for band selection is more useful for Botswana data set. But for KSC data set when the number of selected bands are less than 30, it produces low accuracy compared to RS and VPRS. Afterward, accuracy improves compared to them. NRS could not produce a better result compared to TRS. Thus, TRS is more suitable compared to all the other techniques for KSC data set.

5 Discussion and Conclusion

Rough set theory is capable of handling vague, incomplete, and uncertain data. To handle the drawbacks of classical RS, several variants exist in the literature. The effect of these variants is discussed in terms of hyperspectral image data sets. Since VPRS provides relaxation on the subset operator of RS, it produces a better result compared to RS. But VPRS is dependent on a predefined parameter β to be set manually. RS and VPRS cannot deal with continuous band values directly without applying a suitable discretization technique. TRS can handle continuous band values directly using the concept of similarity. It provides a better result compared to RS and VPRS. It also became dependent on the similarity measure and global similarity threshold value. Another variant of RS, i.e., NRS, uses the concept of neighborhood granule to select the most informative bands. It produces a better result compared to all the remaining techniques presented in this paper except KSC data set. NRS is also dependent on predefined parameter (δ and Δ). From this empirical study, we can conclude that the variants of rough set theory capable of handling continuous band values directly without discretization significantly outperforms.

Although the variants, i.e., VPRS, TRS, and NRS of RS are capable of handling several problems that classical RS cannot, all of them requires additional information during band selection. Automatic computation of the manual parameters for VPRS, TRS, and NRS can be considered as the future scope of this paper.

References

1. Barman B, Patra S (2019) Empirical study of neighbourhood rough sets based band selection techniques for classification of hyperspectral images. *IET Image Process* 13(8):1266–1279
2. Barman B, Patra S (2019) A novel technique to detect a suboptimal threshold of neighborhood rough sets for hyperspectral band selection. *Soft Comput* 23:13709–13719
3. Barman B, Patra S (2020) Variable precision rough set based unsupervised band selection technique for hyperspectral image classification. *Knowl-Based Syst* 193:105414
4. Chang CC, Lin, CJ (2012) Libsvm: a library for support vector machine. Software available at <http://www.csie.ntu.edu.tw/~cjlin/libsvm>
5. Habermann M, Fremont V, Shiguemori EH (2019) Supervised band selection in hyperspectral images using single-layer neural networks. *Int J Remote Sens* 40(10):3900–3926
6. Ham J, Chen Y, Crawford MM, Ghosh J (2005) Investigation of the random forest framework for classification of hyperspectral data. *IEEE Trans Geosci Remote Sens* 43(3):492–501
7. Hu Q, Yu D, Liu J, Wu C (2008) Neighborhood rough set based heterogeneous feature subset selection. *Inf Sci* 178(18):3577–3594
8. Patra S, Modi P, Bruzzone L (2015) Hyperspectral band selection based on rough set. *IEEE Trans Geosci Remote Sens* 53(10):5495–5503
9. Pawlak Z (1991) Rough sets, theoretical aspects of reasoning about data. Kluwer, Dordrecht, The Netherlands
10. Skowron A, Stepaniuk J (1996) Tolerance approximation spaces. *Fundamenta Informaticae* 27(2, 3):245–253
11. Taşkin G, Kaya H, Bruzzone L (2017) Feature selection based on high dimensional model representation for hyperspectral images. *IEEE Trans Image Process* 26(6):2918–2928
12. Xie F, Li F, Lei C, Yang J, Zhang Y (2019) Unsupervised band selection based on artificial bee colony algorithm for hyperspectral image classification. *Appl Soft Comput* 75:428–440
13. Yun O, Ma J (2006) Land cover classification based on tolerant rough set. *Int J Remote Sens* 27(14):3041–3047
14. Zhang C, Sargent I, Pan X, Gardiner A, Hare J, Atkinson PM (2018) VPRS-based regional decision fusion of CNN and MRF classifications for very fine resolution remotely sensed images. *IEEE Trans Geosci Remote Sens* 56(8):4507–4521
15. Ziarko W (1993) Variable precision rough set model. *J Comput Syst Sci* 46(1):39–59

Performance Analysis of Interference Alignment-Based Precoding



Amlan Deep Borah, Md. Anwar Hussain, and Joyatri Bora

Abstract When it comes to the modern multiple-inputs and multiple-output system, i.e., MIMO, the wireless communication system faces a complex challenge in the form of interference mitigation to provide an efficient service. In order to mitigate such challenges, the technology of interference alignment (IA) is an important factor to limit the inter-cell interference of a cellular system. IA technique can increase the system throughput with perfect channel state information in high signal-to-noise (SNR) case. The interference alignment technique also requires feedback technology at least within a cell. This paper discusses the topic of precoder design, user, and antenna scheduling techniques based on IA in a cellular system of two- and three-cell clusters. By obtaining the user's antenna combining vector, the IA scheme aligns the interfering signal from each transmitter of the neighboring cell. We have used zero-forcing beamforming (ZFBM) and minimum mean square error (MMSE)-based precoding to simulate our proposed scheme. On the conclusion of the simulation result, it is tried to showcase the proposed scheme gives better sum-rate performance than the traditional IA-based precoding scheme.

Keywords MIMO · Interference alignment · System throughput · Antenna combining · Sum rate

1 Introduction

In wireless communication system, interference is a major hurdle as mobile users with single and multiple antennas receive signals from single and multiple transmitters with single and multiple antennas of a communication system. To increase the

A. D. Borah (✉) · Md. A. Hussain · J. Bora

North Eastern Regional Institute of Science and Technology, Nirjuli, Arunachal Pradesh, India
e-mail: amlan20deep@gmail.com

Md. A. Hussain

e-mail: ah@nerist.ac.in

J. Bora

e-mail: jb@nerist.ac.in

system performance, MIMO can provide diversity gain multiplexing or array gain by using multiple antennas both at the receiver and transmitter. An increased number of simultaneously serving users that results in the increase of multiuser diversity gain can also increase the system throughput. This can be achieved through linear precoding, a technique for obtaining better system performance by optimizing the interference of a multiuser MIMO system.

Interference is the primary challenge of a communication system [1]. In recent studies, IA is the new aspect to deal with the reduction of inter-cell interference in multicell MIMO system [2]. Firstly, IA was introduced as a coding technique to achieve multiplexing gain [3]. IA was also used as a way to minimize interference-free space in an interference channel for the desired signal [4]. The basic idea of the IA scheme is to compress all interference signals to a predefined dimension of the transmitted signal by the proper design of transceiver to maximize the degree of freedom of the system (DoF). Channel state information (CSI) is important for ideal interference alignment. The precoding techniques use to mitigate the inter-user interference and an IA scheme works on the reduction of the inter-cell interference [5].

The alignment of the interference signal into a subspace dimension of a transmitted signal can provide maximum DoF [6]. Article [7], [8] made a proper study on the feasibility of the IA system and DoF for a downlink multiuser MIMO system. In two-cell cluster, scenario BS can recover desired V symbols using $V + 1$ dimension which a DoF of $\frac{V}{V+1}$ per cell [9]. In [10], IA base zero-forcing (ZF) for multiuser MIMO was proposed. Authors in [9] have discussed the implementation of an IA scheme in two-cell interfering systems with the receive antennas number larger than the transmitting antennas and reciprocal. [11] discussed a two-user (in each cell) two-cell clusters. A joint design of the beamforming vector at the transmitter and user antenna combining factor design to align the interference to a specific direction can eliminate the inter-cell and intra-cell interferences [12]. Sum rate of a two- and three-cell network has been discussed using IA-based precoding aspect for cell-edge users with variable user's position. Orthogonal property is used to select the best users from a large group that increases diversity gain. Antenna scheduling technique is also performed at both the user and the transmitter side that get a better efficiency of the system.

2 System Model

In this work, we consider two different clusters of two and three cells for downlink multiuser MIMO as shown in Figs. 1 and 2. Antenna and user scheduling are used to select the best antennas and users from a larger group to get better system performance. At the transmitter and user, we consider X and Y numbers of antennas in this system, respectively. In a cell, R base station (BS) antennas are selected from X numbers. A total of U numbers of users exists in a cell, where it can serve V numbers of users ($V \leq U$). Users are selected by using both random and orthogonal

Fig. 1 Two cells network of a downlink multiuser MIMO

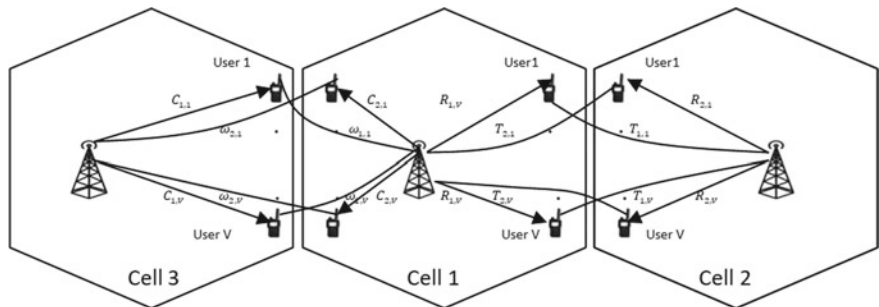
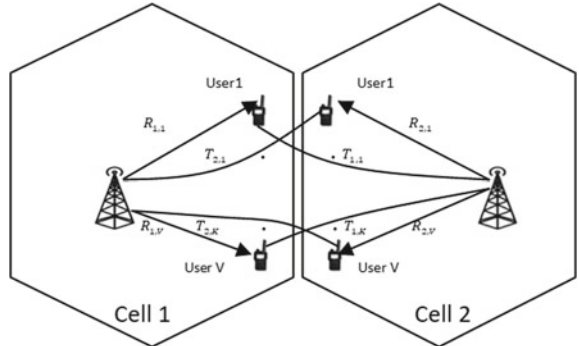


Fig. 2 Three cells network of a downlink multiuser MIMO

user selection techniques. We consider the cell-edge users in the work, where users receive equal power from its own BS and neighboring BS.

The m th user's receive signal in the l th cell can be written as

$$y_{l,m} = R_{l,m}s_l + T_{l,m}s_{3-l} + n_{l,m} \quad (1)$$

The term s_l can be written as

$$s_l = F_l d_l = \sum_{v=1}^V f_{l,v} d_{l,v} \quad (2)$$

In Eq. (1) above, $R_{l,m}$ is the direct channel between transmitter and user and $T_{l,m}$ is the cross-channel between the user and the interfering transmitter. s_l represents the transmitted signal and $n_{l,m}$ is the additive white Gaussian noise with variance $CN(0, 1)$. Whereas shown in (2), $F_l = [f_{l,1} \dots f_{l,V}] \in C^{X \times V}$ is the precoding matrix with $f_{l,m}$ as the beamforming vector of user m in cell l , that satisfies $\|f_{l,m}\|_2^2 = 1$. $E\{x_l^2\} = P$ is the power signal, here transmitter allocates equal power to each user. $d_l = [d_{l,1} \dots d_{l,V}]^\top$ is the data vector with $d_{l,V}$ data symbol.

Since we have considered the case $V \leq U$, the cross-channel is not invertible for this, which results that cross-channel cannot be matched to the reference direction. The Euclidean distance can be minimized by multiplying the m th user of the l th cell received signal with a vector $q_{l,v}$. The proper design of the antenna combining vector can provide this minimization by aligning the interference signal to a reference direction. $q_{l,v}$ can be written as [9]

$$\begin{aligned} q_{l,v} &= \operatorname{argmin} q^H T_{l,V} - v_{\text{ref}}^H \\ \text{s.t. } q &= 1 \end{aligned} \quad (3)$$

The antenna combining factor can be expressed as [12]

$$q_{l,v} = \frac{(T_{l,m} T_{l,m}^H)^{-1} T_{l,m} v_{\text{ref}}}{(T_{l,m} T_{l,m}^H)^{-1} T_{l,m} v_{\text{ref}}} \quad (4)$$

Using the above, received combining signal can be written as

$$y_{l,m} = q_{l,m}^H R_{l,m} x_l + q_{l,m}^H T_{l,m} x_{3-l} + q_{l,m}^H n_{l,m}$$

By using Eq. (2), the above equation can be obtained as

$$\begin{aligned} y_{l,m} &= q_{l,V}^H R_{l,V} \sum_{k=1}^V f_{l,k} d_{l,k} + q_{l,V}^H T_{l,V} \\ &\quad \sum_{k=1}^V f_{3-l,k} d_{3-l,k} + q_{l,V}^H n_{l,m} \end{aligned} \quad (5)$$

Sum rate of V users is obtained as $R_i = V \log_2(1 + \text{SINR}_{i,j})$. So, signal-to-interference plus noise ratio (SINR) of (l, m) th user can be written as

$$\text{SINR}_{l,m} = \frac{\frac{P}{K} |q_{l,V}^H R_{l,V} f_{l,V}|^2}{\sum_{\substack{k=1 \\ k \neq l}}^K |q_{l,V}^H R_{l,V} f_{l,k}|^2 + \frac{P}{K} \sum_{k=1}^V |q_{l,V}^H T_{l,V} f_{3-i,k}|^2 + 1} \quad (6)$$

where in the numerator $\frac{P}{K} |q_{l,V}^H R_{l,V} f_{l,V}|^2$ is the average signal power, in the denominator $\sum_{\substack{k=1 \\ k \neq l}}^V |q_{l,V}^H R_{l,V} f_{l,k}|^2$ is intra-cell interference and $\frac{P}{K} \sum_{k=1}^V |q_{l,V}^H T_{l,V} f_{3-i,k}|^2$ is the inter-cell interference. Using the receive antenna combining, (l, m) th user's detected signal can be written as

$$\begin{aligned} y_{l,m} &= q_{l,V}^H R_{l,V} s_l + q_{l,V}^H T_{l,V} s_{3-l} + q_{l,V}^H n_{l,m} \\ &= r_{l,V}^{\text{eq}} x_l + u_{l,V}^{\text{eq}} s_{3-l} + n_{l,m} \end{aligned}$$

In the equation above, $r_{l,V}^{\text{eq}}$ is the effective direct channel and interfering channel $u_{l,V}^{\text{eq}}$ can be decomposed into two parts having a parallel to v_{ref} ($u_{\parallel v_{\text{ref}}}^{\text{eq}}$) and perpendicular to v_{ref} ($u_{\perp v_{\text{ref}}}^{\text{eq}}$) [12]. Let the interfering channel can be written as $\beta = (u_{l,V}^{\text{eq}})^H$ and also $\beta = \beta_{v_{\text{ref}}} + \beta_{\perp v_{\text{ref}}}$. Here, $\beta_{\perp v_{\text{ref}}}$ causes interference, which can be computed as

$$\beta_{\perp v_{\text{ref}}} = \text{Proj}_{v_{\text{ref}}}((B^{\text{eq}})^H) = \left(I - \frac{v_{\text{ref}}v_{\text{ref}}^H}{v_{\text{ref}}^2} \right) \frac{(B^f B)^H}{\|(B^f B)^H\|} \quad (7)$$

Interfering channel average power is

$$P_{\text{ICI}} = E \left\{ |\beta_{\perp v_{\text{ref}}} s_{3-l}|^2 \right\} = \frac{P}{K} \|\beta_{\perp v_{\text{ref}}}^2\| \quad (8)$$

Transmitter constructs the channel matrix as given below [12]

$$\begin{bmatrix} r_{l,1}^{\text{eq}} \\ \vdots \\ \vdots \\ r_{l,V}^{\text{eq}} \\ v_{\text{ref}}^H \end{bmatrix}$$

From the expression above, the precoding matrix can also be written as shown below,

$$\begin{aligned} \bar{F}_l &= \beta_l^H (\beta_l \beta_l^H)^{-1} \tau \\ &= \beta_l^H (\beta_l \beta_l^H)^{-1} \begin{bmatrix} \sqrt{\gamma}_{l,1} & 0 & 0 \\ \cdot & \cdot & \cdot \\ 0 & 0 & \sqrt{\gamma}_{l,k+1} \end{bmatrix} \\ &= [w_{l,1} \dots w_{l,V} w_{l,V+1}] \begin{bmatrix} \sqrt{\gamma}_{l,1} & 0 & 0 \\ \cdot & \cdot & \cdot \\ 0 & 0 & \sqrt{\gamma}_{l,V+1} \end{bmatrix} \\ &= [\sqrt{\gamma}_{l,1} w_{l,1} \dots \sqrt{\gamma}_{l,V} w_{l,V} \sqrt{\gamma}_{l,V+1} w_{l,V+1}] \\ &= [f_{l,1} \dots f_{l,V} f_{l,V+1}] \end{aligned} \quad (9)$$

In the equation above, $\gamma_{l,V} = \frac{1}{w_{l,V}^2}$ is the power control factor. F_i , the precoding matrix uses to take the first V column from the \bar{F}_l [12]. In our scheme, here we have considered $(V + 1)$ th column as the interfering element for the calculation of SINR. We used the F_i value to obtain the ZFBM and MMSE precoding to analyze the system performance for various user's locations as mentioned below.

3 Result and Analysis

The sum-rate performance of the system has been evaluated in this section. The system with two cells and three cells network is considered as shown in Figs. 1 and 2. We have considered that users are nearer to an edge of a cell, which is also closer to the neighboring cell, considering that users are getting equal power from its own BS and in the interfering BS. User and transmit antenna selection techniques are used to obtain better system performance. Traditional IA-based scheme and the proposed IA-based scheme with ZFBM and MMSE precoding having user and antenna scheduling techniques with low rate-limited feedback have been simulated using MATLAB.

Each cell has a total of U users and V are selected for communication. We used both random and orthogonal user selection techniques and observed the system sum-rate variation. R numbers of the antenna are selected from the X number of BS antennas in each cell, and each user has Y numbers of antennas. In the traditional IA scheme, the first V columns of the matrix obtained from Eq. (9) are considered. But in our scheme, $(V + 1)$ th column is considered as the interfering element for sum-rate calculation. This consideration makes changes in the weighting matrix for precoder design in our proposed scheme due to which the sum rate is increased as shown in Figs. 3 and 4. Also, because of the scheduling applied the sum rate is increased in our scheme.

Figure 3 compares the system performance of a two-cell cluster for both the ZFBM and MMSE precoding. It compares the sum-rate variation with orthogonal and random user selection techniques for both the IA-based approach as mentioned above. Here, $X = 4$ is selected form $R = 80$, where $Y = 2$. Taking similar consideration

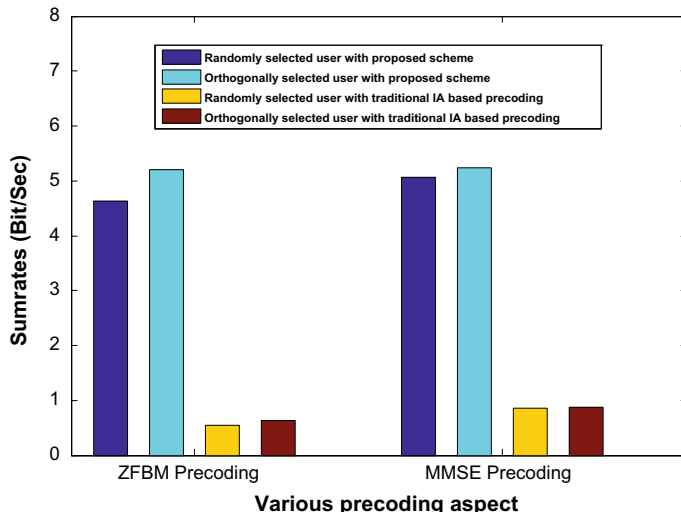


Fig. 3 Sum-rate performance of ZFBM and MMSE precoding with randomly and orthogonally selected user with traditional and proposed IA-based precoding scheme for two microcell

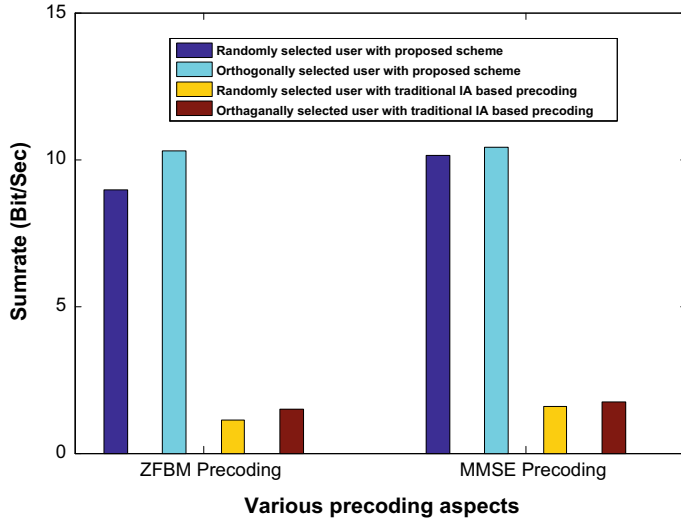


Fig. 4 Sum-rate performance of ZFBM and MMSE precoding with randomly and orthogonally selected user with traditional and proposed IA-based precoding scheme for three microcell

as before, Fig. 4 shows the system sum-rate performance for three-cell network as shown in Fig. 2. Simulated values for both the traditional and proposed IA-based ZFBM and MMSE precoding are shown in Table 1. Sum-rate variation with respect to the random and orthogonal user selection technique is also shown in Table 1.

Table 1 Sum rate obtained for orthogonal and random user selection technique with MMSE and ZFBM precoding for traditional and proposed IA-based scheme

Network types	Schemes	ZFBM		MMSE	
		Random user selection	Orthogonal user selection	Random user selection	Orthogonal user selection
Two-cell network	Proposed IA-based precoding	4.638	5.21	5.0685	5.2415
	Traditional IA-based precoding	0.5383	0.6405	0.8568	0.8722
Three-cell network	Proposed IA-based precoding	8.9629	10.3071	10.138	10.4289
	Traditional IA-based precoding	1.1349	1.4825	1.5837	1.7319

4 Conclusion

A multiuser MIMO system with two cells and three cells network are used to analyze in this work, where users are considered to be placed at the cell edge as shown in Figs. 1 and 2. This paper studies the sum-rate variation using a proposed IA-based scheme and traditional IA-based scheme with ZFBM and MMSE precoding. A comparative study has been made on sum-rate variation using random and orthogonal user selection techniques separately. From the bar diagram plotted in Figs. 3 and 4, it has been proved that for a three cells cluster, sum rate is higher than the two cells network. It has also been concluded that the proposed scheme gives better sum-rate performance than the traditional IA-based ZFBM and MMSE precoding. From the bar diagram, it can be also added that the orthogonal user selection technique gives better outcomes than the random user selection technique and MMSE precoding works better than the ZFBM.

References

1. Jungnickel V, Manolakis K, Zirwas W, Panzner B, Braun V et al (2014) The role of small cells, coordinated multipoint and massive MIMO in 5G. *IEEE Commun Mag* 52(5):44–51
2. Zhou Y, Liu L, Du H, Tian L, Wang X et al (2014) An overview on intercell interference management in mobile cellular networks: from 2G to 5G. In: 2014 IEEE international conference on communication systems. IEEE, Macau, pp 217–221
3. Maddah-Ali MA, Motahari AS, Khandani AK (2008) Communications over MIMO X channel: interference alignment, decomposition, and performance analysis. *IEEE Trans Inform Theory* 54(8):3457–3470
4. Cadambe VR, Jafar SA (2008) Interference alignment and the degrees of freedom for the K user interference channel. *IEEE Trans Inform Theory* 54(8):3425–3441
5. Jindal N (2006) MIMO broadcast channels with finite-rate feedback. *IEEE Trans Inf Theory* 52(11):5045–5060
6. Fadlallah Y, Ferrand P, Cardoso LS, Gorce J-M (2016) Interference alignment for downlink cellular networks: joint scheduling and processing. In: IEEE 17th international workshop on signal processing advances in wireless communications (SPAWC), Jul 2016, Edinburgh, UK, pp 1–5
7. Liu T, Yang C, On the degrees of freedom of asymmetric MIMO interference broadcast channels. In: 2014 IEEE international conference on communications. IEEE, Sydney, Australia, pp 1971–1976
8. Sridharan G, Yu W (2013) Degrees of freedom achieved using subspace alignment chains for three-cell networks. In: 2013 Asilomar conference on signals, systems and computers. IEEE, California, USA, pp 1869–1874
9. Bayesteh A, Mobasher A, Jia Y (2011) Downlink multi-user interference alignment in two-cell scenario, In: 2011 12th Canadian workshop on information theory. IEEE, Kelowna, Canada, pp 182–185
10. Suh C, Ho M, Tse DNC (2011) Downlink interference alignment. *IEEE Trans Commun* 59(9):2616–2626

11. Shin W, Lee N, Lim J-B, Shin C, Jang K (2011) On the design of interference alignment scheme for two-cell MIMO interfering broadcast channels. *IEEE Trans Wireless Commun* 10(2):437–442
12. Zhu Y, Ou Y (2016) Interference alignment-based precoding and user selection with limited feedback in two-cell downlink multi-user MIMO systems. *J Eng Sci Technol Rev* 9(2):115–120

Structural and Optoelectronic Properties of Spin-Coated $\text{CH}_3\text{NH}_3\text{PbCl}_3$ Thin Film Using Non-halide Source of Lead



Paramita Sarkar, S. K. Tripathy, and K. L. Baishnab

Abstract In recent times, methylammonium lead chloride ($\text{CH}_3\text{NH}_3\text{PbCl}_3$) perovskites have great significance as the optoelectronic material. Besides all the promising advantages, there are some problems which need to be resolved, one of such problem is to synthesize well-crystalline, highly homogeneous and the less-defective surface of the perovskites by reducing the synthesis complexity. In this continual search of better properties, we have synthesized of $\text{CH}_3\text{NH}_3\text{PbCl}_3$ film by replacing traditional halide source of lead with a non-halide source of lead. We have also analysed their structural, morphological and optical properties of the film using XRD, FEG-SEM and DRS UV-Vis spectroscopy techniques. The detailed study confirms the cubic structure of the as-prepared film without any contamination. Surface morphology shows the formation of homogeneous spherical particles with an average size of $0.165 \mu\text{m}$. DRS UV-Vis data shows a wide bandgap of 3.7 eV and due to that high transparency in the visible region of light. These outcomes open up the door for $\text{CH}_3\text{NH}_3\text{PbCl}_3$ film as a vital transparent conductor.

Keywords Spin coating · Urbach tail · Hybrid perovskite · Optical properties · Particle size

1 Introduction

Recently, organic-inorganic lead halide (OILH) perovskites APbX_3 ($\text{A}=\text{CH}_3\text{NH}_3^+$; $\text{CH}(\text{NH}_2)_2^+$, etc., and $\text{X}=\text{I}^-$; Br^- ; Cl^-) have gained the attention of researchers. These materials show extraordinary optoelectronic properties, and moreover, they can be easily synthesized via simple cost-effective solution-processable methodologies. The exceptional properties of OILH perovskites include tunable bandgap, high mobility of the charge carriers, higher absorption coefficient, larger diffusion length, etc. These are the reasons which make these materials that fascinating and enable the horizon

P. Sarkar (✉) · S. K. Tripathy · K. L. Baishnab

Department of Electronics and Communication Engineering, National Institute of Technology Silchar, Silchar, Assam 788010, India
e-mail: paramitasarkar2@gmail.com

of its use in the field of optoelectronics like solar cells, UV photodetectors, organic light emitting diodes (LEDs), transparent conductors and lasers [1–5].

Besides all the promising advantages, there are some problems which require special attention before their use in large-scale production. One of such problem is to synthesize well-crystalline, highly homogeneous and the less-defective surface of the perovskites for the better performance of devices. Henceforth, to synthesize high performing devices, the properties of perovskites need to be tuned either by the careful selection of starting materials, preparation methodologies, temperatures, solvents, etc. [6, 7].

The properties of $\text{CH}_3\text{NH}_3\text{PbX}_3$ change dramatically when halide changes from one to another [8, 9]. It has also been observed by the researchers that the properties can be significantly changed by substituting the lead halide precursor salts (i.e. I^- , Br^- , Cl^- sourced) with lead non-halide precursor salts (CH_3COO^- , NO_3^- , etc., sourced) [10]. There are number of reported works on the synthesis of non-halide lead sourced $\text{CH}_3\text{NH}_3\text{PbI}_3$ film, and researchers have attained smooth defect-free surface together with well-crystallinity. Works of the literature suggest that well-crystalline and defect-free surfaces are the utmost requirements for effective device fabrication. One of such notable works has been reported by Moore et al. [11], they have witnessed favourable crystallization kinetics of $\text{CH}_3\text{NH}_3\text{PbI}_3$ using the lead acetate ($\text{Pb}(\text{C}_2\text{H}_3\text{O}_2)_2$) precursor, compared to lead iodide (PbI_2) and lead nitrate ($\text{Pb}(\text{NO}_3)_2$) [9]. Another work shows that acetate ion-based lead salt accelerates the growth of perovskite crystal, which leads to achieving homogeneous and less-defective films [12]. Another group of researchers reported a low-temperature procedure to synthesize uniform films using again the acetate salt, and they have attained 12.5% power conversion efficiency. Similar behaviour of changed morphology and growth mechanism has been stated by many other reports [13–15].

Mostly, a one-step spin-coating methodology is an efficient way for $\text{CH}_3\text{NH}_3\text{PbX}_3$ thin film deposition. Precursor solutions are typically synthesized by dissolving lead halide and methylammonium iodide ($\text{CH}_3\text{NH}_3\text{I}$) into the selected [16, 17]. On the other hand, to acquire high-grade $\text{CH}_3\text{NH}_3\text{PbI}_3$ films using lead iodide, we need an anti-solvent treatment, which is very difficult to control practically [18]. To skip the anti-solvent step, again we need thermal annealing for a longer time. This time-consuming process may limit its use soon [19, 20]. In recent times, non-halide source of lead particularly lead acetate ($\text{Pb}(\text{C}_2\text{H}_3\text{O}_2)_2$) has been commonly used lead source as it does not require an anti-solvent step or thermal annealing for a long time [21–23].

All of the works mentioned above pave the way to modify the properties as well as the crystal growth kinetics by introducing different lead salts. Pieces of the literature suggest that regarding the performances of $\text{CH}_3\text{NH}_3\text{PbX}_3$ perovskite thin films using a non-halide source of lead, $\text{CH}_3\text{NH}_3\text{PbI}_3$ and $\text{CH}_3\text{NH}_3\text{PbBr}_3$ perovskites have been studied mostly till this date, whereas the effect is still under investigation for $\text{CH}_3\text{NH}_3\text{PbCl}_3$ perovskite. As far as we know, there has been no reported work on the thin films of methylammonium lead chloride ($\text{CH}_3\text{NH}_3\text{PbCl}_3$) using lead acetate as the non-halide source of lead via one-step spin-coating methodology. In this work, $\text{CH}_3\text{NH}_3\text{PbCl}_3$ perovskite film has been deposited onto the glass substrate, and their structural, optoelectronic and morphological properties have been studied in detail.

2 Materials and Methodology

2.1 Materials

The starting materials used in this work were in analytical grade purchased from commercial sources and were used without any further refinement. Lead acetate trihydrate ($\text{Pb}(\text{C}_2\text{H}_3\text{O}_2)_2 \cdot 3\text{H}_2\text{O}$, 99%), methylamine hydrochloride ($\text{CH}_3\text{N.HCl}$, ≥98%), *n,n*-dimethylformamide ($\text{C}_3\text{H}_7\text{NO}$, 99.8%) were procured from Sigma-Aldrich. Dimethyl sulfoxide ($\text{C}_2\text{H}_6\text{OS}$ 99%) was purchased from Fisher Scientific.

2.2 Methodology

Methylammonium chloride precursor solution was prepared by dissolving $\text{Pb}(\text{C}_2\text{H}_3\text{O}_2)_2 \cdot 3\text{H}_2\text{O}$ and $\text{CH}_3\text{N.HCl}$ in 1:3 molar ratio in 5 ml *n,n*-dimethylformamide and dimethyl sulfoxide solvent mixture in 3:5 ratio. The acquired solution was stirred in a hot plate at 60 °C for 8 h. Afterwards, the solution was coated onto the glass substrate at 6000 r.p.m. for 1 min in ambient conditions. Before the deposition of thin film, the substrate was pre-cleaned with soap solution, deionized water, ethanol, and acetone and finally dried in an oven. After the completion of the film coating, the coated substrate was annealed at 70 °C for 5 min in an oven and at 60 °C on a hot plate, for 5 min each.

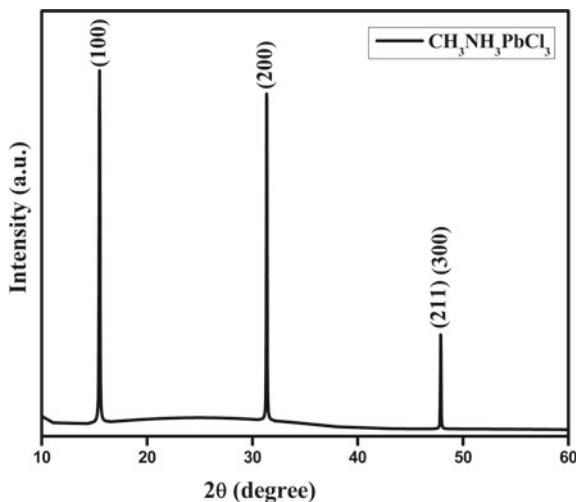
2.3 Characterizations

The structural properties of the film were investigated by Phillips, X'Pert pro diffractometer using $\text{CuK}\alpha$ radiation of 1.5406 Å within the Bragg's angle (θ) range of 10–60° at a step size 0.02° in the ambient conditions. The morphology of the sample was captured by field emission gun scanning electron microscope, FEG-SEM, JEOL (JSM-7600F). Optical properties have been studied using diffuse reflectance spectroscopy (Analytikjena SPECORD). Horiba Jobin Yvon Fluorolog-3 was used to study the photoluminescence (PL) study of the as-prepared perovskites.

3 Results and Discussion

X-ray diffractometer (XRD) study was performed to observe the crystallinity of the synthesized $\text{CH}_3\text{NH}_3\text{PbCl}_3$ perovskite film. Figure 1 shows the XRD pattern of the film. All diffraction peaks are in fair agreement with the reported works for cubic $\text{CH}_3\text{NH}_3\text{PbCl}_3$ perovskite structure, along with space group pm3m [2, 6]. The crystal

Fig. 1 XRD pattern of as-synthesized $\text{CH}_3\text{NH}_3\text{PbCl}_3$ film



planes associated with the diffraction peaks at 15.49° , 31.36° and 47.88° are (100), (200) and (211) (300), respectively. Observed lattice constants are $a = b = c = 5.717 \text{ \AA}$, and the values are in good agreement with other testified works [24, 25]. Absence of any diffraction peaks related to any of the precursor salts confirms the formation of single-phased $\text{CH}_3\text{NH}_3\text{PbCl}_3$ perovskite film. Scherrer's equation has been employed to find out the average crystallite size of the material, and the equation is expressed as follows:

$$D = \frac{0.9\lambda}{\beta_{hkl}\cos\theta} \quad (1)$$

Furthermore, XRD data has been used to calculate some other structural properties [26] such as lattice strain and dislocation density, and the exact values are briefed in Table 1.

Figure 2 illustrates the microstructures of $\text{CH}_3\text{NH}_3\text{PbCl}_3$ film on the glass substrate. The surface of the film is homogeneously covered with spherical-shaped particles. Shapes are regular throughout the surface of the film, and the average particle size is $0.165 \pm 0.02 \mu\text{m}$, which has been calculated with the help of ImageJ software by considering 20 particles. It can be seen from micrographs that some pinholes are present on the surface. A similar type of pinholes for $\text{CH}_3\text{NH}_3\text{PbCl}_3$ thin films has been observed in a few other reported works [4, 27].

Figure 3 represents the reflectance (R) spectra with respect to wavelength (nm) of as-synthesized $\text{CH}_3\text{NH}_3\text{PbCl}_3$ film using diffuse reflectance UV-Vis analysis. Reflectance has been logged within 300–900 nm wavelength. Optical bandgap of the synthesized film can be calculated from reflectance data obtained from diffuse reflectance spectrometer. It is an important parameter to know the material's use as optoelectronic material. Using the well-known Kubelka—Munk relationship, the

Table 1 Properties of as-synthesized $\text{CH}_3\text{NH}_3\text{PbCl}_3$ film

Parameters	This work (using non-halide sourced lead-based $\text{CH}_3\text{NH}_3\text{PbCl}_3$ film)	Other reported works (using halide sourced lead-based $\text{CH}_3\text{NH}_3\text{PbCl}_3$ crystal/film/powder)
Lattice constants (\AA) ($a = b = c$)	5.717	5.67 [2], 5.67 [25], 5.683 [26], 5.68 [28]
Average crystallite size (nm)	106.3	115.72 [4], 50.16 [5]
Dislocation density (lines/ m^2)	9.606×10^{13}	—
Lattice strain	3.35×10^{-4}	—
bandgap (eV)	3.7	2.88 [2], 3.8 [4], 2.97 [5], 3.11 [28], 2.94 [25]

absorption coefficient (α) can be obtained as follows [5]:

$$\alpha \propto F(R) = \frac{(1 - R)^2}{2R} \quad (2)$$

Here, $F(R)$ is the Kubelka—Munk function. Moreover, the optical bandgap has been estimated by using Tauc's plot method. According to Tauc's methodology:

$$\alpha h\nu = A_1(h\nu - E_g)^n \quad (3)$$

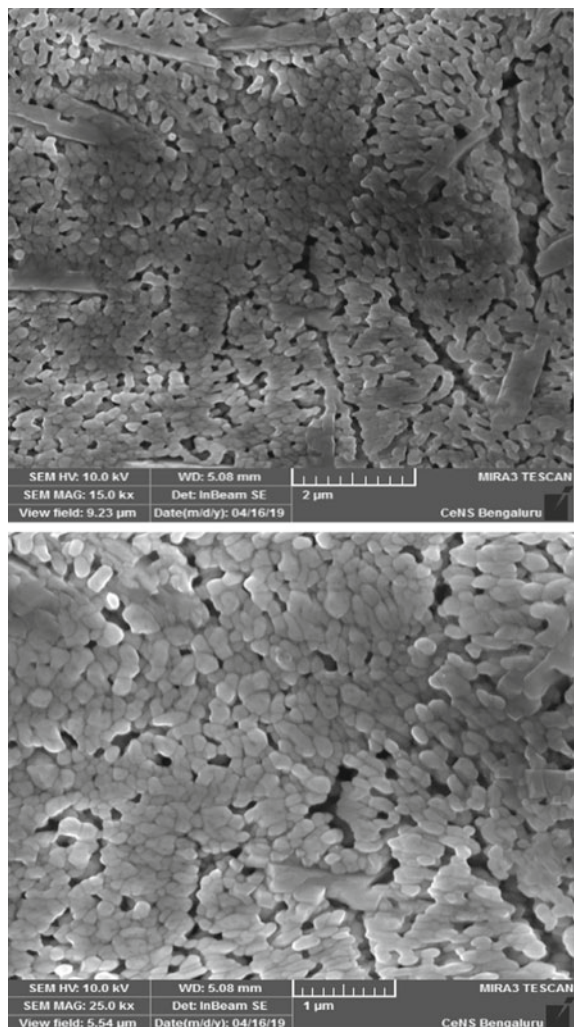
where A_1 is the constant, $h\nu$ is the photon's energy in eV, n is the exponent whose value is dependent on the type of electronic transition occurred in the supporting material. Electronic transitions take places such as direct allowed, direct forbidden, indirect allowed and indirect forbidden for the values of ' n ' are equal to $1/2$, $3/2$, 2 and 3 , respectively. As we have seen in Eq. (2) that α is proportional to $F(R)$ and by taking $n = 2$ (as $\text{CH}_3\text{NH}_3\text{PbCl}_3$ is direct bandgap material), hence Eq. (3) can be written as

$$(F(R).h\nu)^2 = A_2(h\nu - E_g) \quad (4)$$

Extrapolation approach on $(F(R).h\nu)^2$ versus $(h\nu)$ plot (shown in Fig. 4) gives the exact value of bandgap, and the calculated value is 3.7 eV. The obtained value of bandgap is higher than the previously reported values of $\text{CH}_3\text{NH}_3\text{PbCl}_3$ films [29, 30]. The probable reason for achieving higher bandgap may be the thickness of the deposited film due to the experimental procedure.

When film thickness reduces, then size quantization effect comes to the picture, and bandgap may reduce. The film is highly transparent in the visible range of light due to its high bandgap, which is very much appreciable for the materials to be used as a transparent conductor. Previously, many perovskite oxides have shown wide-bandgap nature and have been used as transparent conductors. Few notable works

Fig. 2 FEG-SEM micrographs of as-synthesized $\text{CH}_3\text{NH}_3\text{PbCl}_3$ film



are indium doped Cd_3TeO_6 (bandgap is 3.8 eV), CaTiO_3 (~3.46 eV) and PbTiO_3 (~3.4 eV) [31–34].

4 Conclusion

To find better perovskite film as a transparent conductor, $\text{CH}_3\text{NH}_3\text{PbCl}_3$ film has been fabricated onto a glass substrate using one-step spin-coating methodology using a non-halide source of the lead (lead acetate). Synthesized $\text{CH}_3\text{NH}_3\text{PbCl}_3$ film is a

Fig. 3 Reflectance (%R) versus wavelength (nm) plot of as-synthesized $\text{CH}_3\text{NH}_3\text{PbCl}_3$ film

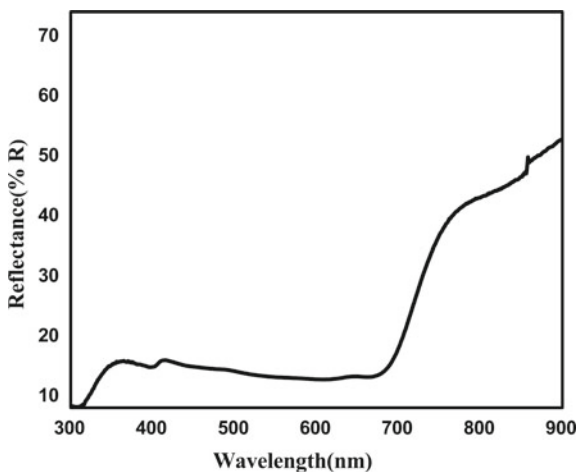
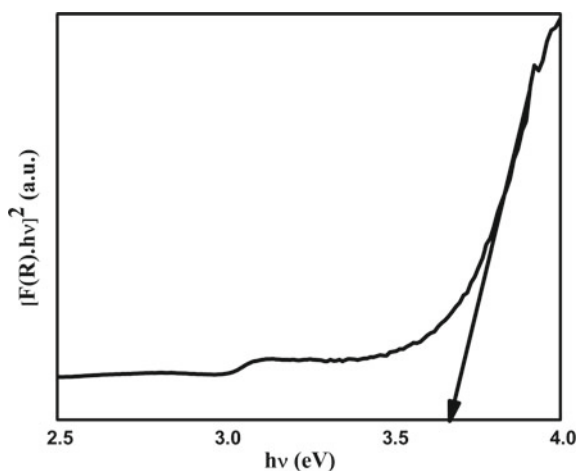


Fig. 4 Tauc's plot for bandgap determination



cubic crystalline structure with space group $\text{pm}3\text{m}$. The average crystallite size, particle size, optical bandgap and few other structural parameters such as lattice strain and dislocation density have been measured. The obtained values have been compared with the available reported works on lead halide sourced $\text{CH}_3\text{NH}_3\text{PbCl}_3$ films/powders/single crystals, due to the lack of available literature of lead acetate-based $\text{CH}_3\text{NH}_3\text{PbCl}_3$ work. All the values are in good agreement with the compared results. Lead acetate sourced $\text{CH}_3\text{NH}_3\text{PbCl}_3$ film shows regular-shaped spherical grains on the surface, and film surface is fully covered, although few pinholes like defects are also seen. Considering the disorders raised due to lead acetate, it can be improved by solvent annealing which can effectively increase the crystallinity of powders and crystallite size. It can be identified as the future scope of work.

Acknowledgements This work was supported by CSIR, New Delhi and ECR scheme (File No. ECR/2016/001404) of SERB, Government of India.

References

1. Wang Q, Lyu M, Zhang M, Yun J, Chen H, Wang L (2015) Transition from tetragonal to cubic phase of organohalide perovskite: The role of chlorine in crystal formation of $\text{CH}_3\text{NH}_3\text{PbI}_3$ on TiO_2 Substrates. *J Phys Chem Lett* 6:4379–4384
2. Maculan G, Sheikh AD, Abdelhady AL, Saidaminov MI, Haque MA, Murali B, Alarous E, Mohammed OF, Wu T, Bakr OM (2015) $\text{CH}_3\text{NH}_3\text{PbCl}_3$ single crystals: inverse temperature crystallization and visible-blind UV-photodetector. *J Phys Chem Lett* 6:3781–3786
3. Tian Y, Ling Y, Shu Y, Zhou C, Besara T, Siegrist T, Gao H, Ma B (2016) A Solution-processed organometal halide perovskite hole transport layer for highly efficient organic light-emitting diodes. *Adv Electron Mater* 2:1600165
4. Sarkar P, Tripathy SK, Baishnab KL, Palai G (2019) Structural, optoelectronic, and morphological study of indium-doped methylammonium lead chloride perovskites. 125:580
5. Sarkar P, Mayengbam R, Tripathy SK, Baishnab KL (2019) Cubic methylammonium lead chloride perovskite as a transparent conductor in solar cell applications: an experimental and theoretical study. *Ind J Pure Appl Phys* 57:891–899
6. Xiao Z, Dong Q, Bi C, Shao Y, Yuan Y, Huang J (2014) Solvent annealing of perovskite-induced crystal growth for photovoltaic-device efficiency enhancement. *Adv Mater* 26:6503–6509
7. Nie W, Tsai H, Asadpour R, Blancon JC, Neukirch AJ, Gupta G, Crochet JJ, Chhowalla M, Tretiak S, Alam MA, Wang HL (2015) High-efficiency solution-processed perovskite solar cells with millimeter-scale grains. *Science* 347:522–525(2015)
8. Mashiyama H, Kurihara Y, Azetsu T (1998) Disordered cubic perovskite structure of $\text{CH}_3\text{NH}_3\text{PbX}_3$ ($\text{X}=\text{Cl}, \text{Br}, \text{I}$). *J Kor Phys Soc* 32:S156–S158
9. Zhang Z, Ren L, Yan H, Guo S, Wang S, Wang M, Jin K (2017) Bandgap narrowing in bi-doped $\text{CH}_3\text{NH}_3\text{PbCl}_3$ perovskite single crystals and thin films. *J Phys Chem* 121:17436–17441
10. Wakamiya A, Endo M, Sasamori T, Tokitoh N, Ogomi Y, Hayase S, Murata Y (2014) Reproducible fabrication of efficient perovskite-based solar cells: X-ray crystallographic studies on the formation of $\text{CH}_3\text{NH}_3\text{PbI}_3$ layers. *Chem Lett* 43:711–713
11. Moore DT, Sai H, Tan KW, Smilgies DM, Zhang W, Snaith HJ, Wiesner U, Estroff LA (2015) Crystallization kinetics of organic–inorganic trihalide perovskites and the role of the lead anion in crystal growth. *J Am Chem Soc* 137:2350–2358
12. Zhang W, Saliba M, Moore DT, Pathak SK, Hörantner MT, Stergiopoulos T, Stranks SD, Eperon GE, Alexander-Webber JA, Abate A, Sadhanala A (2015) Ultrasmooth organic–inorganic perovskite thin-film formation and crystallization for efficient planar heterojunction solar cells. *Nat Commun* 6:6142
13. Forgács D, Sessolo M, Bolink HJ (2015) Lead acetate precursor based pin perovskite solar cells with enhanced reproducibility and low hysteresis. *J Mater Chem A* 3:14121–14125
14. Qing J, Chandran HT, Xue HT, Guan ZQ, Liu TL, Tsang SW, Lo MF, Lee CS (2015) Simple fabrication of perovskite solar cells using lead acetate as lead source at low temperature. *Org Electron* 27:12–17
15. Zhao Q, Li GR, Song J, Zhao Y, Qiang Y, Gao XP (2016) Improving the photovoltaic performance of perovskite solar cells with acetate. *Sci Rep* 6:38670
16. Shen C, Courté M, Krishna A, Tang S, Fichou D (2017) Quinoidal 2,2',6,6'-tetraphenyl-dipyranylidene as a dopant-free hole-transport material for stable and cost-effective perovskite solar cells. *Energy Technol* 5:1852–1858
17. Wolff CM, Zu F, Paulke A, Toro LP, Koch N, Neher D (2017) Reduced interface-mediated recombination for high open-circuit voltages in $\text{CH}_3\text{NH}_3\text{PbI}_3$ solar cells. *Adv Mater* 29:1700159

18. Xiao M, Huang F, Huang W, Dkhissi Y, Zhu Y, Eheridge J, Gray-Weale A, Bach U, Cheng Y-B, Spiccia L (2014) A fast deposition-crystallization procedure for highly efficient lead iodide perovskite thin-film solar cells. *Angew Chem Int Ed* 53:9898–9903
19. Liu Z, Lee E-C Solvent engineering of the electron transport layer using 1,8-diodooctane for improving the performance of perovskite solar cells. *Org Electron* 24:101–105
20. You J, Yang YM, Hong Z, Song T-B, Meng L, Liu Y, Jiang C, Zhou H, Chang W-H, Li G, Yang Y (2014) Moisture assisted perovskite film growth for high performance solar cells. *Appl Phys Lett* 105:183902
21. Qing J, Chandran H-T, Cheng Y-H, Liu X-K, Li H-W, Tsang S-W, Lo M-F, Lee C-S (2015) Chlorine incorporation for enhanced performance of planar perovskite solar cell based on lead acetate precursor. *ACS Appl Mater Interfaces* 7:23110–23116
22. Li C, Guo Q, Wang Z, Bai Y, Liu L, Wang F, Zhou E, Hayat T, Alsaedi A, Tan ZA (2017) Efficient planar structured perovskite solar cells with enhanced open-circuit voltage and suppressed charge recombination based on a slow grown perovskite layer from lead acetate precursor. *ACS Appl Mater Interfaces* 9:41937–41944
23. Liu Y, Liu Z, Lee E-C (2018) Dimethyl-sulfoxide-assisted improvement in the crystallization of lead-acetate-based perovskites for high-performance solar cells. *J Mater Chem C* 6:6705–6713(2018)
24. Zhang Z, Zheng W, Lin R, Huang F (2018) High-sensitive and fast response to 255 nm deep-UV light of $\text{CH}_3\text{NH}_3\text{PbX}_3$ ($\text{X}=\text{Cl}, \text{Br}, \text{I}$) bulk crystals. *R Soc Open Sci* 5:180905
25. Hsu HP, Li LC, Shellaiah M, Sun KW (2019) Structural, photophysical, and electronic properties of $\text{CH}_3\text{NH}_3\text{PbCl}_3$ single crystals. *Sci Rep* 9:13111
26. Studenyak I, Kranjec M, Kurik M (2014) Urbach rule in solid state physics. *Int J Opt Appl* 4:76–83
27. Wang ZK, Li M, Yang YG, Hu Y, Ma H, Gao XY, Liao LS (2016) High efficiency Pb–In binary metal perovskite solar cells. *Adv Mater* 28:6695–6703
28. Nandi P, Giri C, Swain D, Manju U, Topwal D (2019) Room temperature growth of $\text{CH}_3\text{NH}_3\text{PbCl}_3$ single crystals by solvent evaporation method. *Cryst Eng Commun* 21:656–661
29. Zheng E, Yuh B, Tosado GA, Yu Q (2017) Solution-processed visible-blind UV-A photodetectors based on $\text{CH}_3\text{NH}_3\text{PbCl}_3$ perovskite thin films. *J Mater Chem C* 5:3796–3806
30. Zhang Z, Ren L, Yan H, Guo S, Wang S, Wang M, Jin K (2017) Bandgap Narrowing in bi-doped $\text{CH}_3\text{NH}_3\text{PbCl}_3$ perovskite single crystals and thin films. *J Phys Chem C* 121:17436–17441
31. Tetsuka H, Shan YJ, Tezuka K, Imoto H, Wasa K (2005) Transparent conductive In-doped Cd_3TeO_6 thin films with perovskite structure deposited by radio frequency magnetron sputtering. *J Mater Res* 41:2256–2260
32. Balachandran U, Odekkirk B, Eror NG (1982) Electrical conductivity in calcium titanate. *J Solid State Chem* 41:185–194
33. Piskunov S, Heifets E, Eglitis RI, Borstel G (2004) Bulk properties and electronic structure of SrTiO_3 , BaTiO_3 , PbTiO_3 perovskites: an ab initio HF/DFT study. *Comput Mater Sci* 29:165–178
34. Kumar A, Balasubramaniam KR, Kangsabanik J, Vikram, Alam A (2016) Crystal structure, stability, and optoelectronic properties of the organic-inorganic wide-band-gap perovskite $\text{CH}_3\text{NH}_3\text{BaI}_3$: candidate for transparent conductor applications. *Phys Rev* 94:180105–180110

Robust Gunshot Features and Its Classification Using Support Vector Machine for Wildlife Protection



Vivek Singh, Kailash Chandra Ray, and Somanath Tripathy

Abstract In the present study, automatic gunshot sound event detection in forest areas for wildlife protection has been considered. The feature extraction method used is robust to any length of gunshot sound events, which also takes care of the burst of multiple gunshots. First, low-level DWT-based features of large dimension were extracted which projected onto high-level histogram feature vector of small dimension using the bag-of-words approach. Support vector machine (SVM) classifier was considered to classify input audio signals into gunshot or forest ambience. The obtained results are highly reliable with a classification accuracy of 96.04% and area under ROC curve of 0.9866 indicating low false alarming rate. Automatic audio event detection can effectively expand the overall consistency of forest surveillance systems.

Keywords Wildlife protection · Gunshot detection · Discrete wavelet transform · Support vector machine

1 Introduction

Gunshot sound is a vital component of the acoustic world which conveys a situation of emergency for both legal and medical teams. In this paper, a wildlife protection system using automatic detection of gunshot sound event has been considered. Poaching using a firearm is pervasive all over the world. Continuous monitoring of forest areas for such criminal activities using a piece of audio information is the main aim of this study. Gunshot being an impulsive sound event which lasts only for few milliseconds is more challenging to detect than the sustained sound events.

V. Singh (✉) · K. C. Ray (✉) · S. Tripathy
Indian Institute of Technology, Patna, India
e-mail: vivek.pe16@iitp.ac.in

K. C. Ray
e-mail: kcr@iitp.ac.in

S. Tripathy
e-mail: som@iitp.ac.in

In [1], Clavel et al. detected alarming events using GMMs in two steps: in the first step, detected whether sound is alarming or normal and in the second step, it classifies alarming sound into category of shot (e.g. gunshot, rifle shot, etc.), but the results obtained cannot be generalized. Gerosa et al. in [2] also used two classifiers-based approach, respectively, for scream and gunshot against background sound and achieved an accuracy of 93% with very high false rejection rate of 5%. In [3], Chacon et al. compared six gunshot detection algorithm and concluded that feature obtained from discrete wavelet transform performs best. George et al. in [4] reported the advantages of audio analysis using DWT for non-speech signals. In [5], Rabaoui et al. used one-class wavelet base audio feature with SVM and achieved an accuracy of 96.89%. Pittner and Kamarthi in [6] reported how wavelet coefficients could be used for feature extraction of variable length audio events. In [7], Istrate et al. extracted audio feature using wavelet decomposition for telemonitoring medical application and reported a false alarm rate of only 3%. In [8], Oltean et al. extracted audio features based on DWT for detecting alarming event for forest application, reported an accuracy of 95%; however, size of dataset used was very small to be generalized.

Reliable detection and classification of gunshot sound against the background need a robust feature extraction method which can be classified with low complexity machine learning models. In the proposed methodology, the discrete wavelet transform-based audio features were extracted which projected onto high-level histogram features. The classification is achieved using support vector machine classifier. The result shows quite an improvement compared to previously reported work on similar sound classes.

1.1 Existing Methods

Numerous feature extraction and classification methods have been worked upon in the field of automatic recognition of acoustic events. The feature extraction methods are used to highlight the similar features of intraclass sound, whereas discriminative features of inter-class sound. The goal is to achieve both by means of less coefficients. The feature extraction comprises the temporal domain [9], spectral or frequency domain [9], low-level audio descriptors [9], time–frequency [10], cepstral [10], Mel-scaled [5] for getting the prominent features from the acoustic signal. These features were used to train the machine learning model such as deep neural networks [11], RNN [11], CRNN [10], non-negative matrix factorization (NMF) [12], GMM-hidden Markov model (HMM) [13] and support vector machines (SVM) [14] to achieve automatic recognition of acoustic events. Mel-scaled-based audio feature extraction forms a valuable feature for audio classification and is the leading feature extraction technique in reported literature [13].

In our study, low-level time–frequency DWT-based features projected onto high-level histogram features using the bag-of-words approach are used as an audio feature. The proposed feature extraction technique has not been used for gunshot detection

task in any of the reported literature for comparable studies. The feature classification method was achieved using support vector machine (SVM), as SVM is lightweight classifier from hardware point. This study has been done in view of resource-constrained devices.

Paper is organized as follows: Sect. 2 describes the proposed methodology in detail, followed by the experimental procedure in Sect. 3. Gotten results are discussed in Sect. 4. Finally, we conclude the paper, followed by future suggestions in Sect. 5.

2 Proposed Methodology

The objective of the proposed methodology is to classify gunshot sound against the background sound, i.e. forest ambience. In this work, a sound that is assumed to be composed of the small atomic audio unit is considered. A bag-of-words approach, in which the audio to be classified represented by the histogram of occurrences of each atomic audio unit, is employed to form a high-level feature vector from low-level discrete wavelets transform (DWT) coefficients

The proposed architecture for gunshot classification consists of four stages: (a) DWT-based low-level audio features extraction, (b) unsupervised learning of basic audio units using K-means clustering algorithm, (c) high-level feature vector construction and (d) feature classification.

2.1 Dataset Pre-processing

Gunshot data considered in this paper is the subset of airborne [15] gunshot database. The considered gunshot data consists of 290 files of 21 different firearms. The number of gunshots present in each record varies from one event to ten events. Some recordings also contain a burst of multiple gunshots which ranges from two to eight in a row. Hence, this type of gunshot events is also taken care of in the study. Gunshot sound events were isolated to form a dataset of individual gunshot event. In total, the dataset contains 811 individual gunshot events. For background ambience noise, forest sound from freesound.org [16] database is considered, having a total ambience sound of 35 min. Impulsive sound events from forest ambience were extracted and segmented into the small-signal; in total, there were 1113 individual impulsive sound events belongs to forest ambience. Detail of dataset used is summed in Table 1.

Table 1 Detail of dataset used for this study

Class	Gunshot	Forest ambience
Total	811	1113

As audio data considered are obtained from different sources, standardization of data was required. All the dataset converted into single-channel resampled to 16 kHz and normalized in the range $[-1, 1]$.

2.2 DWT-Based Low-Level Features Extraction

An acoustic signal may show sudden changes contained in a few milliseconds. Accordingly, in order to take into account its short-time changeability, the audio stream is fractioned into small frames with 50% overlapping. Each frame is then decomposed using fast DWT into L sub-bands. The DWT analyses acoustic signal at several scales with a different resolution by decomposing the signal into a coarse approximation and detail information. The decomposition of the signal into different scales is achieved by sequential high-pass and low-pass filtering of the time-domain signal. In the fast DWT, only one-sided, i.e. approximated coefficients are decomposed further into sub-bands, whereas detailed coefficients remain intact. Mathematically, a single level of decomposition is expressed by Eq. 1a and 1b.

$$M_{\text{high}}[k] = \sum_n x[n].h[2k - n] \quad (1a)$$

$$M_{\text{low}}[k] = \sum_n x[n].l[2k - n] \quad (1b)$$

where $M_{\text{high}}[k]$ and $M_{\text{low}}[k]$ are the output of the highpass, $h[n]$ and low pass, $l[n]$ filters, respectively; after decimation by 2, the low-level feature vector of a single frame is obtained by appending coefficients of all levels.

2.3 Unsupervised Learning

Fixed set of audio units is achieved by using K-means clustering algorithm. The outcome of K-means clustering is a set of K points that relate to the centroids of the clusters. Each centroid represents a group of similar low-level vectors, and the set $C = \{c_1, \dots, c_K\}$ of the centroids is regarded as the dictionary of basic audio units.

2.4 A High-Level Histogram Feature Vector

Figure 1 depicts the method of building a high-level feature vector, given a dictionary C of cluster's centroids, for every low-level vector v_i , the nearest audio unit c_j is determined. The frequency of each word c_j in a time-limited interval is used to

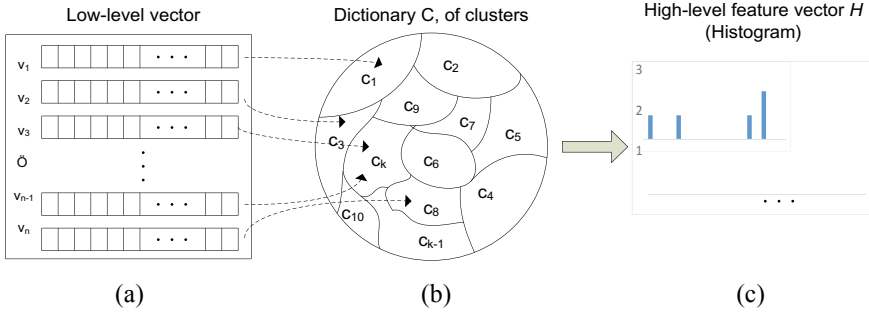


Fig. 1 Building of the high-level histogram feature vector. Every low-level vector v_i (a) is mapped to its closest atomic audio unit c_j in the dictionary (b). Then, the rate of the single atomic audio unit is stored in a histogram, having bins as h_j ($j = 1, \dots, K$) that contains the high-level feature vector (c)

construct a high-level feature vector. Such vector corresponds to the histogram $H = (h_1, \dots, h_K)$, whose bins are computed as:

$$h_j = \sum_{i=1}^M \delta(b_i, j), \quad j = 1, \dots, K \quad (2)$$

where $\delta(\cdot)$ is the Kronecker delta, and b_i is the index of a word within the set C , determined as:

$$b_i = \arg \min_j d(v_i, c_j), \quad j = 1, \dots, K \quad (3)$$

where $d(v_i, c_j)$ is a dissimilarity measure between the vector c_j and the prototype v_i (the Mahalanobis distance is considered).

2.5 Classification

Support vector machine (SVM) is a binary discriminative classifier. In the SVM classification scheme, the selection of the kernel function parameter is entirely data-dependent and chosen empirically. This paper considers the radial basis function (RBF) kernel for implementing SVM approach to classify the gunshot sound events against the forest ambience signals. The RBF kernel is represented by the expression as $(K(x_i, x_j) = \exp^{-\gamma \|x_i - x_j\|^2})$. The regularization parameter C and kernel function argument parameter γ of the classifier are varied in the range of $[2^{-5}, 2^{10}]$ and $[2^{-10}, 2^5]$, respectively, and optimized using PSO [14] technique. In this paper, two classes have been considered, i.e. gunshot and forest ambience, which required only one SVM to be trained. The high-level histogram feature vectors were utilized for training

SVM model. The SVM classifier is particularly suited for the employed acoustic representation since it is able to learn the words that are relevant for a particular class of events and discard that do not contribute to an useful classification, by giving them a little weight. The parameters of the classifier, i.e. C and γ , are slowly tuned using the PSO algorithm in the training phase. The fivefold cross-validation is performed on the training dataset, with the preeminent learning parameter values of C and γ to yield the maximum classification performance. The testing is conducted on the testing dataset, and the performance is presented in the form of the confusion matrix

3 Experiment

The experiment was conducted on detecting gunshot sound events against the background noise, i.e. forest ambience sound. Our approach consists of six stages, viz. pre-processing, low-level DWT feature extraction, K-means clustering, high-level histogram feature extraction, training SVM model and testing. The pre-processing step is discussed in Sect. 2.1.

The training dataset was utilized to obtain the cluster centres using K-means clustering algorithm. First, low-level features of small audio segment, i.e. frame, were extracted. The population of frames kept very high as each frame act as an atomic audio unit. Next paragraph discusses how these atomic audio units are extracted. Every signal in training dataset undergoes proceeding steps.

One signal at a time is taken from the training dataset and segmented into small overlapping (50% hopping with adjacent frames) frames of 16 ms duration, i.e. 256 sample points for 16 kHz sampled signal. Next, each frame undergoes five-level DWT decomposition using *Daubechies4* wavelet. As the number of coefficients varies with levels, a uniform low-level feature vector was obtained by appending coefficients of all five levels together to form a single long feature vector of a frame. This procedure was repeated for all the frames of the signal (Fig. 2).

After performing the above procedure to all the signals from a training dataset of, we get a considerable number of data for unsupervised learning. Unsupervised

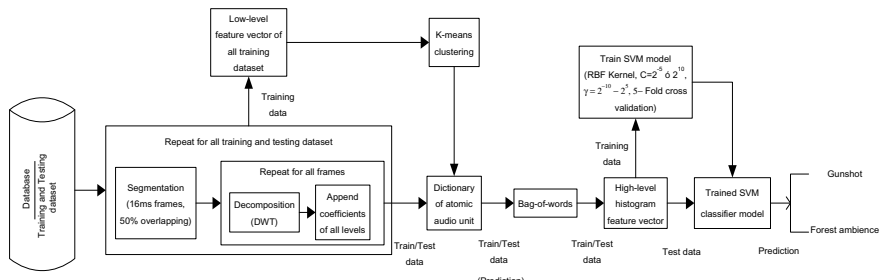


Fig. 2 Block diagram representation of the proposed method

learning treats all the frame-level feature vectors as an individual signal; i.e. K-means clustering algorithm sees all frames as individual signals having a feature vector of length 288. The database is split into a 50/50 manner for training and testing dataset, respectively. $K (= 20)$ number of clusters centre were learned out of the given dataset.

For training the SVM model in a supervised manner, the same training dataset containing individual gunshot events and forest ambience sound was considered. High-level histogram features were extracted out of individual signal. The dimension of the high-level feature vector is the same as the number of clusters. High-level histogram features were obtained by first decomposing the signal using DWT and preparing a feature vector out of it the same as for unsupervised learning. After getting a low-level feature matrix of an individual signal of dimension ($a \times 288$); a may vary with the length of the audio event, each a vector of dimension 288 is predicted for its cluster number. The output of the prediction has a dimension of ($a \times 1$); i.e. each a vector is now representing by its cluster number. The histogram is formed for a percentage of weight-age each cluster has in the particular audio event. The final dimension of the feature vector or the high-level histogram feature is (20×1). After obtaining a high-level histogram feature vector for the whole training dataset, supervised learner, i.e. a support vector machine, is trained as a binary classifier.

For testing purpose, the test dataset is considered. High-level histogram features were extracted and fed into the SVM classifier. The output shows a promising result with a respectable detection accuracy of 96.98%. The main concern in the surveillance-based application is a false alarming rate. The proposed method shows a false alarming rate of only 1.34%, which can be considered as a significant result.

4 Results and Discussion

For training the SVM model, 50%, i.e. 964, of the total available dataset was used. In terms of the number of signals for each class, i.e. forest ambience and gunshot event, 576 and 388, respectively. Fivefold cross-validation was taken into consideration. An SVM model is optimized using particle swarm optimization algorithm. The value for $C = 8$ and $\gamma = 7$ shows an optimum result. Classifier model is trained with an accuracy of 97.19%. Testing data consists of 547 signals for forest ambience and 414 signals for gunshot events. The testing accuracy obtained was 96.04%, which can be considered as remarkable for the amount of dataset. Receivers operating characteristic (ROC) curve as shown in Table 2 under 50/50 data split is also computed; the area under the ROC curve of 0.9884 indicates a low false alarm rate and high true positive rate.

The experiments were also conducted for different sizes of training, and testing dataset splits from the original database. Table 2 sums the results, i.e. confusion matrix and ROC curve of all the different splits. From Table 2, it is observed that, as we increase the size of training data, the accuracy of the proposed methodology does not vary much. Also, improvement in area under ROC curves is not significant for a different number of training examples. Hence, conclusion from the above observation

Table 2 Confusion matrix and ROC curve for different dataset splits

Train/Test	Confusion matrix	ROC curve
50/50	$\begin{matrix} F & G \\ F & 0.96 \ 0.04 \\ G & 0.04 \ 0.96 \end{matrix}$	<p>ROC curve (area = 0.9884)</p>
60/40	$\begin{matrix} F & G \\ F & 0.96 \ 0.04 \\ G & 0.06 \ 0.94 \end{matrix}$	<p>ROC curve (area = 0.9877)</p>
70/30	$\begin{matrix} F & G \\ F & 0.97 \ 0.03 \\ G & 0.06 \ 0.94 \end{matrix}$	<p>ROC curve (area = 0.9887)</p>
80/20	$\begin{matrix} F & G \\ F & 0.98 \ 0.02 \\ G & 0.04 \ 0.96 \end{matrix}$	<p>ROC curve (area = 0.9997)</p>

is that, the proposed feature extraction technique is robust to the size of the training dataset.

The proposed method is independent of the length of the audio events. In gunshot dataset, the length of events varies from 100 to 1200 ms. The proposed model sees all gunshot events as equal length by extracting histogram features, as discussed in Sect. 2.4. The dataset is split in such a way that 8 firearm models are not included in the training set. Though the above constraint, the proposed methodology robustly detects the event into the gunshot class. Thus, our model can be generalized for the completely unseen firearm sounds. In training as well as in testing datasets, a burst of gunshot firing sound is also included. In the testing phase, the proposed system successfully detected all the ten signals of burst gunshot sounds.

5 Conclusion and Future Work

This paper proposes a gunshot detection system against the background sound of forest ambience; for wild areas, surveillance is based on DWT features projected onto high-level histogram features and recognized with support vector machine classifier. In our approach, we have considered that an event has already been detected blindly from the continuous recording, and the audio segment is fed into the proposed system. The detection accuracy of 96.04% with area under ROC curve of 0.9866 was achieved for 50% - 50% split of an available dataset for training and testing, respectively. As future work, authors are working on detection of gunshot events with different SNR from forest ambience.

Acknowledgements MeitY, Government of India, New Delhi, partially supports this work through the project titled ‘Special Manpower Development Program for Chips to System Design’ underneath project reference no. R&D/SP/EE/DEITY/SMD/2015-16/126 and Visvesvaraya PhD Scheme.

References

1. Clavel C, Ehrette T, Richard G (2005) Events detection for an audio-based surveillance system. In: 2005 IEEE international conference on multimedia and expo, Amsterdam, pp 1306–1309
2. Valenzise G, Gerosa L, Tagliasacchi M, Antonacci F, Sarti A (2007) Scream and gunshot detection and localization for audio-surveillance systems. In: 2007 IEEE conference on advanced video and signal based surveillance, London, pp 21–26
3. Chacon-Rodriguez A, Julian P, Castro L, Alvarado P, Hernandez N (2011) Evaluation of gunshot detection algorithms. *IEEE Trans Circ Syst I Regul Pap* 58(2):363–373
4. Tzanetakis G, Essl G, Cook P (2001) Audio analysis using the discrete wavelet transform. In: Proceedings of conference on acoustics and music theory applications, Sept 2001
5. Rabouai A, Davy M, Rossignol S, Ellouze N (2008) Using one-class SVMs and wavelets for audio surveillance. *IEEE Trans Inf Forensics Secur* 3(4):763–775
6. Pittner S, Kamarthi SV (1999) Feature extraction from wavelet coefficients for pattern recognition tasks. *IEEE Trans Pattern Anal Mach Intell* 21(1):83–88
7. Istrate D, Castelli E, Vacher M, Besacier L, Serignat J (2006) Information extraction from sound for medical telemonitoring. *IEEE Trans Inf Technol Biomed* 10(2):264–274
8. Oltean G, Grama L, Ivanciu L, Rusu C (2015) Alarming events detection based on audio signals recognition. In: 2015 International conference on speech technology and human-computer dialogue (SpeD), Bucharest, pp 1–8
9. Mesaros A, Heittola T, Virtanen T (2016) Metrics for polyphonic sound event detection. *Appl Sci* 6(6), Article 162
10. Mesaros A et al (2018) Detection and classification of acoustic scenes and events: outcome of the DCASE 2016 challenge. *IEEE/ACM Trans Audio Speech Lang Process* 26(2):379–393
11. Adavanne S, Politis A, Nikunen J, Virtanen T (2019) Sound event localization and detection of overlapping sources using convolutional recurrent neural networks. *IEEE J Sel Top Signal Process* 13(1):34–48
12. Komatsu T, Toizumi T, Kondo R, Senda Y (2016) Acoustic event detection method using semi-supervised non-negative matrix factorization with a mixture of local dictionaries. In: DCASE 2016 challenge, technical report, Sept 2016

13. Sigtia S, Stark AM, Krstulovi S, Plumbley MD (2016) Automatic environmental sound recognition: performance versus computational cost. IEEE/ACM Trans Audio Speech Lang Process 24(11):2096–2107
14. Raj S, Ray KC (2017) ECG signal analysis using DCT-based DOST and PSO optimized SVM. IEEE Trans Instrum Meas 66(3):470–478
15. <https://www.airbornesound.com/>
16. <https://freesound.org/>

Effect of pH Variations on Zinc Oxide (ZnO) Nanowire Dispersions



Vimal Kumar Singh Yadav and Roy Paily

Abstract This work analyses the effect of pH variations on the morphological properties and dimensional modulation of ZnO nanowires (NWs) aqueous dispersions in de-ionized (DI) water. To observe the effect of lower pH values, different sets of ZnO nanowire dispersions (NWD) have been prepared and a certain amount of drop-casted dispersion has been added with acetic acid, hydrochloric acid (HCl) and sulphuric acid respectively. Further, ammonium hydroxide has been added in the same proportion as the aqueous ZnO NWD to observe the effect of higher pH values. Such a study can be instrumental in the development of ZnO NWDs consisting of well separated, sharp-edged and long nanowires for the fabrication of single-nanowire based electronic devices, which can be applied as sensors, energy harvesters or display units.

Keywords Zinc oxide · Nanowire · pH · Dispersion

1 Introduction

Zinc oxide (ZnO) nanowires (NWs) have been deeply researched due to their unique and attractive material properties, which are being employed in the field of electronics, optics, energy harvesting, and so on [1–3]. ZnO NWs are generally synthesized over the substrate using vapour–liquid–solid (VLS) method with the help of chemical vapour deposition (CVD), laser ablation method, atomic layer deposition (ALD), hydrothermal or solvothermal techniques and so on [4–8]. However, most of the above-mentioned methods use some kind of catalyst or auxiliaries that leads to residual contamination of ZnO NWs [4].

V. K. S. Yadav (✉) · R. Paily

Department of Electronics and Electrical Engineering, Indian Institute of Technology Guwahati, Guwahati, Assam, India

e-mail: vimal.yadav@iitg.ac.in

R. Paily

e-mail: roypaily@iitg.ac.in

Therefore, more efficient method of ZnO NW synthesis requires a contamination-free process that does not alter the original properties of a NW. Shih et al. have reported the synthesis of a ZnO single NW (SNW) using a Ti-assisted CVD in order to avoid catalytic contamination which can control the dimensions of NWs with the help of a diffusion phenomenon taking place during the fabrication process [4]. Lupan et al. have reported the low-temperature solution-based synthesis of Au-modified ZnO NWs with a diameter varying in the range of 10–100 nm [8]. Similarly, Galan et al. have used atomic layer deposition (ALD) to grow ZnO seed layers followed by chemical bath deposition (CBD) of ZnO NWs to produce uniform single crystal ZnO NWs in low-cost [9].

In this work, the effect of acid (lower pH variations) and base addition (higher pH variations) to DI water-based ZnO nanowire-dispersion on the morphology of ZnO NWs, especially on ZnO single-nanowire (SNW) (width or diameter of ZnO wire <500 nm) or single micro-wire (SMW) (width or diameter of ZnO wire >500 nm) is investigated. For this purpose, a commercial ZnO NW powder has been purchased and an optimized dispersion has been prepared utilizing DI water as a dispersion medium and several drops of the prepared dispersion have been drop-casted in μL volume on a cleaned SiO₂/Si substrate and different acids and base have been added to this drop-casted dispersion drop in varied proportions. The optimized acid proportion helps to form sharp-edged and longer ZnO SNW and SMW which can be efficiently used to fabricate discrete electronic components such as micro-resistors, Schottky diodes, and so on [10].

2 Materials and Methods

2.1 Dispersion Preparation

For all the experiments, ZnO Nanowire powder is procured from Sigma Aldrich (Product Id: 773999) and a low surface-tension DI (LST-DI) water is prepared simply by adding 1 mg of sodium dodecyl sulfate (SDS) to 5 mL of DI water to improve the dispersibility of ZnO NWs in the aqueous dispersion as shown in Fig. 1. ZnO NW dispersion is prepared by adding 2 mg of ZnO NW powder in 1200 μL of LST-DI water. The reason to experiment with a very small concentration of ZnO NW dispersion in ‘ μL ’ level as compared to ‘mL’ level is to keep the density of ZnO NWs high so that the effect of acids can be observed clearly. 2 μL of above prepared ZnO NW dispersion is drop-casted on to a cleaned silicon substrate and the initial image is captured with the camera of a Material Printing System (MPS) [11].

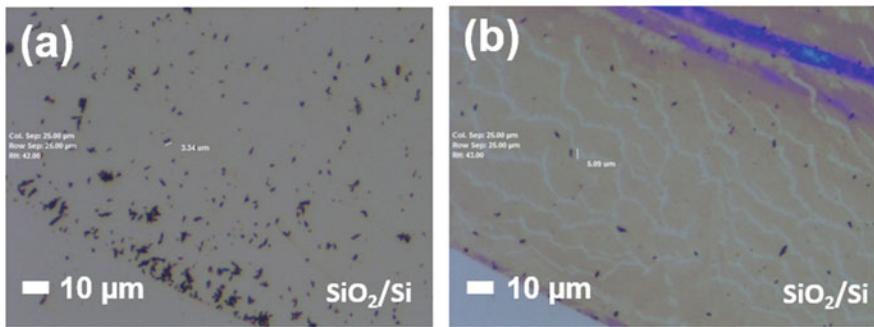


Fig. 1 Optical image showing a portion of ZnO NW dispersion drop in **a** DI water only **b** DI water + SDS after heating. ZnO NWs are in black color

3 Results and Discussion

3.1 Effect of Acid Addition to ZnO NW Dispersion in LST-DI Water

The drop-casted ZnO NW dispersion is in white color as seen from naked eyes. Then, 2 μL of acetic acid, hydrochloric acid (HCl) and sulphuric acid (H₂SO₄) is added to the already drop-casted ZnO NW dispersion to keep the proportion same (1:1). It is observed that (H₂SO₄) dissolves ZnO NWs in all the proportions. HCl also partially dissolves ZnO NWs, however, these NWs turned into micro-particles when heated at ~220 °C as shown in Fig. 2.

When acetic acid is added in 1:1 proportion with NW dispersion, it is observed that within a few seconds, the white color of the dispersion changes to colorless and transparent like LST-DI water as shown in Fig. 3a, b. The ZnO SNW with length <10 μm is almost invisible at this scale as shown in Fig. 3b. Further, acetic acid is

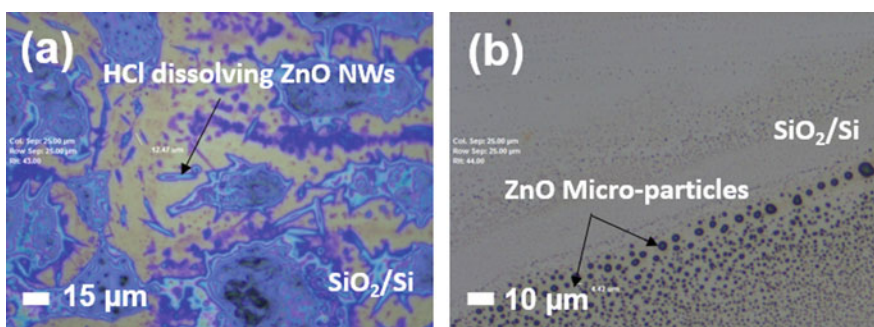


Fig. 2 Optical image showing **a** HCl partially dissolving ZnO NWs **b** NWs converted to micro-particles at high temperatures

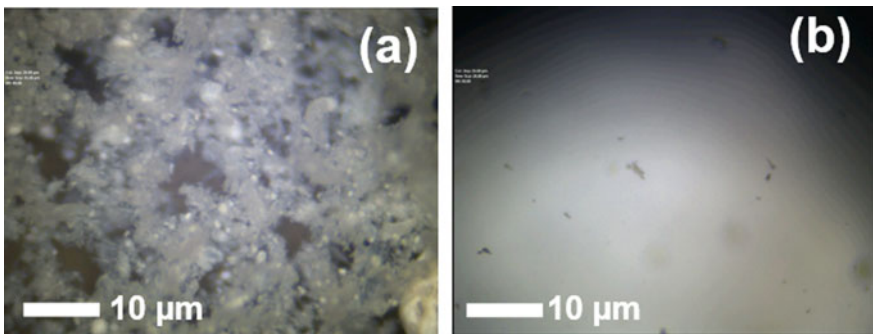


Fig. 3 Optical image showing a portion of 2 μL drop-casted ZnO NW dispersion **a** without acetic acid **b** with acetic acid in 1:1 proportion

added in different volume proportions such as 1:1 (0.5 μL acetic acid in 0.5 μL of NW dispersion), 1:10 (0.5 μL acetic acid in 5 μL of NW dispersion) and 1:40 (0.5 μL acetic acid in 20 μL of NW dispersion) as shown in Fig. 4. It is observed that acetic acid addition to ZnO NW dispersion in different proportions is resulting in long and sharp-edged NWs and therefore has the capability to modulate the morphology of already synthesized ZnO NWs due to its different pH range as compared to H₂SO₄ or HCl [12–14].

It is also observed that acetic acid dissolved all the ZnO NWs in those dispersions in which SDS is not added. This is strong evidence that the, it is the combination of acetic acid and SDS in a proper ratio is mainly responsible for the creation of

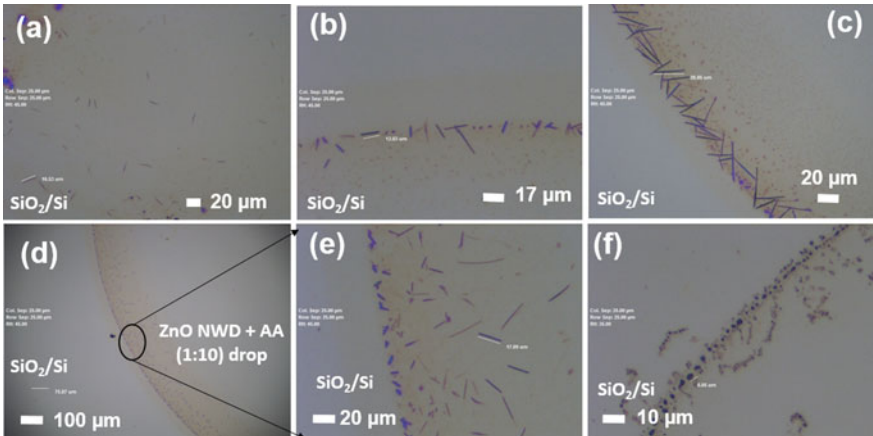


Fig. 4 Optical image showing sharp and long ZnO micro-wires formation after acetic acid addition in **a** 1:1 **b** 1:10 **c** 1:40 proportion **d** 1:10 drop periphery **e** zoomed-in image of encircled region in **d**, **f** ZnO nanowires converting to micro-particles at higher temperatures. AA: acetic acid NWD: NW dispersion

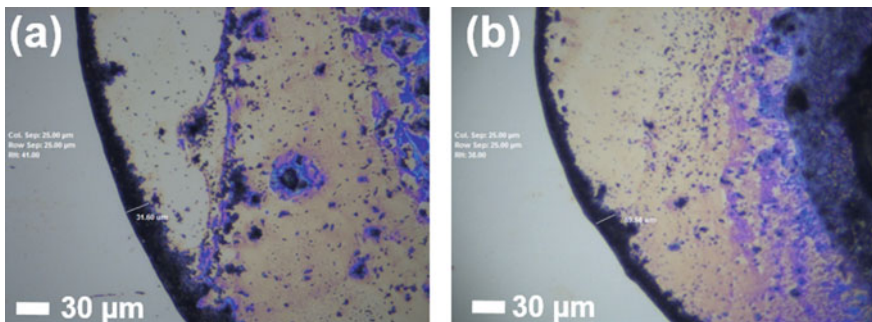


Fig. 5 Optical image showing the formation of ZnO NW mat-cluster ring after NH₄OH addition to ZnO NW aqueous dispersion in **a** 1:20 **b** 1:40 after heating the drop at 180 °C

long, sharp-edged, and highly distinguishable ZnO NWs [15, 16]. However, the dispersion containing acetic acid also converts nanowires and micro-wires into ZnO micro-particles when exposed to high temperatures near ~220 °C as shown in Fig. 4f.

3.2 Effect of Base Addition to ZnO NW Dispersion in LST-DI Water

To observe the effect of adding base (higher pH substance) on the morphology of ZnO NWs, 0.5 μL of ammonium hydroxide (NH₄OH) was added in 0.5 μL (1:1), 10 μL (1:20) and 20 μL (1:40) of ZnO aqueous dispersion (1 mL DI water + 3 mg ZnO NW powder). As observed from the optical images taken from MPS microscope, NH₄OH shows no tendency to either dissolve the NWs or separate them. It forms a ring of ZnO NW mat-cluster of width near 25–50 μm with small, single, and unmodified ZnO NWs scattered randomly along the periphery of the ring as shown in Fig. 5. The width of NW cluster ring increases from ~32 to 60 μm with a dilution ratio, as shown in Fig. 5a, b.

4 Conclusion

This work studies the effect of acetic acid, HCl, H₂SO₄ (acids), and NH₄OH (base), on the morphological changes of ZnO NWs in aqueous dispersions. It is observed that acetic acid with SDS in 1:40 to 1:1 proportion with ZnO NW aqueous dispersion, for ZnO NWD drop-casted volume up to 5 μL, is optimized for ZnO single-nanowire or single micro-wire formation. It is observed that HCl turns NW to micro-particles at high temperature and H₂SO₄ dissolve ZnO NWs completely. ZnO NW micro-mat is formed by the addition of ammonium hydroxide in ZnO NW dispersion in

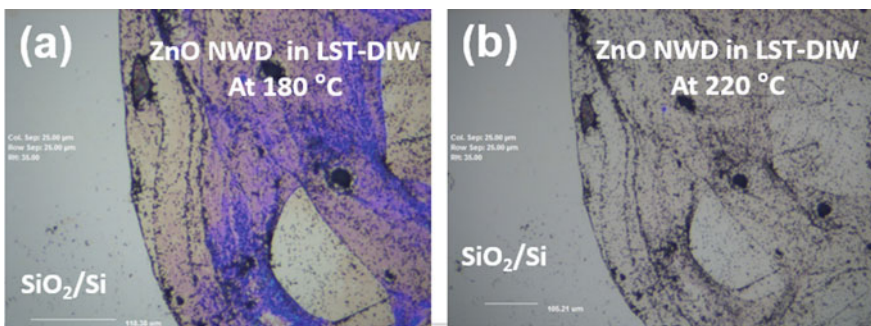


Fig. 6 Optical image showing the effect of annealing temperature on ZnO NWs at **a** 180 °C **b** 220 °C

LST-DI water. The ZnO NWs show appreciable, thermal, and structural stability, at temperatures ~220 °C as shown in Fig. 6a, b.

References

- Zhang Y, Ram MK, Stefanakos EK, Goswami DY (2012) Synthesis, characterization, and applications of ZnO nanowires. *J Nanomater* 2012:22
- Pan ZW, Dai ZR, Wang ZL (2001) Nanobelts of semiconducting oxides. *Science* 291(5510):1947–1949
- Poulin-Vittrant G, Dahiya AS, Boubenia S, Nadaud K, Morini F, Justeau C, Alquier D (2019) Challenges of low-temperature synthesized ZnO nanostructures and their integration into nano-systems. *Mater Sci Semicond Process* 91:404–408
- Shih P-H, Wu S (2017) Growth mechanism studies of ZnO nanowires: experimental observations and short-circuit diffusion analysis. *Nano-materials* 7(7):188
- Shih HY, Chen TT, Chen YC, Lin TH, Chang LW, Chen YF (2009) Size-dependent photoelastic effect in ZnO nanorods. *Appl Phys Lett* 94(2):021908
- Jung M-H, Chu M-J (2014) Synthesis of hexagonal ZnO nanodrums, nanosheets and nanowires by the ionic effect during the growth of hexagonal ZnO crystals. *J Mater Chem C* 2:6675–6682
- Chu Y, Wan L, Wang X, Zhang J (August, 2012) Synthesis and characterization of ZnO nanowires by solvothermal method and fabrication of nanowire-based ZnO nanofilms, pp 366–369
- Lupan O, Postica V, Wolff N, Su J, Labat F, Ciofini I, Cavers H, Adelung R, Polonsky O, Faupel F, Kienle L, Viana B, Paupert T (2019) Low-temperature solution synthesis of Au-modified ZnO nanowires for highly efficient hydrogen nanosensors. *ACS Appl Mater Interfaces* 11(35):32 115–32 126
- Galan-Gonzalez A, Gallant A, Zeze DA, Atkinson D (May, 2019) Controlling the growth of single crystal ZnO nanowires by tuning the atomic layer deposition parameters of the ZnO seed layer. *Nanotechnology* 30(30):305602
- Yadav VKS, Natu G, Paily R (2020) Fabrication and electrical characterization of printed micro-resistors of silver nanoparticles using micro-cantilever based printing technology. *IEEE Trans Compon Packaging Manuf Technol* 10(1):57–64
- BioForce Nanosciences. Accessed April 10, 2019. Available: www.bioforcecenario.com
- S. Edinger, J. Bekacz, M. Richter, R. Hamid, R. Wibowo, A. Pei, and T. Dimopoulos.: Influence of the acetic acid concentration on the growth of Zinc oxide thin films prepared by spray pyrolysis of aqueous solutions," *Thin Solid Films*, vol. 594, pp. 238 – 244, (2015)

13. Jiao B, Zhang X, Wei C, Sun J, Huang Q, Zhao Y (2011) Effect of Acetic acid on ZnO: in transparent conductive oxide prepared by ultrasonic spray pyrolysis. *Thin Solid Films* 520(4):1323–1329
14. Biswal R, Maldonado A, Vega-Perez J, Acosta D, De La Luz Olvera M (2014) Indium doped zinc oxide thin films deposited by ultrasonic chemical spray technique, starting from zinc acetylacetone and indium chloride. *Materials* 7(7):5038–5046
15. Wa Yu H, Wang J, An Yan X, Wang J, Fei Cheng P, Juan Xia C (2019) Effect of surfactants on the morphology and photocatalytic properties of ZnO nanostructures. *Optik.* 185:990–996
16. Usui H (2009) The effect of surfactants on the morphology and optical properties of precipitated wurtzite ZnO. *Mater Lett* 63(17):1489–1492

Intensity Modulated U-Shaped Bent Tapered Optical Fiber Concentration Sensor



Putha Kishore, D. Dinakar, Manchineellu Padmavathi, and L. Obulapathi

Abstract In this paper, a liquid concentration (viscosity) sensor is designed and developed at a low cost using a clad removed U-shaped bent plastic optical fiber (POF). A small portion of POF cladding is removed and bends to form a U-shaped probe for an optimized radius to improve the sensitivity of parameter measurement. The probe is immersed in a viscous liquid, then the interaction of the evanescent field with the ambient viscous liquid in both forward and reverse directions movements of the liquid were recorded. As the probe dipped slowly in and out of the liquid an offset is observed in the response of the sensor, it can be measured as the hysteresis loss in the loop. The offset has been measured in both horizontal (Distance) and vertical (Intensity) directions. The experimental results reveal that the sensor is highly linear with about 0.98 linearities. From the results, It is observed that intensity offset measurement is more suitable than distance offset owing to high sensitivity. Thus, the concentration (or viscosity) of the liquid can be measured using the proposed simple sensor in terms of the offset height and hysteresis area. This sensor is easy to make, simple, low cost, and had inherent advantages of the optical fiber like Immune to EMI, corrosive, small size, flexibility in length. The sensor may found many applications in measuring the viscosities of fluids such as motor oils, petroleum products, chemical solvents, and many other industrial and biological fluids.

Keywords Plastic optical fiber · U-shaped bend · Intensity modulated · Concentration · Viscosity · Hysteresis area

P. Kishore · L. Obulapathi

Department of H&S, Annamacharya Institute of Technology and Science, Rajampet, Kadapa, India

e-mail: kishore.photonics@gmail.com

D. Dinakar (✉)

Department of Physics, National Institute of Technology Warangal, Warangal, India
e-mail: dinakar.anu@gmail.com

M. Padmavathi

Department of Physics, SKR and SKR Government Degree College for Women, Kadapa, India
e-mail: paddu.manchi@gmail.com

1 Introduction

Analysis of the liquid viscosity or concentration enables to open new era applications especially in the fields of Biomedical, chemical, and petroleum industries. The viscosity of a fluid is basically a measure of how sticky it is, and for liquid, it corresponds to the informal concept of thickness also called concentration. Liquid concentration measurement would provide indirect clues for liquid quality monitoring for safeguarding human health. The salinity of liquid is a very important parameter for Mariculture, prediction of climatic changes, Oceanic, marine liquid monitoring, drinking liquid monitoring similarly, blood glucose monitoring an essential task in monitoring the health condition of diabetic patients [1–3]. Thus, the measurement of viscosity has great significance for estimating liquids quality in biotechnology applications, blood protein concentration, salinity of urine, measuring concentrations of contagious chemicals, petrochemicals, and various industrial fluids. Viscometers which are well-established instruments in measuring the viscosity, their usage is limited by constraints such as their voluminous size, inability for remote monitoring applications, aging effects, and highly cost-effective [4, 5].

Several optical methods can be used to detect substance concentrations in an aqueous solution such as absorption, refraction, or a combination of both absorption and refraction of light by the solution. Substance concentration can be investigated more accurately by absorption principle rather than refraction principle in the solution. Here, when a viscous liquid interacts with the fiber guiding mechanism effects the light propagating in the fiber, which results in the change in the profile of the sensor response in forward and reverse directions owing to the viscosity of the liquids. Therefore, this principle of absorption often used to detect substance concentrations.

For the last few decades, fiber optic sensors are well advanced and becoming a substitute for conventional existing sensing technologies. Fiber optic-based sensors have been well known for their inherent advantages like low cost, immunity to electromagnetic interferences, adaptability to other systems, fast response [6, 7]. Many physical and chemical parameters such as displacement, pressure, high temperature, pH, and others were reported to be sensed by various fiber optic techniques. Many special designs in fiber optic sensors are reported for the dedicated application of liquid properties measurement [8–11]. Fiber optic sensor detection of substance concentration by utilizing changes of the substance concentration in solution which will change the refractive index of the solution resulted in the change of refraction direction. This principle has been used to detect the refractive index of chlorinated water and the concentration of the uric acid utilizing side micro bend fiber optic and tapered fiber. Based on the displacement sensor, detection of liquid refractive index, the concentration of liquid can be measured. Based on the displacement sensor, U-bent tapped optical fiber can also be applied to detect the substance concentration in a solution using the principles absorption light by liquid.

Among the many proposed methods, a U-shaped bent tapered fiber-optic intensity-modulated sensor is one of the new methods for sensing the viscosity of the liquids

[10, 12–16]. This sensor yields a switching of its output response when it is dipped into the liquid and taken out from the liquid. If it is closely observed, it gives a hysteresis-like nature of response during the dipping and taking out of the liquid process. From this, the concentration/viscosity of a given liquid can be measured. In this paper, we have explored the hysteresis nature of tapped U shaped bent fiber optic sensor to measure various liquid parameters like concentration, refractive index, and viscosity from the hysteresis nature. The liquid parameters give a linear response which can be taken as a novel way of sensing the properties.

2 Experimental Setup

A simple plastic optical fiber is used as a sensing element and it is bent to U-shape with a calibrated radius. Before using in the experiment the diameter of the sensor probe is calibrated for getting high sensitivity. The schematic experimental setup of the proposed system is shown in Fig. 1. Here, one end of the fiber is coupled with fiber-coupled LED source of 650 nm, $\frac{1}{2}$ watt power, and another end of the fiber is coupled with fiber-coupled matched silicon photodiode (PD). The output from the PD is connected to a digital multimeter via a photodetection circuit to convert the light intensity into an equivalent voltage signal. To enhance the sensing capability of the sensing probe for the applied viscous liquid with various concentrations, the cladding of the sensing area of the optical fiber is removed. The plastic optical fiber of dimensions of around 1470/1500 nm is used in this experiment so that the thickness of the clad is around 30 nm is very small. Clad is removed manually, enough care is taken for the precise dimension and uniformity, and a microscope is also used to verify the uniformity of the optical fiber. At the center of the length of POF, a small portion of about 2 cm the clad is removed. The prepared liquid is filled in a beaker and then it is placed under the sensor probe using a support that is holed with the help of a micro translation stage of precision 0.01 mm.

In this experiment, Glycerin liquid is prepared to study the response of the sensor with various concentrations for the measurement viscosity of the liquid. The Glycerin is mixed in the distilled water from 10 to 50% in volume with an increment of 10. The experiment is conducted with water in a forward direction (downward) that is dipped into the liquid from a fixed position for a distance of 12 mm in steps of 0.05 mm. After a few seconds the probe is removed in the reverse direction (upward) in the same manner as mentioned above. During both forward and reverse directions the intensity of light is measured through the multimeter in terms of voltage for 12 mm distance in steps of 0.05 mm. The experiment is repeated with various concentrations of Glycerin liquid and the sensor response is measured for the movement of the liquid beaker for both directions.

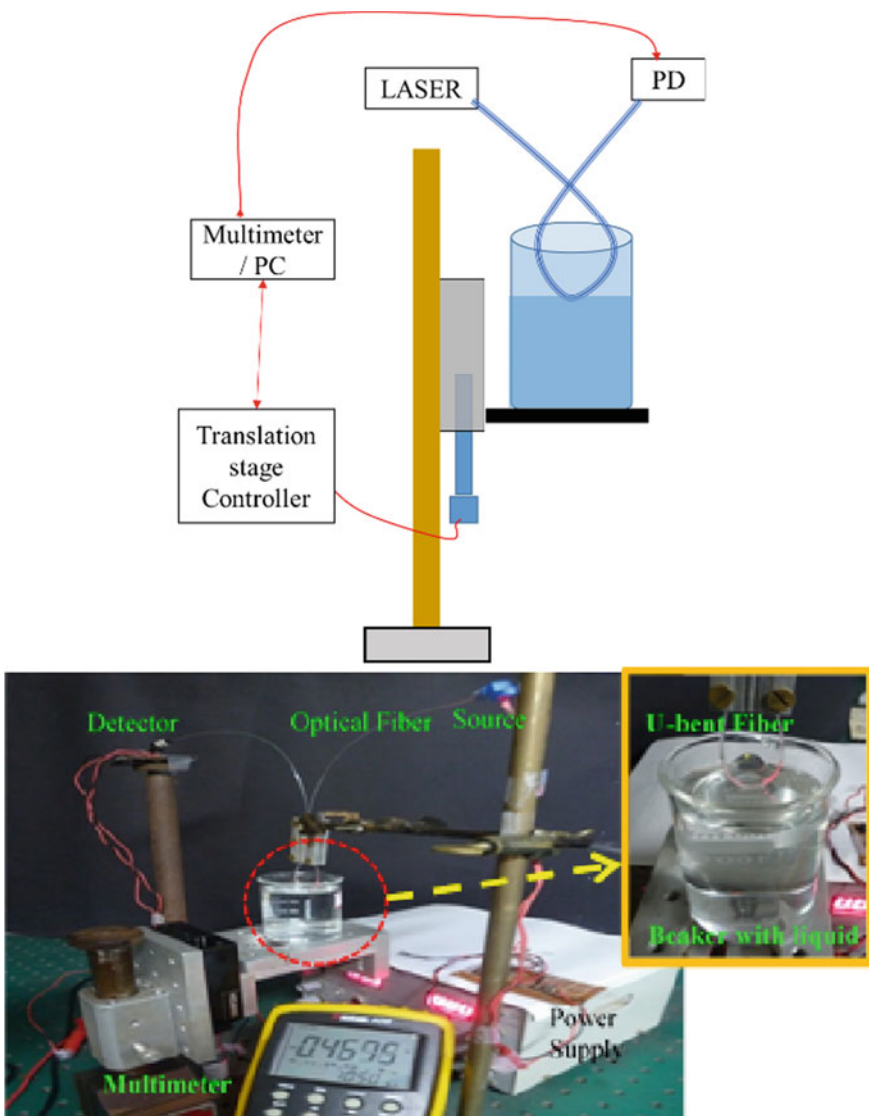


Fig. 1 Schematic and photograph of the experimental setup

3 Results and Discussion

The liquid sample attached to the tip of the sensor head because of the stickiness of the liquid owing to the viscosity. If the concentration (refractive index) of the glycerin solution is higher, then the liquid will stay more time with the sensor end of the u-bent fiber. As the liquid directly interacts with the light at a tapered portion of the fiber by

glycerin solution with higher concentration, causing the light refraction or scatter out from the fiber did not return to the sensing port of the fiber, so the intensity of light (in this case the value of the output voltage detectors) will be reduced. Thus, an increase in glycerin concentration will lead to a change in the value of the peak voltage in forward and reverse directions proximity measurement called intensity offset. Also, change in the distance for change of the intensity also called distance offset. It is clearly showing a hysteresis area between the two paths gives as a measurement of the concentration of liquid (glycerin). The response of the sensor is tested for water and glycerin with different concentrations by recording the sensor output with respect to the displacement of the sensor probe as shown in Fig. 2. It is clearly showing that owing to the viscosity of the liquid, the sensor response does not follow the same path while forward (dipping) and reverse (rising) movement of the liquid from the sensor. If we observe the sensor response for water, there is an offset in both coordinates of the axis. It represents the intensity of light originates with small change and fall of light intensity at different positions.

The offset of displacement for the glycerin liquid of various concentrations (viscosity) has been measured is illustrated in Fig. 3a. It is observed that the sensor follows a linear response with a linearity of about 97% but the sensitivity of the sensor is very less. It has been observed that the response of the sensor with intensity offset for both reverse and forward shown in Fig. 3b. The sensor shows a high linearity response of about 98% and also exhibits high sensitivity. The hysteresis area versus concentration of liquid is plotted as shown in Fig. 3c. It is clearly shown that the sensor following linear response for the concentration with respect to the hysteresis area, with a linearity of about 99% and having high sensitivity.

It is observed that intensity offset or hysteresis area measurements are more suitable than distance offset owing to their high linearity and sensitivity. From the obtained results, it is illustrated that the concentration (or viscosity) of the liquid can be measured in terms of the offset height and/or hysteresis area.

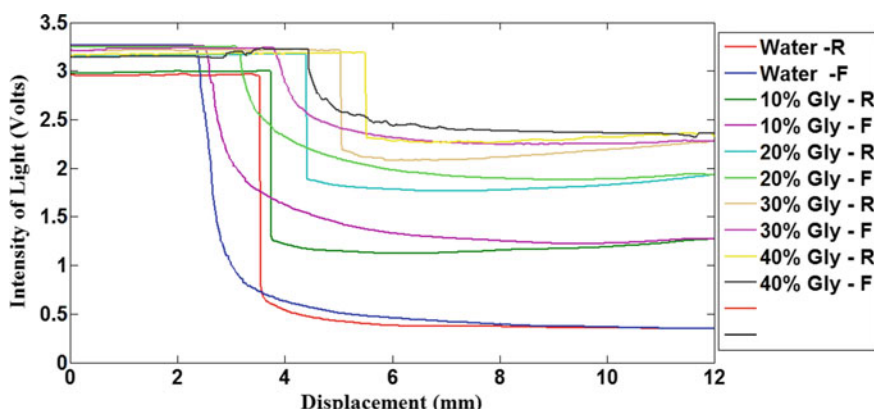


Fig. 2 Response of the sensor for rise and fall of the liquid with different % of glycerine and water

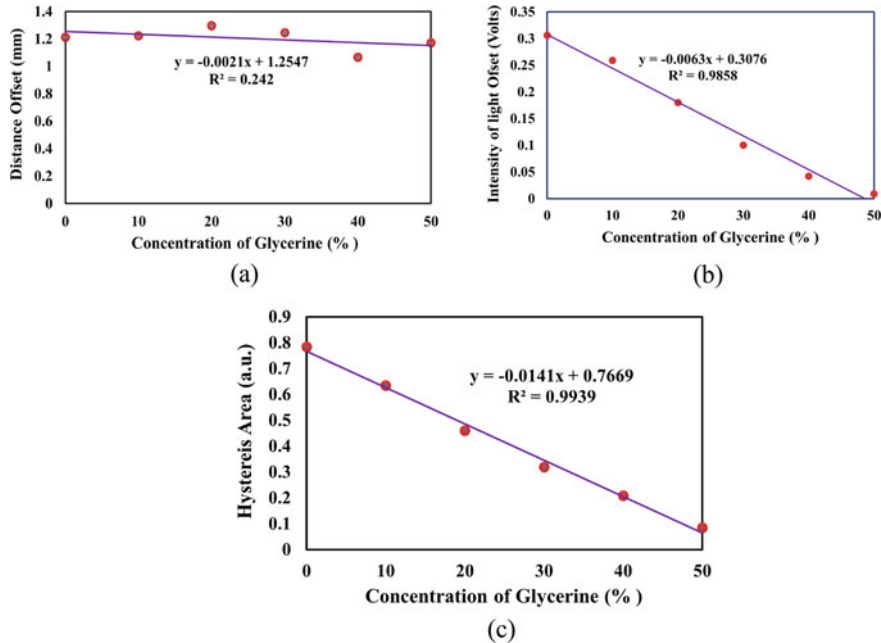


Fig. 3 Experimental results of the sensor **a** distance offset **b** height offset **c** hysteresis area with respect to the viscosity (concentration) of the liquid

The viscosity of the glycerine is calculated from the following empirical formula from the concentration of the liquid [17].

$$\eta = \eta_0 \left(1 + k_1 \frac{L^2}{a^2} c + k_2 \frac{L^4}{a^4} c^2 + \dots \right) \quad (1)$$

where η_0 is the viscosity of a pure liquid, k_1 and k_2 are the constants, L is the length of the molecular distance and a is the radius of the molecule, and c is the % of concentration of the liquid. From the above Eq. 1, the relation between the glycerine concentration and viscosity is drawn along with the hysteresis area measured with respect to the concentration of the liquid. From this, it is easy to find the viscosity of the glycerine liquid as shown in Fig. 4. The simulated viscosity results are almost with the data given in the paper [18]. It represents the measurement of the viscosity of the liquid in terms of hysteresis area. This sensor can also be used to measure the refractive index of the liquid as the concentration is directly related to the refractive index of the liquid.

Thus the proposed sensor may be used to replace many existing optical and chemical viscometers because of the inherent and voluminous advantages of the optical fibres. The sensor may find applications for measuring the viscosities of fluids such

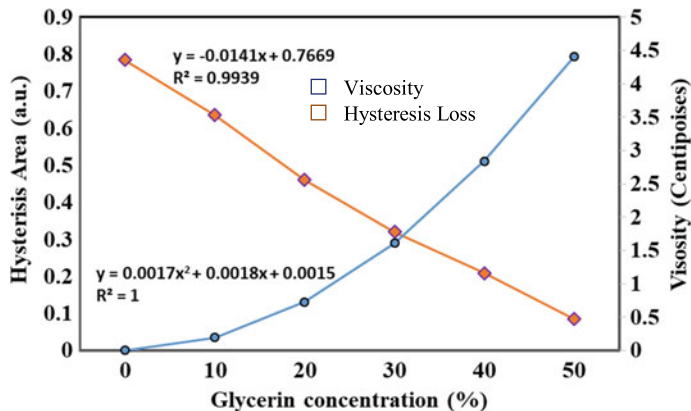


Fig. 4 Response of the sensor for concentration and viscosity

as motor oils, petroleum products, chemical solvents, and many other industrial and biological fluids.

4 Conclusions

The design and development of intensity-modulated plastic optical fiber (POF) viscosity sensor is successfully reported in this paper. The sensor probe is tested for a viscous liquid like Glycerin, by recording the interaction of evanescent field with the ambient viscous liquid in both forward and reverse directions. An offset is observed in the sensor response as the sensor probe dipped slowly in and out of the liquid and measured it in terms of hysteresis loss. The offset has been measured in both horizontal (Distance) and vertical (Intensity) directions. The experimental results reveal that the sensor is highly linear with about 0.98 linearities. From the results, It is observed that intensity offset measurement is more suitable than distance offset owing to high sensitivity. Thus, the concentration (or viscosity) of the liquid can be measured using the proposed simple sensor in terms of the offset height and hysteresis area. This sensor is easy to make, simple, low cost, and had inherent advantages of the optical fiber like Immune to EMI, corrosive, small size, flexibility in length. The sensor may found many applications in measuring the viscosities of fluids such as motor oils, petroleum products, chemical solvents, and many other industrial and biological fluids.

References

1. Gholamzadeh B, Nabovati H (2008) Fiber optic sensors. World Acad Sci Eng Technol 42
2. Yu F, Yin S, Marcel-Dekker (2002) Fiber optic sensor
3. Krohn DA Fiber optic sensors-fundamental and applications. Instrument Society of America
4. Wang Jian-Neng et al (2010) Sensors 10:11174–11188
5. Alexander I, et al (2012) Proceedings of ISOT'12, IEEE. Intl Symp Optomechatronic Technol
6. Udd E et al (1991) Fiber optic smart structures. Wiley INC, New York
7. Dakin, Culshaw b (1988) Optical fiber sensors-principles and components, vol I, Artech, House, Boston
8. Int J Electron Commun Comput Technol (IJECCCT) 3(4) (July, 2013)
9. Jesus Castrellon-Uribe W (February, 2012) Optical fiber sensors: an overview. Center for Research in Engineering and Applied Sciences, CIIC Ap. Autonomous University of Morelos State, UAEM México, ISBN 978-953-307-922-6
10. Golnabi Hossein (2004) Opt Lasers Eng 41:801–812
11. Razani M, Golnabi H (2007) Iranian Phys J 1–2:61–66
12. Natha P, Singh HK, Datta P, Sarma KC (2008) Sensors Actuat A 148:16–18
13. Fidanboylu K, Efendioglu HS (2009) Fiber optic sensors and their applications. In: 5th international advanced technology symposium (IATS-09) May 13–15, Karabuk, Turkey
14. Hizhuoyin S, Ruffin PB, Francis TSY (2008) Fiber optic sensors, 2nd edn. Edited by CRC Press ISBN 13: 978-1-4200-5365-4
15. Barry ArklesGelestInc, Morrisville PA (October, 2008) Hydrophobicity, hydrophilicity and silanes. Paint Coating Magz
16. Pekka Raatikainen U, Ivan Kassamakov b, Roumen Kakanakov b, Mauri Luukkala (1997) Sensors and Actuat A 58:93–97
17. Simha R (1949) J Res Natl Bur Stand RP1981 42:409–418
18. Segur JB, Helen E (1951) Oberstar, industrial and engineering chemistry 43(9):2117–2120

Performance Enhancement for Scattering Effect in Perovskite Solar Cell with Distinct Cathode Materials



Sagar Bhattarai, Arvind Sharma, and T. D. Das

Abstract A comprehensive simulation study has been demonstrated to study perovskite solar cells with imposing scattering interface between TaTm (HTL) and methylammonium lead tri-iodide (MAPI) active layer with a distinct combination of cathodes. The active layer acts as a light-absorbing layer with a bandgap of 1.5 eV. Among the distinct device structures, the highest efficiency is 10.49% at active layer width of 500 nm for Ag as a cathode. Precisely, the present simulated device is also offering the maximum open-circuit voltage (V_{oc}) up to 0.83 V, short circuit current density (J_{sc}) about 16.1 mA cm⁻² and fill factor (FF) of 0.804, respectively, in wavelength spanning from 380 to 780 nm. This simulation results demonstrated an optimal result with imposing of scattering interface in the perovskite layer and it affords several significant strategies for the feasible invention of more efficient PSC.

Keywords HTL · PCE · Active layer · V_{oc} · J_{sc} · FF

1 Introduction

Among the various renewable energy resources offering better device performance and cost-effectiveness, the perovskite solar cell (PSC) is the futuristic substitution for conventional energy resources. The recent advancement in organic-inorganic perovskite solar cells, the methylammonium (MAPI) lead halide has revolutionized due to their high light-harvesting characteristics [1, 2]. Apart from a great absorption characteristic, the MAPI in the PSC has gained extensive attention because of their superior optoelectronic properties like ideal bandgap, high charge mobility, large absorption coefficient, and small exciton binding energy, respectively [3–6]. The MAPI has also fascinated the attention due to outstanding absorbing property which offers a very high *PCE* of the PSC device. To enhance the efficiency of the device, the flexibility in its device structures is very important. Thus, we introduced a scattering interface in the active layer which may cause to enhance the absorption

S. Bhattarai · A. Sharma · T. D. Das (✉)

Department of Basic and Applied Science, National Institute of Technology Arunachal Pradesh, Yupia, Arunachal Pradesh 791112, India

e-mail: tddas@hotmail.com

in the device. Carrying forward, it will also impact the stability of the device. So, the better thoughtful knowledge in the device characteristic machinery is mandatory to optimize efficiency [7, 8]. In that prospective Ag, cathode material offers high device characteristics at a very cheap cost. Meanwhile, the superior electrical property of MAPI organometal halide can be used in solid-state sensitizer as well [9]. As it started in the year of 2009 when Kojima et al. [10] used perovskite in photovoltaic and reported the value of efficiency rates 3.81 and 3.13% for MAPI based PSC with different halide materials [11–13]. Since then numerous study in the field of PSC has been carried out. Thus, the structural property behind the understanding of perovskite solar cell is crucial which is denoted as ABX_3 , where A structure is considered as an organic-inorganic ion, B is a divalent small metallic cation, and X is a halide which binds with cations. By varying the A, B, and X ions, optical and electrical properties of the ABX_3 perovskite structure can be tuned.

In the simulation study, the proposed perovskite solar cells structure of glass /ITO/TaTm/MAPI/C₆₀/Ag or Au, where TaTm acts as P-type material, C₆₀ as N-type material, MAPI functions as an absorber layer, and glass used as a substrate. Also, ITO used as an electrode to the front contact, and Ag used as the back contact. Then the influences of incident light wavelengths and the layer thickness of perovskite absorbers on photovoltaic parameters were predominantly investigated by introducing a scattering layer in the MAPI layer with different cathode materials.

2 Device Simulation Parameters

The present PSC devices are simulated by three input layers; material TaTm acts as ETL, C₆₀ is functioning as HTL, and MAPI is an active layer. ITO is an electrode used in the front contact and silver (Ag) is a cathode in the back contact in the simulated device structure, which is represented in Fig. 1a. Simultaneously, the corresponding energy levels in the corresponding layer of the device level are also represented in Fig. 1b. Perovskite absorber absorbs photons having energy higher than 1.5 eV which creates excitons within this photoactive layer. The parameters utilized for the present study of MAPI based PSC are shown in Table 1, where E_g is bandgap energy in eV scale, N_c and N_v are called effective density of states (EDS) of the conduction band and valence band in m^{-3} , μ_n , and μ_p are the electron and hole mobility in $cm^2/V s$ scale, respectively. The band diagram of the PSC is represented in the simulated device structure.

2.1 Parameters Used During the Simulation of MAPI Based PSC

The simulated PSC device structures are represented as shown below.

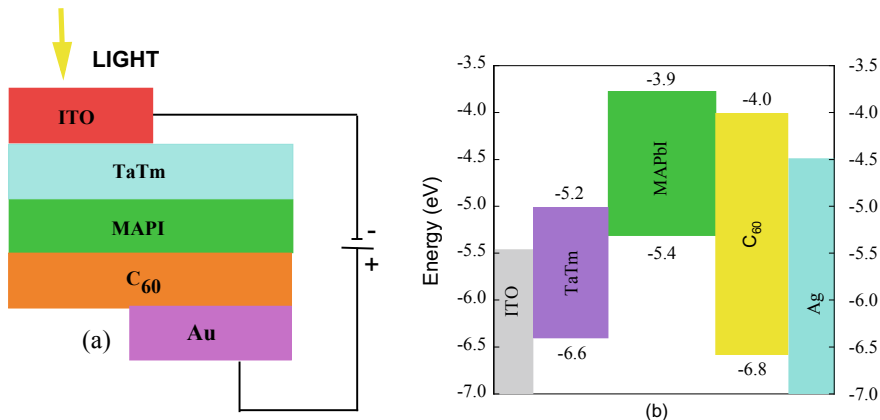


Fig. 1 **a** The schematic layer of simulated PSC device with **b** corresponding energy band diagram with CB and VB for the present study

Table 1 The input parameters in MAPI based PSC

Parameter	Term	ETM (TaTm)	MAPI ($\text{CH}_3\text{NH}_3\text{PbI}_3$)	HTM (C_{60})
d (nm)	Thickness	60	500	40
E_g (eV)	Bandgap	1.4	1.5	2.4
N_c (m^{-3})	EDS in CB	1×10^{27}	1×10^{27}	5×10^{26}
N_v (m^{-3})	EDS in VB	1×10^{27}	1×10^{27}	5×10^{26}
μ_n ($\text{cm}^2/\text{V s}$)	Mobility of electrons	8×10^{-4}	0.01	0.08
μ_p ($\text{cm}^2/\text{V s}$)	Mobility of holes	8×10^{-4}	1	1×10^{-5}

D1(nm) ITO (120)/TaTm (50)/MAPI (without scattering) (500)/ C_{60} (50)/Ag (100)
D2(nm) ITO (120)/TaTm (50)/MAPI (with scattering) (500)/ C_{60} (50)/Ag (100)
D3(nm) ITO (120)/TaTm (50)/MAPI (without scattering) (500)/ C_{60} (50)/Au (100)
D4(nm) ITO (120)/TaTm (50)/MAPI (with scattering) (500)/ C_{60} (50)/Au (100).

3 Results and Discussion

In depicted Fig. 2a, profile for the absorbance describes how much light absorbs out of the harvesting light inside the different device structures D1–D4, respectively. The overall absorbance rate is due to consecutive layers of the device is depicted in the figure, out of which the absorbance spectrum reaches a maximum in the absorber layer interface and reduces at a very fast rate due to the minor diffusion span in charge carriers. Hence, by imposing a scattering layer in the perovskite active layer, the optical path of the incident photon can be increased which results in enhancing the absorbance rate between the wavelength range of 380–780 nm, respectively.

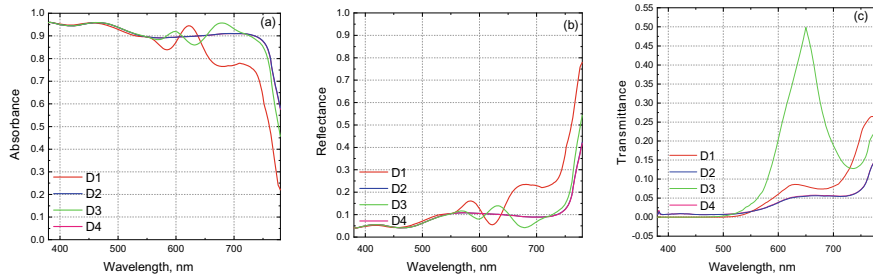


Fig. 2 The variation in **a** absorbance profile measured at different PSC structure over the wavelength at 1.5AM solar spectral irradiance and **b** reflectance and **c** transmittance profile for the PSC devices

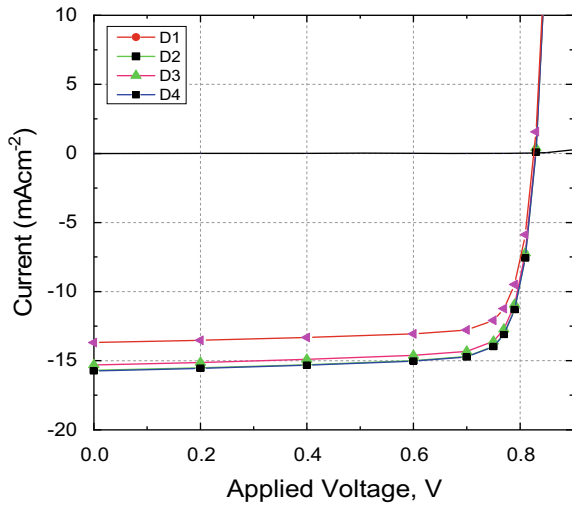
Similarly, in the device D2, the reflective index of the anode material Ag is smaller than anode material Au which results in more light to transmit through the device. Thus, the absorbance profile for device D2 increased up to 90–95% for the perovskite solar cell, due to the triggering the optical pathway by scattering layer throughout the spectrum region.

Figure 2b shows the reflectance spanning over the wavelength for differently structured perovskite solar cell structure D1–D4. It can be noted that the less reflectance results in more effective perovskite solar cell device. Taking into account, in the present study D2 achieved lesser reflectance about 10% since the active layer contains the scattering interface which reduces the reflectance in the active layer influencing the incident light to enter through the device. In D1 and D3 structures, since the optical path is lesser than D2 and D4, it causes more reflectance up to 20 and 30%, respectively, in the PSC. Precisely in D3, the Au layer has a more refractive index than Ag in D1, for which reflectance is more in D3 than D1.

Figure 2c gives the transmittance of the perovskite solar cell for D1–D4 device structures. As more absorbance results in less transmittance rate of the incident light decrease with the scattering layer since it traps more photons in respective active layers of the device. Resulting in decreasing the transmittance in the other layers of the perovskite solar cell. For a 500 nm thick active layer in the perovskite solar cell, we achieved maximum absorbance and minimum reflectance and transmittance for the D2 structure.

The simulated photovoltaic characteristics (J - V curve) are represented through Fig. 3. In the device structure D2, due to imposing a scattering layer in the perovskite active layer gives the best outcome of J_{sc} and FF , respectively. Since J_{sc} is proportional to the field intensity, the active layer which imitates that J_{sc} may be moderated from imposing the scattering layer which enhances the light absorption due to attaining the longer optical path. The lower mobility of charge carriers, regardless of higher absorbance, J_{sc} and V_{oc} value increases for thicker perovskite layer at an externally applied voltage of 1 V. Therefore, in our device structure, we used an optimized thickness in the PSC active layer of 500 nm as reported by Adhikari et al. [14]. Figure 3 shows the dependency of J_{sc} and V_{oc} on device structures D1, D2 under the illumination of AM1.5. Whereas, the PCE of the device in different perovskite

Fig. 3 The photovoltaic characteristics of $J-V$ characteristics at an applied voltage of 1 V across the junction

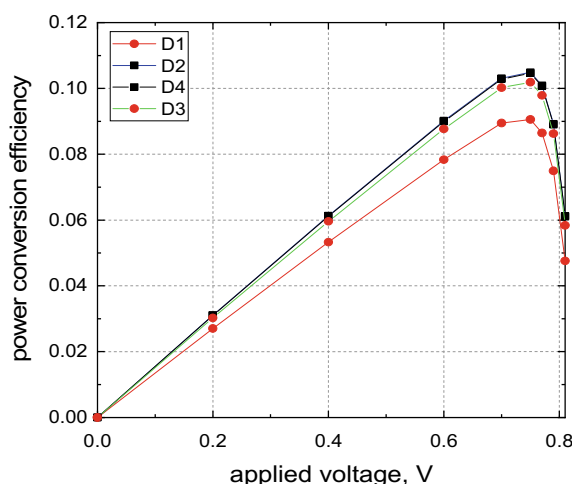


solar structures D1–D4 is calculated, respectively, as shown in Fig. 4. For device D2 of MAPI based perovskite solar cell, we get maximum FF and *PCE* about 10.49%.

As the above figure implies, V_{oc} , J_{sc} , and *FF* of the PSC improved by introducing the scattering interface in the active layer since escalating the layer thickness absorbs photons with longer wavelengths. As the increment in the device parameters for D2 improves the conversion of input power at 1 V of potential. Usually, the results in the generation of excitons further improve the electrical parameters of the PSC device. This relates to more generations in carriers and further optimizes in enhancing device efficiency.

The comparison of different structured PSC structure is given below.

Fig. 4 The power conversion efficiency of PSC structure at AM1.5 illumination and applied voltage 1 V in the PSC



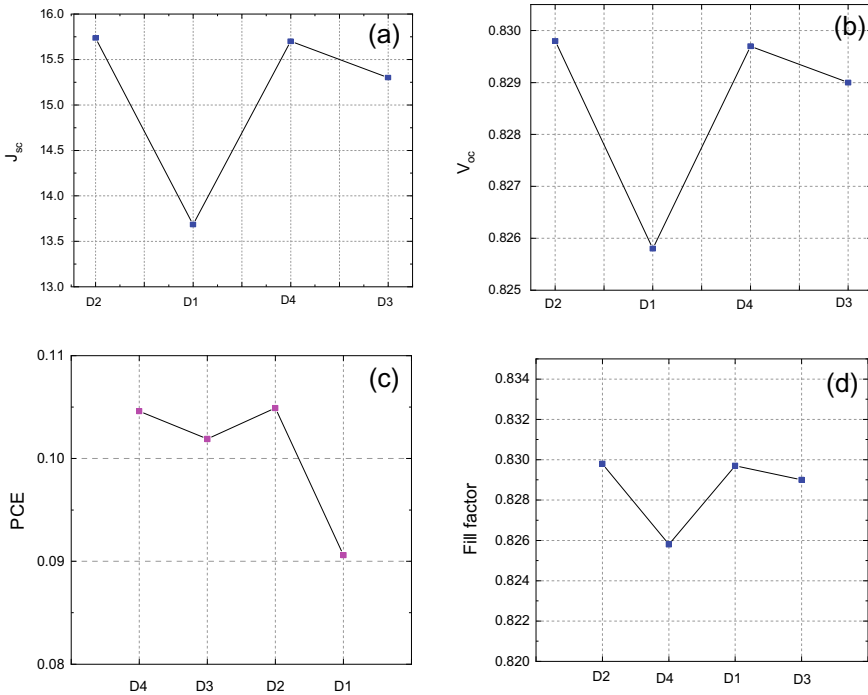


Fig. 5 The simulated result comparison of the different parameters of the MAPI based solar cell

In Fig. 5a, the comparative statement for the different device structure D1–D4 are shown at the AM1.5 illuminance. Current density (J_{sc}) for the device D2 is depicted to be the maximum about $15.7995 \text{ mA cm}^{-2}$ and open-circuit voltage (V_{oc}) of 0.8298 volts is also obtained in the study. Similarly, the D2 device offered optimum power conversion efficiency of 10.49%. Since the scattering effect enhances the voltage and current for higher absorbance in the active layer region triggering the generation of excitons in the simulation study of PSC since a higher generation of excitons enhances the current and voltage in the PSC device [15]. In D2, the effect of more voltage production leads to improving the FF up to 0.834.

4 Summary/Conclusion

In summary, the study of effect due to the scattering layer interface of perovskite solar cell which is introduced between the HTL and MAPI layer with distinct cathode combinations is carried out using a commercially available software package. It is observed that the power conversion efficiency is higher for the perovskite layer with 500 nm thickness. It is also evident from this investigation that with the optimum

perovskite layer thickness, the device parameters like open-circuit voltage (V_{oc}) about 0.8298 V, short circuit current (J_{sc}) as $15.7995 \text{ mA cm}^{-2}$, and fill factor (FF) nearly 0.8035, with PCE reaching significantly high up to 10.49%, respectively, corresponding to the incident light with a wavelength range 350 nm - 800 nm. This result provides pathways for future improvement of PSC with a better suitable optimization mechanism.

Acknowledgements The authors thank the third phase of the Technical Education Quality Improvement Programme (TEQIP-III) under seed grant, NIT Arunachal Pradesh, for financial support. Author Sagar Bhattacharai would like to express his deep and sincere gratitude to TEQIP-III for providing fellowship to carry out his research work.

References

1. Wu HQ, Xue C, Li Y, Zhou P, Liu W, Zhu J, Dai S, Zhu C, Yang S (2019) Simulation of perovskite solar cells by using CuSCN as an inorganic hole-transport material. Mater Res Express 095527
2. Adhikari KR, Gurung S, Bhattacharai BK, Soucase BM (2016) Comparative study on MAPbI₃ based solar cells using different electron-transporting materials. Physica Status Solidi (c), 13:13–17
3. Brabec CJ, Cravino A, Meissner D, Sariciftci NS, Fromherz T, Rispens MT, Sanchez L, Hummelen JC (2001) Origin of the open-circuit voltage of plastic solar cells. Adv Funct Mater 11(5):374–380
4. Tang CW (1986) Two-layer organic photovoltaic cell. Appl Phys Lett 48(2):183–185
5. Brabec (2013) Concepts and realization, vol 60. Springer
6. Gränström M, Petritsch K, Arias AC, Lux A, Andersson MR, Friend RH (1998) Laminated fabrication of polymeric photovoltaic diodes. Nature 395(6699):257–260
7. Zhiliang K, Rong Y, Mi X, Liu T, Han H (2013) Full printable processed mesoscopic CH₃ NH₃ PbI₃/TiO₂ heterojunction solar cells with a carbon counter electrode. Sci Rep 3:3132
8. Shi J, Dong J, Lv S, Yuzhuan X, Zhu L, Xiao J, Xin X, Huijue W, Li D, Luo Y, Meng Q (2014) Hole-conductor-free perovskite organic lead iodide heterojunction thin-film solar cells: high efficiency and junction property. Appl Phys Lett 104(6):063901
9. Burschka J1, Pellet N, Moon SJ, Humphry-Baker R, Gao P, Nazeeruddin MK, Grätzel M (2013) Sequential deposition as a route to high-performance perovskite-sensitized solar cells. Nature 499(7458):316–319
10. Kojima A, Teshima K, Shirai Y, Miyasaka T (2009) Organometal halide perovskites as visible-light sensitizers for photovoltaic cells. J Am Chem Soc 131(17):6050–6051
11. Torabi N, Behjat A, Shahpari M, Edalati S (2015) Development of a silver/polymer nanocomposite interconnection layer for organic tandem solar cells. J Nanophoton 9(1):093049
12. Aharon S, Gamliel S, El Cohena B, Etgar L (2014) Depletion region effect of highly efficient hole conductor free CH₃NH₃PbI₃ perovskite solar cells. Phys Chem Chem Phys 16(22):10512–10518
13. Tress W (2014) Photovoltaic energy conversion in organic solar cells. Springer, Cham, pp 15–65
14. Adhikary P, Venkatesan S, Adhikari N, Maharjan PP, Chenb OAJ, Qiao Q (2013) Enhanced charge transport and photovoltaic performance of PBDDTTT-CT/PC 70 BM solar cells via UV–ozone treatment. Nanoscale 5(20):10007–10013
15. Zhou D, Tiantian Zhou Y, Tian XZ, Yafang T (2018) Perovskite-based solar cells: materials, methods, and future perspectives. J Nanomater 2018:8148072

Need of Techno-Preneurship and Innovations for Community-Level Cancer Screening in Arunachal Pradesh



M. S. Momocha and K. Chaitan

Abstract It is estimated that noncommunicable diseases cause 71% of all death in the world (World Health Organization in India: first to adapt the global monitoring framework on noncommunicable diseases (NCDs). World Health Organization (WHO), Geneva, 2015, [1]). Key noncommunicable diseases are cancer, cardiovascular diseases, and respiratory-related. 61.8% of death in India is due to NCDs. NFHS 4 data shows one-third population faces catastrophic health expenditures and faced distress financing mainly because of hospitalization (Key indicators of social consumption in India: health. NSS 71st round. GoI, Ministry of Statistics and Programme Implementation, New Delhi, 2014, [2]). Out of Pocket Expenditures on hospitalization especially on cancer is highest in India. State diseases burden study 2016, highlighted that in Arunachal Pradesh premature death was 63.7% (SDBS, 2016) and NCDs causing 52.9% death (Indian Council of Medical Research in A report on the cancer burden in North East India, 2012–14, [3]). ICMR 2012–14 reported that in per 100,000 female population Papumpare district of Arunachal Pradesh had the highest Cancer incident (249.0) in the Population-Based Cancer Registration (PBCR) in India. Whereas In per 100,000 male population Papumpare district of Arunachal Pradesh had the second-highest incident of Cancer (230.4) after Aizawl (270.7) in Mizoram (Indian Council of Medical Research in A report on the cancer burden in North East India, 2012–14, [3]). The footfall for NCD screening in the public health system in Arunachal Pradesh during April 2018–Sept 2019 reported 7003 and highest screening was on Oral Cancer (2875) (Ayushman Bharat Health and Wellness Centers (ABHWC) in first 18th months of implementation (April 2018–Sept 2019), [4]). The screening demand generation can be increased if more affordable and accessible technology-based screening services are provided at community-level especially at doorstep along with proper behavior change communications on the risk factors. The paper tried to investigate the Cancer burden and screening services in Arunachal Pradesh and had also objective to oversee the community-level

M. S. Momocha · K. Chaitan (✉)

Department of Management & Humanities, National Institute of Technology Arunachal Pradesh, Itanagar, India

e-mail: chaitandu@gmail.com

M. S. Momocha

e-mail: momocha@nitap.ac.in

demand and supply gap of screening services in Arunachal Pradesh. Secondary data analyzed to meet these objectives. There is high demand for tech-entrepreneurship to meet the demand for screening services of cancer diseases in the community.

Keywords Community cancer screening · Techno-entrepreneurship · Innovations

1 Introduction

Noncommunicable disease (NCD) are chronic diseases mainly cancer, chronic respiratory disease, cardiovascular disease, diabetes, and injuries, and mental health. 80% NCDs are related to lifestyles and risky behaviors like tobacco use in any form, alcohol consumption, inappropriate diet, and physical inactivity which cause physiological changes in the body manifested as high blood pressure, high blood glucose increased, raised body mass index, and waist circumference. The behaviors are developed in various socio-cultural conditions. Study shows in India NCDs are raising at alarming rate and huge economic loses are expected which will hamper the overall development goals if timely preventive majors are not taken. If we achieve a 2% reduction in these diseases our economic growth can increase by one percent. ICMR Estimates that 2.25 million people live with Cancer in India. 1,157,294 new patient registers every year. 413,519 men and 371,302 women died of Cancer in 2018 [3]. Government of India health insurance schemes ABPMJAY data (Sept 2018–July 2019) reflects that 34% of tertiary care claims are related to Oncology [5]. The ABPMJAY schemes are designed for approx. 40% poorest population in India. Seeing the national burden and vulnerability in Arunachal Pradesh the researcher adopted a secondary literature review method to analyze the supply and demand situation of screening services of Cancer diseases in Arunachal Pradesh. Arunachal Pradesh has 98 Operational AB Health and Wellness Centers (Sept 2019) which provided screening of noncommunicable diseases [4]. The state has a population of 13.83 Lakh (Census 2011) and the screening population on NCDs shows 7003 for the period April 2018–Sept 2019 [4]. The screening is being done at HWCs through trained Lab technicians and tablet-based technology is used for MIS data generation and reporting. Tech-entrepreneurship and innovation for doorstep services will help fill the gap in the shortage of screening services.

2 Methodology

The study was done with a literature review, analysis of health department data, reports of research institutions, Government of India Policy documents, reports of Ministry of Health and Welfare were consulted.

3 Key Findings

3.1 Risk Factors/Life Style Diseases

WHO recognized key risk factors on NCD are alcohol use, insufficient physical activity, excess salt intakes, tobacco smoking, raised blood pressure, raised blood glucose, obesity, and air pollution. Hence, NCDs are also called lifestyle diseases.

3.2 Global Disease Burden

World Health Assembly 2013 adopted a global action plan for the prevention and control of NCDs 2013–2020 and recommended member countries to apply 25 comprehensive indicators for positive outcomes of the programs [6].

NCDs cause 71% death worldwide and estimated that 52 million death might occur by 2030 [1]. 50% such death is in lower and middle-income countries. Death due to NCDs is an obstacle for other sustainable development goals and poverty reduction.

The family having NCD patient has a double burden on one side health care cost and on the other had wage loss, time, and income of caring members.

Catastrophic health spending and distress health financing are the two ways economic study of the diseases found in the various literature.

Sustainable development goals targets to reduce one-third premature mortality from noncommunicable diseases through prevention and treatment and promote mental health and wellbeing by 2030.

3.3 Indian Situation

NCDs in India is an increasing trend. 62% of hospitalization is in private hospitals.

Fifty percentages of the family having Cancer patient has to suffer catastrophic spending and 25% of such family fall into poverty [2].

The report of the Global Adult Tobacco Survey (GATS) says hat that 28.6% of adults consume tobacco in various form, it is estimated that 266.8 million tobacco users are in India [7].

3.4 Government of India Initiative to Reduce Out of Pocket Expenditures

Government of India's Ayushman Bharat Pradhan Mantri Jan Arogya Yojana an insurance scheme, covering 40% of the poorest and most vulnerable individuals in the country for secondary and tertiary care.

On the other hand, 150,000 Ayushman Bharat Health Wellness Centers (AB HWCs) are planned for primary care services including screening of NCDs. NCD screening has been planned through these HWCs including outreach activities [8]. This transformation is planned to facilities delivering high-quality, efficient, equitable, and comprehensive care.

ICMR Estimates that 2.25 million people live with Cancer in India. 1,157,294 new patient registers every year. 413,519 men and 371,302 women died of Cancer in 2018.

Government of India health insurance schemes ABPMJAY data (Sept 2018–July 2019) reflects that 34% of tertiary care claims are related to Oncology [5]. The ABPMJAY schemes are designed for the poorest approx. 40% poorest population.

3.5 Vulnerability in Arunachal Pradesh

State diseases burden study 2016, highlighted that in Arunachal Pradesh premature death was 63.7% and among premature death, NCDs caused 52.9% [9].

Risk Factors and their contribution to NCDs are highlighted in Table 1.

ICMR report 2017 highlighted the following figures for Arunachal Pradesh for the Reporting Year 2012–2014.

Table 1 NCD risk factors

Risk factor	Percentage of contribution in death (%)
Malnutrition	14.80
Air pollution	5.1
High blood pressure	5.00
Tobacco use	4.9
Dietary risks	4.7
High fasting plasma glucose	4.00
Wash	3.9
Alcohol and drug use	3.90
Occupational risks	2.6
Impaired kidney function	2.0

In per 100,000 male population Papumpare (230.4) district of Arunachal had the second-highest incident of Cancer after Aizawl (270.7) in Mizoram in the Population-Based Cancer Registration (PBCR) in India.

Whereas in per 100,000 female population Papumpare (249.0) district of Arunachal had the highest incident in the Population-Based Cancer Registration (PBCR) in India.

The report highlighted a total of 1773 (910 male and 863 female) cancer patients registered out of which total 406 (251 Male and 155) death cases recorded [3]. This shows that approx. 23% of Cancer patients could not survive in the reporting period.

The report also highlighted that 61% of Cancer incidents are mostly in four tribes—Nishi 33%, Galo 14%, Monpa 7%, and Apatani 7% [3].

National Family Health Survey (2015–16) says that in Arunachal Pradesh 60% male and 17% female population consume tobacco in the various form [2].

59% of male consumes alcohol. 18–20% population has overweight (male—20%, female—18%), 5.9–8.5% female does screening for breast or Cervical Cancer [2].

Male has high Stomach and liver Cancer whereas the female has high cervical and breast cancer in the state in comparison with the rest of India. The cancer incident and death ratios from 2014 to 2016 has been estimation has been highlighted in Fig. 1 [10].

It shows that the State has Low survival chances of Cancer cases. The death percentage with respect to reported cases during 2014–2016 in Arunachal Pradesh and National average has been shown in Fig. 2.

Medical investigations reported that more than fifty percent of male Cancers and more than twenty-five percent female cases are due to the use of tobacco.

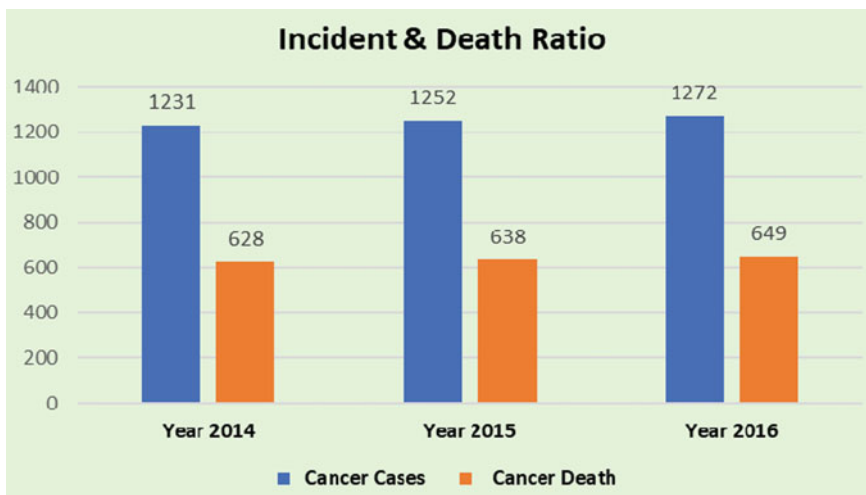


Fig. 1 Cancer incidence versus death in Arunachal Pradesh



Fig. 2 Death percentage India versus Arunachal Pradesh

3.6 *Cancer Screening Situation in the Public Health System in Arunachal Pradesh*

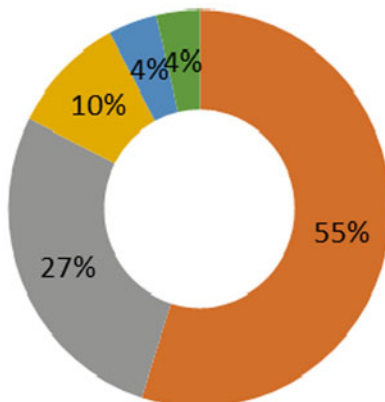
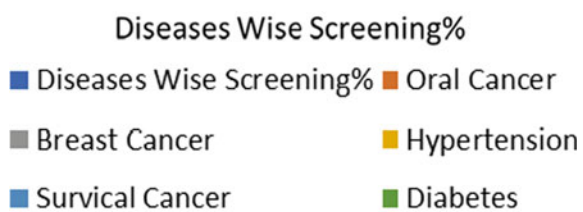
During the period April 2018–Sept 2019 total footfall of screening on NCDs at public health facilities namely Ayushman Bharat Health and Wellness Centers (AB HWCs) in Arunachal Pradesh reported as 7003 [4]. The NCDs are chronic diseases and screening required multiple times. Only three Cancer namely cervical, oral, and breast cancer is being screened across functional health and wellness Centers. The summary of the analysis of demand and supply of screening services is shown in Table 2. An Analysis of Cancer and other diseases screening are shown in Fig. 3.

There is a high gap in the demand and supply of screening services in the population. The NCDs screening gaps analysis is shown in Fig. 4.

The state having 1,383,727 population (Census 2011) and high disease prevalence required more innovation and technological solutions for grass root level screening for Cancers and other NCDs. The interaction with officials of the health departments highlighted the vulnerability and risk factors to be known to the community and health workers. Geographic challenges due to the hilly state and socio-economic characteristics of the community lead to high-risk factors. Community behavior change is a hard task to avoid risk factors in the state. The screening will help to early detection of the diseases and precaution from further risk factors.

Table 2 Population screened on NCD diseases during April 2018–September 2019

Diseases	Screened population (April 2018–Sept 2019)	Suggested rate from the national programme	Adult population above 30 years to be screened based on 2011 census population	% of population having a shortage of screening at HWC
Hypertension	508	37% annually	511,979	99.90
Diabetes	194	37% annually	511,979	99.96
Breast cancer	1442	51% of adult population in 5 years	261,109	99.45
Survical cancer	215	51% of adult population in 5 years	261,109	99.92
Oral cancer	2875	37% annually	261,109	98.90
Total foot fall	7003	Total foot fall estimated	511,979	98.63

Fig. 3 Diseases wise screening percentages

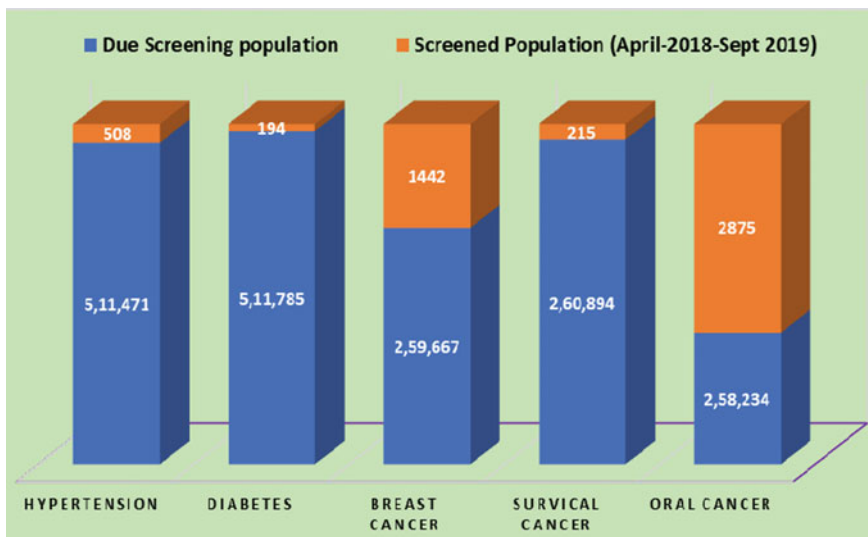


Fig. 4 Gap in NCD screening services in the community

4 Conclusion

NCD prevention framework suggests that multisectoral engagement is required along with community knowledge, attitude, and practice changes to prevent NCD in the community. The data reflects that the risk factors for Cancer burden are high in the state and massive population screening is required at the community-level.

The techno-entrepreneurship for Cancer screening is highly required for affordable and accessible services to fill the shortage of public health Cancer screening system. Further detailed field study is required to find out effective, affordable, and innovation screening solutions for the maximum adult population in the state with geographic and socio-cultural context. Cause for lifestyle behavioral change to be studied for future solutions for reducing risky behaviors in the population. Screening services at private hospitals are to be integrated for policy-level decisions. Current screening policy in the public sector is mainly focused on three high prevalence Cancers. There might be a demand for other Cancer site screening as well.

References

1. World Health Organization (2015) India: first to adapt the global monitoring framework on noncommunicable diseases (NCDs). World Health Organization (WHO), Geneva
2. Key indicators of social consumption in India: health (2014) NSS 71st round, Jan–June 2014. GoI, Ministry of Statistics and Programme Implementation, New Delhi
3. Indian Council of Medical Research. A report on cancer burden in North East India, 2012–14

4. Ayushman Bharat Health and Wellness Centers (ABHWC) in first 18th months of implementation (Apr 2018–Sept 2019). <https://abhwc.nhp.gov.in/download/document/340b49eb2c0937e7b79ad8c1d6b975ad.pdf>. Accessed 18 Jan 2019
5. Can Ayushman Bharat help to tackle cancer burden in India? <https://www.livemint.com/science/health/can-ayushman-bharat-help-tackle-Cancer-burden-in-india-11576396813549.html>. Accessed 18 Jan 2020
6. WHO (2013) Global action plan for the prevention and control of noncommunicable diseases 2013–2020. WHO, Geneva
7. Global adult tobacco survey India fact sheet 2016–17
8. IHME Report (2017) Comprehensive health study in India finds rise of non-communicable diseases. <http://www.healthdata.org/news-release/comprehensive-health-study-india-finds-rise-non-communicable-diseases>
9. India State-Level Disease Burden Initiative Collaborators (2017) Nations within a nation: variations in epidemiological transition across the states of India, 1990–2016 in the Global Burden of Disease Study. Lancet 390:2437–2460. [https://doi.org/10.1016/S0140-6736\(17\)32804-0](https://doi.org/10.1016/S0140-6736(17)32804-0)
10. Press Information Bureau, Government of India, 18 Mar 2018

Phrase-Based Machine Translation of Digaru-English



Rushanti Kri and Koj Sambyo

Abstract The Natural Language Processing (NLP) is mainly associated with the interactivity of computers and natural languages in order to process and analyze natural language data. The machine translation is a subdomain of the NLP which helps us settle language inconceivable issues. The high resourced language such as the European language has been widely studied and used within the discipline of computational linguistics and for Machine Translation whereas several low resourced language such as Digaru spoken by the Tawra Mishmi Tribe of Arunachal Pradesh has yet to be introduced in the Machine Translation field of NLP due to unavailability of data in this data-driven world. In this paper, we have provided freshly collected Digaru-English translation of about 5057 aligned sentence pairs and measured the translation accuracy of the freshly collected data through Statistical Approach of the Machine Translation and provided the unigram score 0.4063 calculated by the BLEU metrics.

Keywords Natural language processing · Statistical machine translation · BLEU score · METEOR · Human evaluation (5–6)

1 Introduction

The Natural Language Processing is an approach based mainly on the set of theories and technologies for analyzing texts. The Machine Translation being a subfield under the NLP has in the past few years garnered the attention of many researchers as well as the public due to the increasing interactions of people from different linguistic backgrounds from across the Globe. This paper is an attempt to provide a comprehensible translation of the Digaru Language used by the Tawra Tribe which is one among the

R. Kri (✉) · K. Sambyo

Department of Computer Science and Engineering, National Institute of Technology Arunachal Pradesh, Yupia, India

e-mail: kirushanti@gmail.com

K. Sambyo

e-mail: sambyo.koj@gmail.com

three of the Mishmi group residing mainly in the eastern side of Arunachal Pradesh with as few as 35,000 native speakers as per the 2001 census. The Digaru language is also considered among the family tree of perhaps the Sino-Tibetian language and also shares the linguistic relationship with the Idu which also belongs to the Mishmi group, they may share few words in common but their linguistic connection is quite puzzling [1]. While many highly resourced languages which have a rich collection of data benefits in providing almost perfect translations from a trained system to a human translator, the low resourced language such as Digaru might in further years disappear if it is not preserved now. Through the computational and linguistic perspective, the structure of Digaru language does not permit us to create a very long sentence due to its unnatural structure as it gets clause from the Hindi language, also due to being a highly tonal language and also due to the involvement of several homographs it gets complicated to write it down in the simpler form [2]. The collection of a completely new corpus and applying several computations on the corpus will provide us with the performance metric of several Machine Translation model for a completely new corpus as well as preserve the corpus of a low resource language such as Digaru. Machine Translation has been present for many years but gained attention only recently. Several Machine Translation approaches have been proposed which includes the RBMT which stands for the Rule-Based Machine Translation, SMT for Statistical Machine Translation, and NMT for the Neural Machine Translation. While many research works are being done based on the NMT approach which is the latest among the three, here in this paper we will use the Statistical Approach for our Corpus with the help of MOSES an opensource Statistical Machine Translation Toolkit and evaluate the translation accuracy that the SMT provides for a completely new corpus with the help of the BLEU, the Bilin-gual Evaluation Understudy which is an algorithm for calculating and judging the translated text quality of the machine-translated corpus from Digaru-English.

2 Related Works

The natural language processing was introduced in the late 1940s where MT was the first computer-based application developed in order to achieve human-like language processing [3]. The Digaru-English corpus is first among the three Mishmi languages which have been introduced to machine translation through this paper. Since it is a completely new corpus there is no history of computations therefore we have selected the phrase-based MT system which lays its priority on meaning preservation as it aims to provide adequate translation [4]. The meaning preservation of the phrase-based MT system is preferable for a low resource language like Digaru as the focus tends towards the meaning instead of the fluency parameters [4]. The SMT system assigns a probability to all set of sentences as it needs several ways to compute the language model probability as well as the translation model probability and also searching for the best source sentence which will provide the highest value [5]. The SMT system makes use of n-gram model to find out the highest probability and rank the words

from the bag of translation where every sentence is chopped into words and every word count provides probability measures for a translation output during decoding [6]. The SMT system uses alignment models such as giza++, MGIZA to provide translation correspondences between a source sentence and its reference translation [7]. The MOSES toolkit has been widely used for SMT by several researchers as well as the industry people to provide faster and reliable translation through a statistical approach [8]. The working order of Moses toolkit starts by first installing all the supporting tools like the MGIZA and mkcls, SRILM, IRSTLM, etc. which are the main building block used during the pre-processing, language and translation model training through Moses and similar translation work has been provided in Ref. [9] where they have given detailed information about their approach to statistical machine translation for their corpus using Moses. The trained models providing the predicted translations are calculated by an automatic metric BLEU which analyzes and counts the n-grams to rank the translated output based on its precision [10].

3 The Statistical Advancement Towards Machine Translation

The main pretension of the machine translation is to provide translation between two languages basically input and an output language. In the past few years Machine Translation has shifted from the Classical approach, i.e., RBMT to the Statistical approach towards machine translation, where the Rule-Based Translation offers a reasonable translation accuracy but is exhausting during the pre-designing set of translation rules and generation based on the form of language structure, according to the syntax of the language and the meaning behind the language of both the source as well as the target language [6]. The SMT creates translations with the underlying support of the statistical models where the parameters are obtained from the analysis of bilingual text corpora [11]. A statistical model does not rely on language features such as the grammar and the language-specific models of translation which provides an advantage over the Rule-Based Translation system and also allows us to build multiple language pairs with minimal modification. Statistical model can be trained on small as well as large data set and increasing the dataset will eventually lead to higher quality translation and capture more of the linguistic aspect of the language.

There are more approaches to machine translation including the Example-Based Machine Translation system and the Neural Machine Translation system which are also corpus-based machine translation system but we have used the statistical approach as it makes use of the predictive algorithms in order to train a translation model that formulates the translation problem with regard to the conditional probability. The SMT model requires methods to compute translation probabilities and also for computing language model probabilities. The implementation of the Bayes Theorem provides with better modelling of the probability distribution $p(\text{elf})$ where e in the target language is the translation of string f in the source language. The Bayes

Theorem, $p(\text{elf}) \propto p(\text{fle})p(e)$, where the translation model $p(\text{fle})$ is the probability that the source string is the translation of target string, and language model $p(e)$ is the probability of seeing that target language string [7].

4 System Description

4.1 Corpus Preparation

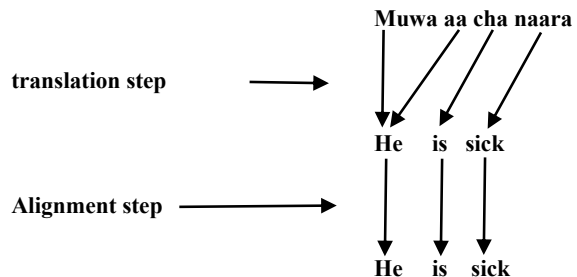
The Corpus preparation of the Digaru-English [12] parallel corpus includes Tokenization which is very helpful for Statistical Machine Translation (SMT) as it divides a sentence into tokens which are separated by spaces, Truecasing which restores case information to badly-cased or non-cased text and avoids irrelevant difference between lowercased and uppercased words and Cleaned which removes long and empty sentences in order to formulate it and make the corpus ready for training, tuning as well as testing purpose.

4.2 The Language Model

To build a reliable language model for SMT system there is the need for time and human cost which results in several difficulties. The language model in Statistical Machine Translation helps with reordering of words and also helps with the word choice which requires less time and human cost compared to the human evaluation of a language model. Also, the prediction is always difficult, especially about the future. In our case, it is the prediction of the next word where assigning probabilities to a sequence of words is essential in machine translation. Language models can be defined as the model that allocates probabilities to a sequence of the word and the n-gram is a model that allocates probabilities to a sequence of word and sentences. The n-gram is a series of n words whereas the bigram or 2-gram is a two-sequence of word, trigram or 3-gram is a three-sequence of word and so on. The main instinct of n-gram model is to approximate the record by just the last few words instead of calculating the probability of a word given its entire record in the history. The presumption that the probability of a word depends exclusively on a previous word is known as Markov model, we can generalize the bigram to the trigram and so on to the n-gram.

We can calculate the unigram probabilities $p(wI) = f(wI)/N$ where $f(wI)$ is the number of times wI is seen in some corpus and N is the total number of words seen in the corpus (by token). The relative frequency estimation, in this case, can be shown to be an instance of maximum likelihood estimation which is an intuitive way to estimate probabilities.

Fig. 1 Word alignment with MGIZA [7]



An open-source machine translation project with very few resources such as our Digaru-English corpus always restricts the quality of the parallel corpus. Word alignment plays an important role in SMT system which can be obtained by increasing language model training data.

4.3 The Translation Model

The translation model is also called as the models of Translation equivalence because they aim to predict whether expressions in different languages have equivalent meanings.

We train a translation model on sentences that have the same definition in each language and the translation quality depends on the size of dataset, i.e., high quantity of the dataset will give better translation quality. The first step to build a translation model is by building an alignment model between the input and the output language [7]. The alignment models provide the best set of alignment links for each sentence in the training corpus. The MGIZA from the Moses toolkit has been used to align our Digaru-English training corpus. Alignment models are a significant part of machine translation as a word-aligned text is mandatory in order to initialize a translation model. The main objective of alignment is to provide an aligned model resulting in the best translation for a particular word or a sentence adding with the fact that it is difficult to corresponds a given word in target sentence to word in a source sentence. We refer to a picture such as that shown in Fig. 1 as an alignment.

4.4 Decoding

The output of the Language model and the output of the Translation model as well as the source sentence is the input for the decoder. The Decoder implements a search for a good translation candidate and tries to find the hypothesis with the highest model score. The computational complexity is a large problem in the decoding process. The inputs may translate in different ways as the search space can become quite large due

Table 1 Corpus description for Digaru-English and German-English parallel corpus

Corpus type	No. of instances
Training data	3246
Tuning data	811
Testing data	1000

to a few reasons such as output word which does not provide direct translation of either word in an input sentence. Decoder customarily utilizes the dynamic programming algorithm and potent search methods like the beam search strategy which is a heuristic-based algorithm for reducing the search space which has a set of possible hypotheses during translation predicted by the combined attempt of the language and translation model.

5 Experimental Design

We have divided the Digaru-English corpus into training, testing and tuning files and also provided a monolingual file for building the language model with English sentences.

The Moses toolkit builds the language model with IRSTLM which promotes algorithm and data structures fit for storing and accessing large n-gram language models, the same is also used for building the recasing model [13]. The language model parameters for our corpus consists of 1 language model builder with IRSTLM = 1, RandLM = 5 where the RandLM uses Bloom Filter for testing and checking whether an element is a member of the set. And the IRSTLM parameters consist of 1 distributed LM training which splits the dictionary into balanced n-gram lists, 20 dictionary number parts, improved-kensor-ney smoothing technique, and 1 memory mapping. The training corpus of Digaru as well as English is trained along with the language model with mkcls and MGIZA for word alignment on 4 cores of the CPU described in Table 1.

6 Result and Analysis

6.1 Scoring Phrases with BLEU/NIST Metrics

The BLEU/NIST score is computed based on the precision of n-grams. Both metrics require a test-set for machine translation system. The Translation from a source sentence or reference sentence to a target sentence or candidate sentence depends on the word orderings and word choices and the results can vary ranging from a perfect translation to a totally unrelated translation [10]. The BLEU metric ranges from 0 to

Table 2 Unigram score for
Digaru-English and
German-English corpus

No.	Corpus type	NIST score	BLEU score
1	Digaru-English	2.3982	0.4063
2	German-English	4.0430	0.6793

1 and the equation for calculating the BLEU score is,

$$\min\left(1, \frac{\text{candidate-length}}{\text{reference-length}}\right) \left(\prod_{i=1}^n \text{precision}_i\right)^{\frac{1}{n}}$$

where BLEU/NIST uses the n-gram precision approach to compute the resemblance between the reference translation and the candidate translation, and if a match is found between the reference and the candidate translation then the n-gram of reference exhausts for next match. The *candidate-length* and *reference-length* from the above equation denote the length of the candidate and the length of the reference translation, respectively and precision score is calculated for the *i*th gram matching [4].

We have calculated the unigram BLEU/NIST score of our relatively small Digaru-English parallel corpus as well as for the German-English corpus consisting equal number of instances with the MOSES an open-source machine translation toolkit. The *unigram* score for both corpora is provided in Table 2.

The score of Digaru-English corpus is low compared to its German-English counterpart mainly due to the high word ambiguity of the Digaru language which directly affects the n-gram count of the Digaru-English corpus.

6.2 About the Automatic Evaluation Metrics: METEOR

METEOR which stands for Metric for Evaluation of Translation with Explicit Ordering is an automatic scoring metrics that generates scores of a translation by calculating the alignments with respect to its exact word, synonym, stemmed word matching and paraphrase matching of the word and sentences. The above three modules provide alignment between the reference and the predicted translation. METEOR provides additional features like the synonym matching, stemming and exact word match which is not a part of the BLEU metrics [14]. METEOR makes use of the precision as well as the recall, unlike the BLEU and NIST metrics which only depends on the precision. Implementation of the precision along with recall provides higher association with the human judgement at sentence level [14]. Let us consider a few notations,

- rt*** No. of unigrams in reference translation
- pt*** No. of unigrams in predicted translation
- mt*** No. of matching unigrams between *rt* and *pt*.

The unigram precision can be obtained by the formula $P = mt/pt$ where P stands for the precision.

The unigram recall can be obtained by, $R = mt/rt$ where R stands for recall.

And, F -measure which is generated during the computation of METEOR score gives the mean of P and R and can be obtained using, $F\text{-measure} = 2 * P * R / P + R$ [4].

6.3 Human Evaluation

The translation quality of output is basically judged relative to its reference translation and the criteria of the judgment are based on its *fluency* and *adequacy* where fluency provides the quality of a language and adequacy provides the measurement of the meaning of the reference translation with respect to their hypothesis translation. The human evaluation is, however, quite expensive because of the time constraint and the financial expense. Linguistic expert in our experiment is my mother and a cousin as they are very well-versed in Digaru Language and is a native of the Tawra Tribe of Arunachal Pradesh. Further, on our paper, we have performed comparative analysis on a few samples from Digaru-English Translation and examined their quality from different perspectives.

6.4 Analysis of Digaru-English Translation

To further examine our translated output from the SMT system we will use *adequacy* and *fluency* as the two main factors to judge the quality of our predicted output. We have taken a few sample sentences from predictions and examined the same for their quality from a different perspective. We have taken the Digaru sentences as the source sentence and on that basis; we will examine the translation quality of the resultant English translation which is the predicted output by MOSES with the actual English translation of the Digaru sentences. **Digaru Test (DT)** will stand for the test sentence, **English Gold (EG)** will stand for the reference sentence in English and **English Predicted (EP)** for the predicted sentence in English.

1. DT: “tya jina”
EG: “Do it now”
EP: “Do it now”

The SMT system has made a perfect prediction for the above sentence and the predicted translation for the Digaru sentence is *adequate* and *fluent*.

2. DT: “boya”
EG: “Don’t go”
EP: “go”

The SMT system has made prediction which has predicted the unigram “go” and therefore it is not *adequate* but is *fluent*.

3. **DT:** “Tom kasa”
EG: “Tom knew”
EP: “Tom knows”

The SMT system has made prediction which is *partially adequate* and is *perfectly fluent*.

4. **DT:** “haa halyo ya kanum jidi”
EG: “I just want to be happy”
EP: “I don’t happy a about”

The SMT system has made prediction which is neither *adequate* nor *fluent*.

5. **DT:** “tom naara”
EG: “tom’s sick”
EP: “tom is sick”

The SMT system has made prediction which is *adequate* as well as *fluent* but here the SMT system automatically interrogates and adds ‘is’ to the predicted sentence.

From the above analysis of the SMT system, we can conclude that the predicted translation gives relatively good translation for a completely new corpus and also gives nearly perfect translations. But for a few sentence pair which has more than three words, it gives a very bad translation which is neither *adequate* nor *fluent*.

7 Summary/Conclusion

The idea of machine translation is to provide a better and faster communication bridge for people belonging to different linguistic backgrounds. Through this paper, we have contributed a small portion of our work to the machine translation community by providing a new corpus Digaru-English with few performance analyses and comparisons with the German-English corpus based on the statistical approach of MT. We have analyzed the translation output based on its *adequacy* and *fluency*. The further work in progress aims to increase the Digaru-English corpus and apply more of the statistical methods and also apply a neural approach to machine translation and generate its performance metric which will improve the *adequacy* as well as the *fluency* believing the fact “more the data better will be the results”.

References

1. Blench R (2017) The ‘Mishmi’ languages, Idu, Tawra and Kman: a mismatch between cultural and linguistic relations. McDonald Institute of Archaeological Research University of Cambridge
2. Sastry GDP (1984) Mishmi grammar, CIIL grammar series-II
3. Liddy ED (2001) Natural language processing. In: Encyclopedia of library and information science, 2nd ed. Marcel Decker, Inc., New York
4. Pathak A, Pakray P, Bentham J (2019) English-Mizo machine translation using neural and statistical approaches. *Neural Comput Appl* 31:7615–7631
5. Bhattacharyya P (2015) Machine translation, xxv, 234 pp. CRC Press, Boca Raton. ISBN: 978-1-4398-8
6. Brown PF, Cocke J, Pietra SAD, Pietra VJD, Jelinek F, Lafferty JD, Mercer RL, Roossin PS (1990) A statistical approach to machine translation. *Comput Linguist* 16(2):79–85
7. Brunning J (2010) Alignment models and algorithm for SMT. University of Cambridge
8. Koehn P, Hoang H, Birch A, Callison-Burch C, Federico M, Bertoldi N, Cowan B, Shen W, Moran C, Zens R et al (2007) Moses: open source toolkit for statistical machine translation. In: Proceedings of the 45th annual meeting of the ACL on interactive poster and demonstration sessions. Association for Computational Linguistics, Stroudsburg, pp 177–180
9. Jabin S, Samak S, Sokphyrum K (2013) How to translate from English to Khmer using Moses. *Int J Eng Invent* 3(2):71–81. e-ISSN: 2278-7461, p-ISSN: 2319-6491
10. Papineni K, Roukos S, Ward T, Zhu W-J (2002) BLEU: a method for automatic evaluation of machine translation. In: Proceedings of the 40th annual meeting of association for computational linguistics (ACL), Philadelphia, pp 311–318
11. Dabre R, Cromieres F, Kurohashi S, Bhattacharyya P (2015) Leveraging small multilingual corpora for SMT using many pivot languages. In: Proceedings of the conference of the North American chapter of the association for computational linguistics: human language technologies, Denver, pp 1192–1202
12. Blench R (2017) A dictionary of Tawra, a language of Arunachal Pradesh, orthographic edition. McDonald Institute of Archaeological Research University of Cambridge
13. Koehn P, Hoang H (2010) Moses, statistical machine translation system. User manual and code guide
14. Denkowski M, Lavie A (2014) Meteor universal: language specific translation evaluation for any target language. In: Proceedings of the EACL 2014 workshop on statistical machine translation

EMT Analysis of Heavy-Duty EVs in Charging Station



Swati Shukla and Gaurav Trivedi

Abstract The catastrophic global energy crisis, which is gripping the world's progress voraciously, requires stringent and long-term solutions. Sooner or later, there will be a complete shift from IC engine based heavy-duty vehicles to electric powered ones. These vehicles will draw a high magnitude of current from the charging stations. This paper presents EMT analysis for heavy-duty electric vehicle (EV) charging stations. A constant current EV charging system has been designed. Simulation is performed for the 24-s duration, considering the various charging scenarios (CS).

Keywords Heavy-duty electric vehicle · Fast charging · Grid-tied-micro-grid · Constant current

1 Introduction

The EV market today is witnessing sharp rise in sales due to a variety of factors like improved technology, better vehicle design, and dipping battery prices. The ever increasing demand for environmentally safe means of transport and increased government spending in EV infrastructure are the other reasons to drive this growth. Big international companies are playing a significant role in popularizing the EV benefits over conventional internal combustion (IC) engine based vehicles. EV market faces several discrepancies in terms of standardization of EV batteries and ratings of charging stations. These discrepancies make it difficult for government and private entities to provide support to the EV manufacturers and customers. Table 1 presents a few types of heavy-duty EV batteries available in the market.

S. Shukla (✉)

Center for Energy, Indian Institute of Technology Guwahati, Guwahati, India
e-mail: swati.shukla@iitg.ac.in

G. Trivedi

Department of Electronics and Electrical Engineering, Indian Institute of Technology Guwahati, Guwahati, India

Table 1 Market specifications of heavy-duty EVs

Serial number	Company	Truck model name	Power rating (kWh)
1	Emoss	EMS 18 Series	240
2	DAF	CF TRUCK	170
3	Daimler	E-FUSO Vision ONE	300
4	Volvo	FL Electric	300

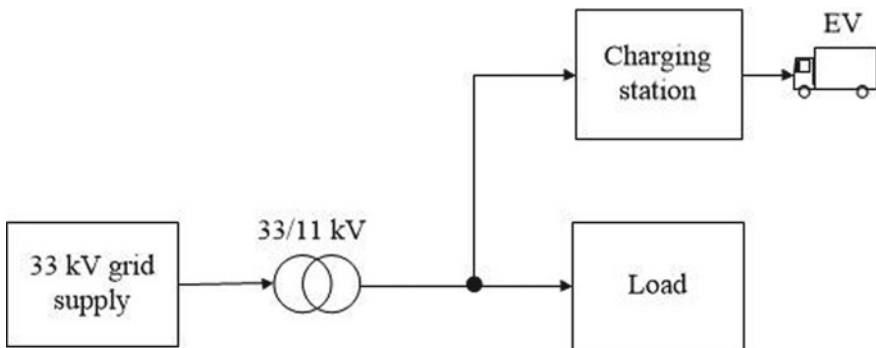
**Fig. 1** Block diagram of the proposed system

Figure 1 shows the block diagram of the distribution network studied in this paper. A grid supply is used to run the dynamic loads of the system, meanwhile charging stations are operated at a stepped-down output voltage in a parallel topology. The analyses of power system behavior due to various real-life situations is carried out in this study, and the detailed result discussion is presented in the later sections of the paper.

The paper is organized as follows. Section 2 discusses the related work carried out in the domains of EV charging. Practical simulation models of a heavy-duty EV battery and modeling of the constant current based EV charger is discussed in Sect. 3, and Sect. 4 presents results/discussion, followed by a conclusion of the entire analysis in Sect. 5.

2 Related Work

Charging station design plays a vital role in determining the popularity of the EV market. Therefore, a lot of studies have been done in this domain. In [1], vehicle to grid (V2G) and vehicle to micro-grid (V2M) implementation have been studied. It can be noted that the power quality and reliability improves when this system is deployed. In another study [2], integration of wind energy system has been done in an active distribution network. Zheng et al. [3] propose an optimal design for the battery

charging/swapping station. Based on the life cycle cost of a battery, an assessment is made for the project, and an improved differential algorithm is used to solve the problem of reinforcing the distribution network. However, the study assumes the EV bus growth forecast to be 25 per year, which can vary significantly for the practical scenario.

In [4], a mathematical model of a single load EV charging has been devised, and actual data of harmonic current has been studied. The internal parameters are considered to be constant. Another study in [5] proposes a heuristic micro-grid for a commercial building, to reduce the dependency of EV charging on the power grid. Marcincin and Medvec [6] check the impact of an active charging station, on micro-grid based geographical locations. In [7], an impact analysis to study the effect of plug-in electric vehicle (PEV) charging on a grid network with medium voltage, has been performed. Three separate charging technologies with three different charging methods have been used to study the impact. In an analysis performed in [8], a study about the penetration of EV charging in residential establishments is shown.

In [9], an analysis to study the impact of EV charging has been performed. The results show that EV charging casts a negative impact on the grid voltage profile, power factor and also leads to increased energy losses. In paper [10], a situation with a micro-grid in islanding operation is considered, where it becomes necessary to perform EV load shedding. In [11], an analysis to study the impact of PEV charging using a low voltage distribution grid has been completed. Various penetration levels have been considered, and the scenarios of slow and fast charging have been discussed. A study in [12] uses Monte Carlo simulation to estimate the power consumption due to fast EV charging. In [13], an analysis to study the impact of EV charging on the distribution network in Los Angeles has been done using real data. The report estimated the usage of charging stations by EV owners under various situations. The proposed study has been performed for 10, 20, and 30% penetration rates of EVs in the area. Paper [14] discusses the possibility of designing a charging station park in a high population density urban area, which consists of slow and fast charging facilities. In [15], it has been studied that EV charging at a commercial building, adds up to the power consumption of the micro-grid and increases the peak demand energy requirement. The analysis in [16] studies the impact of a single line to ground fault condition occurring as a result of EV charging. It has been observed that the node connecting the EV to the grid witnessed an increase in the voltage drop and current rise. In [17], a study of the feeder for the charging station has been performed. In [18], a Monte Carlo based simulation is performed to study the impact of EV charging in power substations of commercial and residential areas. Another paper [19] discusses the impact of an EV charging station on the distribution grid by analyzing the power demand, voltage and current harmonics, voltage swelling and sag, and power loss in distribution transformers. All the studies above, have underlined drawbacks, which this proposed analysis aims to address. The assessments carried out in this paper closely resemble practical situations and are carried out for a range of scenarios. The main objective here is to study the impact of functional EV charging stations on the distribution network.

3 Modeling of the System

3.1 Estimation of the EV Battery Capacity Model

Energy rating of the battery can be estimated by assessing the energy required by the vehicle to travel a distance of 1 km [20]. The mass of the unloaded vehicle is taken to be 24 tons (24,000 kg) and its length, breadth, and height to be 6.7 m, 2.286 m, and 2.286 m, respectively. As per our assumptions, we have considered a vehicle which transports heavy loads between cities, on interconnected high-ways. Hence, once the vehicle achieves its nominal speed, it does not experience any retardation till the destination is reached or the vehicle runs out of charge. It can be assumed that the vehicle with these characteristics will take 15 s to attain a speed of 100 kmph. The resistive forces opposing the truck's motion can be calculated by the following equations (assuming road angle to be zero).

Force due to rolling resistance (F_{roll}):

$$F_{\text{roll}} = f_r Mg$$

Force due to aerodynamic resistance (F_{aero}):

$$F_{\text{aero}} = \frac{A_f C_d \rho V^2}{2}$$

Force due to acceleration resistance (F_{acc}):

$$F_{\text{acc}} = \alpha M \frac{dV}{dt}$$

Table 2 shows the values considered to solve the above equations. Work done by the vehicle to oppose these forces can be calculated by the equation:

$$W = \int F \cdot dS$$

Table 2 Physical quantities for battery design

Serial number	Physical parameter	Value
1	Rolling resistance coefficient (f_r)	0.01
2	Mass of vehicle (M)	24,000 kg
3	Acceleration due to gravity (g)	9.8 m/s ²
4	Frontal area (A_f)	5.225 m ²
5	Drag coefficient (C_d)	0.5
6	Rotational inertia constant (α)	1.1
7	Density of air (ρ)	1.184 kg/m ³

Therefore, the work done by the vehicle against rolling force is 0.049 kWh, against aerodynamic force is 0.0089 kWh and against acceleration, force is 1.0176 kWh. Hence, the total work done by the vehicle to cover a distance of 1 km is 1.0755 kWh. It can thereby be concluded that to cover a distance of 300 km in one charge, a battery with a capacity of approximately 320 kWh needs to be installed.

The battery considered in this paper is a lithium-ion battery for a heavy load EV. Lithium-ion battery is extensively used in EVs due to its property of high energy density and low weight as compared to other battery types of similar capacity. Trucks require batteries with high capacity which can help them to achieve greater travel distances with lesser charging stops. The lithium-ion batteries fulfill this criterion without adding extra weight to the truck.

3.2 Modelling of the EV Charging System

With the EVs dominating the automotive market, charging station infrastructure is still in its niche stage and needs improvement. Various topologies and methodologies have been proposed and tested to make EV charging more efficient. This paper proposes a constant current charging model for an EV battery, suitable for heavy-duty vehicles. The proposed charger can produce a range of constant charging currents, and thus the charging time of the battery can be regulated. The current is controlled by the controller unit presented in Fig. 2.

The charging circuit consists of a universal bridge that acts as a rectifier, a DC link capacitor that produces a constant DC voltage, and a controller. The controller consists of a voltage regulator unit, a current regulating inductor, and a switch. The specification of DC-link capacitance, limiting resistance, and inductance is 58.9 μF , 10 $\text{k}\Omega$, and 100 mH, respectively. The rated voltage of the zener diode is considered

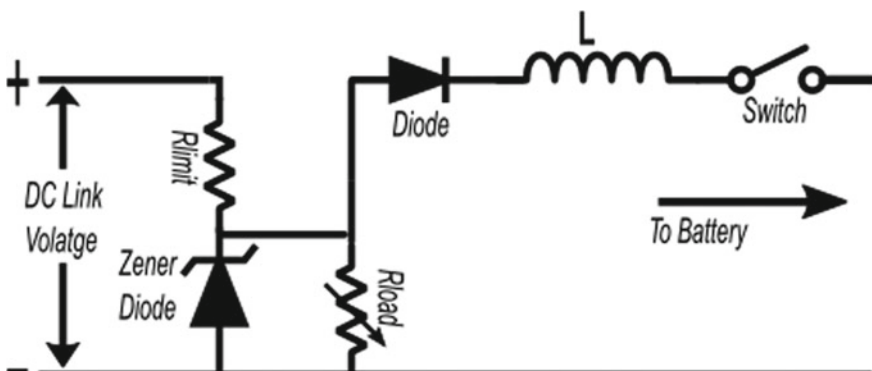


Fig. 2 Controller unit of charger

to be 30 kV for the simulation. Dynamic impedance, knee voltage and the forward voltage drop across the zener diode are considered 0.001 Ω , 400 Ω , and 0.7 V, respectively.

4 Results and Discussion

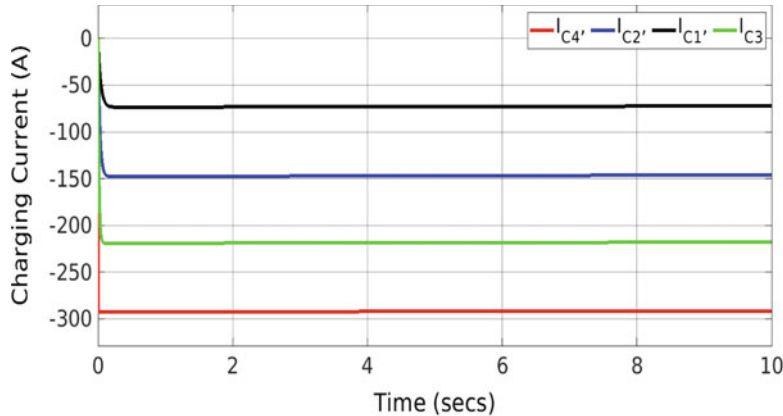
In practical situations, switching between EVs on charging stations may lead to switching transients, which will affect the performance of the charging station. These switching transients might lead to sudden spikes in power consumption or cause high tension faults. Hence, protection devices must be designed and installed at the charging station, to prevent any unnecessary transients in the system. This requires an assessment of the distribution network performance profile, during the time of EV switching. In this study, various charging scenarios (CS) as shown in Table 3, consisting of different charging points and battery topologies, have been assumed. In this study, 4 charging stations (with 12 charging points each), on an 11 kV node of a distribution network have been considered. Table 3 shows, the pattern of switching followed during the analysis.

The EV charger has been designed to give a range of constant current outputs, depending on the requirement. Defining the standard charging current of the charger as 146 A, it will charge the heavy load EV battery in 3.5 h. With this proposed charger model, charging currents between 50 and 200% of the standard value can be achieved. The following graphs depict the charging behavior (SoC) of the battery for the corresponding charging current values.

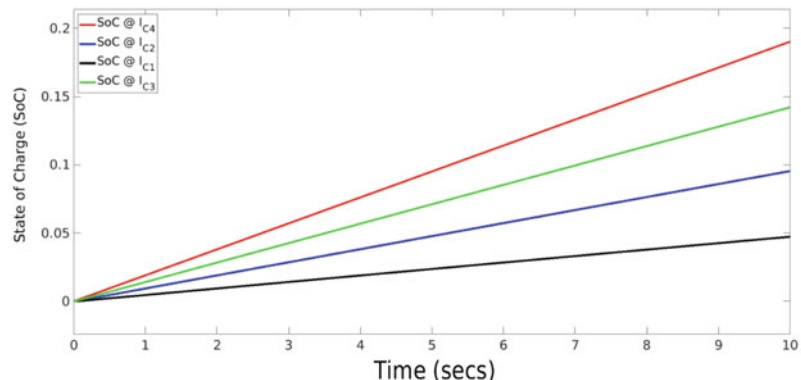
It can be seen from Fig. 3a, b, that the proposed charger can be used to charge the battery to different levels of SoC for the same charging period. A range of charging

Table 3 Switching pattern for EMT analysis

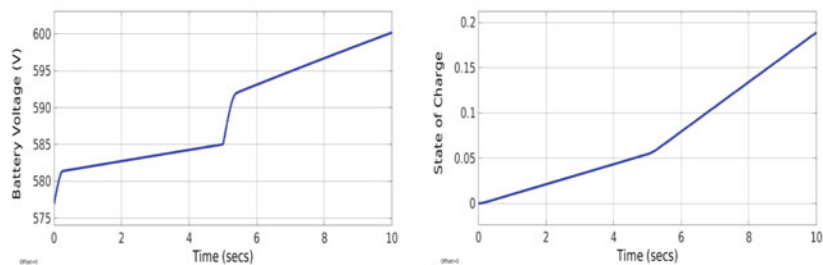
S. No.	Time in s	EVs on charging stations			
		CS1	CS2	CS3	CS4
1	0–1	0	0	0	0
2	1–5	10	10	10	0
3	5–7	0	0	0	0
4	7–8	6	6	6	6
5	8–9	0	0	0	0
6	9–11	6	6	6	6
7	11–15	0	0	0	0
8	15–18	10	10	10	0
9	18–20	0	0	0	0
10	20–24	12	12	12	12



(a) Current characteristic of the EV charging system



(b) SoC of the EV battery for different charging current



(c) Voltage characteristic of the EV battery

(d) SoC of the EV battery

Fig. 3 Characteristics of the EV charging system

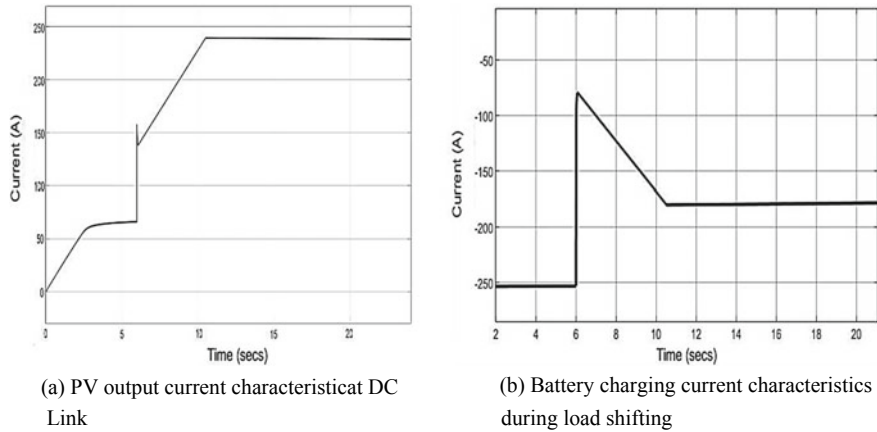


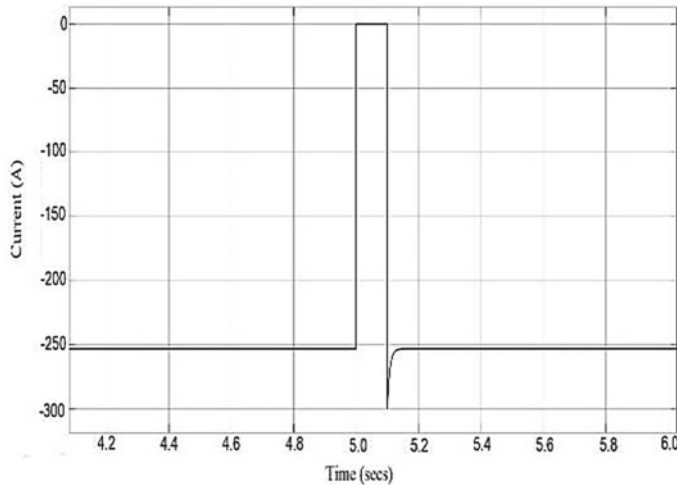
Fig. 4 DC link current characteristic

currents can be achieved by controlling the charger parameters. An increase in the charging current across the battery leads to higher charging rate for the same charging time.

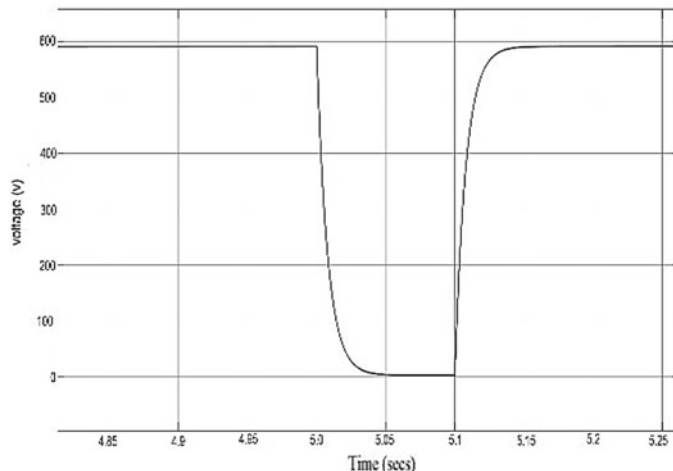
A photo-voltaic (PV) based captive power plant has been modeled to meet the outing of the grid supply. Output current characteristic of PV system at DC link is shown in Fig. 4a. In Fig. 4b, a sharp rise in the EV charging current may be observed during the load shifting (i.e., from grid to PV system). Similarly, transients during short interruption across EV's charging system may be observed in Fig. 5a, b.

5 Conclusion

The design of the charging station is critical for the secure and reliable operation of power distribution network. Various critical design parameters of the charging station can be determined by the EMT analysis. In this paper, a heavy-duty EV battery model has been presented. Design of constant current based EV charging system has also been discussed. A wide range of constant current can be achieved which can regulate the charging time of the battery according to the requirement. The EMT simulation has been performed.



(a) Battery charging current characteristic during switching/interruption



(b) Voltage characteristics across battery during switching/interruption

Fig. 5 Switching analysis across the EV's battery

References

1. Villafáfila-Robles R et al (2011) Electric vehicles in power systems with distributed generation: vehicle to microgrid (V2M) project. In: 11th international conference on electrical power quality and utilisation
2. Shi R et al (2012) Dynamic impacts of fast-charging stations for electric vehicles on active distribution networks. In: IEEE PES innovative smart grid technologies

3. Zheng Y et al (2014) Electric vehicle battery charging/swap stations in distribution systems: comparison study and optimal planning. *IEEE Trans Power Syst* 29(1):221–229
4. Li Q, Xiao X (2013) EV charging and its applications in active distribution systems. In: 2013 IEEE PES innovative smart grid technologies conference (ISGT)
5. Liu N et al (2015) A heuristic operation strategy for commercial building microgrids containing EVs and PV system. *IEEE Trans Ind Electron* 62(4):2560–2570
6. Marcincin O, Medvec Z (2014) Concept of charging stations for electric cars. In: Proceedings of the 2014 15th international scientific conference on electric power engineering (EPE)
7. Bosovic A, Music M, Sadovic S (2014) Analysis of the impacts of plug-in electric vehicle charging on the part of a real medium voltage distribution network. In: IEEE PES innovative smart grid technologies, Europe
8. Torquato R et al (2014) Impact assessment of the two-way operation of plugin electric vehicles on distribution networks. In: 2014 IEEE PES general meeting | conference exposition
9. Joshi K, Lakum A (2014) Assessing the impact of plug-in hybrid electric vehicles on distribution network operations using time-series distribution power flow analysis. In: 2014 IEEE international conference on power electronics, drives and energy systems (PEDES)
10. Sengnongban M, Dechanupaprittha S (2014) Control strategy of PEVs charging for reducing the impact of power fluctuations in micro grid. In: 2014 international electrical engineering congress (IEECON)
11. Bosovic A, Music M, Sadovic S (2015) Analysis of the impacts of plug-in electric vehicle charging on the part of a real low voltage distribution network. In: 2015 IEEE Eindhoven PowerTech
12. Pea-Da B, Dechanupaprittha S (2015) Impact analysis of fast charging to voltage profile in PEA distribution system by Monte Carlo simulation. In: 2015 7th international conference on information technology and electrical engineering (ICITEE)
13. Jiang Z et al (2016) Statistical analysis of electric vehicles charging, station usage and impact on the grid. In: 2016 IEEE power energy society innovative smart grid technologies conference (ISGT)
14. Grackova L, Oleinikova I (2016) Impact of electric vehicle charging on the urban distribution network. In: 2016 57th international scientific conference on power and electrical engineering of Riga Technical University (RTUCON)
15. Moghimi M et al (2016) Impact of PEV behavior on peak demand reduction in a commercial microgrid. In: 2016 Australasian universities power engineering conference (AUPEC)
16. Kumar R, Saxena D (2017) Fault analysis of a distribution system embedded with plug-in electric vehicles. In: 2017 recent developments in control, automation power engineering (RDCAPE)
17. Gómez JR et al (2017) Impact of electric vehicle charging on the distribution system in Cuenca, Ecuador. In: 2017 IEEE PES innovative smart grid technologies conference—Latin America (ISGT Latin America)
18. Longhi G, Borges C, Gruosso G (2018) A model to estimate the impact of electrical vehicles displacement on medium voltage network. In: IECON 2018—44th annual conference of the IEEE industrial electronics society
19. Karmaker AK, Roy S, Ahmed MR (2019) Analysis of the impact of electric vehicle charging station on power quality issues. In: 2019 international conference on electrical, computer and communication engineering (ECCE)
20. Kumar M et al (2012) Analysis of implementing the electric city bus and its coordination with the grid. In: 2012 annual IEEE India conference (INDICON)

Analysis of the Transient Stability of a Multi-machine System with SVC



Srishail K. Bilgundi, M. Shivu, H. Pradeepa, and M. V. Likith Kumar

Abstract Interconnection of remote electric power systems with abundant generation quantity and system load is significantly widespread due to the advancement of the power trade among countries and within countries in various regions of the world. In long-distance AC power transmission, as in interconnected electric power systems, attention to be paid for retaining synchronism besides steady system voltages, notably in combination with faults in the system and line switching. The aim of this paper is to examine the ability of FACTS controller for power flow control and to strengthen the transient stability. A two area two machine systems equipped with SVC is considered for this study, Matlab software is used for simulation.

Keywords Static var compensator · Shunt compensation · Multi-machine system · Transient stability

1 Introduction

Transient stability is vital from the perspective of retaining system security. The development of a fault should not prompt the tripping of generating and the likelihood of successive outages will lead to complete system blackout. Transient stability limit

S. K. Bilgundi (✉) · H. Pradeepa

Department of E&EE, The National Institute of Engineering, Mysuru, Karnataka 570008, India
e-mail: sbilgundi7@gmail.com

H. Pradeepa

e-mail: pradeep3080@nie.ac.in

M. Shivu

Data Analyst, Unilog Content Solutions, Mysuru, Karnataka, India
e-mail: shivu.m04@gmail.com

M. V. Likith Kumar

Department of E&EE, GSSS Institute of Engineering and Technology for Women, Mysuru, Karnataka 570016, India
e-mail: mvlikith2006@gmail.com

is based on the location and magnitude of disturbance and the type of disturbance in the system and also the fault clearance time [1].

For Power system operation, stability and security are critical factors. The power system stabilizers (PSS) are extensively implemented to damp low-frequency oscillations in the range of 0.1–2 Hz. However, PSS may fail to determine the appropriate damping in present-day complicated power systems. Broadly, it is valuable to identify that as loading changes the power parameters of the machine also change accordingly. Hence, PSS adds stability to the discrepancy in loading conditions, specifications and structures of the system. Although PSS provides auxiliary feedback signals, they endure an imperfection of being accountable to produce a considerable discrepancy in the system voltage profile. The utilization of FACTS controllers is highly prominent in power systems [2].

Transient disturbances in power systems have led to the introduction of FACTS controllers like SVC, SSSC, STATCOM, UPFC and IPFC. In stable power systems, when synchronous machines are disturbed, the equilibrium point will either go back to its original state or will reach a new equilibrium state, without loss of synchronism. To increase overall system performance, a lot of research work is already carried out on the cooperation among PSS and FACTS controllers in damping power oscillations [2–7], the parameter tuning of PSS and FACTS controllers is a complicated activity as heavy-handed regional control of PSS and FACTS may lead to destabilizing interactions [2].

2 Proposed Approach

2.1 Introduction to Static Var Compensator (SVC)

The SVC standardizes voltage at its endpoints by consuming reactive power at system voltage beyond the threshold value or by feeding reactive power at system voltage is below the reference value. The SVC and a simplified block diagram of its control system are represented in Fig. 1.

2.2 Description of the Proposed System

A 1000 MVA hydro generation area-1 is interconnected to a remote load area over a 500 kV transmission line of length 700 km. The load Centre consists of 5000 MW + j1500 MVAR inductive load. The power to load is supplied from the remote 1000 MVA area-1 generation and a regional hydro generation area-2 of 5000 MVA. In order to retain system stability for a post fault condition, the ±200 MVar SVC is connected at midpoint of transmission line. Figure 2 represents the single line diagram of the proposed system.

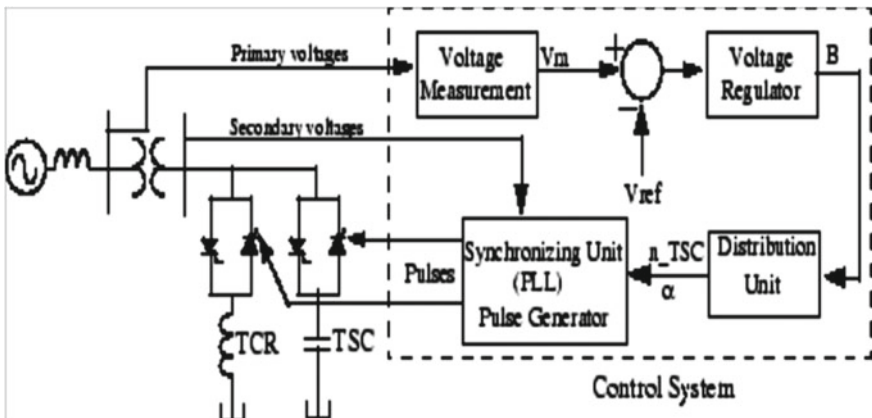


Fig. 1 Single-line diagram of an SVC with its control system block

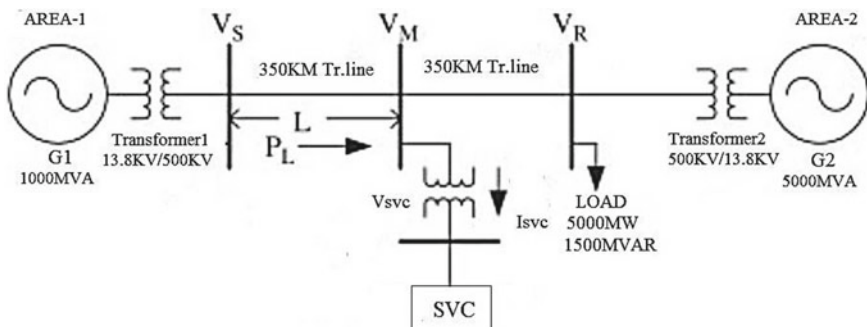


Fig. 2 Single line diagram of the proposed system with SVC at the midpoint of the line

Area-1: 1000 MVA area-1 generator is connected to Bus 1 through a step up transformer-1 (13.8/500 kV, 1000 MVA).

Area-2: 5000 MVA area-2 generator is connected to Bus 3 through a step-up transformer 2 (13.8/500 kV, 5000 MVA).

The two power plants located on the 500 kV systems generate a total power of 6000 MW and is fed to a 5000 MW, 1500 MVar inductive load connected at bus B3. The two machines are designed with a hydro turbine and governor (HTG), IEEE Type-I excitation system, and PSS.

2.3 Cases Considered for Performance Evaluation

The following cases are simulated to evaluate the performance of the system under consideration with SVC connected to transmission line at midpoint.

1. Occurrence of a symmetrical fault
2. Sudden increase of load.

For a stable system, usually, the oscillatory transients that occur after system perturbation will be damped towards a new quiescent condition. These oscillations anyhow cause power flow fluctuations over the transmission lines. If surplus power flow fluctuations in a line connecting to two areas may lead to tripping of protective devices thereby detaching or separating two areas, which may disturb the stability of the tie line. The shunt converter is can produce or consume administrable reactive power based on the requirements [1].

3 Simulation Results of the Proposed System Under Transient Disturbances with SVC Controller

The SVC uses local measurements as input signals to control systems. The Simulink model of the system is shown in Fig. 3.

3.1 Case 1: Occurrence of a Symmetrical Fault

A three-phase to ground symmetrical fault is generated in the system at bus B1 at 1 s for a duration of 6 cycles, i.e., for a time period of $t = 0.1$ s, the following cases are investigated.

1. System with PSS only

The plots of rotor speed of each machine, and tie-line power flow, B_{SVC} a measured voltage in pu, are shown in Figs. 4, 5, 6, 7, 8 and 9. The demagnetizing current rises at the time of fault and remains high even though the fault is cleared, due to increase in the rotor angle. High initial response of the excitation systems with huge ceilings (for field forcing) contributes to 1st swing stability. However, they also affect the damping of subsequent swings. The system becomes unstable even after the clearance of fault.

From Figs. 4 and 5, it is observed that during fault the maximum swing of machine 1 and machine 2 are 68° and 38° , respectively. It also observed that the rotor angle swing is not getting damped and as a result machine 1 goes out of synchronization. The plots of rotor speeds of machine 1 and machine 2, tie line active power, tie line reactive power and terminal voltage are shown in Figs. 6, 7, 8 and 9, respectively.

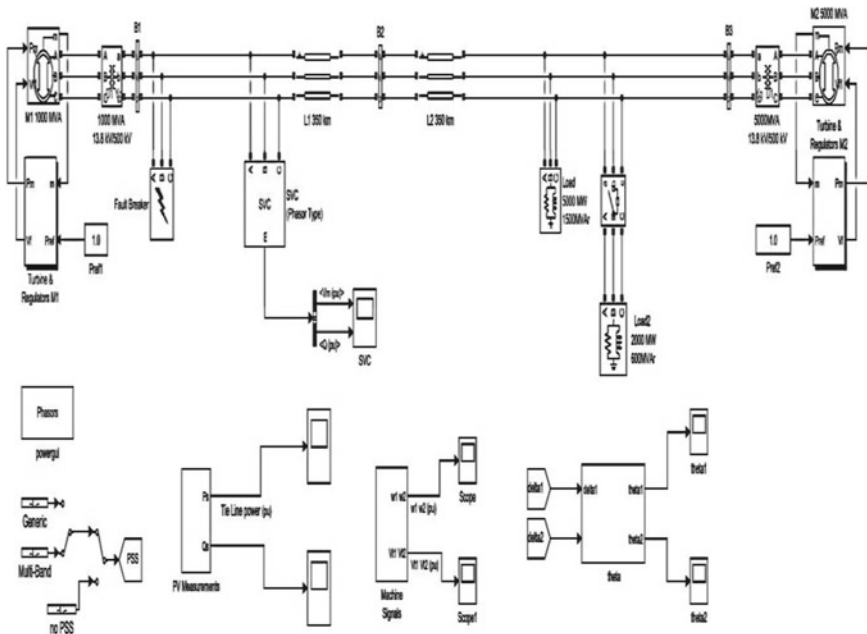


Fig. 3 MATLAB/SIMULINK system model for a symmetrical fault without and with SVC at bus B2

Fig. 4 Plot of rotor angle of machine 1 versus time [system with PSS only]

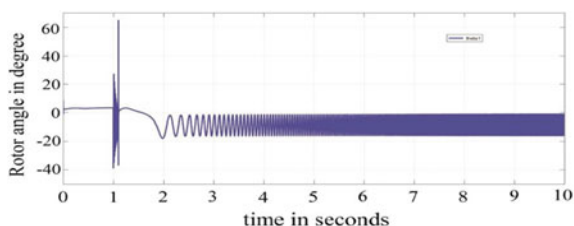


Fig. 5 Plot of rotor angle of machine 2 versus time [system with PSS only]

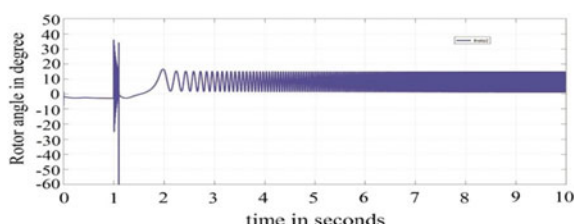


Fig. 6 Plot of rotor speeds of machine 1 and machine 2 versus time [system with PSS only]

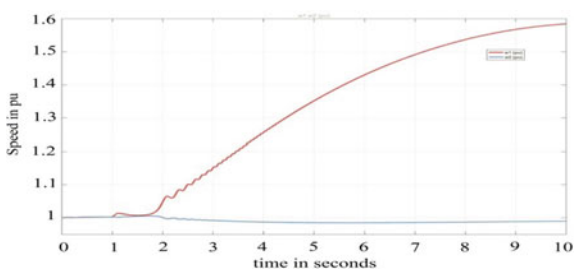


Fig. 7 Plot of tie-line active power versus time [system with PSS only]

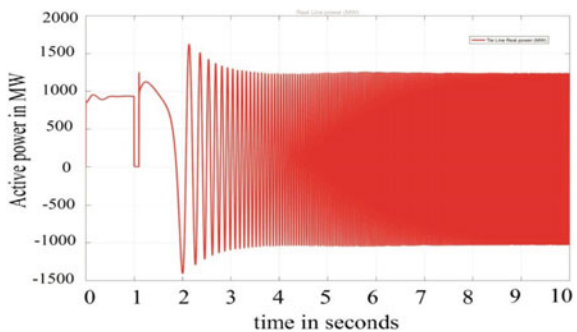


Fig. 8 Plot of tie-line reactive power versus time [system with PSS only]

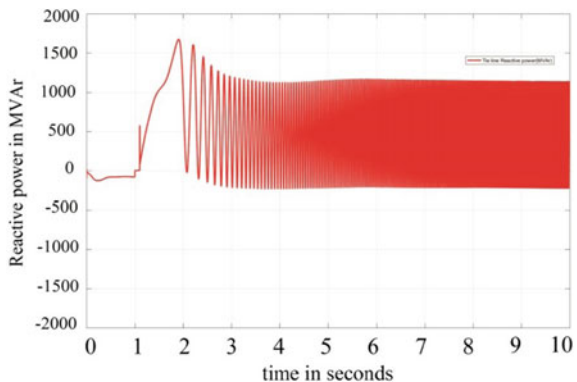
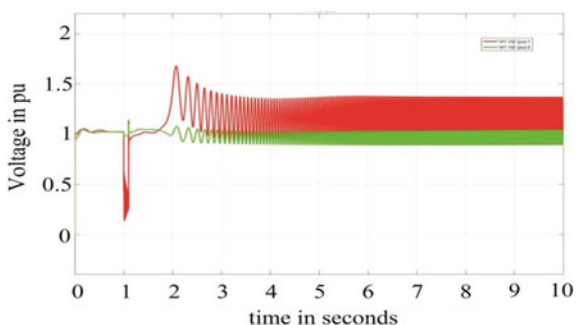


Fig. 9 Plot of terminal voltage versus time



2. System with PSS and SVC

The system has a SVC connected to transmission line at bus B2 i.e., at a transmission line length of 350 km from each of the buses B1 and B3. The plots of rotor angle (with respect to Centre of Inertia), rotor speed of each machine and tie line power flow are shown in Figs. 10, 11, 12, 13, 14 and 15. From the plots it is observed that the system is stable for $t = 0\text{--}1$ s with normal operating conditions (steady state). The system oscillates for short time and become stable with the application of SVC. The primary objective of applying a SVC in transmission network is the fast regulation of voltage at a load or an intermediate bus. The SVC injects a reactive current in phase quadrature with the SVC bus voltage. In the transmission system, the voltage at the middle of the line or some other suitable intermediate point can be maintained with the help of SVC, in case of power flow increment that comes upon instantly

Fig. 10 Plot of rotor angle of machine 1 versus time [system with PSS and SVC]

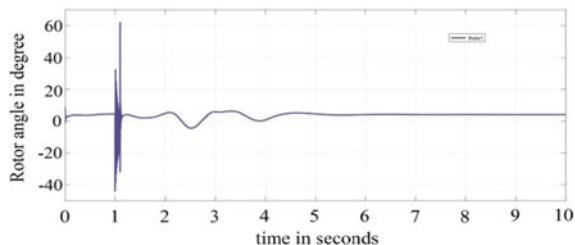


Fig. 11 Plot of rotor angle of machine 2 versus time [system with PSS and SVC]

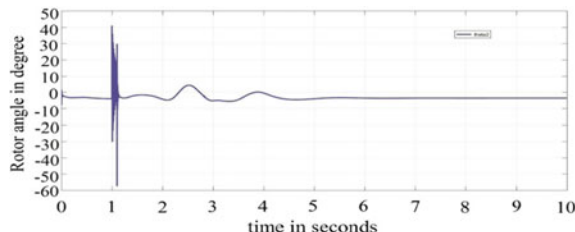


Fig. 12 Plot of rotor speeds of machine 1 and machine 2 versus time [system with PSS and SVC]

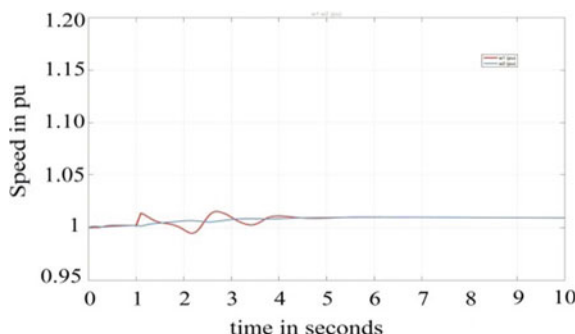


Fig. 13 Plot of tie-line active power versus time [system with PSS and SVC]

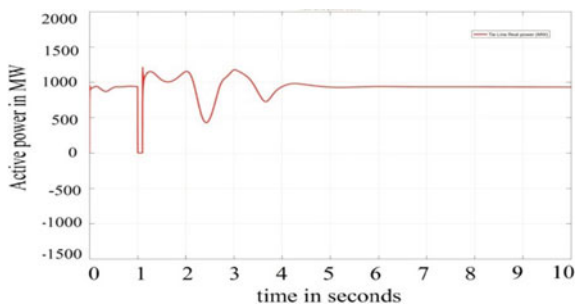


Fig. 14 Plot of tie-line reactive power versus time [system with PSS and SVC]

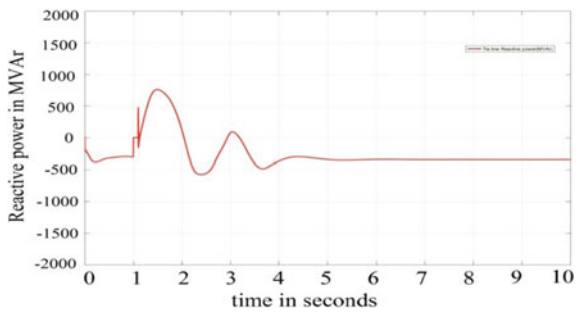
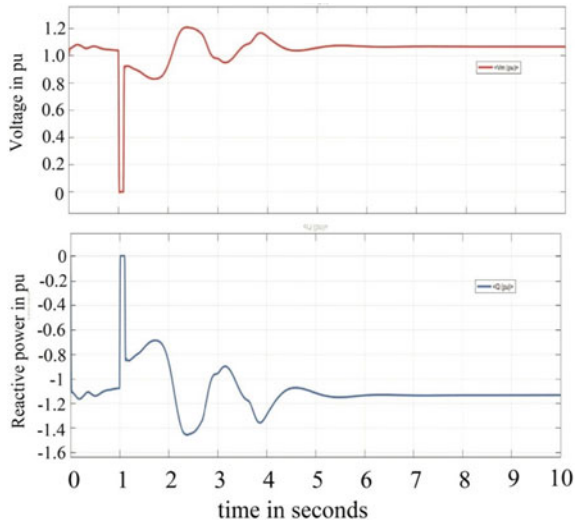


Fig. 15 Plot of bus voltage and reactive power injected by SVC versus time



after clearing the fault. Hence, terminal voltage is improved after clearance of fault thus the transient stability of the system with SVC is improved considerably.

As observed from Figs. 10 and 11 within few cycles the system regains the stability after fault clearance whereas, with only PSS the system loses its stability as seen in

the previous case, it is also observed that there are no power swing oscillations when SVC is present along with PSS. The plots of rotor speeds of machine 1 and machine 2, tie line active power, tie line Reactive power, bus voltage and reactive power injected by SVC are shown in Figs. 12, 13, 14 and 15, respectively.

3.2 Case 2: Sudden Increase of Load

The load in the system is suddenly increased by 20% of normal load at 1 s at bus B3 for a duration of 25 cycles i.e., for a time period of 0.4 s. The Simulink model of the system is shown in Fig. 3.

1. System with PSS only

The plots of rotor angle (with respect to Centre of Inertia), rotor speed, terminal voltage of each machine and tie-line power flow are shown in Figs. 16, 17, 18, 19, 20 and 21. From the plots, it is inferred that the system is stable from 0 to 1 s with normal load conditions (steady-state). When a load connected to the system is increased suddenly, it results in a transient disturbance. The system becomes unstable even after the disconnection of additional load as there is a large decrease in the system voltage.

From Figs. 17 and 18, it is observed that during step increment of load there is a maximum rotor angle swing of 14° and 16° in machine 1 and machine 2, respectively. It is also observed that the rotor angle swing is not getting damped and as a result machine 1 goes out of synchronization. The plots of rotor speeds of machine 1 and machine 2, tie line active power, tie line reactive power, and terminal voltage are shown in Figs. 19, 20, 21 and 22, respectively.

Fig. 16 Plot of rotor angle of machine 1 versus time [system with PSS only for sudden increment in load]

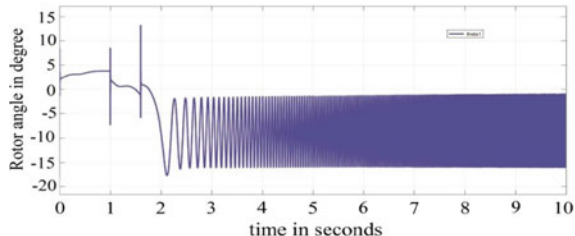


Fig. 17 Plot of rotor angle of machine 2 versus time [system with PSS only for sudden increment in load]

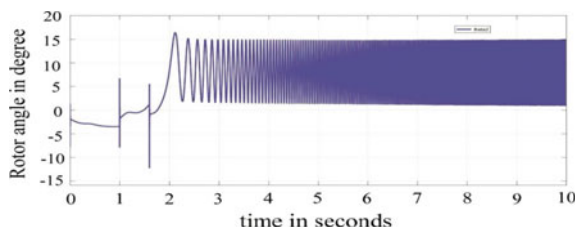


Fig. 18 Plot of rotor speeds of machine 1 and machine 2 versus time [system with PSS only for sudden increment in load]

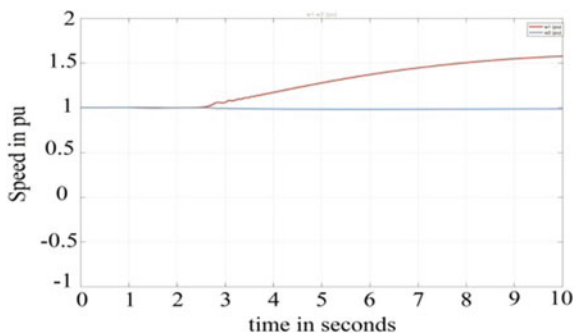


Fig. 19 Plot of tie-line active power versus time [system with PSS only for sudden increment in load]

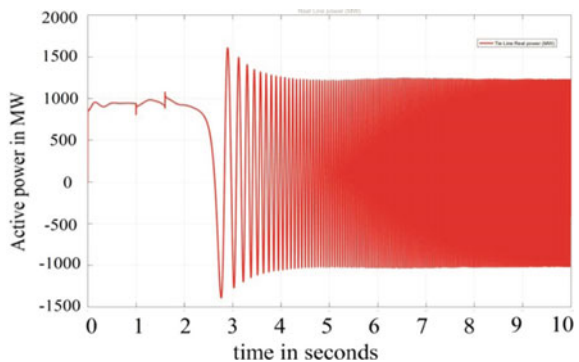


Fig. 20 Plot of tie-line reactive power versus time [system with PSS only for sudden increment in load]

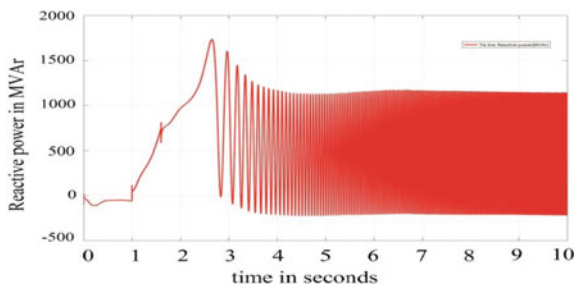


Fig. 21 Plot of terminal voltages of machine 1 and machine 2 versus time [system with PSS only]

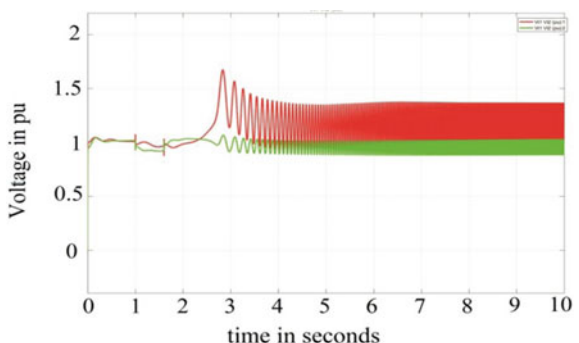
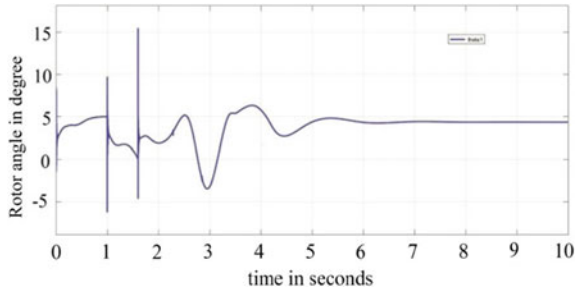


Fig. 22 Plot of rotor angle of machine 1 versus time [system with PSS and SVC for sudden increment in load]



2. System with PSS and SVC

The system has a SVC connected to transmission line at bus B2, i.e., at a transmission line length of 350 km from each of the buses B1 and B3. The plots of rotor angle (with respect to Centre of Inertia), rotor speed of each machine and tie line power flow are shown in Figs. 22, 23, 24, 25, 26 and 27, respectively. From the plots, it is inferred that the system is stable from 0 to 1 s with normal load conditions (steady-state). When the load connected to the system is suddenly increased it results in a

Fig. 23 Plot of rotor angle of machine 2 versus time [system with PSS and SVC for sudden increment in load]

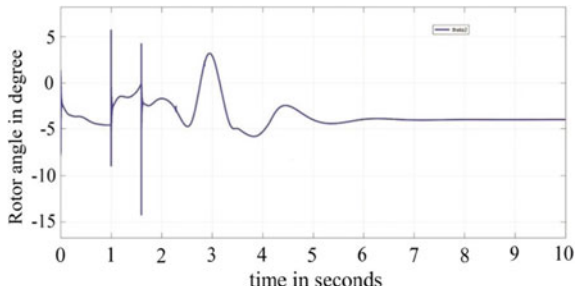


Fig. 24 Plot of rotor speeds of machine 1 and machine 2 versus time [system with PSS and SVC for sudden increment in load]

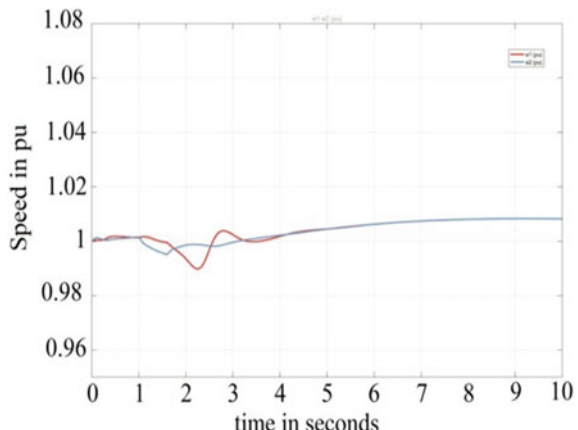


Fig. 25 Plot of tie-line active power versus time [system with PSS and SVC for sudden increment in load]

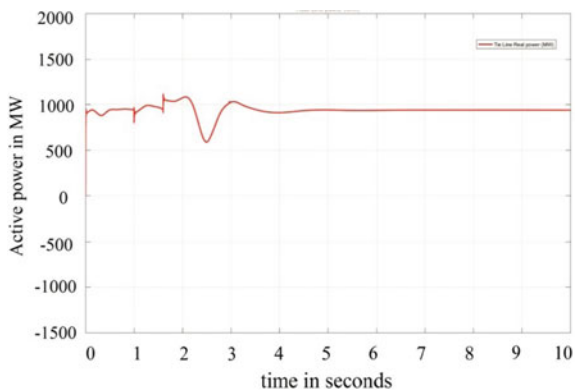


Fig. 26 Plot of tie-line reactive power versus time [system with PSS and SVC for sudden increment in load]

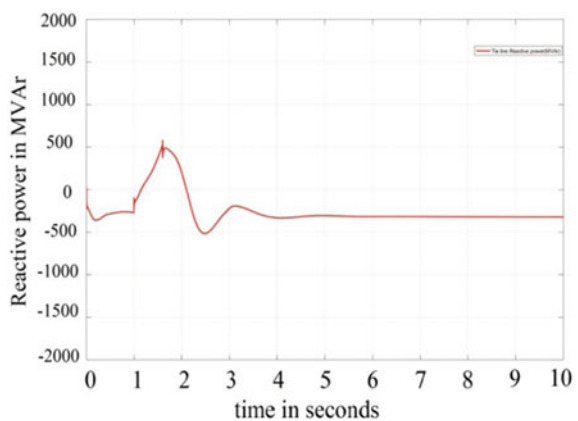
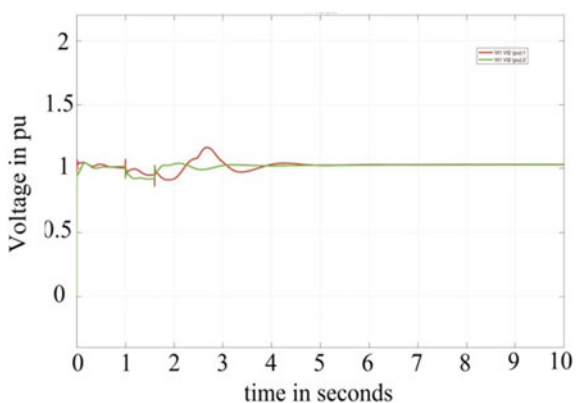


Fig. 27 Plot of terminal voltages of machine 1 and machine 2 versus time [system with PSS and SVC]



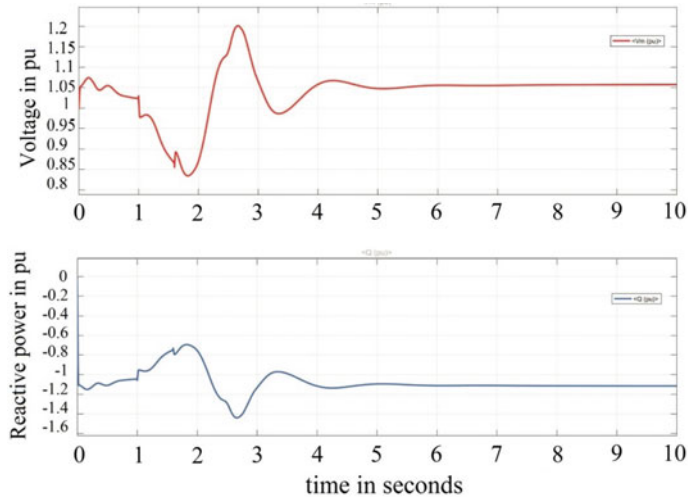


Fig. 28 Plot of bus voltage and reactive power injected by SVC versus time [for sudden increment in load]

transient disturbance. The system oscillates for short period of time and becomes stable with the application of SVC. Whenever an additional load is connected to the system, voltage decreases below the rated value. Thus, the SVC will inject a reactive current ' I_{SVC} ' in negative (capacitive mode operation of SVC). The plots of SVC bus voltage and reactive power injected by SVC are shown in Fig. 28.

As observed from Figs. 22 and 23 within a few cycles the system regains the stability during step increment of load. It is also observed that there are no power swing oscillations in this case. The plots of rotor speeds of machine 1 and machine 2, tie line active power, tie line Reactive power, terminal voltages of machine 1 and machine 2, bus voltage and reactive power injected by SVC are shown in Figs. 24, 25, 26, 27 and 28, respectively.

Summarizing the contributions of this paper; the model developed subjected to different types of transient disturbances is analyzed. The stability of the proposed system with and without SVC is examined by connecting the SVC to transmission line at mid-point. From the results, it is observed that the system effectively damps the power oscillations under transient disturbances.

4 Conclusion

A fast-acting power electronics-based voltage impedance type converters are developed to improve the transient stability to a large extent. In this paper, dynamics of the power system performance are compared with and without SVC in the event of transient disturbances. Proposed FACTS controller is implemented in

MATLAB/SIMULINK. Simulation results indicate that a two area two machine system provides better damping characteristics in the presence of SVC and PSS than PSS alone.

References

1. Patel AD (2015) Comparison of shunt FACTS controllers for the improvement of transient stability of two machine power system using MATLAB modelling. *Int J Sci Res Dev* 3(10) (2015). ISSN (online): 2321-0613
2. Nayak S, Mohapatra SK (2015) Coordinated design of PSS and STATCOM based power oscillation damping controller using MOL algorithm. *Int J Appl Innov Eng Manag (IJAIEM)* 4(12). ISSN 2319 – 4847
3. Zhou E (1993) Application of static VAr compensators to increase power system damping. *IEEE Trans Power Syst* 8(2):655–661
4. Singhal P, Madotra PK (2015) Transient stability enhancement of a multi machine power system using SVC controller. *Int J Emerg Trends Technol Comput Sci* 4(1)
5. Banga A, Kaushik S (2011) Modeling and simulation of SVC controller for enhancement of power system stability. *Int J Adv Eng Technol*
6. Kushwah R, Gupta M (2016) Modelling & simulation of SVC and statcom for enhancement of power system transient stability using Matlab. In: 2016 international conference on electrical, electronics, and optimization techniques (ICEEOT), Chennai, pp 4041–4045
7. Virk PS, Garg VK (2013) Power system stability improvement of long transmission line system by using static var compensator (SVC). *Int J Eng Res Appl* 3(5):1–3(3)

Projection-Based Throughput Computation of Three-Dimensional Geographical Routing Protocol for Multi-hop Wireless Sensor Networks



Afruza Begum and Md. Anwar Hussain

Abstract Three-dimensional multi-hop wireless sensor networks consist of a large number of wireless devices having sensing and communication capabilities to perform a collaborative task for supporting a wide range of applications. In the majority of the existing routing techniques are proposed considering 2D environments, maybe because of working with 3D space is more difficult than 2D space, but in various real-life scenario nodes need to be deployed in 3D space also. An efficient 3D routing technique that gives maximum overall throughput becomes very essential because traditional existing 2D routing techniques are not perfectly applicable in 3D environment. In this paper, we have proposed a projection technique to project the routing paths obtained by our earlier proposed three-dimensional routing protocol and computed the throughput and other performance metrics based on the projection technique to simplify the working difficulties with the route in 3D space and for enhancing the overall network performance. The performance of the proposed technique is evaluated through extensive simulation in Matlab platform in terms of end-to-end throughput, energy consumptions, and end-to-end delay.

Keywords Routing · End-to-end delay · Throughput · Three-dimension · Protocol · Projection

1 Introduction

Multi-hop wireless sensor network consists of number of a wireless device having sensing and communication capabilities to perform a collaborative task. In most of the multi-hop wireless network, communication between wireless devices is done through radio propagation range, for long-distance communication, when the destination is not within the transmission range of sender, one or more intermediate node is

A. Begum (✉) · Md. Anwar Hussain

Department of Electronics and Communication Engineering, NERIST, Itanagar 791109, India
e-mail: afruza.moon@gmail.com

Md. Anwar Hussain

e-mail: bubuli_99@yahoo.com

used as a next-hop relay/forwarder to reach the destination, and this is called multi-hop routing. In last few decades, a large number of geographic routing technique has been proposed, almost all of those techniques are designed for two-dimensional space [1], however, in various real-life scenarios sensor nodes need to deployed in 3D space for important applications like underwater ocean monitoring, forest fire monitoring, weather monitoring, environment, pollution monitoring, etc. 3D embedding in routing gives more accurate network behavior and results. Geographic routing is a very popular and efficient routing technique; it uses location information for routing instead of IP address. Considered that each node in the network knows the location of itself, location of its neighbor and destination using Global Positioning System (GPS) or other centralized location management techniques. In the network of nodes, some of those nodes are considered as *sender or *user and one of those nodes as a *base station or *destination.

End-to-end throughput, delay, and energy consumption are very crucial network parameter for 3D multi-hop wireless sensor network when a huge number of nodes are distributed over an area in a 3D space, it becomes very essential to design routing and scheduling algorithm, which is energy efficient, needs minimum delay and hops to reach the destination, and gives maximum overall throughput. When a user (sender) in multi-hop wireless sensor network is sending packets to the base station (destination), the user node should select such an intermediate node/path to go forward, such that information can be sent in less time (delay) with minimum energy consumptions and gives maximum throughput. Dealing with and implementing 3D routing protocol is much more complicated than dealing with two-dimensional routing. Projecting the path obtained in 3D space into a plane may simplify the task up to some extends.

In this paper, we have presented a projection technique to project the path obtained by our earlier proposed 3D routing and scheduling technique [1] on to a particular plan to simplify the working difficulties with the route in 3D space and enhancing the overall network performance. Performance metrics such as end-end delay and throughput and energy consumption are computed by the proposed projection technique and compared with the performance metrics of origin route in 3D space. Here in the proposed projection technique, each intermediate distance (path) travel by proposed protocol in a 3D multi-hop wireless network is projected onto a particular plan in 3D space, which simplifies the complications of graphing on 3D space. The route obtains from the proposed projected technique consumes less energy, requires a minimum delay, and gives maximum throughput compared to the original route and some existing popular routing protocol. Each sender selects the minimum angle IM node within the transmission range, the line joining the sender and the selected IM is projected on to a particular plane, for each sender/user this process of selection of minimum angle IM and then the projection of selected node on to the plane is repeated till it reached the destination (base station).

The rest of the paper is divided into different sections as follows—Description of related existing works is done in Sect. 2, the methodology and the proposed technique is described in Sects. 3 and 4 is detail about result analysis and performance evaluation and the Sect. 5 is the conclusion and future works.

2 Related Works

Research in three-dimensional wireless networks is gaining popularity because of many applications like natural resource monitoring, pollution monitoring, forest fire monitoring, prediction of natural resources, and many more. In [2], Mariam Akbar et al. introduced a mobile sink AUV and courier node for 3D underwater sensor networks for minimizing energy consumptions. In [3], to improve the performance of the sensor network, the author Ganglia et al. proposed a high-availability data collection scheme based on multiple autonomous underwater vehicles. They have also proposed malfunction discovery and repair mechanisms when the AUV fails to communicate with each other.

In [4], the authors proposed a Robust and Efficient Routing Protocol (RERP) to obtain a static route for the communication between two nodes in the network. They have assigned a rank to every node by a stable network by formulating some important aspects of the sensor. They have selected the least rank sensor nodes for efficient communication. In [5] this paper, Ghoreyshi et al. proposed energy-efficient cluster-based novel mobile data gathering (CMDG) scheme for large-scale UWSNs. The authors have claimed that to deal with the sensors mobility in UWSNs, CMDG is the first AUV tour planning scheme, this technique is applicable in both connected and disconnected networks.

In [6], the authors proposed a prediction-based delay optimization data collection algorithm (PDO-DC). To obtain the corresponding prediction models, delay optimization algorithms, Kernel Ridge Regression (KRR) is utilized via cluster member nodes. Here to reduce the delay, the AUV obtains all the cluster data it traverses by less cluster head nodes. In [7] using the adaptive packet forwarding region (PFR) and selecting fast-forwarding nodes in the PFR, Rubeaai et al. have proposed a three-dimensional real-time routing protocol (3DRTGP) for wireless sensor networks. In 3DRTGP they have used the PFR technique to limits the number of nodes forwarding towards the destination and they also given heuristic solution to the multi-hop wireless networks.

Shah and Kim [8] analyses various issues related to 3D wireless ad hoc and sensor networks, they have discussed mainly 3D underwater sensor networks (UWWSN) and 3D airborne ad hoc networks (AANET's). Design requirements and challenges in 3D AANET's and UWWSN is discussed thoroughly, different researchers have highlighted different issues associated with sensor networks and 3D wireless ad hoc networks.

In [9] Entezami and Christos Politis have proposed a real-time, position-based and energy-efficient protocol for WSNs based on the spanning tree method. When looking for a path to the destination they have used a greedy forwarding approach. To reduce the minimum number of node forwarding they have uses unique restricted parent forwarding regions (PFR), to cover only the parent node, it reduces the radio range. To overcome from dead-end route problem they have used a rainbow mechanism.

In the paper [10], optimized depth-based routing (iAMCTD) has been proposed, which is based on improved adaptive mobility of courier hubs. This protocol is used

for distance communication and mainly for the fisherman to identify the country's border while fishing. In [11], Ahmed et al. proposed two-level redundant transmission control (RTC) approach using some statistical test that ensures the data-similarity, the data similarity from the original data removed before forwarding to the next level by the cluster head and the regional head. Redundant transmission between the mobile sink and cluster head is controlled by the region head. The data-similarity and redundant inner-network transmissions between clusters members are controlled by the cluster head.

In this paper, we have calculated the performance metrics throughput, energy consumption, delay of the proposed 3D routing protocol with the proposed projection method, here the line joining the sender/user node and the selected minimum angle intermediate node of 3D space is projected on to a particular plane to simplify the calculations and working difficulties with the 3D space, this process is repeated till reaches the destination, performance metrics are compared and it is found that the performance of the projection method outperforms the performance of the origin route found in 3D space and the popular typical routing protocol Most Forward Routing (MFR).

3 Protocol Design

In the design of this proposed protocol for multi-hop wireless networks, we have considered that each node knows its location, location of the destination, and locations of neighbors through GPS or some other centralized location management techniques. It is considered that all the nodes in the networks are homogeneous and every node has the transmission range of Tr , nodes are scattered randomly in a uniform manner in a 3D space. Consider a set of U stationery nodes in three-dimensional planes X , Y , Z . When sending information to the base station which is not in the transmission range of sender node, sender node sends information's through one or more intermediate nodes. Any two nodes P and Q can communicate with each other if the Euclidean distance between P and Q is less or equal to its transmission range (Tr), i.e., $|PQ| \leq Tr$.

In the implementation of the proposed protocol, first a reference line from *source to destination is drawn, then within the transmission range, the node which forms a minimum angle with this drawn reference line is considered as an intermediate node to transfer information towards a destination. Suppose P is the source node, and within the transmission range Tr , among all the neighbors the node Q makes minimum angle with the reference line, suppose the node P has location information (P_x, P_y, P_z) , the location of the destination D is (D_{sx}, D_{sy}, D_{sz}) and the location of a neighbor node Q is (Q_x, Q_y, Q_z) .

The vector \vec{PD} is given by $(P_x - D_{sx}, P_y - D_{sy}, P_z - D_{sz})$ and \vec{PQ} is given by $(P_x - Q_x, P_y - Q_y, P_z - Q_z)$. The angle $\angle QPD$, i.e., θ formed by node Q with the reference line drawn from P to D is calculated by using Eq. 1 [1].

$$\theta = \cos^{-1} \left[\frac{\overrightarrow{PQ} \cdot \overrightarrow{PD}}{\|\overrightarrow{PQ}\| \|\overrightarrow{PD}\|} \right] \quad (1)$$

where $(\overrightarrow{PQ} \cdot \overrightarrow{PD})$ is the dot product of \overrightarrow{PQ} and \overrightarrow{PD} . $\|\overrightarrow{PQ}\|$ and $\|\overrightarrow{PD}\|$ is the Euclidean vector norms [7].

The projection of the line joining the sender node and the selected minimum angle intermediate node is done on considering a particular plane (there are infinite number of plans), this minimum angle node Intermediate Node (IM) acts as the new sender node, this new sender node(IM) a reference line is drawn to the destination, then from neighbor list of this new sender node minimum angle node is selected again and projection of the line joining the new sender and the new selected IM is projected on to the plane. The same procedure will be repeated for the selection of IM and project it on to the plane till it reaches the destination/base station.

If the line is perpendicular to the plane, its projection on to the plane is simply the intersection point on the plane, and if the line is parallel to the plane then it is also parallel with its projections onto the plane and orthogonal to the normal vector of the plane. If the line on the 3D space is not parallel also not perpendicular to the plane then the projection of a line onto a plane is the line one end joining the intersection points of line and the plane and the intersection of the normal through the other ends of the line and the plane, or the line joining the two intersections through the normal of the two ends of the line and the plane.

As shown in the Fig. 1, S is the sender and if IM is the selected minimum angle intermediate node, for projecting the selected IM onto the projection plane, need to consider a plane in 3D space, suppose the plan is $ax + by + cz + d = 0$, then calculation of equation of the line is done by joining the sender node and the IM node.

Intersection point of the line and the plane is calculated or the intersections of the normal through ends of the line, S' and IM' is the intersection point of S and IM on to the plane, the projection of line SIM on to plane is $S'IM'$. If $S(sx_1, sy_1, sz_1)$, is the sender and the Intermediate node is $IM(mx_1, my_1, mz_1)$ the intersection point $S'(ip_x, ip_y, ip_z)$ of the line and the plane is calculated from the equation of line by the following equations:

$$ip_x = a * t + sx_1 \quad (2)$$

$$ip_y = b * t + sy_1 \quad (3)$$

$$ip_z = c * t + sz_1 \quad (4)$$

where a, b, c is the normal vectors and the t is the parameter describes a particular point on the line, sx_1, sy_1, sz_1 is the location of the node which needs to project on to the plane. Now putting the values of the equations intersection points (ip_x, ip_y, ip_z)

on the equation of the plane (in x , y , and z).

$$a(at + sx_1) + b(bt + sy_1) + c(ct + sz_1) + d = 0 \quad (5)$$

Solving the Eq. 5, obtained the value of the parameter t .

$$t = -\frac{asx_1 + bsy_1 + csz_1 + d}{a^2 + b^2 + c^2} \quad (6)$$

where d refers to the transition or sliding of plane, so that the plane doesn't pass through the origin a, b, c is the normal vectors, the parameter t describes the particular point on the line. Solving the Eq. 5, obtained the value of the parameter t .

$$Ip_x = sx_1 - a \cdot \frac{asx_1 + bsy_1 + csz_1 + d}{a^2 + b^2 + c^2} \quad (7)$$

$$Ip_y = sy_1 - b \cdot \frac{asx_1 + bsy_1 + csz_1 + d}{a^2 + b^2 + c^2} \quad (8)$$

$$Ip_z = sz_1 - c \cdot \frac{asx_1 + bsy_1 + csz_1 + d}{a^2 + b^2 + c^2} \quad (9)$$

Obtained S' (Ip_x, Ip_y, Ip_z) is the intersection point, i.e., the projection of node S (Fig. 1) of 3D space onto the plane. Similarly, projection of the other end of the line (IM) as shown in Fig. 1 is calculated, it is the intersection of the normal through the

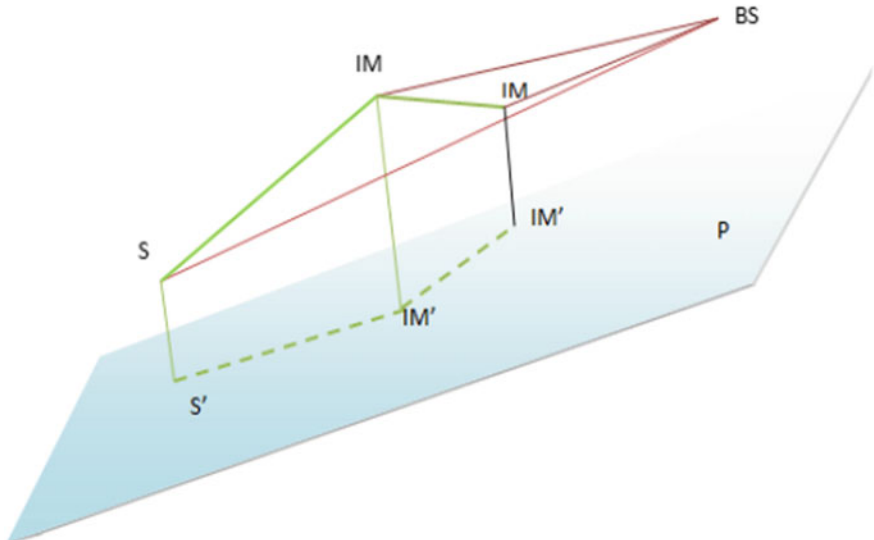


Fig. 1 Projection of the selected path of 3D space on to a plane

point IM . Now joining the two intersection points $S'IM'$ on the plane is a projection of the line SIM of 3D space on to the plane. Now the IM will select another minimum angle IM to go towards the destination. The same procedure of selection of minimum angle node on 3D space and project is on to the 3D plane we have considered will be repeated till it reached the destination node.

4 Performance Evaluation and Result Discussion

Performance of the proposed technique is evaluated by comparing the output metrics of the origin route obtain in the 3D space, the route obtains after projection on to the plane and with route obtain from the popular the typical protocol Most Forward Routing (MFR). We have just considered the route selection techniques of MFR. We have executed in the Matlab platform considering a 3D network environment, the number of the nodes we have increased from 100 to 500, by adding 50 number of nodes every time and each node in the network has the transmission range 2.5 km. For accuracy, we have run each network 100 times and take the average for statistical constant result. We have considered a plane $3x - 2y - 2z + 2 = 0$ for projecting the line joining the sender node and the considered intermediate node (IM) to forward toward the destination. In the networks, all the nodes are scattered randomly, among all the scattered nodes some are considered as a sender/user (S), and one them is considered as a base station (BS). We have considered here the three performance metrics end-to-end throughput, energy consumption, and the end-to-end delay. The commons simulation parameters are tabulated in Table 1 [1].

In unit time, successfully transmitted data amount from source to destination is measured as end-to-end throughput (ETH). Figure 2 depicts the changes of the end to end throughput for an increasing number of nodes deployment for the route obtained by our proposed protocol in the 3D space, route obtained due to projection of the selected route onto the plane and the route obtained by the popular typical protocol MFR. From Fig. 2, it is seen that end-end throughput of the route obtained due to projection on to the plane, gives better performance than the origin route obtained on the 3D space and the MFR because routing in 3D space is much more complicated than routing in 3D plane. Projecting the routes on a 3D plane simplifies

Table 1 Network simulation parameters

Network parameters	Values
Data packet size	1 MB
Network area	$5 \times 6 \times 5$ km
Number of nodes	100–500
Range of node	2.5 km
E_{elec}	50 nJ/bit
E_{amp}	100 pJ bit m ²

the routing process and improve the performance of the routing. From Fig. 2 it is also observed that with increasing network density, average end-to-end throughput increases very slightly, as the number of nodes deployed in the network does not create any considerable changes in the selection process of intermediate nodes (IM) to forward packets toward destination. It is also observed, end-end throughput increases slightly in case of plane compared to 3D space and MFR whenever we calculate routes, with an increasing number of nodes in the networks, this because find route on a plane is easier than challenging 3D space.

The amount of time needed for transmitting information from source to destination is the end-end delay. The Fig. 3 shows the variations of end-to-end delay under increasing number of node deployment for the proposed techniques with the popular existing protocol most forward routing (MFR). From the Fig. 3, it can be observed that end-to-end delay for the route obtain through the projection on the plane is much less than the route obtain in the 3D space and the route obtains by most forward routing(MFR), less delay means better performance. This is because projection on the 3D plane simplifies the complexities of working with 3D space. From Fig. 3, also we have observed that the end-to-end delay decreasing very slightly with the increasing number of node deployment. Because when the transmission range is constant, number of nodes deployed do not create any issue in the position of selected IM nodes to forward packets toward destination.

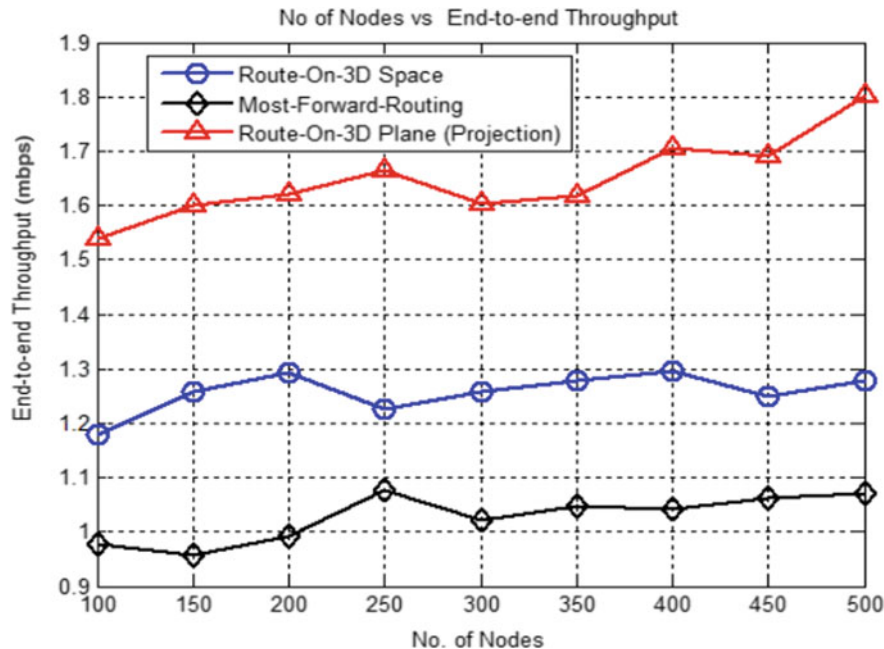


Fig. 2 End-end throughput variation with different number of nodes deployment

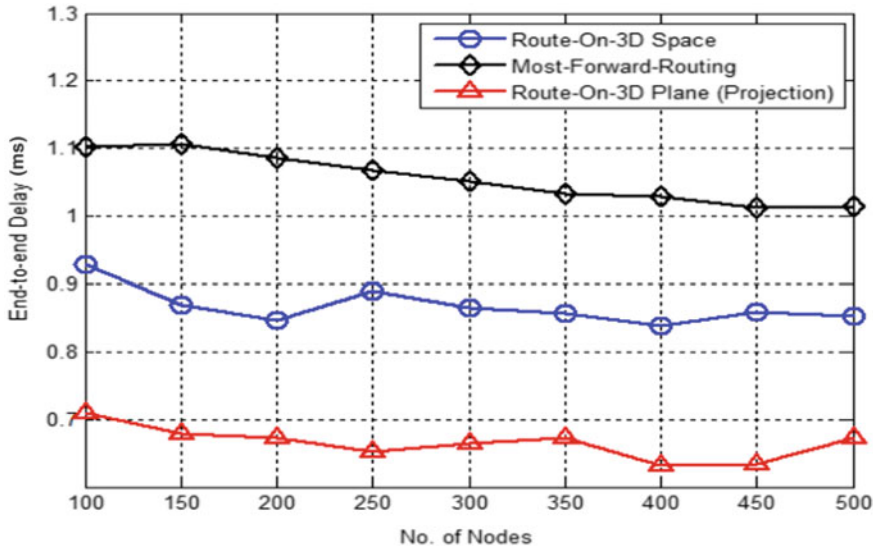


Fig. 3 End-to-end delay variation with different number of nodes deployment

Energy consumption is a very important issue for the nodes deployed in an underwater multi-hop wireless network. Figure 4 depicts the variation in consumption of energy for an increasing number of nodes deployment for the route obtained by the proposed technique in 3D space and the projected route on to the 3D plane, and the typical protocol most forward routing (MFR). From Fig. 4, it is seen that energy consumption for a route in 3D space and the route obtained on the projected 3D plane by proposed technique is considerably less than the existing protocol the Most Forward Routing (MFR) because, in 3D space, selection of the IM node is done based on minimum angle node with the reference line, it chooses the IM nodes which are not too far away from source and destination, so the energy consumption is decreased. It is also observed that with the increasing number of node deployment energy consumption decreases when there is less number of nodes are there in the network, the route through 3D space consumes less energy than the route through 3D plane, but when more number of nodes are there in the network, route though 3D plane consumes less energy than the 3D pace and most forward routing (MFR), this is because with an increasing number of node better *IM* can be found to go forward towards the destination.

5 Conclusion and Future Work

In this paper, we have computed the performance metrics for the proposed three-dimensional routing protocol based on the projection technique, first route discovery

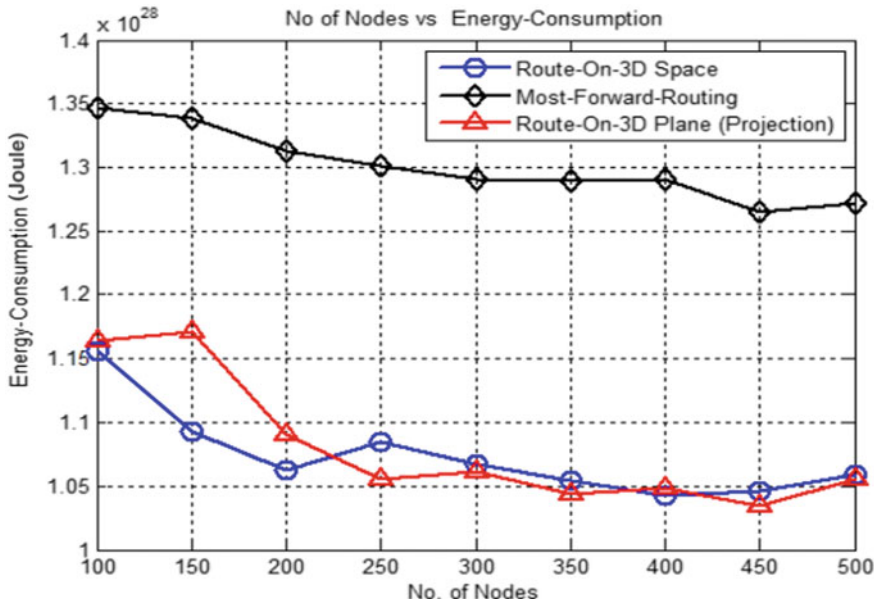


Fig. 4 Energy consumption variation with different number of nodes deployment

is done in 3D space based on the neighbor node that makes a minimum angle with the reference line from sender to destination or base station, then the path obtained on the 3D space is projected on a particular plane to enhance the performance of the route obtained in challenging 3D space. Performance of the proposed techniques is evaluated by calculating the end-end delay and throughput, and energy consumption for each user at the time of computing routes from source to the base station. Output metrics is compared with popular existing protocol, from the result analysis it is observed that the performance metrics of proposed techniques outperform the existing techniques. In future work, our focus will be on developing efficient scheduling techniques so that at a time more than one user can send data without any interference, considering node mobility of the nodes in a network.

*Sender, user, source are used synonymously and the base station and destination are used synonymously.

Acknowledgements This work is fully supported by the Visvesvaraya Ph.D. Scheme, MeitY, Government of India. The authors are thankful to the MeitY, GoI.

References

1. Begum A, Hussain MA, Bora J, Askari SMS (2018) A simple three-dimensional joint routing and scheduling protocol for multi-hop wireless networks. In: 2018 4th international conference on recent advances in information technology (RAIT), pp 1–7. IEEE
2. Akbar M, Javaid N, Khan A, Imran M, Shoaib M, Vasilakos A (2016) Efficient data gathering in 3D linear underwater wireless sensor networks using sink mobility. Sensors 16(3):404
3. Han G, Long X, Zhu C, Guizani M, Zhang W (2019) A high-availability data collection scheme based on multi-auvs for underwater sensor networks. IEEE Trans Mobile Comput
4. Jain R, Rakesh N (2018) Robust and efficient routing in three-dimensional underwater sensor network. In: Proceedings of first international conference on smart system, innovations and computing, pp 107–116. Springer
5. Ghoreyshi SM, Shahrabi A, Boutaleb T, Khalily M (2019) Mobile data gathering with hop-constrained clustering in underwater sensor networks. IEEE Access 7:21118–21132
6. Han G, Shen S, Wang H, Jiang J, Guizani M (2019) Prediction-based delay optimization data collection algorithm for underwater acoustic sensor networks. IEEE Trans Veh Technol
7. AlRubeaai SF, Abd MA, Singh BK, Tepe KE (2016) 3D real-time routing protocol with tunable parameters for wireless sensor networks. IEEE Sensors J 16(3):843–853
8. Shah B, Kim K (2014) A survey on three-dimensional wireless ad hoc and sensor networks. Int J Distrib Sens Netw 10(7):616014
9. Entezami F, Politis C (2015) Three-dimensional position-based adaptive real-time routing protocol for wireless sensor networks. EURASIP J Wireless Commun Netw 2015(1):197
10. Paramesh J, Robin CR (2018) A novel and efficient routing protocol for fishermen using underwater wireless sensor network. J Comput Theor Nanosci 15(4):1226–1232
11. Ahmed G, Zhao X, Fareed MMS, Fareed MZ (2019) An energy-efficient redundant transmission control clustering approach for underwater acoustic networks. Sensors 19(19):4241

Digital Image Processing Based Automatic Fabric Defect Detection Techniques: A Survey



Vaishnavi Raut and Indrasen Singh

Abstract The fabric defect detection is done truly with manual inspection. Automatic fabric investigation is basic to keep up the idea of texture. Fabric examination is present on the reason of modernized pictures of the fabric. The detector gains modernized fabric pictures by picture securing gadgets and transfers it to a PC program to forms the got image. The PC program makes a material assessment to check whether the surface is sans defect or slipped off using Digital picture getting ready systems. Notwithstanding unlimited estimations available, the investigation is up 'til now testing one. This paper shows the requirement, provocation, and methods of automatic fabric defect-recognition program Also, moreover, the paper shows all the chance of available advances related to the fabric defect-recognition program.

1 Introduction

To keep up the nature of the fabric, automatic fabric investigation is significant. It is attractive to deliver the best products in the most brief measure of time is conceivable. Almost 85% of the imperfections are found by the object of the textile industry. Workers improve just 45–65% of their imperfections from seconds or off-standard items. It is basic, to keep these imperfections from reoccurring. A computerized investigation system comprises of a PC based vision system. As they depend on PC, these systems don't endure the downsides of manual examination.

V. Raut (✉) · I. Singh

Department Electronics and Telecommunication Engineering, G H Raisoni College of Engineering, Nagpur 440016, India
e-mail: rautvaishnavi2090@gmail.com

I. Singh

e-mail: indrasen.singh@raisoni.net

1.1 Fabric Inspection

Material review is a significant element in modern producing factories, for example, computerized, mechanized and curative factories. Essentially, Material recognition has two different potential outcomes. First item disconnected review wherein the produced fabric must be examined through the fabric inspection system. The subsequent chances are an online review in which the fabricating procedure can be continually checked for the presence of defects.

1.1.1 Limitation of Manual Inspection

1. It is tough to realize the faults by mortal specialists manually.
2. Manual method needs instruction and they take some period to evolve such expertise.
3. Visible investigation is unvarying or hard, even for the top instruct specialist.
4. The machines give the result faster and accurate than humans.
5. Human inspectors can cause eye fatigue.

1.2 Automated Fabric Inspection

Automated inspection programs are proposed to accelerate absconds distinguishing proof and precision fabric fabricating procedures to diminish work costs, improve the idea of things and augmentation creating an order. In part 2 the requirement and issues of Automated inspection system is sorted, the requirement and issues of an Automated inspection systems have about. In part 3, a chart of Automated material audit program describing the points in levels is introduced. In part 4, classification of each and every believable method open for Automatic inspection systems has been immediately inspected. In part 5, the output of the utilization of different point periods of Automated inspection systems is displayed. At last it is concluded in part 6.

2 Online Fabric Defect Detection System

The accessible material investigation is known as present material investigation where generation and creation limit the works at the same time progressively. The requirement for this Program is from the way that the real-time material investigation technique which is done physically is a difficult task. The significant necessities for an online accessible material investigation Program are as per the following:

1. The framework must work continuously with great outcomes.

2. It should decrease get away from price.
3. It should decrease blunder.
4. It should be hearty and adaptable.
5. It should be of minimal effort and effective.

2.1 Challenges and Difficulties

1. Because of the enormous number of fabric defects classes, the task is challenging.
2. There are between class correspondence and between class varieties of deformities.
3. The depiction of deformities in rugged substance is normally not explained distinctly.
4. There is a huge assortment of texture designs and fabric types.
5. There are arbitrary varieties in scute.
6. The issue of evaluating optical suspicion in difficult times.
7. This assignment has a high information stream.
8. It endures from disturbance effects.

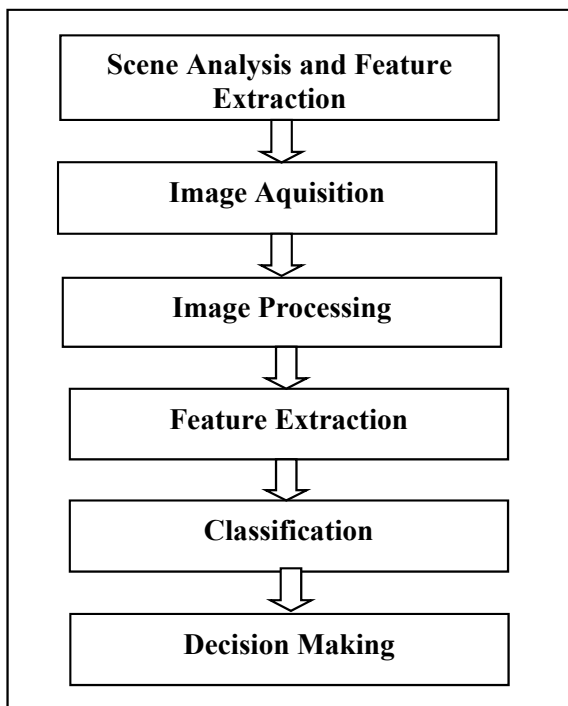
2.2 Deformities in Fabric

Many faults in material happen during fabricating. A portion of these material faults is obvious, while others are definitely not. Be that as it may, some fabric defects might be redressed during weaving and in the wake of fabricating while others are most certainly not. Surface of fabric depends on the experience of the texture. They can be named unpleasant, smooth, smooth, delicate, luxurious, shiny, and so forth. The various surfaces of the fabric preserve upon the kinds of fabricate utilized. The various surfaces of the fabrics rely on the kinds of material used. Fabric materials are utilized to get ready various kinds of texture items in the factories viz. cotton, silk, wool, leather, and linen. Characteristic cloth and manufactured cloth are the two unique kinds of textile cloth. The fabric defects can happen because of machine flaws, opening, Color dyeing, yarn issues, scratch, poor completing, soil spot, excessive stretching, and crack point.

3 Automatic Fabric Inspection System

The advancement of an automatic, i.e., PC visual program for material fault investigation has a few stages as appeared in Fig. 1.

Fig. 1 Methodology of various levels in an automatic fabric inspection system



3.1 Image Acquisition

The basic time of any vision structure is Image procurement. There can be different sorts of cameras utilized for this application, for example, charged coupled gadget camera, CMOS camera, digital camera, and so on. The pixel estimation of these cameras is around 320×420 pixel.

3.2 Image Preprocessing

In picture pretreating levels the collection of procedures that are utilized for the improvement of the visual aspect of an image and furthermore it is utilized to change over the image to a structure, from which it very well may be more qualified for additional survey in the forthcoming levels by a human or instruments.

3.3 Feature Extraction

Feature Extraction is a phase wherein different strategies can be utilized to reproduce the visual substance of images for ordering and recovery reasons. There is a numeral of properties characterized by a picture and there are strategies for figuring every one of these properties. The properties which are more qualified for specific implementation chosen for additional investigation.

3.4 Classification

There are some profitable classifiers, for example, Artificial Neural Network, support vector machines, bunching, and measurable deduction. By revealing whether the fabric is deserted or desert free the characterization organize gives the final product of the whole fabric defect detection process. The preparation stage and testing stage are two stages that requires a classifier utilizing neural systems. The neural system makes the best possible change for its loads in the preparation stage.

4 Classification of Automated Fabric Defect Inspection

The Statistical, unearthly, model-based methodologies are the grouping of Structural methodologies. The surfaces which are made out of natives are the Structural methodologies. These natives' strategy for basic methodologies is as basic as single pixels, a locale with constant gray stages, or line portion. In this way, right off the bat to separate surface natives, and also to show or sum up the spatial situation rules are the primary targets of these methodologies. Geometric connections between natives or taking in measurable properties from surface natives can be gotten by the arrangement administers through demonstrating. Be that as it may, these methodologies are infertile on material fault recognition, fundamentally because of the flexibility of yarns, texture movement, fiber load, commotion, etc.

4.1 Statistical Approaches

Computation of the dimensional dissemination of elements ethics, the fundamental article is to isolate the picture of the reviewed material in the area of different analytical nature. A significant suspicion right now the action is that the insights of defect-free area are unmoving and that these locales reach out above a critical bit of review image. In view of the amount of pixels characterizing the neighborhood highlights, they are grouped these methodologies into first request, second request, what's more,

higher request measurements. The principal request measurements gauge effects like the normal and difference of singular pixel esteem, disregarding the dimensional collaboration between picture elements, next and elevated request measurements then again estimate properties of at least two pixels esteems happening at explicit areas comparative with one another.

4.1.1 Gray-Level Thresholding Approach

To recognize high differentiation fabric defects these are immediate and straightforward mean methodologies. The guideline relies upon the peak or trough that is signal variety because of the appearance of high differentiation defects.

4.1.2 Normalized Cross-Correlation Approach

An image that shows up in another and the relationship coefficient can create a connection plan for defect statement is utilized to find the features in correlation. The straight and proper measure of similar nature between the two images provides the cross-correlation function. The presence of a defect in the merit of this estimate shows any significant variation.

4.1.3 Statistical Moments Approach

The factual details, for instance, Mean, standard deviation, skewness, and kurtosis are given above an area and these characteristics are pre-owned for picture division.

4.1.4 Rank-Order Functions Approach

Based on histogram analysis a picture rank-purpose is a basic measurable strategy used for defects recognition. It is given by the concatenation of grey levels in the scatter diagram and this arrangement is arranged in the arising order. The same information is provided by the histogram and the rank function.

4.1.5 Edge Detection Approach

For image analysis border identification is a conventional strategy. The significant element in the textured images is the appropriation of the edge sum per unit area. The measure of grey level advances in the material picture has address bars, fringe, tip absconds, and other dimensional disruption. Consequently, it has characteristics, as it were, hold for likeness testing, get together assessment, and material fault recognition.

4.1.6 Morphological Operations Approach

The coherent morphology helps depicting the geometrical and essential properties of pictures. Morphological pictures dealing with have significance to molding, marking, gathering, extricating, and coordinating procedures on pictures. The morphological activities are one of the perfect devices for exhausting clamor, in spatially isolated pictures of textures.

4.1.7 Local Linear Transforms Approach

This methodology is emphatically identified with channel bank examination strategies. It gives quantifiable help for the extraction of surface properties by systems for convolution executives (covers). These spreads might be considered as neighborhood discoverers' principal structures, for instance, deserts.

4.1.8 Artificial Neural-Networks Approach

The artificial neural-framework is among the speediest and most flexible classifiers utilized for insufficiency ID due to their non-parametric nature and capacity to portray complex choice change. In the event that the window work is Gaussian, the windowed zones made out of various near rudimentary handling units (neurons) related together into a framework. These neurons are arranged in layers with the data instating the planning at the info layer.

4.2 Structural Approaches

The spectral methodologies involve a major part of the most recent PC vision research work, in view of spatial-frequency area highlights which are delicate to disturbance and force variant than the highlights extricated from a dimensional domain. Incorporeal methodologies are prescribed to be used uniquely for PC visual of constant rugged stuff like material as they require a high level of periodicity.

4.2.1 Fourier Analysis Approach

The Fourier investigation is a worldwide methodology that describes the fabric picture as far as recurrence segments. Fourier approaches have alluring effects of clamor invulnerability, interpretation unchanging, and the ideal portrayal (upgrade) of the occasional highlights. To actualize Fourier examination for material fault recognition, different strategies are used; Optical Fourier Transforms acquired in the visual area by utilizing focal points and spatial channels can be utilized, in any case,

most strategies, carefully actualized, are inferred from Discrete Fourier Transforms and additionally it is Converse which recuperates the pictures in the dimensional area.

4.2.2 Gabor Filters Approach

The Fourier analysis is presented by its old way of spatial reliance through the windowed Fourier change. The windowed Fourier transform turns into the outstanding Gabor change if the window work is Gaussian, which can probably achieve ideal restriction in the dimensional and recurrence areas.

4.3 Model-Based Approaches

The issue of discovering potential bunches in an information set (picture) is a tedious one with a past history. Campbell et al. consolidated images preparing methods with a ground-breaking new measurable procedure to investigate denim fabric. The methodology utilizes model-based grouping to distinguish moderately blackout adjusted deformities. In request to survey the proof for the present of an imperfection, Bayesian data establishment (BIC) is used.

4.3.1 Gauss Markov Random Field (GMRF) Model Approach

The Markov arbitrary fields utilize an exact model of this dependence, the image has essentially random noise. The local logical data in an image is able to capture. The power at every element in the picture relies on the powers of essentially the neighboring elements that are anticipated from this model. This gives a supportive and dependable way for showing setting subordinate components, for instance, pixels, through portraying common impacts among such elements utilizing situation MRF circulation.

4.3.2 Poisson's Model Approach

The stochastic models of some self-decisively present-day finished materials depend upon the chance of the collecting system. One occurrence of such material is the wiry, non-woven material utilized for air filtration that is produced through adhesive advancement.

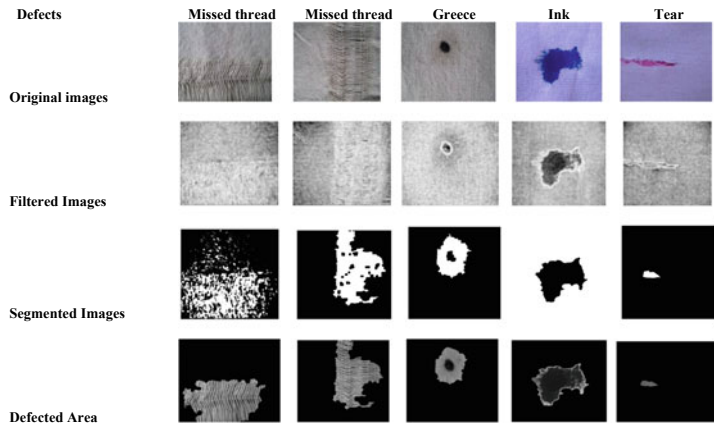


Fig. 2 Results of the images after applying different filtering techniques on original images

5 Results and Discussions

The need to recognize the best techniques is significant as there are different fabrics and fabric defects. The relative examination is significant, as it empowers the scientists to learn and comprehend the distinction dependent on its chance and precision. The computerized pictures of both defects and defect-free are caught by the advanced camera; at that point, this image is preprocessed and the noise is removed and then image is noise-free. By applying the PSO middle separating system, the image appear as shown in Fig. 2. The entropy-based segmentation applied with respect to the separated picture, sectioning out the surrendered area if any in the picture. By then these picture is sent to the Artificial Neural Network classifier, it arranges the pictures in deserted and defect-free groups. To improve more the subsequent advance is executed utilizing PSO based feature selection. Here in the proposed system, five sorts of imperfections are recognized correctly, for example, Tear, Oil Stain, Ink Stain, missed thread (Wept and Warp). The objective here is to demonstrate the advantage of the strategy to identify defects if there should arise an occurrence of genuine fabric and simulated one.

6 Conclusion

In this paper the challenges and need of Automatic Fabric Inspection system is given, a blueprint of the system shows the computerized fabric review which shows the defects in fabric and the cause of the defect is examined. This procedure orchestrates 85% of defects in texture and finds the blemish in the average fabric at a commendable rate and gives 80% gathering precision. A present system and the output has been

given. We have introduced promising outcomes for a computerized texture examination for multi-class imperfection identification and portrayal in texture using both geometric and surface features to get the visual properties.

References

1. Banumathi P, Nasira GM (2012) Fabric inspection system using artificial neural networks. *Int J Comput Eng Sci (IJCES)* 2(5):20–27
2. Banumathi P, Nasira GM (2013) Fourier transform and image processing in automated fabric defect inspection system. *Int J Comput Int Inf (IJCII)*, 3(1):61–64
3. Bodnarova A, Bennamoun M, Kubik K (2000) Suitability analysis of techniques for flaw detection in textiles using texture analysis. *Pattern Anal Appl* 3(3):254–266. <https://doi.org/10.1007/s100440070010>
4. Brzakovic D, Vujoovic N (1996) Designing defect classification systems: a case study. *Pattern Recogn* 29(8):1401–1419. [https://doi.org/10.1016/0031-3203\(95\)00166-2](https://doi.org/10.1016/0031-3203(95)00166-2)
5. Cho CS, Chung BM, Park MJ (2005) Development of real-time vision-based fabric inspection system. *IEEE Trans Ind Electron* 52(4):1073–1079. <https://doi.org/10.1109/TIE.2005.851648>
6. Conci A, Proen a C (2000) A Computer vision approach for textile inspection. *Tex Res J* 70(4)
7. Fatemi-Ghomri N, Palmer PL, Petrou M (1996) Performance evaluation of texture segmentation algorithms based on wavelets. In: Proceedings of the workshop on performance characteristics of vision algorithms (ECCV), Cambridge
8. Gonzales R, Woods R (2008) Digital image processing. Prentice Hall
9. Jansi S, Subhashini P (2013) Particle swarm optimization total variation filter for image denoising. *J Theor Appl Inf Technol* 57(2):169–173
10. He J, Jiang Q (2012) Research on the fabric defect detection method based on improved PSO and NN algorithm. *Int J Dig Cont Technol Appl (JDCTA)* 6(8):177–184. <https://doi.org/10.4156/jdcta.vol6.issue8.21>
11. Kumar TA, Paul V, Priya S (2011) A novel approach to fabric defect detection using digital image processing. *Signal Process Commun Comput Netw Technol (ICSCCN)*. <https://doi.org/10.1109/icscn.2011.6024549>
12. Mak KL, Peng P, Yiu KFC (2009) Fabric defect detection using morphological filters. *Image Vis Comput* 27(10):1585–1592. <https://doi.org/10.1016/j.imavis.2009.03.007>
13. Nasira GM, Banumathi P (2014) Automatic defect detection algorithm for woven fabric using artificial neural network techniques. *Int J Innov Res Comp Comm Eng (IJIRCCE)* 2(1):2620–2624
14. Vyas P, Kakhani M (2015) Fabric fault processing using image processing techniques. *Int J Mult Res Dev* 2(2):29–31
15. Sengottvelan P, Wahi A, Shanmugam A (2008) Automatic fault analysis of textile fabric using imaging systems. *Res J Appl Sci* 3(1):26–31
16. Srinivasan K, Dastor PH, Radhakrishnaiah P, Jayaraman S (1992) FDAS: a knowledge-based frame detection work for analysis of defects in woven textile structures. *J Text Inst* 83(3):431–447

A Balanced Expert System to Manage Parkinson's Disease by Identifying Major Risk Factors: B-TESM-PD



Arpita Nath Boruah, Saroj Kr Biswas, Sivaji Bandyopadhyay,
and Sunita Sarkar

Abstract With changing lifestyles and emergence of modern ways of living, people fail to take enough care of their physical health and increase their chance of falling prey to fatal and non-fatal diseases. With tremendous advancement in science and technology, it is expected to have a system that can help to manage this problem. One of such prevailing diseases is Parkinson's disease (PD). The part of the brain that controls movement, posture, and also emotional imbalance is affected in PD. The symptoms of PD may differ from one individual to another. PD is detected basically in elderly people but now it has turned out to be a chronic disease affecting all age groups. As of its severity it is better to have an expert system which can identify the major risk factors of PD in the early stage and accordingly some measures may be taken to control those risk factors. It would, therefore, be really a great help to the world to have one such expert system for managing a PD. Therefore, this paper proposes an expert system named balanced-transparent expert system for managing-PD (B-TESM-PD) that can identify the major risk factors by generating rules from decision tree (DT). B-TESM-PD encompasses of five phases: preprocessing, rule generation, rule selection, rule pruning and merging, and risk factor identification. The imbalance nature of the PD dataset is treated by the preprocessing stage using a dominant undersampling technique, Tomek Link. Rule generation phase generates rules using decision tree. Rule selection stage selects the transparent rules, rule pruning and merging removes the redundant and inefficient rules from the rule set and then merges the pruned rule set to a single rule, and lastly the major risk factor of

A. N. Boruah (✉) · S. K. Biswas · S. Bandyopadhyay

Computer Science and Engineering Department, National Institute of Technology Silchar, Silchar, Assam 788010, India

e-mail: arpita.boruah@hotmail.com

S. K. Biswas

e-mail: bissarojkum@yahoo.com

S. Bandyopadhyay

e-mail: director@nits.ac.in

S. Sarkar

Computer Science Department, Assam University, Silchar, Assam, India

e-mail: sunitasarkar@rediffmail.com

PD is identified using the risk factor identification phase. The model is validated with the PD dataset collected from UCI repository. Standard decision tree performance is compared with the proposed model.

Keywords Parkinson's disease · Decision tree · Expert system · Hill climbing · Attribute selection · Undersampling

1 Introduction

Parkinson's disease (PD) is among one of the prevailing neurodegenerative disorders around the globe. Conferring to the American Parkinson Disease Association (APDA) [1] more than 10 million individuals have PD. PD can be defined as a progressive neurodegenerative disorder that basically effects the motor as well as the emotional imbalance. The principal symptoms of the disease are formation of tremor, rigidity and stiffness, dysphonia and slowness in motion [2–4].

Along with these, a PD patient may also suffer from emotional disorder of depression, anxiety, panic attacks, tiredness, and constipation [5] which affects day-to-day life. PD mostly occurs among the elderly people of age above 50 [6, 7], due to the demise of particular group of brain cells that are responsible for producing neurotransmitters like dopamine, acetylcholine, serotonin, and also norepinephrine [1, 8]. The degeneration of dopaminergic neurons cause the physical and mental imbalance in the human being leading to PD. The actual reason of PD whether environmental or genetic is still unknown. Several researches have been made for diagnosis of PD and it is about 1–3% of the world population is being suffered from PD. In accordance to the study World Health organization (WHO) [9], the PD growth is increasing and soon it will be one of the most commonly occurring chronic diseases among all age groups. Considering the severity of PD, it is very much essential to prevent it by identifying the major risk factor of the disease.

Extracting the useful and hidden information and their relationship becomes a decisive part of making a data-driven intelligent system. Various data mining (DM) techniques are available which can extract the hidden information and make them use for an expert decision-making system. However, when it aims to recognize the most important risk feature of a disease, it becomes essential to have a transparent system which can make its decision-making process into human understandable form. Among all the classification tools, decision tree (DT) is the most popular and a white box technique which generates a user understandable decision rules. Therefore, DT can be used to find the major risk factors responsible for PD by generating transparent rules. Once the major risk factors are identified, they can be used to manage PD and prevention method can be discovered with very less effort.

Since decades DT, especially, has received a lot of attention because of their universal approximation property and its transparent nature. However, DT assumes balanced training set which is not correct always in case of medical data and hence the classification models that are inclined toward the overrepresented class. Thus, this

paper proposes a decision support system named balanced-transparent expert system for managing-PD (B-TESM-PD) which extracts the transparent decision rules from DT from balanced PD data. The most prominent undersampling technique, Tomek Link [10], is used to make the PD data balanced. Therefore, DT can learn the patterns in both of the classes maintaining uniformity in generating transparent rules. The proposed B-TESM-PD also prunes the generated rules and factors to make the rules more transparent and to identify the major risk factors for PD.

The paper is arranged as follows: Sect. 2 shows the background of PD and various works done on it, Sect. 3 gives the methodology in details, Sect. 4 evaluates the experimental results of the model and comparison, and finally Sect. 5 draws conclusion.

2 Literature Review

Different researchers used different techniques and data to identify PD. Bisalia et al. [11] described PD elaborately. Stuart et al. [12] explained PD as a progressive neurodegenerative disease which causes motor symptoms and visual deficits. Yuvaraj et al. [13] stated that PD has emotional symptoms of depression, sleep disorder, and autonomic impairments. Wang et al. [14] stated that exposure to pesticides may increase the rate of PD. Lee et al. [15] investigated the different applications of digital image processing method to detect the neurological disorder. Stuebner et al. [16] particularly focused on the blood pressure and heart beat rate because in advance stage of PD a patient may have an imbalance blood pressure and thereby can predict any new symptoms of the PD or some other problems. Ramani and Sivagami [17] proposed a classifier model for PD with the higher classification accuracy for vocal data set. Sama et al. [18] used SVM classifier to classify the signals obtained from 12 PD patients using a waist worn triaxial accelerometer. Kim et al. [19] designed an automatic PD detection algorithm using convolution neural network (CNN). Joshi et al. [20] proposed spontaneous non-invasive PD classification by using gait analysis. Little et al. [21] proposed algorithms to measure dysphonia and put forward analysis methods for speech to study voice disorders on the PD patients. The outcomes of the research offer a wide range of voice disorder classes of Parkinson's dataset. Arjmandi and Pooyan [22] proposed an improved algorithm for pathological voice quality assessment. They recognized different voice disorders of the vocal folds and suggested linear discriminant analysis over other detection approach. It is evident from the literature that PD has been studied a lot and different techniques are being proposed for its detection.

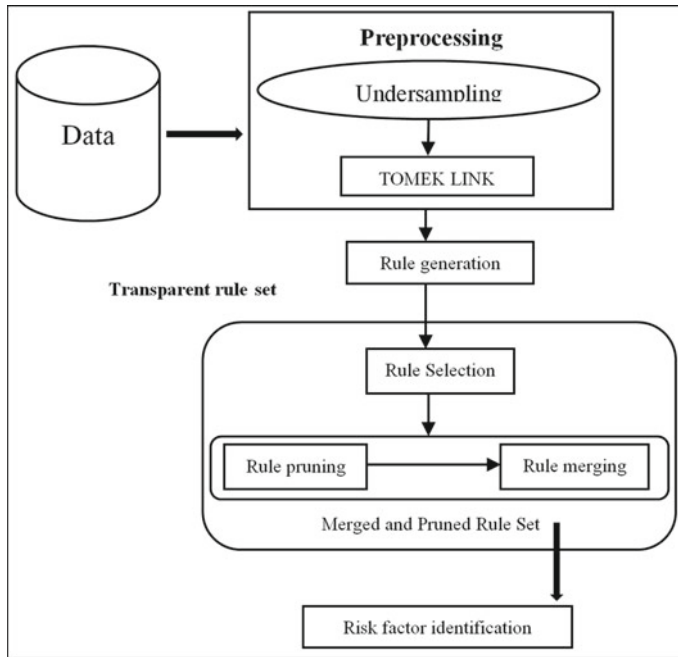


Fig. 1 Balanced-transparent expert system for managing-PD (B-TESM-PD)

3 Proposed Balanced-Transparent Expert System for Managing-PD (B-TESM-PD)

This section describes B-TESM-PD model, which identifies the major risk factors of PD. The proposed B-TESM-PD encompasses of five stages: preprocessing, rule generation, rule selection, rule pruning and merging, and risk factor identification. Rule generation step generates rule set using decision tree (C4.5), rule selection stage selects the transparent rules, rule pruning and merging removes the redundant and incompetent rules from the rule set by using a proposed rule pruning algorithm and then merges the pruned rule set into a single rule, and finally the major risk factors of PD are identified using the risk factor identification phase. The schematic layout of proposed B-TESM-PD is shown in Fig. 1.

4 Results and Discussions

This section is divided into three subdivisions: First subdivision shows the experimental setup and a brief explanation of the PD dataset used in the experiment, and the

second subdivision gives the results. The last section discusses about the important observations.

4.1 Experimental Setup and PD Dataset

The experimentation of the proposed model is performed in PYTHON 2.7 version in Ubuntu environment. The PD dataset [21] is taken from the UCI repository. It contains 197 samples, 23 attributes, and 2 classes. Each column in the dataset is a particular voice measure, and each row corresponds to a patient. The imbalance ratio of PD dataset is 3.06. The purpose of the dataset is to distinguish the healthy and those with PD, according to “status” column which is set to 0 for healthy and 1 for PD. The experiment of the paper is done with 10-fold cross-validation with 70% for training and 30% for testing. The dataset comprises voice perturbation and nonlinear dynamic parameters measured from the acoustic signals of the patients.

- x1 MDVP:F0 (Hz)—Average vocal fundamental frequency
- x2 MDVP:Fhi (Hz)—Maximum vocal fundamental frequency
- x3 MDVP:Flo (Hz)—Minimum vocal fundamental frequency
- x4 MDVP:Jitter(%)—MDVP jitter in percentage
- x5 MDVP:Jitter(Abs)—MDVP absolute jitter in ms
- x6 MDVP:RAP—MDVP relative amplitude perturbation
- x7 MDVP:PPQ—MDVP five-point period perturbation quotient
- x8 Jitter:DDP—Average absolute difference of differences between jitter cycles
- x9 MDVP:Shimmer—MDVP local shimmer
- x10 MDVP:Shimmer (dB)—MDVP local shimmer in dB
- x11 Shimmer:APQ3—Three-point amplitude perturbation quotient
- x12 Shimmer:APQ5—Five-point amplitude perturbation quotient
- x13 MDVP:APQ11—MDVP 11-point amplitude perturbation quotient
- x14 Shimmer:DDA—Average absolute differences between the amplitudes of consecutive periods
- x15 NHR—Noise-to-harmonics ratio
- x16 HNR—Harmonics-to-noise ratio
- x17 RPDE—Recurrence period density entropy measure
- x18 D2—Correlation dimension
- x19 DFA—Signal fractal scaling exponent of detrended fluctuation analysis
- x20 Spread1—Two nonlinear measures of fundamental
- x21 Spread2—Frequency variation
- x22 PPE—Pitch period entropy.

4.2 Results

Rule Generation B-TESM-PD model uses C4.5 algorithm to generate decision rules for each training set, which uses information gain ratio for attribute selection. Each rule is assigned a score function called as worth of rule (WOR).

The rule set of a particular fold along with its WOR value is given in Table 1.

Similarly, the rule sets of the remaining folds are generated along with their WOR values

Rule Selection The rule with the highest WOR is selected from each fold as the best rule for that particular fold. It is seen from Table 1 that **rule no. 8** has the highest WOR value and thus is selected. Similarly, the best rules for the remaining folds are selected and thus the **primary transparent rule set** is formed.

The **primary transparent rule set** is shown in Table 2 and the accuracy obtained by this is 84.61%.

Table 1 Rules and WOR values of the first fold

Rule no.	Rule	WOR
1	$x22 \leq 0.134 \text{ and } x2 \leq 229.18 \text{ and } x17 \leq 0.409$	6.068
2	$x22 \leq 0.134 \text{ and } x2 \leq 229.18 \text{ and } x17 > 0.407$	4.59
3	$x22 \leq 0.134 \text{ and } x2 > 229.18$	34.00
4	$x22 > 0.134 \text{ and } x12 \leq 0.013 \text{ and } x1 \leq 118.141$	6.068
5	$x22 > 0.134 \text{ and } x12 \leq 0.013 \text{ and } x1 > 118.141 \text{ and } x10 \leq 0.171$	23.50
6	$x22 > 0.134 \text{ and } x12 \leq 0.013 \text{ and } x1 > 118.141 \text{ and } x10 > 0.171$	2.83
7	$x22 > 0.134 \text{ and } x12 > 0.013 \text{ and } x20 \leq 0.143$	7.33
8	$x22 > 0.134 \text{ and } x12 > 0.013 \text{ and } x20 > 0.143$	102.33

Table 2 Primary transparent rule set

(1) if ($x22 > 0.134 \text{ and } x12 > 0.013 \text{ and } x20 > 0.143$) then <i>Class==1</i>
(2) if ($x19 > -6.318 \text{ and } x10 > 0.19 \text{ and } x20 > 0.143$) then <i>Class==1</i>
(3) if ($x20 > 0.208 \text{ and } x15 > 0.006$) then <i>Class==1</i>
(4) if ($x22 > 0.134 \text{ and } x13 > 0.02$) then <i>Class==1</i>
(5) if ($x19 > -6.318 \text{ and } x20 > 0.207 \text{ and } x4 > 0.00$) then <i>Class==1</i>
(6) if ($x22 > 0.134 \text{ and } x12 > 0.013 \text{ and } x13 > 0.019$) then <i>Class==1</i>
(7) if ($x22 > 0.134 \text{ and } x13 > 0.02$) then <i>Class==1</i>
(8) if ($x22 > 0.134 \text{ and } x13 > 0.02$) then <i>Class==1</i>
(9) if ($x22 > 0.134 \text{ and } x13 > 0.02$) then <i>Class==1</i>
(10) if ($x22 > 0.104 \text{ and } x8 > 0.005 \text{ and } x17 > 0.404$) then <i>Class==1</i>

Rule Pruning A sequential hill climbing algorithm is applied on the primary transparent rule set. Every time a rule is dropped and the accuracy is computed for that particular rule set and compared with the accuracy of the original rule set. If the accuracy increases or there is no change then that dropped rule is permanently pruned. This process continues till there is no more rules to be pruned which increases the accuracy of the rule set. Rule no. 1 is removed and accuracy is calculated. It is observed that the model produces 84.61% accuracy after removing Rule no. 1 and hence Rule no. 1 is pruned permanently. It is observed that the model produces 81.71% accuracy when Rule no. 2 is removed and hence Rule no. 2 is not pruned. Similar process is done for remaining rules and Table 3 is obtained after one complete iteration.

In the next iteration, Table 3 is treated as input and similar process is done for rule pruning. Finally, Table 4 is obtained by sequential hill climbing procedure and is treated the absolute transparent rule set.

The accuracy of the **absolute transparent rule set** is 85.52%.

Rule Merging Table 4 gives a minimized rule set after rule pruning phase. So, in the rule merging phase, the minimized rule set is merged to form a single rule but the features x_{20} have values with different ranges. The particular feature value is pruned one by one if their absence from the rule increases the accuracy. Feature $x_{20} > 0.143$ and feature $x_{20} > 0.207$ are pruned as by dropping individually it rises the accuracy of classification of positive patterns. Ultimate rule is shown in Table 5.

Risk Factor Identification In the single merged rule obtained in Sect. 4.2, it can be seen that the rule contains seven features $x_{19}, x_{10}, x_{20}, x_{15}, x_4, x_{22}, x_{13}$. In this

Table 3 Rule set after first iteration

(2) if ($x_{19} > -6.318$ and $x_{10} > 0.19$ and $x_{20} > 0.143$) then Class==1
(3) if ($x_{20} > 0.208$ and $x_{15} > 0.006$) then Class==1
(4) if ($x_{22} > 0.134$ and $x_{13} > 0.02$) then Class==1
(5) if ($x_{19} > -6.318$ and $x_{20} > 0.207$ and $x_4 > 0.00$) then Class==1
(6) if ($x_{22} > 0.134$ and $x_{12} > 0.013$ and $x_{13} > 0.019$) then Class==1
(7) if ($x_{22} > 0.134$ and $x_{13} > 0.02$) then Class==1
(8) if ($x_{22} > 0.134$ and $x_{13} > 0.02$) then Class==1
(9) if ($x_{22} > 0.134$ and $x_{13} > 0.02$) then Class==1
(10) if ($x_{22} > 0.104$ and $x_8 > 0.005$ and $x_{17} > 0.404$) then Class==1

Table 4 Absolute transparent rule set

1	if ($x_{19} > -6.318$ and $x_{10} > 0.19$ and $x_{20} > 0.143$) then Class==1
2	if ($x_{20} > 0.208$ and $x_{15} > 0.006$) then Class==1
3	if ($x_{19} > -6.318$ and $x_{20} > 0.207$ and $x_4 > 0.00$) then Class==1
4	if ($x_{22} > 0.134$ and $x_{13} > 0.02$) then Class==1

Table 5 Ultimate rule

If($x19 > -6.318$ and $x10 > 0.19$) or ($x20 > 0.208$ and $x15 > 0.006$)
or ($x19 > -6.318$ and $x4 > 0.004$) or (($x22 > 0.134$ and $x13 > 0.02$)) then
Class=1

Table 6 Misclassification rates (in %) when condition reversed (one attribute)

Testing set	X19	X10	X20	X15	X4	X22	X13
Testing set 1	85.0	95.0	75.0	70.0	85.0	85.0	100
Testing set 2	75.0	90.0	60.0	85.0	85.0	85.0	100
Testing set 3	60	85.0	80.0	65.0	85.0	85.0	80.0
Testing set 4	80	95.0	90.0	100	95.0	100	100
Testing set 5	90.0	90.0	100	100	100	90.0	90
Testing set 6	68.42	63.16	47.37	63.16	63.15	63.16	68.42
Testing set 7	63.16	73.68	68.42	73.68	78.95	84.21	94.74
Testing set 8	100	100	94.74	94.74	100	100	100
Testing set 9	78.95	73.68	73.68	84.21	89.47	94.74	68.42
Testing set 10	57.89	63.16	15.79	78.95	84.21	73.68	57.89
Average	75.84	82.86	70.5	81.47	86.57	86.07	85.94

step, the misclassification rate of each feature is checked by reversing its individual ranges. The higher the misclassification rate the more important is the feature. The misclassification rates are shown in the table below.

It is observed from Table 6 that $x4$ (MDVP jitter in percentage) has the highest misclassification rate, hence this feature is considered as the major risk factor for PD. So if it is the case of selecting a single major risk factor responsible for PD, then $x4$ is selected as the one. By controlling this single feature, PD can be managed up to 86.57%. This process can be further continued to find more risk factors which may be used control PD.

Performance and Comparison of B-TESM-PD with Simple Decision Tree

In addition to accuracy, comprehensibility of the model is also taken into consideration for comparison with simple DT and the same model without using the pre-processing step. Global comprehensibility, which is the total number of deciding rules and local comprehensibility is nothing but the total number of features in the deciding rules.

The experimental results of Table 7 show the performance of the B-TESM-PD with the simple decision tree model.

Table 7 Performance measures (accuracy in %, comprehensibility)

Methods	Accuracy	Global comprehensibility	Local comprehensibility
B-TESM-PD	85.52	4	7
B-TESM-PD (without the preprocessing step)	84.10	4	10
Decision tree	77.86	7	23

4.3 Observations

The B-TESM-PD calculates the rate of misclassification of individual feature by reversing its ranges for the positive patterns only. It identifies the feature with highest misclassification rate as the major risk factor for PD. It is observed that by controlling that particular feature PD can be prevented up to 86.57%. The prevention rate may increase with the increase in the number of risk factors. Although the performance increases with increase in risk factor(s) but at the same time it may be difficult to control more factor(s) responsible for PD. Moreover, from the analysis it is obvious that, even if it is the identification of one risk factor, the disease can be managed significantly. B-TESM-PD is further compared with a simple decision tree and it is clearly evident that the classification accuracy of the B-TESM-PD is much higher than the simple decision tree along with a very high rate of comprehensibility both in terms of global and local. For classification accuracy, both the positive and negative instances are taken into consideration.

5 Conclusion

This paper proposes a rule generation method called B-TESM-PD, to determine important and significant rules and to make a rich transparent system and thereby identifies the major risk factors of PD. The proposed B-TESM-PD extracts the decision rules from the decision tree which are further pruned to increase the transparency of the rule set without sacrificing accuracy. Later a sequential hill climbing method is proposed to prune the rule set to obtain a highly transparent system. Performance of the proposed B-TESM-PD system is measured by global and local comprehensibility, accuracy, precision, recall, and f-measures. Performance of the proposed B-TESM-PD is evaluated with simple decision tree. The overall performance of the B-TESM-PD system is much better than decision tree in terms of accuracy, precision, f-measures, and comprehensibility. The transparent rule finally obtained may contain some attributes or factors which are common with same or different ranges of deciding values. The major factors for PD have been identified by merging and by calculating the misclassification rate of individual features for the positive patterns by reversing its ranges.

Thus, it can be concluded that the B-TESM-PD is a rich transparent system with less decision rules which makes a system efficient, user convincing, and manageable to a great extent for easy prevention of PD and take necessary precautionary measures to control the risk factor thus identified.

The proposed model uses decision tree for rule generation; however, some other machine learning algorithms such as neural network can be used for generating production rules. Moreover, some other optimization techniques can be used in place of hill climbing algorithm in future for pruning the rule set and to get more transparency in the rule set.

References

1. Standaert DG, Saint-Hilaire MH, Thomas CA (2015) Parkinson's disease handbook. American Parkinson Disease Association, New York, USA
2. Lang AE, Lozano AM (1998) Parkinson's disease. *New Zealand J Med* 339:1044–1053
3. Elbaz A, Bower JH, Maraganore DM, McDonnell SK, Peterson BJ, Ahlskog JE, Schaid DJ, Rocca WA (2002) Risk tables for parkinsonism and Parkinson's disease. *J Clin Epidemiol* 55:25–31
4. Van Den Eeden SK, Tanner CM, Bernstein AL, Fross RD, Leimpeter A, Bloch DA, Nelson LM (2003) Incidence of Parkinson's disease: variation by age, gender and race/ethnicity. *Am J Epidemiol* 157:1015–1022
5. Yuvaraj R, Muragappan M, Ibrahim NM, Sundaraj K, Omar MI, Mohamad K, Palaniappan R (2014) Detection of emotions in Parkinson's disease using higher order spectral features from brain's electrical activity. *Biomed Signal Process Control* 108–106
6. Davie CA (2008) A review of Parkinson's disease. *Br Med Bull* 86(1):109–127
7. Sutherland M, Dean P (2017) What is Parkinson's disease? Neuro challenges. Foundation for Parkinson's. <http://www.parkinsonsneurochallenge.org>
8. Jankovic J (2008) Parkinson's disease: clinical features and diagnosis. *J Neurol Neurosurg Psychiatry* 79(4):368–376
9. Organization WH (2011) Global health and ageing. Technical report. US National Institute of Aging
10. Tomek I (1976) Two modifications of CNN. *IEEE Trans Syst Man Cybern* 769–772
11. Bisaglia M, Filograna R, Beltramini M, Bubacco L (2014) Are dopamine derivatives implicated in the pathogenesis of Parkinson's disease? *Ageing Res Rev* 13:107–114
12. Stuart S, Alcock L, Galna B, Lord S, Rochester L (2014) The measurement of visual sampling during real world activity in Parkinson's disease and healthy controls: a structured literature review. *J Neurosci Methods* 222:175–188
13. Yuvaraj R, Muragappan M, Ibrahim NM, Sundaraj K, Omar MI, Mohamad K, Palaniappan R. Optimal set of EEG features for emotional state classification and trajectory visualization in Parkinson's disease. *Int J Psychophysiol* 94(3):482–495. <http://doi.org/10.1016/j.ijpsycho.2014.07.014>
14. Wang A, Costello S, Cockburn M, Zhang X, Bronstein J, Ritz B (2011) Parkinson's disease risk from ambient exposure to pesticides. *Eur J Epidemiol* 547–555
15. Lee H, Guan L, Lee I (2008) Video analysis of human gait and posture to determine neurological disorders. *EURASIP J Image Video Process* 1–12
16. Steubner E, Vichayanrat E, Low DA, Matthias CJ, Isenmann S, Haensch C-A (2013) Twenty-four hour noninvasive ambulatory blood pressure and heart rate monitoring in Parkinson's disease. *Front Neurol* 4
17. Ramani RG, Sivagami G (2011) Parkinson's disease classification using data mining algorithms. *Int Comput Appl* 32(9): 17–22

18. Sama A, Perez-Lopez C, Rodriguez-Matrin D, Catala A, Moreno-Arostegui JM, Cabestany J, de Mingo E, Rodriguez-Molinero A (2017) Estimating bradykinesia severity in Parkinson's disease by analysing gait through a waist-worm sensor. *Comput Biol Med* 84:114–123
19. Kim HB, Lee WW, Kim A, Lee HJ, Park HY, Jeon HS, Kim SK, Jeon B, Park KS (2018) Wrist sensor-based tremor severity quantification in Parkinson's disease using convolutional neural network. *Comput Biol Med* 95:140–146
20. Joshi D, Khajuria A, Joshi P (2017) An automatic non-invasive method for Parkinson's disease classification. *Comput Meth Progr Biomed* 145:135–145
21. Little MA, McSharry PE, Roberts SJ, Costello DA, Moroz IM (2007) Exploiting nonlinear recurrence and fractal scaling properties for voice disorder detection. *Biomed Eng Online* 6(1):23
22. Arjmandi MK, Pooyan M (2012) An optimum algorithm in pathological voice quality assessment using wavelet-packet-based features, linear discriminant analysis and support vector machine. *Biomed Signal Process Control* 7(1):3–19

Bioinformatics Advancements for Detecting Epidemic Disease Using Machine Learning Approaches



Bikash Baruah and Manash Pratim Dutta

Abstract In the twentieth century, many researchers have started working on bioinformatics for disease biomarker detection using genetic information, i.e., DNA microarray dataset and RNA sequencing dataset with machine learning approaches. The journey of this concept starts with the classification technique on DNA microarray dataset by comparing it with reference genome or by deNovo (without reference genome) technique, and lots of different tools were published in different publications. Later, with the availability and advancement of computational power many researchers started working on large RNA sequencing dataset and some tools are published again with significant features. Nowadays, also this area is like a newborn baby and several challenges are still not solved, but it does not have a proper guideline for new researchers to face those challenges. After analyzing so many tools on DNA as well as RNA, we are able to summarize these works with a common workflow, and in this paper, we have proposed a generalized workflow for detecting epidemic diseases like HIV-AIDS, Cancer using machine learning approaches.

Keywords DNA microarray · RNA sequencing · Genome · Sanger · NGS · Differential co-expression

1 Introduction

A recent advancement of bioinformatics [1, 2] is in trend where machine learning approaches are used on DNA microarray [3–6] and RNA-seq dataset [7–10] to identify the progression of epidemic diseases. The effectiveness and reliability of this approach are far better than the traditional techniques. Researchers are working continuously to develop cost-effective and robust algorithms. To obtain the input

B. Baruah (✉) · M. P. Dutta

Department of Computer Science and Engineering, National Institute of Technology Arunachal Pradesh, Papum Pare, India
e-mail: bikash.phd@nitap.ac.in

M. P. Dutta
e-mail: manashpdutta@nitap.ac.in

sequence, basically there are two sequencing methods, i.e., Sanger [11, 12] and NGS [13, 14], and these can be applied either in extracted DNA or RNA of any living being and result obtained will be microarray and RNA-seq, respectively. Now co-expression analysis [15–17], differential expression analysis [16], and differential co-expression analysis [18–22] or hybridized analysis (combination of these analyses) can be used through bi-clustering [23–25] or tri-clustering [26] techniques to detect the disease biomarker [27]. Here, we are proposing one generalized workflow which is fitted in almost all researches of this area. Further, we will extend our work to design robust and cost-effective algorithm to apply Cancer and HIV progression human dataset to identify the highly affected genes.

2 Proposed Model

We have proposed a model given in Fig. 1 which gives a complete workflow starting with DNA and RNA extraction from living cells or tissues followed by sequencing and co-expression analysis. In each step, we try to explain different available techniques. The workflow discussed in this model will certainly help the new researchers of this field, because it was never explained before in such a simple, systematic and step-by-step manner how wet lab and dry lab processes are combined together for detecting disease affected genes. Once sample extraction followed by sequencing is being completed in wet lab, the output of sequencing is taken as the input for dry lab for data analysis. In the following sections, different modules are explained.

2.1 Sample Extraction

Sample can be of two types: DNA and RNA and their extraction process from living or conserved cells, tissues, or virus particles are also different. Though, nowadays, many advanced kits are available for high-quality DNA and RNA extraction [28], the basic steps are almost similar to each other.

2.1.1 DNA Extraction Procedure

- Step 1 Cell lysis to release the DNA.
- Step 2 Centrifuge the sample to separate the DNA from other cellular debris and proteins.
- Step 3 Use chilled isopropanol to precipitate the DNA.
- Step 4 Wash DNA properly with ethanol.
- Step 5 Gel electrophoresis for quality and quantity check of DNA.

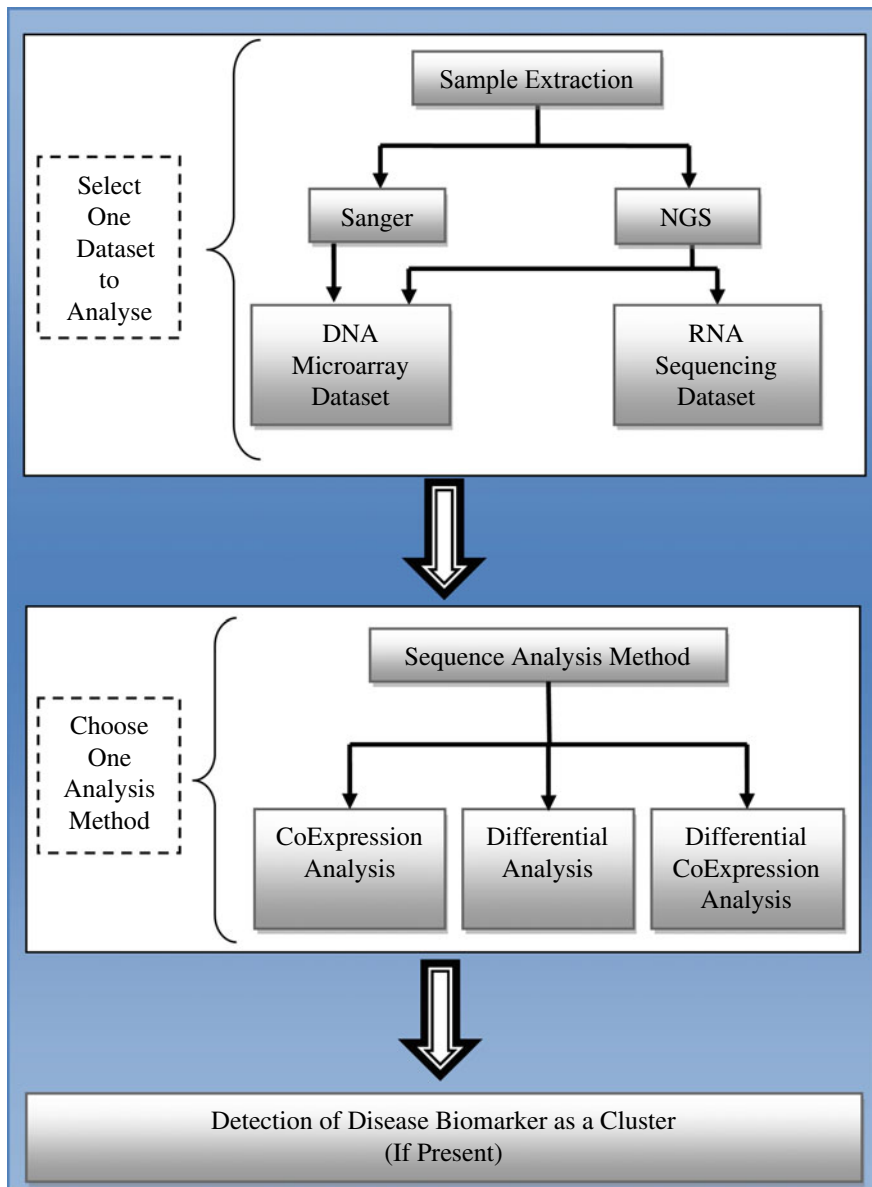


Fig. 1 Proposed model

2.1.2 RNA Extraction Procedure

- Step 1 Cell lysis and dissolution.
- Step 2 Denaturation of proteins and DNA.
- Step 3 RNases inactivation.
- Step 4 Removal of cellular components.
- Step 5 Precipitation of RNA.
- Step 6 Gel electrophoresis for quality and quantity check of RNA.

Once, high-quality sample is extracted from cells, tissues, or virus particles; it becomes ready for sequencing either by Sanger or NGS.

2.2 *Sanger Sequencing*

Frederick Sanger and his colleagues developed Sanger sequencing in 1977, which is known as the first generation sequencing. In complete Human Genome Project, Sanger sequencing is used and completed in 2003. The output of Sanger sequencing gives high-quality data with low noise and robustness. Sanger sequencing method uses dideoxynucleotides (ddNTP) with a hydrogen atom instead of 3' hydroxyl group to sequence the deoxyribonucleic acid (DNA). These modified ddNTPs are able to terminate the polymerization of DNA. Here, DNA sample is divided into four separate samples and each of the four samples contains DNA polymerase and deoxynucleotides (dATP, dGTP, dCTP, and dTTP). In each sample, one of the four dideoxynucleotides (ddATP, ddGTP, ddCTP, or ddTTP) is added. When the bases of unknown strand bind with its complementary ddNTPs, the polymerization will stop as ddNTPs and fragments of DNA are produced. Further, the samples from all four vessels are collected and determine their size by agarose gel electrophoresis. Unknown sequence is determined by arranging the size of fragments from lowest to highest in 5' to 3' order. Many copies of DNA fragments with different lengths are generated to compute the final DNA Microarray dataset which will be further analyzed by applying expression analyzing algorithm to detect the disease biomarker.

2.3 *Next-Generation Sequencing*

Next-generation sequencing (NGS), a more cost-effective and efficient sequencing technology compared to Sanger sequencing, is used to sequence both DNA and RNA. Different machines are available for next-generation sequencing (NGS), but basically it follows three steps to complete the process.

2.3.1 Sample Preparation

It needs custom adapter sequence either by ligation or amplification. These adapter sequences provide universal primers for library hybridization to the sequence chip.

2.3.2 Sequencing Through Machines

Each library fragment is amplified and attached with DNA linkers to hybridize the adapters. This creates clusters of DNA, and each cluster is an individual sequencing read.

2.3.3 Collect Output Data

At the end of sequencing, raw data in the form of reads will be available which can further be analyzed to retrieve the more meaningful and informative result.

NGS can be implemented for both DNA microarray and RNA sequencing. In microarray datasets, gene intensities are in normal distribution; whereas in RNA-seq, it follows either Poisson or negative binomial distribution. The major advantages of RNA-seq over microarray dataset are: DNA microarray has very less sensitivity to gene expressions compared to RNA-seq dataset. RNA-seq can measure approximately 70,000 non-coding [29] RNAs which have an important role in disease biomarker detection; but, it is not possible in microarray.

2.4 Co-expression Analysis

Co-expression analyses are done generally in three steps.

Firstly, individual relationships among genes have to be calculated based on mutual information on each pair of genes. These information are stored in a matrix to describe the similarity or co-expression among the expression patterns of different genes across all the samples. Let us consider an example of five gene co-expression matrix as shown in Table 1.

In Table 1, we can see that maximum and minimum values are one and zero, respectively, for completely identical and complete dissimilar gene pair. Different ways of correlation measures, i.e., (1) Spearman's or Pearson's correlations [30, 31], (2) least absolute error regression [32], and (3) Bayesian algorithm [33] can be used to derive the co-expression matrix shown in Table 1. The values of Table 1 are only to describe the pattern of a co-expression matrix. Bayesian algorithm and least absolute error regression have the advantage to identify causal links.

Secondly, co-expression network has to be constructed using genes as nodes and co-relation between the nodes as edges. Edge can be either weighted versus unweighted

Table 1 5×5 co-expression matrix

	Gene1	Gene2	Gene3	Gene4	Gene5
Gene1	1	0.50	0.67	00	0.32
Gene2	0.50	1	0.39	0.80	0.45
Gene3	0.67	0.39	1	0.20	0.17
Gene4	00	0.80	0.20	1	0.78
Gene5	0.32	0.45	0.17	0.78	1

and signed versus unsigned. Thickness of edge shows the weight of the edge, and the value lies between zero and one.

Weighted Versus Unweighted

Unweighted edged network is the simplest way of constructing co-expression network where interaction between node pairs is binary, i.e., either 0 or 1. By considering the correlation of all gene pairs or node pairs above, a certain threshold to be connected (i.e., 1) and all others be disconnected (i.e., 0).

In a weighted edged network, all nodes are connected to each other with a weighted edge consists of continuous values determining the co-relation between the nodes where value determines the strength. Weighted edge can be of two types: signed and unsigned edges.

Signed Versus Unsigned

In a signed network, edge correlation values lie between -1 (perfect negative correlation) and 1 (perfect positive correlation). An unsigned edge network assigns the correlation values between 0 and 1 so that values less than 0.5 indicate negative correlation and values greater than 0.5 indicate positive correlation.

Thirdly, co-expressed genes are clustered using bi-clustering or tri-clustering technique to group the genes with similar expression patterns across multiple samples. Some well-known clustering algorithms are K-means clustering [34], hierarchical clustering [34], THD-triclus [26], shifting-and-scaling correlation clustering [35], etc. The clusters can be interrogated to identify regulators, functional enrichment, and hub genes for a potential disease gene by using guilt-by-association (GBA) [36] approach, while differential co-expression analysis gives the advantage of comparing modules in different conditions for better identifying disease regulators.

2.5 Differential Expression Analysis

Differential analysis has been done by comparing gene expression datasets of different conditions. For disease detection, minimum two samples have to be considered; one dataset of normal or healthy conditions and another in unhealthy or disease affected conditions. Different statistical tests like t -test, z -test, chi-square test are

applied to analyze whether expressions are in up-regulation (disease is growing) or down-regulation (in control) states. In unhealthy conditions, if more number of samples with a fixed interval can be collected, then differential analysis gives more informative result. Bi-clustering and tri-clustering techniques are used for two datasets and more than two datasets, respectively, to group the genes showing responses in the same conditions.

2.6 *Differential Co-expression Analysis*

Differentially co-expressed analysis is to identify the patterns of correlated gene expression in different conditions. It will always give a more informative picture of the dynamic changes in the gene regulatory networks by comparing the transcriptome of same genome in two conditions. For example, one cluster of genes strongly correlated in one condition may no longer be strongly correlated in another condition. Hence, differential co-expression gives high response to potential disease adaptation in different environments. Differential co-expression analysis can be done in three ways:

2.6.1 Targeted Differential Co-expression

Differential co-expression analysis starts with targeted approach. In general, it is completed in three steps.

Firstly, pre-defined clusters are being surveyed with known annotation file to analyze in different conditions.

Secondly, correlation among genes of individual clusters as well as the correlation within group of clusters has been derived by using the gene correlation expression.

Finally, comparison is done between gene co-expression values in multiple environmental conditions.

2.6.2 Untargeted Differential Co-expression

Untargeted differential co-expression is the latest approach among all bioinformatics sequence analyzer. It is also done in three steps. Unlike targeted in the first step, correlated genes have to be detected which shows different significant behavior in different conditions. Once clustering is completed, rest two steps are similar with targeted approach. In 2009, Southworth et al. [5] applied this approach for the first time which is based on purely untargeted approach for detecting the mice genetic modules correlation with respect to age.

2.6.3 Semi-targeted Differential Co-expression

It is somewhat in between targeted and untargeted, where pre-defined clusters with partial annotation files are used. A strong disadvantage of semi-targeted approach is that it only concerns with those genes which emerge with clusters at least in anyone different environmental conditions.

2.7 Cluster Detection

Once the analysis is being completed by using any of the analysis methods, viz. traditional co-expression analysis, differential expression analysis, or differential co-expression analysis, the affected genes will be discovered. Its efficiency depends on the effectiveness of the algorithm designed by the researchers. Then, these genes are clustered as a module so that this cluster can be used in further drug design.

3 Conclusion

In this paper, we have tried to explain a workflow in a sequential manner for detecting epidemic diseases affected genes using different bioinformatics advancements. In future, we are going to implement these approaches on different DNA, RNA samples to detect Cancer and HIV-AIDS affected genes and will try to cluster them separately, so that our result can help the drug designers at genetic level.

References

1. Tomasz P, Szymon W, Jacek B (2016) Computer representations of bioinformatics models. *Curr Bioinform* 11(5):551–560
2. Agbach CPE (2017) Pathways in bioinformatics: A window in computer science. *Int J Comput Trends Technol* 49(2):83–90
3. Sardaraz M, Tahir M, Ikram AA (2016) Advances in high throughput DNA sequence data compression. *J Bioinf Comput Biol* 14(3):18
4. Ge SX (2017) Exploratory bioinformatics investigation reveals importance of junk DNA in early embryo development. *BMC Genom* 18(1):200
5. Chen S, Liu M, Zhou Y (2018) Bioinformatics analysis for cell-free tumor DNA sequencing data. In: Computational Systems Biology. Humana Press, New York, NY, USA, pp 67–95
6. Zhang J, Huang K (2017) Pan-cancer analysis of frequent DNA come thylation patterns reveals consistent epigenetic landscape changes in multiple cancers. *BMC Genom* 18:1045
7. Van Dam S, Craig T, de Magalhaes JP (2015) Gene friends: a human RNA-seq-based gene and transcript co-expression database. *Nucl Acids Res* 43:1124–1132
8. Zeisel A, Munoz-Manchado AB, Codeluppi S et al (2015) Brain structure cell types in the mouse cortex and hippocampus revealed by single-cell RNA-seq. *347:1138–1142*

9. Fiannaca A, La Rosa M, La Paglia L et al (2015) Analysis of miRNA expression profiles in breast cancer using biclustering. *BMC Bioinform* 16
10. Xue Z, Huang K, Cai C et al (2013) Genetic programs in human and mouse early embryos revealed by single-cell RNA sequencing. *Nature* 500:593–597
11. Sanger F (1980) Google Scholar. http://www.nobelprize.org/nobel_prizes/chemistry/laureates/1980/sanger-bio.html
12. Hutchison C (2007) DNA sequencing: bench to bedside and beyond *Nucleic Acids. Nucl Acids Res.* 35:6227–6237
13. Mardis ER (2008) The impact of next-generation sequencing technology on genetics. *Trends genet. Trends Genet* 24:133–141
14. Shendure J, Ji H (2008) Next-generation DNA sequencing. *Nat Biotechnol* 26:1135–1145
15. Glass K, Huttenhower C, Quackenbush J (2013) Passing messages between biological networks to refine predicted interactions. *PLoS One* 8
16. De Smet R, Marchal K (2010) Advantages and limitations of current network inference methods. *Nat Rev Microbiol* 8:717–729
17. Yue F, Cheng Y, Breschi A et al (2014) A comparative encyclopedia of DNA elements in the mouse genome. *Nature* 515:355–364
18. Amar D, Safer H (2013) Dissection of regulatory networks that are altered in disease via differential co-expression. *PLoS Comput Biol* 9
19. Zeisel A, Munoz-Manchado AB, Codeiluppi S et al (2015) Brain structure cell types in the mouse cortex and hippocampus revealed by single-cell RNA-seq. *Science* 347:1138–1142
20. Bhar A, Haubrock M, Mukhopadhyay A et al (2013) Coexpression and coregulation analysis of time-series gene expression data in estrogen-induced breast cancer cell. *Algor Mol Biol* 8
21. Fiannaca A, La Rosa M, La Paglia L (2015) Analysis of miRNA expression profiles in breast cancer using biclustering. *BMC Bioinform* 16
22. Kakati T, Bhattacharyya DK, Barah P, Kalita JK (2019) Comparison of methods or differential co-expression analysis for disease biomarker prediction. *Comput Biol Med* 10:100–103
23. Madeira SC, Oliveira AL (2004) Biclustering algorithms for biological data analysis: a survey. *IEEE/ACM Trans Comput Biol Bioinform* 1:24–45
24. Wang YK, Print CG, Crampin EJ (2013) Biclustering reveals breast cancer tumour subgroups with common clinical features and improves prediction of disease recurrence. *BMC Genom* 14:102
25. Oghabian A, Kilpinen S, Hautaniemi S, Czeizler E (2014) Biclustering methods: biological relevance and application in gene expression analysis. *PloS One* 9
26. Kakati T, Kashyap H, Bhattacharyya DK (2016) THD-module extractor: an application for CEN module extraction and interesting gene identification for Alzheimer's disease. *Sci Rep* 6
27. Kakati T, Bhattacharyya DK, Barah P, Kalita JK (2019) Comparison of methods for differential co-expression analysis for disease biomarker prediction. *Comput Biol Med* 10:113
28. Tan SC, Yiap BC (2009) DNA, RNA, and protein extraction: the past and the present. *Hindawi Publ Corp J Biomed Biotechnol Article ID* 574398
29. Zhao Y, Li H, Fang S et al (2016) NONCODE 2016: an informative and valuable data source of long non-coding RNAs. *Nucl Acids Res* 44:203–208
30. Guttman M, Donaghey J, Carey BW et al (2011) lincRNAs act in the circuitry controlling pluripotency and differentiation. *Nature* 477
31. Ala U, Piro RM, Grassi E et al (2008) Prediction of human disease genes by human-mouse conserved coexpression analysis. *PLoS Comput Biol* 4
32. van Someren EP, Vaes BL, Steegenga WT et al (2006) Least absolute regression network analysis of the murine osteoblast differentiation network. *Bioinformatics* 22:477–484
33. Friedman N, Linial M, Nachman I et al (2000) Using Bayesian networks to analyze expression data. *J Comput Biol* 7:601–620
34. Haeseler PD (2005) How does gene expression clustering work? *Nat Biotechnol* 23:1499–1501
35. Ahmed H, Mahanta P, Bhattacharyya D, Kalita J (2014) Shifting-and-scaling correlation based biclustering algorithm. *IEEE/ACM Trans Comput Biol Bioinform* 11:1239–1252

36. Chu S, DeRisi J, Eisen M, Mulholland J, Botstein D, Brown PO, Herskowitz I (1998) The transcriptional program of sporulation in budding yeast. *Science* 282:699–705

A Strategic Community Control-Based Power Flow Between Grid-Integrated PV Houses



Jatin M. Soni, Deep V. Patel, Rajendra V. Patel, and Hardik P. Modha

Abstract This paper proposes a controlled power flow between interconnected four photovoltaic (PV) houses and also in grid-connected mode. The voltage and current schemes are used in PV houses. We have applied Perturb and Observe method to obtain maximum power. We have connected battery energy storage system (BESS) at each house by three-phase inverters. When all PV houses are connected, generated power from each PV is supplied to a load of each house. When a load of any house is disconnected, this power is utilized in another house. If there is an excess of power, it is fed to the utility grid. This scheme is validated in MATLAB/SIMULINK in various load condition. The power quality of this scheme is as per the IEEE standard.

Keywords PV rooftop · BESS · Three-phase inverter · Bidirectional energy meter · Utility grid

1 Introduction

The consumption of electricity is continuously increasing. But fossil fuels are decreasing day-by-day. Therefore, the renewable power sources like solar photovoltaic (SPV), wind turbine, geothermal are accepted as alternative source. SPV has gained most attention for research due to its more advantages [1]. SPV is used as rooftop for low power demand or as large solar farm for high power demand. The power at output terminal of SPV varies with solar irradiance and temperature. PV is used in islanded mode or in grid-connected mode [2]. The controller is planned such

J. M. Soni (✉) · D. V. Patel · R. V. Patel · H. P. Modha

Department of Electrical Engineering, Ganpat University, Kherva, Gujarat, India
e-mail: sonijatin1995@gmail.com

D. V. Patel
e-mail: dvp01@ganpatuniversity.ac.in

R. V. Patel
e-mail: hodelec.bspp@ganpatuniversity.ac.in

H. P. Modha
e-mail: hpm01@ganpatuniversity.ac.in

that SPV is synchronized with grid to keep stable system and to supply voltage at desired frequency [3]. Battery energy storage system (BESS) is used to deliver power in shortage of SPV power. In [4], the control of BESS with non-conventional sources is proposed with considering its state-of-charge (SOC). To get maximum power from SPV, maximum power point tracking (MPPT) is used. Perturb and Observe (P&O) method is used. In [5], the algorithm for MPPT is developed. The three-phase inverter is used to interconnect PV houses and grid. This inverter requires pulse width modulation (PWM) gate pulses. Inverter gives proper control of voltage and power, system balancing and quality of power conversion.

The BESS is connected to PV and grid by bidirectional three-phase inverter. It is used for controlling both charging and discharging state. In [6], reactive power control method is given. The active power is controlled by controlling disparity between inverter output voltage and point of common coupling (PCC) voltage [7]. PV houses are interconnected for sharing and utilizing power of other houses. The excess of power is given to utility grid by connecting it. And if there is less SPV power generation, the deficit power is supplied by the grid [8]. The bidirectional energy meter is installed at each PV house terminal. It gives three information: (1) Status of meter (2) How much power is delivered to other house or to grid (3) How much power is delivered from other houses or grid [9]. There is also caterpillar line for indication of direction of power flow. In [10], cluster of PV houses is interconnected. But it does not give information on excess of power and where to use it. This paper has implemented that issue by integrating it with grid.

This paper is prepared as along this path: Sect. 2 gives system configuration and its modeling, Sect. 3 presents control policy for voltage and current control, Sect. 4 gives information about the result attained in different load condition, and Sect. 5 gives conclusion of this paper.

2 System Configuration and Its Modeling

2.1 System Configuration

The four PV houses are interconnected and also connected to utility grid. Each PV houses has bidirectional energy meter at its terminal and PV rooftop system. The main architecture of grid-integrated PV houses is shown (see Fig. 1). Community control panel (CCP) does the power calculation of each house. Each PV house has loads, BESS, three-phase inverter and bidirectional energy meter. SPV and BESS are connected to its load and to grid by unidirectional three-phase inverter and bidirectional three-phase inverter, respectively (see Fig. 2). The lead-acid battery is used which has rating of 5 kW, $24 * 2 = 48$ V, 100 Ah. The load of each house is 12 kW.

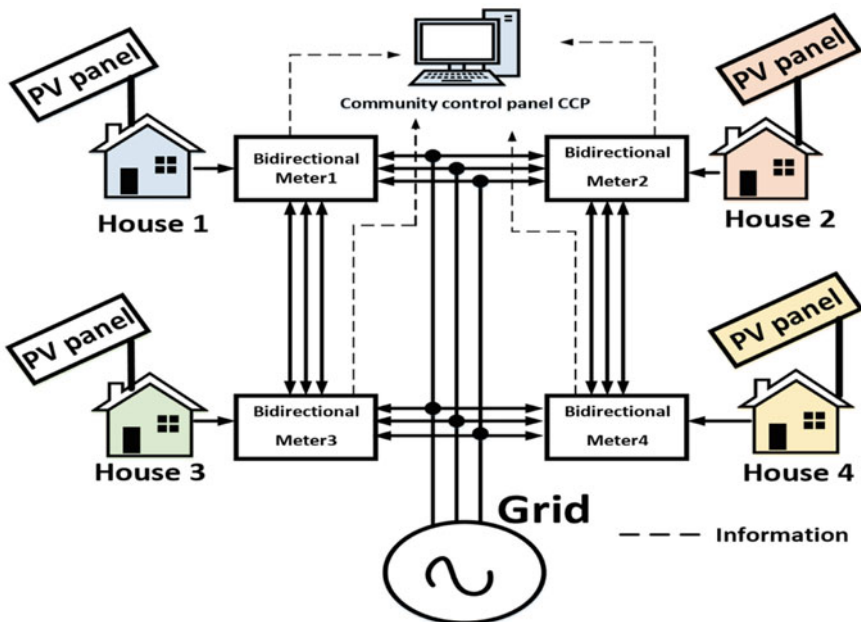


Fig. 1 Main architecture of grid-integrated PV houses

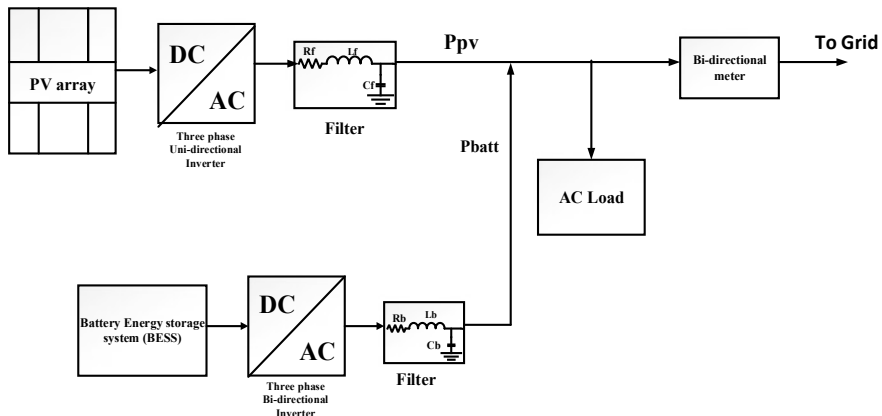
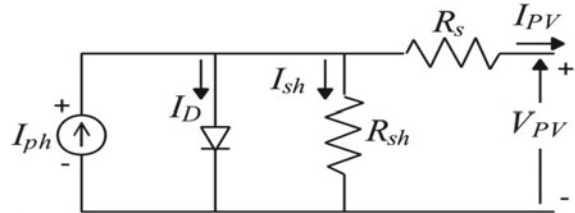


Fig. 2 System configuration in each PV house

2.2 System Modeling

Modeling of PV system and MPPT The inner structure of PV cell is shown (see Fig. 3). There is current source with anti-parallel diode [7]. Output voltage is low

Fig. 3 Internal construction of PV cell



due to voltage drop in series resistance R_s and leakage resistance R_{sh} . The desired output voltage and current is done by connecting cell in series and parallel.

Output voltage of PV system is taken from [8] is as follows:

$$I_{pv} = I_{ph} * I_D - (V_d / R_{sh}) \quad (1)$$

$$I_D = I_0 * (e^{V_d / V_{tA}} - 1) \quad (2)$$

$$V_D = V_{pv} + I_{pv} R_s \quad (3)$$

$$I_{ph} = \lambda * (I_{sc} + A(T - T_{ref})) \quad (4)$$

$$V_{pv} = N_s (A k T / q) * \ln \left\{ N_p I_{ph} - I_{pv} + N_p I_0 / N_p I_0 \right\} - (N_s / N_p) I_{pv} R_s \quad (5)$$

where R_{se} —resistance connected in series, I_{PV} —PV output current, q —electron charge, V_{PV} —obtained output voltage at PV terminal, n_{se} —quantity solar cell series connected, n_p —quantity solar cell parallel connected, K —constant (Boltzmann), A —factor of ideality, T_{cell} —temperature in operation mode, I_{sat} —current when it becomes saturated, I_{ph} —photocurrent, R_{sh} —resistance connected in parallel, I_{sc} —current in short circuit, α —coefficient (temperature), q —charge of electron, T_{ref} —temperature (reference) and E_G —energy gap in PV cell.

MPPT is used to get maximum power. The different MPPT methods are compared in [10]. Perturb and Observe (P&O) method is used because of easy to implement. Diagram of P&O method is shown in Fig. 4. We perturb voltage V , then we examine variation in power P . When we boost voltage in one way, there is raise in power P . We continue this process until we obtain point where voltage increases, power decreases. It is named as maximum power point. V_{dcref} is the reference value of V_{dc} .

Modeling of BESS system The voltage equations in charging and discharging mode for battery are given [10]. $V_{Batt, Ch}$ is charging output voltage, $V_{Batt, DCh}$ is discharging output voltage, V_{Batt} is constant battery voltage, i^* is filtered current, Q is Ah capacity, and $Exp(t)$ is exponential time zone.

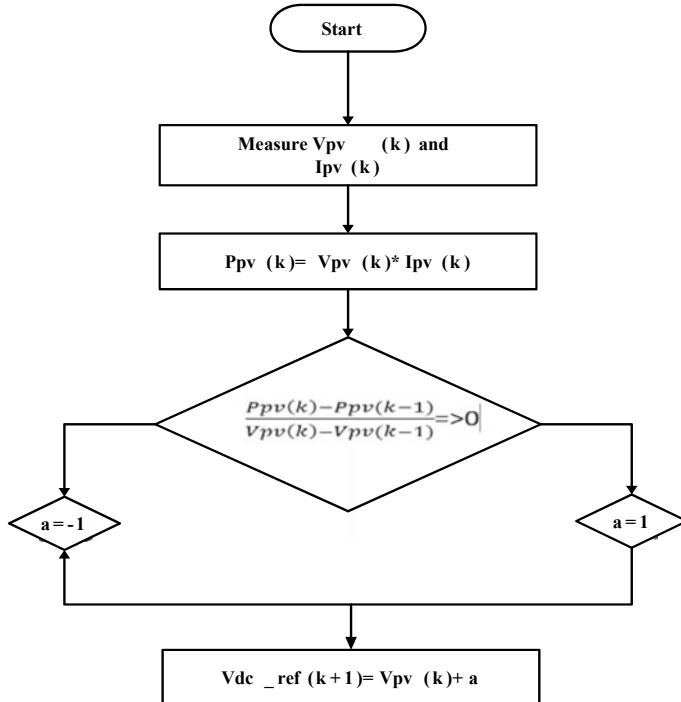


Fig. 4 Diagram of MPPT

$$\begin{aligned}
 V_{\text{Batt,Ch}} = & V_{\text{Batt},0} - R_1 i_{\text{Batt}} - k Q i^*/(i_{\text{Batt}} + 0.1 Q) \\
 & - k Q/(Q - i_{\text{Batt}} i_{\text{Batt}} t + \text{Exp}(t))
 \end{aligned} \quad (6)$$

$$\begin{aligned}
 V_{\text{Batt,Dch}} = & V_{\text{Batt},0} - R_1 i_{\text{Batt}} - k Q i^*/(Q - i_{\text{Batt}} t) \\
 & - k Q i_{\text{Batt}} t/(Q - i_{\text{Batt}} t) + \text{Exp}(t)
 \end{aligned} \quad (7)$$

3 Control Strategy

3.1 SPV and Its Controller

The block diagram of the PV system coupled to load and integrated with the grid is presented in Fig. 5. AC voltage (inverter output) is converted by Park transformation (ABC to DQ transformation). V_d , V_q , I_d and I_q , which are obtained from ABC to DQ (Park transformation) of inverter output voltage, is given to the voltage and current

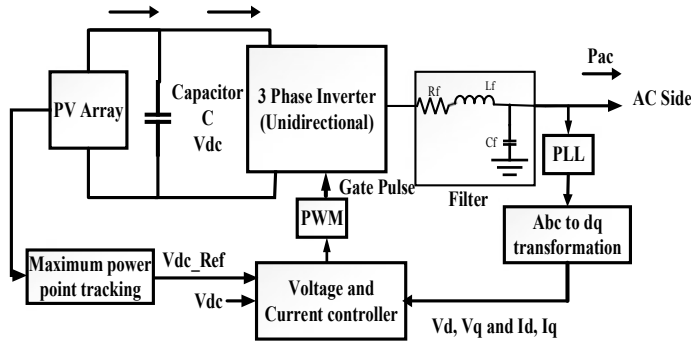


Fig. 5 Block diagram of PV system

controller. To get high power and to control active power given to main grid, a voltage controller is used.

The block diagram of voltage controller is shown in Fig. 6a. According to power balance theory, DC link voltage is as follows:

$$0.5 * C * (dV^2/dt) = P_{PV} - P_{dc} \quad (8)$$

P_{dc} is power at DC side of inverter. If inverter is lossless, P_{dc} is equal to P_{pv} .

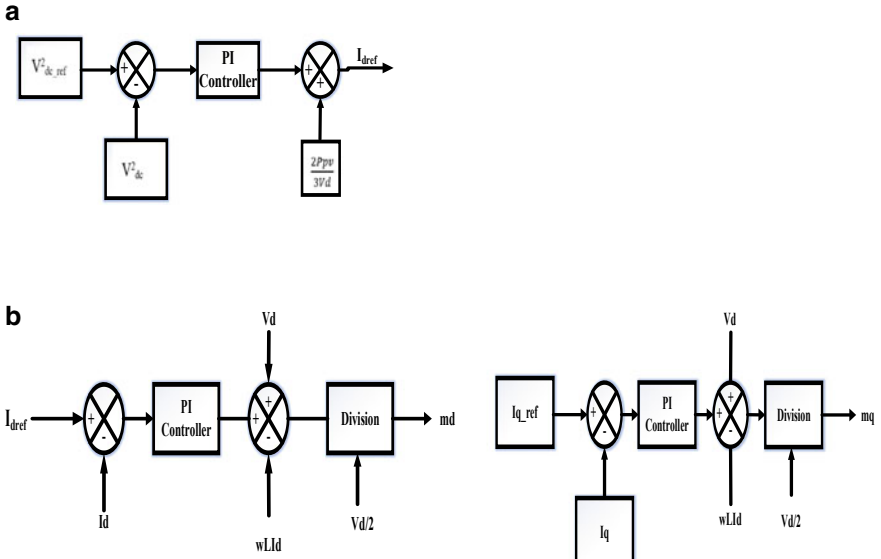


Fig. 6 **a** Voltage controller, **b** current controller

$$P_{ac} = 1.5 * (V_{T_d} i_d + V_{T_q} I_q) \quad (9)$$

V_{T_q} should be zero by using PLL. Equation for I_{dref} is achieved by using feedback linearization technique (FDL).

$$I_{dref} = u_v + \frac{2P_{pv}}{3V_{T_d}} \quad (10)$$

It produces the I_{dref} which is given to the current controller as a reference signal. The control scheme in the current controller is presented in Fig. 6b. Output signals m_d and m_q are converted into m_a , m_b and m_c signal by inverse Park transformation. Then, it is compared with a 2 kHz triangular wave to get the SPWM signal.

3.2 BESS and Its Controller

A block diagram of the BESS system coupled to load is presented in Fig. 7. AC voltage (output from bidirectional three-phase inverter) is converted by Park transformation (ABC to DQ transformation). When we charge the battery, DC voltage at its terminal is kept constant. When the battery is in discharging mode, the AC voltage at inverter output terminal is kept constant. So, value of reference voltage is accepted as per its mode of operation. The PLL is designed such that V_q is zero. The BESS controller is distributed in two categories: (1) voltage controller (2) current controller as shown in Fig. 8a, b. DC voltage of battery is taken as reference in battery charging mode. V_d is taken as reference in battery discharging mode. In current controller, $I_{qref} = 0$. The SPWM signal is attained by the same process as discussed in the PV system.

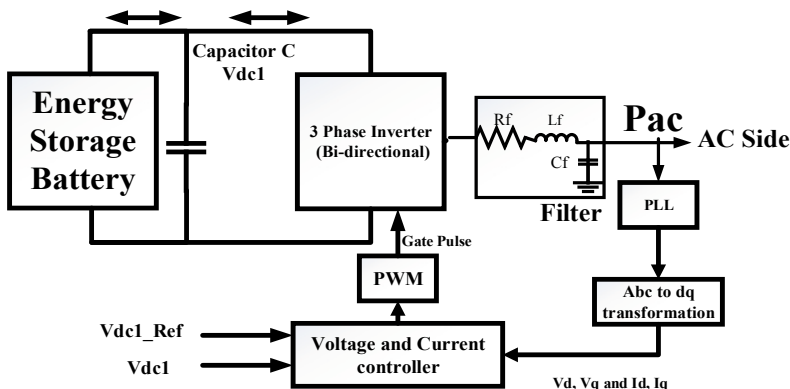


Fig. 7 Single line diagram of BESS system

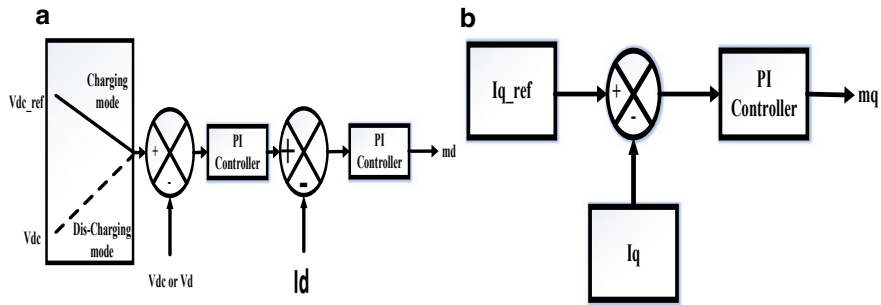


Fig. 8 **a** Voltage controller, **b** current controller

4 Results

The fixed irradiance, fixed temperature, PV output power and BESS output power are 1000 kW/m^2 , 25°C , 10.54 kW and 500 W , respectively, as shown in Fig. 9. Output voltage after transformer is 400 VRMS voltage as shown in Fig. 10.

Case (1) When the load of one house is disconnected: Load of house 1 is disconnected at $t = 3 \text{ s}$ shown in Fig. 11.

Case (2) When the load of two houses is disconnected: Load of house 2 is disconnected at $t = 5 \text{ s}$ grid as shown in Fig. 11.

Case (3) When the load of three houses is disconnected: Load of house 3 is disconnected at $t = 7 \text{ s}$ as shown in Fig. 11.

Case (4) When a load of all house is disconnected: Load of all houses is disconnected at $t = 9 \text{ s}$ as shown Fig. 11.

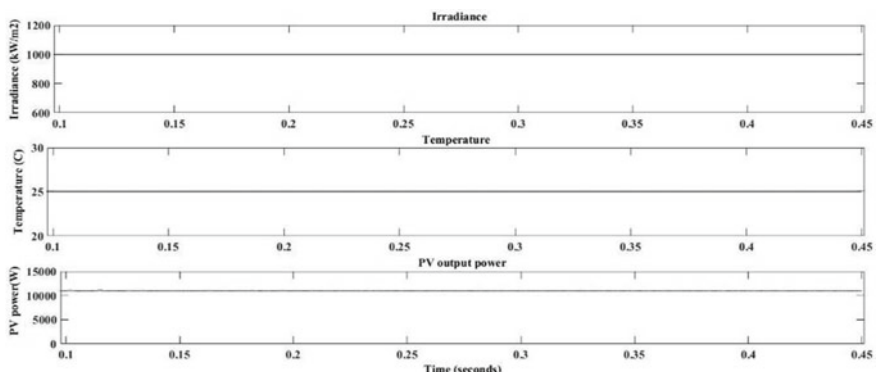


Fig. 9 Irradiance, temperature and PV output power

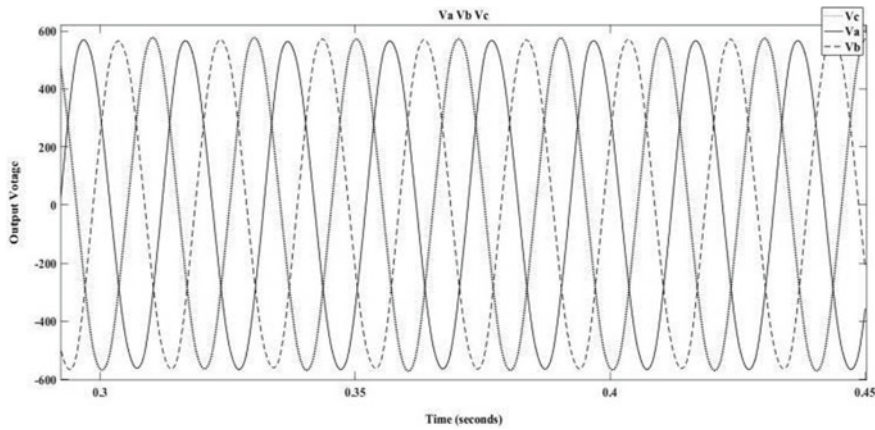


Fig. 10 Output voltage after three-phase inverter

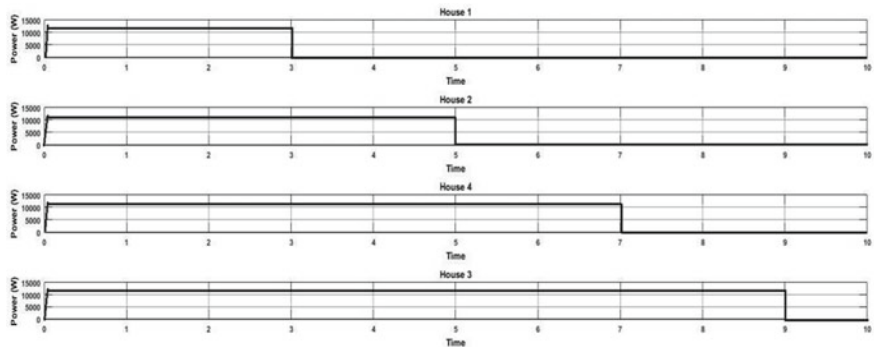


Fig. 11 Load power at each house

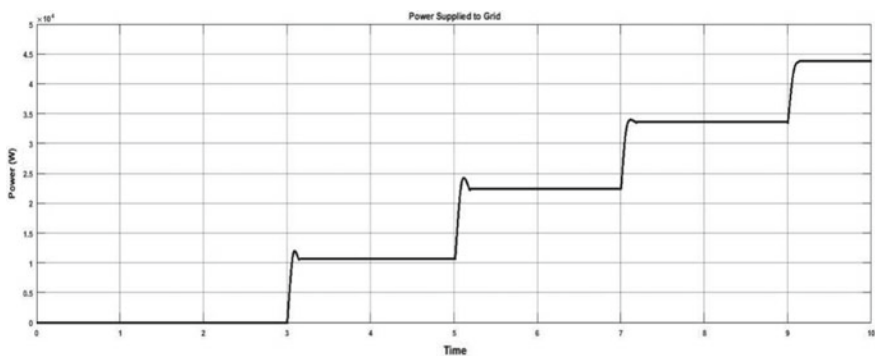


Fig. 12 Power supplied to grid

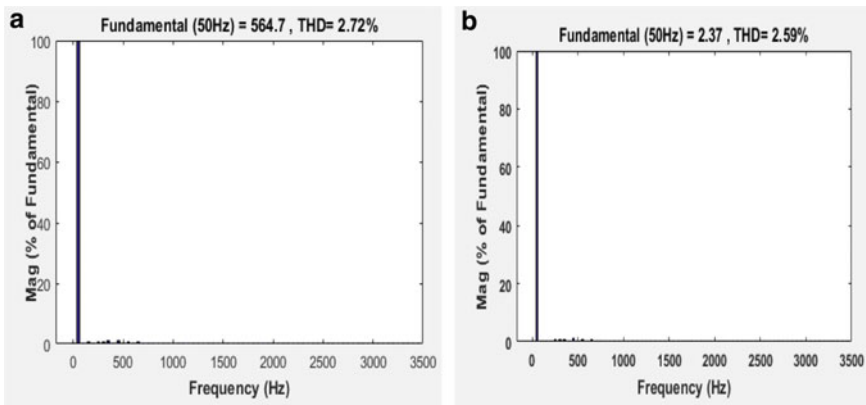


Fig. 13 FFT analysis at each house terminal. **a** Voltage, **b** current

The power supplied to grid in each case is shown in Fig. 12. The total harmonic distortion (THD) analysis of the output voltage is also done at each terminal of the house. And it is as per the IEEE standard as shown in Fig. 13.

5 Conclusion

In this paper, four PV houses are interconnected and also connected to the grid. The load of each house is abounding by PV generation of that house. If load of house is varied or disconnected, the PV power of that house is utilized in other houses. The excess of power, if any, is supplied to grid. The THD of the output voltage and current is as per IEEE 519 standard. So, the issue regarding excess of power is resolved by integrating whole system with grid.

References

1. Mahmood H, Michaelson D, Jiang J (2014) A power management strategy for PV/Battery hybrids system in islanded micro grid
2. Li H, Xu Y, Adhikari S, Rizy DT, Li F, Irminger P (2012) Real and reactive power control of a three phase single stage PV system and PV voltage stability. In: Power and energy society general meeting, 2012, vol 2. IEEE, pp 1–8
3. Blaabjerg F, Teodorescu R, Liserre M et al (2006) Overview of control and grid synchronization for distributed power generation systems. *IEEE Trans Ind Electron* 53(5):1398–1409
4. Mastromauro RA, Liserre M, Dell'Aquila A (2012) Control issues in single stage photovoltaic system: MPPT, current and voltage control. *IEEE Trans Ind Inform* 8(2):241–254
5. Hannan MA, Ghani ZA, Mohamed A, Uddin MN (2014) Real-time testing of a fuzzy logic controller based grid-connected photovoltaic inverter system. In: Industry applications society annual meeting, 5–9 Oct 2014. IEEE, pp 1–8

6. Delfino F, Denegri GB, Invernizzi M, Procopio R (2010) A control algorithm for the maximum power point tracking and the reactive power injection from grid-connected PV system. In: Power and energy society general meeting, 2010, vol 4, no 3, July 2010. IEEE, pp 1–7
7. Eghtedarpour N, Farjah E (2014) Distributed charge/discharge control of energy storages in a renewable-energy-based DC micro-grid. *IET Renew Power Gener* 8(1):45–57
8. Jha RR, Srivastava SC (2016) Fuzzy logic and ANFIS controller for grid integration of solar photo voltaic. In: 2016 IEEE 6th international conference on power systems (ICPS), New Delhi, pp 1–6
9. Jha RR, Srivastava SC, Kumar M (2017) Development of control schemes for a cluster of PV-integrated houses in islanded mode. *IET Gener Transm Distrib J*
10. Soni JM, Pandya MH (2018) Power quality enhancement for PV rooftop and BESS in islanded mode. In: 2018 IEEE 4th international conference on electrical energy system (ICEES), vol 3, Feb 2018, pp 242–247

Classification of Buildings and Vehicles in Google Map Satellite Images Using Random Forest Classifier



Ritik Gautam, Saravanan Chandran , and Jose Hormese

Abstract The Google Map provides an additional feature for observing various places of the landscapes as bird's eye view with the help of the satellite images. Google Map satellite images are developed with the help of geographical information systems (GIS) data, aerial images, drone images, and satellite images with the help of image fusion methods to produce a bird's eye view of a landscape. This proposed research work is intended to classify the buildings and vehicles from the Google Map satellite images that are captured at a zoom level of 20 m. This research work carried out to survey an area for various applications which require number of buildings and number of vehicles. The random forest classifier is used for the pixel classification, and this technique is also referred as pixel segmentation. The random forest classifier produces a result of 87% accuracy.

Keywords Google map · Satellite images · Random forest classifier · Building segmentation · Vehicle segmentation

1 Introduction

Segmentation techniques are extensively used in the field of image processing and computer vision for the applications of object detection and identification [1]. A digital image is subdivided into a number of regions referred as segmented region. The segmented region consists of large number of pixels that have similar properties that represents the image. The segmentation of an image is used in several applications. The segmentation approach is used to identify both the buildings and vehicles in a Google Map satellite images that provide the basis for the work. As urbanization is on the increase, the significance of such satellite images is increasing which can be utilized in diverse applications. Such diverse applications include homeland security, effective resource management, emergency responses, and environmental monitoring as well. These Google Map satellite images are normally captured through

R. Gautam · S. Chandran · J. Hormese

Department of Computer Science and Engineering, NIT Durgapur, West Bengal, India

e-mail: cs@ieee.org

high resolution satellites and have various applications especially in the areas like agriculture, forestry, geology, surveillance, regional planning, and also in education. Having such information helps in rural planning which benefits the residents and the development of various public facilities.

Various approaches have been developed and proposed for applications like extracting road networks [2–8], water regions, green regions, [9] identification of buildings, and vehicles. During the unexpected natural disasters, the loss incurred to assets and people is quite high. If an assessment is prepared in a short time during the disaster period, it provides the technical details of the disaster, quantity of the disaster, area affected by the disaster, etc. Thus, prompt decisions are initiated in short time to control the disaster and start planning for the rescue operation, etc. The significance of the satellite images originates from the fact that it is of high resolution, covers a wide area, and is highly efficient in terms of time. Google Map satellite images are very useful in the context of assessing the damages that are caused in the event of an unexpected disaster. Identifying the impact of the damage is possible to quickly initiate various necessary rescue actions. The field of remote sensing has lot of importance in understanding the extent of land use which helps in understanding the spatial and temporal features. This helps in providing high data availability and computing the data which helps in better understanding the changes. In this research work, classification of buildings and vehicles are carried out and achieved 87% accuracy using random forest classifier algorithm.

2 Related Works

To know about the structure of terrestrial systems, the land cover details are essential. The field of remote sensing generates terrestrial information in a global scale. A methodology is framed for both discrete and continuous land cover that is based on datasets which is time-based and depends on spatial resolution [10]. A method had been proposed that detects eroded and non-forested areas that are tropical. They used image algebra among the colour components that augmented the contrast mainly between green and brown. This helped to differentiate between the areas that are forest and the non-forested parts [11, 12]. Brezonik et al. [13] have specified that images captured from Landsat satellites are useful for estimating various optical characteristics of lakes and various measurements also considered. Prasad et al. [14] have identified that the rapid expansion of urbanization has depleted the water bodies and various infrastructural entities like buildings, roads, parks, and hubs are spreading in a very quick manner. Goswami et al. [15] have specified the importance of recognizing images from satellite images and that it comes under the classification techniques. He proposed artificial neural networks (ANN) for the purpose of object extraction as ANNs are suitable for extracting objects in an automated manner. The data associated with land cover are used extensively in the fields like modelling urban growth, agriculture based on advanced technology, management of coastal regions, and also climate management [16]. Noticed that land cover altered as an

effect of natural disasters like landslides, floods, cyclones, and forest fires. Human interventions like urbanization, deforestation activities, and practices followed in agriculture also lead to alteration in the land cover [17].

The changes that happen in the ecological and physical systems due to human activities, understanding the land cover, help to understand both the ecosystem and the climate models [18]. The conservation of natural resources and its management and to formulate policies for urban and environmental development is essential. Poullis and You [19] proposed a road detection method and classified the method into three categories that are namely region-based, pixel-based, and knowledge-based. Line detectors [20], [21] and ridge detectors [22], [23] are employed for the identification and classification of road points. These interconnected road points are producing road segments that are provided as input to the further processing level stages. The techniques used in deep learning like convolutional neural networks (CNNs) are showing better performance than ANNs as they overcome the pitfalls and they produce better results when compared with machine learning techniques like support vector machines and random forest [24]. Studies have shown that spectral values are supplied in a vector format in one-dimensional format to the CNNs that is used for classification of land cover, but this approach fails to avail full advantage of CNNs that extracts spatial characteristics from images that are in two-dimensional form [25].

3 Methodology

Three hundred Google Map satellite images are collected by cropping various locations. Two hundred images are selected for training, and one hundred images are reserved for testing. The 200 images are marked with red colour for building and green colour for vehicle. These marked images are trained using the random classifier model. Fiji is used for pre-processing the images. The random classifier algorithm is used for training and testing. The Weka has developed the model for classification of building and vehicle. Further, the 100 images are tested using the model.

In a Google Map satellite image, segmentation techniques are used to identify both buildings and vehicles. The image processing tools used for this segmentation are Fiji and Weka. Random forest classifier is used for classification purpose of the above-mentioned images. The classifier is being built with around 200 images in the training set. The classifier is then loaded, and the results are created with a test set of 100 images.

The practice of subdividing an image into various objects or primary parts is the main purpose of segmentation. Once this is accomplished, the extracted regions are applied to different feature extraction algorithms used in both image processing and computer vision applications. This process depends on the application and grouping of pixels based on the intensity values is helpful for separating the required and other objects as well as other parts of the original image. Segmentation is useful for various areas like detection of vehicles, recognition of faces, in the field of medical diagnosis,

and in various other fields as well. It has immense applications in pre-processing steps for image compression techniques and identification of object boundaries. Segmentation algorithms are classified into thresholding, clustering methods, region growing methods, and histogram-based methods. Partitioning an image into different regions that is similar and alike satisfies the similarity property while partitioning an image into several regions that is based on changes in intensity values satisfies the discontinuity property.

In the field of data science, different classification algorithms are available such as random forest, support vector machine, decision trees, logistic regression, Naive Bayes classifier, and few others. One of the frequently used classifiers in this hierarchy is the random forest classifier. The basic idea is the formulation of decision trees, and they are combined together to construct a typical random forest. Any random forest representations are built up using decision trees. Decision trees use features that help to split the data, and the resultant groups formed will be different in various respects.

An open source package for image processing that is based on Java named Fiji is used for this research work. The purpose of Fiji is to provide Java-based plugins that are bundled. Users are provided with a detailed menu supported with broad documentation with tutorials and are robust thereby avoiding installation of different components from various components. Developers use Fiji with version control systems, numerous development channels, infrastructure for prototyping and support numerous scripting languages.

The plugin initiates with two classes and hence producing the binary pixel classification. With the various tools for identifying the region of interest (ROI), users have the freedom to add traces to these classes.

The training set consists of 200 images that are captured from the Google Map satellite images taken at a resolution of 20 m zoom level. The random forest classifier is trained based on this training set, and the classifier is made accordingly. The images that are used for the training purposes are illustrated as follows. The following two images displayed in Figs. 1 and 2 are also employed in the training process.

The two classes that are developed here are namely buildings and vehicles, respectively. The ROI tools are used to indicate the regions present in both the classes from the training images. The pixels that belong to the buildings are marked with red colour, and the pixels corresponding to vehicles are marked with green colour. These boundaries are marked for each class for each and every training image that is being stacked from the training set in the Weka. The resultant classifier images are as follows Figs. 3 and 4.

After the boundaries for each class are being marked for all the images in the training set, as shown in the below images Figs. 5 and 6, the images are trained in Weka. It is noted that the training time depends on the total number of pixels present in each class. Once the training process is completed, the classifier model is saved for testing other images.



Fig. 1 Google Map satellite image 1



Fig. 2 Google Map satellite image 2

4 Results and Discussion

After the classifier is build and then trained, the next step is to perform the testing operations on the classifier developed. A sample test dataset of 100 images is considered for testing, and the results are replicated on these dataset. The classifier is loaded, which was built previously and then click on the generate results option. The results obtained are as shown above.

As mentioned earlier, buildings are mapped with red pixels, and the vehicles are mapped with green pixels. The probability map is shown below where it represents the probability of a pixel that belongs to a particular class that can either be buildings or vehicles. It is noted that for classifiers, the performance has to be augmented with the help of optimization of different parameters (Fig. 7).



Fig. 3 Weka classifier image 1



Fig. 4 Weka classifier image 2

The results obtained are after different stages of optimization techniques. A commonly employed technique used in machine learning is Bayesian optimization. When there are different hyper-parameters that deal with machine learning problems, there arises tuning of the classifier which results in costly evaluations with respect to time and computational resources, respectively. Bayesian optimization is useful to overcome this short coming. A probabilistic model is built, and the posterior predictive distribution is computed that integrates the various true functions. This leads to an optimized proxy function that is cheaper when compared with the true objective.



Fig. 5 Weka test results image 1



Fig. 6 Weka test results image 2

The idea behind this approach is to exploit the amount of randomness to balance the exploration. This approach may not give the best results with respect to neural networks [26] because optimization that is based on a manual scheme is applied.

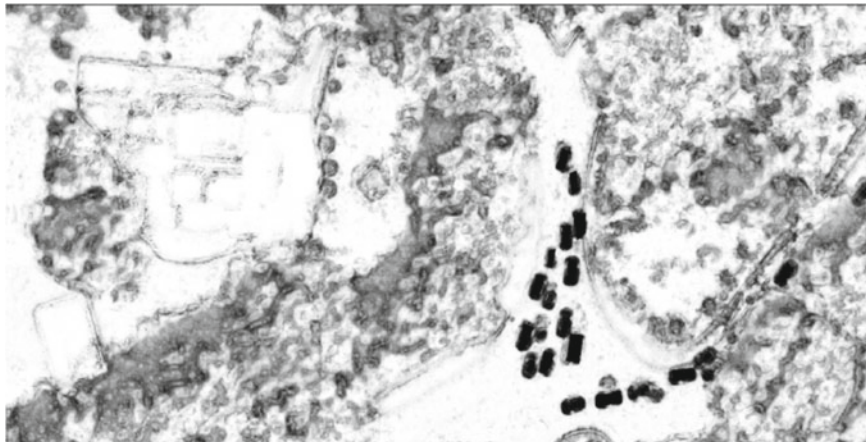


Fig. 7 Weka probability map of the test results

The random forest approach produces the value of accuracy as 0.87 which is computed as the number of true predictions to the entire number of input images. The specificity obtained is 0.91 which matches the negative samples wrongly identified as positive to the whole set of incorrect samples. The precision value obtained is 0.93 which is equal to the proportion of correct positive samples to the whole set of samples that are positive. The recall results come to 0.91 which is denoted as the right positive samples that are predicted to the entire set of samples irrespective of prediction. The F_1 measure that corresponds to the harmonic mean involving both precision as well as recall is 0.92 which depends on the precision of the classifier. The geometric mean comes out to be 0.94 which is related to both sensitivity and specificity.

5 Conclusion

The detection of roads is a critical problem. This is due to complication of road segments like occlusions, discontinuities, different boundaries, and sharp bends. This makes the classification of both buildings and vehicles also difficult. This research article discusses about an approach that classifies buildings and vehicles in Google Map satellite images based on the random forest approach. This provides an informative approach for the classification of both buildings and vehicles. The random forest classifier is employed for this purpose. This research article discusses about an approach in classifying buildings and vehicles with relatively high accuracies. The results can be further improved if the images are processed using deep neural networks that employs deep learning.

References

1. Liu X, Deng Zhidong, Yang Y (2019) Recent progress in semantic image segmentation. *Artif Intell Rev* 52:1089–1106
2. Ruiz JJ, Rubio TJ, Urena MA (2011) Automatic extraction of road intersections from images based on texture characterisation. *Surv Rev* 43(321):212–225
3. Maboudi M, Amini J, Hahn M, Saati M (2016) Road network extraction from VHR satellite images using context aware object feature integration and tensor voting. *Remote Sens Multidis Digital Publ Inst* 8(8):637
4. Coulibaly I, Spiric N, Sghaier MO, Manzo-Vargas W, Lepage R, St-Jacques M (2014) Road extraction from high resolution remote sensing image using multiresolution in case of major disaster. In: Proceedings of 2014 IEEE remote sensing symposium, pp 2712–2715
5. Sghaier MO, Lepage R (2016) Road extraction from very high resolution remote sensing optical images based on texture analysis and beamlet transform. *IEEE J Select Top Appl Earth Observ Remote Sens* 9(5):1946–1958
6. Li M, Stein A, Bikker W, Zhan Qingming (2016) Region-based urban road extraction from VHR satellite images using Binary Partition Tree. *Int J Appl Earth Obs Geoinf* 44:217–225
7. Alshehhi R, Marpu PR (2017) Hierarchical graph-based segmentation for extracting road networks from high-resolution satellite images. *ISPRS J Photogram Remote Sens* 126:245–260
8. Liu R, Song J, Miao Q, Pengfei X, Xue Q (2016) Road centerlines extraction from high resolution images based on an improved directional segmentation and road probability. *Neurocomputing* 212:88–95
9. Kasu NR, Chandran S, Hormese J (2019) Identification of water and green regions in Open-StreetMap using modified densitometry 3 channel algorithm. In: IEEE international conference on advances in computing, communication and control (ICAC3 19), 20–21 Dec 2019, Mumbai, India
10. Colditz RR, Schmidt M, Conrad C, Hansen MC, Dech S (2011) Land cover classification with coarse spatial resolution data to derive continuous and discrete maps for complex regions. *Remote Sens Environ* 115:3264–3275
11. Cruz HO, Eckert M, Meneses JM, Martinez JF (2017) Precise Real-time detection of nonforested areas with UAVs. *IEEE Trans Geosci Remote Sens* 55(2):632–644
12. Mattikalli NM, Richards KS (1996) Estimation of surface water quality changes in response to land use change: application of the export coefficient model using remote sensing and geographical information system. *J Environ Manage* 48(3):263–282
13. Brezonik P, Menken KD, Bauer M (2009) Landsat-based remote sensing of lake water quality characteristics, including chlorophyll and colored dissolved organic matter (CDOM). *Lake Reservoir Manage* 21(4):373–382
14. Prasad PRC, Rajan KS, Bhole V, Dutt C (2009) Is Rapid urbanization leading to loss of water bodies. *J Spat Sci* 2(2):43–52
15. Goswami AK, Gakhar S, Kaur H (2014) Automatic object recognition from satellite images using artificial neural network. *Int J Comput Appl* 95(10)
16. Adam E, Mutanga O, Odindi J, Abdel-Rahman EM (2014) Land use cover classification in a heterogeneous coastal landscape using Rapid-Eye imagery: evaluating the performance of random forest and support vectormachines classifiers. *Int J Remote Sens* 35(10):3440–3458
17. Carlson TN, Arthur ST (2000) The impact of land use land cover changes due to urbanization on surface microclimate and hydrology: a satellite perspective. *Glob Planet Change* 25(1–2):49–65
18. Sterling SM, Ducharne A, Polcher J (2013) The impact of global landcover change on the terrestrial water cycle. *Nature Clim Change* 3(4):385
19. Poullis C, You S (2010) Delineation and geometric modeling of road networks. *ISPRS J Photogram Remote Sens* 65(2):165–181
20. Zhou YT, Venkateswar V, Chellappa R (1989) Edge detection and linear feature extraction using a 2-D random field model. *IEEE Trans Pattern Anal Mach Intell* 11(1):84–95

21. Hedman K, Still U, Lisini G, Gamba P (2010) Road network extraction in VHR SAR images of urban and suburban areas by means of class-aided feature-level fusion. *IEEE Trans Geosci Remote Sens* 48(3):1294–1296
22. Hu J, Razdan A, Femiani JC, Cui M, Wonka P (2007) Road network extraction and intersection detection from aerial images by tracking road footprints. *IEEE Trans Geosci Remote Sens* 45(12):4144–4157
23. Zhang J, Lin X, Liu Z, Shen J (2011) Semi-automatic road tracking by template matching and distance transformation in urban areas. *Int J Remote Sens* 32(23):8331–8347
24. Deng Z, Sun H, Zhou S, Zhao J, Zou H (2017) Toward fast and accurate vehicle detection in aerial images using coupled region-based convolutional neural networks. *IEEE J Sel Top Appl Earth Observ Remote Sens* 10(8):3652–3664
25. Hu F, Xia G-S, Hu J, Zhang L (2015) Transferring deep convolutional neural networks for the scene classification of high-resolution remote sensing imagery. *Remote Sens* 7(11):14680–14707
26. Snoek J, Larochelle H, Adams RP (2012) Practical Bayesian optimization of machine learning algorithms. *Adv Neural Inf Process Syst* 25:2951–2959

Addressing the False Positives in Pedestrian Detection



N. J. Karthika and Saravanan Chandran

Abstract Pedestrian detection is a subfield of object detection that is necessary for several applications such as person tracking, intelligent surveillance system, abnormal scene detection, and intelligent cars. We prepared a dataset for addressing the false positives that occur during the person detection process. Some objects have very similar features to those of a person. If a model is trained using a dataset containing only persons, it leads to several false positives since it cannot differentiate such objects from that of a person. Our dataset includes person and person-like objects (PnPLO). Person-like objects that we introduce in our dataset are statues, mannequins, scarecrows, and robots. We used the SSD model to show that, on training a model using our dataset, we can significantly reduce the false positives during detection when compared to models trained on standard person datasets, thereby improving the precision. The dataset consists of 944 training images, 160 validation images, and 235 images for testing, with a total of 1626 person and 1368 nonhuman labelling.

Keywords Pedestrian detection · Nonhuman detection · Deep learning · SSD · Computer vision

1 Introduction

Humans can instantly recognise any object in an image. We can also simultaneously interpret the location of any object, as well as how the objects interact. The human visual system is very fast as well as accurate, helping us to perform even highly complex tasks such as driving a vehicle, with little conscious thought. Computer

N. J. Karthika · S. Chandran
Computer Science and Engineering, National Institute of Technology,
Durgapur, West Bengal, India
e-mail: karthika.nj@gmail.com

S. Chandran
e-mail: cs@ieee.org

vision is a research area, wherein the researchers try to make the computers work in the same way as to how the human visual system works. The recent trend in this field is the use of deep learning models, which is because various researches [1–5] show that deep learning models have made the computers much faster and accurate in object detection, classification, recognition, and various other computer vision problems. Until the year 2016, state-of-the-art object detection systems with the best accuracy were computationally intensive and too slow to run in real-time (e.g. faster RCNN [1]). Also, the models which ran on real-time were not accurate enough, especially for safety-critical applications. With the advent of SSD model [2], there was a significant improvement in the speed for detection with high accuracy.

Dataset plays a crucial role in problems of object classification, detection, recognition, segmentation, etc. There are many popular datasets widely accepted as benchmarks for object detection problem. ImageNet [6], PASCAL VOC [7], COCO [8], and SUN [9] datasets are few examples. Each of these differs in the type of images, number and type of object labels, and size of datasets.

Pedestrian detection is an object detection problem. It has several real-time applications such as person tracking, robotics, video surveillance, and driverless cars. Research works over the years have been using various approaches for the problem of pedestrian detection, such as part-based detection [10], holistic detection using features like HOG [11], motion-based detection [12], patch-based detection [13], and detection using multiple cameras. As in other object detection problems, deep learning is currently the most used approach in the research related to pedestrian detection [14].

All the research works related to pedestrian detection which use deep learning for training their models make use of person datasets as the benchmark [11, 15, 16]. These datasets consist of only the images of persons in various postures and under different lighting conditions. The popular object detection datasets [6–8] also have person as a class but no object classes to differentiate the person from objects having similar features as persons. Since there are objects such as mannequins and statues that have very similar features as that of a person, a model that is trained with datasets containing only person images will have higher false positives on encountering such objects. Considering this problem, we prepared a dataset (PnPLO) [17] containing persons as well as the objects having features very close to that of a person such as mannequins, statues, scarecrows, and robots. We train SSD model with 300*300 image input size (ssd_300) and show the improvements in precision on testing the newly trained model compared to the model trained on benchmark datasets, namely, COCO [8], INRIA [11], and PASCAL VOC [7]. We can observe considerable improvement in precision with the model trained on our dataset, on testing the models on PnPLO test dataset.

2 Recent Works

Computer vision is a field of study where extensive research is going on, especially with the use of deep learning models. Pedestrian detection or person detection, in general, is one of the topics of eminence in the field of computer vision, because of its wide variety of applications in real-world problems. Video surveillance, driverless cars, and person tracking are some of the applications. Deep learning gained popularity with the advent of AlexNet [3] in the year 2012, followed by many notable research works such as [4, 5, 18].

Most of the recent object detection research works use either faster RCNN [1] or single-shot multibox detector [2] as their backbone network because of their accuracy and speed of SSD. Before the advent of SSD, faster RCNN was widely used because of its excellent accuracy. This model is based on a region proposal network, which is class agnostic. This class agnostic nature of RPN networks leads to high time consumption, as the network needed two rounds of predictions—first, to predict the regions which may contain an object, and then to predict the class of the object present in that region. YOLO [19] considered this disadvantage and proposed to have only one round of prediction by making the region proposals to be class-specific so that the network needs to look at an image only once, thus, saving a great deal of time. As the image passes through the deep convolutional network only once, the model was speedy and could be run real time. Though YOLO worked in real time, it compromised the accuracy by a great deal when compared to the previous state-of-the-art model [1]. Problem with the first version of YOLO was that it could not capture scale variation and failed to detect very small objects. SSD provided a solution for this problem by proposing an auxiliary structure that can perform detections at multiple scales. SSD, therefore, can run in real time with an accuracy comparable to that of faster RCNN.

2.1 SSD Overview

SSD model was the first model that worked in real time with an accuracy as good as the previous state-of-the-art models in object detection. Before SSD, models such as the RCNN series [1, 20, 21] used RPN-based approach, which was time-consuming because of two stages—region proposal, followed by detecting objects in each proposal. The most significant advantage of SSD is its simplicity, with a single network encapsulating all the computations, eliminating the need for a proposal generation as well as the feature resampling stages. Figure 1 shows the architecture of the ssd model.

SSD takes an image and ground truth boxes as input. The model used VGG-16 network [5] as the base network. This network forms the first layers, following which, an auxiliary structure was added to the network to produce detections. For each location in feature maps of different scales, a small set of default boxes of

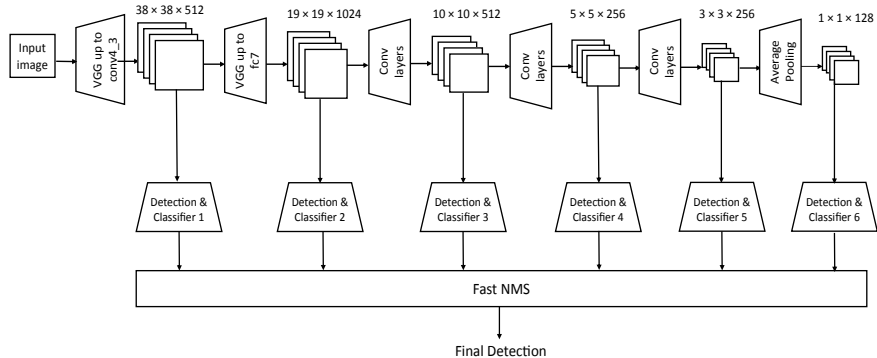


Fig. 1 SSD architecture

varying aspect ratios are evaluated in a convolutional manner. For each default box, confidence scores of all object categories, and the shape offsets are predicted. During training, the default boxes and the ground truth boxes are matched, and the model loss is calculated, which is the weighted sum of confidence loss and the localisation loss. The overall loss is given by :

$$L(x, c, l, g) = \frac{1}{N}(L_{\text{conf}}(x, c) + \alpha L_{\text{loc}}(x, l, g))$$

where L_{conf} and L_{loc} are confidence loss and localisation losses, respectively, and α is the weight term. Confidence loss is the Softmax loss over multiple class confidences (c). Localisation loss is the smooth $L1$ loss [21] between the parameters of ground truth box and the predicted box (l).

2.2 Datasets

Pedestrian detection is a subject of interest in various researches because of its widespread real-life applications. Hence, there are multiple standard datasets available, consisting of person as a class, used for these research works. We have considered three datasets used as benchmarks viz., COCO, INRIA, and PASCAL VOC datasets.

2.2.1 COCO

This dataset contains images of complex everyday scenes of common objects in their natural context. It is a large-scale dataset for object detection. It defines 91 classes, but only 80 classes are used by the data. Segmentations of 11 other classes were not

collected because of problems like too many instances, ambiguity, and difficulty in labelling, too few instances, etc. Compared to the previous datasets such as Imagenet and PASCAL VOC, COCO dataset has more object instances per image and also gives an additional focus on segmenting individual instances of different objects. Person is one among the 80 classes considered in the dataset.

2.2.2 INRIA

The INRIA person dataset has a training set constituting 1128 negative images and 614 positive images, and a testing set with 288 images. First created and used by Dalal and Triggs [11], the static person dataset comprised of people in various positions and orientations, taken in a variety of backgrounds and lighting conditions.

2.2.3 PASCAL VOC

The PASCAL visual object classes (VOC) challenge had been organised annually since the year 2005. The dataset associated with this challenge is publicly available and has been accepted as a benchmark in object detection. It constitutes images as well as annotations in XML format. The dataset consists of 20 classes which include ‘person’ as one among them.

3 PnPLO Dataset

Data plays a critical role in any deep learning research work, enabling the computers to work in the same way as to how the humans do. This is especially true in the field of object detection, where the number and the type of images used for training a deep learning model play a crucial role while applying the model to real-world problems.

All the datasets used as benchmarks for person detection problem contains only images labelled with person objects. Training with such a dataset leads to several false positives while testing, when the images include many objects having features close to that of a person. If an image contains a statue, then a model that was trained with only person images tends to identify the statue as a person, leading to a false positive. To address this problem of false positives, we prepared a dataset containing persons as well as the objects having features similar to a person—person and person-like objects (PnPLO) dataset [17]. We have labelled the person-like objects as ‘nonhuman’.

3.1 *Image Acquisition*

Person images and their corresponding annotation files used for training are considered from the PASCAL VOC 2012 person training dataset, and images for testing are taken from PASCAL VOC 2007 person test set. The nonhuman images are taken from the Internet. These images are completely random, not taken for a specific purpose or a specific event, or from any particular angle. Because of this randomness, we get an unbiased dataset. Some of the nonhuman images also contain person objects in them.

3.2 *Labelling*

The dataset consists of a total of 944 images for training, 160 images in the validation set, and 235 for testing. In the training set, there are 1106 person and 960 nonhuman labellings. In the validation set, there are 203 person and 130 nonhuman labellings. The test set consists of 317 and 278 labellings of person and nonhuman, respectively.

We labelled the nonhuman images using the labelImg tool [22], which is a graphical tool for generating image annotations. This tool saves the annotations in the form of XML files in the format of PASCAL VOC dataset. We have labelled the images for two classes, person and nonhuman class. In the XML annotations of PASCAL VOC dataset, we have removed the annotations marked as difficult since such objects will have similar features for both the classes considered and are difficult for even the human eye to differentiate correctly. We have taken 526 person images for training from the PASCAL VOC 2012 dataset, and 125 images from PASCAL VOC 2007 test list for testing. The number of person and nonhuman objects in the dataset are comparable to avoid any over-fitting or under-fitting problems.

4 Experiment

We first tested the ssd_300 model trained on some standard datasets on the test data of our dataset. The ssd_300 model trained on COCO, INRIA, and PASCAL VOC datasets, respectively, are considered. Since the PASCAL VOC dataset includes person as a class, we used the SSD model trained on this dataset as the initial setting for the model to train on our dataset. This leads to a good initialisation for the model instead of any random weight initialisation methods. We trained this model on our train data for 50 epochs. We limited the number of epochs to 50 as further epochs did not give any considerable improvement in the loss. We have trained the model with a learning rate of 10^{-3} for 10 iterations, then with a learning rate of 10^{-4} , we trained the model up to 30 iterations, and for the final iterations, we used a learning rate of 10^{-5} to train the model. We then used the final trained model to evaluate the test data.



Fig. 2 Evaluation using model trained on PASCAL VOC 07+12 dataset: detecting robot, scarecrow, mannequins, and statues as person



Fig. 3 Evaluation using model trained on PnPLO dataset: robot, scarecrow, mannequins, and statues are correctly detected as nonhumans

We noticed a significant improvement in the precision of person detection after training on our dataset when compared to the precisions obtained on training on datasets containing only persons. This improvement is achieved with the help of PnPLO dataset [17] that considered the objects with features resembling those of a person. Figure 2 shows the evaluation on test images of PnPLO dataset using model trained on PASCAL VOC 07+12 dataset. We can see that the model wrongly detects the person-like images as persons. Figure 3 shows evaluation on the same four images using SSD model trained on PnPLO dataset. We can see that the model is able to differentiate person from other person-like objects.

4.1 Evaluation Metric

Average precision (AP) is the evaluation metric used to compare the performances of the SSD model trained on different datasets. Following metrics are involved in the calculation of average precision.

4.1.1 Intersection Over Union (IOU)

IoU is given by the following formula—the area of overlap over the area of the union of the predicted and ground truth bounding boxes.

$$\text{IoU} = \frac{\text{area of intersection}}{\text{area of union}}$$

IoU is used to measure whether the bounding box predicted by the model is true positive (TP), false positive (FP), or false negative (FN). If the $\text{IoU} > 0.5$, we consider the predicted box to be a true positive. The bounding box is considered to be FP either if $\text{IoU} < 0.5$, or if there are duplicate boxes predicted for the same object in an image. The predicted bounding box is an FN if $\text{IoU} > 0.5$, but a wrong prediction.

4.1.2 Precision

Precision is nothing but the measure of how accurate our predictions are.

$$\text{Precision} = \frac{\text{TP}}{\text{TP} + \text{FP}}$$

4.1.3 Recall

Recall measures how well the model finds all the true positives.

$$\text{Recall} = \frac{\text{TP}}{\text{TP} + \text{FN}}$$

Once the above values are obtained, the precision-recall curve (PR curve) is plotted, as shown in Fig. 4. Average precision is calculated by taking the area under the PR curve.

Table 1 shows the improvement we achieved after training the SSD model on PnPLO dataset. We have compared the performance of the model trained on PnPLO dataset with that trained on three standard datasets, namely, PASCAL VOC 07+12 [7], COCO [8], and INRIA [11] person datasets. Average precision is the metric used to compare the performances.

On evaluating the model trained on COCO, INRIA, and PASCAL VOC, on the test set of our dataset, the average precision obtained was 53.6%, 55.3%, and 61.6%, respectively. After training on our training set, the performance significantly improved to an average precision of 79.8%. Figure 4 shows the precision-recall curve on evaluating the SSD model on our test data.

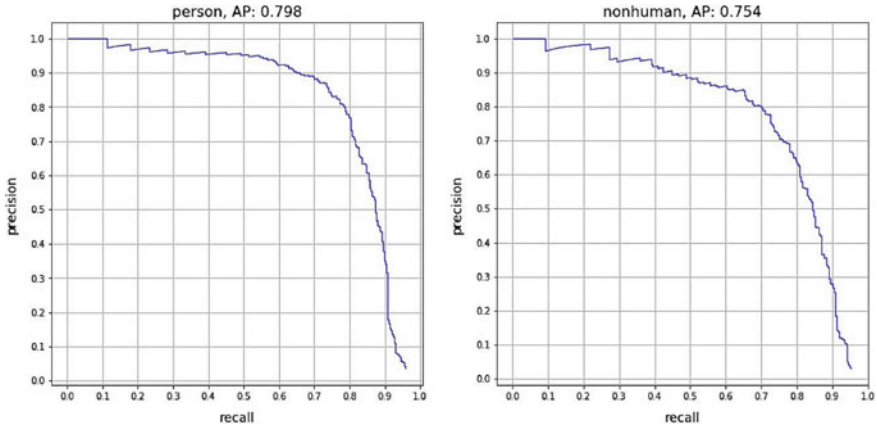


Fig. 4 Precision-recall curve for person and nonhuman on SSD model evaluation on our test data

Table 1 Comparing performance of SSD300 trained on different datasets

Dataset	Average precision (%)
COCO [8]	53.6
INRIA [11]	55.3
PASCAL VOC 07+12 [7]	61.6
PnPLO (ours) [17]	79.8

Bold represents the average precision of SSD300 model on the PnPLO dataset, which we created

5 Conclusion

Various research works are carried out focusing on detection of persons because of its widespread applications such as video surveillance, person tracking, and intelligent cars. These works use datasets comprising of only persons as benchmark dataset. Many objects have features similar to that of a person. A model trained on only persons fails to differentiate these objects from a person and person-like objects. Usage of only person datasets as a benchmark leads to many false positives, detecting person-like objects also to be persons. To overcome this problem, we prepared a person and person-like object (PnPLO) dataset consisting of persons as well as person-like objects such as statues, mannequins, scarecrows, and robots. We trained ssd_300 model on our dataset and tested on PnPLO test data. We show that the performance of the model trained on PnPLO dataset is better than performances of models trained on three standard datasets, namely, COCO, INRIA, and PASCAL VOC. The model trained on our dataset has an average precision of 79.8% compared to 53.3%, 55.6%, and 61.6% for SSD model trained on COCO, INRIA, and PASCAL VOC datasets, respectively.

References

1. Ren S, He K, Girshick R, Sun J (2017) Faster R-CNN: towards real-time object detection with region proposal networks. *IEEE Trans Pattern Anal Mach Intell* 39(6):1137–1149
2. Liu W et al (2016) SSD: Single shot multibox detector. In: Lecture notes in computer science, vol 9905. Springer, pp 21–37
3. Krizhevsky A, Sutskever I, Hinton GE (2012) ImageNet classification with deep convolutional neural networks. *Commun ACM* 56(6):84–90
4. Szegedy C et al (2015) Going deeper with convolutions. In: 2015 IEEE conference on computer vision and pattern recognition (CVPR), Boston, MA, pp 1–9
5. Simonyan K, Zisserman A (2014) Very deep convolutional networks for large-scale image recognition. [arXiv: 1409.1556](https://arxiv.org/abs/1409.1556)
6. Deng J, Dong W, Socher R, Li LJ, Li K, Fei-Fei L (2009) ImageNet: a large-scale hierarchical image database. in: CVPR
7. Everingham M, Van Gool L, Williams CKI, Winn J, Zisserman A (2010) The PASCAL visual object classes (VOC) challenge. *Int J Comput Vis* 88:303–308
8. Lin T-Y, Maire M, Belongie S, Bourdev L, Girshick R, Hays J, Perona P, Ramanan D, Zitnick CL, Dollar P (2014) Microsoft COCO: common objects in context. In: European conference on computer vision (ECCV), Zurich
9. Xiao J, Hays J, Ehinger KA, Oliva A, Torralba A (2010) SUN database: large-scale scene recognition from abbey to zoo. In: CVPR
10. Wang S, Cheng J, Liu H, Wang E, Zhou H (2018) Pedestrian detection via body part semantic and contextual information With DNN. *IEEE Trans Multimedia* 20(11):3148–3159
11. Dalal N, Triggs B (2005) Histograms of oriented gradients for human detection. In: Proceedings of the IEEE computer society conference on computer vision and pattern recognition, pp 886–893
12. Pierard S, Lejeune A, Van Droogenbroeck M (2011) A probabilistic pixel-based approach to detect humans in video streams. In: IEEE international conference on acoustics, speech and signal processing (ICASSP), pp 921–924
13. Leibe B, Seemann E, Schiele B (2005) Pedestrian detection in crowded scenes. In: IEEE computer society conference on computer vision and pattern recognition (CVPR'05), San Diego, CA, USA, vol 1, pp 878–885
14. Karthika NJ, Chandran S (2019) Recent developments in pedestrian detection using deep learning. In: 2019 International conference on computing, communication, and intelligent systems (ICCCIS), Greater Noida, India, pp 353–358
15. Dollr P, Wojek C, Schiele B, Perona P (2012) Pedestrian detection: an evaluation of the state of the art. *IEEE Trans Pattern Anal Mach Intell* 34(4):743–761
16. Geiger A, Lenz P, Urtasun R (2012) Are we ready for autonomous driving? The kitti vision benchmark suite. In: Proceedings of the IEEE conference on computer vision and pattern recognition, pp 3354–3361
17. Karthika NJ, Chandran S. PnPLO Dataset. https://drive.google.com/open?id=1_HSXrAsckZr8-LIZ9ms7LjBxzMwl-3Oa
18. He K, Zhang X, Ren S, Sun J (2016) Deep residual learning for image recognition. In: IEEE conference on computer vision and pattern recognition (CVPR), Las Vegas, NV, pp 770–778
19. Redmon J, Divvala S, Girshick R, Farhadi A (2016) You only look once: unified, real-time object detection. In: 2016 IEEE conference on computer vision and pattern recognition (CVPR), Las Vegas, NV, pp 779–788
20. Girshick R, Donahue J, Darrell T, Malik J (2014) Rich feature hierarchies for accurate object detection and semantic segmentation. In: 2014 IEEE conference on computer vision and pattern recognition, Columbus, OH, pp 580–587
21. Girshick R (2015) Fast R-CNN. In: 2015 IEEE international conference on computer vision (ICCV), Santiago, pp 1440–1448
22. Tzutalin L (2015) <https://github.com/tzutalin/labelImg>

Hybrid CR Network: An Approach Based on Interweave- and Underlay-Type CR Network



Varun Kumar, Mangal Singh, Sarat Kumar Patra, and Poonam Singh

Abstract Increased usage of mobile devices has surged demand for RF spectrum considerably. Cognitive radios (CR) hold tremendous promise for improving spectral efficiency in the wireless system. It provides a fair solution for the dynamic allocation of frequencies between the primary user (PU) and secondary user (SU). Efficient techniques for spectrum holes' estimation in available band maximize the system capacity, but in the limited band, it is tough to provide an unutilized band for SU. Since the secondary network is established where the licensed band is underutilized but if the licensed band is over-utilized, SU may still communicate if interference is lower than I_{th} to the primary user. This paper investigates the capacity of a secondary user with the variation of the power of SU in interweave and underlay network. It provides the novel solution for the performance of SU in hybrid network mode, where SU requires larger bandwidth but the availability of spectrum to the cognitive user is less.

Keywords Cognitive radio · Interweave network · Underlay network · Hybrid spectrum access · CFO

V. Kumar
Indian Institute of Information Technology, Surat, India
e-mail: varun001986@hotmail.com

M. Singh (✉)
Institute of Technology, Nirma University, Ahmedabad, India
e-mail: mangal.etce@gmail.com

S. K. Patra
Indian Institute of Information Technology, Vadodara, India
e-mail: skpatra@iiitvadodara.ac.in

P. Singh
National Institute of Technology, Rourkela, India
e-mail: psingh@nitrk.ac.in

1 Introduction

Increased usage of wireless technology has created a huge demand for high data rate in the wireless scenario. Additionally, a significant number of users in the limited available spectrum have created a scarcity in licensed band. It is expected that nearly 20 billion wireless devices will be utilized over the globe for various application by 2023 [1–3]. Demand for spectral efficiency (SE) along with energy efficiency (EE) is a major challenge in wireless research. Support for high data rate at low power has led to the wireless network densification and also increases the operational cost. From Shannon's channel capacity theorem, system throughput directly depends on SNR or transmitted power which implies that supporting high data rate in limited power is a big problem in wireless communication research. In the other side, optimal resource (time, frequency, power, space, code) allocation in multiple access scenario for uplink (UL) and downlink (DL) also be one of the emerging challenges. Cognitive radio (CR) is one of the possible areas in the field of resource allocation which utilizes the wireless resources opportunistically. CR-based network searches the underutilized license band support for high user density. CR system provides a fair solution for dynamic allocation of frequencies between the primary user (PU) and secondary user (SU) [4]. There are three type of cognitive radio network mode [5]. In the first mode called as interweave networks where spectrum, holes present in the licensed band are allocated to the SU for increasing the overall system capacity. Second mode corresponds, due to unavailability of spectrum in licensed band, the cognitive user utilizes that band in such a way that it produces interference below the threshold limit, called as underlay network. Using the same sub-carrier by the different user, interference could be nullified through intelligent signal processing which is termed as overlay mode for CR system.

1.1 Prior Research, Motivation, and Contribution

In [6], authors describe the interweave CR network with cooperative sensing, considering separate PU decoding for the closest PU receiver. The information observed by secondary base station (SBS) for all closely located SU is highly correlated in cooperative sensing environment. Hence, through soft combination, algorithm for user selection at SBS improvises the overall performance [7]. A solution for an achievable rate under an average transmit power and interference outage constraints has been derived for underlay network [8]. After spectrum sensing, a perfect decision requires based on optimal power. Deterministic and probabilistic model [9] in CR network helps to the optimal allocation of the power between PU and SU, which maximize the overall system capacity. Different literature covers the aspect of optimal power control under various regime. Mung-Chiang et al. worked on the power resource, where they discussed the optimal power allocation among user and base station (BS) through geometrical programming [10, 11] to enhance the capacity. Simultaneously

optimal power allocation among BS and user equipment (UE) solves the problem of high power requirement in uplink and downlink scenario and also maximizes the desired SNR at low power condition [12]. The adaptive deactivation of adjacent sub-carrier provides flexible guard bands between PU and SU and causes mutual interference cancellation in OFDM-based CR system [13].

Above literature mainly covers (1) spectrum sensing, (2) OFDM-based CR network, (3) different optimal power control regime, and (4) different modes (interweave, underlay) for CR system. This paper integrates these various aspects and presents a comprehensive solution for hybrid spectrum access for SU, considering interweave and underlay scenario. Chu et al. have described the hybrid spectrum access in cooperative cognitive network [14] but our work is based on OFDM-enabled single base station (BS) supporting multiple users-based CR system. Interweave and underlay are the two separate aspects for utilizing the frequency resource. Interweave mode requires full spectrum slot, and a lot of work were based on the sensing and allocation of sub-carrier to the cognitive user in this mode. Like interweave, sensing and sub-carrier allocation for underlay mode have also been addressed in the above literature. No paper address these two modes jointly for performance analysis of cognitive user. The numerical result validates the scenario under different real-time constraints with suitable assumption. Performance analysis in interweave, underlay, and hybrid mode has been carried out by an adaptive number of sub-carrier allocation to the SU. This paper investigates the capacity performance enhancement in cognitive radio through hybrid network approach which includes the benefits of interweave and underlay mode.

In summary, major contributions of this paper can be stated as follows:

- Based on spectrum sensing and average information about the interference of PU, we maximize the overall throughput for cognitive user.
- On the basis of two decision threshold, hybrid spectrum access has been implemented. It depends on the channel condition of licensed sub-carrier in OFDMA-based user access mechanism.
- Some other effects like carrier frequency offset which degrade the performance of PU as well as SU have been jointly analyzed.

This paper has been organized as follows, where Sect. 2 covers the related work about conventional CR mode like interweave and underlay. Section 3 describes the system model for proposed method along with classical one. Numerical results have been analyzed in Sect. 4 carried out by the conclusion in Sect. 5.

2 Related Work Based on Interweave and Underlay Toward Achievable Rate

Based on the intuition framed for interweave and underlay mode [5], its extension for cognitive network in OFDM system [15] gives the background of this research.

So OFDM-based interweave and underlay performance analysis has been discussed through two cases.

Case 1: Performance of SU in Interweave Network Generalized frequency response of received wireless signal for OFDM-based system can be expressed as

$$Y_{m,n}(f) = H_{m,n}(f)X_{m,n}(f) + W_{m,n} \quad (1)$$

where $Y_{m,n}(f)$, $H_{m,n}(f)$, $X_{m,n}(f)$, $W_{m,n}$ are the received signal frequency response, transfer function of wireless channel, transmitted symbol, and additive white Gaussian noise of n_{th} sub-carrier for m_{th} time domain sampling index, respectively. Transmitted symbol of n_{th} sub-carrier for m_{th} time domain sampling index can be expressed as

$$X_{m,n}(f) = |X_{m,n}(f)|e^{\frac{j2\pi mn}{N}} \quad (2)$$

where N is the total number of sub-carrier.

In interweave network, PU does not influence the SU. It is mainly affected due to system noise and carrier frequency offset (loss of orthogonality between consecutive sub-carrier). The received power of n_{th} sub-carrier can be expressed as

$$P_{(n)} = \int_{-\tilde{B}_k/2}^{B_k/2} \rho_0(n) \left(\frac{\sin(\pi(f - \frac{n}{T_s})T_s)}{(\pi(f - \frac{n}{T_s})T_s)} \right)^2 df \quad (3)$$

where $P_{(n)}$, $\rho_0(n)$, $T_s = \frac{1}{\Delta f}$, B_k are the power allocation of n_{th} sub-carrier, peak power spectral density of n_{th} sub-carrier, symbol duration, and allocated bandwidth, respectively. At constant bandwidth, if power level of user terminal increases then the power spectral density (PSD) also increases. PSD should not exceed from the maximum limit in such a scenario. In the practical scenario, the upper bound capacity obtained by Jensen's inequality gives the maximum achievable observed capacity. The maximum achievable observed capacity of any random SU in interweave scenario without (CFO) can be expressed as [16].

$$C_{k_s} = \log_2 \left(1 + \frac{\alpha k_{s,n}}{N_{fk_s} - N_{sk_s}} \sum_{n=N_{sk_s}}^{N_{fk_s}} \frac{P_{k_{s,n}} |h_{k_{s,n}}|^2}{\sigma_n^2} \right)$$

$$\alpha k_{s,n} = 1 \forall N_{sk_s} \leq n \leq N_{fk_s}$$

$$\alpha k_{s,n} = 0 \text{ elsewhere} \quad (4)$$

where C_{k_s} is the expected capacity of any k_s^{th} cognitive user. N_{sk_s} and N_{fk_s} are the starting and last sub-carrier number allotted to respective user. It is also expected that all these sub-carriers have not been allocated to any PU or other secondary user. N , B , σ_n^2 are total number of available sub-carriers, total system bandwidth, and noise

variance in license band, respectively. $h_{k_s,n}$ is the channel gain of n^{th} sub-carrier for k_s^{th} SU also $h_{k_s,n} = g_{k_s,n}\sqrt{\beta_{k_s}}$ where $g_{k_s,n}$ and β_{k_s} are the fast fading and slow-fading coefficient and $E\left[\left|g_{k_s,n}\right|^2\right] = 1$. In interweave network, there is no inter-user interference, but the performance of cognitive user is suppressed by only through system noise and CFO.

CFO in SU Sub-carrier

Inter-carrier interference arises mainly due to incorrect (CFO). It occurs due to improper sampling. When l^{th} sub-carrier suffers with CFO ε , then the received l^{th} sub-carrier can be expressed as

$$Y_l = \frac{1}{N} \sum_n \sum_{K=-N/2}^{N/2} X_K H_K e^{-j2\pi(k-l+\varepsilon)n/N} \quad (5)$$

The closed-form equation for observed *SINR* of SU can be expressed as

$$\gamma_1 = \frac{P_{k_s,n} |h_{k_s,n}|^2 \left(\frac{\sin(\pi\varepsilon)}{(\pi\varepsilon)}\right)^2}{0.822 P_{k_s,n} |h_{k_s,n}|^2 \sin(\pi\varepsilon)^2 + \sigma_n^2} \quad (6)$$

Case 2: Performance of SU for underlay network When spectrum holes are unavailable in the licensed band, SU utilizes the licensed band in such a way that power level of SU could not exceed the threshold limit. Adaptive power controlling mechanism can limit excess power transmission from the secondary base station (SBS). Mathematically, the power distribution through the SBS for SU can be expressed as

$$P_{k_s,n} = \min\{I_{\text{th}}, P_{\text{sbs}}\} \quad (7)$$

where $P_{k_s,n}$, I_{th} , P_{sbs} are the optimal power for k_s^{th} SU, interference threshold to PU and transmitted power through SBS respectively. Since in underlay scenario PU is the strong interferer to the secondary, observed achievable capacity in such a scenario can be expressed as

$$C_{k_s} = \log_2 \left(1 + \frac{\frac{1}{N_{fk_s} - N_{sk_s}} \sum_{n=N_{sk_s}}^{N_{fk_s}} P_{k_s,n} |h_{k_s,n}|^2}{\frac{1}{N_{fk_s} - N_{sk_s}} \sum_{n=N_{sk_s}}^{N_{fk_s}} P_{j_p,n} |h_{j_p,n}|^2 + \sigma_n^2} \right) \quad (8)$$

where $P_{j_p,n}$ is the power of j^{th} PU, whose few sub-carrier starting from $n = N_{sk_s}$ to $n = N_{fk_s}$ has been allotted to a random SU where $P_{j_p,n|N_{sk_s} \dots N_{fk_s}} > P_{k_s,n|N_{sk_s} \dots N_{fk_s}}$ and power level of SU should not cross the interference threshold limit. In worst case, scenario achievable capacity in underlay network is jointly influenced by interference and CFO.

When SU and PU suffer with CFO

Under such scenario, the SU performance significantly degrade and observed SINR can be expressed as

$$\gamma_1 = \frac{P_{k_{s,n}} |h_{k_s}|^2 \left(\frac{\sin(\pi\varepsilon)}{(\pi\varepsilon)} \right)^2}{0.822 P_{k_s} |h_{k_s}|^2 \sin(\pi\varepsilon)^2 + P |h_{j_p}|^2 + \sigma_n^2} \quad (9)$$

If CFO arises in PU band then observed SINR can be expressed as

$$\gamma_2 = \frac{P_s |h_s|^2 \left(1 + \frac{0.822 P_p (\sin(\pi\varepsilon))^2}{\sigma_n^2} \right)}{\sigma_n^2 + 0.822 P_p |h_p|^2 (\sin(\pi\varepsilon))^2 + P_p |h_p|^2 \left(\frac{\sin(\pi\varepsilon)}{(\pi\varepsilon)} \right)^2} \quad (10)$$

3 Hybrid Network

Composite network comprises the coexistence of the primary and secondary network in a certain geographical bound. Primary network consists primary base station (PBS) and PU, whereas secondary network is framed by SBS or SU. Here, system model includes the following constraints.

1. Bandwidth allocation for SU should not be greater than B_s Hz for preventing the unauthorized access of large spectrum from the security point of view.
2. Primary users (PU) are assumed to be not very far from the SBS as well as secondary users (SU) such that false alarming issues did not come into the picture.
3. Among the SU, there are no spatial correlation.
4. Expected power level across allocated sub-carriers to the PU remain same.

Hybrid spectrum allocation for SU based on interweave/underlay scenario has been categorized into three steps.

1. Spectrum sensing
2. Decision based on activation threshold
3. Performance analysis for PU and SU.

3.1 Spectrum Sensing Across SBS

In this section, we consider that M_p number of PUs are active in the particular geographical bound and PBS/SBS both receive the signals. PBS remains unaffected, but SBS acquires the information from the PU. During sensing, no uplink and down-link data transmission occur by secondary network till sensing time slot. Only SBS

receives the signal and SU remains inactive during sensing. Within sensing time interval, N_{sub} number of data samples are acquired by SBS. Received data sample is passed through the FFT block across the SBS. For such a system $N_{\text{sub}} > N$ and $\Delta f = B/N$, where Δf is the sub-carrier bandwidth. Two scenarios may be considered for the received signal

$$y_1(t) = \begin{cases} n_1(t) & A_0 \\ s_l(t) + n_l(t) & A_1 \\ \forall & 0 < t < \frac{N_{\text{sub}}}{B} \end{cases} \quad (11)$$

From above equation, $y_l(t)$ is a normal distributed random variable (RV) with mean 0 for hypotheses A_0 implies the absence of PU, whereas for hypotheses A_1 , replicate the presence of PU; the received symbol $y_l(t)$ is a normal distributed RV with mean μ_s . The received power across the SBS can be modeled as

$$P_y(j) = \sum_{i=1}^{M_p} |y_{ij}|^2 = \sum_{i=1}^{M_p} |s_{ij}|^2 + |n_j|^2 \quad (12)$$

where $|s_{ij}|^2$ is the signal power of i^{th} user for j^{th} sample. From above equation, if $i = 0$ (All primary users are inactive), $s_{ij} = 0$; only noise power is considered to be received power. Statistical analysis gives an idea about the power level of different PU whose signals are received across the SBS.

4 Numerical Results

In this section, analytical results have been numerically verified. In multiple access scenario, we have chosen the OFDM-based frequency resource allocation for different users. These users may be PU or SU. We also consider the availability of perfect channel state information CSI between PBS to PU and SBS to SU. Cognitive users also know CSI between itself and PBS/PU. The expected channel variance across each sub-carrier either for SU has been taken unity, i.e., $E[|h_{k_{s,n}}|^2] = 1$. In three different scenarios, SU performance variation has been observed due to nearest reference PU. In LTE-TDD standard, to access multiple users, minimum one resource block (RB) is transferred to any user, where one RB is 0.5 ms and 180 kHz wide in time-frequency frame. One-time slot carries 7 OFDM symbol. In normal cyclic prefix condition, 12 sub-carriers are carried by one resource block. So sub-carrier spacing f is equal to 15 kHz. Total number of available sub-carrier, i.e., $N = 512$. For simplicity, let $B_p = 1.5$ MHz bandwidth has been allocated to the PU and the maximum permissible bandwidth for SU is $B_s = 300$ kHz. In such a wireless network, 5 PU are active and for each PU 100, sub-carriers are allocated. In this

assumption, maximum permissible sub-carrier for SU is 20. As per OFDM-based system constraints, the minimum BW allocation to the cognitive user is 180 kHz and maximum allocated bandwidth is 300 kHz for preventing the unauthorized access of larger licensed band. According to dynamic allocation of the frequency band, the wireless network may allocate the band to SU in three different modes termed as interweave, underlay, and hybrid mode. Figure 1 shows the capacity performance in offset scenario. Under such condition, three modes have shown. In interweave mode, one sub-carrier suffers from 10% CFO due to incorrect sampling, so the achievable rate degrades. In underlay scenario, two cases have been taken. In the first case, 10% CFO arises in one sub-carrier and at same sub-carrier PU acts as an interferer, while in the second case, PU sub-carrier suffers with 10% CFO. Under no CFO and PU as an interfering agent, the performance degradation in such scenario has been shown in Fig. 1. Since power control mechanism in underlay is applied in such a way that SBS did not transmit power more than I_{th} irrespective of maximum power transmit limit by SBS, power constraints from (9) and taking 5 dB as (I_{th}) all curve remain to go to the saturation in underlay scenario. In proposed hybrid spectrum access methodology, 10% CFO has been considered for those sub-carrier which utilizes the PU band and same amount of CFO in the unused band. If all signals are perfectly sampled, then the achievable rate for three modes can be observed from Fig. 2. In the joint scenario, two decision thresholds γ_l and γ_{avg} are used for correct justification about the interweave and underlay band. Here, γ_l and γ_{avg} have been taken 0 dB and 10 dB, respectively, for PU. Out of 500 allocated sub-carrier of PU, best 8 sub-carriers are selected from the PU band. As per assumption, 12 sub-carriers are unused and free from inter-user interference. Eight sub-carriers of PU band having $\gamma_l > \gamma_{avg}$ are aggregated with twelve unused sub-carriers, which fulfill the BW greed for SU. Based on proportionality average, SNR for hybrid spectrum access methodology is formulated. In such a

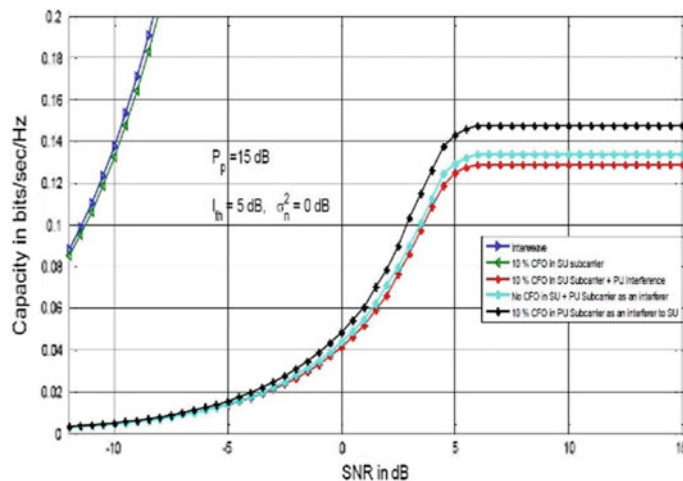


Fig. 1 Observed capacity of cognitive user in offset scenario

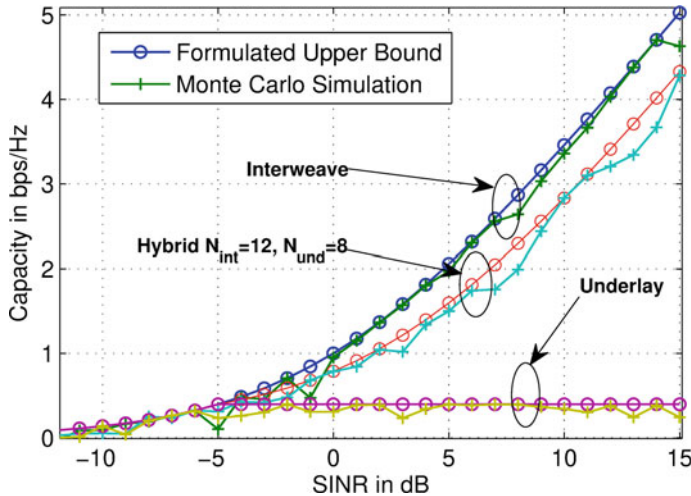


Fig. 2 Capacity in three modes of CR system

condition, I_{agg} be the transmit power and 5 dB is taken for numerical simulation. The analytical curve for the upper bound of a closed-form solution to average achievable rate is obtained from (5), (10) and (13), which are tightly matched to the exact Monte Carlo simulation. Depending on sub-carrier availability in interweave and underlay mode, Fig. 3 depicts the achievable rate performance under different proportionality. In this figure, only upper bound close form expression has been used. Due to increase in the number of unused sub-carrier, the capacity increases with greater extent. Neglecting the impact on statistics for frequency selective at channel, it is

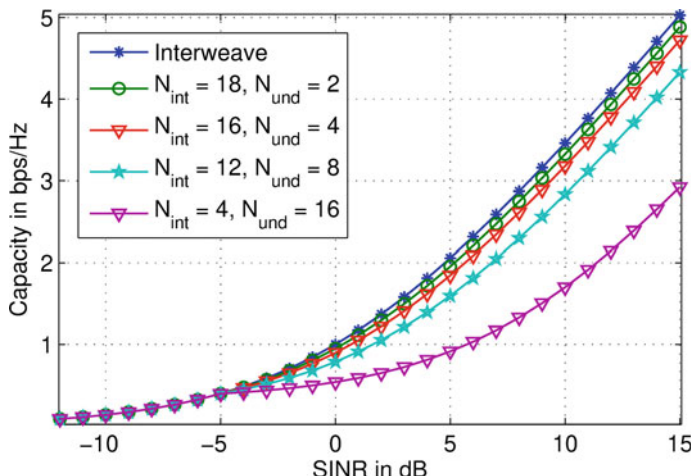


Fig. 3 Capacity in mixed networks for different value of N_{und} and N_{int}

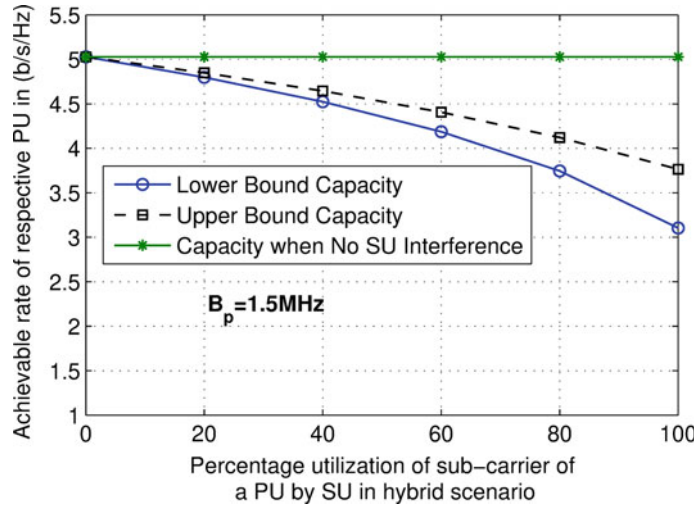


Fig. 4 Achievable rate of PU vs percentage utilization of sub-carrier in hybrid spectrum access methodology where $D_{\text{th}}=1.25$ dB and $I_{\text{th}}=5$ dB

assumed that all selective channels for PU have unit variance $E\left[\left|h_{(j_p,n)}\right|^2\right] = 1$ for PU.

$$\text{Selective Channel} = \frac{B_p}{B_c} = \frac{N_P \Delta f}{B_c} \quad (13)$$

Figure 4 shows the impact of SU on PU. Multiple cognitive users degrade the performance of PU in the nonlinear fashion. For numerical computation, detection and interference threshold have been taken 1.25 and 5 dB, respectively, in underlay scenario. Since 1.5 MHz and 300 kHz bandwidth have been assigned to PU and SU, in this practice, the permissible cognitive users are five where all SU consume maximum bandwidth. Figure 5 depicts two independent scenarios. In the first, when the cognitive user receives power level up to detection threshold than such situation causes less interference to the PU gets upper bound capacity. In the second scenario, when the cognitive user receives the power level up to I_{th} , the PU suffers from more interference and lower bound capacity can be observed if $P_{\text{SU}}=I_{\text{th}}$.

5 Conclusion

In this paper, a detailed analysis has been carried out for SU capacity performance in different CR network mode. In the case of limited BW availability, hybrid spectrum access mode gives moderate solution among another mode like, interweave and underlay. For maintaining fairness among multiple SU, hybrid spectrum access

methodology is more helpful in comparison to interweave and underlay scenario. This technique improvises the cognitive user density providing fairness at the cost of hardware complexity. This paper analyzes the OFDM-based three-mode performance comparison for a single cognitive user. Multiple users' achievable rate performance and their fairness can be an extension of this paper.

References

1. Gohil A, Modi H, Patel SK (2013) 5G technology of mobile communication: a survey'. In: 2013 IEEE international conference on intelligent systems and signal processing (ISSP), pp 288–292
2. Liu Y, Zhang Y, Yu R, Xie S (2015) Integrated energy and spectrum harvesting for 5G wireless communications'. IEEE Netw 29(3):75–81
3. Wu J, Rangan S, Zhang H (2012) Green communications: theoretical fundamentals, algorithms and applications. CRC Press
4. Liang YC, Chen K-C, Li GY, Mahonen P (2011) Cognitive radio networking and communications: an overview. IEEE Trans Veh Technol 60(7):338–340
5. Goldsmith A, Jafar SA, Maric I, Srinivasa S (2009) Breaking spectrum gridlock with cognitive radios: an information theoretic perspective. Proc IEEE 97(5):894–914 (2009)
6. Kusaladharma S, Tellambura C (2015) Interweave cognitive networks with co-operative sensing. In: 2015 IEEE global communications conference (GLOBECOM). IEEE, p 16
7. Bhatti DMS, Nam H (2017) Spatial correlation based analysis of soft combination and user selection algorithm for cooperative spectrum sensing. IET Commun 11(1):3944
8. Sboui L, Rezki Z, Alouini M-S (2013) A unified framework for the ergodic capacity of spectrum sharing cognitive radio systems. IEEE Trans Wirel Commun 12(2):877–887
9. Mallick S, Devarajan R, Rashid MM, Bhargava VK (2012) Robust power allocation designs for cognitive radio networks with cooperative relays. In: 2012 IEEE international conference on communications (ICC). IEEE, pp 167–168
10. Chiang M, Tan CW, Palomar DP, Neill DO, Julian D (2007) Power control by geometric programming. IEEE Trans Wirel Commun 6(7):26402651
11. Boyd S, Kim S-J, Vandenberghe L, Hassibi A (2007) A tutorial on geometric programming. Optim Eng 8(1):671–674
12. Bansal G, Hossain MJ, Bhargava V (2008) Optimal and suboptimal power allocation schemes for OFDM based cognitive radio systems. IEEE Trans Wirel Commun 7(11):4710–4718
13. Weiss T, Hillenbrand J, Krohn A, Jondral FK (2004) Mutual interference in OFDM-based spectrum pooling systems. In: IEEE 59th vehicular technology conference, 2004. VTC 2004-Spring, vol 4. IEEE, pp 1873–1877
14. Chu TMC, Phan H, Zepernick H-J (2014) Hybrid interweave-underlay spectrum access for cognitive cooperative radio networks. IEEE Trans Commun 62(7):21832197
15. Zhang Y, Leung C (2009) Resource allocation in an OFDM based cognitive radio system. In: IEEE Trans Commun 57(7)
16. Shen Z, Andrews JG, Evans BL (2005) Adaptive resource allocation in multiuser OFDM systems with proportional rate constraints. IEEE Trans Wirel Commun 4(6):2726–2737

Intensive Study on Compact Integrated Optic Couplers Using Grating Geometry



Bidyut Deka, Aradhana Dutta, and Partha Pratim Sahu

Abstract In the paper, tooth structured grating-assisted (GA) configuration for 2×2 compact directional coupler (DC), two-mode interference (TMI) coupler and multimode interference (MMI) coupler have reported for an intensive study using a sinusoidal mode simple effective index method (SM-SEIM) centric mathematical model. It is found that beat length of GA-TMI coupler is $\sim 22.3 \mu\text{m}$ which is almost 50% compact in size with comparison to the conventional TMI coupler and is $\sim 25\%$ that for conventional directional coupler. The power imbalance with grating-assisted structures increases as that of fabrication tolerances which are slightly higher compared to conventional TMI coupler.

Keywords Integrated optics · Planar waveguide · Grating · Simple effective index method · Directional coupler · Grating coupler

1 Introduction

The compact planar waveguide-based optical device and its components have become obligatory for implementation of large-scale integration in photonic integrated device (PID) [1–6] for accomplish of increasing bandwidth requirements in contemporary high speed communication. As the fundamental components of integrated circuit, such as optical couplers (DC/TMI/MMI) and switches with smaller in size have been growing interests due to the compactness and simple fabrication process. The

B. Deka (✉)

Department of Physics, Girijananda Chowdhury Institute of Management and Technology (GIMT)-Tezpur, Dekargaon, Sonitpur 784501, Assam, India
e-mail: deka.biduyt@gmail.com

A. Dutta

Department of Physics, Kaliabor College, Kuwarital, Nagaon 782137, Assam, India
e-mail: duttaaradhana@gmail.com

P. P. Sahu

Department of Electronics and Communication Engineering, Tezpur University, Sonitpur 784028, Assam, India
e-mail: pps@tezu.ernet.in

grating-assisted geometry has appeared highly promising and is thus introduced in the integrated optical couplers for further compactness that are very much obligatory for large-scale-integration of PID. Polarization sensitiveness along with higher fabrication tolerances gives additional advantage. The previous works [7–9] have discussed the coupling characteristics with a few detail study such as polarization sensitiveness and fabrication tolerances based on finite difference time domain (FDTD) method for the tooth structure grating-assisted TMI coupler.

In this paper, a detail intensive analysis of compact directional coupler (DC), two-mode interference (TMI) coupler and multimode interference (MMI) coupler with tooth structured grating geometry have been carried out using a sinusoidal mode centric simple effective index method (SM-SEIM) [2, 10–13] based mathematical model for accurate analysis of modal coupled power. Dependence of beat length on coupling separation gap between access waveguides with a fixed value of S bending loss for tooth structured grating-assisted directional coupler (GA-DC), grating-assisted two-mode interference (GA-TMI) coupler and grating-assisted multimode interference (GA-MMI) coupler are shown. Coupling behavior for DC, TMI and MMI couplers with tooth structured grating geometry have discussed and then compared with conventional structures.

2 Grating-Assisted Structure and the Principle

Figure 1 shows three-dimensional (3D) schematic view of 2×2 tooth structured grating-assisted directional coupler (GA-DC) having tooth-shaped grating-assisted coupling region with dimensions (length $\sim L$, coupling separation gap $\sim h$ between

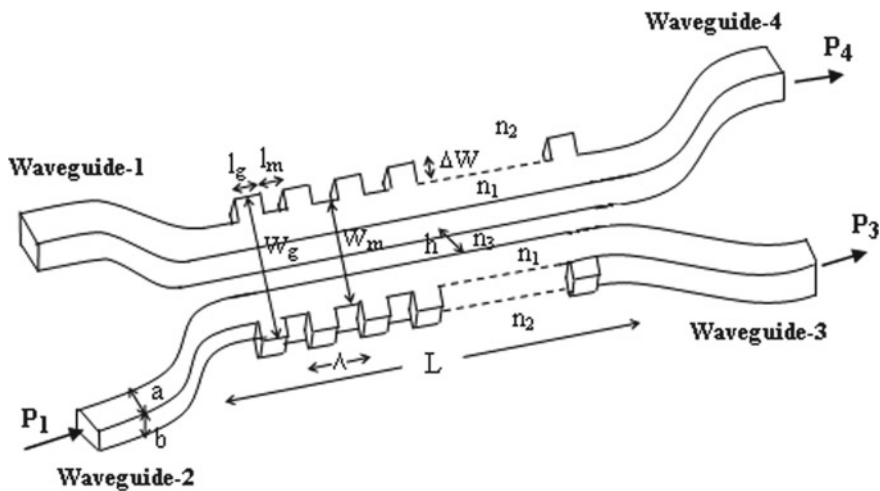


Fig. 1 Schematic 3D view of 2×2 directional coupler with tooth structured grating geometry

the two-channel waveguides), one pair of input single mode access waveguides (Waveguide-1 and Waveguide-2) of core size (width $\sim a$, thickness $\sim b$) and another pair of single mode output access waveguides (Waveguide-3 and Waveguide-4) of similar dimensions, respectively. The coupling region with tooth structured grating geometry is consisting of two-channel waveguides incorporated with tooth structured grating placed close to each other. In the coupling region, the guiding layer of width W_m ($\sim 2a + h$) and grating layer of width W_g ($\sim W_m + 2\Delta W$) are placed alternatively where ΔW is the width of grating teeth. In this study, rectangular tooth structured grating is used for higher compactness and simplification of implementation. The grating structured coupling section is consisting of N total number of grating period, $\Lambda = l_m + l_g$; where l_m denotes the guiding layer's length of width ($S = m$) and l_g gives grating layer's length of width ($S = g$), respectively. Refractive index of core layer and cladding layer are n_1 and n_2 respectively, whereas n_3 is refractive index of coupling gap cladding section. For input power $\sim P_1$ launched at input lower most access Waveguide-2, the respective output optical powers obtained through the Waveguide-3 (as bar state) $\sim P_3$ and Waveguide-4 (as cross state) $\sim P_4$.

Once the mode field with propagation constant $\beta_i(\lambda)$ is launched as input signal through single mode input access Waveguide-2, inside the tooth structured grating-assisted coupling region modes are excited. In coupling section, based on comparative phase difference among the excited modes, light powers are coupled at end of the section through the output single mode access waveguides (Waveguide-3 and Waveguide-4). As fundamental and first-order mode are carrying most of optical power, the beat length which defines the coupling length required for a phase shift $\sim \pi$; of optical coupler with N total number of grating period ($\sim \Lambda$) is found as,

$$L_\pi = [(N + 1)l_m + Nl_g] = \frac{\pi}{[(\beta_{00}^m - \beta_{01}^m) + (\beta_{00}^g - \beta_{01}^g)]} \quad (1)$$

where β_{00}^S and β_{01}^S denote propagation constant for the fundamental and first-order modes irrespective to guiding layer ($S \sim m$) and grating layer ($S \sim g$), respectively. As ($S \sim m, \sim g$), the width, $W_m = W_g$ and Eq. (1) signifies coupling length for conventional structures.

For high-index contrast waveguide, mode field penetration in lateral outside direction of waveguide is negligibly small where input modal field profile of the i th mode, $H_i(x)$ for tooth structured grating-assisted coupling section can be approximated as,

$$H_i(x) = \sin \left[(i + 1) \frac{\pi x}{W_g} \right] \quad (2)$$

Thus, the optical powers at end of tooth structured grating-assisted coupling region are either coupled toward output access waveguides or diminishes out at end of grating structured channel waveguide. Since all guided modes traveling through the grating structured coupling section will contribute to mode field of output access waveguides, thus, mode fields in M th access waveguide can be express as

$$\begin{aligned}
H_M^S(x, L) &= \sum_{\substack{i=0 \\ S=m,g}}^1 H_{M,i}^S(x, L) \\
&= \sum_{\substack{i=0 \\ S=m,g}}^1 c_{M,i} H_i(x) \exp[j(\beta_0^S - \beta_i^S)L]
\end{aligned} \tag{3}$$

where $L = [(N + 1)l_m + Nl_g]$ and $c_{M,i} \approx \sqrt{C_{M,i}^S}$ are contribution coefficient of i th mode at M th access waveguide, estimated using sinusoidal mode centric simple effective index method (SM-SEIM) [10–12] based numerical model as,

$$\begin{aligned}
\frac{C_{M,i}^S}{C_0} &= \frac{\pi^2}{16b^2k^2(n_1^2 - n_2^2)} \\
&\quad \exp\left\{-hk(n_{\text{eff}}^2 - n_2^2)^{1/2}\right\} \left[\exp\left\{bk(n_1^2 - n_2^2)^{1/2}\right\} - \exp\left\{-bk(n_1^2 - n_2^2)^{1/2}\right\} \right] \\
&\quad + \frac{\pi^2}{16b^2k^2(n_1^2 - n_3^2)} \\
&\quad \exp\left\{-hk(n_1^2 - n_3^2)^{1/2}\right\} \left[\exp\left\{bk(n_1^2 - n_3^2)^{1/2}\right\} - \exp\left\{-bk(n_1^2 - n_3^2)^{1/2}\right\} \right]
\end{aligned} \tag{4}$$

where for TE mode,

$$C_0 = \frac{0.4}{F_C} \times \frac{\left(n_1^2 - n_{\text{eff(TE),}S}^2\right)\sqrt{n_{\text{eff(TE),}S}^2 - n_2^2}}{n_{\text{eff(TE),}S}(n_1^2 - n_3^2) \left[W_S + \frac{2}{k_0\sqrt{n_{\text{eff(TE),}S}^2 - n_2^2}} \right]} \tag{5}$$

$$F_c = \frac{3(1 + 0.2h)}{\{13.5 + 185(\beta_0^S - \beta_i^S)\} h} \tag{6}$$

$$n_{\text{eff(TE),}S} = \beta_{\text{TE}(i)}^S \left(\frac{\lambda}{2\pi} \right); \quad S = m, g \tag{7}$$

The normalized output coupling power at M th access waveguide of tooth structured grating-assisted directional coupler (GA-DC) can be written as,

$$\frac{P_{M,i}(x, L)}{P_{1,i}(x, 0)} = \frac{\left| \sum_{\substack{i=0 \\ S=m,g}}^1 H_{M,i}^S(x, L) \right|^2}{\left| \sum_{\substack{i=0 \\ S=m,g}}^1 H_{1,i}^S(x, 0) \right|^2} \tag{8}$$

$$\begin{aligned}
& \approx \sum_{\substack{i=0 \\ S=m,g}}^1 C_{M,i}^S H_i^2(x) \\
& + \sum_{\substack{i=0 \\ S=m,g}}^1 \sum_{\substack{j=1+i \\ S=m,g}}^1 \left[2\sqrt{C_{M,i}^S C_{M,j}^S} H_i(x) H_j(x) \right. \\
& \quad \left. \times \cos \left\{ \sum_{\substack{i=0, j=i+1 \\ S=m,g}}^1 [(N + q_S)(\beta_i^S - \beta_j^S)] l_S \right\} \right] \quad (8)
\end{aligned}$$

where $P_M^i = |H_{M,i}^S(x, L)|^2$ and $i, j = 0, 1$ denotes even mode and odd mode such that $j > i$, $q_S = 0, 1$ refers to grating layer ($S \sim m$) and guided layer ($S \sim g$), respectively, total number of grating period $\sim N$ and $C_{M,i}^S$, $C_{M,j}^S$ are the contribution coefficients for i th, j th modes that signifies the field contribution into output access waveguides which can estimated from Eqs. (4), β_i , β_j = propagation constants for i th and j th mode that are calculated using dispersive equations [2]. The guiding width length $\sim l_m$ and grating width length $\sim l_g$ are determined by using the following relation (9) [8, 9],

$$l_S = \frac{\lambda}{4n_{\text{eff}(j,S)}}; \quad S = m, g \quad (9)$$

2.1 Result and Discussion

Figure 2 shows schematic layout of three-dimensional (3D) tooth structured 2×2 grating-assisted directional coupler (GA-DC) along with the beam propagation results at the bar coupling (P_3/P_1) state and cross-coupling (P_4/P_1) state with $W_m = 3.0 \mu\text{m}$, $h = 0.5 \mu\text{m}$, $\Delta W = 0.25 \mu\text{m}$, $\Delta n = 5\%$, $a = 1.5 \mu\text{m}$, $b = 1.5 \mu\text{m}$, $\lambda \sim 1.55 \mu\text{m}$ obtained by using optiBPM software. It is also show light wave propagation on half coupling (3-dB) state of GA-DC coupler and cross-coupling point obtained by optiBPM software that is based on finite difference time domain (FDTD) method [6, 12]. From the study found that the cross-coupling point is obtained at coupling length of $45.1 \mu\text{m}$ which is almost close to that obtained by SEIM based on sinusoidal modes.

The schematic 3D layout of 2×2 tooth structured grating-assisted two-mode interference (GA-TMI) coupler is shown in Fig. 3 along with the beam propagation results at bar coupling (P_3/P_1) point and cross-coupling (P_4/P_1) point found by using optiBPM software for $W_m = 3.0 \mu\text{m}$, $h = 0 \mu\text{m}$, $a = 1.5 \mu\text{m}$, $b = 1.5 \mu\text{m}$, $\Delta W =$

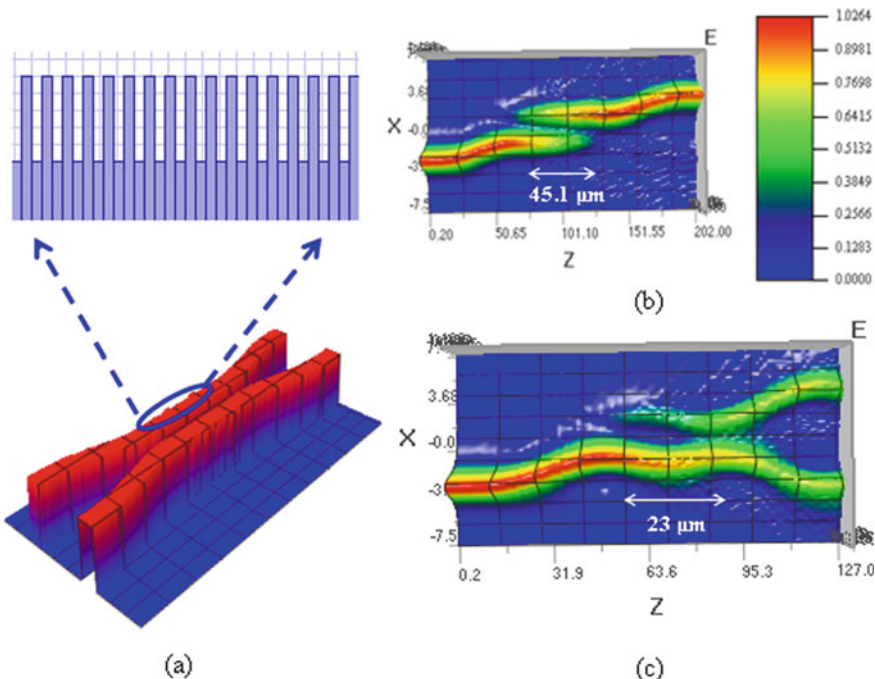


Fig. 2 Tooth structured 2×2 grating-assisted directional coupler (GA-DC) along with (a) 3D schematic layout and BPM simulation results for (b) cross-state of beat length $\sim 45.1 \mu\text{m}$ and (c) 3-dB coupler of beat length $\sim 23 \mu\text{m}$

$0.25 \mu\text{m}$, $\Delta n = 5\%$, $\lambda \sim 1.55 \mu\text{m}$, respectively. It is found that cross-coupling beat length $\sim 22.3 \mu\text{m}$ which is equivalent to the result obtained by SM-SEIM.

Figure 4 shows 3D device layout of the tooth structured 2×2 grating-assisted multimode interference (GA-MMI) coupler along with beam propagation simulation results estimated using optiBPM software at the bar coupling (P_3/P_1) state and cross-coupling (P_4/P_1) state with $W_m = 7.0 \mu\text{m}$, $\Delta n = 5\%$, $\Delta W = 0.25 \mu\text{m}$, $h = 4 \mu\text{m}$, $a = 1.5 \mu\text{m}$, $b = 1.5 \mu\text{m}$, $\lambda \sim 1.55 \mu\text{m}$. The coupling length of GA-MMI coupler obtained as $\sim 40.1 \mu\text{m}$ and 3-dB coupler of beat length $\sim 20.2 \mu\text{m}$, respectively. Further, a comparative analysis for beat length (L_π) versus Δn (%) for tooth structured GA-MMI, GA-DC and GA-TMI couplers with teeth height $\Delta W \sim 0.25 \mu\text{m}$ and that of conventional couplers (structures with $\Delta W \sim 0 \mu\text{m}$) is shown in the plot Fig. 5. The figure signifies that as Δn increases, the beat length reduces. This is obtained that GA-TMI coupler has the lesser beat length compared to other types of couplers.

In Fig. 6, the relative study of normalized bar and cross-states coupling powers distribution has shown with respect to grating numbers ($\sim N$) which can be estimated using Eqs. (1)–(9) for tooth structured grating-assisted two-mode interference (GA-TMI) coupler of coupling separation gap, $h \sim 0.0 \mu\text{m}$, directional coupler (GA-DC) for $h \sim 0.5 \mu\text{m}$ and multimode interference (GA-MMI) coupler for $h \sim 4.0 \mu\text{m}$ with

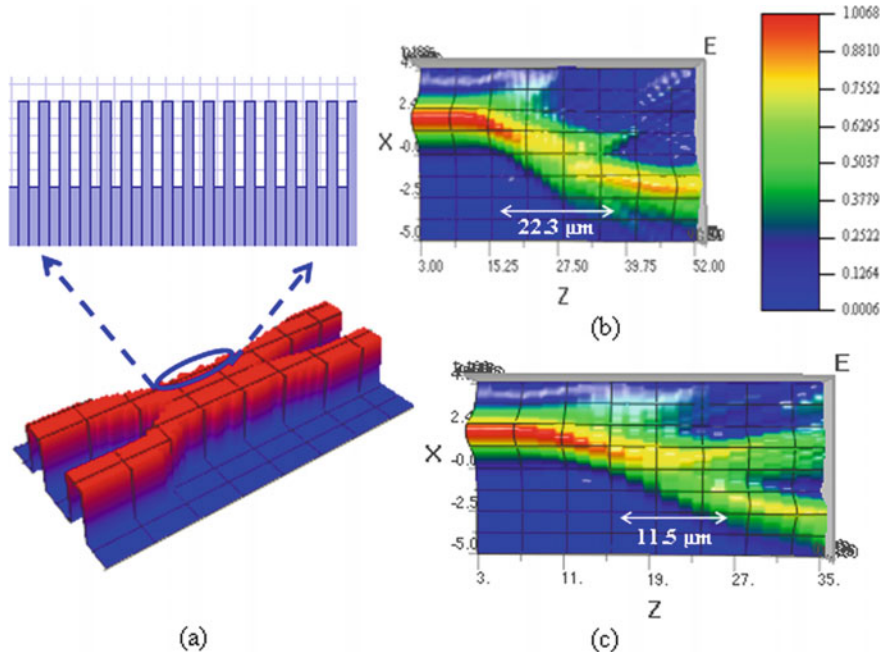


Fig. 3 Tooth structured 2×2 grating-assisted TMI (GA-TMI) coupler along with (a) 3D schematic layout and BPM simulation results for (b) cross-coupling state of beat length $\sim 22.3 \mu\text{m}$ and (c) 3-dB coupler of beat length $\sim 11.5 \mu\text{m}$

$\Delta n = 5\%$, cladding index ~ 1.45 , $a = b = 1.5 \mu\text{m}$, $\Delta W \sim 0.25 \mu\text{m}$, $l_m = l_g = 0.27 \mu\text{m}$ and wavelength (λ) $\sim 1.55 \mu\text{m}$, respectively. From Fig. 7, it is observed that the peak cross-state coupling power (P_4/P_1) is found at beat lengths corresponding to the values of $N \sim 41, 70$, and 85 with respect to the tooth-shaped GA-TMI, GA-MMI and GA-DC, respectively. Thus, the beat lengths for GA-DC, GA-MMI and GA-TMI couplers calculated using Eqs. (1) are $\sim 45.1 \mu\text{m}$, $40.1 \mu\text{m}$ and $22.3 \mu\text{m}$, respectively.

Further, these planar waveguide-based conventional DC, TMI coupler and MMI coupler with waveguide designed parameters are then fabricated and experimentally tested using waveguide materials, SiON as the core layer along with SiO_2 cladding layer. From the experimental results as shown in Fig. 7, the beat lengths of conventional TMI coupler ($h = 0 \mu\text{m}$, $\Delta W = 0 \mu\text{m}$) and conventional MMI coupler (with $h = 4 \mu\text{m}$, $\Delta W = 0 \mu\text{m}$) are found as $\sim 45 \mu\text{m}$ and $\sim 80 \mu\text{m}$, respectively, whereas for conventional DC (with $h = 0.5 \mu\text{m}$, $\Delta W = 0 \mu\text{m}$) is $\sim 91 \mu\text{m}$ with $\Delta n = 5\%$. In the graph, respective cross and 3-dB coupling points are indicated by the dot, and star signs show optiBPM simulation results along with experimental results and SEM photographs of developed DC, TMI coupler and MMI coupler, respectively.

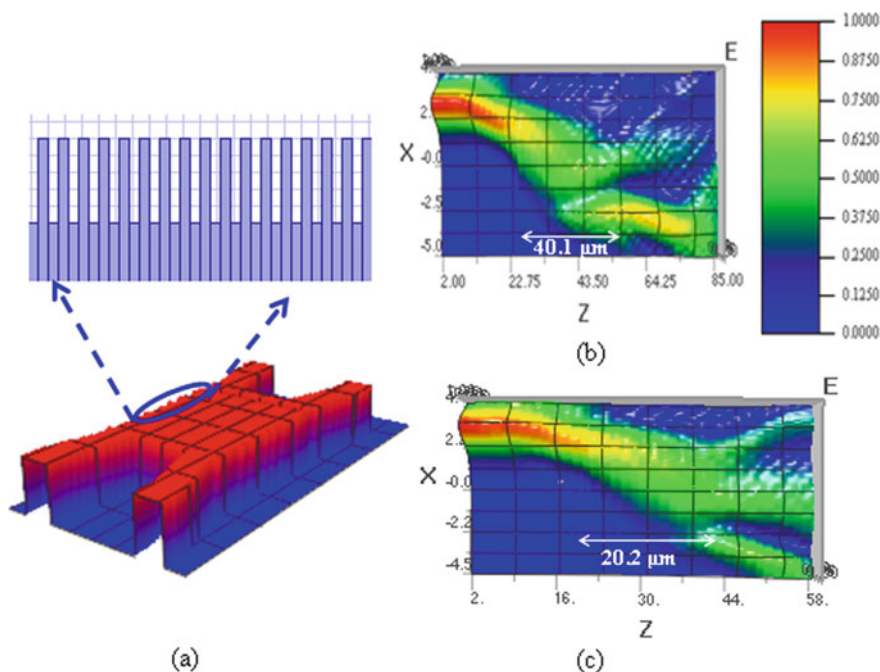
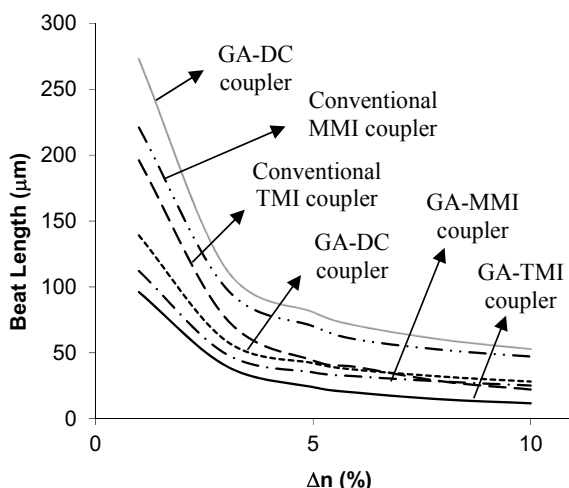


Fig. 4 Tooth-shaped GA-MMI coupler with (a) 3D layout and BPM results for (b) cross-coupling state of $L_{\pi} \sim 40.1 \mu\text{m}$ and (c) 3-dB coupler of $L_{\pi} \sim 20.2 \mu\text{m}$, respectively

Fig. 5 Beat length (L_{π}) versus index contrast (Δn) for tooth structured grating geometry with $\Delta W \sim 0.25 \mu\text{m}$ and conventional structures (where $\Delta W \sim 0 \mu\text{m}$)



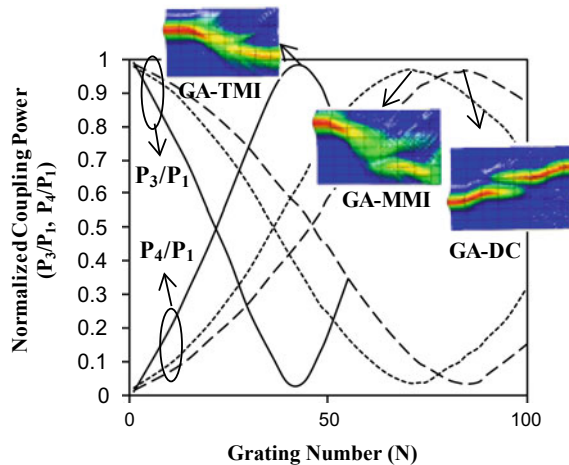


Fig. 6 Normalized bar and cross-state coupling power distribution versus grating number for tooth structured GA-TMI coupler with coupling gap, $h = 0.0 \mu\text{m}$ (solid line), multimode interference (GA-MMI) coupler (dashed lines) for $h = 4.0 \mu\text{m}$ and directional coupler (GA-DC) (dotted lines) for $h = 0.5 \mu\text{m}$ with cladding index ~ 1.45 , $\Delta n = 5\%$, $a = 1.5 \mu\text{m}$, $b = 1.5 \mu\text{m}$, $\Delta W = 0.25 \mu\text{m}$ and $\lambda \sim 1.55 \mu\text{m}$, respectively

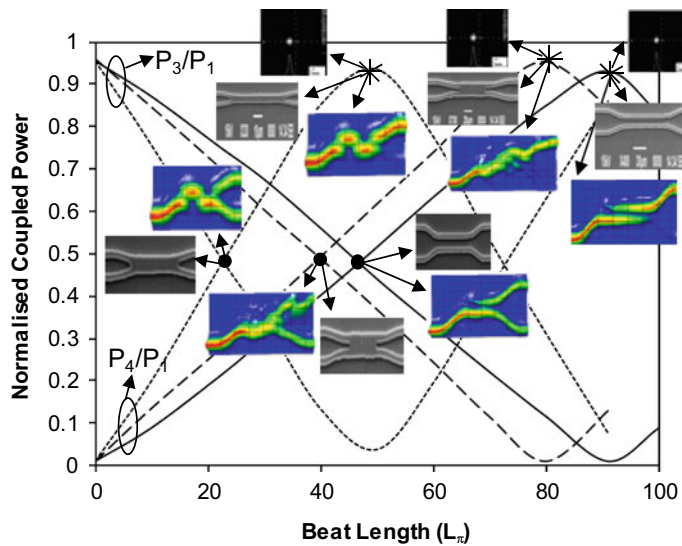


Fig. 7 Normalized coupling power versus beat length using SM-SEIM-based mathematical model for conventional TMI coupler, MMI couplers and directional coupler, along with BPM simulation results and experimental results, respectively

3 Summary

In the paper, a detail comparative study of coupling behavior for tooth structured grating-assisted two-mode interference (GA-TMI) coupler, multimode interference (GA-MMI) coupler and directional coupler (GA-DC) have been presented using a mathematical model based on sinusoidal mode centered simple effective index method (SM-SEIM). The results are compared to the conventional coupler geometry and verified with beam propagation method (BPM) simulation results obtained by using commercially available optiBPM software. It is established that GA-TMI coupler has shorter beat length compared to other couplers.

Acknowledgements The author thankfully acknowledge the help and supports for the fabrication work, carried out at the CENSE under INUP at Indian Institute of Sciences (IISc.), Bangalore which have been sponsored by DIT, MCIT, Government of India.

The author dully acknowledges the financial support provided for this work under collaboration research scheme of TEQIP-III from Assam Science and Technology University, Guwahati, Assam. The author also appreciates fruitful discussions held with Dr. Bharat Kakati.

References

- Chin MK, Lee CW, Lee SY, Darmawan S (2005) High-index-contrast waveguides and devices. *Appl Opt* 44:3077–3086
- Nishihara H, Haruna M, Suhara T (1989) Optical integrated circuits. McGraw-Hill, New York
- Das AK, Sahu PP (2006) In: IEEE wireless and optical communication network conference, Digital No- 01666673, vol 1
- Sahu PP (2009) Parabolic tapered structure for an ultracompact multimode interference coupler. *Appl Opt* 48:206–211
- Chan HP, Chow CK, Das AK (2003) A wide angle X-junction polymeric thermo optic digital switch with low crosstalk. *IEEE Photon Tech Lett* 15:1210–1212
- Passaro VMN (2000) Optimal design of grating-assisted directional couplers. *J Lightwave Tech* 18:973–984
- Hardy A (1984) Exact derivation of the coupling coefficient in corrugated waveguides with rectangular tooth shape. *IEEE J Quantum Electron* 20:1132–1139
- Tsai TY, Lee ZC, Gau CS, Chen FS, Chen JR, Chen CC (2004) A novel wavelength-division-multiplexer using grating assisted two-mode interference. *IEEE Photon Tech Lett* 16:2251–2253
- Tsai TY, Lee ZC, Chen JR, Chen CC, Fang YC, Cha MH (2005) A novel ultra compact two-mode-interference wavelength division multiplexer for 1.5 μm operation. *IEEE J Quantum Electron* 41:741–746
- Chiang KS (1991) Effective index method for the analysis of optical waveguide couplers and arrays: an asymptotic theory. *J Lightwave Tech* 9:62–72
- Wang Q, Farrell G, Freir T (2006) Effective index method for planar lightwave circuits containing directional couplers. *J Opt Commun* 259:133–136
- Deka B, Sahu PP (2009) Transformation relationship of directional coupler with multimode interference coupler and two mode interference coupler. *J Opt* 38:75–87
- Deka B, Sahu PP (2011) Tooth-shaped grating-assisted structure for compact multimode interference (MMI) coupler. *Appl Opt* 50:E193–E199

Effect of AlN Spacer Layer on the Proposed MIS-AlGaN/GaN HEMT



Ravi Ranjan, Nitesh Kashyap, and Ashish Raman

Abstract This paper presents a comparison between AlGaN/GaN high electron mobility transistor (HEMT) with and without AlN spacer layer between AlGaN and GaN interface. Two AlN layers are used in the proposed design, one AlN layer is used as an interfacial passivation layer between Al_2O_3 and AlGaN layer. 2DEG is formed at the interface of AlN and GaN. Spacer layer enhances the mobility of carrier in the channel. Due to higher mobility, current density and drain current of the spacer layer HEMT are larger than HEMT without spacer. The results with spacer-MIS-HEMT are compared with MIS-HEMT without spacer, which shows that the spacer-MIS-HEMT provides better ON-OFF current, transconductance, cutoff frequency (11 GHz), and ON to OFF current ratio is (10^{11}).

Keywords Gallium nitride (GaN) · Spacer layer · Dopingless · HEMT · MIS

1 Introduction

Silicon has been mostly used in many electronics devices. But due to some limitation of silicon over higher bandgap material, silicon is not preferred for high power devices. Wider bandgap compound semiconductor is used for power devices and radio frequency application such as radar, mobile tower and automobiles. III-group nitrides have many advantages over silicon and other larger bandgap material (GaAs and SiC) that is saturation velocity and thermal conductivity. Table 1 gives the material and electrical properties of GaAs, 4H-SiC, Si and GaN. Due to above advantage, III-group nitrides are used for power applications [1]. AlGaN/GaN hetero-structure-based HEMT is better choice for high power and high frequency application [2].

R. Ranjan (✉) · N. Kashyap · A. Raman

Dr. B. R. Ambedkar National Institute of Technology Jalandhar, Jalandhar 144011, India

e-mail: ranjan.ravi80@gmail.com

N. Kashyap

e-mail: kashyapn@nitj.ac.in

A. Raman

e-mail: ramana@nitj.ac.in

Table 1 Physical and electronics property of GaN, Si, 4H-SiC and GaAs [1, 3, 5]

Property	Si	4H-SiC	GaN	GaAs
Energy band (eV)	1.12	3.2	3.4	1.4
$V_s (10^7 \text{ cm/s})$	1	2	3	1.3
$\mu (\text{cm}^2/\text{Vs})$	1350	800	1300	6000
ϵ	11.8	9.7	9.5	13.1
$E_{cr} (\text{MV/cm})$	0.25	3	4	0.4
Thermal conductivity, $k (\text{W/cmK})$	1.5	4.9	1.3	0.5

The drain current is flow through channel, formed through two-dimensional electron gases (2DEG). Due to different bandgap of AlGaN and GaN layer, 2DEG is formed at the interface mobility of electrons (carriers) present in 2DEG is higher than mobility of electron in other three terminal devices [4]. Due to higher mobility of carrier, some of the carriers move toward Schottky gate side, and due to this, the leakage current of the device is increased. Metal insulator semiconductor HEMT (MIS-HEMT) is used to reduce the gate leakage current and enhance the performance of the device. Different insulators are used in MIS-HEMT are Si_3N_4 , Al_2O_3 , HfO_2 .

Above dielectric is used to reduce leakage current. In the proposed design, Al_2O_3 is used as a gate passivation. And AlN layer is used to interfacial layer between dielectric and AlGaN layer. Lattice of AlGaN and dielectric do not match, so why AlN layer is used [6].

In AlGaN/GaN HEMT, channel is formed at the interface of AlGaN and GaN. Due to interface roughness scattering at the interface of AlGaN and GaN, the mobility of carrier will reduce. A spacer layer (AlN) is used to enhance the carrier mobility, current density at the (2DEG), transconductance and cutoff frequency [7].

The aim of this paper is to propose and discuss the spacer layer AlGaN/GaN HEMT and compare it with AlGaN/GaN HEMT without spacer. The analog performance of both the devices is discussed, and the results are compared. The spacer layer AlGaN/GaN HEMT provides better drain current, transconductance, cutoff frequency and ON-resistance.

2 Device Structure and Simulation Parameters

A larger bandgap material is grown on lower bandgap material for HEMT design. AlGaN/GaN HEMT is designed by growing AlGaN layer on top of GaN layer [8]. Due to the discontinuities in the conduction band between AlGaN and GaN, the 2DEG is formed at the interface [9, 10]. A potential well is created at the GaN side of device. Because of the uniform lattice in GaN, spontaneous polarization field is generated. When larger lattice size material (AlGaN) is grown upon lower lattice size material (GaN) than strain is induce at the AlGaN side and due to this spontaneous and piezoelectric polarization field is generated at the AlGaN [11]. A electric field is

Table 2 Parameters

Parameters	Proposed HEMT
AlGaN doping	Nil
GaN doping	Nil
AlGaN thickness (nm)	20
L_G (μm)	1.2
Work function of gate (eV)	5.05
Al_2O_3 thickness (nm)	4
Device length (μm)	2
AlN thickness (nm)	2

generated in the AlGaN layer because of piezoelectric polarization. To compensate the positive charges at the AlGaN, electron is generated at the GaN side. There is not any requirement of doped AlGaN for generation of 2DEG at the interface (Table 2).

In the proposed HEMT, is shown in Fig. 1. AlGaN layer is grown upon GaN with the composition (mole fraction) of Al in GaN is 0.25. No any external doping is required to AlGaN for formation of 2DEG. Si is used as a substrate [12]. GaN is deposited on the Si substrate with thickness of 0.184 μm . On the top of the GaN, spacer AlN layer is grown with thickness 1 nm. Due to different lattice of GaN and AlGaN, the channel electron degradation takes place at the channel. The 2DEG wave function is mostly present in GaN, but there is a small part of wave function that penetrates the AlGaN barrier, leading to alloy-disorder scattering. AlN layer reduces

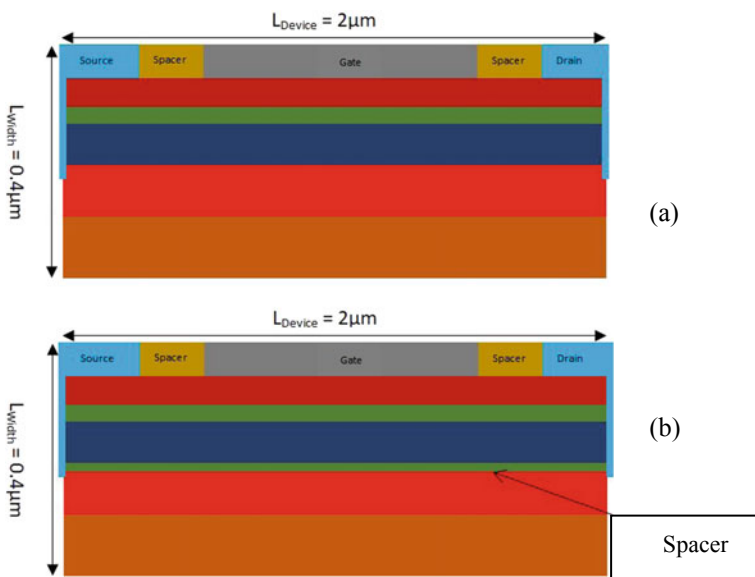


Fig. 1 **a** AlGaN/GaN HEMT without spacer **b** AlGaN/GaN HEMT with spacer

the alloy-disorder scattering. Hence, mobility of electron increases in 2DEG, and carrier density increases at the interface. The spacing between the source and drain to gate is 10 nm. The second source and drain are present at the boundary of device up to upper part of GaN layer for reduction in series resistance. The silicon substrate is used for the mechanical support of device, and thickness of Si is 0.2 μm . The 2-D schematic of HEMT with and without spacer layer is shown in Fig. 1.

3 Simulation Results and Discussion

Both the above designs (with spacer and without spacer) are simulated at same gate voltage and work function. Fig. 2a, b shows the 2-DEG formation in ON-state condition at the interface of two different bandgap materials such as AlGaN and GaN interface in case of HEMT without spacer and at the interface of AlN and GaN with spacer. In both cases of HEMT, 2DEG forms in similar fashion at the interface. Due to reduction in alloy-disorder scattering, the depth of 2-DEG below Fermi level is slightly more in case of spacer layer HEMT shown in Fig. 2b. Higher depth of 2-DEG, the current density at the interface is more. The higher current density and mobility increase the drain current in case of HEMT with spacer.

Electron concentration of both the devices with spacer and without spacer is shown in Fig. 3a, b, respectively. Because of interface roughness, the concentration of carrier layer HEMT is slightly larger than HEMT without spacer. From the graph, the current will flow through drain to source by only one carrier, i.e., electrons.

Figure 4a shows the transfer characteristics of designed HEMT. Due to higher current density and mobility, the drain current of spacer layer HEMT is larger than without spacer layer HEMT. Spacer layer HEMT shows higher I_{ON} to I_{OFF} ratio than conventional HEMT. The OFF-state current of spacer layer HEMT is lower than HEMT without spacer layer because of lower minority concentration of channel.

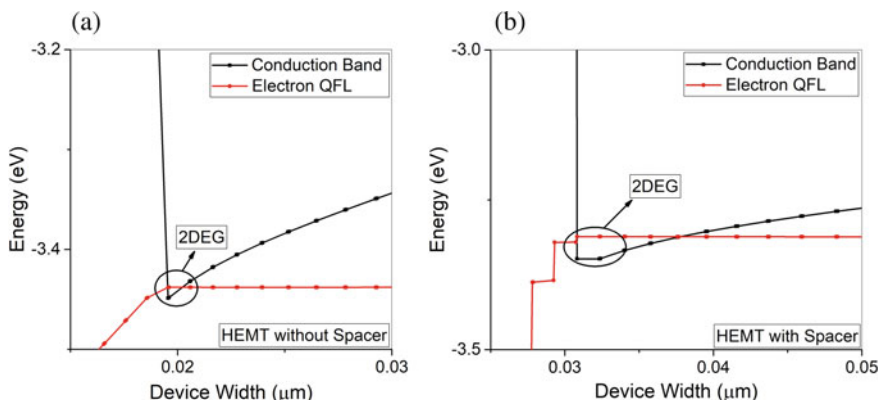


Fig. 2 2DEG of HEMT **a** without spacer **b** with spacer

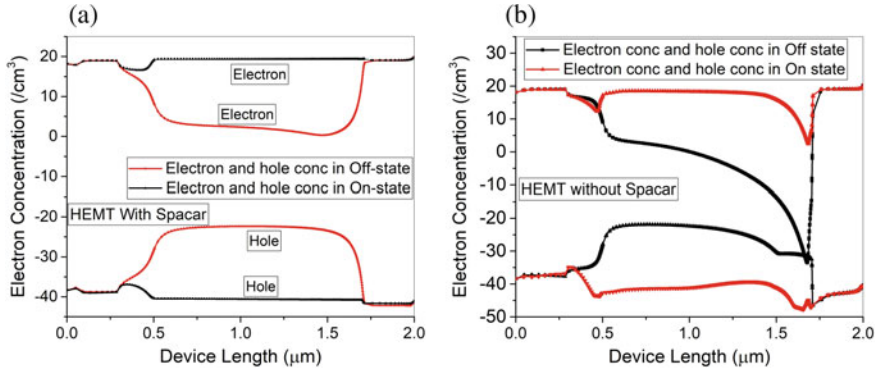


Fig. 3 Electron concentration with respect to device length of HEMT **a** with spacer **b** without spacer layer

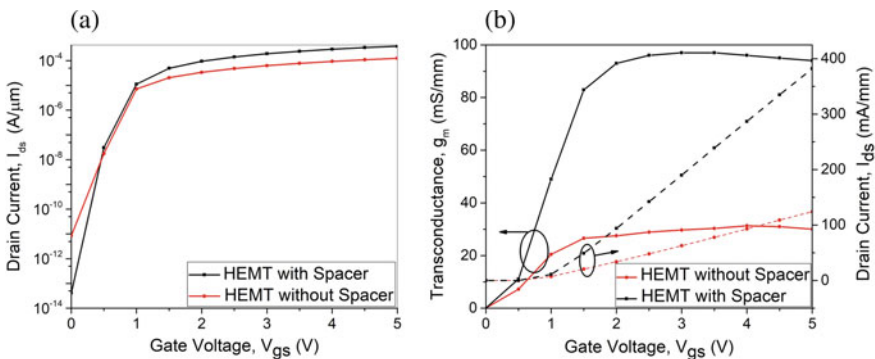


Fig. 4 **a** Transfer characteristics of HEMT with and without spacer at $V_{ds} = 10 \text{ V}$. **b** Transconductance, g_m , and drain current, I_{ds} , with respect to V_{gs} at $V_{ds} = 10 \text{ V}$

All the simulation is done on $V_{ds} = 10 \text{ V}$. At $V_{gs} = 5 \text{ V}$, the ON-state currents are 125 mA/mm and 380 mA/mm of HEMT without spacer and spacer layer, respectively. Figure 4b shows the transconductance and drain current with V_{gs} . Due to higher ON-state current of the spacer layer HEMT, the transconductance of spacer layer HEMT is larger than without spacer HEMT.

From Eq. 1, transconductance is directly proportional to the slope of log (drain current), and due to higher drain current I_{ds} , the transconductance of spacer HEMT is larger than that of the without spacer HEMT. Transconductance of spacer and without spacer layer HEMT is 96 mS/mm and 24 mS/mm, respectively.

$$g_m = \frac{\partial I_{ds}}{\partial V_{gs}} \quad (1)$$

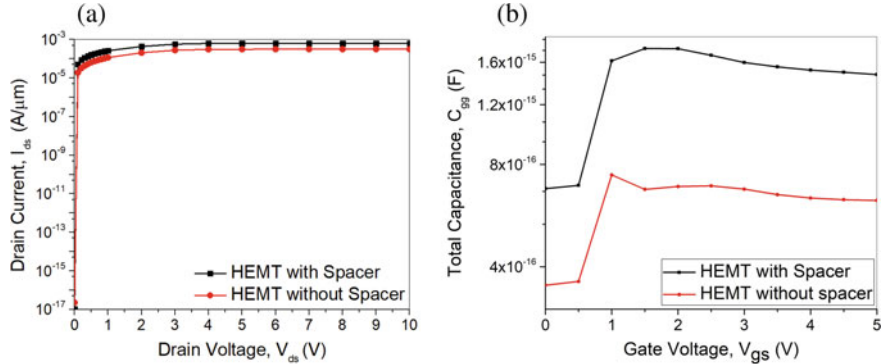


Fig. 5 Drain current, I_D , as a function of drain voltage, V_{ds} , for GAA and Planar-MIS-HEMT at $V_{gs} = 5$ V. **b** Total capacitance, C_{gg} with respect to gate voltage, V_{gs} , at $V_{ds} = 10$ V

Transconductance (g_m) and drain current (I_{ds}) graph with gate voltage, V_{gs} , are shown in Fig. 4b. Dotted line shows the drain current for both the devices that is in the order of mA scale, and solid line shows the transconductance of both the devices.

Figure 5a shows the graph between drain current with drain voltage. Because of higher carrier density, the drain current of spacer HEMT is larger than without spacer layer HEMT.

Figure 5b shows the total capacitance, C_{gg} ($C_{gg} = C_{gd} + C_{gs}$), of both devices at $V_{ds} = 10$ V where C_{gd} is the gate-to-drain capacitance and C_{gs} is the gate-to-source capacitance. The value of C_{gg} is higher in the case of the spacer HEMT and in comparison with HEMT without spacer device. The switching behavior of device depends upon total capacitance. From Eq. (2), the cutoff frequency, f_T , of device depends on transconductance and total capacitance. Cutoff frequency is directly proportional to g_m and inversely proportional to C_{gs} .

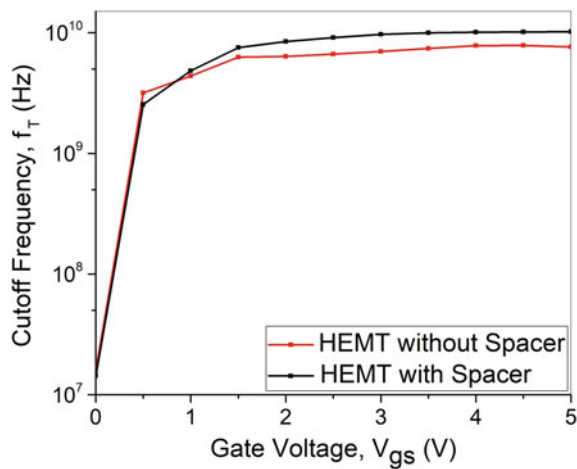
Due to larger value of transconductance of spacer layer AlGaN/GaN HEMT, the cutoff frequency of spacer layer HEMT is larger than without spacer layer. Figure 6 shows the cutoff frequency, f_T , with gate voltage, V_{gs} , at $V_{ds} = 10$ V.

$$f_T = \frac{g_m}{2\pi C_{gg}} \quad (2)$$

4 Conclusion

AlGaN/GaN HEMT is design for microwave and RF frequency application. Spacer layer AlGaN/GaN HEMT is compared without spacer layer in terms of their RF and analog characteristics. AlN is used as a spacer layer between AlGaN and GaN layer. By using spacer layer, the depth of 2DEG is higher than HEMT without spacer.

Fig. 6 Cutoff frequency, f_T , with respect to gate voltage, V_{gs} at $V_{ds} = 10$ V



Dopingless AlGaN layer is used to facilitate the formation of 2DEG at the interface of GaN. Carrier density and mobility of carriers are larger in spacer layer HEMT. Spacer layer HEMT provides better analog performance than HEMT without spacer layer. ON-state current, transconductance, ON-resistance and cutoff frequency of GAA-HEMT is higher as compared to HEMT without spacer.

References

- Wong YY, Chiu YS, Luong TT, Lin TM, Ho YT, Lin YC, Chang EY (2012) 10th IEEE international conference on semiconductor electronics (ICSE), pp 729–732, IEEE
- Xiao-Guang H, De-Gang Z, De-Sheng J (2015) Chinese physics B 24(6):067301
- Hsieh TE, Chang EY, Song YZ, Lin YC, Wang HC, Liu SC, Salahuddin S, Hu CC (2014) IEEE Electron Device Lett 35(7):732–734
- Hwang IH, Eom SK, Choi GH, Kang MJ, Lee JG, Cha HY, Seo KS (2018) Physica status solidi (a) 215(10):1700650
- Roccaforte, Fabrizio, Greco G, Fiorenza P, Iucolano F (2019) Materials 12(10)
- Oka T, Nozawa T (2008) IEEE Electron Device Lett 29(7):668–670
- Ye PD, Yang B, Ng KK, Bude J, Wilk GD, Halder S, Hwang JCM (2005) Appl Phys Lett 86(6):063501
- Ohno Y, Kuzuhara M (2001) IEEE Trans Electron Devices 48(3):517–523
- Palacios T, Chakraborty A, Heikman S, Keller S, DenBaars SP, Mishra UK (2005) IEEE Electron Device Lett 27(1):13–15
- Kumar TV, Balamurugan NB (2018) AEU-Int J Electron Commun 94:19–25
- Radhakrishnan SK, Subramaniyan B, Anandan M, Nagarajan M (2017) Int J Electron Commun 2018 83:462–469. <https://doi.org/10.1016/j.aeue.2017.10.029>
- Ranjan R, Kashyap N, Raman A (February 2020) Appl Phy A

Enhancement of Isolation in MIMO Antenna System



**Neelima Koppala, Sree Lochan Kanthi Kumar Kuppachi,
Rohith Sai Kumar Gajula, Bhanu Ravindranath Kasturi,
and Rupa Sree Jangam**

Abstract In this presented document, the analysis of the isolation is improved with the help of an antenna array which consists of eight radiators divided into four ports. Each port consists of two radiators for which we are going to increase the isolation. The number of antennas is greater than one which leads us to the multiple-input multiple output (MIMO). MIMO is the thing that we are used for achieving high data rates for the upcoming smart mobiles. This design purely deals with providing the isolation between any two antenna elements. There are many techniques to improve isolation, among them this document deals with the defective ground structures, parasitic elements. This design operates at a frequency of 3 GHz with isolation parameter range of (-26.0619 to -42.9525) dB.

Keywords MIMO · 5G · Isolation · Dual polarization

1 Introduction

In modern life, high data rates and channel band width are the key parameters of the communication system. To influence these parameters, we need to study modern

N. Koppala

Department of Electronics and Communication Engineering, Center of VLSI and Embedded Systems, Sree Vidyanikethan Engineering College, Tirupathi, India

e-mail: neelumtech17@gmail.com

S. L. K. K. Kuppachi (✉) · R. S. K. Gajula · B. R. Kasturi · R. S. Jangam

Department of Electronics and Communication Engineering, Sree Vidyanikethan Engineering College, Tirupathi, India

e-mail: ramamachavolu@gmail.com

R. S. K. Gajula

e-mail: royalrohith88@gmail.com

B. R. Kasturi

e-mail: kbhanuravindranath98@gmail.com

R. S. Jangam

e-mail: rsreejangam@gmail.com

communication systems which includes MIMO. This MIMO technology has more advantages than single input devices, comparatively MIMO has best channel band width and data rates. The main challenge in MIMO is keeping isolation high between many elements in antenna array. MIMO was been introduced at BELL laboratories at period called the BLAST period, which stands for Bell-Layered Space Time.

Because of the mutual coupling between any two elements and high similarity in channel degrades the performance of MIMO antenna system [1–4]. From past years, researchers have developed many methods to overcome the mutual coupling. Among them, we used two methods. They are 1. Defected ground structure and 2. Parasitic elements [5] isolation [6] and the defected ground structures in turn allows the antenna to radiate in both sides.

The slotted antenna element contains a square ring as a defective ground structure and antenna fed with rectangular micro strip lines. In advance, we have a circular-shaped ring that acts as a parasitic element which is used to reduce mutual coupling between elements. In the design, we have placed these antennas and ground as a slots at the ends of square-shaped structure [7]. The single element slot antenna fundamental properties have been discussed in the following Sections.

2 Single Element Antenna

In this single element antenna, we are going to deal with the single port from four ports total antenna which consists of eight element antenna.

Figure 1 shows the single slotted antenna with two parasitic elements, two feed elements and one ground structure. Here, the substrate used is a FR4 dielectric with a height of 1.6 mm. The ground structure is taken in the form of a rectangular shape at the bottom of the substrate. Two antennas are placed at the corner of the substrate with help of design parameters so that it passes from the structure of ground placed bottom of the substrate. Two circular-shaped rings are taken into consideration that these are acts as the parasitic elements which can radiate, through which we can reduce mutual coupling (Table 1).

This table shows the design parameters for single slot antenna L_f represents the length of feed, W_f represents the width of the feed, W represents the length of outer rectangle in ground plane, W_1 represents the length of inner rectangle in the ground

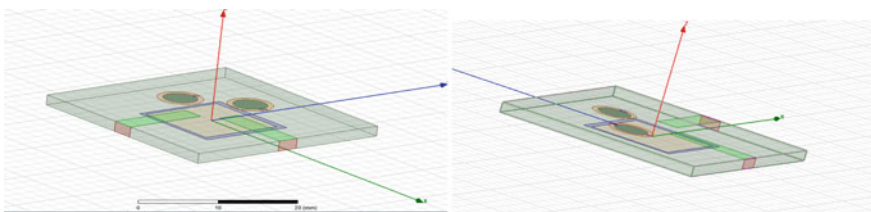


Fig. 1 The proposed single slot antenna

Table 1 The values of the design parameter

Parameter	Dimension (mm)
W	13.4
h_s	1.6
W_f	3
L_f	11.75
W_s	30
W_1	11.9
W_2	13.15
S	0.75
S_1	0.75
L_1	9
d	5.95
r	3

plane, S is the width of ground plane rectangle, r is the radius of the circular ring which acts as a parasitic elements.

Figure 2 shows the development of single element antenna in stages; this development is done in HFSS design.

Substrate contains a material called FR4 dielectric substrate which is used because it can be easily available and can be designed easily with less cost; its dimensions mainly consists of 1.6 mm height and a width of $(75 \times 75) \text{ mm}^2$.

Figure 3 shows the excitation of radiators in single element antenna, (a) shows excitation of one element where the other is not excited, (b) shows the excitation of other element where the first one is kept constant.

Main inference from this Figs. 3 and 4 is that the voltage level is increased from 0.7 to 1 V which means by increasing the elements in the design, we can able to increase voltage levels.

Considering the results of this antenna, we have best return loss at $s(1, 1)$ when both the radiators are excited and the value is -14.4429 dB where the standard value goes like this it should be more than -10 dB . Voltage standing wave ratio (VSWR) is best when both are excited in a frequency of 3 GHz which is 1.4679, usually the VSWR must be in a range of 1–2.

Considering the isolation parameter which how much one element is different from other, to obtain the good performance, usually this isolation parameter value must be more than -15 dB .

We have the isolation parameter value as $S(1, 2) = -18.414 \text{ dB}$, which is also the best one at frequency of 3 GHz range.

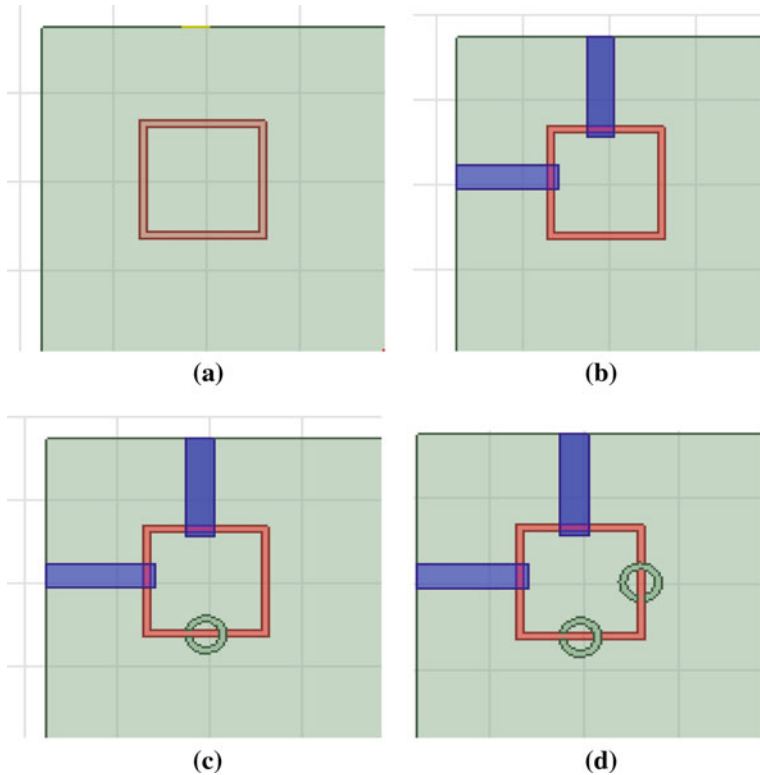


Fig. 2 **a** Ground plane present at the bottom of substrate, **b** extends by adding feed, **c** added with parasitic elements and **d** final structure

3 Introduction to the Eight Element Antenna

First, we proposed a two element radiating element antenna, for the purpose of the using this in the smart phone or the upcoming livelihood the need for the antennas increases drastically. So we designed an eight element antenna [8] to increase the performance characteristics of the device and as well as to increase the device capability.

While comparing the values of the parameters like gain, the eight element antenna meets the required levels.

The metrics that can be used to compare the designs of EDAC Codes for memories are given as below.

The above design is the eight element antenna design that has been designed [9] to meet the required levels. The substrate used is the Fr-4 material. The design challenges that are faced to design the model are:

1. Mutual coupling
2. In situ performance

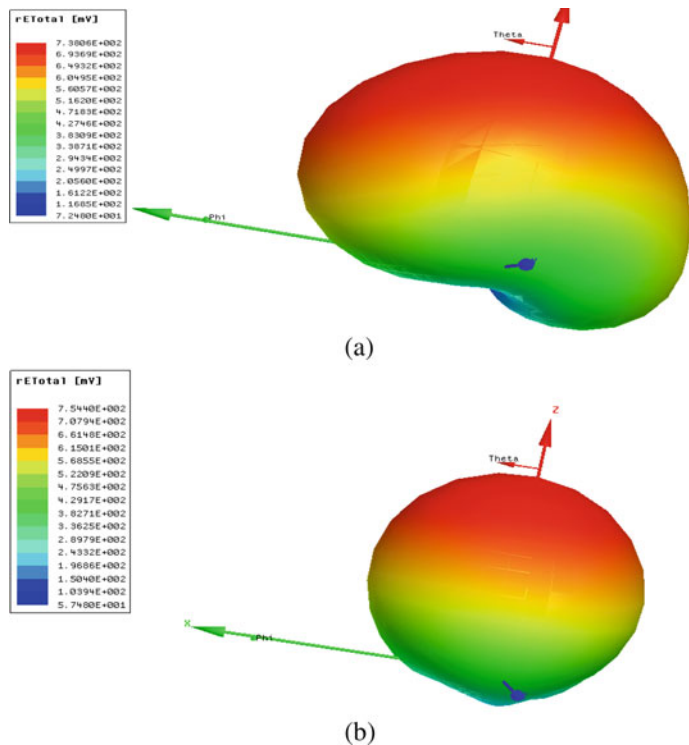


Fig. 3 **a** Single element excitation, **b** second element excitation

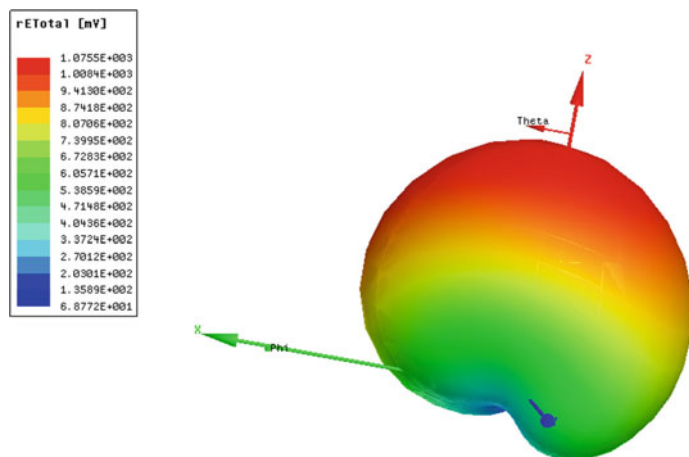


Fig. 4 2 elements radiated

3. Antenna size.
1. Mutual coupling:

Mutual coupling is the interference of the radiation pattern between the two element antenna array.

2. In situ performance

In situ performance is the characteristic representation of an every element in an array within itself.

3. Antenna size

The size of the antenna is a design challenge because we are designing this design to an smart phone device; size compatibility is a must in those designs.

4 Design of the Element Antenna

Figure 5 displays the schematic of the designed [10] 8 element antenna. The designed is arranged on an FR-4 dielectric medium which has a permittivity of 4.4 and the overall dimension is of $75 \times 75 \text{ mm}^2$ and an dual-polarized square ring slot antenna of size $27 \times 27 \text{ mm}^2$ (Table 2).

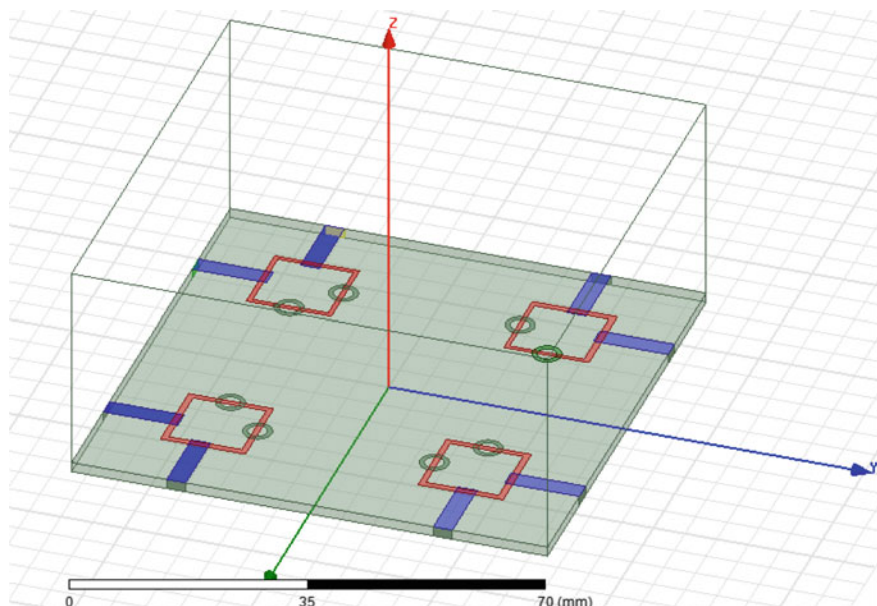


Fig. 5 The eight element antenna

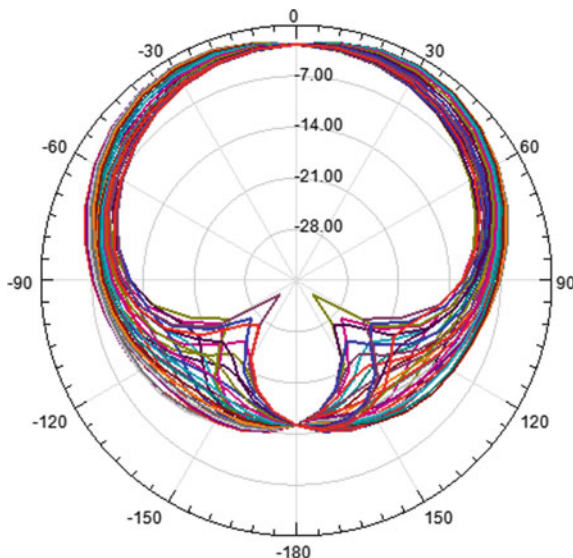
Table 2 Design parameters

Parameter	Dimension (mm)
W	13.4
h_s	1.6
W_f	3
L_f	11.75
W_s	30
W_1	11.9
W_2	13.15
S	0.75
S_1	0.75
L_1	9
d	5.95
r	3

5 Performance Characteristics

The output of the design is showed in the 2D and 3D polar plots (Fig. 6).

Figure 7 shows the 3D polar plot of an eight element radiators radiation pattern when all the antennas are radiated at a time which consists of 2.8 V of voltage level where as Figure 8 shows the radiation pattern when the single port is radiated from four port or eight element antenna which exists in the planar mode, when all the ports are radiated which explains that the design is directional so that this can be viewed

Fig. 6 2D polar plot

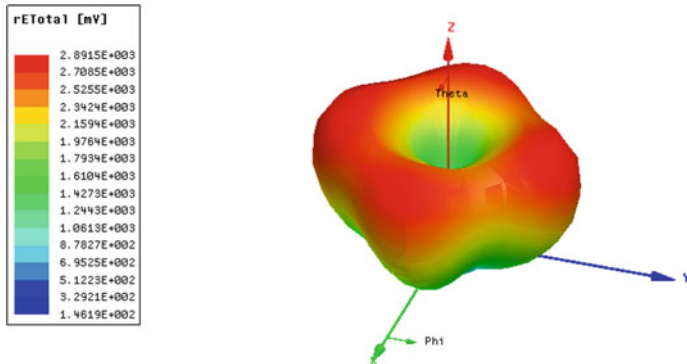


Fig. 7 3D polar plot (all ports exited)

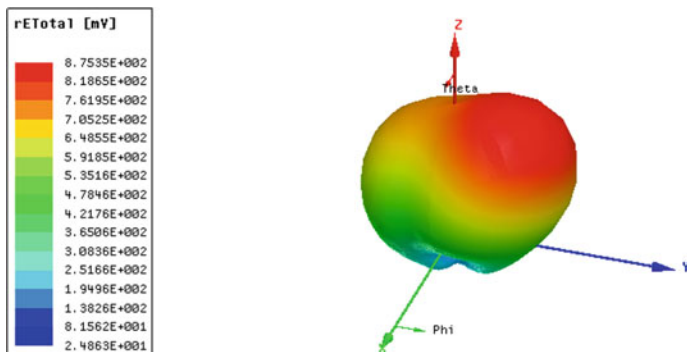


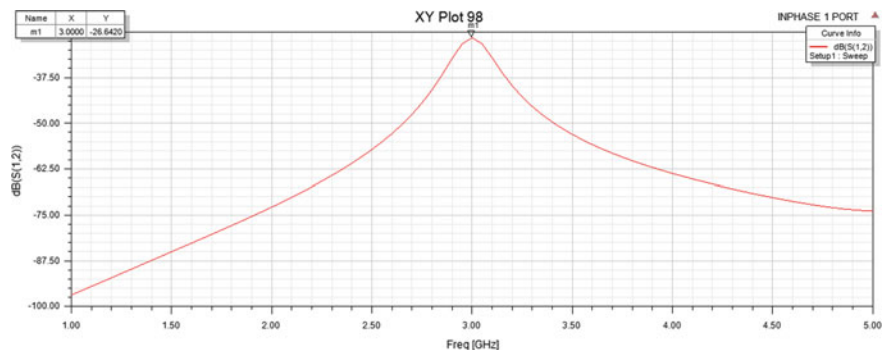
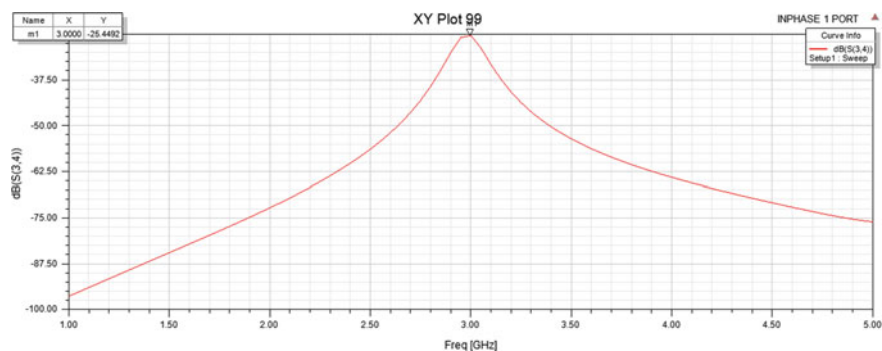
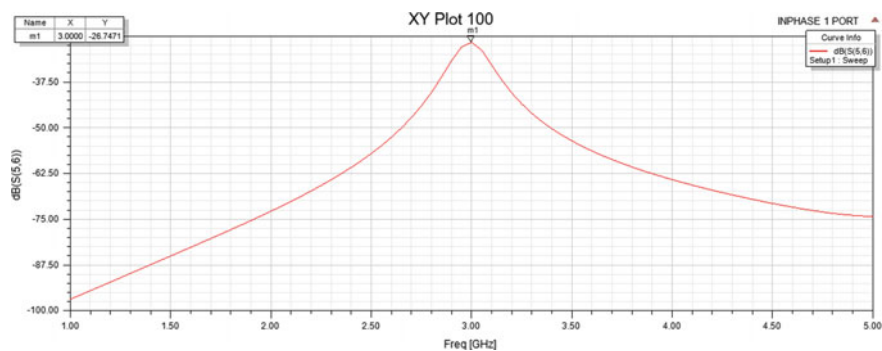
Fig. 8 3D polar plot (one port exited)

in MIMO. As we are designing this to the smart phone 5G networks, the MIMO concept is very useful to give high data rates.

The main parameter of this design is to give the isolation between 2 antenna elements. Figure 5 shows the eight element antenna design. The isolation should be more at the nearby elements 1 and 2, 3 and 4, 5 and 6, 7 and 8. The required isolation should be showed between these pairs; hence, they are the nearby elements; the rest of the elements are far away & the isolation is quite normal for them. For proving the isolation between these elements, we are going for the S -parameter due to its measurement of the power. The next following graphs show the isolation between those pairs.

The minimum isolation between two antenna elements should be -15 dB. The above graphs show the isolation between these pairs and the isolation is of the values.

From Fig. 9, it shows $S(1, 2)$: -26.6420 dB, from Fig. 10 it shows $S(3, 4)$: -25.4492 dB, from Fig. 11 it shows $S(5, 6)$: -26.7471 dB and from Fig. 12 it shows $S(7, 8)$: -26.0619 dB these values show that more than -15 dB which is best.

**Fig. 9** $S(1, 2)$ **Fig. 10** $S(3, 4)$ **Fig. 11** $S(5, 6)$

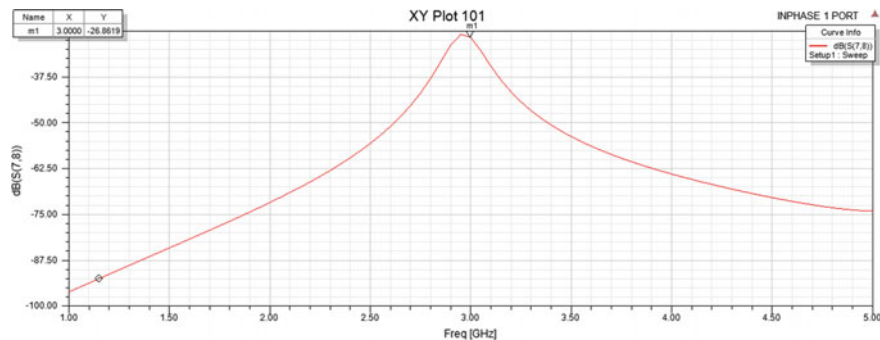


Fig. 12 $S(7, 8)$

According to this designed model, the antenna elements shows a good performance in S parameters at 3 GHz.

6 Conclusion

The structure of the proposed MIMO antenna consists of dual-polarized square ring slot antenna placed at the corners of smart phone PCB which intern reduces mutual coupling antenna elements, these circular rings act as the parasitic structures at the top of the dielectric substrate, rectangular ground structures are placed at the bottom of substrate acts as defective ground structures by using parasitic, defective ground structures, the mutual coupling is reduced which in turn increases isolation which is in a range of -26.0619 to 45.9525 dB at operating frequency 3 GHz. This design antenna offers good performance characteristics at 3 GHz applications.

References

- Qin Z, Wen GY, Zhang M, Wang J (March, 2016) Printed eight-element MIMO system for compact and thin 5G mobile handset. *Electron Lett* 52(6):416–418
- Hussain R, Alreshaid AT, Podilchak SK, Sharawi MS (2017) Compact 4G MIMO antenna integrated with a 5G array for current and future mobile handsets. *IET Microw Antennas Propag* 11(2):271–279
- Al-Hadi AA, Ilvonen J, Valkonen R, Viikari V (2014) Eight-element antenna array for diversity and MIMO mobile terminal in LTE 3500 MHz band. *Microw Opt Technol Lett* 56(6):1323–1327
- Wong KL, Lu JY, Chen LY, Li WY, Ban YL, Li C (December, 2015) 16 antenna array in the smartphone for the 3.5 GHz MIMO operation. In: 2015 Asia-Pacific microwave conference (APMC), Nanjing, China, pp 1–3
- Statement: improving consumer access to mobile services at 3.6–3.8 GHz. Accessed: Oct. 21, 2018

6. Li Y, Zou H, Wang M, Peng M, Yang G (March, 2018) Eight-element MIMO antenna array for 5G/Sub-6 GHz indoor micro wireless access points. In: Proceedings of international workshop on antenna technology (IWAT), Nanjing, China, pp 1–4
7. Yang HH, Quel YQS (2017) Massive MIMO meet small cell. In: Springer briefs in electrical and computer engineering. Springer, Cham, Switzerland. https://doi.org/10.1007/978-3-319-43715-6_2
8. Nadeem Q-U-A, Kammoun A, Debbah M, Alouini M-S Design of 5G full dimension massive MIMO systems. *IEEE Trans Commun* 66(2):726–740
9. Osseiran A, Boccardi F, Braun V, Kusume K, Marsch P, Maternia M, Queseth O, Schellmann M, Schotten H, Taoka H, Tullberg H, Uusitalo MA, Timus B, Fallgren M Scenarios for 5G mobile and wireless communications: the vision of the METIS project. *IEEE Commun Mag* 52(5):26–35
10. Sun L, Feng H, Li Y, Zhang Z Compact 5G MIMO mobile phone antennas with tightly arranged orthogonal-mode

Stochastic Frontier Model Approach of Technical Efficiency for Paddy Farming in Odisha



Priyabrata Bhoi, Deepak Kumar Swain, Subhadra Mishra, Debahuti Mishra, Gour Hari Santra, and Samarjeet Borah

Abstract Paddy production with utilising efficient technology will boost the production and economy simultaneously. Technical efficiency approach is adopted for perfect utilisation of inputs. The study is carried out between the years 2001 and 2016. The secondary data are collected from DES, India, and for Odisha, the data are generated from scheme “Comprehensive scheme to study cost of cultivation of principal crops in Odisha” conducted by OUAT, Bhubaneswar. Different parameters are considered, and the efficiency is obtained by stochastic frontier model or stochastic frontier production function. Total fertiliser and casual labour show statistical significant effect. The significant shifting of mechanisation from 2001 to 2016 can be visible clearly.

P. Bhoi

Department of Agricultural Economics, FAS, Siksha ‘O’ Anusandhan Deemed to be University, Bhubaneswar, Odisha 751030, India

e-mail: Priyabratas3@gmail.com

D. K. Swain

Department of Agricultural Statistics, FAS, Siksha ‘O’ Anusandhan Deemed to be University, Bhubaneswar, Odisha 751030, India

e-mail: dsagrico14@gmail.com

S. Mishra

Department of Computer Science and Application, CPGS, OUAT, Bhubaneswar, Odisha 751030, India

e-mail: mishra.subhadra@gmail.com

D. Mishra (✉)

Department of Computer Science and Engineering, ITER, Siksha ‘O’ Anusandhan Deemed to be University, Bhubaneswar, Odisha 751030, India

e-mail: debahutimishra@soauniversity.ac.in

G. H. Santra

Department of Soil Science and Agricultural Chemistry, FAS, Siksha ‘O’ Anusandhan Deemed to be University, Bhubaneswar, Odisha 751030, India

e-mail: santragh@gmail.com

S. Borah

Department of Computer Applications, Sikkim Manipal University, Gangtok, Sikkim, India

e-mail: samarjeetborah@gmail.com

Keywords Production function · Stochastic frontier model · Cobb–Douglas function · Technical efficiency · Paddy production

1 Introduction

One of the poor faces of India is Odisha. The livelihood of 70% people depends on agriculture. Rice is staple crop and food of the people of Odisha. The State possess 29.14 lakh ha of high land, 17.55 lakh ha of medium land and low land of 15.11 lakh ha summing up to 61.80 lakh ha of cultivated area. Paddy cropping covers around 41.24 lakh ha and 3.31 lakh ha area in *kharif* and *rabi*, respectively (DAFE, BBSR). To feed the hunger, the production should be alleviated efficiently by judicious utilisation of the inputs, due to their scarcity. The knowledge of technical efficiency of different crops is an important tool for policy formulation. Production performance of crops can be improved from past efficiency observation. Efficiency studies have corroborated the possibility of increasing the crop productivity without incremental in input application which is described by Ali and Chaudhry [1], Umesh and Bisaliah [2] and Gaddi et al. [3]. The efficiency of production completely depends on the kind of technology used and the potential of producer explored to exploit it. The production growth rate can be increased through improved technology, efficient use of technology, facilitation of technological innovations via institution and rural infrastructure development through public investment explained by Kalirajan and Shand [4]. Resource use pattern and production efficiencies of various farms provide guidelines for national policy and planning as well proportional resource allocation to different farms. An economy can be benefited in several ways from inefficiency studies as it is one of essential factor for growth of productivity. The estimation on the extent of inefficiency can also aid in finding out the potential technology to enhance the agricultural productivity. Kalirajan et al. [5] confirmed that boosting technical efficiency is a prime approach to harvest the potential profits of the existing technology rather than setting for new technology. Shanmugam and Venkataramani [6] found that without increasing the input application the increment of crop production is also possible. Determinants of technical efficiency and allocative efficiency can be accomplished by stochastic frontier production function conferred by Mruthyunjay et al. [7]. A study was conducted on the productivity of resource and technical efficiency of paddy in Thrissur district of Kerala, where stratified random sampling technique was used by Suresh and Reddy [8] to collect the farm-level data of 71 farmers.

2 Materials and Method

2.1 Data Collection

The study used the secondary data compiled from the Department of Economics and Statistics (DES), Ministry of Agriculture, Govt. of India. Odisha has generated data from the scheme “Comprehensive scheme to study cost of cultivation of principal crops in Odisha” being implemented by the Orissa University of Agriculture and Technology, Bhubaneswar. The current study perused data of input use and output produced in paddy crop for the year 2001–02 and 2016–17, a gap of 15 years for technical efficiency estimation and comparison.

2.2 Technical Efficiency

The Cobb–Douglas form of stochastic frontier production function can be employed to obtain technical efficiency of different crops at farm level. Meeusen et al. [9] and Aigner et al. [10] firstly published this model. The important feature of this model is estimation of technical efficiency at farm level for different data types like cross-sectional and panel data by Battese and Coelli [11]. The disturbance term splits into a two-sided random error, in which one will check random effects beyond the control of firm, another is efficiency component. The R Frontier package 1.0 which is developed by Coelli et al. [12] estimate the ML estimates and individual farm’s technical efficiencies.

The Cobb–Douglas form of stochastic frontier model is given by,

$$Y_i = \beta_0 \times \prod_{j=1}^n X_{ij}^{\beta_j} \times e^{D_{ki} + (v-u)}$$

where

Y = Output in $q\text{ ha}^{-1}$ or ' ha^{-1}

X_i = Vector of inputs

β_j = Estimated coefficient of i th input

D_{ki} = Vector of k th dummy variable

v_i = Asymmetrical random term and assumed to be normally

distributed $[N(0, \sigma_v^2)]$

u_i = Farm-specific technical inefficiency assumed to follow
a half normal distribution

To obtain technical efficiency, the farm will have its own stochastic production frontier $f(X_i, \beta) \exp(v_i)$; a deterministic part $f(X_i, \beta)$ common to all farm and producer-specific part $\exp(v_i)$. The technical efficiency can be obtained as follows,

$$\text{TE}_i(\mu_i) = \frac{f(X_i, \beta) \exp(v_i - u_i)}{f(X_i, \beta) \exp(v_i)} = \exp(-u_i)$$

where

f = Cobb-Douglas form of the production function

$\text{TE}(\mu_i)$ = Technical efficiency of individual farm.

3 Result and Discussion

The technical efficiency in paddy was based on estimated parameters which are given in Table 1.

In 2001, fertiliser, seed and casual labour were the main inputs which when applied in increased amount improved the yield significantly. In that period, farmers were not using mechanisation which is clear from the coefficient which is zero. σ^2 value showed highly significant which means the model is stochastic rather than deterministic. γ value is almost near to 1 (0.97***), dominance of efficiency over random errors. This means, the factors like fertiliser, seed and casual labour were the major component of technology in 2001, and their utilisation management was responsible for 97% variation in the yield of paddy. It also indicates that the technology frontiers must be changed for further yield augmentation as the current technology was saturated and only 3% possibility was there for other factors to have any effects on yield.

In 2016, the scenario changed due to shift in the technology level as 15 years is a period long enough time for technology frontiers to change. From the table, it is evident that in 2016, mechanisation has already been adopted by Odisha farmers, and it has highly significant impact on yield; however, seed and fertiliser have now lost its significance in affecting yield. σ^2 value showed highly significant which means the model is stochastic rather than deterministic. γ value is almost near to is very low (0.35) and is non-significant which indicates the dominance of random factors

Table 1 ML estimates of stochastic frontier production function of paddy for the years 2001 and 2016, Odisha

Parameters	2001	2016
(Intercept)	3.92*** (0.31)	1.38*** (0.14)
Family labour (Man versus hours)	0.01 (0.00)	0.011 (0.009)
Casual labour (Man versus hours)	0.01** (0.00)	-0.002 (0.002)
Machine labour (Hours)	0.00 (0.00)	0.009*** (0.001)
Total fertiliser (Kg)	0.21*** (0.01)	0.49*** (0.019)
Seed (Kg)	0.28*** (0.06)	-0.005 (0.017)
σ^2	0.09*** (0.01)	0.013*** (0.003)
γ	0.97*** (0.01)	0.35 (0.28)
Log likelihood value	157.19	39
Mean efficiency	0.82	0.95

* is a significance level of 0.1 indicates a 10% risk of concluding that a difference exists when there is no actual difference. Similarly for ** and *** we have 5% and 1% risk of conclusion respectively.

not included in the model over input technical efficiency. This also indicates that the farmer has the possibility of increasing their current level of input efficiency to a higher level before any technological change is required. The current level of technology must be exploited for further augmentation of yield in paddy.

The similar comparative study on paddy crop was carried out in Punjab by Bhoi et al. [13] in which the technological frontiers, efficiency and maximum likelihood estimates were used.

4 Conclusion

The present study is based on stochastic frontier production approach for technical efficiency study in paddy production. MLE estimates of different parameter clarified the scenario of the study. The visible difference of adoption of mechanisation from 2001 to 2016 has great impact on production of paddy.

References

1. Ali M, Chaudhry MA (1990) Inter-regional farm efficiency in Pakistan's Punjab: a frontier production function study. *J Agric Econ* 41:62–74
2. Umesh KB, Bisaliah S (1991) Efficiency of groundnut production in Karnataka: frontier profit function approach. *Ind J Agric Econ* 46:20
3. Gaddi GM, Mundinasmani SM, Hiremath GK (2002) Resource use efficiency in groundnut production in Karnataka—an economic analysis. *Agric Sit Ind* 58:517–522
4. Kalirajan K P, Shand RT (1989) A generalized measure of technical efficiency. *Appl Econ* 21:25–34
5. Kalirajan KP, Obwona MB, Zhao S (1996) A decomposition of total factor productivity growth: the case of Chinese agricultural growth before and after reforms. *Amer J Agric Econ* 78:331–338
6. Shamugam KR, Venkataramani A (2006) Technical efficiency in agricultural production and its determinants: an exploratory study at the district level. *Madras Sch Econ* 10
7. Mruthyunjaya SK, Rajashekharappa MT, Pandey LM, Ramanarao SV, Narayan P (2005) Efficiency in Indian edible oilseed sector: analysis and implications. *Agric Econ Res Rev* 18:153–166
8. Suresh A, Reddy TK (2006) Resource-use efficiency of paddy cultivation in Peechi command area of Thrissur district of Kerala: an economic analysis. *Agric Econ Res Rev* 19:159–171
9. Meeusen W, Van den Broeck J (1997) Efficiency estimation from Cobb-Douglas production functions with composed error. *Int Econ Rev* 435–444
10. Aigner D, Lovell CK, Schmidt P (1997) Formulation and estimation of stochastic frontier production function models. *J Econ* 6:21–37
11. Battese GE, Coelli TJ (1991) Frontier production functions, technical efficiency and panel data: with application to paddy farmers in India. Department of Econometrics, University of New England, Australia
12. Coelli T, Henningsen A, Henningsen MA (2013) Package ‘frontier’
13. Bhoi PB, Singh J, Sachdeva J (2017) Farm specific technical efficiency in paddy production and its determinants in Punjab. *Ind J Econ Dev* 13(3):493–499

Improving Security Concerns of Mobile Cloud Computing Environment with Quantum Cryptographic Techniques



Sudhanshu Maurya , Kuntal Mukherjee , and R. Badlishah Ahmad

Abstract In the current scenario, mobile cloud computing (MCC) is termed as speedily developing field of IT. With the development of mobile phones and success of the Internet, computational resources have become cheaper, easily accessible, ubiquitous, distributed, and powerful tool for all types of organizations. Mobile cloud computing is a computational model in which services are offered on mobile phones in an on-demand fashion. Most of the service provider are concerned with privacy and security issues. In this endeavor, security concerns of MCC are discussed and proposed a new quantum cryptography (QC)-based encryption and decryption method. Proposed technique allows the users to store and process the user's data through strengthened cryptographic method.

Keywords Security · Mobile cloud computing · Quantum cryptography

1 Introduction

Amalgamation of Internet, mobile device, and cloud computing (CC) environment is referred as mobile cloud computing (MCC). Hence, the services offered by cloud for mobile devices are named as MCC [1]. It uses the technology of CC to deliver services as well as applications to mobile phones [2]. This amalgamation brings out advanced computational resources at the fingertips of mobile phone users and cloud providers [3]. The concept of the cloud computing which is offered by grid computing, application service provisioning, to makes it easier for its client to utilize

S. Maurya ()

School of Computing, Graphic Era Hill University, Bhimtal Campus, Dehradun, Uttarakhand, India

e-mail: dr.sm0302@gmail.com

S. Maurya · R. B. Ahmad

School of Computer and Communication Engineering, Universiti Malaysia Perlis (UniMAP), Arau, Malaysia

K. Mukherjee

Department of Computer Science, BIT Mesra, Ranchi, Jharkhand, India

the services offered by cloud environment [4, 5]. Google proposed cloud computing in the year of 2007 and dragged a prodigious attention from idea phase to real-life utilization phase in a very short span of time [6]. It extended the capacity of storage and computing, the ability of data service and system trading capacity of mobile devices. Google believes that the CC must provide clients data and data storing in secure, easily accessible and credible manner [7]. CC provides the facility to update application and services as per the requirement and concern of the users [8]. In simple terms, CC is an effervescent environment where user receives the resources as utility over the Internet [9]. It comes with many perks like efficiency, flexibility, scalability, etc. It uses “pay-per-use” policy for delivery of user desired services over the cloud environment [10]. Despite of these positives, it is severely affected by privacy and security issues [11]. This legacy of limitations is further carried forward by mobile cloud computing. It is because of scarcity that strong algorithms for resource security cannot be implemented with mobile phones [12]. There is a need of deploying well-structured job scheduling algorithms between cloud and mobile nodes to solve this issue [13]. Unfortunately, most of the users are not aware of these issues associated with cloud computing and mobile cloud computing [14].

This manuscript presents the security aspects of MCC and proposed novel encryption and decryption technique based on quantum cryptography. In literature review section, basics of security, cryptography, security requirements have been discussed. In next section, we propose a new cryptographic technique for encryption and decryption. Further, summarizing the paper with result analysis and conclusion.

2 Literature Review

Hidden script communiqué has been proficient for almost four thousand years ago. In Egypt, a secret script has been outlined around 1900 B.C [15]. Cryptography has been used ever since there was a need to hide a message. In the ancient times, people replaced the original words with digits or symbols [16]. Many other classical cryptographic methodologies were implemented in the yester decade. ISO 27001 has defined cloud computing security as—“safeguarding data’s confidentiality, availability as well as its integrity.” Authenticity, non-repudiation, accountability and reliability. Security in cloud computing is a new and emerging research sector as a subdiscipline of network security, computer security and information security.

It comprises of technologies, policies, data protection and such related cloud infrastructure. In another sense, CC has being associated to large number of businesses inventively. Productivity of these varied methods leads to privacy and security risks [17–19]. Security is referred to as an arrangement that decides for the privilege of accessing and altering information.

Security in cloud is divided into two broad visions: Making of a security strategy and then checking for the successful accomplishment of the security goal as per that strategy by code execution. The strategy differentiates sharply that who has the permission to carry out what operation and on what data set through validation and

authorizations. After adaptation of cloud services client has not confident about the integrity, recovery of data, privacy and security of data [20]. A protected framework is a structure where information cannot be seen or changed by a customer without appropriate approval being explicitly endorsed by the security technique [21].

2.1 User's Security Requirements

Security in cloud processing has various implications. For instance: having a protected cloud from a supplier perspective does not imply that it is secure for clients point. Furthermore, unfortunately, greatest clients deliberate that with client username and a secret key to get to their record is sufficient protected [22].

Confidentiality: It alludes to the protection information undisclosed. It is upheld by specialized instruments like encryption and control on access and legitimate backings too [20]. It gives an answer for some beneath referenced treats:

Unsecured Cloud Service User Access: As we know that most of the services and resources delivered through a remote connection. There is always the risk of fraud, phishing and others. Username, password and other credentials are often reused, which may increase the impact of these attacks [18, 23].

Data leakage: There are two prospects in this, first some organizations might store their data at servers of another nation. Second, even after deletion by the client, data may be remains on the provider's server [24].

Availability: It alludes to utilize the framework at whatever point required. It is bolstered by acceptable design and limit working by the cloud supplier, notwithstanding that all around characterized arrangements and terms of the understanding are likewise required [20]. Approximate all of the cloud service providers' offer availability for their servers up to 99.99% [25].

Accountability: It maps the activities in the framework to responsible gatherings and bolstered by get to control, verification and vigorous personality notwithstanding that the capacity to record associations and critically review the tracks and record pernicious ones [20].

2.2 Provider's Security Requirements

The criteria of security may be minimal distinctive when contrasted with clients: At one side, it is tied in with picking up the client's belief, with a decent notoriety in the cloud advertise. On next side, cloud suppliers dropping their command over the information they are developing. Keep information secured on own servers, exchanging

Table 1 Analysis of security preventing methods

Category	Solution	Users			Providers	
		Security				
		Confidentiality	Availability	Accountability		
Formal approaches	Clear SLA	Partially	Yes	Yes	Partially	
	Data protection approaches/policies	Partially	Partially	Yes	Partially	
Managerial approaches	Data life cycle	Yes	Yes	Partially	Yes	
	Virtual machine image management system	Partially	Does not impact	Yes	Yes	
	Client based privacy manager	Yes	Partially	Yes	Partially	

of information to other, reinforcement of their whole architecture or erasing the information. Every one of these concerns must be settled on according to the decision of the suppliers and execution of it must be leveled out. A large portion of the businesses and analyst use cryptographic procedure for information security. Encryption is a very notable method for information security, comprehensively named secrecy, legitimacy and information protection in a cloud domain with the assistance of keys [26]. At execution part information encryption is finished by the encryption key and information is decoded by the utilization of decryption key.

In Table 1, examination of few security forestalling methods like Clear SLA [27, 28], data protection approaches/policies [29, 30], data life cycle [31], virtual machine image management system [30, 32] and client-based privacy manager [33] for all stakeholders of the cloud has been discussed.

Data encryption method is effectively performed when information/data are little in dimensions, yet it may get quite a while the information is huge. This method in distributed computing condition can influence its start to finish execution. Some of the time it is difficult to send and actualize in the cloud [34]. In this manuscript, a new cryptographic technique is being proposed which is based on quantum mechanics. Quantum mechanics was originally developed as a theory to describe the behaviors of microscopic substances like electrons or atoms [35, 36].

Ambiguity in the theory of quantum mechanics has directed toward a new paradigm referred as quantum cryptography (QC) [37]. It was proposed by Brennet and Brassard, based on the no-cloning theorem in the 1970s [38], it means a qubit cannot be copied or manipulated without changing its actual stage [37]. QC explores the fundamentals of quantum physics where it is impossible to quantify a state of a random polarized photon congaing information with zero disturbance [39]. It gives us perfectly secure data transfer. Various opportunities and market trends of mobile cloud computing have been discussed in the research work of [40] and also give a roadmap for security measures.

2.3 Proposed Quantum Encryption and Decryption Algorithm

The criteria encryption has always been depicted as better resolution to secure data. As per Sosinsky, symmetric cryptosystem is efficient for cloud environment. Cloud being handling bulks of data is the reason behind the introduction of symmetric cryptosystem based on quantum cryptography in this work [41].

A qubit may take binary data simultaneously that is zero and one. In Dirac representation, it is represented as:

$$|\Psi\rangle \geq \alpha|0\rangle + \beta|1\rangle$$

where: $|0\rangle \geq \begin{bmatrix} 1 \\ 0 \end{bmatrix}$ and $|1\rangle \geq \begin{bmatrix} 0 \\ 1 \end{bmatrix}$ and α, β are composite quantities having the credibility as binary numbers that is 0 and 1 discretely [42]. According to Dirac equation as per the free particle solution, the state $\begin{bmatrix} 1 \\ 0 \end{bmatrix}$, while ups to $\begin{bmatrix} 0 \\ 1 \end{bmatrix}$ state that denotes the roll down of subatomic elements. Finally, after merging both states, we get a table like structure of the matrix $D = \begin{bmatrix} 1 & 0 \\ 0 & 1 \end{bmatrix}$.

We acknowledge zero as minus one and get $D_w = \begin{bmatrix} 1 & -1 \\ -1 & 1 \end{bmatrix}$.

Here, w is served as dimensions of the matrix in $2w$ form. For higher value of D_w , $D = D \otimes D$ is needed.

The example of the matrix of size 4×4 is given in Fig. 1.

Generate a random natural number and replace “-1” by that number. Hence, obtained matrix D_w is considered as the key matrix for encryption and decryption operations. Algorithm 1 is responsible for encryption and Algorithm 2 for the decryption.

Fig. 1 Matrix $D_{4 \times 4}$, where -1 is replaceable

$$D_{4 \times 4} = D_{2 \times 2} \otimes D_{2 \times 2}$$

$$D_{4 \times 4} = \begin{bmatrix} 1 & -1 & -1 & 1 \\ -1 & 1 & 1 & -1 \\ -1 & 1 & 1 & -1 \\ 1 & -1 & -1 & 1 \end{bmatrix}$$

ALGORITHM 1: For Encrypting Message (Plain Text) into Cipher Text

Procedure Encryption (M) [Where M is Message]

Step 1. Reading Plaintext M and represent it into matrix format M.

Step 2. Obtain D_w (as mentioned above) in such a way that its determinant is non zero.

Step 3. [Obtain Determinate of D_w]

$$\eta \leftarrow |D_w|$$

Step 4. [Encryption of Plain Text M into CT]

$$CT \leftarrow (D_w \times M) \times \eta$$

Where CT is cipher text and D_w is proposed matrix.

End
ALGORITHM 2: For Decrypting Cipher Text into Message (Plain Text)

Procedure Decryption (CT) [Here CT is Cipher Text]

Step 1. Read Cipher Text CT.

Step 2. [Decrypt the Cipher Text]

$$M \leftarrow \frac{D_w^{-1} \times CT}{\eta}$$

Where D_w^{-1} is inverse of proposed Matrix D_w and η is determinant of D_w

Step 3. [Display the Message]

Print plain text M

End

3 Experimental Setup and Result Analysis

Overall proposed algorithms are implemented in a cloud environment consisting of a master-slave node system. Scheduling of jobs to different slaves is the work of master node. Master Node is Acer Swift 5 Corei7-1065G7 with 16 GB RAM and SSD is 512 GB and slave nodes are ACER Aspire 3 Core i3 processor with

4 GB of RAM. A fast LAN is used for data communication between the nodes. We have compared our proposed algorithm with the famous Hill Cipher algorithm. The comparative observations of time taken, in encrypting and decrypting, are shown in below figures. Figure 2 depicts the results for message length of 2 while Fig. 3 shows the results for message length of 4.

Time complexity in encryption using Algorithm 1 is $O(n^2)$ whereas talking about the case decryption using Algorithm 2 is $O(n^3)$. In addition to the above results, the nature of Dirac matrices is combinatorial. On the analysis of all results shown in the below figures, some observation made are as follows:

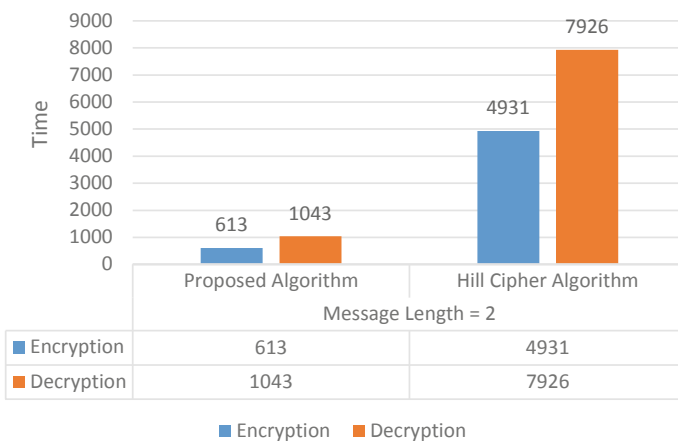


Fig. 2 Encryption and decryption time in millisecond (message length 2)

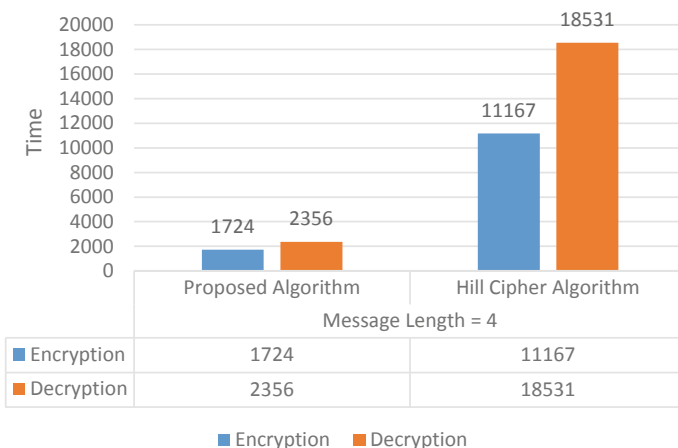


Fig. 3 Encryption and decryption time in millisecond (message length 4)

1. The time taken in encryption and decryption differ approximately linearly with respect to the length of message.
2. Time taken in encryption is lower than that taken in decryption.

4 Conclusion

In this endeavor, security and privacy parameters regarding cloud computing have been discussed. Symmetric key cryptography is used in cloud for securing data. The techniques presently in use are not sufficient so a new technique has been presented in this paper. A comparative study of the proposed Algorithm with Hill Cipher algorithm is done. The proposed algorithm is better at the processing time aspect of encryption and decryption.

References

1. Sanaei Z, Abolfazli S, Gani A, Khokhar RH (2012) Tripod of requirements in horizontal heterogeneous mobile cloud computing. In: International conference on computing, information systems and communications, Singapore, pp 217–222
2. Liu F, Shu P, Jin H, Ding L, Yu J, Niu D, Li B (2013) Gearing resource-poor mobile devices with powerful clouds: architecture, challenges, and applications. IEEE Wirel Commun Mag Special Issue Mobile Cloud Comput 20(3):14–22
3. Khan AR, Othman M, Madani SA, Khan SU (2014) Survey of mobile cloud computing application models. IEEE Commun Surv Tut 16(1):393–413
4. Ahmed M, Sina AAI, Chowdhury R, Ahmed M, Rafiee MMH (2012) An advanced survey on cloud computing and state-of-the-art research issues. Int J Comput Sci Issues 9(1):201–207
5. Pearson S (2012) Privacy, security and trust in cloud computing. HP Laboratories, HPL-2012-80R1
6. Li J, Liu JZ (2010) Influence of cloud computing on educational informationization of china rural areas. In: The proceedings of information science and engineering conference, pp 281–283
7. Meng K (2008) A walk in the cloud: uncovering cloud computing. China Netw World 12–14
8. Mell P, Grance T (2010) The NIST definition of cloud computing. Technical Report. Available Online at <http://www.blogjava.net/zamber/archive>
9. Furht B, Escalante A (2010) Handbook of cloud computing. Springer, New York
10. Maurya S, Mukherjee K (2015) A literature survey on mobile cloud computing. Int J Appl Eng Res 10(79):329–334
11. Kuyoro SO, Ibikunie F, Awodele O (2011) Cloud computing security issues and challenges. Int J Comput Netw (IJCN) 3(5):247–255
12. Malik S, Chaturvedi MM (2013) Privacy and security in mobile cloud computing: review. Int J Comput Appl 80(11):20–26
13. Popovic K, Hocenski Z (2010) Cloud computing security issues and challenges. In: Proceedings of the 33rd international convention MIPRO, pp 24–28
14. Chen D, Zhao H (2012) Data security and privacy protection issues in cloud computing. In: International conference on computer science and electronic engineering (ICCSSEE), pp 23–25
15. Kahn D (1996) The code breakers: the comprehensive history of secret communications from ancient times to the internet. Enigmas Books, New York
16. Pfleeger CP, Pfleeger SL (2003) Security in computing. Prentice Hall, USA

17. Wang L, Laszewski GV, Younge A, He X, Kunze M, Tao J, Fu C (2010) Cloud computing: a perspective study. *New Gener Comput* 28(2):137–146
18. Robinson N, Valeri L, Cave J, Starkey T, Graux H, Creese S, Hopkins P (2010) The cloud: understanding the security, privacy and trust challenges. TR-933-EC, prepared for unit F.5, directorate-general information society and media, European Commission
19. Kadam K, Paikrao R, Pawar A (2013) Survey on cloud computing security. *Int J Emerg Technol Adv Eng* 3(12):239–249
20. Friedman AA, West DM (2010) Privacy and security in cloud computing. *Issues Technol Innov Center Technol Innov Brookings* 3:1–13
21. Maurya S, Mukherjee K (2016) A novel method for secured cloud-health-care-system. *Int J Control Theory Appl* 9(19):9291–9303
22. Meryeme A, Hanan EB (2015) Security, privacy and trust in cloud computing: a comparative study. In: International conference on cloud technologies and applications (CloudTech), pp pp 23–30
23. Alvi FA, Choudary BS, Jaferry N, Pathan E (2012) A review on cloud computing security issues and challenges. In: International conference on mobility for life, Chiang Rai, Thailand
24. Kangchan L (2012) Security threats in cloud computing environments. *Int J Secur Appl* 6(4):25–32
25. Habib SM, Ries S, Muhlhauser M (2010) Cloud computing landscape and research challenges regarding trust and reputation. In: IEEE 7th international conference on ubiquitous intelligence and computing and 7th international conference on autonomic and trusted computing, Xian, Shaanxi, China, pp 410–415
26. Eloff JHP, Eloff MM, Dlamini MT, Zielinski MP (2009) Internet of people, things and services—the convergence of security, trust and privacy. In: 3rd companionable workshop—IoPTS, Novotel Brussels—Brussels, pp 1–8
27. Barron C, Yu H, Zhan J (2013) Cloud computing security case studies and research. *World Congr Eng*, London, U.K., II, pp 1287–1291
28. Arora P, Chaudhry R, Satinder WE, Ahuja P (2012) Cloud computing security issues in infrastructure as a service. *Int J Adv Res Comput Sci Softw Eng* 2(1):1–7
29. Srinivasamurthy S, Liu DQ (2010) Survey on cloud computing security technical report. Indiana University—Purdue University, Fort Wayne, Indiana. Available online at: http://salsahpc.org/CloudCom2010/Poster/cloudcom2010_submission_67.pdf
30. Khan AW, Khan SU, Ilyasand M, Azeem MI (2012) A literature survey on data privacy/protection issues and challenges in cloud computing. *IOSR J Comput Eng* 1(3):28–36
31. Pearson S, Shen Y, Mowbray M (2009) A privacy manager for cloud computing. In: IEEE international conference on cloud computing (CloudCom 2009), lecture notes in computer science, Springer book series cloud computing, vol 5931, pp 99–106
32. Pearson S, Charlesworth A (2009) Accountability as a way forward for privacy protection in the cloud. In: IEEE international conference on cloud computing (CloudCom 2009), lecture notes in computer science, Springer book series Cloud Computing, vol 5931, pp 131–144
33. Miranda M, Pearson S (2009) A client-based privacy manger for cloud computing. In: Proceedings by ACM digital library of fourth international ICST conference on communication system software and middleware—COMSWARE’09, Dublin, Ireland, Article No. 5
34. Choubey S, Namdeo MK (2015) Study of data security and privacy preserving solutions in cloud computing. In: International conference on green computing and internet of things (ICGCloT-2015), pp 1101–1106
35. Dirac PAM (1978) The principles of quantum mechanics, 4th edn. Oxford University Press, 1958. Reprinted-1978, Oxford, UK
36. Landau LD, Lifshitz EM (1987) Quantum mechanics (nonrelativistic theory), 3rd edn. Pergamon Press, New York, First print-1977. Reprinted-1987
37. Falahati A, Meshgi H (2009) Using quantum cryptography for securing wireless LAN networks. In: IEEE international conferences on signal processing system, Singapore, pp 698–701
38. Bennett C, Brassard G (2014) Quantum cryptography: public—key distribution and coin tossing. In: IEEE international conference on computer systems and signal processing,

- Bengaluru, India, pp 175–179, 1984. Reprint published by Elsevier J Theor Comput Sci 560(Part 1):7–11
- 39. Huang X, Wijesekera S, Sharma D (2009) Quantum cryptography for wireless network communications. In: IEEE 4th international symposium on wireless pervasive computing, pp 01–05
 - 40. Chang RS, Gao J, Gruhn V, He J, Roussos G, Tsai WT (2013) Mobile cloud computing research—issues, challenges and needs. In: IEEE seventh international symposium on service-oriented system engineering, pp 442–453
 - 41. Sosinsky B (2011) Cloud computing bible, 1st edn. Wiley India Pvt. Ltd., India, pp 6–42
 - 42. Djellab R, Benmohammed M (2012) Securing encryption key distribution in WLAN via QKD. In: IEEE international conference on cyber-enabled distributed computing and knowledge discover, pp 160–165

Author Index

A

- Aarthi, R., 199
Adhikary, Tathagata, 11
Afroj, Md. Asif, 143
Agrawal, Rajeev, 521
Agrawal, Sunil, 465
Agrawal, Vanita, 839
Ahmad, R. Badlishah, 1141
Ahmed, Tanvir, 89
Al Miraz, Mehedhi, 143
Angadi, Sachin, 155
Ansari, Sahil, 831
Anwar Hussain, Md., 1017
Arundhati, Priya, 753

B

- Babu, Korra Sathy, 177
Baishnab, Krishna Lal, 899, 929
Bandyopadhyay, Sivaji, 673, 1039
Banerjee, Abhik, 541, 595, 617
Banik, Santanu, 241
Barman, Barnali, 909
Barman, Rahul, 653
Baro, Utpal Chandra, 839
Baruah, Bikash, 1051
Baruah, Manali, 831
Baruah, Smriti, 743
Basak, Piyali, 11
Begum, Afruza, 1017
Bharti, Manisha, 295, 337
Bharti, Sneha, 295, 337
Bhattacharjee, Utpal, 99, 513
Bhatarai, Sagar, 965
Bhavani, Pilla Devi, 231
Bhavani, R., 419
Bhoi, Priyabrata, 1135

- Bilgundi, Srishail K., 1003
Biswas, Saroj Kr., 653, 673, 1039
Borah, Amlan Deep, 919
Borah, Janmoni, 731
Borah, Kunal, 329
Borah, Samarjeet, 1135
Borah, Shekhar Suman, 285
Bora, Joyatri, 485, 731, 743, 919
Borkakoty, Hsuvas, 387
Boruah, Arpita Nath, 1039
Bulo, Yaka, 221
Buragohain, Arunav, 831

C

- Chaitan, K., 973
Chakraborty, Ashis, 253
Chakraborty, Swarnendu K., 697
Chandran, Saravanan, 1073, 1083
Chanu, Thingbaijam Rajkumari, 21
Chatterjee, Saibal, 329
Chhetri, Rupa, 839
Chintesh, I., 575

D

- Daimari, Raja Jwbhasa, 853
Dan, Sanket, 63, 241, 253
Das, Amitesh, 707
Das, Dolly, 673
Das, Santos Kumar, 177, 187, 211
Das, T. D., 965
Datta, Brajagopal, 813
Datta, Manishankar, 607
Datta, Shrayasi, 885
Debela, Tamiru, 863, 875
Deka, Aniruddha, 853

Deka, Bidyut, 1105
 Deshmukh, Prashant, 211
 Deshmukh, Tanmay, 357
 Dev, Chandana, 387
 Devi, Kshetrimayum Linthoinganbi, 731
 Devi, Swagata, 899
 Dinakar, D., 957
 Doso, Oying, 265
 Dutta, Aradhana, 1105
 Dutta, Jiten Chandra, 377, 429
 Dutta, Manash Pratim, 1051
 Dutta, P. K., 565
 Dutta, Subrata, 253

G

Gajula, Rohith Sai Kumar, 1123
 Ganguly, Amrita, 387
 Gao, Sarsing, 265
 Gautam, 813
 Gautam, Ritik, 1073
 Ghole, Mukund Subhash, 555
 Ghosh, Chim moy, 885
 Ghosh, Mourina, 285
 Ghosh, Pritam, 63, 241, 253
 Gogoi, Mriganka, 565
 Goswami, Joyeeta, 77
 Guchhait, Pabitra Kumar, 541, 595
 Guha, Koushik, 899
 Gupta, Lalita, 167

H

Hajra, Dilip Kumar, 241
 Halder, B., 439
 Hampannavar, Santoshkumar, 805
 Haripriya, B., 775
 Hasibuzzaman, Md., 143
 Hazarika, Kabyashree, 429
 Hijam, Somokanta, 21
 Himabindu, N., 805
 Hormese, Jose, 1073
 Husainee, Kauser, 357
 Hussain, Israfil, 839
 Hussain, Md. Anwar, 919
 Hussain, Sarfraz, 475

I

Ieswaria, S., 419

J

Jamwal, Anbesh, 521

Jangam, Rupa Sree, 1123
 Jena, Sisir Kumar, 641
 Joshi, Manoj, 133
 Jyothsana, A., 307

K

Kabir, Md. Monirul, 89
 Karimulla, Shaik, 347
 Karthika, N. J., 1083
 Kashyap, Nitesh, 1115
 Kasturi, Bhanu Ravindranath, 1123
 Kaur, Baljit, 295, 337, 367
 Kaushik, Rajasve, 585, 607
 Keshwani, Gaurav, 377, 429
 Kishore, Putha, 957
 Koppala, Neelima, 1123
 Kri, Rushanti, 983
 Kumari, Pallavi, 407
 Kumar, Piyush, 485
 Kumar, Prashant, 585, 607
 Kumar, Rajesh, 475
 Kumar, Raman, 585, 607
 Kumar, Rishi Kant, 585, 607
 Kumar, Varun, 1093
 Kumar, Vickey, 367
 Kumar, Vinod, 1
 Kunamalla, Sarangam, 395
 Kuppachi, Sree Lochan Kanthi Kumar, 1123

L

Laskar, Naushad Manzoor, 899
 Latif, Abdul, 839
 Likith Kumar, M. V., 1003

M

Machavaram, Venkata Raghunadh, 275
 Mahanta, Pinakeswar, 685
 Maity, Santanu, 743
 Majumder, Suman, 885
 Malemnganbi, Rajkumari, 37
 Manasani, Swapna, 805
 Mandal, Satyendra Nath, 63, 241, 253, 885
 Mandi, Rajashekhar P., 805
 Marchang, Ningrinla, 627
 Maurya, Sudhanshu, 1141
 Maurya, Sudhir, 617
 Meghwal, Virendra Kumar, 507
 Meher, Preetisudha, 49
 Meitei, Moirangthem Goldie, 627
 Meitei, Sorokhaibam Nilakanta, 329
 Miah, Md. Aman, 143

Mia, Nasim, 89
 Mishra, Debahuti, 1135
 Mishra, Madhusudhan, 99, 485
 Mishra, Shashidhar, 187
 Mishra, Subhadra, 1135
 Mitra, A., 439
 Mittal, Namita, 507
 Modha, Hardik P., 1061
 Momocha, M. S., 973
 Mudang, Tagiya, 109
 Mukherjee, Kaushal, 707
 Mukherjee, Kaushik, 63, 241, 253
 Mukherjee, Kuntal, 1141
 Murugananthan, V., 453
 Mustafi, Subhranil, 63, 241, 253

N
 Nandan, Durgesh, 575
 Nandhan, Durgesh, 231
 Naskar, Syamal, 241
 Nath, Sourav, 899
 Neroula, Sujan, 533
 Ningthoujam, Sanjit, 697
 Nistala, Bheema Rao, 275, 395, 495, 823
 Nongmeikapam, Kishorjit, 775
 Nyodu, Karter, 663

O
 Obulapathi, L., 957
 Okramcha, Maxon, 21

P
 Padmavathi, Manchineellu, 957
 Paily, Roy, 949
 Panigrahi, Rakhee, 719
 Pani, Santosh Kumar, 753
 Panwar, Maj Sunil Kumar, 685
 Parashar, Shivam, 485
 Patel, Deep V., 1061
 Patel, Rajendra V., 1061
 Pathak, Uddipta, 831
 Patidar, Akshay, 521
 Patjoshi, Rajesh Kumar, 719
 Patnaik, Abinash, 485
 Patra, Aswini K., 485
 Patra, Sarat Kumar, 1093
 Patra, Swarnajyoti, 909
 Paul, Bikram, 685
 Phukan, Hillol, 863, 875
 Pradeepa, H., 1003
 Pradhan, Adarsh, 831

Prakash, Sai, 495
 Preethi, V., 231
 Priyadarsini, Lima, 211
 Priya, R., 419
 Pudur, Rajen, 407
 Purkayastha, Biswajit, 653

R
 Rajak, Mrinal Kanti, 407
 Raju, A. B., 155
 Raman, Ashish, 1115
 Raman, Rahul, 317
 Ranjan, Ashish, 133
 Ranjan, Ravi, 1115
 Rashed, Md. Jahidul Islam, 143
 Raut, Vaishnavi, 1029
 Ravi, Mancharla, 221
 Ray, Anjan Kumar, 555
 Ray, Kailash Chandra, 939
 Ray, Sangram, 885
 Roy, Kunal, 63, 241, 253
 Roy, O. P., 1
 Roy, Sahadev, 707
 Roy, Subhojit, 241
 Roy, Suvadip, 541

S
 Saha, Ashim, 77
 Saha, T., 439
 Sahu, Partha Pratim, 1105
 Saifullah, Mohammad Khalid, 89
 Sakthivel, G., 453
 Sakuru, K. L. V., 495
 Samal, K. Krishna Rani, 177
 Sambyo, Koj, 983
 Santra, Gour Hari, 1135
 Saring, Yang, 783
 Sarkar, Paramita, 929
 Sarkar, Santanu, 187
 Sarkar, Sunita, 653, 673, 1039
 Sarker, Avijit, 143
 Sasmal, Sajal, 783
 Satyanarayana, V., 575
 Sharma, Arpan, 485
 Sharma, Arvind, 965
 Sharma, Monica, 521
 Sharma, Santanu, 533
 Sharma, Suruchi, 295, 337, 367
 Shimray, Benjamin A., 37
 Shivani, 585
 Shibu, M., 1003

Shopon, Md, [763](#)
 Shufian, Abu, [143](#)
 Shukla, Swati, [993](#)
 Sindhuja, R., [119](#)
 Singh, Anil Kumar, [109](#)
 Singh, Ankur, [285](#)
 Singh, Arvind Kumar, [99](#), [513](#)
 Singh, Girdhari, [507](#)
 Singh, Gurpartap, [465](#)
 Singh, Indrasen, [1029](#)
 Singh, Jiwanjot, [863](#), [875](#)
 Singh, Karam Bharat, [133](#)
 Singh, Lukram Dhanachandra, [49](#)
 Singh, Mangal, [1093](#)
 Singh, Poonam, [1093](#)
 Singh, Renu, [99](#), [485](#), [513](#)
 Singh, Vivek, [939](#)
 Sinha, Khushboo, [27](#)
 Sinha, Rohan, [317](#)
 Sivakumar, D., [199](#)
 Sivaraman, J., [307](#), [347](#)
 Sohi, B. S., [465](#)
 Soni, Badal, [653](#)
 Soni, Jatin M., [1061](#)
 Srinivasan, S., [119](#)
 Srivastava, Harshit, [187](#)
 Suresh, Yellasiri, [155](#)
 Swain, Deepak Kumar, [1135](#)

T

Thakur, Hiranya Ranjan, [377](#), [429](#)
 Thoudam, Archana, [595](#)
 Tilak Babu, S. B. G., [575](#)
 Tiwari, Praveen, [685](#)
 Tripathy, S. K., [929](#)
 Tripathy, Somanath, [939](#)
 Trivedi, Gaurav, [475](#), [685](#), [993](#)
 Trivedi, Y. N., [27](#)
 Tumma, Sunil Kumar, [823](#)

V

Valluvan, M., [453](#)
 Verma, Abhishek, [295](#), [337](#)
 Vijaya, Samudra, [663](#)

Y

Yadav, Menka, [791](#)
 Yadav, Vimal Kumar Singh, [949](#)
 Yaragatti, Udaykumar R., [155](#)

Z

Zimik, Mayanmi, [485](#)